Sādhanā (2023)48:206
https://doi.org/10.1007/s12046-023-02249-2

Secure and privacy in healthcare data using quaternion based neural network and encoder-elliptic curve deep neural network with blockchain on the cloud environment

P SUGANTHI[1,*] and R KAVITHA[2]

[1]Department of CSBS, Thiagarajar College of Engineering, Madurai, India
[2]Department of IT, Velammal College of Engineering and Technology, Madurai, India
e-mail: suga.pathma@gmail.com

MS received 13 July 2022; revised 8 June 2023; accepted 8 July 2023

Abstract. The security and privacy of healthcare data are crucial aspects within the healthcare industry, as accurate diagnoses rely on medical professionals accessing patient healthcare data. Similarly, patients often require access to their data. However, ensuring that sensitive health data is shared securely while prioritizing privacy is essential. This paper proposes an innovative solution called the quaternion based neural network, Advanced Data Security Architecture in Healthcare Environment (ADSAH), which combines Elliptical curve cryptography (ECC) with a blockchain mechanism and a Deep Fuzzy Based Neural Network (DFBNN) to safeguard cloud-stored health data. The proposed approach begins by encoding the input medical data using an encoder and then encrypting the encoded data using ECC techniques. The secret key for encrypting the data is securely stored within a blockchain framework. The key is divided into blocks to enhance security, and the SHA algorithm is employed to identify key events within these blocks. These key events are subsequently stored in a cloud storage system. A modified genetic algorithm is utilized to generate the encryption and decryption key. This algorithm is explicitly tailored to secure healthcare data. Authorized patients or physicians can access medical data using the secret key to decrypt and retrieve the necessary information. The performance of the proposed network is evaluated by considering factors such as time and cost and is compared against existing studies. The evaluation demonstrates notable improvements, including a reduction in the time required for the encryption and decryption process, as well as a decrease in transaction and execution costs when compared to previous research. By incorporating ECC with a blockchain mechanism and DNN, the ADSAH approach offers an advanced solution for ensuring the security and privacy of cloud-stored health data. It provides robust encryption and facilitates efficient and cost-effective access to authorized individuals while safeguarding sensitive health information.

Keywords. Healthcare data; security; deep neural network; improved quaternion based neural network; blockchain mechanism; elliptic curve cryptography.

1. Introduction

The healthcare industry is of paramount importance as it delivers vital medical services and continually strives to enhance patient outcomes through technological advancements, innovative treatments, and public health initiatives [1]. Despite these advancements, ensuring the security and privacy of patient data remains a pressing concern within the healthcare sector. While healthcare professionals require access to patient healthcare data for accurate diagnoses and effective treatments, it is equally vital to prioritize the secure and private sharing of sensitive health information [2]. Protecting patient's privacy is imperative to maintain trust and confidentiality in healthcare interactions. To address these concerns, robust measures must be implemented to safeguard patient data against unauthorized access, breaches, and misuse. Achieving a balance between data accessibility and privacy preservation is paramount in the healthcare industry, as it allows for effective healthcare delivery while respecting patient rights [3].

Therefore, comprehensive and reliable solutions are needed to establish stringent security measures and ensure the utmost privacy protection in the healthcare data ecosystem. Maintaining patient data privacy has become increasingly challenging with the digitization of healthcare records and the widespread use of cloud storage systems [4, 5]. Existing techniques for securing healthcare data often need to be revised to address privacy concerns

*For correspondence
Published online: 23 September 2023

adequately [6]. These techniques may need more robust encryption mechanisms, efficient access controls, and secure storage methods [7, 8]. As a result, healthcare organizations face the risk of data breaches, unauthorized access, and misuse of sensitive patient information [9]. This paper proposes a novel solution called the Advanced Data Security Architecture in Healthcare Environment (ADSAH) to address these challenges and enhance the security and privacy of cloud- stored health data. ADSAH combines Elliptical curve cryptography (ECC) [10] with a blockchain mechanism and deep Fuzzy Based Neural Network (DFBNN) [11] to provide a comprehensive and practical approach to safeguarding patient data [12, 13]. The ADSAH technique presents numerous advantages in overcoming the shortcomings of current privacy protection methods. It leverages advanced encryption techniques, specifically Elliptical curve cryptography (ECC), to establish a robust layer of data security and ensure the utmost confidentiality of sensitive information. Through integrating a blockchain framework, ADSAH provides a secure storage mechanism for encryption keys, enhancing critical management practices and mitigating the risk of unauthorized access. Additionally, ADSAH integrates a modified genetic algorithm [14, 15], enabling efficient encryption and decryption processes that significantly reduce time requirements and enhance overall system performance. This combination of cutting-edge encryption, secure key storage, and optimized algorithms makes ADSAH an effective solution for bolstering data privacy in healthcare settings. Through integrating ECC (blockchain) and DNN, the proposed ADSAH enables secure access and retrieval of medical data for authorized individuals like patients and physicians. This integration ensures efficient and controlled data sharing while upholding patient privacy. By addressing the limitations of existing methods, ADSAH provides a comprehensive and advanced solution to safeguard patient data in cloud-based healthcare environments. The incorporation of ECC strengthens data security, while the utilization of DNN-based DFBNN processes the encrypted data using deep learning capabilities and fuzzy logic to handle uncertainty and imprecision. It performs analysis and decision-making tasks on the encrypted data while preserving its confidentiality. By utilizing the proposed ADSAH, healthcare organizations can protect patient data effectively while facilitating seamless and protected access for authorized users.

The main contributions of the paper are as follows.

- Introducing a ground-breaking approach called the Advanced Data Security Architecture in Healthcare Environment (ADSAH) that addresses the secure handling of patient data within healthcare settings.
- The ADSAH technique incorporates Elliptical Curve Cryptography (ECC) with a blockchain mechanism, Deep Fuzzy Based Neural Network (DFBNN), to ensure healthcare data's seamless and efficient transfer.
- Within the Blockchain mechanism, the keys are converted into blocks, and subsequently, the SHA algorithm is employed to recognize and process them.

The experiments are conducted to demonstrate the effectiveness of the proposed technique.

1.1 *Blockchain*

Recent growth of blockchain technology assists in solving the interoperability challenges in healthcare and plays a major role in maintaining patient's record at the centre of ecosystem. Thereby, blockchain improves the privacy, security and interoperability. Generally, blockchain can be used in sharing and accessing the medical record of patients and also in remote monitoring. Blockchain is used in medical data management system which permits patients to maintain ownership over the available records.

The main advantages of using the blockchain are

- Single point failure and performance bottlenecks are avoided.
- Patients may view and manage their data.
- The blockchain guarantees the consistency, precision, simplicity, completeness, and timeliness of medical data history.
- The patient network participants may see every step of the blockchain procedure.
- The data insertions are also unchangeable. Unauthorised alterations have been discovered.

1.2 *Privacy preservation*

The major focus is on how to completely manage privacy problems and forecast efficacy, especially when it comes to sensitive medical data kept in third parties. As a result, in order to prevent the loss of privacy associated with medical data, data mining techniques for privacy preservation should be developed. Accordingly, Machine Learning (ML) algorithms possess innate abilities of effective learning. Such abilities could be employed in blockchain for enhancing the smartness of the chain. This integration could also be valuable in enhancing the security of blockchain distributed ledger. With the ability in predicting the system behavior, using various ML algorithms optimizes blockchain mechanisms. No privacy preservation approach currently in use provides the necessary privacy protection. It is quite effective, practical and useful. The capacity of blockchain to provide adequate privacy protection is represented by security analysis. The objective of the study involves:

1. To use improved quaternion based neural network cryptography, elliptical curve cryptography to generate

keys, encrypt data, and decode data in order to protect shared data.
2. To implement blockchain technology, which converts keys into blocks and then recognises them using the ADSHA algorithm.
3. To put the encrypted data in a cloud storage system and provide authorised patients and clinicians access to it.

1.3 *Novelty of the proposed system*

Proposed framework permits the clinicians for transferring their data in encrypted format to cloud which hosts the corresponding network. A neural network is fed with input (plain text) and neurally based pseudo-random numbers (in vector form). Results of process include weights and cipher text in hidden-layers. In accordance with the changes in weight based on the pseudo-random number, cipher text alters in accordance with it. Hence, this permits the model to be highly secured. The study proposes Modified Genetic Algorithm, wherein, based on fitness-function, keys are generated and these keys are utilized for encryption. Such encrypted predictions could be sent to secret-key owner who could decrypt them. The proposed system is highly secured as the training-input adjusts its weight in accordance with the trained data.

As the model quickly and easily provides overall output, plain text encryption is accomplished easily for producing cipher text in less time with the updated key-generation approach. With the use of several nodes and hidden layers, it enhances the model complexity, thereby affording high cryptosystem security. The keys generated with Modified Genetic Algorithm are integrated with the hidden weights. Thus, even when an intruder attempts to hack any data, it is not possible to decrypt it. Owner of the data could possess confidence upon their data as it is safely stored in cloud. The proposed system seems to exist as a potential-source for the public-key cryptographic approaches which does not rely on the number theoretic-operations and possess memory and time complexities. The outcomes reveal the better performance of the proposed system while comparison with conventional studies in accordance with security. In blockchain, third-parties are not needed for verifying the transactions. The consensus approaches are utilized for maintaining the consistency of data on the blockchain networks. The ethereum possess 3 kinds of consensus approaches (PoS-Proof of Stake, PoW-Proof of Work and PoA-Proof of Authority). In this study, PoW consensus approach is executed in the fusion-chain with Ethereum as it assists only PoW. This approach is implemented with full-node type, block creation and block validation, wherein, CPU overhead tends to increase. To ensure the smooth and effective transfer of healthcare data, the ADSAH approach combines Elliptical Curve Cryptography (ECC) with a blockchain mechanism known as Deep Fuzzy Based Neural Network (DFBNN).

2. Related works

This study aims to evaluate the performance of various encryption and decryption schemes for securing medical data transmitted wirelessly. The study assesses the execution time, throughput, average data rate, and information entropy of encryption schemes such as Blowfish, DES, AES, RC4, RSA, ECC, CBE, MTLM, and CEC [16]. This paper proposes a hybrid cryptographic algorithm combining RC4, ECC, and SHA-256 to enhance the security of sensitive information in IoT-based intelligent irrigation systems. By encrypting the RC4 key with ECC and applying SHA-256 for hashing, the proposed scheme ensures data integrity and protection against known attacks [17]. This paper addresses the privacy and efficiency challenges in IoT devices and applications that rely on continuous data collection. The paper presents a hybrid approach where the initial layers of a deep neural network are run on the IoT device, and the output is sent to the cloud for further processing. To ensure privacy, the paper introduces Siamese fine-tuning to prevent unwanted inferences in the data [18]. This paper uses blockchain technology to enhance healthcare systems by improving health record management, insurance billing, and data security. It explores solutions such as Hyperledger Fabric, Composer, Docker Container, and Hyperledger Caliper to measure the performance of blockchain-based systems. This paper aims to propose GuardHealth, a decentralized Blockchain system for innovative electronic medical records (EMRs), ensuring secure and privacy-preserving data sharing. GuardHealth focuses on managing confidentiality, authentication, and data preservation while utilizing consortium Blockchain, smart contracts, and a trust model with Graph Neural Network (GNN) for malicious node detection [19]. The proposed framework addresses the challenges of log record protection and real-time anomaly detection in IoT systems. By leveraging Blockchain and smart contracts, it ensures data integrity and automates anomaly detection, overcoming issues with high communication overhead and tampering vulnerability in existing methods [20]. This paper addresses the privacy and control issues associated with centralized health data storage in IoT systems. The proposed scheme, Healthchain, utilizes blockchain technology to preserve the privacy of health data by encrypting it and implementing fine-grained access control [21]. This paper aims to shed light on the constraints of conventional health information technology in delivering personalized and patient- centric care. It underscores the transformative potential of blockchain technology in overcoming these limitations by offering decentralized and secure solutions for data access, storage, and payment systems in healthcare

[22]. This study aims to address the security vulnerabilities in a multiserver authentication scheme proposed by Wang *et al* to manage the increasing number of users in a mobile network. The authors demonstrate the insecurity of Wang *et al* scheme against various attacks and propose an improved scheme to mitigate these security weaknesses [23]. The focus is on addressing the security, privacy, and trust issues in intelligent healthcare, a crucial aspect of smart cities. The authors propose a human-in- the-loop-aided (HitL-aided) scheme to preserve privacy in intelligent healthcare. The scheme incorporates a block design technique to obfuscate health indicators and introduces the concept of human-in-the-loop to enable privacy-controlled access to health reports [24]. This paper aims to address the research challenge of achieving efficient data search and sharing in cloud-assisted IoT systems while ensuring sensor data security in healthcare applications. The authors propose a solution called proxy re-encryption with equality test (PRE- ET) by combining the concepts of proxy re-encryption (PRE) and public key encryption with equality test (PKE-ET) [25]. This paper aims to address the security and privacy concerns in IoT-enabled healthcare infrastructure by proposing a novel encryption scheme. The scheme combines elliptic curve cryptography, Advanced Encryption Standard (AES), and Serpent to secure healthcare data [26]. The paper discusses using cryptographic algorithms for access contro l in IoMT-based healthcare systems, emphasizing algorithms like RC6, elliptic curve digital signature, and SHA256 for data integrity. It highlights how adopting high-security algorithms enhances availability and confidentiality and protects sensitive information from implantable devices, strengthening healthcare services [27]. This research addresses the challenge of storing and securely transferring healthcare data by proposing the LRO-S encryption method. This method combines lionized remora optimization and improved security algorithms to generate secure keys for the serpent encryption algorithm [28]. This paper addresses the security concerns in transmitting ECG data to cardiologists for telecardiology services. The proposed method focuses on securing the ECG transmission using a triple data encryption standard (3-DES) for encryption and a water cycle optimization (WCO) algorithm for authentication [29]. This research addresses the security concerns in healthcare data and services by proposing a content-aware DNA computing system for encrypting medical images [30]. This research addresses the security and privacy concerns of storing and accessing patients' health data in cloud computing environments. The vulnerability of patient data to various cyberattacks necessitates the implementation of encryption mechanisms to protect sensitive health information. This paper proposes a hybrid cryptography approach to securely share health data over the cloud, ensuring data privacy and secrecy [31–33].

2.1 *Significance of blockchain in healthcare sector*

As the study focuses on blockchain in healthcare, significance and usage of blockchain in healthcare as claimed by conventional studies are presented to afford a comprehensive view about it in existing researches [34–36].

The recommended study has explained about the significance of blockchain in health care during pandemic situation. The application of blockchain technology includes digital data storage, public surveillance system, disease control, supporting the supply chain of medical parts, healthcare instruments tracking, enhanced the transparency during treatment of patients, assist in storing and transferring the information related to treatment, helps in efficient healthcare management and provides better healthcare protection [37, 38].

2.2 *Research gap*

The recommended study has confessed that blockchain technology is prone to have information decay, lack of scalability and non-standardization. Hence, the new approaches may be integrated with blockchain technology to overcome the existing drawbacks.

As the healthcare services are complex in nature, the blockchain technology is still in a budding stage. Therefore, more empirical base is needed to make the existing mechanism highly conclusive and emphatic which may reduce the complexity of the existing system.

Scalability acts as a major limitation, as validation needs more time because of the authorization of transactions from majority of nodes. Additionally, complexity of blockchain and need for extensive network of users is considered as another disadvantage. And also, privacy preservation acts as a major limitation in using blockchain technology in health care.

3. Methodology

Through the implementation of the proposed work improved quaternion neural network cryptography is used to encrypt the shared healthcare data in order to achieve strong security. The ADSAH, a robust security framework is established for encrypting shared health data. This approach incorporates key generation, encryption, and decryption processes to optimize complexity and execution time. The overall process is depicted in figure 1, showcasing the seamless flow of data security measures. In the ADSAH framework, private medical data uploaded by physicians is encrypted using the ECC encryption technique. The secret key associated with the encrypted data is securely stored using blockchain technology, utilizing a block-based storage approach. Key events within these blocks are identified using the SHA algorithm, bolstering

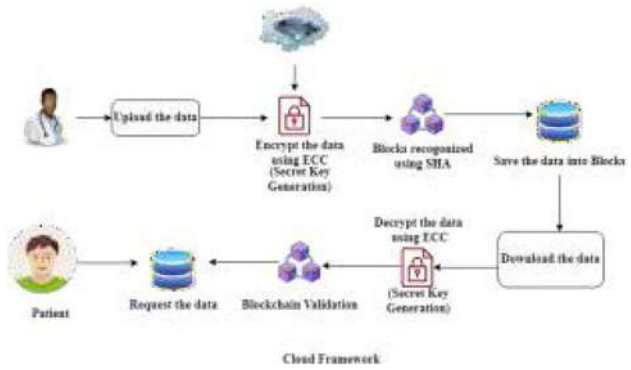

Figure 1. An implementation framework for the proposed methodology.

security measures. The encrypted and secured data is then stored in a cloud storage system, ensuring its accessibility and integrity. Using the secret key, authorised patients or medical professionals can access the medical information. The data is decrypted using the ADSAH encryption and decryption processes, enabling the retrieval of secure medical data. The data remains protected and stored within the cloud environment throughout the process, safeguarding its confidentiality and privacy (figures 2 and 3).

3.1 *Proposed ADSAH*

3.1.1 *Elliptic curve cryptography (ECC) algorithm:* In hospital management, the security of user-related data, encompassing patient information, medical records, and medication details, holds immense

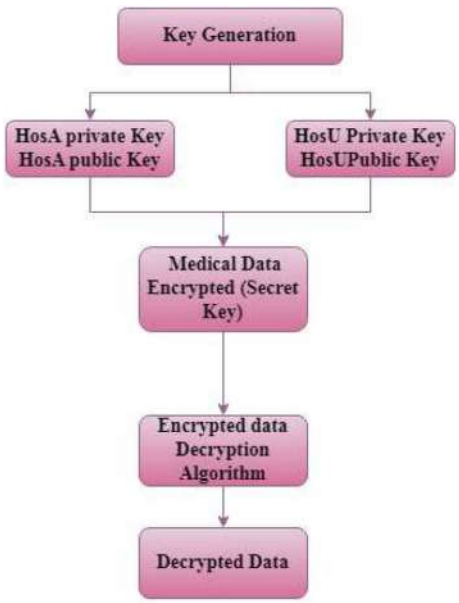

Figure 2. ECC Encryption process workflow.

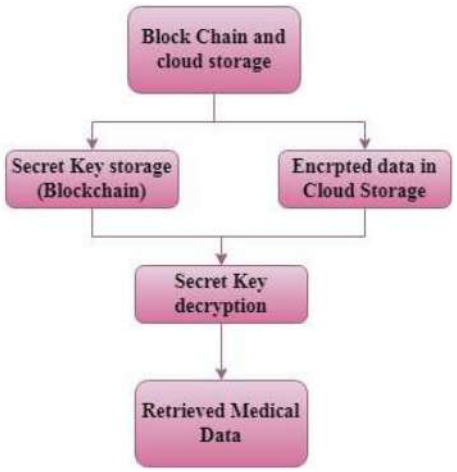

Figure 3. ECC Decryption process workflow.

significance. However, hospitals encounter significant challenges in ensuring data security. To tackle this issue, this paper proposes the adoption of the elliptic curve cryptography (ECC) algorithm for encryption and decryption processes. ECC is an asymmetric cryptographic algorithm that utilizes private and public keys for encryption and decryption operations. One notable advantage of ECC over non-ECC algorithms like RSA and DSA is its ability to provide equivalent security with smaller key sizes. In other words, ECC achieves the same level of protection as different algorithms while requiring shorter key lengths. The name "elliptic curve cryptography" stems from using elliptic curves as the foundation of its mathematical framework. Elliptic curves are described by cubic functions, specifically equations of degree 3. The equation of an elliptic curve follows the form $y^2 = x^3 + (a * x) + b$, where a and b are constants defining the curve. The coordinates of the elliptic curve equation are represented as (x_1, y_1), (x_2, y_2) and so on [32]. By harnessing the power of elliptic curves and their underlying mathematical principles, the ECC algorithm provides a secure and efficient solution for encrypting and decrypting sensitive user data within the realm of hospital management. It offers robust security while minimizing the required key sizes, making it appropriate for safeguarding confidential information within healthcare systems.

The process begins by initiating the algorithm. For each user, their username and password are obtained. If the user's credentials are authenticated, they are granted access to a secret key within the system. This authentication check is performed iteratively, allowing multiple users to be established. If a user is found invalid during the authentication process, the algorithm proceeds to handle this case. It displays a message indicating the user is invalid and then exits the algorithm. Once the authentication process is completed, the algorithm moves on to the next phase, which involves storing the data securely in a cloud storage

system using blockchain technology. This integration ensures the data integrity and provides a secure and decentralized storage solution. After the data is securely stored, the algorithm reads the plain text data. The next step involves initiating the ECC encryption process in the Edge Server. During this process, public and private keys are generated using Algorithm 1, which will be crucial for the subsequent encryption and decryption operations. Following key generation, the algorithm performs the encryption process using Algorithm 2. This process transforms the plain text data into an encrypted form, ensuring its confidentiality and protection against unauthorized access. To enable the decryption of the encrypted data, a request for the decryption process is made in the Edge Server. If the user is authenticated for decryption, the algorithm performs the decryption process using Algorithm 3. This process utilizes the previously generated keys to decrypt the encrypted data and retrieve the original plaintext. Once the decryption process is completed, the data is securely stored in the cloud server and blockchain technology. This dual storage approach enhances the security and persistence of the data. Finally, authenticated users are granted access to view their data securely. This ensures privacy and confidentiality by restricting data access only to authorized individuals

Algorithm 1- public, private, and secret Key Generation

Input: User $HosU$ data; Key size: 516 bits
Output: public, private, and secret key of $HosU\&HosA$
Step 1: create E
Step 2: generate G
Step 3: for-each User $HosU$ do;
Step 4: create private and public keys of $HosA$
Step 5: create private keyN_{HosA} of $HosA$; where $N_{HosA} <$ n
Step 6: compute public key P_{HosA} of $HosA$; where $P_{HosA} = N_{HosA}(G)$
Step 7: create the private key and Public key of $HosU$
Step 8: create private key $N_{HosU}$of $HosU$; where $N_{HosU} < n$
Step 9: compute public key P_{HosU} of $HosU$; where $P_{HosU} = N_{HosU} * G$
Step 10: create a secret key of $HosA$; $kHosA = N_{HosA} * P_{HosU}$
Step 11: create secret key of N_{HosU}; $kHosU = N_{HosU} * P_{HosA}$
Step 12: end for-each;

According to Algorithm 1, the aim is to generate public, private, and secret keys for Hospital Users *HosU* and the Hospital Authority *HosA*. The key size is specified as 516 bits. First, a variable E is created. Then, a point G is generated. For each Hospital User *HosU* in the system, the algorithm proceeds a private key and public key are created for the Hospital Authority *HosA*. The private key is denoted as N_{HosA}, where N_{HosA} is a randomly generated value that is less than the total number of keys n. The public key of *HosA*, denoted as P_{HosA}, is computed as the scalar multiplication of N_{HosA} and G: $P_{HosA} = N_{HosA}(G)$. Similarly, private and public keys are created for the Hospital User *HosU*. The private key for *HosU* is denoted as N_{HosU}, and it is randomly generated such that $N_{HosU} < n$. The public key of *HosU*, denoted as P_{HosU}, is computed as $P_{HosU} = N_{HosU} * G$. To establish the secret key for each entity, the algorithm performs the following calculations: The secret key of HosA, kHosA, is computed as the scalar multiplication of N_{HosA} and P_{HosU}: *HosA*; $kHosA = N_{HosA} * P_{HosU}$. Similarly, the secret key of *HosU*, *kHosU*, is computed as $kHosU = N_{HosU} * P_{HosA}$. These steps are repeated for each Hospital User in the system.

Algorithm 2- plain text PT to cipher text CP_{pt}

Input: plain text PT
Output: cipher text CP_{pt}
Step 1: read PT
Step 2: encode $PT -> EP => EP_{pt}$
Step 3: compute CP
Step 4: compute CP_{pt}; $CP_{pt} = \{K * G, EP_{pt} + K * P_{HosU}\}$
Step 5:compute $X - coordinate = K * G$; $Y - coordinate = EP_{pt} + K * P_{HosU}$

The algorithm 2 takes a plain text message PT as input and aims to produce a cipher text CP_{pt} as output. First, the plain text message PT is read. Next, the plain text message PT is encoded, resulting in an encoded message EP_{pt}, which represents the transformed version of the original message using a specific encoding scheme. Then, the algorithm proceeds to compute the cipher text CP. The cipher text CP_{pt} is calculated using the formula: $CP_{pt} = \{K * G, EP_{pt} + K * P_{HosU}\}$, where K is a randomly generated scalar value, G is a predefined point, and P_{HosU} is a public key associated with the Hospital User. The computation of CP_{pt} involves two components: the X-coordinate and the Y-coordinate. The X- coordinate is determined by multiplying $K * G$, while the Y-coordinate is obtained by adding $EP_{pt} + K * P_{HosU}$.

Algorithm 3- cipher text CP_{pt} **to** plain text PT

Input: Cipher text
Output: Plain text
Step 1: get cipher point CP_{pt} at receiver end
Step 2: compute $Z = KG * N_{HosU}$
Step 3: subtract Z from Y coordinates and compute the following:
Step 4: $HosU < -EP_{pt} + K * P_{HosU} - (Z)$
Step 5: $HosU < -EP_{pt} + K * P_{HosU} - (KG * N_{HosU})$
Step 6: $HosU < -EP_{pt} + K * P_{HosU} - K * P_{HosU}$ $where\ P_{HosU} = N_{HosU} * G$
Step 7: $HosU < -EP_{pt}$

The algorithm 3 aims to decrypt a cipher text and retrieve the original plain text message. Given the cipher text, the receiver obtains the cipher point CP_{pt} as an input. To decrypt the cipher text, the receiver computes Z by multiplying the predefined point $KG * N_{HosU}$ associated with the Hospital User. Next, the algorithm subtracts Z from the Y coordinates of the cipher point and performs the following computations:

$$HosU < -EP_{pt} + K * P_{HosU} - (Z)$$

$$HoSU < -EP_{pt} + K * P_{HosU} - (KG * N_{HosU})$$

$$HosU < -EP_{pt} + K * P_{HosU} - K *$$

P_{HosU} where $P_{HosU} = N_{HosU} * G$ Finally, the algorithm simplifies the expression to: $HosU < -EP_{pt}$

3.1.2 *Deep fuzzy based neural network (DFBNN):* In this section we discussed about the DFBNN which is based On Deep Neural Network (DNN) concept. The proposed ADSAH technique employs a combination of ECC and DFBNN algorithms for secure data analysis and decision-making. It starts by encrypting the data using ECC, which utilizes elliptic curves and cryptographic keys to ensure confidentiality during transmission or storage. The encrypted data, along with other relevant information, is securely stored, such as in a blockchain or secure database. The DFBNN, which combines deep learning and fuzzy logic, is then used for data analysis. The figure 4 depicts the DFBNN architecture, which is made up of several layers, nodes, and fuzzy rules, and it is trained on labeled data to learn patterns and relationships in the encrypted data. The DFBNN processes the encrypted data using deep learning capabilities and fuzzy logic to handle uncertainty and imprecision. It performs analysis and decision-making tasks on the encrypted data while preserving its confidentiality. When the analysis is complete, the encrypted results are retrieved, and the private key associated with ECC encryption is used to decrypt the data back to its original form, allowing for interpretation or further use.

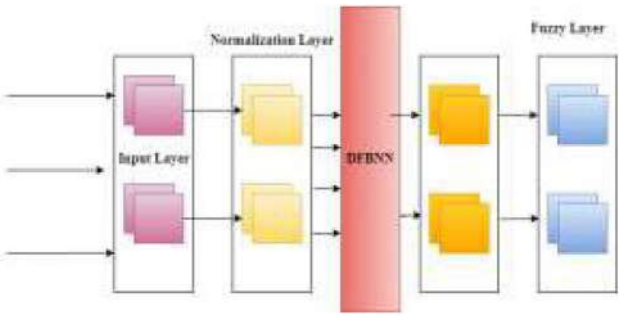

Figure 4. DFBNN Architecture.

Step 1: Initialization:
$DaTr$ = Data for training (scene data and situation labels).
$DaTr_m = m$ number of training data $DaTr$.
X_i = For input X, ith input of the scene data
$\hat{X}_i$ = Input normalized data.
$F_{train}()$ = Function to train the hidden layers of deep network
Fun_{act} =Activation function for the deep neural network
DNN_{imp} = Improved deep neural network (DNN)
$F_{norml}()$ =For input normalization
F_{fuzz_out} =Output Fuzzification
$Fout\_DNN_{imp}$ =Training of the DNN_{imp}
Step 2: Offline training of the DNN_{imp}
Step 3: $i \leftarrow 0$;
Step 4: $do\ i++$
Step 5: $\hat{X}_i \leftarrow F_{norm}(DaTr)$;
Step 6: $F_{train}(Fun_{act}, \hat{X}_i)$;
Step 7: $while\ i > DaTr_m$ is false go back to line 2
Step 8: $Ftrain_{DNN_{imp}(DNN_{imp},DaTr)}$;
Step 9: Online training of the DNN_{imp}:
Step 10: $t \leftarrow 0$;
Step 11: $do\ t++$
Step 12: $\hat{X}_i \leftarrow$Normalized (X_i);
Step 13: $\hat{b_i} \leftarrow Fout_{DNN\,imp}(\hat{X}_i, DNN_{imp})$;
Step 14: $p_i \leftarrow F_{fuzz_{out}}(\hat{b_i})$;
Step 15: $while\ DaTr \geq DaTr_{max}$ is false, go back to line 9

The algorithm starts with an initialization step, where the necessary variables and functions are defined. These include the training data $DaTr$, the number of training data $DaTr_m$, input variables X_i normalized input data $\hat{X}_i$, functions for training the hidden layers of the deep network

F_{train}, activation function for the deep neural network Fun_{act}, the improved deep neural network DNN_{imp}, functions for input normalization F_{norml} and output fuzzification F_{fuzz_out}, and the training of the improved DNN $Fout\_DNN_{imp}$. In the offline training phase, the DNN_{imp} is trained using the training data $DaTr$. Then, in a loop starting from Step 3, the algorithm iterates through the training process. Each iteration involves normalizing the input data and training the hidden layers of the deep network. The loop continues until the condition $i > DaTr_m$ is false, and then DNN_{imp} is further trained. The online training phase begins with initializing the variable t. In the subsequent loop, the algorithm performs online training. It involves normalizing the input data and obtaining the output of the DNN_{imp} $\widehat{b_i}$ for the normalized input. Fuzzifying the output p_i using $F_{fuzz_{out}}\left(\widehat{b_i}\right)$ and repeating the process until the condition $DaTr \geq DaTr_{max}$ is false. The algorithm continues to iterate through the online training phase until the desired criteria for the maximum number of training data $DaTr_{max}$ or the maximum number of iterations $DaTr_{max}$ are met. the training of the improved DNN $Fout\_DNN_{imp}$. In the offline training phase, the DNN_{imp} is trained using the training data $DaTr$. Then, in a loop starting from Step 3, the algorithm iterates through the training process. Each iteration involves normalizing the input data and training the hidden layers of the deep network. The loop continues until the condition $i > DaTr_m$ is false, and then DNN_{imp} is further trained. The online training phase begins with initializing the variable t. In the subsequent loop, the algorithm performs online training. It involves normalizing the input data and obtaining the output of the DNN_{imp} $\hat{b_i}$ for the normalized input. Fuzzifying the output pi using $F_{fuzz_{out}}(\hat{b_i})$ and repeating the process until the condition $DaTr \geq DaTr_{max}$ is false. The algorithm continues to iterate through the online training phase until the desired criteria for the maximum number of training data $DaTr_{max}$ or the maximum number of iterations $DaTr_{max}$ are met.

3.1.3 *Modified genetic algorithm (GA):* As we discussed earlier, in the context of the proposed ADSAH system, a modified genetic algorithm can be used to generate encryption and decryption keys. The genetic algorithm is a search and optimization technique inspired by natural selection and genetics. Figures 5 and 6 illustrates the process of key generation using genetic algorithm [14].

Figure 7 represents the framework for the practical implementation of the model. The cloud framework will be based on the hospital networks. The doctors could create new files and add them to the network, which will be protected using the proposed techniques. The files stored in the cloud server would be accessed by the patient based on privacy, and they could only read the data.

Algorithm 2- Modified Genetic Algorithm for Key Generation

$P(t) - Pop(i)$

Input: *Initialised the data*

Output: *Generated Key*

1. $i \leftarrow 0$
2. *Init_Population* $[Pop(i)]$; *Initialises the population.*
3. *Eval_Population* $[Pop(i)]$; *Evaluates the population.*
4. *While not terminating,*
5. *do*
   $Pop'(i)$
   $\leftarrow$ *Variation* $[Pop(i)]$; *Creates new solutions*
   Eval_Population $[Pop'(t)]$; *Evaluates the new solutions*
   $Pop(i+1) \leftarrow$ *ApplyGeneticOperators*
   $[Pop'(i) U\ Q]$; *Next, generation pop.*
   $i \leftarrow i + 1$;
   end while.
6. *Population having maximum fitness value is selected as key.*

4. Results and discussion

This part presents the findings from the performance analysis, comparison analysis, and environmental setup conducted during the execution of the proposed system.

4.1 *Environmental setup*

In our proposed work, the evaluation is conducted by implementing programs using the Java programming language version 1.8. The computer system used for the evaluation consists of an Intel Core i5 processor with a clock speed of 3.30 GHz. It is equipped with 8 GB of RAM and runs on the Windows 8 operating system, which is a 64-bit OS. This specific hardware and software configuration is chosen to provide a suitable computing environment for our experiments. The Intel Core i5 processor offers a good balance between performance and cost, while the 8 GB of RAM ensures sufficient memory capacity for running the programs and handling the computational tasks involved for training and evaluation. By utilizing this, we can execute our programs efficiently and collect relevant data to evaluate the performance of the proposed ADSAH.

4.2 *Comparative analysis*

4.2.1 *Uploading time:* According to figure 8, for the data size of 1MB, ADSAH achieves an uploading time of 3.98 milliseconds, which is significantly lower than the other methods such as CE (5.6 ms), LR (10.89 ms), RCE (5.6 ms), DOM (5.6 ms), and ECC-CRT (4.38 ms). This indicates that ADSAH has optimized the uploading process for faster data transfer. As the data size increases to 2MB, ADSAH still maintains its superiority with an uploading time of 6.2 ms, outperforming CE (8.68 ms), LR (16.24 ms), RCE (8.68 ms), DOM (8.68 ms), and ECC-CRT (5.42

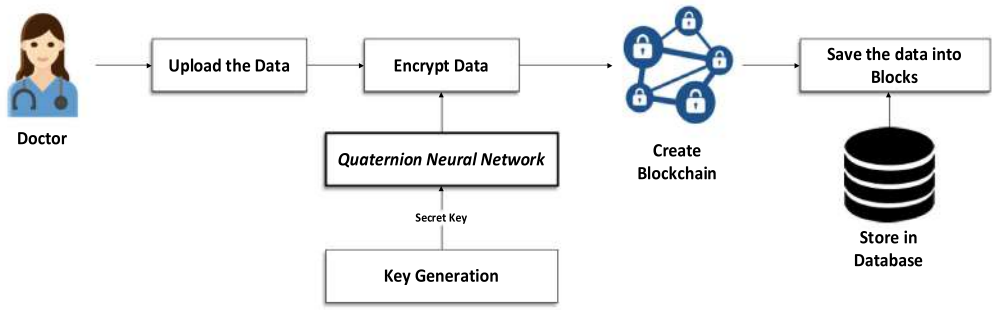

Figure 5. Key generation for the doctor.

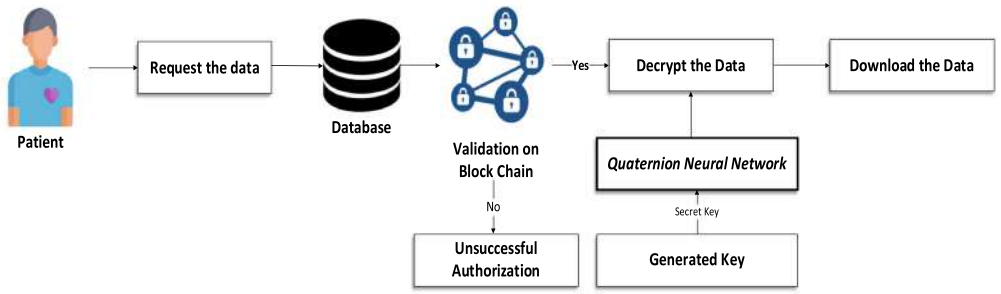

Figure 6. Key generation for the patient.

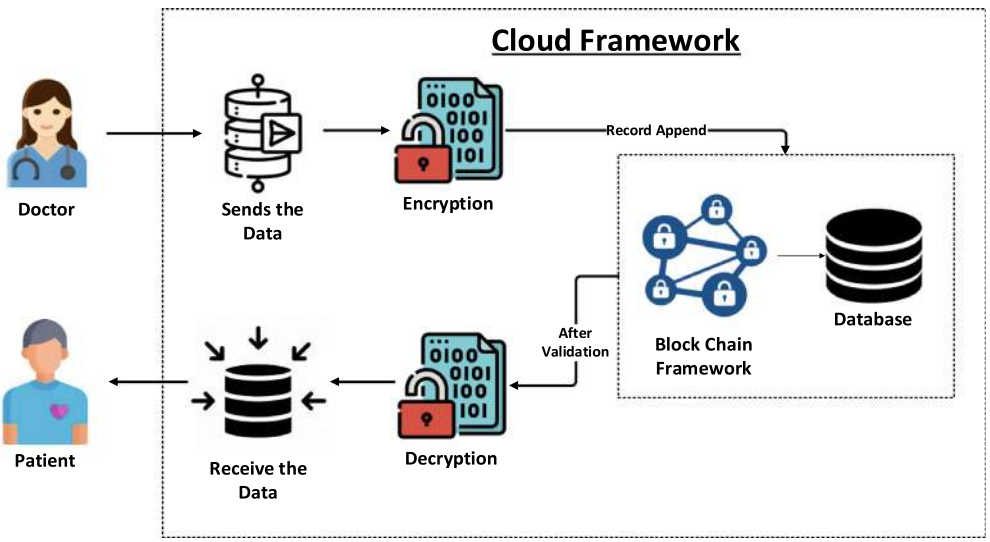

Figure 7. An implementation of overall framework.

ms). The trend continues as the data size grows. For 4MB, 6MB, 8MB, and 10MB, ADSAH consistently exhibits lower uploading times compared to the other methods. This demonstrates that ADSAH has been designed to efficiently handle larger data sizes and minimize the time required for data uploading.

4.2.2 *Downloading time:* ADSAH, the proposed method, demonstrates faster data retrieval compared to other methods for a data size of 1MB, achieving a downloading time of 3.23ms. This superiority is maintained as the data size increases to 2MB, with ADSAH recording a downloading time of 4.89ms,

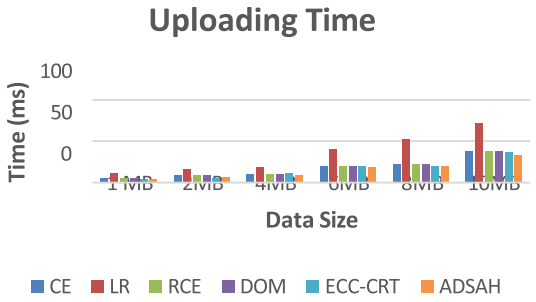

Figure 8. Uploading time.

outperforming the alternative methods. This trend continues for larger data sizes, such as 4MB, 6MB, 8MB, and 10MB. When it comes to the data size of 10 MB it achieving the time with 31.98 ms when compared with the other CE, LR, RCE, DOM, ECC-CRT as 34.92 ms, 34.92ms, 34.92ms, 35ms, 33.89ms respectively, was clearly depicted in figure 9. Where ADSAH consistently exhibits lower downloading times compared to the other methods. These findings highlight the efficiency and effectiveness of ADSAH in facilitating faster data retrieval, regardless of the data size.

4.2.3 *Encryption time comparison:* Figure 10 represents the encryption time comparison for different encryption methods at various input data sizes (in KB), the term of time evaluated in terms of (milliseconds). The encryption times are provided for the following methods: 3DES & ECC & SHA-256, RC4 & 3DES & SHA-256, AES & RC4 & SHA-256, AES & 3DES & SHA-256, RC4 & AES & SHA-256, and the proposed ADSAH method. By analyzing the figure, we can observe that the proposed ADSAH method consistently demonstrates lower encryption times compared to the other encryption methods for all data sizes. This indicates that ADSAH is more efficient in terms of encryption time. For example, at a data size of 200 KB, the proposed ADSAH method has an encryption time of 19.63 ms, while the other methods range from 28 ms to 35 ms. Similarly, at larger data sizes, such as

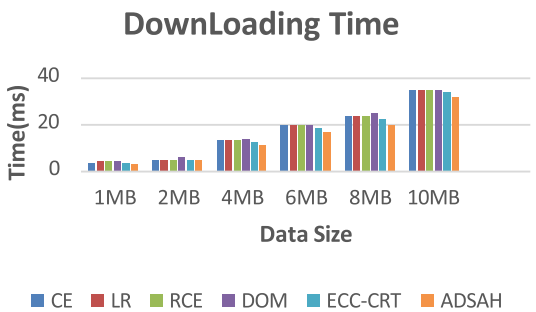

Figure 9. Downloading time.

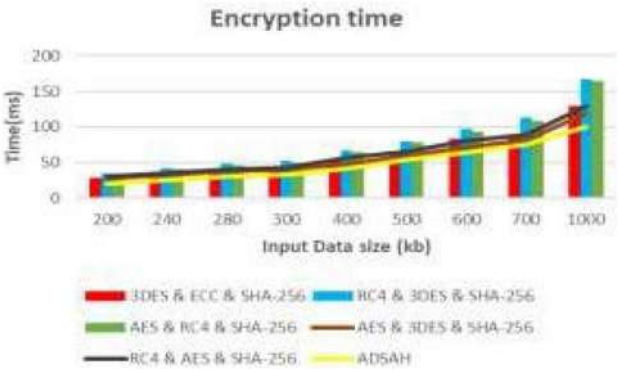

Figure 10. Encryption time comparison of the proposed model.

1000 KB, the proposed ADSAH method has an encryption time of 100.63 ms, outperforming the other methods with encryption times ranging from 119 ms to 168 ms. These results highlight the efficiency of the proposed ADSAH method in terms of encryption time. It offers faster encryption compared to the other methods, making it a more time-effective solution for securing data.

4.2.4 *Decryption time:* Figure 11 represents the decryption time comparison for different decryption methods at various input file sizes (in KB). The decryption times are provided for the following methods: 3DES & ECC & SHA-256, RC4 & 3DES & SHA- 256, AES & RC4 & SHA-256, AES & 3DES & SHA-256, RC4 & AES & SHA-256, and the proposed ADSAH method. By analyzing figure 8, we can observe that the proposed ADSAH method consistently demonstrates lower decryption times compared to the other decryption methods for all file sizes. This indicates that ADSAH is more efficient in terms of decryption time. For example, at a file size of 200 KB, the proposed ADSAH method has a decryption time of 17.66 ms, while the other methods range from 28 ms to 33 ms. Similarly, at larger file sizes, such as 1000 KB, the proposed ADSAH method has a decryption

Figure 11. Decryption time comparison of the proposed model.

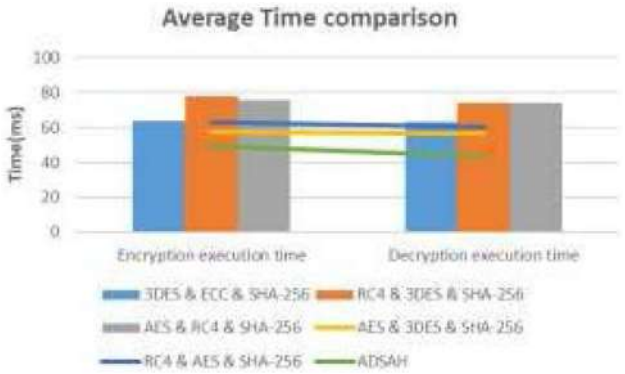

Figure 12. Average time comparison for encrypting and decrypting a file for the proposed model and the previous model.

time of 96.82ms, outperforming the other methods with decryption times ranging from 120 ms to 165 ms. These results highlight the efficiency of the proposed ADSAH method in terms of decryption time. It offers faster decryption compared to the other methods, making it a more time-effective solution for retrieving secured data. By minimizing the decryption time, ADSAH enhances the overall efficiency of the system, enabling quick access to decrypted data while ensuring its security.

4.2.5 *Average time comparison:* Figure 12 presents the average time comparison for encryption and decryption execution using different methods: 3DES & ECC & SHA-256, RC4 & 3DES & SHA-256, AES & RC4 & SHA-256, AES & 3DES & SHA-256, RC4 & AES & SHA- 256, and the proposed ADSAH method. In terms of encryption execution time, the proposed ADSAH method demonstrates the best performance with an average time of 49.28 ms. It outperforms the other methods, which range from 57.44 ms to 77.88 ms. This indicates that ADSAH offers faster encryption execution, making it more efficient in terms of time. Similarly, in terms of decryption execution time, the proposed ADSAH method shows superior performance with an average time of 43.44 ms. The other methods have average times ranging from 56.33 ms to 74.33 ms. Once again, ADSAH outperforms the alternatives, providing faster decryption execution. The performance of the proposed ADSAH method can be attributed to its optimized encryption and decryption algorithms, which are specifically designed to minimize execution time while maintaining data security. By reducing the average time required for encryption and decryption, ADSAH enhances the overall performance of the system, enabling efficient and timely data processing From table 1, it has been observed that, Scheme I has regarded to afford security for different attack methods like user anonymity, offline password attacks, stolen smart card attacks and server impersonation attack. Similarly, Scheme II has considered to afford security to offline password attacks, stolen smart card attacks, replay attacks, three factor secrecy and perfect forward secrecy. On contrary, the proposed method has considered to provide security for all the kinds of considered attacks as depicted in table 1 which confirms its ability than other schemes.

In addition, comparison has been performed in accordance with computational cost and the outcomes are shown in table 1.

From table 2, it has been revealed that, the existing methods have consumed high computational cost in comparison with the proposed system. Lower the computational cost, higher is the efficacy of the method. Hence, the proposed algorithm has been found to be effective than conventional algorithms.

Table 2. Comparison of computation cost.

Scheme	Overall computation cost (ms)
Existing algorithm	74.33
Proposed algorithm	49.28

Table 1. Security Performance comparison.

Attack methods	Scheme I	Scheme II	Proposed Method
User anonymity	√	×	√
Offline password attacks	√	√	√
Stolen smart card attacks	√	√	√
Known session- specific temporary information attack	×	×	√
User impersonation attack	×	×	√
Server impersonation attack	×	×	√
Replay attacks	√	√	√
Perfect forward secrecy	×	√	√
Three-factor secrecy	×	√	√

5. Conclusion

The suggested new novel solution improved quaternion based neural network and ADSAH with a blockchain mechanism maintained in a cloud environment secures private health data. The innovative approach to addressing the security and privacy risks associated with cloud-based healthcare data. To reduce complexity and time, the proposed cryptography approach performed the key generation, encryption, and decryption processes.

The blockchain system is used to manage multiple hash events, where the secret key is saved and handled by the ADSAH algorithm. A further enhancement in security is provided by the updated genetic algorithm's key generation process. The data is encrypted and kept securely in the cloud. Using the secret key, the authorised patient or doctor can access the confidential health information, after which the data is decrypted. The assessment findings demonstrate that compared to the previous study, the suggested approach reduces the time required for encryption and decryption. Comparatively, the cost of transaction and execution was also decreased as a result of the complexity reduction. It addresses the security and privacy challenges associated with healthcare data, providing a promising solution for the healthcare industry.

References

[1] Duan X, Guo D, Liu N, Li B, Gou M and Qin C 2020 A new high capacity image steganography method combined with image elliptic curve cryptography and deep neural network. *IEEE Access* 8: 25777–25788

[2] Itoo S, Khan A A, Kumar V, Alkhayyat A, Ahmad M and Srinivas J 2022 CKMIB: Construction of key agreement protocol for cloud medical infrastructure using blockchain. *IEEE Access* 10: 67787–67801

[3] Zala K, Thakkar H K, Jadeja R, Singh P, Kotecha K and Shukla M 2022 PRMS: design and development of patients' E-healthcare records management system for privacy preservation in third party cloud platforms. *IEEE Access* 10: 85777–85791

[4] Haddad A, Habaebi M H, Islam M R, Hasbullah N F and Zabidi S A 2022 Systematic review on AI-blockchain based E-healthcare records management systems. *IEEE Access*. https://doi.org/10.1109/ACCESS.2022.3201878

[5] Madine M M, Salah K, Jayaraman R, Yaqoob I, Al-Hammadi Y, Ellahham S and Calyam P 2020 Fully decentralized multi-party consent management for secure sharing of patient health records. *IEEE Access* 8: 225777–225791

[6] Gupta D N, Kumar R and Ansari S H 2022 Federated learning for an IoT application. In: *Federated Learning for IoT Applications*, Springer International Publishing, Cham, pp. 53–66

[7] Rasina Begum B and Chitra P 2021 ECC-CRT: an elliptical curve cryptographic encryption and Chinese remainder theorem based deduplication in cloud. *Wirel. Pers. Commun.* 116(3): 1683–1702

[8] Hamza R, Yan Z, Muhammad K, Bellavista P and Titouna F 2020 A privacy-preserving cryptosystem for IoT E-healthcare. *Inf. Sci.* 527: 493–510

[9] Ilokah M and Eklund J M 2020 A secure privacy preserving cloud-based framework for sharing electronic health data. In: *2020 42nd Annual International Conference of the IEEE Engineering in Medicine & Biology Society (EMBC)*, IEEE, pp. 5592–5597

[10] Christo M S, Jesi V E, Priyadarsini U, Anbarasu V, Venugopal H and Karuppiah M 2021 Ensuring improved security in medical data using ECC and blockchain technology with edge devices. *Secur. Commun. Netw.* 2021: 1–13

[11] Kwabena O A, Qin Z, Zhuang T and Qin Z 2019 Mscryptonet: multi-scheme privacy-preserving deep learning in cloud computing. *IEEE Access* 7: 29344–29354

[12] An J, Fu L, Hu M, Chen W and Zhan J 2019 A novel fuzzy-based convolutional neural network method to traffic flow prediction with uncertain traffic accident information. *IEEE Access* 7: 20708–20722

[13] Amosov O S, Ivanov Y S and Amosova S G 2019 Recognition of abnormal traffic using deep neural networks and fuzzy logic. In: *2019 International Multi-Conference on Industrial Engineering and Modern Technologies (FarEastCon)*, IEEE, pp. 01–05

[14] Soni A and Agrawal S 2013 Key generation using genetic algorithm for image encryption. *Int. J. Comput. Sci. Mob. Comput. (IJCSMC)* 2(6): 376–383

[15] Tanwar S, Parekh K and Evans R 2020 Blockchain-based electronic healthcare record system for healthcare 4.0 applications. *J. Inf. Secur. Appl.* 50: 102407

[16] Adedeji K B, Nwulu N I, Aigbavboa C and Gbadamosi S L 2019 Assessment of encryption and decryption schemes for secure data transmission in healthcare systems. In: *2019 IEEE AFRICON*, IEEE, pp. 1–6

[17] Mousavi S K, Ghaffari A, Besharat S and Afshari H 2021 Improving the security of internet of things using cryptographic algorithms: a case of smart irrigation systems. *J. Ambient Intell. Human. Comput.* 12: 2033–2051

[18] Osia S A, Shamsabadi A S, Sajadmanesh S, Taheri A, Katevas K, Rabiee H R, Lane N D and Haddadi H 2020 A hybrid deep learning architecture for privacy-preserving mobile analytics. *IEEE Internet of Things J.* 7(5): 4505–4518

[19] Wang Z, Luo N and Zhou P 2020 GuardHealth: blockchain empowered secure data management and graph convolutional network enabled anomaly detection in smart healthcare. *J. Parallel Distrib. Comput.* 142: 1–12

[20] Wu T Y, Yang L, Lee Z, Chen C M, Pan J S and Islam S H 2021 Improved ECC-based three-factor multiserver authentication scheme. *Secur. Commun. Netw.* 20(21): 1–14

[21] Xie X, Fang Y, Jian Z, Lu Y, Li T and Wan G 2020 Blockchain-driven anomaly detection framework on edge intelligence. *CCF Trans. Network.* 3: 171–192

[22] Xu J, Xue K, Li S, Tian H, Hong J, Hong P and Yu N 2019 Healthchain: a blockchain-based privacy preserving scheme for large-scale health data. *IEEE Internet of Things J.* 6(5): 8770–8781

[23] Yaeger K, Martini M, Rasouli J and Costa A 2019 Emerging blockchain technology solutions for modern healthcare infrastructure. *J. Sci. Innov. Med.* 2(1)

[24] Yassein H R, Abidalzahra A A and Al-Saidi N M 2021 A new design of NTRU encryption with high security and performance level. In: *AIP Conference Proceedings*, Vol. 2334, No. 1, AIP Publishing LLC, p. 080005

[25] Zhou T, Shen J, He D, Vijayakumar P and Kumar N 2020 Human-in-the-loop-aided privacy-preserving scheme for smart healthcare. *IEEE Trans. Emerg. Top. Comput. Intell.* 6(1): 6–15

[26] Li W, Jin C, Kumari S, Xiong H and Kumar S 2022 Proxy re-encryption with equality test for secure data sharing in Internet of Things-based healthcare systems. *Trans. Emerg. Telecommun. Technol.* 33(10): e3986

[27] Das S and Namasudra S 2022 A novel hybrid encryption method to secure healthcare data in IoT-enabled healthcare infrastructure. *Comput. Electr. Eng.* 101: 107991

[28] Nagarajan S M, Deverajan G G, Kumaran U, Thirunavukkarasan M, Alshehri M D and Alkhalaf S 2021 Secure data transmission in internet of medical things using RES-256 algorithm. *IEEE Trans. Ind. Inform.* 18(12): 8876–8884

[29] Almalawi A, Khan A I, Alsolami F, Abushark Y B and Alfakeeh A S 2023 Managing security of healthcare data for a modern healthcare system. *Sensors* 23(7): 3612

[30] Raheja N and Manocha A K 2022 IoT based ECG monitoring system with encryption and authentication in secure data transmission for clinical health care approach. *Biomed. Sign. Process. Control* 74: 103481

[31] Wu Y, Zhang L, Berretti S and Wan S 2022 Medical image encryption by content-aware DNA computing for secure healthcare. *IEEE Trans. Ind. Inform.* 19(2): 2089–2098

[32] Karuppiah S V and Gurunathan G 2021 Secured storage and disease prediction of E-health data in cloud. *J. Ambient Intell. Human. Comput.* 12: 6295–6306

[33] Boumezbeur I and Zarour K 2022 Improving privacy-preserving healthcare data sharing in a cloud environment using hybrid encryption. *Acta Inform. Prag.* 3: 361–379

[34] Jiang H, Wang M, Zhao P, Xiao Z and Dustdar S 2021 A utility-aware general framework with quantifiable privacy preservation for destination prediction in LBSs. *IEEE/ACM Trans. Netw.* 29(5): 2228–2241

[35] Qiao F, Li Z and Kong Y 2023 A privacy-aware and incremental defense method against GAN-based poisoning attack. *IEEE Trans. Comput. Soc. Syst.*

[36] Han S, Ding H, Zhao S, Ren S, Wang Z, Lin J, Zhou S 2023 Practical and robust federated learning with highly scalable regression training. *IEEE Trans. Neural Networks Learn Syst.*

[37] Luan D, Liu A, Wang X, Xie Y, Wu Z, Zhang W 2022 Robust two-stage location allocation for emergency temporary blood supply in postdisaster. *Discrete Dyn. Nat. Soc.*

[38] Song Y, Xin R, Chen P, Zhang R, Chen J, Zhao Z 2023 Identifying performance anomalies in fluctuating cloud environments: A robust correlative-GNN-based explainable approach. *Future Gener. Comput. Syst.* 145: 77–86

Secure and privacy in healthcare data using quaternion based neural network and encoder–elliptic curve deep neural network with blockchain on the cloud environment

Published: 23 September 2023

Volume 48, article number 206, (2023) Cite this article

Sādhanā

Aims and scope

Submit manuscript

P Suganthi & R Kavitha

Abstract

The security and privacy of healthcare data are crucial aspects within the healthcare industry, as accurate diagnoses rely on medical professionals accessing patient healthcare data. Similarly, patients often require access to their data. However, ensuring that sensitive health data is shared securely while prioritizing privacy is essential. This paper proposes an innovative solution called the quaternion based neural network, Advanced Data Security Architecture in Healthcare Environment (ADSAH), which combines Elliptical curve cryptography (ECC) with a blockchain mechanism and a Deep Fuzzy Based Neural Network (DFBNN) to safeguard cloud-stored health data. The proposed approach begins by encoding the input medical data using an encoder and then encrypting the encoded data using ECC techniques. The secret key for encrypting the data is securely stored within a blockchain framework. The key is divided into blocks to enhance security, and the SHA algorithm is employed to identify key events within these blocks. These key events are subsequently stored in a cloud storage system. A modified genetic algorithm is utilized to generate the encryption and decryption key. This algorithm is explicitly tailored to secure healthcare data. Authorized patients or physicians can access medical data using the secret key to decrypt and retrieve the necessary information. The performance of the proposed network is evaluated by considering factors such as time and cost and is compared against existing studies. The evaluation demonstrates notable improvements, including a reduction in the time required for the encryption and decryption process, as well as a decrease in transaction and execution costs when compared to previous research. By incorporating ECC with a blockchain mechanism and DNN, the ADSAH approach offers an advanced solution for ensuring the security and privacy of cloud-stored health data. It provides robust encryption and facilitates efficient and cost-effective access to authorized individuals while safeguarding sensitive health information.

References

1 Duan X, Guo D, Liu N, Li B, Gou M and Qin C 2020 A new high capacity image steganography method combined with image elliptic curve cryptography and deep neural network. *IEEE Access* 8: 25777–25788

Article Google Scholar

2 Itoo S, Khan A A, Kumar V, Alkhayyat A, Ahmad M and Srinivas J 2022 CKMIB: Construction of key agreement protocol for cloud medical infrastructure using blockchain. *IEEE Access* 10: 67787–67801

Article Google Scholar

3 Zala K, Thakkar H K, Jadeja R, Singh P, Kotecha K and Shukla M 2022 PRMS: design and development of patients' E-healthcare records management system for privacy preservation in third party cloud platforms. *IEEE Access* 10: 85777–85791

Article Google Scholar

4 Haddad A, Habaebi M H, Islam M R, Hasbullah N F and Zabidi S A 2022 Systematic review on AI-blockchain based E-healthcare records management systems. *IEEE Access*. https://doi.org/10.1109/ACCESS.2022.3201878

Article Google Scholar

5 Madine M M, Salah K, Jayaraman R, Yaqoob I, Al-Hammadi Y, Ellahham S and Calyam P 2020 Fully decentralized multi-party consent management for secure sharing of patient health records. *IEEE Access* 8: 225777–225791

Article Google Scholar

6 Gupta D N, Kumar R and Ansari S H 2022 Federated learning for an IoT application. In: *Federated Learning for IoT Applications*, Springer International Publishing, Cham, pp. 53–66

7 Rasina Begum B and Chitra P 2021 ECC-CRT: an elliptical curve cryptographic encryption and Chinese remainder theorem based deduplication in cloud. *Wirel. Pers. Commun.* 116(3): 1683–1702

Article Google Scholar

8 Hamza R, Yan Z, Muhammad K, Bellavista P and Titouna F 2020 A privacy-preserving cryptosystem for IoT E-healthcare. *Inf. Sci.* 527: 493–510

Article MathSciNet MATH Google Scholar

9 Ilokah M and Eklund J M 2020 A secure privacy preserving cloud-based framework for sharing electronic health data. In: *2020 42nd Annual International Conference of the IEEE Engineering in Medicine & Biology Society (EMBC)*, IEEE, pp. 5592–5597

10 Christo M S, Jesi V E, Priyadarsini U, Anbarasu V, Venugopal H and Karuppiah M 2021 Ensuring improved security in medical data using ECC and blockchain technology with edge devices. *Secur. Commun. Netw.* 2021: 1–13

Article Google Scholar

11 Kwabena O A, Qin Z, Zhuang T and Qin Z 2019 Mscryptonet: multi-scheme privacy-preserving deep learning in cloud computing. *IEEE Access* 7: 29344–29354

Article Google Scholar

12 An J, Fu L, Hu M, Chen W and Zhan J 2019 A novel fuzzy-based convolutional neural network method to traffic flow prediction with uncertain traffic accident information. *IEEE Access* 7: 20708–20722

Article Google Scholar

13 Amosov O S, Ivanov Y S and Amosova S G 2019 Recognition of abnormal traffic using deep neural networks and fuzzy logic. In: *2019 International Multi-Conference on Industrial Engineering and Modern Technologies (FarEastCon)*, IEEE, pp. 01–05

14 Soni A and Agrawal S 2013 Key generation using genetic algorithm for image encryption. *Int. J. Comput. Sci. Mob. Comput. (IJCSMC)* 2(6): 376–383

Google Scholar

15 Tanwar S, Parekh K and Evans R 2020 Blockchain-based electronic healthcare record system for healthcare 4.0 applications. *J. Inf. Secur. Appl.* 50: 102407

Google Scholar

16 Adedeji K B, Nwulu N I, Aigbavboa C and Gbadamosi S L 2019 Assessment of encryption and decryption schemes for secure data transmission in healthcare systems. In: *2019 IEEE AFRICON*, IEEE, pp. 1–6

17 Mousavi S K, Ghaffari A, Besharat S and Afshari H 2021 Improving the security of internet of things using cryptographic algorithms: a case of smart irrigation systems. *J. Ambient Intell. Human. Comput.* 12: 2033–2051

Article Google Scholar

18 Osia S A, Shamsabadi A S, Sajadmanesh S, Taheri A, Katevas K, Rabiee H R, Lane N D and Haddadi H 2020 A hybrid deep learning architecture for privacy-preserving mobile analytics. *IEEE Internet of Things J.* 7(5): 4505–4518

Article Google Scholar

19 Wang Z, Luo N and Zhou P 2020 GuardHealth: blockchain empowered secure data management and graph convolutional network enabled anomaly detection in smart healthcare. *J. Parallel Distrib. Comput.* 142: 1–12

Article Google Scholar

20 Wu T Y, Yang L, Lee Z, Chen C M, Pan J S and Islam S H 2021 Improved ECC-based three-factor multiserver authentication scheme. *Secur. Commun. Netw.* 20(21): 1–14

Google Scholar

21 Xie X, Fang Y, Jian Z, Lu Y, Li T and Wan G 2020 Blockchain-driven anomaly detection framework on edge intelligence. *CCF Trans. Network.* 3: 171–192

Article Google Scholar

22 Xu J, Xue K, Li S, Tian H, Hong J, Hong P and Yu N 2019 Healthchain: a blockchain-based privacy preserving scheme for large-scale health data. *IEEE Internet of Things J.* 6(5): 8770–8781

Article Google Scholar

23 Yaeger K, Martini M, Rasouli J and Costa A 2019 Emerging blockchain technology solutions for modern healthcare infrastructure. *J. Sci. Innov. Med.* 2(1)

24 Yassein H R, Abidalzahra A A and Al-Saidi N M 2021 A new design of NTRU encryption with high security and performance level. In: *AIP Conference Proceedings*, Vol. 2334, No. 1, AIP Publishing LLC, p. 080005

25 Zhou T, Shen J, He D, Vijayakumar P and Kumar N 2020 Human-in-the-loop-aided privacy-preserving scheme for smart healthcare. *IEEE Trans. Emerg. Top. Comput. Intell.* 6(1): 6–15

Article Google Scholar

26 Li W, Jin C, Kumari S, Xiong H and Kumar S 2022 Proxy re-encryption with equality test for secure data sharing in Internet of Things-based healthcare systems. *Trans. Emerg. Telecommun. Technol.* 33(10): e3986

Article Google Scholar

27 Das S and Namasudra S 2022 A novel hybrid encryption method to secure healthcare data in IoT-enabled healthcare infrastructure. *Comput. Electr. Eng.* 101: 107991

Article Google Scholar

28 Nagarajan S M, Deverajan G G, Kumaran U, Thirunavukkarasan M, Alshehri M D and Alkhalaf S 2021 Secure data transmission in internet of medical things using RES-256 algorithm. *IEEE Trans. Ind. Inform.* 18(12): 8876–8884

Article Google Scholar

29 Almalawi A, Khan A I, Alsolami F, Abushark Y B and Alfakeeh A S 2023 Managing security of healthcare data for a modern healthcare system. *Sensors* 23(7): 3612

Article Google Scholar

30 Raheja N and Manocha A K 2022 IoT based ECG monitoring system with encryption and authentication in secure data transmission for clinical health care approach. *Biomed. Sign. Process. Control* 74: 103481

Article Google Scholar

31 Wu Y, Zhang L, Berretti S and Wan S 2022 Medical image encryption by content-aware DNA computing for secure healthcare. *IEEE Trans. Ind. Inform.* 19(2): 2089–2098

Article Google Scholar

32 Karuppiah S V and Gurunathan G 2021 Secured storage and disease prediction of E-health data in cloud. *J. Ambient Intell. Human. Comput.* 12: 6295–6306

Article Google Scholar

33 Boumezbeur I and Zarour K 2022 Improving privacy-preserving healthcare data sharing in a cloud environment using hybrid encryption. *Acta Inform. Prag.* 3: 361–379

Article Google Scholar

34 Jiang H, Wang M, Zhao P, Xiao Z and Dustdar S 2021 A utility-aware general framework with quantifiable privacy preservation for destination prediction in LBSs. *IEEE/ACM Trans. Netw.* 29(5): 2228–2241

35 Qiao F, Li Z and Kong Y 2023 A privacy-aware and incremental defense method against GAN-based poisoning attack. *IEEE Trans. Comput. Soc. Syst.*

36 Han S, Ding H, Zhao S, Ren S, Wang Z, Lin J, Zhou S 2023 Practical and robust federated learning with highly scalable regression training. *IEEE Trans. Neural Networks Learn Syst.*

37 Luan D, Liu A, Wang X, Xie Y, Wu Z, Zhang W 2022 Robust two-stage location allocation for emergency temporary blood supply in postdisaster. *Discrete Dyn. Nat. Soc.*

38 Song Y, Xin R, Chen P, Zhang R, Chen J, Zhao Z 2023 Identifying performance anomalies in fluctuating cloud environments: A robust correlative-GNN-based explainable approach. *Future Gener. Comput. Syst.* 145: 77–86

Author information

Authors and Affiliations

Department of CSBS, Thiagarajar College of Engineering, Madurai, India
P Suganthi

Department of IT, Velammal College of Engineering and Technology, Madurai, India
R Kavitha

Corresponding author

Correspondence to P Suganthi.

Rights and permissions

About this article

Cite this article

Suganthi, P., Kavitha, R. Secure and privacy in healthcare data using quaternion based neural network and encoder-elliptic curve deep neural network with blockchain on the cloud environment. *Sādhanā* **48**, 206 (2023). https://doi.org/10.1007/s12046-023-02249-2

Received	Revised	Accepted
13 July 2022	08 June 2023	08 July 2023

Published
23 September 2023

DOI

https://doi.org/10.1007/s12046-023-02249-2

Keywords

Healthcare data security deep neural network improved quaternion based neural network blockchain mechanism elliptic curve cryptography

IETE Journal of Research ›
Latest Articles

Research Article

Optimized Dictionary-based Sparse Regression Learning for Health Care Monitoring in IoT-based Context-Aware Architecture

S. Kamalesh & A. Muthukrishnan

Published online: 25 Sep 2023

Cite this article https://doi.org/10.1080/03772063.2023.2255567 Check for updates

Abstract

Several context-aware systems have been recently developed to provide physiological data about the health and well-being of each individual. But, there is a delay in sending data to the cloud when monitoring the patient's health. So, to overcome such types of delays, in this manuscript, a Dictionary-based Sparse Regression Learning with Golden Jackal Optimization is proposed to monitor the healthcare data in IoT-based context-aware architecture (DSRL-GJO-HD-CAA-IOT). Initially, the input data are gathered from real-time datasets. Afterward, data are fed to pre-processing. Pre-processing data include the collection, data storage, and data redundancy phase. For the redundancy phase, structural interval gradient filtering (SIGF) is used to delete the repeated data. Then, the pre-processing output is fed to feature extraction. The feature is extracted using structured optimal graph-based sparse feature extraction. After that, the extracted features are given to Dictionary-based Sparse Regression Learning (DBSRL) optimized with the Golden Jackal Optimization algorithm for effectively classifying regular, irregular, and critical conditions of patients. The proposed DSRL-GJO-HD-CAA-IOT approach is implemented in OMNeT++. The performance of the proposed DSRL-GJO-HD-CAA-IOT approach attains 3.10%, 7.12%, 7.73%, and 6.7% high accuracy, 24.13%, 13.04%, 29.51%, and 17.81% higher scalability, and 2.29%, 5.36%, 1.55%, and 3.91% higher response time than the existing methods.

KEYWORDS: Cloud layer Dictionary-based sparse regression learning fog layer Golden Jackal optimization Internet of Things structured optimal graph

Disclosure statement

No potential conflict of interest was reported by the author(s).

Additional information

Notes on contributors

S. Kamalesh

S Kamalesh received BE degree in ECE from VLB Janakiammal College of Engineering and Technology, Coimbatore affiliated to Bharathiar University, Coimbatore, Tamilnadu in 2002. ME Degree in CSE from MepcoSchlenk Engineering College, Sivakasi, affiliated to Anna University, Chennai, Tamil Nadu in 2007. He completed his PhD degree in information and communication engineering, Anna University, Chennai, Tamilnadu in 2018. He is currently working as a professor in Department of Information Technology in Velammal College of Engineering and Technology,Madurai, India. His research interests include wireless sensor networks, IoT, AI, and ML etc.

A. Muthukrishnan

A Muthukrishnan received a bachelor of engineering degree in electrical and electronics engineering from RVS College of Engineering and Technology affiliated to Anna University Chennai, India in 2005 and master of engineering in VLSI design from Anna University Coimbatore, India in 2009. He received his PhD degree in information and communication engineering from Anna University Chennai, India in 2016. He is currently working as an associate professor in Department of Computer Science and Engineering in Vel Tech Rangarajan Dr. Sagunthala R&D Institute of Science and Technology Chennai, India. He had thirteen years of teaching and research experience in information and communication Engineering. His current research interest includes wireless sensor networks, IOT, VLSI design and its applications, and wireless communications. He was the recipient of the best achiever award of the Anna university regional campus Madurai in recognition of his outstanding research work in the area of wireless sensor networks in 2016. **Email:** muthuathi@gmail.com

Issue Purchase

- 30 days online access to complete issue
- Article PDFs can be downloaded
- Article PDFs can be printed

USD 100.00

Add to cart

* Local tax will be added as applicable

Related Research

People also read | Recommended articles | Cited by

‹ Back

SN Computer Science

A System Review on Fraudulent Website Detection Using Machine Learning Technique

Authors: P. Saraswathi, J. V. Anchitaalagammai, R. Kavitha Authors Info & Claims

SN Computer Science, Volume 4, Issue 6 • Oct 2023 • https://doi.org/10.1007/s42979-023-02084-6

Published: 13 September 2023 Publication History

Abstract

At present, scams and malicious websites are one of the most widespread and dangerous problems on the website. It brings enormous economic suffering and irretrievable losses to companies and individuals. This approach can strengthen the Internet's legitimacy and impose sanctions on criminals who engage in prohibited or malicious activities. However, governments still need a derivation to classify websites as dangerous or non-dangerous. However, several malicious and counterfeit goods are published on fraudulent websites to cheat consumers and make high and unfair profits. Due to the proliferation of such fraudulent websites, it is difficult to detect and identify them through manual inspection. Phishing attacks include various attacks, including spoofing malicious-based, DNS-based, data theft, email/spam, web-based delivery, and telephone-based phishing. We propose an integrated machine learning (ML) framework for fraudulent website detection to solve this problem. Artificial neural networks (ANN), support vector machine (SVM), random forests (RF), and K-nearest neighbor (K-NN) are algorithms to detect phishing websites accurately. Some URLs can be used to classify them as appropriate or phishing. Data from publicly available phishing websites can be collected from the UCIrvine ML repository for training and testing. Then, the results can be predicted using the features of the dataset. We conduct an in-depth literature review and propose methods for detecting phishing websites using ML methods.

References

1. Maktabar M, Zainal A, Maarof M, Kassim M: Content-based fraudulent website detection using supervised machine learning techniques. *Adv Intell Syst Comput* (2018) 734, 294 - 304. 10.1007/978-3-319-76351-4_30

2. Yang R, Zheng K, Wu B, Wu C, Wang X: Phishing website detection based on deep convolutional neural network and random forest ensemble learning. *Sensors (Basel)* (2021) 21(24), 8281 10.3390/s21248281.PMID:34960375;PMCID:PMC8709380

3. Rao RS, Pais AR: Detection of phishing websites using an efficient feature-based machine learning framework. *Neural Comput Appl* (2019) 31, 3851 - 3873. 10.1007/s00521-017-3305-0

Recommendations

Back

- Phishing is among the most concerning issues in a constantly changing world.…

Abstract

Phishing is among the most concerning issues in a constantly changing world. The increasing use of the Internet has led to a new way of stealing data, known as cybercrime. Cybercrime refers to stealin…

SN Computer Science

SAINT '11: Proceedings of the 2011 IEEE/IPSJ International Symposium on Applications and the Internet

In recent years, spam mails intending for ``One-click fraud" or ``Phishing" have become increasing. As one anti-spam technology, DNSBL based on the URLs or their corresponding IP addresses in the messages is well used. However, some spam mails that ...

Read More

Spam Mail Discrimination System Based on Behavior of DNS Servers Associated with URLs

SAINT '12: Proceedings of the 2012 IEEE/IPSJ 12th International Symposium on Applications and the Internet

As one of anti-spam technologies, DNSBL based on the URLs or their corresponding IP addresses in the messages is well used. However, some spam mails cannot be filtered by conventional DNSBLs since the spammers create websites using various techniques ...

Read More

0 Comments

Share

Best Newest Oldest

Nothing in this discussion yet.

View Issue's Table of Contents

Back

SN Computer Science

Early Risk Prediction of Diabetes Categorization Using Fuzzy K-Means Clustering Algorithm

R. Sangeethapriya
Assistant professor, Department of Information Technology, Sona college of Technology, Salem 636 005, Tamil Nadu

S. Gomathi
Assistant Professor, Department of Computer Science and Engineering, Dr. N.G.P Institute of Technology, Coimbatore 641048, Tamil Nadu.

B. Dhiyanesh
Associate Professor, Department of Computer Science and Engineering, Dr. N.G.P Institute of Technology, Coimbatore 641048, Tamil Nadu

J. K. Kiruthika
Assistant Professor (Sr.G), Department of Computer Science and Engineering, KPR Institute of Engineering and Technology, Coimbatore 641407, Tamil Nadu

P. Saraswathi
Assistant Professor, Department of Information Technology, Velammal College of Engineering and Technology, Madurai 625009, Tamil Nadu.

K. Divya
Assistant Professor, Department of Electrical and Electronics Engineering, Karpagam Institute of Technology, Coimbatore 641021, Tamil Nadu.

Keywords: Feature Selection, Classification, Clustering, Fuzzy Rules, Machine learning, diabetes

ABSTRACT

Diabetes mellitus (DM) is a metabolic disease that primarily results in high blood glucose levels. There are distinct clinical types, with Type 1 and Type 2 being the most common forms of diabetes. A significant increase has been observed in the number of young people suffering from type 1 diabetes over the past few years for this reason. Diabetes can become chronic with a long latency period in childhood and adolescence, as the symptoms in the early stages can be vague. This can make timely detection and treatment complex, possibly leading to delayed treatment. It is important to detect or prevent diabetes early. It can cause many complications, and the prediction of diabetes is not accurate for further analysis using previous methods. We introduced the new proposed method using learning (ML) approaches to overcome the issues. Based on the Fuzzy K-means Clustering and Support Vector Machine (FKMC-SVM) for deciding the classification model for diabetic prediction using a standard dataset, for an accurate result, Initially collected, the diabetic dataset is from the standard repository, and the second step is pre-processing to reduce the imbalanced data, normalizing the values from the dataset using Z-Score normalization, and then selecting the features based on the margin values using Threshold Recursive Feature Elimination (TRFE) to eliminate the values from the pre-processing dataset based on the maximum threshold values of the recursive features in the dataset. Then the fuzzy-based method is used to decide diabetes using fuzzy logic to create interpretable models and to diagnose diabetes early based on these classifiers, FKMC and SVM, and to design fuzzy rules. FKMC refers to a collection of data points where the points in one location share similarities or connections but differ from those in another cluster. Additionally, optimizing support vector machines with larger datasets may provide more accurate results and predict the likelihood of diabetes in both Type 1 and Type 2. This combined algorithm, F-KMC-SVM, compares the precision, accuracy, recall, and F1-score of different ML techniques used to classify diabetic patients.

DOWNLOADS

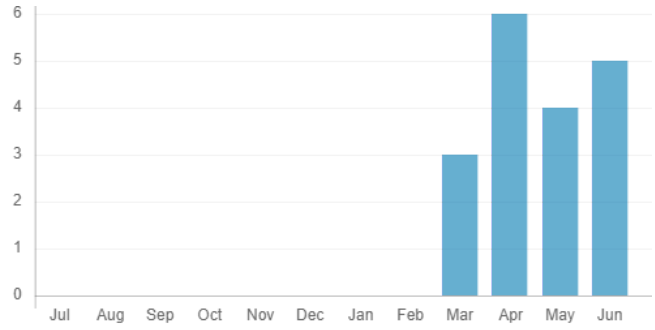

REFERENCES

U. Ahmed et al., "Prediction of Diabetes Empowered With Fused Machine Learning," IEEE Access, vol. 10, pp. 8529-8538, 2022.

P. G. Shynu, V. G. Menon, R. L. Kumar, S. Kadry and Y. Nam, "Blockchain-Based Secure Healthcare Application for Diabetic-Cardio Disease Prediction in Fog Computing," IEEE Access, vol. 9, pp. 45706-45720, 2021.

M. Goyal, N. D. Reeves, S. Rajbhandari and M. H. Yap, "Robust Methods for Real-Time Diabetic Foot Ulcer Detection and Localization on Mobile Devices," IEEE Journal of Biomedical and Health Informatics, vol. 23, no. 4, pp. 1730-1741, July 2019.

M. Z. M. Shamim, S. Alotaibi, H. S. Hussein, M. Farrag and M. Shiblee, "Diagnostic Accuracy of Smartphone-Connected Electrophysiological Biosensors for Prediction of Blood Glucose Level in a Type-2 Diabetic Patient Using Machine Learning: A Pilot Study," IEEE Embedded Systems Letters, vol. 14, no. 1, pp. 27-30, March 2022.

M. Gadaleta, A. Facchinetti, E. Grisan and M. Rossi, "Prediction of Adverse Glycemic Events From Continuous Glucose Monitoring Signal," IEEE Journal of Biomedical and Health Informatics, vol. 23, no. 2, pp. 650-659, March 2019.

X. Zeng, H. Chen, Y. Luo and W. Ye, "Automated Diabetic Retinopathy Detection Based on Binocular Siamese-Like Convolutional Neural Network," IEEE Access, vol. 7, pp. 30744-30753, 2019.

H. Kaushik, D. Singh, M. Kaur, H. Alshazly, A. Zaguia and H. Hamam, "Diabetic Retinopathy Diagnosis From Fundus Images Using Stacked Generalization of Deep Models," IEEE Access, vol. 9, pp. 108276-108292, 202.

V. K. Daliya, T. K. Ramesh and S. -B. Ko, "An Optimised Multivariable Regression Model for Predictive Analysis of Diabetic Disease Progression," IEEE Access, vol. 9, pp. 99768-99780, 2021.

G. Annuzzi et al., "Impact of Nutritional Factors in Blood Glucose Prediction in Type 1 Diabetes Through Machine Learning," IEEE Access, vol. 11, pp. 17104-17115, 2023.

M. K. Hasan, M. A. Alam, D. Das, E. Hossain and M. Hasan, "Diabetes Prediction Using Ensembling of Different Machine Learning Classifiers," IEEE Access, vol. 8, pp. 76516-76531, 2020.

Beneyto, A. Bertachi, J. Bondia and J. Vehi, "A New Blood Glucose Control Scheme for Unannounced Exercise in Type 1 Diabetic Subjects," IEEE Transactions on Control Systems Technology, vol. 28, no. 2, pp. 593-600, March 2020.

R. Ferdousi, M. A. Hossain and A. E. Saddik, "Early-Stage Risk Prediction of Non-Communicable Disease Using Machine Learning in Health CPS," IEEE Access, vol. 9, pp. 96823-96837, 2021.

M. S. Islam, M. K. Qaraqe, S. Belhaouari and G. Petrovski, "Long Term HbA1c Prediction Using Multi-Stage CGM Data Analysis," IEEE Sensors Journal, vol. 21, no. 13, pp. 15237-15247, 1 July1, 2021.

W. Wang, S. Wang, X. Wang, D. Liu, Y. Geng and T. Wu, "A Glucose-Insulin Mixture Model and Application to Short-Term Hypoglycemia Prediction in the Night Time," IEEE Transactions on Biomedical Engineering, vol. 68, no. 3, pp. 834-845, 2021.

Aliberti et al., "A Multi-Patient Data-Driven Approach to Blood Glucose Prediction," IEEE Access, vol. 7, pp. 69311-69325, 2019.

S. Huang, J. Li, Y. Xiao, N. Shen and T. Xu, "RTNet: Relation Transformer Network for Diabetic Retinopathy Multi-Lesion Segmentation," in IEEE Transactions on Medical Imaging, vol. 41, no. 6, pp. 1596-1607, 2022.

F. Haque, M. B. I. Reaz, M. E. H. Chowdhury, F. H. Hashim, N. Arsad and S. H. M. Ali, "Diabetic Sensorimotor Polyneuropathy Severity Classification Using Adaptive Neuro Fuzzy Inference System," IEEE Access, vol. 9, pp. 7618-7631, 2021.

M. M. Abdelsalam and M. A. Zahran, "A Novel Approach of Diabetic Retinopathy Early Detection Based on Multifractal Geometry Analysis for OCTA Macular Images Using Support Vector Machine," IEEE Access, vol. 9, pp. 22844-22858, 2021.

He, T. Li, N. Li, K. Wang and H. Fu, "CABNet: Category Attention Block for Imbalanced Diabetic Retinopathy Grading," IEEE Transactions on Medical Imaging, vol. 40, no. 1, pp. 143-153, Jan. 2021.

Y. Zhou, B. Wang, L. Huang, S. Cui and L. Shao, "A Benchmark for Studying Diabetic Retinopathy: Segmentation, Grading, and Transferability," IEEE Transactions on Medical Imaging, vol. 40, no. 3, pp. 818-828, March 2021.

Gothane, Suwarna, K. Srujan Raju, Saikumar Tara, and P. Devika. "Unsupervised learning towards hierarchical clustering." In AIP Conference Proceedings, vol. 2477, no. 1. AIP Publishing, 2023.

J. Narasimharao, A. V. Reddy, R. Regulagadda, P. Sruthi, V. Venkataiah and R. Suhasini, "Analysis on Rising the Life Span of Node in Wireless Sensor Networks Using Low Energy Adaptive Hierarchy Clustering Protocol," 2023 IEEE 5th International Conference on Cybernetics, Cognition and Machine Learning Applications (ICCCMLA), Hamburg, Germany, 2023, pp. 651-659, doi: 10.1109/ICCCMLA58983.2023.10346731.

Madala, S., Suvarna Vani, K., Jalapally, P., Srujan Raju, K., Somasekhar, G. (2022). Framework for Diabetic Retinopathy Classification. In: Satapathy, S.C., Bhateja, V., Favorskaya, M.N., Adilakshmi, T. (eds) Smart Intelligent Computing and Applications, Volume 2. Smart Innovation, Systems and Technologies, vol 283. Springer, Singapore. https://doi.org/10.1007/978-981-16-9705-0_58

PDF

PUBLISHED

24.03.2024

HOW TO CITE

Sangeethapriya, R. ., Gomathi, S. ., Dhiyanesh, B. ., Kiruthika, J. K. ., Saraswathi, P. ., & Divya, K. . (2024). Early Risk Prediction of Diabetes Categorization Using Fuzzy K-Means Clustering Algorithm. *International Journal of Intelligent Systems and Applications in Engineering*, *12*(20s), 423–431. Retrieved from https://ijisae.org/index.php/IJISAE/article/view/5154

More Citation Formats

ISSUE

Vol. 12 No. 20s (2024)

SECTION

Research Article

Most read articles by the same author(s)

- G. Gokila Deepa, B. Dhiyanesh, C. B. Selva Lakshmi, T. Yawanikha, I. Janani, R. Radha, Enhancing Chronic Kidney Disease Diagnosis with an Optimized Fuzzy Deep Neural Network: A Polycystic Kidney Disease Perspective , International Journal of Intelligent Systems and Applications in Engineering: Vol. 12 No. 20s (2024)
- A. Asha, B. Dhiyanesh, G. Kiruthiga, L. Shakkeera, Vinodkumar Jacob, Anita Venaik, Efficient Coronary Heart Disease Prediction: Enhanced Neural Network with Chaos Salp Decision and Feature Optimization , International Journal of Intelligent Systems and Applications in Engineering: Vol. 12 No. 20s (2024)
- A. Baseera, B. Dhiyanesh, Parveen Begam Abdul Kareem, P. Shanmugaraja, V. Anusuya, Integrative Approach for Precision Prediction of Chronic Kidney Disease: Anfis-Based Feature Selection and DCNN Classification , International Journal of Intelligent Systems and Applications in Engineering: Vol. 12 No. 20s (2024)

Similar Articles

- Vinayak Kishan Nirmale, C. Madhusudhana Rao, Mylapalli Ramesh, M. Nirmala, S. Girinath, Nellore Manoj Kumar, Fuzzy Integrated Latent Dirichlet Allocation Algorithm for Intrusion Detection in Cloud Environments , International Journal of Intelligent Systems and Applications in Engineering: Vol. 12 No. 17s (2024)

You may also start an advanced similarity search for this article.

ANNOUNCEMENTS

Information for Authors

March 6, 2023

Information for Authors:

We are pleased to inform that we are now collaborating with **Elsevier Digital Commons** for much better visibility of journal. Further authors will be able to observe their citations, metric like PlumX from journal website itself. **IJISAE** will be in transition from **OJS** to **Digital Commons framework** in next few months so if their is any queries or delays contact directly on ***editor@ijisae.org***

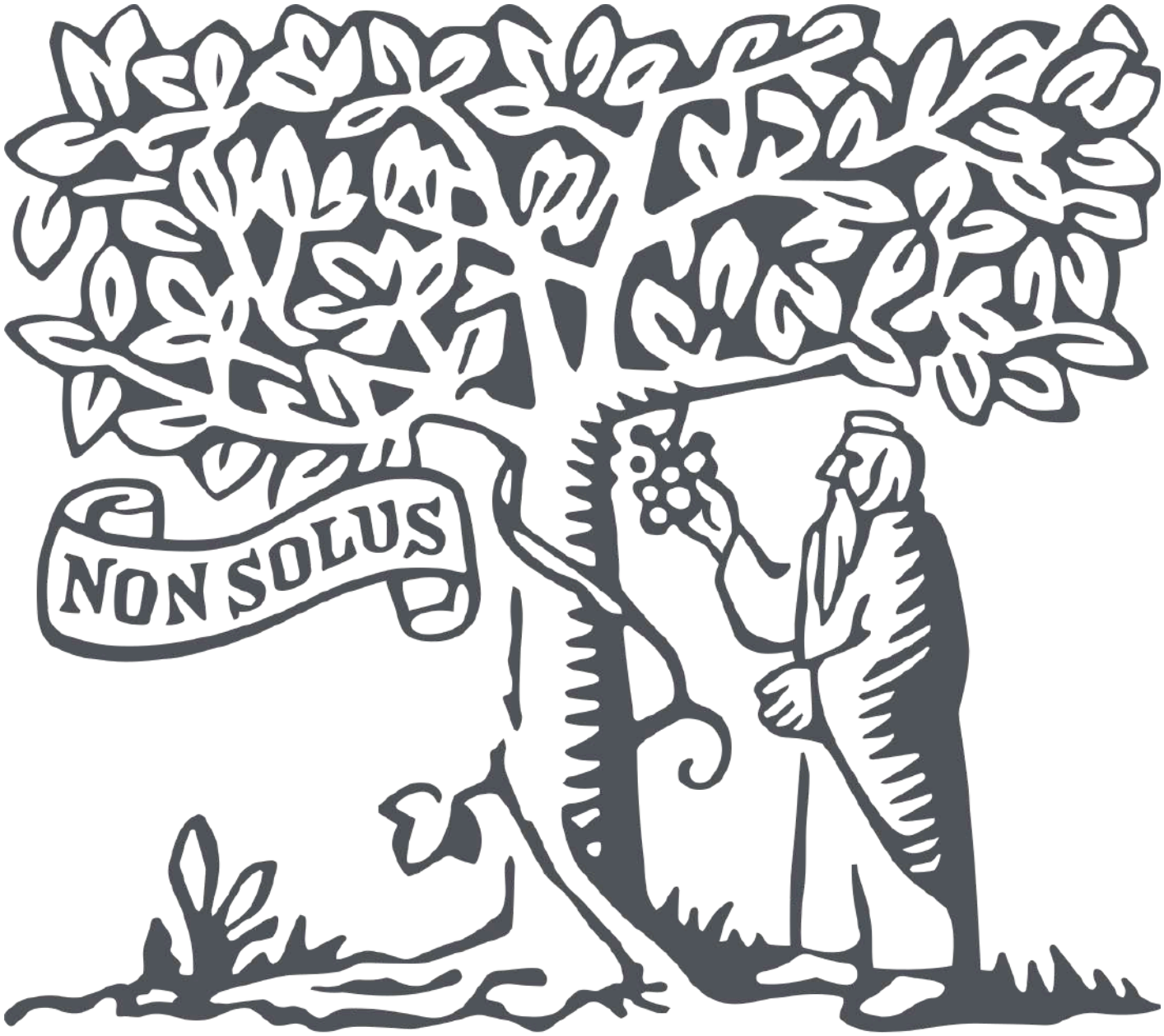

ELSEVIER

Editorial Team
Focus and Scope
Author Guidelines
Indexing
Publishing Process
New Submission
Publishing Ethics
Contact

Peer Review Process

INFORMATION

For Readers

For Authors

For Librarians

Indexed By

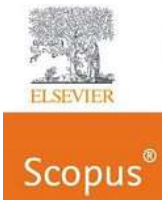

MOST READ

Ontology-based Multi-Agent System on Fuzzy Markup Language in Healthy Lifestyle
1285

Classification of Rice Varieties Using Artificial Intelligence Methods
820

Applications of Integration and Differentiation in Real Life
624

Advancements in Computing: Emerging Trends in Computational Science with Next-Generation Computing
463

Abstractive Long Text Summarization using Large Language Models
431

Quick links for:
Authors

- **Register** as a new author
- **Track** the status of your submissions
- **Submit** a new manuscript
- **Update** the details in your profile
- **Show the guidelines** for authors

Quick links for:
Peer Reviewers

- **Register** as a new Peer Reviewer
- **Overview** of a current review
- **Process** for undertaking reviews

Quick links for:
Editor and Section Editors

- **Overview** of new submissions
- **Assign** submissions to reviewers
- **Track progress** of revisions
- **Select** submissions for copy editing

Quick links for:
Editor and Publisher

- **Overview** of new submissions
- **Assign** submissions to Section Editors

Current Issue | Archives | Submit a manuscript | About the Journal
ISSN: 2147-6799

International Journal of
INTELLIGENT SYSTEMS AND APPLICATIONS IN ENGINEERING
ISSN:2147-6799 www.ijisae.org Original Research Paper

Optistroke: Harnessing Bat Algorithm-Driven Stacked Ensembles for Enhanced Stroke Prediction Using Machine Learning

Divya K [1], Sangeethapriya R [2], Gomathi S [3], Dhiyanesh B [4], Kiruthika J.K [5] Saraswathi P [6]

Submitted: 17/01/2024 **Revised**: 25/02/2024 **Accepted**: 03/03/2024

Abstract: Strokes are considered to be one of the most serious medical conditions in the world and must be diagnosed at an early stage so that the consequences for the patients can be minimized. The proposed BatOptiStroke is a novel technique that increases stroke prediction accuracy by using a stacked ensemble model powered by the Bat Algorithm (BA). To capture a wide range of prediction skills, BatOptiStroke combines a diversified selection of base models, such as Extreme Gradient Boosting (XGBoost), K Nearest Neighbors (KNN), and Support Vector Machines (SVM). By modifying the placements and velocities of the bats that reflect the fundamental models, the BA continuously optimizes the group's efficiency. This results in increased stroke prediction accuracy. On a sizable dataset of stroke patients, the BatOptiStroke framework's efficiency is thoroughly assessed in comparison to that of each of the base models and alternative ensemble approaches. Evaluation metrics validate BatOptiStroke's stroke prediction capabilities. The combined model set consistently outperforms individual base models, improving prediction accuracy and overall performance. Along with increased 97% accuracy, 89% precision, 95% recall, and a 93% F1 score, BatOptiStroke also contributes.

Keywords: *Stacked Ensemble, Gradient Descent, Prediction, Optimization, Machine Learning, Healthcare, Stroke*

1. Introduction

The World Health Organization (WHO) estimates that stroke accounts for 11% of all mortality globally and leaves millions permanently disabled. Stroke impacts individuals beyond the afflicted to their families, the healthcare system, and society as a whole [1]. The early detection and immediate treatment of a stroke are crucial to improving patient outcomes and reducing stroke disability. Access to competent medical care and prompt diagnosis of stroke symptoms are crucial elements that substantially impact patient survival and recovery. However, due to the multifactorial nature of stroke, accurate and reliable stroke prediction is difficult [2].

Artificial intelligence and machine learning in healthcare have garnered attention. These technologies make possible data analysis, disease detection, and prediction. Learning is one of the most successful approaches to improving prediction accuracy. Improved-accuracy ensembles are formed by bringing together models and leveraging each model's strengths to enhance accuracy. Specifically, stacked ensembles offer hope for industry sectors such as healthcare and banking, as well as weather forecasting [3]. In this study, a novel approach called the BatOptiStroke framework is proposed. It employs a Bat Algorithm (BA) directed by a stacked ensemble for stroke prediction. By taking advantage of DAO benefits, this framework also shows how group thinking can be used to resolve challenges in predictive modelling for strokes. BatOptiStroke equips a variety of abilities. We have included XGBoost, KNN, and SVM models. Thus, by moving the bat positions and classes in these models, the ensemble performance is dynamically optimised, and stroke predictions are made [4].

BatOptiStroke aims to enhance stroke forecast accuracy. This advance will help experts perform coolly in crucial situations where people's lives are almost at risk. BatOptiStroke improves on earlier models by combining base models and totally different features in one package. Also, the ensemble predictions improved after optimization using the Bat algorithm, which led to a rise in our model's precision.

This document introduces several significant technical innovations. BatOptiStroke presents an innovative way of thinking about stroke prediction. It combines the Bat algorithm-based stacked ensembles with various base models to optimize performance. It blends distinct predictive capabilities and requires little handwork from the designer. Thanks to the dynamic optimization ability introduced by the Bat Algorithm, this ensemble exploits the information space for better forecasting accuracy [5]. Secondly, experimental studies have shown that the BatOptiStroke ensemble improves stroke prediction accuracy. BatOptiStroke easily beats all kinds of single models and other existing ensemble methods in many evaluations on a large dataset of stroke scenarios. Because of its improved prediction accuracy and excellent performance, the ensemble is a reliable tool for assessing stroke risk [6]. Not only will accuracy be enhanced, but there are many practical applications for the BatOptiStroke system. Quick and exact stroke predictions can identify those at high risk when they are proven to be true. Healthcare workers will be able to intervene effectively with them. Early therapy can be significant for stroke control because it can greatly curtail adverse effects, boosting long-term outcomes [7].

In addition, BatOptiStroke will give you ideas for drawing accurate

[1] *Assistant Professor/EEE, Karpagam Institute of Technology, Coimbatore*
[2] *Assistant professor/IT, Sona college of Technology, Salem*
[3] *Assistant Professor/CSE, Dr.N.G.P Institute of Technology, Coimbatore.*
[4] *Associate Professor/CSE, Dr.N.G.P Institute of Technology, Coimbatore*
[5] *Assistant Professor/CSE, KPR Institute of Engineering and Technology, Coimbatore*
[6] *Assistant Professor/IT, Velammal College of Engineering and Technology, Madurai*

**** Corresponding Author Email: dhiyanu87@gmail.com***

NJC

ROYAL SOCIETY OF CHEMISTRY

PAPER

Cite this: *New J. Chem.*, 2024, **48**, 2962

$Zn@ZrO_2$ nanoparticles decorated on naringin-based sensor for electrochemical detection of *p*-nitrophenol and *o*-nitrophenol†

Ramesh Madhaiyan,[a] Umamatheswari Seeman, *[a] Sankar Chinnusamy *[b] and Jayavel Ramasamy[c]

Received 23rd November 2023,
Accepted 9th January 2024

DOI: 10.1039/d3nj05410a

rsc.li/njc

The development of modest and accurate electrochemical sensors for organic waste in water systems is of the highest priority. This study describes a method for synthesizing a $Zn@ZrO_2$ nanoparticle decorated naringin (NG) nanocomposite ($Zn@ZrO_2$/NG). Several techniques, such as XRD, FTIR, XPS, HR-SEM, EDX and HR-TEM, were used to investigate the morphology, structure and molecular properties of the $Zn@ZrO_2$/NG nanocomposite. The electrochemical properties of $Zn@ZrO_2$/NG were investigated using CV and DPV. The proposed sensor displayed strong linearity for *p*-nitrophenol (PNP) and *o*-nitrophenol (ONP) from 1 μM to 500 μM, with LOD of 1.14 μM and 1.03 μM, and sensitivity of 5.055 and 3.385 μA mM^{-1} cm^{-2}, respectively. In addition, the fabricated sensor possesses good sensitivity, great reproducibility, and high stability for the detection of PNP and ONP. The enhanced sensitivity of the sensor towards the detection of PNP and ONP could pave way for the detection of PNP and ONP in real samples.

1. Introduction

Nitrophenol is a highly harmful organic substance widely used as a precursor and intermediate for the manufacture of various products.[1,2] In particular, *p*-nitrophenol (PNP) and *o*-nitrophenol (ONP) are essential raw materials for the manufacture of various products, such as polymers, pharmaceuticals, dyes, leather, petroleum, pesticides, explosives and rubber.[3,4] Even at low concentrations, nitrophenol is a highly hazardous material, causing severe damage to the liver, kidney, blood, and central nervous system of humans, as well as being harmful to the environment.[5] Moreover, it is nondegradable, persisting for long periods in the environment. With the presence of a nitro group, phenols are highly polar in nature, so phenols are easily soluble in water and can produce damaging effects on the environment. Thus, it is imperative to develop a quick, inexpensive, and simple analytical method for the highly sensitive and accurate sensing of PNP and ONP. Currently, various techniques are available for the detection and removal of PNP and ONP, like capillary electrophoresis,[6] high performance liquid chromatography,[7] Raman spectroscopy,[8] gas chromatography,[9] and fluorescence/luminescent[10–12] and electrochemical methods.[13] However, these methods of analysis have some limitations, such as difficulty in operation, high cost, and long processing times. In comparison to these conventional detection techniques, the electrochemical method is the most promising analytical method because of its low cost, fast response, inexpensive instrumentation, simple operation, and ability to carry out its analysis *in situ*.[14–16]

However, the main challenges of using conventional electrodes that need to be overcome are their poor sensitivity and selectivity towards specific toxic and hazardous chemicals and their electrochemical detection in the presence of other interfering species. As a consequence, it is highly desirable to develop novel electrodes for the selective detection of *ortho*/*para*-nitrophenols.[17] The electrochemical response can be enhanced by modifying the surface of the electrode with an active substance, such as simple metal and metal oxide nanomaterials or nanocomposites. For example, Ag,[18] Au,[19] ZrO_2,[20] ZnO, AgO_2,[21] and Fe_2O_4[22] nanomaterials have great electrochemical detection capability for nitrobenzene because they are excellent catalysts. ZrO_2 nanoparticles are the most suitable materials for immobilizing molecules with oxygen-containing compounds because of their stability at high temperature,

[a] *PG and Research Department of Chemistry, Government Arts College (Affiliated to Bharathidasan University), Tiruchirappalli – 620 022, Tamil Nadu, India. E-mail: drsumamatheswari@gmail.com; Tel: +91-8438288510*
[b] *Department of Chemistry, Velammal College of Engineering and Technology, Madurai – 625 009, Tamil Nadu, India. E-mail: sankschem@gmail.com; Tel: +91-9944585257*
[c] *Centre for Nanoscience and Technology, Anna University, Chennai – 600 025, Tamil Nadu, India*

† Electronic supplementary information (ESI) available. See DOI: https://doi.org/10.1039/d3nj05410a

inability to react with chemicals, nontoxicity, and strong attraction to oxygen-containing compounds. These ZrO_2 nanoparticles also contain a three-dimensional platform with limited angles that can be changed to allow direct electron transfer between the protein and the conductor.[20] Owing to its appealing properties, ZrO_2 has been widely used in electrochemical sensors. Moreover, ZnO NPs are n-type semiconductors with a significant excited binding energy of 60 meV and a band gap value of 3.2 eV. ZnO nanoparticles exhibit excellent chemical stability, low cost, and nontoxicity. They also demonstrate the positive aspects of electrochemical sensors, such as excellent analyte interactions and electron transfer.[23] In the last few years, many research groups have developed Zn/ZnO-based electrochemical sensors to determine 4-nitrophenol, such as Ag_2O–ZnO nanocomposites,[24] GO/ZnO nanohybrids,[25] ZnO/RuO_2 NPs[26] and Co-doped ZnO-based hybrid nanocomposites.[27] Flavonoids are beneficial plant-derived secondary metabolites. Flavonoids are polyphenols with great anticancer, antibacterial, anti-inflammatory, antiviral, and antimicrobial abilities.[28] Additionally, their neutral functional groups, such as amine and hydroxyl groups, make them easy to dissolve in water and attach to metals.[29] Naringin is an important nutrient and flavanone glycoside made from naringenin and neohesperidose, which are both found in citrus products, such as grapefruit.[30] It has many benefits, such as antitumor, antiallergic, antimicrobial, and biosensor functions.[31–34] For example Sasya *et al.* developed an enzymeless electrochemical detection of superoxide based on naringin-copper nanocomposites, and the sensor exhibited good sensitivity in the range of 0.2–4.2 μM with a response time of <1 s.[35]

However, based on a literature review, a naringin-loaded Zn@ZrO_2 nanocomposite has not yet been developed for the quantification of nitrophenol derivatives. The present study describes the synthesis and biosensing applications for PNP and ONP based on Zn@ZrO_2/NG nanocomposites for the first time. Herein, a nanocomposite Zn@ZrO_2/NG was synthesized by the functionalization of Zn@ZrO_2 on an NG surface, which was then fabricated onto a GCE surface (Scheme 1) to produce an electrochemical sensor for accurate sensing of PNP and ONP. Additionally, the practicability of the Zn@ZrO_2/NG nanocomposite in drinking and river water was analyzed.

2. Experimental section

2.1. Chemicals

Zinc oxide (ZnO), zirconyl chloride octahydrate ($ZrOCl_2{\cdot}8H_2O$), ammonium hydroxide (NH_4OH), deionized water (DI water), ethanol (Et), *p*-nitrophenol (PNP), *o*-nitrophenol (ONP), bisphenol A (BPA), uric acid (UA), ascorbic acid (AA), glucose (Glu), hydrogen peroxide (H_2O_2), calcium chloride ($CaCl_2$), ferric chloride ($FeCl_3$), phosphate buffer solution (PBS), nitrobenzene (NB), 2-nitrotoluene (2-NT), 4-nitrotoluene (4-NT), 2,4-dinitrotoluene (DNT), aniline, and 3-nitroaniline (3-NA) were obtained

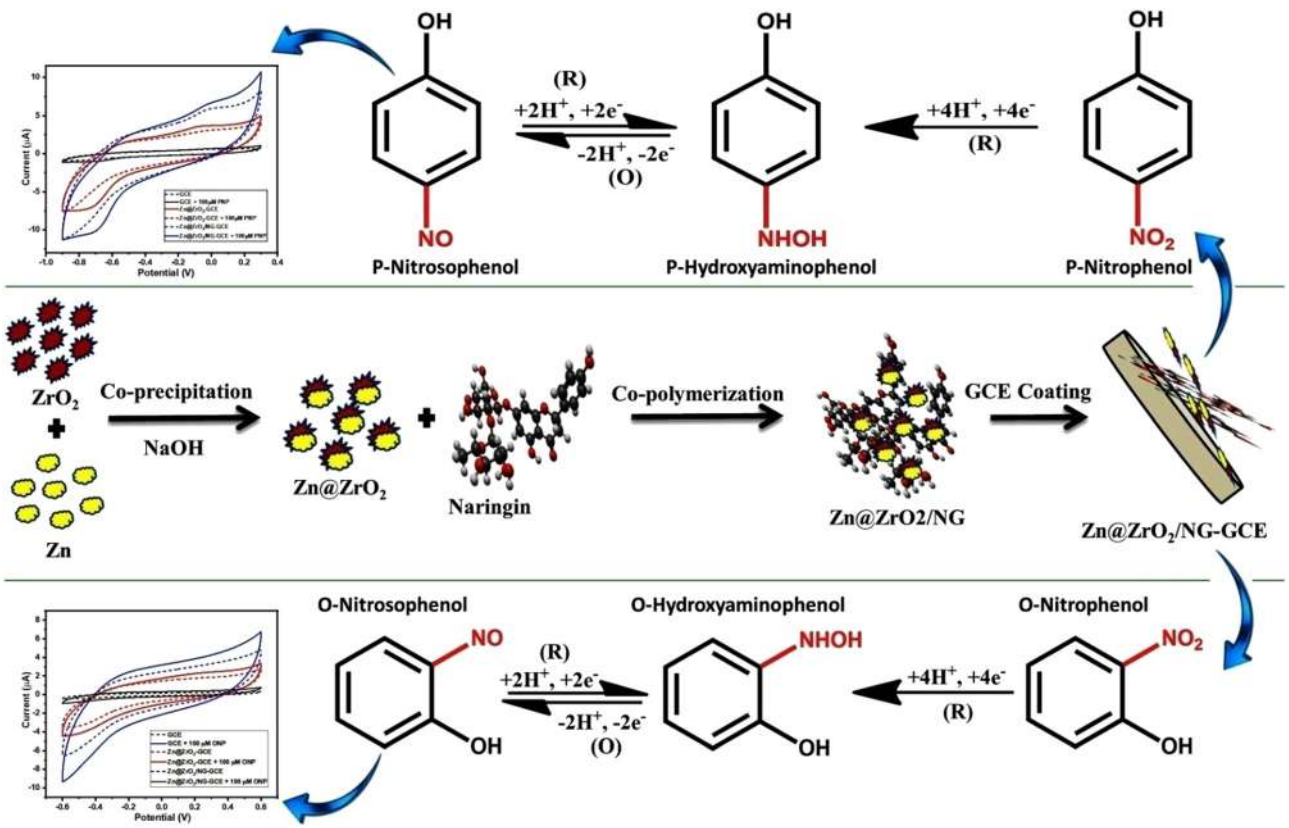

Scheme 1 Schematic diagram for the electrochemical detection of PNP and ONP.

from Sigma Aldrich and Sisco Research Laboratory, Pvt. Ltd and used without further purification.

2.2. Preparation of Zn@ZrO_2 nanoparticles

The fabrication steps are illustrated in Scheme 1. First, 1.61 g of $ZrOCl_2 \cdot 8H_2O$ and 0.20 g of ZnO were dissolved in 50 mL of DI water. After vigorous stirring for 5 min, NH_4OH solution was slowly added, maintaining the pH at 10, and stirred at room temperature for 4 h. After the reaction was complete, the product was centrifuged and washed numerous times in a DI water and ethanol mixture and dried at 80 °C overnight. Finally, the obtained product was annealed at 400 °C for 5 h at a heating rate of 5 °C min^{-1}.

2.3. Preparation of Zn@ZrO_2/NG nanocomposites

Zn@ZrO_2/NG nanocomposites were synthesized based on our previously reported procedure,[20] with novelty in the modification part which was done in a single step. Three different concentrated Zn@ZrO_2/NG nanocomposites, Zn@ZrO_2/NG(1 : 5), Zn@ZrO_2/NG(2 : 5), and Zn@ZrO_2/NG(3 : 5), were synthesized. Zn@ZrO_2 NPs (1 g%) and naringin (5 g%) were dissolved in a 50 : 50 ethanol : water mixture. The reaction mixture was stirred vigorously until the solution reached homogeneity. After adjusting the pH to 10 by adding 4 M NaOH solution, the resulting mixture was ultrasonicated for 2 h. The obtained product was washed with DI water and ethanol and dried at 80 °C overnight. Finally, the obtained product was annealed at 200 °C for 5 h at a heating rate of 5 °C min. The same method was used to synthesize the other two concentrated nanocomposites, Zn@ZrO_2/NG(2 : 5) and Zn@ZrO_2/NG(3 : 5). The fabricated Zn@ZrO_2/NG nanocomposites were characterized using various techniques.

2.4. Fabrication of Zn@ZrO_2/NG-GC electrode

Initially, 4 mg of Zn@ZrO_2/NG nanocomposite was dispersed in 500 μL of ethanol and 10 μL of 10% Nafion solution under ultrasonic conditions for 30 min. Then, 10 μL of dispersed Zn@ZrO_2/NG slurry was drop coated on the cleaned GCE surface and dried at ambient temperature. The as-prepared Zn@ZrO_2/NG-GC electrode was used for the electrochemical detection of PNP and ONP, in CV and DPV.

2.5. Electrochemical measurements

Electrochemical studies were undertaken with a CHI600E workstation with a working electrode of Zn@ZrO_2/NG-GCE, reference electrode of Ag/AgCl, and counter electrode of Pt wire. All experiments were carried out in a phosphate buffer solution (pH = 5). The electrocatalytic activity of Zn@ZrO_2/NG-GCE towards PNP and ONP was studied by cyclic voltammetry in the potential range of −0.9 to 0.3 V for PNP and −0.6 to 0.6 V for ONP with a scan rate of 50 mV s^{-1}. Then, the quantitative estimation of PNP and ONP was carried out using DPV with a range of potential of −0.95 to −0.75 V for PNP and −0.75 to −0.45 V for ONP.

3. Results and discussion

3.1. Characterization of the Zn@ZrO_2/NG nanocomposite

The composition ratio of the constituents in the sensor is important to determine their uniqueness. Thus, metal

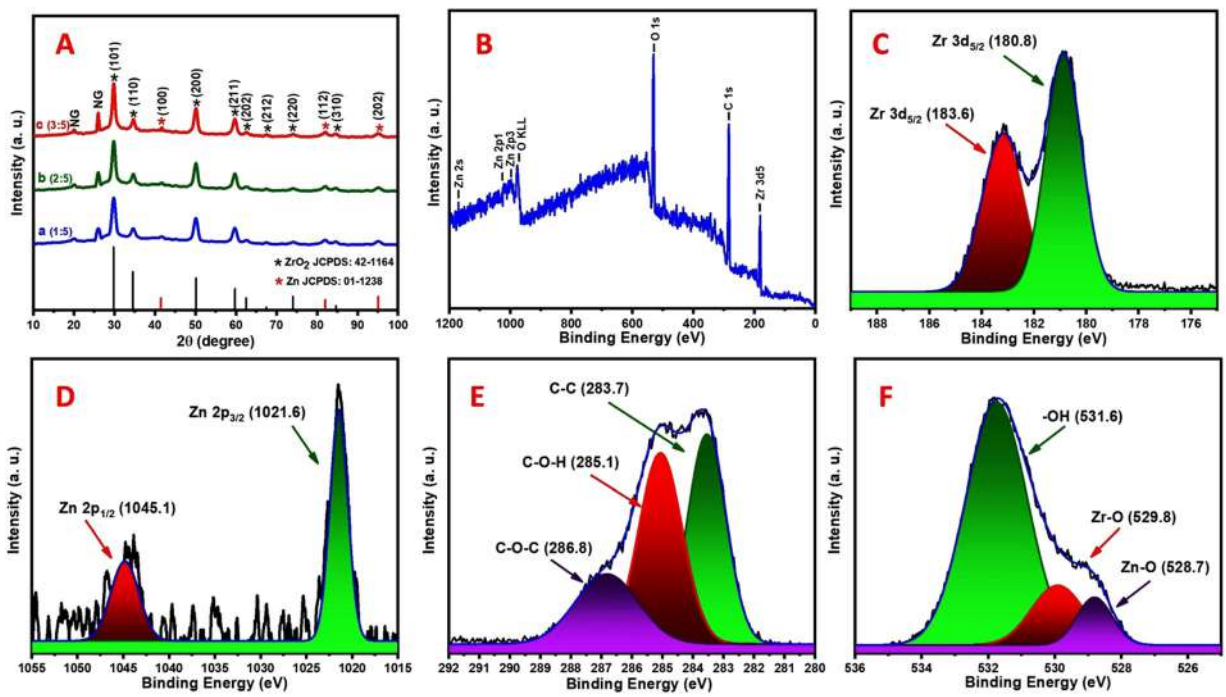

Fig. 1 (A) XRD patterns of the Zn@ZrO_2/NG nanocomposite with different concentrations of Zn@ZrO_2 NPs. (B) XPS survey spectrum of the Zn@ZrO_2/NG nanocomposite. (C) Zr 3d spectrum, (D) Zn 2p spectrum (E) C1 spectrum and (F) O1 spectrum.

nanocomposites were synthesized at three concentration Zn@ZrO_2/NG ratios of 1 : 5 (a), 2 : 5 (b), and 3 : 5 (c). The 1 : 5 (a), 2 : 5 (b), and 3 : 5 (c) crystal structures of Zn@ZrO_2/NG nanocomposites are shown in Fig. 1A. The characteristic diffraction peaks located at 29.8, 34.8, 50.1, 59.8, 62.5, 67.5, 74.1, 84.6 correspond to the (101), (110), (200), (211), (202), (212), (220), and (310) crystal planes of the tetragonal structure of ZrO_2, according to the JCPDS data for ZrO_2 (JCPDS 42-1164).[36] Conversely, the diffraction peaks located at 41.7°, 82.12°, 95.2° (2θ) correspond to (100), (112), (202) reflections, respectively, and agree with the crystal planes of the hexagonal structure of Zn (JCPDS 01-1238).[37] These results suggest a mixture of both crystalline phases, which is commonly observed in a ZrO_2 matrix, when calcined at a similar temperature. The additional diffraction peaks were attributed to the naringin substrate. These results demonstrate the successful synthesis of the Zn@ZrO_2/NG nanocomposite. The particle size of the nanocomposites was determined using the Debye–Scherrer equation, and the calculated average particle sizes were 10, 13, and 14 nm. The results revealed that the particle size increased with increasing concentration of Zn@ZrO_2 NPs.

The FTIR spectra of Zn@ZrO_2/NG(1 : 5), (2 : 5) and (3 : 5) nanocomposites were recorded in the range 400–4000 cm^{-1} (Fig. S1, ESI†). The band appearing at 1086.16 cm^{-1} is ascribed to C–O–C stretching vibrations and that at 1354.15 cm^{-1} is due to CH and CH_2 stretching vibrations of the naringin molecule. The bands appearing at 1610.27 and 3412.64 cm^{-1} are due to the bending and stretching vibrations of –OH in the naringin molecule. A distinct peak at 646.64 cm^{-1} corresponds to the M–OH peak and is observed for all samples. Therefore, the FTIR study suggests that the OH group of naringin binds to the Zn@ZrO_2 group of the synthesized nanoparticles.[38]

The chemical configuration and elemental arrangement of the Zn@ZrO_2/NG nanocomposite were determined by XPS, and the survey spectrum is shown in Fig. 1B. In Fig. 1C, the high-resolution XPS spectrum of Zr $3d_{5/2}$ could be fitted to two peaks at 180.8 and 183.6 eV corresponding to Zr $3d_{5/2}$ and Zr $3d_{3/2}$. For Zn, in the XPS spectrum of Zn 2p (Fig. 1D), we observe two obvious peaks at 1021.6 and 1045.1 eV, which indicate Zn $2p_{3/2}$ and Zn $2p_{1/2}$. This confirms that Zn is dispersed among the ZrO_2 lattice and exists in the form of divalent ions,[39] which supports the conclusion of XRD results. In the Zn 2p spectra shown in Fig. 1D, two peaks are located at 1021.6, 1045.1 eV for Zn $2p_{3/2}$ and Zn $2p_{1/2}$. In Fig. 1E, the C 1s spectrum presents three peaks located at 283.7, 285.1 and 286.8 eV, corresponding to C–C, C–O–H and C–O–C, respectively. As shown in Fig. 1F, the O1s spectrum has three distinct peaks at 528.7, 529.8 and 531.6 eV relating to Zn–O, Zr–O and –OH. Consequently, the Zn@ZrO_2/NG nanocomposite had been effectively fabricated.

The structures of Zn@ZrO_2/NG(1 : 5), Zn@ZrO_2/NG(2 : 5) and Zn@ZrO_2/NG(3 : 5) nanocomposites were examined by HR-SEM, as depicted in Fig. 2A–C. The image of the prepared nanocomposites shows a random agglomeration of pure sphere-shaped Zn@ZrO_2 NPs on the naringin surface. Zn@ZrO_2/NG nanocomposites consist of spherical Zn@ZrO_2 particles with sizes 1 : 5 = 10, 2 : 5 = 13 and 3 : 5 = 14 nm, which are dispersed across the surface of the naringin. The presence of different concentrations of Zn@ZrO_2 NPs on the surface of the naringin results in a change in the particle size and an increase in surface area and number of active sites, which improves the electron transport during the redox process. The EDX spectrum (inset to Fig. 2A–C) indicates the presence of Zn, Zr, O and C atoms in Zn@ZrO_2/NG nanocomposites without any impurities.

The structures of Zn@ZrO_2/NG nanocomposites were further confirmed by HR-TEM analysis (Fig. 2D–F). The prepared

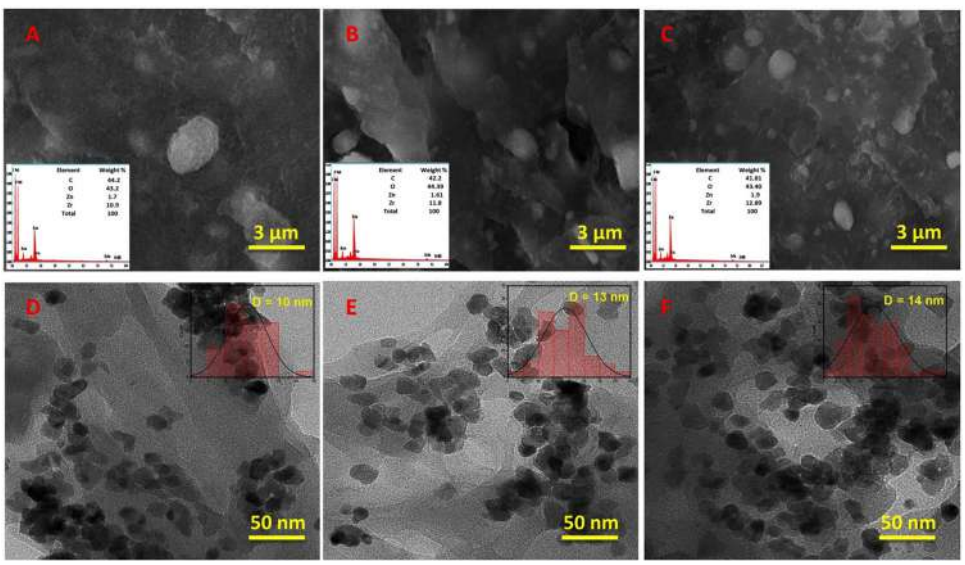

Fig. 2 (A) HR-SEM image of Zn@ZrO_2/NG(1 : 5) (inset: EDS spectrum), (B) HR-SEM image of Zn@ZrO_2/NG(2 : 5) (inset: EDS spectrum), (C) HR-SEM image of Zn@ZrO_2/NG(3 : 5) (inset: EDS spectrum). (D) HR-TEM image of Zn@ZrO_2/NG(1 : 5) (inset: histogram plot), (E) HR-TEM image of Zn@ZrO_2/NG(2 : 5) (inset: histogram plot), (F) HR-TEM image of Zn@ZrO_2/NG(3 : 5) (inset: histogram plot).

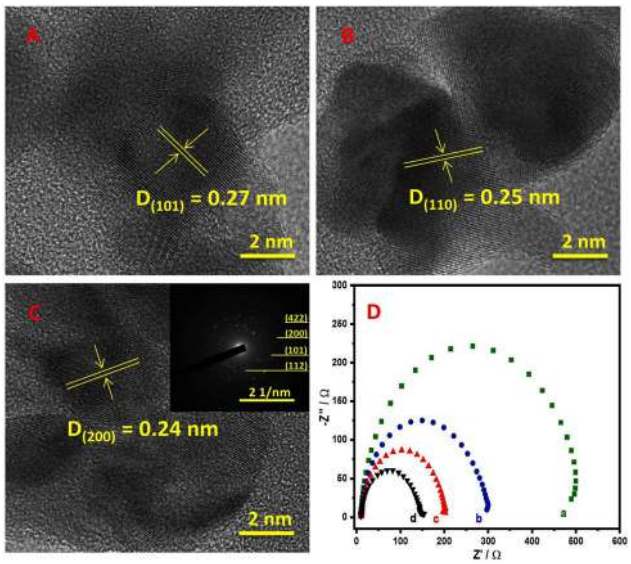

Fig. 3 (A) IFFT image of Zn@ZrO_2/NG(1 : 5) nanocomposite. (B) IFFT image of Zn@ZrO_2/NG(2 : 5) nanocomposite. (C) IFFT image of Zn@ZrO_2/NG(3 : 5) nanocomposite. (D) EIS spectrum of Zn@ZrO_2/NG nanocomposites.

nanocomposites were clearly observed to be spherical in shape and agglomerated in the foliated structure of naringin where the particle sizes of the composites were 1 : 5 = 10, 2 : 5 = 13 and 3 : 5 = 14 nm.

The HR-TEM images in Fig. 3A–C further revealed that the particles have distinct lattice fringes, corresponding to $D_{(101)}$ = 0.27, $D_{(110)}$ = 0.25 and $D_{(200)}$ = 0.24 nm of the tetragonal plane of Zn@ZrO_2 (JCPDC 42-1164). The crystalline structure of the Zn@ZrO_2/NG composite is clearly shown in the inset to Fig. 3C, which corresponds to the SAED. The SAED pattern shows the interplanar distances, $D_{(112)}$ = 1.92, $D_{(101)}$ = 1.17, $D_{(200)}$ = 0.97 and $D_{(422)}$ = 0.77, which well matched JCPDS 42-1164 where the composites are polycrystalline in nature.

3.2. Electrochemical response towards PNP

3.2.1. Electrochemical impedance spectroscopy (EIS). Electrochemical impedance spectroscopy (EIS) is a useful method for measuring the electron conduction behavior of the interface between fabricated electrodes and an electrolyte. The EI spectrum was obtained for four different electrodes, bare GCE (a), Zn@ZrO_2/NG-GCE(1 : 5) (b), Zn@ZrO_2/NG-GCE(2 : 5) (c) and Zn@ZrO_2/NG-GCE(3 : 5) (d) in the presence of 5 mM $K_3[Fe(CN)_6]$, as shown in Fig. 3D. In the highest frequency band, nearly all electrodes showed one semicircle.

The electrocatalytic activity of the fabricated electrode can be calculated from the standard change in current density (I_0) according to eqn (1):[40]

$$I_0 = RT/nFR_{ct} \quad (1)$$

The current densities (I_0) of fabricated electrodes were 0.0513, 0.0855, 0.128 and 0.188 μA cm^{-2}. From the results, the Zn@ZrO_2/NG(3 : 5) electrode shows a higher standard change current density (I_0 = 0.188 μA cm^{-2}) than other electrodes, which indicates that Zn@ZrO_2/NG-GCE(3 : 5) shows good electrocatalytic activity. Therefore, we chose the Zn@ZrO_2/NG-GCE(3 : 5) electrode for further electrochemical analysis.

3.3. Electrochemical detection of *p*-nitrophenol by cyclic voltammetry (CV)

The electrocatalytic behavior of fabricated Zn@ZrO_2/NG electrodes was examined by CV measurements. The CV experiments were carried out in a phosphate buffer solution at a pH of 5.0 and at a scan rate of 50 mV s^{-1} with and without 100 μM of PNP (Fig. 4A). No redox peaks were observed in the bare GCE. The fabricated Zn@ZrO_2-GCE exhibited a significant reduction peak (red) at −0.79 V. However, the modified Zn@ZrO_2/NG-GCE(3 : 5) exhibits a high reduction peak (red) at −0.79 V and a reversible peak (ox) at −0.05 V in the presence of 100 μM of PNP. This result confirmed that the Zn@ZrO_2/NG-GC(3 : 5) nanocomposite exhibits higher sensitivity for the detection of 4-nitrophenol.

Investigation into the kinetics of the electrode reaction was performed with CV at different scan rates. Fig. 4B illustrates the CV curves of the reduction of 100 μM of PNP on Zn@ZrO_2/NG-GCE obtained at different scan rates from 10 to 100 mV s^{-1}. It can be observed that the reduction peak current linearly increases with increasing scan rate. The insert in Fig. 4B shows the linear relationship between the reduction peak current (I_p) and scan rate (ν) in the range of 10–100 mV s^{-1}. The electrochemical process is governed by diffusion, as illustrated by the linear behaviour of I_{pc} *vs.* the square root of the scan rate (ν) with linear regression given by $I_{pa} = -1.119x - 0.869$ (R^2 = 0.98841) and $I_{pc} = 0.724x - 0.906$, R^2 = 0.99081 (inset Fig. 4B). The observed peak current at −0.79 V can be ascribed to the *p*-nitrophenol being directly reduced to the corresponding *p*-nitrosophenol with the transfer of six electrons and protons in the reduction side. Reversible redox conversions take place between *p*-hydroxyaminophenol and *p*-nitrosophenol, resulting in the appearance of an oxidation peak at −0.05 V. Based on an earlier report, a possible mechanism for the fabricated electrode reaction is proposed in Scheme 1.[41]

3.3.1. Differential pulse voltammetry (DPV) analysis. The DPV technique was used to optimize the electrochemical parameters to investigate the correlation between the reduction peak current and concentration of PNP. Fig. 4C illustrates the DPV spectra obtained at three sets of concentration (1–500 μM) (see Table S1 in ESI†) of PNP in a phosphate buffer solution at pH 5 and at a scan rate of 50 mV s^{-1}. At 0.79 V, the PNP reduction peak current linearly increased with increasing concentration of PNP. Furthermore, the linear regression equation inset in Fig. 4C gives $I_{pc} = -0.0353x - 3.456$ with an R^2 of 0.99782. The estimated LOD for the fabricated Zn@ZrO_2/NG-GC electrode was 1.14 μM, calculated from LOD = $3\sigma/S$ (σ = standard deviation, S = slope of the calibration plot)[42] and sensitivity = 5.055 μA mM^{-1} cm^{-2} which was calculated with S = slope of the curve/active surface area.[43] We compare the obtained results with other non-enzymatic nitrophenol sensors using metal/metal oxide/organic molecules in Table S2 (ESI†).

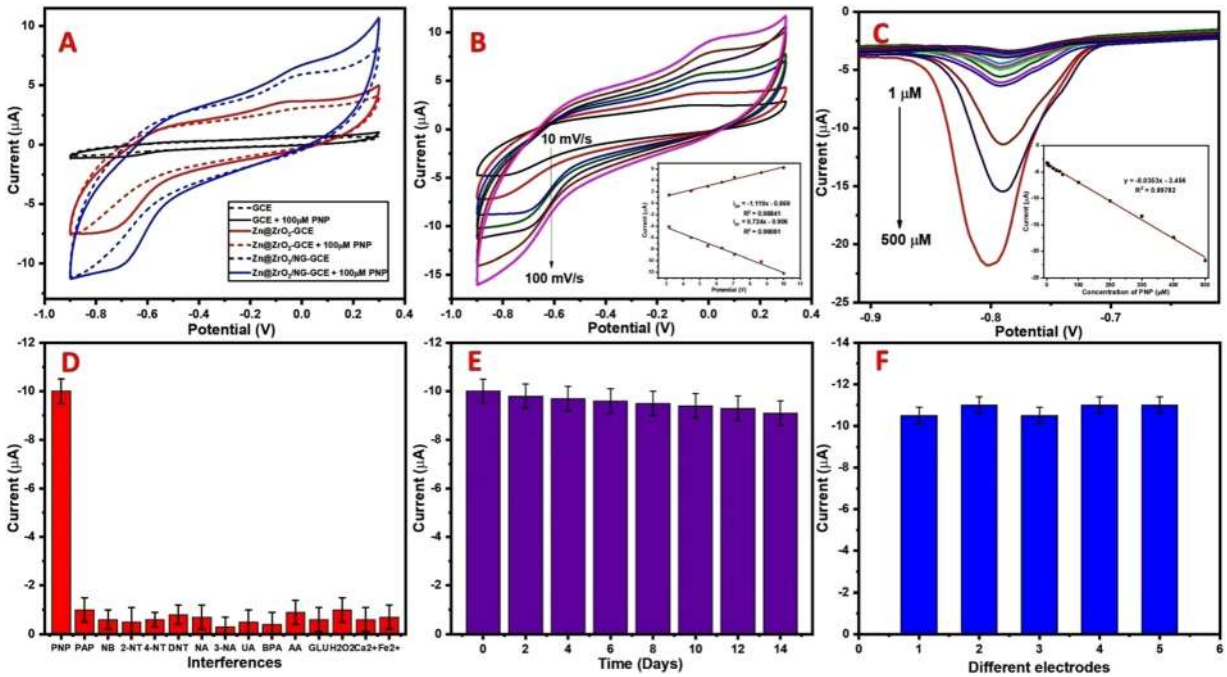

Fig. 4 (A) CVs of bare GCE, Zn@ZrO_2-GCE and Zn@ZrO_2/NG-GCE in a solution containing 100 μM of PNP at a scan rate of 50 mV s^{-1}. (B) CVs of various scan rates (10–100 mV s^{-1}). (C) DPV spectrum for Zn@ZrO_2/NG-GCE at various concentrations of PNP (1–500 μM). (D) Interference analysis. (E) Stability study recorded up to 14 days with 100 μM of PNP. (F) Reproducibility analysis.

The $ZnZrO_2$/NG electrode provided exceptional electrocatalytic activity as well as a broad linear detection range and a low LOD for PNP. These exceptional properties are a result of the large specific area, high porosity and synergistic relationships of the modified electrodes.

3.3.2. Selectivity, stability and reproducibility. In addition, an anti-interference study was conducted to assess the selectivity of Zn@ZrO_2/NG-GCE because environmental water contains numerous organic and inorganic contaminants. The influence of neighboring organic compounds like NB, 2-NT, 4-NT, 2,4-DNT, aniline, 3-NA, PAP, BPA, UA, AA, Glu, H_2O_2 and inorganic ions like Ca^{2+} and Fe^{2+} on the detection of PNP was studied, which showed almost no interference with the current response (Fig. 4D). Hence, it is suggested that Zn@ZrO_2/NG-GCE has remarkable anti-interference and selectivity for the detection of PNP. To determine the electrochemical capability of Zn@ZrO_2/NG-GCE, a study was carried out to examine its stability and reproducibility. Fig. 4E exhibits the stability of the reduction current for PNP detection for 14 consecutive days. The low RSD for PNP (3.01%) demonstrates that Zn@ZrO_2/NG is more stable. We examined the reproducibility of PNP detection under ideal conditions and compared it with five modified electrodes using the same method (Fig. 4F). The peak current response to PNP can be well repeated, indicating that Zn@ZrO_2/NG shows excellent reproducibility.

3.3.3. Real-sample analysis. Finally, the practicability of Zn@ZrO_2/NG-GCE was investigated by the standard addition method to determine PNP in real water samples. The water samples were filtered before the experiment to remove any suspended contaminants. Different concentrations of PNP were introduced to these water samples to allow further study. The concentration of PNP in the above water samples was determined by the DPV method and a linear regression equation between current and concentration (Fig. S3A and B, ESI†). The average recoveries of PNP ranged from 98% to 99.3%, and the RSD ranged from 1.04% to 1.56% (Table 1), indicating a high level of accuracy and feasibility in determining the presence of PNP in real water samples with fabricated Zn@ZrO_2/NG-GCE.

3.4. Electrochemical behavior of ONP on Zn@ZrO_2/NG

CV was used to investigate the electrochemical activity of Zn@ZrO_2/NG-GCE towards *o*-nitrophenol. Fig. 5A shows the CV curves of bare GCE, Zn@ZrO_2-GCE and Zn@ZrO_2/NG-GCE with and without the addition of 100 μM of ONP in PBS

Table 1 Determination of the concentrations of PNP and ONP in tap and river water with the $ZnZrO_2$/NG-GCE sensor

Analytes	Sample	Spiked amount (μM)	Found amount (μM)	Recovery (%)	RSD (%)
PNP	Tap water	5	4.93	98.6	1.21
		10	9.8	98	1.56
		15	14.9	99.3	1.40
	River water	5	4.91	98.2	1.42
		10	9.86	98.6	1.51
		15	14.83	98.8	1.04
ONP	Tap water	5	4.95	99	1.74
		10	9.83	98.3	1.14
		15	14.85	99	1.51
	River water	5	4.94	98.8	1.72
		10	9.87	98.7	1.54
		15	14.93	99.5	1.02

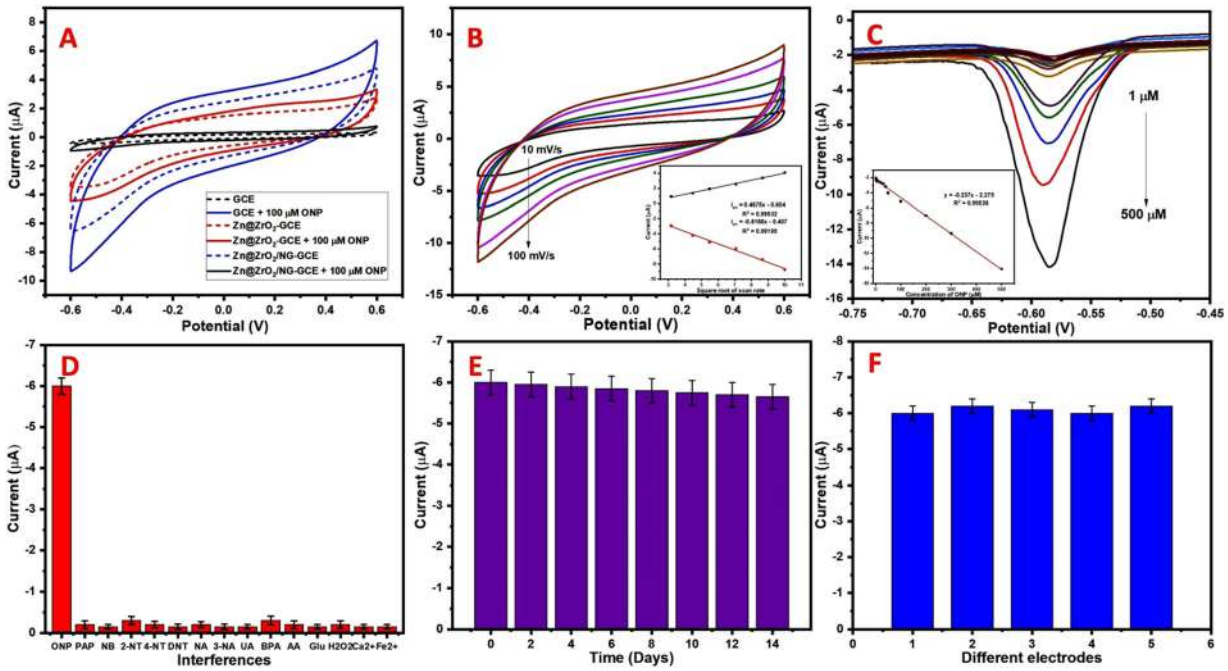

Fig. 5 (A) CVs of bare GCE, Zn@ZrO_2-GCE and Zn@ZrO_2/NG-GCE in a solution containing 100 μM of ONP at a scan rate of 50 mV s^{-1}. (B) CVs of various scan rates (10–100 mV s^{-1}). (C) DPV spectrum for Zn@ZrO_2/NG-GCE at various concentrations of ONP (1–500 μM). (D) Interference analysis. (E) Stability study recorded up to 14 days with 100 μM of ONP. (F) Reproducibility analysis.

solution. Either with or without ONP, there is no particular current response on the bare GCE. In addition, the redox peak current increased gradually on Zn@ZrO_2-GCE and Zn@ZrO_2/NG-GCE, indicating enhanced electrochemical detection of ONP. The redox peak potential of ONP on Zn@ZrO_2/NG-GCE exhibits a high current response at −0.58 V compared to bare GCE and Zn@ZrO_2-GCE due to the enhanced electrocatalytic action, high surface area and excellent conductivity of the Zn@ZrO_2/NG-GC electrode. Fig. 5B shows CV plots of Zn@ZrO_2/NG-GCE obtained at various scan rates from 10 to 100 mV s^{-1} with 100 μM of ONP in PBS solution. The peak current linearly increased with increasing scan rate. The inset to Fig. 5B illustrates the correlation plot between I_{pc} and the square root of scan rate, indicating that the observed process is diffusion controlled with linear regression equations, I_{pa} = $0.4675x - 0.654$ (R^2 = 0.99352) and $I_{pc} = -0.8188x - 0.417$ (R^2 = 0.99195). A possible mechanism for the reaction of the fabricated Zn@ZrO_2/NG-GCE is exhibited in Scheme 1.

3.4.1. Differential pulse voltammetry (DPV) analysis. The electrochemical performance of the Zn@ZrO_2/NG-GC(3 : 5) electrode was investigated by DPV in PBS solution containing various concentrations of ONP (1–500 μM). The reduction peak current increased linearly with increasing ONP concentration at −0.58 V (Fig. 5C). The fabricated Zn@ZrO_2/NG-GC electrode displayed a significant level of linearity in the relationship between the current response and the concentration of ONP with linear regression equation, $I_{pc} = -0.0353x - 3.456$ with correlation R^2 = 0.99782 (inset to Fig. 5C). The LOD of the fabricated Zn@ZrO_2/NG-GC electrode is 1.03 μM and the sensitivity is 3.385 μA mM^{-1} cm^{-2}. The linearity, sensitivity and LOD of the fabricated Zn@ZrO_2/NG-GCE in the detection of ONP were compared with earlier reports, as shown in Table S3 (ESI†). The obtained results demonstrate that the developed Zn@ZrO_2/NG-GCE sensor exhibits significant potential for the detection of ONP.

3.4.2. Selectivity, reproducibility, repeatability and stability. The selectivity of the fabricated electrode was examined with commonly used interference substances, such as NB, 2-NT, 4-NT, 2,4-DNT, aniline, 3-NA, PAP, UA, BPA, AS, Glu, H_2O_2, Ca^{2+} and Fe^{2+}, in PBS solution, which have minimal impact on the current response (Fig. 5D). Therefore, it is suggested that the Zn@ZrO_2/NG-GC electrode exhibits notable selectivity in the detection of ONP. Fig. 5D gives the results that the Zn@ZrO_2/NG-GC sensor shows satisfactory selectivity in the interference experiment and the relative standard deviation (RSD) is less than ±3.12%. The addition of *p*-nitrophenol has a slight influence on the detection of *o*-nitrophenol, which can be recognized in the reduction potentials of *o*-nitrophenol and 4-NP being different as well as the Zn@ZrO_2/NG-sensor possessing excellent selectivity.

A study was carried out to assess the reproducibility and stability of the fabricated electrode to establish its electrochemical capabilities. Fig. 5E presents the stability curve displaying the reducing current for ONP detection over a period of 14 days. The related standard deviation of ONP (2.10%) indicates that the Zn@ZrO_2/NG electrode exhibited a higher level of stability. The reproducibility of ONP detection was further assessed for the five fabricated Zn@ZrO_2/NG-GC electrodes using the same method (Fig. 5F). ONP detection exhibits a very repeatable peak current response, suggesting that the Zn@ZrO_2/NG material possesses outstanding reproducibility.

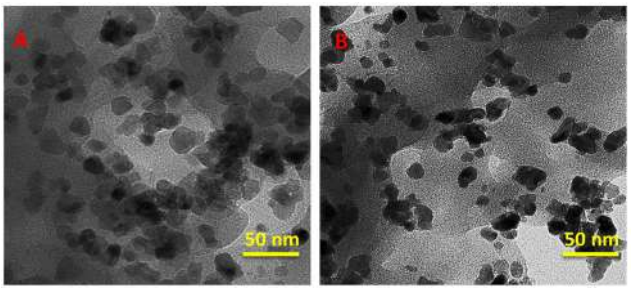

Fig. 6 HR TEM morphology of Zn@ZrO_2/NG-GCE before (A) and after (B) the reduction of nitrophenol.

3.4.3. Real sample analysis. The practicability of the fabricated Zn@ZrO_2/NG-GCE sensor was assessed by the standard addition method to quantify ONP in real water samples. Various concentrations of ONP in water samples were evaluated using the DPV method (Fig. S4A and B, ESI†). The average recoveries of the sensor in detecting ONP in real water samples ranged from 98.7% to 99.5% with a RSD of 1.02% to 1.74%, as shown in Table 1. The results suggest that the developed Zn@ZrO_2/NG-GCE sensor exhibits the possibility of precise, selective and highly sensitive detection of ONP in water samples.

3.4.4. Analysis of sensor surface morphology by HR-TEM. The stability of Zn@ZrO_2/NG-GCE was confirmed by analyzing the surface of Zn@ZrO_2/NG-GCE using HR-TEM at room temperature. HR-TEM was recorded before and after the detection of PNP and ONP using CV, as shown in Fig. 6. The images show similar spherical morphology of Zn@ZrO_2/NG-GCE before and after the electrochemical reaction, which proves the stability of the electrode. Moreover, the electrochemical reaction of PNP and ONP did not affect the surface morphology of Zn@ZrO_2/NG-GCE.

4. Conclusion

In summary, the sensing ability of a naringin–metal/metal oxide complex has been investigated for the first time. A Zn@ZrO_2/NG nanocomposite was synthesized *via* a simple and cost-effective method. The effectiveness of the fabricated composite was assessed in terms of its electrochemical sensing capability for PNP and ONP. The Zn@ZrO_2/NG nanocomposite modified GCE possesses smaller interface electron transfer resistance and electrons are more easily transferred by the surface of the Zn@ZrO_2/NG nanocomposite modified GCE than by the bare electrode. Based on the observed results, it was found that the Zn@ZrO_2/NG fabricated GCE showed exceptional efficacy in the electrochemical detection of PNP and ONP with an LOD for PNP of 1.14 μM and for ONP of 1.03 μM. The fabricated sensor exhibits excellent selectivity and stability when used for the estimation of PNP and ONP in real water samples. Hence, new sensing platforms which consist of Zn@ZrO_2/NG nanocomposites produced from MOFs exhibit promising potential for the detection of various analysts present in the environment.

Author contributions

Ramesh: formal analysis, data curation, writing – original draft, validation. Umamatheswari: supervision, investigation, formal analysis, data curation, validation, writing – review & editing, conceptualization, methodology. Sankar: resources, formal analysis, data curation, writing – review & editing. Jayavel: supporting the project.

Conflicts of interest

The authors declare that they have no known competing financial interests or personal relationships that could have appeared to influence the work reported in this paper.

Acknowledgements

The authors express their sincere gratitude to the Centre for Nanoscience and Technology, Anna University and SRM Central Instrumentation Facility (SCIF) for providing all necessary instrument facilities.

References

1 X. Tu, F. Gao, X. Ma, J. Zou, Y. Yu, M. Li, F. Qu, X. Huang and L. Lu, *J. Hazard. Mater.*, 2020, **396**, 122776, DOI: **10.1016/j.jhazmat.2020.122776**.
2 S. Manivannan, S. An, J. Jeong, M. Viji and K. Kim, *ACS Appl. Mater. Interfaces*, 2020, **12**, 17557–17570, DOI: **10.1021/acsami.0c01704**.
3 F. Subhan, S. Aslam, Z. F. Yan and M. Yaseen, *J. Colloid Interface Sci.*, 2020, **578**, 37–46, DOI: **10.1016/j.jcis.2020.05.093**.
4 G. D. Zhu, Q. Tang, M. H. Huang, J. M. Yang, R. Xu and J. Y. Liu, *Sens. Actuators, B*, 2020, **320**, 128593, DOI: **10.1016/j.snb.2020.128593**.
5 L. Hu, F. Peng, D. Xia, H. He, C. He and Z. Fang, *ACS Sustainable Chem. Eng.*, 2018, **6**, 17391–17401, DOI: **10.1021/acssuschemeng.8b05169**.
6 N. H. Al-Shaalan, I. Ali, Z. A. Alothman, L. H. Al-Wahaibi and H. Alabdulmonem, *Sep. Sci. Technol.*, 2021, **56**(6), 1095–1101, DOI: **10.1080/01496395.2020.1748653**.
7 V. Boddu, S. Kim, J. Adkins, E. Weimer, T. Paul and R. Damavarpu, *Int. J. Environ. Anal. Chem.*, 2017, **97**(11), 1053–1064, DOI: **10.1080/03067319.2017.1381235**.
8 Y. Zhang, Y. Hu, G. Li and R. Zhang, *Microchim. Acta*, 2019, **186**, 477, DOI: **10.1007/s00604-019-3618-z**.
9 M. P. Belda, M. J. S. Lopez, N. Campillo, P. Vinas and M. H. Cordoda, *Talanta*, 2018, **189**, 543–549, DOI: **10.1016/j.talanta.2018.07.043**.
10 N. Xiao, S. G. Liu, S. Mo, N. Li, Y. J. Ju, Y. Ling, N. B. Li and H. Q. Luo, *Talanta*, 2018, **184**, 184–192, DOI: **10.1016/j.talanta.2018.02.114**.
11 A. C. Giachia, A. E. Psalti, A. D. Pournara, M. J. Manos, C. Pappa, K. Triantafyllidis and T. Lazarides, *J. Mater. Chem. C*, 2022, **10**, 12307–12315, DOI: **10.1039/D2TC02494B**.

12 J. Ru, Y. X. Shi, S. C. Fu, Q. Guo, L. L. Li and Y. L. Wang, *Inorg. Chim. Acta*, 2023, **555**, 121574, DOI: **10.1016/j.ica.2023.121574**.
13 F. M. M. Tchieno and I. K. Tonle, *Rev. Anal. Chem.*, 2018, **37**, 20170019.
14 J. A. Adkins, K. Boehle, C. Friend, B. Chamberlain, B. Bisha and C. S. Henry, *Anal. Chem.*, 2017, **89**, 3613–3621, DOI: **10.1021/acs.analchem.6b05009**.
15 M. Kolar, T. Oraz, V. Jovanovski and S. B. Hocevar, *Sens. Actuators, B*, 2021, **330**, 129338, DOI: **10.1016/j.snb.2020.129338**.
16 B. M. Hryniewicz, E. S. Orth and M. Vidotti, *Sens. Actuators, B*, 2018, **257**, 570–578, DOI: **10.1016/j.snb.2017.10.162**.
17 J. Li, L. He, J. Jiang, Z. Xu, M. Liu, X. Liu, H. Tong, Z. Liu and D. Qian, *Electrochim. Acta*, 2020, **353**, 136579, DOI: **10.1016/j.electacta.2020.136579**.
18 A. M. Mostafa, E. A. Mwafy, N. S. Awwad and H. A. Ibrahium, *J. Mater. Sci.: Mater. Electron.*, 2021, **32**, 11978–11988, DOI: **10.1007/s10854-021-05827-4**.
19 M. A. Ehsan, M. A. AzizA, A. Rehman, A. S. Hakeem, M. A. A. Qasem and S. H. A. Ahmad, *J. Electrochem. Soc.*, 2018, **165**, B302–B309, DOI: **10.1149/2.1141807jes**.
20 M. Ramesh, C. Sankar, S. Umamatheswari and R. Jayavel, *New J. Chem.*, 2023, **47**, 15099, DOI: **10.1039/D3NJ02177G**.
21 N. Dimcheva, *Curr. Opin. Electrochem.*, 2020, **19**, 35–41, DOI: **10.1016/j.coelec.2019.09.008**.
22 G. G. Gerent and A. Spinelli, *J. Hazard. Mater.*, 2017, **330**, 105–115, DOI: **10.1016/j.jhazmat.2017.02.002**.
23 K. Shamsa, P. S. M. Rajaitha, S. Vinoth, C. Murugan, P. Rameshkumar and A. Pandikumar, *Microchim. Acta*, 2020, **187**, 552, DOI: **10.1007/s00604-020-04525-y**.
24 U. Chakraborty, G. Bhanjana, Kannu, N. Kaur, R. Sharma, G. Kaur, A. Kaushik and G. R. Chaudhary, *J. Hazard. Mater.*, 2021, **416**, 125771, DOI: **10.1016/j.jhazmat.2021.125771**.
25 P. Senthil Kumar, P. Ga, N. Elavarasan and B. S. Sreeja, *Chemosphere*, 2023, **313**, 137345, DOI: **10.1016/j.chemosphere.2022.137345**.
26 M. T. Uddin, M. M. Alam, A. M. Asiri, M. M. Rahman, T. Toupance and M. A. Islam, *RSC Adv.*, 2020, **10**, 122–132, DOI: **10.1039/C9RA08669B**.
27 K. Mariappan, S. Sakthinathan, S. M. Chen and T. W. Chiu, *Colloids Surf., A*, 2024, 133147, DOI: **10.1016/j.colsurfa.2024.133147**.
28 M. Khater, D. Ravishankar, F. Greco and H. M. Helen, *Future Med. Chem.*, 2019, **11**, 2845–2867, DOI: **10.4155/fmc-2019-0237**.
29 D. Mandial, P. Khullar, H. Kumar, G. K. Ahluwalia and M. S. Bakshi, *ACS Omega*, 2018, **3**, 15606–15614, DOI: **10.1021/acsomega.8b01776**.
30 R. Sangubotla, B. A. Lakshmi, S. Kim and J. Kim, *Appl. Surf. Sci.*, 2020, **510**, 145417, DOI: **10.1016/j.apsusc.2020.145417**.
31 Z. Memariani, S. Q. Abbas, S. S. Ul-Hassan, A. Ahmadi and A. Chabra, *Pharmacol. Res.*, 2021, **171**, 105264, DOI: **10.1016/j.phrs.2020.105264**.
32 M. Yu, D. You, J. Zhuang, S. Lin, L. Dong, S. Weng, B. Zhang, K. Cheng, W. Weng and H. Wang, *ACS Appl. Mater. Interfaces*, 2017, **9**, 19698–19705, DOI: **10.1021/acsami.7b05296**.
33 S. Bothra, Y. Upadhyay, R. Kumar, S. K. A. Kumar and S. K. Sahoo, *Biosens. Bioelectron.*, 2017, **90**, 329–335, DOI: **10.1016/j.bios.2016.11.066**.
34 Y. C. Lin, T. Wu and Y. W. Lin, *Anal. Methods*, 2018, **10**, 1624–1632, DOI: **10.1039/C8AY00308D**.
35 S. Madhurantakam, S. Selvaraj, N. Nesakumar, S. Sethuraman, J. B. B. Rayappan and U. M. Krishnan, *Biosens. Bioelectron.*, 2014, **59**, 134–139, DOI: **10.1016/j.bios.2014.03.029**.
36 A. A. Ashkarran, S. A. A. Afshar, S. M. Aghigh and M. Kavianipour, *Polyhedron*, 2010, **29**, 1370–1374, DOI: **10.1016/j.poly.2010.01.003**.
37 M. I. Khalil, O. Atici, A. Lucotti, S. Binetti, A. Le Donne and L. Magagnin, *Appl. Surf. Sci.*, 2016, **379**, 91–97, DOI: **10.1016/j.apsusc.2016.04.062**.
38 M. M. AbdElhady, *Int. J. Carbohydr. Chem.*, 2012, **2012**, 1–6, DOI: **10.1155/2012/840591**.
39 P. Ji, Z. Mao, Z. Wang, X. Xue, Y. Zhang, J. Lv and X. Shi, *Nanomaterials*, 2019, **9**, 983, DOI: **10.3390/nano9070983**.
40 H. Ibrahim and Y. Temerk, *Microchem. J.*, 2022, **178**, 107425, DOI: **10.1016/j.microc.2022.107425**.
41 R. Huang, D. Liao, Z. Liu, J. Yu and X. Jiang, *Sens. Actuators, B*, 2021, **338**, 129828, DOI: **10.1016/j.snb.2021.129828**.
42 M. Ramesh, C. Sankar, S. Umamatheswari, R. Ganapathi Raman, R. Jayavel, D. Choi and A. G. Ramu, *RSC Adv.*, 2023, **13**, 20598–20609, DOI: **10.1039/D2RA08140G**.
43 M. Ramesh, C. Sankar, S. Umamatheswari, J. Balamurugan, R. Jayavel and M. Gowran, *Int. J. Biol. Macromol.*, 2023, **226**, 618–627, DOI: **10.1016/j.ijbiomac.2022.11.318**.

ACS APPLIED NANO MATERIALS

www.acsanm.org Article

Sonochemical Synthesis of Ag-Functionalized Fe_2O_3 Nanocomposites for the Highly Sensitive Electrochemical Detection of Ractopamine and H_2O_2

M. Ramesh, S. Umamatheswari,* C. Sankar,* and R. Jayavel

Cite This: *ACS Appl. Nano Mater.* 2024, 7, 2929−2938 Read Online

ACCESS | Metrics & More | Article Recommendations | Supporting Information

ABSTRACT: Herein, we report an electrochemical sensor for the detection of ractopamine (RA) and hydrogen peroxide (H_2O_2), based on a silver (Ag)-functionalized Fe_2O_3-modified glassy carbon electrode (AFO-GCE). This environment friendly nanosensor is synthesized by a simple and cost-effective ultrasonic technique and characterized by FT-IR, P-XRD, XPS, EIS, HR-SEM and HR-TEM. The obtained results suggest that the average size of the nanoparticles is between 14 and 22 nm. EIS is also performed to prove the fabricated electrode has faster electron transfer and permits a diffusion-controlled process. The fabricated sensor exhibits superior electrocatalytic activity in RA detection with good linearity of 1.0 nM−5.847 μM, sensitivity of 2.28 μA mM^{-1} cm^{-2}, limit of detection (LOD) of 1.35 nM and H_2O_2 detection with high linearity from 10 μM to 6.85 mM, sensitivity of 27.2 μA mM^{-1} cm^{-2}, and LOD of 1.98 μM with respectable selectivity, excellent reproducibility, and long-term stability. Further, the sensor is effectively employed for the detection of RA in chicken and pork samples and detection of H_2O_2 in milk samples with an extensive recovery range of 95−98%.

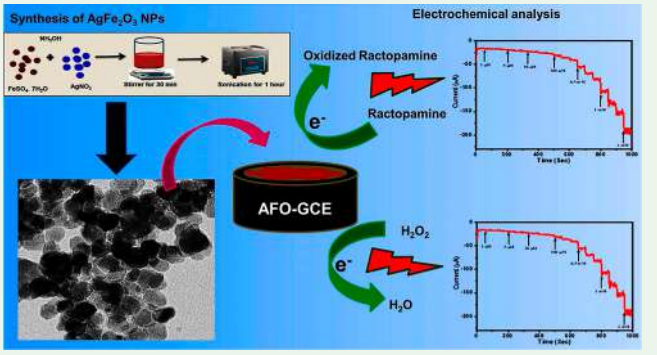

KEYWORDS: *$AgFe_2O_3$, nanomaterial, ractopamine, hydrogen peroxide, sensor*

1. INTRODUCTION

Ractopamine (RA) is a β-adrenergic receptor agonist derived from phenylethylamine.[1] It plays a significant role in the treatment of respiratory illnesses such as lung diseases and asthma.[1] However, it is unethically utilized in animal feed to promote the development of muscle tissues and reduce the accumulation of body fat via a direct effect on adipose tissues.[2] Due to their disrupted metabolism, the drug residues can enter the human body through the food chain and can cause significant health issues in humans, including heart palpitations, muscle tremors, uneasiness, chills, and vomiting.[3] As per the Codex Alimentarius Commission, the maximum residual limits (MRLs) of RA in beef and pork are 0.01 mg/kg in meat, 0.04 mg/kg in the liver, and 0.09 mg/kg in the kidney.[4,5] The FAO/WHO Joint Expert Committee on Food Additives (JECFA) has proposed setting the MRL of RA for cattle and pork to 5 mg/kg.[1,6] However, in China, the EU, and Russia, RA is not permitted for use in livestock and poultry farming, and importing any products containing RA is outright forbidden. In recent years, monitoring of RA residue in animal-derived foods (such as pork, beef, and lamb) has attracted great attention from government regulators and the food industry.[7]

Hydrogen peroxide (H_2O_2) is an important chemical reagent in the food industry, biomedical field, environmental remediation, and industrial equipment. Additionally, it serves as a mild antiseptic for cleaning and bleaching purposes.[8,9] H_2O_2 is harmful to living and nonliving things in three main ways: it corrodes things, makes oxygen gas, and peroxidizes fats. Concentrated H_2O_2 is acidic, and its exposure may damage nearby tissues. It is also possible for large amounts of oxygen to be produced when highly concentrated H_2O_2 (>35%) is used.[11] Moreover, it has considerable consequences for biological reactions involving enzymes, which have the potential to produce serious illnesses such as cardiovascular diseases, cancer, and Alzheimer's disease.[10] The consumption of H_2O_2 is restricted. The U.S. Food and Drug Administration (USFDA) has approved a permissible limit of <0.5 ppm of H_2O_2 in packaged drinking water.[11]

Therefore, creating an effective, reliable, and sensitive sensor for the detection of RA and H_2O_2 is necessary for various processes as well as for human health. Standard titrimetry,[12]

Received: November 3, 2023
Revised: January 5, 2024
Accepted: January 5, 2024
Published: January 22, 2024

Scheme 1. Schematic Diagram for Electrochemical Detection of RA and H_2O_2

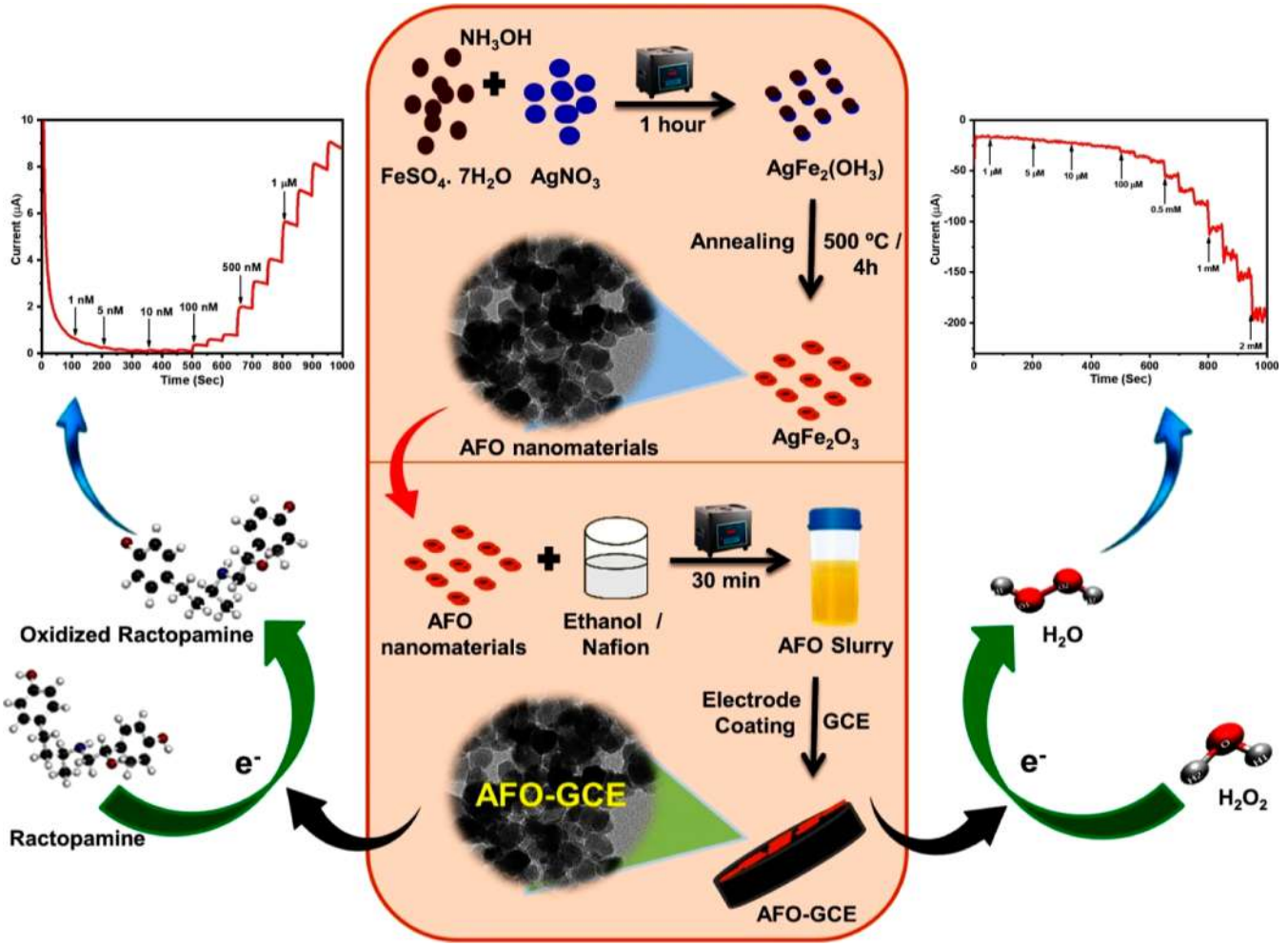

spectrophotometry,[13] chemiluminescence,[14] and high-performance liquid chromatography (HPLC) are some of the sensing technologies that have been reported. Even though these technologies have numerous advantages, complex sample preparation, extensive pretreatment time, high cost, complex process of the instrument, and other shortcomings limit their wide application. Among them, electrochemical approaches[1,15,16] have received the most attention due to their user-friendliness, low costs, quickness, and excellent sensitivity, which make the sensing of RA and H_2O_2 by electrochemical methods more competitive.[17] For instance, Balram et al. have developed a zinc ferrite-decorated three-dimensional graphene system that can sensitively and rapidly detect RA.[18] Recently, Zhang et al. have prepared silver-anchored 3DG electrochemical sensors for RA detection with a low detection limit of 0.12 μM.[19] Similarly, various research groups reported the detection of H_2O_2 based on an electrochemical approach. For example, Kannan et al. synthesized a functionalized Co_3O_4 nanocomposite for electrochemical detection of H_2O_2 with a low detection limit of 0.28 μM.[20] Furthermore, the synthesis of Mn@FeNi−S/graphene oxide nanocomposite is considered a highly valuable and effective electrocatalyst for the nonenzymatic electrochemical detection of H_2O_2.[21]

On the other hand, metal nanoparticles (NPs) are considered "star products" in chemically modified electrodes due to their several outstanding properties.[22] In particular, magnetic NPs are being extensively used in biological applications like MRI, drug loading and delivery, and sensors.[23−25] Among them, Fe_2O_3 nanomaterials are extensively fabricated in sensor applications due to their unique properties, like ease of preparation, tiny size, excellent biocompatibility, high specific surface area, nontoxicity, good conductivity, and magnetic properties.[26] Nanocomposites based on Fe_2O_3 have also shown promise for use in supercapacitors, electrochemical sensors, solar cells, transducers, and Li-ion storage devices. Nowadays, Fe_2O_3 is used as a suitable nanomaterial for an effective electrocatalyst for nonenzymatic electrochemical sensors. Liu et al. have reported the one-pot synthesis of porphyrin-functionalized γ-Fe_2O_3 NPs for the detection of glucose and H_2O_2.[27] Additionally, silver nanoparticles (Ag NPs) stand out enough to be noticed because of their antimicrobial, electrocatalytic, optical, synthetic, natural properties, etc.[28−30] Ag NPs-oxidized green rust nanohybrids for a novel and effective nonenzymatic H_2O_2 electrochemical sensor have been reported by Njima and Legrand.[31]

Numerous studies have shown that the most effective nanomaterials can be produced by modifying the size and morphology of NPs or by integrating them with carbon or polymers,[32,33] organic molecules,[34−36] and other metals and metal oxides.[37,38] Similarly, the detection ability was enhanced by changing the electronic configuration of the elements

https://doi.org/10.1021/acsanm.3c05236
ACS Appl. Nano Mater. 2024, 7, 2929−2938

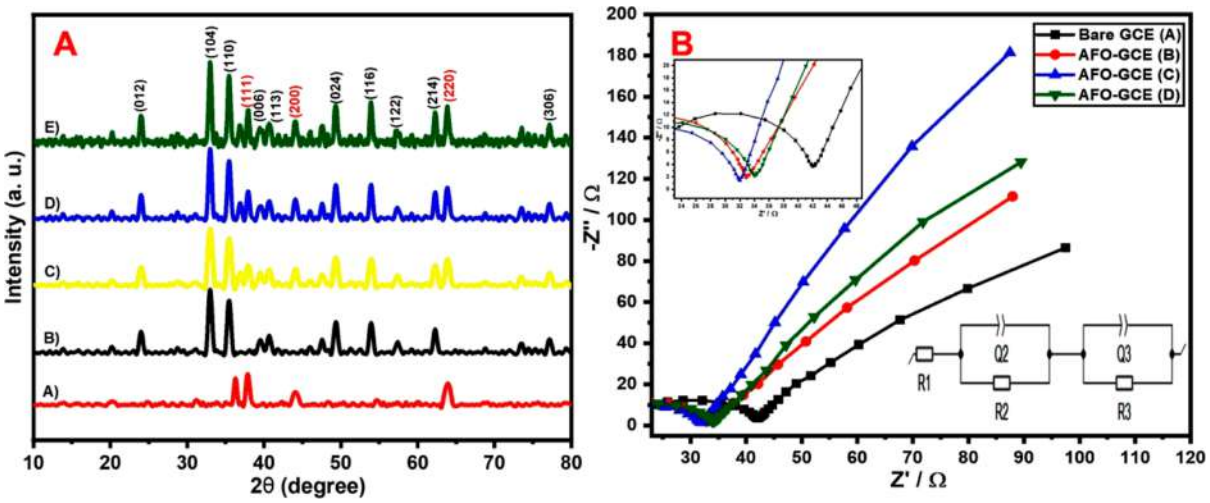

Figure 1. (A) Powder XRD pattern of AFO NPs with different concentrations of Ag. (B) EIS spectra of bare GCE and AFO NPs with different concentrations of Ag.

(Fe_2O_3 NPs), such as the oxidation state of Fe and O_2. Consequently, our research focuses primarily on the ability of Fe_2O_3 NPs in this regard, which gives the premise for the electrochemical sensing of RA and H_2O_2.

Based on the above observation, nanosphere-based Fe_2O_3 nanocatalysts enhance the electrocatalytic performance toward RA and H_2O_2 detection. To the best of our knowledge, the electrochemical detection application of a Ag-functionalized Fe_2O_3 nanocomposite (AFO) has not been reported yet. Therefore, we have reported a facile one-pot synthesis of AFO using an ultra-sonochemical process, as the nanomaterials acquired by ultra-sonication revealed a higher specific surface area and pore volume. Finally, the applicability of the fabricated method was evaluated using different real samples, such as pork and chicken liver (RA) and milk (H_2O_2).

2. EXPERIMENTAL SECTION

2.1. Materials. Ferrous sulfate heptahydrate ($FeSO_4{\cdot}7H_2O$), silver nitrate ($AgNO_3$), ammonia solution (NH_3OH), urea (NH_2CONH_2), RA, H_2O_2, potassium chloride (KCl), ascorbic acid (AA), sodium hydroxide (NaOH), dopamine (DA), and uric acid (UA) were purchased from Sigma-Aldrich, India. The sulfonated tetrafluoroethylene polymer support is known as Nafion. It is used for electrode fabrication, for enhancing the affinity, and aids for good adhesion between the electrode surface and fabricated nanomaterials. All chemicals were of analytical grade (≥95% pure) and used without further purification. A detailed discussion of the methods and characterization techniques is provided in the Supporting Information.

2.2. One-Pot Synthesis of AFO NPs. In a typical procedure, 0.5 M of $FeSO_4{\cdot}7H_2O$ and 0.01 M of $AgNO_3$ were dissolved in 50 mL of demineralized water to form a homogeneous solution at ambient temperature. After that, NH_4OH was gradually added to the reaction mixture until the pH reached 9.5 with continuous stirring. Subsequently, the mixture was subjected to sonication using the Elmasonic EASY 60H model ultrasonicator at a frequency of 37 kHz and a power output of 150 W for a duration of 60 min to obtain a stable dispersion of the AFO composite, which was then filtered and washed with an ethanol and water mixture 6−7 times. The brown-colored AFO NPs were finally dried in a hot air oven at 80 °C for 12 h and annealed at 500 °C for 4 h. We used the same procedure to synthesize different concentrations (0.3 and 0.05 M) of AFO NPs.

2.3. Fabrication of the AFO-Modified Glassy Carbon Electrode. The glassy carbon electrode (GCE) was refined with alumina (0.5 μM) powder. Subsequently, the electrode was thoroughly cleaned by subjecting it to sonication with a 1:1 mixture of ethanol and deionized water. The cleaned electrode was dried in a hot air oven for 10 min. Then, 10 μL of 10% Nafion and 0.5 mg of AFO NPs were added into 500 μL of EtOH, and the total mixture was dispersed under ultrasonic conditions for 30 min. Then, 5 μL of dispersed AFO slurry was coated on top of the GCE and dried normally. Finally, the fabricated AFO-modified GCE (AFO-GCE) was used to detect RA and H_2O_2.

2.4. Sample Preparation. The real samples were prepared by slight modification of a previously described method.[39] First, pork and chicken livers were selected as real samples and crushed individually. Spiked samples were prepared by injecting a known concentration of RA into the pork and chicken liver samples; the stock solution is prepared without addition of RA. In the second step, 4 mL (0.1 M) of $HClO_4$ was added to 2.0 g of crushed real samples, and the mixture was ultrasonicated for 30 min. The mixture was then heated in water at 80−90 °C for 45 min. The supernatant was collected by centrifuging the mixture at 7000 rpm for 20 min. The pH of the collected supernatant was adjusted to 10 using 10% Na_2CO_3. NaCl (1.5 g) was also added. The solution was extracted with 5 mL of isopropanol−ethyl acetate (v/v = 2:3), and RA was back-extracted into the HCl solution and repeated several times. Finally, the solution was diluted to 10 mL with NaOH (pH 12).

3. RESULTS AND DISCUSSION

3.1. Characterization of AFO NPs. *3.1.1. XRD and FT-IR Spectral Analyses.* The AFO nanocomposite was synthesized by a simple one-pot synthesis process by using an ultrasonic method without the addition of a reducing agent (Scheme 1). The synthesized AFO NPs' were characterized using FT-IR, XRD, HR-SEM, HR-TEM, EIS, and XPS. At the first stage, XRD and FT-IR spectra were recorded, which confirmed the crystalline nature, phase formation, and functional groups of AFO NPs.

The functional groups of different concentrations of AFO NPs were characterized by FT-IR spectroscopy in the wavelength range of 400 to 4000 cm^{-1}, as shown in Figure S1. The broad absorption band at 3429.54 cm^{-1} is attributed to the OH stretching vibration band. The band absorbed at 468.12 cm^{-1} corresponds to the Fe_2O_3 band,[40] and a stretching vibration band of Ag−O is found at 552.66 cm^{-1}.

The XRD patterns of Ag NPs (A), Fe_2O_3 NPs (B), 0.01 M Ag-doped Fe_2O_3 NPs (C), 0.03 M Ag-doped Fe_2O_3 NPs (D), and 0.05 M Ag-doped Fe_2O_3 NPs (E) are shown in Figure 1A.

https://doi.org/10.1021/acsanm.3c05236
ACS Appl. Nano Mater. 2024, 7, 2929−2938

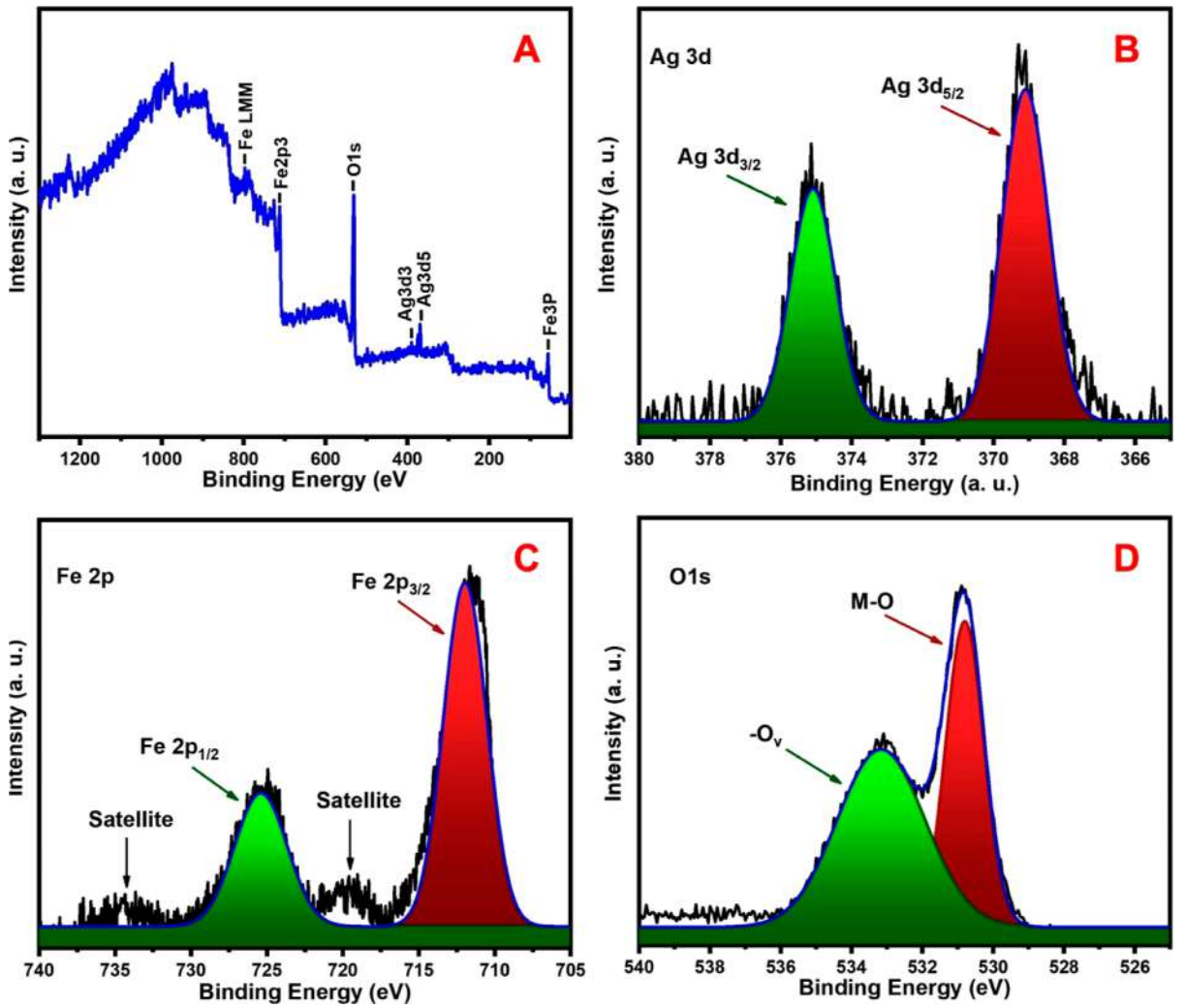

Figure 2. XPS spectrum of AFO NPs. (A) Survey spectrum, (B) Ag 3d, (C) Fe 2p, and (D) O 1s.

The peaks situated at 24.11, 33.14, 35.57, 39.65, 40.80, 49.33, 54.05, 57.49, 62.33, 63.86, and 77.24 correspond to (012), (104), (110), (006), (113), (024), (116), (122), (214), (300), and (306), respectively. The presence of highly intense sharp diffraction peaks at 33.14, 35.57, 49.33, and 54.05 indexed to (104), (110), (024), and (116) reflections, respectively, elucidated the good crystalline nature of AFO nanomaterials with a perfectly matched rhombohedral crustal system and $R\bar{3}$space group of Fe_2O_3 (JCPDS. No. 24-0072).[41] The additional peaks involved at 37.99 and 44.10 clearly show the presence of Ag in the synthesized AFO nanomaterials. The XRD patterns of the silver system demonstrated an increase in the intensity of the diffraction peaks of silver with increasing silver concentration. This is related to the increase in the size of the AFO nanomaterials (14, 17, and 22 nm), as observed in the patterns.

3.1.2. EIS Analysis. EIS is a useful analytical tool for measuring the electrochemical surface area and electron conduction behavior of the interface between fabricated electrodes and the electrolyte. EIS and CV curves were used to evaluate the impedance alterations and interface characteristics of the bare and modified AFO-GC electrodes. EIS was carried out using $[Fe(CN)_6]^{3-/4-}$ as the redox probe and over the frequency range of 0.01 to 120.000 Hz for GCE (A), 0.01 M Ag-doped Fe_2O_3-GCE (B), 0.03 M Ag-doped Fe_2O_3-GCE (C), and 0.05 M Ag-doped Fe_2O_3-GCE (D), depicted in Figure 1B. The impedance spectra show two regions: one is semicircular and the other is a linear region. The semicircular region indicates the charge-transfer resistance (R_{ct}) in the higher-frequency region, whereas the lower-frequency region represented by the linear part indicates the diffusion-limited process.[42,43]

The electroactive surface area of the AFO-GCE (0.03 M) was characterized by CV at varying scan rates from 10 to 100 mV s^{-1}. Thus, the electroactive surface area of the AFO-GCE (0.03 M) was calculated by the Randles-Sevcik equation (eq 1).

$$I_{Pa} = 2.69 \times 10^5 A n^{3/2} C_o n D^{1/2} \varphi^{1/2} \quad (1)$$

Here, I_{pa} is the peak current, A is the effective surface area, n is the number of electrons transferred for $Fe(CN)_6^{3-/4-}$ (n = 1), C is the concentration of $Fe(CN)_6^{3-/4}$, D is the diffusion coefficient of $Fe(CN)_6^{3-/4-}$ (7.7×10^{-6} cm^2/s), and φ is the scan rate (V s^{-1}). As a result, the active surface areas of bare GCE and AFO-GCE (0.03 M) were 0.0751 and 0.52 cm^2, respectively.

The charge-transfer resistance (R_{ct}) of the bare GCE and AFO-modified GCE of different concentrations—AFO-GCE (0.01 M), AFO-GCE (0.03 M) and AFO-GCE (0.05 M)—was 42.01, 32.88, 31.97, and 34.09 Ω, respectively. From the

https://doi.org/10.1021/acsanm.3c05236
ACS Appl. Nano Mater. 2024, 7, 2929−2938

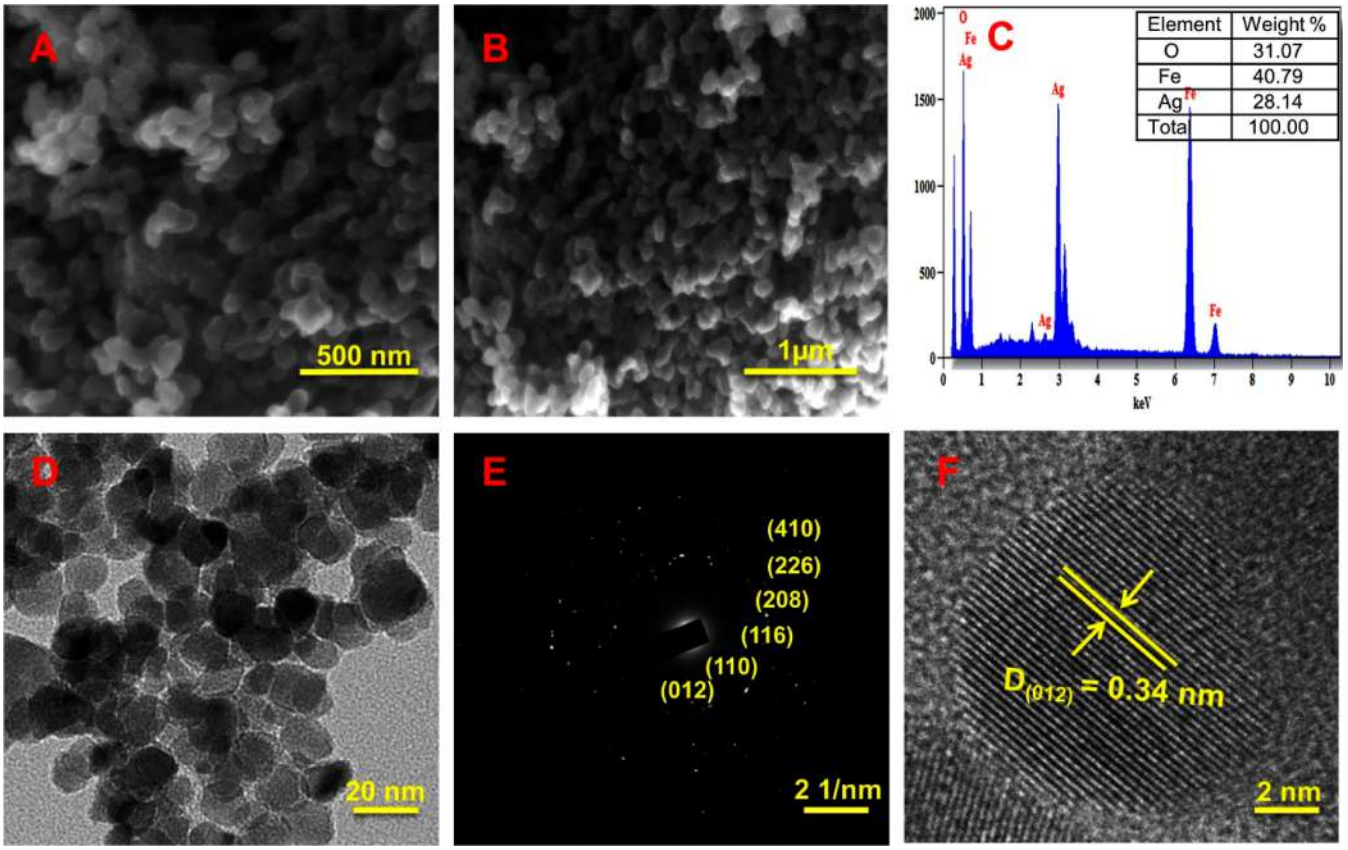

Figure 3. (A,B) HR-SEM images, (C) EDX elemental analysis, (D) HR-TEM image, (E) SAED pattern, and (F) IFFT image of AFO NPs.

obtained results, the AFO-GCE (0.03 M) had excellent conductivity and better electrocatalytic activity than the other electrodes. Further, the heterogeneous electron-transfer rate constant (k_{et}) was calculated from eq 2.[43]

$$k_{et} = RT/(F^2R_{ct}AC) \quad (2)$$

Here, R is the universal gas constant (R = 8.314 J K^{-1} mol^{-1}), F is Faraday's constant (F = 96,485 C mol^{-1}), R_{ct} is the charge-transfer resistance (Ω), A is the surface area of the electrode (cm^2), and C is the concentration of the $[Fe(CN)_6]^{3-/4-}$ solution (mol cm^{-3}). The measured k_{et} values of the bare GCE and AFO-GCE (0.03 M) were 1.18×10^{-4} and 3.09×10^{-4} cm s^{-1}, respectively.

In addition, the electrocatalytic activity of the fabricated electrode can be calculated from the standard change in the current density (I_o) by eq 3.[44]

$$I_o = RT/nFR_{ct} \quad (3)$$

The fabricated electrode, AFO-GCE (0.03 M), shows a higher standard change current density (I_o = 0.803 μA cm^{-2}) than the bare GCE (I_o = 0.611 μA cm^{-2}), which indicates that AFO-GCE (0.03 M) has good electrocatalytic activity.

3.1.3. XPS Analysis. The elemental composition and metal oxidation states of the fabricated AFO NPs were thoroughly studied by XPS. The XPS survey spectrum of the AFO (0.03 M of Ag) NPs is shown in Figure 2A in the range of 0−1300 eV. The XPS spectrum of the Ag 3d core-level photoelectron area is shown in Figure 2B; the peaks located at 369.1 and 375.1 eV are attributed to Ag $3d_{5/2}$ and Ag $3d_{3/2}$, respectively, whose binding energies are generally described for the metallic Ag^0 state.

Figure 2C shows the deconvoluted XPS spectrum of Fe, The presence of two peaks linked to Fe $2p_{3/2}$ and Fe $2p_{1/2}$ in the range of 712.1 and 726.3 eV, respectively, indicates the 3+ oxidation state of Fe in AFO NPs. Figure 2D exhibits two distinct peaks at 530.8 and 533.1 eV, which emerge from deconvolution of the XPS spectrum of O 1s. The presence of a metal−oxygen bond in the AFO NPs was revealed by the appearance of a new peak at 531.2 eV, which was attributed to lattice oxygen. The undercoordinated lattice oxygen, hydroxyl group-chemisorbed oxygen, or defect oxide is shown to be strongly linked to the peak at 533.1 eV. The above XPS result confirmed the formation of AFO NPs.

3.1.4. HR-SEM and HR-TEM Analyses. The HR-SEM analysis confirmed the appearance of spherical-shaped particles that were evenly distributed and displayed the same aggregation (Figure 3A,B). EDX analysis was also used to determine the elemental composition of the AFO NPs (Figure 3C). The obtained results confirmed the presence of Ag (28.14%), Fe (40.79%), and O (31.07%), and the EDX elemental mapping analysis of AFO NPs is shown in Figure S2.

HR-TEM was used to reconfirm the morphology and size of the AFO NPs (Figure 3D). The image clearly shows that most of the particles have spherical and irregular shapes. The shapes of all the different concentration AFO NPs were spherical and aggregated and were nearly dispersed, as shown in Figure S3. The average particle sizes of the AFO NPs were found to be 14, 17, and 22 nm. This clearly suggests that with increasing concentrations of Ag—0.01, 0.03, and 0.05 mM—with Fe_2O_3 nanomaterials, the particle size increased. The selected area electron diffraction (SAED) pattern reveals that the diffractions were indexed to D = 3.3, 2.4, 1.6, 1.3, 1.0, and

https://doi.org/10.1021/acsanm.3c05236
ACS Appl. Nano Mater. 2024, 7, 2929−2938

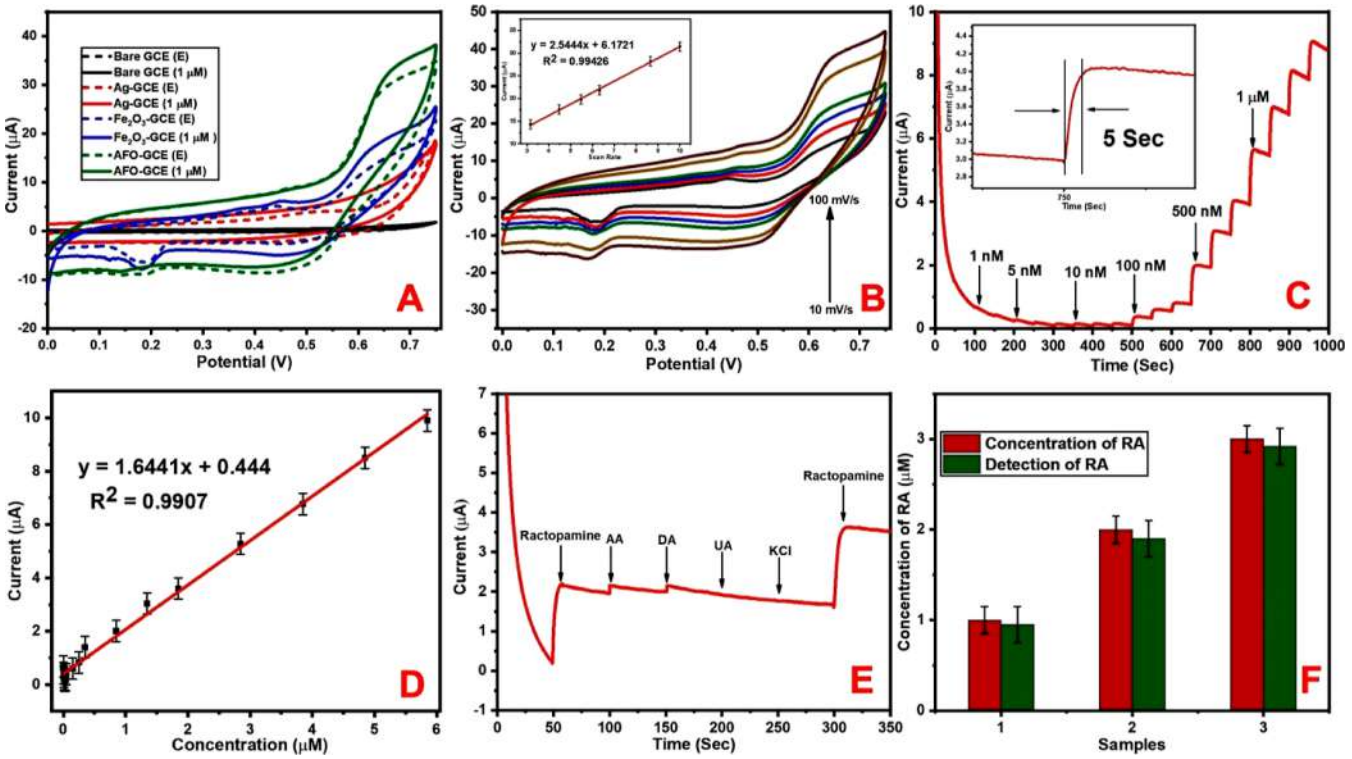

Figure 4. (A) CV plot of different electrodes with and without 1 μM RA in the electrolyte at 50 mV/s. (B) CV plot of different scan rates of 10−100 mV/s (inset: correlation plot of current vs square root of scan rate). (C) Amperometric i−t curve for increasing concentrations of RA (inset: fast response curve). (D) Calibration plot of current vs concentration of RA. (E) Anti-interference study recorded with AA, DA, UA, and KCl. (F) Practicability study in chicken and pork samples.

0.9 corresponding to (012), (110), (116), (208), (226), and (410) diffraction planes, respectively, of the rhombohedral crustal system of AFO NPs, which are in good agreement with the XRD patterns, as shown in (Figure 3E). The inverse fast Fourier transform (IFFT) image (Figure 3F) of AFO revealed a lattice fringe spacing distance D = 0.34 nm, which corresponds to the (012) plane of the AFO NPs. The SAED pattern and IFFT interplanar D-spacing perfectly matched the JCPDS No: 24-0072.

3.2. Electrochemical Sensing of RA by AFO NPs. *3.2.1. CV Analysis.* CV was used to analyze the electrochemical oxidation of RA on various modified AFO electrodes in 0.1 M NaOH. The electrolyte solutions consisted of three types: (a) 0.1 M acetate buffer solutions with pH values of 3.0, 4.0, and 5.0; (b) 0.1 M phosphate buffer solutions with pH values of 6.0, 7.0, 7.5, and 8.0; and (c) 0.1 M NaOH with acetic acid solutions with pH values of 10, 11, 12, 13, and 14. Figure S5 illustrates the effect of pH on the oxidation peak current of RA. The oxidation peak current of RA progressively increased as the pH increased from 3.0 12.0. Nevertheless, the oxidation peak current of RA declined when the pH exceeded 12. To achieve optimal sensitivity, a NaOH solution at pH 12 was chosen for the detection of RA. The CV curves of the bare GCE, Ag-GCE, Fe_2O_3-GCE, and AFO-GCE with the addition of 1.0 μM RA in 0.1 M N_2-saturated NaOH at a scan rate of 50 mV/s are depicted in Figure 4A.

In Figure 4A, the bare GCE did not show any oxidation peak, even at a high potential. Likewise, the Ag-GCE does not show any major differences compared to the Fe_2O_3-GCE when it comes to the weak oxidation of RA, and the only difference is the slightly increased anodic peak current. However, in contrast to the measurements taken with the AFO-GCE, the response of the AFO-GCE is highly enhanced in the presence and absence of RA, as shown in Figure 4A.

Therefore, the AFO-GCE may have generated excellent electrochemical oxidation of RA. Figure S6A shows the CV plot of various molar concentrations of RA (1 to 10 μM) for further analysis of electrochemical oxidation using an AFO-GCE. It was observed that the current response linearly increased with increasing concentrations of RA. Besides, RA is electrochemically oxidized, and the oxidation mechanism of RA is shown in Scheme 2.[45]

In addition, to investigate the kinetics for oxidation of RA, CV was performed at different scan rates between 10 and 100 mV/s in the potential range from 0 to 0.75 V in 1.0 μM RA (Figure 4B). As a result, the anodic peak current increased linearly with increasing scan rate, and E_p shifted toward a higher positive value along with an increase in the oxidation current. This observation suggests irreversible electron-transfer kinetics for RA oxidation at the AFO-GCE surface.[46] The linear regression equation for the relationship between current and square root of the scan rate is $I(\mu A) = 1.544x + 6.172$ (R^2 = 0.99426). The remarkable electrical conductivity capabilities of the AFO NPs illuminate its enormous opportunity in future sensing applications.

3.2.2. Chronoamperometry Analysis. Chronoamperometry (CA) was used to evaluate the sensitivity of the newly fabricated AFO-GCE for the detection of RA. Figure S6B shows the CA plot of different potentials 0.6, 0.65, 0.7, and 0.75 V by the addition of 0.5 in 1 μM RA at every 50 s intervals. As a result, the potential range of 0.65 V reveals a high response to the electrochemical oxidation of RA. Therefore, 0.65 V was chosen for the amperometric studies. The CA i−t curves were obtained by gradually increasing the

https://doi.org/10.1021/acsanm.3c05236
ACS Appl. Nano Mater. 2024, 7, 2929−2938

Scheme 2. Oxidation Mechanism of RA Based on AFO-GCE

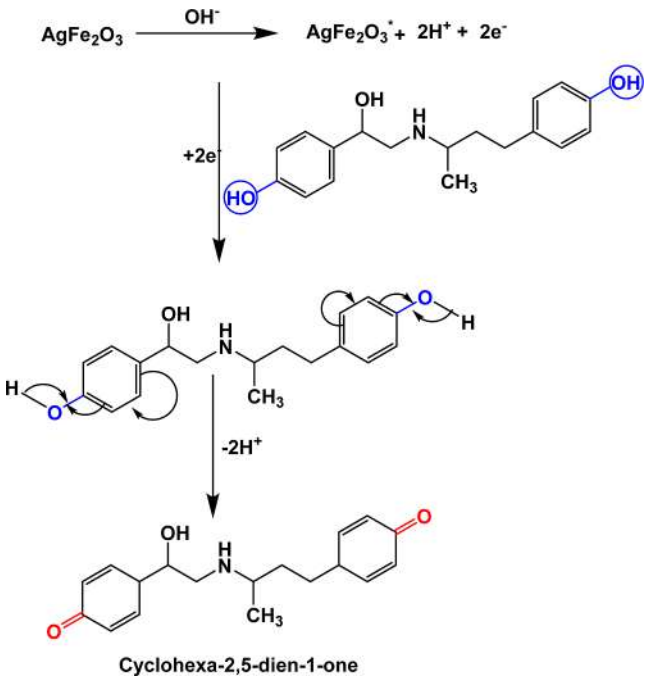

added RA concentration (1 nM−5.847 μM) for every 50 s in the electrolyte solution at 0.65 V with continuous stirring (Figure 4C). As a result, with the increase of added RA concentration, owing to an increase in the oxidation current, the steady-state current value was reached within 5 s, indicating the effective sensing ability of the AFO-GCE. Furthermore, the calibration plot illustrates the linearity of oxidation current response vs concentration of RA between 1.0 nM and 5.847 μM, as displayed in Figure 4D. The linear current response is described as I (μA) = 1.6441x + 0.444, with a correlation coefficient R^2 = 0.9907. The sensitivity of the AFO-GCE was determined as 2.28 μA mM^{-1} cm^{-2} from the calibration plot (slope/active surface area), and the limit of detection (LOD) is 1.35 nM, which is calculated from the equation LOD = 3 Sb/S (where Sb = standard deviation of current response and S = sensitivity).[47] This is considerably less than that of the majority of the other relevant sensors listed in Table S1.

3.2.3. Selectivity, Stability, Reproducibility, and Repeatability of the Sensor. The selectivity of the fabricated AFO-GCE was evaluated using a variety of interferences, such as AA, DA, UA, and KCl in 0.1 M NaOH solution with continuous stirring. However, the AFO-GCE responds extremely weakly to the addition of 0.1 mM UA, AA, DA, and KCl (Figure 4E). These results demonstrate that these interferences had no noticeable effect on the amperometric curve for the AFO-GCE; therefore, the fabricated electrode exhibited good selectivity for the detection of RA.

The reproducibility of the five freshly prepared AFO-GCEs was analyzed for RA detection using the amperometric response (Figure S6C). The current responses of the five electrodes exhibited a relative standard deviation (RSD) of 2.39%. These results suggest that the AFO-GCE has good reproducibility. The stability of the fabricated AFO-GCE was analyzed by CV plot for the 1st and 10th days with 1.0 μM RA in 0.1 M NaOH at 50 mV/s (Figure S6D). Distinctly, the 1st and 10th days' current responses were almost 95% identical. The obtained results indicated that the fabricated AFO-GCE exhibited good reproducibility and high stability.

3.2.4. Real-Sample Analysis. The practicability of the fabricated AFO-GCE was determined by recording the amperometric response at three different spiked concentrations of RA (1.0, 2.0, and 3.0 μM) in a 0.1 M NaOH solution containing chicken and pork sausages (Figure 4F). Hence, the three spiked concentrations of the RA recovery values were calculated and are listed in Table 1. The fabricated AFO-GCE sensor exhibited an extraordinary recovery range from 95 to 97.5% with RSD = 1.59 to 1.84% and from 97 to 98% with RSD = 1.64 to 1.72% for the detection of RA in chicken and pork sausages.

Table 1. RA Detection in Chicken and Pork Samples

samples	spiked RA (μM)	detection of RA (μM)	recovery (%)	RSD (n = 3) (%)
chicken	1.0	0.95	95	1.61
	2.0	1.92	96	1.84
	3.0	2.93	97.5	1.59
pork	1.0	0.97	97	1.64
	2.0	1.95	97.5	1.68
	3.0	2.96	98	1.72

3.3. Electrochemical Sensing of H_2O_2 by AFO NPs.

3.3.1. CV Analysis. Metal oxide NPs, particularly Ag and Fe_2O_3, exhibit excellent electrocatalytic activity for the reduction of H_2O_2. Therefore, it would be interesting to investigate the electrocatalytic activity of AFO NPs for H_2O_2 reduction. Figure 5A shows the CV plots of bare GCE, Ag-GCE, Fe_2O_3-GCE, and AFO-GCE in electrolyte solution with and without 1 mM H_2O_2 at 50 mV/s. Distinctly, the fabricated AFO-GCE displays decent electrocatalytic ability toward reduction of H_2O_2 and a noticeable peak at about −0.45 V, while no performance is observed at the bare GCE and a slight performance at Ag-GCE and Fe_2O_3-GCE.

In addition, the CV curve of the AFO-GCE was recorded with 1.0 mM H_2O_2 at different scan rates of 10−50 mV/s in 0.1 M NaOH. The cathodic peak current increased linearly with increasing scan rates (10 to 50 mV/s), as shown in Figure 5B. The linear regression equation I (A) = −1.7577x − 5.4655 (R^2 = 0.99532) showed a satisfactory linear response with the cathodic peak current and square root of the scan rate (Figure 5B **inset**). Figure S7A shows the CV plot of the fabricated AFO-GCE at various concentrations of H_2O_2 (0.1−1.0 mM) at 50 mV/s. The cathodic current response increased linearly with increasing H_2O_2 concentration. The AFO-GCE exhibited a slight increase in the cathodic current and a decrease in the oxidation current in the opposite electrochemical reaction, demonstrating that the Fe^{3+}/Fe^{2+} redox method can promote the reduction of H_2O_2 at negative potentials.[31]

$$Fe^{3+} + e^- \rightarrow Fe^{2+} \quad (4)$$

The reaction between Fe^{2+} and H_2O_2 is given below

$$H_2O_2 + Fe^{2+} \rightarrow 2Fe^{3+} + 2OH^- \quad (5)$$

Similarly, H_2O_2 reduction using the Ag electrode is given below[48]

$$H_2O_2 + e^- \rightarrow OH_{ads} + OH^- \quad (6)$$

$$OH_{ads} + e^- \rightarrow OH^- \quad (7)$$

https://doi.org/10.1021/acsanm.3c05236
ACS Appl. Nano Mater. 2024, 7, 2929−2938

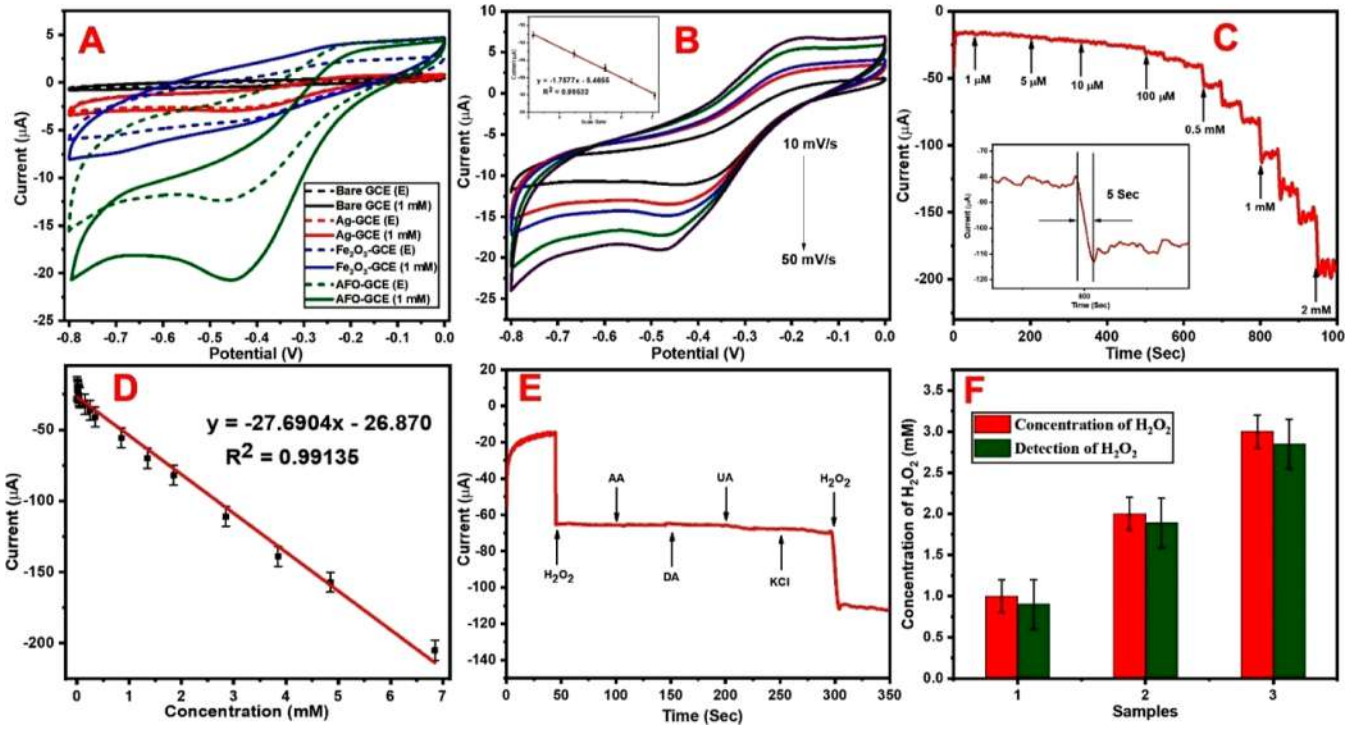

Figure 5. (A) CV plot of different electrodes with and without 1 mM H_2O_2 in the electrolyte at 50 mV/s. (B) CV plot of different scan rates of 10−100 mV/s (inset: correlation plot of current vs square root of scan rate). (C) Amperometric $i-t$ curve for increasing concentrations of H_2O_2 (inset: fast response curve). (D) Calibration plot of current vs concentration of H_2O_2. (E) Anti-interference study recorded with AA, DA, UA, and KCl. (F) Practicability in milk sample.

The overall reduction reaction of H_2O_2 in NaOH solution is as follows

$$H_2O_2 + 2e^- \rightarrow 2OH^- \quad (8)$$

3.3.2. CA Analysis. Amperometric ($i-t$) measurements were used to evaluate the electrocatalytic activity of fabricated AFO-GCE for H_2O_2 reduction. Figure S7B shows the CA plot of different potentials −0.4, −0.45, and −0.5 V with the addition of 0.5 and 1 mM concentrations of H_2O_2 in the electrolyte solution with continuous stirring. Thus, the potential range of −0.45 V illustrates the great response to the electrochemical reduction of H_2O_2. Therefore, −0.45 V was selected for the following measurements. The amperometric $i-t$ curve of H_2O_2 reduction at the fabricated AFO-GCE was studied by consecutive addition of H_2O_2 (1 μM to 5.848 mM) in 30 mL of 0.1 M NaOH in the potential range of −0.45 V with continuous stirring (Figure 5C). As a result, every addition of H_2O_2 led to an increase in the current response, and the steady-state value was reached within 5 s, indicating the effective sensing activity of the AFO-GCE. Figure 5D shows the calibration graph of the reduction current vs H_2O_2 concentration. It can be assumed that the AFO-GCE shows a linear range from 1 μM to 5.848 mM, which is described as I (μA) = −27.6904 × −26.870 with a correlation coefficient R^2 = 0.99135 and a sensitivity S = 27.2 μA cm^{-2} mM^{-1}. The LOD was calculated to be 1.08 μM. This is considerably less than that of the majority of the other relevant sensors listed in Table S2.

3.3.3. Selectivity, Stability, Reproducibility, and Repeatability of the Sensor. To determine the selectivity of the AFO-GCE toward H_2O_2 detection, several electrocatalytic interferences, such as UA, AA, DA, and KCl, were used in the CA technique. The CA measurement was performed by the addition of 1.0 mM H_2O_2, 0.1 mM AA, DA, UA, and KCl, and the addition of 1 mM H_2O_2. Figure 5E shows that before and after adding interference, the addition of 1 mM H_2O_2 generated a significant current response at almost the same level. As a result, the interference had no noticeable effect on the CA current response of the AFO-GCE with good selectivity toward H_2O_2 detection. The reproducibility of five fabricated AFO-GCEs toward the H_2O_2 sensor was analyzed by the amperometric method. Figure S7C shows the histogram plot of five AFO-GCEs, exhibiting the RSD value = 2.5%. Then, the long-time stability of the AFO-GCE was tested before and after 10 days with 1 mM H_2O_2 by CV at the scan rate of 50 mV/s. Figure S7D shows that the current response before and after 15 days was almost the same at 95%. The fabricated AFO-GCE exhibited good reproducibility and long-term stability for H_2O_2 detection.

3.3.4. Real-Sample Analysis. The practicability of the fabricated AFO-GCE was determined by the amperometric response recorded in three different concentrations of H_2O_2 (1, 2, and 3 mM) in 0.1 M NaOH solution containing milk sample (Figure 5F). Hence, the spiked three concentrations of H_2O_2 recovery values were calculated and are shown in Table 2. As a result, the fabricated AFO-GCE sensor exhibits extraordinary recovery range from 95.5 to 97% with RSD = 1.09 to 1.60% for H_2O_2 detection in milk sample.

4. CONCLUSIONS

In summary, we successfully fabricated AFO NPs via a facile, one-pot, cost-effective sonochemical synthesis method for the first time. The obtained AFO NPs had good nanostructures, high activity, easy electron release, and excellent stability for the electrochemical sensing processes. In particular, AFO-modified GCEs exhibited high selectivity, sensitivity, and

https://doi.org/10.1021/acsanm.3c05236
ACS Appl. Nano Mater. 2024, 7, 2929−2938

Table 2. H_2O_2 Detection in Milk Sample

S.No	spiked H_2O_2 (mM)	detection of H_2O_2 (mM)	recovery (%)	RSD (n = 3) (%)
1	1.0	0.96	96	1.18
2	2.0	1.91	95.5	1.09
3	3.0	2.92	97	1.60

detection limits for RA and H_2O_2. Furthermore, AFO NPs were applied for the detection of RA in chicken and pork samples and H_2O_2 in milk samples with excellent sensing abilities. The proposed biosensor showed outstanding selectivity in the presence of a potentially active interference. Thus, this study provides a new strategy for the design and synthesis of highly active, stable, and novel-structured metal−metal oxide catalysts for electrochemical sensor applications.

■ ASSOCIATED CONTENT

Supporting Information

The Supporting Information is available free of charge at https://pubs.acs.org/doi/10.1021/acsanm.3c05236.

Brief description of instrumentation methods; electrochemical measurement; real-sample preparation for H_2O_2; FT-IR spectrum for AFO nanomaterial with different concentrations of Ag; elemental mapping of AFO nanomaterial; HR-TEM image of AFO nanomaterial with histogram plots; effect of Ag concentration and temperature; optimization of pH; CV plot for different concentrations of RA (1−10 μM); amperometric plot of different potentials; reproducibility test for the histogram plot and CV plot of stability test; comparison tables for the recently reported electrochemical RA and H_2O_2 sensors; and CV plot for different concentrations of H_2O_2 (0.1−1 mM) (PDF)

■ AUTHOR INFORMATION

Corresponding Authors

S. Umamatheswari − *PG and Research Department of Chemistry, Government Arts College (Affiliated to Bharathidasan University), Tiruchirappalli 620 022 Tamil Nadu, India*; orcid.org/0000-0003-0872-9923; Phone: +91-84382 88510; Email: drsumamatheswari@gmail.com

C. Sankar − *Department of Chemistry, Velammal College of Engineering and Technology, Madurai 625 009 Tamil Nadu, India*; Phone: +91-9944585257; Email: sankschem@gmai.com

Authors

M. Ramesh − *PG and Research Department of Chemistry, Government Arts College (Affiliated to Bharathidasan University), Tiruchirappalli 620 022 Tamil Nadu, India*

R. Jayavel − *Centre for Nanoscience and Technology, Anna University, Chennai 600 025 Tamil Nadu, India*

Complete contact information is available at: https://pubs.acs.org/10.1021/acsanm.3c05236

Notes

The authors declare no competing financial interest.

■ ACKNOWLEDGMENTS

The authors are thankful to the Centre for Nanoscience and Technology, Anna University, and SRM Central Instrumentation Facility (SCIF) for providing research facilities. One of the authors M. Ramesh acknowledges the Department of Collegiate Education Tamil Nadu for giving Research Scholar Stipend.

■ REFERENCES

(1) Bai, W.; Huang, H.; Li, Y.; Zhang, H.; Liang, B.; Guo, R.; Du, L.; Zhang, Z. Direct preparation of well-dispersed graphene/gold nanorod composites and their application in electrochemical sensors for determination of Ractopamine. *Electrochim. Acta* **2014**, *117*, 322−328.

(2) Duan, J.; He, D.; Wang, W.; Liu, Y.; Wu, H.; Wang, Y.; Fu, M.; Li, S. The fabrication of nanochain structure of gold nanoparticles and its application in ractopamine sensing. *Talanta* **2013**, *115*, 992−998.

(3) Sairi, M.; Arrigan, D. W. M. Electrochemical detection of ractopamine at arrays of micro-liquid | liquid interfaces. *Talanta* **2015**, *132*, 205−214.

(4) UN Food Safety Body Sets Limits on Veterinary Growth Promoting Drug. Codex Alimentarius Commission Adopts Maximum Residue Levels. 2012. http://www.fao.org/news/story/en/item/150953/icode. accessed April 29, 2020.

(5) *Residue Valuation of Certain Veterinary Drugs, Meeting 2010: Evaluation of Data on Ractopamine Residues in Pig Tissues*; Joint FAO/WHO Expert Committee on Food Additives: Rome, Italy, 2010; Vol. *52*.

(6) Haasnoot, W.; Stouten, P.; Lommen, A.; Cazemier, G.; Hooijerink, D.; Schilt, R. Determination of fenoterol and ractopamine in urine by enzyme immunoassay. *Analyst* **1994**, *119*, 2675−2680.

(7) Lam, H. M.; Remais, J.; Fung, M. C.; Xu, L.; Sun, S. S. M. Food supply and food safety issues in China. *Lancet* **2013**, *381*, 2044−2053.

(8) Song, M.-J.; Hwang, S. W.; Whang, D. Amperometric hydrogen peroxide biosensor based on a modified gold electrode with silver nanowires. *J. Appl. Electrochem.* **2010**, *40*, 2099−2105.

(9) Chen, S.; Yuan, R.; Chai, Y.; Hu, F. Electrochemical sensing of hydrogen peroxide using metal nanoparticles: a review. *Microchim. Acta* **2013**, *180*, 15−32.

(10) Ensafi, A. A.; Zandi-Atashbar, N.; Ghiaci, M.; Taghizadeh, M.; Rezaei, B. Synthesis of new copper nanoparticle-decorated anchored type ligands: Applications as nonenzymatic electrochemical sensors for hydrogen peroxide. *Mater. Sci. Eng., C* **2015**, *47*, 290−297.

(11) Watt, B. E.; Proudfoot, A. T.; Vale, J. A. Hydrogen Peroxide Poisoning. *Toxicol. Rev.* **2004**, *23* (1), 51−57.

(12) Hurdis, E. C.; Romeyn, H.; Romeyn. Accuracy of determination of hydrogen peroxide by cerate oxidimetry. *Anal. Chem.* **1954**, *26*, 320−325.

(13) Hsu, C.-C.; Lo, Y.-R.; Lin, Y.-C.; Shi, Y.-C.; Li, P.-L. A spectrometric method for hydrogen peroxide concentration measurement with a reusable and cost-efficient sensor. *Sensors* **2015**, *15*, 25716−25729.

(14) Hanaoka, S.; Lin, J.-M.; Yamada, M. Chemiluminescent flow sensor for H_2O_2 based on the decomposition of H_2O_2 catalyzed by cobalt (II)-ethanolamine complex immobilized on resin. *Anal. Chim. Acta* **2001**, *426*, 57−64.

(15) Fan, J.; Bian, X.; Niu, Y.; Bai, Y.; Xiao, X.; Yang, C.; Yang, J.; Yang, J. Formation of three-dimensional nano-porous silver films and application toward electrochemical detection of hydrogen peroxide. *Appl. Surf. Sci.* **2013**, *285*, 185−189.

(16) Li, J. R.; Zhuang, Z. X.; Guo, Z.; Liu, Z. G.; Huang, X. J. Framework-derived Fe_2O_3/Mn_3O_4 nanocubes as electrochemical catalyst for simultaneous analysis of Cu(II) and Hg(II). *Electrochim. Acta* **2021**, *399*, 139412.

(17) Ramezani, H.; Azizi, S. N.; Hosseini, S. R. NaY zeolite as a platform for preparation of Ag nanoparticles arrays in order to construction of H_2O_2 sensor. *Sens. Actuators, B* **2017**, *248*, 571−579.

(18) Balram, D.; Lian, K. Y.; Sebastian, N.; Alharthi, S. S.; Al-Saidi, H. M.; Kumar, D. Nanomolar electrochemical detection of feed additive ractopamine in meat samples using spinel zinc ferrite

decorated 3-dimensional graphene nanosheets to combat food fraud in livestock industries. *Food Chem.* **2024**, *437*, 137868.
(19) Zhang, Q.; Ma, S.; Zhuo, X.; Wang, C.; Wang, H.; Xing, Y.; Xue, Q.; Zhang, K. An ultrasensitive electrochemical sensing platform based on silver nanoparticle-anchored 3D reduced graphene oxide for rifampicin detection. *Analyst* **2022**, *147*, 2156−2163.
(20) Kannan, P.; Maiyalagan, T.; Pandikumar, A.; Guo, L.; Veerakumar, P.; Rameshkumar, P. Highly sensitive enzyme-free amperometric sensing of hydrogen peroxide in real samples based on Co_3O_4 nanocolumn structures. *Anal. Methods* **2019**, *11*, 2292−2302.
(21) Manavalan, S.; Ganesamurthi, J.; Chen, S. M.; Veerakumar, P.; Murugan, K. A robust Mn@FeNi-S/graphene oxide nanocomposite as a high-efficiency catalyst for the non-enzymatic electrochemical detection of hydrogen peroxide. *Nanoscale* **2020**, *12*, 5961−5972.
(22) Manavalan, S.; Veerakumar, P.; Chen, S. M.; Karuppusamy, N.; Keerthia, M. Development of robust multifunctional CrNiCo-P/GCN catalyst for oxygen evolution reaction, electrochemical sensing, and photodegradation of roxarsone. *Nanoscale* **2022**, *14*, 16233−16248.
(23) Jiang, J.; Lin, X.; Ding, D.; Diao, G. Enzyme-free homogeneous electrochemical biosensor for DNA assay using toehold-triggered strand displacement reaction coupled with host-guest recognition of Fe_3O_4@SiO_2@β-CD nanocomposites. *Biosens. Bioelectron.* **2018**, *114*, 37−43.
(24) Kuang, Y.; Zhang, J.; Xiong, M.; Zeng, W.; Lin, X.; Yi, X.; Luo, Y.; Yang, M.; Li, F.; Huang, Q. A novel nanosystem realizing curcumin delivery based on Fe_3O_4@carbon dots nanocomposite for Alzheimer's disease therapy. *Front. Bioeng. Biotechnol.* **2020**, *8*, 614906.
(25) Poo-arporn, Y.; Pakapongpan, S.; Chanlek, N.; Poo-arporn, R. P. The development of disposable electrochemical sensor based on Fe_3O_4-doped reduced graphene oxide modified magnetic screen-printed electrode for ractopamine determination in pork sample. *Sens. Actuators, B* **2019**, *284*, 164−171.
(26) Sobhanardakani, S.; Zandipak, R.; Sahraei, R. Removal of Janus green dyefrom aqueous solutions using oxidized multi-walled carbon nanotubes. *Toxicol. Environ. Chem.* **2013**, *95*, 909−918.
(27) Liu, Q.; Zhang, L.; Li, H.; Jia, Q.; Jiang, Y.; Yang, Y.; Zhu, R. One-pot synthesis of porphyrin functionalized γ-Fe_2O_3 nanocomposites as peroxidase mimics for H_2O_2 and glucose detection. *Mater. Sci. Eng., C* **2015**, *55*, 193−200.
(28) Li, D.; Hong, B.; Fang, W.; Guo, Y.; Lin, R. Preparation of Well-Dispersed Silver Nanoparticles for Oil-Based Nanofluids. *Ind. Eng. Chem. Res.* **2010**, *49*, 1697−1702.
(29) Ramesh, M.; Sankar, C.; Umamatheswari, S.; Raman, R. G.; Jayavel, R.; Choi, D.; Ramu, A. G. Silver-functionalized bismuth oxide ($AgBi_2O_3$) nanoparticles for the superior electrochemical detection of glucose, NO_2^- and H_2O_2. *RSC Adv.* **2023**, *13*, 20598−20609.
(30) Mafune, F.; Kohno, J.; Takeda, Y.; Kondow, T.; Sawabe, H. Structure and Stability of Silver Nanoparticles in Aqueous Solution Produced by Laser Ablation. *J. Phys. Chem. B* **2000**, *104*, 8333−8337.
(31) Achraf Ben Njima, M.; Legrand, L. Ag nanoparticles-oxidized green rust nanohybrids for novel and efficient non-enzymatic H_2O_2 electrochemical sensor. *J. Electroanal. Chem.* **2022**, *906*, 116015.
(32) Huang, Q.; Lin, X.; Chen, D.; Tong, Q. X. Carbon Dots/α-Fe_2O_3-Fe_3O_4 nanocomposite: Efficient synthesis and application as a novel electrochemical aptasensor for the ultrasensitive determination of aflatoxin B1. *Food Chem.* **2022**, *373*, 131415.
(33) Madhaiyan, R.; Chinnusamy, S.; Seeman, U.; Ramasamy, J. A facile synthesis of $CuZrO_2$ nanoparticle functionalized chitosan for capable and stable non-enzymatic electrochemical detection of glucose and H_2O_2. *New J. Chem.* **2023**, *47*, 15099−15110.
(34) Tajik, S.; Beitollahi, H.; Nejad, F. G.; Dourandish, Z.; Khalilzadeh, M. A.; Jang, H. W.; Venditti, R. A.; Varma, R. S.; Shokouhimehr, M. Recent developments in polymer nanocomposite-based electrochemical sensors for detecting environmental pollutants. *Ind. Eng. Chem. Res.* **2021**, *60*, 1112−1136.
(35) Fall, B.; Diaw, A. K. D.; Fall, M.; Sall, M. L.; Lo, M.; Gningue-Sall, D.; Thotiyl, M. O.; Maria, H. J.; Kalarikkal, N.; Thomas, S. Synthesis of highly sensitive rGO@CNT@Fe_2O_3/polypyrrole nanocomposite for the electrochemical detection of Pb^{2+}. *Mater. Today Commun.* **2021**, *26*, 102005.
(36) Madhu, R.; Veeramani, V.; Chen, S. M.; Veerakumar, P.; Liu, S. B..; Miyamoto, N. Functional porous carbon−ZnO nanocomposites for high-performance biosensors and energy storage applications. *Phys. Chem. Chem. Phys.* **2016**, *18*, 16466−16475.
(37) Veerakumar, P.; Sangili, A.; Chen, S. M.; Vinothkumar, V.; Balu, S.; Hung, S. T.; Lin, K. C. Zinc and Sulfur Codoped Iron Oxide Nanocubes Anchored on Carbon Nanotubes for the Detection of Antitubercular Drug Isoniazid. *ACS Appl. Nano Mater.* **2021**, *4*, 4562−4575.
(38) Li, Y. H.; Zhang, N.; Chen, J. X.; Li, R. J.; Li, L.; Li, K. Y. Fabrication of α-Fe_2O_3/TiO_2 Bi-functional composites with hierarchical and hollow structures and their application in water treatment. *J. Nanopart. Res.* **2016**, *18*, 36.
(39) Cao, L.; Ding, Q.; Liu, M.; Lin, H.; Yang, D. P. Biochar-Supported Cu2+/Cu+ Composite as an Electrochemical Ultrasensitive Interface for Ractopamine Detection. *ACS Appl. Bio Mater.* **2021**, *4*, 1424−1431.
(40) Kang, X.; Wu, Z.; Liao, F.; Zhang, T.; Guo, T. Ag/α-Fe_2O_3 hallow microspheres: preparation and application for hydrogen peroxide detection. *J. Solid State Chem.* **2015**, *229*, 266−271.
(41) Gunes, F.; Aykac, A.; Erol, M.; Erdem, Ç.; Hano, H.; Uzunbayir, B.; Sen, M.; Erdem, A. Synthesis of hierarchical heterocomposite of grephene foam/α-Fe_2O_3 nanowires and its application on glucose biosensors. *J. Alloys Compd.* **2022**, *895*, 162688.
(42) Darabi, R.; Shabani-Nooshabadi, M. $NiFe_2O_4$-rGO/ionic liquid modified carbon paste electrode: An amplified electrochemical sensitive sensor for determination of Sunset Yellow in the presence of Tartrazine and Allura Red. *Food Chem.* **2021**, *339*, 127841.
(43) Amudi, K.; Yigit, A.; Menges, N.; Talay Pınar, P. Highly selective electrochemical sensor for new generation targeted-anticancer drug Ibrutinib using newly synthesized nanomaterial GO-NH-B(OH)2@AgNPs modified glassy carbon electrode. *Measurement* **2023**, *216*, 112978.
(44) Ibrahim, H.; Temerk, Y. Surface decoration of functionalized carbon black nanoparticles with nanosized gold particles for electrochemical sensing of diuretic spironolactone in patient plasma. *Microchem. J.* **2022**, *178*, 107425.
(45) Liu, Z.; Zhou, Y.; Wang, Y.; Cheng, Q.; Wu, K. Enhanced oxidation and detection of toxic ractopamine using carbon nanotube film-modified electrode. *Electrochim. Acta* **2012**, *74*, 139−144.
(46) Begum, H.; Islam, M. N.; Ben Aoun, S.; Safwan, J. A.; Shah, S. S.; Aziz, M. A.; Hasnat, M. A. Electrocatalytic reduction of nitrate ions in neutral medium at coinage metal-modified platinum electrodes. *Environ. Sci. Pollut. Res.* **2022**, *30*, 34904−34914.
(47) Ramesh, M.; Sankar, C.; Umamatheswari, S.; Balamurugan, J.; Jayavel, R.; Gowran, M. Hydrothermal synthesis of $ZnZrO_2$/chitosan ($ZnZrO_2$/CS) nanocomposite for highly sensitive detection of glucose and hydrogen peroxide. *Int. J. Biol. Macromol.* **2023**, *226*, 618−627.
(48) Kurowska, E.; Brzozke, A.; Jarosz, M.; Sulka, G. D.; Jaskula, M. Silver nanowire array sensor for sensitive and rapid detection of H_2O_2. *Electrochim. Acta* **2013**, *104*, 439−447.

International Journal of Biological Macromolecules 264 (2024) 130533

Contents lists available at ScienceDirect

International Journal of Biological Macromolecules

journal homepage: www.elsevier.com/locate/ijbiomac

Synthesis of silver-bismuth oxide encapsulated hydrazone functionalized chitosan ($AgBi_2O_3$/FCS) nanocomposite for electrochemical sensing of glucose, H_2O_2 and *Escherichia coli* O157:H7

M. Ramesh [a], S. Umamatheswari [a,*,1], P.M. Vivek [b], C. Sankar [c,*,1], R. Jayavel [d]

[a] PG and Research Department of Chemistry, Government Arts College (Affiliated to Bharathidasan University), Tiruchirappalli 620 022, Tamil Nadu, India
[b] Department of Chemistry, Vel Tech Rangarajan Dr. Sagunthala R&D Institute of Science and Technology (Deemed University), Chennai 600 062, Tamil Nadu, India
[c] Department of Chemistry, Velammal College of Engineering and Technology, Madurai 625 009, Tamil Nadu, India
[d] Centre for Nanoscience and Technology, Anna University, Chennai 600 025, Tamil Nadu, India

ARTICLE INFO

Keywords:
$AgBi_2O_3$
1,3,5-Triazine chitosan
Glucose
H_2O_2
E. coli O157:H7

ABSTRACT

In this work, silver-bismuth oxide encapsulated 1,3,5-triazine-bis(4-methylbenzenesulfonyl)-hydrazone functionalized chitosan (SBO/FCS) nanocomposite was synthesized by a simple hydrothermal method. The amine ($-NH_2$) group was functionalized by the addition of cyanuric acid chloride followed by 4-methylbenzenesulfonol hydrazide. The SBO/FCS has been characterized by FT-IR, X-ray diffraction, XPS, HR-SEM, HR-TEM, AFM, and thermogravimetry (TGA). Under the optimum conditions, the SBO/FCS sensor showed brilliant electrochemical accomplishment for the sensing of glucose and H_2O_2 by a limit of detection (LOD) of 0.057 μM and 0.006 μM. It also showed linearity for glucose 0.008–4.848 mM and for H_2O_2 of 0.01–6.848 mM. Similarly, the sensor exhibited a low sensitivity to glucose (32 μA mM^{-1} cm^{-2}) and a good sensitivity to H_2O_2 (295 μA mM^{-1} cm^{-2}). In addition, that the prepared electrode could be used to sense the glucose and H_2O_2 levels in real samples such as blood serum and HeLa cell lines. The screen printed electrode (SPE) immunosensor could sense the *E. coli* O157:H7 concurrently and quantitatively with a linear range of 1.0×10^1–1.0×10^9 CFU mL^{-1} and a LOD of 4 CFU mL^{-1}. Likewise, the immunosensor efficiently detect spiked *E. coli* O157:H7 in milk, chicken, and pork samples, with recoveries ranging from 89.70 to 104.72 %, demonstrating that the immunosensor was accurate and reliable.

1. Introduction

In the past few decades, rapid population growth, modernization, and lifestyle have had serious adverse effects on people's health and lives. For example, glucose is an important compound that provides energy for daily activities. The normal glucose concentration in the blood, ranging from 3.0 to 8.0 mM (80–120 mg/dL), can support the normal activity of tissues in the body. Meanwhile, hyperglycemia is a condition in which blood glucose concentrations exceed the usual range, known as diabetes mellitus (DM), and is a major metabolic disorder caused by high blood glucose levels. Diabetes is one of the most common and serious chronic diseases affecting public health. If this trend continues, it is expected to be 6th leading source of mortality worldwide by 2030 [1]. Continuous monitoring of blood glucose levels is the primary approach to detect diabetic or hyperglycemic conditions and prevent stroke, heart attack, kidney failure and blindness [2–4].

Likewise, hydrogen peroxide (H_2O_2) is a reactive oxygen species (ROS) that mostly results from protein folding, cell respiration, metabolic metabolism in organisms, and regulated biochemical reactions in animals and plants. It is also used in chemical, food, and environmental industries because of its significant redox ability. It is also one of the most prominent oxygen reactive species produced by the human system. Normal H_2O_2 levels in organisms guarantee signal transduction and the regular physiological function of cells. Diabetes, cancer, cardiac disorders, and Alzheimer's disease are major diseases associated with excess H_2O_2 [5–8]. Glucose and H_2O_2 concentrations in biological bodies are highly associated with physiological health. The immediate recognition of glucose and H_2O_2 in biological bodies is advantageous to find out the

* Corresponding authors.
E-mail addresses: drsumamatheswari@gmail.com (S. Umamatheswari), sankschem@gmail.com (C. Sankar).
[1] †Equal contribution.

https://doi.org/10.1016/j.ijbiomac.2024.130533
Received 10 November 2023; Received in revised form 19 February 2024; Accepted 27 February 2024
Available online 29 February 2024

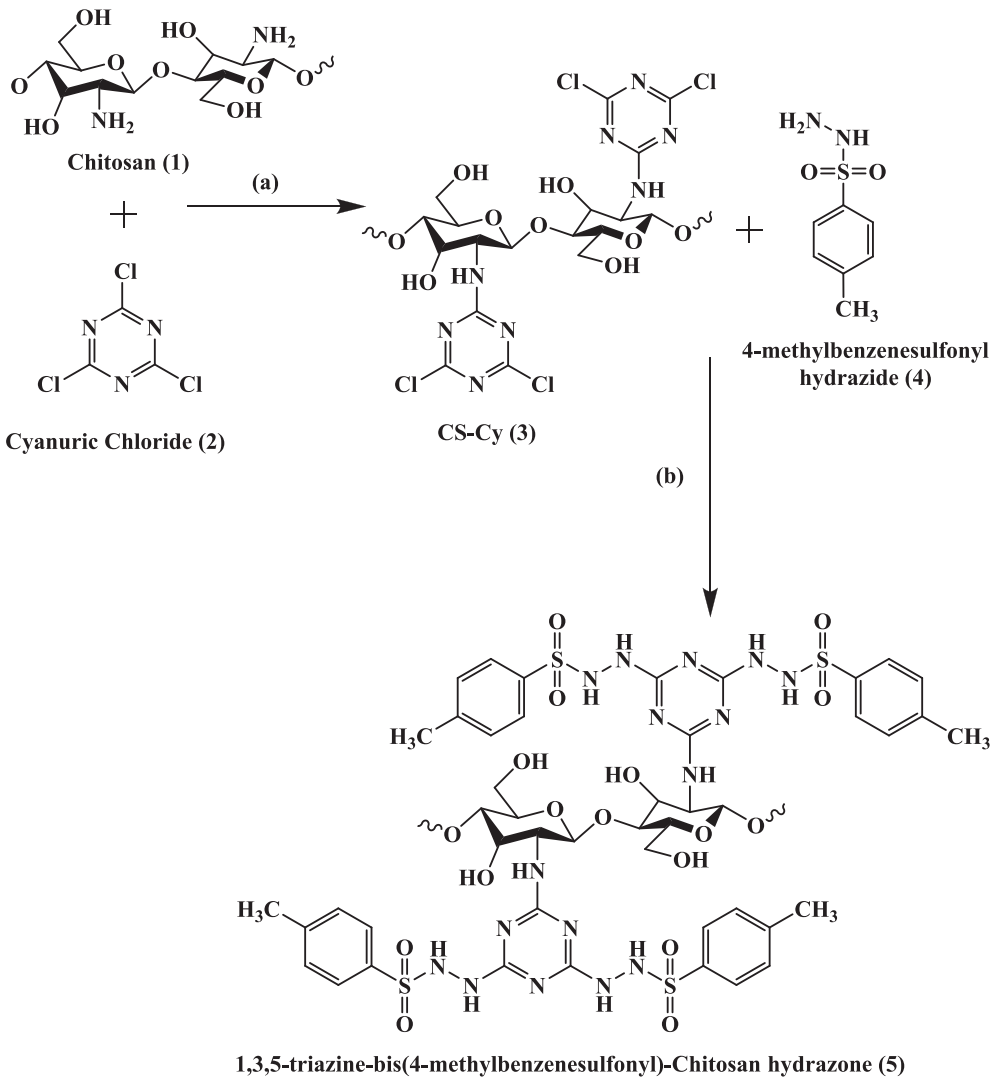

Scheme 1. Synthesis of hydrazone functionalized chitosan (**5**).

relationship of inherent small molecule-disease; in fact, on-time and accurate diagnosing of diseases is important in monitoring the progression of the disease. Therefore, it is vital and essential to develop a rapid and sensitive glucose and H_2O_2 detection strategy for the early diagnosis and treatment.

As we all know, bacterial pathogens are the most common cause of food poisoning. *Escherichia coli* bacteria, which are widespread in both food and humans, have recently emerged as a major cause of concern over the safety of our food supply [9]. It is essential to develop a fast and reliable method for identifying food borne pathogens to prevent and treat food borne infections [10]. Traditional culture-based procedures for identifying harmful pathogens require extensive time to find, even though they are the "gold standard" [11].

Over the past two decades, several research groups have reported numerous cutting-edge identification techniques, such as enzyme-linked immunosorbent assay (ELISA), polymerase chain reaction (PCR), DNA probes, gene chip technologies, titrimetry, fluorescence, spectrophotometry, calorimetry, and gas chromatography methods were effectively used to monitoring the glucose H_2O_2 and *E. coli* levels [12–25]. These methods are able to operate in near-real-time, exhibit high sensitivity and reproducibility, and can be carried easily [16]. Although these approaches can demonstrate strong specificity and high sensitivity for detection, their widespread implementation is hindered by a number of drawbacks, such as high cost, high technical requirements, and difficult detection processes. Obviously, the electrochemical method is promising and has several advantages, such as low cost, straightforward equipment, ease of use, high sensitivity, selectivity, and appropriateness for on-site sensing [26–28]. Thus, it is essential to develop a reliable signal multiplication approach to boost the sensitivity of the sensor.

Furthermore, metal-organic frameworks (MOFs) have drawn growing interest due to their tunable pore sizes, diverse structures, and abundant functional designs [29,30]. Compared with transition metals, silver (Ag) and bismuth metal organic frameworks, especially Ag/BiO-MOFs, have been studied widely due to their outstanding purity, strong van der Waals force, color, large Stokes shift, higher energy band gap, good optical, electrical properties, high oxygen-ion conductivity, along with noticeable photocatalytic activity, photoluminescence, long decay lifetime, and undisturbed emissive energy [31–33]. Recently, many Ag/Bi-MOFs were used as an ideal material for detecting small molecules, pathogenic bacteria, gases, and explosives [34–37].

To the best of our knowledge, this is the first time that a silver-doped Bi_2O_2/FCS (SBO/FCS) nanocomposite has been used for triad applications (Scheme 1). We also aimed to develop an electrochemical biosensor for direct, label-free detection of bacterial pathogens by modifying the gold-based screen-printed electrode with SBO/FCS to investigate their electrochemical stability during measurements. The fabricated electrode exhibited excellent efficiency in detecting low concentrations of glucose, H_2O_2, and *E. coli* in real samples.

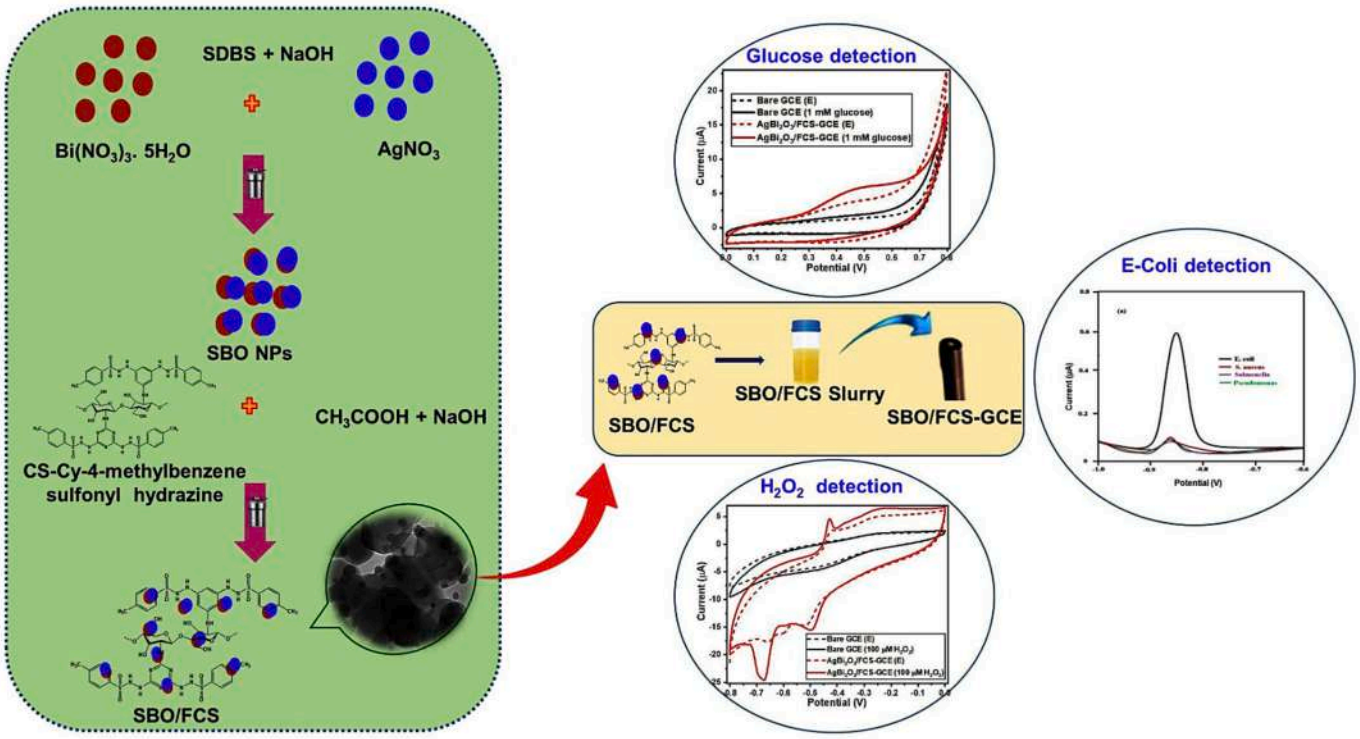

Scheme 2. Schematic representation for the fabrication of SBO, SBO/FCS nanocomposite.

2. Experimental

2.1. Materials and reagents

Chitosan, cyanuric chloride, 4-methylbenzenesulfonohydrazide, bismuth nitrate ($Bi(NO_3)_3.5H_2O$), zinc sulphate ($ZnSO_4$), silver nitrate ($AgNO_3$), sodium dodecylbenzene sulfonate (SDBS), glucose, sodium nitrite ($NaNO_2^-$), sodium hydroxide (NaOH), deionized water (DI), bovine serum albumin (BSA), hydrogen peroxide (H_2O_2), 2-methylimidazole, borax solution, zinc acetate (CH_3COOZn), and urea (NH_2CONH_2) were obtained from Sigma Aldrich, India. Abcam (India) provided the *E. coli* antibody. The non-pathogenic MTCC type *E. coli* strain was obtained from CSIR-Institute of Microbial Technology (IMTECH), Chandigarh, India, under the supervision of CSIR-IMTECH. Sodium acetate (CH_3COONa), dopamine (DA), potassium hydroxide (KOH), ascorbic acid (AA), sodium bicarbonate ($NaHCO_3$), uric acid (UA), and potassium chloride (KCl), were acquire from SRL Pvt. Lt. (India). The entire experiments were carried out using deionized (DI) water.

2.2. Synthesis of 1,3,5-triazine-bis(4-methylbenzenesulfonyl)-chitosan hydrazone (FCS) (5)

The synthesis of hydrazone functionalized chitosan (FCS) **5** was carried out by a two-step process (Scheme 1). In this study medium molecular weight (MMW) chitosan was used. In the initial stage: cyanuric chloride (0.02 mol) and chitosan (0.01 mol) were dissolved in 50 mL of acetic acid. Then, 0.5 mM of triethyl amine was added in this dispersion under vigorous stirring over a period of 10 h at 85–90 °C. After completion of the reaction, the reaction mixture was diluted by adding 200 mL of brine solution to it. A solid mass of 2,6-dichloro-6-chitosan-*s*-triazine chitosan was formed, filtered and recrystallized using ethanol as a solvent.

In the subsequent stage, the 2,6-dichloro-6-chitosan-*s*-triazine **3** (0.01 mol) was added into a stirred solution of 0.05 mol 4-methylbenzenesulfonylhydrazone (**4**) in the 50 mL of methanol in the presence of 0.5 mmol sodium acetate. Then, the total reaction mixture was refluxed for 10 h. Upon completion, a solid product was obtained by filtration, and washed with a mixture of warm water and ethanol (1:1) and recrystallized by ethanol. The obtained product was characterized by ^1H and ^{13}C NMR spectra.

2.3. Fabrication of $AgBi_2O_3$ (SBO) nanoparticles

The SBO NPs was fabricated by hydrothermal approach. Solution (a), 20 mL of DI water inclosing 0.2 M of $Bi(NO_3)_3.5H_2O$ and 2 mL HNO_3. Solution (b), 0.05 M $AgNO_3$ dispersed in 50 mL of DI water and stirred continuously 20 min. Subsequently, 0.5 g of SDBS was added into the reaction mixture at constant stirring, followed by addition of 4.0 M NaOH the pH of the reaction mixture was attained at 10. Then the reaction mixture was transformed into 100 mL of autoclave and heated for 12 h at 120 °C. The obtained solid mass was washed 5 times by DI water and dried at 80 °C for 12 h. Finally the product was well grained and annealed at 500 °C for 4 h.

2.4. Synthesis of SBO/FCS nanocomposite

During a typical synthesis of SBO/FCS nanocomposite, first 0.25 g of FCS (**5**) dissolved in 20 mL of ethanol. Subsequently, 20 mL of a 0.5 g aqueous SBO NPs was added into the reaction mixture with constant stirring at ambient temperature for 30 min. After adding 5 M of NaOH to that mixture, which was adjusted to have a pH of 10, a gel was produced. The obtained gel was heated for 10 h at 100 °C in an autoclave. The resulted solid mass was washed numerous times by the mixture of ethanol and DI water, dried at 100 °C for a period of 12 h and the reaction scheme was shown in Scheme 2.

2.5. Fabrication of the screen printing electrochemical immunosensor

The SBO/FCS fabricated GC electrode was used for the detection of glucose and H_2O_2. The fabrication of SBO/FCS GCE is given in the supporting information. Similarly the detection of *E. coli* was carried out

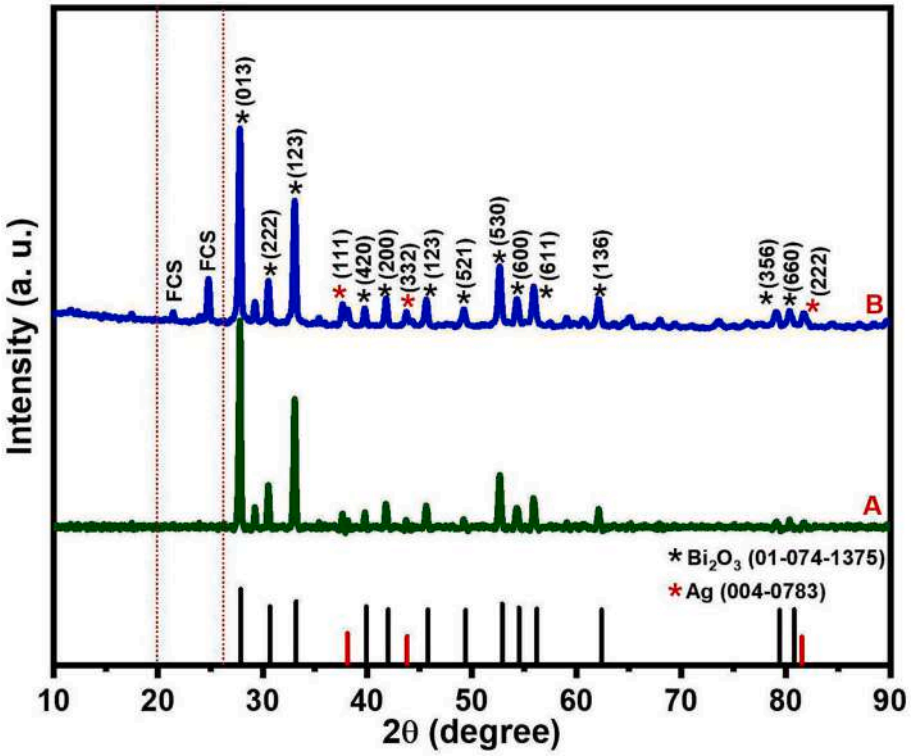

Fig. 1. XRD pattern of SBO NPs and SBO/FCS nanocomposite.

by SBO/FCS fabricated screen printing electrochemical (SPE) immunosensor (Scheme S1). In this method, 3 mm diameter Au used an electrode and fabricated by screen printing technique. The electrode was subjected into activation through treatment with a solution consisting of sulfuric acid and 30 % hydrogen peroxide, usually referred to as piranha solution. A volume of 5.0 μL of piranha solution was precisely deposited over the working electrode, after which it was allowed to remain undisturbed for a period of 30 s. Following that, the electrode underwent a comprehensive rinsing process using double-distilled water. Subsequently, the electrode surface was subjected to a drying process, followed by incubation in a 50 μL solution of the recently prepared slurry consisting of SBO (self-assembled monolayer of biotinylated oligonucleotides) and FCS (fetal calf serum) for duration of 12 h. This step aimed to facilitate the creation of a self-assembly monolayer (SAM) on the surface of the electrode. In the subsequent stage, the surface of SPE@SBO/FCS was modified by the incorporation of an amino group. This was achieved by adding 2 wt% of polyethyleneimine (PEI) in 100 μL of phosphate buffer solution at a pH of 7.4. Consequently, SPE@SBO/FCS/PEI was obtained. Subsequently, the electrode surface was subjected to a thorough rinsing with water, followed by a drying process utilizing a vacuum dryer.

Antibody conjugated SPE@SBO/FCS/PEI electrode was fabricated as follows two stages. In the stage first the SPE@SBO/FCS/PEI washed five times with PBS solution and the excess amount of buffers solution was removed. Then 0.20 wt% of glutaraldehyde containing 2 mL of PBS was added and sonicated for 30 min. In the second stage 20 μg/mL antibody capture of anibody-*E.coli* Ab, 0.01 M of PBS were added into the above the electrode surface. The total reaction mixture was incubated in 2 h and the obtained electrode was denoted as SPE@SBO/FCS/PEI-Ab. The electrode washed by 200 μL of PBS-20 buffer solution and dispersed in 1.0 mL of PBS. Subsequently, the electrode treated with 5 mL of 5 mm of BSA and sonicated 15 min. The blocking agent BSA was block the non-specific binding sites present in the electrode. Finally, the obtained SPE@SBO/FCS/PEI-Ab-BSA was suspended in to PBS solution and reserved at <4 °C for future use.

2.6. Real samples preparation

Human serum albumin (HSA) was acquired from Sigma Aldrich India. The stock solution was prepared by the addition of 0.5 μg of HAS into 50 mL of 1.0 M NaOH. The standard addition method (SAM) was utilized for the detection and determination of glucose in real samples. Known concentrations of glucose (0.5, 1.0, and 1.5 mM) were spiked in to the diluted serum samples and recovery of the glucose was evaluated.

Furthermore, for detection of H_2O_2 HeLa was selected as real sample models. HeLa cells were cultured in Dulbecco's Modified Eagle's Medium which contained 10 % *v*/v fetal bovine serum (FBS), 0.25 mg/mL G418, 1 % penicillin and streptomycin, 4 mM L-glutamine and 1 ng/mL doxycycline and grown at 37 °C and subcultured every 3 days, respectively. All the HeLa cells were maintained as monolayer cultures in a humidified atmosphere at 37 °C with 5 % CO_2 incubator. After three days, they were rinsed carefully several times phosphate buffer saline (PBS). Finally, 3 mL of PBS was added into test well and used for amperometric testing at −0.7 V potential.

To assess the performance of the fabricated biosensor, low fat milk, chicken and pork were used as real samples. All the real samples were purchased from local market. Samples were spiked with different concentration of *E. coli* to obtain the final concentrations of 3×10^3, 3×10^4 and 3×10^5 CFU·mL^{-1}. Stripping Voltammogram (DPV) was performed for the samples, and according to the calibration plot, the recovery percentage and RSD% were determined. It is also important to mention that we used a sample of low-fat milk purchased from the supermarket without special preparation or screening.

The raw pork and chicken samples were cut into small pieces, placed on a sterile plate, and subjected to UV light treatment for 1 h to remove the bacteria on the surface of raw samples. Then the raw samples were spiked with 3×10^3, 3×10^4 and 3×10^5 CFU·mL^{-1} of *E. coli* O157:H7. The spiked samples were allowed to dry in laminar flow for 1 h min.

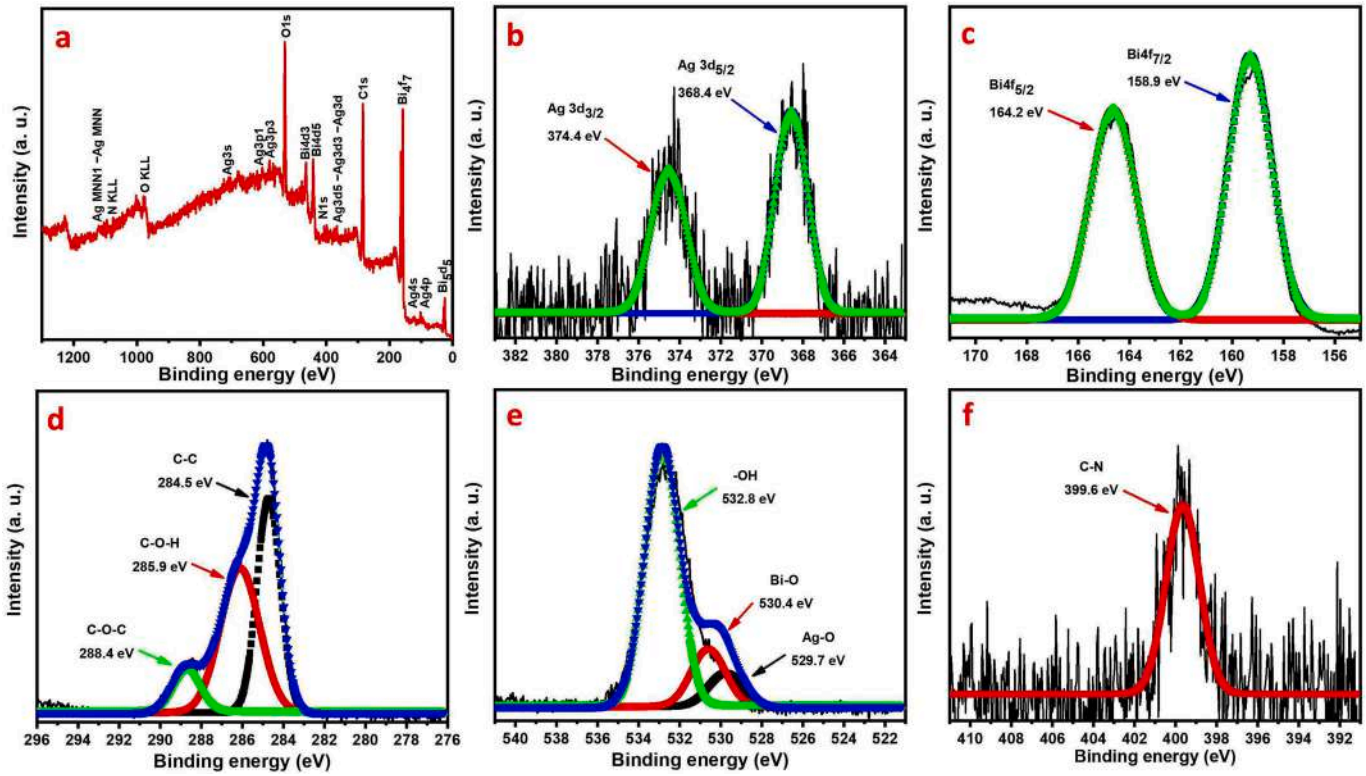

Fig. 2. XPS analysis of SBO/FCS nanocomposite. a) survey spectrum, b) Ag 3d spectrum, c) Bi 4f spectrum, d) C1s spectrum, e) O1s spectrum, f) N1s spectrum.

2.7. Electrochemical measurement

Electrochemical measurements were analyzed by CHI600E electrochemical workstation and data was analyzed CHI software with standard three electrode system, fabricated SBO/FCS-GCE used as a working electrode, silver/silver chloride (3 M KCl salt) and platinum wire were used as a reference and counter electrode. Cyclic voltammetry (CV) was recorded in 0.1 M aqueous NaOH at the potential range from 0 to 0.8 V and − 0.8 to 0 V for glucose and H_2O_2 respectively, at the scan rate 50 mVs^{-1}. The chronoamperometry (CA) also recorded in 0.1 M aqueous NaOH at potential of glucose 0.5 V and H_2O_2–0.68 V with continuous stirring.

3. Result and discussion

3.1. Synthesis of functionalized chitosan

The distinct reactivity of the three chlorine atoms in cyanuric chloride enables their substitution with diverse nucleophiles through temperature control. This phenomenon is being referred to commonly known as temperature-controlled selectivity. In addition, it is worth noting that cyanuric chloride exhibits favorable selectivity in nucleophilic substitution reactions involving the amino-to-hydroxyl group, a phenomenon usually referred to as functional group selectivity. Herein, we have synthesized a functionalized chitosan natural biopolymer by the reaction between cyanuric chloride and 4–methylbenzenesulfonyl hydrazide involving hydrazone linkage as given in Scheme 1. In the 1st step, cyanuric chloride **1** was treated with chitosan, one chorine could be replaced by the amine group (−NH_2) of chitosan to yield 2,4-dichloro-6-chitosan-*s*-triazine **3**. In the subsequent stage, compound **3** was reacted with two equiv. of 4–methylbenzenesulfonyl hydrazide to gives corresponding hydrazone derivative **5** with high yield.

3.2. Characterization of SBO and SBO/FCS nanocomposites

The chemical structure of the target molecule **5** was further confirmed by ^1H and ^{13}C NMR spectroscopy, and the NMR spectra are shown in Figs. S1 and S2 (Supporting Information). The ^1H NMR spectrum clearly shows that the multiplet centred at 7.1–7.8 ppm signals corresponds to the aromatic protons of hydrazone. The chitosan ring protons H_3, H_4, H_5, and H6 merged with the solvent DMSO-d_6 peak at 3.37 ppm. In hydrazone, the methyl proton at C-4 appeared as a singlet at 1.19 ppm equivalent to three protons, which confirmed the presence of a methyl group. In the ^{13}C NMR spectrum, the chemical shifts between δ 60 and 80 ppm were assigned to the carbons of the chitosan backbone. There were four weak signals in the downfield region δ 180.53, 177.19, 129.23 and 128.98 ppm. The chemical shift at 180.53 and 177.19 ppm are due to the 1,3,5-triazin (-C=N) carbons and another two weak signals δ 129.23 and 128.98 ppm are due to the ipso carbon of 4–methylbenzenesulfonyl hydrazide. All the observed chemical shifts were confirmed by the formation of target molecule **5**.

The XRD pattern of the newly fabricated SBO NPs and SBO/FCS nanocomposite is depicted in Fig. 1. All the diffraction peaks are identified and compared with the *JCPDS No* of Ag (00–004-0783) and Bi_2O_3 (01–074-1375), shown in Fig. 1A. The XRD pattern of Ag assign to the cubic system, Fm3m space group and Bi_2O_3 assign to the cubic system with space group 123. The XRD peaks observed at 2θ = 38.05, 43.74, 81.60 corresponds to (111), (332), (222) are crystalline planes of Ag and 2θ = 27.86, 30.64, 33.2, 39.9, 42.0, 45.8, 49.4, 52.9, 54.5, 56.2, 62.4, 79.4 and 80.8 corresponding to the (013), (222), (123), (420), (332), (431), (521), (530), (600), (611), (136), (356) and (660) crystalline planes of Bi_2O_3 respectively. Further peaks at 21.43 and 24.84 reveal chitosan's presence in the SBO/CS nanocomposite (Fig. 1B). The high intense sharp diffraction peaks are depict the synthesized nanocomposite is in good crystalline nature. The crystalline size of the nano composite is determined by the Debye-Scherrer equation and the estimated average crystalline size of SBO NPs is 14 ± 2 and SBO/FCS is 20 ± 2 nm.

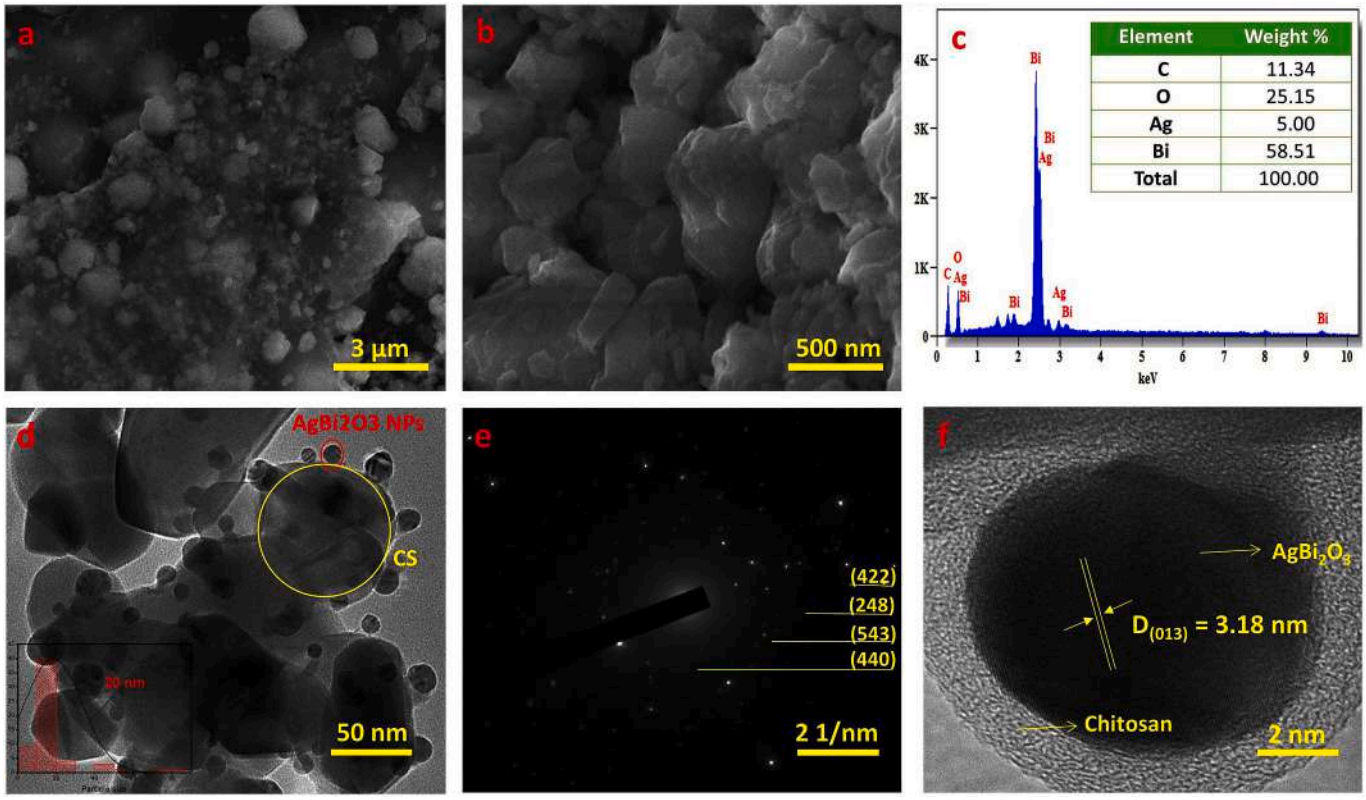

Fig. 3. a & b) HR-SEM images of SBO/FCS nanocomposite. c) EDS spectrum of the nanocomposite. d) HR-TEM image of SBO/FCS nanocomposite (inset: particle size distribution of histogram plot). e) SAED pattern, f) IFFT image.

The bonding nature, surface chemistry and functional groups of the SBO and SBO/FCS NPs was studied by FTIR spectroscopy and shown in Fig. S3. The peaks between 400 and 600 cm-^{1} indicate the Bi—O vibration band, whereas the sharp peak 830 cm^{-1} is attributable to the Ag band. The band appeared at 3428 and 1633 cm^{-1} are corresponds to vibration of hydroxide (O—H) and carbonyl (C=O) stretchings (Fig. S3A). The broad peak appeared at 1082 cm^{-1} and 1382 cm^{-1} are ascribed to C-O-C and O—H stretching vibrations. The intense peaks at 1591 and 2925 cm^{-1} associated to the -CH and -CH_2 stretching vibrations. The multiple distinct peaks indicate that chitosan is present in this nanocomposite (Fig. S3B).

The XPS used to confirm the surface composition and elements oxidation state such as Ag, Bi, C, O, N in SBO/FCS (Fig. 2). The survey spectrum Fig. 2a clearly depicts the presence of Ag 3d, Bi 4f, C1s, O1s and N1s. The core Ag 3d spectrum Fig. 2b depicted two prominent peaks at 364.4 and 374.4 eV, conforming to Ag 3$d_{5/2}$ and Ag 3$d_{3/2}$, which imply the presence of Ag [38]. According to the Fig. 2c, the dual peaks of 158.9 and 164.2 eV are identical with Bi 4$f_{7/2}$ and Bi 4$f_{5/2}$, respectively

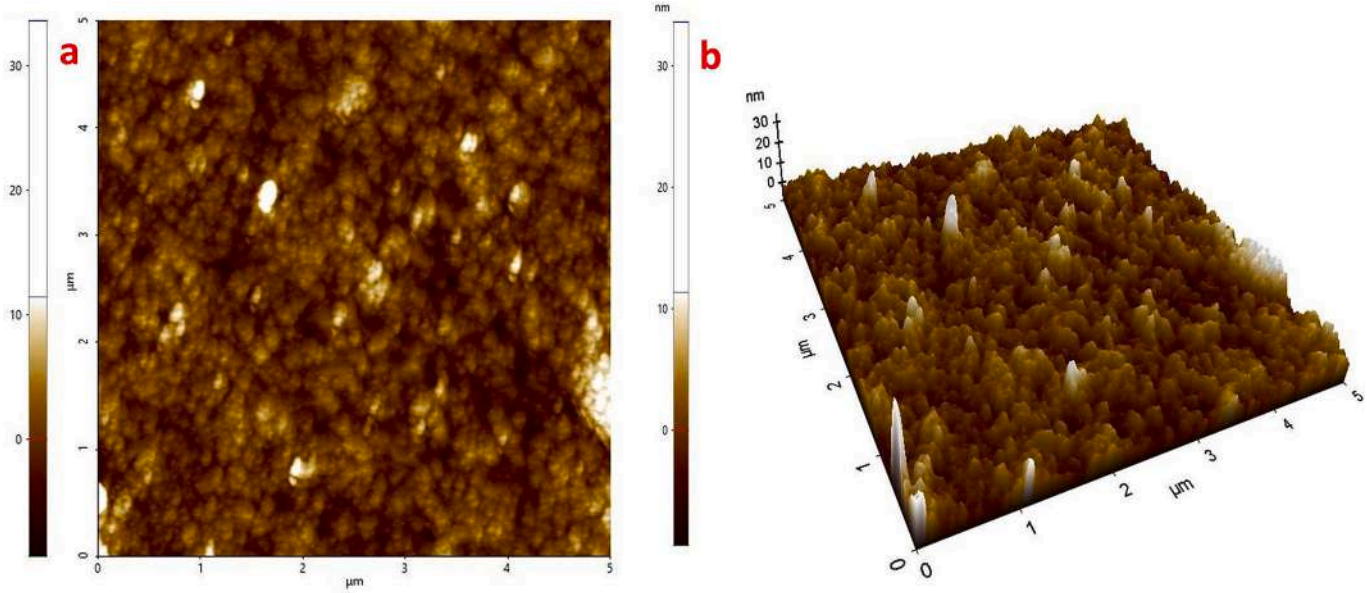

Fig. 4. AFM image of the SBO/FCS nanocomposite. a) 2D image. b) 3D image.

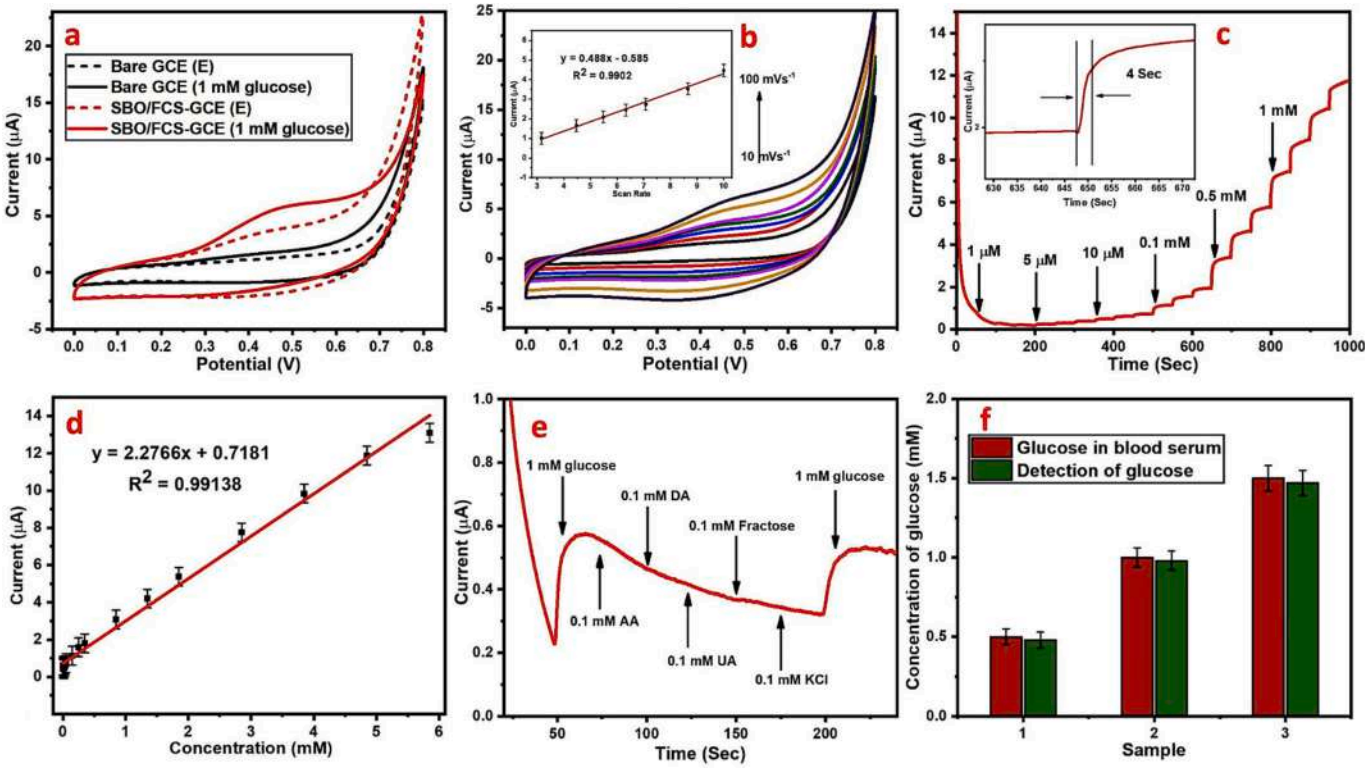

Fig. 5. a) CV plot of different electrodes (Bare GCE and SBO/FCS-GCE) with and without 1 mM glucose. b) CV plot of different scan rate with 1 mM glucose. c) Amperometric i-t curve for increasing concentration of glucose (1 μM to 5.848 mM). d) Calibration plot of glucose sensor. e) Anti interference study. f) Real sample analysis.

with a band gap of 5.3 eV ratifying Bi^{3+} is the primary oxidation state of bismuth in the SBO/CS nanocomposite [39]. Fig. 2d shows the C1s spectrum demonstrated the three main peaks observed at 284.5, 285.9 and 288.4 eV corresponds to C—C, C-O-H and C-O-C, respectively [25]. In addition three oxygen peaks were found at 529.7, 530.4 and 532.8 eV which belong to Ag—O, Bi—O and –OH, respectively [40] (Fig. 2e). The N1s spectrum in Fig. 2f shows the one main peak observed at 399.6 eV which can be ascribed to the C—N band in the chitosan core [25].

3.3. Evaluation of morphology by SEM and TEM analyses

To explore the morphology and particle size of the SBO/FCS nanocomposite was carried out by HR-SEM and HR-TEM is given in Fig. 3. Fig. 3a and b shows the HR-SEM image of the nanocomposite, it clearly depicts in a spherical shaped of SBO NPs and irregular shaped monocrystalline cluster of chitosan molecule. As a result the spherical shaped metal NPs were effectively embedded on the chitosan surface and the average particle size of this nanocomposite is 20 ± 1 nm. As seen in Fig. 3c, the purity and chemical constitution of the SBO/FCS NPs were analyzed by EDS. The presence of peaks for the components C, O, Ag, and Bi confirms the formation of $AgBi_2O_3$/FCS nanocomposite.

The HR-TEM (Fig. 3d) shows the spherical shaped SBO NPs (red color circle) was embedded on the functionalized chitosan's surface (yellow color circle) with a particle size of 20 nm. The HR-TEM images Fig. S4a and S4b, showed that the most of the NPs had a darker shell and a lighter core part, and that the SBO nanoparticles were embedded on the chitosan surface. The precise chitosan-incorporated $AgBi_2O_3$ nanocomposite structure is given, and it shows how the outlines of the hybrid nanocomposite are distinct and the nanoparticles seem to be clearly immersed in the polymeric medium. The SAED pattern of synthesized SBO/CS (Fig. 3e) undoubtedly depict the particles are polycrystalline nature with the inter planar distance D = 1.76, 1.40, 1.07 and 0.82 corresponds to (440), (543), (248) and (422). The lattice fringe of the SBO/FCS nanocomposite can be seen in the inverse fast Fourier transform analysis (IFFT) image (Fig. 3f). The D value of 3.18 nm corresponds to the (013) plane, and the dark parts of the image indicate the $AgBi_2O_3$ and the lighter parts indicate the chitosan molecule. The root mean square (RMS) roughness of SBO/FCS nanocomposite is frequently assessed using AFM. The two dimension and three dimension surface topography image of the nanocomposite was displayed in Fig. 4a and b. The estimated average RMS was only 0.92 μm. These findings enable to determine that the SBO/FCS nanocomposite is physically homogeneous. The particle diffusion and particulate interaction are strongly correlated with the volume of nanocomposite and the specific surface constituent of the chitosan membrane. The interaction between hydrazone functionalized chitosan and $AgBi_2O_3$ nanoparticles are thought to be the cause of the thickness producing a multilayered system.

The pore size and specific surface area (SSA) of the SBO/FCS NPs were further determined by means of the N_2 adsorption-desorption isotherm. The slight rise in adsorption seen with increasing pressure in the early part of the adsorption curve can be attributed to the monolayer-multilayer adsorption of N_2 molecules on SBO/FCS surface (Fig. S5). However, the type IV isotherm (hysteresis loop) is obtained at high pressure due to gas capillary condensation, which is consistent with the IUPAC-defined mesoporous structure of the material (Schneider, 1995). We calculate the mean average pore size distribution and surface area to be 7 nm and 132.2 m^2/g respectively, using the conventional equations. These findings proved that the NPs have an exceptionally large active surface area and desirable characteristics for biosensing.

3.4. TGA analysis

To calculate how much amount of hydrazone functionalized chitosan is present in the metal nanocomposite, a thermogravimetric analysis (TGA) of the SBO/FCS was performed. A weight loss of SBO/FCS nanoparticles in the presence of N_2 is seen in Fig. S6. The SBO/FCS TGA

curve may be divided into two distinct phases of weight reduction. The first is the initial sample weight loss up to 150 °C owing to evaporation of water molecules (moisture). Between 250 and 400 °C, however, the most significant weight loss occurred (about 27 %), along with the degradation of organic (chitosan) molecule. Using the difference in weight percentage at the conclusion of the TGA curves for pure SBO NPs and SBO/FCS, we may infer that SBO/FCS contains roughly 10 wt% of chitosan molecule.

3.5. Electrochemical detection of glucose

3.5.1. Cyclic voltammetry

The electrochemical behaviour of unmodified GCE and SBO/FCS-GCE were recorded by CV at a sweep rate of 50 mV/s, in ambient temperature. In Fig. 5a, the unmodified GCE didn't show any noticeable peak. On the other hand, the SBO/FCS-GCE displays a fine anodic peak was observed at 0.45 V with the addition of 1.0 mM glucose. It is apparently suggest that the oxidation peak of glucose increased after the modification of GCE with SBO/FCS. It reveals that the Ag NPs and FCS were enlightening the performance of the electrode.

Further, the effect of scan rate on the electrochemical behaviour of glucose was observed by varying the scan rate from 10 to 100 mV/s (Fig. 5b). The result suggests that both oxidation and reduction peak currents were increased linearly with increasing scan rate, which can be expressed by linear regression equation I_{pa} (μA) = 2.118x − 9.405. The square root of the scan rate was plotted against the peak current that showed a linear curve with an R^2 value of 0.9902. It indicate that electrochemical oxidation reaction of glucose over SBO/FCS electrodes is a diffusion-controlled process

Also, the sensitivity of the electrode was determined by CVs at varying concentrations of glucose from 1 to 10 mM and shown in Fig. S7a. In absence of glucose, there was no discernible current response. At same time while increasing the concentration of glucose, the anodic peak potentials (Ea) were shifted into the positive direction. The current density was directly proportional to the concentration of glucose. These results indicate that the electron transfer involved a diffusion controlled process.

The electrode projects a potential oxidation process for the glucose during the anodic sweep, and BiO^+ may be oxidized into BiO^{3+}. The electrochemical oxidation of glucose using NPs is given in the following mechanism.

$$BiO_3 + 3OH^- \rightarrow BiOOH + H_2O + e^- \quad (1)$$

$$BiOOH + C_6H_{12}O_6 \rightarrow BiO_3 + C_6H_{10}O_6 \quad (2)$$

3.5.2. Chronoamperometry

Based on the observed electrochemical behaviour from CV, the chronoamperometric i-t responses of the SBO/FCS modified GC electrode with addition of 0.5 mM glucose at various potentials were investigated and given in Fig. S7b. It demonstrates that the potential goes to 0.4, 0.5, and 0.6 V, the oxidation peak current increases significantly. The oxidation current response of the modified SBO/FCS-GC electrode gives an outstanding response at 0.5 V potential. Therefore, 0.5 V was chosen as the optimal potential for chronoamperometric analysis and shown in Fig. 5c.

The amperometric response of the SBO/FCS was studied by the progressive addition of glucose to a 0.1 M aqueous NaOH at regular intervals. The electrode initiates a rapid response upon the addition of glucose, reaching a steady state current of 90 % within 4 s. This shows that the electrode is sensitive to glucose very quickly and well. The electrode calibration plot is depicted in Fig. 5d, illustrating the variation in glucose concentration from 1 μM to 5.848 mM. From the calibration plot (current vs. glucose concentration), the current response increased linearly with increasing the concentration of glucose. The calibration plot is determined to be linear with a correlation coefficient R^2 is 0.99138 and the linear regression equation y = 2.2766× + 0.7181 with a limit of detection 0.057 μM. The SBO/FCS electrode also exhibited a high sensitivity of 32 μA mM^{-1} cm^{-2} by dividing the slope of the linear part of the calibration plot by the surface area of the electrode's [41]. When the results of the new sensor and proposed method are compared to those reported in the literature, the fabricated SBO/FCS sensors shows a similar or same LOD, linear range, and sensitivity for detecting glucose (Table S1).

Table 1
Determination the concentrations of glucose in human serum albumin (HSA) SBO/FCS-GCE sensor.

Sample	Spiked Amount (mM)	Detection Amount (mM)	Recovery (%)	RSD (%) (n = 3)
Glucose (HSA)	0.5	0.48	96	2.27
	1.0	0.98	98	2.63
	1.5	1.47	98	2.78

Selectivity is an important parameter in sensor for particular application, Fig. 5e displays the selectivity of the electrode in presence of common interferences such as AA, DA, UA, and KCl. After adding 1.0 mM glucose and 0.1 mM of each interference into the electrolyte at 0.5 V, the chronoamperometric current response of the SBO/FCS electrode clearly shows the current response increases with each addition of glucose; however, signal was not significantly impacted in the presence of interferences. It shows, the fabricated SBO/CS-GC electrode can be used for the selective detection of glucose.

The stability of the SBO/FCS was investigated by CV on the 1st - 15th days (Fig. S8a). The current response of glucose is nearly 93 % same before and after 15 days of oxidation. It clearly indicates that the SBO/FCS modified GCE electrode exhibit good stability. To study the reproducibility of the SBO/FCS electrode towards the oxidation of glucose, five freshly fabricated electrodes were evaluated by relating their current response in 0.1 M NaOH with 1 mM glucose (Fig. S8b). The RSD of all five electrodes was 2.2 %, indicating that SBO/FCS was highly reproducible.

3.5.3. Viability in real samples

The good sensing ability of SBO/FCS demonstrates its suitability for detecting glucose in real samples, which was evaluated by identifying the amount of glucose in human serum albumin samples. Known concentrations of glucose (0.5, 1.0, and 1.5 mM) were added in to the diluted serum samples and recovery of the glucose was evaluated (Fig. 5f and Table 1). The glucose recoveries at the SBO/CS sensor ranged from 96 to 98 %, with an RSD of 2.27 to 2.78 %. Similarly, the glucose level measured by the SBO/FCS sensor for the standard addition of glucose in the serum samples was extremely similar to the glucose level discovered by the commercial device. These analyses reveal that the fabricated SBO/FCS sensor can be applied for the practical analysis of glucose in clinical specimens.

3.6. Electrochemical detection of H_2O_2

3.6.1. Cyclic voltammetry

The electrochemical reduction the SBO/FCS NPs was examined by cyclic voltammetry in 1.0 mM H_2O_2 at 50 mV/s. The CV responses of unmodified GCE and SBO/FCS modified GCE with and without addition of H_2O_2 were shown in Fig. 6. There was no peak observed in bare GCE with and without 1.0 mM H_2O_2 (Fig. 6a). Interestingly, a high enhanced reduction current response was observed at −0.68 V for the SBO/FCS-GC electrode. Similarly the reduction activity of the SBO/FCS-GC electrode towards H_2O_2 was assessed at various concentrations ranging from 1.0 to 10 mM. Fig. S9a shows the reduction current enhanced gradually with increasing amount of H_2O_2. The rise in reduction peak current shows that the modified SBO/FCS electrode could have a large surface

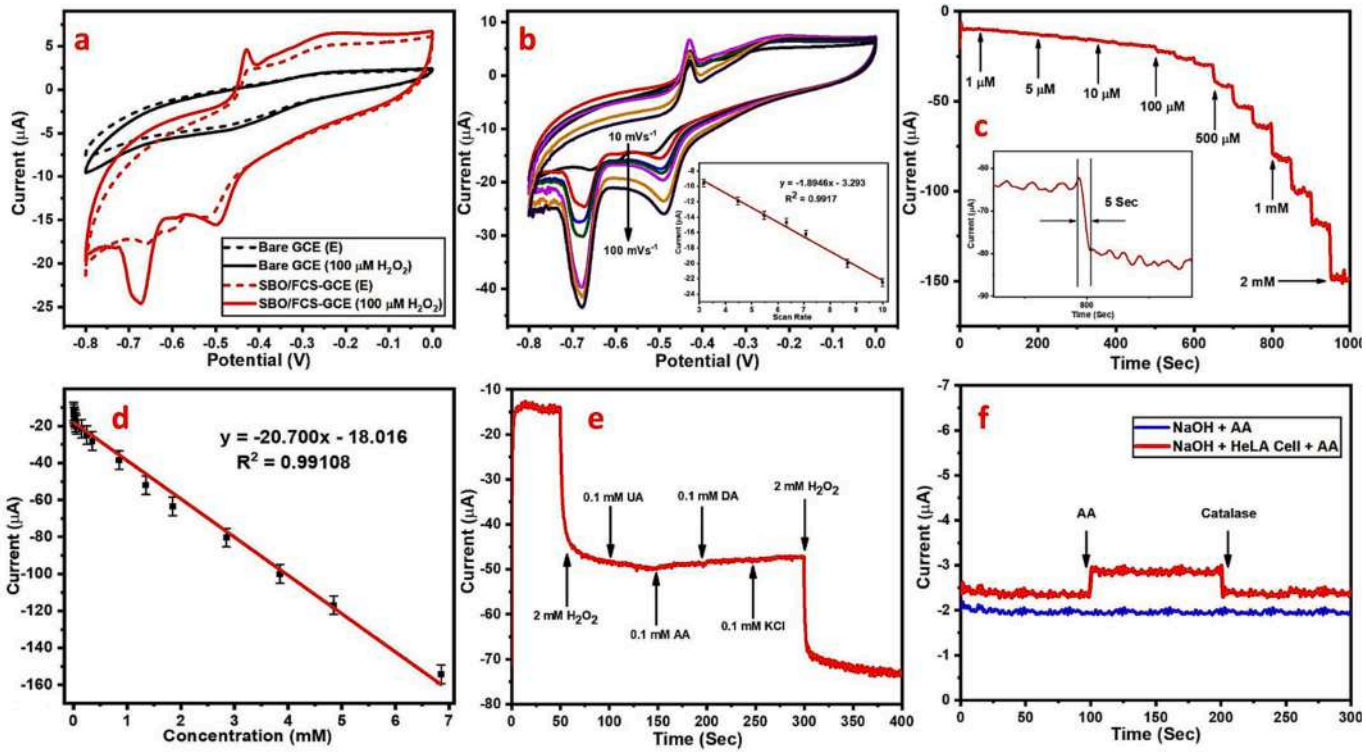

Fig. 6. a) CV plot of different electrodes (Bare GCE and SBO/FCS-GCE) with and without 1 mM H_2O_2. b) CV plot of different scan rate with 1 mM H_2O_2. c) Amperometric i-t curve for increasing concentration of H_2O_2 (1 μM to 6.848 mM). d) Calibration plot of H_2O_2 sensor. e) Anti interference study. f) Real sample analysis.

area and a higher concentration of SBO/FCS electrode could help reduce H_2O_2 through electrocatalytic reductions. Because SBO/FCS possesses a high specific surface area, they also have a large area where H_2O_2 can stick to them. Because of this, electrodes with a superior SSA will get more H_2O_2 on their surfaces, flow of electrons capacity will make it easier for them. When H_2O_2 introduced in the NaOH solution, the reduction mechanism followed the following reactions [42].

$$H_2O_2 + e^- \leftrightarrow OH(ads) + OH^- \quad (3)$$

$$OH(ads) + e^- \leftrightarrow OH^- \quad (4)$$

$$OH^- + 2H^+ \leftrightarrow 2H_2O \quad (5)$$

The effect of scan rate on the electrocatalytic reduction reaction was studied by cyclic voltammetry with various scan rates of 10–100 mVs^{-1}. The reduction peak current increased linearly with increasing scan rate. The linear regression equation for the correlation coefficient of cathodic current (Ipc) and square root of scan rate ($v^{1/2}$) was found to be y = −1.8946× - 3.293, R^2 = 0.9917 (Fig. 6b). These results show the fabricated SBO/CS-GC electrode has outstanding electrocatalytic reduction of H_2O_2.

3.6.2. Chronoamperometry

Fig. S9b illustrates the amperometric (i-t) curve of H_2O_2 reduction by the fabricated SBO/FCS-GC electrode at different potentials at −0.5, −0.6, −0.7 and − 0.8 V. The observed reduction current response of the fabricated SBO/FCS-GC electrode at −0.7 V exhibits an excellent response for H_2O_2 detection. As a result, the potential −0.7 V was preferred for the further amperometric analysis. Fig. 6c shows the amperometric i-t curve of fabricated SBO/FCS-GCE with sequential addition of H_2O_2 from 1.0 μM to 6.848 mM into NaOH electrolyte at −0.7 V potential with stirring condition. When H_2O_2 is added, the electrode responds quickly, and it takes <5 s to get a steady state current of 94 %. This shows that electrode was very sensitive and works quickly. The current slowly increased with the increasing amount of H_2O_2 and there was a good relationship between the amount of H_2O_2 (1.0 M to 6.848 mM) and the reduction current (Fig. 6d).

The calibration plot between the concentration of H_2O_2 and reduction current (Fig. 6d) shows good correlation co-efficient ($R^2 = 0.99108$) with a high sensitivity 295 μA mM^{-1} cm^{-2} and a LOD of 0.006 μM. It indicates, the modified electrode exhibited a superior sensitivity and a lower detection limit when compared to other recent publications on non-enzymatic sensors based transition metal nanoparticles (Table S2).

The fabricated SBO/FCS sensor's selectivity was examined with common interferences for H_2O_2. 0.1 mM concentration of AA, DA, UA, 0.5 mM of KCl and 2 mM of H_2O_2 were tested with sensor at a − 0.7 V potential (Fig. 6e). The observed result indicates that the sensor reacts immediately to H_2O_2, but it does not show any response to other interferences. However, the magnitudes of the current response of the initial and final addition of H_2O_2 are similar. For each addition of interferences, a negligible amount of response was observed, confirming that the fabricated sensor shows good selectivity for the sensing of H_2O_2

The sensors stability and reproducibility was also tested by CV at the scan rate of 50 mV/s, The reduction current was observed with an RSD of 1.56 and the electrode's stability was found to be nearly 96 % the same on the 1st - 15th days (Fig. S10a). Further the reproducibility of the fabricated sensor was analyzed towards the reduction of H_2O_2, freshly prepared five electrodes was recorded by relating current response in electrolyte solution in presence of H_2O_2 (Fig. S10b). The five electrodes exhibit the RSD value is 1.54 % as a result, the fabricated SBO/FCS-GCE sensor having good stability and outstanding reproducibility.

3.6.3. Viability in real samples

We use HeLa cancer cell line to test how well the SBO/FCS sensor works for detecting H_2O_2 in real time. As shown in Fig. 6f, SBO/FCS was placed in the suspension of HeLa cells, the flow of current didn't changed much, while adding ascorbic acid into HeLa cell lines there was a big change in the flow of current, which indicates that live HeLa cells were

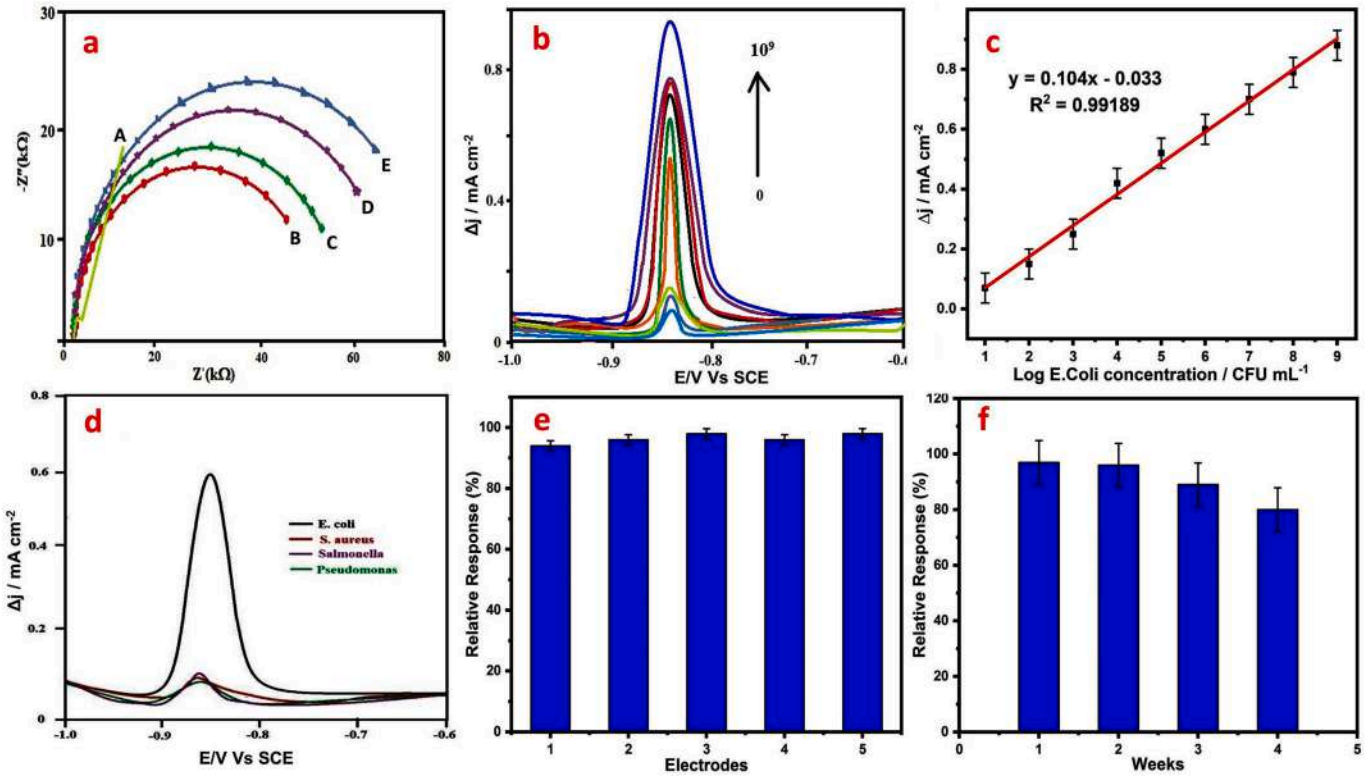

Fig. 7. a) EIS of bare SPE (A), SPE@SBO/FCS (B), SPE@SBO/FCS/PEI-Ab (C), SPE@SBO/FCS/PEI-Ab-BSA (D), and SPE@SBO/FCS/PEI-Ab-BSA-*E.coli* O157:H7 (E), containing mixture of 5.0 mM of $K_3Fe(CN)_6$ and $K_4Fe(CN)_6$. b) DPV for SPE@SBO/FCS/PEI-Ab-BSA with different concentration of *E. coli* O157:H7. c) Calibration plot of *E. coli* O157:H7 sensor. d) DPV for selectivity study for *E. coli* O157:H7. e) Reproducibility plot. f) Stability study.

giving off H_2O_2. So, it was very important for SBO/FCS to be able to detect H_2O_2 by living cells in real time. Our results showed that SBO/FCS might be a good way to track the H_2O_2 in living cells produce in real time.

3.7. Electrochemical detection of E.coli O157:H7

3.7.1. Electrochemical impedance spectroscopy analysis (EIS)

The pathogenic bacteria's can be detected by calculating the electron-transfer resistance (R_{ct}) in electrochemical impedance spectroscopy (EIS) and it is a wonderful technique as well. Fig. 7a shows the EIS of bare SPE (A), SPE@SBO/FCS (B), SPE@SBO/FCS/PEI-Ab (C), SPE@SBO/FCS/PEI-Ab-BSA (D), and SPE@SBO/FCS/PEI-Ab-BSA-*E. coli*O157:H7 (E). Both $K_3Fe(CN)_6$ and $K_4Fe(CN)_6$ acted as redox probes. In Fig. 7a, both semicircle and straight line impedance spectra can be seen, indicating that electron transfer and diffusion are occurring. The charge transfer resistance (R_{ct}) was anticipated to be 31.5 W based on the bare gold plated-SPE's extremely narrow semicircle and line EI spectrum. The R_{ct} value shows that the probe's redox reaction is extremely rapid. SBO/FCS-SPE has a high R_{ct} value of 598 Ω compared to bare gold plated-SPE, indicating that the deposition of SBO/FCS on SPE was successful. SPE@SBO/FCS/PEI-Ab-BSA electrode was then incubated in 1.0 mL of 10^4 CFU m/L *E. coli* O157:H7 with PBS at 35 °C for 1 h to produce the SPE@SBO/FCS/PEI-Ab-BSA-*E.coli* O157:H7, which has R_{ct} value of 3212 Ω.

3.8. Differential pulse stripping voltammogram (DPV) analysis

Further, differential pulse stripping voltammogram (DPV) was employed to understand the electrochemical process of (i) SPE@SBO/FCS and (ii) SPE@SBO/FCS/PEI-Ab and the change in current as a function of potential is displayed in Fig. S11. The current increased significantly for SPE@SBO/FCS@PEI-Ab, confirming the binding of the anti-*E. coli* antibody to the electrode. After the immobilization of anti-*E. coli* the peak potential was shifted slightly to the left, which indicates facile electron transfer on the electrode surface. The peak current increased as the amount of *E. coli* (CFU mL^{-1}) increased, indicating that antigen-antibody complexes coated the electrode surface (Fig. 7b). Fig. 7b exhibits DPVs for sensing of *E. coli* O157:H7 by SPE@SBO/FCS/PEI-Ab-BSA electrode as a signal tags. Even at low concentrations (1.0×10^3 CFU mL^{-1}) of *E. coli* O157:H7, a current signal can be observed (Fig. 7b). A linear relationship ($R^2 = 0.9919$) between the logarithm of the amount of *E. coli* O157:H7 from 1.0×10^1 to 1.0×10^9 CFU mL^{-1} and the peak current density (Fig. 7c). Peak current density is directly proportional to the amount of *E. coli* O157:H7 and the fabricated electrode shows a detection limit of 4 CFU mL^{-1} (S/N = 3). The performance of the fabricated SBO/FCS biosensor is revealed to be equivalent to or superior to that of the reported electrodes in Table S3. The selectivity of the biosensors was analyzed by SPE@SBO/FCS/PEI-Ab-BSA as signal tag. Fig. 7d and S12 demonstrate that the immunosensor has significant response to *E. coli* O157:H7 detection but a much poorer sensitivity to other pathogens. The immune biosensor is particularly effective in detecting *E. coli* O157:H7 because to the specific interaction between the *E. coli*-Ab and the antigen found on the surface of *E. coli* cells.

A sensor's reliability depends on its ability to function consistently throughout several analysis runs when using a single electrode or multiple electrodes made using the same technique. The reproducibility of the SBO/FCS based biosensor for *E. coli* O157:H7 was analyzed for five successive reading in 1.0×10^4 CFU mL^{-1} of *E. coli* O157:H7 (Fig. 7e). The resulting current response showed an RSD of 1.74 %, confirming that the immunosensor possess excellent reproducibility. Another important consideration in assessing the sensor performance is the stability of the immunosensor during extended periods of storage. The immunosensor maintained 90 % of its early response for first and second week after it was reduced (Fig. 7f), which indicates that the immunosensor is found to be an excellent stability up to two weeks of storage

Table 2
Detection results and recoveries of the immunosensor in milk, chicken and pork samples.

Sample	Spiked (CFU mL^{-1})	Found (CFU mL^{-1})	Recovery (%)	RSD (%, n = 3)
Milk	3×10^3	2.7×10^3	90.0	2.8
	3×10^4	2.5×10^4	83.3	3.0
	3×10^5	2.6×10^5	86.6	3.1
Chicken	3×10^4	2.8×10^4	93.3	2.7
	3×10^4	3.1×10^4	103.3	2.4
	3×10^5	2.9×10^5	96.6	2.9
Pork	3×10^4	2.6×10^4	86.6	2.4
	3×10^4	2.7×10^4	90.0	2.9
	3×10^5	3.2×10^5	106.6	2.9

towards detection of *E. coli* O157:H7.

3.8.1. Viability in real samples

To promote the analysis of the immunosensor's viability in real samples, milk, chicken, and pork were used as real sample model. In order to make an accurate estimation, the standard addition methodology was adopted. The real samples were analyzed at three different concentrations spiked with *E. coli* O157:H7 sample solution (**Fig. S13**), and the results were given in Table 2. The SPE@SBO/FCS/PEI-Ab-BSA exhibited a recovery range from 86 to 106 % with an RSD of 2.4 to 3.1 %. The results indicate that the SPE@SBO/CSPEI-Ab-BSA sensor could be highly feasible for the detection of *E. coli* O157:H7 in real samples.

4. Conclusion

In conclusion, we have successfully proposed an electrochemical sensor for non-enzymatic glucose and H_2O_2 detection used SBO/FCS. According to the experimental data demonstrated the SBO/FCS NPs have good electrocatalytic activity for the oxidation of glucose and reduction of H_2O_2, the response reached steady state within 4 and 5 s. The surface displayed linearity from 0.008 to 4.848 mM of glucose and 0.01–6.848 mM of H_2O_2, sensitivity of glucose 32 μA mM^{-1} cm^{-2} and H_2O_2 295 μA mM^{-1} cm^{-2}, detection limit of glucose 0.057 μM and H_2O_2 0.006 μM. Similarly, SPE@SBO/FCS/PEI-Ab-BSA/*E.coli* O157 has been design and fabricated in a single tags for a sensitive detection of *E. coli* O157:H7. The biosensor has a detection limit of 4 CFU mL^{-1}, which is one of the lowest detection limits. In addition to its high selectivity, the developed immunobiosensor efficiently detected *E. coli* O157:H7 in real samples such as milk, chicken and pork, indicating a viable tool for sensitive detection of *E. coli*. All of these observations imply that the fabricated sensor is a desirable and effective method for practical glucose, H_2O_2 and *E. coli* O157:H7 monitoring and provide a unique perspective on the possible applications of SBO/FCS in the area of electrochemical sensor.

CRediT authorship contribution statement

M. Ramesh: Formal analysis, Data curation, Conceptualization. **S. Umamatheswari:** Writing – review & editing, Investigation, Formal analysis, Data curation. **P.M. Vivek:** Resources. **C. Sankar:** Writing – review & editing, Writing – original draft, Resources, Data curation. **R. Jayavel:** Resources.

Declaration of competing interest

The authors declare that they have no known competing financial interests or personal relationships that could have appeared to influence the work reported in this paper.

Data availability

Data will be made available on request.

Acknowledgements

The authors are express sincere thanks to the Centre for Nanoscience and Technology, Anna University and SRM Central Instrumentation Facility (SCIF) for providing the all necessary instrument facilities. Mr. M. Ramesh likes to thank the Department of Collegiate Education Tamil Nadu for financial support as Research Scholar Stipend.

Appendix A. Supplementary data

Supplementary data to this article can be found online at https://doi.org/10.1016/j.ijbiomac.2024.130533.

References

[1] T. Jadoon, T. Mahmood, K. Ayub, Silver gluster (Ag_6) decorated coronene as non-enzymatic sensor for glucose and H_2O_2, J. Mol. Graph. Model. 103 (2021) 107824, https://doi.org/10.1016/j.jmgm.2020.107824.
[2] M. Asif, The prevention and control the type-2 diabetes by changing lifestyle and dietary pattern, J. Educ. Health Promot. 3 (2014) 1, https://doi.org/10.4103/2277-9531.127541.
[3] Diagnosis and classification of diabetes mellitus, Diabetes Care 37 (2014) S81–S90, https://doi.org/10.2337/dc14-S081.
[4] S. Vasudevan, I.B. Hirsch, Interference of intravenous vitamin C with blood glucose testing, Diabetes Care 37 (2014) 93–94, https://doi.org/10.2337/dc13-2452.
[5] S.K. Maji, S. Sreejith, A.K. Mandal, X. Ma, Y. Zhao, Immobilizing gold nanoparticles in mesoporous silica covered reduced graphene oxide: a hybrid material for cancer cell detection through hydrogen peroxide sensing, ACS Appl. Mater. Interfaces 6 (2014) 13648–13656, https://doi.org/10.1021/am503110s.
[6] Z. Li, Y. Xin, W. Wu, B. Fu, Z. Zhang, Topotactic conversion of copper (I) phosphide nanowires for sensitive electrochemical detection of H_2O_2 release from living cells, Anal. Chem. 88 (2016) 7724–7729, https://doi.org/10.1021/acs.analchem.6b01637.
[7] R. Weinstain, E.N. Savariar, C.N. Felsen, R.Y. Tsien, In vivo targeting of hydrogen peroxide by activatable cell-penetrating peptides, J. Am. Chem. Soc. 136 (2014) 874–877, https://doi.org/10.1021/ja411547j.
[8] M.P. Mattson, Pathways towards and away from alzheimer's disease, Nature 430 (2004) 631–639, https://doi.org/10.1038/nature02621.
[9] P.S. Mead, L. Slutsker, V. Dietz, L.F. McCaig, J.S. Bresee, C. Shapiro, P.M. Griffin, R. V. Tauxe, Food-related illness and death in the United States, Emerg. Infect. Dis. 5 (1999) 607, https://doi.org/10.3201/eid0505.990502.
[10] E.C. Alocilja, S.M. Radke, Market analysis of biosensors for food safety, Biosens. Bioelectron. 18 (2003) 841, https://doi.org/10.1016/S0956-5663(03)00009-5.
[11] A.P. Dufour, E.R. Strickland, V.J. Cabelli, Membrane filter method for enumerating Escherichia coli, Appl. Environ. Microbiol. 41 (1981) 1152–1158, https://doi.org/10.1128/aem.41.5.1152-1158.1981.
[12] N.V. Klassen, D. Marchington, H.C. McGowan, H_2O_2 determination by the I3-method and by $KMnO_4$ titration, Anal. Chem. 66 (1994) 2921–2925, https://doi.org/10.1021/ac00090a020.
[13] J. Odo, K. Matsumoto, E. Shinmoto, Y. Hatae, A. Shiozaki, Spectrofluorometric determination of hydrogen peroxide based on oxidative catalytic reactions of phydroxyphenyl derivatives with metal complexes of thiacalix arenetetrasulfonate on a modified anion-exchanger, Anal. Sci. 20 (2004) 707–710, https://doi.org/10.2116/analsci.20.707.
[14] A.C. Pappas, C.D. Stalikas, Y.C. Fiamegos, M.I. Karayannis, Determination of hydrogen peroxide by using a flow injection system with immobilized peroxidase and long pathlength capillary spectrophotometry, Anal. Chim. Acta 455 (2002) 305–313, https://doi.org/10.1016/S0003-2670(01)01600-2.
[15] M. Ramesh, C. Sankar, S. Umamatheswari, R. Ganapathi Raman, R. Jayavel, D. Coi, A.G. Ramu, Silver-functionalized bismuth oxide ($AgBi_2O_3$) nanoparticles for the superior electrochemical detection of glucose, NO_2^- and H_2O_2, RSC Adv. 13 (2023) 20598–20609, https://doi.org/10.1039/D2RA08140G.
[16] M. Uttamchandani, J.L. Neo, B.N. Ong, S. Moochhala, Applications of microarrays in pathogen detection and biodefence, Trends Biotechnol. 27 (2009) 53–61, https://doi.org/10.1016/j.tibtech.2008.09.004.
[17] L. Yang, W. Deng, C. Cheng, Y. Tan, Q. Xie, S. Yao, Fluorescent immunoassay for the detection of pathogenic bacteria at the single-cell level using carbon dots-encapsulated breakable organosilica nanocapsule as labels, ACS Appl. Mater. Interfaces 10 (2018) 3441, https://doi.org/10.1021/acsami.7b18714.
[18] X. Zhang, J. Shen, H. Ma, Y. Jiang, C. Huang, E. Han, B. Yao, Y. He, Optimized dendrimer-encapsulated gold nanoparticles and enhanced carbon nanotube nanoprobes for amplified electrochemical immunoassay of *E. coli* in dairy product based on enzymatically induced deposition of polyaniline, Biosens. Bioelectron. 80 (2016) 666, https://doi.org/10.1016/j.bios.2016.02.043.
[19] S. Wang, W. Deng, L. Yang, Y. Tan, Q. Xie, S. Yao, Copper-based metal–organic framework nanoparticles with peroxidase-like activity for sensitive colorimetric

detection of *Staphylococcus aureus*, ACS Appl. Mater. Interfaces 9 (2017) 24440, https://doi.org/10.1021/acsami.7b07307.
[20] M. Xu, R. Wang, Y. Li, Electrochemical biosensors for rapid detection of *Escherichia coli* O157:H7, Talanta 162 (2017) 511, https://doi.org/10.1016/j.talanta.2016.10.050.
[21] S.L. Zhao, H.J. Yin, L. Du, L.C. He, K. Zhao, L. Chang, Z.Y. Tang, Carbonized nanoscale metal–organic frameworks as high performance electrocatalyst for oxygen reduction reaction, ACS Nano 8 (2014) 12660–12668, https://doi.org/10.1021/nn505582e.
[22] S. Dang, Q.-L. Zhu, Q. Xu, Nanomaterials derived from metal-organic frameworks, Nat. Rev. Mater. 3 (2018) 17075, https://doi.org/10.1038/natrevmats.2017.75.
[23] P. Zhao, S. Chen, J. Zhou, S. Zhang, D. Huo, C. Huo, A novel Fe-hemin-metal organic framework supported on chitosanreduced graphene oxide for real-time monitoring of H_2O_2 released from living cells, Anal. Chem. Acta 1128 (2020) 90–98, https://doi.org/10.1016/j.aca.2020.06.008.
[24] M. Ramesh, C. Sankar, S. Umamatheswari, R. Jayavel, A facile synthesis of $CuZrO_2$ nanoparticle functionalized chitosan for capable and stable non-enzymatic electrochemical detection of glucose and H_2O_2, New J. Chem. 47 (2023) 15099–15110, https://doi.org/10.101039/D3NJ02177G.
[25] M.A. Rashed, J. Ahmed, M. Faisal, S.A. Alsareii, M. Jalalah, F. Harraz, A., Highly sensitive and selective thiourea electrochemical sensor based on novel silver nanoparticles/chitosan nanocomposite, Colloid. Surf. A Phys. Eng. Asp. 644 (2022) 128879, https://doi.org/10.1016/j.colsurfa.2022.128879.
[26] N. Zou, X. Wei, Z. Zong, X. Li, Z. Wang, X. Wang, A novel enzymatic biosensor for detection of intracellular hydrogen peroxide based on 1-aminopyrene and reduced graphene oxides, J. Chem. Sci. 131 (2019) 1–8, https://doi.org/10.1007/s12039-019-1604-y.
[27] T. Liu, Y. Guo, Z. Zhang, Z. Miao, X. Zhang, Z. Su, Fabrication of hollow CuO/PANI hybrid nanofibers for non-enzymatic electrochemical detection of H_2O_2 and glucose, Sensors Actuators B Chem. 286 (2019) 370–376, https://doi.org/10.1016/j.snb.2019.02.006.
[28] Y. Liu, H. Li, S. Gong, Y. Chen, R. Xie, Q. Wu, J. Tao, F. Meng, P. Zhao, A novel nonenzymatic electrochemical biosensor based on the nanohybrid of bimetallic PdCu nanoparticles/carbon black for highly sensitive detection of H_2O_2 released from living cells, Sensors Actuators B Chem. 290 (2019) 249–257, https://doi.org/10.1016/j.snb.2019.03.129.
[29] G. Li, Q. Xue, J. Feng, W. Sui, Electrochemical biosensor based on nanocomposites film of thiol graphene-thiol chitosan/nano gold for the detection of carcinoembryonic antigen, Electroanalysis 27 (2015) 1–9, https://doi.org/10.1002/elan.201400524.
[30] Y. Chang, F. Gao, T. Wu, Q. Pan, L. Liu, Q. Song, Electrochemical detection of protein kinases with methylene blue-functionalized Zr-based metal-organic frameworks as signal labels, Int. J. Electrochem. Sci. 18 (2023) 100338, https://doi.org/10.1016/j.ijoes.2023.100338.
[31] V. Fruth, M. Popa, D. Berger, R. Ramer, M. Gartner, A. Ciulei, M. Zaharescu, Deposition and characterization of bismuth oxide thin films, J. Eur. Ceram. Soc. 25 (2005) 2171–2174, https://doi.org/10.1016/j.jeurceramsoc.2005.03.025.
[32] H.T. Fan, X.M. Teng, S.S. Pan, C. Ye, G.H. Li, L.D. Zhang, Optical properties of δ-Bi_2O_3 thin films grown by reactive sputtering, Appl. Phys. Lett. 7 (2005) 8231916, https://doi.org/10.1063/1.2136351.
[33] Y. Tian, F.L. Wang, Y.X. Liu, F. Pang, X. Zhang, Green synthesis of silver nanoparticles on nitrogen-doped graphene for hydrogen peroxide detection, Electrochim. Acta 146 (2014) 646–653, https://doi.org/10.1016/j.electacta.2014.08.133.
[34] Y. Chang, J. Lou, L. Yang, M. Liu, N. Xia, L. Liu, Design and application of electrochemical sensors with metal–organic frameworks as the electrode materials or signal tags, Nanomaterials 12 (2022) 3248, https://doi.org/10.3390/nano12183248.
[35] Y. Dong, C. Duan, Q. Sheng, J. Zheng, Preparation of Ag@zeolitic imidazolate framework-67 at room temperature for electrochemical sensing of hydrogen peroxide, Analyst 144 (2019) 521–529, https://doi.org/10.1039/C8AN01641K.
[36] M. Hu, H. He, F. Xiao, C. Liu, Bi-MOF-derived carbon wrapped bi nanoparticles assembly on flexible graphene paper electrode for electrochemical sensing of multiple heavy metal ions, Nanomaterials 13 (2023) 2069, https://doi.org/10.3390/nano13142069.
[37] A. Anum, M. Altaf Nazir, S.M. Ibrahim, S.S. Ahmad Shah, A.A. Tahir, M. Malik, M. A. Wattoo, A. Rehman, Synthesis of Bi-metallic-sulphides/MOF-5@graphene oxide nanocomposites for the removal of hazardous moxifloxacin, Catalysts 13 (2023) 984, https://doi.org/10.3390/catal13060984.
[38] L.L. Tian, K.D. Xia, W.P. Hua, X.H. Zhong, Y.L. Chen, C. Yang, L. Li, A wide linear range and stable H_2O_2 electrochemical sensor based on Ag decorated hierarchical Sn_3O_4, Electrochim. Acta 231 (2017) 190–199, https://doi.org/10.1016/j.electacta.2017.02.052.
[39] L. Chen, L. Miao, Y. Chen, Y. Gao, J. Di, An enzyme-free photoelectrochemical glucose sensor based on coupling $BiVO_4$ with gold nanoparticles, Mater. Sci. Semicond. Process. 125 (2021) 105632, https://doi.org/10.1016/j.mssp.2020.105632.
[40] A. Koyappayil, S. Berchmans, M.-H. Lee, Dual enzyme-like properties of silver nanoparticles decorated Ag_2WO_4 nanorods and its application for H_2O_2 and glucose sensing, Colloids Surf. B: Biointerfaces 189 (2020) 110840, https://doi.org/10.1016/j.colsurfb.2020.110840.
[41] M. Ramesh, C. Sankar, S. Umamatheswari, J. Balamurugan, R. Jayavel, M. Gowran, Hydrothermal synthesis of $ZnZrO_2$/chitosan ($ZnZrO_2$/CS) nanocomposite for highly sensitive detection of glucose and hydrogen peroxide, Int. J. Biol. Macromol. 226 (2023) 618–627, https://doi.org/10.1016/j.ijbiomac.2022.11.318.
[42] A.K. Mohiuddin, S. Jeon, Highly efficient Ag doped δ-MnO2 decorated graphene: comparison and application in electrochemical detection of H2O2, Appl. Surf. Sci. 592 (2022) 153162, https://doi.org/10.1016/j.apsusc.2022.153162.

ScienceDirect

Materials Today: Proceedings

Available online 23 August 2023

In Press, Corrected Proof What's this?

Thermo-hydraulic performance of nanofluids composed of functionalized MWCNT

Ganimisetti Srinivasa Rao [a], V. Subha [b], S. Jagan Raj [c], Syed Farrukh Rasheed [d], M. Rashmi [e], K. Suganandam [f]

Show more

Share Cite

https://doi.org/10.1016/j.matpr.2023.08.084

Get rights and content

Abstract

The nanofluids can be utilized as the potential candidates for reducing wear between two metal surfaces. In this work, the characterization and rheological behavior of the ionic liquid 1-ethyl, 3-methylimidazolium dicyanamide had been performed, and its dispersions with different types of carbon nanotubes were compared. It was determined that the viscous behavior of nanofluids was in steady-state shear flow. Then, the study of tribology was performed to study the behavior of the dispersions as a lubricant. Particularly, AISI 316L stainless was used as the specimen considering its potential application in a number of machine parts. Hence, the wear behaviour of the nanofluid was studied by using them as the lubricant 0n AISI 316L steel surfaces. The specimen showed the better thermo-hydraulic performance, since its increments for the convective coefficient were higher.

Introduction

To the detriment of the growing demand of the world's energy consumption nowadays, the generation and use of energy has become a fundamental issue in the world. The high costs and the increasing use of fossil fuels have led to everyone's concern about the scarcity of these non-renewable resources [1]. Thus, large industries concerned about the lack of natural resources have made large investments and efforts in the development of high-performance systems and devices, to find solutions to reduce energy consumption and improve their efficiency, enabling more efficient consumption, in addition to avoid damage to the environment and the depletion of resources in the long term [2], [3]. Carbon-based materials are used in several recent studies targeting electrochemical applications, due to their properties, structure and abundance, together with the fact that they are environmentally benign. Among these materials, graphene stands out, the most recent allotrope of carbon. Graphene is an ordered material of carbon atoms in a flat sheet format, forming a monoatomic layer, organized in hexagonal cells, which presents structural properties such as high electronic mobility and transport unique in nature, with excellent mechanical, chemical and thermal properties [4], [5].

Conventional fluids in which a suspension of solid particles is used, which can be obtained by dispersing different nanoparticles of manometric size, with an interval of 1–100nm, are called nanofluids. Nanofluids consisting of Graphene nanoparticles (GNP) is one of the most promising fluids in heat transfer, due to its relatively high thermal conductivity of 5000W/m. K.

During the past decades, a wide variety of porous materials have been used to be functionalized with amino species for CO_2 capture, but the development of nanoscience and nanotechnology in recent years offers numerous opportunities and innovative solutions in this field [6], [7]. That is why there is a promising technique that is chemical adsorption on nanomaterials functionalized with organic molecules that contain amino groups [3]. The use of ionic liquids has aroused great interest in recent years, both scientifically and technologically, as a consequence of their physicochemical properties [8], [9]. They are the object of study since they present potential industrial applications, such as lubrication, due to their high viscosity and their great thermal and chemical stability. Another of its great industrial applications is as a green solvent, since due to its ionic nature it has a low vapor pressure, which means that it has low volatility, thus reducing the emission of vapors into the atmosphere and therefore reducing the environmental impact [10], [11], [12].

Carbon nanotubes have also generated great interest at the scientific level because their properties can be modified by adsorption of atoms or molecules on the outer walls of carbon nanotubes [13], [14]. Then they can obtain changes in the physical properties of the surface of these nanoparticles, and thus vary their solubility and dispersion [10].

They can be composed of one (single-walled) two (double-walled) or more (multiwalled) seamless, concentric sheets of graphene consisting of sp2-hybridized carbon atoms coiled into the shape of thin hollow cylinders [15], [16], [17].

The dispersion of carbon nanotubes in a base fluid, in our case, in the ionic liquid 1-ethyl-3-methylimidazolium dicyanamide (EMM DCA), allows us to obtain fluids with very specific characteristics, helping the development of new nanofluids [18], [19], [20]. Nanofluids, in other words, are a two-phase system with a solid phase (carbon nanotubes) dispersed in another liquid phase (EMM DCA). This work focus on the characterization and rheological behavior of the ionic liquid and its dispersions with different carbon nanotubes, as well as its potential tribological applications, such as wear protection of metal surfaces.

Section snippets

Materials and methodology

Literature [1] investigated the specimen with the best percentage of ES residue as a cement substitute and its effect was studied in terms of workability (W) and compressive strength (CS) [21], [22]. Four types of mixing ratios were prepared with 0%, 5%, 10% and 15%.

In this work, the ionic liquid (LI) 1-ethyl-3-methylimidazolium dicyanamide (EMM DCA) is used, whose molecular formula is $C_8H_{11}N_5$ and its molecular weight is 177.21 g/mol (Fig. 1).

EMM DCA is a yellow liquid solvent formed by…

Preparation of the dispersions

The experimental procedure is shown in Fig. 2. To prepare the dispersions, 0.04g of nanotubes are mixed in an Agatha mortar with 1-ethyl-3-methylimidazolium dicyanamide until reaching the 4g of dispersion required at 1% concentration [23], [24]. Next, manual grinding is carried out for 10 minutes where a black dispersion is obtained. This dispersion is transferred to a vial and, subsequently, it is subjected to sonication at 30°C for half an hour [25], [26]. Finally, the vial corresponding…

Particle size analysis by laser diffraction

Firstly, a study of the distribution of the different types of carbon nanotubes (EMM DCA (I), Aligned (II), multi-walled carbon nanotubes (MWCNT) (III), single-walled carbon nanotubes (SWCNT) (IV) has been carried out. As a result of the tests, a volume distribution function is obtained (Fig. 3).

In the previous images it is seen that all the dispersions follow a normal distribution, forming a Gaussian bell, which shows great symmetry in the distribution of the particles. In the aligned ones, it …

Conclusions

This work studied the feasibility of manufacturing, using and improving the thermal exchange, present in different types of heat exchangers, through the use of nanofluids with MWCNT. Conclusions are,

- The addition of III and SWCNTs nanotubes improves friction and wears between the steel discs and the sapphire ball punch and, therefore, improves the lubricating capacity with respect to EMM DCA.…
- Its use can be implemented in different industries, it uses heat exchangers and water as the working…

…

CRediT authorship contribution statement

Ganimisetti Srinivasa Rao: Writing – original draft, Conceptualization, Investigation. **V. Subha:** Supervision, Methodology. **S. Jagan Raj:** Formal analysis, Writing – review & editing. **Syed Farrukh Rasheed:** Validation, Writing – review & editing. **M. Rashmi:** Data curation. **K. Suganandam:** Writing – review & editing.…

Declaration of Competing Interest

The authors declare that they have no known competing financial interests or personal relationships that could have appeared to influence the work reported in this paper.…

References (37)

B. Jóźwiak *et al.*
Rheology of ionanofluids—A review
J. Mol. Liq. (2020)

R. Sharma *et al.*
Characterization of ZnO/nanofluid for improving heat transfer in thermal systems
Mater. Today:. Proc. (2022)

S.N. Dinesh *et al.*
Investigating the single pass baffled solar air heater (SAH) with an organic PCM (OPCM)
Mater. Today:. Proc. (2022)

G. Thilak *et al.*
Analyzing thermal characteristics of an inorganic phase change material
Mater. Today:. Proc. (2022)

D. Muruganandam *et al.*
Enhancing heat transfer rate in heat exchanger using nano particles of the natural Glay
Mater. Today:. Proc. (2020)

R. Ramesh *et al.*
Microstructural characterization and tensile behavior of Nd: YAG laser beam welded thin high strength low alloy steel sheets
Mater. Sci. Eng. A (2020)

M. Balaji *et al.*
Augmenting agility in production flow through ANP
Mater. Today:. Proc. (2021)

M.L. Rinawa *et al.*

Analyzing an evacuated tube solar water heating system using twin-nano/paraffin as phase change material
Mater. Today:. Proc. (2022)

Y.D. Dwivedi *et al.*
Experimental study on the treatment of urban garment industry wastewater to mitigate groundwater contamination using a solar evaporative still
Urban Clim. (2023)

P.M.J. Stalin *et al.*
Utilization of zinc-ferrite/water hybrid nanofluids on thermal performance of a flat plate solar collector—a thermal modeling approach
Environ. Sci. Pollut. Res. (2022)

View more references

Cited by (0)

Recommended articles (0)

View full text

J Mater Sci: Mater Electron (2024) 35:718

Investigations on Mo dye-doped PPLT single crystals for possible non-linear optical applications

K. Savitha[1], K. Saravanan[2,*], and K. Suganandam[3]

[1] *Department of Chemistry, Salem Sowdeswari College, Salem, Tamil Nadu 636010, India*
[2] *PG and Research Department of Chemistry, Thiruvalluvar Government Arts College, Rasipuram, Tamil Nadu 637401, India*
[3] *Department of Chemistry, Velammal College of Engineering and Technology, Madurai, Tamil Nadu 625009, India*

Received: 12 December 2023
Accepted: 27 March 2024

ABSTRACT

We report pure Piperazinium L-tartrate (PPLT) and methyl orange (MO) dye-doped PPLT for third-order NLO applications. The crystals were grown by slow evaporation solution growth technique at ambient conditions. Both single-crystal and powder XRD evinces the monoclinic system with space group of P21. Formation of PPLT and incorporation of MO dye in PPLT was confirmed through Fourier transform infrared (FTIR) study. Calculated hardness number and stiffness constant with Vicker's Micro hardness study portrays the soft nature of the title crystals. The decrease in bandgap of PPLT is due to the additional energy levels introduced between the valence band and conduction band which in turn increases the net polarizability of the crystal. The thermal behavior of the PPLT crystal was investigated by thermogravimetric and differential thermal analysis (TG–DTA). The third-order nonlinear optical properties such as nonlinear refractive index (n_2), absorption co-efficient (β) and susceptibility ($\chi(3)$) were studied by Z-scan technique at 632.8 nm using He–Ne laser.

1 Introduction

Si-based integrated circuits (ICs), which are dominated by Si CMOS technology, have reached their physics limit. The influences of quantum effects, parasitic parameters, and process parameters on data transmission applications are also reaching their limits, as the rapid development of microelectronics has led to higher requirements for data transmission technology [1–5]. The widespread use of synthetic dyes in various industries has reflected in series of risks to the human health and aquatic life because of the mutagenic, bio-accumulative, carcinogenic and toxic properties. In addition, discharging dyes into aquatic environment decreases the transmission of solar light, decreases dissolved oxygen (DO) level, suppress photosynthesis which means a decrease in plant survival. Dyes-containing wastewater is a significant polluter of the environment and has taken more attention because most of the dyes are chemically and photolytically stable which make them resistant towards temperature and conventional aerobic and anaerobic biological degradation processes [6–10]. The development of photonic technology during the past decade has intensified research activities on searching for new materials that display unusual and interesting NLO properties. New NLO materials are the key elements to future photonic technologies, in which their functions can

Address correspondence to E-mail: ksaravanantgac@gmail.com

https://doi.org/10.1007/s10854-024-12486-8
Published online: 06 April 2024

be integrated with other electrical, optical and magnetic components that have become important in this era of optical communications. The most important advantages of organic materials are the possibility of unique diversity and the ability to be tailored with a variety of chromospheres for the exogenous variables that stimulate photonic functions in a desirable manner, therefore, for example, different NLO processes can be adopted for applications [11–14]. The application of NLO materials are widespread in the field of solid-state technology that includes harmonic generators, optical computing, telecommunications, laser lithography, image processing, sensors, diode lasers and overall optical systems. The superiority of organic materials has been realized because of their versatility and the possibility of tailoring material properties by molecularly engineering them for particular end uses [15–19]. In addition, organic materials also exhibit large nonlinear figures of merit, high-damage thresholds and ultrafast response time. With these views, recently the studies on third-order NLO properties of organic molecular and polymeric materials have been focused and progressing rapidly [20, 21].

Piperazine is an organic material and it plays an important role in the most complex molecules and this material is studied well in several fields. Piperazine is a secondary amine with a molecular formula of $C_4H_{10}N_2$. Piperazines were originally named because of their chemical similarity with piperidine, which is found in the black pepper plant [22]. It is also found in a number of biologically active compounds, including several marketed drugs and it is considered to be a privileged structure in drug discovery, even piperazine ring is frequently used as a building block for pharmaceuticals [23, 24]. Recently, it has been found that some polycationic ligands, including piperazine ring, exhibit a substantial degree of selective RNA binding [25], not only that, the broad family of piperazinium material was subjected to crystallographic [26, 27] and vibrational [28] investigations. The efficiency of nonlinear response from these combinations depends on the choice of cation. It suggests that the selection of different cations to form a salt with L-tartaric acid can improve the SHG activity of the organic salt. In this aspect, molecules of six membered ring structure, piperazine (PPZ) has been investigated with L-tartaric acid. During the combination of tartaric acid with piperazine, two proton is transferred from the carboxylic acid group to the piperazine nitrogen resulting piperazinium cation (PPZ^{2+}) and tartrate anion ($Tart2^{-}$). Tartrate anions provide a rigid environment for the incorporation of cations to form acentric salts i.e. NLO materials [29]. Moreover, PPLT is basically a transparent material and is highly transparent in the visible region. Hence addition of organic dyes like methyl orange (MO) and it could avail a visible absorption to the host and this change in band structure could influence the nonlinear absorption behavior of the system. MO dyes find a wide range of applications in light-emitting diodes, organic semiconductors, photo catalytic activity, waste water management, energy storage devices, thermal printing, biology, medical fields as wound healing, photo dynamic therapy, pharmaceutical chemistry, etc., [30–32]. Also, the chromophore of MO shows excellent nonlinear optical behavior especially the reverse saturable absorption. Therefore, PPLT has been chosen as host material for the present work and organic azo dye (methyl orange) has been chosen as a dopant in order to analyze the changes in the optical limiting behaviors. The optical, mechanical, dielectric and thermal properties have of the crystal were also studied to identify the suitability of the crystal for nonlinear optical applications.

2 Experimental

2.1 Materials

The substances employed for the cultivation of PPLT and MO doped PPLT crystals consist of piperazine, L-tartaric acid, and methyl orange (MO) ($C_{14}H_{14}N_3NaO_3S$). The crystals are cultivated using chemicals of analar grade.

2.2 Crystal growth process

Initially, the saturation point at room temperature to grow the pure PPLT single crystals was identified. For MO-doped PPLT, the doping concentration was taken in the ratio of 1:0.05 M. pH of both pure PPLT and MO-doped PPLT solutions were maintained at 7 and 5, respectively. After 4 h of vigorous stirring, both the solutions were filtered and sealed with perforated sheet and left undisturbed for slow evaporation at ambient condition. Figure 1a and b show the harvested pure and MO-doped PPLT single crystals after

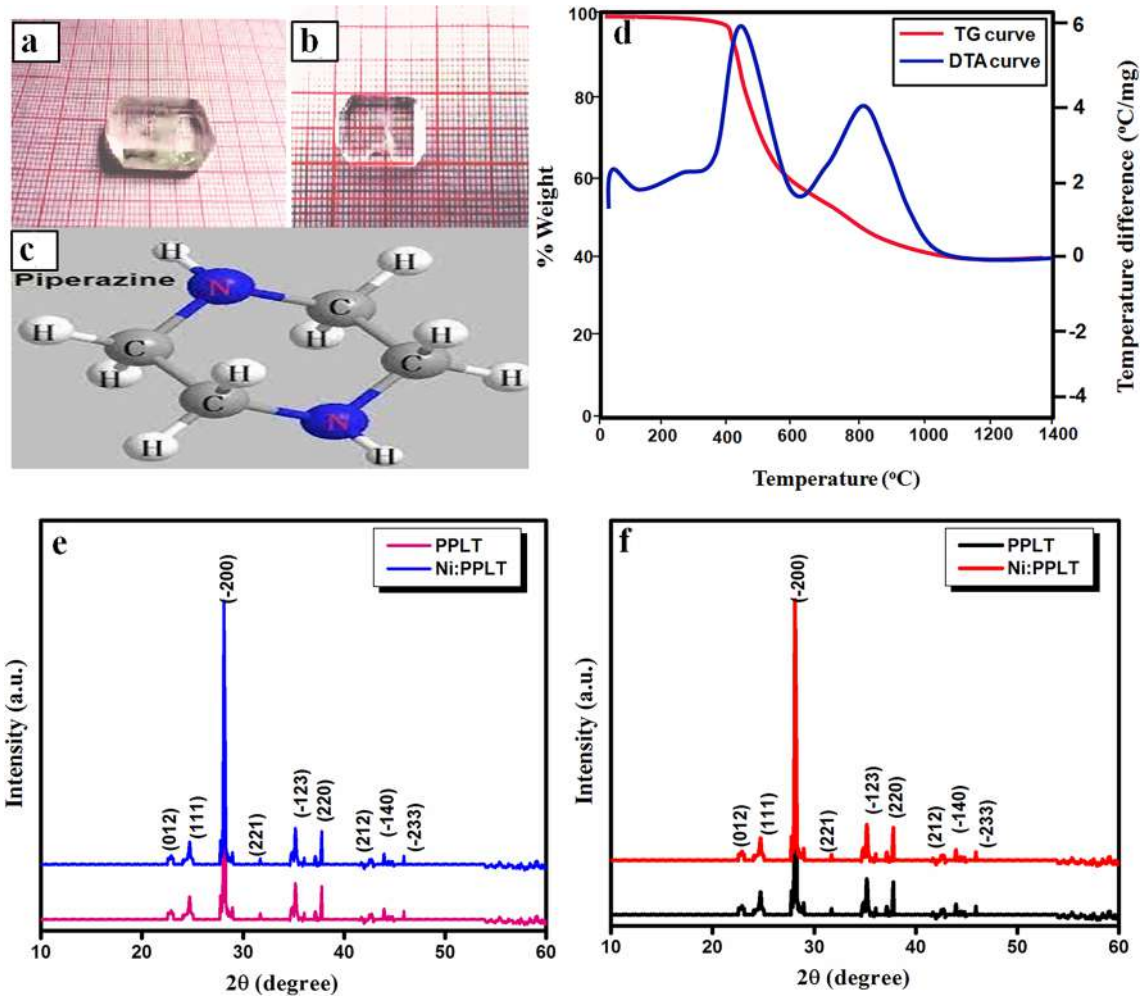

Fig. 1 Photograph of grown crystals **a** PPLT; **b** MO:PPLT; **c** molecular structure of PPLT; **d** TG–DTA curves of PPLT; **e** Single crystal XRD pattern of pure and MO doped PPLT crystals; **f** powder XRD pattern of pure and MO doped PPLT crystals

a period of 35 and 45 days, respectively. The molecular structure of PPLT was shown in Fig. 1c.

2.3 Characterization techniques

The thermal stability of the title compound was assessed by (Q 500 HI-RES TGA analyzier) TG/DTA analysis. The pristine crystals and doped PPLT were subjected to single crystal X-ray diffraction (XRD) studies using an ENRAF NONIUS CAD4 X-ray diffractometer with a MoKa radiation ($k = 0.71073$ Å). Molecular structure and the functional group associated with grown crystals were identified by Perkin–Elmer Fourier transform infrared (FTIR) spectrometer. Mechanical stability of the crystals were tested under Vickers Microhardness Tester (Shimadzu HMV-2). The absorption and the transmission spectra of PPLT and MO-doped PPLT were studied between wavelengths 200–1200 nm using Perkin-Elmer UV–Vis spectrometer. The third-order nonlinear optical properties of PPLT crystal were measured by Z scan technique.

3 Results and discussion

3.1 Thermal, structural and elemental analysis

The thermo-gravimetric (TG) and differential thermal analyses (DTA) were conducted under a nitrogen environment, spanning a temperature range from room temperature to 773 K (Fig. 1d). Upon analysing the TGA arc, it was seen that it shows a little reduction in weight beginning at 496 K as a

result of the deterioration of the PPLT molecule. No significant reduction in weight was detected between temperatures of 308 K and 507 K, which indicated the absence of physically adsorbed liquid. The significant reduction in weight seen between 506 and 774 K can be attributed to the breakdown of the PPLT molecule into gaseous form. The DTA analysis revealed the presence of two endothermic reactions occurring at temperatures of 535 K and 695 K, which may be attributed to the disintegration of the chemical. Since no distinct endothermic reaction was detected below 506 K, it may be concluded that the PPLT undergoes decomposition without undergoing a melting process. Therefore, the PPLT crystal has the potential to be utilised in applications with temperatures as high as 506 K. The unit cell characteristics and crystal morphology were identified using single crystal X-ray diffraction analysis using an ENRAF NONIUS CAD4 X-ray diffractometer that was equipped with MoKa radiation ($k = 0.71073$ Å) (Fig. 1e). The PPLT crystal is classified as belonging to the monoclinic framework, with a space group of P21. The estimated lattice characteristics for this crystal are $a = 6.4259$ Å, $b = 9.1327$ Å, $c = 9.3567$ Å, and a volume of $V = 519.12$ Å3. The calculated cell parameters figures are consistent with the values published in the literature [33]. When comparing the XRD pattern of MO dye doped PPLT crystal with the pure KDP crystal structure, it was seen that the 2 theta values shifted slightly to the left. This means that the 2 theta values fell somewhat, resulting in an increase in the d-spacing range. The powder XRD data indicate the presence of a monoclinic crystalline unit and a small shift in the peak after incorporating MO (Fig. 1f). This is a result of the integration of MO dye into the PPLT crystal. The methyl orange dye aims to exert dominance over the PPLT and enhance its transparency.

3.2 FTIR analysis

Molecular structure and the functional group associated with grown crystals were FTIR. Figure 2a and b shows the recorded FTIR spectra of pure and MO doped PPLT crystals, respectively. The spectra give the necessary information about the molecular arrangements of the crystals. The intense and wide band corresponding to the stretching vibrations of the hydroxyl group, which is strongly involved in hydrogen bonding, is seen at a wavenumber of 3453 cm^{-1} [34]. The peak at 3369 cm^{-1} corresponds to the O–H vibrations

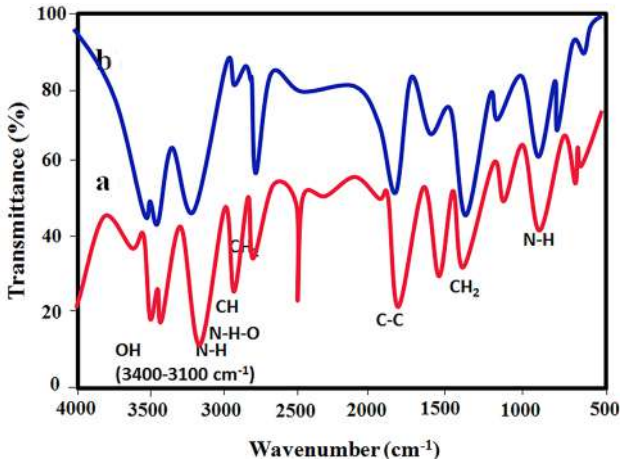

Fig. 2 FTIR spectra of **a** pure PPLT and **b** MO-doped PPLT crystals

Table 1 Vibration assignments of pure and MO-doped PPLT crystals

Vibration		Assignments
PPLT	Mo doped PPLT	
3456	3487	O–H stretching
3134	3094	N–H stretching
2956	2987	CH stretching
2831	2878	CH_2 stretching
2776	2756	C-H stretching
1616	1648	NH_2 stretching
1567	1578	CH_2 stretching
1415	1428	CH_2 stretching
784	813	Piperazine aromatic ring

that stretch [35]. The C–H stretching vibration is identified at a wavenumber of 3065 cm^{-1} [36]. The C–H stretching mode vibrations caused by molecular orbital (MO) occur at a frequency of 2676 cm^{-1}. The peak seen at 1844 cm^{-1} corresponds to the stretching vibrations of the CO band [37]. The in-plane deformations of NH_2 are identified by their characteristic frequencies of 1645 cm^{-1} and 1421 cm^{-1}. The presence of C–CH in-plane deformations is responsible for the peak seen at 1345 cm^{-1}. The spectral band assignments of MO-doped PPLT crystals are presented in Table 1, which provides additional evidence of the effective integration of dye into the host material.

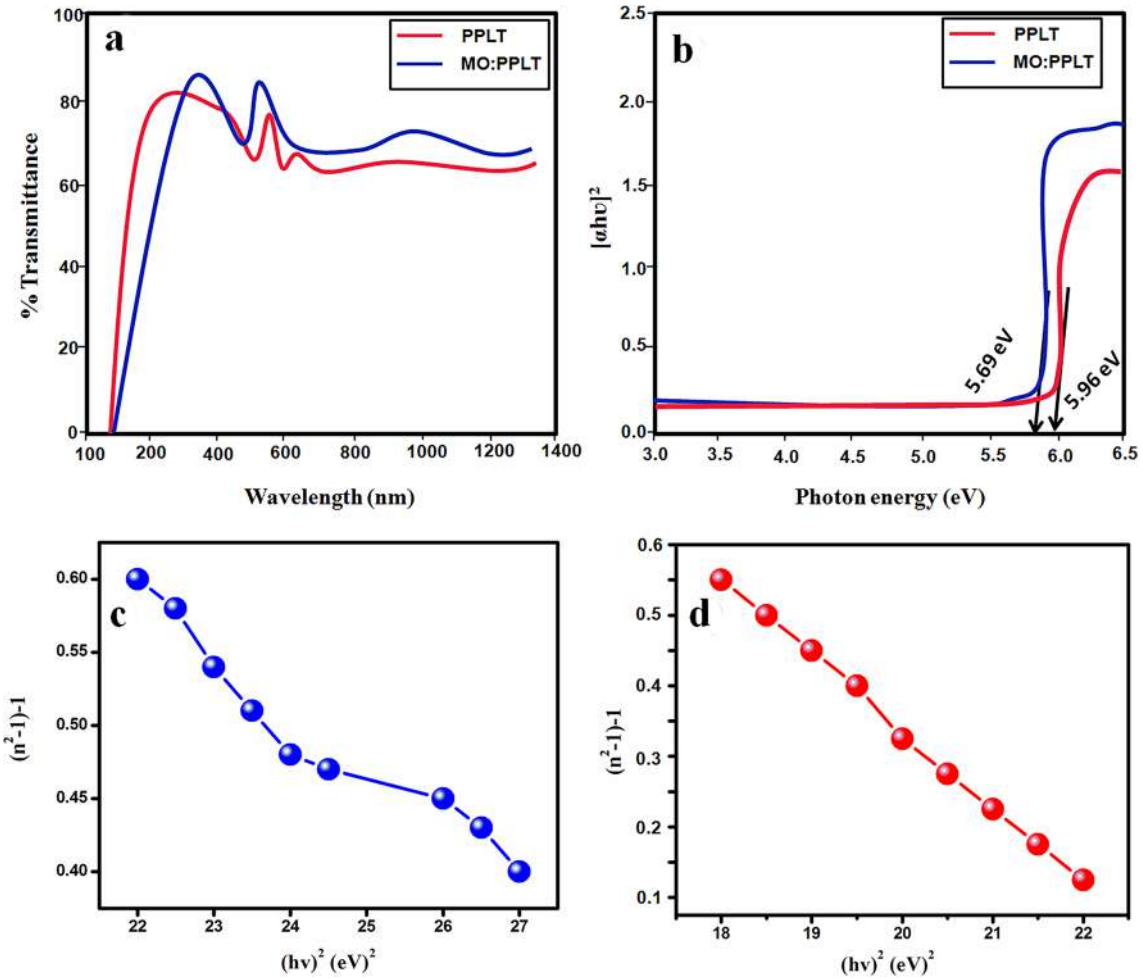

Fig. 3 **a** UV–Vis transmittance spectra; **b** band gap plot; the refractive index dispersion below the energy band gap for **c** PPLT **d** MO-doped PPLT

3.3 UV–Vis transmittance spectra analysis

UV–Vis–NIR transmission spectral studies of pure and doped LLM crystals were carried out using Perkin—Elmer Lambda 35 double beam UV–Vis–NIR spectrophotometer in the range of 150–1300 nm. Figure 3a shows the transmittance spectrum of pure and MO-doped PPLT single crystals. One of the most important considerations in the choice of a material for optical applications is its optical damage tolerance. As high-optical intensities are involved in nonlinear processes, the materials must be able to withstand high-power intensities. Crystals possessing high transparency in an extensive range of wavelength can be used for optical device fabrication. MO doping has considerably increased the absorbance of PPLT and red-shifted its cut-off wavelength to 250 nm. This has resulted in decreased optical band gap of the doped crystals. This red-shift confirms the addition of a host molecule in the parent material. It is a well known fact that the MO dye contains one azo group and two phenyl rings. This azo group acts as a bridge between two phenyl rings and the OH–LT groups of the tartrate molecule. This modifies the optical properties of the PPLT crystals. Hence, the inclusion of MO dye molecules introduces the additional energy levels between the valence band and conduction bands. Due to this, the bandgap of MO doped PPLT crystals is decreased to 5.69 eV from 5.96 eV which is for pure PPLT (Fig. 3b). Hence, alteration in band structure along with change in visible absorption is observed in MO doped PPLT crystals. The dependence of refractive index on photon energy below inter band absorption edge ($h\upsilon < E_g$) is given as [38] $n^2(\lambda) = 1 + E_0E_d/(E_0^2 - E_2^2)1$; where E_0 = Single

oscillator energy, E_d = Dispersion energy, $E = hm$ = Photon energy. The moments of single oscillator dispersion spectra (M_{-1} and M_{-3}), Static refractive index (n_0) and Oscillator strength (f) are calculated using the following expression:

$$M_{-1} = E_d/E_o,\ M_{-3} = E_d/Eo_3 \quad (1)$$

$$n_o = \nu 1 + E_d/E_o.f = E_oE_d \quad (2)$$

Figure 3c and d shows the refractive index distribution below the bandgap energy for pure and Mo doped PPLT crystals. Matching experimental evidence with straight lines yields the single oscillator energy (E_0), dispersion energy (E_d), and momentum of such oscillator models (M_{-1} and M_{-3}). Table 2 indicates that the single oscillator energy (E_0) decreases when MO is doped in PPLT crystals. Because it correlates to the material's average bond strength, this number should be as low as possible, suggesting that the crystal has high nonlinear optical quality.

Table 2 Dispersive parameters of pure and MO-doped PPLT crystals

Sample	E_d (eV)	E_0 (eV)	M_{-1}	M_{-3}
PPLT	1.63	4.92	0.2565	0.00498
Ni:PPLT	1.424	5.24	0.2201	0.01883

3.4 Photoluminescence spectra analysis

Photoluminescence intensity is highly dependent on the crystalline and structural perfection of the crystal. The dye incorporation in the solid crystal tunes the emission of light depending upon nature of dyes and their characteristic absorption. Moreover, the fluorescence also finds wide application in the branches of biochemical, medical and chemical research fields for analyzing organic compounds. The excitation spectrum was recorded in the range 250–350 nm and the sample was excited at 300 nm. The emission spectrum was measured in the range 300–500 nm. The emission spectrum of pure and MO-doped PPLT is given in Fig. 4a. Peaks were observed between 420 and 480 nm in the emission spectrum. The result indicates that a MO-doped PPLT crystal has a blue fluorescence emission. The high-luminescence emission intensity in the dye-doped crystal shows the good crystalline nature as a result of dye doping and it can be useful for optoelectronic device applications.

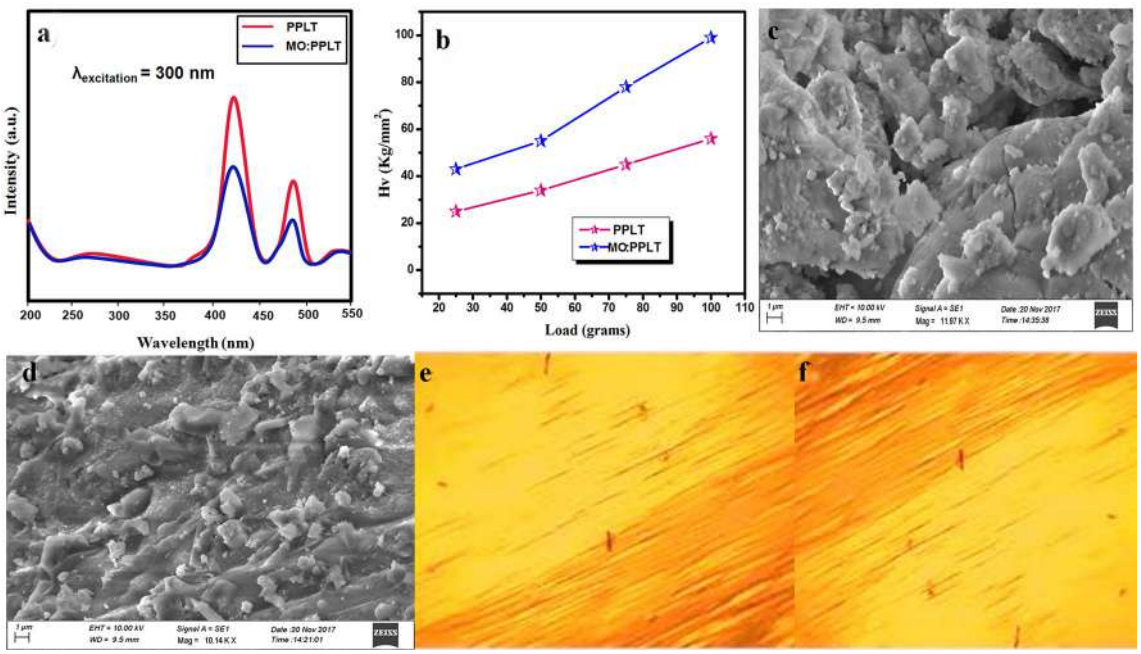

Fig. 4 **a** PL spectra; **b** hardness study; SEM images of **c** PPLT; **d** MO:PPLT; Optical etching photograph images; **(e)** PPLT; **(f)** MO:PPLT

3.5 Harness and etching studies

Hardness measurement is a valuable non-destructive testing technique for determining the hardness of materials [39]. The mechanical stability of the PPLT crystal, both in its pure form and when doped with MO, was assessed by Vickers microhardness tests. The indentations were meticulously created with a dwell duration of 10 s, employing weights ranging from 10 to 100 g. The researchers measured the average length of the diagonal and calculated the Vickers Hardness number (VHN) using the formula $Hv = 1{:}8544P/d^2$ Kg/mm^2, where 'P' represents the force exerted in kilogrammes and 'd' represents the width of the diagonal of the indentation imprint in micrometres. The relationship between the hardness number (Hv) and the load (P) for the PPLT crystals doped with MO is seen in Fig. 4b. Both pure PPLT and MO doped PPLT exhibit an increase in hardness as the applied load increases, thereby confirming the reverse indentation size effect (RISE) [40]. By incorporating MO into PPLT by doping, a significant enhancement in the hardness measurement was seen. This phenomenon occurs because the MO dye, being a large molecule, occupies the empty spaces inside the PPLT crystal structure, leading to a densely packed lattice. The SEM provides information relating to morphology, phase distribution and crystal structure The SEM images for the pure and MO-doped PPLT crystals were recorded and are display in Fig. 4c and d. The SEM images of all the samples are agglomerated morphology. All the particles are uniformly distributed, however some of the particles in all the samples were found to be in regular shapes (spherical). In addition, the second metal doped is more agglomerated than pure samples. Etching is the selective dissolution of the crystal which reveals the crystal symmetry and lattice defects [41, 42]. Etch patterns observed on surface such as spirals, hillocks and step pattern, etc. yield considerable information on the growth process and growth mechanism of the crystal. When a surface is etched, well-defined etch patterns are produced at the dislocation sites. The etching studies were carried out on the grown crystals of pure and MO-doped PPLT crystals using polarized high-resolution optical microscope. The surfaces of the samples were polished and then etched in doubly distilled water at room temperature for 10 s. Then dried with a filter paper and examined under an optical microscope in reflection mode. Figure 4e and f illustrate the typical etch patterns observed on the pure and MO doped PPLT crystals. The etching shows predominant straight striations on the grown crystal. The size of the pit increases with the increase of etching time. The pit pattern remains the same. The observed etch pits are due to the layered growth of the crystal. This shows how the crystal would have been formed from the solution.

3.6 Dielectric study

The dielectric constant (ε) and dielectric loss (tan δ) of both pure and doped crystals were measured using the usual parallel plate capacitor method. The experiments were conducted at various temperatures ranging from 30–50 °C and in the frequency range of 50 Hz–5 MHz. An LCR metre (HIOKI 3536) was used for the tests. A flat PPLT crystal, which had been farmed and doped with MO, underwent polishing. The opposing faces of the crystal were then covered with graphite to provide a highly conducting surface layer, facilitating Ohm's contact. The sample's capacitance was determined by altering the frequency range from 50 Hz to 5 MHz. The dielectric constant was determined by applying the formula $\varepsilon' = Cd/(\varepsilon_0 A)$. The variables in the equation are defined as follows: A represents the area of the crystal plate, d represents the thickness of the crystal, and ε_0 represents the permittivity of the dielectric of free space. Figure 5a–d illustrates the dielectric value of both pure and MO-doped PPLT crystals. The plot demonstrates a reduction in the dielectric constant as the frequency increases, reaching a saturation value in the upper frequency range. The high dielectric constant at low frequency is attributed to the existence of several forms of polarisation, including electronic, ionic, orientation, and space charge. The space charge polarisation is contingent upon the level of purity and flawlessness of the sample. The impact of this phenomenon is significant under high temperature conditions, although it is not discernible in the low frequency range. Crystals possessing a high-dielectric constant result in the dissipation of power. Materials with low dielectric constant have little losses, making them suitable for high-speed electro-optic modulations [43]. The frequency-dependent dielectric loss of pure MO-doped PPLT is seen in Fig. 5c and 5d. The presence of low dielectric loss at high frequencies in a particular sample indicates that

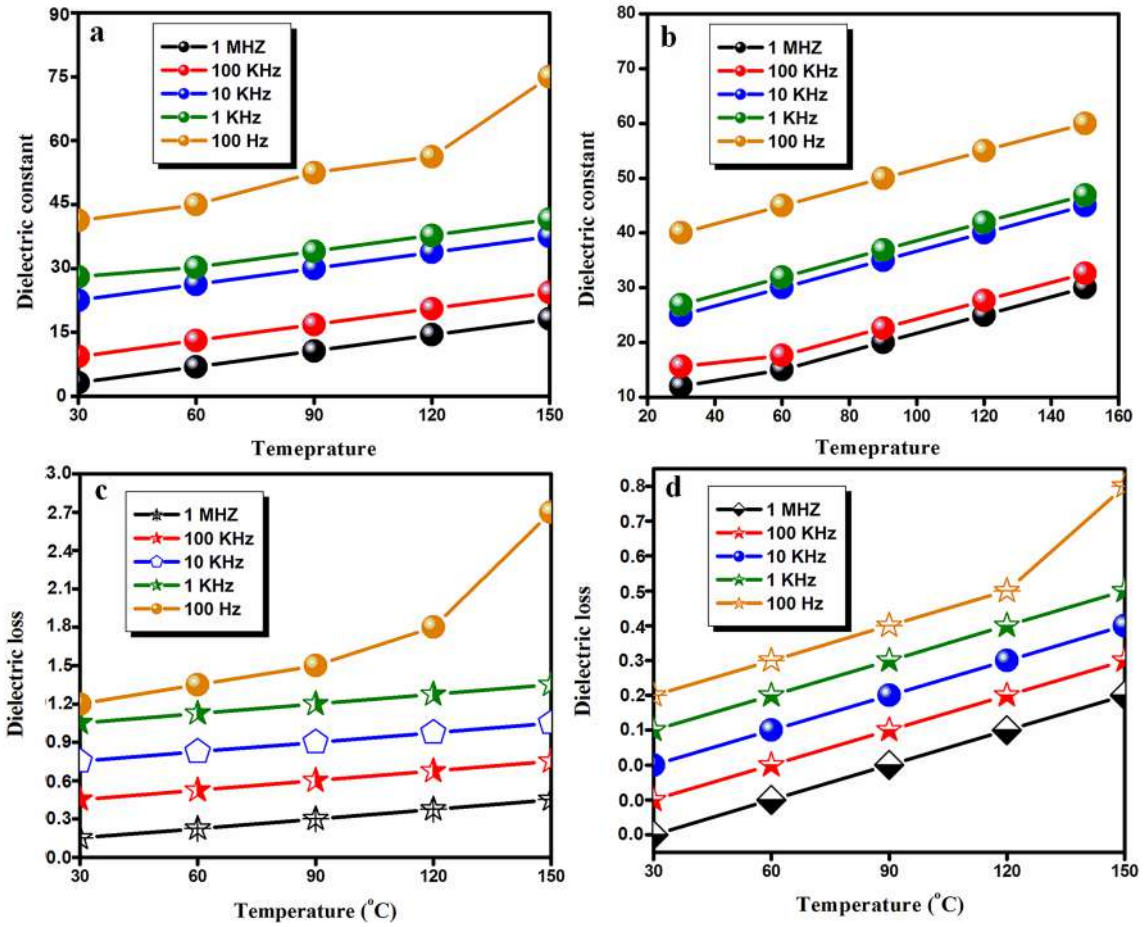

Fig. 5 Variation of dielectric constant as a function of frequency **a** PPLT; **b** MO:PPLT; Dielectric loss of **c** PPLT; **d** MO:PPLT crystals

the sample has improved optical quality and fewer flaws. This property is crucial for the effective use of nonlinear optical materials [44]. MO-doped PPLT single crystals exhibit higher dielectric loss in comparison to pure PPLT crystals. The increase in polarisation in the MO-doped PPLT single crystal may be attributed to the rise in dipole moment per unit volume.

3.7 AC conductivity test

The LCR metre was employed to quantify the alternating current (AC) conductivity of both pure PPLT and MO-doped PPLT crystals throughout a temperature range of 323 K to 373 K, using a fixed frequency of 1 kHz. A damp cloth polishing sheet was utilised to both cut and polish the samples. Effective connections to electricity are established using silver-plated electrodes positioned on opposing surfaces. The amount of resistance values were directly acquired from the LCR metre. The alternating current (AC) conductivity was calculated using the formula: $AC = 2fCt/A$, where f represents the frequency of the applied field. Figures 6a–d depict the alternating current conductivity, dielectric constant, and dielectric loss of pure PPLT and MO-doped PPLT crystals at different temperatures. The alternating current (AC) conductivity has a positive correlation with increasing temperature, and it further increases upon the introduction of MO doping. Metallic oxides (MO), which facilitate the mechanism of free electrical conduction within crystals, are accountable for the enhanced alternating current (AC) conductivity. The plots in Fig. 6c and d depict Jonscher's results for pure and doped PPLT crystals, demonstrating the highly dispersive nature resulting from the presence of only alternating current (AC) conductivity [42, 45, 46]. The values of s and A are determined based on the slope and intercept of the plots stated above. Table 3 presents the Jonscher's plot parameters for pure and MO-doped PPLT crystals.

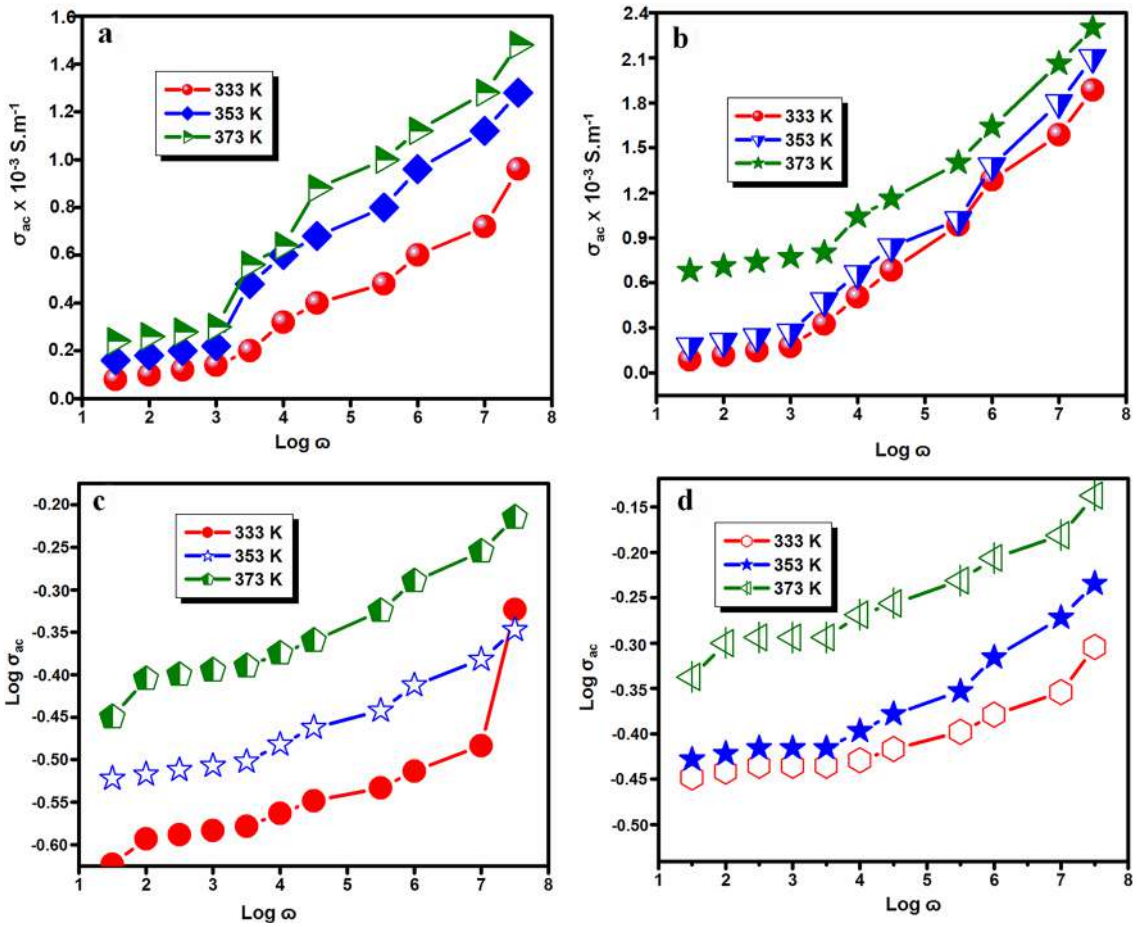

Fig. 6 **a** and **b** AC conductivity of PPLT and MO-doped PPLT; Jonscher's plot of **c** pure PPLT crystal **d** MO-doped PPLT crystal

Table 3 Josher's plot parameters pure and MO-doped PPLT crystals

Temperature (*K*)	S-Parameter		$A \times 10^{-9}$ (s.m^{-1}.rad^{-n})	
	PPLT	Ni:PPLT	PPLT	Ni:PPLT
323	0.57612	0.44090	2.4	78.1
353	0.53491	0.47651	3.2	86.9
373	0.51201	0.40897	4.4	143.7

3.8 Z-scan measurement

The nonlinear absorption (NLA) and nonlinear refraction (NLR) of pure PPLT and MO-doped PPLT were measured using open aperture (OA) and closed apertures (CA) Z-scan experiments, respectively. The third-order nonlinear optical (NLO) susceptibility was also found. The 785 nm spectrum continuous wave laser beam, with a peak power of 50 mW, was focused and transmitted through the grown material. The sample was transferred onto the sample stage, moving from the source to the detector in the same direction as the beam transmission. The beam's penetration was measured at the far field for several sample placements, both with and without an aperture in front of the detector. Subsequently, a graph was constructed correlating the transmittance with the location of the sample. Figure 7 illustrates the CA mode of PPLT and MO doped PPLT. Nonlinear absorption is often caused by several phenomena, including saturable absorption (SA), reverse saturable absorption (RSA), which is a result of two-photon absorption (2PA), multiphoton absorption (MPA), excited-state absorption (ESA), or free carrier absorption (FCA) [47]. The presence of reverse saturable absorption (RSA) is revealed by the valley-like optical absorption (OA) curve of pure and MO-doped PPLT, as shown in Fig. 7a and b. The closed aperture (CA) approach allows for the observation of either the negative or positive lens, which leads to either self-defocusing or self-focusing behaviour of

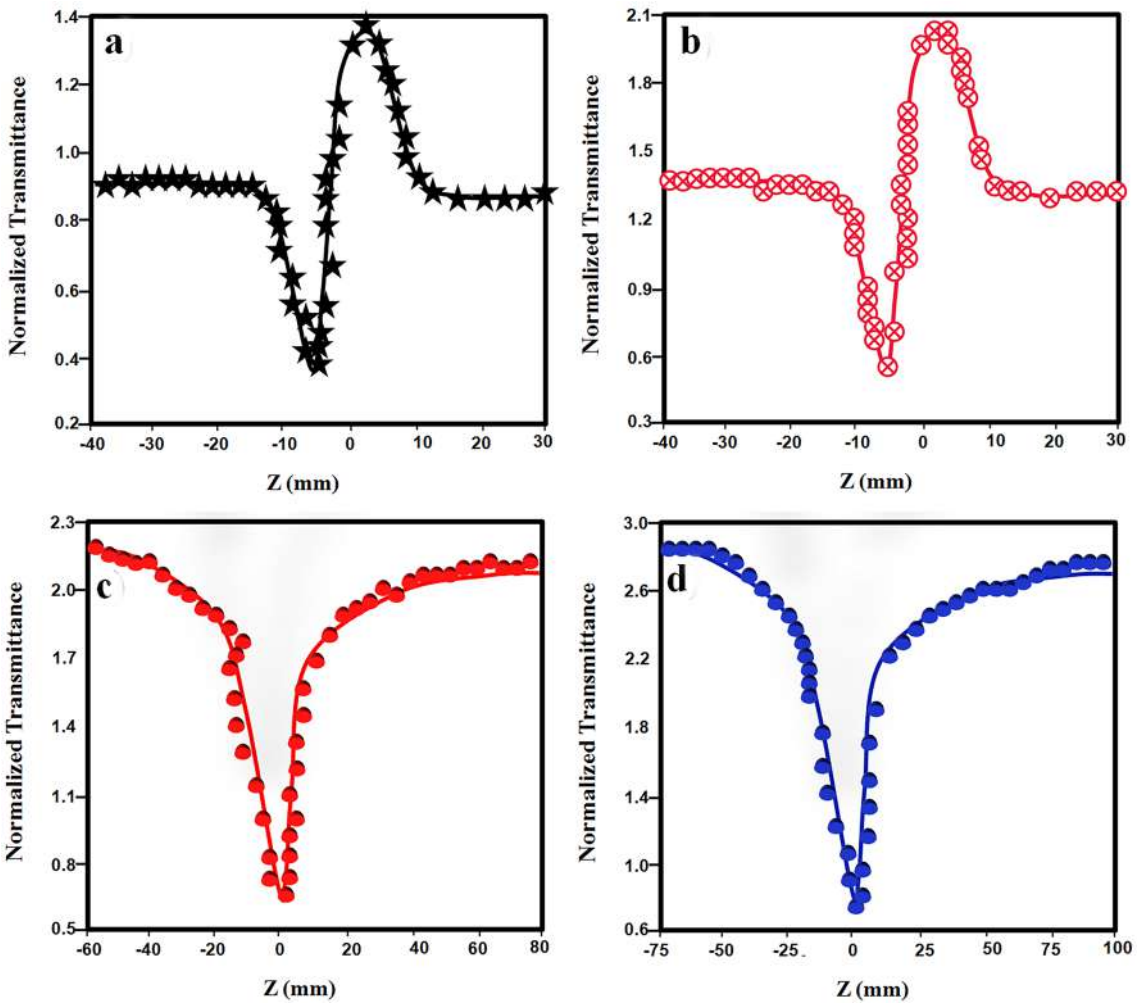

Fig. 7 Z-scan spectra of **a** PPLT; **b** MO:PPLT (open aperture); **c** PPLT; **d** MO:PPLT (close aperture)

Table 4 Optical details of Z- scan setup and measured parameters

Laser beam wavelength (λ)		632.8 nm
Lens focal length (f)		8.5 cm
Optical path distance (Z)		117 cm
Aperture radius (ra)		2 mm
Spot-size diameter in front of the aperture (ωa)		1 mm
Incident intensity at the focus (Z = 0)		15 MW/cm^2
Sample thickness (L)		2 mm
Effective thickness		1.81 mm
Nonlinear refractive index (n2)	PPLT	MO doped PPLT
10–7 cm^2/W	3.17	3.11
Nonlinear absorption coefficient (β)cm/W	1.35	1.99
Third-order nonlinear susceptibility ($\chi 3$) 10^{-3} esu	1.41	2.87
Figure of Merit (FOM)	28.91	20.92

the sample (see Fig. 7c and d). The higher values of the third-order nonlinear optical (NLO) coefficients in MO-doped PPLT compared to PPLT may be attributed to the enhanced delocalized movement of p-electrons caused by the dye. This, in turn, leads to an increased net polarizability of the MO-doped PPLT [48]. The parameter values are displayed in Table 4.

4 Conclusion

Good quality single crystals of pure and MO dye doped PPLT were grown from aqueous solution by slow evaporation method. The lattice parameter was confirmed by single crystal X-ray diffraction (XRD) and it belongs to the monoclinic system with the space group of P21/c. The FTIR spectral analysis confirms the functional groups present in the grown crystal. UV–Vis NIR spectrum shows that the crystal becomes transparent in entire visible region and the cut-off wavelength is found to be 250 nm. The optical band gap was calculated using Tauc's plot and it was found to be 5.96 eV and 5.69 eV for PPLT and MO doped PPLT single crystals, respectively. The MO dye-doped crystals have strong absorption in the visible region and high transmittance in the near-IR region, since it acts as a good candidate for optical applications. The high luminescence emission intensity in the dye-doped crystal shows the good crystalline nature as a result of dye doping. From the dielectric study, it is observed that dye-doped crystal has higher dielectric constant and lower dielectric loss at various temperatures. The higher values of dielectric constant with low losses concluded that the title crystal is more useful for optoelectronic and NLO applications. Z-scan experimental result confirms the relatively large value of nonlinear optical absorption (β) and refractive index (n^2) and hence MO doped PPLT crystal has large value of third order nonlinear susceptibility ($\chi(3)$) which is most suitable for optical limiting applications. The results obtained from the various studies suggest that the MO-doped PPLT crystal may be suitable for the device fabrication like optical limiting and photonic devices.

Author contributions

K. Savitha, study conceptualization and writing (original draft) the manuscript K. Saravanan data curation, formal analysis and writing (review and editing). K. Suganandam, formal analysis and writing (review and editing).

Funding

The authors have not disclosed any funding.

Data availability

The data that support the findings of this study are available from the corresponding author, upon reasonable request.

Declarations

Conflict of interest The authors have no relevant financial or non-financial interests to disclose.

Ethical approval The authors declare that there are no human cells and tissues are used in this manuscript.

References

1. S. Serna, V. Vakarin, J.-M. Ramirez, J. Frigerio, A. Ballabio, X. Le Roux et al., Nonlinear properties of Ge-rich $Si_{1-x}Ge_x$ materials with different Ge concentrations. Sci. Rep. **7**, 14692 (2017)
2. Y. Miao, G. Wang, Z. Kong, Xu. Buqing, X. Zhao, X. Luo, H. Lin et al., Review of Si-based GeSn CVD growth and optoelectronic applications. Nanomaterials **11**, 2556 (2021)
3. M. Jose, Escalante, non-linear behavior of germanium electronic band structure under high strain. Comput. Mater. Sci. **152**, 223–227 (2018)
4. Z. Kong, G. Wang, R. Liang, Su. Jiale, M. Xun, Y. Miao et al., Growth and strain modulation of GeSn alloys for photonic and electronic applications. Nanomaterials **12**, 981 (2022)
5. Yu. Shuangfeng, F. Pang, H. Liu, X. Li, J. Yang, T. Wang, Compositing orbital angular momentum beams in

$Bi_4Ge_3O_{12}$ crystal for magnetic field sensing. Appl. Phys. Lett. **111**, 091107 (2017)
6. H.A. Khayoon, M. Ismael, A. Al-nayili, H.A. Alshamsi, Fabrication of $LaFeO_3$-nitrogen deficient g-C_3N_4 composite for enhanced the photocatalytic degradation of RhB under sunlight irradiation. Inorg. Chem. Commun. **157**, 111356 (2023)
7. M.A.A.H. Allah, H.A. Alshamsi, Green synthesis of AC/ZnO nanocomposites for adsorptive removal of organic dyes from aqueous solution. Inorg. Chem. Commun. **157**, 111415 (2023)
8. A.A. Kadhem, H.A. Alshamsi, Biosynthesis of Ag-ZnO/rGO nanocomposites mediated *Ceratophyllum demersum* L. leaf extract for photocatalytic degradation of Rhodamine B under visible light. Biomass Convers. Biorefinery. **26**, 1–9 (2023)
9. M.A.A.H. Allah, H.A. Alshamsi, Facile green synthesis of ZnO/AC nanocomposites using *Pontederia crassipes* leaf extract and their photocatalytic properties based on visible light activation. J. Mater. Sci. Mater. Electron. **34**, 1263 (2023)
10. N.S. Salman, H.A. Alshamsi, Synthesis of sulfonated polystyrene-based porous activated carbon for organic dyes removal from aqueous solutions. J. Polym. Environ. **30**, 5100–5118 (2022)
11. P.J. Kim, J.H. Jeong, M. Jazbinsek, S.B. Choi, I.H. Baek, J.T. Kim, F. Rotermund, H. Yun, Y.S. Lee, P. Gunter, O.P. Kwon, Highly efficient organic THz generator pumped at near-infrared: quinolinium single crystals. Adv. Funct. Mater. **22**, 200–209 (2012)
12. P.J. Kim, M. Jazbinsek, O.P. Kwon, Selective growth of highly efficient electrooptic stilbazolium crystals by sequential crystal growth in different solvents. Cryst. Growth Des. **11**, 3060–3064 (2011)
13. D.W. Chen, J.J. Yeh, Aleandrite laser frequency doubling in β-BaB_2O_4 crystals. Opt. Lett. **13**, 808–810 (1988)
14. G.D. Boyd, R.C. Miller, K. Nassau, W.L. Bond, A. Savage, $LiNbO_3$: an efficient phase matchable nonlinear optical material. Appl. Phys. Lett. **5**, 234–236 (1964)
15. C. Chen, Y. Wu, A. Jiang, B. Wu, G. You, R. Li, S. Lin, New nonlinear-optical crystal: LiB_3O_5. J. Opt. Soc. Am. B **6**, 616–621 (1989)
16. G.R. Kumar, S.G. Raj, R. Mohan, R. Jayavel, Influence of isoelectric pH on the growth linear and nonlinear optical and dielectric properties of L-threonine single crystals. Cryst. Growth Des. **6**, 1308–1310 (2006)
17. P. N. Prasad, D. J. Williams, Wiley, 1991.
18. A.V. Alex, J. Philip, S. Brahadeeswaran, H.L. Bhat, Ultrasonic measurement of the elastic constants of sodium p-nitrophenolate dihydrate single crystals. Phys. Rev. B **62**, 2973–2975 (2000)
19. X. Zhang, M. Li, Z. Shi, Z. Cui, Prepare organic/inorganic hybrid nonlinear optical material containing two-dimensional spindle-type chromophores. Mater. Lett. **65**, 1404–1406 (2011)
20. Y. Takahashi, H. Adachi, T. Taniuchi, M. Takagi, Y. Hosokawa, S. Onzuka, S. Brahadeeswaran, M. Yoshimura, Y. Mori, H. Masuhara, T. Sasaki, H. Nakanishi, Organic nonlinear optical DAST crystals for electro-optic measurement and terahertz wave generation. J. Photochem. Photobiol. A: Chem. **183**, 247–252 (2006)
21. T. Pal, T. Kar, G. Bocelli, L. Rigi, Synthesis, growth, and characterization of l-arginine acetate crystal: a potential NLO material. Cryst. Growth Des. **3**, 13–16 (2003)
22. S. Gunasekaran, B. Anita, Spectral investigation and normal coordinate analysis of piperazine. Indian J. Pure Appl. Phys. **46**, 833–838 (2008)
23. T. Eicher, S. Hauptmann, *The Chemistry of Heterocycles* (Wiley, Hoboken, 2003)
24. T. Suzuki, N. Fukazawa, K. San-nohe, W. Sato, O. Yano, T. Tsuruo, Structure-activity relationship of newly synthesized quinoline derivatives for reversal of multidrug resistance in cancer. J. Med. Chem. **40**, 2047–2052 (1997)
25. A.W. McConnaughie, J. Spychala, M. Zhao, D. Boykin, W.D. Wilson, Design and synthesis of RNA-specific groove-binding cations: implications for antiviral drug design. J. Med. Chem. **37**, 1063–1069 (1994)
26. D. Havlicek, J. Plocek, I. Nemec, R. Gyepes, Z. Micka, The crystal structure, vibrational spectra, and thermal behavior of piperazinium(2+) selenate monohydrate and N, N′-dimethylpiperazinium(2+) selenate dihydrate. J. Solid State Chem. **150**, 305–315 (2000)
27. D. Havlicek, V. Chudoba, I. Nemec, I. Cisarova, Z. Micka, Preparation, crystal structure, vibrational spectra and thermal behaviour of piperazinium(2+) selenite monohydrate and piperazinium(2+) diselenite. J. Mol. Struct. **606**, 101–116 (2002)
28. J. Plocek, D. Havlicek, I. Nemec, I. Cisarova, Z. Micka, The crystal structure, vibrational spectra, and thermal behavior of dilithium piperazinium(2+) selenate tetrahydrate and dilithium N, N′-dimethylpiperazinium(2+) selenate tetrahydrate. J. Solid State Chem. **170**, 308–319 (2003)
29. M.K. Marchewka, S. Debrus, A. Pietraszko, A.J. Barnes, H. Ratajczak, Crystal structure, vibrational spectra and nonlinear optical properties of L-histidinium-L-tartrate hemihydrate. J. Mol. Structure **656**, 265–273 (2003)
30. M. Nageshwari, P. Jayaprakash, C.R. Kumari, G. Vinitha, M.L. Caroline, Growth, spectral, linear and non-linear

optical characteristics of an efficient semiorganic acentric crystal:L-valinium L-valine chloride. Phys. B **511**, 1–9 (2017)
31. M. Ghodrati, M. Mousavi-Kamazani, S. Zinatloo-Ajabshir, $Zn_3V_3O_8$ nanostructures: facile hydrothermal/solvothermal synthesis, characterization, and electrochemical hydrogen storage. Ceram. Int. **46**, 28894 (2020)
32. S. Zinatloo-Ajabshir, M. Baladi, M. Salavati-Niasari, Enhanced visible-light-driven photocatalytic performance for degradation of organic contaminants using $PbWO_4$ nanostructure fabricated by a new, simple and green sonochemical approach. Ultrason. Sonochem. **72**, 105420 (2021)
33. C.B. Aakeroy, G.S. Bahra, M. Nieuwenhuyzen, Piperazinium l-tartrate. Acta Cryst **52**, 1471–1473 (1996)
34. T. Balakrishnan, G. Bagavannarayana, K. Ramamurthi, Growth, structural, optical, thermal and mechanical properties of ammonium penta borate single crystals. Spectra Chim. Acta A **71**, 578–583 (2008)
35. R.N. Jayaprakash, P. Kumaradass, Growth and characterization of urea L-valine an organic non linear optical crystal. Orient. J. Chem. **29**, 1409–1414 (2018)
36. S. Moitra, T. Kar, Growth and characterization of L-valine-a non linear optical crystal. Cryst. Res. Technol. **45**(1), 70–74 (2010)
37. K. Vikram, R. Nandi, R.K. Singh, Low temperature Raman study of a liuid crystalline system 4-decycloxybenzoic acid (4DBA). Spectrochim. Acta A **112**, 377–383 (2013)
38. J.H. Joshi, S. Kalainathan, D.K. Kanchan, K. Chaudhari, M.J. Joshi, K.D. Parikh, Crystal growth, structural, optical, photoluminescence, electrical and third-order nonlinear optical studies of pure and methylene blue dye-doped ammonium dihydrogen phosphate crystals. J. Mater. Sci. Mater. Electron. **34**, 1–3 (2023)
39. A.N. Vigneshwaran, A.A. Joseph, C.R. Raja, A study on the properties of potassium penta borate crystals. Optik **127**, 5365–5369 (2016)
40. K. Sangwal, On the reverse indentation size effect and microhardness measurement of solids. Mater. Chem. Phys. **63**, 145 (2000)
41. K. Sangwal, R.B. Heimann, *Etching of Crystals: Theory, Experiments and Applications* (Elsevier, Amsterdam, 1987)
42. H. Joshi, D.K. Kanchan, H.O. Jethva, M.J. Joshi, K.D. Parikh, Dielectric relaxation, protonic defect, conductivity mechanism, complex impedance and modulus spectroscopic studies of pure and L-threonine doped ammonium dihydrogen phosphate. Ionics **24**, 1995–2016 (2018)
43. S. Gopinath, S. Barathan, R. Rajasekaran, Comparative study of thiourea metal complexes crystals. Adv. Mater. Res. **584**, 112–115 (2012)
44. C. Balarew, R. Duhlew, Application of the hard and soft acids and bases concept to explain ligand coordination in double salt structures. J. Solid State Chem. **55**, 1–6 (1984)
45. K. Funke, Jump relaxation in solid electrolytes. Prog. Solid State Chem. **22**, 111–195 (1993)
46. J.H. Joshi, G.M. Joshi, M.J. Joshi, K.D. Parikh, Complex impedance, FT-Raman, and photoluminescence spectroscopic studies of pure and L-phenylalanine doped ammonium dihydrogen phosphate single crystals: the correlation with hydrogen bonding defect. Ionics **25**, 3223–3245 (2019)
47. S. Ramakanth, S. Hamad, S.V. Rao, K.C.J. Raju, Magnetic and nonlinear optical properties $BaTiO_3$ nanoparticles. AIP Adv. **5**, 057139 (2015)
48. J.H. Joshi, S. Kalainathan, D.K. Kanchan, M.J. Joshi, K.D. Parikh, Crystal growth, AC electrical and nonlinear optical studies of pure and di-methionine doped ammonium dihydrogen phosphate single crystals. Mater. Sci. Mater. Electron. **30**, 2985–2993 (2019)

ChemistrySelect

Research Article
doi.org/10.1002/slct.202304974

Chemistry Europe
European Chemical Societies Publishing

www.chemistryselect.org

Design, Synthesis, and Anticancer Activity of N-1 Terminal Segment of α-(2, 5,7-Tri-tert-butylindol-3-yl)alanine-Incorporated Short Peptides

Rajavenkatesh Krishnamoorthy,*[a] Meenakshi Singh,[b] Parthiban Anaikutti,[c] Mahesh Chand Pavar,[d] Esthar Selvaraj,[e] Saravanakumar Rajagopal,[e] and Rajendran Babhu Vignesh[f]

Using a minimallised approach,we designed and synthesized N-terminal modified peptides ***W***-KRGNKWLA-$CONH_2$ (P1) and ***W***-ARGDGGNGRGA-$CONH_2$ (P2) using Fmoc-Chemistry solid phase peptide synthesis protocol. High-performance liquid chromatograms and mass spectrometry (LCMS and analytical HPLC) were employed to determine the purity and molecular weight of the peptide. Surface tension measurements are used to evaluate peptide surface activity. The primary structure of the peptideis anlaysed by NMR spectroscopy. Circular dichroism studies demonstrate that the secondary structure of the peptide changes minimally when it attached to anionic lipid bilayers (POPC:POPG). According to a steady-state fluorescence experiment, peptides P1 and P2 preferentially interact with anionic (POPC:POPG) lipid bilayers rather than zwitterionic (POPC) lipid bilayers. The peptide P2 interacts preferentially with anionic lipid membranes and has an anticancer effect due to RGD and NGR binding motifs. The cytotoxicity of the MTT experiment demonstrated that both normal and cancerous cells could lower peptide concentrations below their IC_{50} levels. Molecular docking also supports *in-vitro* anticancer research. Both peptides P1 and P2 were non-toxic to vero cells and appeared to be more promising as it demonstrated wide spectrum anticancer activity.

1. Introduction

Cancer is one of the leading causes of death worldwide, according to a recent global assessment, and the emergence of several chemotherapy drugs is based on its mechanism.[1] Anticancer drugs have limited efficacy against cancerous cells.[2] Despite these therapeutic limitations in cancer, it remains one of the most promising techniques for reducing systemic side effects in normal cells.[3,4] Numerous natural or manufactured cationic linear or cyclized peptides with extensive antibacterial and anticancer action have been identified.[5,6] In this regard, a new class of 5-fluoro-2′-deoxyuridine prodrugs conjugated with the cyclic peptide CNGRC synthesized and showed good antiproliferative activity.[7] The monomeric and dimeric NGR-^{64}Cu-labeled peptides were synthesized by the Chen et al. group and remarkably used for microPET imaging of CD13 receptor expression.[8–10] Surface receptors such as $\alpha v\beta 3$ and $\alpha v\beta 5$ integrins are extremely attractive to cancer cells, owing to their strong binding affinities with the peptides indicated above.[11,12] APN (or) CD13,[13] VEGFRs (vascular endothelial growth factor receptors),[14,15] and matrix metalloproteinase's (MMPs).[16] Furthermore, certain biological marker techniques have been developed based on peptide binding to cancer cell receptors. These indicators' differential expressions have been extensively researched and employed as appealing targets for selective drug delivery.[17–20] Simple terminal modifications such as C-terminal amidation, N-terminal acetylation, and end-labeling have contributed to the alteration of the properties of antimicrobial peptides (AMPs) and anticancer peptides (ACPs), improving the screening of these selective peptide variants towards anticancer and antibacterial properties based on their sequence design method.[21–23] Any N-terminal peptide labelling procedure might, in theory, monitor the stepwise synthesis of peptides. In contrast, they have been coupled to doxorubicin,[24] cisplatin,[25] and molecular imaging probes such as the cyanine dye Cy5.5,[26] FITC,[27] dansyl,[28] and rhodamine,[29] which have also been reported in the literature. A few studies have suggested that cancer cell membranes differ from normal cell membranes due to aberrant anionic components.[30–32] The RGD

[a] *Dr. R. Krishnamoorthy*
Organic and Bioorganic Chemistry Laboratory CSIR-Central Leather Research Institute (CSIR-CLRI), Adyar, Chennai-600020, Tamil Nadu, India
E-mail: krajavenkateshkcmp5@gmail.com
rajavenkateshk2@gmail.com

[b] *M. Singh*
Department of Drug Discovery and Development, Auburn University, Auburn Alabama, AL, USA

[c] *P. Anaikutti*
Centre for GMP extraction facility (Dept. of Biotechnology), National Institute of Pharmaceutical Education and Research, Guwahati-781101, Assam, India

[d] *M. C. Pavar*
Syngene International Ltd, Bengaluru-560099, Karnataka, India

[e] *E. Selvaraj, S. Rajagopal*
Department of Chemistry, Sethu Institute of Technology, Kariapatti, Virudunagar-626115, Tamil Nadu, India

[f] *R. B. Vignesh*
Department of Chemistry, Velammal College of Engineering and Technology, Viraganoor,
Madurai-625009, Tamil Nadu, India

Supporting information for this article is available on the WWW under https://doi.org/10.1002/slct.202304974

and NGR tripeptide motifs have recently been linked to cancer cell-selective binding due to their affinity for integrin and aminopeptidase N (CD13) receptors.[33–37] As a result, numerous tumour-homing peptides have been developed that target RGD or NGR motifs.[38–42]

Based on the spatial position and arrangement of tryptophan-active peptide adsorption and activity, the previous study found that the mode of action of anticancer peptides against different cancer cells influences the diverse structural orientations acting on the membrane.[43,44] The sensitivity and polarity of the tryptophan environment make the emission/fluorescence properties essential for the potential biological study of peptides and their dynamic properties.[45]

From the above literature reviews, we have predicted that incorporating both RGD and NGR motifs in peptide sequences would increase the anticancer activity.This study aims to design and synthesize two N-terminally modified peptides based on NGR and RGD motifs, ***W***-KRGNKWLA-$CONH_2$ (P1) and ***W***-ARGDGGNGRGA-$CONH_2$ (P2). Figure 1 depicts the expected final structures of the ***W***-based peptides P1 and P2. Surface tension tests revealed that peptides had detergent-like surface-active capabilities due to their high hydrophobicity and cationic nature.We use circular dichroism biophysical and steady-state fluorescence investigations to look at the dynamic structural changes of peptide and lipid model membranes as well as peptide-lipid-membrane interactions. Because of the presence of NGR and RGD residues, the molecular docking data demonstrate that peptides P1 and P2 preferentially bind to the anionic lipid bilayer (POPC : POPG) over the zwitterionic (POPC). To that purpose, synthetic peptides (P1 and P2) having strong interactions with topoisomerase, catalase, and estrogen synthase were examined for cancer cell killing using MTT assay results; all peptides P1 and P2 showed anticancer activity. For better results of their IC_{50} values regarding the selectivity of the peptides for cancer cells, the assessment of their cytotoxic properties in three human cell lines was provided.

2. Materials and Methods

2.1.Chemical and reagents

The MBHA Rink amide resin, diisopropylethylamine, 1-hydroxybenzotriazole, 3-(4,5-dimethyl-2-thiazolyl)-2,5-diphenyl-2H-tetrazolium bromide, trifluoroacetic acid, thioanisole, and ethanedithiol, as well as the peptide synthesis vessel, were purchased from Sigma Aldrich - Merck Chemicals Pvt. Ltd. The lipids employed in this study, such as 2-oleoyl-1-palmitoyl-sn-glycerol-3-phosphocholine (POPC) and 2-oleoyl-1-palmitoyl-sn-glycero-3-phospho-rac-(1-glycerol) sodium salt (POPG), were purchased from Sigma Aldrich Chemical Inc. Lipids in Alabama. From Spectrochem Pvt. Ltd. (Mumbai, India), solvents such as acetonitrile, water, dichloromethane, dimethylformamide, chloroform, and methanol were purchased. Water from the NANO pure A filtration system was used to make buffer solutions. In this investigation, all of the compounds were used without further purification.

2.2. Peptide Synthesis

Both peptides were synthesized using MBHA Rink amide resin and the Fmoc-chemistry process. The rink amide resin was neutralized using a 5% DIPEA solution. To synthesize all peptides, all amino acids were linked as HBTU with one equivalent of HOBT and 2.5 equivalents of DIPEA. When the synthesis was finished, the Fmoc protective moiety was removed using 20% Piperidine in DMF. To initiate N-terminal coupling, the resins were subjected to 2,5,7-tri-tert-butylindol-3-yl)alanine (***W***), accompanied by HBTU (1.0 eq.), HOBT (1.0 eq.) and DIPEA (2.5 eq.), for peptides P1 and P2 at ambient temperature.[46] Before drying under vacuum, the resin was carefully washed with suitable solvents such as dimethylformamide, dichloromethane, acetic acid, and diethyl ether. The

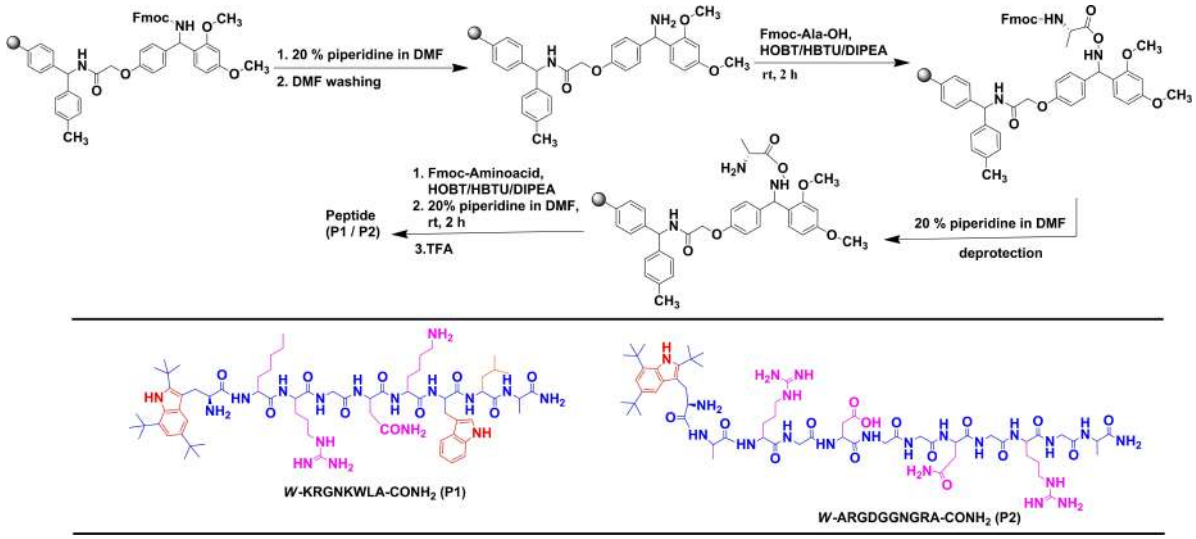

Figure 1. The schematic line structure of synthetic peptides **P1** and **P2**. Both peptides started with MBHA Rink amide resin (0.2 mmol), 20% piperdine in DMF, Fmoc-Aminoacids (1.0 mmol), HBTU (1.0 mmol), HOBT (0.8 mmol), DIPEA (1.5 mmol).

peptides were extracted from the resin for nearly two hours at room temperature using a combination of trifluoroacetic acid, thioanisole, and ethanedithiol (9.0:0.5:0.5, v/v). The crude peptide was obtained after filtration of the cleavage mixture, concentration, and drying with diethyl ether. The crude peptide was then centrifuged and dried with air before being kept at 4 °C. As a result, the molecular mass of the synthesized peptides was determined using a MALDI-TOF apparatus (Microflex LT, Bruker Diagnostics, Germany) and ESI-MASS spectrum analysis and the structure of the both peptide analysed by NMR spectroscopy (Bruker 500 MHZ).

2.3. Reversed-phase high-performance liquid chromatography (RP-HPLC)

At room temperature, the purity of the produced peptides was determined using RP-HPLC (Waters 1525 Binary HPLC) equipped with a C-18 reverse-phase column (4.6 mm×150 mm). Before injecting the sample, the column was thoroughly cleaned with solvents. The peptide solution was injected into the column in 25 μL at a concentration of 3 mg mL-1. The samples were eluted in the following manner: 5–15 min, an isocratic elution of 95% eluent A (0.1% trifluoroacetic acid (TFA) in water) and 5% eluent B (0.1% TFA in acetonitrile); 15–40 min, a linear gradient elution to 5% eluent A and 95% eluent B; 40–48 min, a linear gradient elution back to 95% eluent A and 5% eluent B for all peptides.The flow rate was set at1 mL per minute, and the wavelength of the UV detector was 280 nm. The retention time of peptides (P1 & P2) are given in Table 1.

2.4. Surface Activity

The surface-active properties of the prepared peptides were estimated by calculating their surface tension (π, mN/ m) at the air/water interface using a multiwell plate with the Micro trough X instrument (Kibron Inc., Helsinki, Finland). The multiwall plate was thoroughly washed, and 350 μL of 10 mM Tris buffer (containing 150 mM NaCl, pH 7.4) was added. After injecting peptide solution (10.0 μM) into the subphase *via* a micro-syringe, the surface tension was examined using a Wilhelm plate attached to a Delta Pi microbalance (Kibron Inc., Helsinki, Finland). All the experiments were performed at 20 ± 1 °C.

2.5. Preparation of Small Unilamellar Vesicles

Sonication was used to create small unilamellar vesicles (SUVs). POPC and a POPC:POPG (1:1) mixture of synthetic lipids were dissolved in a chloroform : methanol (9:1) mixture and dried under a N_2 environment. The dry lipids were dehydrated to a concentration of one milliliter in PBS buffer (10 mM sodium phosphate, 150 mM NaCl, 2 mM EDTA, pH 7.4) and vigorously mixed with a vortex mixer before being stored for 15 minutes under sonication in an ice-water bath at 25 °C using an ultrasonic device with a titanium tip. When the lipid suspension was clear, an aliquot was tested for vesicle dispersion using dynamic light scattering measures (N4 Plus, Coulter Corporation, USA), which confirmed the presence of a considerable population of smaller unilamellar vesicles. As a result, the little unilamellar vesicles.The small unilamellar vesicles thus obtained were used for binding experiments without delay.

2.6. Fluorescence spectroscopy

The steady-state fluorescence emission spectra of the peptides and peptide-lipid mixes were acquired using an Agilent Technologies Cary Eclipse Fluorescence Spectrometer. The intrinsic fluorescence of the peptides' modified tryptophan (***W***) was used to determine the extent of lipid binding. The excitation wavelengths for peptides P1 and P2 were adjusted to 280 nm with a bandwidth of 5 nm. After repeated quantities of lipids were added to the peptide solution (10.0 μM for peptides P1 and P2), spectra were recorded in PBS buffer for 5 minutes to allow for an equilibrium-binding peptide.

2.7. Circular dichroism analysis

A JASCO J-715 spectropolarimeter was used to study circular dichrosim spectra. The sample was collected in a quartz cuvette (path length = 0.1 cm) with a peptide/lipid (SUVs) ratio of 1:50 and 1:100. At 25 °C, measurements were taken at a scan rate of 50 nm/min from 197 to 250 nm. The spectra were normalized for concentration and path length by subtracting an average of four scans of each control sample without peptide from buffer and SUVs with the corresponding peptide sample. Peptides P1 and P2 (10.0 μM) were incubated with SUVs (64 μg) in PBS buffer solvent at room temperature for approximately 4 minutes before collecting CD spectra.

Table 1. The sequence of peptides and their properties.

Peptide name	Peptide sequence	Molecular weight (calculated)	HPLC retention time (min)	Net charge
P1	***W***-KRGNKWLA-$CONH_2$	1323.8400 (1323.8543)	25.7	+4
P2	***W***-ARGDGGNGRGA-$CONH_2$	1339.7503 (1339.7500)	24.1	+2

2.8. Cell cultures

The peptides were tested for anticancer activity against various cancer cell lines, including HeLa-derived cell lines (Hep-2), hepatocellular carcinoma cell lines (HepG2), human skin cancer cell lines type 3 (A375), and breast cancer cell lines (MCF-7), as well as cytotoxicity to normal cells. All of the cells were obtained from the National Centre for Cell Sciences (NCCS), Pune, India. At a plating density of 10,000 cells per well, cells were treated in 96-well plates in 100 μL of media containing 5% FBS. It was incubated for 48 hours before adding chemicals at 37 °C, 5% CO_2, 95% air, and 100% relative humidity.

2.9. Anticancer activity MTT Assay

The synthesized peptides were evaluated for their anticancer properties against human cancer cell lines (Hep-2, HepG2, A375, and MCF-7) using a 3-(4,5 dimethythiazol-2-yl)-2,5-diphenyl tetrazolium bromide (MTT) assay and compared to positive control. For the screening test, the cells were treated in 96-well plates in 100 μL of medium comprising 5% FBS at a plating density of 10,000 cells/well and incubated at 37 °C, 5% CO_2, 95% air, and relative humidity (100%) for 48 hours before adding peptide compounds. After 48 hours, compounds were added at various concentrations and incubated at 37 °C, 5% CO_2, 95% air, and relative humidity (100%) for 48 hours. Triplicates were kept, and the medium without the sample acted as a control. After 48 hours, 50 μL of MTT (5 mg/mL) in triple distilled water was added to each well and incubated at 37 °C for 4 hours. The medium with MTT was drained, and the formed formosan crystals were solubilized in 100 μL of DMSO, and then the absorbance at 570 nm was measured using a microplate reader (Bio-Rad, USA). The potential of the designed peptide to specifically target the cancer cells was analyzed using a confocal fluorescence microscope (Leica Microsystems, Germany) to image the peptide localization in both normal and cancer cell lines. The percent of cell inhibition was determined using the following equation formula (1) and summarized in Table 2.

$$\text{Cell inhibition } (\%) = \text{100-Absorbance (Sample)/Absorbance (control)} \times 100 \quad (1)$$

2.10. Molecular docking of synthetic peptides

Once a complex has been optimized synthetically and biologically, molecular docking studies strengthen the molecular mechanism, interactions, and binding of protein-synthetic peptide complexes. So, to study these complexes, protein structures were retrieved from the protein data bank with PDB ID:3ERD and PDB ID:5GWK. (https://www.rcsb.org). The retrieved structures and designed peptides (P1 and P2) were prepared by using the Protein Preparation Wizard utility in Maestro.[47] To minimize, an Optimized Potential for Liquid Simulations-4 (OPLS-4) force field was used.[48] PROPKA algorithm was used to predict and analyze, the protonation state of ionizable residues and the tautomeric ionizationstates of His residues of proteins and synthetic peptides, respectively.[49]

2.11. Receptor Grid Generation and Molecular Docking Studies

Receptor grid generation is the primary step before docking. The grid box is the centroid of residue (28 Å). For grid generation,default parameters, grid for peptide docking, and OPLS-4 were used. The glide docking program and SP peptide docking mode were used for molecular docking.[47]

3. Results and Discussion

3.1. Peptide Design and Synthesis

Recently, in current clinical research development, the Asn-Gly-Arg (NGR) and Arg-Gly-Asn (RGD) motifs containing many antitumor homing peptides have been developed, owing to its strong binding to aminopeptidase N (APN) or CD13 receptor and integrin protein types.[33–42] Thus, to demonstrate our suggestion, two short peptides, ***W***-KRGNKWLA-$CONH_2$ (**P1**) and ***W***-ARGDGGNGRGA-$CONH_2$ (**P2**), were synthesized at the N-terminus with α-(2,5,7-tri-tert-butyl) tryptophan (***W***) having RGD and NGR sequences (to enhance the anticancer activity) and synthetic yield of the peptides having 90%. To create peptides using the conventional solid-phase peptide synthesis method, we used Fmoc-aminoacids and MBHA Rink amide resin. We added lysine and alanine residues to the N-terminus before conjugating modified tryptophan residues, which are likely to

Table 2. Anticancer activity of peptides.

S.No		*In Vitro* anticancer studies (IC_{50}, μM)				
	Peptide sequence	Hep-2	HepG2	MCF-7	A375	Vero
1	***W***-KRGNKWLA-$CONH_2$ (**P1**)	12 ± 0.6	33 ± 0.9	22 ± 3.5	34 ± 1.5	43 ± 6.5
2	***W***-ARGDGGNGRA-$CONH_2$ (**P2**)	9 ± 0.05	11 ± 3.0	12 ± 0.51	23 ± 2.1	38 ± 3.2
3	Doxorubicin	10 ± 0.2	1 ± 0.08	0.5 ± 0.12	12 ± 0.15	16 ± 1.5

[a]Results are the average of three independent experiments. Hep2- Laryngeal carcinoma; HepG2-hepatocellular carcinoma; MCF-7- Breast carcinoma; A375-Human skin cancer; Vero-Normal cell.

increase cell penetration. Figure 1 depicts the peptides' final structure, which was supported by an NMR spectroscopy analysis (Supplementary Figures S1–S4). The N-terminal labeling and formation of 7 amide back-bone protons appeared at δ 8.6–7.2 ppm, side chain aromatic protons were located at δ 7.2–6.7 ppm, aliphatic protons δ 4.5–1.27 ppm for P1 and 10 amide back-bone protons appeared at 8.5–7.3 ppm side chain aromatic protons δ 7.3–6.7 ppm, aliphatic protons were located at δ 4.5–0.5 ppm, for P2 are observed in the ^{1}H-NMR spectrum (Supplementary Figures S1 and S3) and 2D TOSCY NMR spectrum (Supplementary Figures S2 and S4) of both peptides P1 and P2, which confirmed the total correlation between the peptide sequences from the cross peaks and diagonal peaks. The peptide P1 and its purity and molecular weight and purity of the peptide P1 and P2 were confirmed by mass spectroscopic analysis and HPLC chromatograms. As a result, the purity of the peptides P1 and P2 is 98.5% in Figure 2A. ESI mass spectrometric analysis of peptide P1 showed the m/z value to be 1323.8400, which matched well with the calculated m/z value (1323.8543), and similarly, the calculated mass (m/z = 1339.7500) of peptide P2 was confirmed by MALDI mass analysis (m/z = 1339.7503) in Figure 2B.

Based on membrane binding studies, we predicted that peptides with a greater degree of surface activity would generally have a higher affinity for the lipid membrane. Additionally, NGR and RGD peptides have a strong and selective binding relationship to membrane receptors, including APN/CD13 and v3, which are significantly increased in the majority of tumour cells, making them predominantly tumour-specific. These characteristics led us to investigate the in vitro binding and penetrating capabilities of the cell membrane. The anticancer activity of the synthesized peptides was tested using human cancer cell lines such as Hep-2, HepG2, A375, MCF-7, and Vero cells.[50] Using a confocal microscope, the N-terminally modified amino acid-containing peptides' capacity and selectivity for uptake by cancer cells were examined. To evaluate the cytotoxic activity of these synthesized pentameric peptides containing aminopeptidase N (CD13) binding motif and Asn-Gly_Arg (NGR) motif, we performed a set of assays and found that these peptides are showing potential activity toward cancerous cells (Table 3). In contrast to that, we found out that out of four different cancerous cell lines, (HepG2, MCF-7, HeP-2, and A375), the P1 and P2 are most active towards Hep-2 cells. The potential inhibitory concentration (IC_{50}) for P1 and P2 on HeP-2 cell lines is at 9.06 and 12.5 μM when compared to FDA approved drug Doxorubicin without showing toxic effects to normal Vero cell (Figure 3). These results suggest that, that the anticancer effect of the peptides is caused by their greater hydrophobicity and surface activity. These characteristics encourage more effective electrostatic interaction-based peptide

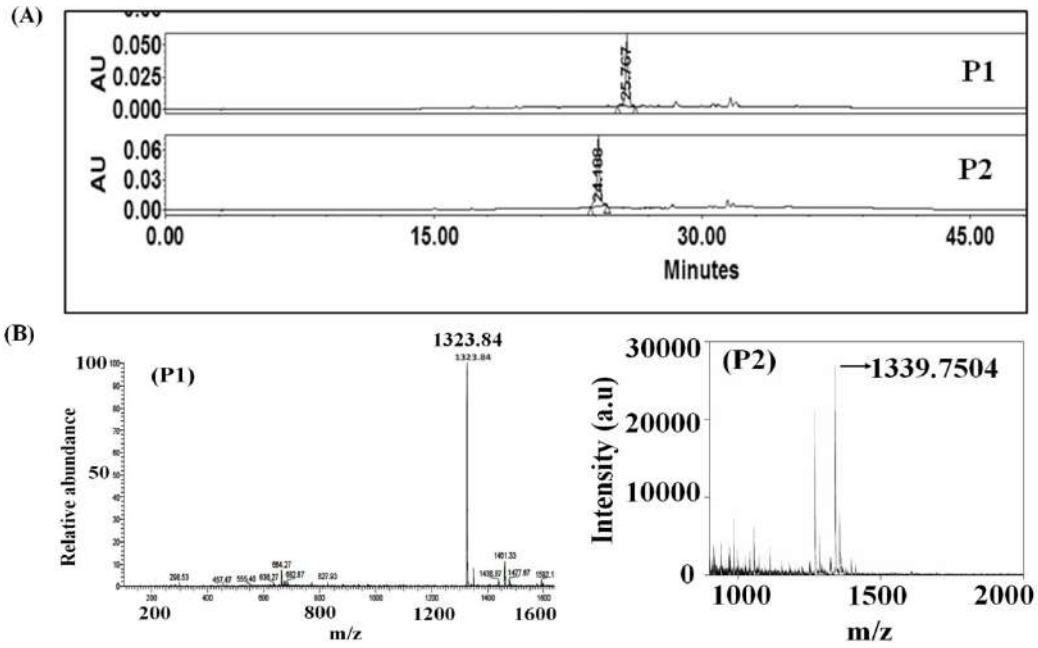

Figure 2. (A) RP-HPLC profiles and (B) Mass spectrum of peptides **P1** and **P2**.

Table 3. Table representing Docking score and interactions shown by peptide P1 and peptide P2 when docked in 3ERD and 5GWK.

PDB ID	Ligand	SP Gscore (kcal/mol)	Interactions
3ERD	**P1**	−7.691	Gln 375, Lys 362, Asn 359, Glu 380, Glu 542, Hid 555
	P2	−9.916	Leu 549, Hid 555, Glu 380, Glu 542, Asp 538, Asp 351; Tyr 537, Asn 348 (Water mediated H-bond)
5GWK	**P1**	−9.732	DNA intercalator; DG13, DC11
	P2	−11.121	DNA intercalator; DG 13, DC12, DC11, DG10, and Arg 804

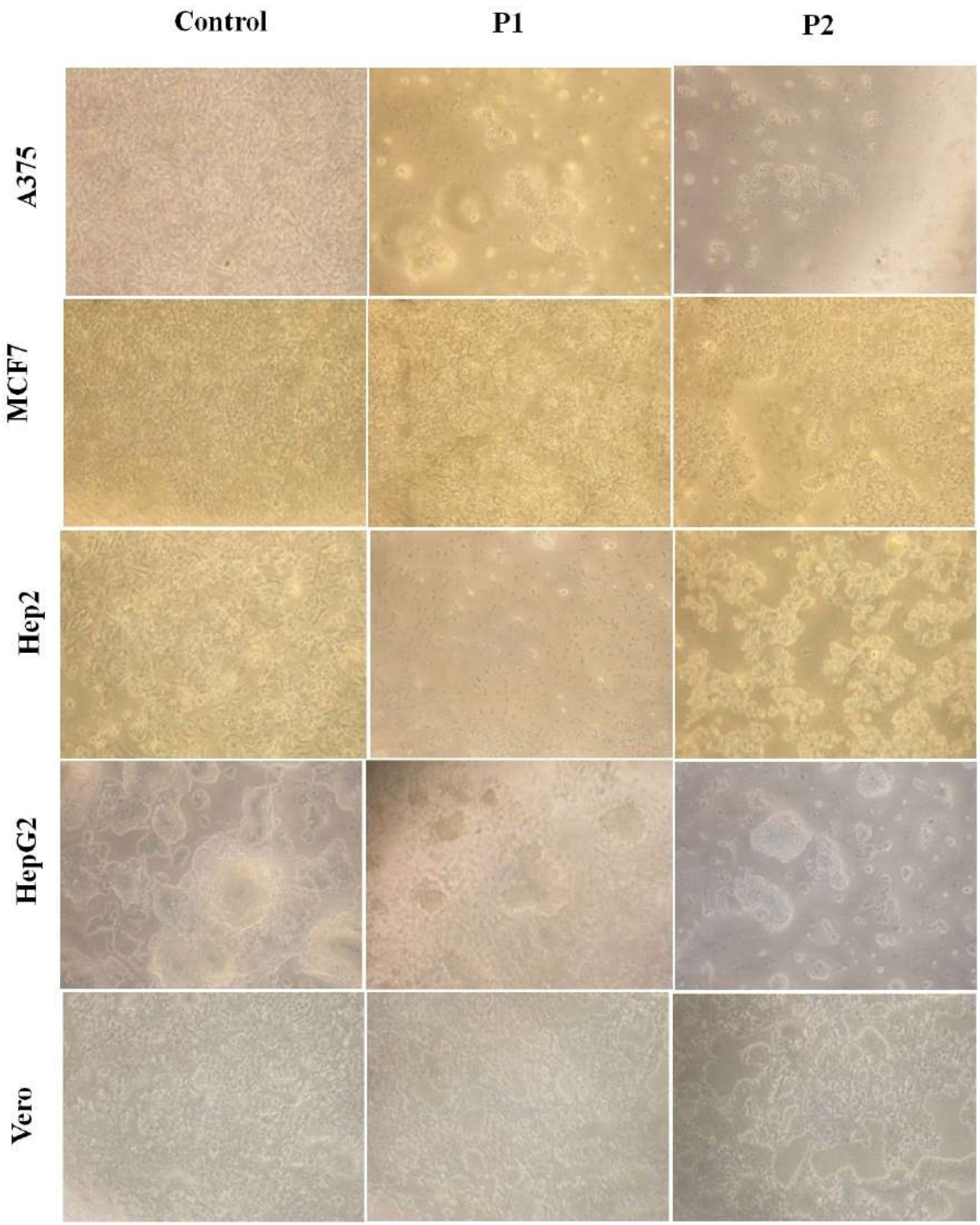

Figure 3. Cell viability assay: normal Vero cell and cancer cells (Hep-2, HepG2, A375, and MCF-7) showing no cytotoxic effects against normal cells. sacle bar 2 microns.

binding to the outer membrane of cancer cells. As a result, these peptides could be employed to efficiently localize them on the surface of cancer cells and kill them. Peptide P2 (***W***-ARGDGGNGRGA-$CONH_2$), on the other hand, has lower IC_{50} values than peptide P1 (***W***-KRGNKWLA-$CONH_2$). These IC_{50} values are nearly identical to the inhibitory value of Doxorubicin (Table 2).[51,52] The peptide P2′s improved capacity to reduce water surface tension correlates well with the lower IC_{50} values obtained for peptide P2. This selectivity towards cancerous cells suggests that these peptides can bind to protein-expressed in cancerous cells than normal tissues (Table 2) which is further validated via molecular docking studies.

3.2. Surface activity property of peptides

Numerous bioactive peptides, particularly antimicrobial peptides, have been found to have detergent-like surface-active properties. The air-water interface is where these peptides exhibit interfacial action.[53,54] The capacity of peptides to permeabilize lipid bilayer membranes has been linked to their interfacial activity. We observed changes in the surface tension of the Tris buffer solution when the synthetic peptides (10.0 μM) were added. The interfacial affinity of peptides was determined using the observed fluctuation in surface tension.[55] The surface tension reduced over time after the addition of the peptide to the buffer's sub-phase, as depicted in Figure 4, and it eventually achieved its equilibrium value. At 20 °C, the Tris buffer surface tension was 58.87 mN/m. The surface tension attained equilibrium after injecting P1 and P2 into the Tris buffer sub-phase, and the equilibrium surface tension values were observed to be 48.45 mN/m and 50.42 mN/m, respectively. This concludes that, P1 and P2 are surface active (P2 < P1), and upon addition of 10.0 μM, the surface tension of Tris buffer decreased by 10.42 mN/m and 8.45 mN/m respectively.[56]

3.3. Secondary structure of peptides

We acquired the circular dichroism spectra of P1 and P2 in a trisbuffer at room temperature to better understand the nature of peptide-lipid interactions in the peptides' cell-selective interactions. P1 may have a random coil structure because a neat solution of P1 (10.0 μM) in a tris buffer revealed a single negative minimum at 198 nm (Figure 5). P1 and P2 both showed a single negative minimum at 200 and 204 nm, respectively, when POPC SUVs (64 μg) were added before being tested in a tris buffer (Figure 5). The CD profiles of P1 and P2 were not appreciably changed by POPC vesicles. When peptide P2 was added to the anionic POPC:POPG vesicles, it indicated that the peptide backbone had been reoriented to create a more ordered secondary ß-structure on the anionic lipid membrane and that P1 had slightly changed to an orderly structure.[57]

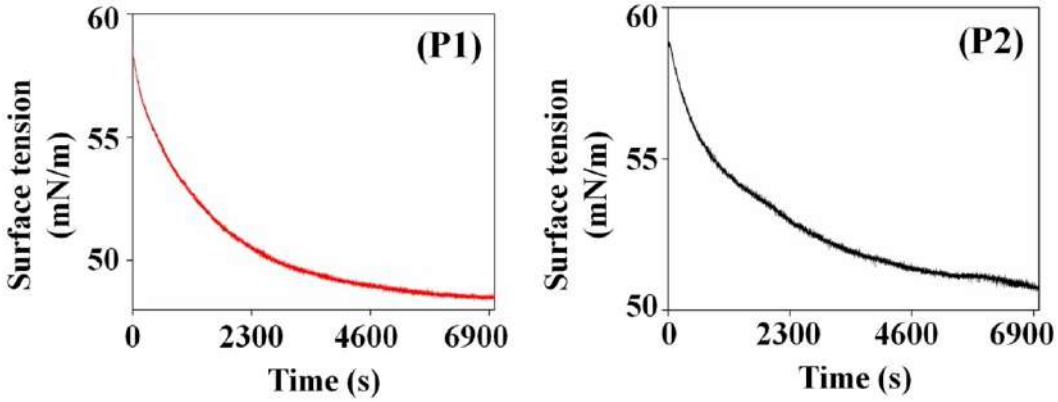

Figure 4. Surface activity is achieved from peptide adsorption to the air/water interface. The surface tension of Tris-HCl buffer (58.87 mN/ m at 20 ± 1 °C) decreases once peptides **P1** and **P2** (10.0 μM) are injected into the subphase of the buffer. The observed surface tension decreased for **P1** = 10.42 and **P2** = 8.45 (mN/m).

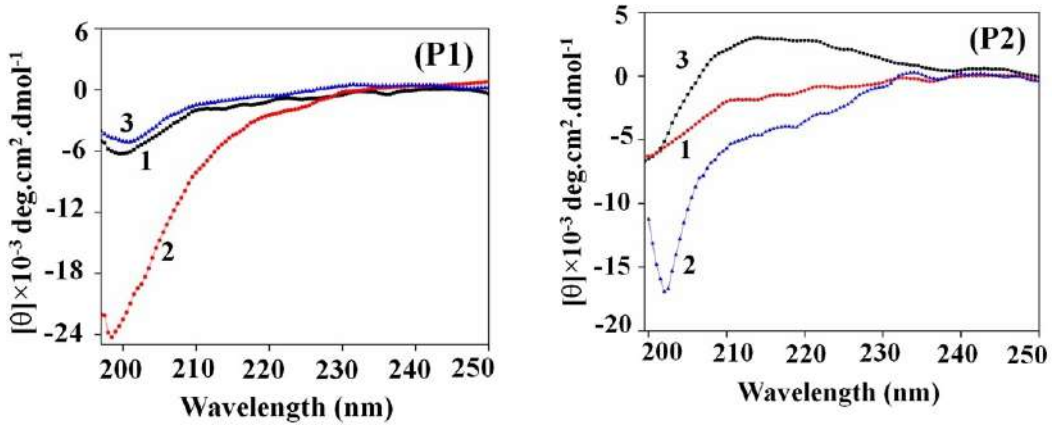

Figure 5. Circular dichroism spectra of peptides **P1** and **P2** (10.0 μM) in PBS buffer (1), and with small unilamellar vesicles of POPC (2) and POPC:POPG (3).The lipid concentration was 64 μg/mL.

3.4. Mechanism of cancer cell-selective binding of peptides

The capacity of the N-terminally modified peptides to attach to membranes was verified using steady-state fluorescence measurements. The electrostatic interaction between the anionic membrane (POPC:POPG) and the zwitterionic membrane (POPC), as suggested by extensive studies on the mechanism of killing bacteria and cancer cells by membrane-active peptides, would be a crucial element in eliciting their antibacterial and anticancer activity.[56,57] So, using tiny unilamellar vesicles (lipid bilayer membranes) made of POPC and a POPC:POPG (1:1) mixture, we studied the selective layer interactions of peptides P1 and P2 (10.0 μM).[57] To test the binding affinity of peptides towards zwitterionic POPC and anionic POPC:POPG (1:1) vesicles and fluorescence which contains both native and modified tryptophan (P1 and P2) (Figure 6). The enhanced

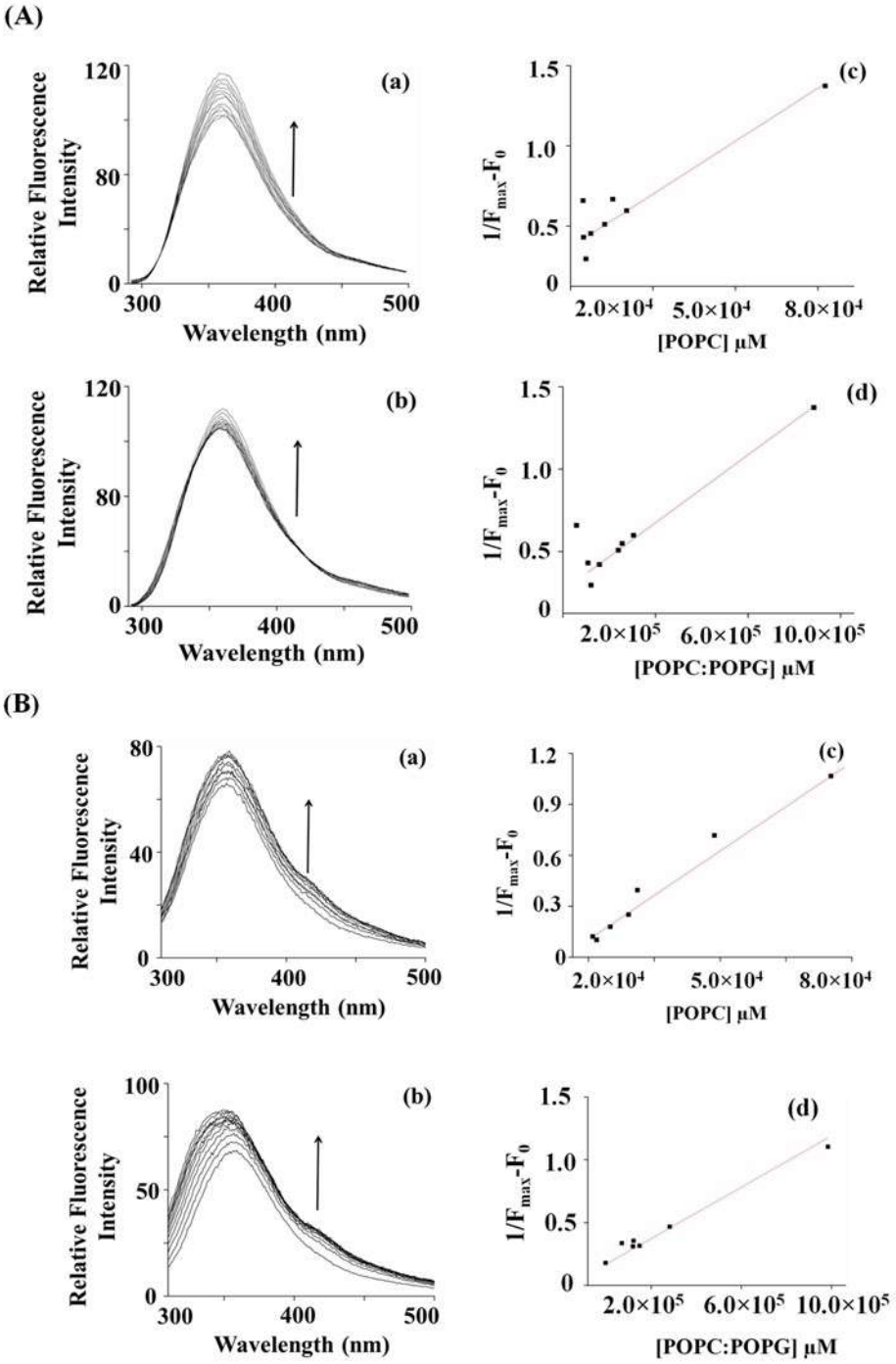

Figure 6. Enhancement of intrinsic fluorescence from peptides (A) **P1** (***W***-KRGNKWLA-$CONH_2$ = 10.0 μM) upon binding to POPC **(a)** and POPC:POPG **(b)** vesicles and followed by binding constants values are **(c)** 1.3154×10^5 M and **(d)** 1.2012×10^4 M. Similarly,(B) **P2** (***W***-ARGDGGNGRGA-$CONH_2$ = 10.0 μM) upon binding to POPC **(a)** and POPC:POPG **(b)** vesicles and followed by binding constants values are **(c)** 1.5381×10^6 M and **(d)** 1.0284×10^4 M respectively.

extent of the intensity rise upon binding and the driver of the blue shift exhibited in Figure 6 may both be related to the presence of native tryptophan. This is in line with the hypothesis that tryptophan binds to bilayers and causes variations in the depth of penetration related to lipid composition.[46]

Despite the NGR motif being present in peptide P1, P2 differs from P1 in that it is longer and more hydrophobic (Figure 2A and Table 1). P1 had a higher affinity for the anionic POPC:POPG membrane (binding constant: 1.3154×10^{5} M) than the zwitterionic POPC membrane (1.2012×10^{4} M). It's interesting to note that peptide P2 had a stronger affinity for POPC:POPG lipid vesicles (1.5381×10^{6} M) than it did for POPC (1.0284×10^{4} M). It is critical to understand that peptide P2 has a higher affinity for anionic POPC:POPG lipid vesicles than peptide P1. This result is well correlated with the anticancer activity of peptide P2 could be higher owing to the presence of NGR and RGD binding motifs compared to one NGR group present in P1. The interaction of P2 with integrin and CD13 on cancer cells (receptor-ligand interactions) could be the first stage in killing the cells.

3.5. Molecular docking of synthetic peptide and protein

The docking analysis of peptides (P1 and P2) docked in 3ERD and 5GWK showed that peptides P1 and P2 formed a Hydrogen bond interaction, as shown in Figure 7. The best conformation for the peptide was chosen based on the better glide score (SP Gscore).[58]

Docking of synthetic peptides into 3ERD: Peptide P2 established deterministic hydrogen bond interactions with the active site with an SP docking score (SP Gscore −9.916 kcal/mol) compared with Peptide P1 (SP Gscore −7.691 kcal/mol) which might be a reason for its good activity. This synthetic peptide P2 has numerous hydrogen bond interactions with amino acid residues (Leu 549, Hid 555, Glu 380, Glu 542, Asp 538, Asp 351, and Tyr 537) (as shown in Figure 7A and Figure 7B). Water-mediated interactions are the potential for protein-peptide binding which can be observed in peptide P2 (Asn 348). This additional interaction is a strong validation of why P2 (as shown in Table 3) is more active when compared to peptide (P1). However, peptide P1 shares hydrogen bond interactions with protein amino acid residues (Gln 375, Lys 362, Asn 359, Glu 380, Glu 542, and Hid 555), it is not entirely engulfed in the cavity which is predominantly surrounded by hydrophobic residues and makes fewer interactions with the residues of the receptor.

Docking of synthetic peptides into 5GWK:The results obtained from molecular docking suggest that bothsynthetic peptides intercalated within the cytosine and guanine-rich regions of the major groove of the DNA base pair. It could be seen that peptide P2 is sandwiched between DNA bases and shares significant hydrogen bonding interactionat DG 13, DC

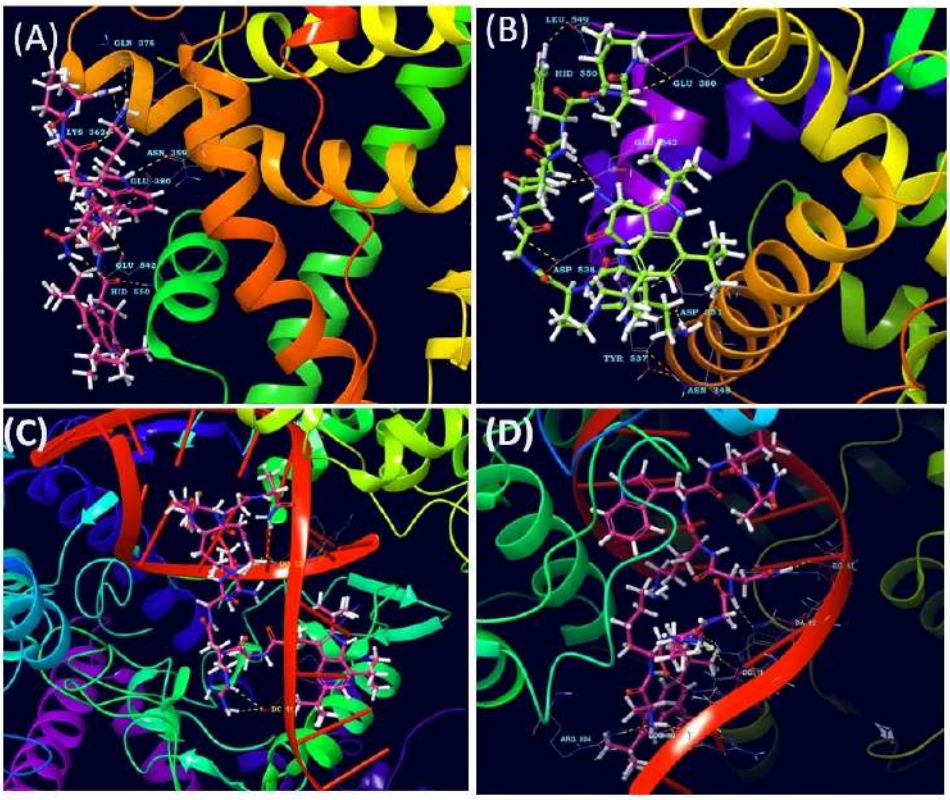

Figure 7. 3D binding representation of docked complex of the synthetic peptide with human estrogen receptor alpha (PDB ID: 3ERD) (A) **P1** and (B) **P2** and with Human topoisomerase II alpha (PDB ID: 5GWK) (C) **P1** and (D) **P2** through non-covalent bonding interaction.

12, DC 11, and DG 10 (SP Gscore −11.121 kcal/mol). One additional hydrogen bonding interaction between the NH_2 group and the charged residue Arg 804 on the peptide chain (is shown in Figure 7C and Figure 7D. However, if we look into peptide P1, they do not bury deep in the binding site. Instead, they extend farther out of the groove. It shows two hydrogen bond interactions with SP Gscore −9.732 kcal/mol, i.e., DC 13 and DC 11 with DNA major grooves, and there is no additional interaction with protein. Thus, the hydrogen bond interactions play a significant role in stabilizing the synthetic peptide and DNA complex.

4. Conclusions

The CD13-binding motifs in the P1 and P2 peptide sequences were chosen to specifically target and kill cancer cells. The role of the trialkylated tryptophan amino acid (***W***) at the N-terminus of the peptides P1 and P2 was included in the design. For the solid-phase peptide synthesis (SPPS) approach, we used Fmoc-amino acids and Rink amide resin to combine various amino acids. NGR is present in peptide P1, and RGD as well as NGR motifs are present in peptide P2. Mass spectrometry analysis and Reverse-phase HPLC (RP-HPLC) chromatogram verified the peptides' structural integrity and purity of the peptide.In addition, to check the interfacial affinity, we performed the surface tension activity of synthesized peptides (P1 and P2). Furthermore, a change in the conformational transitionis observed from an unordered to an ordered structure by circular dichroism and the structure is finally confirmed by 1D and 2D NMR spectroscopy analysis. Likewise, we found that the secondary ß-structure change in the Peptide P2 CD profile is due to the anionic (POPC:POPG) zwitterionic (POPC) lipid membrane. The selective anticancer activity demonstrates that due to structural variation in P2 as compared to P1 makes it more selective towards Hep-2 cells which is further confirmed by molecular docking studies (PDB ID 5GWK, PDB ID 3ERD).Two binding motifs found in P2-NGR and RGD could be the cause of this dramatic increase in activity. So, these peptides can be considered as templates for future cancer clinical treatment as they serve, good solubility, low toxicity, high selectivity, low manufacturing cost, biocompatibility, and enhanced therapeutic index.

Acknowledgements

The authors heartly thank to Dr. S. Thennarasu, Former Chief Scientist & Head, CSIR-Central Leather Research Institute (CSIR-CLRI), Adyar, Chennai-600020, Tamil Nadu, India for providing research support.There is no external funding research support for carrying out this work

Conflict of Interests

The authors declare no conflict of interest.

Data Availability

The data that support the findings of this study are available from the corresponding author upon reasonable request.

Keywords: Solid phase peptide synthesis · Steady-State fluorescence spectroscopy · Peptide-lipid binding interaction · Surface activity · Anticancer activity

[1] S. Riedl, D. Zweytick, K. Lohner, *Chem. Phys. Lipids.* **2011**, *164*, 766–81.
[2] A. T. Y. Yeung, S. L. Gellatly, R. E. W. Hancock, *Cell. Mol. Life Sci.* **2011**, *68*, 2161–2176.
[3] E. Ruoslahti, S. N. Bhatia, M. J. Sailor, *Cell Biol.* **2010**, *188*,759–768.
[4] Z. Liu, K. Wu, *Recent pat. on Anti-Cancer Drug Discov.* **2008**, *3*, 202–208.
[5] N. Papo, Y. Shai, *Cell. Mol. Life Sci.* **2005**, *62*, 784–790.
[6] D. W. Hoskin, A. Ramamoorthy, *Biochem. Biophysics Acta.* **2008**, *1778*, 357–375.
[7] Z. Zhang, H. Hatta, K. Tanabe, S. I. Nishimoto, *Pharm.Res.* **2005**, *22*, 381–389.
[8] K. Chen, W. Ma, G. Li, W. Wang, L. P. Yap, L. D. Hughes, R. Park, P. S. Conti, *Mol. Pharmaceutics.* **2013**, *10*, 417–427.
[9] W. Arap, R. Pasqualini, E. Ruoslahti, *Science.* **1998**, *279*, 377–380.
[10] F. Curnis, A. Sacchi, L. Borgna, F. Magni, A. Gasparri, A. Corti, *Nat. Biotechnol.* **2000**, *18*, 1185–1190.
[11] K. Chen, X. Chen, *Theranostics.* **2011**, *1*, 189–200.
[12] P. C. Brooks, R. A. F. Clark, D. A. Cheresh, *Science.* **1994**, *264*, 569–571.
[13] M. Wickström, R. Larsson, P. Nygren, J. Gullbo, *Cancer Sci.* **2011**, *102*, 501–508.
[14] D. J. Hicklin, L. M. Ellis, *J. Cliln. Oncol.* **2005**,*23*, 1011–1027.
[15] T. Veikkola, M. Karkkainen, L. Claesson-Welsh, K. Alitalo, *Cancer Res.* **2000**, *60*, 203–212.
[16] S. Silletti, T. Kessler, J. Goldberg, D. L. Boger, D. A. Cheresh, *Proc. Natl. Acad. Sci. U. S. A.* **2001**, *98*,119–124.
[17] J. S. Desgrosellier, D. A. Cheresh, *Nat. Rev. Cancer.* **2010**, *10*, 9–22.
[18] T. M. Allen, *Nat. Rev. Cancer.* **2002**, *2*, 750–763.
[19] A. Wallbrunn, J. Waldeck, C. Höltke, M. Zühlsdorf, R. Mesters, W. Heinde, M. Schäfers, C. Bremer, *J. of Biomed. Opt.* **2008**, *13*, 011007.
[20] M. Oostendorp, K. Douma, T. M. Hackeng, A. Dirksen, M. J. Post, M. van, A. M. J. Zandvoort, W. H. Backes, *Cancer Res.* **2008**, *68*, 7676–7683.
[21] R. Krishnamoorthy, P. Adhikari, P. Anaikutti, *RSC Adv.* **2023**, *13*, 15594–15605.
[22] R. Krishnamoorthy, P. Anaikutti, *RSC Adv.* **2023**, *13*, 36439–36454.
[23] E. Jr Crusca, A. A. Rezende, R. Marchetto, M. J. S. Mendes-Giannini, W. Fontes, M. S. Castro, E. M. Cilli, *Biopolymers.* **2011**, *96*, 41–48.
[24] Y. Van Hensbergen, H. J. Broxterman, Y. W. Elderkamp, J. Lankelma, J. C. Beers, M. Heijn, *Biochem Pharmacol.* **2002**, *63*, 897–908.
[25] M. W. Ndinguri, R. Solipuram, R. P. Gambrell, S. Aggarwal, R. P. Hammer, *Bioconjug Chem.* **2009**, *20*, 1869–1878.
[26] D. Donald, C. Noting, W. John Gore, *Curr. Org. Synth.* **2011**, *8*, 521–534.
[27] M. Jullian, A. Hernandez, A. Maurras, K. Puget, M. Amblard, J. Martinez, *Tetrahedron Lett.* **2009** *50*, 260–263.
[28] J. M. Walker, *Methods Mol. Biol.* **1984**, *1*, 203–212.
[29] E. Birtalan, B. Rudat, D. K. Kölmel, D. Fritz, S. B. L. Vollrath, U. Schepers, S. Braise, *Biopolymers.* **2011**, *96*, 694–701.
[30] F. Schweizer, *Eur. J. Pharmacol.* **2009**, *625*,190–194.
[31] I. Dobrzynska, B. Szachowicz-Petelska, S. Sulkowski, Z. Figaszewski, *Mol. Cell Biochem.* **2005**, *276*, 113–119.
[32] D. H. Dube, C. R. Bertozzi, *Nat. Rev. Drug Discov.* **2005**, *4*, 477–488.
[33] S. T. Henrique's, Y. H. Huang, K. J. Rosengren, H. G. Franquelim, F. A. Carvalho, A. Johnson, S. Sonza, G. Tachedjian, M. A. Castanho, N. L. D. Daly, J. Craik, *J. Biol. Chem.* **2011**, *286*, 24231–24241.
[34] A. Parthiban, M. Kumaravel, J. Muthukumaran, R. Rukkumani, R. Krishna, H. Surya Prakash Rao, *Med. Chem. Res.* **2016**, *25*, 1308–1315.
[35] K. N. Sugahara, T. Teesalu, P. P. Karmali, V. R. Kotamraju, L. Agemy, *Science.* **2010**, *328*, 1031–1035.
[36] E. Koivunen, D. A. Gay, E. Ruoslahti, *J. Biol. Chem.* **1993**, *268*, 20205–20210.
[37] E. Koivunen, B. Wang, E. Ruoslahti, *J. Cell Biol.* **1994**, *124*, 373–80.
[38] A. Gautam, P. Kapoor, K. Chaudhary, R. Kumar, *Curr. Med. Chem.* **2014**, *21*, 2367–2391.
[39] R. Liu, X. Li, W. Xia, K. S. Lam, *Adv. Drug Deliv. Rev.* **2017**, *110*, 13–37.

[40] O. H. Aina, R. Liu, J. L. Sutcliffe, J. Marik, J. C. X. Pan, K. S. Lam, *Mol. Pharmaceutics.* **2007**, *4*, 631–51.
[41] O. H. Aina, J. Marik, R. Liu, D. H. Lau, K. S. Lam, *Mol. Cancer Ther.* **2005**, *4*, 806–813.
[42] M. Mikawa, H. Wang, L. Guo, R. Liu, J. Marik, Y. Takada, K. S. Lam, D. Lau, *Mol. Cancer Ther.* **2004** *3*, 1329–1334.
[43] N. Wiradharma, M. Khan, L. K. Yong, C. A. Hauser, S. V. Seow, S. Zhang, Y. Y. Yang, *Biomater.* **2011**, *32*, 9100–9108.
[44] A. J. De Jesus, T. W. Allen, *Biochem. Biophysics Acta.* **2013**, *1828*, 864–876.
[45] A. S. Ladokhin, *Anal. Biochem.* **1999**, *276*, 65–71.
[46] A. R. Ferreira, C. Teixeira, C. F. Sousa, L. J. Bessa, P. Gomes, P. Gameiro, *Membranes.* **2021**, *11*, 48.
[47] Schrödinger Release 2022-3: Protein Preparation Wizard; Epik, Schrödinger, LLC, New York, NY, 2021; Impact, Schrödinger, LLC, New York, NY; Prime, Schrödinger, LLC, New York, NY, **2021**.
[48] C. Lu, C. Wu, D. Ghoreishi, W. Chen, L. Wang, W. Damm, G. A. Ross, M. K. Dahlgren, E. Russell, C. D. Von Bargen, R. Abel, *J. Chem. Theory Comput.* **2021**, *7*, 291–4300.
[49] D. C. Bas, D. Rogers, J. Jensen, *Proteins.* **2008**, *73*, 765–783.
[50] T. Mossman, *J. Immunol. Methods.* **1983**, *65*, 55–63.
[51] K. Rajavenkatesh, S. Meenakshi, A. Parthiban, L. E. Paul, D. Sivasankaran, S. Thennarsu, *Bioorg.Chem.* **2023**, *134*, 106434.
[52] A. Parthiban, R. Sivasankar, B. Rajdev, R. N. Asha, T. C. Jeyakumar, R. Periakaruppan, V. G. M. Naidu, *J. Mol. Struct.* **2022**, *1270*, 133885.
[53] H. Brockman, *Curr. Opin. Struct. Biol.* **1999**, *9*, 438–443.
[54] S. Deshayes, T. Plénat, G. Aldrian-Herrada, G. Divita, C. Le Grimellec, F. Heitz, *Biochem.* **2004**, *43*, 7698–7706.
[55] C. Peetla, S. Vijayaraghavalu, V. Labhasetwara, *Adv. Drug Deliv. Rev.* **2013**, *30*, 65–98.
[56] K. Rajavenkatesh, M. Padmaja, I. Janani, S. Aishwarya, K. Purna Sai, S. Thennarasu, *Chem.Biol. Drug Des.* **2020**, *96*, 610–623.
[57] S. Thennarasu, R. Huang, P. D.-K. Lee, L. Yang, Z. Maloy, A. Chen, . Ramamoorthy, *Biochem.* **2010**, *49*, 10595–10605.
[58] A. H. Morgan, E. S. O. Luis, R. N. Matthew, J. S. David, J. P. Thaddeus, E. T. Katharine, D. V. Timothy, A. C. Gregory, *Biochim. Biophys. Acta, Biomembr.* **2019**, *1861*, 182984.

Manuscript received: December 11, 2023

Journal of Environmental Chemical Engineering 12 (2024) 112266

Contents lists available at ScienceDirect

Journal of Environmental Chemical Engineering

journal homepage: www.elsevier.com/locate/jece

Efficient interfacial charge transfer of hierarchical crinkled (2D/2D) $Ti_3C_2T_x$ MXene assembled on perforated GO heterojunction for enhanced degradation of organic dye

Sivakumar Vigneshwaran [a], Palliyalil Sirajudheen [b], Rajendran Babhu Vignesh [c], Do-Gun Kim [d], Seok-Oh Ko [a,*]

[a] Environmental System Laboratory, Department of Civil Engineering, Kyung Hee University-Global Campus, 1732 Deogyong-daero, Giheung-Gu, Yongin-Si, Gyeonggi-Do 16705, Republic of Korea
[b] Department of Chemistry, Pocker Sahib Memorial Orphanage College, Tirurangadi, Malappuram, Kerala 676 306, India
[c] Department of Chemistry, Velammal College of Engineering and Technology, Viraganoor, Tamil Nadu 625009, India
[d] Department of Environmental Engineering, Sunchon National University, 255 Jungang-ro, Suncheon, Jellanam-do 57922, Republic of Korea

ARTICLE INFO

Keywords:
Holey graphene oxide
MXene
Photodegradation
Organic dye
Pseudo-first order kinetics
Reusability

ABSTRACT

In this research work, a simple hydrothermal technique was employed to synthesize a novel holey graphene oxide (HGO) intercalated MXene (MX) hybrid composite and utilized for the enhanced removal of methylene blue (MB) dyes by irradiation using visible light. The fabricated HGO@MX catalyst exhibited excellent catalytic activity, and the degraded efficiency achieved was around 99% for MB with a minimum irradiation time of 60 min. The HGO@MX nano-matrix has better photocatalytic action over HGO because of its increased light absorption ability, efficient charge transference, appropriate band synchronization, and less charge carrier recombination between HGO and MX. A significant number of active sites are provided on the composite surface by the synergistic interaction between HGO and MXene, which leads to outstanding photodegradation behavior and can increase the mass-transfer rates and chemical processes. The radicals the HGO@MX hybrid catalyst generates are non-toxic and effectively mineralize the selected organic dye. Additionally, HGO@MX showed great potential with 82% degradation efficiency after five repetitive runs for MB with minimal loss of catalytic activity. The as-synthesized HGO@GO catalytic material was systematically examined through SEM, TEM, XPS, XRD, FTIR, TGA-DTA, and Raman analysis. The LC-MS technique described the degradation pathway of MB and the obtained intermediates. Finally, MB dye degradation and catalytic mechanism pathways were investigated thoroughly based on the obtained experimental data. The results show that HGO@MX is a promising photocatalytic material for the oxidation of MB from the aqueous environment.

Main finding: The hydrothermal approach was adopted to create the hybrid photocatalyst 2D/2D holey graphene oxide on MXene, which demonstrated enhanced photocatalysis and photo endurance.

1. Introduction

Dyes are carcinogenic and mutagenic, causing health problems in living organisms [1]. The complex aromatic structures of dye molecules are usually non-biodegradable and make them resistant to heat, oxidation and light [2,3]. Among the all-traditional techniques, photocatalytic degradation is one of the promising methods in water remediation which is highly efficient, cost-effective, has the feasibility of operation and produces a low level of secondary pollution [4,5].

In the presence of charged particles (electrons and holes), the selected photocatalytic material undergoes reduction and oxidation processes on its surface, producing active radical species ($\bullet O_2^-$ and $\bullet OH$) and aiding in the degradation process of dyes in an aqueous environment [6–8]. Many inorganic materials, such as oxides of Ti and Zn, have been used as photocatalysts for the degradation of organic molecules for the past few decades, however, both exhibit low catalytic activity due to their large band gaps[9]. In place of TiO_2 [10], ZnO [11], and other semiconductors, there are some carbonaceous materials that exhibit excellent photocatalytic properties [12,13]. Moreover, the formation of heterojunction photocatalytic materials (^2D–^2D carbonaceous

* Corresponding author.
E-mail address: soko@khu.ac.kr (S.-O. Ko).

https://doi.org/10.1016/j.jece.2024.112266
Received 20 September 2023; Received in revised form 14 February 2024; Accepted 18 February 2024
Available online 20 February 2024

composites) exhibits high resistance to the relocation of charge carriers as well as increases the separation rate of electrons (e^-) and holes (h^+) [14]. Therefore, 2D/2D composite can be better alternative as a novel photocatalytic carbonaceous material for the degradation of recalcitrant organic pollutants.

Graphene oxide (GO) has great potential to be used as a photocatalytic agent due to its large surface area [15], special chemical structure [16], and chemical stability [17]. The functionality of GO, such as carboxyl (COOH), epoxy (C-O-C), and hydroxyl (OH) arranged randomly on the edges and basal planes of GO, allowing easy chemical modifications [18,19]. Therefore, GO effectively creates a network with other organic and inorganic materials through ionic and covalent bonds. However, the inexorable insertion of functional groups via over-oxidation causes defective spots on the sp^2 hybridized graphene carbon plane, making GO less conductive [20]. The creation of oxidative cavities within the basal surface of graphene sheets has just acknowledged much consideration in developing GO morphologies; the resulting material is referred to as holey graphene oxide (HGO). HGO differs from GO in that it has considerably higher catalytic centers because of the increased periphery recognized to holes [21]. The HGO with holes affords interlayer transport pathways of electrons across the holey graphene plane and ultimately binds to the surface to heterostructures, thus overcoming the intrinsic heterojunction thus promotes charge separation and electron transport. The distinctive porosity structure of HGO makes it simple to interact with both organic and inorganic molecules, which has several uses in band gap optimizations. Because of its strong electrical conductivity, wide operative surface areas, and significantly more accessible edge activities for ion diffusion, it can create an unhindered channel using 2D materials for fast electron transit. Therefore, the HGO acts as a space interlayer to improve the electrochemical performance of doping material.

Following this HGO, a family of innovative 2D transition carbonitrides of metals such as MXene has recently received much attention in water treatment for multiple applications with the general formula $M_{n+1}X_nT_x$ (where n=0, 1, 2, and 3). In this equation, M represents transition metals, X stands for either carbon or nitrogen, and T represents surface edges such as –O, –F, or –OH, which are obtained after the etching of the A (III-group elements) layer from the MAX precursors [22,23]. The MAX phase has exceptionally stable chemical characteristics and excellent mechanical strength due to a covalent link between M and X and a metallic bond between M and A. MXene could act as an excellent co-catalyst due to its excellent metallic conductivity [24], large surface area [25], exceptional hydrophilicity [26], different active sites and low band gap [27–29]. Due to their great electrical conductivity, MXenes may operate as charge-transfer intermediaries and control their capacity to capture light, while their functionality governs how they interact with other materials, such as HGO. Furthermore, by combining HGO with MXene, we expect MXenes can be a tuner for complex composites which can efficiently separate the photogenerated electrons and holes, resulting in a lower recombination rate [30]. In addition, (2) MXene surface terminations (e.g., –O, –OH, –F) could be an asset in producing more active sites on the surface and also at interfaces and enhance the intimate contact with the HGO [31]. In order to obtain enhanced photocatalytic activity, we used in-plane pores structure of HGO with interlayered channels between MXene to prepare HGO@MX nanocomposite. The intimate contact of HGO with MX can promote the development of a “synergistic effect” so that multiple interfaces in the composite induce interfacial polarization; therefore, the binary composite exhibits excellent photocatalytic performances towards methylene blue.

In this study, holey graphene oxide intercalated MXene (HGO@MX) catalytic material was fabricated via a simple co-precipitation technique. Our literature review shows no studies regarding the photocatalytic degradation of dyes using the combination of HGO and MXene hybrid material under visible irradiation. The prepared photocatalytic material before and after degradation was systematically characterized using FTIR, XRD, SEM, TGA, UV-DRS, XPS, and LC-MS analysis. In particular, the regeneration experiments were similarly steered to confirm the firmness of the prepared photocatalyst hybrid. The activity of the photocatalyst HGO@MX was explored via the removal kinetics of MB in an aqueous environment.

2. Experimental section

2.1. Chemicals and reagents

The supplemental material in **Text S1** provides a complete list of all the reagents with grade information. The physio-chemical characteristics of the selected dyes are presented in Table S1.

2.2. Fabrication of modified holey graphene oxide intercalated MXene (HGO@MX) hybrid composite

The binary *HGO@MX* catalyst composites were fabricated using docile hydrothermal and freeze-drying processes as follows,

2.2.1. Preparation of direct HF-etched MXene ($Ti_3C_2T_x$)

In the synthesis process through direct etching procedure, 5 g of Ti_3AlC_2 was added gradually to a 100 mL of 50 wt% hydrofluoric acid (HF) while stirring using Teflon magnetic bar. Slow addition of MXene powder is necessary to minimize excessive bubbling formed due to the exothermic reaction. The etching process was then allowed to proceed at room temperature (~23ºC) for 5 hours under stirring at 300 rpm. The sample then be separated using centrifugation (5 min per cycle at 3500 rpm) and washed with deionized water until the pH value is almost neutral. The pH value was determined by using a pH paper indicator. The sediments were re-washed with 1000 mL of deionized water via vacuum-assisted filtration using a polyvinyl difluoride (PVDF) filter membrane with 0.22 μm pore size filters. The sample was let to dry in vacuum oven for 24 hours at 80ºC.

2.2.2. Synthesis of HGO via chemical etching

Graphene oxide (GO) was prepared from graphite by using a modified Hummers-Offeman method [32]. About 2 g of flake-graphite and 1 g of $NaNO_3$ were added into the H_2SO_4 (96 mL) solution and the reaction contents were placed in an ice bath with constant agitation. Then, 6 g of $KMnO_4$ was added drop by drop to the above mixture with vigorous stirring at below 20 °C for 2 h. The obtained green thick paste was then mixed with 150 mL of DI water for 18 h at room temperature while stirring, followed by diluting 240 mL of DI water. After standing 30 min, the obtained solid residue was purified by washing, centrifuging and dried for 2 h and then the obtained product is denoted as GO. Subsequently, 5 mL of 30% H_2O_2 solution was added into the 200 mL of GO dispersion, and the reaction suspension was sealed in a Teflon-lined autoclave at 180 °C. Finally, the obtained yellowish brown HGO powder was washed with DI water followed by ethanol. At last, the final products were continuously stirred and filtered for 2 h at 100 °C [32–34].

2.2.3. Fabrication of modified HGO@MX nanocomposite

HGO@MX films were fabricated by the following procedure. Specifically, the various ratio of MXene and HGO was added on the beaker with ethanol/aqueous dispersions were mixed *via* magnetic stirring and hydrothermal treatment for 30 min to achieve MXene-HGO composite colloidal suspensions. Finally, the holey graphene oxide intercalated MXene (HGO@MX) framework was washed with DI water several times and naturally cooled down at ambient temperature. After filtration, the dried HGO@MX catalyst was freeze dried and used for further catalytic experiments.

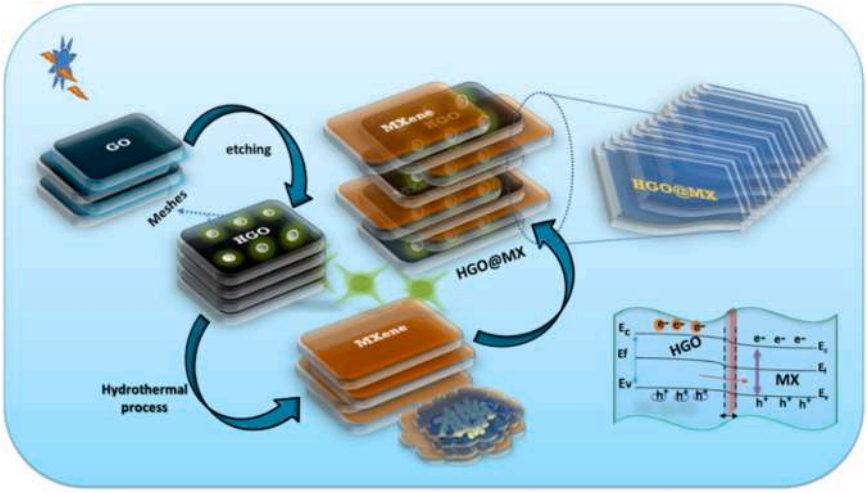

Scheme 1. Sample fabrication route for the synthesis of HGO@MX nanocomposites.

2.3. Characterization techniques

All of the characterization procedures used to evaluate the physiochemical and photocatalytic characteristics of the manufactured catalysts are summarized in **Text S2**.

2.4. Evaluation of prepared photocatalyst

The supplemental information, **Text S3**, fully explains the experimental methodology and catalytic procedures utilized to assess photocatalytic performances.

3. Results and discussion

3.1. Crystal structure and crystallite phase

The surface functionality of the synthesized materials was investigated via FTIR spectroscopy. The FTIR spectra of GO, MX, HGO, and HGO@MX hybrid catalyst are depicted in Fig. 1. Different absorption peaks were obtained to describe the successful synthesis of prepared materials. The spectra of GO and HGO was exhibited at 3400, 1723, 1630, 1385, 1221 and 1055 cm^{-1} correspond to the –OH, –C═O, C═C, C–OH, O–H and C–O stretching, suggesting the presence of carboxyl, hydroxyl, and epoxy oxygen in both GO and HGO. The intensity of peak (C–OH) of HGO is decreased compared to the GO, which is indicated the –OH removed partially in the reaction. The presence of –OH stretching and –NH stretching vibration of all prepared materials was responsible for the vibration mode at 3431 and 1626 cm^{-1}, respectively. The peaks at 2924 and 2860 cm^{-1} were interrelated to the symmetric and asymmetric stretching vibration of $–CH_2$ in all prepared materials [35]. The corresponding stretching modes of –C═O and –C–O in all materials were attributed to 1719 and 1063 cm^{-1}. Additionally, the prominent peak at 563 cm^{-1} corresponds to the –Ti-O of MXene [36]. The change in chemical composition of the HGO@MX catalyst after loading of HGO on MX sheets was confirmed by the shifting and reduction of peak positions in the HGO@MX material, which is shown in the FTIR spectrum of the HGO@MX. For instance, the reduced peak intensities were noted at 3431, 2924, 1626, and 1063 cm^{-1}, the disappearance of peaks at 1384 cm^{-1}; and shifted peaks from 1063 to 1042 cm^{-1} and 563–609 cm^{-1} clearly indicated that the selected HGO was successfully draped into the MX sheets.

The crystallographic information of prepared materials was studied by XRD analysis. Fig. 2 shows the XRD spectra of MX and the HGO@MX hybrid catalyst. The XRD pattern of MX exhibits the strong characteristic peaks at 8.91° and 18.09°, which are responsible for the MX. Similar results were reported for the MXene sheets in the literature by *Liu et al.,* [37]. Also, the XRD spectra of MX showed the additional peaks at 16.22°, 22.94°, 27.13°, 34.29°, 36.81°, 38.89°, 41.89°, and 60.64° [38]. The slightly increased peak intensities of these oxygenous groups in the

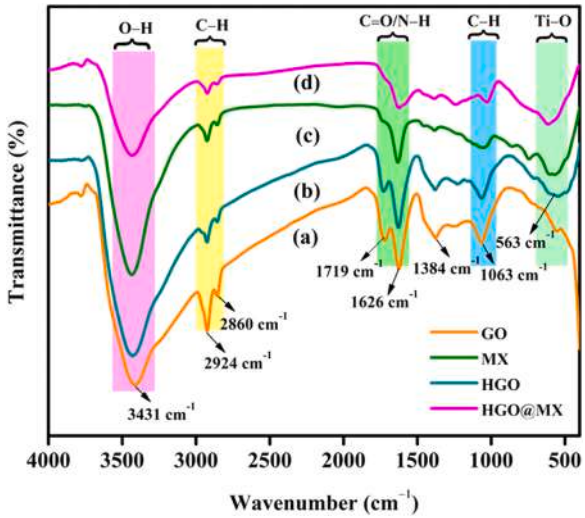

Fig. 1. FTIR spectra of GO, MX, HGO and HGO@MX nanocomposites.

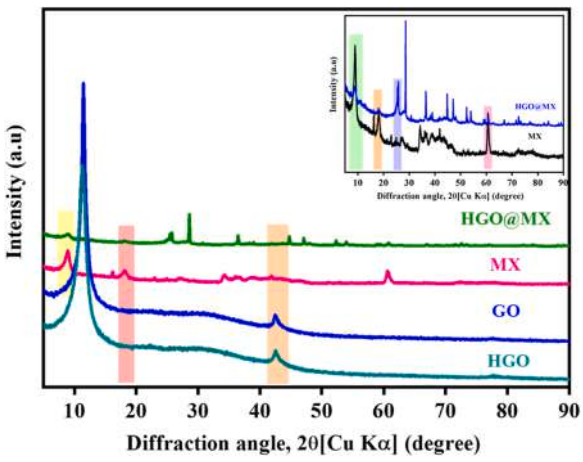

Fig. 2. XRD patterns of GO, MX, HGO and HGO@MX (inset: enlargement of MX and HGO@MX) nanocomposites.

HGO compared to those in GO may suggest the incorporation of some more oxygen atoms into HGO after the H_2O_2 etching step, due to the oxidation of carbon atoms by concentrated H_2O_2. This is further supported by the XPS results in Table S3, which shows that the relative atomic percentage of oxygen in HGO is slightly higher than that in GO. The XRD pattern of the HGO@MX catalyst reflects the peaks of the HGO and MX materials. This statement was confirmed by the peaks of 8.96°, 12.69°, 18.10°, and 60.82°, which are responsible for the HGO and MX in the prepared HGO@MX catalyst. The small peak at 12.69° (002) was attributed to the presence of HGO in the HGO@MX composite. Sharp peaks of the HGO@MX clearly demonstrate its better crystalline properties and thus it facilitates accelerated charge transfer between heterogenous HGO and MXene.

3.2. Morphological characterization and the element analysis

The SEM analysis was used to investigate the surface morphology of the as-prepared HGO@MX photocatalyst in detail. Fig. 3(a-f) depicts the SEM images of the HGO@MX hybrid composite in different magnifications. The prepared photocatalyst demonstrates the layered morphology according to the SEM images of the HGO@MX material. The formation of small sized in-plane holes were observed on the sheet plate of the prepared catalyst clearly manifested that stretch and damage of carbon framework of the GO (inset) which is probably generated by the H_2O_2 etching and ultimately leaving GO with a holey-like structure (Fig. 3(a)). The closed layered structure of the MAX phase is clearly visible in the SEM image. whereas, the MXene layers take on scrunched shapes and have a hard texture with many ridges Fig. 3(b). Cross-sectional SEM pictures of a $Ti_3C_2T_x$ composite that are layered, sleek, and orderly. Comparing Fig. 3(b) to (c), a top-view SEM image reveals that the layers are distinct from one another. The Ti_3C_2 layers have the largest specific surface areas, according to the partial enlarged SEM image of MX layers, which is 20 nm on average [39]. Moreover, the dense layer on the surface of MX exhibits outstanding hydrophilicity and electronic properties for the prepared photocatalyst. These properties help to improve the degradation efficiency during the dye treatment process [40]. The process of various state of research that aligns on the possibility of sepiolite structural formation.

After the HGO deposition, the surface does not have any pores but shows some wrinkles (Fig. 3(e)), confirming the deposition of the HGO on layers. The random distribution of HGO on MX was clearly confirmed by the SEM observation. The equal distribution of HGO intercalated over the surface of MXene, which may surprisingly increase the surface area and thus greatly induces light absorption capacity. The surface area of the as prepared HGO@MX nanocomposite was relatively high due to the increase in the interlayer distance (1.31 nm) of MXene, which led to the formation of plenty of active sites on the catalyst when compared to pristine HGO. The inter-layer of the MXene which adheres to the surface of Holey GO, shows the existence of a multi layered bubble pouch-like structure as shown in Fig. 3(b).

The overlapping of carbon layers has been further validated by energy dispersive spectroscopy (EDX) with elemental mapping, whereas the uniform distribution of oxygen and nitrogen points to the layered phenomena in the freshly produced nanocomposite. In addition, it is obvious from Fig. S3, the EDAX and mapping analysis that the Ti, Al, C, O, and F components in HGO@MX nanocomposite was well synthesized. Fig. 4(a) displays the TEM pictures of the HGO@MX flakes together with the corresponding EDAX elemental mapping analysis in Fig. S3**.** We measured a single layer of MXene with a thickness of 3.604 nm. The TEM image amply illustrates the incorporation of HGO nanoparticles into the space between the numerous layers of MXene (Fig. 4(b)). On the surface of multi-layered MXenes, a large number of HGO nanoparticles are also adsorbed. It is worthy to note that the HGO layers were present on the surface of the multi-layered as well as between the layers of the MXene also are evenly well dispersed over the HGO@MX.

Notably, the MXene flakes exhibit a big size and a smooth surface that enable them to stack preferentially and produce more durable structures, thus giving them an advantage in the application of photocatalyst. HGO nanosheets and MX were found to overlap to varying degrees, and as a result, a well-defined cylindrical stretching structure

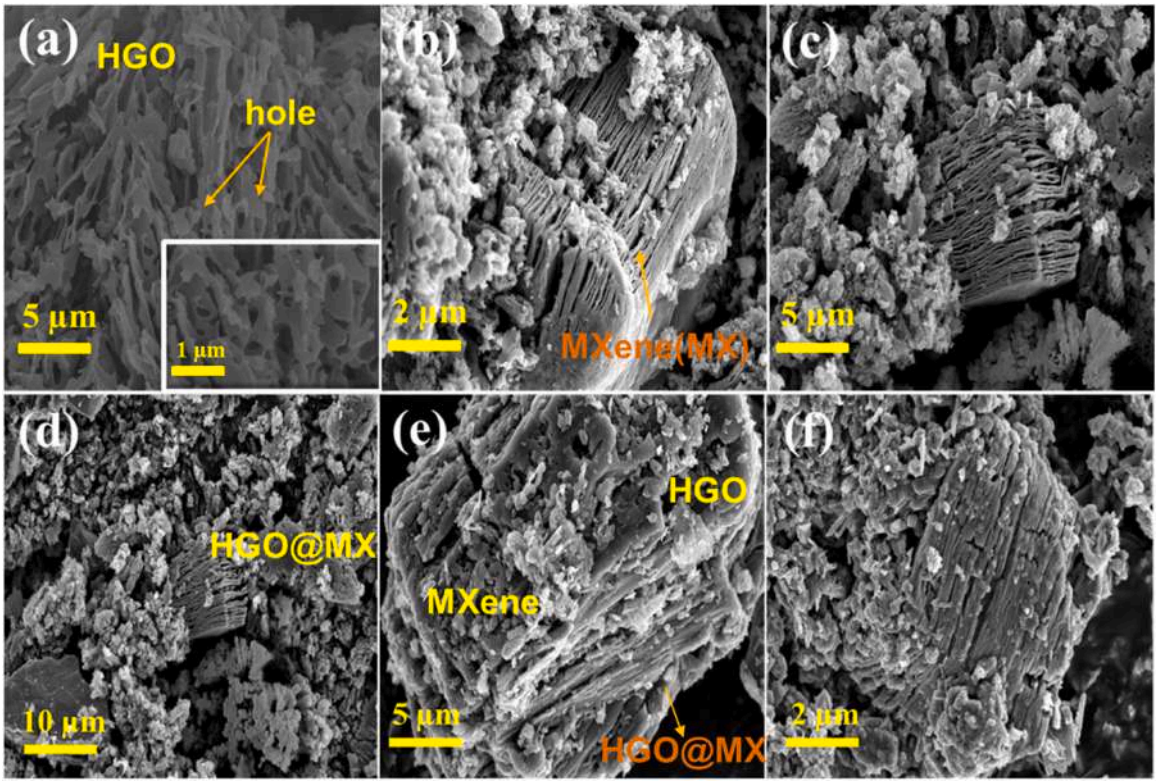

Fig. 3. SEM images of (a) HGO, (b-c) MX, and (d-f) HGO@MX nanocomposites.

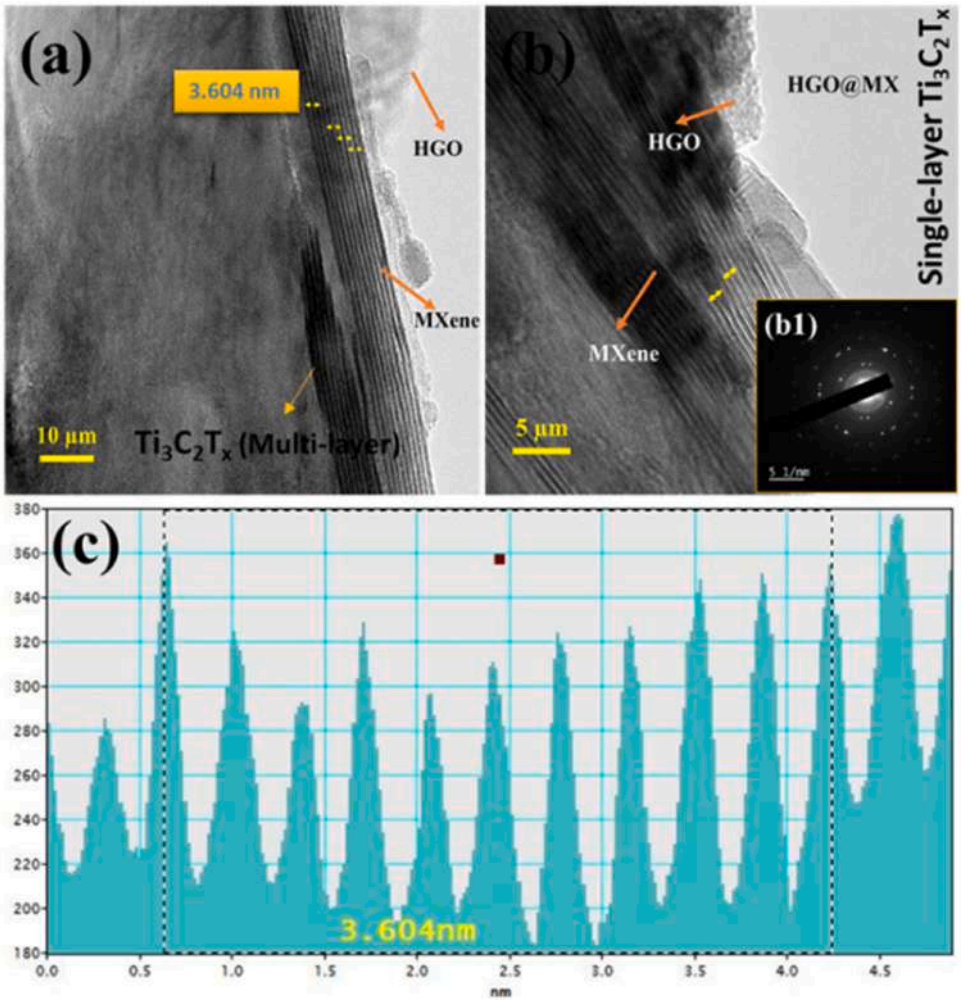

Fig. 4. (a) TEM images of $Ti_3C_2T_x$ (MXene); (b) single layered $Ti_3C_2T_x$ in HGO@MX nanocomposites ((b1) inset SAED pattern) and (c) line profile diagram of as prepared material.

was seen. This might highlight the increased specific surface area and active sites. The ultrathin-layered MX nanosheets are uniformly distributed in solution and in contact with HGO nanosheets. This is advantageous for enabling the stretching of HGO nanosheets via substantial physical coupling and is crucial for carrying electrons during the photocatalytic reaction. The SEM, TEM, and EDAX mapping studies' unambiguous outline of the MX-grafted, ultra-thin HGO nanosheets shows that the designed heterojunction was successfully built using the MX nanosheets and HGO. The SAED pattern of Fig. 4(b1) shows discrete spots are found to be organized in the shape of circular rings, which correlated to a hexagonal phase that comprises the (200), (102), and MX (001), (100) of HGO. The d-spacing gained from XRD and TEM images

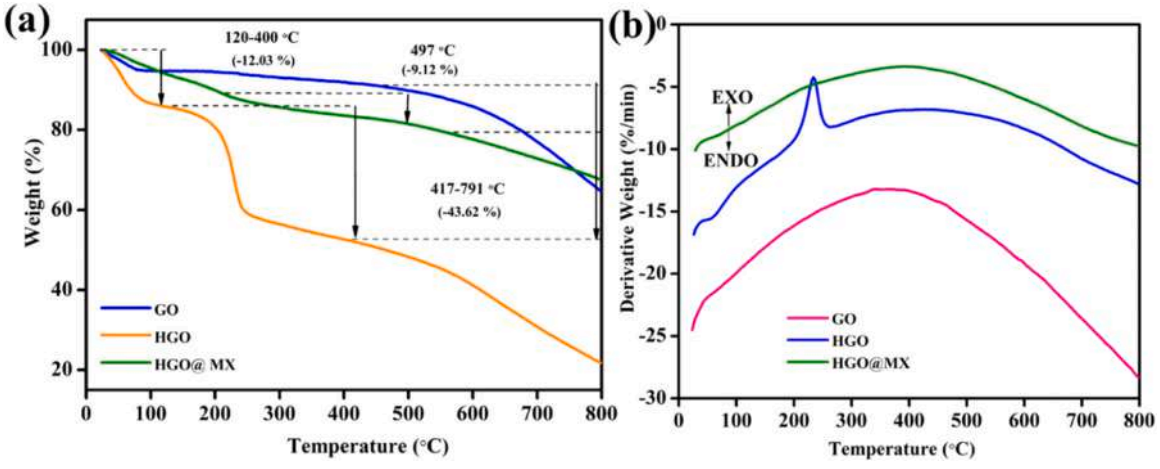

Fig. 5. (a) TGA, and (b) DTA analysis of GO, HGO and HGO@MX nanocomposites.

are compatible.

3.3. Thermal analysis

The stability of the prepared materials was studied by the TGA analysis and depicted in Fig. 5. The TGA profile of the HGO, GO, and HGO@MX photocatalyst were shown in Fig. 5(a). It has been found that all three materials exhibit the first degradation step just below 100 °C. This weight loss corresponds to the removal of water molecules present in the pores of the catalyst during its preparation. The second weight loss was observed in the range of 100–250 °C and this may be due to the functional groups like hydroxide, carboxylic, epoxide, etc., for HGO [41]. The third weight loss was observed at above 480 °C due to the Ti_3C_2 MX sheets. The second and final weight loss of the prepared HGO@MX photocatalyst occurs in the range of 250–800 °C due to the release of functional groups and the decomposition of HGO and MX sheets. It is worthy to note that the pure $Ti_3C_2T_x$ MXene decomposes at about 785 °C [42]. The TGA thermogram shows that the HGO@MX photocatalyst has much thermal stability than the HGO and GO sheets. It is anticipated that the carbene fragments inside and in the close proximity of the cavities in the HGO are stabilized by π–π interaction between the carbide and the graphene oxide moiety. Such a collective interaction can result in the high thermal stabilization of intercalated MX-HGO composite.

Moreover, the intercalations of HGO nanosheets among the MXene matrices during the hydrothermal process inhibit the self-restacking of MXene flakes and retain high density, increasing the thermal stability of the nano matrix [43]. The DTA curves initially exhibit a pattern like an endothermic reaction, but at high temperatures, turn into an exothermic reaction Fig. 5(b).

3.4. Surface elemental analysis

The elemental compositions of the prepared HGO and HGO@MX photocatalyst were characterized by XPS analysis. The XPS survey spectra of HGO and HGO@MX photocatalysts are shown in Fig. 6(a). The inclusion of oxygen-containing functional groups in HGO creates ample opportunities for the creation of hydrogen bonds across MXene and HGO sheets, preventing MXene from self-stacking and improving both the migration and separation characteristics of the nanocomposite. A wide scan XPS spectrum of HGO shows the presence of C 1 s and O 1 s at the binding energies of 287 and 532.9 eV. The wide scan XPS spectrum of prepared HGO@MX catalyst shows the presence of C 1 s, O 1 s, Ni 1 s, F 1 s, Al 2p, and Ti 2p at the binding energies of 287, 532.9, 402, 684.7, 74, and 459 eV as depicted in Fig. 6(b-f). Similar XPS spectrums were reported by *Wang et al.*,[44] and *Halim et al.*,[45] for HGO and MX, respectively. The peak of C–C upsurges from the inclusion of HGO. The peak intensity of C–Ti is debilitated because of the HGO introduction, which diminishes the quantity of MXene in the MX@HGO nanocomposite. Besides, the C-C linkage with polymerized HGO and MXene enabled photoelectron motion to decrease the electron-hole pair charge recombination. Based on the results, the HGO was successfully intercalated into the MX sheets.

Herein, the nitrogen adsorption–desorption was performed at 77 K to verify the mitigative restacking structures of the MXene and the results are depicted in Fig. 7. According to the IUPAC classification, the isotherms of all samples show the characteristic type IV with H3 hysteresis loop. This implies the mesoporous structure. The samples HGO, MX and HGO@MX show a specific surface area of 168.25, 48.12 and 86.28 $m^2 \cdot g^{-1}$, respectively. The type IV isotherm is obtained with pore diameter 2.103, 1.514 and 1.301 nm for HGO, MX and HGO@MX hybrid as depicted in Table S2. Based on the Brunauer-Emmett-Teller (BET) results, the HGO exhibited a much higher specific surface area of ~168 $m^2 \cdot g^{-1}$ which is distinctly superior to than that of pristine GO (~127 $m^2 \cdot g^{-1}$), probably because of the holes. Also, the MX has a specific surface area of only 48.12 m^2/g due to its severely restacking dense structure, limiting the approachability of MXene flakes to electrolyte ions. Amazingly, the surface area of HGO@MX was achieved as 86.28 m^2/g, which is distinctly superior to pure MX. This is because the holey graphene itself possesses a high surface area on account of the

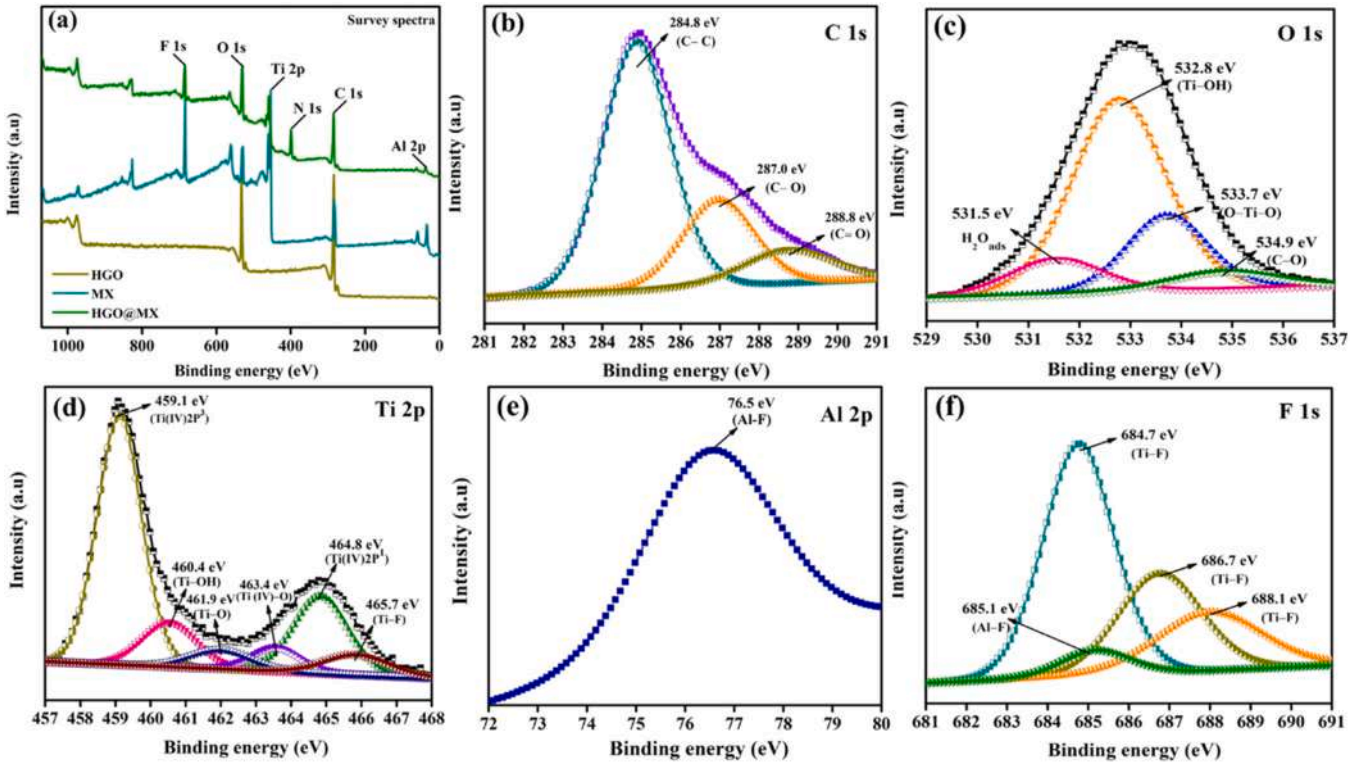

Fig. 6. (a) Survey spectra of HGO and HGO@MX, (b) C1s, (c) O1s, (d) Ti 2p, (e) Al 2p and (f) F 1 s of HGO@MX nanocomposites.

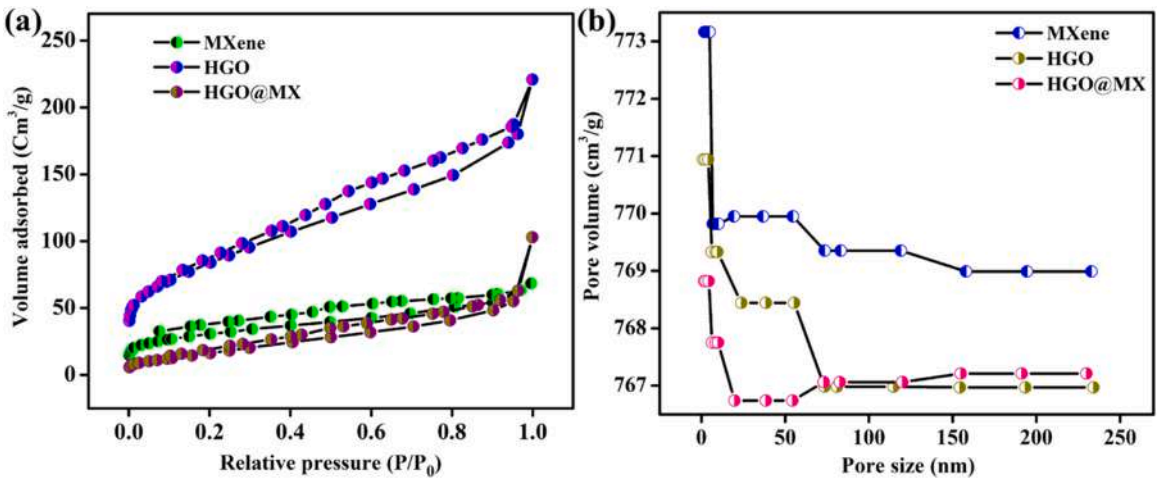

Fig. 7. (a) BET surface area and (b) pore size distribution curves of MXene, HGO and HGO@MX nanocomposites.

presence of abundant nanopores in the basal plane. The presence of abundant nanopores on the HGO surface, whereas the GO has no pores. Furthermore, the incorporation of holey graphene into the MXene layers can effectively reduce its severe stacking, resulting in the formation of a highly interconnected pore connectivity channel, which is very advantageous for accelerating the transport of electrons [43]. Meanwhile, HGO@MX exhibited a more prominent pore size distribution with mesoporous structures in the range of 1–3 nm, which could be ascribed to the nanopores in the basal plane of HGO@MX nanocomposite. This is because the holey graphene itself possesses a high surface area on account of the presence of abundant nanopores in the basal plane. In addition, the introduction of holey graphene into the MXene layers can effectively reduce its severe restack, forming a highly interconnected pore connectivity channel, which is very favorable to accelerate the transport and diffusion of ions in heterojunction requiring fast charge/discharge processes.

Interestingly, the addition of MX on the surface of HGO provides higher pore volume to surface area of materials tend to have greater adsorption capacity (larger particle size). As can be seen from the data, as surface area grows, so does the average pore diameter and the pore size distribution. Table. S2, provides a summary of the variables that were utilized to compute the pore size distributions. This will end up with the enhancement of the photocatalytic performance. The BET results propose an adsorption assisted oxidation of pollutant dyes from the contaminated water.

Zeta potential measurements were used to investigate the surface characteristics of as-obtained hybrids. Fig. S2 summarizes the results, which reveal that the negative zeta potential value of GO (–8.06) is transformed to the greater charge for HGO (–6.31 mV) due to lowering of surface charge of COO^-. This might be related to the conversion of GO to HGO, which results in a partial loss of oxygen and carboxylic groups, which is responsible for the lower negative zeta potential value. MX, on the other hand, has a very low zeta potential (−29.9) value. However, the nanocomposite HGO@MX hybrid shows an increase in zeta potential (−18.3 mV) due to reduced functional groups on the edges. The enhancement in MX surface charge potential of the HGO@MX hybrid is indicative of MX binding onto HGO, which has previously been shown to stack onto graphene rings through π-π interaction. Furthermore, chelation between MX nanosheets and HGO nanosheets, as well as hydrogen bonding interactions between MX nanosheets, might be driving forces for layer-by-layer assembly, which ultimately hold the charge of the HGO@MX nanocomposite.

The optical characteristics of the HGO@MX catalyst nanocomposite are analyzed using UV-Vis spectra and depicted in Fig. S3, which have an absorption band spanning from 320 to 520 nm and an absorption edge at 410 nm. In the area of visible light, the HGO@MX catalyst exhibits a wide absorption edge. The photocatalytic process at the heterojunctions was improved by the increase in light absorption in the visible region. For the HGO@MX catalyst nanocomposite, the average value of E_g determined from the linear plot of $(h)^{1/2}$ vs hν was 2.7 eV. Compared to bare HGO and MXene materials, the band gap edge is observed in the visible light range. Hence, the HGO@MX catalyst can be stimulated by visible light and create additional electron-hole pairs, the increase in band gap makes it possible for the HGO@MX nanocomposite to function as an effective photocatalyst in dye molecular mineralization.

In semiconductor-based photodegradation processes, photoluminescence (PL) studies are very important for the photo-induced electron/hole pair recombination analysis. The prepared HGO@MX demonstrated a strong emission centered at 450 nm when excited at 360 nm (Fig. 8(a)). Photoluminescence studies have demonstrated that the PL peak can be systematically blue-shifted as the MX composition is decreased. The addition of MXene has significantly altered the peak intensity of the HGO@MX composite. A subsequent decrease in the intensity of emission suggests lower recombination of e^-/h^+ pairs. The excitation wavelength of the photocatalyst will gradually reduce due to the recombination of electrons and holes present in it. When the ratio of peak intensities is disturbed over a portion of the disordered functional groups, the degradation process is significantly slowed. MXenes act as suitable electron acceptors to suppress the charge carrier recombination process. According to our results, the composite HGO@MX exhibits the greatest deterioration toward MB. Furthermore, the capacity of the catalyst is greater as the nanocomposite dose is raised above 25%. This behavior can be related to the fact that excessive catalyst dose prevents the catalyst from absorbing visible light, hence lowering photocatalytic activity.

Raman spectra of MXene-based composite exhibit a prominent band at 1594 cm^{-1}, which is triggered due to the chaotic shape and bond stretch motion of the sp^2-hybridized carbons. Because of the flaws created by the holes in the HG nanosheets, the I_D/I_G value of HGO was 0.93, greater over HGO@MX (0.90). The abundance of functional groups on the hole edges may cause dipoles, resulting in the desirable polarization loss. Furthermore, the oxygen-containing functional groups on the surface of HGO promote hydrogen bond formation with the MXene sheets, preventing MXene self-stacking and strengthening the layered structure of HGO, as estimated from Fig. 8(b).

3.5. Evaluation of photocatalytic and kinetic performance

Irradiation time was used to study the photo-mineralization efficiency of the HGO@MX nanocomposite. Fig. 9(a) shows the photocatalytic activity for MB dye degradation over MX, HGO, GO@MX and HGO@MX samples when exposed to dark and visible light. The mixtures

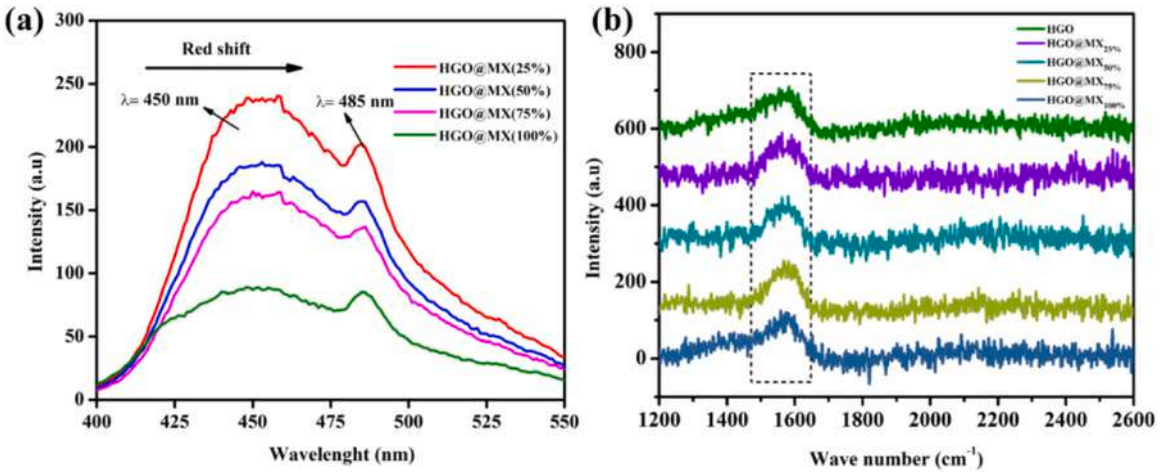

Fig. 8. (a) Photoluminescence (PL) and (b) Raman scattering spectra of the various ratio of HGO@MX nanocomposites.

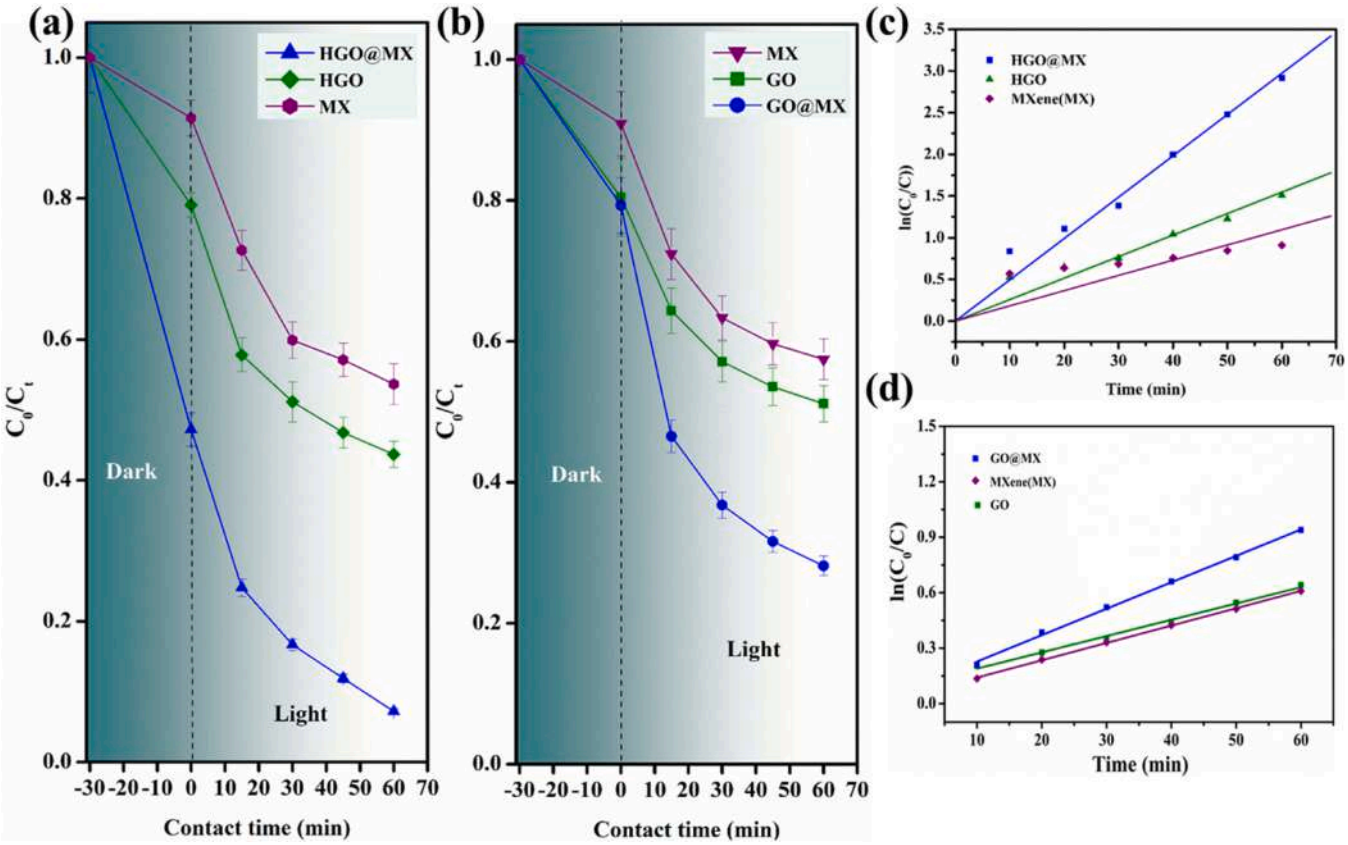

Fig. 9. (a, b) Dropping of MB quantity (C/C_0) in the occurrence of the fabricated photocatalysts; and (c, d) a linear plot of light illumination time vs $\ln(C_0/C)$ for 0–60 min for mineralization of MB in perceptible light irradiation. (Investigational settings: 0.1 g/L photocatalyst, Preliminary dye quantity of 50 mg/L, intensity of light of 0.16 mW/cm^2, and temperature of 24.7 °C).

are stirred in the dark for one hour to avoid the adsorption effect prior to photocatalytic degradation. Under visible light irradiation, the HGO@MX composites exhibit greater photodegradation capacities than bare MX, HGO and GO@MX, indicating that the incorporation of HGO with MXene can boost photocatalytic activity than the GO@ MX due to higher defective(active) sites as depicted in Fig. 9(b). The abundant in-plane pores of HGO with few nanometers size (≈0.406 nm) possess high intrinsic double layer at edges form heterojunction compared to GO. This increase of the number of active sites together with the reasonable design and enhancement of the active site activity facilitate the high performance. Moreover, the HGO@MX blend retards the recombination of e^--h^+ pairs as they can act as p-n junction. By the irradiation study it was evident that within 60 minutes of light exposure, the GO@MX and HGO@MX nanocomposite had degraded the MB dye molecule to their maximal efficiency, which was 81% and 99% for MB dye as shown in Fig. S4(b).

The enhancement in deprivation capacity was ascribed to the enhanced Eg of HGO@MX and GO@MX nanocomposite which would improve the deprivation proficiency of the catalyst in the visible range. The plot of ln (C_o/C) versus time (t) for different concentrations C_o of MB

(Fig. 9 (a)) fits well with the experimental data to pseudo-first-order kinetics as shown in Eq. (1)

$$r = -\frac{dC}{dt} = kC \quad (1)$$

Where "*k*" represents the pseudo-first-order rate constant; "C" is the equilibrium concentration of the stock solution with the integration of C_0 at time $t = 0$, which represents to $C = C_0$

It showed that there were line fitting results between $\ln(C_t/C_0)$ and t, showing the Langmuir-Hinshelwood first-order reaction kinetic model representing the removal rate of MB using HGO@MX and GO@MX (Fig. 9(c, d)). The observed regression coefficient (R^2) was 0.9999, 0.970, 0.864, and 0.749, respectively, when the initial pH of the dye varies between 5.0 and 9.0 as shown in Table S3. As shown in Fig. S4, the enhanced dye mineralization was attained at pH 6.03 and 7.09 (99% and 92.5%, respectively) within 60 min than the GO@MX. On solution pH, the MB molecules present in quinone and azo structures with conjugated π-system are responsible for the adsorption on HGO@MX nanocomposite as shown in **Text S4**.

The oxidation of the pollutants exhibits an impressive efficiency of about 99% for MB dyes within 60 min whereas the GO@MX exhibit degradation efficiency of 81%. The photodegradation capacities of HGO@MX nanocomposite compared with various catalysts reported in previous works for the removal of MB are listed in Table S4.

3.6. Elucidation of active species, total organic carbon (TOC), and H_2O_2 generation

The production of reactive species by the incidents of perceptible light is a key factor in the photo—mineralization of organic dyes. The information about the trapping of species in the study is given in Text S5. The findings also show that the •OH and $\bullet O_2^-$ radical is the predominant species involved in the photocatalytic oxidation activity by HGO@MX nanocomposite (Fig. S5). The results confirm that the hydroxyl (•OH) and superoxide ($\bullet O_2^-$) radical played a key role in the photodegradation of the MB dye molecules and was primarily involved as the active, reactive species. On the other hand, the other radicals do not significantly impact the photodegradation of MB dye molecules. The outcomes demonstrated that $\bullet O_2^-$ radicals play a potential role in the active photo mineralization of MB in visible light irradiation.

The mineralization of parent dye molecules into final products such as CO_2 and H_2O were determined by TOC analysis (Fig. S6(a)). The TOC content diminished 0.87 ppm from 50 ppm, after 1 h of photocatalytic oxidation of dye, which provides more to the adsorption, photolysis, and photodegradation during dye removal. Also, the substantial fall of TOC was used to scrutinize the mineralization of MB in the HGO@MX matrix by Eq. (2):

$$\text{TOC} \quad (\%) = \text{TOC}/\text{TOC}_0 \times 100 \quad (2)$$

that concerning the extent of the elimination process, the HGO@MX hybrid photocatalyst Where, TOC_0 and TOC are the former and final concentration of dye MB in the HGO@MX photocatalyst, as shown in Fig. S6(a). The lower degree of mineralization of about 32% occur on adsorption of dye on composite and the decolorization (photolysis) occur due to the destruction of the azo group with 48% efficiency, whereas on light irradiation the complete mineralization may occur of about 82% on HGO@MX/Vis system with formation of stable intermediate products for their breakdown of chain molecule on dye by oxidation *via* reactive oxygen species upon photogenerated e^- and h^+ on H_2O_2 production (Fig. S6(b)) with various amount of catalyst from 0 to 30 mg/L by KI dosimetry method discussed detailed in **Text S6**.

3.7. Photodegradation pathway and intermediates of MB catalyzed by HGO@MX

The intermediates formed in the depreciation of each MB dye molecule were identified and examined using the LC-MS analytical method. Fig. S7 (upper) and (lower) show the positive and negative ESI values before and after MB degradation in the HGO@MX system. A potential mechanism for mineralization is shown in Fig. 7. For MB dye molecules, the LC-MS investigation and the values of *m/z* are crucial in determining several deprivation intermediary phases, including chromophore cleavage, de-ethylation, ring-rupture, and mineralization. The attack of the •OH radical initiates the collapse of MB dye molecules by swapping of one of their benzene aromatic rings with OH groups. As a result, the generation of intermediates with *m/z* values of 357(DP2), 343 (DP3), 325(DP4), and 293(DP5), respectively, take place. In addition, the N-C bond heterolytic cleavage triggered the demethylation of precursors complexes which further deteriorate into less complex or lower organic molecules with *m/z* =74, *m/z* =65, and *m/z* =56(DP11–13). Additionally, products of ring-opened low molecular weight substances, such as butane, sulfoxylic acid, etc., also are produced. Further attacks on intermediates by the OH radicals result in the formation of H_2O, CO_2, and inorganic salts as the final products.

3.8. Intrinsic mechanism for the highly efficient photocatalytic performance of HGO@MX heterojunction in MB degradation

The mechanism behind the mineralization of MB using HGO@MX under light irradiation was displayed in Scheme 2. The HGO@MX was capable of enhanced photodegradation efficiency for MB dye and was partly owing to the increased adsorption of MB by the MXene. Since the functional groups like hydroxyl (OH-), carboxyl (COO-), epoxy, aluminum (Al^{3+}), and fluoride (F^-) ions were present on the surface of the HGO@MX nanocomposite, enhancing the number of pollutants to be reacted with OH radicals. This is due to the fact that introducing holey graphene into the layers MXene may significantly expand the space between layers and ameliorate the heaping of the MXene nanosheets, resulting in a larger utilizable surface area of the ions of the electrolyte. Moreover, upon irradiation of holey graphene and MXene flakes, the nanopores in holey graphene may significantly facilitate the flow of ions across the whole surface area and trigger the creation of charge carriers to form an intense nanopore-linked network to form p-n heterojunction. HGO, on the other hand, functions as a space to stop MXene from self-restacking effectively and creates a highly connected network of nanopores that may greatly speed up the process of charge separation and minimize the recombining of electron and hole couples. The enhanced degradation efficiency of the pollutants on HGO@MX shows that the interconnected hole interrelation with petite diffusion pathways is favorable for fast charge transport which favors the higher degradation rate towards pollutant removal.

Under optical irradiation, photoexcited electrons of the hetero HGO@MX 2D/2D p-n junction emerge out from VB of HGO and move to the adjacent CB. Photoelectrons can swiftly move from the conduction band (CB) of HGO to MX through remotely comparable hetero-junction because the electric field of MX is much more energetic than that of the CB potential of HGO. A vast number of electrons produced on the surface of MX in a typical decomposition process interacted with O_2 to create superoxide radicals ($\bullet O_2^-$). Meanwhile, the hydroxyl ions (OH^-) and water adsorbed on the catalyst surface interacted with photogenerated holes to produce hydroxyl radicals (•OH).

The photocatalysis reaction mechanisms in the presence of H_2O_2 under visible light irradiation were summarized as follows:

$$HGO@MX \xrightarrow{hv} (h^+ + e^-)HGO@MX \quad (3)$$

$$OH^- + h^+(HGO) \rightarrow \bullet OH + e^- \quad (4)$$

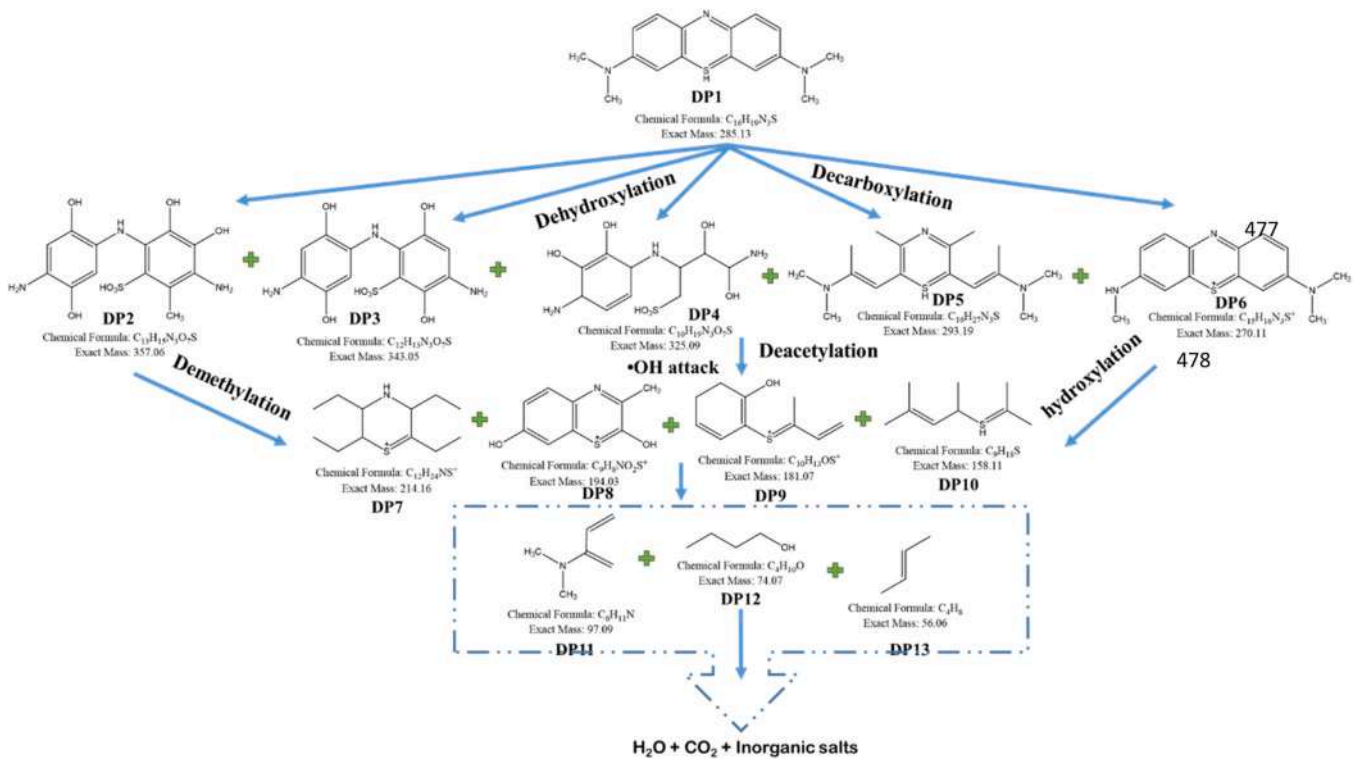

Fig. 10. By-products formed during photo-degradation of MB by the HGO@MX photocatalyst. (Investigational settings: 0.1 g/L photocatalyst, Original concentration of 50 mg/L, intensity of light of 0.16 mW/cm^2, and 24.7 °C).

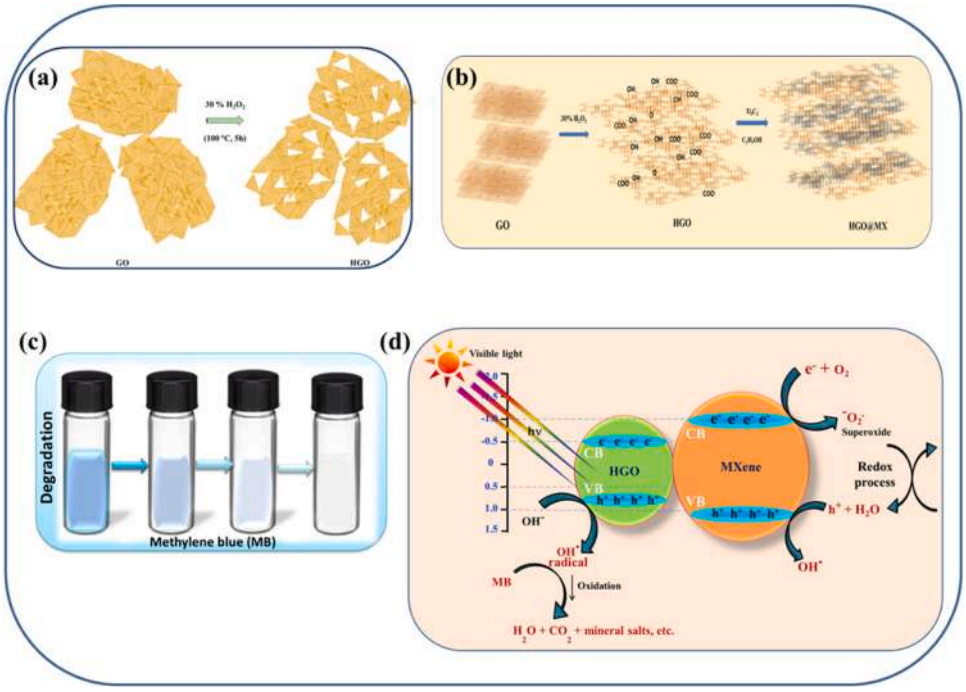

Scheme 2. Schematic illustration of (a-b) typical synthesis route to HGO and HGO@MX structure; (c) pictorial design of degradation of MB dye; (d) possible reaction mechanism of HGO@MX nanocomposite.

$$O_2 + e^-(MX) \rightarrow \bullet O_2^- \quad (5)$$

$$\bullet O_2^- + H^+ \rightarrow \bullet OOH \rightarrow \bullet OH \quad (6)$$

$$\bullet OH + \bullet OH \rightarrow H_2O_2 \quad (7)$$

$$H_2O_2 + e^-(MX) + H^+ \rightarrow \bullet OH + H_2O \quad (8)$$

The H_2O molecules confined in the holes are induced photolytically and produce •OH radicals. The generated •OH radical could act as a prevailing oxidant for the fractional or total degradation of MB dye molecules. The h^+ on the VB of the photocatalyst also has the capability

to oxidize the dye molecules [46,47] . The electron excited to the CB was subjugated by the dissolved molecules of oxygen in the reaction mixture and produced $\bullet O_2^-$ radicals. The inclusive photo-excited e^--h^+ pair shift makes a number of radicals, including $\bullet O_2^-$, •OH, and h^+, which are further added to the overall dye degradation process. Due to the fact that a retarded combination rate of e^-/h^+ subsequently their separation leads to a quicker formation of reactive species, delayed recombination of pairs of e^- and h^+, works a significant part in the photocatalyst's efficiency. The HGO@MX hybrid showed improved catalytic activity towards the photocatalytic degradation of MB due to the excellent charge/mass transfer capacity of HGO, slight size and unvarying scattering of the particles, and close contact between HGO and MX for encouraging synergistic effects.

3.9. Photostability and recyclability

In a practical perspective, a photocatalyst must have high reusability and stability. In this investigation, five successive cycles were used to validate the reusability of the photocatalyst HGO@MX. The photocatalyst after degradation study was recovered by centrifugation for the reusability test. The recovered catalyst was washed with ethanol and dried under a vacuum at 100 °C for 10 h. The reusability test demonstrated that the HGO@MX photocatalyst remained stable and only slightly lost photocatalytic activity after being recycled four times (Fig. 11). The long-term reliability of the fabricated photocatalyst with regard to of both morphology and structural features was also studied. The XRD and FT-IR patterns of the HGO@MX catalyst before and after the photodegradation study was the same (Fig. S8(a, b)). This demonstrates the structural stability of the synthesized catalyst. Again, the TEM morphology of treated catalyst strongly supports the sample's morphological solidity with even surface as shown in Fig. S8(c, d). These findings demonstrate that the new HGO@MX nanocomposite has remarkable reusability and stability, which makes it suitable for the effective oxidation of MB dye molecules in the Vis system.

4. Conclusions

The holey graphene oxide draped MXene (HGO@MX) hybrid architecture was successfully fabricated using a simple co-precipitation method. Experimentally, it was found that the as-synthesized HGO@MX hybrid photocatalyst was found to be effective for the removal of MB dye molecules under visible-light irradiation in aqueous media. During the photocatalytic process, HGO and MX act as the medium for electron transfer and the production of radicals, respectively. The HGO@MX hybrid material exhibits an oxidation efficacy of 99% for MB with a respective irradiation time of 60 min using visible light irradiation, respectively. As a result, the Vis/HGO@MX system was considered to be important for the photocatalytic oxidation of both MB from aqueous media. The radicals $\bullet O_2^-$ and •OH were responsible for the photodegradation of MB dyes. Moreover, the presence of HGO on MX material was absolutely enhanced the photocatalytic activity during the degradation of MB under light irradiation. The primary mechanisms of MB removal were described via cleavage of oxidation of the C-H bond, de-carboxylation, C-N bond, and de-chlorination process. The photocatalytic efficiency of selected dyes remained at 82% after five repetitive cycles, which clearly demonstrates the excellent stability of the HGO@MX hybrid composite. According to the above statements, this investigation describes that the HGO@MX hybrid material was a suitable candidate for the degradation of organic dyes from aquatic phase.

CRediT authorship contribution statement

Seokoh Ko: Funding acquisition, Methodology, Project administration, Validation, Writing – review & editing. **Do-Gun Kim:** Validation, Writing – review & editing. **Rajendran Babhu Vignesh:** Investigation, Methodology. **Palliyalil Sirajudheen:** Investigation, Methodology.

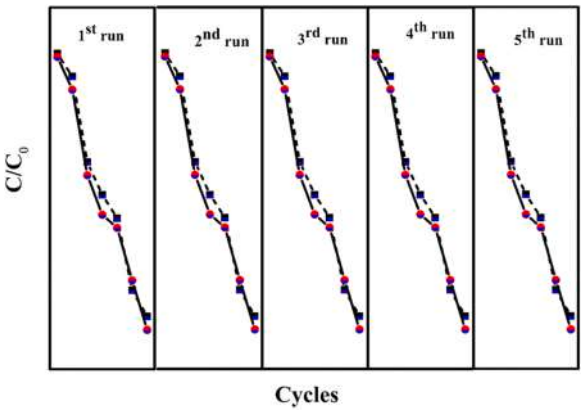

Fig. 11. Cycle curves of photocatalytic degradation of MB solution with the HGO@MX for 5 cycles of reuse.

Sivakumar Vigneshwaran: Conceptualization, Investigation, Methodology, Validation, Writing – original draft.

Declaration of Competing Interest

The authors declare that they have no known competing financial interests or personal relationships that could have appeared to influence the work reported in this paper.

Data availability

Data will be made available on request.

Acknowledgement

The National Research Foundation of Korea (NRF) grant (No. 2022R1A2B5B02001584) financed by the Korean government (MSIT) provided funding for this work.

Appendix A. Supporting information

Supplementary data associated with this article can be found in the online version at doi:10.1016/j.jece.2024.112266.

References

[1] M. Ghanbari, M. Bazarganipour, M. Salavati-Niasari, Photodegradation and removal of organic dyes using cui nanostructures, green synthesis and characterization, Sep Purif. Technol. 173 (2017) 27–36, https://doi.org/10.1016/j.seppur.2016.09.003.
[2] V.L. Louros, V. Silva, C.P. Silva, V. Calisto, M. Otero, V.I. Esteves, R. Freitas, D.L. D. Lima, Sulfadiazine's photodegradation using a novel magnetic and reusable carbon based photocatalyst: Photocatalytic efficiency and toxic impacts to marine bivalves, J. Environ. Manag. 313 (2022), https://doi.org/10.1016/j.jenvman.2022.115030.
[3] S. Vigneshwaran, P. Karthikeyan, C.M. Park, S. Meenakshi, Boosted insights of novel accordion-like (2D/2D) hybrid photocatalyst for the removal of cationic dyes: Mechanistic and degradation pathways, J. Environ. Manag. 273 (2020) 111125, https://doi.org/10.1016/j.jenvman.2020.111125.
[4] L. Yao, X. He, J. Lv, G. Xu, Z. Bao, J. Cui, D. Yu, Y. Wu, Efficient degradation of ciprofloxacin by Co_3O_4/Si nanoarrays heterojunction activated peroxymonosulfate under simulated sunlight: Performance and mechanism, J. Environ. Chem. Eng. 10 (2022), https://doi.org/10.1016/j.jece.2022.107397.
[5] C. Chuaicham, K. Sekar, V. Balakumar, J. Uchida, T. Katsurao, H. Sakabe, B. Ohtani, K. Sasaki, Efficient photocatalytic degradation of emerging ciprofloxacin under visible light irradiation using BiOBr/carbon quantum dot/saponite composite, Environ. Res 212 (2022), https://doi.org/10.1016/j.envres.2022.113635.
[6] K. Saravanakumar, A. Fayyaz, S. Park, Y. Yoon, Y.M. Kim, C.M. Park, Hierarchical $CoTiO_3$ microrods on $Ti_3C_2T_x$ MXene heterostructure as an efficient sonocatalyst for bisphenol A degradation, J. Mol. Liq. 344 (2021), https://doi.org/10.1016/j.molliq.2021.117740.
[7] J. Hu, X. Jing, L. Zhai, J. Guo, K. Lu, L. Mao, BiOCl facilitated photocatalytic degradation of atenolol from water: Reaction kinetics, pathways and products,

Chemosphere 220 (2019) 77–85, https://doi.org/10.1016/j.chemosphere.2018.12.085.
[8] J. Wang, X. Chang, Y. Zhao, H. Xu, G. He, H. Chen, A novel Bi_2WO_6/BiOBr/RGO photocatalyst for enhanced degradation of ciprofloxacin under visible light irradiation: Performance, mechanism and toxicity evaluation, Diam. Relat. Mater. 128 (2022), https://doi.org/10.1016/j.diamond.2022.109274.
[9] Y.C. Liu, J.Q. Wang, Y. Wang, C.L. Chen, X. Wang, Z. Xiang, Sonocatalytic degradation of ciprofloxacin by BiOBr/$BiFeO_3$, Appl. Catal. A Gen. 643 (2022), https://doi.org/10.1016/j.apcata.2022.118776.
[10] Z. Mehrabadi, H. Faghihian, Comparative photocatalytic performance of TiO_2 supported on clinoptilolite and TiO_2/Salicylaldehyde-NH_2-MIL-101(Cr) for degradation of pharmaceutical pollutant atenolol under UV and visible irradiations, J. Photochem. Photobio. A Chem. 356 (2018) 102–111, https://doi.org/10.1016/j.jphotochem.2017.12.042.
[11] D. van Thuan, T.B.H. Nguyen, T.H. Pham, J. Kim, T.T. Hien Chu, M.V. Nguyen, K. D. Nguyen, W.A. Al-onazi, M.S. Elshikh, Photodegradation of ciprofloxacin antibiotic in water by using ZnO-doped g-C_3N_4 photocatalyst, Chemosphere 308 (2022), https://doi.org/10.1016/j.chemosphere.2022.136408.
[12] I. Ahmad, R. Bano, M.A. Sheraz, S. Ahmed, T. Mirza, S.A. Ansari, Photodegradation of levofloxacin in aqueous and organic solvents: A kinetic study, Acta Pharm. 63 (2013) 223–229, https://doi.org/10.2478/acph-2013-0011.
[13] M. Jeon, B.M. Jun, S. Kim, J. Cho, C.M. Park, C.E. Choong, M. Jang, Y. Yoon, Sonodegradation of amitriptyline and ibuprofen in the presence of $Ti_3C_2T_x$ MXene, J. Hazard. Mater. Lett. 2 (2021), https://doi.org/10.1016/j.hazl.2021.100028.
[14] A.A. Fauzi, A.A. Jalil, N.S. Hassan, F.F.A. Aziz, M.S. Azami, T.A.T. Abdullah, M.F. A. Kamaroddin, H.D. Setiabudi, An intriguing Z-scheme titania loaded on fibrous silica ceria for accelerated visible-light-driven photocatalytic degradation of ciprofloxacin, Environ. Res 211 (2022), https://doi.org/10.1016/j.envres.2022.113069.
[15] R. Krishna, E. Titus, O. Okhay, J. Campos Gil, J. Ventura, E. Venkata Ramana, J.J. A. Gracio, Rapid Electrochemical Synthesis of Hydrogenated Graphene Oxide Using Ni Nanoparticles, 2014. www.electrochemsci.org.
[16] T. Bhattacharjee, S. Rahman, D. Deka, M.K. Purkait, D. Chowdhury, G. Majumdar, Synthesis and characterization of exfoliated beta-cyclodextrin functionalized graphene oxide for adsorptive removal of atenolol, Mater. Chem. Phys. 288 (2022), https://doi.org/10.1016/j.matchemphys.2022.126413.
[17] K. Thakur, B. Kandasubramanian, Graphene and Graphene Oxide-Based Composites for Removal of Organic Pollutants: A Review, J. Chem. Eng. Data 64 (2019) 833–867, https://doi.org/10.1021/acs.jced.8b01057.
[18] X. Hu, D. Bai, Y. Wu, S. Chen, Y. Ma, Y. Lu, Y. Chao, Y. Bai, A facile synthesis of reduced holey graphene oxide for supercapacitors, Chem. Commun. 53 (2017) 13225–13228, https://doi.org/10.1039/c7cc07475a.
[19] X. Chen, Z. Feng, J. Gohil, C.M. Stafford, N. Dai, L. Huang, H. Lin, Reduced Holey Graphene Oxide Membranes for Desalination with Improved Water Permeance, ACS Appl. Mater. Interfaces 12 (2020) 1387–1394, https://doi.org/10.1021/acsami.9b19255.
[20] J. Qin, X. Zhang, C. Yang, M. Cao, M. Ma, R. Liu, ZnO microspheres-reduced graphene oxide nanocomposite for photocatalytic degradation of methylene blue dye, Appl. Surf. Sci. (2016), https://doi.org/10.1016/j.apsusc.2016.09.043.
[21] J.H. Jeong, G.W. Lee, Y.H. Kim, Y.J. Choi, K.C. Roh, K.B. Kim, A holey graphene-based hybrid supercapacitor, Chem. Eng. J. 378 (2019), https://doi.org/10.1016/j.cej.2019.122126.
[22] J. Chen, Q. Huang, H. Huang, L. Mao, M. Liu, X. Zhang, Y. Wei, Recent progress and advances in the environmental applications of MXene related materials, Nanoscale 12 (2020) 3574–3592, https://doi.org/10.1039/c9nr08542d.
[23] W. Qiang, X. Qu, C. Chen, L. Zhang, D. Sun, Ti_3C_2 MXene derived (001)TiO_2/Ti_3C_2 heterojunctions for enhanced visible-light photocatalytic degradation of tetracycline, Mater. Today Commun. 33 (2022), https://doi.org/10.1016/j.mtcomm.2022.104216.
[24] X. Chen, R. Yang, X. Wu, Printing of MXene-based materials and the applications: a state-of-the-art review, 2d Mater 9 (2022). https://doi.org/10.1088/2053-1583/ac8009.
[25] A. Javaid, S. Latif, M. Imran, N. Hussain, M. Bilal, H.M.N. Iqbal, MXene-based hybrid composites as photocatalyst for the mitigation of pharmaceuticals, Chemosphere 291 (2022), https://doi.org/10.1016/j.chemosphere.2021.133062.
[26] M. Zhang, J. Ruan, L. Wang, Z. Zhao, W. Shao, J. Li, Z. Chen, C. Gu, W. Qiao, MXene-like carbon sheet/carbon nanotubes derived from metal-organic frameworks for efficient removal of tetracycline by non-radical dominated advanced oxidation processes, Sep Purif. Technol. 300 (2022), https://doi.org/10.1016/j.seppur.2022.121851.
[27] J.K. Im, E.J. Sohn, S. Kim, M. Jang, A. Son, K.D. Zoh, Y. Yoon, Review of MXene-based nanocomposites for photocatalysis, Chemosphere 270 (2021), https://doi.org/10.1016/j.chemosphere.2020.129478.
[28] B. Sun, F. Tao, Z. Huang, W. Yan, Y. Zhang, X. Dong, Y. Wu, G. Zhou, Ti_3C_2 MXene-bridged Ag/Ag_3PO_4 hybrids toward enhanced visible-light-driven photocatalytic activity, Appl. Surf. Sci. 535 (2021), https://doi.org/10.1016/j.apsusc.2020.147354.
[29] V. Soni, P. Singh, H.H. Phan Quang, A.A. Parwaz Khan, A. Bajpai, Q. van Le, V. K. Thakur, S. Thakur, V.H. Nguyen, P. Raizada, Emerging architecture titanium carbide ($Ti_3C_2T_x$) MXene based photocatalyst toward degradation of hazardous pollutants: Recent progress and perspectives, Chemosphere 293 (2022), https://doi.org/10.1016/j.chemosphere.2022.133541.
[30] M. ben Ali, H. Elhouichet, S. Szunerits, R. Boukherroub, Recent advances on semiconductor/MXene hybrids for harvesting light and photoelectrochemical water oxidation: A mini review, Chem. Eng. J. 450 (2022), https://doi.org/10.1016/j.cej.2022.138381.
[31] D.N. Nguyen, G.S. Gund, M.G. Jung, S.H. Roh, J. Park, J.K. Kim, H.S. Park, Core-shell structured MXene@carbon nanodots as bifunctional catalysts for solar-assisted water splitting, ACS Nano 14 (2020) 17615–17625, https://doi.org/10.1021/acsnano.0c08436.
[32] S. Li, Y. Huang, N. Zhang, M. Zong, Synthesis of holey reduced graphene oxide covered in the FeCo@SiO2 and their enhanced electromagnetic absorption properties, J. Compos Mater. 53 (2019) 1973–1983, https://doi.org/10.1177/0021998318817358.
[33] J. Zhao, Y.Z. Zhang, F. Zhang, H. Liang, F. Ming, H.N. Alshareef, Z. Gao, Partially Reduced Holey Graphene Oxide as High Performance Anode for Sodium-Ion Batteries, Adv. Energy Mater. 9 (2019), https://doi.org/10.1002/aenm.201803215.
[34] S. Vigneshwaran, D.G. Kim, S.O. Ko, Tuning of interfacial HGO@CLS nanohybrid S-scheme heterojunction with improved carrier separation and photocatalytic activity towards RhB degradation, Chemosphere 340 (2023), https://doi.org/10.1016/j.chemosphere.2023.139914.
[35] Y. Lin, Y. Liao, Z. Chen, J.W. Connell, Holey graphene: a unique structural derivative of graphene, Mater. Res Lett. 5 (2017) 209–234, https://doi.org/10.1080/21663831.2016.1271047.
[36] S. Kim, S.N. Nam, C.M. Park, M. Jang, N. Taheri-Qazvini, Y. Yoon, Effect of single and multilayered $Ti_3C_2T_X$ MXene as a catalyst and adsorbent on enhanced sonodegradation of diclofenac and verapamil, J. Hazard Mater. 426 (2022), https://doi.org/10.1016/j.jhazmat.2021.128120.
[37] K. Liu, H. Zhang, T. Fu, L. Wang, R. Tang, Z. Tong, X. Huang, Construction of BiOBr/Ti_3C_2/exfoliated montmorillonite Schottky junction: New insights into exfoliated montmorillonite for inducing MXene oxygen functionalization and enhancing photocatalytic activity, Chem. Eng. J. 438 (2022), https://doi.org/10.1016/j.cej.2022.135609.
[38] Y. Li, Z. Yin, G. Ji, Z. Liang, Y. Xue, Y. Guo, J. Tian, X. Wang, H. Cui, 2D/2D/2D heterojunction of Ti_3C_2 MXene/MoS_2 nanosheets/TiO_2 nanosheets with exposed (001) facets toward enhanced photocatalytic hydrogen production activity, Appl. Catal. B 246 (2019) 12–20, https://doi.org/10.1016/j.apcatb.2019.01.051.
[39] H. Alnoor, A. Elsukova, J. Palisaitis, I. Persson, E.N. Tseng, J. Lu, L. Hultman, P.O. Å. Persson, Exploring MXenes and their MAX phase precursors by electron microscopy, Mater. Today Adv. 9 (2021), https://doi.org/10.1016/j.mtadv.2020.100123.
[40] S.K. Sharma, A. Kumar, G. Sharma, D.V.N. Vo, A. García-Peñas, O. Moradi, M. Sillanpää, MXenes based nano-heterojunctions and composites for advanced photocatalytic environmental detoxification and energy conversion: A review, Chemosphere 291 (2022), https://doi.org/10.1016/j.chemosphere.2021.132923.
[41] Z. Jiang, Y. Shi, Z.J. Jiang, X. Tian, L. Luo, W. Chen, High performance of a free-standing sulfonic acid functionalized holey graphene oxide paper as a proton conducting polymer electrolyte for air-breathing direct methanol fuel cells, J. Mater. Chem. A Mater. 2 (2014) 6494–6503, https://doi.org/10.1039/c4ta00208c.
[42] R. Liu, W. Li, High-Thermal-Stability and High-Thermal-Conductivity $Ti_3C_2T_x$ MXene/Poly(vinyl alcohol) (PVA) Composites, ACS Omega 3 (2018) 2609–2617, https://doi.org/10.1021/acsomega.7b02001.
[43] Z. Fan, Y. Wang, Z. Xie, D. Wang, Y. Yuan, H. Kang, B. Su, Z. Cheng, Y. Liu, Modified MXene/Holey Graphene Films for Advanced Supercapacitor Electrodes with Superior Energy Storage, Adv. Sci. 5 (2018), https://doi.org/10.1002/advs.201800750.
[44] D.H. Wang, Y. Hu, J.J. Zhao, L.L. Zeng, X.M. Tao, W. Chen, Holey reduced graphene oxide nanosheets for high performance room temperature gas sensing, J. Mater. Chem. A Mater. 2 (2014) 17415–17420, https://doi.org/10.1039/c4ta03740e.
[45] J. Halim, K.M. Cook, M. Naguib, P. Eklund, Y. Gogotsi, J. Rosen, M.W. Barsoum, X-ray photoelectron spectroscopy of select multi-layered transition metal carbides (MXenes), Appl. Surf. Sci. 362 (2016) 406–417, https://doi.org/10.1016/j.apsusc.2015.11.089.
[46] Q. Liu, L. Ai, J. Jiang, MXene-derived TiO_2@C/g-C_3N_4 heterojunctions for highly efficient nitrogen photofixation, J. Mater. Chem. A Mater. 6 (2018) 4102–4110, https://doi.org/10.1039/c7ta09350k.
[47] H. Song, Y. Wang, Z. Ling, D. Zu, Z. Li, Y. Shen, C. Li, Enhanced photocatalytic degradation of perfluorooctanoic acid by Ti_3C_2 MXene-derived heterojunction photocatalyst: Application of intercalation strategy in DESs, Sci. Total Environ. 746 (2020), https://doi.org/10.1016/j.scitotenv.2020.141009.

Journal of Engineering Education Transformations ,
Volume 37 , No. 2 , October 2023 , ISSN 2349-2473, eISSN 2394-1707

10.16920/jeet/2023/v37i2/23155

Challenges and Opportunities in Online Computer Science & Engineering Education: A Study in Velammal College of Engineering & Technology, Madurai

Dr. P. Alli[1], Dr. Janaki Bojiah[2] , Mrs. C. B. Selva Lakshmi[3], Mrs. K. Santha Sheela[4]
[1,2,3,4] Velammal College of Engineering & Technology, Madurai, India.
[1]alli_rajus@vcet.ac.in
[2]bj@vcet.ac.in
[3]cbsl@vcet.ac.in
[4] kss@vcet.ac.in

Abstract: Owing to the entry of COVID-19, starting from the year 2000, India managed online education well for more than a year and a half. Now, the question is to understand whether the online mode of education is as effective as the face-to-face classes. This study intends to focus on identifying the challenges and finding the opportunities to enhance the quality of online engineering education with respect to Computer Science and Engineering (CSE) branch. A survey was conducted using a questionnaire involving the chosen 2nd year, 3rd year, and 4th year students of CSE department, Velammal College of Engineering & Technology, Madurai (VCET), who have had the experience of acquiring knowledge through both offline and online modes. The spreadsheet software was used to filter, organize as well as visualize quantitative data, and descriptive methodology was adopted for the data analysis. The result of the study will lay a scope to understand the existing gaps in online CSE education and the proposed ideas to fill the same enhancing the resources. Further, this study may play a pivotal role in making effective online CSE education at par with face-to-face classes completely possible and preferable.

Dr. P. Alli
Velammal College of Engineering & Technology, Madurai, India.
alli_rajus@vcet.ac.in

Keywords: COVID-19; CSE; digital skills; online education; Velammal College of Engineering & Technology

1. Introduction

With the emergence of Corona Virus (COVID-19) at the end of 2019 in China and its gradual encroachment into India in the year 2000, there were quite a lot of lifestyle changes worldwide. The sudden closure of educational institutions resulted in abrupt stoppage of flow of knowledge. To compensate this, the online education came into picture with a lot of challenges (Garcia-Morales et al., 2021; Pilav-Velic et al., 2021). The students were not mentally prepared and the faculty members were not completely trained (Jain & Sharma, 2022). In addition, the educationists were in a state of flux as to whether to invest in online resources or not (Asfour & Alkharoubi, 2023). In course of time, with COVID-19, not being completely controlled, the education was rendered to the students through online mode (Wong, 2023).

Velammal College of Engineering & Technology (VCET), Madurai, offers undergraduate programmes in the following streams namely Civil Engineering, Computer Science and Engineering, Electrical and Electronics Engineering, Electronics and Communication Engineering, Information Technology and Mechanical Engineering; also, it offers post graduate programmes in the above-mentioned disciplines except the Civil Engineering. VCET became the forerunner to start the online

classes using Google Meet efficiently. With a simple demonstrative session by the IT personnel and with limited resources and intermittent network connection, the members of VCET started to manage the flow of knowledge using the smart devices. Thus, VCET assured business continuity, flow of communication, and undisrupted knowledge transfer. The paper intends to analyze the challenges and drawbacks faced by the students with respect to online computer science and engineering education so that strategies could be devised towards addressing the identified problems to enhance the teaching learning process.

2. Literature Review

With the intervention of Corona Virus (COVID-19) in the end of 2019 in Wuhan, China (Sansa, 2020), the scare of being infected by the same has started getting into the nerves of each of the countries across the world. The World Health Organization proclaimed COVID-19 to be a Public Health Emergency of International Concern on 30 January 2020 (Wee et al., 2020). Gradually the widespread of COVID-19 in various countries was witnessed. India is not an exception to this, as in course of time, it witnessed the entry of COVID-19 in Kerala on 30 January 2020 (Jayesh & Sreedharan, 2020). As a course of action, travel ban, the immediate closure of educational institutions, recreation centres, malls, etc., came into picture followed by a series of lock down which disturbed the normal routine of the people. Initiatives were taken by the government to educate people about the spread of the pandemic through print and audio as well as video messages (Shaanxi Normal University, 2020). This pandemic situation affected every aspect of life including education.

As urged by (Hodges et al., 2020) and endorsed by (COL, 2020; OECD, 2020), Emergency Remote Teaching (ERT) is a quick alternate arrangement to manage the pandemic situation (Bozkurt & Sharma, 2020) to ensure the consistent flow of education by redefining the teaching methods which (Millman, 2020) calls as "pandemic pedagogy." As a measure to cope with the pandemic situation, distance learning was adopted by the educational institutions (Wu, 2020; CDC, 2020) so that social distancing could be guaranteed. Though it was initially a challenging task to manage education during the lock down situation (Wang, 2020), things started falling in place gradually. In course of time, the world witnessed many educational institutes adopting online education and continuously putting efforts to assure better learning environment (Murphy, 2020). The burning issue during the pandemic with respect to online classes was the drive amidst the faculty and students to adopt it as an alternative. Teachers with 'work from home' (Hubbard, 2020) option found it hard to handle the task (Luo et al., 2020).

Meanwhile, the limitations and the challenges that were brought by COVID-19 on educationists with respect to education occupied the majority of the literature (Huber & Helm, 2020; Judd et al., 2020; NFER, 2020) out of which some came up with meticulous action plans to handle remote teaching commendably (Ferdig et al., 2020) and the rest appreciated the transformation of mindset of the stakeholders in this regard (Moorhouse, 2020; Zhang et al., 2020). UNESCO Director-General Audrey Azoulay observes this globe-wide educational disruption as an education crisis (Education International, 2020) and (UNESCO, 2020) acknowledges that the online education is the only way to cater to the knowledge transfer. Online education promises and provides study materials anytime, anywhere which contributes to learning at their own pace and convenience (Gewin, 2020). Due to this and advancement of digitalization, noted universities like Tsinghua, Peking, Harvard, MIT, Yale, Oxford and Cambridge had already brought online education in place in the last decade (Bao, 2020) itself.

Online platforms like MS Teams facilitates the effective transfer of AV materials instantly (Barteit et al., 2020) and this helps in commanding students' enthusiasm and contribution resulting in meaningful learning (König, 2020). Broadcasting of audio files, telecasting of video lectures, relay of MOOCs (courses), and NPTEL courses also facilitate distant learning (University of British Columbia, 2020). Blended learning which is a combination of online and offline classes facilitate connectivity through Google form, Learning Management System like Moodle, Blackboard, Canvas etc., for assigning tasks and evaluating the performance of the students. Active learning helps students in knowledge acquisition much faster than any other way. The interaction between faculty and students are supported by LMS as instant messaging could be tiring.

With the emergence of online assignment submission and online tests, the genuineness of the person submitting the assessment and the originality

of the submission are questionable (Borge & Mercier, 2019). Monitoring of students during assessments is still a challenge as there has been hesitation and reluctance sensed amidst the students especially girls (Sanderson, 2020). In addition, the study by (Flores et al., 2020) pinpoints that despite spending more time in making online teaching effective, there was hardly any creditable student participation or engagement. The need for the inculcation of artificial intelligence (Lim, 2020) to impart education in online mode more effectively has become the need of the hour (World Bank, 2020). Online education (McKimm et al., 2020; Goh & Sanders, 2020) has become indispensable and so in the post pandemic era, one should be prepared for a mix of online and offline classes for the same syllabus (Zhu, 2020). Hence, it calls for an attention to update advancements in the digital literacy and the education tools to bring in an effective teaching learning process (Jandrić, 2020). This aspect forms the crux of the study that was conducted on CSE students of Velammal College of Engineering & Technology (VCET), Madurai.

3. Methodology

Keeping in mind to identify the opportunities and challenges with respect to information acquisition pertaining to Computer Science and Engineering branch of study, a questionnaire consisting of 20 MCQs was made (Littlefield, 2018). It was based on multiple choice questions with varied number of options depending on the context. Convenient sampling method was adopted. The students of CSE branch who had the experience of online education were chosen to be the samples for the study. Formal permission was acquired from the head of the institution as well as the CSE department to conduct the survey. The purpose of the study and the questions were explained to the students. The students were given the choice to agree or disagree to be the part of the survey. In addition, to assure confidentiality, the identities of the students are not revealed to anyone. The survey was conducted employing a Google Form shared through their respective class WhatsApp groups. 100 students filled up the questionnaire, however, only 81 responses were considered for the study. The other 19 were incomplete and distorted. The result of Cronbach Alpha reliability test considering all the items present in the questionnaire was 0.834 which is highly significant in terms of reliability. After confirming the validity, the MS Excel Spreadsheet software tool was used to filter, organize as well as visualize quantitative data, and descriptive methodology was adopted for the data analysis.

4. Data Analysis

Out of 81 total respondents of 2nd, 3rd, and 4th year students of CSE branch, 48 were female students and 33 were male students; 25.9% from 2nd year, 58% from 3rd year, and 16.1% from 4th year of study. 96.3% of the respondents claimed to have the experience of both online and face-to-face learning experiences with respect to online CSE education; 93.8% asserted to have got the basic digital literacy to access online classes before taking them up. It can be interpreted that online education was not a new phenomenon before the pandemic period very specifically in Madurai region. The youngsters of today have got exposed to the basic digitals skills as they are more familiar with social media applications, webinars, Skype calls etc. which is acknowledged by (Suharto & Ambarwangi, 2021) as well. This has enriched their digital experience and so adopting to online education and tools became an easy task.

When asked about the items they enjoyed in online classes, 45.7% mentioned that online classes facilitate them to study at their own pace; 30.9% felt relieved that there wasn't any need for commuting to college; 11.1% felt listening to recorded lectures recurrently made them learn better; 6% felt good about the lack of need to dress up and be appealing whereas 5% enjoyed online assessments, and 1.3% considered flexible submission of assignments to be enjoyable. It is very significant to note that most students like to study at their own pace without any peer pressure or the regulations imposed by the instructors which is in line with the findings of (Gewin, 2020). However, whether the students opting for this will be able to learn time management remains a question that needs further probing.

When enquired about the methods that engaged them personally to learn digitally, 33.3% mentioned small group work, 29.6% voted for project-based learning, 27.2% opted for individual assignment, and 9.9% liked the large group tasks. This clearly suggests that small group tasks are considered more effective with the complementary skills helping each other. The small group also facilitates easy and effective coordination which may not be possible effectively in large group coordination and communication. Task based learning is almost equally preferred because division of the work, following up of the same, and consolidating of the results happen instantly and aptly

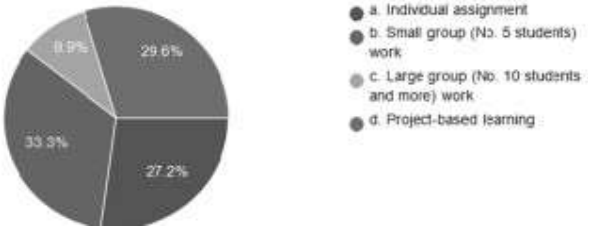

Fig.1: The methods engage personally to learn digitally

(Lambert et al., 2023). When a specific task is assigned, 56.8% preferred working in a small group, 33.3% opted for working in pairs and 9.9% wanted to work individually.

When questioned about the digital approaches that motivated them to learn, 32.1% mentioned that animations really make them stay tuned and this is confirmed by (Maisaroh & Endahati, 2022; Mansor et al., 2020; Schneider et al., 2023), 28.4% mentioned that PPT presentations are good to learn from, 14.8% were enthusiastic about online exercises, 9.9% liked all kinds of audio-visual materials, 8.6% were thrilled about using digital pen and slate whereas 6.2% preferred the white board and pen. It is worthy to note that the art of writing is losing its momentum be it using digital pen and slate or white board and pen. The students of today are ready to type out and feel reluctant to write. This may be due to their mobile addiction where they communicate via social media in the form of texting, voice messaging, and voice or video calling. Added to this, with their mobile phones, they are quite used to prediction of words or text as well.

When asked about their experience with online learning from home digitally, 67.9% mentioned that they are comfortable learning at their own pace at home whereas 21% mentioned that they get distracted with various activities like people chatting, watching tv, visitors, external noise etc. 8.6% mentioned the difficulties they faced with respect to inconsistent flow of Internet and how they had to suffer carrying the device from a place to another place looking for strong signal strength of the network, and 2.5% complained that the home situation is only challenging and it is not at all favorable for learning. This calls for an attention of providing equally a conducive atmosphere at home also to facilitate effective learning as reflected by (Barai, 2020; Keser Aschenberger, 2023).

When commenting about the type of video lectures that made their learning effective, 61.7% mentioned that the video lectures delivered by their faculty to be more effective following the video lectures delivered by unknown experts, video lectures delivered by reputed overseas universities, and lastly NPTEL video lectures which is contrary to the findings of (University of British Columbia, 2020). This calls for an attention with respect to analyzing the effectiveness of NPTEL lectures as these are considered to be one of the major development programmes to upskill oneself. We need to understand the reasons behind the least preference of NPTEL lectures and motivate students to overcome those and to actively learn from those. Students' preference for the video lectures delivered by their faculty encapsulates that they are designed in accordance with the students' frame of reference and meant for getting better grades in their exams.

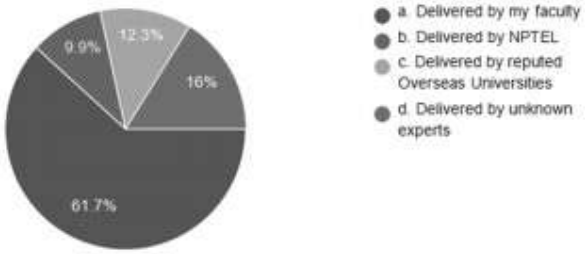

Fig.2: Video lecture effective for learning

When given a choice about the most preferred method for clearing doubts, 45.7% wanted to ask the instructor and clarify their doubts directly whereas 32.1% preferred to go through the online material providing additional explanation, and 22.2% preferred to post the query in the discussion forum to get inputs from the instructor as well as peers. Despite various means, asking the instructors directly and clarifying the doubts stands the most popular and preferred as the instructor can provide explanation keeping in mind the level of understanding of the student/students. Secondly, the instructor may give relevant examples and additional information with respect to the issue which may not be possible when you look for information online. Hence, when they post a query and when the peers respond, there is still a

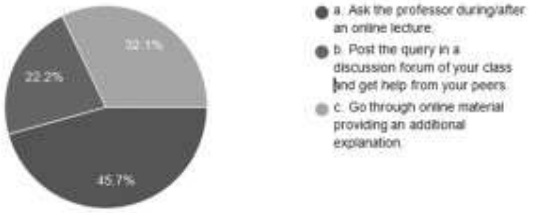

Fig. 3: Methods for clearing doubts in online learning

lack of confirmation till the instructor intervenes. This acknowledges the indispensable role of instructor support be it online or offline which is in line with the study by (Mohd Basar et al., 2021; Nagi & Bojiah, 2020).

When clarified about the sense of being comfortable using a cell phone or computer camera to show their face only for the purpose of identification during demos, presentations, or exams, 69.2% agreed without any hesitation and mentioned that there wasn't any problem about it which is contrary to the findings of (Sanderson, 2020). However, 18.5% felt awkward and found it to be objectionable whereas 12.3% remained in a state of confusion as to what to say. Most students agreeing for the motion is a good sign of understanding the importance of academic integrity as we do not have an option to confirm who is carrying out the assessment. If the instructor does not check, he or she may end up assessing someone else instead of the specified student.

When examined about the challenges they faced when taking classes in a fully online environment, 42% mentioned that inconsistent flow of Internet is the major challenge. The students suffer attendance issues owing to this and at times they may have to shuttle in and out of the online class due to intermittent network which will affect the smooth transfer of knowledge. This may hamper the building up of rapport with the instructor and the peers as well. Following this, 34.6% mentioned that they have sensed a lack of concentration during online classes, 12.3% complained about the unavailability of smart devices that makes online classes more effective and lastly, 11.1% did not have enough private space to do their online classes peacefully. This again stresses the importance of having a peaceful and conducive atmosphere to facilitate learning at home.

When commenting on the online class platforms like Zoom or Google Meet, 39.5% mentioned that they felt socially disconnected with their peers as they did not have the opportunity to share and care for each other in person which reflects the results of the study conducted by (Hehir, 2021). They missed the real time discussion and clarification that contribute towards learning. 38.3% mentioned that they could not focus and follow lectures, 12.3% felt online classes to be ineffective, and 9.9% felt no inclination to acquire knowledge from online classes. Being socially disconnected with peers and instructor drastically affect the mental make-up of the students. This could be the major reason for finding online classes to be ineffective and lacking in commanding student engagement and participation.

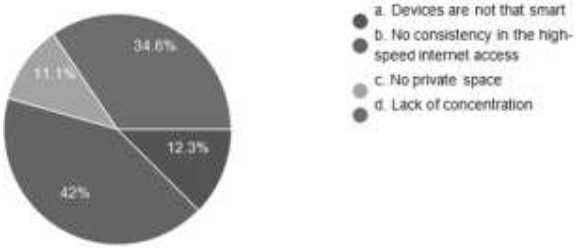

Fig. 4: Challenges of online environment

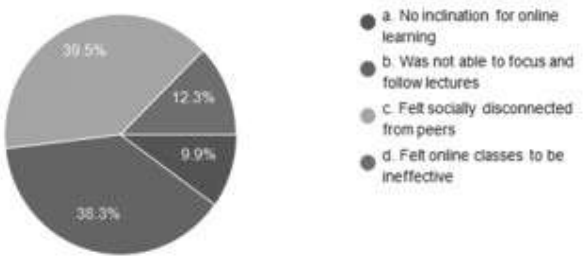

Fig. 5: Challenges in Zoom/Google Meet classes

In terms of instructional mode and materials, 45.7% felt that there was a much-pronounced lack of communication, 19.8% had issues using software, 18.5% faced issues pertaining to accessing and submitting assessments, 8.6% could not access course materials with ease, and 7.4% could not understand the instructions completely. This may be due to the unpreparedness from both the faculty and the students' side. Online education was adopted as a matter of emergency service (COL 2020; Hodges et al., 2020; OECD 2020) and so neither faculty nor students had ample formal training to equip themselves for this mode of education. The faculty members tended to use the same instructional materials and assessments for the course (Dayal, 2023) which is a matter of serious concern as to how they will fit in when there is a change in the mode of delivery.

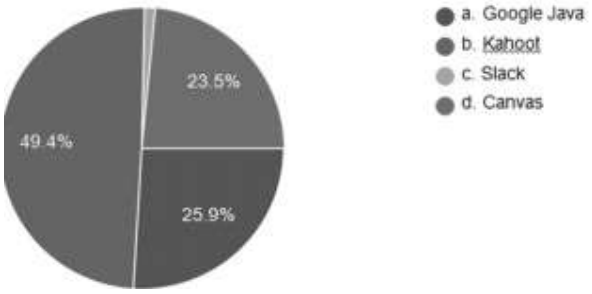

Fig. 6 : Tools for assignment submission

With respect to online mode of instruction, the overall experience was rated to be 43.2% of satisfied level and 18% of very satisfied level. This clearly indicates that the students are ready for online education as the dissatisfied level and very dissatisfied level stand at 3.5% and 2%. However, 33.3% stands neutral as to what to decide calls for a redressal of equipping the faculty and students to be trained enough to involve in online classes and developing of the course content and instructional materials that suit the purpose of education in online mode. Nevertheless, 46.9% stated that the online mode is good for semi-theoretical courses, 42% recommended online mode for theoretical courses, and 11.1% insisted that it fits in for lab courses as well. More than 10% suggesting that online mode is good for lab courses is a good sign because with no big technical support, lab courses were conducted online to keep up with the knowledge transfer flow during pandemic. This recommendation from students suggests that with proper training and resources, effective teaching of lab courses through online is possible.

When asked about their suggestions to make lab courses effective through online mode, 33.3% voted for 3D enhanced practical sessions, 16.1% suggested to enhance IT infrastructure, 14.8% recommended a Learning Management System (LMS) to be in place, 13.6% voted for hybrid or blended mode of learning, 11.1% recommended digitalizing scientific materials, and safeguarding educational platforms. It is very clear to comprehend that the IT infrastructure should be enhanced to accommodate LMS to impart 3D sessions using digitalized instructional materials and education tools to make the user experience a fruitful one.

For the submission of assignment, 49.4% preferred Kahoot!, 25.9% preferred Google Java, 23.5% preferred Canvas, and 1.2% preferred Slack. Kahoot! is a social learning platform, with users of the game gathered around a common screen such as an interactive whiteboard, projector or a computer monitor. The site can also be used through screen-sharing tools, like Zoom or Google Classroom. Students find it easy to comprehend through Kahoot! be it a short answer or writing the answer in detail. Hence, the students prefer to use this platform for assignment submission. As Kahoot! is user-friendly, game-based, and simple process of accessing, it is proved to have more liking from the students (Altawalbeh & Irwanto, 2023; Sinnivasagam & Hua, 202

Second preference is given to Google Java as it ensures that every assignment or work given to the students is done in the right way (Baharum et al., 2020; Skalka et al., 2020). Students get automatic evaluation after submitting their assignment and it makes sure that the student gets marks after satisfying all the requirements of the project assigned. For this reason, Google Java may be considered easy to handle from the instructors' points of view whereas it is said to be hard to handle as evident from the students' responses. These are not so familiar to students owing to its complexities and the lack of training. The studies by (Marachi & Quill, 2020; Ragupathi & Pinto, 2022) explain the varied features of Canvas and their effectiveness in enhancing the learning experience in detail. Though Canvas is also preferred as equal as Google Java, it does not seem to be very popular amidst the samples; Slack is the least preferred and it is quite possible that the tool is unexplored. Hence, it is important to train the people involved and use a variety of tools for the enrichment of learning experience.

When they are asked to suggest innovative teaching methodologies for online mode of teaching, 61.7% suggested game-based learning, 19.8% wanted pre-recorded video lectures, 11.1% recommended mind map, and 7.4% wanted class blog. Though, game-based learning cannot be suitable for all the courses, it seems to command more student engagement. Pre-recorded lectures have its own flavour of favouring students with the recurrent use for more clarity as these are demonstrative in nature. The preference for mind map and class blog are least rated as these may command some participation at the students' end. This clearly suggests that the students want something readymade and easy to access to manage their study.

51.9% suggested that the complete online engineering education was not effective whereas 48.1% felt that it is effective. Amongst this, a greater number of boys and a smaller number of girls have found online education to be very effective. 54.3% disagreed to enroll for an online postgraduate course but 45.7% agreed to get admitted. Amongst this, a greater number of boys and a smaller number of girls agreed to take up their post graduate degree programme completely online.

5. Conclusion

It is concluded that there are many niceties abiding

online learning. Studying at our own pace of time and convenience, exploring novel education tools for online mode of education, engaging in small group works for performing tasks, watching animations, listening to recorded lectures by the faculty, clarifying doubts instantly through the learning platform, game-based learning, and online submissions through Kahoot! to name a few. However, the overall responses suggest that a completely online CSE education will not be effective and majority disagreeing to enroll into a completely online post graduate course highlights the need to address the gap. The suggestions to include 3D sessions with digitally modified instructional materials, arrange for proper training of the faculty members and students, incorporate more game-based assessments, employ varied education tools, invest in high-speed Internet connectivity, and other IT infrastructure are to be taken seriously to embark onto this journey.

6. Recommendations

- Hand written assessments are losing its charm owing to the emerging technologies. Hence, this study intends to recommend typing of the answers from the beginning of the college level education. These days there is no concern for any hand written manuscript and in the college level education, checking the knowledge of spelling is also not the priority. Moreover, the similarity index will significantly find out and report the originality of the submission. It is recommended to have the plagiarism software to be embedded in the LMS platforms that is provided for task submission. The students also can check and verify at their ends which will help them work further and submit again.

- For online education to be more effective, counselling sessions should be arranged for family members of the wards stressing the importance of maintaining a quiet private space which is conducive for online learning.

- It is recommended to identify the challenges pertaining to NPTEL courses so that these could be improved to make the students attend them willingly.

- It is recommended to recognize the changing role of the faculty from instructor to facilitator so as to train him or her in the light of digital literacy to equip them to make the teaching learning process more striking.

- It is recommended to find out ways and means to monitor students during examinations using recognition of facial expressions, movement of eye balls, gestures, and postures.

- It is recommended to develop smart devices meant ideally for educational purposes so that there are no distractions to the learners in any manner.

- Online education comes with a lot of issues pertaining to the social disconnection. It is recommended for the instructors to incorporate a lot of interactive tools with respect to group work to let the students collaborate and learn better.

- It is recommended to have a mix of online and offline modes of education when imparting engineering courses as this will help in social interaction and hands-on learning. For these reasons, students enjoy blended or hybrid models to realize the ease of learning at their own convenient pace as well as learning practically interacting with peers and instructors.

- The LMS platforms like Kahoot! needs intense promotion amidst students. More LMS platforms should be introduced to the students for the ease and engagement of the students with the content and the instructional materials.

- Game-based learning proves to be commanding more attention and interest. It is time to explore the concept of the Metaverse which is undeniably becoming a part of every technology that makes our lives easier. It is recommended to bring in 3D technology, establish virtual learning environment embedding artificial intelligence, augmented reality, mixed reality etc., to make the learning experience vivid and participatory. However, it is also suggested that one should know that the self in the real world and the self in the virtual world are two different identities. Nevertheless, the self in the virtual world could be an alter ego of the real identity. It becomes compulsory for the instructors to clarify all these to the students before they expose the students to this kind of environment to avoid the student's tendency to suffer identity crisis.

7. Future Research

The correlation between studying at their own pace and time management should be analyzed. In addition to the effectiveness of online delivery and digital

instructional materials, the need for a peaceful ambience at home is still stressed by a considerable number of students. Further probing in this regard should be carried out in the Indian context in general and Madurai context to be specific. Game-based learning seems to be promising in commanding student engagement however, whether it contributes towards academic performance remains a query. The effectiveness of 3D materials, education tools, formal training on online education, peer learning, and online lab courses still need in-depth analysis with respect to Madurai context.

8. Limitations

The study is based on the responses from the sample size of 81 from an institute. Hence, the findings cannot be generalized. Further, the study was conducted only on the students of CSE major which further restricts itself to idealize the findings with respect to CSE education as a whole.

References

[1] Altawalbeh, Khitam & Irwanto, Irwanto. (2023). Game-Based Learning: The Impact of Kahoot! on a Higher Education Online Classroom.

[2] Asfour, O. S. & Alkharoubi, A. M. (2023). Challenges and opportunities in online education in Architecture: Lessons learned for Post-Pandemic education, Ain Shams Engineering Journal, https://doi.org/10.1016/j.asej.2023.102131

[3] Baharum, Aslina & Moung, Ervin & Ismail, Ismassabah & Ismail, Rozita & Majalin, Mazliah & Mat Noor, Noorsidi Aizuddin. (2020). A Preliminary Study of Difficulties in Learning Java Programming for Secondary School. International Journal of Advanced Trends in Computer Science and Engineering. 9. 302 - 306. 10.30534/ijatcse/2020/4591.42020.

[4] Bao, W. (2020). COVID -19 and online teaching in higher education: A case study of Peking University. Human Behavior and Emerging Technologies, 2(2), 113-115. https://doi.org/10.1002/hbe2.191

[5] Barai, B. (2020). Need Of A Proper Home Environment Conducive To Promote Creative Potential Of The Learners During Covid19 Crisis.

[6] Barteit, S., Guzek, D., Jahn, A., Bärnighausen, T., et al. (2020). 'Evaluation of e-learning for medical education in low-and middle-income countries: A systematic review'. Computers & Education, 145, 103726. https://doi.org/10.1016/j.compedu.2019.103726

[7] Borge, M., & Mercier, E. (2019). Towards a micro-ecological approach to CSCL. International Journal of Computer-Supported Collaborative Learning, 14(2), 219-235. https://doi.org/10.1007/s11412-019-09301-6

[8] Bozkurt, A., & Sharma, R.C. (2020). Emergency remote teaching in a time of global crisis due to Corona Virus pandemic. Asian Journal of Distance Education, 15 (1): i–vi.

[9] CDC. Public Health Recommendations after Travel-Associated COVID-19 Exposure. Centers for Disease Control and Prevention. Coronavirus Disease 2019 (COVID-19). https://www.cdc. gov/coronavirus/2019-ncov/php/risk-assessment.html. Accessed 6 August 2022.

[10] COL. (2020). Guidelines on Distance Education during COVID-19. Burnaby: COL.

[11] Dayal S. Online education and its effect on teachers during COVID-19-A case study from India. PLoS One. 2023 Mar 2;18(3):e0282287. doi: 10.1371/journal.pone.0282287. PMID: 36862704; PMCID: PMC9980775.

[12] Education International. (2020). Guiding Principles on the COVID-19 Pandemic. https://www.ei-ie.org/en/detail/16701/guiding-principles-on-the-covid-19-pandemic

[13] Ferdig, R. E., Baumgartner, R., Hartshorne, R., Kaplan-Rakowski, R., & Mouza, C. (Eds). (2020). "Teaching, technology, and teacher education during the COVID-19 pandemic: Stories from the field." Association for the Advancement of Computing in Education (AACE). https://www.learntechlib.org/p/216903/

[14] Flores, M. A., Machado, E.A., & Alves, P.

(2020). "Ensino E Avaliação a Distância Em Tempos De COVID-19 Nos Ensinos Básico E Secundário Em Portugal." Webinar, July 3.

[15] Garcia-Morales, J.V., Garrido-Moreno, A., & Martin-Rojas, R. (2021). The Transformation of Higher Education After the COVID Disruption: Emerging Challenges in an Online Learning Scenario. Front. Psychol., 12, 616059. [CrossRef]

[16] Gewin, V. (2020) Five tips for moving teaching online as COVID19 takes hold. Nature 580:295–296

[17] Goh, P. S. & Sandars, J. (2020). 'A vision of the use of technology in medical education after the COVID-19 pandemic'. MedEdPublish, 9. https://doi.org/10.15694/mep.2020.000049.1

[18] Hehir, E., Zeller, M., Luckhurst, J. et al. (2021). Developing student connectedness under remote learning using digital resources: A systematic review. Educ Inf Technol 26, 6531–6548 https://doi.org/10.1007/s10639-021-10577-1

[19] Hodges, C., Moore, S., Lockee, B., Trust, T., & Bond, A. (2020). The difference between emergency remote teaching and online learning. Educ. https://er.educause.edu/articles/2020/3/the-differencebetween-emergency-remote-teaching-and-online-learning

[20] Hubbard, B. (2020). Coronavirus fears terrify and impoverish migrants in the Persian Gulf. New York Times, 13 April. https://www.nytimes.com/2020/04/13/world/middleeast/persian-gulf-migrants-coronavirus.html. Accessed 4 August 2022.

[21] Huber, S. G., & C. Helm. (2020). "COVID-19 and Schooling: Evaluation, Assessment and Accountability in Times of Crises—Reacting Quickly to Explore Key Issues for Policy, Practice and Research with the School Barometer." Educational Assessment, Evaluation and Accountability 32 (2): 237–270. doi:10.1007/s11092-020-09322-y.

[22] Jain, M. & Sharma, S. (2022). Online Education: Challenges, Opportunities and Future Prospects. International Journal of Advanced Research in Commerce, Management & Social Science, 5(1): 35-44

[23] Jandrić, P. (2020). Postdigital research in the time of Covid-19. Postdigital Science and Education, 2, 233 – 238. https://doi.org/10.1007/s42438-020-00113-8.

[24] Jayesh, S. & Sreedharan, S. (2020). Analysing the Covid-19 Cases in Kerala: a Visual Exploratory Data Analysis Approach. SN Compr Clin Med. 2020;2(9):1337-1348. doi: 10.1007/s42399-020-00451-5.

[25] Judd, J., B. A. Rember, T. Pellegrini, B. Ludlow, & J. Meisner. (2020). "'This Is Not Teaching': The Effects of COVID-19 on Teachers." https://www.socialpublishersfoundation.org/knowledge_base/this-is-not-teaching-the-effects-of-covid-19-on-teachers/

[26] Keser Aschenberger, F., Radinger, G., Brachtl, S. et al. (2023). Physical home learning environments for digitally-supported learning in academic continuing education during COVID-19 pandemic. Learning Environ Res 26, 97–128. https://doi.org/10.1007/s10984-022-09406-0

[27] König, L. (2020). 'Podcasts in higher education: teacher enthusiasm increases students' excitement, interest, enjoyment, and learning motivation'. Educational Studies, 1-4. https://doi.org/10.1080/03055698.2019.1706040

[28] Lambert, C., Aubrey, S., & Bui, G. (Ed.). (2023). The Role of the Learner in Task-Based Language Teaching Theory and Research Methods. Routledge. https://doi.org/10.4324/9781003227267

[29] Lim, Ida. Covid-19: What are Malaysia's public universities doing? Online classes and more... Malay Mail. https://www.malaymail.com/news/malaysia/2020/03/16/covid-19what-are-malaysias-public-universities-doing-online-classes-and-mo/1847071, 2020 (accessed 8 August 2022).

[30] Littlefield, J. (January 14, 2018). The Difference Between Synchronous and Asynchronous Distance Learning. https://www.thoughtco.com/synchronous-distance-learning-asynchronous-distance-learning-1097959.

[31] Luo, Yu-Meng, Wei Liu, Xiao-Guang Yue, & Marc A. Rosen. 2020. Sustainable Emergency Management Based on Intelligent Information Processing. Sustainability 12: 1081.

[32] Maisaroh, S. & Endahati, N. (2022). The Effectiveness of Multimedia Animation-Based Integrative Learning Model During Covid-19 Pandemic at Primary School. UPY International Conference on Education and Social Science 2022.

[33] Mansor, Noor Rohana & Zakaria, Rosdi & Rashid, Roswati & Arifin, Raihan & Hairiel, Baidruel & Zakaria, Ruslimi & Razak, Mohd. (2020). A Review Survey on the Use Computer Animation in Education. IOP Conference Series Materials Science and Engineering. 917. 012021. 10.1088/1757-899X/917/1/012021.

[34] Marachi, R. & Quill, L. (2020). The case of Canvas: Longitudinal datafication through learning management systems, Teaching in Higher Education, 25:4, 418-434, DOI: https://doi.org/10.1080/13562517.2020.1739641

[35] McKimm, J., Gibbs, T., Bishop, J. and Jones, P. (2020). 'Health Professions' Educators' Adaptation to Rapidly Changing Circumstances: The Ottawa 2020 Conference Experience'. MedEdPublish, 9. https://doi.org/10.15694/mep.2020.000047.1

[36] Milman, N. B. (2020). Pandemic pedagogy. Phi Delta Kappan.

[37] Mohd Basar, Zulaikha., Mansor, Azlin Norhaini, Jamaludin, Khairul Azhar, & Alias, Bity Salwana. (2021). The Effectiveness and Challenges of Online Learning for Secondary School Students – A Case Study. Asian Journal of University Education, 17(3).

[38] Moorhouse, B. L. (2020). Adaptations to a face-to-face initial teacher education course 'forced' online due to the COVID-19 pandemic. Journal of Education for Teaching 1–3. doi:10.1080/02607476.2020.1755205.

[39] Murphy, M. P. A. (2020). COVID-19 and emergency eLearning: Consequences of the securitization of higher education for post-pandemic pedagogy. Contemporary Security Policy, 1-14. https://doi.org/10.1080/13523260.2020.1761749

[40] Nagi, M. & Bojiah, J. (2020). Real Classes Vs Online Classes: A Comparative Study on the Chosen Course of HRM Students of Gulf University, Kingdom of Bahrain. International Journal of Emerging Technologies in Learning, 15(18). https://doi.org/10.3991/ijet.v15i18.15267

[41] NFER. 2020. "Schools' Responses to Covid-19. Pupil Engagement in Remote Learning." https://www.nfer.ac.uk/schools-responses-to-covid-19-pupil-engagement-in-remote-learning/

[42] OECD. (2020). "Education Responses to Covid-19: Embracing Digital Learning and Online Collaboration." https://www.oecd.org/coronavirus/policy-responses/education-responses-tocovid-19-embracing-digital-learning-and-online-collaboration-d75eb0e8/

[43] Pilav-Velic´, A., Jahic´, H., Okicˇic´, J., Selimovic´, J., & Grabovica, E. (2021). Emergency remote learning acceptance among higher education students during COVID-19 pandemic. Proc. Rij. Fac. Econ. J. Econ. Bus., 39, 325–347. [CrossRef]

[44] Ragupathi, K. & Pinto, K. (2022, 07 Sep). Guiding principles to a well-designed Canvas course, Teaching and Learning with Canvas at NUS Blog. https://blog.nus.edu.sg/canvas/2022/09/07/guiding-principles-to-a-well-designed- canvas-course/

[45] Sanderson, D. (2020). UAE students speak out against webcam policy for online exams. The National, 13 April. https://www.thenational.ae/uae/education/uae-

students-speak-out-against-webcam-policy-foronline-exams-1.1005549. Accessed 14 August 2022.

[46] Sansa, N.A. (2020). Analysis for the Impact of the COVID - 19 to the Petrol Price in China (March 2, 2020). Accessed 08/08/2022, available from https://ssrn.com/abstract=3547413.

[47] Schneider, S., Krieglstein, F., Beege, M., & Rey, G. D. (2023). Successful learning with whiteboard animations – A question of their procedural character or narrative embedding? Heliyon, 9(2).

[48] Shaanxi Normal University. 2020. The First Mental Health Guidance Manual of the "War on Resistance to Epidemic" Was Formally Published by Our Publishing House. Available online: http://news.snnu.edu.cn/info/1012/22155.htm (accessed on 11 August 2022).

[49] Sinnivasagam, P., & Hua, T. K. (2023). Gamification Functionality and Features of Kahoot!! in Learning—ESL Teachers and Students' Perceptions. Open Journal of Social Sciences, 11, 404-421. https://doi.org/10.4236/jss.2023.112027

[50] Skalka, Ján & Benko, Ľubomír & Boryczka, Mariusz & Landa, Jaromír & Rodriguez-del-Pino, Juan. (2020). Java fundamental. 10.17846/2020-java1.

[51] Suharto, S. & Ambarwangi. S. (2021). Social Media as a Learning Media to Improve Digital Literacy and Creation, Proceedings of the 4th International Conference on Arts and Design Education (ICADE 2021).

[52] UNESCO (2020). COVID-19 Educational Disruption and Response. https://en.unesco.org/covid19/educationresponse. Retrieved Feb 2020

[53] University of British Columbia (2020). Flexible Learning. http://flexible.learning.ubc.ca.

[54] Wang, G. et al., 2020. Mitigate the effects of home confinement on children during the COVID-19 outbreak. The Lancet. 395.10228. 945–947. http:// doi.org/10.1016/S0140-6736(20)30547-X

[55] Wee, S. L., Jr, McNeil, D.G., Jr, and Hernández, J. C. W.H.O. Declares Global Emergency as Wuhan Coronavirus Spreads. The New York Times (2020). Available online at: https://www.nytimes.com/2020/01/30/health/coronavirus- world- health- organization.html (accessed August 13, 2022).

[56] Wong, Sing Yun. (2023) Digitalization challenges in education during COVID-19: A systematic review, Cogent Education, 10:1, 2198981, DOI: 10.1080/2331186X.2023.2198981

[57] World Bank. (2020). Guidance Note on Remote Learning and COVID-19 (English). Washington, D. C.: World Bank Group. Accessed 08/08/2022 available from http://documents.worldbank.org/curated/en/

[58] Wu Z, McGoogan, J.M. (2020) Characteristics of and important lessons from the coronavirus disease 2019 (COVID-19) outbreak in china: summary of a report of 72314 cases from the Chinese center for disease control and prevention. JAMA. https ://doi.org/10.1001/jama.2020.2648

[59] Zhang, W., Y. Wang, L. Yang, and C. Wang. 2020. "Suspending Classes without Stopping Learning: China's Education Emergency Management Policy in the COVID-10 Outbreak." Journal of Risk and Financial Management 13 (3): 1–6. doi:10.3390/jrfm13030055.

[60] Zhu, X. (2020). Building up National Online Teacher Education System. Research in Education Development, 40(2), 3. https://doi.org/10.14121/j.cnki.1008-3855.2020.02.002.

Elevated CNN Based Secured Sensor Image Data Communication for HAR: IIOT

| Conference paper | First Online: 01 April 2023

| pp 211–220 | Cite this conference paper

International Virtual Conference on Industry 4.0

(IVCI 2021)

P. Alli & J. Dinesh Peter

Part of the book series: Lecture Notes in Electrical Engineering ((LNEE,volume 1003))

Included in the following conference series:

International Virtual Conference on Industry

Abstract

The Industrial Internet of Things (IIOT) is constituted by the development of the Internet of Things into the fields of manufacturing, monitoring, and management. It enables industries to make use of data communication and control by leveraging the capabilities of smart machines and real-time analysis. Our proposed work concentrates on the application of IIOT along with two contributions: the first one is to secure sensor based image, video and audio communication and the other one is the detection of human activity. Initially, the human activities data are captured by the camera sensors which is attached in the employee ID card that sensor monitors the employee activities as a motion image along with vibrations and sound signals. All this information is securely communicated to the smart office dashboard with the help of an efficient encryption algorithm namely Software Defined Network along with Stochastic Honey Overlapping Based Dual Helix Scan (SDN-SHODHS), that secures the communication in the access network. In the second phase to detect employee activity, we propose an efficient Elevated Deep Convolutional Neural Network that gives the best efficient result compared to all other existing works. Our proposed framework achieves secure sensor data image, audio and video communication and accurate human activity recognition in terms of encryption and decryption time, precision, recall and F-measure.

Similar content being viewed by others

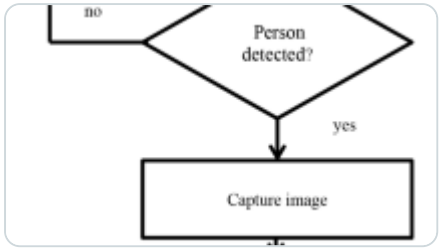

A secured deep learning based smart home automation system

Article | Open access
29 August 2024

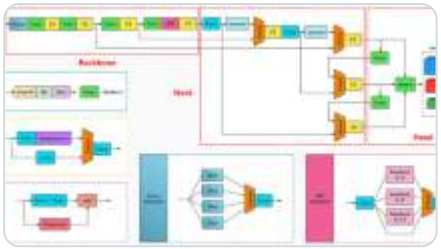

100+ FPS detector of personal protective equipment for worker safety: A deep learning approach for green edge computing

Article | 15 November 2021

Enhancement of IoT Security by Integration of Convolutional Neural Network and Image Processing

Chapter | © 2022

References

1. Vermesan O, Friess P (eds) (2013) Internet of things: converging technologies for smart environments and integrated ecosystems. River publishers

Google Scholar

2. Bhide VH, Wagh S (2015) I-learning IoT: an intelligent self learning system for home automation using IoT. In: 2015 International conference on communications and signal processing (ICCSP). pp 1763–1767

Google Scholar

3. Nagy J, Oláh J, Erdei E, Máté D, Popp J (2018) The role and impact of Industry 4.0 and the internet of things on the business strategy of the value chain—the case of Hungary. Sustainability 10(10):3491

Google Scholar

4. Ronao CA, Cho SB (2016) Human activity recognition with smartphone sensors using deep learning neural networks. Expert Syst Appl 59:235–244

Article Google Scholar

5. Lin J, Yu W, Zhang N, Yang X, Zhang H, Zhao W (2017) A survey on internet of things: architecture, enabling technologies, security and privacy, and applications. IEEE Internet Things J 4(5):1125–1142

Article Google Scholar

6. Wang X, Ong SK, Nee AY (2018) A comprehensive survey of ubiquitous manufacturing research. Int J Prod Res 56(1–2):604–628

Article Google Scholar

7. Jain S, Chandrasekaran K (2020) Industrial automation using Internet of Things. In: Security and privacy issues in sensor networks and IoT. IGI Global, pp 28–64

Google Scholar

8. Castro D, Coral W, Rodriguez C, Cabra J, Colorado J (2017) Wearable-based human activity recognition using an iot approach. J Sens Actuator Netw 6(4):28

Article Google Scholar

9. Zhang H, Xiao Z, Wang J, Li F, Szczerbicki E (2019) A novel IoT-perceptive human activity recognition (HAR) approach using multihead convolutional attention. IEEE Internet Things J 7(2):1072–1080

Article Google Scholar

10. Hassan MM, Uddin MZ, Mohamed A, Almogren A (2018) A robust human activity recognition system using smartphone sensors and deep learning. Futur Gener Comput Syst 81:307–313

Article Google Scholar

11. Jain A, Kanhangad V (2017) Human activity classification in smartphones using accelerometer and gyroscope sensors. IEEE Sens J 18(3):1169–1177

Article Google Scholar

12. Khan PW, Byun Y (2020) A blockchain-based secure image encryption scheme for the industrial Internet of Things. Entropy 22(2):175

Google Scholar

Author information

Authors and Affiliations

Velammal College of Engineering and Technology, Madurai, India

P. Alli

Karunya Institute of Technology and Sciences, Coimbatore, India

J. Dinesh Peter

Corresponding author

Correspondence to P. Alli .

Editor information

Editors and Affiliations

School of Computer Science and Engineering, Vellore Institute of Technology, Chennai, India

R. Jagadeesh Kannan

School of Computer Science and Engineering, Vellore Institute of Technology, Chennai, India

S. Geetha

Department of Science and Engineering, Manchester Metropolitan University, Manchester, UK

Sravanthi Sashikumar

Academic Lead Industry 4.0, Manchester Metropolitan University, Manchester, UK

Carl Diver

Rights and permissions

Copyright information

About this paper

Cite this paper

Alli, P., Dinesh Peter, J. (2023). Elevated CNN Based Secured Sensor Image Data Communication for HAR: IIOT. In: Kannan, R.J., Geetha, S., Sashikumar, S., Diver, C. (eds) International Virtual Conference on Industry 4.0. IVCI 2021. Lecture Notes in Electrical Engineering, vol 1003. Springer, Singapore. https://doi.org/10.1007/978-981-19-9989-5_18

.RIS .ENW .BIB

DOI
https://doi.org/10.1007/978-981-19-9989-5_18

Published
01 April 2023

Publisher Name
Springer, Singapore

Print ISBN
978-981-19-9988-8

Online ISBN
978-981-19-9989-5

eBook Packages
Engineering
Engineering (R0)

Publish with us

Policies and ethics

An IoT-Based Pregnancy Complexity Identification Using Machine Learning

G. Vinoth Chakkaravarthy, Raja Lavanya, P. Alli

Source Title: Technological Tools for Predicting Pregnancy Complications (/book/technological-tools-predicting-pregnancy-complications/329620)

Pages: 8
DOI: 10.4018/979-8-3693-1718-1.ch013

Abstract

Pregnancy complications have the potential to seriously injure both the mother and the developing baby, increasing the risk of morbidity and mortality. Early detection of high-risk pregnancies is crucial to reducing the likelihood of such issues and improving the health outcomes for mothers and babies. The authors suggest an IoT-based system that uses machine learning to recognise pregnancy complications as a solution to this problem. The system uses a variety of sensors to collect information from pregnant women, including blood pressure, heart rate, foetal heart rate, and temperature sensors. This collected data is then analyzed using machine learning algorithms using supervised learning algorithms for classification and regression analysis. The study's findings indicate that the suggested system can effectively recognize pregnancy complications with high levels of accuracy, sensitivity, specificity, and AUC. The system holds great potential in enhancing maternal and fetal health outcomes by enabling the early detection and intervention of high-risk pregnancies.

Chapter Preview

Top

2. Literature Survey

Numerous research studies have suggested employing IoT-based sensors and ML algorithms for monitoring pregnancy and identifying complications. This section presents an overview of some of the relevant research works conducted in this field.

The paper titled “IoT-Based Risk Level Prediction Model for Maternal Health Care in the Context of Bangladesh” presents a study that explores the potential of IoT and machine learning in predicting the risk level of maternal health in Bangladesh (Ahmed & Kashem, 2020). In order to forecast the risk level of maternal health in real-time, the paper addresses the difficulties in maternal health care in Bangladesh and suggests a risk prediction model that makes use of IoT-based sensors and machine learning algorithms. The study also discusses the design and implementation of the suggested system and assesses its effectiveness using a number of measures.

An overview of an IoT-based wearable system that makes use of accelerometers and machine learning for tracking foetal movement is provided in the paper titled An IoT-based wearable system using accelerometers and machine learning for foetal movement monitoring (Zhao et al, 2019). The technology seeks to offer a non-invasive and economical means for tracking foetal movements, which is a crucial sign of the health of the foetus. A variety of criteria, including accuracy, sensitivity, specificity, and positive predictive value (PPV), are used in the study to assess the system's performance. The findings show that the suggested method has the ability to precisely identify foetal movements and has the potential to be a helpful tool for foetal monitoring throughout pregnancy. According to the findings, the suggested approach had high accuracy rates of 96.6%, 92.1% sensitivity, 98.2% specificity, and PPV.

Complete Chapter List

Search this Book: Full text search terms

Reset

Chapter 5

Wearable Sensors and AI Algorithms for Monitoring Maternal Health (/chapter/wearable-sensors-and-ai-algorithms-for-monitoring-maternal-health/332209) (pages 66-87)

D. Sathya, S. P. Siddique Ibrahim, D. Jagadeesan

Preview Chapter (/viewtitlesample.aspx?id=332209&ptid=329620&t=Wearable Sensors and AI Algorithms for Monitoring Maternal Health&isxn=9798369317181) **$37.50** Add to Cart

Chapter 6

Ethical Considerations for Wearable Sensors and AI Algorithms: Fetal Heart Rate Monitoring (/chapter/ethical-considerations-for-wearable-sensors-and-ai-algorithms/332210) (pages 88-123)

Prasath Nithiyanandam, A. Arun, J. Sreemathy, R. Lakshminarayanan

Preview Chapter (/viewtitlesample.aspx?id=332210&ptid=329620&t=Ethical Considerations for Wearable Sensors and AI Algorithms: Fetal Heart Rate Monitoring&isxn=9798369317181) **$37.50** Add to Cart

Chapter 7

Wearable Sensors and AI Algorithms for Pregnant Women (/chapter/wearable-sensors-and-ai-algorithms-for-pregnant-women/332211) (pages 124-140)

A. Vinora, E. Lloyds, R. Nancy Deborah, A. Gobinath, G. Sivakarthi

Preview Chapter (/viewtitlesample.aspx?id=332211&ptid=329620&t=Wearable Sensors and AI Algorithms for Pregnant Women&isxn=9798369317181) **$37.50** Add to Cart

Chapter 8

Predicting Pregnancy Complications Using Machine Learning (/chapter/predicting-pregnancy-complications-using-machine-learning/332212) (pages 141-160)

Manav Dewan, Aman Mudgal, Pallavi Pandey, Yogita Yashveer Raghav, Tanu Gupta

Preview Chapter (/viewtitlesample.aspx?id=332212&ptid=329620&t=Predicting Pregnancy Complications Using Machine Learning&isxn=9798369317181) **$37.50** Add to Cart

Chapter 9

Depression and Mood Monitoring for Pregnant Women Using IoT-Based Wearables (/chapter/depression-and-mood-monitoring-for-pregnant-women-using-iot-based-wearables/332214) (pages 162-185)

Delshi Howsalya Devi, R. Naresh, C. N. S. Vinoth Kumar, S. Senthilkumar, Asis Jovin

Preview Chapter (/viewtitlesample.aspx?id=332214&ptid=329620&t=Depression and Mood Monitoring for Pregnant Women Using IoT-Based Wearables&isxn=9798369317181) **$37.50** Add to Cart

Chapter 10

Machine Learning-Based Monitoring Devices for Pregnant Women (/chapter/machine-learning-based-monitoring-devices-for-pregnant-women/332215) (pages 186-198)

Selvanayaki Palanisamy, Muthanantha Murugavel A. S, Sathiyamurthi Pattusamy, S. Deepa

Preview Chapter (/viewtitlesample.aspx?id=332215&ptid=329620&t=Machine Learning-Based Monitoring Devices for Pregnant Women&isxn=9798369317181) **$37.50** Add to Cart

Chapter 11

Machine Learning-Based Devices for Pregnant Women (/chapter/machine-learning-based-devices-for-pregnant-women/332216) (pages 199-204)

Gnana King, Vishnu Rajan, Jensha Haennah

Preview Chapter (/viewtitlesample.aspx?id=332216&ptid=329620&t=Machine Learning-Based Devices for Pregnant Women&isxn=9798369317181) **$37.50** Add to Cart

Chapter 12

Wearable Sensors and AI Algorithms for Pregnant Women: Integrating Wearable Mitered Meander Antenna Sensors for Continuous Breathing Monitoring (/chapter/wearable-sensors-and-ai-algorithms-for-pregnant-women/332217) (pages 205-220)

A. Gobinath, P. Rajeswari, Suresh Kumar, M. Anandan

Preview Chapter (/viewtitlesample.aspx?id=332217&ptid=329620&t=Wearable Sensors and AI Algorithms for Pregnant Women: Integrating Wearable Mitered Meander Antenna Sensors for Continuous Breathing Monitoring&isxn=9798369317181) **$37.50** Add to Cart

Chapter 13

An IoT-Based Pregnancy Complexity Identification Using Machine Learning (/chapter/an-iot-based-pregnancy-complexity-identification-using-machine-learning/332219) (pages 222-229)

G. Vinoth Chakkaravarthy, Raja Lavanya, P. Alli

Preview Chapter (/viewtitlesample.aspx?id=332219&ptid=329620&t=An IoT-Based Pregnancy Complexity Identification Using Machine Learning&isxn=9798369317181) **$37.50** Add to Cart

Chapter 14

Prediction of Pregnancy Complications Using Machine Learning and Deep Learning Algorithms (/chapter/prediction-of-pregnancy-complications-using-machine-learning-and-deep-learning-algorithms/332220) (pages 230-246)

Bharati Sanjay Ainapure

Preview Chapter (/viewtitlesample.aspx?id=332220&ptid=329620&t=Prediction of Pregnancy Complications Using Machine Learning and Deep Learning Algorithms&isxn=9798369317181) **$37.50** Add to Cart

Chapter 15

Prediction of Pregnancy Complications in Fetal Heart Rate Using Hybrid Supervised Learning Model Enhanced With Compressive Sensing (/chapter/prediction-of-pregnancy-complications-in-fetal-heart-rate-using-hybrid-supervised-learning-model-enhanced-with-compressive-sensing/332221) (pages 247-274)

Sivasankari Jothiraj, Sridevi Balu, S. Premalatha, Nagarani Nagarajan

Preview Chapter (/viewtitlesample.aspx?id=332221&ptid=329620&t=Prediction of Pregnancy Complications in Fetal Heart Rate Using Hybrid Supervised Learning Model Enhanced With Compressive Sensing&isxn=9798369317181) **$37.50** Add to Cart

Chapter 16

Analyzing Skin Cancer Detection Efficiency With Convolutional Neural Networks (/chapter/analyzing-skin-cancer-detection-efficiency-with-convolutional-neural-networks/332223) (pages 276-288)

N. Nagarani, S. Seronica, S. Rajalakshmi, S. J. Sherine Santhi

Preview Chapter (/viewtitlesample.aspx?id=332223&ptid=329620&t=Analyzing Skin Cancer Detection Efficiency With Convolutional Neural Networks&isxn=9798369317181) **$37.50** Add to Cart

Chapter 17

Implementation of Machine Learning Models for Analyzing the Correlation and Classification of Complications in Pregnancy Using Amniotic Fluid (/chapter/implementation-of-machine-learning-models-for-analyzing-the-correlation-and-classification-of-complications-in-pregnancy-using-amniotic-fluid/332224) (pages 289-302)

Santhi Palanisamy, K. Deepa, M. Sathya Sundaram

Preview Chapter (/viewtitlesample.aspx?id=332224&ptid=329620&t=Implementation of Machine Learning Models for Analyzing the Correlation and Classification of Complications in Pregnancy Using Amniotic Fluid&isxn=9798369317181) **$37.50** Add to Cart

Chapter 18

Improving Maternal Health by Predicting Various Pregnancy-Related Abnormalities Using Machine Learning Algorithms (/chapter/improving-maternal-health-by-predicting-various-pregnancy-related-abnormalities-using-machine-learning-algorithms/332225) (pages 303-326)

K. Nandhini, J. Jayapriya, M. Vinay

Preview Chapter (/viewtitlesample.aspx?id=332225&ptid=329620&t=Improving Maternal Health by Predicting Various Pregnancy-Related Abnormalities Using Machine Learning Algorithms&isxn=9798369317181) **$37.50** Add to Cart

Chapter 19

Machine Learning Algorithms for Pregnant Women (/chapter/machine-learning-algorithms-for-pregnant-women/332226) (pages 327-350)

Priyadarsan Parida, Sonali Dash, Ranjita Rout

Preview Chapter (/viewtitlesample.aspx?id=332226&ptid=329620&t=Machine Learning Algorithms for Pregnant Women&isxn=9798369317181) **$37.50** Add to Cart

About the Contributors

View Full PDF (/pdf.aspx?tid=332228&ptid=329620&ctid=17&t=About the Contributors&isxn=9798369317181)

Index

View Full PDF (/pdf.aspx?tid=332229&ptid=329620&ctid=17&t=Index&isxn=9798369317181)

Statistical performance review on diagnosis of leukemia, glaucoma and diabetes mellitus using AI

Rengaraju Perumalraja, B. Felcia Logan's Deshna, N. Swetha

First published: 21 January 2024
https://doi.org/10.1002/sim.10004

Abstract

The growth of artificial intelligence (AI) in the healthcare industry tremendously increases the patient outcomes by reshaping the way we diagnose, treat and monitor patients. AI-based innovation in healthcare include exploration of drugs, personalized medicine, clinical diagnosis investigations, robotic-assisted surgery, verified prescriptions, pregnancy care for women, radiology, and reviewed patient information analytics. However, prediction of AI-based solutions are depends mainly on the implementation of statistical algorithms and input data set. In this article, statistical performance review on various algorithms, Accuracy, Precision, Recall and F1-Score used to predict the diagnosis of leukemia, glaucoma, and diabetes mellitus is presented. Review on statistical algorithms' performance, used for individual disease diagnosis gives a complete picture of various research efforts during the last two decades. At the end of statistical review on each disease diagnosis, we have discussed our inferences that will give future directions for the new researchers on selection of AI statistical algorithm as well as the input data set.

Open Research

DATA AVAILABILITY STATEMENT

Data sharing is not applicable to this article as no new data were created or analyzed in this study.

REFERENCES

1 Amin MM, Kermani S, Talebi A, Oghli MG. Recognition of acute lymphoblastic leukemia cells in microscopic images using K-means clustering and support vector machine classifier. *J Med Signal Sens*. 2015; **5**(1): 49-58. doi:10.4103/2228-7477.150428

View | PubMed | Google Scholar

2 Moradiamin M, Samadzadehaghdam N, Kermani S, Talebi A. Enhanced recognition of acute lymphoblastic leukemia cells in microscopic images based on feature reduction using principle component analysis. *Front Biomed Technol*. 2015; **2**: 128-136.

Google Scholar

3 Kasani PH, Park SW, Jang JW. An aggregated-based deep learning method for leukemic B-lymphoblast classification. *Diagnostics (Basel).* 2020; **10**(12): 1064. doi:10.3390/diagnostics10121064

View | PubMed | Web of Science® | Google Scholar

4 Sallam NM, Saleh A, Ali HA, Abdelsalam MM. An efficient strategy for blood diseases detection based on grey wolf optimization as feature selection and machine learning techniques. *Appl Sci*. 2022; **12**(21):10760. doi:10.3390/app122110760

View | CAS | Google Scholar

Measurement: Sensors 30 (2023) 100906

Contents lists available at ScienceDirect

Measurement: Sensors

journal homepage: www.sciencedirect.com/journal/measurement-sensors

CPS in block chain smart city application based on distributed ledger based decentralized technique

T. Hemalatha [a,*], K. Sangeetha [b], K. Sasi Kala Rani [c], K.V. Kanimozhi [d], M. Lawanyashri [e], K. Santhi [e], R. Deepalakshmi [f]

[a] Department of AI&DS, PSNA College of Engineering & Technology, Dindigul, TN, India
[b] Department of Computer Science and Engineering, Panimalar Engineering College, Chennai, TN, India
[c] Department of Computer Science and Engineering, Sri Krishna College of Engineering & Technology, Coimbatore, TN, India
[d] Department of CSE, Saveetha School of Engineering, Saveetha Institute of Medical and Technical Sciences, Chennai, TN, India
[e] SITE, Vellore Institute of Technology, Vellore, TN, India
[f] Department of Computer Science and Engineering, Velammal College of Engineering and Technology, India

ARTICLE INFO

Keywords:
Block chain
Cyber physical system
Pervasive computing
Smart city
Distributed ledger based decentralized database

ABSTRACT

This article offers a brief overview about cyber-physical systems enabled by blockchain (CPS). Dissects various blockchain-enabled CPS reported on the operations and blockchain characteristics used in the literature. Base of its time sensitiveness and throughput requirements, we identify and categories key common CPS operations that can be activated by blockchain. We also develop blockchain features and categories in terms of diverse levels of benefits to CPS like security, privacy, immutability, tolerance of defects, interoperability's, data origin, atomicity, automation, information/service sharing and trust. This paper provides an overview of the concept of intelligent cities as well as emerging technologies and a quick overview of cyber-physical systems. It then discusses CPS' potential role in the development of intelligent city apps and some real-life examples of CPS adaptation for city smart projects. A decentralized database based on distributed ledgers has been introduced. Distributed ledgers are a distributed database with a network connection node. These nodes include ledgers that list transactions with timestamps.

1. Introduction

CPS (cyber-physical systems) are an architectural paradigm that combines pervasive sensing and communication technology to give many economic and societal benefits. In other terms, it's a cyber-enhanced physical system or process. These components are tightly interconnected, which indicates that one component's functionality is reliant on the functionality of the other. In recent years, CPS has experienced exponential expansion in areas such as energy, health, transportation, and the Industrial Internet of Things (IIoT). Stability, dependability, robustness, security, and privacy are key areas of research when creating smart, efficient, and flexible systems. Rapid advances in enabling technology, on the other hand, have exposed such systems to substantial and profound hazards. We would forfeit the enormous benefits that such risks can give if they are not managed. By effectively establishing trust among nodes, blockchain has the ability to develop new foundations for most distributed systems. It is a crucial technology for decentralization and plays a significant role in the CPS area (see Tables 1 and 3).

Blockchain is a promising solution to address the mentioned CPS problems because of its prominent qualities of decentralized, anonymity, and security. The blockchain is an immutable, distributed ledger that stores data in blocks that are connected via cryptographic techniques in a peer-to-peer network. Although the Bitcoin blockchain's principal use is to transfer funds between members of a trustless network without the necessity of trusted intermediaries, blockchains with varying capacities have since grown to accommodate different applications. When stated parameters are met, smart contracts on Ethereum and Hyperledger blockchains, for example, can run self-executing programming.

The paper's main structure is as follows: Section 2 contains a literature review based on our approach. Section 3 Contain cyber-physical systems (CPS) and pervasive sensing to demonstrate how blockchain

* Corresponding author.
E-mail addresses: hemashek@gmail.com (T. Hemalatha), sangeethakalyaniraman@gmail.com (K. Sangeetha), sasikalaranik@skcet.ac.in (K. Sasi Kala Rani), kanimozhikv.sse@saveetha.com (K.V. Kanimozhi), lawanyaraj@gmail.com (M. Lawanyashri), ksanthi@vit.ac.in (K. Santhi), rdl@vcet.ac.in (R. Deepalakshmi).

https://doi.org/10.1016/j.measen.2023.100906
Received 15 February 2023; Received in revised form 19 June 2023; Accepted 2 October 2023
Available online 17 October 2023

Table 1
Application domains of CPS.

SYSTEM	APPLICATION
Healthcare	Medical equipment, health network administration
Industrial Control system	Electronic automotive, railway Vehicle networks, systems, Management of aviation and aviation
Transportation	Monitoring and control of physical infrastructure
Smart grid	Generation of electricity and distribution, construction, and environmental management
Smart city	Detection of mobile phones Congestion in the streets Parking with Insight

Table 3
Compares DDS with DLBD on various characteristics.

Characteristics	DDS	DLBD
Energy Consumption	**0.75**	**0.63**
Scalability	**0.69**	**0.88**
Security	**0.84**	**0.87**

technology can help the economy and society and 3.1 contain Distributed ledger based decentralized database with cyber-physical CPS systems in smart city application. The experimental section is in Section 4. The paper comes to an end in Section 5.

2. Litrature survey

Blockchain-based solutions for CPS using over-simplified system models does not fully represent the System dynamics, requirements and restriction [1]. more realistic system model, real-world data sets, proof-of-concept and pilot trials are necessary to build blockchain solutions that can be applied to real-world CPS. While some blockchain platforms include test networks and performance evaluation tools, the performance of large networks or complex CPS applications cannot be evaluated [2]. Blockchain-enabled cyber-physical systems, a succinct yet thorough examination (CPS). The functioning of several blockchain-enabled CPS documented in the literature, and the blockchain properties used. Security, privacy, immutability, toleration for faults, interoperability, sharing of data/service and trust are properties of blockchain that can be divided into different CPS benefits [3]. Creation of conceptual principles for the design of cyber-physical systems of food production. According to the results, modern foods have a cyber-physical character that is crucial to the development of healthier and more sustainable food systems. Using machine learning methodologies to collect, integrate and analyses data relating to biomass production and processing at different levels from a molecule to a global level, it is possible to accurately analyses food systems and estimate upscaling benefits and potential negative social-attitude rebound effects [4]. A thorough review of the use of blockchain in current information systems as a service. According to some of the most relevant findings in the survey, the structure of blockchain, modern cloud and cutting-edge computing paradigms are essential to enabling new participants to widely adopt and develop blockchain technologies in today's vibrant global market.

The introduction of Log-Flow, an IoT, CPS, and blockchain technology-based logistics financed platform. We called for the use of digital assets to accelerate the physical and information movement across the LC in order to facilitate logistics financings [5]. For building digital assets with mobile sensors and IoT technologies, Digital Twining and IoT technologies were used [6]. If 5 limitations can be addressed effectively, 6 are widely recognized as a four contributor to the reduction and increase in consumption and sustainability. The development of Smart Product-Service System (SPSS) in which 8 Smart Connected Products (SCP) play a critical part for the connection of 9 physical components and specialized services to create value, has also been driven by the development of advanced Information and Communication Technology (ICT) [7,21]. Create a multi-layer taxonomy to demonstrate how BT is used in different business models in intelligent city. The article explores the business model and technological aspects of a blockchain-based smart city application. Identify archetypes of BT startups in several areas, including economic sharing, privacy and security, and the Internet (IoT).

Determining whether an application blockchain is legitimate or not. Such apps should solve a business problem that cannot be more efficiently solved with various technology, that has an identifiable actors' network of assets and transactions [8], and that requires the trust of recorded transactions that include properties such as immutability, finality, origin and consensus [9]. Various researchers are keen to undertake research on the subject of cyber-physical systems. We present an overview of several problems with CPS devices in our article, which endanger user security and privacy [10]. On this basis, a secure architecture for CPS applications was developed as a solution to deep learning adoption blockchain. Conceptual discussions on DAM have been presented. Our future studies will be shaped by the implementation and evaluation of the proposed DAM model. As it also places the authorities in a chain of verifiers or certifiers, DAM can be seen as a conceptual approach to the governance of blockchain enabled multi-agent ecosystems [11,12]. The main characteristics, components and functional features of CPS are decentralized consensus approaches. The survey also shared the importance of BC as a facilitator for ensuring faith and validation in the CPS ecosystems. There are three objectives for this type of survey. Initially, the proposed survey will examine the review process systemically based on research issues and quality screening issues [13]. A blockchain-KM protocol, which can accelerate transaction processing without sacrificing the benefits of traditional blockchain. Planed Blockchain-KM protocol transforms the whole private chain to a blockchain, and users are required to mine or lease the wireless spectrum. After a miner has obtained the license for spectrum access, he will send messages over wireless networks. The miner may also auction off the authorization when the miner no longer wants to broadcast messages [14]. This book bridges a gap between sustainable development and CE literature by providing a set of rules on how technology has a role to play in a sustainable society. An essential conflict and problem is how far these emerging technologies' negative environmental effects can be offset by their sustainability advantages.

This study suggests that technological improvements are going to continue to accelerate so that everyone is not able to keep up with the change rate. During the process, many industries already miss the opportunities that data offers because of a lack deficiency and awareness of what data and artificial intelligence may offer [15]. Commercial houses can share the same set of UAVs as blockchain technology that guarantees confidence and openness [16]. A range of UAV security and privacy vulnerabilities and possible blockchain-based solutions have been discovered for addressing these threats [17]. The service function of an intelligent city information management system should first and foremost be highlighted in the CPS architecture. We offer a CPS physical architectural model for the intelligent city based on the architecture framework for service [18]. A Hybrid Smart City Cyber Security Architecture (HSCCA) method is used to investigate threats and to generate safe data. To build a we ensure that crucial variables such as useful data collection, store, retrieval, and a well-organized high-level HSCCA network are taken into consideration [19]. As a result of the blockchain-AI convergence paradigm, the intelligent city sector is changing. It brings together companies, administrations and even countries. Blockchain-AI is known and highly esteemed thanks to its decentralized character and peer-to-peer qualities [20]. Use Telecom Data, Hotspots Extraction and SNA, a method to create a CPSS model on big data platforms. The suggested CPSS model incorporates high-traffic areas in urban centers and incorporates central network features to determine the relevance of each node. This selects the ten most occupied

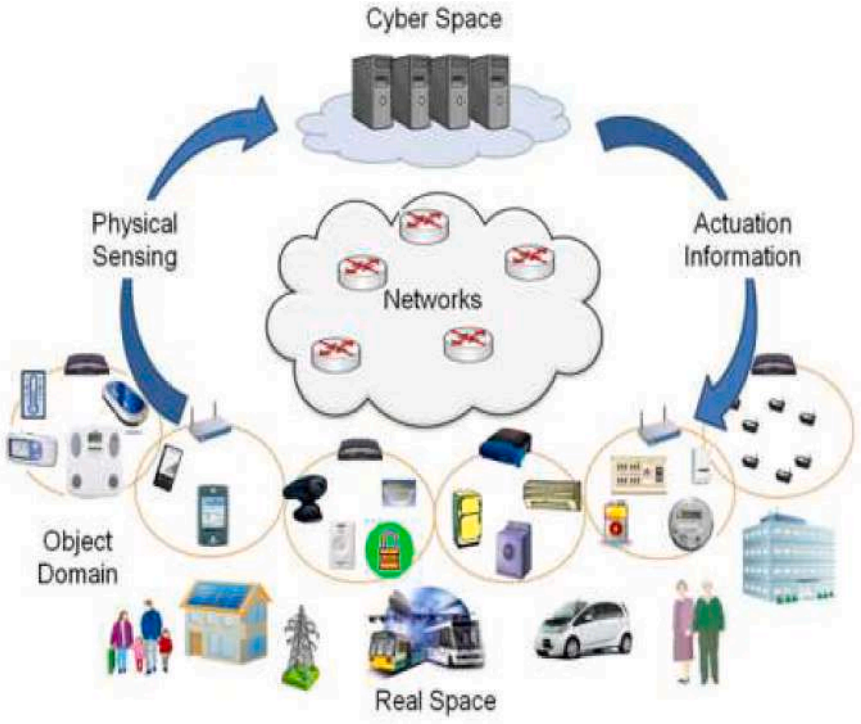

Fig. 1. Block diagram for Cyber - Physical Systems in Blockchain.

regions in a clever city in our proposed model.

2.1. Blockchain limitations

- The use of block size and the time needed to calculate the hash is restricted and therefore does not increase as many devices are connected. • Under some circumstances, transaction charges or some other forms of mineral compensation are necessary.
- The requirements of the blockchain participants in computing and storage are large, as the entire ledger must be stored and participating as endorsers or miners in the transaction verification process.
- Although the concept of a single bank is not as centralized, it relies still on a few large companies, such as miners.

3. Proposed model

A cyber-physical system based on block chains is a mechanism closely linked with the internet and its end users and manages or monitors computerized algorithms. In a cyber-physical system, the physical and software components are tightly integrated, with each working on different temporal and spatial scales. Blockchain technology was initially associated with bitcoin, but in recent years, its potential applications in domains such as smart contracts, logistics, and the administration of multi-actor systems have been investigated. Researchers and developers hope to boost people's trust in both digital and local communities by using the possibilities of Blockchain. Because of its decentralized and open nature, Blockchain systems may easily accomplish this, giving a single source of truth and a single starting point for future initiatives.

3.1. CYBER-PHYSICAL systems (CPS)

Cyber-physical systems are linked together in CPSs to offer crucial services. The smart grid, for example, makes extensive use of data collected from the physical system. The cyber system collects and analyses data, and then uses economic and corrective activities to alter the physical system's operation. Despite the need of integrating cyber and physical systems, the tight coupling of physical and cyber systems introduces new sorts of dangers. When cyber-attacks are involved, on the one hand, the cyber system may have a negative impact on the physical system. Untimely and/or forged directives, for example, may cause damage to the facilities or possibly set off a chain of events. On the other hand, a considerable number of the CPS's key functions rely on precise data and measurements from the physical system. Sensor, device, and communication line failures result in insufficient data, processing delays, and failures to send critical commands. As a result, the physical system's reliability is compromised.

3.1.1. Blockchain applications for cyber-physical systems (CPS)

A cyber-physical system based on Block Chain is one that includes strict coordination and a combination of physical and computer aspects. Intelligence control systems (ICS) and sensor-based systems are two common applications of CPS (SBS). SBS, such as wireless sensor networks and smart building management systems, use a network of dispersed sensors to gather and monitor environmental or system data and send it to a central system for processing. Automatic pilot avionics, distributed robotics, process control systems, smart grid operation, medical monitoring, and autonomous vehicle systems are all examples of ICS. In this subject, the benefits and applications of blockchain technology in cybersecurity are discussed. Fig. 1 illustrates this.

Cyber computing can be used to acquire, regulate and interact more resourcefully with physical infrastructure and systems. The CCI maintains and maintains large physical systems and infrastructures through the Internet of Things (IoT). Cloud computing technology is now integrated into CCI. For instance, in the case of a Smart Health System, people can access and process the medical data they store in the cloud (including medical video and images) through virtual components (machines, server). In addition, patient safety records are collected dynamically and processed in remote diagnostics and mobile health (by means of medical devices and signal processing sensors) before sent for further transmission and analysis to wireless sensor networks.

Governance and smart living: In the infrastructure of living and governance, CPS has a greater role to play. CPS is an open database collection that provides information on several topics from a non-textual

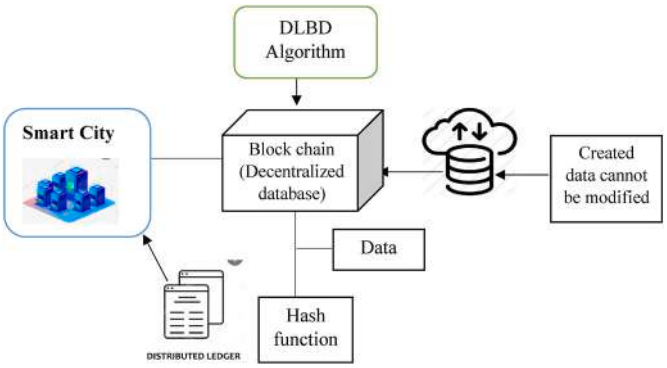

Fig. 2. Distributed ledgers provide a distributed database with nodes.

perspective (biodiversity, weather, geographical, medical, utilities, and so on). This information/data is frequently derived from public administration programmers supported or developed by a public entity that distributes the information/data through social media. Individuals may use open databases to access comprehensive information and information regarding recreation, social services, health, transport and other matters. Governance and living are the two modern fields in which CPS can play an active role. Electronic voting, intelligent water management, smart transit, and smart waste disposal are some of CPS' potential manifestations.

Public Safety System: The CPS has a major impact on progress in the public security sector as part of its efforts. The technological changes that change the interaction between government officials, government agencies and transport fleets mean that interoperability is no longer just a motto; communities' benefit. The country's broadband public safety net, "FirstNet," is the first in its kind, for example. The first one is now the "First Responder Network Authority." Where fully functional, FirstNet includes, besides data transfer, audio, photo and video communication.

A mathematical model for a DSS like this. While it is widely assumed that all models are incorrect, as shown by G.E. Pelham Box, some are beneficial. We hope that the model described in this study will be useful in making decisions. The mathematical model is defined as follows:

$$S = \frac{\sum_{i}^{N} a_i w_i}{N} \tag{1}$$

A sensor plot can be used in some instances, to compare the applicability of the decentralized Distributed Leader based database to different applications such as the university database and the associated car databases, for example, in the mathematical model, a simple numerical output for decision-making. When there are many independent variables, all with different measurement scales, spectrum visualization is very useful.

3.2. *Distributed ledger based decentralized database for cyber-physical*

A distributed ledger is a "record system" duplicated and maintained in sync between several network nodes, without a "master" copy of the directory. More specifically, the ledger is implemented in physical DLT systems as a timed and unchangeable linear record sequence. Only if new records have been validated by pairs of consents to ensure that documents are true and cannot be deleted or withdrawn after commitment can change the sequence. The integrity of records and sequences will be protected by strong cryptographic techniques. In view of the decentralized nature both of the leader and of the consensus mechanism it is only by taking over significant numbers of its kernels - $N/3 + 1$ to $N/2 + 1$ depending on the consensus mechanism, where "N" is the total number of knots - that we can compromise or bring down a "pure DLT.

Because of the components depicted in Fig. 2, Blockchain is able to achieve these qualities. Distributed ledgers provide a distributed database with nodes that form a network link between users. Ledgers, which are ordered lists of transactions with timestamps, reside within these nodes. Only within the database can these ledgers be appended, ensuring a safe mechanism to track transactions without the need for a central authority to verify them. The first generation of Blockchains used a P2P transaction model, which was later replaced by Smart Contracts in the second generation. Smart Contracts are pieces of software that regulate the flow of ledgers between nodes.

4. Experimental result

Our proposed Distributed ledgers (DLBD) approach was tested using the NS 2.35 simulator. Fig. 3 shows the characteristics of the three parameters for DDS and DLBD applications. The total score in all metrics is 0.75, where the above values are plugged into Equation (1), as compared to 0.63 in the connected vehicle data base. The score is 1.0. This framework helps establish the equally suitable decentralized database technique based on distributed headers for either database.

A more primitive approach could take longer and be more

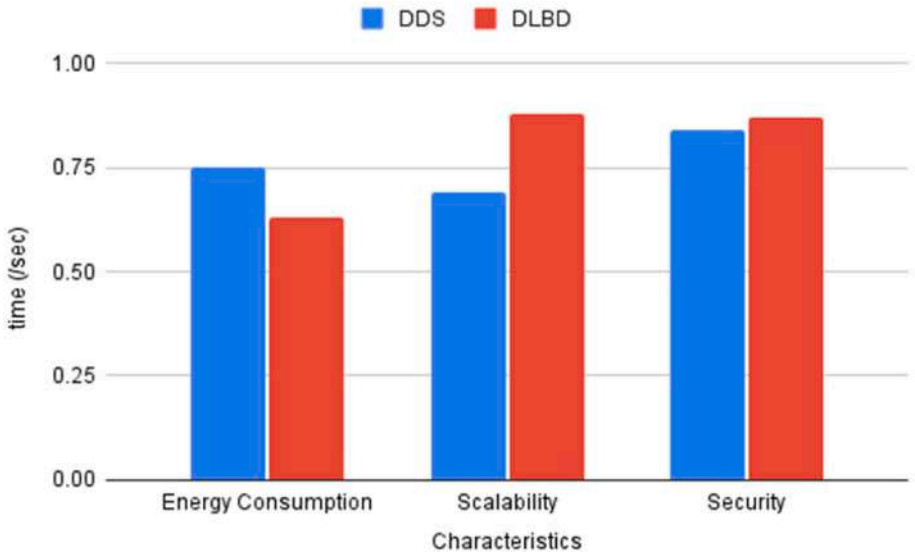

Fig. 3. Performance of DLBD

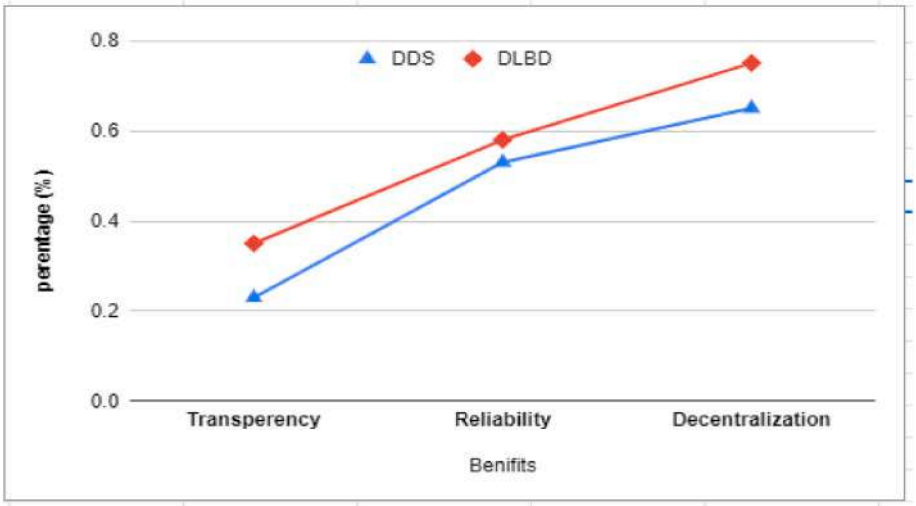

Fig. 4. Benefits of Block chain Technology using ledger based decentralized database.

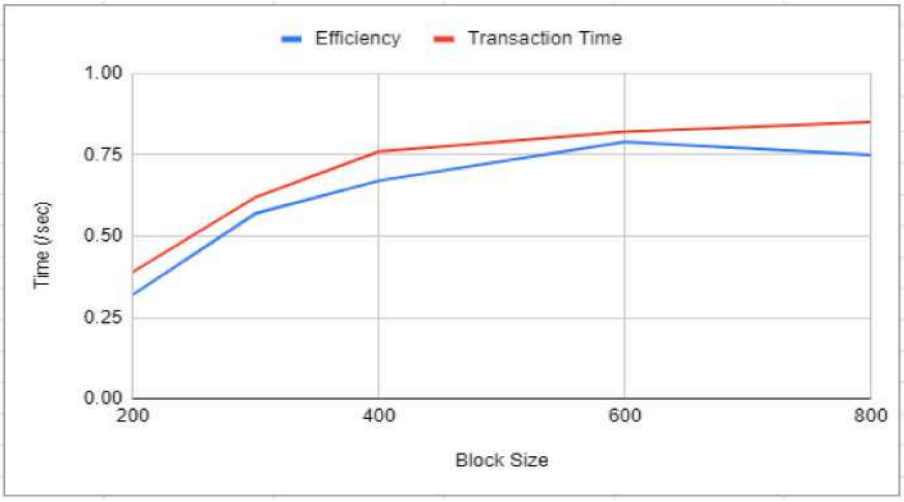

Fig. 5. Block Chain technique is to calculating the efficiency and transaction time.

susceptible to human error. All of this demands the involvement of a third party, as depicted in Fig. 3. By offering a ledger-based decentralized system that allows all users to access the same data, blockchain eliminates the need for several data storage methods. Data will be more easily accessible, and organizational efficiency will be enhanced.

Fig. 4 shows the benefits of block chain technology using ledger based decentralized database. Fig. 5 illustrates how the Block Chain approach calculates efficiency and transaction time, resulting in a higher output result. When compared to other methods, CPS-based Block chain technology provides an effective methodology for increasing efficiency and transaction time.

5. Conclusion

This paper provides CPS with decentralized ledger database techniques like blockchain or are used. CPS are physical world control systems that control and monitor our environment. Blockchain and its inherent combination of consensus algorithms can use distributed data stored on the record and secure protocols in order to build security, scalability, and reliability in such systems. This paper describes how applications, including the smart city, have benefited by distributing the risk of a centralized architecture to validated information across the network. This paper describes the decentralized data base technique used by blockchain technology, a common database built only by adding new data, authenticated users with high encoding, and using economic incentives to promote the administration and safe updating of immigrants. But the future will likely and ultimately lead to intelligence, and cyber-physical cities are closer to reality than ever before.

Declaration of competing interest

The authors declare that they have no known competing financial interests or personal relationships that could have appeared to influence the work reported in this paper.

Data availability

No data was used for the research described in the article.

References

[1] V. Dedeoglu, A. Dorri, R. Jurdak, R.A. Michelin, R.C. Lunardi, S.S. Kanhere, A. F. Zorzo, A Journey in Applying Blockchain for Cyberphysical Systems. 2020 International Conference on COMmunication Systems & NETworkS, COMSNETS), 2020, https://doi.org/10.1109/comsnets48256.2020.9027487.

[2] W. Zhao, C. Jiang, H. Gao, S. Yang, X. Luo, Blockchain-enabled cyber-physical systems: a review, IEEE Internet Things J. 1 (2020), https://doi.org/10.1109/jiot.2020.3014864. –1.
[3] S. Smetana, K. Aganovic, V. Heinz, Food supply chains as cyber-physical systems: a path for more sustainable personalized nutrition, Food Eng. Rev. (2020), https://doi.org/10.1007/s12393-020-09243-y.
[4] D. Berdik, S. Otoum, N. Schmidt, D. Porter, Y. Jararweh, A survey on blockchain for information systems management and security, Inf. Process. Manag. 58 (1) (2021), 102397, https://doi.org/10.1016/j.ipm.2020.102397.
[5] A. Rachana Harish, X.L. Liu, R.Y. Zhong, G.Q. Huang, Log-flock: a blockchain-enabled platform for digital asset valuation and risk assessment in E-commerce logistics financing, Comput. Ind. Eng. (2020), 107001, https://doi.org/10.1016/j.cie.2020.107001.
[6] Clyde Zhengdao Li, Zhe Chen, Xue Fan, TR Kong Xiang, Bing Xiao, Xulu Lai, Yiyu Zhao, A blockchain-and IoT-based smart product-service system for the sustainability of prefabricated housing construction, J. Clean. Prod. 286 (2021), 125391.
[7] Blockchain and distributed ledger technology use cases, in: H. Treiblmaier, T. Clohessy (Eds.), Progress in IS (2020), https://doi.org/10.1007/978-3-030-44337-5.
[8] A.J.M. Milne, A. Beckmann, P. Kumar, Cyber-physical trust systems driven by blockchain, IEEE Access 8 (2020) 66423–66437, https://doi.org/10.1109/access.2020.2984675.
[9] Advanced multimedia and ubiquitous engineering, in: J.J. Park, V. Loia, Y. Pan, Y. Sung (Eds.), Lecture Notes Electrical Eng. (2021), https://doi.org/10.1007/978-981-15-9309-3.
[10] Alper Kanak, Niyazi Ugur, Salih Ergun, Diamond accountability model for blockchain-enabled cyber-physical systems, in: 2020 IEEE International Conference on Human-Machine Systems (ICHMS), IEEE, 2020, pp. 1–5.
[11] U. Bodkhe, D. Mehta, S. Tanwar, P. Bhattacharya, P.K. Singh, W.-C. Hong, A survey on decentralized consensus mechanisms for cyber physical systems, IEEE Access 8 (2020) 54371–54401, https://doi.org/10.1109/access.2020.2981415.
[12] L. Tan, N. Shi, C. Yang, K. Yu, A blockchain-based access control framework for cyber-physical-social system big data, IEEE Access (2020) 1, https://doi.org/10.1109/access.2020.2988951. –1.
[13] X. Fan, Y. Huo, Blockchain based dynamic spectrum access of non-real-time data in cyber-physical-social systems, IEEE Access 8 (2020) 64486–64498, https://doi.org/10.1109/access.2020.2985580.
[14] Behzad Esmaeilian, Joe Sarkis, Kemper Lewis, Sara Behdad, Blockchain for the future of sustainable supply chain management in Industry 4.0, Resour. Conserv. Recycl. 163 (2020), 105064.
[15] D.G. Broo, U. Boman, M. Törngren, Cyber-physical systems research and education in 2030: scenarios and strategies, J. Ind. Inf. Integr. (2020), 100192, https://doi.org/10.1016/j.jii.2020.100192.
[16] T. Alladi, V. Chamola, N. Sahu, M. Guizani, Applications of blockchain in unmanned aerial vehicles: a review, Vehicular Commun. (2020), 100249, https://doi.org/10.1016/j.vehcom.2020.100249.
[17] Recent trends in intelligent computing, communication and devices, in: V. Jain, S. Patnaik, F. Popenţiu Vlădicescu, I.K. Sethi (Eds.), Adv. Intell. Syst. Comput. (2020), https://doi.org/10.1007/978-981-13-9406-5.
[18] S. Sengan, S. V, S.K. Nair, I. V, M. J, L. Ravi, Enhancing cyber-physical systems with hybrid cyber security architecture for secure public data-smart network, Future Generat. Comput. Syst. (2020), https://doi.org/10.1016/j.future.2020.06.028.
[19] S. Singh, P.K. Sharma, B. Yoon, M. Shojafar, G.H. Cho, I.-H. Ra, Convergence of Blockchain and Artificial Intelligence in IoT Network for the Sustainable Smart City, Sustainable Cities and Society, 2020, 102364, https://doi.org/10.1016/j.scs.2020.102364.
[20] A. Jasmine Gnana Malar, C. Agees Kumar, A. Gnana Saravanan, Iot based sustainable wind green energy for smart cites using fuzzy logic based fractional order darwinian particle swarm optimization, Measurement 166 (2020), https://doi.org/10.1016/j.measurement.2020.108208.
[21] Farhan Amin, Gyu Sang Choi, Hotspots analysis using cyber-physical-social system for a smart city, IEEE Access 8 (2020) 122197–122209, https://doi.org/10.1109/ACCESS.2020.3003030.

Chapter 15
Healthcare 5.0: Unveiling the Future of Integrated Medicine

J. Shanthalakshmi Revathy
https://orcid.org/0000-0003-1724-7117
Velammal College of Engineering and Technology, India

J. Mangaiyarkkarasi
https://orcid.org/0000-0003-1431-9584
NMSS Vellaichamy Nadar College, India

ABSTRACT

The chapter explores the transformative shift from traditional to integrated healthcare. It delves into technology, patient empowerment, interdisciplinary collaboration, data-driven decision-making, and preventive healthcare. The role of AI in diagnostics and treatment, along with the use of big data for improved outcomes, resource allocation, and disease surveillance, is highlighted. The chapter advocates for a proactive healthcare model, emphasizing early intervention and ethical considerations. It explores virtual reality and augmented reality's potential in medical practices and discusses the impact of telemedicine on accessible and convenient patient care, especially in underserved areas. This concise overview provides insights into the future of integrated medicine in Healthcare 5.0.

1. INTRODUCTION

In an integrated medical future, individuals become active participants in their own health, and technology acts as an enabler rather than a replacement for interpersonal relationships. A different, innovative and empathetic approach that maintains the principles of Healthcare 5.0 seems, providing the prospect of a community that feels more peaceful, well-being, and joyful. "Healthcare 5.0" is the next stage in development in healthcare, indicating an evolution of paradigms from traditional approaches to a comprehensive, focused on patients approach. Addressing the mind, body, and spirit is vital since true healing extends beyond simply alleviating symptoms. The chapter analyses the core elements of healthcare

DOI: 10.4018/979-8-3693-1874-4.ch015

5.0 by examining the revolutionary roles that artificial intelligence (AI) and machine learning (ML) are playing in changing diagnosis and treatments. It also focuses at the promise of precision medicine, which uses genetic data to personalise care for patients and enhance outcomes (Vale, El-Sharif, and Ali 2022).

The chapter also highlights how important it is to encourage cooperation between technology experts, researchers, and healthcare professionals in order to establish a setting where knowledge and creativity are freely exchanged. Through shedding light on the importance of this cooperative framework, the story reveals how it acts as a driving force behind revolutionary developments in healthcare. By fostering a synergy that breaks through conventional silos, this integrated strategy pushes the sector towards new frontiers of discovery and application.

Furthermore, the investigation explores the crucial function that patient empowerment plays in the Healthcare 5.0 framework. The importance of increased health knowledge and patient involvement in treatment choices is emphasised. In this Healthcare 5.0 vision, the convergence of inclusivity, creativity, and compassion drives medical advancement while simultaneously establishing the groundwork for a society that is not just happier and healthier but also more intricately connected through shared information and well-being.

1.1 Evolution of Healthcare: From Traditional to Integrated Medicine

Strictly focusing on treating certain ailments or symptoms with accepted medical procedures—frequently involving drugs and surgery—was the hallmark of traditional healthcare. With little regard for their general health or lifestyle choices, individuals under this approach sought medical assistance for specific symptoms. An individual with persistent headaches, for example, may be prescribed painkillers by their physician. This treatment targets the symptoms rather than probing deeper into underlying issues like anxiety, inadequate sleep, or malnutrition (Lemmen, Simic, and Stock 2021).

An important trend towards integrated medicine evolved as medical knowledge grew and patient outcomes were examined. This method adopted a more holistic viewpoint, accounting for a patient's emotional health as well as lifestyle, heredity, environment, and other aspects. Rehabilitating individual illnesses became less significant than treating the individual's condition as a whole. A patient with chronic back pain may receive physical therapy, chiropractic care, and stress reduction using mindfulness methods as part of the growing approach. In order improve general well-being, this multifaceted strategy seeks to tackle the underlying causes of pain in addition to just relieving it.

This evolution in healthcare signifies a progression from conventional, isolated medical practices to a cohesive approach that integrates traditional and modern medicine, as depicted in Figure 1. The emphasis is now on a comprehensive understanding of patients and a commitment to addressing health issues at their roots, reflecting a more patient-centered and holistic paradigm.

Alternatively referred to as holistic or integrative medicine, integrated medicine is the combination of evidence-based complementary and alternative therapies with standard medical procedures. Personalised treatment plans, patient empowerment, and active involvement in the healing process are at the centre of this approach. Using cutting-edge diagnostics, genetics, and technology, integrated medicine precisely customises interventions to meet each patient's specific needs.

Imagine an instance in integrated medicine where a patient with cancer receives a customised treatment plan. It incorporates alternative methods like acupuncture, yoga, and meditation with conventional treatments like radiation or chemotherapy in an effortless way. This method places holistic nature seeks to enhance the patient's general state of life as well as their health throughout the duration of therapy, in

Figure 1. Evolution of healthcare: From traditional to integrated medicine

addition to fighting the illness. Thus, integrated medicine embodies a patient-centered philosophy that brings together the best aspects of complementary and traditional medicine to provide a more thorough and customised medical experience.

1.2. Definition and Concept of Healthcare 5.0

The healthcare industry has witnessed a significant and recent transformation as "Healthcare5.0." This places great emphasis on the patient, incorporating advanced technology, collaborative teamwork, and a comprehensive understanding of the patient's well-being. The goal is to seamlessly integrate data-driven technologies, personalized medicine, and patient empowerment to actively involve patients in their healthcare decisions (Seetharaman, Krishnan, and Schneider 2021). By utilizing wearable technology and medical monitoring apps, Healthcare 5.0 continuously collects data on various health indicators, sleep patterns, and activity levels. This data equips healthcare providers with a thorough understanding of the patient's condition, enabling them to tailor their plans accordingly by integrating it into the patient's digital health record.

Healthcare 5.0 is an evolving revolutionary change in the medical field, emphasising a patient-centric strategy that leverages advanced technologies, cooperative collaboration, and an in-depth understanding of the well-being of people. By integrating data-driven technologies, personalised medicine, and allowing patients to take an active role in their medical decisions, it aims to accomplish an easy transition. Employing wearable devices and medical monitoring apps, Health 5.0 gathers real-time data on the health of an individual, sleeping habits, and activity level. Since the fact because this data is integrated into the patient's electronic health record, physicians may use it to gain an in-depth understanding of the patient's condition and adjust their treatment plans accordingly. The idea of Healthcare 5.0 is an enhancement over past healthcare models, emphasising the significance of patient contribution, safeguarding, and welfare as a whole. It makes optimal use of the advantages of AI, ML, and big data in order to improve diagnosis, treatment, and care coordination while encouraging collaboration among healthcare professionals from various disciplines.

Through Healthcare 5.0, patients with chronic diseases such as diabetes can receive personalised treatment programmes that use lifestyle factors, genetic analysis, and data from wearable devices. The patient takes an active role in self-monitoring, makes informed decisions, and consults with physicians

Figure 2. Health industry revolution

virtually through the use of virtual health platforms. Figure 2 illustrates the revolutionary changes and innovations that are reshaping healthcare delivery, technology, and services.

1.3 The Current Gaps in Knowledge or Limitations Identified in the Existing Research

Current healthcare systems often suffer from fragmented data across various platforms and institutions. Seamless data integration and exchange are crucial for comprehensive patient care and analysis but pose significant technological and policy challenges. While AI holds immense potential for personalized medicine and predictive analytics, ethical considerations regarding bias, transparency, and accountability require careful attention. Additionally, existing algorithms may not adequately capture the complexity of individual health factors and social determinants of health. The integration of technology should not overshadow the importance of human connection and patient-centered care. Building trust with patients and ensuring equitable access to these advancements remain crucial challenges. Successfully implementing Healthcare 5.0 requires adapting existing clinical workflows and training healthcare professionals on utilizing new technologies effectively. Resistance to change and the need for robust training programs hinder seamless integration.

Current legal and regulatory frameworks may not adequately address data privacy, ownership, and liability concerns with advanced healthcare technologies. Adapting these frameworks to ensure ethical and responsible implementation is essential. Implementing and maintaining sophisticated Healthcare 5.0 infrastructure and technologies can be expensive. Equitable access and affordability for resource-constrained settings require innovative solutions and partnerships. Many aspects of Healthcare 5.0 remain theoretical or in early stages of development. Rigorous research and robust clinical trials are necessary to validate the efficacy and safety of these technologies before widespread adoption. Healthcare 5.0 must go beyond individual-level interventions and address the broader social, economic, and environmental factors that impact health outcomes. Integrating social determinants of health into the framework is crucial for achieving true health equity. The healthcare landscape is constantly evolving, requiring Healthcare 5.0 systems to be adaptable and capable of learning from new data and emerging technologies. Building adaptive frameworks for continuous improvement is essential for long-term sustainability.

1.4 Purpose and Scope of the Chapter

This chapter's goal is to examine and clarify the healthcare industry's revolutionary transition from conventional methods to the integrated approach of Healthcare 5.0. The chapter seeks to emphasise the importance of patient-centric care, technological integration, and collaboration in influencing the future of healthcare by looking at the major turning points and conceptual framework.

Historical overview: This chapter will give a general account of how healthcare has changed throughout time, showing how old techniques gave way to integrated medicine.

Integrated Medicine: Extensive explanations of the ideas and methods of integrated medicine, emphasising its patient-centered methodology and providing instances of effective integrative treatment in the actual world.

The concept of Healthcare 5.0 and its essential components—such as the use of contemporary technologies, patient empowerment, and precision medicine—are described.

Applications in real time: demonstrating the impact of Healthcare 5.0 on patient outcomes and experiences while demonstrating its real-time use in a variety of healthcare contexts.

Future Consequences: talking about how Healthcare 5.0 might affect public health programmes, research, and healthcare delivery in the future.

Through an exploration of these facets, the chapter aims to offer a thorough comprehension of the development of healthcare and the revolutionary possibilities of Healthcare 5.0 in moulding a more effective, patient-focused, and cohesive healthcare framework.

2. FOUNDATIONS OF HEALTHCARE 5.0

Healthcare 5.0 denotes a revolutionary epoch in medical history, where patient-centered care, multidisciplinary collaboration, and state-of-the-art technologies combine to determine the future course of healthcare delivery. This chapter delves into the fundamental ideas of Healthcare 5.0, highlighting the significance of interdisciplinary collaboration and the transformative power of technological advancements in driving this ground-breaking paradigm shift.

2.1 Interdisciplinary Collaboration in Healthcare

The integration of various medical professions and specialists is depicted in Figure 3 as a means of improving patient care through all-encompassing and holistic approaches.

2.1.1 Collaborative Approach in Healthcare Delivery

Patient care was often fragmented in traditional healthcare since medical specialists typically worked independently in inflexible silos. Healthcare 5.0, on the other hand, encourages multidisciplinary cooperation and collaboration and brings together healthcare professionals from many specialties to work together to collaboratively address patient requirements. Dismantling divisions improves communication and information flow, which improves decision-making and patient outcomes (Johnson et al. 2021). An example of a collaborative healthcare setting involves a team of primary care physicians, endocrinologists, cardiologists, mental health specialists, and nutritionists treating a patient with multiple chronic

Figure 3. Multidisciplinary cooperation in the medical field

illnesses, such as diabetes, hypertension, and depression. The team works together to develop a comprehensive care plan that considers all aspects of the patient's health, leading to improved quality of life and more effective management.

2.1.2 Integration of Medical Disciplines for Comprehensive Care

Healthcare 5.0 places a strong emphasis on the integration of medical specializations in recognition of the human body's complexity as a networked system. This integration enables a comprehensive picture of a patient's condition, leading to more accurate diagnoses and customised treatment plans. Healthcare 5.0 integrates evidence-based alternative and complementary therapies with standard medicine to promote overall wellbeing and patient empowerment (Mehrabi et al. 2019). A patient with chronic pain may benefit from an integrated approach that combines pain management techniques like physical therapy and medicine with complementary therapies like acupuncture and meditation for stress reduction. This comprehensive therapy plan of action addresses emotional and psychological issues in addition to the physical causes of pain, leading to improved pain alleviation and general health.

2.2 Technological Advancements in Healthcare 5.0

2.2.1 Artificial Intelligence and Machine Learning

AI and ML, you know, are crucial elements in Healthcare 5.0 that change a lot of aspects of healthcare delivery. Therefore, these tools analyze massive amounts of data, identify patterns in the data, and provide meaningful information for customized treatment plans, early sickness detection, and improved patient outcomes. Additionally, AI-powered diagnostic tools and decision support systems have made it possible for healthcare workers to make clinical decisions more rapidly and accurately. For example, AI systems are completely capable of analyzing medical images, such as MRIs and X-rays, to assist radiologists in more precisely identifying irregularities. Additionally, medical teams can anticipate patient readmission risk by utilizing machine learning (ML) models.

2.2.2 Internet of Things (IoT) in Healthcare

The Internet of Things (IoT) consists of networked sensors and gadgets that gather and share data. IoT-enabled wearables and medical devices enable patients to track their health in real-time in Healthcare 5.0, enabling remote patient monitoring and early health issue detection. By giving medical professionals access to vital patient data, these gadgets enhance treatment efficiency and coordination (Beede et al. 2020). For instance, IoT-enabled glucose monitors can provide information to healthcare practitioners while continuously monitoring the blood sugar levels of diabetic patients. This makes it possible for medical staff to remotely track changes in blood sugar levels and promptly intervene or modify a patient's treatment regimen. The networked integration of medical systems and devices, shown in Figure 4, allows for data sharing and remote monitoring to enhance patient outcomes and healthcare productivity.

2.2.3 Big Data Analytics and Predictive Modelling

Large-scale databases are tapped into using big data analytics in Healthcare 5.0 to find trends, patterns, and correlations that guide evidence-based medical decisions. Forecasting illness patterns, identifying patient populations at high risk, and allocating resources optimally in healthcare institutions are all made possible by predictive modeling. For instance, big data analytics can forecast the occurrence of disease outbreaks, like flu epidemics, by analyzing demographic information, electronic health records, and environmental factors. Public health authorities can use this information to strategically allocate medical resources and put preventive measures into place.

2.2.4 Telemedicine and Virtual Care

In Healthcare 5.0, telemedicine and virtual care have become increasingly popular, particularly in the wake of the COVID-19 epidemic. By facilitating virtual diagnosis, digital health monitoring, and remote consultations, these technologies increase access to healthcare services while lessening the strain on traditional healthcare facilities. Example: Using a virtual telemedicine platform, a patient in a remote

Figure 4. Internet of things (IoT) in healthcare

location can consult with a specialist in a nearby city. This eliminates the need for the patient to make lengthy trips by giving them rapid access to professional medical advice.

2.2.5 Wearable Devices and Remote Patient Monitoring

In Healthcare 5.0, wearable technology has gained popularity as it enables patients to continuously monitor their health parameters. By keeping an eye on vital signs, exercise, sleep habits, and other health indicators, these gadgets help patients and medical professionals address diseases early on. An illustration of this would be a patient with heart disease who wears a smartwatch to track heart rhythm and rate. The patient's medical team receives an alert from the gadget if it notices any abnormalities, which triggers timely follow-up care to avoid any complications.

These fundamental components spur innovation and revolutionize healthcare delivery as Healthcare 5.0 develops. While technological innovations empower patients and healthcare providers to make informed decisions, enhance outcomes, and build a more connected and patient-centric healthcare ecosystem, interdisciplinary teamwork assures a holistic approach to patient care (van Berkel, Sarsenbayeva, and Goncalves 2023). By embracing these pillars, Healthcare 5.0 has the ability to transform contemporary medicine and improve people's quality of life everywhere. In Figure 5, real-time medical data is provided and health metrics are tracked through the use of portable devices, which improves patient participation and allows for proactive healthcare management.

3. KEY COMPONENTS OF HEALTHCARE 5.0

Healthcare 5.0 embodies a patient-centric approach that leverages cutting-edge technology and interdisciplinary collaboration to transform the landscape of healthcare. This chapter delves into the core components of Healthcare 5.0, highlighting the significance of personalized and precision medicine, patient-centered care, prevention, and care coordination to optimize patient outcomes and improve overall well-being.

Figure 5. Wearable devices and remote patient monitoring

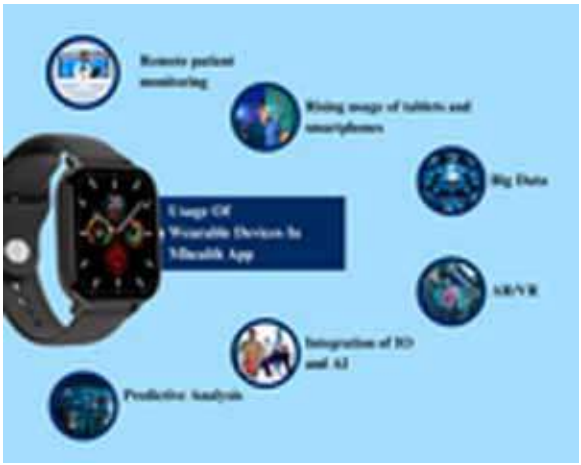

3.1 Personalized and Precision Medicine

3.1.1 Genomic Medicine and Targeted Therapies

In Healthcare 5.0, genomic medicine plays a pivotal role in tailoring treatments based on a patient's genetic makeup. Advancements in genomic sequencing enable healthcare providers to identify specific genetic variations that influence disease susceptibility, response to medications, and disease progression. Targeted therapies focus on addressing these genetic anomalies, maximizing treatment efficacy, and minimizing adverse effects. *Example:* In the case of certain cancers, genomic profiling of the tumor can reveal specific genetic mutations. Targeted therapies can then be prescribed to inhibit the growth of cancer cells with precision, sparing healthy cells and improving treatment outcomes (Wazid, Das, et al. 2022).

3.1.2 Biomarkers and Diagnostic Advancements

Healthcare 5.0 incorporates biomarkers as valuable tools for early disease detection, risk assessment, and treatment monitoring. Biomarkers are measurable indicators that provide insights into a patient's health status at the molecular level. Diagnostic advancements, such as liquid biopsies and novel imaging techniques, aid in the identification of biomarkers, enabling early interventions and personalized treatment strategies. *Example:* Biomarker testing in cardiovascular disease helps identify patients at high risk of heart attacks. This allows healthcare professionals to implement preventive measures, such as lifestyle modifications and medication, to reduce the risk of adverse cardiac events. Figure 6 involves tailoring medical treatments and interventions to individual characteristics, genetics, and health profiles, optimizing effectiveness and minimizing side effects.

3.2 Patient-Centered Care and Shared Decision-Making

3.2.1 Empowering Patients in Their Healthcare Journey

Healthcare 5.0 emphasizes the empowerment of patients as active participants in their healthcare journey. Patient-centered care recognizes the unique needs, values, and preferences of individuals, fostering a collaborative partnership between patients and healthcare providers. Patients are encouraged to take ownership of their health, make informed decisions, and actively engage in shared decision-making.

Figure 6. Personalized and precision medicine

Example: Through patient-centered care, a diabetic patient is involved in setting personalized treatment goals, choosing appropriate medication options, and deciding on lifestyle modifications. This approach fosters adherence to the treatment plan and enhances overall treatment success (Wazid, Bera, et al. 2022).

3.2.2 Shared Decision-Making Tools and Patient Education

Healthcare 5.0 integrates shared decision-making tools and patient education resources to facilitate informed choices and enhance health literacy. Decision aids, educational materials, and interactive platforms empower patients to understand their health conditions, available treatment options, and potential risks and benefits, enabling them to make well-informed decisions. *Example:* A shared decision-making tool for prostate cancer treatment options presents patients with detailed information about surgery, radiation therapy, and active surveillance. With this knowledge, the patient can collaboratively decide on the most suitable treatment based on their preferences and priorities. Figure 7 illustrates the process of involving patients in medical choices by providing them with information, resources, and interactive tools to make informed decisions aligned with their preferences and values.

3.3 Prevention and Wellness Promotion

3.3.1 Focus on Proactive and Preventive Measures

Healthcare 5.0 shifts the focus from reactive treatment to proactive prevention. Preventive measures, such as vaccinations, screenings, and lifestyle interventions, are prioritized to identify and address health risks before they escalate into chronic conditions. By emphasizing prevention, Healthcare 5.0 aims to reduce the burden of disease and improve overall population health. *Example:* Immunization programs prevent the spread of infectious diseases, such as measles and influenza. By vaccinating individuals, Healthcare 5.0 contributes to herd immunity, protecting vulnerable populations and reducing the occurrence of outbreaks.

Figure 7. Shared decision-making tools and patient education

3.3.2 Integrating Lifestyle Medicine and Behavioural Health

Healthcare 5.0 recognizes the crucial role of lifestyle factors and behavioural health in maintaining overall well-being. Lifestyle medicine interventions, including nutrition counselling, exercise prescriptions, and stress management, are incorporated into patient care plans to support health promotion and disease prevention. *Example:* A patient at risk of developing type 2 diabetes receives lifestyle medicine counselling, including dietary recommendations and physical activity plans. These interventions empower the patient to make positive lifestyle changes, potentially preventing or delaying the onset of diabetes. Figure 8 outlines strategies, interventions, and education aimed at proactively maintaining and improving individuals' health, reducing the risk of diseases, and enhancing overall well-being.

3.4 Continuum of Care and Care Coordination

3.4.1 Seamless Transition Across Healthcare Settings

Healthcare 5.0 prioritizes the seamless transition of patients across different healthcare settings to ensure continuous and coordinated care. Effective care coordination involves clear communication between healthcare providers, smooth transitions from hospital to home or rehabilitation facilities, and the integration of services to avoid gaps in care (Rahman et al. 2023). *Example:* A patient undergoing hip replacement surgery receives coordinated care from the hospital team, the physical therapist, and the home health nurse during post-operative recovery. This integrated approach supports the patient's successful rehabilitation and reduces the risk of complications.

3.4.2 Integrated Electronic Health Records and Interoperability

Healthcare 5.0 leverages electronic health records (EHRs) to consolidate patient information, ensuring healthcare providers have access to comprehensive medical histories, test results, and treatment plans. Interoperability allows EHRs to seamlessly exchange information between different healthcare systems, enhancing care coordination and reducing redundancies. *Example:* With interoperable EHRs, a patient's

Figure 8. Prevention and wellness promotion

primary care physician can easily access the medical records from a recent hospital visit, facilitating informed decision-making and providing comprehensive care. Figure 9 depicts the seamless sharing and exchange of patient health information across different healthcare systems and providers, enabling comprehensive and coordinated care while maintaining data accuracy and privacy.

4. BENEFITS AND IMPACTS OF HEALTHCARE 5.0

Healthcare 5.0 represents a transformative approach to medicine, harnessing advanced technologies and patient-centered practices to revolutionize healthcare delivery. This chapter explores the far-reaching benefits and impactful outcomes of Healthcare 5.0, ranging from improved health outcomes and enhanced patient experiences to more efficient and cost-effective healthcare delivery. Figure 10 illustrates the transformative effects of the fifth wave of healthcare evolution, characterized by patient-centric care, advanced technologies, data-driven insights, and improved outcomes, ultimately leading to enhanced patient experiences and population health.

4.1 Improved Health Outcomes

4.1.1 Early Disease Detection and Prevention

One of the significant benefits of Healthcare 5.0 is the early detection and prevention of diseases. Through the integration of advanced diagnostics, predictive modelling, and patient monitoring technologies, Healthcare 5.0 enables healthcare providers to identify health risks and diseases at their earliest stages. Timely interventions allow for early treatment, preventing the progression of diseases and reducing long-term complications.

Impact: Early detection of conditions such as cancer, cardiovascular diseases, and diabetes can lead to more successful treatment outcomes, increased survival rates, and improved quality of life for patients.

Figure 9. Integrated electronic health records and interoperability

Figure 10. Benefits and impacts of Healthcare 5.0

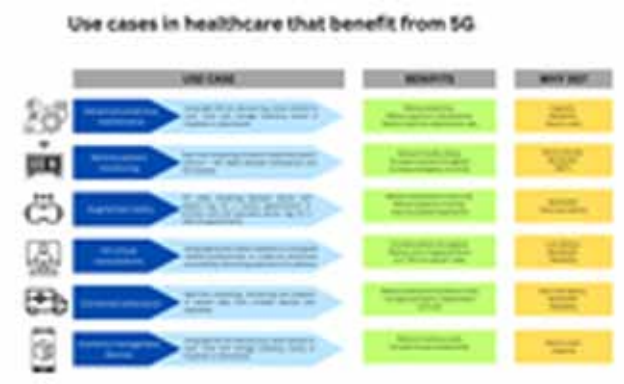

4.1.2 Enhanced Treatment Outcomes and Reduced Complications

Healthcare 5.0 leverages personalized and precision medicine to tailor treatments based on an individual's unique characteristics. By integrating genomic medicine, targeted therapies, and biomarker-driven approaches, Healthcare 5.0 optimizes treatment efficacy and minimizes adverse effects. Additionally, patient-centered care and shared decision-making ensure that treatment plans align with patients' preferences and needs, resulting in improved treatment adherence and outcomes (Paterick et al. 2017).

Impact: Enhanced treatment outcomes translate to reduced hospital readmissions, lower healthcare costs, and improved overall patient well-being.

4.2 Enhanced Patient Experience and Engagement

The table 1 outlines how modern healthcare practices and technologies contribute to improving the overall patient experience and engagement.

Table 1. Enhanced patient experience and engagement

Factors	Patient Engagement	Patient Experience
Goals	Drive better health and outcomes. Empower patients and loved ones to be active in their own care. Reduce costs.	Drive better health and outcomes. Exceed expectations. Reduce suffering. Brand differentiation.
Stakeholders	Patient, likely others.	Patient, likely others.
Context	Patient's own health.	All-encompassing (access communication, food, etc.)
Patent involvement (Behaviors and ownership)	Required	Not required (through in an ideal experience, patient are partners and co-designers)
Time	Patient, likely others	Transactional and Longitudinal
Use of health self-management tool/services	Yes	No
Validated measurement	Patient Activation Measure (PAM) PROMIS, Patient Health Engagement (PHE) Scale	HCAHPS, CGCAHPS, etc.

4.2.1 Accessible and Convenient Healthcare Services

Healthcare 5.0 embraces telemedicine, virtual care, and remote patient monitoring, enabling patients to access healthcare services conveniently from their homes or remote locations. Virtual consultations and digital health platforms eliminate geographical barriers and reduce wait times, ensuring patients receive timely medical attention.

Impact: Increased accessibility and convenience result in higher patient satisfaction, improved healthcare utilization, and better adherence to treatment plans.

4.2.2 Empowered Patients in Managing Their Health

Healthcare 5.0 places patients at the center of their healthcare journey, fostering patient empowerment and engagement. Through shared decision-making, patient education, and health monitoring tools, patients are actively involved in making informed choices about their health and treatment options. This collaborative approach promotes self-management and encourages patients to take ownership of their well-being.

Impact: Empowered patients are more likely to comply with treatment regimens, adopt healthier lifestyles, and proactively manage chronic conditions, leading to better health outcomes and reduced healthcare utilization.

4.3 Efficient and Cost-Effective Healthcare Delivery

4.3.1 Streamlined Care Processes and Reduced Inefficiencies

Healthcare 5.0 optimizes care delivery through interoperable electronic health records, AI-driven diagnostics, and care coordination platforms. These technologies streamline care processes, reducing administrative burdens and eliminating redundant procedures. Additionally, interdisciplinary collaboration promotes efficient communication among healthcare teams, ensuring a coordinated approach to patient care.

Impact: Streamlined care processes improve healthcare provider productivity, reduce wait times for patients, and enhance overall healthcare system efficiency.

4.3.2 Optimal Resource Utilization and Healthcare Expenditure

Healthcare 5.0 emphasizes prevention and proactive interventions, reducing the burden of disease on healthcare systems. By identifying high-risk populations and implementing preventive measures, Healthcare 5.0 reduces the need for costly treatments and hospitalizations. Moreover, personalized medicine and targeted therapies lead to better treatment efficacy, reducing wasteful spending on ineffective treatments (O'Regan et al. 2008).

Impact: Optimal resource utilization results in cost savings for healthcare institutions and payers, allowing for reinvestment in improved patient care and technological advancements.

In conclusion, the benefits and impacts of Healthcare 5.0 are far-reaching, transforming healthcare delivery across the globe. Improved health outcomes through early disease detection and precision medicine, enhanced patient experiences, and engagement through accessible healthcare services, and efficient,

cost-effective care delivery are the hallmarks of Healthcare 5.0. By leveraging advanced technologies and patient-centric practices, Healthcare 5.0 represents the future of medicine, promising better health and well-being for individuals and societies as a whole.

5. CHALLENGES AND CONSIDERATIONS IN IMPLEMENTING HEALTHCARE 5.0

Healthcare 5.0 represents a promising future for healthcare, but its successful implementation comes with several challenges and considerations. This chapter explores the critical obstacles and factors that must be addressed to realize the full potential of Healthcare 5.0.

5.1 Ethical and Legal Implications

5.1.1 Privacy and Security of Patient Data

With the integration of advanced technologies and interconnected devices, patient data becomes more vulnerable to breaches and cyberattacks. Healthcare 5.0 must prioritize robust data security measures to protect sensitive patient information. Balancing data accessibility for medical research and treatment purposes with patient privacy rights poses a significant ethical challenge.

Consideration: Implementing strict data encryption, access controls, and regular security audits can safeguard patient data while complying with privacy regulations such as HIPAA.

5.1.2 Ethical Considerations in Using AI and IoT in Healthcare

Healthcare 5.0 relies heavily on AI and IoT, raising ethical concerns regarding algorithm transparency, bias, and accountability. Decisions made by AI systems in diagnosis and treatment plans must be explainable and understandable by healthcare professionals and patients. Ensuring that AI models are fair and do not perpetuate existing biases is crucial.

Consideration: Ethical frameworks and guidelines for the responsible use of AI and IoT in healthcare need to be established, and healthcare professionals should be involved in the development and validation of AI algorithms.

5.2 Workforce Readiness and Training

5.2.1 Preparing Healthcare Professionals for Integrated Care

Healthcare 5.0 demands a shift in the roles and responsibilities of healthcare professionals. Interdisciplinary collaboration and patient-centered care require effective communication and teamwork skills. Training healthcare professionals to work effectively in a multidisciplinary environment may pose challenges due to differing education backgrounds and institutional cultures (Mbunge, Jiyane, and Muchemwa 2022).

Consideration: Integrating interprofessional education into medical training and providing ongoing professional development opportunities can prepare healthcare professionals for collaborative care.

5.2.2 Upskilling and Adapting to Technological Advancements

As Healthcare 5.0 incorporates advanced technologies, the workforce needs to be proficient in leveraging these tools effectively. Some healthcare professionals may face challenges in adopting new technologies or may fear the displacement of traditional roles.

Consideration: Offering continuous training and support in using healthcare technologies can help healthcare professionals embrace innovations and enhance their technological fluency.

5.3 Infrastructure and Interoperability

5.3.1 Integration of Healthcare Systems and Data Sharing

Healthcare 5.0 requires seamless integration and interoperability among different healthcare systems, electronic health records, and medical devices. Legacy systems and proprietary formats may hinder data exchange and collaboration among healthcare providers.

Consideration: Investing in interoperable health IT solutions and fostering industry-wide data exchange standards can facilitate smoother data sharing and continuity of care.

5.3.2 Standardization and Interoperability Challenges

Healthcare 5.0 involves the integration of various technologies, which may use different data formats and standards. Achieving full interoperability among these technologies poses technical challenges and requires cooperation between vendors and healthcare institutions. Encouraging industry collaboration and promoting the adoption of international standards, such as HL7 and FHIR, can foster interoperability and data sharing (Maxhelaku and Kika 2019).

The implementation of Healthcare 5.0 faces several challenges, ranging from ethical and legal concerns surrounding data privacy and AI usage to the need for workforce readiness and training. Infrastructure and interoperability challenges also play a crucial role in realizing the full potential of integrated medicine and advanced technologies. Addressing these challenges requires a collaborative effort from healthcare stakeholders, policymakers, and technology providers to ensure that Healthcare 5.0 can effectively transform healthcare delivery, improve patient outcomes, and promote a more patient-centric and connected healthcare ecosystem.

6. CASE STUDIES AND EXEMPLARY MODELS OF HEALTHCARE 5.0

Healthcare 5.0 has witnessed successful implementations across various healthcare settings, showcasing the transformative power of integrated medicine and advanced technologies. This chapter examines exemplary models and real-world case studies that exemplify the principles and benefits of Healthcare 5.0.

6.1 Successful Implementations of Integrated Medicine

6.1.1 Collaborative Healthcare Networks and Accountable Care Organizations

Case Study: Geisinger Health System

Geisinger Health System, based in Pennsylvania, USA, is a pioneering example of an integrated health network that embodies the principles of Healthcare 5.0. Geisinger focuses on value-based care delivery through its ProvenCare® program, which utilizes evidence-based clinical pathways and interdisciplinary care teams to optimize patient outcomes(Lampley and Therrien 2023).

Impact: Geisinger's ProvenCare® program has shown remarkable results in reducing complications, readmissions, and overall healthcare costs for specific conditions, such as heart failure and joint replacement surgeries.

6.1.2 Integrated Health Systems and Population Health Management

Case Study: Kaiser Permanente

Kaiser Permanente, a large integrated health system in the United States, emphasizes population health management through its comprehensive approach to patient care. The organization leverages EHRs, data analytics, and care coordination to proactively identify health risks, manage chronic conditions, and promote preventive measures among its patient population (Nathaniel et al. 2021).

Impact: Kaiser Permanente's population health management approach has led to improved health outcomes, reduced hospitalizations, and better patient engagement, contributing to higher patient satisfaction rates.

6.2. Real-World Examples of Healthcare 5.0 in Action

6.2.1 Remote Patient Monitoring for Chronic Disease Management

Case Study: University of Mississippi Medical Center (UMMC)

UMMC implemented a remote patient monitoring program for patients with chronic conditions, such as hypertension, diabetes, and heart failure. Patients use wearable devices and IoT-enabled health monitoring tools to transmit vital data, such as blood pressure, blood glucose levels, and weight, to healthcare providers in real-time. Healthcare teams use this data to track patients' health status and intervene promptly if any abnormalities are detected (Peyroteo et al. 2021).

Impact: The remote patient monitoring program at UMMC has led to improved patient adherence to treatment plans, early detection of health issues, and reduced hospitalizations among chronic disease patients.

6.2.2 AI-Powered Clinical Decision Support Systems

Case Study: IBM Watson for Oncology

IBM Watson for Oncology is an AI-powered clinical decision support system that assists oncologists in formulating personalized cancer treatment plans. The system analyzes vast amounts of medical literature, clinical trial data, and patient records to provide evidence-based treatment recommendations aligned with the patient's specific cancer type, stage, and genetic profile (Somashekhar et al. 2017).

Impact: IBM Watson for Oncology has demonstrated its ability to assist oncologists in making more informed treatment decisions, potentially expanding treatment options, and improving patient outcomes.

These case studies and exemplary models demonstrate the successful implementation of Healthcare 5.0 principles in real-world healthcare settings. Collaborative healthcare networks, integrated health systems, remote patient monitoring, and AI-powered clinical decision support systems showcase the transformative potential of integrated medicine and technology in improving patient care, enhancing outcomes, and optimizing healthcare delivery. As more healthcare organizations and institutions embrace Healthcare 5.0, the potential for positive impact on patient well-being and the future of medicine continues to grow.

7. FUTURE DIRECTIONS AND OUTLOOK

Healthcare 5.0 holds immense potential to revolutionize the healthcare landscape and improve patient outcomes. As the field continues to evolve, several anticipated advancements and societal implications are likely to shape the future of Healthcare 5.0.

7.1 Anticipated Advancements in Healthcare 5.0

7.1.1 Genomic Medicine and Personalized Therapeutics

Genomic medicine is expected to become increasingly prevalent in Healthcare 5.0. Advancements in genetic sequencing technologies and bioinformatics will enable more comprehensive and affordable genome profiling. As a result, personalized therapeutics tailored to an individual's genetic makeup will become more commonplace, optimizing treatment efficacy and minimizing adverse effects(Streeter, Beron, and Iyer 2017).

Anticipated Impact: Personalized therapeutics will lead to more precise and targeted treatments for various diseases, increasing treatment success rates and enhancing patient quality of life.

7.1.2 Advancements in AI and Machine Learning Applications

AI and machine learning will continue to drive significant advancements in Healthcare 5.0. AI-powered diagnostic tools, predictive modeling, and decision support systems will become more sophisticated and accurate, empowering healthcare professionals with data-driven insights. Additionally, AI-driven robotics and automation may enhance surgical precision and streamline administrative processes.

Anticipated Impact: AI advancements will improve diagnostic accuracy, streamline healthcare workflows, and potentially alleviate healthcare workforce shortages, leading to more efficient and cost-effective healthcare delivery.

7.2 Societal Impact and Implications

7.2.1 Accessible Healthcare for Underserved Populations

Healthcare 5.0 has the potential to address healthcare disparities and improve accessibility for underserved populations. Telemedicine and virtual care platforms can bridge the gap between patients and healthcare providers in remote or rural areas. Moreover, AI-driven diagnostics and point-of-care technologies may enhance early disease detection and treatment in resource-limited settings.

Anticipated Impact: Improved accessibility to healthcare services can lead to better health outcomes and reduced healthcare disparities among marginalized communities.

7.2.2 Redefining the Role of Healthcare Professionals

Healthcare 5.0 will reshape the roles and responsibilities of healthcare professionals. With the integration of AI and automation, routine tasks may be delegated to technology, allowing healthcare professionals to focus on more complex and patient-centric aspects of care. Emphasizing patient education and empowerment will further shift the role of healthcare professionals from being purely authoritative to collaborative partners in patients' health journeys.

Anticipated Impact: Redefining the role of healthcare professionals will enhance patient engagement, improve communication, and foster stronger therapeutic relationships.

In conclusion, the future of Healthcare 5.0 holds exciting possibilities with anticipated advancements in genomic medicine, AI applications, and personalized therapeutics. As these technologies mature and become more accessible, healthcare delivery is expected to become more precise, efficient, and patient-centered (Xu, Wermus, and Bauman 2011). Moreover, the societal impact of Healthcare 5.0 is poised to extend accessibility to healthcare services for underserved populations and redefine the roles of healthcare professionals, enhancing patient care and well-being across the globe. By embracing the principles of integrated medicine and leveraging cutting-edge technologies, Healthcare 5.0 is poised to shape a more connected, efficient, and patient-centric healthcare ecosystem in the years to come.

8. CONCLUSION

This book chapter provides a comprehensive exploration of Healthcare 5.0, envisioning a transformative future for healthcare delivery through integrated medicine. The evolution from traditional practices to patient-centric care and interdisciplinary collaboration characterizes this paradigm shift. Anchored in personalized and precision medicine, patient-centered care, prevention, and care coordination, Healthcare 5.0 empowers patients, optimizes treatment outcomes, and enhances proactive health management. The paradigm offers numerous benefits, including improved health outcomes via early disease detection and precision medicine, enriched patient experiences, and efficient, cost-effective healthcare delivery. However, challenges such as ethical, legal, workforce, and infrastructure considerations must be navigated

for successful integration. Real-world case studies showcasing collaborative networks, remote patient monitoring, and AI-driven clinical decision support systems underscore the potential of merging medicine and technology in Healthcare 5.0's success.

Envisioning the future of integrated medicine within the Healthcare 5.0 framework anticipates transformative advancements in healthcare. This future encompasses precise personalized treatments through genomic medicine and AI, patient empowerment fostering accessible care, collaborative healthcare professional efforts integrating AI, telemedicine, and data sharing, a holistic approach emphasizing well-being, and efficient, cost-effective healthcare via technology-driven solutions and coordinated care. Ultimately, Healthcare 5.0 embodies a patient-centered, collaborative, and technology-empowered paradigm poised to revolutionize healthcare, promising enhanced patient outcomes, inclusivity, and a more interconnected and streamlined healthcare landscape, with the potential to shape a healthier and empowered society.

REFERENCES

Beede, E. (2020). A Human-Centered Evaluation of a Deep Learning System Deployed in Clinics for the Detection of Diabetic Retinopathy. In *Proceedings of the 2020 CHI Conference on Human Factors in Computing Systems* (pp. 1–12). ACM. doi:10.1145/3313831.3376718

Johnson, K. B., Wei, W.-Q., Weeraratne, D., Frisse, M. E., Misulis, K., Rhee, K., Zhao, J., & Snowdon, J. L. (2021). Precision Medicine, AI, and the Future of Personalized Health Care. *Clinical and Translational Science*, *14*(1), 86–93. doi:10.1111/cts.12884 PMID:32961010

Lampley, K., & Therrien, N. (2023). *Geisinger Ambulatory Pharmacy Care Program Field Notes.* https://stacks.cdc.gov/view/cdc/126232

Lemmen, C., Simic, D., & Stock, S. (2021). A Vision of Future Healthcare: Potential Opportunities and Risks of Systems Medicine from a Citizen and Patient Perspective—Results of a Qualitative Study. *International Journal of Environmental Research and Public Health*, *18*(18), 9879. doi:10.3390/ijerph18189879 PMID:34574802

Lilhore, U. K., Dalal, S., Faujdar, N., Margala, M., Chakrabarti, P., Chakrabarti, T., Simaiya, S., Kumar, P., Thangaraju, P., & Velmurugan, H. (2023). Hybrid CNN-LSTM model with efficient hyperparameter tuning for prediction of Parkinson's disease. *Scientific Reports*, *13*(1), 14605. doi:10.1038/s41598-023-41314-y PMID:37669970

Lilhore, U. K., Dalal, S., Faujdar, N., Simaiya, S., Dahiya, M., Tomar, S., & Hashmi, A. (2024). Unveiling the prevalence and risk factors of early stage postpartum depression: A hybrid deep learning approach. *Multimedia Tools and Applications*, 1–35. doi:10.1007/s11042-024-18182-3

Lilhore, U. K., Manoharan, P., Sandhu, J. K., Simaiya, S., Dalal, S., Baqasah, A. M., Alsafyani, M., Alroobaea, R., Keshta, I., & Raahemifar, K. (2023). Hybrid model for precise hepatitis-C classification using improved random forest and SVM method. *Scientific Reports*, *13*(1), 12473. doi:10.1038/s41598-023-36605-3 PMID:37528148

Lilhore, U. K., Poongodi, M., Kaur, A., Simaiya, S., Algarni, A. D., Elmannai, H., Vijayakumar, V., Tunze, G. B., & Hamdi, M. (2022). Hybrid model for detection of cervical cancer using causal analysis and machine learning techniques. *Computational and Mathematical Methods in Medicine*, *2022*, 2022. doi:10.1155/2022/4688327 PMID:35572826

Lilhore, U. K., Simaiya, S., Pandey, H., Gautam, V., Garg, A., & Ghosh, P. (2022). Breast cancer detection in the IoT cloud-based healthcare environment using fuzzy cluster segmentation and SVM classifier. *Proceedings of RACCCS*, *2021*, 165–179.

Lilhore, U. K., Simaiya, S., Prasad, D., & Guleria, K. (2020). A hybrid tumor detection and classification based on machine learning. *Journal of Computational and Theoretical Nanoscience*, *17*(6), 2539–2544. doi:10.1166/jctn.2020.8927

Maxhelaku, S., & Kika, A. (2019). Improving interoperability in healthcare using HL7 FHIR. In *Proceedings of the 47th International Academic Conference*. International Institute of Social and Economic Sciences. doi:10.20472/IAC.2019.047.012

Mbunge, E., Sipho'esihle, J., & Muchemwa, B. (2022). Towards Emotive Sensory Web in Virtual Health Care: Trends, Technologies, Challenges and Ethical Issues. *Sensors International*, *3*, 100134. doi:10.1016/j.sintl.2021.100134

MehrabiN.2019). *A Survey on Bias and Fairness in Machine Learning*. http://arxiv.org/abs/1908.09635

Nathaniel, T. I., Goodwin, R. L., Fowler, L., McPhail, B., & Black, A. C. Jr. (2021). An Adaptive Blended Learning Model for the Implementation of an Integrated Medical Neuroscience Course During the Covid-19 Pandemic. *Anatomical Sciences Education*, *14*(6), 699–710. doi:10.1002/ase.2097 PMID:33915035

O'Regan, D., Shah, S., Mirsadraee, S., Al-Ruzzeh, S., Karthik, S., & Jarvis, M. (2008). Implementation of a Process-Orientated Multidisciplinary Approach (POMA), a System of Cost-Effective Healthcare Delivery within a Cardiac Surgical Unit. *Quality & Safety in Health Care*, *17*(6), 459–463. doi:10.1136/qshc.2006.021279 PMID:19064663

Onyema, E. M., Lilhore, U. K., Saurabh, P., Dalal, S., Nwaeze, A. S., Chijindu, A. T., Ndufeiya-Kumasi, L. C., & Simaiya, S. (2023). Evaluation of IoT-Enabled hybrid model for genome sequence analysis of patients in healthcare 4.0. *Measurement. Sensors*, *26*, 100679. doi:10.1016/j.measen.2023.100679

Paterick, T. E., Patel, N., Tajik, A. J., & Chandrasekaran, K. (2017). Improving Health Outcomes Through Patient Education and Partnerships with Patients. *Baylor University Medical Center Proceedings, 30*(1), 112–13. https://www.tandfonline.com/doi/full/10.1080/08998280.2017.11929552

Peyroteo, M., Ferreira, I. A., Elvas, L. B., Ferreira, J. C., & Lapão, L. V. (2021). Remote Monitoring Systems for Patients With Chronic Diseases in Primary Health Care: Systematic Review. *JMIR mHealth and uHealth*, *9*(12), e28285. doi:10.2196/28285 PMID:34932000

Rahman, A., Hossain, M. S., Muhammad, G., Kundu, D., Debnath, T., Rahman, M., Khan, M. S. I., Tiwari, P., & Band, S. S. (2023). Federated Learning-Based AI Approaches in Smart Healthcare: Concepts, Taxonomies, Challenges and Open Issues. *Cluster Computing*, *26*(4), 2271–2311. doi:10.1007/s10586-022-03658-4 PMID:35996680

Seetharaman, M., Krishnan, G., & Schneider, R. H. (2021). The Future of Medicine: Frontiers in Integrative Health and Medicine. *Medicina, 57*(12), 1303. https://www.mdpi.com/1648-9144/57/12/1303

Somashekhar, S. P., Sepúlveda, M.-J., Norden, A. D., Rauthan, A., Arun, K., Patil, P., Ethadka, R. Y., & Kumar, R. C. (2017). Early Experience with IBM Watson for Oncology (WFO) Cognitive Computing System for Lung and Colorectal Cancer Treatment. *Journal of Clinical Oncology*, *35*(15, suppl), 8527–8527. doi:10.1200/JCO.2017.35.15_suppl.8527

Streeter, Beron, & Iyer. (2017). Precision Medicine. *Otolaryngologic Clinics of North America, 50*(4), 765–73. https://linkinghub.elsevier.com/retrieve/pii/S0030666517300609

Vale, D., El-Sharif, A., & Ali, M. (2022). Explainable Artificial Intelligence (XAI) Post-Hoc Explainability Methods: Risks and Limitations in Non-Discrimination Law. *AI and Ethics*, *2*(4), 815–826. doi:10.1007/s43681-022-00142-y

van Berkel, N., Sarsenbayeva, Z., & Goncalves, J. (2023). The Methodology of Studying Fairness Perceptions in Artificial Intelligence: Contrasting CHI and FAccT. *International Journal of Human-Computer Studies*, *170*, 102954. doi:10.1016/j.ijhcs.2022.102954

Wazid, M., Bera, B., Das, A. K., Mohanty, S. P., & Jo, M. (2022). Fortifying Smart Transportation Security Through Public Blockchain. *IEEE Internet of Things Journal*, *9*(17), 16532–16545. doi:10.1109/JIOT.2022.3150842

Wazid, M., Das, A. K., Mohd, N., & Park, Y. (2022). Healthcare 5.0 Security Framework: Applications, Issues and Future Research Directions. *IEEE Access : Practical Innovations, Open Solutions*, *10*, 129429–129442. doi:10.1109/ACCESS.2022.3228505

Xu, E., Wermus, M., & Bauman, D. B. (2011). Development of an Integrated Medical Supply Information System. *Enterprise Information Systems*, *5*(3), 385–399. doi:10.1080/17517575.2011.566630

Chapter 2
Machine Learning Algorithms for Natural Disaster Prediction and Management

Shanthalakshmi Revathy J.
https://orcid.org/0000-0003-1724-7117
Velammal College of Engineering and Technology, India

Mangaiyarkkarasi J.
https://orcid.org/0000-0003-1431-9584
NMSS Vellaichamy Nadar College, India

ABSTRACT

Natural disasters, such as floods, earthquakes, tsunamis, and landslides, pose significant threats to communities and ecosystems. This investigation explores the application of machine learning (ML) techniques in addressing the challenge. ML, a subset of artificial intelligence, involves creating models and algorithms that enable computers to learn from data, offering accurate disaster predictions without explicit programming. Various ML algorithms, including random forest for flood and wildfire prediction, support vector machine for earthquake forecasting, and decision tree for landslide risk assessment, are employed due to their ability to process complex datasets. Beyond prediction, ML plays a vital role in disaster management, optimizing resource allocation, refining emergency response plans, and enhancing evacuation strategies. Real-world case studies illustrate how ML contributes to mitigating disaster damage, emphasizing its role in proactive measures for disaster prevention and management.

INTRODUCTION

Natural disasters are harmful impacts on society created by natural hazard events. A natural disasters can cause severe damage to life, property, and causes some other impacts on environment. Such events can include a wide range of geological phenomena, such as quakes, volcanic eruption, and landslides, along with weather patterns such as hurricanes, tornadoes, floods or forest fires (Kansal et al. 2015). Across

DOI: 10.4018/979-8-3693-3362-4.ch002

the world, and with a demand for efficient emergency preparation, response and recovery strategies, the impact of disasters is widespread. The sudden release of energies that can lead to mass destruction is a natural consequence of the volcanic disasters caused by Earth's dynamic processes. Whereas, Meteorological disasters are due to climatic changes, and may lead to floods and landslides. These events are unpredictable and mitigation measures should be made to secure people. These disasters not only create impact on human society but also create long term consequences on economies, ecosystem and infrastructures. There is a need for some techniques and methodologies to predict the possibilities of the disasters. These may help us to be aware of the hazards and be prepared with the mitigation measures. In this paper we see how ML algorithms are used to predict natural disasters (Suliman Munawar et al. 2019). ML algorithms have wide range of knowledge based on the training data. They create patters based on the information from the learning data. Machine learning algorithms aid in the creation of resilient early warning systems by evaluating both historical and current data. They are versatile and can adapt to address different types of natural disasters. Rather than traditional methods, ML models provide more accurate predictions. ML algorithms can effectively process and analyze large data from various resources. These advantages made ML suitable for predicting natural disasters. Also, there are some other techniques to predict natural disasters. There are several algorithms in ML that are used in this prediction ranging from ensemble learning like random forests to neural networks (Gopal et al. 2020). This paper proposes an ensemble model using K-means clustering, LightGBM, and XGBoost algorithms to predict earthquakes based on seismic, GNSS, and environmental data (Joshi, Vishnu, and Mohan 2022). This study utilizes Random Forest and Support Vector Machines to predict landslide susceptibility in vulnerable areas using satellite imagery and LiDAR data (Tanyu et al. 2021). Not only for prediction, are some ML algorithms used for management after disasters. Image processing plays a major role in management after floods. ML models can analyze the damages from the satellite images and they can process data from sensors and drones to identify the affected regions. When used in disaster management, machine learning models can drastically lower the number of fatalities and property damage. The use of machine learning algorithms for natural catastrophe management and prediction is demonstrated in this study.

LITERATURE SURVEY

When using data mining and machine learning techniques for inference and decision-making in disaster situations, the literature review examines several approaches in disaster management and explores their procedural applications, strengths, and limits. The table 1 summarizes the surveyed research papers from 2015 to 2023, highlighting their methodologies, respective pros and cons, and the overall inference drawn from each study.

Table 1. Literature survey

Reference	Methodology	Pros	Cons	Inference
(Arinta and Andi W.R. 2019)	Big data and ML is used in early warning of disaster management.	These algorithms helps in predicting natural disasters and post disaster management. The data collection is made simple.	The data is collected from tweets. So the model is trained from that data.	ML algorithms are most effective and suitable to predict natural disasters.
(Li et al. 2019)	Methods such as Logistic regression, Naïve Bayes, AdaBoost and Random Forest are used to assess the risk of flood on watersheds.	These algorithms are effective for large datasets and resistant to overfitting. They are computationally efficient.	They may sensitive to outliers and noisy data.	The random forest model provides best results for prediction.
(Ekpezu et al. 2021)	Employed Convolutional Neural Network (CNN) and Long Short-Term Memory (LSTM) networks, both effective in pattern recognition and sequential data analysis.	Achieved impressive classification rates of 99.96% (CNN) and 99.90% (LSTM) for natural disaster sound classification.	Practical implementation challenges in real-time scenarios, especially for early warning systems, might need further exploration and resolution.	Deep learning effectively classified natural disaster sounds with high accuracy, highlighting potential for early detection despite practical deployment concerns.
(Mahajan and Sharma 2022)	Regression, ML Algorithms	Early disaster warning	Challenges in long-term prediction	Various ML techniques aid accurate rainfall prediction
(Khalaf et al. 2018)	Describes Random Forest Classifier, Support Vector Machines (SVM), and Levenberg-Marquardt training algorithm.	Utilizes various machine learning algorithms for flood severity prediction. - Introduces a novel flood dataset. - Demonstrates classification into normal, abnormal, and high-risk floods.	SVM produces inferior results compared to random forest model. - Neural network models (LEVNN and RF) performed better in performance measures.	Machine learning algorithms, especially random forest, offer better accuracy in flood severity prediction.
(Kansal et al. 2015)	Comparison of machine learning methods (SVM, regression, decision trees, neural networks) for forest fire prediction	High accuracy of regression for forest fire detection- Fast detection compared to other machine learning techniques	No specific mention of the dataset or its size- Limited explanation of feature selection or engineering	Regression proves most effective for fast and accurate forest fire detection, outperforming other ML techniques based on this study.
(Maspo et al. 2020)	Overview of supervised, unsupervised, and reinforcement learning types in ML	Outlines the process of systematic literature review for flood prediction methods.	Narrow scope within recent 5 years, may miss older yet relevant studies.	Systematic review conducted through specific search terms; focused on recent studies within a defined period
(Gupta and Roy 2020)	Real-time monitoring, prediction, and control system for flood management as a Decision Support System (DSS).	Integrates various methods for comprehensive flood management.	Requires extensive data validation and verification.	The study presents a comprehensive flood control framework using DSS, ML, and MCDM, highlighting effective strategies categorized by social, environmental, and economic scenarios.
(Zheng et al. 2021)	Full Parameter Time Complexity (FPTC) Analysis	Provides an estimation of running time without executing the code - Helps in quick algorithm selection for LULC classification during emergencies	Relies on theoretical analysis, actual running time might vary - Requires prior knowledge of algorithmic complexity	Combining FPTC with coefficient ω aids in precise prediction of algorithm running time for emergency managers, aiding rapid decision-making with limited time and remote sensing data.
(Tiu et al. 2022)	Enhancing rainfall prediction in the Dungun river basin (1996-2016) using Variational Mode Decomposition (VMD), Bagging, Boosting, Bagging-VMD, and Boosting-VMD as pre-processing, coupled with Artificial Neural Network (ANN) and Support Vector Regression (SVR) base models for improved accuracy.	Enhanced prediction accuracy using data pre-processing techniques. - Comparative analysis of different pre-processing methods. - Demonstrates superiority of Boosting-ANN model for river water level prediction.	Specific focus on one river basin may limit generalization. - Limited discussion on real-time implementation challenges.	Boosting-ANN, employing Boosting with Variational Mode Decomposition, emerges as the most effective model, showcasing superior predictive performance with the lowest RMSE, MAPE, MAE, and highest NSE.
(Tufail et al. 2023)	Utilized various machine learning techniques, including neural networks and ensemble methods, to analyze historical space weather data.	Improved accuracy in space weather predictions, aiding in better preparation for potential disruptions.	Dependency on the availability and quality of historical space weather data.	Demonstrated the effectiveness of machine learning in predicting space weather events, offering valuable insights for early warning systems.
(Xu et al. 2022)	Applied deep learning techniques, including convolutional neural networks (CNNs), to analyze satellite imagery and atmospheric data.	Enhanced accuracy in predicting hurricane intensity, crucial for evacuation and response planning.	Computational intensity and resource requirements for training deep learning models.	Showcased superior performance in hurricane intensity prediction compared to traditional methods.

METHODOLOGY

Disaster management encompasses a range of activities aimed at preventing or mitigating the adverse effects of natural hazards such as earthquakes, floods, wildfires, and human-induced disasters like technological accidents or intentional attacks(Chamola et al. 2021). Data-driven approaches have emerged as powerful tools for disaster management, enabling the extraction of valuable insights from vast amounts of data to inform decision-making and improve disaster resilience. The methodology for data-driven disaster management typically involves the following steps:

Data Collection: Collect pertinent information from a range of sources, such as government databases, social media, sensor networks, satellite photography, and historical documents. This data may consist of text, photos, audio, and video, and it may be organised, semi-structured, or unstructured. Depending on the type of disaster and the information needs of the disaster management, several data sources will be employed. Table 2 summarizes available data set for Natural Disaster Prediction and Management.

Table 2. Data set available for natural disaster prediction and management

Category	Dataset	Description	Source	Image Source
Prediction	Earthquake Early Warning System Data	Real-time data from seismic stations in Japan	National Research Institute for Earth Science and Disaster Resilience (NIED)	Image of seismic waveforms and earthquake detection: https://www.eri.u-tokyo.ac.jp/en/
	Global Historical Earthquake Catalog (GHEC)	Comprehensive earthquake data since 1900	U.S. Geological Survey (USGS)	Image of global earthquake map: https://earthquake.usgs.gov/earthquakes/search/
	Flood Forecast and Warning System Data	Water level, precipitation, and streamflow data for flood forecasting	National Oceanic and Atmospheric Administration (NOAA)	Image of flood forecast map: https://dashboard.waterdata.usgs.gov/
	Landslide Susceptibility Mapping Data	Satellite imagery and geospatial data for landslide prediction	NASA Earth and Open Science Platform (EOSPO)	Image of landslide susceptibility map: https://earthobservatory.nasa.gov/images/89937/a-global-view -of-landslide-susceptibility
Management	OpenStreetMap	Collaborative mapping data for infrastructure and resource allocation	OpenStreetMap Foundation	Image of OpenStreetMap visualization: https://www.openstreetmap.org/
	Global Earthquake Damage Model (GEDM)	Earthquake damage estimates for different scenarios	The World Bank	Image of earthquake damage assessment: https://datacatalog.worldbank.org/search/dataset/0038576/Glo bal-earthquake-hazard
	Hurricane Harvey Twitter Dataset	Social media data for analyzing public sentiment and needs	Kaggle	Image of Twitter data visualization: https://www.kaggle.com/datasets/dan195/hurricaneharvey
	UNOSAT Emergency Dashboard	Satellite imagery and analysis for disaster response	United Nations Satellite Programme (UNOSAT)	Image of UNOSAT satellite imagery: https://unosat.org/products/

Data Preprocessing: Cleanse and prepare the data for analysis by handling missing values, outliers, and inconsistencies. This may involve data imputation, normalization, and feature engineering. To guarantee the accuracy and dependability of the data utilised for analysis, data preparation is crucial.

Exploratory Data Analysis: Using descriptive statistics, visualisations, and correlation analysis, learn about the properties, distributions, and relationships of the data. Finding patterns, trends, and abnormalities in the data that could point to impending disasters or weaknesses can be aided by this preliminary investigation.

Feature Engineering: To increase machine learning models' capacity for prediction, add new features or modify current ones. Data mining algorithms, statistical methods, and domain knowledge can all be used in feature engineering. Feature engineering is to produce features that are applicable to the current issue and that machine learning models can utilise efficiently.

Model Selection and Training: Select the best machine learning algorithms for the job in light of the data that is available and the nature of the issue. Supervised learning techniques like logistic regression, decision trees, and linear regression as well as unsupervised learning algorithms like k-means clustering and anomaly detection algorithms are frequently employed in disaster management. Utilising metrics like accuracy, precision, and recall, assess the models' performance as you train them on the prepared data. In order to minimise error on the training data, model training entails optimising the parameters of the machine learning algorithm. To make sure that the trained models can effectively generalise to new data, model evaluation is crucial. This figure 1 illustrates the dynamic interplay between model prediction and monitoring in the context of disaster management.

Figure 1. Model monitoring

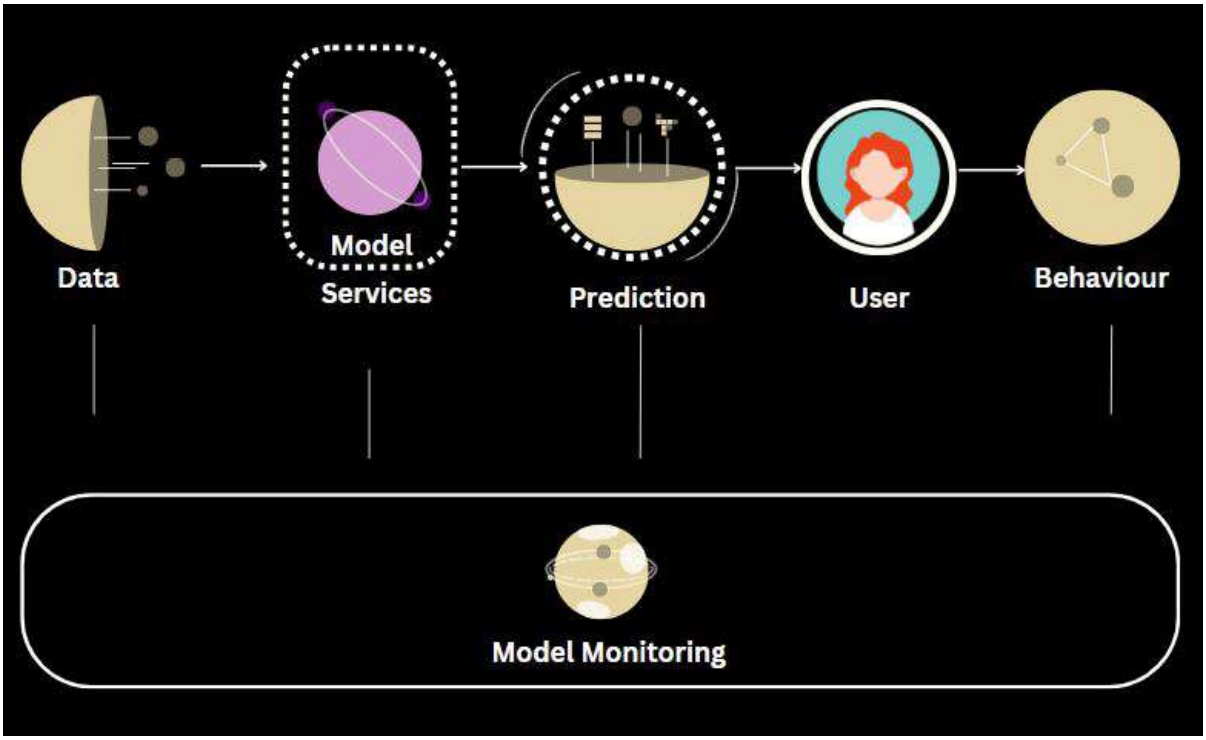

Model Deployment: Integrate the trained models into operational systems for real-time predictions and decision support. This may involve developing web applications, integrating the models with existing decision support systems, or deploying the models on edge devices.

Model Monitoring and Maintenance: Continuously monitor the performance of the deployed models, retrain them as new data becomes available, and adapt them to changing conditions. This ensures that the models remain accurate and relevant over time.

Interpretation of Data

Data interpretation plays a crucial role in disaster management, transforming raw data into meaningful information that can guide decision-making and inform disaster response strategies. This process involves understanding the context, limitations, and potential biases of the data to derive accurate and actionable insights.

Contextual Understanding: Consider the historical, geographical, and social context of the data to interpret it correctly. Understand the underlying factors and processes that have influenced the data's collection and analysis. For example, interpreting satellite imagery of a wildfire requires an understanding of the local vegetation, weather patterns, and human activities that may have contributed to the fire's development.

Data Limitations: Recognize the limitations of the data, such as missing values, sampling biases, and measurement errors. Account for these limitations when interpreting the results and making decisions. For instance, understanding the limitations of a sensor network's coverage area is crucial when using sensor data to assess the extent of flooding.

Bias Detection: Identify and address any potential biases in the data that could lead to inaccurate interpretations. This may involve examining data collection methodologies, sampling techniques, and data processing procedures. For example, being aware of potential biases in social media data is essential when using this data to gauge public sentiment during a disaster.

Visualization and Communication: Employ effective data visualization techniques to communicate findings clearly and concisely to stakeholders and decision-makers. Use charts, graphs, and maps to illustrate patterns, trends, and anomalies in the data. Effective data visualization can enhance the understanding and utilization of data-driven insights in disaster management.

Data Types in Disaster Management

Disaster management is a complex and multifaceted undertaking that requires the effective utilization of a wide range of data types. The figure 2visually conveys the diverse landscape of data types employed in research papers, these data types can be broadly classified into five categories:

- **Unstructured Textual Data:** This type of data includes news articles, incident activity reports, announcements, social media posts, and other forms of unstructured text. It provides valuable insights into public sentiment, emerging trends, and potential threats.
- **Structured Textual Data:** This category of data include structured text documents such as damage assessment forms, situational reports, 9-1-1 CAD data, and others. It offers comprehensive details on the type and scope of disasters, the distribution of resources, and the actions taken in response.

Figure 2. Most commonly used data types

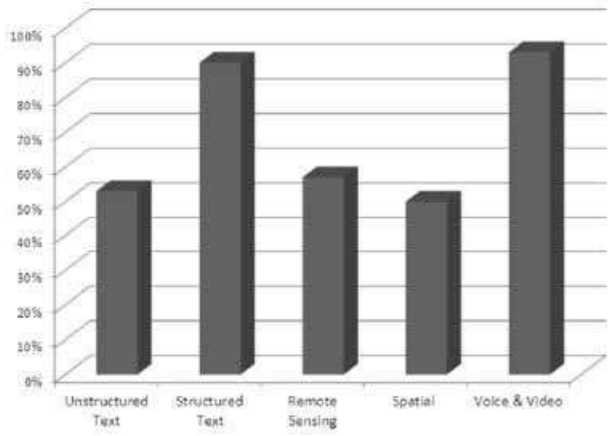

- **Remote Sensing Data:** This type of data includes satellite imagery, aerial photography, and sensor data. It provides a comprehensive overview of the affected area, enabling disaster managers to assess damage, monitor infrastructure, and track the movement of natural hazards.
- **Spatial Data:** This category of data include information from satellite and aerial imagery, graphical information systems (GIS), and other spatial data formats. It offers a geographical framework for comprehending the dangers, weaknesses, and response tactics associated with disasters.
- **Voice and Video Data:** This type of data includes radio communication, news broadcasts, and other forms of voice and video data. It provides real-time information about the unfolding situation, enabling disaster managers to make informed decisions and coordinate response efforts.

Challenges in Data Utilization

The diversity of data types used in disaster management poses several challenges for data analysis and utilization. These challenges include:

- **Data Integration:** Combining data from disparate sources and ensuring data consistency and quality are essential for effective analysis.
- **Real-time Processing:** Real-time or almost real-time data analysis is frequently needed for disaster management in order to facilitate decision-making.
- **Uncertainty and Incompleteness:** Disaster data often contains uncertainties and missing values, requiring robust analytical methods that can handle incomplete information.
- **Heterogeneity of Data Formats:** Data from different sources may have different formats and structures, requiring data harmonization and transformation.

DATA MINING AND MACHINE LEARNING

Disaster management has been completely transformed by data mining and machine learning techniques, which make it possible to find patterns, trends, and anomalies in data that would otherwise go undetected. With the use of these tools, one can gain a deeper understanding of the risks, vulnerabilities, and potential repercussions of disasters by extracting insightful information from massive and complicated datasets.

Data Mining

To find hidden patterns, trends, and connections in big datasets, data mining techniques are applied. These methods can be used for many different types of disaster management assignments, such as:

- **Risk Assessment:** Identify areas with high susceptibility to natural hazards and assess the potential impact of disasters.
- **Vulnerability Analysis:** Determine the vulnerability of infrastructure, communities, and individuals to different types of disasters.
- **Anomaly Detection:** Detect unusual patterns in sensor readings, social media data, or financial transactions that could indicate an impending disaster.
- **Knowledge Discovery**: Uncover hidden relationships between variables that can inform disaster management strategies.

Machine Learning

Machine learning algorithms are able to forecast future events, like the probability of earthquakes, the spread of wildfires, or the paths of storms, by learning from past data. This figure 4 illustrates the components and processes of an Early Warning and Detection System designed for disaster management. The system is depicted as a comprehensive framework with interconnected elements contributing to timely alerts and efficient response strategies.

These algorithms can be used to:

- **Early Warning Systems**: Develop early warning systems that can predict the occurrence of disasters and provide timely alerts to affected communities.
- **Resource Allocation:** Optimize the allocation of resources, such as personnel, equipment, and supplies, to areas of greatest need during and after disasters.
- **Damage Assessment:** Estimate the extent of damage caused by disasters using satellite imagery, aerial photography, and sensor data.
- **Recovery Planning:** Develop informed recovery plans that prioritize reconstruction efforts and address long-term economic impacts.

Figure 3. Early warning and detection system

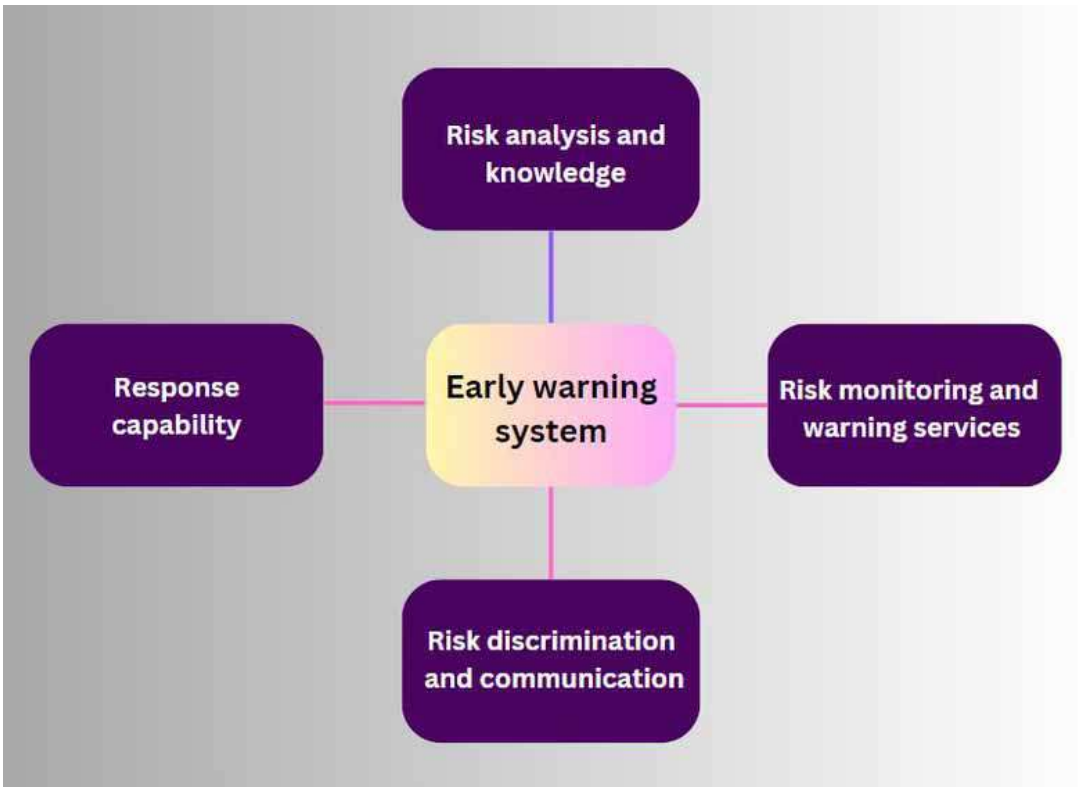

DATA ANALYSIS IN DISASTER MANAGEMENT

The availability and comprehensive utilization of data pose significant challenges. While extensive data volumes may exist, harnessing their full potential remains problematic. The idea of a jurisdiction in its "normal" state highlights how difficult it is to gather and analyse information about possible risks and their effects. To close this gap, creating a knowledge base from past incident reports helps define typical system parameters, create boundaries, and convert possible events into likely situations. This process enriches data-driven methods, enabling the detection of anomalies—events deviating from the norm.

Various data-driven early warning systems leverage anomaly detection, such as disease outbreak detection or fire detection. Anomalies are identified by considering multiple correlated factors influencing data variations. However, reliance on simulated data for system development and validation presents challenges. While widely accepted, simulated data may lack complexity, suffer from bias towards original event data, or fail to represent practical events accurately. Thus, thorough evaluation of model performance using real-world data remains crucial for validating the practicality of these systems (Arinta and Andi W.R. 2019).

Efficient data analysis in disaster management involves navigating the complexities of available data, understanding historical incidents, and deploying innovative methods to detect anomalies and predict potential events. Integrating these approaches contributes significantly to enhancing disaster preparedness and response mechanisms.

Mitigation

The main goals of mitigation efforts in disaster management are to lower the likelihood of disasters and lessen their possible effects. Notably, data mining and machine learning (DM and ML) play pivotal roles in preventing various threats posed by both natural and human-made disasters. These technologies play a crucial role in identifying potential terrorist threats by means of network analysis, detecting nuclear hazards through the utilisation of social networks and sensor data fusion, and utilising facial recognition in crowded environments. Monitoring changing conditions and their effects on community infrastructure is made more effective by combining DM and ML with static data. This integrated approach enhances the prioritization of preventive actions, potentially averting incidents before they occur.

Additionally, through the integration of spatial data and the analysis of evacuee behaviour, DM supports evacuation planning during the readiness phase. It aids in identifying potential threat areas and monitoring public safety websites for indicators of public awareness. ML applications in early warning systems, whether for floods, tsunamis, or chemical and nuclear threats, rely on anomaly detection. Identifying anything deviating from the norm flags it for human review, thereby improving the responsiveness to potential threats. The proactive detection of dangers, effective resource allocation, and general improvement of preparedness measures are all greatly aided by the application of DM and ML technologies in disaster mitigation. This figure 4 provides an overview of the key components and strategies involved in the mitigation phase of disaster management.

Figure 4. Mitigation

Preparedness

Data analysis aids in resource allocation, evacuation planning, and risk communication during the readiness stage. Data mining techniques, for instance, can optimise evacuation routes according to population density and traffic trends. Hurricane trajectories and wildfire spread can be predicted by machine learning models, enabling prompt resource deployment and evacuation.

Response

In the reaction stage, data analysis unifies information from multiple sources, including social media, mobile devices, and sensor networks, to enable real-time situational awareness. This real-time data fusion enables responders to make informed decisions regarding search and rescue operations, resource deployment, and damage assessment.

Recovery

The recovery phase focuses on restoring normalcy and rebuilding communities following a disaster. Data analysis is essential for assessing damage, estimating recovery costs, and allocating resources effectively. Satellite imagery and aerial photography can provide a comprehensive overview of the damage, while social media monitoring can gauge public sentiment and identify emerging needs. Data mining techniques can be used to analyze insurance claims and economic indicators to determine the long-term economic impact of the

DISCUSSION

The talk titled "Machine Learning Algorithms for Natural Disaster Prediction and Management" explores the complex field of technological advances in catastrophe resilience in further detail. This conversation goes beyond new developments and moral dilemmas to include other aspects that are vital to comprehending the consequences, difficulties, and wider social effects of utilizing machine learning algorithms in natural disaster response (Parmar, Mistree, and Sompura 2017).

Advanced Predictive Modeling: The potential of machine learning methods to improve natural catastrophe prediction modeling is unparalleled. The discourse delves deeper into the complexity of these models, highlighting their capacity to absorb large-scale datasets instantly. Machine learning algorithms improve their forecast accuracy by incorporating sensor inputs, satellite pictures, and historical data, allowing for a more sophisticated comprehension of intricate environmental patterns. These models' capacity for adaptive learning makes them excellent instruments for forecasting, greatly enhancing early warning systems.

Dynamic Adaptability: The dynamic adaptability of machine learning algorithms is a noteworthy feature. These algorithms improve their predictions over time by constantly changing in response to fresh data inputs. The talk emphasizes how these models are self-learning, showing how they may adjust to shifting circumstances, unanticipated factors, and new patterns. This flexibility makes predictive models more useful in disaster management plans by ensuring that they continue to be applicable and efficient in the face of changing natural events.

Integration of Geospatial Technologies: The effectiveness of machine learning algorithms is further improved by the inclusion of geospatial technologies. Predictive modeling gains spatial dimensions from remote sensing technology and Geographic Information Systems (GIS). The conversation delves into how the combination of machine learning and geospatial technologies allows for a finer-grained comprehension of regions that are vulnerable to disasters, hence enabling more focused interventions and efficient use of resources. Optimizing preparedness and reaction for disasters depends on this synergy. This figure 5 illustrates the application of geospatial technologies in the context of disaster management, showcasing the key components and functionalities that contribute to improved decision-making and response efforts.

Interdisciplinary Collaboration: A crucial aspect of the conversation centers on the necessity of interdisciplinary cooperation. Expertise from a variety of disciplines, such as data science, engineering, social sciences, and meteorology, is needed for effective disaster management. Algorithms for machine learning facilitate interdisciplinary cooperation by giving specialists a platform to come together and capitalize on their specialized knowledge. The integration of these fields of study promotes a comprehensive strategy for disaster resilience that takes into account social and infrastructure elements in addition to environmental ones.

Figure 5. Geospatial technologies

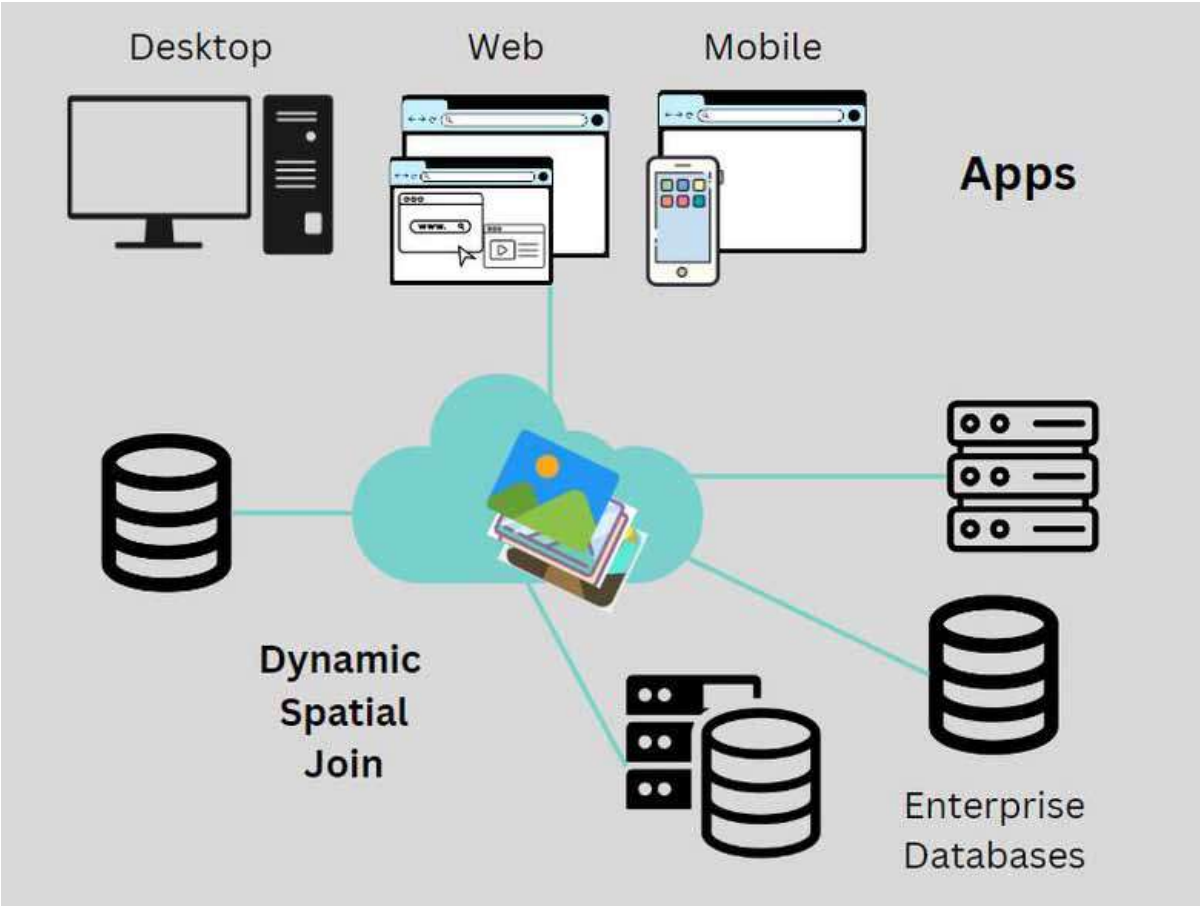

Challenges in Algorithmic Implementation: Although there is much promise in machine learning algorithms, the implementation challenges are acknowledged in the discussion. Interpretability and explainability issues can arise from the complexity of algorithmic models, particularly deep learning neural networks. Building trust amongst stakeholders—including legislators, first responders, and the communities impacted by disasters—becomes imperative when these issues are addressed.

Resource Allocation and Scalability: The practical aspects of scalability and resource allocation are also covered. Significant resources are needed for the implementation of machine learning algorithms in natural disaster management, including personnel with specialized knowledge and technological infrastructure. The discourse adeptly navigates the obstacles linked to resource limitations, underscoring the significance of adaptable and scalable solutions that can be tailored to varying geographic locations and degrees of technological infrastructure.

Public Awareness and Education: The significance of public education and awareness is something that is frequently missed in the discussion of machine learning for disaster management. The conversation looks at ways to explain predictive results to the general public in an understandable way. Communities are empowered and prepared to participate actively in disaster resilience initiatives when they are informed about the potential and constraints of machine learning models.

To sum up, this thorough analysis highlights the subtleties involved in incorporating machine learning algorithms into the prediction and management of natural disasters. In order to improve resilience in the face of natural disasters, technology-driven solutions are discussed in detail in this discourse, covering everything from dynamic adaptability and advanced predictive modeling to interdisciplinary collaboration and resource allocation issues. As these technologies advance, resolving issues and encouraging cooperation will be essential to realizing their full potential and building societies that are more informed, resilient, and adaptable.

CONCLUSION

The integration of machine learning algorithms into natural disaster prediction and management represents a pivotal shift, offering unprecedented potential yet accompanied by multifaceted challenges. These algorithms, with their adaptive learning capabilities and real-time data assimilation, elevate predictive modeling to unparalleled accuracy. However, their implementation demands a nuanced approach due to interpretability issues, resource allocation concerns, and the imperative of ensuring ethical use. The collaboration across disciplines emerges as a cornerstone, fostering a comprehensive approach to disaster resilience. By amalgamating expertise from diverse fields, these algorithms catalyze collective intelligence, acknowledging the intricate interplay of environmental, social, and infrastructural factors in disaster mitigation. Yet, the path forward mandates a careful balance between technological innovation and ethical responsibility, ensuring these advancements benefit communities while mitigating potential risks. Sustained efforts are paramount, urging continual research, technological advancements, and community involvement. A future where technology and disaster resilience converge to foster safer societies hinges upon persistent dedication to moral conduct, inclusivity, and ongoing collaborative endeavors. Responsible utilization of machine learning algorithms holds the promise of transforming disaster preparedness and response, driving us toward a future where societies are better equipped to navigate the unpredictable nature of natural disasters.

REFERENCES

Arinta, R. R., & Emanuel, A. W. R. (2019). Natural Disaster Application on Big Data and Machine Learning: A Review. In *In 2019 4th International Conference on Information Technology, Information Systems and Electrical Engineering (ICITISEE)* (pp. 249–254). IEEE. https://ieeexplore.ieee.org/document/9003984/ doi:10.1109/ICITISEE48480.2019.9003984

Chamola, V., Hassija, V., Gupta, S., Goyal, A., Guizani, M., & Sikdar, B. (2021). Disaster and Pandemic Management Using Machine Learning: A Survey. *IEEE Internet of Things Journal*, *8*(21), 16047–16071. https://ieeexplore.ieee.org/document/9295332/. doi:10.1109/JIOT.2020.3044966 PMID:35782181

Ekpezu, A. O., Wiafe, I., Katsriku, F., & Yaokumah, W. (2021). Using Deep Learning for Acoustic Event Classification: The Case of Natural Disasters. *The Journal of the Acoustical Society of America*, *149*(4), 2926–2935. https://pubs.aip.org/jasa/article/149/4/2926/1068002/Using-deep-learning-for-acoustic-event. doi:10.1121/10.0004771 PMID:33940915

Gopal, L. S., Prabha, R., Pullarkatt, D., & Ramesh, M. V. (2020). Machine Learning Based Classification of Online News Data for Disaster Management. In *In 2020 IEEE Global Humanitarian Technology Conference (GHTC)* (pp. 1–8). IEEE. https://ieeexplore.ieee.org/document/9342921/ doi:10.1109/GHTC46280.2020.9342921

Gupta, T., & Roy, S. (2020). A Hybrid Model Based on Fused Features for Detection of Natural Disasters from Satellite Images. In *IGARSS 2020 - 2020 IEEE International Geoscience and Remote Sensing Symposium* (pp. 1699–1702). IEEE. https://ieeexplore.ieee.org/document/9324611/ doi:10.1109/IGARSS39084.2020.9324611

Joshi, A., Vishnu, C., & Krishna Mohan, C. (2022). Early Detection of Earthquake Magnitude Based on Stacked Ensemble Model. *Journal of Asian Earth Sciences: X*, *8*, 100122. https://linkinghub.elsevier.com/retrieve/pii/S2590056022000433

Kansal, A., Singh, Y., Kumar, N., & Mohindru, V. (2015). Detection of Forest Fires Using Machine Learning Technique: A Perspective. In *In 2015 Third International Conference on Image Information Processing (ICIIP)* (pp. 241–245). IEEE. https://ieeexplore.ieee.org/document/7414773/ doi:10.1109/ICIIP.2015.7414773

Khalaf, M. (2018). A Data Science Methodology Based on Machine Learning Algorithms for Flood Severity Prediction. In *In 2018 IEEE Congress on Evolutionary Computation (CEC)* (pp. 1–8). IEEE. https://ieeexplore.ieee.org/document/8477904/ doi:10.1109/CEC.2018.8477904

Li, X., Yan, D., Wang, K., Weng, B., Qin, T., & Liu, S. (2019). Flood Risk Assessment of Global Watersheds Based on Multiple Machine Learning Models. *Water (Basel)*, *11*(8), 1654. https://www.mdpi.com/2073-4441/11/8/1654. doi:10.3390/w11081654

Mahajan, D., & Sharma, S. (2022). Prediction of Rainfall Using Machine Learning. *4th International Conference on Emerging Research in Electronics, Computer Science and Technology, ICERECT 2022,* *9*(01).

Maspo, N.-A., Bin Harun, A. N., Goto, M., Cheros, F., Haron, N. A., & Mohd Nawi, M. N. (2020). Evaluation of Machine Learning Approach in Flood Prediction Scenarios and Its Input Parameters: A Systematic Review. *IOP Conference Series. Earth and Environmental Science*, *479*(1), 012038. https://iopscience.iop.org/article/10.1088/1755-1315/479/1/012038. doi:10.1088/1755-1315/479/1/012038

Munawar, S., Hafiz, F. U., Hammad, A., & Ali, T. H. (2019). *After the Flood: A Novel Application of Image Processing and Machine Learning for Post-Flood Disaster Management Construction Engineering and Management at NUST Pakistan View Project Smart City Management: Applications of Disruptive Technologies View Proj*. Research Gate. https://www.researchgate.net/publication/337773028

Parmar, A., Mistree, K., & Sompura, M. (2017). Machine Learning Techniques For Rainfall Prediction: A Review Machine Learning View Project Rainfall Prediction Using ANN View Project Machine Learning Techniques For Rainfall Prediction: A Review. *International Conference on Innovations in information Embedded and Communication Systems*.

Tanyu, B. F., Abbaspour, A., Alimohammadlou, Y., & Tecuci, G. (2021). Landslide Susceptibility Analyses Using Random Forest, C4.5, and C5.0 with Balanced and Unbalanced Datasets. *Catena*, *203*, 105355. https://linkinghub.elsevier.com/retrieve/pii/S0341816221002149. doi:10.1016/j.catena.2021.105355

Tiu, E. S. K., Huang, Y. F., Ng, J. L., AlDahoul, N., Ahmed, A. N., & Elshafie, A. (2022). An Evaluation of Various Data Pre-Processing Techniques with Machine Learning Models for Water Level Prediction. *Natural Hazards*, *110*(1), 121–153. https://link.springer.com/10.1007/s11069-021-04939-8. doi:10.1007/s11069-021-04939-8

Tufail, S., Riggs, H., Tariq, M., & Sarwat, A. I. (2023). Advancements and Challenges in Machine Learning: A Comprehensive Review of Models, Libraries, Applications, and Algorithms. *Electronics (Basel)*, *12*(8), 1789. https://www.mdpi.com/2079-9292/12/8/1789. doi:10.3390/electronics12081789

Xu, X.-Y., Shao, M., Chen, P.-L., & Wang, Q.-G. (2022). Tropical Cyclone Intensity Prediction Using Deep Convolutional Neural Network. *Atmosphere (Basel)*, *13*(5), 783. https://www.mdpi.com/2073-4433/13/5/783. doi:10.3390/atmos13050783

Zheng, X., Jia, J., Guo, S., Chen, J., Sun, L., Xiong, Y., & Xu, W. (2021). Full Parameter Time Complexity (FPTC): A Method to Evaluate the Running Time of Machine Learning Classifiers for Land Use/Land Cover Classification. *IEEE Journal of Selected Topics in Applied Earth Observations and Remote Sensing*, *14*, 2222–2235. https://ieeexplore.ieee.org/document/9317826/. doi:10.1109/JSTARS.2021.3050166

Measurement: Sensors 28 (2023) 100810

Contents lists available at ScienceDirect

Measurement: Sensors

journal homepage: www.sciencedirect.com/journal/measurement-sensors

Blink talk: A machine learning-based method for women safety using EEG and eye blink signals

K. Shanmuga Priya [a,*], S. Vasanthi [a], Nithyanandhan R [b], Vinoth Chakkaravarthy G [c], Golda Jeyasheeli P [d], Karthiga M [e], Pandi C [f]

[a] Department of EEE, University College of Engineering, Dindigul, 624709, Tamilnadu, India
[b] Department of CSE, S.A Engineering College, Thiruverkadu, Chennai, 600077, Tamilnadu, India
[c] Department of CSE, Velammal College of Engineering and Technology, Madurai, 625009, Tamilnadu, India
[d] Department of Computer Science and Engineering, Mepco Schlenk Engineering College, Sivakasi, 626005, Tamilnadu, India
[e] Department of Electronics and Communication Engineering, Bannari Amman Institute of Technology, Erode, 638401, Tamilnadu, India
[f] Department of Computer Science and Engineering, Veltech Multitech Dr.Rangarajan Dr.Sakunthala Engineering College, Avadi, 600062, Chennai, India

ARTICLE INFO

Keywords:
Women safety
Machine learning
Stacked denoising autoencoder (SDAE)
Multiclass support vector machine (MSVM)
EEG
Discrete wavelet transform

ABSTRACT

Women's safety is currently thought to be a big issue in both urban and rural settings. A variety of smart gadgets and software were created to provide women with security. There are a lot of smart gadgets and applications on the market, but they don't offer a good answer and are too expensive. In this research, a novel machine learning-based Blink Talk method has been proposed for women safety. EEG based on some blink talk algorithms for eye blink detection. Initially, the EEG and eye blink signals are pre-processed using Discrete wavelet transform (DWT). The pre-processed signals are fed into Stacked Denoising autoencoder (SDAE) for extracting the features. In the next phase, the extracted features are used to classify the emotions of women through Multiclass Support vector machine (MSVM). The classification results are sad, happy, normal, and fear; finally, fear emotion is converted into text using GSM to the saved contacts and nearby police station and GPS scan the near radius surrounding people to send the alert and help request message for the help needed person. The experimental results reveal that the suggested approach provides high accuracy range of 98.04%. then the traditional machine learning techniques.

1. Introduction

Women's safety is in danger in today's globe, particularly in India. In the twenty-first century, women have made significant contributions to society and have joined males in a variety of industries [1]. Women's crimes, such as harassment, molestation, eve-teasing, rape, kidnapping, and domestic abuse, are not decreasing, but rather increasing [2]. The government has taken many pre-emptive measures to prevent these misbehaving acts, but nothing has changed the number of crimes and they remain untouched. Currently, there are more crimes committed against women than ever before. Harassment of women occurs not only at night or during the evening, but also during the day at home, at work, and even while shopping. Women are often scared of strangers and worried about their safety. About 80% of our country's women are concerned about their safety [3].

According to survey findings, more than 370,000 incidences of women's crime were reported in 2020, and women's crime is gradually increasing. Uttar Pradesh has 49,385 such incidents, followed by West Bengal (36,439), Rajasthan (34,535), Maharashtra (31,954), and Madhya Pradesh (31,954). (31,954). (25,640) [4]. The majority of crimes against women (30.2%) were committed by a husband or his family, followed by attacks on women with the goal of disturbing modesty (19.7%), kidnapped and abducted of women (19.0%), and rape (15.0%). (7.2%)

An electroencephalogram (EEG) is a method of measuring neuronal activity using non-stationary electric potential signals from the scalp of the brain [5]. A wide range of research has been conducted on brain–computer interfaces (BCIs) based on electroencephalograms (EEGs) for the purpose of women safety [6]. In EEG applications, efficient algorithms are becoming increasingly important for detecting and rejecting artifacts [7]. During an EEG, electrodes are put to the scalp to record the electrical activity of the brain. This approach provides high

* Corresponding author.
E-mail address: shanmuga86819481@gmail.com (K.S. Priya).

https://doi.org/10.1016/j.measen.2023.100810
Received 29 September 2022; Received in revised form 10 March 2023; Accepted 20 May 2023
Available online 22 May 2023

temporal resolution and is safe, simple, and inexpensive to employ [8]. EEG data are frequently recorded and connected to physiological and cognitive activities to better understand these processes. Wearable EEG headsets are growing in popularity among those who want to analyze their statistics on mental health, meditation, mindfulness, and sleep [9, 20].

Electrical field disturbances are very dangerous to EEG signals. Eye blinks, in particular, drastically reduce the signal-to-noise ratio (SNR) of recorded EEG readings by generating electric impulses when the retina and cornea, or the eyes and eyelids, create an electric dipole. EEG interpretations become unclear or may even be inaccurate due to eye-blink artifacts in the EEG output. Therefore, it may be helpful to identify and eliminate eye-blink components from any EEG investigation [10]. The EEG may be utilized to get physiological data such as consciousness levels, sleep phases, or simple eye blinks. The two types of Eye Blinks are reflexive Eye Blinks and deliberate Eye Blinks. The simplest response is the reflexive eye blink because it doesn't involve any cerebral structures. Intentional eye blinking, on the other hand, includes various parts of the cerebral cortex [11,12].

In the current circumstances, Women want to work and be outside, yet there is a lack of safety; many schemes, devices and techniques have been established for women safety still it has some limitations such as low-frequency noise removal, this is because of the chances of loss of data inherent in the EEG signal. So, this paper proposes ML-based methods in eye blink and EEG artifact detection for providing solutions to the women safety. When an eye blink is detected, the suggested method will activate and send the victim's information and location to the closest police station. The main contribution of our proposed technique,

- The main purpose of this study is to detect the need of paralyzed people using blink talk.
- In pre-processing stage, DWT (Discrete Wavelet Transform) is used for filtering the eye blinks in EEG signals to avoid an erroneous brain activity analysis.
- In feature extraction stage, Stack Denoising autoencoder is used to exact the reflexive Eye Blink and the intentional Eye Blink features.
- The Multiclass classification is performed by Multiclass Support Vector Machine (MSVM) for classifying the signals extracted from the features.
- The classified brain waves are converted into text and the text message is sent to the nearby police station via the GSM module.
- The proposed Machine learning-based Blink Talk method is evaluated based on its specificity, and accuracy.

The remainder of this study was organized into five sections as follows. Section 2 outlines the literature survey, Section 3 includes the proposed method named Blink talk, Section 4 comprises results and discussion and finally, Section 5 encloses with the conclusion and future enhancement.

2. Literature survey

In recent days several tools and methods were introduced by the investigators mostly to progress the women safety with EEG signal. Some of those methods are deliberate briefly in this section.

In 2018, Singh, H., Singh, J. et al. [13] presented a real-time eye blink detection method. In the experiment, blinking is detected in both controlled and natural environments. Blinks (both eyes blinking simultaneously), and left and right winks are detected by the blink detector. Eye blinks left winks, and right winks were detected with 96, 92, and 88% accuracy in this study.

Yasoda, K. et al. [14] presented a fuzzy kernel support vector machine to automatically classify WICA artifacts in 2020. The suggested technique removes EEG signal artifacts from the raw dataset automatically. The proposed technique constantly improves artifact component detection and achieves a classification accuracy of 86.1%.

In 2021 Sivachitra, M. et al. [15] proposed Women Safety Patrolling Robotic system to ensure the women's safety. In order to patrol in its designated region with the least amount of human interaction, the suggested technique makes the best use of its characteristics, including sound sensors, ultrasonic sensors, ESP cameras, and IoT. This means that the community of women will benefit more from the proposed night patrolling robot.

In 2021 Nivedetha, B. [16], suggested approach makes the best use of its capabilities, including sound sensors, ultrasonic sensors, ESP cameras, and IoT, to patrol in its designated region with the least amount of human involvement. This means that the community of women will benefit more from the proposed night patrolling robot. The suggested system aims to protect women in society by giving them wearable technology, encouraging them to be brave in any circumstance, and leveraging the Internet of Things to convey the appropriate message in an encrypted format.

In 2021 Tayal, S. et al. [17] proposed a simple and cost-effective women's safety device design and hardware implementation using GSM, NodeMCU, and GPS modules are suggested. A push button on this safety device must be pressed by a woman in the event that she detects any risk. In this situation, GPS locates the women fast, and a GSM module sends an emergency message to contacts who have been saved, as well as to a nearby police control room. Additionally, the buzzer signals passersby to assist the women. As a result, comprehensive protection for women is guaranteed.

In 2021 Hariharan, K. et al. [18] proposed an application with a machine learning mechanism for warning and protecting female cab passengers. The software also has extra features like real-time location monitoring and incorrect route prediction. The advantage of this application is that it has an auto mode for use in emergency scenarios. Three machine learning models have also been tried, and the SVM classifier performs the best with our dataset, with an accuracy of 89.5%.

In 2021 Gomathy, C.K. and Geetha, M.S [19] have proposed an Arduino-powered wearable safety gadget for women. This device is meant to protect ladies in case they encounter any threat. To communicate with other devices and provide alerts to them, the device employs wireless sensor networks. The user's location is shared immediately with the appropriate authorities and stored contacts via GPS and GSM. The proposed method enables many users to manage device functionality, and the switch's built-in authentication feature speeds up fault detection and correction.

Various technologies and techniques were focused on women's safety with EEG signals according to the research review. Our proposed machine learning-based Blink Talk method improves accuracy and reduces the computational cost.

3. Proposed methodology

The proposed machine learning-based Blink talk method aims to bring out a solution for Women's safety without any outward or internal harm to their bodies Due to the fact that none of the components come into close contact with the women, the proposed blink talk model is significantly safer and costs less than earlier models shown in Fig. 1.

3.1. Data acquisition

A peaceful setting, ten participants between the ages of 21 and 31 provided the raw EEG data and eye blinks. During one session, 6 to 8 trials of 20 s each of EEG signals were recorded. The volunteer was required to blink 8 to 12 times during each trial. recorded the EEG signals of women in two sessions separated by more than two weeks, whereas the signals of the other women were recorded in one session. MATLAB was used to process the EEG data from the Neurosky headgear.

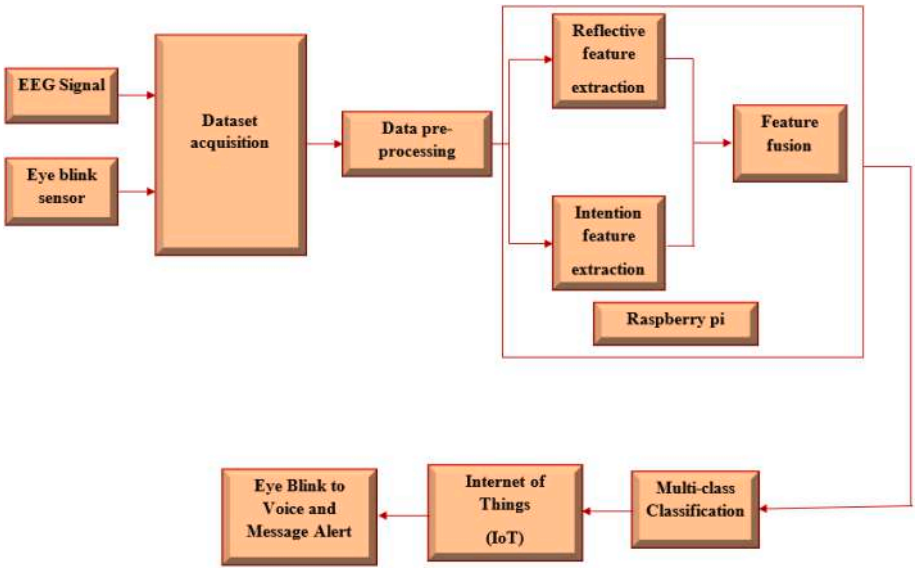

Fig. 1. The overall workflow of the proposed Blink Talk method.

3.2. Data pre-processing

For time-frequency analysis, wavelet transforms are employed. It is a technique for data transformation that divides the data into several frequency components and analyses each component according to its resolution at that scale. Non-stationary signals include EEG signals. In the study, DWT was used to split the collected EEG signals into their frequency components, and properties of the frequency bands at the decomposition levels were retrieved. The discrete values of dilation and translation are represented by the parameters A and B in the discrete wavelet transform. It is usual to practice discretizing the dilation factor A using a logarithmic scale in order to link it to B by making B proportional to A. Therefore, the normalized wavelet function can be discretized as follows,

$$\varphi(x,y) = \frac{1}{A_0^x}\varphi\left(\frac{T - yB_0A_0^x}{A_0^x}\right) \quad (1)$$

which is the result by taking $A = A_0^x$, and $B = yB_0A_0^x$, respectively, the integers *x,y* translation, regulate dilation, respectively. A_0 is the fixed dilation phase that is larger than 1. $B_0$is the location parameter that is larger than 0.

3.3. Feature extraction

The pre-processed signals' redundant and irrelevant data are removed at the crucial phase of feature extraction. The stacked autoencoder is a multi-autoencoder ANN design that is taught using a greedy layer-wise training technique. Each autoencoder is made up of a middle layer, an output layer, and an input layer. The following autoencoder of the layered autoencoder shown in Fig. 2 receives input from a middle layer output.

The stacking autoencoder is extended by the SDAE. SDAE's input signals are tainted by noise. To decode and recover the blurred original input G $P = \{p_1, p_2, \ldots p_n\}$. These distorted input signals are transferred using a sigmoid function to a hidden layer with units as,

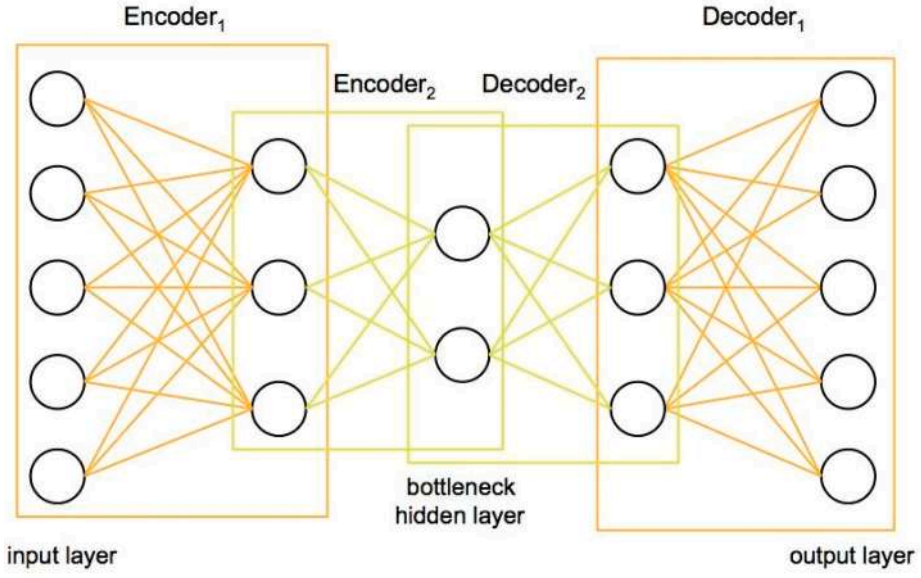

Fig. 2. Structure of stacked denoising autoencoder (SDAE).

$$S = f_{1,\theta}(P_1) = z(WP_1 + b) \tag{2}$$

$$p(u) = \frac{1}{1 + e^{-u^2}} \tag{3}$$

where W, q, and f represent the weight matrices, bias, and activation function of the encoder on the first autoencoder, and S represents the signal on the middle layer of the first autoencoder, respectively. The weight and bias matrices are chosen at random during initialization. The uncorrupted input $Q = \{q_1, q_2, \ldots q_n\}$ the estimation of P, can be reconstructed by the decoder of the first autoencoder as,

$$Y = g_{2,\theta}(Z_1) = z(S^{'}Q_1 + b^{'}) \tag{4}$$

where S′, b', and g are the weight matrices, bias, and nonlinear function of the decoder for the first autoencoder, respectively. To make the feature vectors of the signals produced by the autoencoder smaller, statistical characteristics are added to the set of wavelet coefficients.

3.4. Feature fusion

Feature concatenation is a crucial step in the domain of eye blink pattern recognition. The various feature vectors are sequentially fused to build a finalized feature vector for eye blink detection. The main rationale for conducting this step is to consolidate all descriptor data into a single feature vectors column, which can be effective in reducing the error rates. The structural and geometric features are extracted by the SDAE by eliminating the irrelevant features of the input image as feature set 1 and 2. Then the fusion selection method selects the relevant or particular features from extracted features and these features are fused for the classification process.

3.5. Multi-class classification

A support vector machine (SVM) is an important supervised learning approach and a useful technique for data classification. SVM identifies binary classes by locating and employing a hyperplane class border that maximizes the margin in the training dataset. The support vectors are the training data samples that flow along hyper planes at the class border, and the margins are the gap between both the support vectors and the class border hyperplanes. Binary classification is done by SVM, which can distinguish between two classes. Multiclass classification is not natively supported by SVM. It makes binary categorization and dividing data points into two classes easier. The similar approach is used for multiclass classification after breaking the issue down into several binary classification problems.

3.6. Eye blink to voice and message alert

The research study's final module is this one. One of Python's modules, "imutils," has a dictionary of face landmarks. contains points for the right and left eyes, respectively, which can be used to access the eyes. The eye aspect ratio (EAR) value has been utilized to identify blinks in real time. Calculating and averaging the EAR of each eye's blinking results in the EAR of both eyes blinking. When the eye is shut, the EAR value steadily approaches 0. The face is detected and the blink detection system records the eye blinking.

Algorithm. Eye Blink Detection Algorithm

1. Point feature extraction.
2. Eye aspect ratio (EAR) calculation.
3. Calculation of time duration.
4. Based on the duration of eye blink the input is considered as dot or dash.
5. Dot-Dash sequence measure code is converted into normal text.
6. Dot - Dash sequence is stored in an array.
7. This sequence is converted into the respective letter.

The eye blinks are recognized using the EAR formula following the eye detection from the face. Now, the voice will be created from the eye blink. Blinks from that initial eye must be noticed. When the eyes are open, the EAR is constant; when they close, it becomes 0. Therefore, the colour red is used to represent an open eye, while the colour green is used to represent a closed eye. The eye-aspect ratio is,

$$EAR = \frac{||v_2 - v_6|| + ||v_3 - v_5||}{2||v_1 - v_4||} \tag{5}$$

Where v_1, v_2, v_3, v_4, v_5 and v_6 landmarks on eye with (x,y) coordinates. Each number on the virtual keys represents a specific requirement for the people who are paralyzed. Durations of single and double eye blinks are not constrained. Like when using the Morse Alphabet, respondents were requested to leave a little waiting period at the end of each letter as they entered words using their eyes only. In-letter space is the term for this brief pause in the letters. On the other hand, individuals chose for themselves the length of time between a single and double eye blink. However, this period's length must be shorter than the one that follows each letter. The system's only constraint during data entering is this.

In order to take Fig. 3's blink detection action, the woman must keep her eyes closed for a duration of between one and 5 s. Eye aspect ratio is estimated based on which voluntary and involuntary blinks are differentiated. If any voluntary blinks are detected, count of the blinks is used to identify the emotions. Then, the fear emotion is converted into via voice call and text message is sent by the GSM module about task given for particular count of blinks. To turn the blink into voice, a GMS module included from the dlib library converts the speech into a text message and sends it to the nearby police station.

4. Results and discussions

The experimental design for the research was put into practise using the machine learning toolkit MATLAB 2019b. In this result analysis, the EEG signals were used for detecting eye blinking for classifying the emotions of women.

4.1. Performance analysis

In this research the performance evaluation of the proposed Blink talk based on machine learning is calculated based on specificity, accuracy and sensitivity.

$$spe = \frac{tn}{tn + fp} \tag{6}$$

$$sen = \frac{tp}{tp + fn} \tag{7}$$

$$acc = \frac{tp + tn}{total\ no.of\ samples} \tag{8}$$

False positives and negatives are referred to as fp and fn, respectively, in place of true positives and true negatives of the samples, tp and tn, respectively.

In this proposed study, a testing methodology is used to classify the emotions of the women for their safety. From Table 1, it is clear that the

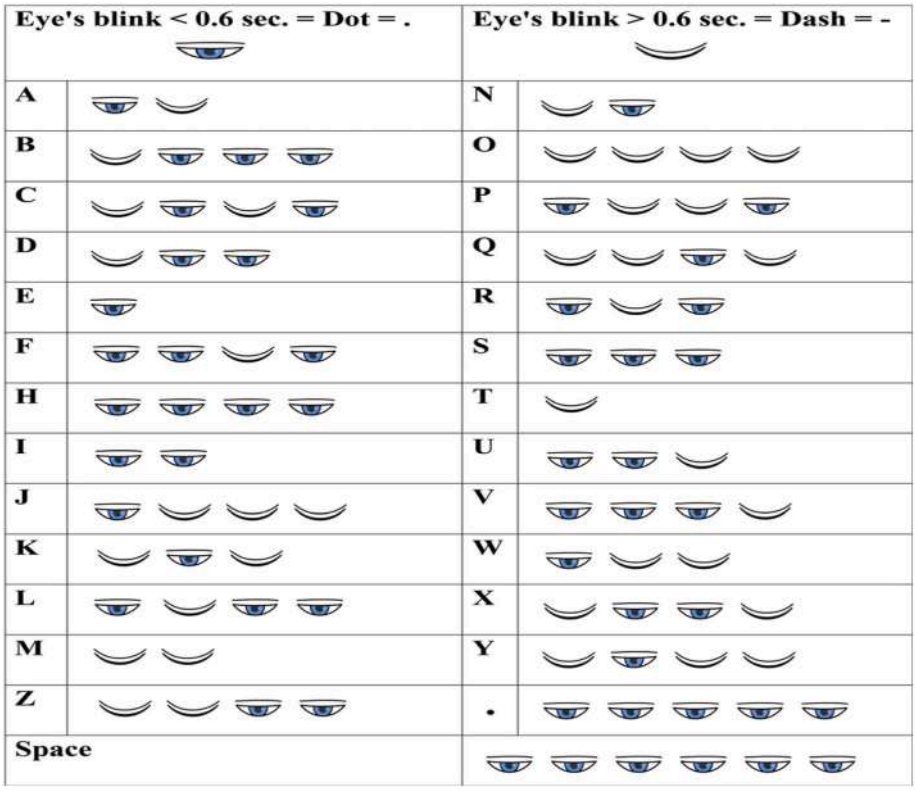

Fig. 3. Morse code of eye blink.

Table 1
Performance analysis of MSVM with SVM.

Models	SVM	MSVM
Testing accuracy	92.58	98.04
Training accuracy	94.29	97.85

suggested MSVM classifiers performs better than the traditional SVM. Utilizing the metrics of specificity, sensitivity, and accuracy, the effectiveness of the suggested model was assessed. The testing accuracy is determined based on the raw dataset and testing accuracy is taken from the real time signals as input is given in Fig. 4. Further, training and testing loss is also evaluated based on the epochs is shown in Fig. 5 for

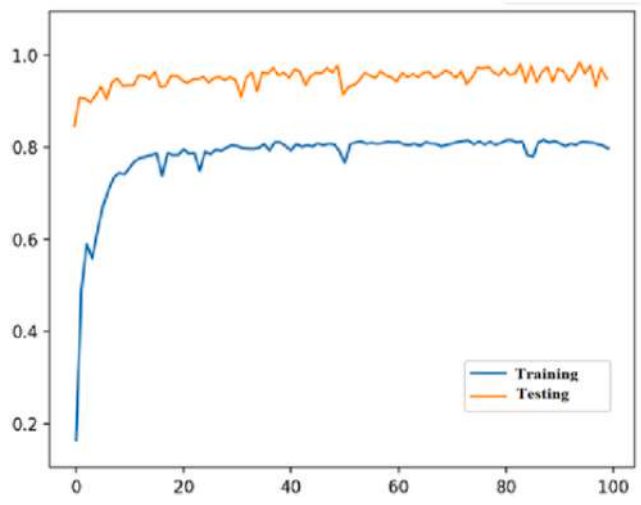

Fig. 4. Training and testing accuracy of the proposed method.

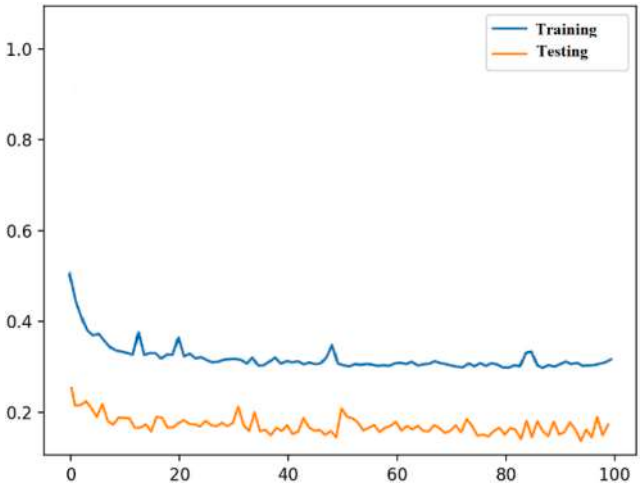

Fig. 5. Training and testing loss of the proposed method.

multiclass SVM. This lower loss rate could lead to a higher accuracy.

4.2. Comparative analysis

Each ML classifier's performance was evaluated to demonstrate how much more effective the outcome of the suggested method is. The sensitivity, specificity, and accuracy of each classifier are used to determine the classification, and the MSVM classifier achieved an accuracy of 98.04%. The Stacked Denoising Auto-encoder and Multi-class SVM classifier integration produces a classification accuracy rate that is higher than that of the existing models. The four conventional machine learning classifiers, including SVM, RF, NB, and KNN's suggested MSVM model, are compared.

Table 2 shows the comparative performance of each classifier, and

Table 2
Comparative analysis of ML classifiers.

Classifiers	Accuracy	Sensitivity	Specificity
KNN	85.25	83.69	84.28
NB	91.23	92.54	93.25
RF	92.59	90.25	89.63
SVM	94.29	91.85	90.65
MSVM	98.04	96.25	96.48

Table 3
Comparative analysis of ML feature extractors.

Models	Accuracy	Sensitivity	Specificity
PCA	84.53	83.89	80.77
LDA	92.05	90.25	91.68
GLCM	93.85	89.32	91.89
AE	95.06	92.52	93.26
SDAE	98.04	95.28	95.45

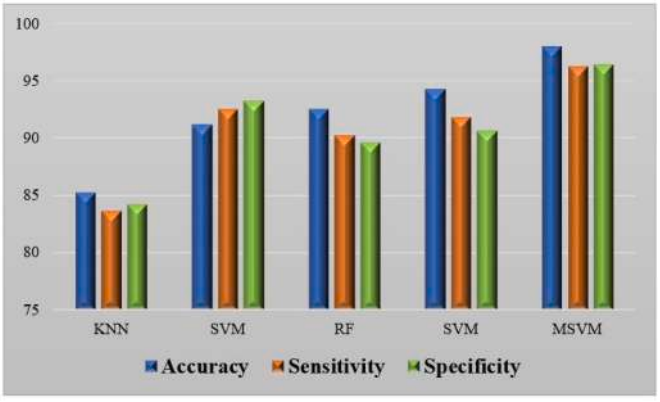

Fig. 6. Graphical comparison of machine learning classifiers.

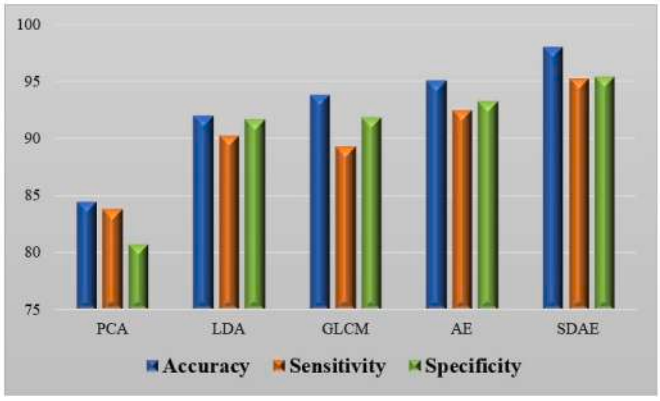

Fig. 7. Graphical comparison of machine learning techniques.

Fig. 6 shows a graphical comparison. Table 3 shows the relative effectiveness of each ML technique, and Fig. 7 shows a graphical comparison.

Table 2 displays the results of a comparison between the proposed SDAE model and the four conventional ML feature extraction techniques (PCA, LDA, GLCM, and AE). From the above comparison the SDAE yields higher accuracy than the existing models.

5. Conclusion

In this research, a novel ML based Blink Talk technique has been proposed for women safety. EEG based on some blink talk algorithms for eye blink detection. Initially, the EEG and eye blink signals are pre-processed using Discrete wavelet transform (DWT). The pre-processed signals are fed into Stacked Denoising autoencoder (SDAE) for extracting the features. The next stage uses the extracted features to categorize the emotions of women using a multiclass SVM. The classification results are sad, happy, normal, and fear; finally, fear emotion is converted into text using GSM to the saved contacts and nearby police station and GPS scan the near radius surrounding people send the alert and help request message for the help needed person. The experimental findings show that the suggested approach offers high accuracy within a 98.04% range than the traditional machine learning techniques. The suggested classification model will be built to accurately anticipate the different emotions in the future using deep learning techniques.

CRediT authorship contribution statement

K. Shanmuga Priya: Conception and design of study, Drafting the manuscript, Approval of the version of the manuscript to be published. **S. Vasanthi:** Acquisition of data, Revising the manuscript critically for important intellectual content, Approval of the version of the manuscript to be published. **Nithyanandhan R:** Formal analysis, Analysis and/or interpretation of data, Approval of the version of the manuscript to be published. **Vinoth Chakkaravarthy G:** Formal analysis, Analysis and/or interpretation of data, Approval of the version of the manuscript to be published. **Golda Jeyasheeli P:** Approval of the version of the manuscript to be published. **Karthiga M:** Drafting the manuscript, Approval of the version of the manuscript to be published. **Pandi C:** Revising the manuscript critically for important intellectual content, Approval of the version of the manuscript to be published.

Declaration of competing interest

No conflict of interest exists between authors to publish this paper.

Data availability

The data that has been used is confidential.

References

[1] B. Sathyasri, U.J. Vidhya, G.J. Sree, T. Pratheeba, K. Ragapriya, Design and implementation of women safety system based on Iot technology, Int. J. Recent Technol. Eng. 7 (6S3) (2019).
[2] B.S. Bala, M. Swetha, M. Tamilarasi, D. Vinodha, Survey on women safety using IOT, International Journal of Computer Engineering in Research Trends 5 (2) (2018) 16–24.
[3] A. Mojahed, N. Alaidarous, H. Shabta, J. Hegewald, S. Garthus-Niegel, Intimate partner violence against women in the Arab countries: a systematic review of risk factors, Trauma Violence Abuse 23 (2) (2022) 390–407.
[4] D.K. Tran, T.H. Nguyen, T.N. Nguyen, Detection of EEG-based eye-blinks using a thresholding algorithm, European Journal of Engineering and Technology Research 6 (4) (2021) 6–12.
[5] A. Palumbo, N. Ielpo, B. Calabrese, An FPGA-embedded brain-computer interface system to support individual autonomy in locked-in individuals, Sensors 22 (1) (2022) 318.
[6] S. Zhu, T. Yu, T. Xu, H. Chen, S. Dustdar, S. Gigan, D. Gunduz, E. Hossain, Y. Jin, F. Lin, B. Liu, Intelligent Computing: the Latest Advances, Challenges and Future, 2022 arXiv preprint arXiv:2211.11281.
[7] J. Cao, L. Chen, D. Hu, F. Dong, T. Jiang, W. Gao, F. Gao, Unsupervised eye blink artifact detection from EEG with Gaussian mixture model, IEEE Journal of Biomedical and Health Informatics 25 (8) (2021) 2895–2905.
[8] M. Agarwal, R. Sivakumar, Blink: a fully automated unsupervised algorithm for eye-blink detection in eeg signals, in: 2019 57th Annual Allerton Conference on Communication, Control, and Computing (Allerton), IEEE, 2019, September, pp. 1113–1121.
[9] D. Hu, J. Cao, X. Lai, J. Liu, S. Wang, Y. Ding, Epileptic signal classification based on synthetic minority oversampling and blending algorithm, IEEE Transactions on Cognitive and Developmental Systems 13 (2) (2020) 368–382.
[10] C.R. Rashmi, C.P. Shantala, EEG artifacts detection and removal techniques for brain computer interface applications: a systematic review, International Journal of Advanced Technology and Engineering Exploration 9 (88) (2022) 354.
[11] R. Akhter, F. Ahmad, F.R. Beyette, Automated detection of ERP artifacts of auditory oddball paradigm by unsupervised machine learning algorithm, in: 2022 IEEE

Conference on Computational Intelligence in Bioinformatics and Computational Biology (CIBCB), IEEE, 2022, August, pp. 1–8.
[12] A. Boudaya, S. Chaabene, B. Bouaziz, H. Batatia, H. Zouari, S.B. Jemea, L. Chaari, A convolutional neural network for artifacts detection in EEG data, in: Proceedings of International Conference on Information Technology and Applications, Springer, Singapore, 2022, pp. 3–13.
[13] H. Singh, J. Singh, Real-time eye blink and wink detection for object selection in HCI systems, Journal on Multimodal User Interfaces 12 (1) (2018) 55–65.
[14] K. Yasoda, R.S. Ponmagal, K.S. Bhuvaneshwari, K. Venkatachalam, Automatic detection and classification of EEG artifacts using fuzzy kernel SVM and wavelet ICA (WICA), Soft Comput. 24 (21) (2020) 16011–16019.
[15] M. Sivachitra, T. NaveenRaj, V.G. Rekhasri, N. Sowmiyaa, Women safety night patrolling robot, Annals of the Romanian Society for Cell Biology (2021) 15706–15714.
[16] B. Nivedetha, Wearable device for women safety using IOT, JAC (J. Antimicrob. Chemother.): A Journal of Composition Theory 14 (6) (2021) 94–97.
[17] S. Tayal, H.P.G. Rao, A. Gupta, A. Choudhary, Women safety system design and hardware implementation, in: 2021 9th International Conference *on Reliability, Infocom Technologies And Optimization (Trends And Future Directions) (ICRITO)*, IEEE, 2021, September, pp. 1–3.
[18] K. Hariharan, R.R. Jain, A. Prasad, M. Sharma, P. Yadav, S.S. Poorna, K. Anuraj, A comprehensive study toward women safety using machine learning along with android app development, in: Sustainable Communication Networks and Application, Springer, Singapore, 2021, pp. 321–330.
[19] C.K. Gomathy, M.S. Geetha, Women safety device using Iot, International Journal of Scientific Research in Engineering and Management (IJSREM) 5 (10) (2021) 1–9.
[20] M. Wang, J. Wang, X. Cui, T. Wang, T. Jiang, F. Gao, J. Cao, Multidimensional feature optimization based eye blink detection under epileptiform discharges, IEEE Trans. Neural Syst. Rehabil. Eng. 30 (2022) 905–914.

Chapter 1
Engineering Next-Generation Wireless Experiences Through Radar and RF Front End System Designs

J. Mangaiyarkkarasi
https://orcid.org/0000-0003-1431-9584
N.M.S.S. Vellaichamy Nadar College, India

J. Shanthalakshmi Revathy
https://orcid.org/0000-0003-1724-7117
Velammal College of Engineering and Technology, India

ABSTRACT

This chapter explores the synergy between radar and radio frequency (RF) front-end systems, ushering in a new era of wireless connectivity. It discusses the collaborative potential of radar and RF, emphasizing their role in enhancing security, reducing interference, and boosting adaptability. The chapter covers radar-based spectrum sensing, which enhances network efficiency, particularly in high-frequency scenarios like 5G. Radar and RF enable precise localization for IoT and autonomous vehicles, surpassing the capabilities of GPS. The chapter highlights radar's contributions to security, threat detection, and reducing signal interference. Radar-assisted RF improves vehicle communication, cooperative driving, and traffic management. In environmental monitoring and disaster management, radar augments RF for early warnings. This integration offers transformative potential, benefiting diverse applications and offering theoretical and practical insights for researchers and engineers. Radar and RF convergence offers a more connected, adaptable, and efficient wireless future.

DOI: 10.4018/979-8-3693-0916-2.ch001

1. INTRODUCTION

1.1 Evolution of Wireless Technologies

The evolution of wireless technologies has been a remarkable journey that has fundamentally transformed the way we communicate, connect, and interact with the world around us. Starting from the early days of radio communication in the late 19th century, wireless technologies have progressed through numerous generations, each marked by significant advancements.

The first generation of wireless communication primarily focused on analog voice transmission, enabling long-distance communication via radio waves. With the advent of the second generation (2G), digital technologies emerged, allowing for more efficient voice transmission and the introduction of text messaging. However, it was the third generation (3G) that truly revolutionized the landscape by enabling mobile data connectivity, laying the groundwork for basic internet browsing and limited multimedia services on mobile devices (Gunasekaran & Harmantzis, 2007). The subsequent generations, including 4G and its advanced variant LTE (Long-Term Evolution), brought about substantial increases in data speeds and paved the way for video streaming, mobile applications, and the mobile-centric digital lifestyle we experience today. As demand for data-intensive applications soared, the industry responded with the ongoing deployment of the fifth generation (5G), promising ultra-high speeds, ultra-low latency, and the capacity to support the Internet of Things (IoT) on an unprecedented scale.

This evolutionary trajectory is not only defined by technological advancements but also by the ever-expanding scope of wireless applications. From personal communication to industrial automation, healthcare, transportation, and beyond, wireless technologies have woven themselves into the fabric of modern society. As we stand at the cusp of the sixth generation (6G), with visions of even faster speeds, seamless connectivity, and transformative use cases such as holographic communication and sentient environments, the journey of wireless evolution continues to unfold, promising a future where the boundaries of connectivity are pushed even further (Tightiz et al., 2020) .

1.2 Demand for Enhanced Wireless Experiences

The relentless surge in the demand for enhanced wireless experiences underscores the pivotal role that connectivity plays in our lives. As we navigate an increasingly digital world, the need for seamless, high-quality wireless interactions has become non-negotiable. Modern society relies on wireless technology not just for communication, but also for a spectrum of activities that range from remote work

and virtual education to entertainment streaming and IoT-enabled smart living. This multifaceted reliance places tremendous pressure on wireless networks to deliver robust performance in terms of speed, reliability, and low latency.

Consumers expect to effortlessly connect with loved ones, colleagues, and information resources regardless of their physical location. This has led to an insatiable demand for faster data speeds that can support high-definition video streaming, online gaming, and real-time collaboration (Arbab-Zavar et al., 2019). Additionally, as evolving technologies viz augmented reality (AR), virtual reality (VR), and autonomous vehicles become more prominent, the necessity for wireless networks to handle massive data loads with minimal delay becomes paramount. The demand for enhanced wireless experiences isn't limited to individuals; industries are also capitalizing on wireless advancements to optimize processes, increase efficiency, and unlock new business models. Smart engineering, telemedicine, smart cities, and precision farming are just a few examples of sectors that rely heavily on seamless wireless connectivity.

In essence, the demand for enhanced wireless experiences is a reflection of our interconnected world's expectations and aspirations. As technology continues to evolve, wireless networks must rise to the challenge, continuously innovating to meet the soaring expectations of users and the expanding horizons of applications.

2. FUNDAMENTALS OF RADAR AND RF FRONT END SYSTEMS

2.1 Radar Principle

Radar (Radio Detection and Ranging) is a transformative technology based on the principle of using radio waves to detect and locate objects in its vicinity. Figure 1 explains the basic principle of Radar

Figure 1. Basic principle of radar

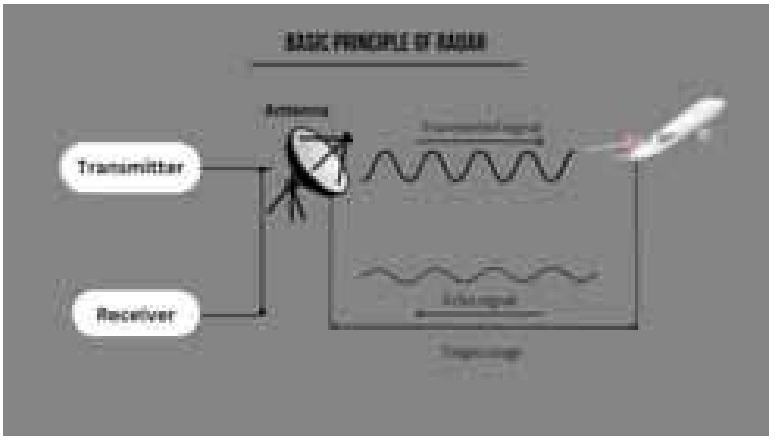

It operates by emitting radio frequency signals and then analyzing the echoes that bounce back from objects, allowing for the determination of their distance, speed, direction, and even size[(Ghorbanian et al., 2019). Range of radar is important in the designing of radar syatems which is expressed in equation (1)

$$R^4 = \sqrt{PsG^2\sigma\lambda^{2/}4\pi 3P_E} \tag{1}$$

Where, Ps – transmitted power, σ- cross section of radar, G-Antenna gain, P_E – received power

Antenna gain is expressed in equation (2) given below,

$$\mathrm{G} = \frac{4\pi Ak_a}{\lambda^2} \tag{2}$$

Where, A – area of antenna, K_a – efficiency, λ -wavelength

2.2 Applications

Radar's applications are diverse and span multiple fields. In aviation, radar is instrumental for air traffic control, weather monitoring, and collision avoidance systems. In meteorology, it aids in tracking storms and assessing precipitation patterns. Military applications include surveillance, target tracking, and missile guidance. Additionally, radar plays a pivotal role in maritime navigation, helping ships and boats avoid collisions and providing information about sea conditions. Furthermore,

radar has found its way into automotive safety, enabling features like adaptive cruise control and autonomous emergency braking. Its utility extends to geology, where ground-penetrating radar helps archaeologists and geologists discover subsurface features (Bruder, 2013). As technology advances, radar's versatility continues to expand, offering innovative solutions across domains and contributing significantly to our modern way of life.

2.3 Role of RF Front End Systems in Wireless Communication

The RF (Radio Frequency) front end is the gateway that bridges the physical world of electromagnetic signals with the digital realm of wireless communication systems. It plays a critical role in shaping, processing, and converting radio signals, forming a crucial interface between the transmitting and receiving elements of wireless devices.

In the realm of wireless communication, the RF front end system's significance cannot be overstated. It is accountable for responsibilities like signal amplification, filtering, modulation, and demodulation (Zhao et al., 2021). Figure 2 depicts the RF front end design.

Figure 2. RF front end design

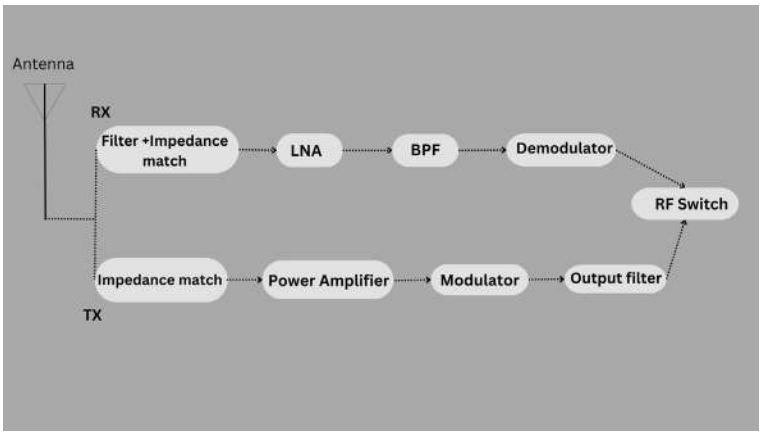

Signal amplification ensures that weak transmitted signals reach their intended destinations, while filtering helps eliminate unwanted noise and interference, enhancing signal quality. Modulation and demodulation processes allow data to be encoded onto carrier waves for transmission and decoded at the receiving end, enabling information exchange.

RF front end systems are tailored to the specific requirements of various wireless technologies, whether it's cellular networks, Wi-Fi, Bluetooth, or satellite communication. The design and capabilities of the RF front end directly influence the overall performance of wireless devices, determining factors like signal strength, data rate, range, and energy efficiency.

As wireless communication evolves to accommodate higher data rates, broader frequency ranges, and enhanced connectivity, the RF front end system's role becomes even more pivotal. The amalgamation of innovative technologies such as beamforming, massive MIMO, and millimeter-wave communications requires sophisticated RF front end designs to manage complex signal processing and ensure optimal performance (F. Liu et al., 2023) and hence the RF front end system serves as the cornerstone of wireless communication, enabling the translation of information between the analog and digital domains, and ultimately shaping the quality and efficiency of our modern wireless experiences.

3. INTEGRATION OF RADAR AND WIRELESS COMMUNICATION

3.1 Radar-Communication Coexistence Challenges

Radar – communication coexistence challenges are listed below.

***Spectrum Congestion*:** Radar and communication systems often operate within limited frequency bands, leading to potential spectrum congestion as the demand for both applications increases. Coordinating frequency usage becomes crucial to avoid interference.

***Interference Mitigation*:** The strong transmission power of radars can interfere with nearby communication devices. Innovative interference mitigation techniques are needed to ensure that radar signals do not disrupt communication services and vice versa.

***Dynamic Frequency Allocation*:** Both radar and communication systems require adaptable frequency allocation to accommodate changing operational needs. Developing dynamic spectrum sharing mechanisms is essential to prevent conflicts.

***Signal Isolation*:** Radar and communication systems emit strong electromagnetic signals that can unintentionally leak into neighboring frequency bands, causing cross-interference. Effective signal isolation techniques are necessary to maintain signal purity (Feng et al., 2020).

***Antenna Sharing*:** Efficient sharing of antennas for radar and communication can be challenging due to different radiation patterns and operational requirements.

Co-designing antennas to cater to both applications while minimizing interference is a complex task.

***Power Efficiency*:** Balancing power consumption is crucial as both radar and communication systems need to manage energy usage. Energy-efficient designs are required to ensure sustainable coexistence.

***Latency and Timing*:** Communication systems demand low latency, while radar applications require precise timing for target detection. Synchronizing these different timing requirements without compromising performance is a significant challenge.

***Protocol Compatibility*:** Radars and communication devices follow different protocols and communication standards. Ensuring that coexisting systems can understand each other's signals and protocols is essential for effective coordination.

***Regulatory Compliance*:** Regulatory frameworks and standards may differ for radar and communication technologies. Navigating these regulations while ensuring seamless coexistence can be complex, particularly in international deployments.

***Adaptive Algorithms*:** Developing adaptive algorithms that allow real-time adjustments in transmission parameters based on environmental conditions, interference levels, and operational needs is critical to address coexistence challenges effectively (R. Liu et al., 2021)

3.2 Spectrum Sharing Process and Managing Interference

Spectrum sharing process and interference are pivotal aspects of modern wireless ecosystems. As the demand for wireless services grows, effectively allocating and sharing the limited frequency spectrum becomes paramount. Sophisticated technologies and protocols are essential to ensure that different wireless systems, such as radar and communication, can coexist harmoniously without causing harmful interference. Figure 3 explains the process of spectrum sharing types.

Figure 3. Spectrum sharing types

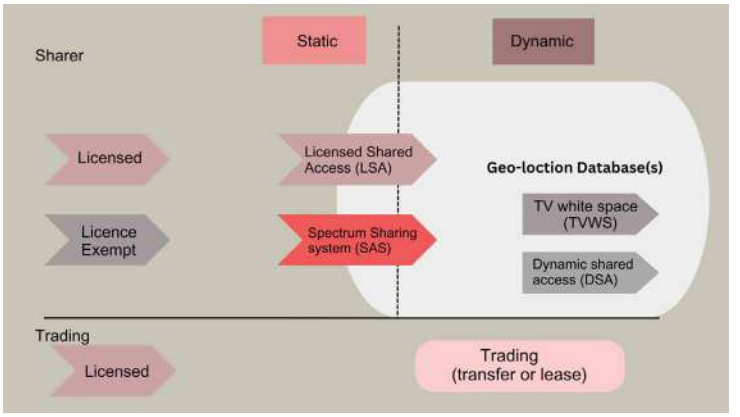

Dynamic spectrum admittance techniques, cognitive radio, and adaptive modulation are among the strategies employed to optimize spectrum utilization (Zheng et al., 2023). By intelligently managing interference and facilitating efficient spectrum sharing, these approaches enhance overall wireless performance, enabling diverse applications to thrive within the same frequency bands.

4. ADVANCED ANTENNA TECHNOLOGIES FOR NEXT-GENERATION WIRELESS

4.1 MIMO and Massive MIMO Systems

Multiple-Input Multiple-Output (MIMO) machinery has developed wireless communication by dramatically enhancing data rates, reliability, and spectral efficacy. MIMO systems employ several antennas at both the transmitting and receiving ends, exploiting spatial diversity to transmit and receive several data streams simultaneously over the similar frequency channels (Elijah et al., 2022). This technique mitigates signal fading, increases capacity, and improves overall system performance. Figure 4 explains Massive MIMO Techniques for 5G.

Figure 4. Massive MIMO systems for 5G

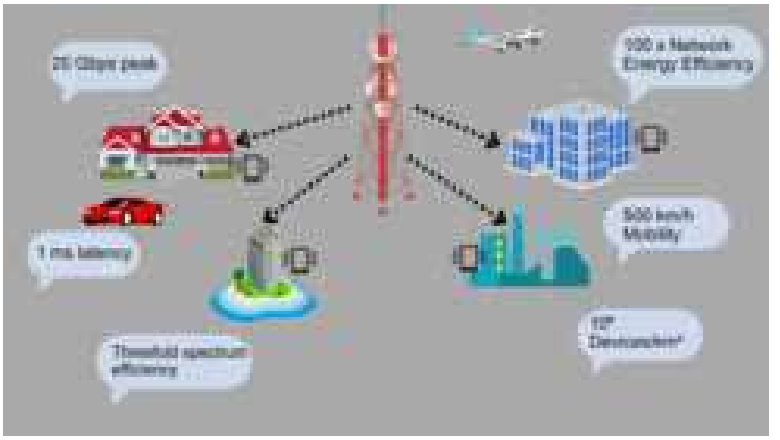

Massive MIMO takes MIMO to the next level by installing a large number of antennas at the base station. This architecture further boosts spectral efficiency and user experience. By utilizing spatial multiplexing techniques and beamforming, massive MIMO method increases signal-to-noise ratio, extends coverage, and reduces interference. The technology is particularly effective in crowded environments and for providing high-speed connectivity to a large number of users (Wei et al., 2023).

Massive MIMO's ability to serve multiple users concurrently, along with its resistance to fading and its potential for energy efficiency, makes it a cornerstone of future wireless networks. This technology aligns well with the demands of 5G and beyond, where the focus is on accommodating diverse applications such as augmented reality, Internet of Things (IoT), and ultra-high-definition streaming. As the wireless landscape continues to evolve, MIMO and massive MIMO systems will play a pivotal role in achieving the insatiable appetite for higher data rates, seamless connectivity, and enhanced user experiences.

4.2 Beamforming and Directional Antennas

Beamforming and directional antennas are instrumental technologies in wireless communication, allowing for targeted signal transmission and reception, improved link quality, and enhanced spectral efficiency. Beamforming involves shaping and directing radio frequency signals in specific directions, optimizing signal strength towards intended receivers while minimizing interference in other directions.

Directional antennas, a key component of beamforming, focus radio waves in a specific direction rather than uniformly radiating in all directions. This enables greater signal reach, reduced interference, and improved resistance to noise and fading. By

concentrating signal energy towards the intended user or device, directional antennas enhance communication reliability and increase system capacity (Hassanien et al., 2016).

Beamforming and directional antennas are particularly advantageous in urban and dense environments where interference and signal degradation are common challenges. They enable better coverage, support higher data rates, and extend the reach of wireless networks. Moreover, they contribute to energy efficiency as less power is wasted on signals propagating in unneeded directions. These technologies find applications in various domains, from cellular networks to Wi-Fi routers, satellite communications, and even vehicular networks. They are integral to improving the quality of service, ensuring consistent connectivity, and supporting the diverse demands of modern wireless communication, such as IoT, streaming media, and real-time applications. As wireless systems advance, beamforming and directional antennas will continue to play a pivotal role in influencing the upcoming of wireless experiences

5. ADAPTIVE RF FRONT END DESIGNS

5.1 Dynamic Spectrum Access Techniques

Dynamic Spectrum Access (DSA) techniques are pivotal to understand the rising claim for the wireless communication by optimizing the utilization of available frequency spectrum. DSA allows for the efficient sharing of spectrum resources between various users, applications, and services in real-time, maximizing spectral efficiency while minimizing interference (Zhang et al., 2020). Figure 5 explains various dynamic Spectrum Access Techniques

Figure 5. Dynamic spectrum access techniques

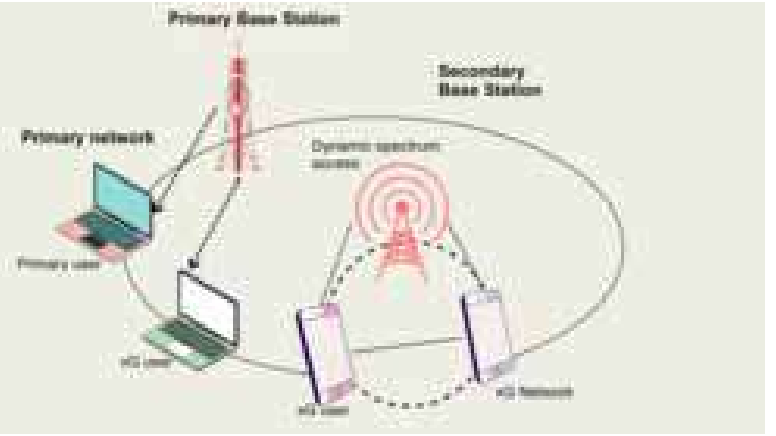

One key aspect of DSA is cognitive radio, where devices are equipped with the intelligence to sense and adapt to their surrounding radio environment. Cognitive radios can identify underutilized frequency bands or "white spaces" and opportunistically access them without causing interference to licensed users. This technology not only enhances spectrum utilization but also promotes the coexistence of diverse wireless services. Another approach is the use of spectrum databases that maintain information about available frequencies, regulatory rules, and usage patterns. When a device seeks to establish a connection, it queries the database for suitable frequency bands. This database-driven approach ensures compliance with regulatory requirements and minimizes conflicts.

DSA techniques hold immense potential for addressing spectrum scarcity and enabling innovative wireless applications. They are especially beneficial in scenarios where spectrum resources are unevenly distributed or underutilized. However, challenges remain, including interference management, accurate spectrum sensing, and ensuring fair access for various users (Y. Wu et al., 2023). As wireless technology evolves, DSA techniques are important in generating more flexible, efficient, and adaptable wireless communication schemes that cater to the dynamic demands of our interconnected world.

5.2 Reconfigurable RF Front End Architectures

Reconfigurable RF front end architectures are a transformative paradigm in wireless communication design, offering unprecedented flexibility and adaptability. These architectures enable wireless devices to dynamically adjust their radio frequency

circuitry to accommodate varying operating conditions, frequency bands, and communication standards.

Traditional RF front ends are fixed, designed for specific frequency ranges and communication protocols. Reconfigurable architectures, on the other hand, integrate tunable components such as filters, amplifiers, and antennas that can be adjusted in real-time. This adaptability allows devices to efficiently switch between different modes of operation, optimizing performance while conserving power. One approach involves software-defined radios (SDRs), where signal processing and modulation schemes are controlled through software, enabling rapid reconfiguration for diverse applications (Ma et al., 2021). Additionally, tunable components like varactor diodes or MEMS (Micro-Electro-Mechanical Systems) devices allow for dynamic adjustments of resonant frequencies and bandwidths.

Reconfigurable RF front ends offer a multitude of benefits, including reduced manufacturing costs by catering to multiple frequency bands with the same hardware, enhanced coexistence in spectrum-sharing environments, and improved resilience against interference. They also play a crucial role in future-proofing devices as new wireless standards emerge.

6. MILLIMETER WAVE AND BEYOND FOR ENHANCED WIRELESS

6.1 Millimeter Wave Frequency Bands and Characteristics

Millimeter wave frequency bands, often abbreviated as mmWave bands, refer to a range of radio frequency (RF) wavelengths that fall within the millimeter range, typically between 30 GHz (gigahertz) and 300 GHz (Björnson et al., 2019). These frequencies occupy a higher portion of the electromagnetic spectrum than those commonly used for traditional wireless communication, such as cellular networks. Some of the well-known millimeter wave frequency bands include: 24 GHz to 100 GHz, 57 GHz to 86 GHz and 94 GHz to 300 GHz.

Millimeter wave frequencies offer the advantage of providing larger bandwidths, which can support extremely high data rates. This makes them suitable for next-generation wireless technologies, such as 5G and after that. However, millimeter waves have shorter propagation distances and can be more susceptible to atmospheric absorption and obstacles like buildings or foliage, which can limit their coverage area. To overcome these challenges, technologies like beamforming and advanced antenna designs are employed to direct and focus the signals (Kaushik et al., 2021). Millimeter wave frequencies are key players in unlocking the potential of ultra-fast

wireless communication, enabling high-definition video systems, augmented reality systems, virtual reality systems, and Internet of Things in urban environments.

Millimeter wave frequency bands possess several distinctive characteristics that make them unique within the electromagnetic spectrum (Mishra et al., 2019). These characteristics shape their applications, advantages, and challenges. The important characteristics includes, high frequency, large Bandwidth, short wavelength, propagation challenges, spatial multiplexing, beamforming, line-of-sight dependency, high data rates and short range communications.

Millimeter wave frequency bands offer remarkable potential for high-speed, high-capacity wireless communication. While they come with unique challenges related to propagation and coverage, their advantages in terms of data rates, spatial multiplexing, and directional capabilities position them as a crucial component of the wireless technology landscape (Ahmed et al., 2021).

6.2 Benefits and Challenges of Millimeter Wave Communications

Millimeter wave technology presents a myriad of advantages that are shaping the landscape of wireless communication. First and foremost, its high data rates are a game-changer, addressing the insatiable appetite of data-intensive 4K video applications, virtual reality, and augmented reality systems. This is made possible by the massive bandwidth availability within the millimeter wave spectrum, which can put up the ever-growing number of connected devices and data-hungry services(Dokhanchi et al., 2019) . One of the remarkable features of millimeter waves is their efficient spatial reuse due to their short wavelengths. This enables multiple devices to operate in close proximity using the same frequency band without causing interference, greatly optimizing spectrum utilization. Moreover, their small antenna size, a direct consequence of the short wavelength, allows for the integration of multiple antennas in compact devices, fostering advanced beamforming techniques for improved signal quality and coverage. The ultra-low latency capabilities of millimeter wave communication are instrumental in online gaming, remote control surgery, and autonomous vehicles, where split-second decisions are critical. Additionally, their short-range and high directionality enhance security and privacy by reducing the risk of eavesdropping and unauthorized access, making them suitable for high-security applications.

Millimeter waves find utility in wireless backhaul solutions, offering high-capacity connections between cellular base stations and the core network, ensuring reliable and high-speed data transfer (Griffiths et al., 2015). Furthermore, this technology future-proofs networks, as it can easily accommodate the anticipated surge in data consumption as demands continue to escalate.

Some significant challenges of millimetre wave communications are propagation loss, atmospheric absorption, obstruction sensitivity, signal penetration, costly infrastructure, complex beamforming, device design challenges, regulatory hurdles, interference and crowding, trade-off between coverage and capacity (Cohen et al., 2018)

7. ENABLING TECHNOLOGIES FOR ENHANCED RADAR CAPABILITIES

7.1 Pulse-Doppler Techniques for Target Tracking

Pulse-Doppler techniques for target tracking involve advanced signal processing methods that utilize the Doppler frequency shift of radar echoes to accurately detect and track moving objects. Figure 6 shows Pulse Doppler processing of signal

Figure 6. Pulse doppler processing of signal

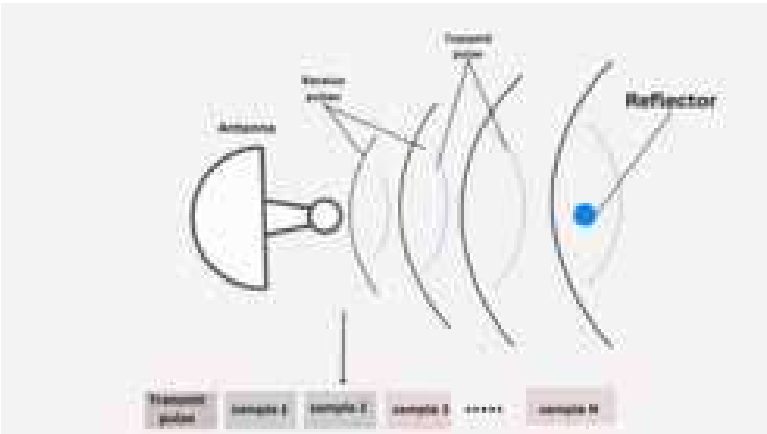

Here are some prominent Pulse-Doppler techniques used in target tracking:

***Constant False Alarm Rate (CFAR)*:** CFAR techniques adaptively adjust the detection threshold rely on the statistical properties of the received signal. This helps discriminate between true target echoes and clutter caused by stationary objects or environmental factors.

Moving Target Indication (MTI): MTI techniques employ multiple radar pulses to detect and track moving targets while suppressing the returns from stationary

objects. Doppler filtering or cancellers are used to eliminate clutter returns, enhancing the visibility of moving targets.

***Pulse-Pair Techniques*:** Pulse-pair processing compares the phase difference between successive radar pulses to estimate the target's Doppler shift. This technique reduces the impact of Doppler ambiguities and improves velocity accuracy.

***Stretch Processing*:** Stretch processing involves using linear frequency modulation in transmitted pulses. This spreads the received echoes in the frequency domain, making Doppler shifts more discernible and improving target detection (Dokhanchi et al., 2018).

***Clutter Map Tracking*:** Clutter map tracking builds a spatial representation of the radar environment to distinguish between actual targets and clutter. This method enhances target tracking accuracy by effectively filtering out unwanted signals.

Doppler Ambiguity Resolution: Modern radar systems employ techniques like staggered pulse repetition frequency (PRF) to mitigate Doppler ambiguities, allowing accurate tracking of fast-moving targets.

***Space-Time Adaptive Processing (STAP)*:** STAP combines information from multiple radar snapshots to suppress clutter and interference, improving detection and tracking of low-observable targets in complex scenarios.

***Frequency Modulated Continuous Wave (FMCW) Radar*:** FMCW radars use continuous transmission and frequency modulation to measure both range and Doppler shift, enabling simultaneous target tracking and velocity estimation.

***Multi-Channel Processing*:** Multi-channel processing involves using multiple receive channels to enhance the signal-to-noise ratio and enable efficient Doppler processing for tracking.

***Kalman Filtering*:** Kalman filtering is a recursive estimation technique used for target tracking. It combines measurement data with a dynamic model to predict and update target state information, leading to accurate and smooth tracking results (Kumari et al., 2018).

These Pulse-Doppler techniques, among others, are crucial for extracting valuable information from radar echoes, allowing for the precise detection, localization, and tracking of moving objects even in challenging and cluttered environments.

7.2 Synthetic Aperture Radar (SAR) for Imaging

Synthetic Aperture Radar (SAR) is a powerful remote sensing technology that revolutionizes imaging in various fields, from earth observation and environmental monitoring to disaster assessment and military reconnaissance. Unlike optical imaging, SAR operates independently of daylight and weather conditions, making it an invaluable tool for obtaining detailed images regardless of environmental constraints. Figure 7 shows synthetic aperture radar.

Figure 7. Synthetic aperture radar

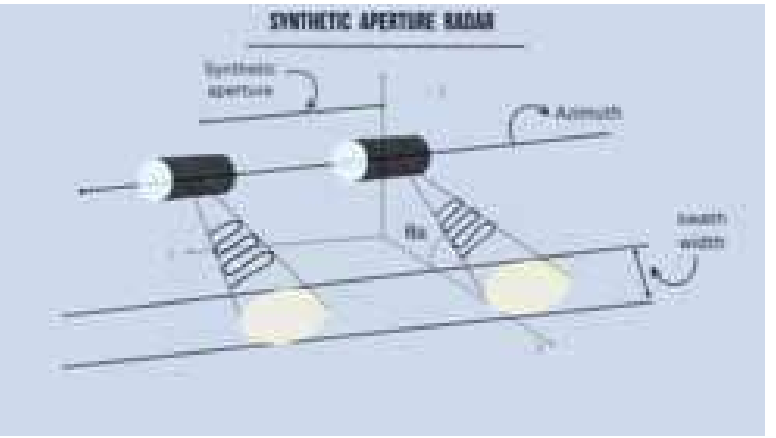

SAR imaging involves emitting microwave signals towards the Earth's surface from an airborne or space borne platform. The signals reflect off the target and return to the sensor, where they are recorded over multiple passes or pulses. By combining the information collected from these multiple perspectives, SAR effectively creates a "synthetic aperture," simulating a larger antenna that produces higher-resolution images (K. Wu et al., 2023). The key advantage of SAR lies in its ability to generate detailed, high-resolution images with consistent quality. It can penetrate cloud cover, haze, and even dense vegetation, providing critical information for disaster response, crop monitoring, deforestation assessment, and more. Additionally, SAR's capability to detect subtle changes over time makes it ideal for monitoring landscape alterations, tracking glacier movements, and studying ground deformation due to earthquakes or subsidence.

However, SAR imaging does present challenges such as complex signal processing, the need for accurate platform positioning, and issues related to speckle noise in resulting images. Nonetheless, its versatility, accuracy, and applicability across various domains have solidified Synthetic Aperture Radar as an indispensable tool for capturing detailed and reliable imagery of Earth's surfaces from space or the sky.

8. CO-DESIGN AND OPTIMIZATION OF RADAR-COMMUNICATION SYSTEMS

8.1 Cross-Layer Design Considerations

Cross-layer design considerations in radar communication involve optimizing interactions and trade-offs between different protocol layers to enhance overall system performance. Here are some key cross-layer design considerations in radar communication:

i. ***Physical Layer to Data Link Layer*:** Optimizing modulation schemes and coding techniques to suit the radar waveform characteristics while maintaining efficient data transmission and error correction mechanisms.
ii. ***Physical Layer to Network Layer*:** Coordinating radar transmission timing and power control to minimize interference with other communication systems and ensure efficient use of available spectrum resources.
iii. ***Physical Layer to Transport Layer*:** Balancing radar waveform characteristics, such as pulse repetition interval, with transport layer requirements to ensure timely and reliable data delivery (Zarakovitis et al., 2012).
iv. ***Physical Layer to MAC (Medium Access Control) Layer*:** Coordinating radar transmission schedules with MAC protocols to avoid collisions and ensure fair access for both radar and communication devices.
v. ***MAC Layer to Network Layer*:** Prioritizing radar signals over data communication during critical radar operations, and dynamically adjusting traffic prioritization based on network congestion and radar requirements.
vi. ***MAC Layer to Transport Layer*:** Adapting MAC layer parameters like access priority and contention resolution to optimize latency and reliability for both radar sensing and communication.
vii. ***Network Layer to Application Layer*:** Ensuring radar's quality of service requirements align with application-specific needs, such as tracking accuracy, object recognition, or target classification.
viii. ***Network Layer to Security Layer*:** Implementing security mechanisms to protect radar and communication data, considering the unique vulnerabilities and requirements of both systems.
ix. ***Network Layer to QoS (Quality of Service) Layer*:** Allocating network resources to ensure that both radar and communication systems meet their respective QoS targets while avoiding resource contention.
x. ***Network Layer to Energy Management Layer*:** Coordinating energy-efficient operation by optimizing the active and sleep periods of radar and communication devices to extend battery life.

By carefully addressing these cross-layer considerations, radar communication systems can achieve effective coexistence, minimize interference, and provide optimal performance for radar sensors and wireless systems.

8.2 Joint Optimization of Radar and Communication Performance

Joint optimization of radar and communication performance involves a holistic approach to designing systems that seamlessly integrate radar sensor and wireless communication functionalities. This approach recognizes the synergy between the two systems and leverages their interactions to achieve enhanced overall performance (Ashraf et al., 2023).

One key aspect of joint optimization is efficiently sharing spectrum resources between radar and communication systems. By dynamically allocating frequency bands and time slots based on real-time requirements, both radar and communication services can coexist without causing harmful interference. This shared spectrum usage optimizes spectral efficiency and maximizes the utility of the available bandwidth. Figure 8 clearly explains Joint Optimization of Radar and Communication

Figure 8. Joint optimization of radar and communication

Furthermore, joint optimization considers the interchanges between radar sensing and communication tasks. For instance, radar can adapt its transmission parameters to minimize interference with communication devices during critical communication moments. Conversely, communication systems can prioritize data transmission while accommodating radar's sensing needs during less sensitive communication

periods. In the context of infrastructure, co-locating antennas and sharing hardware components between radar and communication systems can lead to cost savings and efficient space utilization. This approach reduces the physical footprint and lowers deployment expenses.

Ultimately, joint optimization seeks to create a synergistic relationship where radar and communication systems not only coexist harmoniously but also enhance each other's performance. By sharing resources, adapting parameters, and aligning operational strategies, this approach leads to more capable, versatile, and responsive systems that address the demands of both radar sensing and wireless communication in a unified manner.

9 CASE STUDIES: INTEGRATING RADAR INTO WIRELESS SYSTEMS

9.1 Automotive Radar and V2X Communication

Automotive radar and Vehicle-to-Everything (V2X) communication are pivotal technologies reshaping the landscape of transportation safety and efficiency. These interconnected systems work in tandem to create smarter and safer road environments.

Automotive radar employs radar technology to enable vehicles to sense their surroundings. This includes detecting nearby vehicles, pedestrians, and obstacles, providing critical data for collision avoidance, adaptive cruise control, and autonomous driving functions. Radar sensors use the Doppler effect to measure relative speed and distance accurately, even in adverse weather conditions (Rauch et al., 2011).

V2X communication, on the other hand, leverages wireless communication to establish connections between vehicles and infrastructure elements such as traffic lights, road signs, and even pedestrians' smartphones. This bi-directional communication allows vehicles to share real-time information about their location, speed, and intentions, enhancing situational cognizance and enabling innovative safety structures like intersection collision evasion and cooperative adaptive cruise control. Figure 9 shows the v2x communication.

Figure 9. v2x communication

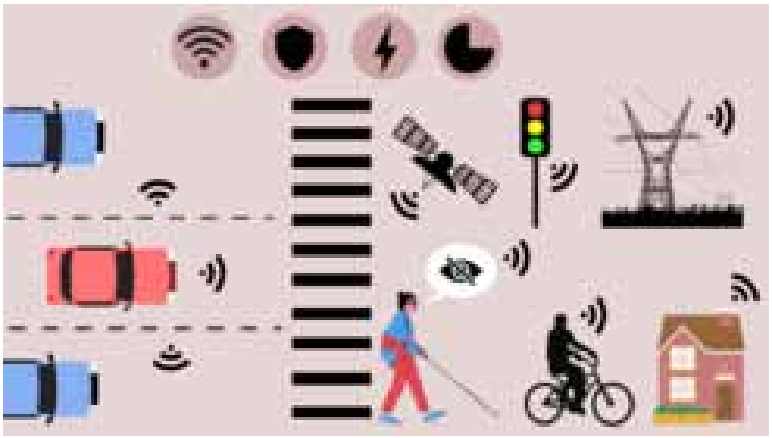

Together, automotive radar and V2X communication create a comprehensive safety net. Radar systems provide immediate object detection and short-range obstacle awareness, while V2X communication extends this awareness to encompass a broader environment, including non-line-of-sight scenarios. This collaborative approach enhances collision mitigation capabilities and supports the realization of fully autonomous vehicles.

Automotive manufacturers and researchers are continually advancing these technologies to ensure effective coexistence, optimal resource allocation, and reliable communication in complex driving scenarios. The combined power of automotive radar and V2X communication promises safer roads, reduced traffic congestion, and a future of smarter, more efficient transportation systems.

9.2 5G NR and Radar Integration for Industrial Applications

The integration of 5G New Radio (NR) and radar technologies holds significant promise for revolutionizing industrial applications, particularly in sectors like manufacturing, logistics, and automation. 5G NR's high data rates, low latency, and network sharing capabilities, coupled with radar's object detection and ranging prowess, create a potent synergy that can reshape industrial processes.

5G NR's ultra-reliable low-latency communication (URLLC) abilities enhance real-time control and communication between machines and systems, allowing for precise coordination and efficient resource management. This is essential for time-sensitive industrial tasks, such as robotics, where split-second decisions are crucial (Aijaz, 2020). Radar technology complements this by offering accurate object detection and tracking, enabling collision avoidance, automated guided

vehicles (AGVs) routing, and asset tracking within industrial environments. Radar's resilience to adverse conditions like dust, smoke, and poor lighting further solidifies its reliability in demanding settings (Liang et al., 2023).

The integration of 5G NR and radar enables seamless communication between machines, devices, and central control units, resulting in improved production efficiency, reduced downtime, and enhanced worker safety. For instance, AGVs can benefit from radar-based navigation and collision avoidance systems while communicating critical status updates through 5G networks (Li et al., 2023).

As industries progressively embrace Industry 4.0 concepts, the amalgamation of 5G NR and radar is poised to create an ecosystem where machines collaborate intelligently, leading to heightened productivity, optimized processes, and safer work environments. The synergy between these technologies exemplifies the transformative potential of combining wireless communication and radar sensing in industrial applications (Qian et al., 2022).

9.3 Recent Advances in Radar Design

The enduring essence of the fundamental radar range equation continues to serve as a wellspring of inspiration for pioneering designs and innovations in both civilian and military radar systems (Brown & Li, 2023).

In the contemporary radar landscape, this enduring equation has given rise to a plethora of cutting-edge technologies. These encompass a range of technologies, such as Multiple Inputs, Multiple Output systems, Digital Beam Forming methods, Active Electronically Steered Array radar, millimeter-wave radar, Passive Coherent Location Radar Systems, semiconductor Power Amplifiers, and advanced techniques for signal coding and Digital Signal Processing in radar systems. These advanced technologies have played a pivotal role in shaping the landscape of modern radar systems (Tan et al., 2023). Researchers have introduced an innovative hybrid substrate integrated checkerboard metasurface (CMS) that combines resonance-based and dispersion techniques to enhance radar stealth, effectively reducing the radar cross section (RCS) of flat metallic targets (Wang et al., 2023). To attain a broader bandwidth, the researchers employed both single and dual resonant artificial magnetic conductor meta-atoms, featuring adjusted cell topologies. The investigation delved into the resonance mechanism, providing a comprehensive insight into the reflective behaviors of these meta-atoms. A prototype of the RCS reducer was fabricated and measured, aligning closely with theoretical simulations. The improved 8 dB RCS drop in experimental results was attributed to the dielectric substrate's dispersion effects. This innovative design sets a benchmark for economical CMS in radar evasion applications. Radar design development is shown in Figure 10.

Figure 10. Radar design development

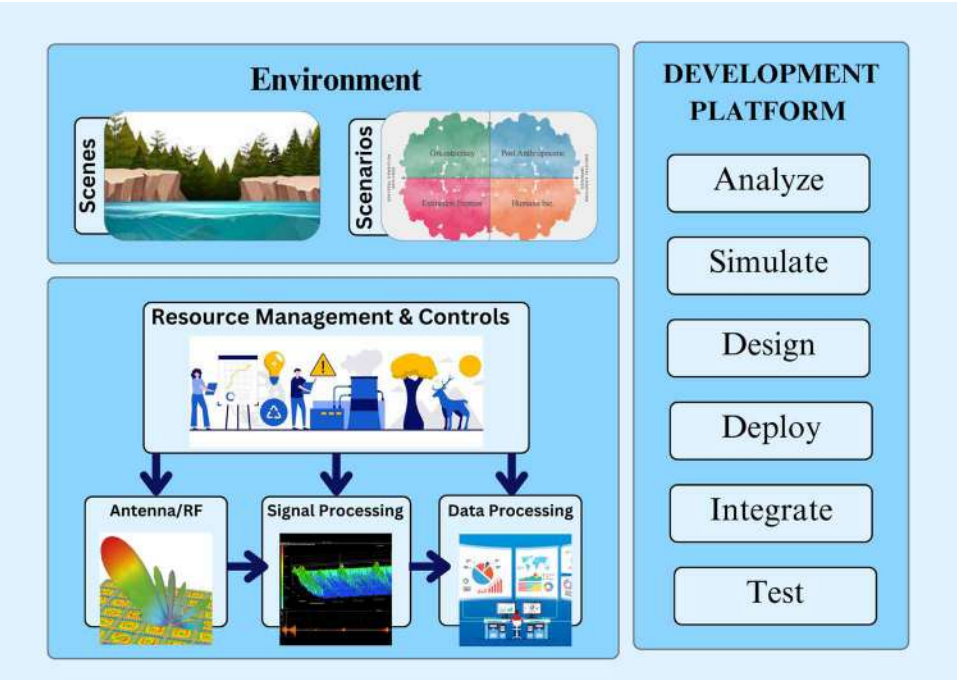

Nowadays, leveraging modeling and simulation tools within the radar system design process offers comprehensive benefits. By utilizing MATLAB and Simulink as the core platform for radar system development we can achieve better performance.

This comprehensive radar simulation and development framework offers a wide array of capabilities. It facilitates the interactive adjustment of radar parameters and waveform optimization, taking into account considerations based on the radar range equation and link budget. The framework expedites the development process with its extensive algorithm libraries with encompassing functions It supports modeling across a range of scenarios, including ground-based, airborne, ship-borne, space-based, and automotive radar systems, accommodating both moving targets and radar platforms. Additionally, it can create phased array systems, evaluate their presentation in diverse conditions using accurate synthetic data, and generate radar signals for machine and deep learning models. This framework seamlessly integrates RF component models and complex antenna designs, enhancing radar system design fidelity. It also streamlines the debugging and testing of complete radar models in the early project stages, minimizing the risk of costly redesigns. Furthermore, it automates the translation of MATLAB- Simulink methods into code

for positioning on DSP and programmable gate array, making the implementation process more efficient.

10. OVERCOMING TECHNICAL AND REGULATORY HURDLES

10.1 Regulatory Framework for Radar and Wireless Integration

The integration of radar and wireless technologies necessitates a well-defined regulatory framework to ensure coexistence, minimize interference, and promote efficient spectrum utilization. Regulatory bodies worldwide play a vital role in establishing rules that govern the deployment and operation of such integrated systems.

One key challenge in radar and wireless integration lies in allocating spectrum resources in a way that prevents harmful interference between these systems. Moreover, regulatory frameworks need to address issues related to spectrum sharing and coordination. Dynamic spectrum access mechanisms, such as geolocation databases and spectrum sensing, can aid in avoiding interference between radar and wireless networks. Additionally, regulations must ensure that both radar and wireless communication systems comply with emission limits to prevent excessive interference (Huseien & Shah, 2022).

International harmonization is also essential. Radar and wireless technologies transcend geographical boundaries, making it crucial for regulatory frameworks to align internationally. This ensures consistency and interoperability, allowing integrated systems to function seamlessly across regions.

As technologies evolve, regulatory bodies must remain agile and adaptive to accommodate advancements in radar and wireless communication. They play a pivotal role in enabling innovation while safeguarding against potential disruptions and conflicts. By establishing clear guidelines and standards, regulatory frameworks foster a conducive environment for the successful integration of radar and wireless technologies to create safer, more efficient, and interconnected systems.

10.2 Addressing Privacy and Security Concerns

Addressing privacy and security concerns in the integration of radar with wireless systems is crucial to ensure the protection of sensitive information and maintain user trust. Some significant points are shown in figure 11.

Figure 11. Privacy and security concerns

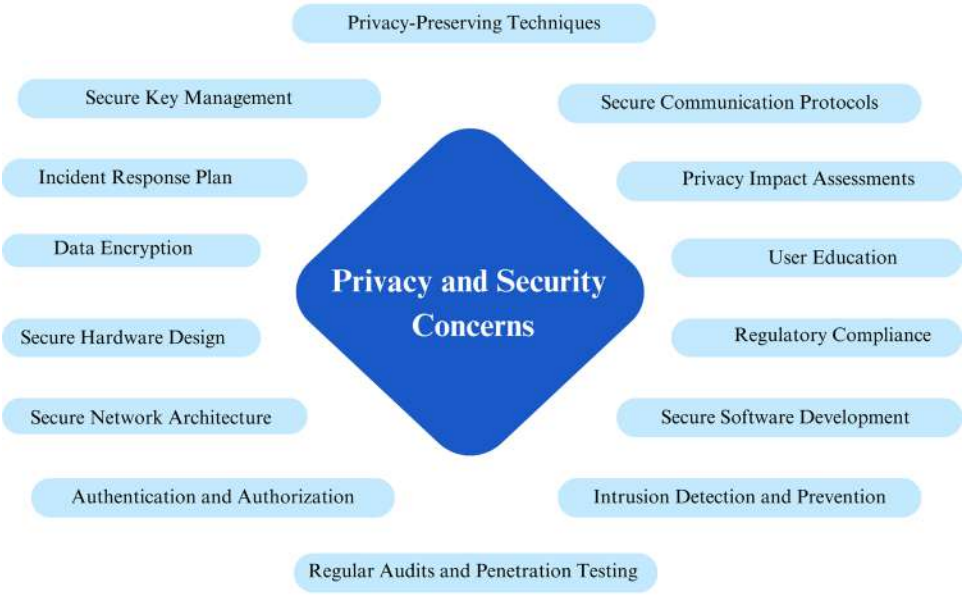

i. ***Data Encryption*:** Implement robust encryption mechanisms for both radar and wireless communication data to prevent unauthorized access and eavesdropping (You et al., 2021).
ii. ***Authentication and Authorization*:** Employ strong authentication methods to confirm the distinctiveness of devices and users before granting access to the network or radar system.
iii. ***Secure Key Management*:** Establish secure key management practices to safeguard encryption keys and ensure they are not compromised.
iv. ***Privacy-Preserving Techniques*:** Utilize privacy-preserving techniques like differential privacy to anonymize and aggregate data while still extracting meaningful insights.
v. ***Secure Software Development*:** Follow secure software development practices to minimize vulnerabilities and ensure that software and firmware updates are free from security flaws.
vi. ***Secure Communication Protocols*:** Use secure communication protocols that protect data integrity and confidentiality during transmission.

vii. ***Regular Audits and Penetration Testing*:** Conducting regular security audits and penetration testing to categorise vulnerabilities and flaws in the system's defenses.
viii. ***User Education*:** Educate users and stakeholders about the importance of security measures, best practices, and potential risks associated with the integrated system.
ix. ***Secure Hardware Design*:** Utilize hardware security features to prevent physical attacks and tampering of devices.
x. ***Secure Network Architecture*:** Design the network architecture with security in mind, realising firewalls, intrusion detection, and network division.
xi. ***Incident Response Plan*:** Develop a comprehensive incident reaction plan to handle security breaches and lessen the control on the integrated system.

By addressing these points, stakeholders can foster a secure and privacy-respecting environment for the incorporation of radar with wireless communication systems, mitigating risks and building user confidence in the technology's capabilities.

11.FUTURE DIRECTIONS IN RADAR-ENHANCED WIRELESS EXPERIENCES

11.1 Integration With 6G and Beyond

Integration with 6G and beyond represents a forward-looking approach to technology convergence, where radar and wireless communication systems synergistically coexist to shape the future of interconnected environments. As we approach the era beyond 5G, the integration of radar and wireless technologies holds immense potential to create innovative solutions that transcend traditional boundaries.

6G envisions a hyper-connected world, where data rates reach terabits per second, latency becomes nearly imperceptible, and diverse applications benefit from seamless connectivity. Integrating radar into this vision can lead to transformative advancements. For instance, combining radar's precise sensing capabilities with ultra-high-speed wireless communication can create unparalleled situational awareness for autonomous vehicles, enabling real-time collision avoidance even in complex urban scenarios(F. Liu et al., 2022). Moreover, radar's ability to penetrate obstacles and harsh weather conditions can enhance the reliability of communication networks. This is especially relevant for applications like disaster response, where integrated systems can ensure continuous connectivity in adverse situations.

The integration of radar and 6G wireless communication also has implications for security and privacy. Radar can be employed to detect and mitigate wireless signal

jamming and cyberattacks, fortifying the resilience of communication networks against malicious actors.

As we look even further ahead to 7G and beyond, integration can amplify the potential for holistic sensing and communication ecosystems. Radar systems could play a pivotal role in creating intelligent environments that adapt in real-time based on both wireless communication and radar-sensed data. This could lead to urban infrastructure that self-adjusts traffic signals based on real-time vehicle movements, resulting in optimized traffic flow and reduced congestion.

However, this integration also introduces challenges such as harmonizing complex waveforms, addressing interference between radar and advanced wireless networks, and managing cross-layer optimizations effectively. Collaborative research development across disciplines will be essential to realize the potential of this integration (Shafie et al., 2022).

In conclusion, the integration of radar with 6G and beyond holds tremendous promise for reshaping our world's communication and sensing capabilities. As these technologies converge, they can revolutionize industries, enhance safety, and drive innovations that propel us toward a more interconnected and intelligent future.

11.2 AI-Driven Adaptations for Dynamic Environments

In dynamic and rapidly changing environments, the integration of artificial intelligence (AI) offers remarkable opportunities for adaptive systems that can respond intelligently to evolving conditions. AI-driven adaptations empower systems to make real-time decisions, optimize performance, and ensure efficiency in the face of uncertainties and fluctuations.

One of the basic strengths of AI lies in its skill to process large data from several sources. This data can be leveraged to generate comprehensive situational awareness, allowing systems to understand the environment's current state and predict its future dynamics. For instance, in autonomous vehicles, AI can process sensor data to assess road conditions, weather, traffic patterns, and even pedestrians' behavior, enabling the vehicle to adapt its driving strategy accordingly (Drinan et al., 2012).

Machine learning algorithms, a subset of AI, enable systems to learn patterns and trends from historical data. This enables AI-driven adaptations to recognize recurring scenarios and make informed decisions. In manufacturing, AI can optimize production processes by predicting equipment failures and adjusting operations in real-time to minimize downtime.

AI-driven adaptations are particularly relevant in sectors like healthcare and disaster management. In healthcare, AI can continuously monitor patients' vital signs and detect anomalies, triggering alerts to medical staff for timely intervention. In

disaster management, AI can analyze incoming data from various sources to predict natural disasters and dynamically allocate resources to affected areas.

However, challenges exist, including the need for robust AI models that can generalize well in diverse scenarios and the ethical considerations around AI-driven decision-making.

Ultimately, AI-driven adaptations for dynamic environments promise to revolutionize how we interact with technology. As AI systems become more adept at processing data, learning from it, and making real-time adjustments, they will enable a new level of efficiency, safety, and responsiveness in sectors ranging from transportation to healthcare, from manufacturing to emergency response, and beyond. The synergy between AI and dynamic environments can reshape industries and improve quality of life on a global scale.

11.3 Achievements in Next-Gen Wireless Experiences

The realm of next-generation wireless experiences has seen remarkable achievements that are transforming the way we connect, communicate, and interact. These achievements are shaping a future where wireless technologies offer unprecedented capabilities and cater to the diverse demands of our interconnected world.

i. ***5G Revolution*:** One of the most notable achievements has been the rollout of 5G networks. With faster data rate, low latency, and massive device connections, 5G has unlocked new possibilities for real-time applications and the Internet of Things (IoT).
ii. ***Massive MIMO and Beamforming*:** Massive Multiple-Input Multiple-Output (MIMO) technology and advanced beamforming techniques have enabled networks to provide higher data rates and improved coverage, enhancing user experiences even in densely populated areas.
iii. ***Edge Computing*:** The integration of edge computing with wireless networks has brought computation nearer to data sources, decreasing latency and empowering time-sensitive applications like autonomous vehicles and industrial automation.
iv. ***IoT Connectivity*:** Next-gen wireless technologies have facilitated seamless IoT connectivity, allowing for a myriad of devices to communicate and interact with each other. This has led to advancements in smart homes, industrial IoT, and connected healthcare.
v. ***Enhanced Mobile Broadband*:** Faster and more reliable wireless connections have propelled enhanced mobile broadband experiences, enabling high-quality streaming, online gaming, and other bandwidth-intensive activities (Sahu et al., 2021).

vi. ***Wireless Power Transfer*:** Achievements in wireless power transfer have led to the development of technologies that wirelessly charge devices, from smartphones to electric vehicles, without the need for physical connectors.
vii. ***Smart Cities*:** Wireless technologies have been pivotal in the evolution of smart cities, enabling intelligent transportation systems, smart energy grids, and efficient urban management.
viii. ***Cognitive Radio and Spectrum Sharing*:** Cognitive radio techniques have facilitated dynamic spectrum sharing, optimizing spectrum utilization and addressing the challenge of spectrum scarcity.
ix. ***Wireless Healthcare*:** Wireless medical devices and telemedicine solutions are transforming healthcare delivery, allowing for remote monitoring, diagnosis, and treatment.
x. ***AI-Driven Wireless Networks*:** The incorporation of AI and machine learning with wireless networks has led to autonomous network management, predictive maintenance, and optimized resource allocation.

These achievements collectively mark a significant shift in the wireless landscape, fostering innovation, economic growth, and improved quality of life. As wireless technologies continue to advance, their transformative impact will likely extend to realms yet unexplored, paving the way for a future where connectivity is seamless, intelligent, and deeply integrated into our daily lives.

11.4 Potential Societal and Industrial Impact

The convergence of radar and wireless communication technologies holds immense potential for generating significant societal and industrial impact:

i. ***Safer Transportation*:** Integration can enhance collision avoidance systems, enabling safer roadways through improved radar-based object detection and real-time V2X communication for timely alerts to drivers.
ii. ***Smart Cities*:** Radar-wireless integration can contribute to efficient traffic management, waste collection, and energy distribution, transforming urban environments into smart and sustainable hubs.
iii. ***Industrial Automation*:** The combination can optimize manufacturing processes by using radar for precise object tracking and wireless communication for real-time data sharing, leading to increased productivity and reduced downtime.
iv. ***Agricultural Innovation*:** By providing accurate soil moisture data through radar and enabling remote control of machinery using wireless communication, agriculture can become more efficient and sustainable.

v. ***Healthcare Advancements*:** Integration can support wearable health devices that monitor patients' vital signs through radar and transmit data wirelessly for remote medical diagnosis and treatment (Lyu et al., 2021) .
vi. ***Emergency Response*:** Radar communication can assist in disaster management by enabling through-wall sensing for locating survivors, while wireless communication maintains connectivity for coordinated response efforts.
vii. ***Environmental Monitoring*:** Both technologies combined can facilitate real-time monitoring of pollution levels, weather patterns, and natural disasters, enhancing our understanding of and ability to respond to environmental changes.
viii. ***Supply Chain Efficiency*:** Radar can improve logistics by enabling precise asset tracking, while wireless communication supports real-time inventory management and coordination across the supply chain.
ix. ***Remote Sensing*:** The synergy can lead to more accurate weather forecasting, remote sensing for scientific research, and space exploration applications.
x. ***New Business Models*:** Radar-wireless integration can foster the creation of innovative services and business models, propelling economic growth and opening doors to new market opportunities.

The societal and industrial impact of integrating radar and wireless communication is profound. This synergy has the power to transmute various sectors, enhancing safety, efficiency, and class of life on a global scale while ushering in new possibilities for innovation and technological advancement.

CONCLUSION

In conclusion, the book chapter on "Engineering Next-Generation Wireless Experiences through Radar and RF Front End System Designs" sheds light on the synergistic potential of integrating radar and wireless communication technologies. This integration marks a pivotal step towards creating interconnected ecosystems that transcend traditional boundaries and enhance our ability to sense, communicate, and interact in dynamic environments.

Throughout the chapter, we have delved into the evolution of wireless technologies, the demand for enhanced wireless experiences, radar principles, RF front-end systems, and various cross-layer considerations. We've explored the challenges and benefits of coexistence between radar and communication, and examined advanced techniques like MIMO, beamforming, and dynamic spectrum access. Moreover, the chapter delved into reconfigurable RF front-end architectures and the regulatory aspects governing the integration of radar and wireless systems.

The societal and industrial impact of this integration is vast, with potential implications for transportation, healthcare, smart cities, agriculture, and beyond. This chapter underscores the crucial role that radar and RF front-end designs play in shaping the future of wireless technologies, opening avenues for innovation, economic growth, and improved quality of life.

As the world accelerates towards the realization of 5G, 6G, and beyond, the intersection of radar and wireless communication is poised to redefine how we perceive, connect, and interact with our environment. The book chapter underscores the importance of interdisciplinary collaboration and continuous research to harness the full potential of this integration, fostering a world where technology not only amplifies human capabilities but also ushers in a new era of connectivity and intelligence. Ultimately, by engineering next-generation wireless experiences through radar and RF front-end system designs, we pave the way for a future where communication and sensing are seamlessly intertwined, shaping a world that is safer, smarter, and more connected than ever before.

REFERENCES

Ahmed, A., Zhang, Y. D., & Hassanien, A. (2021). Joint Radar-Communications Exploiting Optimized OFDM Waveforms. *Remote Sensing (Basel)*, *13*(21), 4376. doi:10.3390/rs13214376

Aijaz, A. (2020). Private 5G: The Future of Industrial Wireless. *IEEE Industrial Electronics Magazine*, *14*(4), 136–145. doi:10.1109/MIE.2020.3004975

Arbab-Zavar, B., Palacios-Garcia, E., Vasquez, J., & Guerrero, J. (2019). Smart Inverters for Microgrid Applications: A Review. *Energies*, *12*(5), 840. doi:10.3390/en12050840

Ashraf, M., Tan, B., Moltchanov, D., Thompson, J. S., & Valkama, M. (2023). Joint Optimization of Radar and Communications Performance in 6G Cellular Systems. *IEEE Transactions on Green Communications and Networking*, *7*(1), 522–536. doi:10.1109/TGCN.2023.3234258

Björnson, E., Sanguinetti, L., Wymeersch, H., Hoydis, J., & Marzetta, T. L. (2019). Massive MIMO is a reality—What is next? *Digital Signal Processing*, *94*, 3–20. doi:10.1016/j.dsp.2019.06.007

Brown, M., & Li, C. (2023). Advancement of PMCW Radar and Its Board-Level Prototyping. *2023 IEEE 16th Dallas Circuits and Systems Conference (DCAS)*, 1–4. 10.1109/DCAS57389.2023.10130242

Bruder, J. A. (2013). IEEE Radar standards and the radar systems panel. *IEEE Aerospace and Electronic Systems Magazine*, *28*(7), 19–22. doi:10.1109/MAES.2013.6559377

Cohen, D., Mishra, K. V., & Eldar, Y. C. (2018). Spectrum Sharing Radar: Coexistence via Xampling. *IEEE Transactions on Aerospace and Electronic Systems*, *54*(3), 1279–1296. doi:10.1109/TAES.2017.2780599

Dokhanchi, S. H., Mysore, B. S., Mishra, K. V., & Ottersten, B. (2019). A mmWave Automotive Joint Radar-Communications System. *IEEE Transactions on Aerospace and Electronic Systems*, *55*(3), 1241–1260. doi:10.1109/TAES.2019.2899797

Dokhanchi, S. H., Shankar, M. R. B., Stifter, T., & Ottersten, B. (2018). OFDM-based automotive joint radar-communication system. *2018 IEEE Radar Conference (RadarConf18)*, 902–907. 10.1109/RADAR.2018.8378680

Drinan, D. P., Zale, A. V., Webb, M. A. H., Taper, M. L., Shepard, B. B., & Kalinowski, S. T. (2012). Evidence of Local Adaptation in Westslope Cutthroat Trout. *Transactions of the American Fisheries Society*, *141*(4), 872–880. doi:10.1080/00028487.2012.675907

Elijah, O., Abdul Rahim, S. K., New, W. K., Leow, C. Y., Cumanan, K., & Kim Geok, T. (2022). Intelligent Massive MIMO Systems for Beyond 5G Networks: An Overview and Future Trends. *IEEE Access : Practical Innovations, Open Solutions*, *10*, 102532–102563. doi:10.1109/ACCESS.2022.3208284

Feng, Z., Fang, Z., Wei, Z., Chen, X., Quan, Z., & Ji, D. (2020). Joint radar and communication: A survey. *China Communications*, *17*(1), 1–27. doi:10.23919/JCC.2020.01.001

Ghorbanian, M., Dolatabadi, S. H., Masjedi, M., & Siano, P. (2019). Communication in Smart Grids: A Comprehensive Review on the Existing and Future Communication and Information Infrastructures. *IEEE Systems Journal*, *13*(4), 4001–4014. doi:10.1109/JSYST.2019.2928090

Griffiths, H., Cohen, L., Watts, S., Mokole, E., Baker, C., Wicks, M., & Blunt, S. (2015). Radar Spectrum Engineering and Management: Technical and Regulatory Issues. *Proceedings of the IEEE*, *103*(1), 85–102. doi:10.1109/JPROC.2014.2365517

Gunasekaran, V., & Harmantzis, F. C. (2007). Emerging wireless technologies for developing countries. *Technology in Society*, *29*(1), 23–42. doi:10.1016/j.techsoc.2006.10.001

Hassanien, A., Amin, M. G., Zhang, Y. D., & Ahmad, F. (2016). Dual-Function Radar-Communications: Information Embedding Using Sidelobe Control and Waveform Diversity. *IEEE Transactions on Signal Processing*, *64*(8), 2168–2181. doi:10.1109/TSP.2015.2505667

Huseien, G. F., & Shah, K. W. (2022). A review on 5G technology for smart energy management and smart buildings in Singapore. *Energy and AI*, *7*, 100116. doi:10.1016/j.egyai.2021.100116

Kaushik, A., Masouros, C., & Liu, F. (2021). Hardware Efficient Joint Radar-Communications with Hybrid Precoding and RF Chain Optimization. *ICC 2021 - IEEE International Conference on Communications*, 1–6. 10.1109/ICC42927.2021.9500661

Kumari, P., Choi, J., Gonzalez-Prelcic, N., & Heath, R. W. (2018). IEEE 802.11ad-Based Radar: An Approach to Joint Vehicular Communication-Radar System. *IEEE Transactions on Vehicular Technology*, *67*(4), 3012–3027. doi:10.1109/TVT.2017.2774762

Li, H., Liu, Y., Liao, G., & Chen, Y. (2023). Joint Radar and Communications Waveform Design Based on Complementary Sequence Sets. *Remote Sensing (Basel)*, *15*(3), 645. doi:10.3390/rs15030645

Liang, C., Li, Y., Hu, X., Wang, Y., Zhang, L., Wang, M., & Guo, J. (2023). Coherent-on-Receive Synthesis Using Dominant Scatterer in Millimeter-Wave Distributed Coherent Aperture Radar. *Remote Sensing (Basel)*, *15*(6), 1505. doi:10.3390/rs15061505

Liu, F., Cui, Y., Masouros, C., Xu, J., Han, T. X., Eldar, Y. C., & Buzzi, S. (2022). Integrated Sensing and Communications: Toward Dual-Functional Wireless Networks for 6G and Beyond. *IEEE Journal on Selected Areas in Communications*, *40*(6), 1728–1767. doi:10.1109/JSAC.2022.3156632

Liu, F., Zheng, L., Cui, Y., Masouros, C., Petropulu, A. P., Griffiths, H., & Eldar, Y. C. (2023). Seventy Years of Radar and Communications: The road from separation to integration. *IEEE Signal Processing Magazine*, *40*(5), 106–121. doi:10.1109/MSP.2023.3272881

Liu, R., Li, M., Liu, Q., & Swindlehurst, A. L. (2021). Dual-Functional Radar-Communication Waveform Design: A Symbol-Level Precoding Approach. *IEEE Journal of Selected Topics in Signal Processing*, *15*(6), 1316–1331. doi:10.1109/JSTSP.2021.3111438

Lyu, Y., Zhang, Y., Liu, Y., Chen, W., Zhang, X., Xu, W., Wu, C., Wang, L., Zeng, H., Sheng, X., Yang, R., Wang, Z., Kuang, K., & Fei, W. (2021). Analysis of Potential Disruptive Technologies in the Electronics and Information Field Towards the Intelligent Society. *Engineering (Beijing)*, *7*(8), 1051–1056. doi:10.1016/j.eng.2021.05.004

Ma, D., Shlezinger, N., Huang, T., Liu, Y., & Eldar, Y. (2021). FRaC: FMCW-Based Joint Radar-Communications System Via Index Modulation. *IEEE Journal of Selected Topics in Signal Processing*, *15*(6), 1348–1364. doi:10.1109/JSTSP.2021.3118219

Mishra, K. V., Bhavani Shankar, M. R., Koivunen, V., Ottersten, B., & Vorobyov, S. A. (2019). Toward Millimeter-Wave Joint Radar Communications: A Signal Processing Perspective. *IEEE Signal Processing Magazine*, *36*(5), 100–114. doi:10.1109/MSP.2019.2913173

Qian, J., Liu, Z., Lu, Y., Zheng, L., Zhang, A., & Han, F. (2022). Radar and Communication Spectral Coexistence on Moving Platform with Interference Suppression. *Remote Sensing (Basel)*, *14*(19), 5018. doi:10.3390/rs14195018

Rauch, A., Klanner, F., & Dietmayer, K. (2011). Analysis of V2X communication parameters for the development of a fusion architecture for cooperative perception systems. *2011 IEEE Intelligent Vehicles Symposium (IV)*, 685–690. 10.1109/IVS.2011.5940479

Sahu, C. K., Young, C., & Rai, R. (2021). Artificial intelligence (AI) in augmented reality (AR)-assisted manufacturing applications: A review. *International Journal of Production Research*, *59*(16), 4903–4959. doi:10.1080/00207543.2020.1859636

Shafie, A., Yang, N., Han, C., Jornet, J. M., Juntti, M., & Kurner, T. (2022). Terahertz Communications for 6G and Beyond Wireless Networks: Challenges, Key Advancements, and Opportunities. *IEEE Network*, 1–8. doi:10.1109/MNET.118.2200057

Tan, B., Ma, Z., Zhu, X., Li, S., Zheng, L., Huang, L., & Bai, J. (2023). Tracking of Multiple Static and Dynamic Targets for 4D Automotive Millimeter-Wave Radar Point Cloud in Urban Environments. *Remote Sensing (Basel)*, *15*(11), 2923. doi:10.3390/rs15112923

Tightiz, L., Yang, H., & Piran, M. J. (2020). A Survey on Enhanced Smart Micro-Grid Management System with Modern Wireless Technology Contribution. *Energies*, *13*(9), 2258. doi:10.3390/en13092258

Wang, C., Wang, R.-Z., Zhang, S.-J., Wang, H., & Wang, W.-S. (2023). Reducing radar cross section of flat metallic targets using checkerboard metasurface: Design, analysis, and realization. *Journal of Applied Physics*, *134*(4), 044902. Advance online publication. doi:10.1063/5.0154916

Wei, Z., Wang, Y., Ma, L., Yang, S., Feng, Z., Pan, C., Zhang, Q., Wang, Y., Wu, H., & Zhang, P. (2023). 5G PRS-Based Sensing: A Sensing Reference Signal Approach for Joint Sensing and Communication System. *IEEE Transactions on Vehicular Technology*, *72*(3), 3250–3263. doi:10.1109/TVT.2022.3215159

Wu, K., Zhang, J. A., Huang, X., & Guo, Y. J. (2023). OTFS-Based Joint Communication and Sensing for Future Industrial IoT. *IEEE Internet of Things Journal*, *10*(3), 1973–1989. doi:10.1109/JIOT.2021.3139683

Wu, Y., Lemic, F., Han, C., & Chen, Z. (2023). Sensing Integrated DFT-Spread OFDM Waveform and Deep Learning-Powered Receiver Design for Terahertz Integrated Sensing and Communication Systems. *IEEE Transactions on Communications*, *71*(1), 595–610. doi:10.1109/TCOMM.2022.3225920

You, X., Wang, C.-X., Huang, J., Gao, X., Zhang, Z., Wang, M., Huang, Y., Zhang, C., Jiang, Y., Wang, J., Zhu, M., Sheng, B., Wang, D., Pan, Z., Zhu, P., Yang, Y., Liu, Z., Zhang, P., Tao, X., ... Liang, Y.-C. (2021). Towards 6G wireless communication networks: Vision, enabling technologies, and new paradigm shifts. *Science China. Information Sciences*, *64*(1), 110301. doi:10.1007/s11432-020-2955-6

Zarakovitis, C. C., Ni, Q., Skordoulis, D. E., & Hadjinicolaou, M. G. (2012). Power-Efficient Cross-Layer Design for OFDMA Systems With Heterogeneous QoS, Imperfect CSI, and Outage Considerations. *IEEE Transactions on Vehicular Technology*, *61*(2), 781–798. doi:10.1109/TVT.2011.2179817

Zhang, Z., Du, Z., & Yu, W. (2020). Mutual-Information-Based OFDM Waveform Design for Integrated Radar-Communication System in Gaussian Mixture Clutter. *IEEE Sensors Letters*, *4*(1), 1–4. doi:10.1109/LSENS.2019.2946735

Zhao, J., Li, J., & Yi, Y. (2021). Research on Radar Communication Integrated Signal Based on 64QAM-LFM. *2021 International Wireless Communications and Mobile Computing (IWCMC)*, 1151–1155. doi:10.1109/IWCMC51323.2021.9498961

Zheng, J., Chu, P., Wang, X., & Yang, Z. (2023). Inner-Frame Time Division Multiplexing Waveform Design of Integrated Sensing and Communication in 5G NR System. *Sensors (Basel)*, *23*(15), 6855. doi:10.3390/s23156855 PMID:37571638

J.Natn.Sci.Foundation Sri Lanka 2023 51 (2): 225 - 235
DOI: http://dx.doi.org/10.4038/jnsfsr.v51i2.11080

RESEARCH ARTICLE

Photonics Technology

Simulation and numerical analysis of SOA- based all optical NAND gate for high data rate communication

V Anusooya[1], S Ponmalar[2], MSK Manikandan[3] and S Gobalakrishnan[4]

[1] *Department of Electronics and Communication Engineering, Amrita College of Engineering and Technology, Tamil Nadu 629901, India.*
[2] *Department of Computer Science and Engineering, Velammal College of Engineering and Technology, Tamil Nadu 625009, India.*
[3] *Department of Electronics and Communication Engineering, Thiagarajar College of Engineering, Tamil Nadu 625015, India.*
[4] *Department of Nanotechnology, Noorul Islam Centre for Higher Education, Tamil Nadu 629180, India.*

Submitted: 18 Febuary 2022; Revised: 15 August 2022; Accepted: 28 October 2022

Abstract: As a result of the development of advanced semiconductor-based optical switching devices and their commercialization, concepts and technologies in all-optical signal processing have evolved significantly in the past few years. Universal gates are required for the realization of logical processes in photonic computing. In this study, a straightforward and small-footprint all-optical NAND gate was created utilizing semiconductor optical amplifier and simulated at high data rates between 10 to 40 Gbps. Numerical analysis of the performance of the suggested NAND gate for various input combinations and semiconductor optical amplifier (SOA) is shown. A numerical study is carried out by varying the wavelength, injection current, confinement factor, and optical elements such as sources, amplifiers, and filters. Unique results were obtained at a 10 Gbps to 40 Gbps data rate for NRZ-L user-defined bit sequences. This type of all-optical NAND gate will be the perfect alternative in the field of all-optical computing to realize a high-speed optical communication network. An extinction ratio of 15.323 dB is achieved at a high data rate of 40 Gbps. The output spectrum of the designed NAND logic is also obtained for a wide input spectrum and the system responds selectively to the input wavelength at 1548.3 nm, which is the probe signal wavelength.

Keywords: Cross-gain modulation, erbium doped fibre amplifier, extinction ratio, gain saturation, optical logic gate, semiconductor optical amplifier.

INTRODUCTION

Considerable research has gone into making all-optical integrated circuits, which are widely useful for doing ultrafast computing to handle ultrahigh bandwidth in the field of communication engineering technology. This technology is very helpful in developing miniaturized and noise-free integrated circuits, which are very difficult to realize using conventional electronic components. Among all the digital logic gates, these are the primary elements for performing any kind of function in electronic circuits. Therefore, similar kinds of gates will be replaced by optical logic gates so that all functions can be done with light.

All-optical logic gates are unique due to their small physical size, negligible electronic interference, excellent immunity against short circuits, and high bandwidth transmission with negligible loss. Implementing a nonlinear medium is essential to complete the design of an all-optical system which plays a major role in modulating the input light signals into the desired output. At a data rate of 80 Gbps, the configuration of the NAND logic gates employing a semiconductor optical amplifier (SOA) and PC-SOA with Mach-Zehnder interferometer (MZI) structure has been designed to achieve an extinction ratio of 7.1 dB and 16.2 dB, respectively (Heydarian *et al*., 2022). In addition, a three-input all-optical NAND gate that makes use of polarisation rotation in an SOA was demonstrated. The goal of this demonstration was to achieve a high extinction ratio with an unsaturated gain of 30 dB, despite the fact that the output signals had non-uniform amplitudes (Mukherjee & Raja, 2020).

* Corresponding author (v.anusooya@gmail.com; https://orcid.org/0000-0003-2608-5738)

The design of all-optical logic gates comprises an encoding system, a frequency generator, and a frequency converter. For the representation of binary states, hybrid encoding techniques are preferred. A four-wave mixing semiconductor amplifier was adopted to develop a frequency generator, and a cross-polarization rotation effect was adopted to develop a frequency convertor. With these designed components, a universal all-optical NAND logic system has been studied (Mukherjee *et al*., 2019). The use of filters along with SOA can help improve the efficiency of the NAND gate.

Continuous improvement is made by the research community from the existing SOA-based NAND gate designs into the SOA-MZI configuration, which enables high switching efficiency, ER ratio, and high bit rate operation (Mehra *et al*., 2012). To achieve miniaturization, an integrated SOA-based MZI was used at a data rate of 10 Gbps, which opens a new horizon to realize all-optical routing (Ye *et al*., 2006). The enhancement of the existing design has been attained by introducing a distributed Bragg reflector laser integrated SOA. By increasing the signal rate between 1.25 Gbps and 10 Gbps, the extinction ratio was reduced from 28 dB to 6 dB (Yu *et al*., 2014).

Kim *et al*. (2006a) found that the NAND, NOR, and their combinations have the best chance of being able to do all kinds of logical operations in the future high-capacity optical communication networks. Excellent recovery time and high-speed operations have been achieved at 5 ps and 10 Gb/s, respectively, using nonlinear vertical-cavity semiconductor gates (Porzi *et al*., 2008). All-optical AND and NAND gates were designed using silicon-based micro ring resonators, which showed the free carrier dispersion effect (Ibrahim *et al*., 2003). To achieve 15 dB at 10 Gbps, one research team developed a structure with parallel SOA and MZI logic gates. These gates include XOR, OR, NOR, and NAND (Kim *et al*., 2006b).

To obtain an ER of 11 dB and a low penalty of 2.3 dB with a gate operating data rate of 42.6 Gbps, differently switched SOAs are used in a MZI configuration (Dailey *et al*., 2009). The design and modelling of an all-optical NAND gate employing an SOA with a high ER of 15.323 and a data rate of 40 Gbps are reported in this research. The necessary mathematical support from the current literature is used to effectively address the theoretical background of the EDFA and SOA. User defined random input sequences were used in the NAND gate simulations, and the accompanying numerical analyses are documented. The performance of the designed NAND operation was compared with those reported previously.

MATERIALS AND METHODS

Design arrangement

Figure 1 shows the block diagram of the proposed SOA-based all-optical NAND gate. It consists of an EDFA along with a TWSOA, which is the important optical component for the design of the NAND gate. As input sequences, A and B are combined by the optical multiplier and amplified by the EDFA, whereas the reference or probe signal from a continuous wave laser is combined with the amplified input data by an X-coupler. Continuous laser light from port 3 can be used as a reference signal to achieve an all-optical NAND gate function.

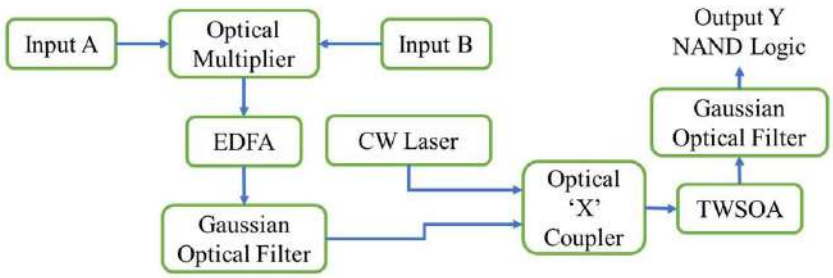

Figure 1: Block diagram representation of proposed NAND gate

Working principles of NAND logic

In the principles of operation, the two binary inputs A and B are converted into an analog waveform using an optical pulse generator, and will be given to the multiplier, which generates the multiplication of binary data. It looks like an AND logic operation. The Erbium-Doped Fibre Amplifier is used to boost the output of the multiplier. It has the lowest loss in all of the optical fibre telecommunication wavelength bands, so it can also be used to make up for signal loss as it travels.

The amplified data is further processed through a tuned Gaussian optical filter to get a specific centre wavelength. A continuous wave laser is employed to generate a probe or reference signal. An optical X coupler receives a combined input and probe signal simultaneously and its outputs are fed to a TWSOA where cross gain modulation (XGM) of carrier induced changes takes place in accordance with the changes in the input A and B (intensity modulation). During cross gain modulation, the gain is changed in SOA by the effect of gain saturation.

The modulated output wavelength of continuous wave (CW) laser is caused by gain variations of the intensity modulated input signals. The output of SOA module carries data that precisely matches the intensity-modulated input signals. The output signal is influenced by the directional characteristics of two signals, such as the reference signal and combined input signals, which can both enter the SOA in a co-directional or counter-directional manner. The optical bandpass filter receives the output of the amplifier.

The Gaussian optical filter centred at wavelength 1548.3 nm and bandwidth 40 GHZ selects the desired NAND operation. To get the optimum performance, the SOA parameters were adjusted. When inputs A and B are high, XGM can be generated at SOA, producing a low output (logic 0). If any one of the inputs is low, then the multiplier output is also low and then the output of SOA corresponds to CW laser only, which is the logic high output (logic 1). By filtering and amplifying the power of the CW laser, the NAND output can be seen.

The 'X' coupler is used to couple the output of the multiplier and the output of the CW laser; the coupling coefficient selected was 0.5 dB. The semiconductor optical amplifier receives the coupler output as its input. When either input A or B, or both, is low, a high-power output is produced. Because the multiplier output is low, cross gain modulation cannot take place. On the other hand, the CW laser reference signal makes the logic output high.

The XGM modulated signal can be generated with the combined use of the multiplier output and the signal from the continuous wave laser, whereas the output of the multiplier is high when all the two inputs are logic high. The Gaussian optical filter is used to select a preferred centre frequency from the SOA output and to remove unwanted noise. Then the output will be considered as logic "0". At least one of the inputs goes to zero (low), the output logic becomes logic "1", which indicates that the constructed logic gate reflects the NAND operations.

Theoretical background of EDFA and SOA

Erbium-doped fibre amplifiers (EDFA) are used to boost signals with a loss of less than 0.2 dB/km in the 1550 nm wavelength range. The amplification is purely optical and independent of the data rate (Durhuus *et al*., 1996). The proposed NAND gate has EDFA parameters of 2.2 μm for the core radius and doping radius. The EDFA's numerical aperture is 0.24, and the losses at 1500 nm are 0.1 dB/m. The wavelength and power for forward transmission are 1553 nm and 100 mW, respectively. Similar to this, the EDFA's backward pump wavelength and power are 980 nm and 0 mW, respectively. This demonstrates that there will be no back reflection while the gate is operating.

Simulated emission is the guiding principle behind the operation of the amplifier in erbium-doped fibre (Nakazawa *et al*., 1989). When the data is introduced into the fibre at a wavelength ranging from 1520 nm to 1560 nm, the desired result of stimulated emission can be attained. During the stimulated emission process, the signal is amplified by the photon that is just made (Agrawal, 1997).

The rate equation stated the working principles of EDFA. The population of the upper, middle, and ground state is represented byP_u, P_m andP_g, respectively. When T_p is the pumping rate, T_{ab} is the absorption of photons from the signal and τ_{12} is the lifetime of spontaneous emission, the following equations can be written as

$$\frac{dP_g}{dt} = \frac{P_m}{\tau_{mg}} + T_{ab}\left(P_m - P_g\right) - T_p\left(P_g - P_u\right), \quad \ldots(1)$$

$$\frac{dP_m}{dt} = \frac{P_u}{\tau_{um}} - T_{ab}\left(P_m - P_g\right), \quad \ldots(2)$$

$$\frac{dP_u}{dt} = -\frac{P_u}{\tau_{um}} + T_p\left(P_g - P_u\right). \quad \ldots(3)$$

In a SOA, population inversion refers to the condition, in which the population of electrons in the conduction band exceeds the population of holes in the valence band, $P_m > P_g$. Under steady state conditions, the time derivatives are not present. Since the photon lifetime at state u is much smaller than the lifetime of a photon at state m, the population of the excited state is defined by the Boltzmann distribution, β.

The population of upper level is $P_u = P_m\, e^{-\frac{E_u - E_m}{K_T}} = \beta P_m$, $\ldots(4)$

where $\beta = e^{-\frac{E_u - E_m}{K_T}}$,

From (1), $\frac{P_m}{\tau_{mg}} + T_{ab}\left(P_m - P_g\right) - T_p\left(P_g - P_u\right) = 0.$

This gives the inversion level as

$$n = \frac{P_m}{P_m - P_g} = \frac{\left(T_p + T_{ab}\right)\tau}{T_p\tau(1-\beta) - 1}. \quad \ldots(5)$$

Equations (1) to (4) related with population inversion, while (5) shows the degree of inversion needed for a signal to successfully flow through the EDFA (Desurvire, 1994). The inversion level n is thus related to both the probe and input signal powers, probe signal wavelength through β (Sabella & Lugli, 1999).

The nonlinear optical effect and the carrier density of SOA can be theoretically analysed by rate equations (Ishikawa, 2008). The device considered for this work is the Travelling Wave Semiconductor Optical Amplifier (TWSOA), which is used to amplify modulated light signals in which the input signal power and the internal noise have an impact on the gain of SOA. Gain saturation will occur if the input power is high, which will decrease the lasing operation in SOA (Liou *et al*., 1997), which will result in low output.

The carrier recombination lifetime decides the gain dynamics of the SOA and the condition underneath specified appears the carrier density which is created spatially along the whole length of the active region of the device. The carrier recombination lifetime decides the gain dynamics of the SOA and the condition underneath specifies the carrier density, which is created spatially along the whole length of the active region of the device. It combines the forward and turn-around traveling signal as well as the ASE mentioned in (6) (Manimaran & Madhan, 2020). The dynamic equation for the change in carrier density inside the device's active zone is provided by

$$\frac{dn(z)}{dt} = \frac{1}{edLW} - R\left(n(z)\right) - \frac{\Gamma}{dw}\left\{\sum_{k=1}^{N_s}\left[\!\left[g_m\left(v_k, n(z)\right)\left(N_{sk}^{+}(z) + N_{sk}^{-}(z)\right)\right\}\right] - \left[\!\left[\frac{2\Gamma}{dw}\left\{\sum_{k=1}^{N_m - 1}\left[\!\left[g_m\left(v_k, n(z)\right)K_j\left(N_j^{+}(z) + N_j^{-}(z)\right)\right\}\right]\right]\right.\right.\right., \quad \ldots(6)$$

where Γ is the confinement factor, g_m is the material gain, while *L, W* are the length and the width of the active region of the SOA, respectively. The recombination rate is $R\left(n(z)\right)$, an emitted photon in the positive and negative Z-direction are $N_{sk}^{+}(z)$ and $N_{sk}^{-}(z)$. For the transverse electric (*TE*) mode, the spontaneous emission

photon rate is $N_j^+(z)$, and for the transverse magnetic (TM) mode, it will be $N_j^-(z)$. The carrier density can be altered within the active region by varying a few parameters or processes which are shown in (6). The infused current, unconstrained radiative and nonradiative recombination, forecast recombination process of carriers, invigorated recombination by the signal, and ASE photons. In the case of a traveling wave amplifier, the mirror losses will not affect the photon lifetime (Eisenstein, 1989; Obermann *et al*., 1997). In the proposed system, the parameters chosen for the SOA are confinement factor Γ = 0.35, length L = 0.5 mm, width W = 3 μm, height H = 80 nm, Line width enhancement factor = 5, differential gain $A_d = 27.8 \times 10^{-021} m^2$.

RESULTS AND DISCUSSION

The study of this numerical simulation explored the dynamics transfer characteristics of the NAND gate for user-defined or random sequence input of A and input B with a data rate of 40 Gbps. The wavelength of 1553.05 nm and 1557.75 nm was selected for A and B with a power of -1.21 dBm and -0.223 dBm, respectively. The centre wavelength of the Gaussian optical filter is 1555.40 nm, which is the average wavelength of both inputs A and B, whereas the wavelength, injection current, and power of the probe or reference signal are 1548.3 nm, 0.95A, and -2.6 dBm, respectively.

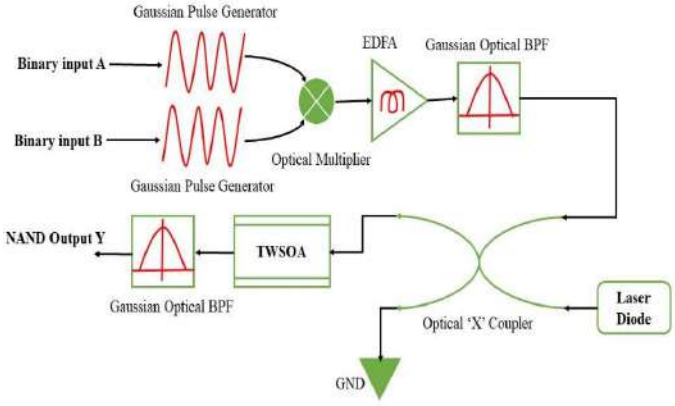

Figure 2: The schematic diagram of the proposed NAND gate design

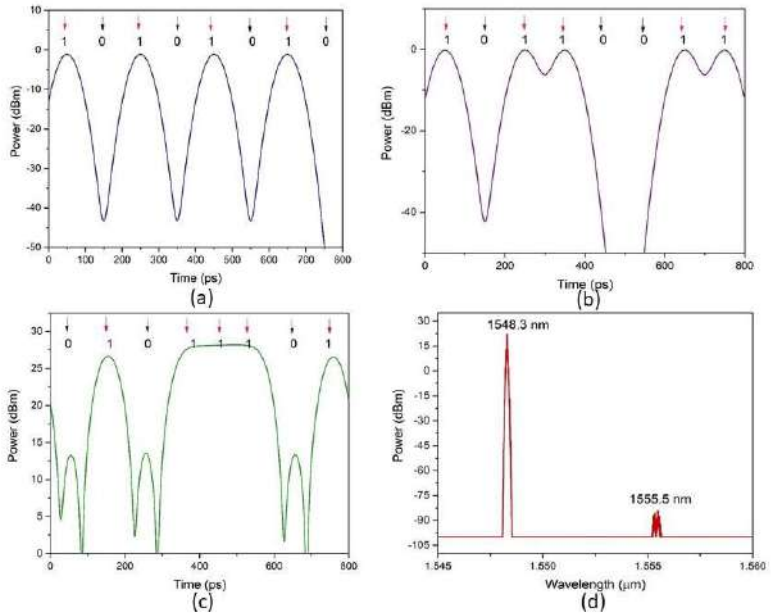

Figure 3: (a). Input sequence A; (b) Input sequence B; (c) Output of NAND logic; (d) Output Power spectrum of designed NAND logic.

The SOA parameters are set as 0.5 mm length, 3 μm width, 80 nm height, and the optical confinement factor is 0.35. The centre wavelength of the Gaussian optical filter placed before SOA is 1555.4 nm and after SOA is 1548.3 nm. Figure 2 shows the schematic of the proposed NAND gate. Figures (3a) and (3b) represent the user-defined input sequence of A: 10101010 and B: 10110011, and Figure (3c) shows the output of NAND logic Y: 01011101. From the NAND gate logic output, we observe that, the output power for logic 1 is 28.575 dBm and the output power for logic 0 is 13.252 dBm. The figure (3d) shows the output spectrum of the NAND logic and it was measured for different wavelengths ranging from 1545 to 1560 nm. The system gives a highly selective response at a 1548.3 nm input wavelength with about 28.5 dBm of output power. All other wavelengths are forbidden from transmission. Around 1555.5 nm, a small output signal (-82 dBm) arises, but it is negligible when compared to 28.5 dBm. Table 1 shows the proposed NAND gate logic output for user-defined input sequences with corresponding logical outputs with power in dBm.

Table 1: Truth table for NAND gate logic (user defined input)

User defined sequence		NAND gate logic	Output power
Input 1 logic	Input 2 logic	$y = \overline{A * B}$	(dBm)
1	1	0	13.252
0	0	1	28.575
1	1	0	13.252
0	1	1	28.575
1	0	1	28.575
0	0	1	28.575
1	1	0	13.252
0	1	1	28.575

Numerical analysis

The analysis of the proposed design can be performed by varying the parameters as well as the optical components. Different wavelengths of output for NAND logic can be observed. At a wavelength of 1548.3 nm, the performance of the pump laser is compared with the CW laser output shown in Figure 4. Even though the optical output power of the pump laser is more stable than the CW laser output, we have chosen a continuous wave laser, which is mainly used in optical low-loss applications.

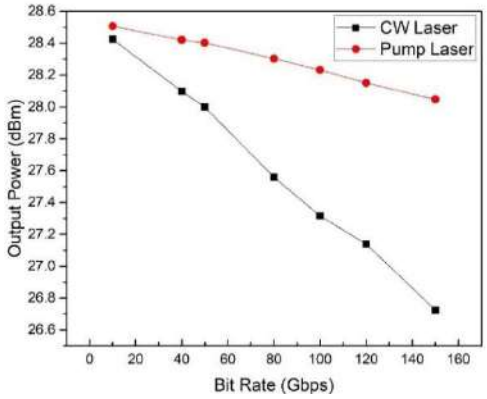

Figure 4: Output optical power at various data rates for CW and pump lasers

The impact of various types of amplifiers on the output power of NAND logic can be seen in Figure 5, in which we observe that the output is greater in optical fibre amplifiers and TWSOA. Likewise, filters were also tested to identify the better performance of the proposed logic gate. In the input stage of the proposed system, the impact of filters is high, but in the case of filters at the output stage, no impact is there, as mentioned in Table 2.

Table 2: Types of filters (vs) output power at λ= 1548.3 nm and bandwidth= 10 GHz

Sl. no	Types of filters	Output power (dBm)
1	Trapezoidal optical filter	27.416
2	Gaussian optical filter	28.575
3	Butterworth optical filter	28.202
4	Bessel optical filter	28.202
5	Fabry Perot optical filter	24.217
6	Optical digital filter	26.622
7	Periodic optical filter	28.231

The selected components from the analysis can be used for the design of a universal optical NAND gate. Figure 4 shows the relationship between the optical laser source and the operating data rate. Here the same structure can be further tested for various data rates of 10 Gbps to 200 Gbps.

Finally, the required performance can be attained at a bit rate from 10 Gbps to 40 Gbps. Afterward, its output power value can be reduced considerably, and finally, no proper transmission has occurred at a speed of 180 Gbps to 200 Gbps. The rate of change of output power for pump laser and CW laser was calculated from the plot based on the simulated output values of 0.00382 dBm/Gbps and 0.0126 dBm/Gbps, respectively. In order to improve the quality of the output signal, it is recommended to use the appropriate filter in front of the SOA.

In this study, various filters have been analysed and their outputs are observed and listed in Table 2. From the tabulated values, it is obvious that the Gaussian filter and Periodic Optical filter showed better output power compared to other filters, and their output power values are 28.575 dBm and 28.231 dBm, respectively. Since the Gaussian optical filter shows the best output power and also has an optimum shape to get high resolution in the output, it has been selected for the development of the NAND gate logic system.

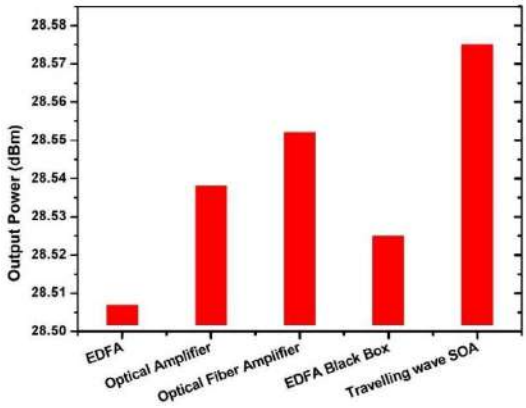

Figure 5: Output optical power for different amplifiers

Figure 6, shows the tuning of the wavelength of the carrier signal in order to get the maximum output power, which will favour efficient information transmission. After doing a large-scale variation from 1400 nm to 1600 nm, it has been identified that the system responds better around 1548 nm. Then, the signal wavelength varied from 1548.0 to 1548.9 nm with an increment of 0.1 nm. The output power is maximal when the wavelength is set as 1548.3 nm. The output power drastically decreases on the higher and lower side of the spot of 1548.3 nm, which can be interpreted as the window being optimum for the proposed system. The third optical window, which has a wavelength between 1400 and 1600 nm, was identified in the literature as an appropriate one for achieving low-loss transmission.

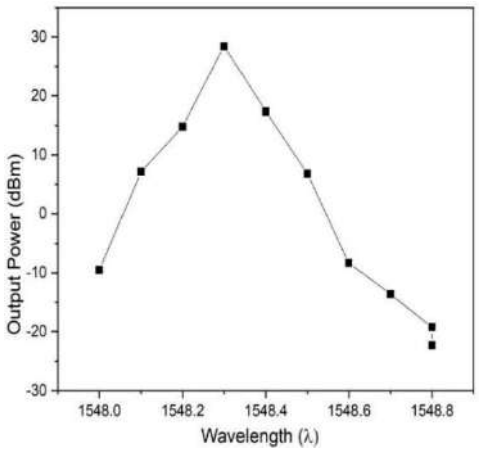

Figure 6: Wavelength (vs) output optical power using CW laser.

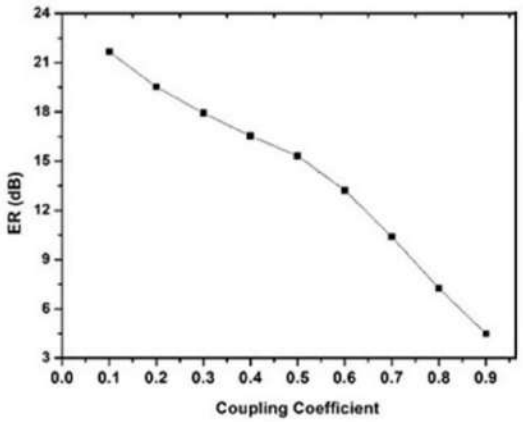

Figure 7: The response of ER to variation in coupling coefficient.

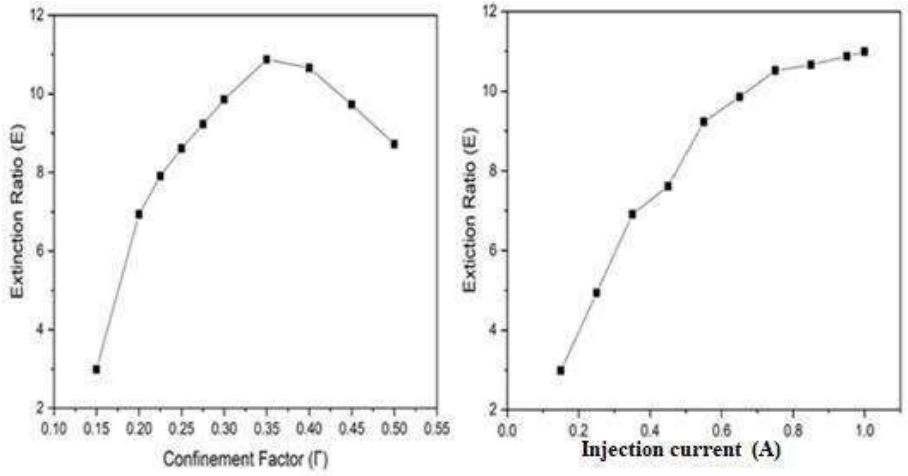

Figure 8: Relationship between confinement factor, injection current and extinction ratio at 10 Gbps data rate.

In telecommunications and optical systems, the extinction ratio (ER) is a measure of the contrast or ratio of power between the "on" and "off" states of an optical signal which considered as an important factor in evaluating the performance of the system at a particular data rate.

The performance of the NAND gate is verified using the Extinction Ratio (ER) as shown in Figure 7, by adjusting the coupling coefficient of the X-coupler. According to this, ER ratio increases if the coupling coefficient is smaller than 0.5. The ER is decreased when the coupling coefficient lies between 0.5 and 0.9. The NAND logic operation will not function correctly, after the coupling coefficient approaches one. The coupling coefficient selected for the current work is 0.5 in order to achieve an appropriate NAND gate logical operation at a high data rate of 40 Gbps. Moreover, both the confinement factor and injection current varied independently and the extinction ratio based on the output results is shown in Figure. 8. The confinement factor and the injection current of 0.35 and 0.95 A, respectively, produced an excellent extinction ratio of 15.323 dB. The same high extinction ratio can be maintained for the high-speed data rate of 10 Gbps to 40 Gbps. Similarly, the important parameters such as the Extinction Ratio (ER) and Bit Error Rate (BER) were calculated and listed in Table 3.

Table 3: Calculated parameters of the designed NAND logic system

Sl. No	Parameters	Metrics
1	Extinction ratio	15.323 dB
2	Bit error rate (BER)	4.27×10^{-26}

Table 4: Comparison of NAND gate designs

Sl. no.	Author name and year	Title	Optical components used	Data rate (Gbps)	Extinction ratio (dB)
1	Heydarian *et al*., 2022	Design and analysis of an all-optical NAND logic gate using a photonic crystal semiconductor optical amplifier based on the Mach–Zehnder interferometer structure	SOA	80	7.1
			PC-SOA	80	16.2
2	Mukherjee *et al*., 2019	All-optical logic gate NAND using semiconductor optical amplifiers with simulation	Two SOA	10	13.0
3	Oliveira *et al*., 2019	New design of all-optical logic universal NAND gate formed by NOT (A AND B) gates using Michelson Interferometer based on semiconductor optical amplifier	SOA- MI	10	-
4	Yu *et al*., 2014	All-optical decision gate with extinction ratio improved scheme using a SOA-DBR laser	SOA-DBR Laser	10	24
5	Mehra *et al*., 2012	All optical universal logic Gates Design and Simulation using SOA	Two SOA	40	8.75
6	Mehra *et al*., 2012	SOA based all-optical NAND gates and their comparison	SOA- filter	80	9.73
			SOA- MZI	80	11.09
7	Nakarmi *et al*., 2012	Demonstration of all-optical NAND gate using single-mode Fabry–Pérot laser diode	Fabry Perot laser diode	10	14.6

We deduce from the comparison table that the majority of research on the design of all-optical NAND gates for optoelectronic integrated circuits has a data rate of 10 Gbps. If the data rate rises, the extinction ratio may decline. With a single SOA and filter combination, the NAND gate in the proposed work is created with a high data rate of 40 Gbps and an enhanced extinction ratio of 15.323 dB.

CONCLUSION

A unique all-optical NAND gate using a single TWSOA has been developed and implemented in this study, and by numerical simulation, a high ER of 15.323 dB at a data rate of 10 Gbps to 40 Gbps is achieved. Additionally, the functionality of all-optical NAND gate is examined in various scenarios. By adjusting the input data, SOA, CW laser, or optical filter parameters, the maximum extinction ratio for the NAND gate was achieved. Calculated values for the ER and BER were 15.323 dB and 4.27×10^{-26} respectively.

Conflict of interest

The authors declare that there is no conflict of interest.

Acknowledgement

The authors acknowledge the Department of Electronics and Communication Engineering, Government College of Engineering Tirunelveli for providing software facility for the successful completion of the proposed work.

REFERENCES

Agrawal G.P. (1997). *Fiber-optic Communication Systems*, 2nd edition. John Wiley & Sons, Inc., USA.

Desurvire E. (1994). *Erbium Doped Fiber Amplifiers*. John Wiley & Sons, Inc., USA.

Dailey J.M., Ibrahim S.K., Manning R.J., Webb R.P., Lardenois S., Maxwell G.D. & Poustie A.J. (2009). 42.6 Gbit/s fully integrated all-optical XOR gate. *Electronics Letters* **45**(20): 1047–1049.

Durhuus T., Mikkelsen B., Joergensen C., Lykke Danielsen S. & Stubkjaer K.E. (1996). All-optical wavelength conversion by semiconductor optical amplifiers. *Journal of Lightwave Technology* **14**(6): 942–954.
DOI: https://doi.org/10.1109/50.511594

Eisenstein G. (1989). Semiconductor optical amplifiers. *IEEE Circuits and Devices Magazine* **5**(4): 25–30.
DOI: https://doi.org/10.1109/101.29899

Heydarian K., Nosratpour A. & Razaghi M. (2022). Design and analysis of an all-optical NAND logic gate using a photonic crystal semiconductor optical amplifier based on the Mach–Zehnder interferometer structure. *Photonics and Nanostructures-Fundamentals and Applications* **49**: 100992.
DOI: https://doi.org/10.1016/j.photonics.2022.100992

Ibrahim T.A., Grover R., Kuo L.C., Kanakaraju S., Calhoun L.C. & Ho P.T. (2003). All-optical AND/NAND logic gates using semiconductor microresonators. *IEEE Photonics Technology Letters* **15**(10): 1422–1424.
DOI: https://doi.org/10.1109/LPT.2003.818049

Ishikawa H. (2008). Ultrafast all-optical signal processing devices. In: *Ultrafast All-Optical Signal Processing Devices*. John Wiley & Sons, Inc., USA.
DOI: https://doi.org/10.1002/9780470758694

Kim J.-Y., Kang J.-M., Kim T.-Y. & Han S.-K. (2006a). All-optical multiple logic gates with XOR, NOR, OR, and NAND functions using parallel SOA-MZI structures: theory and experiment. *Journal of Lightwave Technology* **24**(9): 3392–3399.
DOI: https://doi.org/10.1109/JLT.2006.880593

Kim J.-Y., Kang J.-M., Kim T.-Y. & Han S.-K. (2006b). 10 Gbit/s all-optical composite logic gates with XOR, NOR, OR and NAND functions using SOA-MZI structures. *Electronics Letters* **42**(5): 303–304.
DOI: https://doi.org/10.1049/el:20063501

Liou K.Y., Koren U., Burrows E.C., Zyskind J.L. & Dreyer K. (1997). A WDM access system architecture based on spectral slicing of an amplified LED and delay-line multiplexing and encoding of eight wavelength channels for 64 subscribers. *IEEE Photonics Technology Letters* **9**(4): 517–519.
DOI: https://doi.org/10.1109/68.559407

Manimaran P. & Madhan M.G. (2020). Bandwidth characteristics of TWSOA based inline detector configurations for near infrared communications. *Optical and Quantum Electronics* **52**(1): 32.
DOI: https://doi.org/10.1007/s11082-019-2143-y

Mehra R. & Tripathi J.K. (2012). All optical universal logic gates design and simulation using SOA. *IJCEM International Journal of Computational Engineering and Management* **15**: 41–45.

Mehra R., Jaiswal S. & Dixit H. K. (2012). SOA based all-optical NAND gates and their comparison. 2012 *Third International Conference on Computer and Communication Technology*, 23-25 November, Allahabad, India, pp. 175–177.
DOI: https://doi.org/10.1109/ICCCT.2012.42

Mukherjee K. & Raja A. (2020). Three Input NAND gate using semiconductor optical amplifier. *2020 IEEE VLSI Device Circuit and System (VLSI DCS 2020)*, Kolkata, India, 18–19 July, pp. 142–145.

Mukherjee K., Raja A. & Maji K. (2019). All-optical logic gate NAND using semiconductor optical amplifiers with simulation. *Journal of Optics* **48**(3): 357–364.
DOI: https://doi.org/10.1007/s12596-019-00555-9

Nakarmi B., Rakib-Uddin M., Hoai T. Q. & Won Y. H. (2010). Demonstration of all-optical NAND gate using single-mode Fabry–Pérot laser diode. *IEEE Photonics Technology Letters* **23**(4): 236–238.
DOI: https://doi.org/10.1109/LPT.2010.2098863

Nakazawa M., Kimura Y. & Suzuki K. (1989). Efficient Er3+-doped optical fiber amplifier pumped by a 1.48 μm InGaAsP laser diode. *Applied Physics Letters* **54**(4): 295–297.

Oliveira J.M., Silva H.A.B.D., Oliveira L.A.D., Sousa F.B.D., Oliveira J.E.D., Sousa F.M.D. & Costa M.B.C. (2019). New design of all-optical logic universal NAND gate formed by NOT (A AND B) gates using Michelson interferometer based on semiconductor optical amplifier. *Journal of Computational and Theoretical Nanoscience* **16**(7): 2712–2719.
DOI: https://doi.org/10.1166/jctn.2019.8236

Obermann K., Koltchanov I., Petermann K., Diez S., Ludwig R. & Weber H. G. (1997). Noise analysis of frequency converters utilizing semiconductor-laser amplifiers. *IEEE Journal of Quantum Electronics* **33**(1): 81–88.
DOI: https://doi.org/10.1109/3.554895

Porzi C., Guina M., Bogoni A. & PotÌ L. (2008). All-optical NAND/NOR logic gates based on semiconductor saturable absorber etalons. *IEEE Journal of Selected Topics in Quantum Electronics* **14**(3): 927–937.
DOI: https://doi.org/10.1109/JSTQE.2008.919754

Sabella R. & Lugli P. (1999). High speed optical communications. In: *High Speed Optical Communications*, pp. 207–232. Springer, USA.
DOI: https://doi.org/10.1007/978-1-4615-5275-8

Ye X., Ye P. & Zhang M. (2006). All-optical NAND gate using integrated SOA-based Mach-Zehnder interferometer. *Optical Fiber Technology* **12**(4): 312–316.
DOI: https://doi.org/10.1016/j.yofte.2005.12.001

Yu L.-Q., Lu D. & Zhao L.-J. (2014). All-optical decision gate with extinction ratio improved scheme using an SOA-DBR laser. *IEEE Photonics Technology Letters* **26**(21): 2126–2129.
DOI: https://doi.org/10.1109/LPT.2014.2349274

Chapter 4
Multiferroic Marvels Paving the Way for Energy Harvesting

J. Mangaiyarkkarasi
https://orcid.org/0000-0003-1431-9584
N.M.S.S. Vellaichamy Nadar College, India

J. Shanthalakshmi Revathy
https://orcid.org/0000-0003-1724-7117
Velammal College of Engineering and Technology, India

ABSTRACT

This chapter explores the revolutionary realm of multiferroic materials, focusing on their dual ferroelectric and ferromagnetic properties and their pivotal role in energy harvesting. It classifies key materials, including Bismuth Ferrite and Gadolinium Manganite, highlighting their suitability for energy conversion. The intricate mechanisms of multiferroicity, encompassing piezoelectric and magnetoelectric effects, are unveiled. Examining different phases, such as ferroelectric and ferromagnetic, illuminates their multifunctional behavior. Advanced characterization techniques, like X-ray diffraction, are crucial for harnessing these materials. Various energy harvesting mechanisms, such as piezoelectric and thermoelectric, are explored, emphasizing multiferroics' versatility. Applications, challenges, and future directions, including enhanced efficiency and integration into flexible devices, are discussed. In conclusion, this chapter provides a comprehensive exploration of multiferroic materials, showcasing their potential to revolutionize energy harvesting for a sustainable future.

DOI: 10.4018/979-8-3693-2003-7.ch004

1. INTRODUCTION

Energy harvesting plays a vital role in addressing the rising demand for sustainable and self-sufficient power sources. It enables the efficient capture and utilization of energy from diverse sources like solar radiation, vibrations, heat differentials, and more. This sustainable energy generation reduces our reliance on finite fossil fuels and minimizes environmental impact. Energy harvesting is essential for powering remote or low-power devices, ensuring their continuous operation without the need for frequent battery replacements or extensive wiring (Xu et al. 2017). Additionally, it has applications in IoT sensors, wearable technology, and various off-grid scenarios, making it an integral part of the transition towards cleaner, more resilient energy solutions. Multiferroic materials have attracted substantial interest in the recent years because of their latent applications in energy harvesting. These materials exhibit the coexistence of multiple ferroic orders, such as ferroelectricity and ferromagnetism, making them uniquely suited for converting different types of energy into electrical power. This convergence of properties opens up exciting possibilities for developing highly efficient and compact energy harvesting devices (Lee et al. 2021). Ferroelectricity is a property that allows certain materials to maintain a permanent electric polarization when subjected to an external electric field, while ferromagnetism enables materials to retain a permanent magnetic polarization when exposed to an external magnetic field. Multiferroic materials possess both these characteristics, making them exceptionally versatile for energy conversion (Mehta, Islam, and Imran 2023). One of the most hopeful applications of multiferroic materials is energy harvesting. Energy harvesting implicates the capture and renovation of various energy sources like mechanical vibrations, thermal gradients, or electromagnetic fields, into electrical energy for powering small electronic devices or sensors (Sun, MacManus-Driscoll, and Wang 2020). Multiferroic materials can be employed to design energy harvesters that efficiently convert these diverse energy sources into electrical power. For instance, multiferroic nanogenerators can harness mechanical vibrations and deformations to generate electricity. When exposed to mechanical strain, these materials generate voltage and current, offering the opportunity to harness and utilize the energy for powering low-energy electronic devices or storing it for future use. Additionally, multiferroic materials can be integrated into thermoelectric devices to efficiently convert waste heat into electricity, a process known as thermoelectric energy harvesting.

The exclusive properties of multiferroic materials like, their simultaneous ferroelectric and ferromagnetic behavior, make them promising candidates for energy harvesting applications. Their versatility in converting mechanical, thermal, and electromagnetic energy into electrical power opens up exciting opportunities for

creating self-sustaining and environmentally friendly energy solutions (Chen et al. 2019). As ongoing research in this field progresses, we can expect the emergence of groundbreaking energy harvesting devices based on multiferroic materials, potentially transforming the way we supply power to electronic systems.

2. CLASSIFICATION OF MULTIFERROIC MATERIALS

Materials exhibiting multiferroicity, marked by the simultaneous presence of multiple ferroic orders, can be categorized into different groups according to their distinct properties and behaviors. Figure 1 shows the representation of multiferroic material.

Figure 1. Representation of multiferroic material

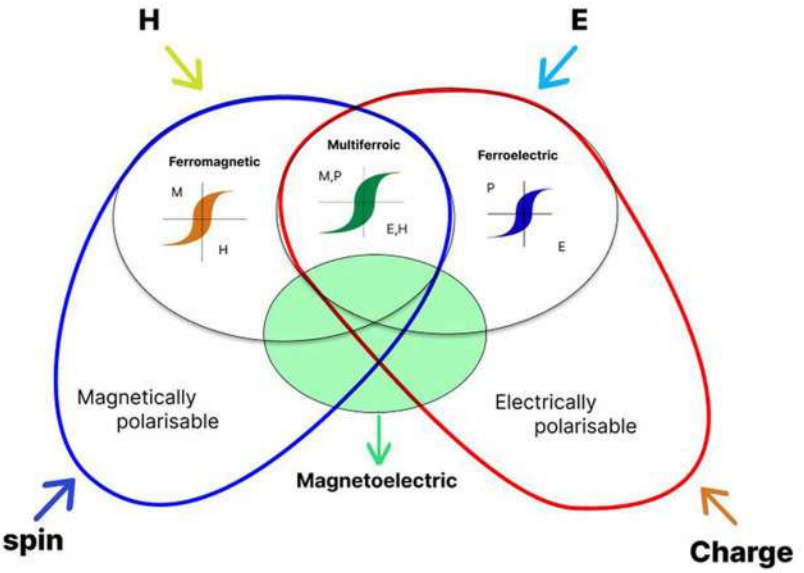

Here are some common classifications of multiferroic materials is depicted in Figure 2.

Figure 2. Classification of multiferroic materials

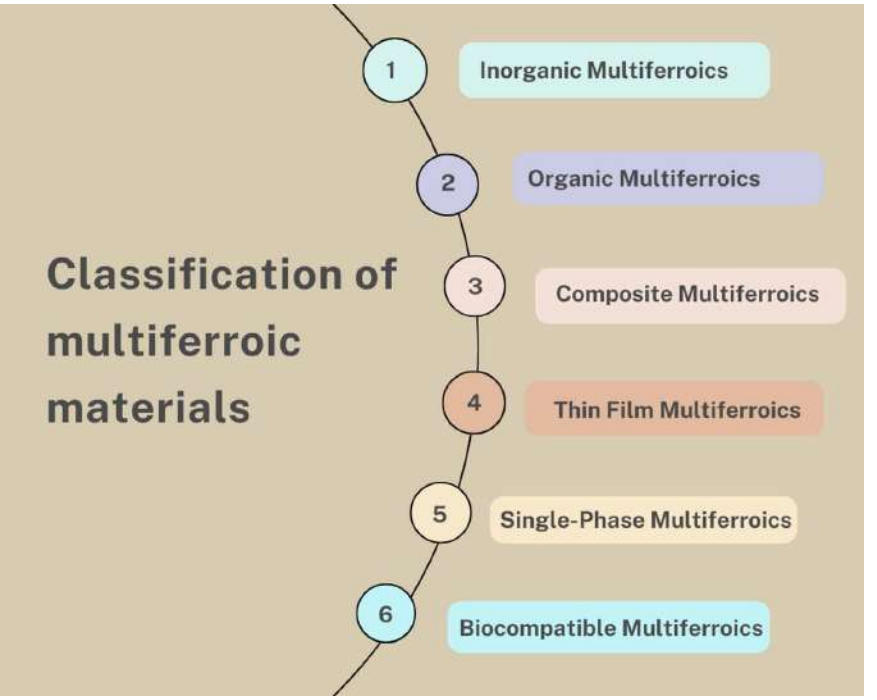

Main classification include type-I and type II multiferroics. Type-I multiferroics exhibit both ferroelectric and ferromagnetic orders within the same phase, where the two orders are intimately coupled. They often possess strong magneto-electric coupling suitable for various memory devices. Type-II multiferroics are materials where ferroelectricity and ferromagnetism coexist in different phases or structural domains. These materials might not exhibit strong direct coupling between the ferroelectric and ferromagnetic properties. They are often characterized by complex structures and phase transitions (Chorsi et al. 2019). Further they are classified as,

i. ***Inorganic Multiferroics***: Inorganic multiferroics are typically composed of transition metal oxides, perovskite structures, and other crystalline compounds. Examples include bismuth ferrite ($BiFeO_3$), which exhibits robust ferroelectricity and antiferromagnetism.

ii. ***Organic Multiferroics***: Organic multiferroics consist of organic compounds and molecules. They are relatively less common than their inorganic counterparts but offer the advantage of being more lightweight and flexible. However, their ferroic properties are often weaker.

iii. ***Composite Multiferroics***: Composite multiferroics are materials created by combining multiple components, such as ferroelectric and ferromagnetic materials, to induce multiferroic behavior. These composites often exhibit enhanced properties and can be tailored for specific applications (Fan 2021).

iv. ***Thin Film Multiferroics***: Thin film multiferroics are multiferroic materials deposited as thin layers on substrates (Xu et al. 2018). They are essential in microelectronic applications, such as sensors and memory devices, where thin film technology is prevalent.

v. ***Single-Phase Multiferroics***: Single-phase multiferroics are materials where both ferroelectricity and ferromagnetism coexist within the same crystal structure. These materials are particularly desirable for straightforward device integration and strong coupling between properties (Sezer and Koç 2021).

vi. ***Biocompatible Multiferroics*:** Biocompatible multiferroics are a subset of multiferroic materials suitable for use in biomedical applications. These materials are non-toxic and can be integrated into medical devices, offering opportunities for advanced diagnostics and therapies (Shirvanimoghaddam, Johnson, and Lance 2016).

The classification of multiferroic materials is important for understanding their unique properties and tailoring them for specific applications (Mangaiyarkkarasi and Shanthalakshmi Revathy 2023). Researchers continue to explore and develop new multiferroic materials and composites, expanding the possibilities for their use in various technologies, from memory devices to energy harvesting systems and beyond.

3. MECHANISMS OF MULTIFERROICITY

The mechanism of multiferroicity is a fascinating and complex phenomenon that involves the simultaneous coexistence and coupling of ferroelectricity and ferromagnetism in a material. Understanding the underlying mechanisms is crucial for the development of advanced electronic devices and technologies. There are several key mechanisms that contribute to multiferroicity.

Spin-Orbit Coupling: One of the fundamental mechanisms behind multiferroicity is the spin-orbit coupling. In materials with strong spin-orbit interactions, the electron spins are strongly coupled to the orbital motion of electrons. This coupling can lead to the induction of ferroelectric polarization, creating ferroelectricity in the material. Additionally, due to the correlated nature of electron spins, ferromagnetism can coexist with ferroelectricity in the same material (Dong, Xiang, and Dagotto 2019).

Charge Ordering and Jahn-Teller Effect: In some multiferroic materials, charge ordering occurs, leading to the formation of polar structures. The Jahn-Teller effect, which causes distortions in the crystal lattice due to interactions between electrons and phonons, can also contribute to ferroelectricity. These structural distortions can coexist with ferromagnetic order, resulting in multiferroic behaviour.

Magnetic Exchange Interactions: Multiferroicity can also be driven by magnetic exchange interactions. In some materials, specific magnetic interactions between ions can lead to a breaking of spatial inversion symmetry, resulting in ferroelectric polarization (Muthukrishnan, Mohammed Yusuf Ansari, and Abdul Kader 2023). When these magnetic exchange interactions are strong, it can lead to ferroelectricity and ferromagnetism coexisting in the same material.

Multiferroic Domain Formation: Multiferroic materials often exhibit domain structures where regions with different ferroelectric and magnetic orientations coexist. These domains can be manipulated and controlled through external fields, such as electric or magnetic fields. The coupling between these domains allows for the efficient switching between ferroelectric and magnetic states, making multiferroic materials valuable for memory and sensor applications (Geng et al. 2014). Figure 3 explains the different types of domain wall formation in multiferroic materials. In this figure arrows denote the orientation of polarization or magnetization vectors. (a) Ising-type wall (b) Bloch-type wall(c) Néel-type wall (d) Neutral 180° wall. (e) Head-to-head wall, (f) Tail-to-tail wall.

Figure 3. Multiferroic domain formation

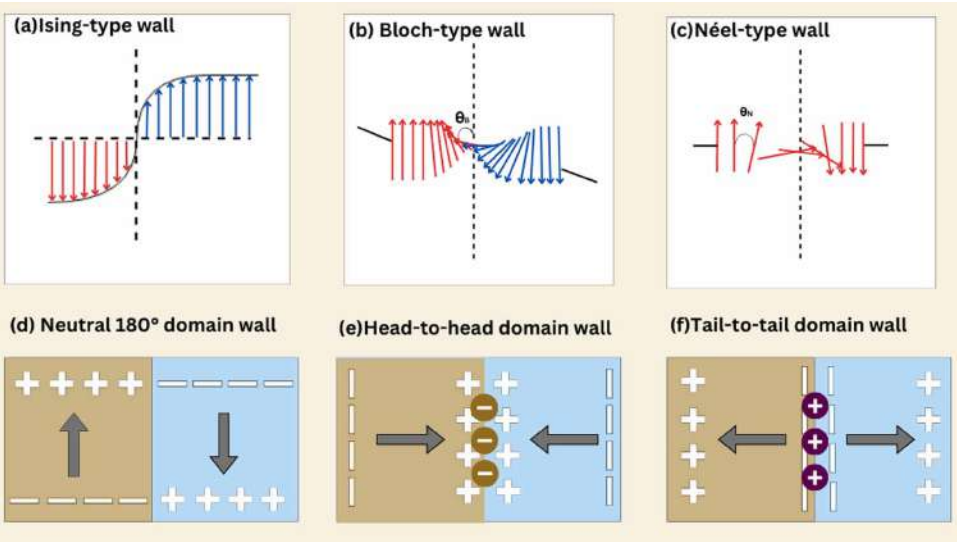

Pressure and Temperature Effects: Multiferroic behavior can be induced or enhanced by external factors like pressure and temperature. Changing these conditions can modify the crystal structure and electronic interactions in the material, thereby influencing its multiferroic properties.

The mechanisms of multiferroicity is a subject of ongoing research, as scientists aim to discover and engineer new multiferroic materials with improved properties and potential applications. Multiferroic materials have the potential to revolutionize electronics, memory devices, and sensors, offering new opportunities for energy-efficient technologies and information storage and processing (Krishan, Kaur, and Mehta 2023).

Different structural and electronic configurations that multiferroic materials can exhibit are referred as multiferroic phases and are useful to know the properties and applications. Multiferroic materials are known for their coexistence of ferroelectric and ferromagnetic order, and the specific arrangement of atoms and electronic states within these materials can lead to various multiferroic phases. Here are some common multiferroic phases which are shown in Figure 4.

Figure 4. Multiferroic phases

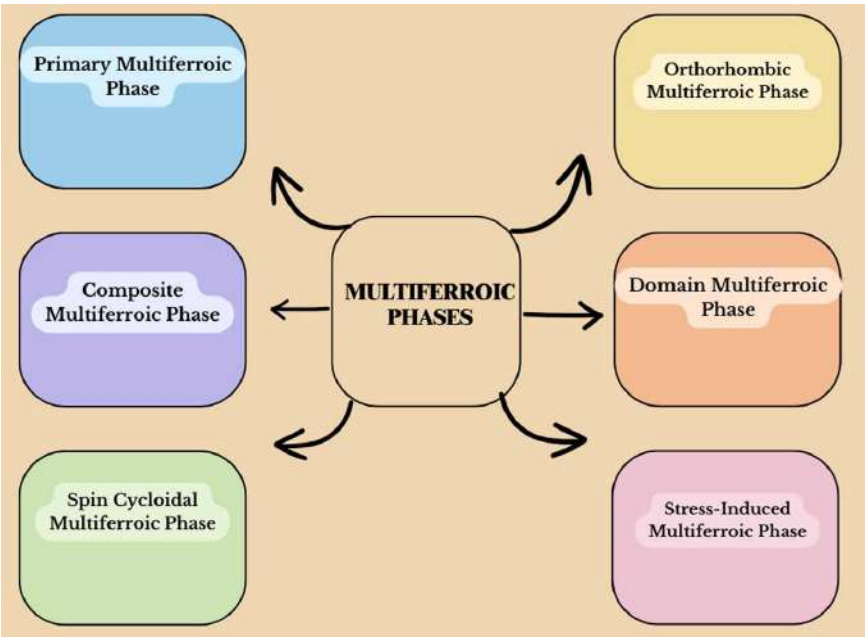

Primary Multiferroic Phase: In this phase, both ferroelectric and ferromagnetic domains can form and coexist, making it a critical starting point for studying multiferroic behavior.

Composite Multiferroic Phase: Composite multiferroic phases involve the incorporation of different materials, often one with ferroelectric properties and another with ferromagnetic properties. By combining these materials, a multiferroic response can be engineered. These phases can offer enhanced properties (Remya et al. 2020).

Spin Cycloidal Multiferroic Phase: This phase involves a helical or cycloidal arrangement of magnetic moments, which gives rise to ferroelectricity. Materials with this phase can exhibit unique magnetic and electric properties (Ravi 2020).

Orthorhombic Multiferroic Phase: Some multiferroic materials exhibit an orthorhombic crystal structure, where the lattice is distorted, leading to ferroelectricity. This structural distortion is often induced by magnetic interactions and can result in strong magneto-electric coupling.

Domain Multiferroic Phase: Multiferroic materials often display domain structures where regions with different orientations of ferroelectric and magnetic polarization coexist. These domains can be manipulated and controlled using external electric or magnetic fields, enabling the design of various multiferroic devices, such as memory and logic elements (Panneer Muthuselvam and Bhowmik 2010).

Stress-Induced Multiferroic Phase: Some materials can exhibit multiferroicity under specific conditions, such as applied stress or pressure. This stress-induced multiferroic phase arises due to changes in the crystal lattice structure and electronic behavior under mechanical strain.

4. MAGNETIC AND FERROELECTRIC COUPLING

The coupling of magnetic and ferroelectric properties denotes the interplay and correlation between the magnetic and ferroelectric characteristics within a material. In multiferroic materials, these properties coexist, and understanding their coupling is crucial for various technological applications (Aguiar et al. 2015). Certain multiferroic materials demonstrate an immediate coupling between magnetic and ferroelectric orders which signifies that alterations in one property directly impact the other. This strong coupling is highly desirable for efficient multiferroic device applications. In other cases, there may be no direct correlation between ferroelectric and magnetic properties. However, they can still be influenced by common underlying factors, like structural distortions or spin-orbit coupling. Mechanisms of Coupling are important to analyse the multiferroic material for a specific application. In materials with

strong spin-orbit coupling, the electron spins are coupled to the orbital motion of electrons. This can lead to the induction of both ferroelectricity and ferromagnetism and contributes to their coupling (Krishan, Kaur, Singh, et al. 2023).

Magnetic exchange interactions between ions in a crystal lattice can induce ferroelectric polarization. The relative alignment of magnetic moments affects the distribution of charge within the material, which, in turn, influences the ferroelectric properties (MuthuKrishnan, Mohammed Yusuf Ansari, and Abdul Kader 2023). In some magnetic interactions, often in materials with non-collinear spin arrangements, can induce ferroelectricity. This magnetic frustration leads to complex magnetic structures, which can have a profound impact on the ferroelectric behavior. In some cases, coupling arises due to structural distortions in the crystal lattice. These distortions can influence both the electric and magnetic properties of the material. The ability to manipulate ferroelectric and magnetic domains through an external field enables data storage and retrieval. Multiferroic memories are shown in Figure 5.

Figure 5. Multiferroic memories

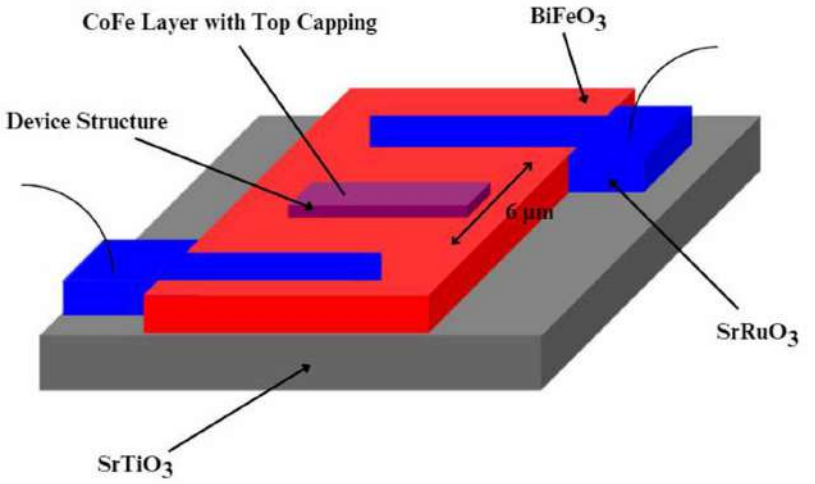

The interconnection of magnetic and ferroelectric properties can be utilized for sensor applications. For example, the multiferroic materials can be used to detect both magnetic and electric fields simultaneously. Understanding the coupling between ferroelectricity and ferromagnetism is crucial for the progress of efficient energy harvesters, which convert mechanical energy, thermal gradients, or other energy sources into electrical power. Magnetic and ferroelectric coupling is also of

interest in spintronics, where spin and charge are coupled to enable novel electronic devices with lower power consumption (Jing et al. 2023).

4.1 Principles of Energy Harvesting With Multiferroic Materials

Multiferroic materials exhibit a strong coupling between their ferroelectric and ferromagnetic properties. This unique coupling allows them to respond to a broad spectrum of external stimuli, including mechanical vibrations, temperature gradients, and electromagnetic fields. Energy harvesting with multiferroic materials is based on the following principles: Piezoelectric and magnetoelectric effects are two important phenomena related to the coupling of mechanical, electrical, and magnetic properties in certain materials.

Piezoelectric Effect

The piezoelectric effect is the capability of specific materials to produce an electric charge when exposed to mechanical deformation or stress. Conversely, these materials can also produce mechanical vibration when subjected to an external electric field (Chan et al. 2019). This bidirectional relationship between mechanical and electrical properties is the basis of the piezoelectric effect which is depicted in figure 6.

Figure 6. Piezoelectric effect

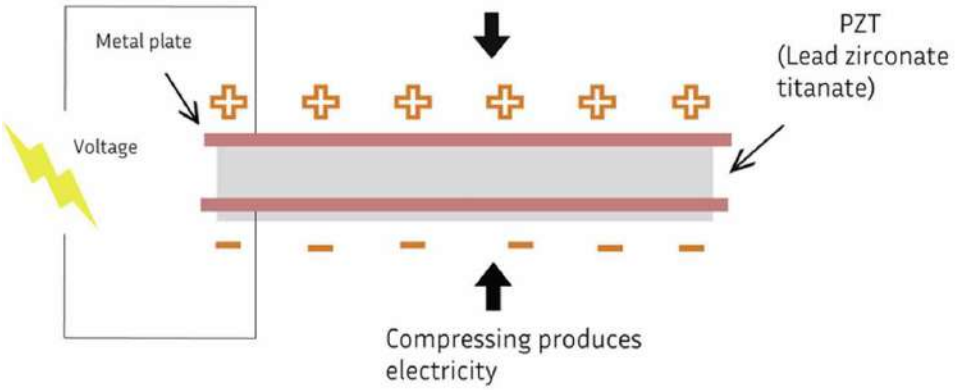

Typical piezoelectric materials encompass quartz, lead zirconate titanate (PZT), and diverse piezoelectric polymers. These materials find frequent applications in sensors, actuators, and ultrasound devices, owing to their capacity to transform

mechanical energy into electrical signals. Piezoelectric materials are mostly used in sensors for pressure, acceleration, and force measurements and actuators employed in devices that require precise and rapid mechanical motion, such as inkjet printers and autofocus cameras. Piezoelectric materials are used in energy harvesting systems to capture and convert mechanical energy into electrical energy.

Magnetoelectric Effect

The magnetoelectric effect is the occurrence in which an external magnetic field triggers an electric polarization in a material, and reciprocally, an external electric field has the ability to induce a magnetic polarization. The coupling between magnetic and electric properties is uncommon and is observed in particular multiferroic materials. Multiferroic materials are essential for the magnetoelectric effect, as they exhibit both ferroelectric and ferromagnetic properties. Bismuth ferrite ($BiFeO_3$) is a renowned multiferroic material that demonstrates the magnetoelectric effect. Magnetoelectric materials can be used in sensors for detecting weak magnetic fields with high sensitivity. Figure 7 explains magneto electric sensors

Figure 7. Magneto electric sensors

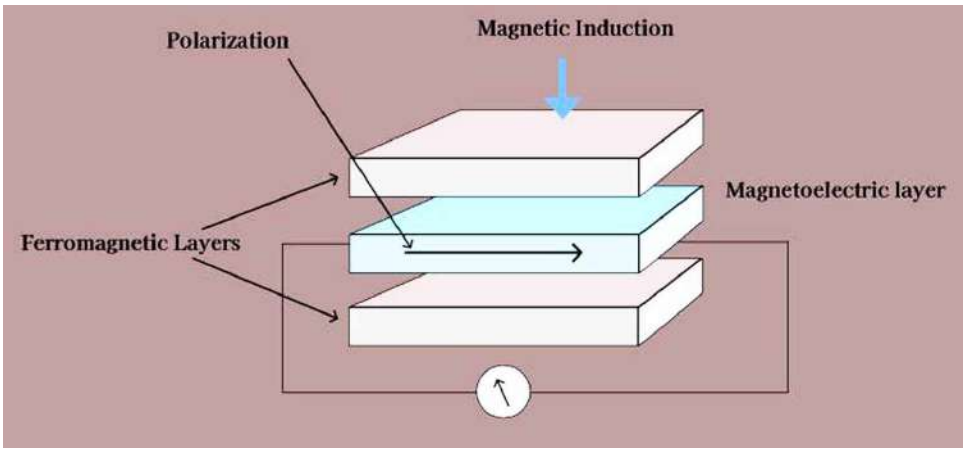

5. CHARACTERIZATION TECHNIQUES FOR MULTIFERROIC MATERIALS

Characterizing multiferroic materials involves a range of techniques to assess their magnetic, ferroelectric, and structural properties. Here are some common

characterization methods used for multiferroic materials are structural, ferroelectric, magnetic, magnetic-ferroelectric coupling and electric-magnetic Coupling.

Structural Characterizations

X-ray Diffraction (XRD): XRD is used to analyze the crystal structure, phase transitions, and lattice parameters of multiferroic materials.

Transmission Electron Microscopy (TEM): TEM produces high-resolution imaging to study the microstructure, defects, and domain structures within multiferroic materials.

Scanning Electron Microscopy (SEM): SEM used to analyse the surface morphology and microstructure of multiferroic samples.

Atomic Force Microscopy (AFM): AFM can be used to visualize surface topography and domain structures with high resolution.

Ferroelectric Characterizations

Polarization vs. Electric Field (P-E) Loops: This method measures the ferroelectric polarization with respect to the applied electric field. It provides information about the ferroelectric hysteresis and coercive field. Figure 8 explains PE loop of ABO_3 type multiferroic.

Dielectric Spectroscopy: Dielectric spectroscopy is used to investigate the dielectric properties of ferroelectric materials with respect to frequency and temperature. It helps in understanding polarization dynamics.

Pyroelectric Measurements: Pyroelectric measurements involve detecting changes in polarization with temperature variations, which can reveal the presence of ferroelectric domains and phase transitions (Cuadras, Gasulla, and Ferrari 2010).

Magnetic Characterizations

Magnetization vs. Magnetic Field (M-H) Loops: These loops provide information about the magnetic properties of multiferroic materials, viz., magnetic hysteresis, magnetic susceptibility, and saturation magnetization.

Magnetic Resonance Techniques: Methods like electron paramagnetic resonance (EPR) and nuclear magnetic resonance (NMR) can be engaged to probe the magnetic behavior, including spin states and magnetic ordering.

Magnetic Force Microscopy (MFM): MFM is a scanning probe microscopy procedure that allows the imaging of magnetic domains and domain walls in multiferroic materials.

Figure 8. P-E loop of ABO_3 type multiferroic

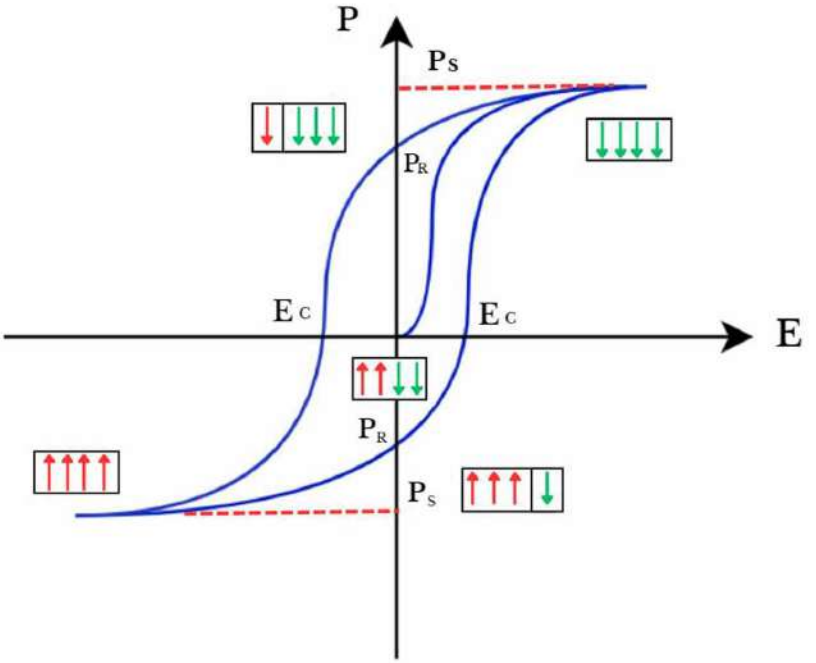

Magnetic-Ferroelectric Coupling

Magneto-optical Kerr Effect (MOKE): MOKE is used to study the coupling between magnetic and ferroelectric properties by analyzing changes in light polarization due to magnetization variations. Figure 9 shows magneto optical kerr effect (Lacerda and de Lazaro 2020).

Piezoresponse Force Microscopy (PFM): PFM helps in the characterization of ferroelectric domains and their response to external electric fields, which can be related to the magnetic behaviour (Sahu, Mondal, and Dewangan 2019).

Electric-Magnetic Coupling

Magneto capacitance Measurements: These measurements study the changes in the dielectric properties of a system with applied magnetic field, providing insight into the electric-magnetic coupling.

Electromagnetic Resonance Techniques: These techniques investigate the interactions between electric and magnetic fields, such as magnon-photon coupling and magnetoelectric resonances.

Figure 9. Magneto optical Kerr effect

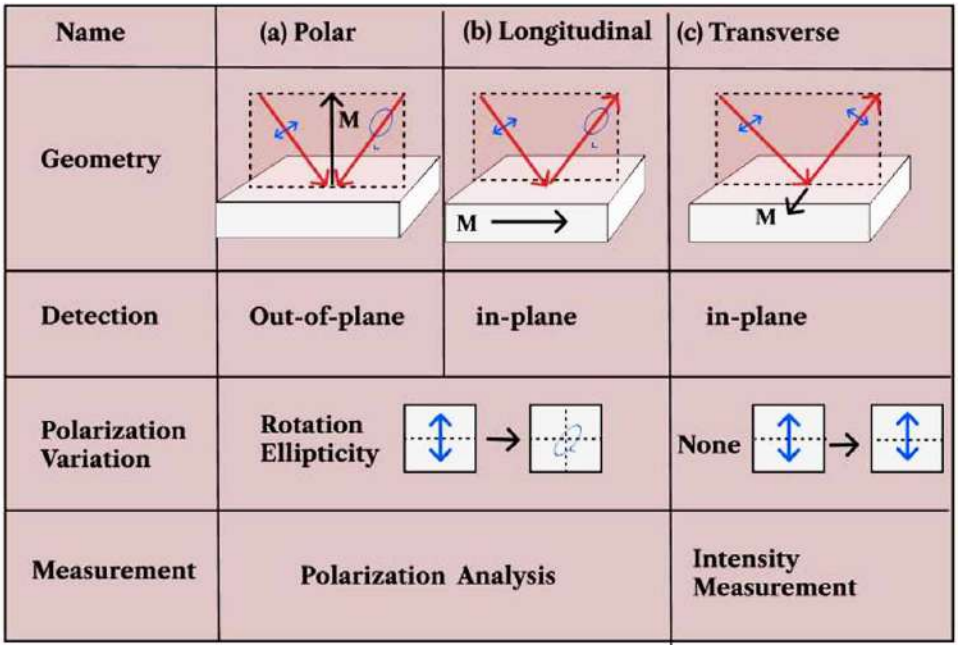

Characterizing multiferroic materials often requires a combination of these techniques to fully understand their properties and behavior, as these materials are complex and exhibit a range of interconnected properties (Rani, Kolte, and Gopalan 2019).

6. APPLICATIONS OF MULTIFERROIC MATERIALS

Multiferroic materials have unique properties that make them suitable for certain applications, particularly in the fields of electronics, sensors, and also in energy conversion. Here is a list of applications for multiferroic materials.

Memory Devices: Multiferroic materials are used in non-volatile memory devices where the coupling among ferroelectric and ferromagnetic properties allows for the manipulation and storage of data.

Magnetic Sensors: The strong coupling among magnetic and ferroelectric characteristics enables the development of highly sensitive sensors for detecting weak magnetic fields, which find applications in areas like geophysics and medical imaging (Sriramdas et al. 2020).

Spintronic Devices: Multiferroic materials are being explored for spintronic devices, which rely on the spin of electrons for information processing. This can lead to lower power consumption and faster electronic devices.

Energy Harvesting: Multiferroic materials play a crucial role in energy harvesting systems, where they transform mechanical vibrations, thermal gradients, and various energy sources into electrical power. This utilization provides sustainable and effective solutions for energy needs (Kishore and Priya 2018).

Tunable Microwave Components: The electric-field control of magnetic characters in multiferroics can be harnessed to create tunable microwave components like filters, phase shifters, and antennas, leading to versatile communication devices.

Piezoelectric Actuators: Multiferroic materials can be used to design high-performance actuators for precise and rapid mechanical motion (Zeng et al. 2018). These are applied in various devices, including inkjet printers and autofocus cameras.

Magnetoelectric Sensors: The magnetoelectric coupling in multiferroic materials allows for the development of sensors that can simultaneously detect both electric and magnetic fields, making them useful in a widespread applications (Narita and Fox 2018).

Medical Devices: Multiferroic materials are employed in medical devices, such as ultrasound transducers and magnetic resonance imaging (MRI) sensors, to improve sensitivity and imaging quality (Parvez Mahmud et al. 2018).

Voltage-Controlled Magnetic Devices: By utilizing the voltage-induced changes in magnetic properties, multiferroic materials can enable voltage-controlled magnetic switches and sensors.

Optical Devices. The manipulation of magnetic properties through electric-field variation in multiferroics holds the potential to advance the creation of optical devices for data transmission and telecommunications.

Biomedical Devices: Researchers are investigating the use of biocompatible multiferroic materials in controlled drug delivery systems and implantable devices.

Environmental Sensors: Multiferroic materials can be utilized in environmental monitoring devices like sensors for detecting pollutants, magnetic fields, and seismic activity.

Quantum Computing: The strong coupling between electric and magnetic properties in multiferroics holds promise for their use in quantum computing, a field with enormous potential for solving complex problems.

Smart Materials: Multiferroic materials are employed as smart materials that can modify their properties with respect to external stimuli. They are used in applications like adaptive optics and vibration control systems.

The versatility of multiferroic materials makes them a subject of ongoing research, with potential applications across a wide range of technologies, from information storage and processing to sensors and energy-efficient devices. Energy harvesting with multiferroic materials is an innovative and promising field that focuses on converting various ambient energy sources into electrical power (Annapureddy et al. 2018).

7. MULTIFERROIC ENERGY HARVESTING

Multiferroic energy harvesting offer advantages over traditional piezoelectric or electromagnetic harvesters by providing improved energy conversion efficiency. Ongoing research aims to optimize the design and performance of multiferroic energy harvesters for various applications, including wearable electronics and remote sensor networks which are discussed below.

Wireless Sensor Networks: Multiferroic energy harvesting is particularly useful in powering wireless sensor networks (WSNs). These networks are used for environmental monitoring, structural health monitoring, and many other applications. Energy harvesters utilizing multiferroic materials offer a sustainable power source for sensors, eliminating the necessity for battery replacement and lowering maintenance costs.

Vibrational Energy Harvesters: Multiferroic materials can efficiently convert mechanical vibrations from sources such as machinery, vehicles, or foot traffic into electrical energy. These energy harvesters can be integrated into infrastructure or wearable devices to capture mechanical vibrations and extend the operational life of electronic components (Liu et al. 2022).

Thermal Energy Harvesting: Multiferroic materials with strong thermoelectric properties can be used to capture waste heat from industrial processes, exhaust systems, or electronic devices. This harvested energy can be used to power low-energy sensors or supplement other power sources in various applications.

Environmental Sensors: Energy harvesting with multiferroic materials is beneficial for environmental monitoring sensors. These sensors can be deployed in remote or hard-to-reach locations to gather data on environmental conditions, viz., temperature, humidity and quality of air.

Medical Implants: Multiferroic energy harvesters have the potential to power medical implants, such as pacemakers or drug delivery devices. By utilizing energy from mechanical motions or temperature gradients within the human body, these implants can operate without the need for frequent surgeries to replace batteries.

Wearable Technology: Wearable devices, like smartwatches and fitness trackers, can benefit from multiferroic energy harvesters. These devices can capture energy from user movements and environmental vibrations, extending battery life and reducing the need for recharging.

IoT Devices: Multiferroic energy harvesting contributes to the development of energy-efficient Internet of Things (IoT) devices. These devices can operate independently in remote or harsh environments, collecting and transmitting data without relying on conventional power sources (Amrillah et al. 2021).

Energy-Efficient Electronics: Multiferroic materials can be integrated into various electronic devices to enhance their energy efficiency. For example, they can be used in combination with low-power microcontrollers and sensors to create self-powered systems.

Although the potential of multiferroic energy harvesting is promising, there remain challenges to address. These include optimizing material properties, enhancing energy conversion efficiency, and scaling up production. Ongoing research in this field aims to make strides in developing more practical and efficient multiferroic energy harvesters for diverse applications. This progress contributes to the realization of a more sustainable and energy-efficient future.

7.1 Significant Energy Harvesting Methods

This section elucidates significant energy harvesting methods utilizing multiferroic systems.

Piezoelectric and Piezomagnetic Energy Harvesting

The Piezoelectric and Piezomagnetic energy Harvester has garnered significant attention due to its capability to transform magnetic energy into electrical power. Nevertheless, it faces challenges in sustaining electrical energy for nanosystems and mitigating the intrinsic fragility of piezoelectric and piezomagnetic materials. As a solution, Tao Fan (Fan 2021) introduces a novel concept: an energy harvesting system has been devised, consisting of a nanoporous beam that combines piezoelectric and piezomagnetic properties, integrated with a storage circuit for optimal energy efficiency. The design envisions a nanoporous beam structured as a sandwich composite, incorporating a core made of both piezoelectric and piezomagnetic materials, along with outer interface layers (Queraltó et al. 2020).

Biomechanical Energy Harvesting

Biomechanical means of energy harvesting from multiferroic materials represents a cutting-edge approach in the field of renewable energy technology. Multiferroic materials possess a unique combination of both ferroelectric and ferromagnetic properties, making them exceptionally attractive for producing energy from various mechanical systems, like human motion and vibrations in the environment (Wu et al. 2021).

The principle behind this innovative technology lies in the capability of multiferroic systems to change mechanical strain and motion into electrical energy. When subjected to stress or movement, these materials generate voltage, which can be efficiently harvested and stored for various applications. This presents a likely solution for powering wearable devices, sensors, and even medical implants through the natural movements of the human body.

The energy harvesting module with multiferroic properties comprises a permanent magnet capable of movement, converting mechanical energy into magnetic energy. One of the key advantages of using multiferroic materials for biomechanical energy harvesting is their high energy conversion efficiency, durability, and adaptability to different environmental conditions. Researchers are continually exploring the potential of these materials in creating self-powered systems that reduce the reliance on traditional batteries and contribute to sustainable energy solutions.

As technology advances, the integration of multiferroic materials in wearable devices and environmental sensors is expected to become more prevalent, offering a greener and more sustainable way to meet our growing energy demands while reducing the environmental impact of traditional power sources.

Thermal Energy Harvesting

Thermal energy harvesting from multiferroic materials is a promising frontier in renewable energy technology. Multiferroic materials, renowned for their unique combination of ferroelectric and ferromagnetic properties, demonstrate exceptional potential for efficiently converting temperature variations into electrical energy. This occurrence, known as the pyroelectric effect, allows multiferroic materials to generate voltage when exposed to temperature fluctuations. Ba0.85Ca0.15Ti0.9-xSnxZr0.10O3 has been reported as an excellent moltiferroic material for thermal energy harvestimg. The applications for thermal energy harvesting from multiferroic materials are diverse. They can be integrated into sensors, environmental monitoring systems, and self-powered devices, capitalizing on the naturally occurring temperature differences in their surroundings. This innovative approach can reduce the reliance

on traditional power sources and minimize environmental impact (Khobragade and Patel 2020).

One significant advantage of multiferroic materials in thermal energy harvesting is their ability to work in a wide range of temperature conditions, making them suitable for various environments. As technology continues to advance, the utilization of these materials in renewable energy solutions has the potential to improve sustainability, energy efficiency, and reduce our dependence on fossil fuels.

Energy harvesting with multiferroic materials presents a range of exciting opportunities for sustainable power generation. However, it also comes with its share of challenges. Here, we'll explore both the opportunities and the obstacles in this emerging field:

7.2 Opportunities and Obstacles in Energy Harvesting

i. ***Sustainability***: Energy harvesting with multiferroic materials provides a sustainable and environmentally friendly means of generating electricity. It reduces our reliance on non-renewable energy sources and minimizes the environmental impact associated with battery disposal.

ii. ***Battery Replacement***: Multiferroic energy harvesters can replace or supplement batteries in various applications, such as wireless sensor networks and wearable technology. This eliminates the need for frequent battery replacements, reducing maintenance costs and downtime.

iii. ***Remote and Harsh Environments***: These energy harvesters offer the ability to power sensors and devices in remote or harsh environments where replacing batteries or using traditional power sources is challenging. Examples include remote environmental monitoring and offshore sensor networks (Oliveira et al. 2021).

iv. ***Self-Powered Devices***: Multiferroic energy harvesters enable the development of self-powered devices that can operate autonomously, reducing the need for frequent human intervention or maintenance.

v. ***Enhanced Efficiency***: Multiferroic materials, which combine ferroelectric and ferromagnetic properties, can achieve elevated conversion efficiencies. This characteristic renders them well-suited for applications where energy efficiency is of paramount importance.

vi. ***Miniaturization***: Multiferroic energy harvesters can be miniaturized, allowing their integration into small and compact electronic devices, including IoT sensors and wearable technology.

vii. ***Medical Implants***: These energy harvesters can be used to power medical implants, enhancing patient safety by eliminating the need for battery replacement surgeries (Zaeimbashi et al. 2019).

7.3 Challenges in Energy Harvesting

i. ***Energy Conversion Efficiency***: Achieving high energy conversion efficiency with multiferroic materials remains a challenge. Researchers are working to optimize material properties and device designs to maximize power output.
ii. ***Material Selection***: Identifying and developing suitable multiferroic materials that exhibit strong coupling between ferroelectricity and ferromagnetism is critical. Some of these materials can be rare or difficult to produce in large quantities.
iii. ***Cost***: The cost of manufacturing multiferroic materials can be higher than traditional materials, posing an economic challenge, particularly for widespread adoption.
iv. ***Environmental Variability***: Energy harvesting efficiency can vary significantly with environmental conditions. Variations in temperature, humidity, and mechanical vibrations can impact the performance of multiferroic energy harvesters (Oliveira et al. 2023).
v. ***Scalability***: Scaling up the production of multiferroic materials and energy harvesting devices to meet commercial demand is a complex task that requires addressing various manufacturing and quality control issues.
vi. ***Integration Challenges***: Integrating multiferroic energy harvesters into existing systems or devices can be challenging due to differences in form factor and power characteristics. This requires innovative designs and engineering solutions.
vii. ***Longevity and Durability***: The lengthy stability and durability of multiferroic materials and devices under several conditions need to be thoroughly assessed to ensure their reliability.
viii. ***Standardization***: Developing industry standards and guidelines for the characterization, testing, and use of multiferroic energy harvesters is essential to promote consistency and compatibility across applications.

8. CASE STUDIES: MULTIFERROIC MARVELS IN ACTION

Multiferroic materials have been gaining attention for their unique properties and their potential in various technological applications. Here are a few case studies highlighting the use of multiferroic materials in real-world applications:

i. ***Multiferroics in Energy Harvesting***: Researchers at a leading university developed a novel energy harvesting device using a multiferroic composite material. This device captured both mechanical vibrations and temperature gradients, converting them into electrical power. They installed this technology in

a remote environmental monitoring system in a forest. The device autonomously powered sensors that collected data on temperature, humidity, and air quality. It eliminated the need for frequent battery replacements and significantly reduced maintenance costs.

ii. ***Multiferroics in Medical Implants***: A medical technology company successfully incorporated multiferroic materials into the design of a new type of cardiac pacemaker. These multiferroic-based pacemakers capture energy from mechanical movements within the human body and use it to recharge the battery. As a result, patients experience fewer battery replacements, which can be invasive and costly. The pacemakers have demonstrated reliability and extended battery life.

iii. ***Wearable Multiferroic Sensors***: A start-up company focused on wearable technology developed a fitness tracker powered by multiferroic materials. The device used the piezoelectric effect of multiferroic materials to convert the user's movements into electrical energy. As a result, the fitness tracker's battery life was significantly extended, reducing the need for frequent recharging (Krishna Rao, Kumar Rajagopal, and Chandrasekaran 2023). Users appreciated the convenience and sustainability of the device, which quickly gained popularity in the market.

iv. ***Self-Powered Environmental Sensors***: A multinational corporation invested in the development of self-powered environmental sensors for their industrial facilities. They integrated multiferroic energy harvesters into the sensor design. These sensors were deployed in various locations to monitor temperature, pressure, and humidity. The self-powered sensors eliminated the need for cumbersome and expensive wiring, and they provided reliable data collection even in remote areas.

v. ***Multiferroics in Wireless Sensor Networks***: A government agency aimed to improve their environmental monitoring capabilities in remote regions. They implemented a wireless sensor network powered by multiferroic energy harvesters. These sensors continuously collected data on soil moisture and weather conditions, helping in disaster prediction and agricultural planning. The use of multiferroic materials allowed for long-term, autonomous operation of the sensor network without frequent battery replacements.

These case studies demonstrate the practical applications of multiferroic materials in diverse fields, including environmental monitoring, healthcare, and wearable technology. Multiferroic-based devices are not only extending battery life but also contributing to sustainability and efficiency by reducing the environmental impact associated with traditional power sources. The continued development and

integration of multiferroic materials in various technologies hold the promise of a more sustainable and self-powered future.

9. FUTURE DIRECTIONS IN MULTIFERROIC RESEARCH

Multiferroic systems have captured the imagination of researchers and engineers due to their latent for various technological advancements (Rahmati et al. 2023). As researchers continue to unravel the unique properties of multiferroics, several exciting future directions in multiferroic research are emerging:

i. ***Tailoring Multiferroic Materials***: The search for new multiferroic materials with enhanced properties and operational temperatures remains a key focus. Researchers are exploring ways to engineer and tailor multiferroics to meet specific application requirements. This includes modifying crystal structures, doping, and thin-film deposition to enhance multiferroic performance.

ii. ***Energy Harvesting and Conversion***: Multiferroic materials hold great promise for energy harvesting, converting ambient sources of mechanical, thermal, and electromagnetic energy into electrical power. Future research will likely concentrate on optimizing the efficiency and scalability of multiferroic energy harvesters for various applications, from IoT devices to medical implants.

iii. ***Advanced Memory and Computing Devices***: Multiferroic memory devices, which offer the potential for non-volatile, energy-efficient, and high-density data storage, are an area of active research. Exploring the scalability and reliability of multiferroic memory for next-generation computing is a significant direction.

iv. ***Magnetoelectric Coupling***: Understanding and enhancing the magnetoelectric coupling in multiferroic materials is a key research area. This coupling holds promise for novel electronic and spintronic devices, where control over both electric and magnetic properties is essential.

v. ***Biocompatible Multiferroics***: The development of biocompatible multiferroic materials for medical applications, such as controlled drug delivery and neuromorphic devices, is an emerging direction. Researchers are focusing on materials that are safe for implantation in the human body and can interface with biological systems (Garcia-Gonzalez and Landis 2020).

vi. ***Environmental and Structural Sensors***: The use of multiferroic materials in sensors for environmental monitoring, structural health, and security applications is expected to grow. These sensors can operate in harsh conditions and contribute to data collection for climate studies, infrastructure maintenance, and defense.

vii. ***Quantum Technologies:*** Multiferroic materials could contribute to the advancement of quantum technologies, including applications in quantum

computing and quantum communication. Researchers are investigating the potential of multiferroics to enable the manipulation of qubits and quantum states.

viii. ***Standardization and Commercialization***: As multiferroic technologies mature, the establishment of standards and guidelines for characterization, testing, and application will become increasingly important. This will facilitate the commercialization of multiferroic products and their integration into existing technology ecosystems.

ix. ***Collaboration and Interdisciplinary Research***: The future of multiferroic research will involve greater collaboration between materials scientists, physicists, electrical engineers, and other experts. Interdisciplinary approaches will be crucial to address the complex challenges and opportunities presented by multiferroic materials.

x. ***Global Energy Solutions***: The potential incorporation of multiferroic energy harvesters could play a crucial role in the shift toward cleaner and more sustainable energy sources. Future research may focus on integrating multiferroic technologies into global energy solutions, including grid systems, remote power generation, and smart cities.

The unique properties and potential applications of multiferroic materials offer exciting opportunities for advancements in technology, energy harvesting, and beyond. With continued research and development, multiferroics are expected to become an integral part of future technologies.

10. CONCLUSION

Multiferroics have introduced novel opportunities in the field of energy harvesting, providing creative solutions to address key challenges in sustainable power generation. These remarkable materials, with their coexistence of ferroelectric and ferromagnetic properties, have demonstrated great promise across various applications. Multiferroic materials have enabled the development of self-sustaining systems in remote and harsh environments, eliminating the need for frequent battery replacements and reducing maintenance costs. They have found their way into wearable technology, powering devices by harnessing human motion, furthering the evolution of portable electronics. In healthcare, they are enhancing the reliability of medical implants, contributing to patient well-being. Moreover, the incorporation of multiferroics in environmental and structural sensors is revolutionizing the way we monitor our surroundings, ensuring safety and efficiency.

As we look ahead, the future of multiferroic research holds exciting prospects, from further optimizing material properties to exploring emerging applications in quantum technologies and beyond. The marriage of science, engineering, and innovation in the realm of multiferroics is not only reshaping our technological landscape but also taking us one step closer to a sustainable and self-powered future. In this transformative journey, multiferroic marvels continue to pave the way for more efficient, eco-friendly, and autonomous energy solutions, leaving an indelible mark on the path to a greener, smarter world.

REFERENCES

Aguiar, E. C., Ramirez, M. A., Cortes, J. A., Rocha, L. S., Borsari, E., & Simões, A. Z. (2015). Magnetoelectric Coupling of LaFeO3/BiFeO3 Heterostructures. *Ceramics International*, *41*(10), 13126–13134. doi:10.1016/j.ceramint.2015.07.043

Amrillah, T., Hermawan, A., Wulandari, C. P., Muthi'Ah, A. D., & Simanjuntak, F. M. (2021). Crafting the Multiferroic BiFeO 3 -CoFe 2 O 4 Nanocomposite for next-Generation Devices: A Review. *Materials and Manufacturing Processes*, *36*(14), 1579–1596. doi:10.1080/10426914.2021.1945096

Annapureddy, V., Na, S.-M., Hwang, G.-T., Kang, M. G., Sriramdas, R., Palneedi, H., Yoon, W.-H., Hahn, B.-D., Kim, J.-W., Ahn, C.-W., Park, D.-S., Choi, J.-J., Jeong, D.-Y., Flatau, A. B., Peddigari, M., Priya, S., Kim, K.-H., & Ryu, J. (2018). Exceeding Milli-Watt Powering Magneto-Mechano-Electric Generator for Standalone-Powered Electronics. *Energy & Environmental Science*, *11*(4), 818–829. doi:10.1039/C7EE03429F

Chan, D. Q., Quan, T. Q., Kim, S.-E., & Duc, N. D. (2019). Nonlinear Dynamic Response and Vibration of Shear Deformable Piezoelectric Functionally Graded Truncated Conical Panel in Thermal Environments. *European Journal of Mechanics. A, Solids*, *77*, 103795. doi:10.1016/j.euromechsol.2019.103795

Chen, A., Su, Q., Han, H., Enriquez, E., & Jia, Q. (2019). Metal Oxide Nanocomposites: A Perspective from Strain, Defect, and Interface. *Advanced Materials*, *31*(4), 1803241. Advance online publication. doi:10.1002/adma.201803241 PMID:30368932

Chorsi, M. T., Curry, E. J., Chorsi, H. T., Das, R., Baroody, J., Purohit, P. K., Ilies, H., & Nguyen, T. D. (2019). Piezoelectric Biomaterials for Sensors and Actuators. *Advanced Materials*, *31*(1), 1802084. Advance online publication. doi:10.1002/adma.201802084 PMID:30294947

Cuadras, A., Gasulla, M., & Ferrari, V. (2010). Thermal Energy Harvesting through Pyroelectricity. *Sensors and Actuators. A, Physical*, *158*(1), 132–139. doi:10.1016/j.sna.2009.12.018

Dong, S., Xiang, H., & Dagotto, E. (2019). Magnetoelectricity in Multiferroics: A Theoretical Perspective. *National Science Review*, *6*(4), 629–641. doi:10.1093/nsr/nwz023 PMID:34691919

Fan, T. (2021). Energy Harvesting from a Nanopiezoelectric/Piezomagnetic Sandwich Beam with Porous Properties. *The Journal of Sandwich Structures & Materials*, *23*(7), 3280–3302. doi:10.1177/1099636220926863

Garcia-Gonzalez, D., & Landis, C. M. (2020). Magneto-Diffusion-Viscohyperelasticity for Magneto-Active Hydrogels: Rate Dependences across Time Scales. *Journal of the Mechanics and Physics of Solids*, *139*, 103934. doi:10.1016/j.jmps.2020.103934

Geng, Y., Das, H., Wysocki, A. L., Wang, X., Cheong, S.-W., Mostovoy, M., Fennie, C. J., & Wu, W. (2014). Direct Visualization of Magnetoelectric Domains. *Nature Materials*, *13*(2), 163–167. doi:10.1038/nmat3813 PMID:24292421

Jing, Q., Liu, Z., Cheng, X., Li, C., Ren, P., Guo, K., Yue, H., Xie, B., Li, T., Wang, Z., & Shu, L. (2023). Boosting Piezo-Photocatalytic Activity of BiVO4/BiFeO3 Heterojunctions through Built-in Polarization Field Tailoring Carrier Transfer Performances. *Chemical Engineering Journal*, *464*, 142617. doi:10.1016/j.cej.2023.142617

Khobragade, S., & Patel, S. (2020). Thermal Energy Harvesting Capabilities in Lead-Free Ba0.85Ca0.15Ti0.9−xSnxZr0.10O3 Ferroelectric Ceramics. *Journal of Electronic Materials*, *49*(2), 1194–1203. doi:10.1007/s11664-019-07821-3

Kishore, R., & Priya, S. (2018). A Review on Low-Grade Thermal Energy Harvesting: Materials, Methods and Devices. *Materials (Basel)*, *11*(8), 1433. doi:10.3390/ma11081433 PMID:30110947

Krishan, R., Kaur, M., & Mehta, S. (Eds.). (2023). *Innovative Smart Materials Used in Wireless Communication Technology*. IGI Global. doi:10.4018/978-1-6684-7000-8

Krishan, R., Kaur, M., Singh, J., Mehta, S., & Goyal, V. (Eds.). (2023). *Digital Transformation – Modernization and Optimization of Wireless Networks*. Nova Science Publishers. doi:10.52305/TTVQ3854

Lacerda & Lazaro. (2020). Magneto-Optical Coupling and Kerr Effect in PbNiO3, PbCrO3, and PbMnO3 Multiferroics: An Excited-States Approach. *Journal of Magnetism and Magnetic Materials, 514*, 167176. doi:10.1016/j.jmmm.2020.167176

Lee, O. J., Misra, S., Wang, H., & MacManus-Driscoll, J. L. (2021). Ferroelectric/Multiferroic Self-Assembled Vertically Aligned Nanocomposites: Current and Future Status. *APL Materials*, *9*(3), 030904. Advance online publication. doi:10.1063/5.0035366

Liu, S., Xiang, F., Cheng, Y., Luo, Y., & Sun, J. (2022). Multiferroic and Magnetodielectric Effects in Multiferroic Pr2FeAlO6 Double Perovskite. *Nanomaterials (Basel, Switzerland)*, *12*(17), 3011. doi:10.3390/nano12173011 PMID:36080048

Mangaiyarkkarasi, J., & Shanthalakshmi Revathy, J. (2023). Design and Fabrication Techniques for Nonlinear Metamaterials and Metasurfaces for Wireless Communication. In Metamaterial Technology and Intelligent Metasurfaces for Wireless Communication Systems. IGI Global. doi:10.4018/978-1-6684-8287-2.ch004

Mehta, S., Islam, F., & Imran, A. (Eds.). (2023). *Innovations in Engineering and Food Science*. IGI Global. doi:10.4018/979-8-3693-0819-6

Muthukrishnan, R. M., Mohammed Yusuf Ansari, P., & Abdul Kader, S. M. (2023). Analysing the Super Exchange Interaction of Fe3+-O2—Cr3+ on Multiferroic Structured BiFeO3/LaCrO3 Nanocomposite. *Physica B, Condensed Matter*, *665*, 415030. doi:10.1016/j.physb.2023.415030

MuthuKrishnan, R. M., Mohammed Yusuf Ansari, P., & Abdul Kader, S. M. (2023). Engineering and Analysing the Super Exchange Interaction of Fe3+- O2− - V5+ on Novel Multiferroic BiFeO3/BiVO4 Nanocomposite. *Journal of Solid State Chemistry*, *326*, 124224. doi:10.1016/j.jssc.2023.124224

Narita, F., & Fox, M. (2018). A Review on Piezoelectric, Magnetostrictive, and Magnetoelectric Materials and Device Technologies for Energy Harvesting Applications. *Advanced Engineering Materials*, *20*(5), 1700743. Advance online publication. doi:10.1002/adem.201700743

Oliveira, R. C., Volnistem, E. A., Astrath, E. A. C., Dias, G. S., Santos, I. A., Garcia, D., & Eiras, J. A. (2021). La Doped BiFeO3 Ceramics Synthesized under Extreme Conditions: Enhanced Magnetic and Dielectric Properties. *Ceramics International*, *47*(14), 20407–20412. doi:10.1016/j.ceramint.2021.04.049

Oliveira, R. C., Volnistem, E. A., de Melo, M. A. C., Cótica, L. F., Santos, I. A., Eiras, J. A., Garcia, D., Süllow, S., Menzel, D., Litterst, F. J., Baabe, D., Davanse da Silveira, L. G., & Dias, G. S. (2023). On the Enhanced Dielectric and Magnetic Properties of BiFeO3 Ceramics Sintered under Meta-Stable Conditions. *Applied Materials Today*, *32*, 101790. doi:10.1016/j.apmt.2023.101790

Panneer Muthuselvam, I., & Bhowmik, R. N. (2010). Mechanical Alloyed Ho3+ Doping in CoFe2O4 Spinel Ferrite and Understanding of Magnetic Nanodomains. *Journal of Magnetism and Magnetic Materials*, *322*(7), 767–776. doi:10.1016/j.jmmm.2009.10.057

Parvez Mahmud, M. A., Huda, N., Farjana, S. H., Asadnia, M., & Lang, C. (2018). Recent Advances in Nanogenerator-Driven Self-Powered Implantable Biomedical Devices. *Advanced Energy Materials*, *8*(2), 1701210. Advance online publication. doi:10.1002/aenm.201701210

Queraltó, A., Frohnhoven, R., Mathur, S., & Gómez, A. (2020). Intrinsic Piezoelectric Characterization of BiFeO3 Nanofibers and Its Implications for Energy Harvesting. *Applied Surface Science*, *509*, 144760. doi:10.1016/j.apsusc.2019.144760

Rahmati, A. H., Jia, R., Tan, K., Zhao, X., Deng, Q., Liu, L., & Sharma, P. (2023). Theory of Hard Magnetic Soft Materials to Create Magnetoelectricity. *Journal of the Mechanics and Physics of Solids*, *171*, 105136. doi:10.1016/j.jmps.2022.105136

Rani, A., Kolte, J., & Gopalan, P. (2019). Investigation on the Structural, Multiferroic and Magnetoelectric Properties of BaTi1-XNixO3 Ceramics. *Ceramics International*, *45*(5), 5312–5320. doi:10.1016/j.ceramint.2018.11.229

Rao, K., Subha, R. K. R., & Chandrasekaran, G. (2023). Fiber Optic Sensors for Gas Detection: An Overview on Spin Frustrated Multiferroics. In Metal-Oxide Gas Sensors. IntechOpen.

Ravi, S. (2020). High Curie Temperature and Room Temperature Magnetoresistance in Pr2FeCrO6 Material for Spintronics Applications. *Materials Letters*, *278*, 128448. doi:10.1016/j.matlet.2020.128448

Remya, K. P., Prabhu, D., Justin Joseyphus, R., Chandra Bose, A., Viswanathan, C., & Ponpandian, N. (2020). Tailoring the Morphology and Size of Perovskite BiFeO3 Nanostructures for Enhanced Magnetic and Electrical Properties. *Materials & Design*, *192*, 108694. doi:10.1016/j.matdes.2020.108694

Sahu, S. A., Mondal, S., & Dewangan, N. (2019). Polarized Shear Waves in Functionally Graded Piezoelectric Material Layer Sandwiched between Corrugated Piezomagnetic Layer and Elastic Substrate. *The Journal of Sandwich Structures & Materials*, *21*(8), 2921–2948. doi:10.1177/1099636217726330

Sezer, N., & Koç, M. (2021). A Comprehensive Review on the State-of-the-Art of Piezoelectric Energy Harvesting. *Nano Energy*, *80*, 105567. doi:10.1016/j.nanoen.2020.105567

Shirvanimoghaddam, M., Johnson, S. J., & Lance, A. M. (2016). Design of Raptor Codes in the Low SNR Regime with Applications in Quantum Key Distribution. In *2016 IEEE International Conference on Communications (ICC)*. IEEE. 10.1109/ICC.2016.7510800

Sriramdas, R., Kang, M.-G., Meng, M., Kiani, M., Ryu, J., Sanghadasa, M., & Priya, S. (2020). Large Power Amplification in Magneto-Mechano-Electric Harvesters through Distributed Forcing. *Advanced Energy Materials*, *10*(8), 1903689. Advance online publication. doi:10.1002/aenm.201903689

Sun, X., MacManus-Driscoll, J. L., & Wang, H. (2020). Spontaneous Ordering of Oxide-Oxide Epitaxial Vertically Aligned Nanocomposite Thin Films. *Annual Review of Materials Research*, *50*(1), 229–253. doi:10.1146/annurev-matsci-091719-112806

Wu, H., Tatarenko, A., Bichurin, M. I., & Wang, Y. (2021). A Multiferroic Module for Biomechanical Energy Harvesting. *Nano Energy*, *83*, 105777. doi:10.1016/j.nanoen.2021.105777

Xu, Z., Bykova, J., Baniasadi, M., Moreno, S., Zhou, Z., Das, N., Bandi, S., Xi, Y., Qian, D., Baughman, R. H., & Minary-Jolandan, M. (2017). Bioinspired Multifunctional Ceramic Platelet-Reinforced Piezoelectric Polymer Composite. *Advanced Engineering Materials*, *19*(2), 1600570. Advance online publication. doi:10.1002/adem.201600570

Xu, Z., Liu, Y., Dong, L., Closson, A. B., Hao, N., Oglesby, M., Escobar, G. P., Fu, S., Han, X., Wen, C., Liu, J., Feldman, M. D., Chen, Z., & Zhang, J. X. J. (2018). Tunable Buckled Beams with Mesoporous PVDF-TrFE/SWCNT Composite Film for Energy Harvesting. *ACS Applied Materials & Interfaces*, *10*(39), 33516–33522. doi:10.1021/acsami.8b09310 PMID:30199624

Zaeimbashi, M., Lin, H., Dong, C., Liang, X., Nasrollahpour, M., Chen, H., Sun, N., Matyushov, A., He, Y., Wang, X., Tu, C., Wei, Y., Zhang, Y., Cash, S. S., Onabajo, M., Shrivastava, A., & Sun, N. (2019). NanoNeuroRFID: A Wireless Implantable Device Based on Magnetoelectric Antennas. *IEEE Journal of Electromagnetics, RF and Microwaves in Medicine and Biology*, *3*(3), 206–215. doi:10.1109/JERM.2019.2903930

Zeng, S., Zhang, C., Wang, K., Wang, B., & Sun, L. (2018). Analysis of Delamination of Unimorph Cantilever Piezoelectric Energy Harvesters. *Journal of Intelligent Material Systems and Structures*, *29*(9), 1875–1883. doi:10.1177/1045389X17754273

Received: 21 June 2023 | Revised: 13 November 2023 | Accepted: 15 December 2023

DOI: 10.1002/mop.33993

RESEARCH ARTICLE

WILEY

Simulation of all-optical NOR gate design with improved extinction ratio using semiconductor optical amplifier

Anusooya Vadukanathan[1] | **Gobalakrishnan Suyambragasam**[2] | **Ponmalar Sivaraj**[3] | **Manikandan Moola Seetharamaier Kasiviswanathan**[4]

[1]Department of ECE, Rajalakshmi Engineering College, Chennai, Tamil Nadu, India

[2]Department of Physics, Rajalakshmi Engineering College, Chennai, Tamil Nadu, India

[3]Department of CSE, Velammal College of Engineering and Technology, Madurai, Tamil Nadu, India

[4]Department of ECE, Thiagarajar College of Engineering, Madurai, Tamil Nadu, India

Correspondence
Anusooya Vadukanathan, Department of ECE, Rajalakshmi Engineering College, Thandalam, Chennai, Tamil Nadu, 602105, India.
Email: prof.v.anusooya@gmail.com

Abstract

Optical computers, leveraging the advantages of light characteristics, hold the potential to outperform electronic computers significantly. The role of all-optical logic gates is pivotal in realizing such high-performance computing systems. This research introduces a streamlined design for an all-optical NOR logic gate utilizing a semiconductor optical amplifier. The proposed gate operates at a remarkable data rate of 40 Gbps, achieving an excellent extinction ratio of 20.285 dB. Notably, the design exhibits very low dispersion ($-0.029 \times 10^{+006}$ ps/nm) and an impressively low bit error rate of 4.27×10^{-26}.

KEYWORDS

all-optical logic gate, cross-gain modulation, extinction ratio, Kerr effect, NOR gate, semiconductor optical amplifier

1 | INTRODUCTION

Optics is rapidly becoming the most promising prospective answer in comparison to electronics because of its ability to deliver parallel data processing at lower costs and at a greater speed than electrical computers, which are nearly 100 000 times quicker than optical computers.[1] High-speed all-optical logic gates are generated using binary phase-shift keyed signals and on–off keyed signals.[2] All-optical NOR logic gates are important components for all-optical communication and computing systems. They can be used to implement a variety of logic functions, including arithmetic operations, data processing, and signal routing. Semiconductor optical amplifiers (SOAs) and related devices such as SOA-Mach–Zehnder interferometers (SOA-MZIs), quantum dot SOAs (QD-SOAs), optically dense reflective SOAs (OD-RSOAs), and SOA-delayed interferometers (SOA-DIs), highly nonlinear fiber, micro-scale and nanoscale waveguides, and photonic crystal structures have been widely used to implement all-optical NOR logic gates.[3] One of the simplest designs for an all-optical NOR gate using SOAs is the parallel SOA-MZI structure. This design consists of two SOA-MZIs connected in parallel, with the two input signals applied to the two SOA-MZIs, respectively. The output signal from each SOA-MZI is then combined using a power combiner.[4] In a study, a single QD-SOA-based MZI was used to simulate a fast all-optical NOR gate. Data signals of the same wavelength can be converted into logic gates with excellent quality and logical correctness.[5] An RSOA-based optical NOR gate architecture using soliton pulses, achieving extinction ratio (ER ~ 14 dB), contrast ratio (~15 dB), and Q value (~90 dB) for future optical logic processors.[6] The NOR logic function is implemented by exploiting the

cross-gain modulation (XGM) effect in SOAs. When two optical signals are input into an SOA, they interact with each other and with the SOA, resulting in a change in the gain and phase of both signals. The magnitude and phase of this change depends on the power of the two input signals.[7] One design for a QD-SOA-based NOR gate uses a single QD-SOA and QD-RSOA with two input ports and a single output port. The two input ports are used to input the two input signals, and the output port is used to output the NOR logic function.[8] The paper introduces and experimentally validates an all-optical NOR logic gate operating at a speed of 1 Tbps. This is achieved through the utilization of a turbo-switch Mach–Zehnder interferometer (TSMZI) in conjunction with the ultrafast SOA-DI. The quality factor (QF) using a serially DI after the QD-SOAs-TSMZI is 21, surpassing values of 14.3 and 7.5 achieved with QD-SOAs-TSMZI and QD-SOAs-MZI, respectively.[9] In addition to SOA, photonic crystal also becoming an important platform for all-optical gate design in recent years. Researchers proposed an all-optical 3-input NOR gate using photonic crystals. Three resonant rings and the Kerr effect regulate light-output interaction in the gate. Simulations have confirmed the device's operational capability and NOR gate logical table compliance.[10] Another study on universal logic gates in a single silicon mirroring resonator using mode conversion has been reported. The gates have a switching speed of 0.2 ps, an ultrahigh QF, and require low power. Simulations have shown that the gates function correctly and have a QF of around 1500 for NOT and NAND gates, and 2400 for NOR gates.[11] A single microring resonator has been used by researchers to make high-speed, low-power all-optical ternary logic switches. Using different light polarization states, the gates show the three types of logic states.[12] The use of linear optics in a novel design for an all-optical NOR gate has just been documented in the scientific literature.[13] Even people still seek to SOA for all-optical logic gate design despite the prevalence of other platforms for constructing such gates. Recently, Bosu and Bhattacharjee[14] reported on the use of dibit-based OR and NOR gates built on a RSOA. Design and simulation of all-optical frequency encoded logic gates XOR and XNOR also found in a recent report[15] realized using QD-SOAs. Currently, this paper presents a simulation of an all-optical NOR gate design using SOA with improved ER. It is possible to achieve BERs of 10^{-26} or lower using current optical communication technologies. As the technology continues to improve, it is likely that even lower BERs will be possible.[16–18]

2 | DESIGN AND WORKING PRINCIPLES OF OPTICAL NOR LOGIC GATE

In the design of all-optical NOR gate as shown in Figure 1, two binary inputs are generated using pseudorandom sequence generator. Then these two binary inputs are converted into a pulse waveform using a Gaussian pulse generator and both the corresponding input waveforms will be given to the summer, which generates the addition of binary data. Its looks like an OR logic gate operation. The summer output is amplified using an erbium-doped fiber amplifier (EDFA) produces the lowest loss in the complete optical fiber telecommunication wavelength bands, which is also used for the compensation of loss during long-distance communication. The properties of EDFA includes core radius $r = 2.2\,\mu m$, erbium-doping radius $= 2.2\,\mu m$, the

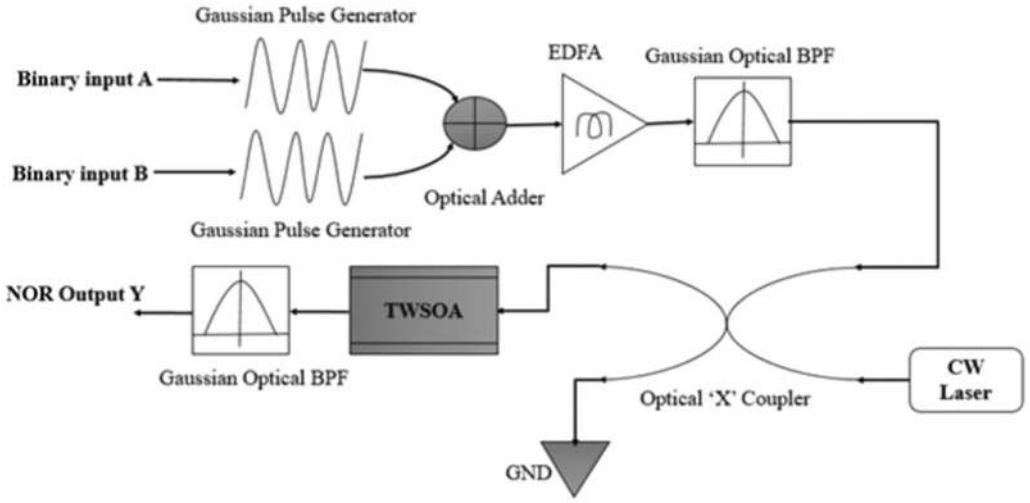

FIGURE 1 The schematic diagram of the proposed NOR gate design. CW, continuous wave; EDFA, erbium-doped fiber amplifier; TWSOA, traveling wave semiconductor optical amplifier.

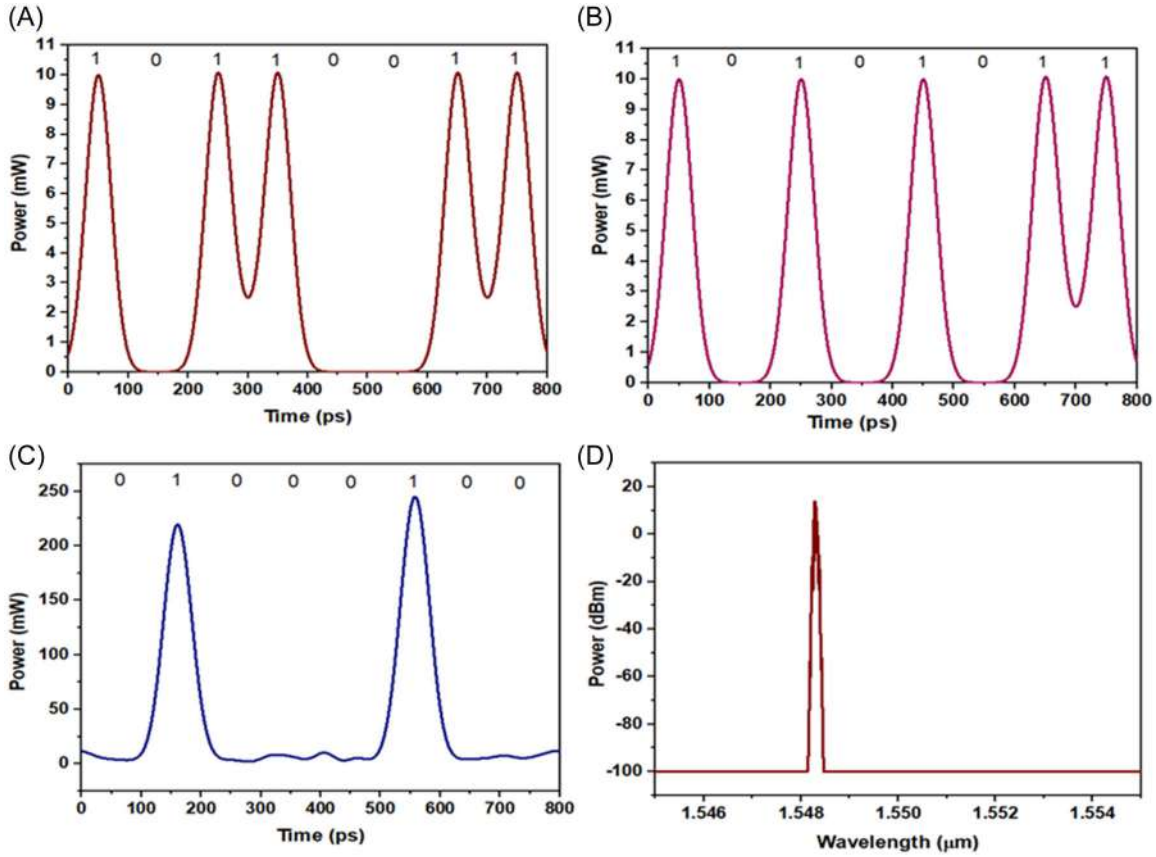

FIGURE 2 (A) Input 1 sequences, (B) Input 2 sequences, (C) Output NOR logic and (D) NOR logic output power spectrum.

TABLE 1 Proposed NOR logic gate truth table.

User-defined sequence		NOR gate logic	Output power (mW)	Output power (dBm)
Input 1 logic	Input 2 logic	$y = A \bar{+} B$		
1	1	0	2.28	3.579
0	0	1	243.45	23.864
1	1	0	2.28	3.579
1	0	0	2.28	3.579
0	1	0	2.28	3.579
0	0	1	243.45	23.864
1	1	0	2.28	3.579
1	1	0	2.28	3.579

TABLE 2 Calculated and measured parameters of the designed NOR logic system.

Parameters	Metrics
Extinction ratio	20.285 dB
Optical output power (logic 1)	23.864 dBm
Optical output power (logic 0)	3.579 dBm
Dispersion	$-0.029 \times 10^{+006}$ ps/nm
Bit error rate	4.27×10^{-26}
Data rate	40 Gbps

metastable lifetime is 10 ms, numerical aperture is 0.24, wavelength is 1550 nm. In EDFA backpropagation is avoided and the forward and the backward pump power is 100 and 0 mW, respectively. The noise threshold was −100 dB.

The properties of the traveling wave semiconductor optical amplifier (TWSOA) were chosen for the better performance of the NOR logic gate are injection current $I = 0.55$ A, length 0.5 mm, width 3 μm, height 80 nm. The optical confinement factor was 0.3, the differential gain is $2.8e^{-021}$ m^2, and the linewidth enhancement factor is 5.

The user-defined or a random sequence of two inputs can be generated at a wavelength of 1549.3 and 1550.7 nm and input power 10 and 10 mW, respectively with a data rate of 40 Gbps. These two binary inputs are converted into an optical pulses using an optical pulse generator and that will be given to the optical adder, which generates the addition of the two optical pulses. It looks like an OR Logic gate operation. The optical adder output is amplified by the EDFA and the amplified adder

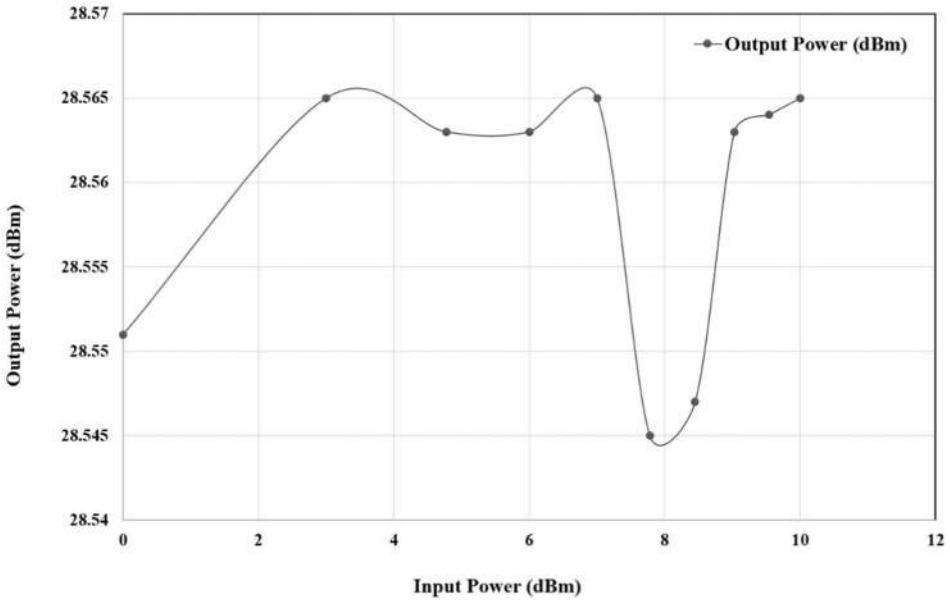

FIGURE 3 Optimization and selection of input power based on the output response of gate.

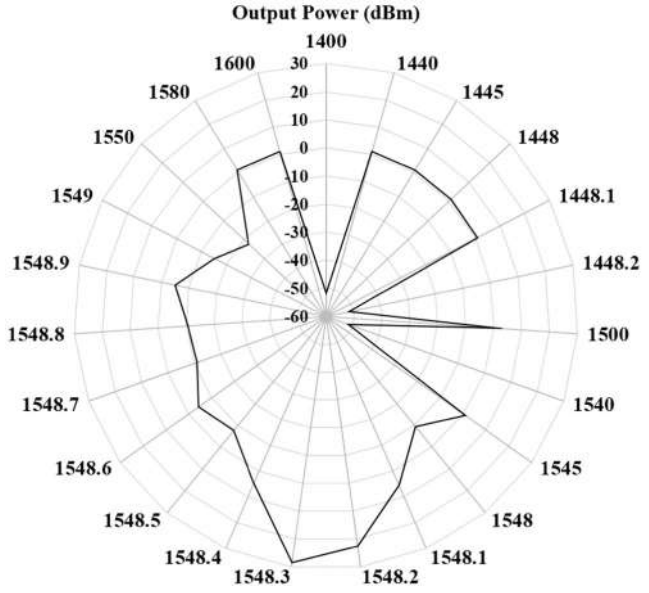

FIGURE 4 Optimization and selection of probe signal wavelength based on its corresponding output response.

output is given to one of the inputs of the 2 × 2 coupler, the probe or reference signal can be generated at a wavelength of 1548.3 nm and 5 mW power using a continuous wave (CW) laser which is always high. This probe signal along with combined inputs is simultaneously fed into the TWSOA using an X coupler. The coupler throughput is amplified using a TWSOA, which act as a loss compensator during signal propagation. A Gaussian optical bandpass filter is tuned to select only the required wavelength of the amplified data with the center wavelength which is the average wavelength of both the inputs and the reference signal. Inside the TWSOA, XGM of carrier-induced changes takes place in accordance with the changes in the two inputs (intensity modulation). During XGM, the intensity-modulated input signal modulates the gain in SOA through the gain saturation effect.

The CW from CW laser at the output wavelength is modulated by the gain variation intensity-modulated input signals. At the output of SOA, the probe or reference signal carries the same information as intensity-modulated input signals. The combined input signals and the CW reference signal can be applied to the TWSOA either codirectionally or counter-directionally. After TWSOA, the CW is given to the optical bandpass filter. The optical bandpass filter centered at wavelength 1548.3 nm and bandwidth 10 GHz selects the desired NOR gate operation. The SOA parameters are required to be adjusted for optimum performance. No XGM will generate at TWSOA only when both the inputs are low (logic 0), the output of the adder will be low and the output power of SOA will be corresponding to the reference signal only, which will show a high-level output of logic "1" because the power of CW laser is filtered and amplified to get the NOR gate output.

When anyone or both the data pumps are at logic 1, XGM will be generated because the output of the adder will be 1 and the output will correspond to the peak of the CW laser. The output of the adder is high only when any one or both the inputs are high so the output of the adder and CW laser will together generate the XGM signal. The output of SOA is filtered with the band pass filter of the center frequency of the CW laser to remove the unwanted signal.

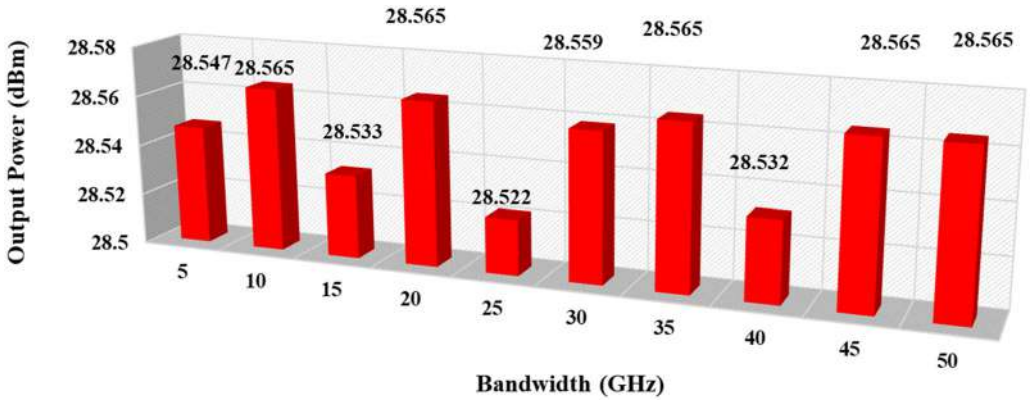

FIGURE 5 Relationship between Gaussian filter bandwidth and the output response of NOR gate.

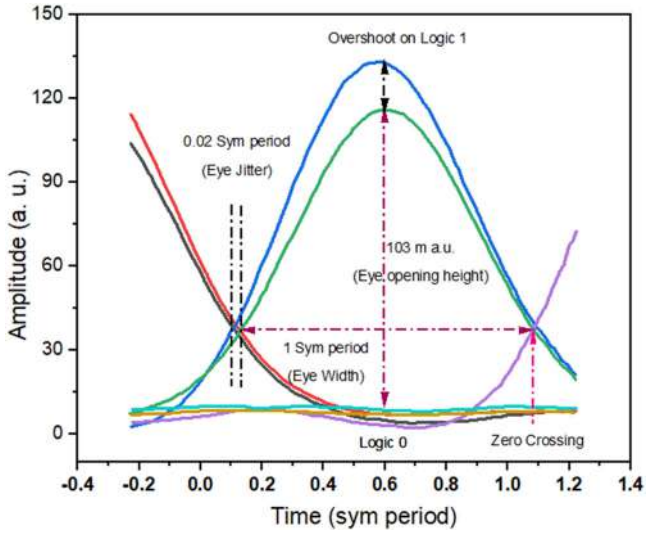

FIGURE 6 Eye pattern for the proposed NOR logic gate design.

So, a lower value of output power will be obtained when gain saturation occurs. Then the output will be considered as logic "0." As in the NOR logic, we have a logic high when both data inputs are zero.

3 | SIMULATION RESULTS AND DISCUSSIONS

The input sequences 1 and 2 are taken as 10110011 and 10101011, respectively and the corresponding NOR logic output is 01000100 verified successfully using an all-optical NOR gate using SOA as depicted in Figure 2A–D.

The optical output power for the designed gate is 243.45 mW (23.864 dBm) for logic 1 and 2.28 mW (3.579 dBm) for logic 0 as mentioned in Table 1. The calculated and measured parameters of the designed NOR logic system is depicted in Table 2.

4 | ANALYSIS OF THE DESIGNED ALL-OPTICAL NOR GATE

The analysis of the designed NOR logic gate involved systematic variations in different parameters, including input power, wavelength, and the bandwidth of the Gaussian bandpass filter. The output response of the NOR gate for the wide range of the input power from 0 dBm to 10 dB was investigated and depicted in Figure 3. Form the graph, it was evident that the output power was high at an input power of 3, 7 and 10 dBm. But based on the specific performance requirement, 10 dBm (10 mW) were chosen for the proposed NOR gate design. The relationship between the wavelength from 1400 to 1600 nm and the corresponding optical power output of the NOR gate was studied and the corresponding responses were plotted in Figure 4. It was observed that the NOR gate resonates only at the specific wavelength of 1548.3 nm and its performance was reduced nonlinearly for the remaining wavelengths.

NOR gate performance can be detuned by the bandwidth of the bandpass filter.[19] The ER and QF are notably influenced by the bandwidth of the optical Gaussian bandpass filter. A narrower bandwidth enhances both the ER and QF.[20] In this study, Figure 5 illustrates the change in output power for different bandwidths of Gaussian band-pass filters. Interestingly, the output power of the peak transmission at a specific frequency fluctuates within a range of 28.565–28.522 dBm for various band-pass filters. Stable and high output power was consistently achieved with bandwidths of 10, 20, 35, 45, and 50 GHz. Implementing low-bandwidth filters can help improve the signal-to-noise ratio and reduce crosstalk.

The eye diagram displays the superposition of many individual logic bits. The vertical axis represents the signal's amplitude, while the horizontal axis represents time. The eye opening refers to the region where the signal remains above

TABLE 3 Comparative study of all-optical NOR gate design using SOA.

S no.	Type of gates	Scheme	Speed	Extinction ratio (dB)	Quality factor (QF)	References
1	NOR	QD-SOA-MZI	160 Gbps	9.12	9.49	[5]
2	NOR	QD-SOA	160 Gbps	11.27	3.75	[20]
3	NOR	Two parallel SOA-MZI	10 Gbps	15	11.761	[21]
4	NOR	SOA-MZI	10 Gbps	3.82	5.86	[22]
	NOR	SOA-MZI along with MUX	10 Gbps	4.77	6.87	
5	NOR	Two parallel SOA-MZIs	80 Gbps	23.92	15.7	[23]
6	NOR	SOA & DI	80 Gbps	15.198	12.05	[24]
7	NOR	QD-RSOA	1 Tbps	15	10	[8]
8	NOR	Single SOA	40 Gbps	20.262	13.067	Present work

Abbreviations: DI, delayed interferometer; MZI, Mach–Zehnder interferometer; QD, quantum dot; RSOA, reflective semiconductor optical amplifier; SOA, semiconductor optical amplifiers.

the threshold level for both logic 1 and logic 0. The eye height is the difference between the maximum and minimum signal levels within this eye opening. The proposed gate exhibits an eye diagram, as depicted in Figure 6. This eye diagram boasts a commendable eye opening of 0.03 a.u. and minimal eye jitter of only 0.02 symbol periods. The signal's amplitude measures 0.1 a.u., with the zero crossing occurring at 0.05 a.u. Additionally, there is a slight overshoot on logic 1, measuring 0.5 a.u., although this does not pose a significant concern.

All-optical logic gates have been developed through the collaborative efforts of numerous researchers, utilizing various combinations of optical components such as SOAs, SOA-MZIs, SOA-DIs, and more. The complexity of designing logic gates increases with the number of components used. The comparison of the present work with the existing research work was reported in Table 3. However, this research has yielded a simple and compact design for an all-optical NOR logic gate, employing just a single SOA. In the context of optical integrated circuits, simplicity and compactness are essential for achieving optimal performance. The proposed NOR gate was crafted using only one SOA, and the system underwent simulation using OptiSystem at a high data rate of 40 Gbps. The outcome was an impressive improvement in the ER, reaching 20.285 dB. This result is remarkable considering that existing reports typically feature ERs of around 15 dB.

5 | CONCLUSION

The input sequences, denoted as 1 and 2 with values 10110011 and 10101011, respectively, undergo successful verification using an all-optical NOR gate employing a SOA at a high data rate of 40 Gbps. The optical output power for the designed gate is measured at 23.864 dBm for logic 1 and 3.579 dBm for logic 0. The spectrum analysis reveals that the maximum logic output is achieved at a wavelength of 1548.3 nm, while at all other wavelengths, the output is zero, indicating the absence of a signal. The calculated improved ER for the proposed NOR gate design is determined to be 20.58.

ACKNOWLEDGMENTS

The authors acknowledge the Department of Electronics and Communication Engineering, Alagappa Chettiar Government College of Engineering and Technology, Karaikudi, for providing software facilities that contributed to the successful completion of the proposed work.

DATA AVAILABILITY STATEMENT

Data sharing is not applicable to this article as no datasets were generated or analyzed during the current study.

REFERENCES

1. Kazanskiy NL, Butt MA, Khonina SN. Optical computing: status and perspectives. *Nanomaterials*. 2022;12(13):2171. doi:10.3390/nano12132171
2. Hu H, Zhang X, Zhao S. High-speed all-optical logic gate using QD-SOA and its application. *Cogent Phys*. 2017;4(1):1388156. doi:10.1080/23311940.2017.1388156
3. Jiao S, Liu J, Zhang L, et al. All-optical logic gate computing for high-speed parallel information processing. *Opto-Electron Sci*. 2022;1(9):220010. doi:10.29026/oes.2022.220010
4. Kim JY, Han SK, Lee S. All-optical multiple logic gates using parallel SOA-MZI structures. Paper presented at: 2005 IEEE LEOS Annual Meeting Conference Proceedings; October 2005. pp. 133-134. doi:10.1109/LEOS.2005.1547914
5. Dimitriadou E, Zoiros KE. Proposal for all-optical NOR gate using single quantum-dot semiconductor optical amplifier-based Mach–Zehnder interferometer. *Opt Commun*. 2012; 285(7):1710-1716. doi:10.1016/j.optcom.2011.11.122

6. Mukherjee K, Maji K, Raja A, Mandal MK. All-optical soliton based universal logic NOR utilizing a single reflective semiconductor optical amplifier (RSOA. *Photon Netw Commun*. 2022;43(2):101-108. doi:10.1007/s11107-021-00956-6
7. Jhon YM, Choi KS, Byun YT, Lee S. All-optical OR/NOR bi-functional logic gate by using cross-gain modulation in semiconductor optical amplifiers. *J Korean Phys Soc*. 2010;56(4):1093-1096. doi:10.3938/jkps.56.1093
8. Wang Y, Wang H, Kong X, Yang S, Hu M, Gong Q. Research on output characteristics based on QD-SOA and QD-RSOA cross gain modulation all-optical logic NOR gate. *Opt Quantum Electron*. 2021;53:715. doi:10.1007/s11082-021-03372-2
9. Kotb A, Guo C. All-optical OR and NOR gates using quantum-dot semiconductor optical amplifiers-assisted turbo-switched Mach–Zehnder interferometer and serially delayed interferometer at 1 Tb/s. *Optik*. 2020;218:164879. doi:10.1016/j.ijleo.2020.164879
10. Mehdizadeh F, Soroosh M. Designing of all optical NOR gate based on photonic crystal. *Indian J Pure Appl Phys*. 2016;54(01):35-39.
11. Bharti GK, Rakshit JK, Singh MP, Yupapin P. Design of all-optical universal logic gates using mode-conversion in single silicon microring resonator. *J Nanophoton*. 2019;13(3):1. doi:10.1117/1.JNP.13.036002
12. Hossain M, Rakshit JK, Zoiros KE. Microring resonator-based all-optical parallel pseudo random binary sequence generator for rate multiplication. *Opt Quantum Electron*. 2022;54(8):525. doi:10.1007/s11082-022-03908-0
13. Mondal H, Goswami K, Sen M, Khan WR. Design and analysis of all-optical logic NOR gate based on linear optics. *Opt Quantum Electron*. 2022;54(5):272. doi:10.1007/s11082-022-03624-9
14. Bosu S, Bhattacharjee B. Dibit-based OR and NOR gates using reflective semiconductor optical amplifier. *J Nonlinear Opt Phys Mater*. 2023;32(2):2350046. doi:10.1142/S0218863523500467
15. Mukherjee K. Numerical simulation of Tb/s all-optical reconfigurable frequency encoded OR and AND gate using quantum dot semiconductor optical amplifier-based Mach–Zehnder interferometer. *J Nonlinear Opt Phys Mater*. 2023;32(2):2350043. doi:10.1142/S0218863523500431
16. Kaur S, Kaur J, Sharma A. Predicting the performance of radio over free space optics system using machine learning techniques. *Optik*. 2023;281:170798. doi:10.1016/j.ijleo.2023.170798
17. Anusooya V, Ponmalar S, Manikandan MSK, Gobalakrishnan S. Simulation and numerical analysis of SOA-based all optical NAND gate for high data rate communication. *J Natl Sci Found Sri Lanka*. 2023;51(2):225-235. doi:10.4038/jnsfsr.v51i2.11080
18. Margarat M, Caroline BE, Vinothini M. Design of all-optical universal gates and verification of Boolean expression using SOA-MZI. Paper presented at: 2018 IEEE international conference on system, computation, automation and networking (ICSCA) (1-6); July 2018. doi:10.1109/ICSCAN.2018.8541238
19. Azzam ES, Aly MH. FWM in DCF based four-input all-optical NOR/AND gate. *Opt Quantum Electron*. 2018;50:166. doi:10.1007/s11082-018-1432-1
20. Komatsu K, Hosoya G, Yashima H. All-optical logic NOR gate using a single quantum-dot SOA-assisted an optical filter. *Opt Quantum Electron*. 2018;50:131. doi:10.1007/s11082-018-1384-5
21. Joo-Youp K, Jeung-Mo K, Tae-Young K, Sang-Kook H. All-optical multiple logic gates with XOR, NOR, OR, and NAND functions using parallel SOA-MZI structures: theory and experiment. *J Light Technol*. 2006;24(9):3392-3399.
22. Singh P, Tripathi DK, Dixit HK. Designs of all-optical NOR gates using SOA based MZI. *Optik*. 2014;125(16):4437-4440. doi:10.1016/j.ijleo.2014.02.032
23. Kotb A, Zoiros KE, Guo C. All-optical XOR, NOR, and NAND logic functions with parallel semiconductor optical amplifier-based Mach–Zehnder interferometer modules. *Opt Laser Technol*. 2018;108:426-433. doi:10.1016/j.optlastec.2018.07.027
24. Kotb A, Guo C. All-optical multifunctional AND, NOR, and XNOR logic gates using semiconductor optical amplifiers. *Phys Scr*. 2020;95(8):085506. doi:10.1088/1402-4896/aba057

How to cite this article: Vadukanathan A, Suyambragasam G, Sivaraj P, Kasiviswanathan MMS. Simulation of all-optical NOR gate design with improved extinction ratio using semiconductor optical amplifier. *Microw Opt Technol Lett*. 2024;66:e33993. doi:10.1002/mop.33993

Chapter 19
Pregnancy in the Digital Age:
A New Era of Healthcare Technologies

J. Shanthalakshmi Revathy
https://orcid.org/0000-0003-1724-7117
Velammal College of Engineering and Technology, India

J. Mangaiyarkkarasi
https://orcid.org/0000-0003-1431-9584
N.M.S.S. Vellaichamy Nadar College, India

ABSTRACT

Digital healthcare technologies have the potential to revolutionize prenatal care by giving expectant moms real-time access to health information and assistance. This chapter reviews the current state of digital health technologies in pregnancy care. It discusses their capacity to enhance patient results, boost patient involvement, and lower healthcare expenses. Mobile apps have become increasingly popular for tracking pregnancy progress, providing educational resources and connecting patients with health-care providers. Healthcare professionals can monitor vital signs using wearable technology like smart watches and activity trackers. The use of telemedicine enables patients in rural or underserved areas to receive healthcare services through remote consultations and virtual appointments. However, there are also limitations and challenges associated with digital health technologies in pregnancy care. This chapter is based on a survey of the most recent research findings and literature on the application of digital health technology, including articles from peer-reviewed journals.

1. INTRODUCTION: THE CHANGING LANDSCAPE OF PREGNANCY CARE

Pregnancy is a unique and transformative experience that brings about significant changes in the lives of women and their families. Over the years, pregnancy care has undergone significant changes due to advances in technology and innovations in healthcare delivery. The digital age has ushered in a new era of healthcare technologies that have transformed the way pregnancy care is delivered, monitored, and managed (Bagalkot et al., 2018). In the past, pregnancy care was primarily delivered in a traditional

DOI: 10.4018/978-1-6684-8974-1.ch019

healthcare setting, where women would visit their obstetrician or midwife for routine check-ups and ultrasounds. However, with the advent of digital health technologies, pregnancy care has expanded beyond the traditional healthcare setting, allowing women to receive care remotely, from the comfort of their homes. Mobile health applications, wearable's, telemedicine, and virtual consultations are just a few examples of technologies that are transforming pregnancy care. These technologies not only increase women's access to personalised, real-time information about their health and the wellbeing of their unborn children, but they also provide healthcare professionals with more data to manage pregnancies (Peyton et al., 2014). Mobile health applications are one of the most popular and regularly utilised technologies in pregnancy care for tracking and managing pregnancies. These apps offer women a wealth of information about their pregnancy, including advice on nutrition, exercise, and prenatal care. They also allow women to track their symptoms, monitor their weight, and record their baby's movements.

Wearable technology is another innovative technology that is transforming pregnancy care. The health parameters of the mother and foetus, such as heart rate, blood pressure, and foetal movement, can be continuously monitored with wearable technology. This technology allows for early detection of potential complications, and can also provide women with greater peace of mind throughout their pregnancy (Mukhopadhyay, 2015). Telemedicine and virtual consultations have also become increasingly popular in pregnancy care. Women may now consult with their healthcare practitioners remotely thanks to these technology, which eliminates the need for in-person consultations. Women who reside in rural regions or have restricted mobility would particularly benefit from this because it eliminates the need for them to go far for care (DeNicola et al., 2020). Artificial intelligence (AI) is another technology that is transforming pregnancy care. AI has the potential to analyse vast volumes of data and give healthcare professionals new perspectives on patient treatment. It can also be used to predict potential complications, such as preterm labour or preeclampsia, allowing for early intervention and management (Oprescu et al., 2020). Personalized medicine and genomics are also playing an increasingly important role in pregnancy care. Advances in genomics have allowed healthcare providers to better understand the genetic makeup of both mother and baby, allowing for personalized care and early detection of potential genetic abnormalities (Ginsburg & Willard, 2009). Social media and online communities have also transformed pregnancy care, providing women with a wealth of information and support throughout their pregnancy journey. Expectant mothers can leverage online communities to connect with each other, exchange experiences, and seek advice. Such communities also offer a platform for education and knowledge-sharing (Chan & Chen, 2019). Even though digital health technologies provide numerous advantages for prenatal care, some ethical issues and difficulties need to be resolved. Concerns include issues with data security and privacy as well as the potential for healthcare practitioners to place an undue emphasis on technology at the expense of face-to-face interactions with patients. The field of pregnancy care has seen considerable changes as a result of the development of digital technologies. Pregnancy care is being offered in a completely new way, thanks to the development of technology like wearable's, telemedicine, AI, personalised medicine, genomics, and online communities. Despite the numerous advantages offered by these technologies, there are ethical and practical challenges that must be addressed to ensure that their use in pregnancy care is safe, efficient, and centered around the patient's needs.

2. MOBILE HEALTH APPLICATIONS FOR PREGNANCY TRACKING AND MANAGEMENT

Mobile health applications (apps) have become increasingly popular in pregnancy care, offering women a convenient and accessible way to track and manage their pregnancies. These apps can provide a wealth of information about pregnancy, including advice on prenatal care, nutrition, exercise, and fetal development. They can also help women monitor their symptoms, record their weight, and track their baby's movements (Dahl et al., 2018). The fact that mobile health applications provide women more control over pregnancy is one of its most important advantages. With real-time access to personalized information and advice, women can make informed decisions about their health and their baby's health. They can also use the app to communicate with their healthcare provider, ask questions, and receive guidance on how to manage any concerns or complications that may arise. There are many different types of mobile health apps available for pregnancy tracking and management, each with its unique features and benefits (Bachiri et al., 2016). Some apps offer daily tips and reminders, while others provide a more comprehensive suite of tools and resources for pregnancy management. For example, some pregnancy apps offer a calendar that tracks the due date and provides information about fetal development, including weekly updates on the baby's size, weight, and developmental milestones. Others may include a symptom tracker, allowing women to monitor their symptoms and alert their healthcare provider if they experience any concerning changes.

Some pregnancy apps also offer features that allow women to track their weight, blood pressure, and glucose levels, providing them with real-time feedback on their health status (Garg et al., 2022). Those with pre-existing medical issues or those who are more likely to experience pregnancy complications may find this to be very beneficial. Pregnancy problems such as gestational diabetes, preeclampsia, and high blood pressure have been handled in a variety of ways by mobile apps designed for self-management during pregnancy (Iyawa et al., 2021).

Table 1. Quantitative information about health apps for pregnancy tracking and management

Statistics	Information
Number of mobile health apps for pregnancy in app stores	1000+
Top downloaded a pregnancy app	The Bump
Percentage of expectant mothers who use pregnancy apps	80%
Most common features of pregnancy apps	Due date calculator, pregnancy tracker, symptom tracker, kick counter
Percentage of pregnancy apps that share user data with third parties	70%
Percentage of pregnancy apps that have been found to have security vulnerabilities	50%
The average cost of a pregnancy app	$2.99
Percentage of pregnancy apps that are available in multiple languages	75%
Percentage of pregnancy apps that have been clinically validated	20%
Percentage of healthcare providers who recommend pregnancy apps to patients	60%

Table 1 provides quantitative information about health apps for pregnancy tracking and management. The table includes data such as the number of apps analysed, the types of features offered, the average rating of the apps, and the percentage of apps that offer medical advice. This information can help researchers and healthcare professionals better understand the landscape of pregnancy-related mobile apps and their potential benefits and limitations. In order to detect foetal movements, women can keep track of their infant's activity levels and notify their healthcare physician if they see any changes or have any concerns. This feature can provide women with greater peace of mind and can also help healthcare providers detect potential complications, such as fetal distress or reduced fetal movement. One potential downside of mobile health apps is that they can sometimes provide conflicting or inaccurate information. Before making any significant changes to how they are managing their pregnancy based on advice they have gotten from an app, women should always speak with their healthcare professional. Overall, mobile health apps have the potential to revolutionize pregnancy care, providing women with greater access to personalized information and resources to help them manage their pregnancy (Gyselaers et al., 2019). With careful selection and appropriate use, mobile health apps can be a valuable tool for women and their healthcare providers in promoting healthy pregnancies and positive pregnancy outcomes.

Table 2. Popular mobile apps for tracking and managing pregnancy health

Mobile Health Application	Developer	Platform	Features
Glow Nurture	Glow Inc.	iOS, Android	Due date calculator, symptom tracker, personalized insights, community forum
Ovia Pregnancy Tracker	Ovia Health	iOS, Android	Daily articles, weight tracker, kick counter, food safety lookup
The Bump	The Knot Inc.	iOS, Android	Weekly updates, 3D interactive visuals, appointment tracker, contraction timer
What to Expect	Everyday Health Inc.	iOS, Android	Baby size visualizer, community support, daily pregnancy news, appointment tracker
BabyCenter Pregnancy Tracker	BabyCenter	iOS, Android	Fetal development videos, contraction timer, kick counter, community support
Pregnancy+	Health & Parenting Ltd.	iOS, Android	Fetal size visualizer, baby names database, kick counter, personalized diary
Sprout Pregnancy	Med ART Studios	iOS, Android	Weight tracker, contraction timer, appointment tracker, baby size visualizer
WebMD Pregnancy	WebMD LLC	iOS, Android	Pregnancy news, symptom tracker, medication lookup, community forum
Kegel Trainer	Olson Applications Ltd.	iOS, Android	Kegel exercise tracker and reminders, customizable workouts, progress charts
Full Term - Contraction Timer	Mustansir Golawala	iOS, Android	Contraction timer, pregnancy and labour information, exportable data

Table 2 lists popular mobile apps for tracking and managing pregnancy health. The table includes the names of the apps, their ratings, and the types of features they offer. This information can be helpful for individuals who are pregnant or planning to become pregnant and are looking for a mobile app to assist them with tracking their pregnancy, monitoring their health, and accessing information about

pregnancy-related topics. The table can also be useful for healthcare professionals who may recommend these apps to their patients as a tool for managing their pregnancy health

3. WEARABLE TECHNOLOGY FOR MATERNAL AND FETAL MONITORING

Wearable technology is becoming an increasingly popular tool for maternal and fetal monitoring, offering women and their healthcare providers real-time data on maternal and fetal health status (Runkle et al., 2019). These devices are designed to be worn on the body, providing continuous monitoring of various physiological parameters and transmitting data wirelessly to healthcare providers. One of the most common uses of wearable technology in pregnancy care is fetal monitoring. In order to monitor the mother's uterine contractions and foetal heart rate, sensors are applied to her belly. These sensors can be incorporated into a wearable device such as a belt or a patch that is worn on the mother's belly. The data collected by the device can be transmitted wirelessly to the healthcare provider's office for real-time monitoring and analysis. Maternal monitoring with wearable technologies can track variables like heart rate, blood pressure, and glucose levels. This can be especially helpful for women with pre-existing medical conditions or those who are more likely to encounter pregnancy difficulties because it provides real-time input on maternal health status (Piwek et al., 2016).

Figure 1. The overall design of the system for wearable medical equipment
Source: Dias and Paulo Silva Cunha (2018)

Figure 1 shows the overall architecture which has four modules: (A) Body Area Network (BAN) to collect physiological data, (B) Data Logger or Portable Unit to store and transmit data, (C) Data Analysis for offline review of collected data, and (D) Real-Time Monitoring for live data visualization. It offers a comprehensive system for monitoring and analysing physiological data in real-time, enabling healthcare professionals to provide personalized care to patients.

There are wearable devices available that are specially designed for use during labour and delivery. Throughout labour and delivery, these gadgets continuously check on the mother's and fetus's health. This enables healthcare professionals to closely observe the progress of labour and detect any potential complications. Important vital indications like the mother's heart rate, blood pressure, oxygen levels, and fetal heart rate can all be monitored by the devices. These devices may include sensors that monitor contractions, fetal heart rate, and maternal vital signs, as well as provide alerts if any parameters fall outside of normal ranges (Nguyen et al., 2018). Another use of wearable technology in pregnancy care is for remote monitoring. This allows healthcare providers to monitor maternal and fetal health status from a distance, using sensors and wireless technology to transmit data to a central monitoring station. Women who reside in rural locations or are unable to frequently attend their doctor's office may find this to be of particular benefit. Wearable technology can also be integrated with other technologies, such as mobile health apps, to provide women with a comprehensive suite of tools and resources for pregnancy management. For example, a wearable device that tracks fetal heart rate could be integrated with a mobile health app that provides information about fetal development and offers tips on prenatal care.

While wearable technology has many potential benefits for maternal and fetal monitoring, there are also some potential drawbacks. For example, wearable devices may not be suitable for all women, especially those with skin sensitivities or allergies. They may also be expensive and may not be covered by insurance. In addition, there is a risk that wearable devices may provide false alarms or inaccurate data, leading to unnecessary interventions or anxiety for the mother. Healthcare providers need to carefully evaluate the data provided by wearable devices and use their clinical judgment to determine the appropriate course of action (Runkle et al., 2019). In conclusion, wearable technology has the potential to revolutionize maternal and fetal monitoring, providing women and their healthcare providers with real-time data on maternal and fetal health status. With careful selection and appropriate use, wearable technology can be a valuable tool for promoting healthy pregnancies and positive pregnancy outcomes.

4. TELEMEDICINE AND VIRTUAL CONSULTATIONS IN PREGNANCY CARE

Recent years have seen a rise in the use of telemedicine and virtual consultations for prenatal care, particularly in the wake of the COVID-19 pandemic. Telemedicine involves the use of telecommunications technology to provide remote healthcare services, including consultations, diagnoses, and treatment. Virtual consultations in pregnancy care can take various forms, including video conferencing, phone calls, and instant messaging. These consultations provide an opportunity for healthcare providers to communicate with their patients in real time, without the need for in-person visits.

Figure 2. Telemedicine process

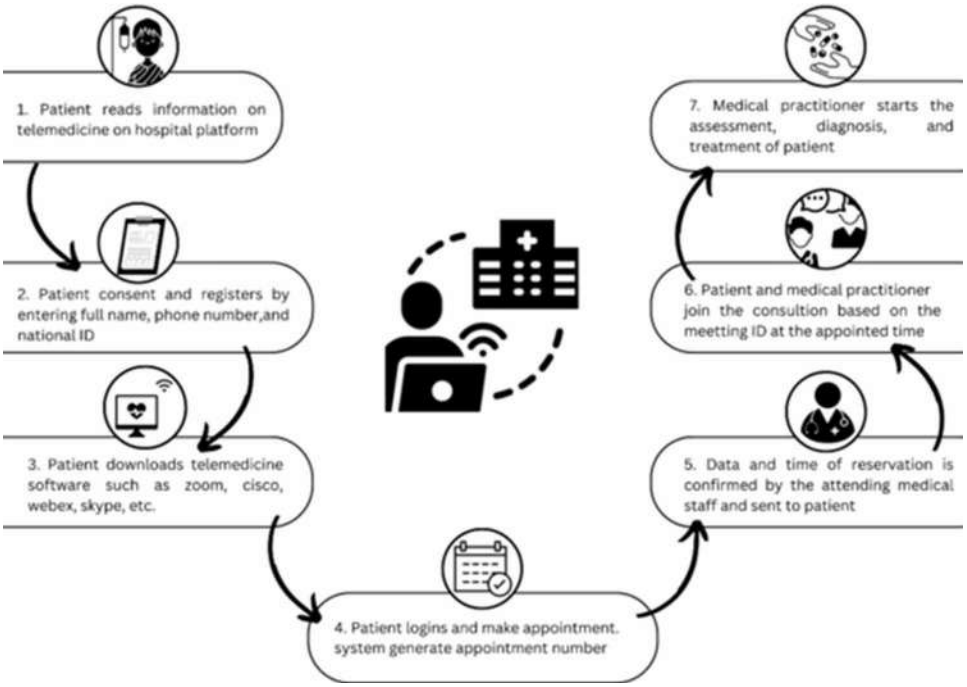

In Figure 2, the telemedicine process is depicted as a tool for treating patients remotely. Telemedicine provides the capacity to transfer saved movies or static images for later inspection by the receiving physician, storing pertinent medical data such as physical findings and patient concerns. Patients can opt for asynchronous telemedicine methods like email, health apps, patient portal messages, or e-consults, or synchronous methods like telephone, videoconferencing, or virtual software platforms. It can be particularly beneficial for women residing in remote or underserved areas, as it provides access to healthcare services that may not be locally available. Additionally, women facing mobility issues or living far from healthcare provider's offices can also benefit from telemedicine. In addition, telemedicine can be a more convenient and flexible option for women with busy schedules, allowing them to schedule consultations at a time that is convenient for them (Aziz et al., 2020).

Figure 3. The proliferation of virtual software platforms and telemedicine

The many factors that could affect how frequently consumers and medical professionals use telemedicine and virtual software platforms are highlighted in Figure 3. These elements can be generally categorised using the social, organisational, and technological characteristics. Social factors refer to the cultural and societal influences that can impact the acceptance and utilization of telemedicine. For example, patients may have concerns about the quality of care they will receive through telemedicine or may feel more comfortable with traditional in-person visits. Healthcare providers may also be hesitant to adopt telemedicine due to concerns about patient privacy and the accuracy of remote diagnoses. Organizational factors relate to the structures and processes within healthcare organizations that can facilitate or hinder the implementation of telemedicine. These considerations cover things like finance and resource availability, the willingness of healthcare organisations to adopt new technology, and the degree of integration of telemedicine into current healthcare systems. Technological factors refer to the capabilities and limitations of the technologies used in telemedicine, such as the availability and reliability of internet connectivity, the quality of video conferencing software, and the accuracy of remote diagnostic tools.

Virtual consultations can be used for a range of pregnancy-related issues, including prenatal care, postpartum care, and lactation support. For example, a woman may have a video consultation with her healthcare provider to discuss her prenatal care plan, or to receive advice on managing common pregnancy symptoms such as nausea and fatigue. Virtual consultations can also be used for monitoring maternal and fetal health status, such as checking blood pressure or fetal heart rate. In some cases, women may be provided with at-home monitoring equipment that can be used to track these parameters and transmit data to their healthcare provider. One of the key benefits of telemedicine and virtual consultations is that they can help reduce the need for in-person visits, which can help reduce the risk of exposure to infectious diseases such as COVID-19. For pregnant women, who are probably more at risk for COVID-19

problems, this can be especially crucial. However, there are also some potential drawbacks to telemedicine and virtual consultations. For example, some women may feel more comfortable with in-person visits and may have difficulty building a rapport with their healthcare provider over video or phone. In addition, there may be technical issues or limitations with the technology used for virtual consultations, which could impact the quality of care provided (Ghimire et al., 2022). In conclusion, telemedicine and virtual consultations have emerged as important tools for pregnancy care, providing women with greater flexibility and access to healthcare services. While there are some potential drawbacks, with appropriate use and careful evaluation, telemedicine and virtual consultations can be a valuable addition to traditional in-person care.

5. THE ROLE OF ARTIFICIAL INTELLIGENCE IN PREGNANCY CARE

Personalized and data-driven ways to monitoring the health of the mother and foetus offered by artificial intelligence (AI) have the potential to revolutionise prenatal care. Electronic health records and wearable technology are only two examples of the types of data that AI systems can analyse in order to spot patterns and forecast future health outcomes. One area where AI has shown promise is in predicting and preventing preterm birth, a leading cause of infant mortality and morbidity. AI algorithms can analyse various risk factors, such as maternal age and medical history, to identify women at high risk of preterm birth. This information can then be used to develop targeted interventions and preventions, such as preterm labour monitoring and medication(Oprescu et al., 2020). AI can also be used to monitor fetal health during pregnancy. For instance, foetal heart rate monitor data can be analysed by AI algorithms to find patterns that can suggest foetal distress, enabling early intervention and possibly averting negative outcomes like stillbirth.

Figure 4. AI and ML in maternal and fetal health data analysis

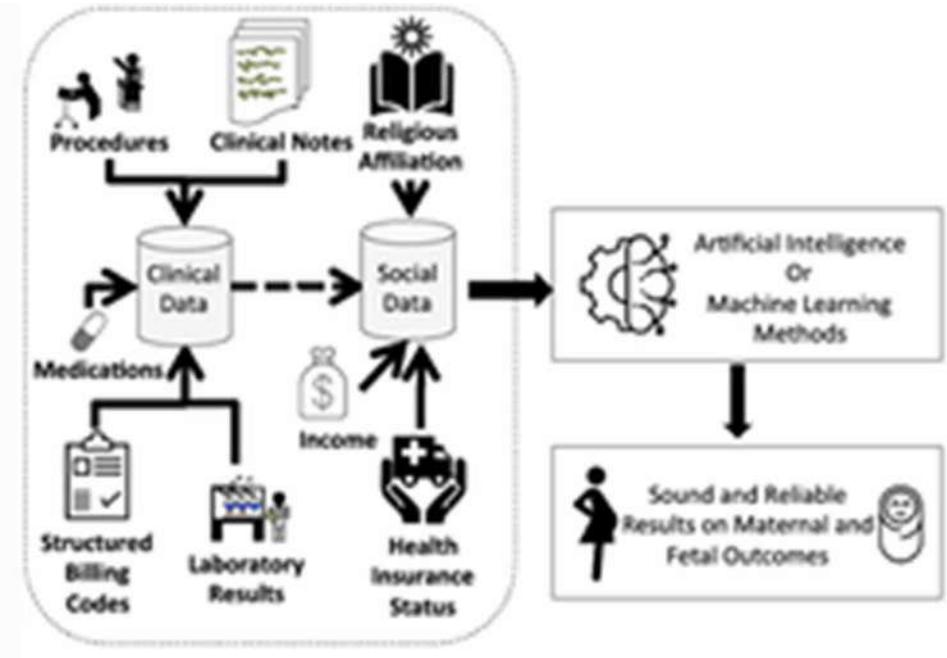

Artificial intelligence (AI) and machine learning (ML) enable the processing of enormous amounts of clinical data to acquire insights and improve patient outcomes, and these technologies have the potential to dramatically change the healthcare sector. Figure 4 shows how artificial intelligence (AI) and machine learning (ML) can be used to process different data sources, including as genetic data, medical imaging data, and electronic health records, to create solid and reliable conclusions about mother and foetus outcomes. In order to find patterns and risk factors linked to negative outcomes, like preterm birth or hypertension, massive datasets of maternal and foetal health records can be analysed using AI and ML, for instance. The creation of personalised treatment programmes and the identification of at-risk patients can both be accomplished using the prediction models created from these data. Moreover, AI and ML can be used to examine ultrasound or MRI scan data to find anomalies and abnormalities that could be signs of foetal distress or other issues. Additionally, these technologies can be used to evaluate genetic information to spot potential risk factors and create individualised treatment strategies based on the unique genetic profiles of patients. Another potential use for AI in pregnancy care is in improving the accuracy of ultrasound imaging. AI algorithms can analyse ultrasound images and identify abnormalities with greater accuracy and speed than human experts, allowing for earlier and more accurate diagnoses. In addition, AI technologies can be used to provide personalized recommendations for maternal and fetal health based on individual patient data. For example, AI algorithms can analyse a woman's medical history, lifestyle factors, and other data to develop personalized recommendations for prenatal care and monitoring. However, there are also some potential drawbacks to the use of AI in pregnancy care. For example, there may be concerns about the accuracy and reliability of AI algorithms, and there is a need for careful evaluation and validation of these technologies before they can be widely adopted. Furthermore, there may be concerns about the impact of AI on the patient-provider relationship, as some women may prefer a more human-centered approach to healthcare. It's crucial to make sure AI is applied in a transparent, moral, and patient-focused manner. As a result of its ability to provide individualised and data-driven approaches to monitoring maternal and foetal health, AI has the potential to revolutionise the way that pregnant women are cared for. While there are some potential drawbacks and concerns, with appropriate use and careful evaluation, AI technologies can be a valuable addition to traditional pregnancy care approaches (Iftikhar et al., 2020).

In a 2019 survey conducted by M3 Global Research, a majority of obstetricians and gynecologists in the United States reported being interested in using AI in their practice. Of the 308 physicians surveyed, 63% expressed interest in using AI to predict pregnancy complications, while 57% were interested in using AI to monitor fetal health (Emin et al., 2019). A 2020 survey by BabyCenter and Zebra Technologies found that nearly half of the expectant mothers in the United States are interested in using wearable devices and other technologies to monitor their health during pregnancy. The survey also found that many mothers were interested in using AI-powered tools to predict and prevent pregnancy complications. A 2021 survey by the American College of Obstetricians and Gynecologists (ACOG) found that while many obstetricians and gynecologists are interested in using AI in their practice, there are also concerns about the accuracy and reliability of AI technologies. Of the 609 physicians surveyed, 59% reported being interested in using AI for fetal monitoring, while 47% were interested in using AI for predicting preterm birth. However, many physicians also expressed concerns about the need for validation and verification of AI algorithms, as well as concerns about the impact of AI on the patient-provider relationship.

Overall, these survey reports suggest that there is growing interest in the use of AI in pregnancy care, both among healthcare providers and expectant mothers. However, there are also concerns about the ac-

curacy and reliability of AI technologies, as well as the potential impact on the patient-provider relationship. The efficacy and suitability of AI in pregnancy care will require more investigation and analysis.

6. PERSONALIZED MEDICINE AND GENOMICS IN PREGNANCY CARE

Personalized medicine and genomics have the potential to revolutionize pregnancy care by tailoring treatment and management strategies to individual patients based on their unique genetic makeup and health history (Sufriyana et al., 2020).

Figure 5. Prenatal testing

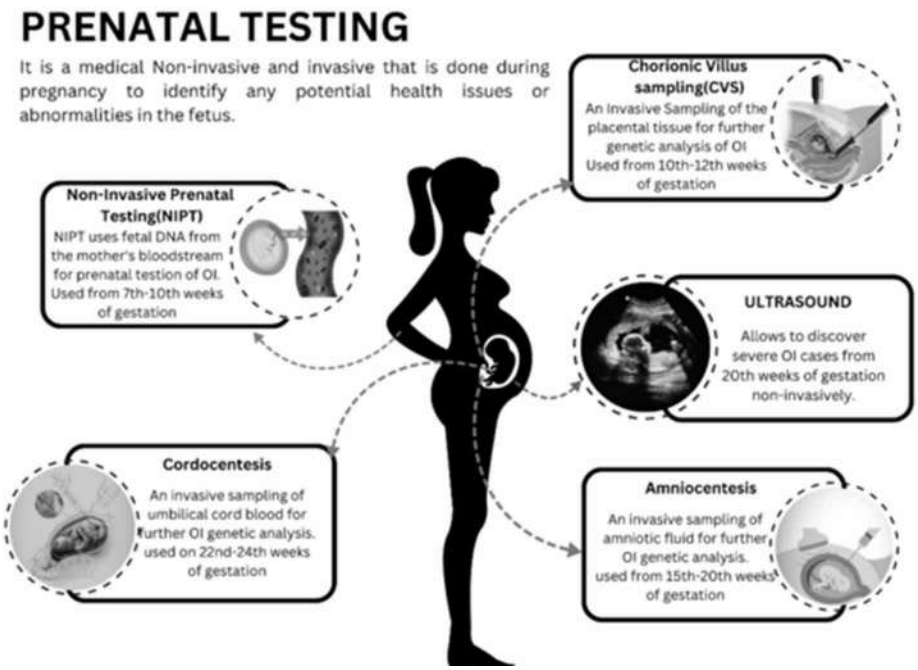

Prenatal Testing is the term used to describe medical tests carried out during pregnancy to look for potential health problems in the growing foetus. The figure 5 show different types of prenatal testing and how they are performed. These tests can help to identify genetic disorders, birth defects, or other conditions that may require medical attention at or after birth. Prenatal testing can be done through various methods, such as ultrasound, blood tests, and genetic screening. Prenatal testing aims to educate parents and medical professionals about potential risks to the foetus and arm them with the knowledge they need to make decisions about the pregnancy and the baby's health. It is significant to remember that not all prenatal tests are required or acceptable for all pregnancies, and the choice to undergo prenatal testing should be based on the unique circumstances and medical history of the patient in collaboration with a healthcare provider.

Here are some of the ways personalized medicine and genomics could impact pregnancy care:

Early identification of genetic risks: Genomic testing can identify potential genetic risks for both the mother and the fetus early in the pregnancy. This allows for more proactive management and monitoring of potential complications, such as preeclampsia or gestational diabetes (Peters et al., 2015).

Individualized treatment plans: With a better understanding of a patient's genetic makeup, healthcare providers can tailor treatment plans and medication dosages to optimize outcomes and minimize potential side effects.

Prevention and early intervention: In order to implement earlier intervention and prevention measures, personalised medicine can assist in identifying individuals who are highly susceptible to particular illnesses. For example, genomic testing can identify patients with a high risk for preterm labour, allowing for earlier interventions to prevent premature birth.

Enhanced prenatal screening: Genomic testing can improve the accuracy and reliability of prenatal screening, allowing for earlier detection and treatment of genetic disorders such as Down syndrome.

Personalized nutrition and lifestyle recommendations: A patient's genetic makeup can impact their nutritional needs and response to certain lifestyle interventions. Personalized medicine and genomics can help identify these individual needs, allowing for more personalized and effective nutrition and lifestyle recommendations.

While there are many potential benefits to personalized medicine and genomics in pregnancy care, there are also some ethical, legal, and social implications that need to be carefully considered (Guttmacher et al., 2010). For example, concerns about privacy, informed consent, and the potential for genetic discrimination will need to be addressed as these technologies become more widely used. Despite these challenges, personalized medicine and genomics hold great promise for improving pregnancy outcomes and providing more individualized care.

7. SOCIAL MEDIA AND ONLINE COMMUNITIES FOR PREGNANCY SUPPORT AND EDUCATION

Social media and online communities have become increasingly popular platforms for pregnancy support and education. Here are some of the ways these platforms can benefit pregnant women:

Access to support and information: Pregnant women have a platform to interact with others who are going through similar circumstances thanks to social media and online groups. This may be especially helpful for women who lack access to local support networks or who prefer the privacy of online conversation.

Sharing experiences and resources: Online communities provide a space for pregnant women to share their experiences, ask questions, and share resources. This can help women feel more connected and informed, and can also provide a source of emotional support during a potentially stressful time.

Educational resources: Social media and online communities can also provide educational resources on topics such as pregnancy nutrition, exercise, and childbirth preparation. This information can be particularly helpful for first-time mothers who may not have access to other educational resources.

Patient advocacy: Social media and online communities can also provide a platform for patient advocacy and raising awareness of important issues in pregnancy care, such as maternal mortality rates and access to healthcare services.

While social media and online communities can be valuable sources of support and information, there are also some potential drawbacks (Zhu et al., 2019). Online communities may not always provide

accurate or reliable information, and there is a risk of misinformation spreading quickly through these platforms. Additionally, some women may feel overwhelmed or anxious by the amount of information available online, particularly if they encounter conflicting advice or opinions. Despite these challenges, social media and online communities can be valuable tools for pregnant women to connect with others, access information, and find support during this important time.

8. ETHICAL CONSIDERATIONS AND CHALLENGES IN THE DIGITAL AGE OF PREGNANCY CARE

As with any emerging technology, the digital age of pregnancy care presents several ethical considerations and challenges (Topçu & Brown, 2019). Here are some of the key issues to consider:

Privacy and security: The collection, storage, and sharing of personal health information through digital technologies raise important privacy and security concerns. Healthcare providers and technology companies must ensure that patient data is kept secure and that patients are informed of how their information will be used and shared.

Equity and access: Digital technologies have the potential to expand access to prenatal care, but they run the risk of escalating already-present health inequities if some populations cannot access or pay them. Healthcare providers must ensure that digital technologies are used in a way that promotes equity and does not further marginalize vulnerable populations.

Informed consent: Before participating in these programmes, patients must be fully aware of the advantages and disadvantages of digital technology and must provide their informed consent. This can be challenging given the rapidly evolving nature of these technologies and the potential for patients to be overwhelmed by the amount of information available.

Bias and discrimination: Artificial intelligence and machine learning technologies may inadvertently perpetuate biases or discriminate against certain populations. Healthcare providers and technology companies must take steps to mitigate these risks and ensure that their algorithms are fair and unbiased.

Regulation and oversight: As digital technologies become increasingly integrated into pregnancy care, there is a need for regulatory oversight to ensure that these technologies are safe, effective, and ethical. This can be challenging given the rapidly evolving nature of these technologies and the difficulty of regulating software and digital platforms.

Overall, while digital technologies hold great promise for improving pregnancy care, it is important to be mindful of the ethical considerations and challenges that arise with their use (Carissoli et al., 2016). Healthcare providers and technology companies must work together to ensure that these technologies are utilised in a way that fosters equity, privacy, and patient autonomy.

9. FUTURE DIRECTIONS AND OPPORTUNITIES FOR PREGNANCY CARE TECHNOLOGY

As technology continues to advance, there are several promising directions and opportunities for pregnancy care technology. Here are a few potential areas of growth:

Integration of data from multiple sources: With the increasing availability of wearable devices, mobile health applications, and other monitoring technologies, there is a wealth of data available on maternal

and fetal health. Integrating and analysing this data from multiple sources could lead to more personalized and effective pregnancy care.

On the basis of enormous amounts of data, patterns are discovered and results are forecasted using artificial intelligence and machine learning. These technologies could be used to develop predictive models for pregnancy complications or to identify patients who are at high risk for certain conditions (Bjelica et al., 2020).

Expansion of telemedicine and virtual consultations: Pregnant women, especially those who live in rural or underserved areas, have already showed potential in gaining access to healthcare services thanks to telemedicine and virtual consultations. As technology continues to improve, there is potential to expand these services even further, improving access and convenience for patients.

Development of more specialized devices and technologies: There is potential to develop more specialized devices and technologies for pregnancy care, such as sensors for monitoring uterine contractions or devices for monitoring fetal movements. These technologies could provide more detailed and accurate information on maternal and fetal health.

Use of virtual and augmented reality: Virtual and augmented reality technologies could be used to simulate prenatal and childbirth experiences, providing patients with a more immersive and realistic understanding of what to expect during pregnancy and childbirth (van den Heuvel et al., 2018).

As these technologies continue to evolve and improve, it will be important to carefully evaluate their effectiveness, safety, and ethical implications. By doing this, we can keep raising the standard and accessibility of prenatal care, which will ultimately lead to better results for mothers and their newborns.

10. CONCLUSION: THE PROMISE AND PITFALLS OF PREGNANCY CARE IN THE DIGITAL AGE

In the digital age, pregnancy care has been transformed by the use of various technologies, such as mobile health applications, wearable devices, telemedicine, and artificial intelligence. These innovations could increase pregnancy care's accessibility, effectiveness, and quality by offering women individualised, data-driven techniques to monitoring their own and their unborn children's health. However, there are also some potential pitfalls and challenges associated with the use of these technologies. For example, there may be concerns about the accuracy and reliability of some technologies, as well as the impact on the patient-provider relationship. There might also be problems with data security and privacy, as well as the possibility of unequal access to and usage of these technology.

It is important to carefully evaluate and validate these technologies before they are widely adopted, and to ensure that they are used in a way that is transparent, ethical, and patient-centered. This includes addressing potential biases and disparities, ensuring that patients have access to comprehensive and accurate information, and preserving the human element of healthcare. Overall, the digital age offers both promise and pitfalls for pregnancy care. With strategic navigation of the obstacles and effective utilization of available technologies, it is possible to enhance the health results and overall experiences of expectant mothers and their loved ones.

REFERENCES

Aziz, A., Zork, N., Aubey, J. J., Baptiste, C. D., D'Alton, M. E., Emeruwa, U. N., Fuchs, K. M., Goffman, D., Gyamfi-Bannerman, C., Haythe, J. H., LaSala, A. P., Madden, N., Miller, E. C., Miller, R. S., Monk, C., Moroz, L., Ona, S., Ring, L. E., Sheen, J.-J., ... Friedman, A. M. (2020). Telehealth for High-Risk Pregnancies in the Setting of the COVID-19 Pandemic. *American Journal of Perinatology*, *37*(08), 800–808. doi:10.1055-0040-1712121 PMID:32396948

Bachiri, M., Idri, A., Fernández-Alemán, J. L., & Toval, A. (2016). Mobile personal health records for pregnancy monitoring functionalities: Analysis and potential. *Computer Methods and Programs in Biomedicine*, *134*, 121–135. doi:10.1016/j.cmpb.2016.06.008 PMID:27480737

Bagalkot, N., Verdezoto, N., Lewis, M., Griffiths, P., Harrington, D., Mackintosh, N., & Noronha, J. A. (2018). Towards Enhancing Everyday Pregnancy Care. *Proceedings of the 9th Indian Conference on Human-Computer Interaction*, 71–74. 10.1145/3297121.3297130

Bjelica, D., Bjelica, A., Despotović-Zrakić, M., Radenković, B., Barać, D., & Đogatović, M. (2020). Designing an IT Ecosystem for Pregnancy Care Management Based on Pervasive Technologies. *Health Care*, *9*(1), 12. doi:10.3390/healthcare9010012 PMID:33374164

Carissoli, C., Villani, D., & Riva, G. (2016). *An Emerging Model of Pregnancy Care*., doi:10.4018/978-1-4666-9986-1.ch007

Chan, K. L., & Chen, M. (2019). Effects of Social Media and Mobile Health Apps on Pregnancy Care: Meta-Analysis. *JMIR mHealth and uHealth*, *7*(1), e11836. doi:10.2196/11836 PMID:30698533

Dahl, A. A., Dunn, C. G., Boutté, A. K., Crimarco, A., & Turner-McGrievy, G. (2018). Mobilizing mHealth for Moms: A Review of Mobile Apps for Tracking Gestational Weight Gain. *Journal of Technology in Behavioral Science*, *3*(1), 32–40. doi:10.100741347-017-0030-6

DeNicola, N., Grossman, D., Marko, K., Sonalkar, S., Butler Tobah, Y. S., Ganju, N., Witkop, C. T., Henderson, J. T., Butler, J. L., & Lowery, C. (2020). Telehealth Interventions to Improve Obstetric and Gynecologic Health Outcomes. *Obstetrics and Gynecology*, *135*(2), 371–382. doi:10.1097/AOG.0000000000003646 PMID:31977782

Dias, D., & Paulo Silva Cunha, J. (2018). Wearable Health Devices—Vital Sign Monitoring, Systems and Technologies. *Sensors (Basel)*, *18*(8), 2414. doi:10.339018082414 PMID:30044415

Emin, E. I., Emin, E., Papalois, A., Willmott, F., Clarke, S., & Sideris, M. (2019). Artificial Intelligence in Obstetrics and Gynaecology: Is This the Way Forward? *In Vivo (Athens, Greece)*, *33*(5), 1547–1551. doi:10.21873/invivo.11635 PMID:31471403

Garg, N., Arunan, S. K., Arora, S., & Kaur, K. (2022). Application of Mobile Technology for Disease and Treatment Monitoring of Gestational Diabetes Mellitus Among Pregnant Women: A Systematic Review. *Journal of Diabetes Science and Technology*, *16*(2), 491–497. doi:10.1177/1932296820965577 PMID:33118397

Ghimire, S., Gerdes, M., Martinez, S., & Hartvigsen, G. (2022). *Virtual Prenatal Care: A Systematic Review of Pregnant Women' and Healthcare Professionals' Experiences*. Needs, and Preferences for Quality Care. doi:10.37766/inplasy2022.9.0070

Ginsburg, G. S., & Willard, H. F. (2009). Genomic and personalized medicine: Foundations and applications. *Translational Research; the Journal of Laboratory and Clinical Medicine*, *154*(6), 277–287. doi:10.1016/j.trsl.2009.09.005 PMID:19931193

Guttmacher, A. E., McGuire, A. L., Ponder, B., & Stefánsson, K. (2010). Personalized genomic information: Preparing for the future of genetic medicine. *Nature Reviews. Genetics*, *11*(2), 161–165. doi:10.1038/nrg2735 PMID:20065954

Gyselaers, W., Lanssens, D., Perry, H., & Khalil, A. (2019). Mobile Health Applications for Prenatal Assessment and Monitoring. *Current Pharmaceutical Design*, *25*(5), 615–623. doi:10.2174/1381612825666190320140659 PMID:30894100

Iftikhar, P. M., Kuijpers, M. V., Khayyat, A., Iftikhar, A., & DeGouvia De Sa, M. (2020). Artificial Intelligence: A New Paradigm in Obstetrics and Gynecology Research and Clinical Practice. *Cureus*. Advance online publication. doi:10.7759/cureus.7124 PMID:32257670

Iyawa, G. E., Dansharif, A. R., & Khan, A. (2021). Mobile apps for self-management in pregnancy: A systematic review. *Health and Technology*, *11*(2), 283–294. doi:10.100712553-021-00523-z

Mukhopadhyay, S. C. (2015). Wearable Sensors for Human Activity Monitoring: A Review. *IEEE Sensors Journal*, *15*(3), 1321–1330. doi:10.1109/JSEN.2014.2370945

Nguyen, K., Bamgbose, E., Cox, B. P., Huang, S. P., Mierzwa, A., Hutchins, S., Caso, B., Culjat, M., Connelly, C., Lacoursiere, D. Y., & Singh, R. S. (2018). Wearable Fetal Monitoring Solution for Improved Mobility During Labor & Delivery. *2018 40th Annual International Conference of the IEEE Engineering in Medicine and Biology Society (EMBC)*, 4397–4400. 10.1109/EMBC.2018.8513321

Oprescu, A. M., Miro-Amarante, G., Garcia-Diaz, L., Beltran, L. M., Rey, V. E., & Romero-Ternero, M. (2020). Artificial Intelligence in Pregnancy: A Scoping Review. *IEEE Access : Practical Innovations, Open Solutions*, *8*, 181450–181484. doi:10.1109/ACCESS.2020.3028333

Peters, D. G., Yatsenko, S. A., Surti, U., & Rajkovic, A. (2015). Recent advances of genomic testing in perinatal medicine. *Seminars in Perinatology*, *39*(1), 44–54. doi:10.1053/j.semperi.2014.10.009 PMID:25444417

Peyton, T., Poole, E., Reddy, M., Kraschnewski, J., & Chuang, C. (2014). Every pregnancy is different. *Proceedings of the 2014 Conference on Designing Interactive Systems*, 577–586. 10.1145/2598510.2598572

Piwek, L., Ellis, D. A., Andrews, S., & Joinson, A. (2016). The Rise of Consumer Health Wearables: Promises and Barriers. *PLoS Medicine*, *13*(2), e1001953. doi:10.1371/journal.pmed.1001953 PMID:26836780

Runkle, J., Sugg, M., Boase, D., Galvin, S. L., & Coulson, C., C. (. (2019). Use of wearable sensors for pregnancy health and environmental monitoring: Descriptive findings from the perspective of patients and providers. *Digital Health*, *5*. doi:10.1177/2055207619828220 PMID:30792878

Sufriyana, H., Husnayain, A., Chen, Y.-L., Kuo, C.-Y., Singh, O., Yeh, T.-Y., Wu, Y.-W., & Su, E. C.-Y. (2020). Comparison of Multivariable Logistic Regression and Other Machine Learning Algorithms for Prognostic Prediction Studies in Pregnancy Care: Systematic Review and Meta-Analysis. *JMIR Medical Informatics*, *8*(11), e16503. doi:10.2196/16503 PMID:33200995

Topçu, S., & Brown, P. (2019). The impact of technology on pregnancy and childbirth: Creating and managing obstetrical risk in different cultural and socio-economic contexts. *Health Risk & Society*, *21*(3–4), 89–99. doi:10.1080/13698575.2019.1649922

van den Heuvel, J. F., Groenhof, T. K., Veerbeek, J. H., van Solinge, W. W., Lely, A. T., Franx, A., & Bekker, M. N. (2018). eHealth as the Next-Generation Perinatal Care: An Overview of the Literature. *Journal of Medical Internet Research*, *20*(6), e202. doi:10.2196/jmir.9262 PMID:29871855

Zhu, C., Zeng, R., Zhang, W., Evans, R., & He, R. (2019). Pregnancy-Related Information Seeking and Sharing in the Social Media Era Among Expectant Mothers: Qualitative Study. *Journal of Medical Internet Research*, *21*(12), e13694. doi:10.2196/13694 PMID:31799939

Ad Hoc & Sensor Wireless Networks, Vol. 58, pp. 53–77
Reprints available directly from the publisher
Photocopying permitted by license only
DOI: 10.32908/ahswn.v58.8995

MoDT: Interest Forwarding in Named Data Networking Based Vehicular Ad Hoc Networks by Predicting the Mobility Using Direction and Timer

PADMA DEVI S[1,*] AND DHANALAKSHMI K[2]

[1]*Department of Computer Science and Engineering, Velammal College of Engineering and Technology, Madurai, Tamil Nadu – 625009, India*
[2]*Department of Computer Science and Engineering, PSNA College of Engineering and Technology, Dindigul, Tamil Nadu-624622, India*

Received: February 10, 2022. Accepted: February 12, 2023.

Vehicular Ad hoc Networks (VANET) play a vital role in building Intelligent Transportation Systems (ITS). Since VANET is highly dynamic, it's very difficult to implement an IP-based communication system for ITS. Named Data Networking (NDN) is an alternative to IP-based networking applications. In this case, content is retrieved based on its name rather than its IP address. The proposed system focuses primarily on the interest-forwarding strategy for content retrieval. Since traditional NDN uses blind flooding to broadcast the interest, it causes a broadcast storm. Many different techniques, such as location-based, scheduling-based, priority-based, and clustering-based NDN have been proposed to control the broadcast storm problem. The proposed scheme is a Mobility Prediction using Direction and Timer for Interest Forwarding strategy for Named Data Networking (MoDT-NDN) that selects only a tiny proportion of forwarders based on Link Availability Time and Direction. MoDT-NDN is compared to Classic NDN and RA-NDN strategies. The results show that MoDT-NDN outperforms both classic NDN and RA-NDN.

Keywords: Named data networking, content centric networking, flooding, broadcast storm problem, interest forwarding strategy, location-based forwarding

*Corresponding author: E-mail address: paddevima@gmail.com

1 INTRODUCTION

Vehicular Ad hoc networks act as a backbone for Intelligent transportation systems. Vehicle-Vehicle to communication and Vehicle to infrastructure communication (Figure 1) is done with the help of VANETs. Even though VANETs are initially used to exchange information related to driver safety, nowadays real-time traffic information is also communicated. Mostly position-based information like "Which nearby restaurant is good?", "In which parking area, a lot is free?", and" Which Road is congestion-free to use?" are sent by the vehicles. Existing works mainly concentrate on routing and content dissemination techniques in VANET. Content routing in VANET imposes several challenges[1–4]. When a vehicle requests a particular data, it has to know the source from which it can extract the data. Mostly in VANET applications, it is very difficult to identify the source. Though a centralized server solves this problem, information gathering and dissemination among vehicles take a long delay. We cannot ensure a very good packet delivery ratio due to the dynamic nature of the VANET.

Many data dissemination techniques [5]–[7] have been proposed that work with the TCP/IP implementation. There are two main drawbacks, first in a low-density vehicle scenario, it results in data loss since it is very difficult to maintain the path between vehicles. To maintain the path between the vehicles, IP address assignment is necessary. Second, In a highly dynamic environment, it's very difficult to assign an IP address to the vehicles.

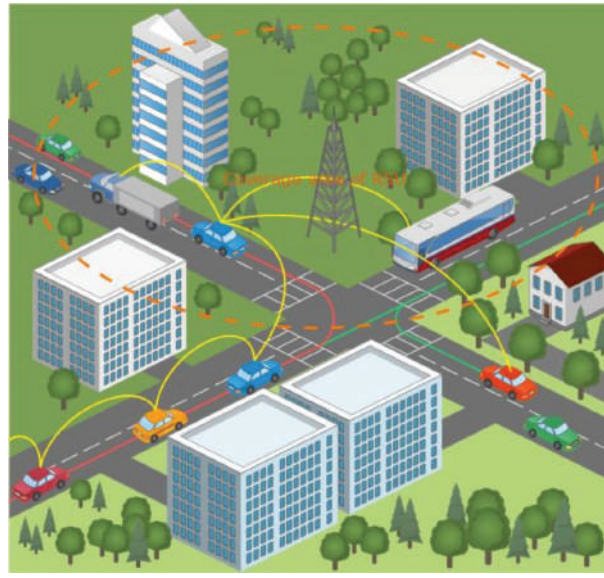

FIGURE 1
VANET with V2V Communication and V2R Communication

Named data networking provides a good solution to the challenges that are raised due to IP address strategies. Communication in NDN is purely consumer-oriented. NDN has three data structures: "the content store (CS), the Pending Interest Table (PIT), and the Forwarding Information Base (FIB)". Here a consumer will initiate the communication by sending an interest, for example, City/Area/Free parking lot. When a router or an intermediate node receives an interest, it checks its content store; if the node has content that is relevant to the interest, it will forward the content to the consumer If the matching content cannot be found in the CS, the node will search for it in its PIT table. If that interest is already in the PIT table, the received interest is discarded; instead, the node records the receiving and sending interfaces for that PIT entry, and the forwarding strategy identifies the forwarder based on the FIB.

If the interest reaches the producer, content is transferred in the reverse path hop by hop so that the content can reach all its consumers. The content is also cached in the forwarder's content store so that it can serve the future request for that interest and the corresponding interest from the PIT is also removed.

A lot of works have been proposed for V2V dissemination [7] in NDN-based VANETs, like probabilistic-based, location-based, Clustering-based, Timer-based, Push-based, Pull based, etc.. data dissemination techniques. Some works combine the approaches to improve the packet delivery ratio or to reduce the dissemination time. The main challenge is in the case of a highly dynamic network it's very difficult to find the required content with minimum delay. For example, consider a scenario where node A is the requester node, node S is the only node having the cached content of that interest. When A sends the request, S would have moved out of that area. So, A's interest will be forwarded infinitely throughout that area and the interest packet would have dropped when the timer expires. This results in packet loss which affects the packet delivery ratio. In the case of a high-density network, without one central coordinator, packet loss rate and packet delivery time may increase. The central arbiter can collect information from other nodes, process the information, and disseminate the information to other nodes. Establishing an infrastructure may incur the cost and processing the information may increase the delay, but by using that central administrator we can improve content dissemination. Considering that feature we make use of Independent Road-side units in our work, which has the same configuration as on-board units in the vehicle used to collect the information specific to that area and disseminate that information to the node which is interested in it.

In our work, we mainly concentrate on interest forwarding strategy,

- Interest will be disseminated by the consumer with the name of the content that has to be retrieved.

- Each forwarder will be selected based on the Link Availability Time (LAT) and the direction.
- The timer is set by calculating the time required for the interest to travel to the zone from which it needs the content
- When the content is found, it is sent to the consumer using the information in PIT. It solves the reverse path partitioning problem.

2 RELATED WORKS

VANET is highly dynamic which results in frequent disconnections. It will have an impact on network performance, causing the packet delivery ratio to drop and communication latency to increase. Data dissemination is critical for communication in the VANET. VANET communication can be unicast, multicast, or broadcast.

The primary function of name-based networking is to extract content based on its name and cache the data to make retrieval easier. Here the interest is broadcasted, to find the source of the data, and data is sent to the consumer on a multi-hop basis.

Several techniques for curbing the broadcast storm challenge all through interest forwarding have been proposed. One approach is to restrict the forwarders from rebroadcasting the data. The main schemes that focus attention on this concept are delay-based, probability-based, Geo-based, and Cluster-based data dissemination approaches.

Geo-based data dissemination

Milojevic et al. [8] propose a location awareness algorithm that provides message location context without any positioning system. Vehicles create a spatio-temporal database to develop a spatial understanding of their environment. This method reduces the number of sent and received packets, as well as packet collision and network load. The authors of [9] evaluated a distributed message delivery system in which multiple connected vehicles (CV) operated concurrently with data transfer between RSUs and various transportation centers. The measured latencies in this system are less than the recommended latency requirement for CV applications. Bitam et al. [10] developed a hybrid routing protocol that applies to both highway and urban scenarios. A topology-based approach is used when the density is high; otherwise, a geography-based approach is used. It demonstrates a significant improvement in packet delivery ratio and average end-to-end delay. Bian et al. [11] redesigned the NDN forwarding strategy to incorporate the concept of geo-based routing, making it appropriate for urban VANET scenarios. It searches the neighbor table for neighbors who are closer to the data source or for the farthest neighbors who are closest to the data source. To meet the reliability criteria, Chuang et al [12] proposed a “density-aware emergency message extension protocol (DEEP)” in which a message is quickly dispatched to the hot spot and sent to

all vehicles in the area. This scheme achieves a low dissemination delay and a high level of reliability. DEEP, on the other hand, cannot be used in a complex environment. In [13]Ahmed et al. presented CODIE, a scheme for controlling data flooding in naive NDN. When a request is received, the vehicle records the number of hops required for the data packet to return. It sends fewer copies of data packets that have a similar interest satisfaction rate as vehicular named data networking (VNDN), and it also reduces overall interest satisfaction delay. Dehaghani et al. [14] develop a novel forwarding strategy by modifying the NDN structure with a redundancy elimination approach. It demonstrated that it can maintain proper network performance in wireless networks with dynamic topologies. To control the flow of data in wireless sensor networks, Almesaeed and Jedidi proposed dynamic directional routing (DDR). Mobile nodes choose the next hop in data routing towards the sink based on a particular predefined search angle that ultimately decides the possible candidate of a next-hop node. This method improves the packet delivery ratio and allows for shorter router lengths. [15]. [16] Kim et al created an algorithm that uses in-network caching to reduce network packet transmissions. It dispatches content in a unicast manner to avoid issues with multicast delivery. This scheme effectively eases the damage caused by a broken path in a unicast relay by incorporating a localized path recovery algorithm.

Priority-based data dissemination

The authors of [17] presented a unique mechanism for retrieving named content in which interest and data packets are disseminated over the 802.11 OCB interface by prioritizing high-priority interest packets over low-priority ones.

Scheduling-based data dissemination

Chen et al. recommended the Guaranteed Time Slot (GTS) scheme in [18] for effectively planning several vehicles' access to Road Side Units (RSUs) in vehicular sensor networks. It performs better in terms of latency. Amadeo et al. [19] augmented the CCN framework to support content delivery over IEEE 80211p vehicular technology. It employs a straightforward counter-based approach, along with deferred transmission time and interest retransmission patterns. The results show that the content delivery mechanism is efficient enough.

Probabilistic-based data dissemination

The authors of [20] developed a new data dissemination scheme in VANETs depending on directional clustering and probabilistic broadcasting which allows us to solve key challenges such as long latency, high collision probability, and poor data visibility while incurring additional overheads during clustering initialization and maintenance.

Clustering-based data dissemination

[21] Cheng and Huang work hard to make VANET clusters as stable as possible to cut management costs and enhance communication quality. The rela-

tive mobility metric is used to counter the effects of vehicle distance, speed, and maximum displacement. It performs admirably in terms of reliability and packet delivery cost. The [22] algorithm is designed to find clusters with the least amount of relative mobility and proximity between cluster heads and cluster members. The resulting clusters are unfluctuating, with a longer average lifespan of cluster heads and a reduced average rate of cluster head change. A stochastic analysis of single-hop cluster stability in a highway VANET with a single lane as a focus is presented by Abboud and Zhuang [23]. It shows a high degree of concurrence between analytical and simulation results. The authors of [24] proposed a distributed clustering algorithm (DCA-DS) based on dominating sets for the Internet of Vehicles. In this case, the cluster head is the node with the greatest span, and its neighbors are the cluster members. When compared with the conventional N-hop algorithm, DCA-DS yields good results.

RSU-assisted data dissemination

Rahim et al [24] investigated and proposed a solution for improving the broadcasting performance of the DSRC safety message at intersections while taking into account the IEEE 802.11p enhanced distributed channel access mechanism. They used RSU at the intersection center to relay the safety messages once to improve overall broadcast performance. [25] describes a new protocol called Roadside unit assisted named data network (RA-NDN), in which the RSU functions as a Stand Alone (SA) node. One advantage of deploying SA-RSUs has improved network connectivity. The RA-NDN protocol improves ad hoc communication performance by increasing the data received ratio and throughput while decreasing total dissemination time and traffic load. Belmekki et.al [26] investigate vehicular communications at road intersections. They show that direct transmission is better for high vehicle densities and hybrid transmission is better for low vehicle densities. They demonstrate that the non-line-of-sight scenario performs better at intersections.

Blockchain-based computation offloading

[27] Performed extensive research into the technology of blockchain and machine learning integration. [28]carries out a study on the massive IOT made possible by 6G. The authors provide a brief explanation of how 6G's four-tier network, aided by edge computing, satisfies the IOT applications' need for full coverage.

[29] developed the "Dual-side Dynamic Joint task offloading & Resource allocation algorithm in Vehicular networks (DDORV)" using Lyapunov optimization theory, which solves optimization problems on the Vehicular Terminal (VT) side and Mobile-RSU (MRSU) side in an integrated framework in each frame.

[30] put forth an innovative mobile edge computing-enabled wireless blockchain platform that allows for the caching of block cryptographic hashes and the offloading of computationally taxing mining tasks to neighboring edge computing nodes.

[31]suggested a unique blockchain-based approach with an adjustable block size for mobile edge computing and video streaming. They implemented an incentive system to encourage collaboration between consumers, transcoders, and content producers.

Deep Reinforcement learning-based approach
By utilizing recent advancements, [32] developed the maximization of the cache-assisted proactive interference alignment network as a deep reinforcement challenge. The central scheduler in this scenario is in charge of collecting channel state information from each participant and transmitting the node's fundamental behavior to the deep Q structure to ascertain the optimal method for user selection.

To enhance the efficiency of next-generation vehicular networks, [33] proposed an integrated framework that can enable the interactive collaboration of networking, caching, and computational capabilities. For high-quality engaging and interactive video services, [34] recommended lowering the long-term energy demand of THz wireless access-based MEC systems.

3 PRELIMINARIES

In this section, we present all the preliminaries that are required to understand our proposed work.

3.1 Assumptions

1. In the network, we assume that each vehicle has a radio device for short-range communication as well as a GPS device to determine the vehicle's position and speed.
2. Every vehicle in the network collects neighborhood information with periodic HELLO messages (i.e) BEACONS
3. Road Side Units (RSU) are used, mainly to collect region-specific information

3.2 System Model

a. Network Model: The network we considered have linear roads which consist of many lanes and vehicles travel in both directions at different speeds.

b. Channel Model: In this case, the Nakagami-m distribution [26] is used to calculate the likelihood of successful data packet transmission between two vehicles i and j

$$P_{ij}^{f}(d_{ij}) = 1 - F_d(r_T, m, \varphi) = e^{-\frac{mr_T}{\varphi}\sum_{i=1}^{m}\frac{\left(\frac{-mr_T}{\varphi}\right)^{i-1}}{(i-1)!}}$$

$F_d(r_T, m, \varphi)$. denotes the cumulative distribution function for receiving signal power r_T. In this equation, r_T denotes the reception threshold of a signal, φ is the average received signal power level, and m denotes the fading parameter, which is a function of the intervehicle distance between vehicles i and j.[20]

$$m\left(d_{ij}\right) = \begin{cases} 1, d_{ij} \geq 150m \\ 1.5, 50m \leq d_{ij} < 150\,m \\ 3, d_{ij} < 50\,m \end{cases}$$

4 PROPOSED SYSTEM

In a named data networking-based VANET, the source sends an interest in data search, where the producer's address is unknown to the source. In MoDT-NDN, the source will be sending the Interest packet with the structure as shown in Figure 2. The interest packet is identified by the interest's name and ID. The GPS coordinates of the source vehicle are indicated by the source location. The source vehicle's current speed is denoted by speed. The Time to Live field stores the lifetime of the interest message. The timestamp contains information about when the time interest packet is generated. If necessary, the signature field is used to verify the source's authentication.

Interest Name
Interest ID
Source Location
Speed
Time to Live
Time Stamp
Signature of the Consumer

FIGURE 2
Structure of Interest Packet

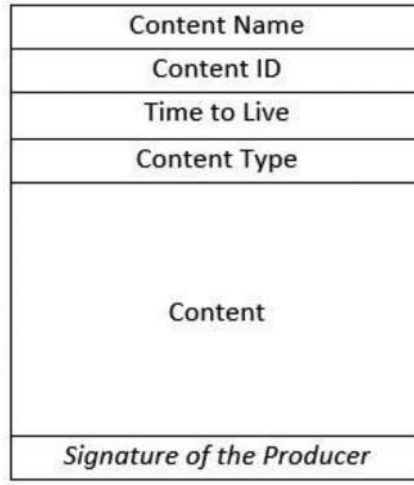

FIGURE 3
Structure of Data Packet

Figure 3 depicts the data packet structure, which contains information such as the content name and content ID to identify the content. Time to Live denotes the lifespan of a content packet. The content type is used to store either normal or emergency content. The content field contains the information requested by the consumer. Finally, the Signature field is used to verify the authenticity of the producer vehicle, if necessary.

Content Naming is still an open research issue in NDN. Normally NDN-based networks use either flat naming or hierarchical naming structure [35]. Flat name increases routing table size and minimizes network scalability, whereas hierarchical names provide name aggregation, reduces routing table size, and improves network scalability. MoDT-NDN follows a hierarchical naming scheme to improve the efficiency of the proposed work.

Classic NDN follows three data structures namely Content Store (CS), Pending Interest Table (PIT), and Forwarding Information Base (FIB). When a node receives an interest packet, it will check the CS first. If the content is available, the node will immediately send the data packet to that interest forwarder, else it will check the PIT. If the interest is already available in the PIT, it will discard it else it will aggregate interest to the PIT and in the next step, it will select a forwarder from FIB, then forward the interest to that forwarder[36]. Interest will be forwarded to interfaces stored in the FIB for that corresponding interest. If no forwarders are available, classic NDN follows Blind Flooding (BF) technique where interest is broadcasted to all vehicles in its transmission range, which results in a broadcast storm problem.

To avert the broadcast storm problem, only a few potential forwarders must be chosen. Broadcasting in an ad hoc network is typically done in one of three ways: proactive, reactive, or hybrid. In the Proactive approach, each

node gathers information about its surroundings and stores it in a table. When forwarding a packet, it will choose a neighbor from the table. However, this approach is unsuitable for a highly dynamic environment such as a VANET. On-demand approaches do not use tables to store neighborhood information; instead, packet size grows because it carries the entire path information from source to destination. These approaches are appropriate for a small network; however, they cannot guarantee a good packet delivery ratio for VANETs where the network size is unknown.

MoDT-NDN addresses the broadcast storm and network partitioning issues. When an interest packet needs to be forwarded, it employs a hybrid approach that collects neighborhood information. Instead of storing information about all neighbors, it selects forwarders based on direction and speed, which is then stored in FIB. MoDT-NDN effectively uses NDN data structures to reduce the overhead of storing neighborhood information in separate tables. It selects only a few forwarders based on direction and vehicle speed, thereby resolving the broadcast storm and network portioning issues.

4.1 Forwarder Selection Process

When a Vehicle has to forward the interest, it collects the neighborhood information through beacons The beacons consist of Beacon ID, Vehicle ID, and Position (i.e) GPS coordinates of the neighbor along with the speed and time stamp. To mitigate the broadcast storm problem, only a few forwarders have to be selected among the neighbors. The important question that arises here is, what should be the nature of the forwarder? Forwarders selected should move in the direction of the producer and forwarders should have stable link availability time.

Let us assume that now the interest packet is at V_i, now V_i has to choose a forwarder. V_{i+} receives a beacon message from all its neighbors.

The beacon message format is

Beacon ID	Vehicle ID	Position	Speed	Timestamp

Each Vehicle informs about its position and its speed to its neighbors through periodic beacons. The receiver predicts the Link Availability Time (LAT) of each neighbor. The neighbors with the largest LAT are chosen as a forwarder. The speed of V_i is distributed over the range of $(0, V_{max})$ and the direction of the vehicle is distributed over the range of $(0, \pi)$.

In Figure 4, V_i is the interest source, V_j is under potential forwarder selection. Let us assume V_j is in position (x_j, y_j) at time t_1 and at time t_2 it is at the position (x_d, y_d) (i.e) at the transmission range of V_i. Therefore, the distance between V_i and V_j^{t2} (i.e V_j at time t_2) is R, which is the transmission range of V_i.

Using cosine law

$$D_j^2(\Delta t) = R^2 + D_{ij}^2 - 2RD_{ij}\cos\theta_i \quad (1)$$

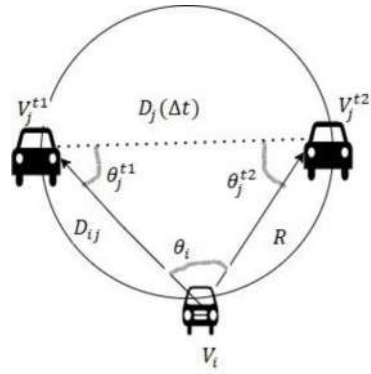

FIGURE 4
Calculating Angles between the Vehicles

$$D_j\left(\Delta t\right) = \sqrt{R^2 + D_{ij}^2 - 2RD_{ij}\cos\theta_i} \tag{2}$$

$$\vartheta_j LAT_j = \sqrt{R^2 + D_{ij}^2 - 2RD_{ij}\cos\theta_i} \tag{3}$$

$$LAT_j = \frac{\sqrt{R^2 + D_{ij}^2 - 2RD_{ij}\cos\theta_i}}{\vartheta_j} \tag{4}$$

Here Δt is $t_2 - t_1$, D_j is distance travelled by V_j from time t_1 to t_2, R is the transmission range of V_i, D_{ij} is the distance between V_i and V_j.

Using (4) Link Availability Time of all neighborhood vehicles has been estimated. The vehicle with the greatest LAT is chosen as a forwarder. The procedure is repeated by checking the forwarder's direction toward the producer's direction. The angle between the forwarder and the approximate position of the producer is calculated as θ_k. Let us consider that the current position of the forwarder is (x_1, y_1) and the approximate position of the producer at the destination is (x_2, y_2) then the angle can be calculated as

$$radian = atan2\left(y_2 - y_1, x_2 - x_1\right) \tag{5}$$

$$\theta_k = radian * \frac{180}{\pi} \tag{6}$$

$$\theta_k = \begin{cases} 0, Neighbor\ is\ moving\ in\ same\ direction\ w.r.t\ producer \\ \leq 90^0, Producer\ and\ Neighbor\ are\ not\ in\ same\ direction \\ 180^0, Producer\ and\ Neighbor\ are\ in\ opposite\ direction \end{cases} \tag{7}$$

If $d_i^{m,n}$ denotes the distance traveled by vehicle V_i from zone m to zone n then the time required to travel can be computed using

$$t_i^{m,n} = \frac{d_i^{m,n}}{v_i} \tag{8}$$

Expiry time for the interest packet can be set using

$$Expiry\_timer = t_i^{m,n} + t_{delay} \tag{9}$$

Here t_{delay} represents packet delay in transmission

Let us consider a scenario as depicted in Figure 5, Vehicle C initiates forwarding of interest with id interest1. In the case of Classic NDN, the Blind Flooding technique is followed, so C broadcasts interest to all the vehicles in its transmission range which results in a broadcast storm problem. In MoDT-NDN, the received beacon direction and Link Availability time are calculated. Neighbors traveling in the same direction as the consumer and who have the longest link availability time is chosen as a forwarder. In Figure 5 when C initiates interest forwarding, it collects neighborhood information through beacons, Vehicles 1,2,3,10,11,12 will send their information to Vehicle C. MoDN -NDN chooses vehicles 1 and 3 as a forwarder, C updates its FIB, also Vehicles 1 and 3 updates its PIT.

Similarly, Vehicles 3 and 6 choose their forwarders (Figure 6 and Figure 7). When the interest reaches Vehicle P where the content requested by C is cached, it checks its CS first, since the content is available it forwards the content toward C using PIT.

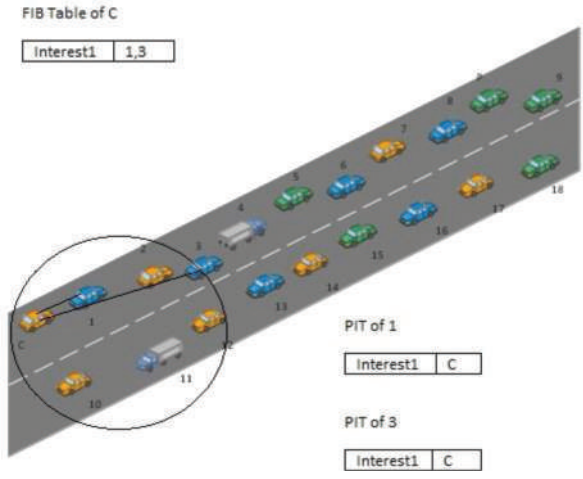

FIGURE 5
Interest Forwarding at node C

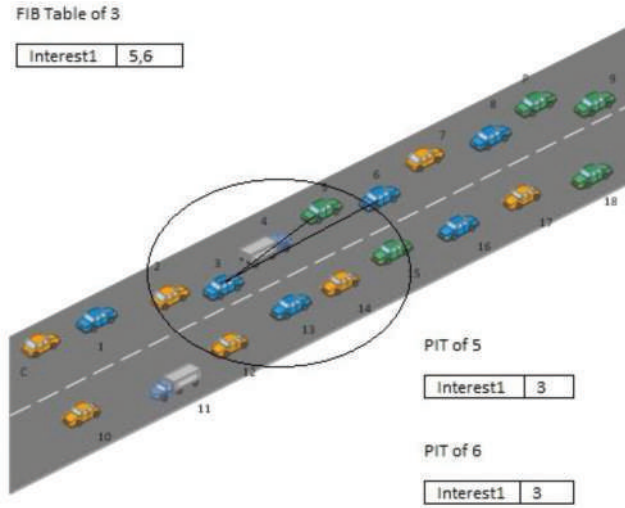

FIGURE 6
Interest Forwarding at node 3

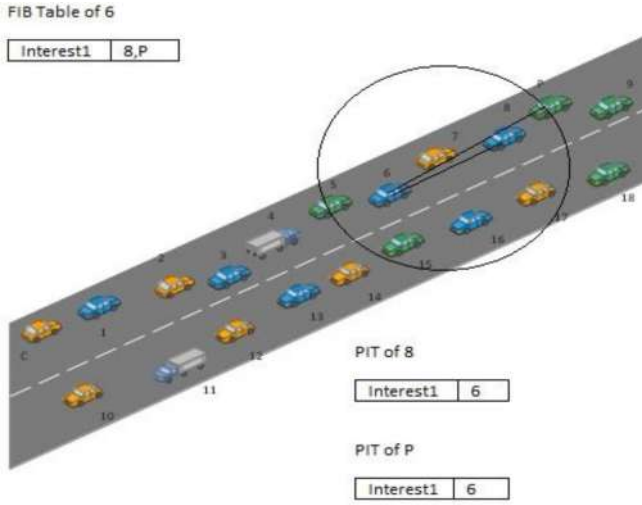

FIGURE 7
Interest Forwarding at node 6

4.2 Content Dissemination

MoDT-NDN solves the Reverse Path Partitioning problem that mainly occurs during the content dissemination process. Here the forwarders are selected based on stable link availability time and direction. Therefore, when vehicle X receives interest from vehicle Y, and if X is having the requested content, then it can disseminate the content in the reverse path by retrieving incoming interface information from PIT.

Algorithm 1: Forwarder ForwarderSelection(Vehicle$_i$)

//Returns the forwarder that is chosen from a set of neighbors for the ith vehicle

```
1.   Struct Vehicle
     {
       ID: identifier
       P: GPS coordinates
       S: Velocity
       TS: TimeStamp
     }N_i{} Neighbour set
2.   Broadcast BEACON (ID_i, P_i, S_i, TS_i) message to all the Vehicles
     in its Transmission Range
3.   Receive BEACON (ID, P, S, DIR) messages from its neighbors
4.   Max_LAT=0,k=0
5.   For each received BEACON(j)
6.       Calculate LATj and θ_k
7.       If(θ_k == 0) then
8.           Forwarder[k]=j; LAT[k]=LAT_j; k++;
         Endif
9.   For each Forwarder[k]
           If(LAT[k]> Max_LAT)
10.            Max_LAT  =LAT[k]
               F=k;
11.  Return F
```

Algorithm 2: Consumerinterestforwarding ()

```
1.   At Consumer
2.       C-Consumer
3.       P-Producer
4.       F-Forwarder
5.       I_i-Interest
6.       C initiates the search of the interest I_i
7.       Sets the timer for interest I_i
8.       F=ForwarderSelection ()
9.       Send the interest to F
10.      Add F to FIB for the interest I_i
```

Algorithm 3: Forwarderinterestforwarding ()

```
At Forwarder
    Checks the content store CS
    If the content is available
        Return the content to the consumer by retrieving the forwarder address from PIT
    else
        Check the PIT
        If the interest available in the PIT
            Discard the interest I_i, append the forwarder address for the Interest I_i in PIT
        Else
            Add the interest to the PIT
            Set the Forwarder address as the Incoming interface for Interest I_i in PIT
    F=ForwarderSelection ()
    Send the interest to F
    Add f to FIB
```

Algorithm 4: ContentForwarding ()

```
When Content is received,
If the received node is  not a Consumer
        Check for interest in PIT
        Locate the source for the Interest I_i
        Forward the content to the source
Add the content to the content store
Remove the interest from PIT
```

5 PERFORMANCE EVALUATION

MoDT-NDN-based VANET is evaluated with the NS3 simulator and compared to the classic-NDN algorithm and the RA-NDN. Classic NDN searches for content using three data structures, CS, PIT, and FIB, but it uses blind flooding to forward the interest message, resulting in a broadcast storm and

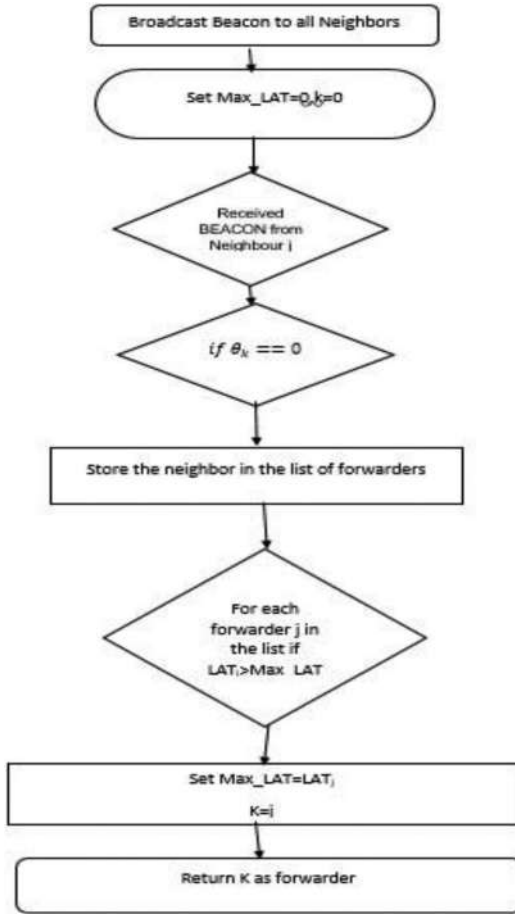

FIGURE 8
Forwarder Selection Process

network partitioning problem. RA-NDN employs a specialized infrastructure, a standalone RSU, to effectively store the contents, which improves content search; however, it retains the traditional NDN approach for interest forwarding and content search. MoDT-NDN focuses primarily on an interest-forwarding strategy that prevents broadcast storms and reverse path partitioning. It also employs standalone RSU to avoid the issue that arises as a result of the vehicle that cached the content moving out of the zone. The mobility model is created using VANET MOBISIM. For radio propagation, the Nakagami-m model is used, and the MAC layer is implemented using IEEE 802.11 DCF. The received signal strength is represented by a dual-slope piecewise linear model [3]

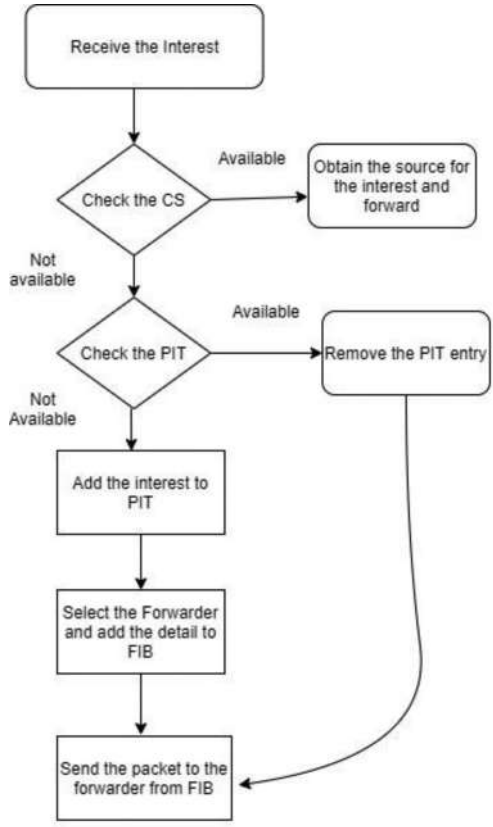

FIGURE 9
Interest Forwarding at Forwarder

$$P(d) = \begin{cases} P(d_0) - 10\alpha_1 log_{10}\left(\frac{d}{d_0}\right) + \chi\sigma_1, d_0 \le d \le d_c \\ P(d_0) - 10\alpha_1 log_{10}\left(\frac{d}{d_0}\right) - 10\alpha_2 log_{10}\left(\frac{d}{d_c}\right) + \chi\sigma_2 \\ d > d_c \end{cases}$$

Here, "d is the distance between i and j. $P(d_0)$ denotes the signal strength throughout the distance d_0. $\alpha_1 \, and \, \alpha_2$ are path loss components, d_c is the critical distance which is computed as $d_c = \frac{4 \propto_i \propto_j}{\lambda}$ where $\propto_i and \propto_j$ denotes the antenna heights of vehicles i and j. λ denotes the wavelength of the

electromagnetic wave at 5.9 GHz. $\chi\sigma_1 \, and \, \chi\sigma_2$ are zero-mean normally distributed random variables with the standard deviation $\sigma_1 and \sigma_2$ respectively".

5.1 Simulation

The Simulation scenario is designed as a two-way highway with four zones. The Poisson distribution is used to place vehicles on the road. The number of vehicles per km ranges from 10 to 200. The road length between zones is approximately 10 km. Three NDN protocols are compared here: Classic NDN, RA-NDN, and MoDT-NDN, with simulation results, averaged over 50 runs.

5.2 Performance Metrics

1. Network Load (NL): Total number of interest packets generated in the network

$$NL = \sum_{i=1}^{N} Number\ of\ interest\ packets\ generated\ by\ each\ vehicle,$$

   where x_i is the number of generated interests from vehicle i and N is the number of vehicles in the network.
2. Packet Delivery Ratio (PDR): Ratio of the number of packets of interest successfully reached the producer and the number of interest packets generated

$$PDR = \frac{\sum_{i=1}^{N} \begin{matrix} Number\ of\ interest\ packets\ that\ are\ received \\ sucessfully\ \ by\ the\ producer from\ the\ vehicle\ i \end{matrix}}{NL}$$

3. Average Latency: Average time that a packet has taken to reach the producer from the consumer node.

$$AL = \frac{\sum_{i=1}^{N} time\ taken\ by\ each\ sucessful\ \ packet\ to\ reach\ producer}{NL}$$

   Where t_i is the time taken by an interest packet to reach the producer from the consumer.
4. Packet loss: Average number of packets that are dropped in the network.

$$Packet\ loss = \frac{\sum_{i=1}^{N} Number\ of\ \ packets\ that\ are\ dropped}{NL}$$

Parameter	Value
Physical Layer	Nakagami-m
MAC Layer	802.11 DCF
Transmission range	200m
Simulation duration	500 s
Number of Vehicles	10-200 Vehicles/Km
Road Length	10 km
Number of Lanes	2
Zones	4
Interest Life time	4 s
Vehicle Maximum speed	80 Km/hr
Interest packet size	25 bytes
Simulation runs	50

TABLE 1
Simulation Parameter

5. Throughput: Rate of successful interest packet delivery in the network

$$Throughput = \frac{Total\ number\ of\ packets\ generated\ in\ the\ network}{Total\ time\ that\ is\ required\ by\ each\ packet\ to\ reach\ producer}$$

6. Average velocity: Average speed taken by the vehicles to travel in each direction

$$Average\ Velocity = \frac{Total\ Speed\ of\ all\ vehicles\ travelling\ in\ all\ directions}{Total\ Number\ of\ vehicles\ travelling\ in\ all\ directions}$$

5.3 Performance Analysis

Figure 10 depicts a comparison of vehicle density and packet delivery ratio. The graph shows that the network is initially sparse because the number of vehicles is low, so PDR is also low. As a result, the forwarder selection process becomes extremely difficult. When network density increases, PDR improves as well.

Figure 11 illustrates the relationship between vehicle density and latency. Because classic NDN employs a flooding strategy, the time required to reach the destination node is lengthy. RA-NDN does not employ any specialized forwarding strategy but instead employs RSUs, which eliminates the problem of infinite content search and, as a result, reduces latency. MoDT selects only a few forwarders based on direction and Link Availability time to eliminate broadcast storms, reducing latency even further when compared to RA-NDN.

From Figure 12, it is evident that Packet Delivery Ratio dips when velocity increases. In MoDT-NDN we consider speed along with direction for interest

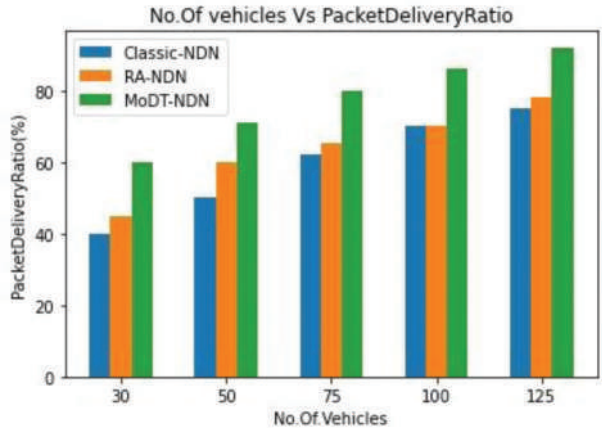

FIGURE 10
No. of Vehicles Vs PacketDeliveryRatio

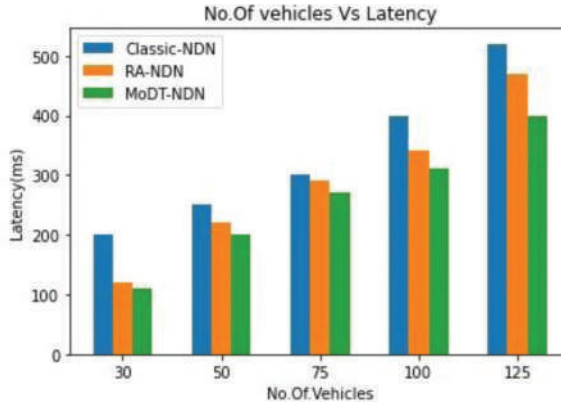

FIGURE 11
No. of Vehicles Vs Latency

forwarding, therefore compared to classic-NDN and RA-NDN, MoDT-NDN yields better results.

When the velocity of a vehicle increases, it affects the latency in interest forwarding. In Figure 13, we can conclude that latency in MoDT-NDN is less than in classic-NDN and RA-NDN.

Figure 14 represents the PDR for various vehicle densities as the vehicle's velocity increases. PDR may decrease when the velocity increases rapidly, but it improves significantly when the vehicle density increases.

Figure 15 shows when the vehicle density is less, the packet generation rate is less, therefore packet drop is also less. But when the vehicle density increases, packet drop also increases, compared to the other two techniques, the packet drop rate is less in MoDT-NDN.

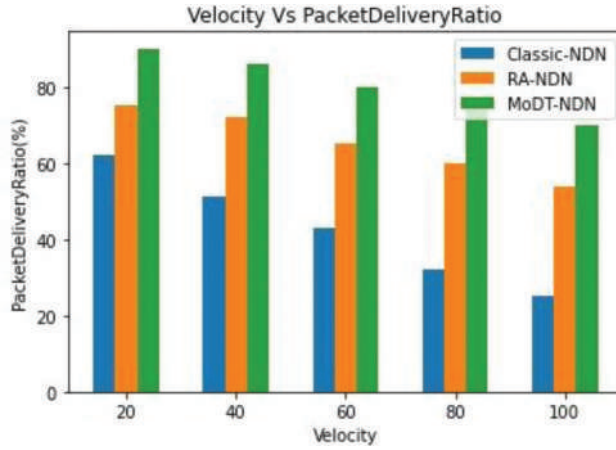

FIGURE 12
Velocity Vs PacketDeliveryRatio

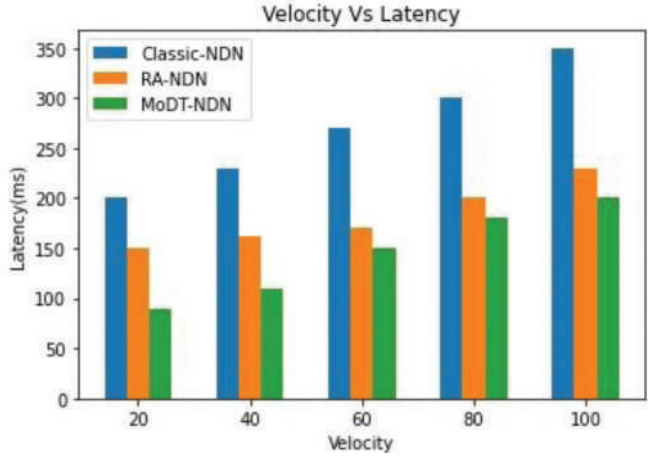

FIGURE 13
Velocity Vs Latency

Figure 16 captures how throughput improves as the number of vehicles in the network grows. According to the graph, the most important reason for this increase in MoDT-NDN is its simplicity, which ensures a high packet delivery ratio. Because it uses an On-demand approach and selects the forwarder solely based on information from the beacon messages, the forwarder selection process is simplified, which reduces the packet's latency to reach the destination.

Figure 17 proves that traffic load is reduced in MoDT-NDN. The primary reason for this is that it chooses only a few forwarders to forward the interest packet to avoid unnecessary flooding.

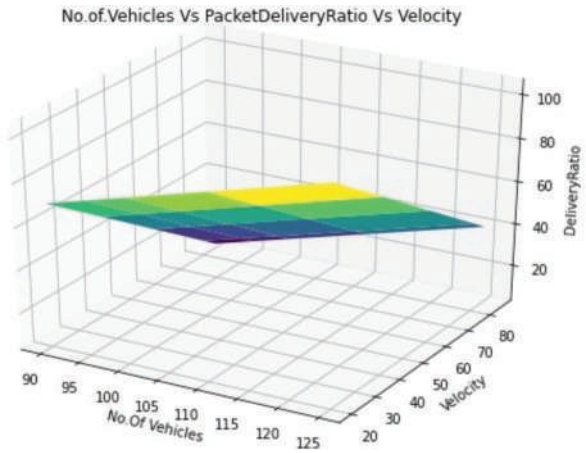

FIGURE 14
No. of Vehicles Vs PacketDeliveryRatio Vs Velocity

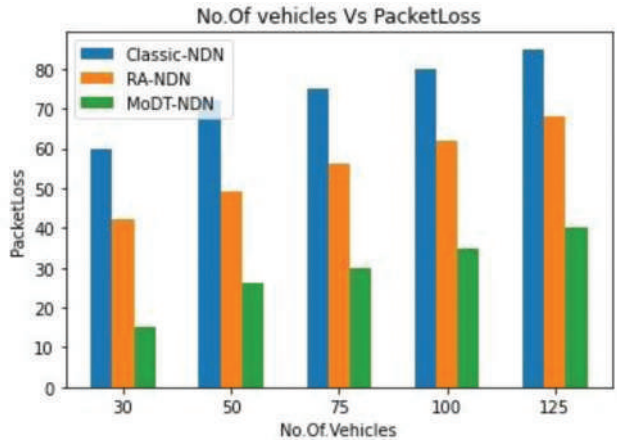

FIGURE 15
No. of Vehicles Vs PacketLoss

6 CONCLUSION

Searching for content whose source is not known is time-consuming. This task is made easier by named data networking, in which interest is broadcasted in search of content. When the content is discovered, it is directed to the consumer. The primary task for content dissemination in VANET is interest forwarding. The most common problems encountered during interest forwarding are broadcast storm and network partitioning. To select the forwarder, we devised a novel strategy that combines a hybrid approach with direction and velocity. In terms of packet delivery ratio and latency, simulation results show

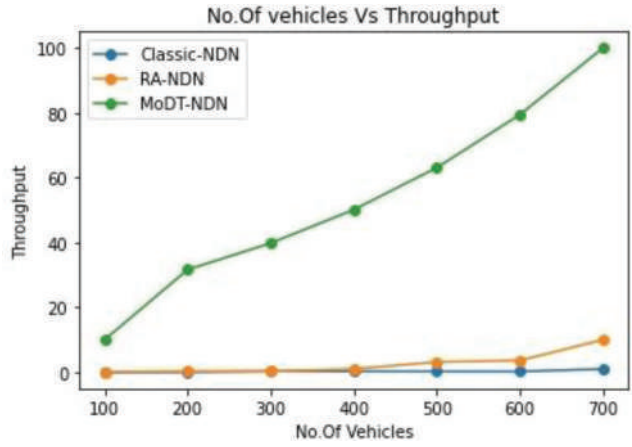

FIGURE 16
No. of Vehicles Vs Throughput

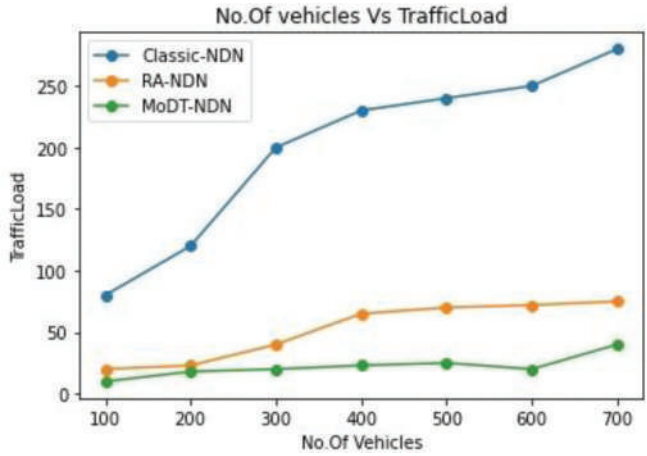

FIGURE 17
No. of Vehicles Vs TrafficLoad

that MoDT-NDN outperforms classic NDN and RA-NDN. In the future, evaluating the trustworthiness of the content could be done to ensure its authenticity.

REFERENCES

[1] K. Ahed, M. Benamar, A. A. Lahcen, and R. el Ouazzani, "Forwarding strategies in vehicular named data networks: A survey," *Journal of King Saud University - Computer and Information Sciences*. King Saud bin Abdulaziz University, 2020. doi: 10.1016/j.jksuci.2020.06.014.

[2] J. Nzouonta, N. Rajgure, G. Wang, and C. Borcea, "VANET routing on city roads using real-time vehicular traffic information," *IEEE Trans Veh Technol*, vol. 58, no. 7, pp. 3609–3626, 2009, doi: 10.1109/TVT.2009.2014455.

[3] W. Liang, Z. Li, H. Zhang, S. Wang, and R. Bie, "Vehicular Ad Hoc networks: Architectures, research issues, methodologies, challenges, and trends," *International Journal of Distributed Sensor Networks*, vol. 2015. Hindawi Publishing Corporation, 2015. doi: 10.1155/2015/745303.

[4] R. W. L. Coutinho, A. Boukerche, and A. A. F. Loureiro, "Design Guidelines for Information-Centric Connected and Autonomous Vehicles," *IEEE Communications Magazine*, vol. 56, no. 10, pp. 85–91, Oct. 2018, doi: 10.1109/MCOM.2018.1800134.

[5] X. Shen, X. Cheng, L. Yang, R. Zhang, and B. Jiao, "Data dissemination in VANETs: A scheduling approach," *IEEE Transactions on Intelligent Transportation Systems*, vol. 15, no. 5, pp. 2213–2223, Oct. 2014, doi: 10.1109/TITS.2014.2313631.

[6] R. Ghebleh, "A comparative classification of information dissemination approaches in vehicular ad hoc networks from distinctive viewpoints: A survey," *Computer Networks*, vol. 131. Elsevier B.V., pp. 15–37, Feb. 11, 2018. doi: 10.1016/j.comnet.2017.12.003.

[7] M. Chaqfeh, A. Lakas, and I. Jawhar, "A survey on data dissemination in vehicular ad hoc networks," *Vehicular Communications*, vol. 1, no. 4. Elsevier Inc., pp. 214–225, 2014. doi: 10.1016/j.vehcom.2014.09.001.

[8] M. Milojevic and V. Rakocevic, "Location-aware data aggregation for efficient message dissemination in vehicular ad hoc networks," *IEEE Trans Veh Technol*, vol. 64, no. 12, pp. 5575–5583, Dec. 2015, doi: 10.1109/TVT.2015.2487830.

[9] Y. Du *et al.*, "A Distributed Message Delivery Infrastructure for Connected Vehicle Technology Applications," *IEEE Transactions on Intelligent Transportation Systems*, vol. 19, no. 3, pp. 787–801, Mar. 2018, doi: 10.1109/TITS.2017.2701799.

[10] S. Bitam, A. Mellouk, and S. Zeadally, "HyBR: A Hybrid Bio-inspired Bee swarm Routing protocol for safety applications in Vehicular Ad hoc NETworks (VANETs)," *Journal of Systems Architecture*, vol. 59, no. 10 PART B, pp. 953–967, 2013, doi: 10.1016/j.sysarc.2013.04.004.

[11] C. Bian, T. Zhao, X. Li, and W. Yan, "Boosting named data networking for efficient packet forwarding in urban VANET scenarios," in *IEEE Workshop on Local and Metropolitan Area Networks*, May 2015, vol. 2015-May. doi: 10.1109/LANMAN.2015.7114718.

[12] M. C. Chuang and M. C. Chen, "DEEP: Density-aware emergency message extension protocol for VANETs," *IEEE Trans Wirel Commun*, vol. 12, no. 10, pp. 4983–4993, Oct. 2013, doi: 10.1109/TWC.2013.090413.121697.

[13] S. H. Ahmed, S. H. Bouk, M. A. Yaqub, D. Kim, H. Song, and J. Lloret, "CODIE: Controlled Data and Interest Evaluation in Vehicular Named Data Networks," *IEEE Trans Veh Technol*, vol. 65, no. 6, pp. 3954–3963, Jun. 2016, doi: 10.1109/TVT.2016.2558650.

[14] N. N. Dehaghani, R. Sadeghi, and S. M. F. Imani, "REF: A Novel Forwarding Strategy in Wireless NDN," *Wirel Pers Commun*, vol. 117, no. 2, pp. 1025–1042, Mar. 2021, doi: 10.1007/s11277-020-07909-8.

[15] R. Almesaeed and A. Jedidi, "Dynamic directional routing for mobile wireless sensor networks," *Ad Hoc Networks*, vol. 110, Jan. 2021, doi: 10.1016/j.adhoc.2020.102301.

[16] D. Kim, J. H. Kim, C. Moon, J. Choi, and I. Yeom, "Efficient content delivery in mobile ad-hoc networks using CCN," *Ad Hoc Networks*, vol. 36, pp. 81–99, Jan. 2016, doi: 10.1016/j.adhoc.2015.06.007.

[17] M. Amadeo, C. Campolo, and A. Molinaro, "Priority-based content delivery in the internet of vehicles through named data networking," *Journal of Sensor and Actuator Networks*, vol. 5, no. 4, Dec. 2016, doi: 10.3390/jsan5040017.

[18] C. Chen, Q. Pei, and X. Li, "A GTS Allocation Scheme to Improve Multiple-Access Performance in Vehicular Sensor Networks," *IEEE Trans Veh Technol*, vol. 65, no. 3, pp. 1549–1563, Mar. 2016, doi: 10.1109/TVT.2015.2412613.

[19] M. Amadeo, C. Campolo, and A. Molinaro, "Enhancing content-centric networking for vehicular environments," *Computer Networks*, vol. 57, no. 16, pp. 3222–3234, Nov. 2013, doi: 10.1016/j.comnet.2013.07.005.

[20] L. Liu, C. Chen, T. Qiu, M. Zhang, S. Li, and B. Zhou, "A data dissemination scheme based on clustering and probabilistic broadcasting in VANETs," *Vehicular Communications*, vol. 13, pp. 78–88, Jul. 2018, doi: 10.1016/j.vehcom.2018.05.002.

[21] X. Cheng and B. Huang, "A center-based secure and stable clustering algorithm for VANETs on highways," *Wirel Commun Mob Comput*, vol. 2019, 2019, doi: 10.1155/2019/8415234.

[22] B. Hassanabadi, C. Shea, L. Zhang, and S. Valaee, "Clustering in Vehicular Ad Hoc Networks using Affinity Propagation," *Ad Hoc Networks*, vol. 13, no. PART B, pp. 535–548, Feb. 2014, doi: 10.1016/j.adhoc.2013.10.005.

[23] K. Abboud and W. Zhuang, "Stochastic modeling of single-hop cluster stability in vehicular ad hoc networks," *IEEE Trans Veh Technol*, vol. 65, no. 1, pp. 226–240, Jan. 2016, doi: 10.1109/TVT.2015.2396298.

[24] M. Noor-A-Rahim, G. G. Nawaz Ali, H. Nguyen, and Y. L. Guan, "Performance Analysis of IEEE 802.11p Safety Message Broadcast with and Without Relaying at Road Intersection," *IEEE Access*, vol. 6, pp. 23786–23799, Apr. 2018, doi: 10.1109/ACCESS.2018.2829897.

[25] S. Tiennoy and C. Saivichit, "Using a Distributed Roadside Unit for the Data Dissemination Protocol in VANET with the Named Data Architecture," *IEEE Access*, vol. 6, pp. 32612–32623, May 2018, doi: 10.1109/ACCESS.2018.2840088.

[26] B. E. Y. Belmekki, A. Hamza, and B. Escrig, "Cooperative vehicular communications at intersections over Nakagami-m fading channels," *Vehicular Communications*, vol. 19, Oct. 2019, doi: 10.1016/j.vehcom.2019.100165.

[27] Y. Liu, F. R. Yu, X. Li, H. Ji, and V. C. M. Leung, "Blockchain and Machine Learning for Communications and Networking Systems," *IEEE Communications Surveys and Tutorials*, vol. 22, no. 2, pp. 1392–1431, Apr. 2020, doi: 10.1109/COMST.2020.2975911.

[28] F. Guo, F. R. Yu, H. Zhang, X. Li, H. Ji, and V. C. M. Leung, "Enabling Massive IoT Toward 6G: A Comprehensive Survey," *IEEE Internet of Things Journal*, vol. 8, no. 15. Institute of Electrical and Electronics Engineers Inc., pp. 11891–11915, Aug. 01, 2021. doi: 10.1109/JIOT.2021.3063686.

[29] J. Du, F. R. Yu, X. Chu, J. Feng, and G. Lu, "Computation offloading and resource allocation in vehicular networks based on dual-side cost minimization," *IEEE Trans Veh Technol*, vol. 68, no. 2, pp. 1079–1092, Feb. 2019, doi: 10.1109/TVT.2018.2883156.

[30] M. Liu, F. R. Yu, Y. Teng, V. C. M. Leung, and M. Song, "Computation offloading and content caching in wireless blockchain networks with mobile edge computing," *IEEE Trans Veh Technol*, vol. 67, no. 11, pp. 11008–11021, Nov. 2018, doi: 10.1109/TVT.2018.2866365.

[31] M. Liu, F. R. Yu, Y. Teng, V. C. M. Leung, and M. Song, "Distributed Resource Allocation in Blockchain-Based Video Streaming Systems with Mobile Edge Computing," *IEEE Trans Wirel Commun*, vol. 18, no. 1, pp. 695–708, Jan. 2019, doi: 10.1109/TWC.2018.2885266.

[32] Y. He *et al.*, "Deep-reinforcement-learning-based optimization for cache-enabled opportunistic interference alignment wireless networks," *IEEE Trans Veh Technol*, vol. 66, no. 11, pp. 10433–10445, Nov. 2017, doi: 10.1109/TVT.2017.2751641.

[33] Y. He, N. Zhao, and H. Yin, "Integrated networking, caching, and computing for connected vehicles: A deep reinforcement learning approach," *IEEE Trans Veh Technol*, vol. 67, no. 1, pp. 44–55, Jan. 2018, doi: 10.1109/TVT.2017.2760281.

[34] J. Du, F. R. Yu, G. Lu, J. Wang, J. Jiang, and X. Chu, "MEC-Assisted Immersive VR Video Streaming over Terahertz Wireless Networks: A Deep Reinforcement Learning Approach," *IEEE Internet Things J*, vol. 7, no. 10, pp. 9517–9529, Oct. 2020, doi: 10.1109/JIOT.2020.3003449.

[35] D. Saxena, V. Raychoudhury, N. Suri, C. Becker, and J. Cao, "Named Data Networking: A survey," *Computer Science Review*, vol. 19. Elsevier Ireland Ltd, pp. 15–55, Feb. 01, 2016. doi: 10.1016/j.cosrev.2016.01.001.

[36] L. Zhang *et al.*, "Named Data Networking (NDN) Project," 2010. [Online]. Available: http://named-data.net/techreports.html

Design and Fabrication Techniques for Nonlinear Metamaterials and Metasurfaces for Wireless Communication

J. Mangaiyarkkarasi, J. Shanthalakshmi Revathy (/affiliate/j-shanthalakshmirevathy/450287/)

Source Title: Metamaterial Technology and Intelligent Metasurfaces for Wireless Communication Systems (/book/metamaterial-technology-intelligent-metasurfaces-wireless/312573)

Pages: 28
DOI: 10.4018/978-1-6684-8287-2.ch004

Abstract

The chapter explores the development and manufacturing of tailored nonlinear metamaterials and metasurfaces for wireless communication. It covers design and fabrication techniques, material selection and characterization, and design considerations. The chapter also examines simulation and modelling techniques, advanced fabrication methods, integration into wireless communication systems, and characterization and testing processes. It addresses reliability and scalability challenges, the role of nonlinear effects, and the significance of reliability testing and performance characterization. Economic, scalability, and sustainability considerations are discussed, along with case studies and future trends in design and fabrication techniques. The chapter strongly emphasizes the potential of nonlinear metamaterials for enhancing wireless communication and aids as a valuable source for experts in the field.

Chapter Preview

Top

Overview Of Design And Fabrication Techniques

To understand the design and fabrication techniques of nonlinear metamaterials and metasurfaces for wireless communication, it is essential to have the knowledge of their classifications (Quevedo-Teruel & Chen, 2021). Some common classification categories for nonlinear metamaterials and metasurfaces based on the properties, in the context of wireless communication are,

Complete Chapter List

Search this Book: Full text search terms

Reset

Chapter 1

Metamaterials-Based Antenna for 5G and Beyond (/chapter/metamaterials-based-antenna-for-5g-and-beyond/328941) (pages 1-35)

Smrity Dwivedi

Preview Chapter (/viewtitlesample.aspx?id=328941&ptid=312573&t=Metamaterials-Based Antenna for 5G and Beyond&isxn=9781668482872) **$37.50** Add to Cart

Chapter 2

Review of Antenna Performance Based on Metamaterials (/chapter/review-of-antenna-performance-based-on-metamaterials/328942) (pages 36-63)

Devendra Kumar Somwanshi

Preview Chapter (/viewtitlesample.aspx?id=328942&ptid=312573&t=Review of Antenna Performance Based on Metamaterials&isxn=9781668482872) **$37.50** Add to Cart

Chapter 3

Prospect of Dynamic Metasurface Array Antenna System With Machine Learning (/chapter/prospect-of-dynamic-metasurface-array-antenna-system-with-machine-learning/328943) (pages 64-81)

Rupesh Kumar

Preview Chapter (/viewtitlesample.aspx?id=328943&ptid=312573&t=Prospect of Dynamic Metasurface Array Antenna System With Machine Learning&isxn=9781668482872) **$37.50** Add to Cart

Chapter 4

Design and Fabrication Techniques for Nonlinear Metamaterials and Metasurfaces for Wireless Communication (/chapter/design-and-fabrication-techniques-for-nonlinear-metamaterials-and-metasurfaces-for-wireless-communication/328944) (pages 82-109)

J. Mangaiyarkkarasi, J. Shanthalakshmi Revathy

Preview Chapter (/viewtitlesample.aspx?id=328944&ptid=312573&t=Design and Fabrication Techniques for Nonlinear Metamaterials and Metasurfaces for Wireless Communication&isxn=9781668482872) **$37.50** Add to Cart

Chapter 5

Metamaterial-Based Absorber (/chapter/metamaterial-based-absorber/328945) (pages 110-120)

Mehaboob Mujawar, Subuh Pramono

Preview Chapter (/viewtitlesample.aspx?id=328945&ptid=312573&t=Metamaterial-Based Absorber&isxn=9781668482872) **$37.50** Add to Cart

Chapter 6

Study of Novel Design of Multi-Band and Broad-Band Metamaterial Microwave Absorber (/chapter/study-of-novel-design-of-multi-band-and-broad-band-metamaterial-microwave-absorber/328946) (pages 121-135)

Alkesh Agrawal, Bhagwant Singh

Preview Chapter (/viewtitlesample.aspx?id=328946&ptid=312573&t=Study of Novel Design of Multi-Band and Broad-Band Metamaterial Microwave Absorber&isxn=9781668482872) **$37.50** Add to Cart

ISSN 1330-3651 (Print), ISSN 1848-6339 (Online)
https://doi.org/10.17559/TV-20221128071759
Original scientific paper

Intelligent Intrusion Detection System using Enhanced Arithmetic Optimization Algorithm with Deep Learning Model

S. KAVITHA*, N. UMA MAHESWARI, R. VENKATESH

Abstract: The widespread use of interoperability and interconnectivity of computing systems is becoming indispensable for enhancing our day-to-day actions. The susceptibilities deem cyber-security systems necessary for assuming communication interchanges. Secure transmission needs security measures for combating the threats and required developments to security measures that counter evolving security risks. Though firewalls were devised to secure networks, in real-time they cannot detect intrusions. Hence, destructive cyber-attacks put forward severe security complexities, requiring reliable and adaptable intrusion detection systems (IDS) that could monitor unauthorized access, policy violations, and malicious activity practically. Conventional machine learning (ML) techniques were revealed for identifying data patterns and detecting cyber-attacks IDSs successfully. Currently, deep learning (DL) methods are useful for designing accurate and effective IDS methods. In this aspect, this study develops an intelligent IDS using enhanced arithmetic optimization algorithm with deep learning (IIDS-EAOADL) method. The presented IIDS-EAOADL model performs data standardization process to normalize the input data. Besides, equilibrium optimizer based feature selection (EOFS) approach is developed to elect an optimal subset of features. For intrusion detection, deep wavelet autoencoder (DWAE) classifier is applied. Since the proper tuning of parameters of the DWNN is highly important, EAOA algorithm is used to tune them. For assuring the simulation results of the IIDS-EAOADL technique, a widespread simulation analysis takes place using a benchmark dataset. The experimentation outcomes demonstrate the improvements of the IIDS-EAOADL model over other existing techniques

Keywords: arithmetic optimization algorithm; deep learning; feature selection; intrusion detection; security

1 INTRODUCTION

The usage of Internet applications and services is gradually increasing in number of applications like e-commerce and e-learning, which escalates concerns regarding privacy and security. With this usage, breaching cybersecurity using additional and recently established hacking and phishing tools has simultaneously improved for violating the Integrity, Confidentiality, and Availability (CIA) principles. Malicious software (malware) refers to a code that allows to bypass access controls, steal data, or compromise or harm an Internet of Things (IoT) system, a software system, or a computer network [1]. For this reason, dissimilar protection approaches like anti-malware, firewalls, and encryption tools were employed to prevent cyberattacks, whereas digital forensics technique has been utilized to examine the attacks. The emergence of new cyberattacks and zero-day attacks makes the defence against them considerable security problems in the extensive network [2]. An Intrusion Detection System (IDS) can be referred to software application or device that is regarded as a defensive wall. The basic function of the IDS is to monitor the behaviour and activity of network traffic for identifying malicious and abnormal activities and generate reports and alerts of these behaviours. Fig. 1 depicts the architecture of IDS.

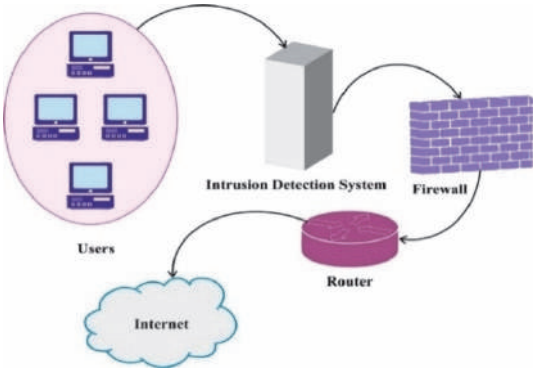

Figure 1 Framework of Intrusion Detection Systems

The IDS would be referred as software or hardware system that works in an automatic manner which helps to monitor the actions which are carried out within the system. It is widely applied with respect to security method and IDS alert is used for system administrators to produce a log based on attack while it predicts the occurrence of any event in host or a network. The IDS can be implemented inside a network on the basis of required action. It is used for detecting the attacks based on maximum patterns and procedures that have distinct signature. Thus, prediction of IDS improves the number of rules. However, presence of massive rules does not refer the input data to be related with alternate procedures. Hence, more amounts of rules tend to machine overhead. Rather than using a typical IDS, an intelligent and robust IDS is required because different systems have the capacity of hiding suspicious network traffic [3]. The classification of IDS depends on different conditions namely the data source and the response and detection models. Network-and Host-based models are the most important classes of IDS based on the data source, whereas signature-and anomaly based models are the major technologies based on the detection technique [4]. IDS handles an enormous quantity of data in the network traffic where data contains irrelevant, noisy, and redundant features that affect the performance of IDS and consume further resources. Consequently, dimension reduction was required for enhancing the efficacy of IDS [5].

With adequate computing power and massive quantity of information gathered from interconnected devices [6], DL model has been taken into account to improve the security of IoT with respect to user behaviors analysis, intrusion detection, privacy preserving, and vulnerabilities [7]. DL technique and particularly CNN is used to identify, learn, and extract complicated patterns and features directly from raw IoT information thereby enhancing the utility of the devices to effectively potential possible attacks and threats in the IoT platform [8]. Furthermore, DL model is very effective in automated feature extraction instead of dependent on conventional machine learning

(ML) method that demands handcrafted statistical features. Over the last few years, researcher workers had proposed different approaches for IDSs [9]. Various ML approaches have been developed for security problems. Additionally, DL model is utilized in IoT environments like generative adversarial networks (GAN) to improve the device utility and secure user private information [10]. Feature selection techniques have proven great performance in IDS with different classifications. Recently, metaheuristics optimization algorithm has been devised for many challenging issues, involving feature selection.

This study develops an intelligent IDS using enhanced arithmetic optimization algorithm with deep learning (IIDS-EAOADL) method. The presented IIDS-EAOADL method performs data standardization process to normalize the input data. Besides, equilibrium optimizer based feature selection (EOFS) approach is developed to elect an optimal subset of features. For intrusion detection, deep wavelet autoencoder (DWAE) classifier is applied. Since the proper tuning of parameters of the DWNN is highly important, EAOA algorithm is used to tune them. For assuring the simulation results of the IIDS-EAOADL technique, a widespread simulation analysis takes place using benchmark dataset.

2 RELATED WORKS

In [11], an artificial neural network (ANN) can be used for the detection of abnormal action in a medical IoT mechanism. The detection precision is based on the features that were granted to the ANN. The crucial and challenging problem of network traffic is choosing the significant and discriminatory features as it has a substantial effect on the learning procedure. In this presented technique, the butterfly optimized approach is a metaheuristic optimized technique used for selecting the best features for the learning procedure in an ANN. Fatani et al. [12] introduce a potential AI-related system for IDS in IoT systems. The metaheuristics (MH) algorithms and deep learning advancements are used by the authors that ensure effectiveness in resolving complicated engineering complexities. Moreover, feature extracting technique utilizing CNN is devised by the authors for extracting appropriate features. In addition, the authors advanced an innovative feature selecting approach utilizing an innovative variant of the transient search optimization (TSO) technique, termed TSODE, and leverage the operatives of differential evolution (DE) method.

Alzaqebah et al. [13] present an altered bio-inspired approach, which is the GWO that improves the efficiency of the IDS in identifying normal as well as anomalous traffic in the networks. The key developments include the smart initializing stage that integrates the filter and wrapper techniques for assuring the informative features that are added in initial iterations. Moreover, to tune the parameters of ELM, the authors approved the Extreme Learning Machine (ELM), modified GWO, and high-speed classification method. Fatani et al. [14] projected creative feature selecting and extracting algorithms for the IDS by making use of the benefits of the swarm intelligence (SI) approaches. Additionally feature extracting system based on the CNN is devised by the author. Then an alternative feature selection (FS) method utilizing the recently advanced Aquila optimizer (AQU) and SI algorithm.

In [15], an IDS can be presented that uses ML and data mining ideas for detecting network intrusion paradigms. In the presented technique, an ANN was utilized as a learning technique. The meta-heuristic algorithm including the swarm-related method can be employed for minimizing ID errors. To reduce ID error rate, the Grasshopper Optimization Algorithm (GOA) was utilized for more accurate and better learning of ANNs. The role of the GOAMLP method was to reduce the ID error in the NN through selection of valuable variables like weight and bias. In [16], an innovative IDS can be modelled that uses the butterfly optimization algorithm (BOA), for executing FS. And to assess the ability of the features which is chosen for predicting assaults, a multi-layer perceptron (MLP) classifier was employed. With a view to enhancing the MLP method, not just the gradient descent (GD) training approach along with 2 meta-heuristic techniques, GA, and PSO were employed for optimizing the classifier structure. In [17], a wrapper FS method for IDS is devised. This technique will make use of the pigeon inspired optimizer for using the selective procedure. A novel technique to binarize a continual pigeon inspired optimizer was modelled and made a comparison with the conventional way of binarizing continual SI methods.

3 THE PROPOSED MODEL

In this study, a new IIDS-EAOADL algorithm was presented for intrusion detection process. To attain this, the presented IIDS-EAOADL model performs data standardization process to normalize the input data. Next, a novel EOFS technique is developed to elect an optimal subset of features. Followed by, the EAOA with DWAE classifier is applied to recognize and classify intrusions. Fig. 2 demonstrates the block diagram of the IIDS-EAOADL approach.

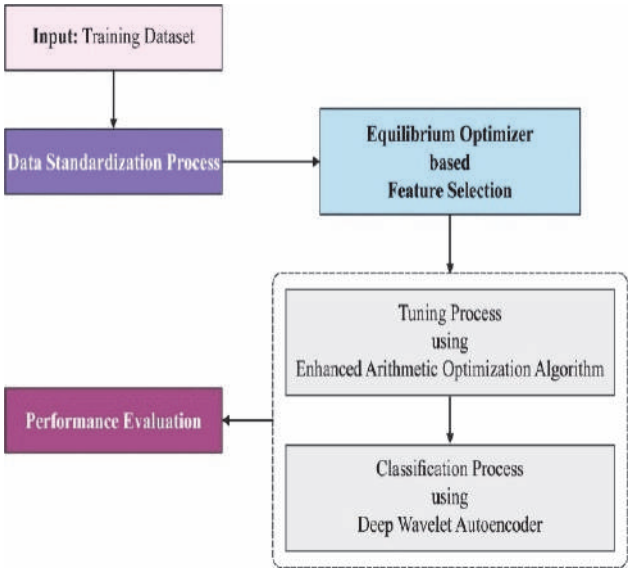

Figure 2 Block diagram of IIDS-EAOADL approach

3.1 Feature Selection Using EOFS Model

In this study, a novel EOFS technique is formulated to elect an optimal subset of features. The EO algorithm is a

metaheuristic technique stimulated by the law of physics that is used to evaluate the equilibrium state [18]. Similar to other optimization techniques, the EO algorithm originated from initial population of the particles. The following equation demonstrates the initial population of the EOA with *n* particles.

$$P_z^{'} = P_{\text{Min}} + \Re_z \left(P_{\text{Max}} - P_{\text{Min}} \right), z = 1, 2, 3, ..., n \tag{1}$$

where $P_z^{'}$ indicates the primary concentration of particle z, P_{Max} represents maximal number of dimensions, P_{Min} signifies minimal number of dimensions, n depicts overall amount of particles, and $\Re_z$ implies random value lies in [0, 1]. For finding the equilibrium state of particle, all the particles in the population are estimated to define the objective function. Next, the concentration updating approach is carried out according to the equilibrium pool that comprises 4 optimum candidate particles and it is mathematically expressed as follows.

$$P_{\text{New}} = P_r + \frac{g_R}{\gamma}\left(1 - f\right) + \left(P - P_r\right) \cdot f \tag{2}$$

Now, P denotes present concentration vector, P_r shows random concentration vector, generation rate is represented by g_R, the exponential term is indicated by f, and the random vector is characterized by γ which is fixed to [0, 1].

Furthermore, the exponential term f and generation rate g_R are evaluated as follows.

$$g_R = \begin{cases} 0.5 R_1 \left(P_r - \gamma P \right) f, \text{ if } R_2 \geq g_p \\ 0, \text{ if } R_2 < g_p \end{cases} \tag{3}$$

$$f = C_1 \, si \, gn\left(\lambda - 0.5\right) \cdot \left(e^{-\gamma \left(1 - \left(t / t_{\text{Max}}\right)\right) C_2 \left(t / t_{\text{Max}}\right)} - 1 \right)$$

Here, R_1 and R_2 indicate the random values within [0, 1], λ represents the random vector amongst zero and one, C_1 and C_2 are constants set to 2 and 1, correspondingly. Likewise, the generation probability g_R is fixed to 0.5; t and t_{Max} depicts existing and overall iterations, correspondingly.

Next, every concentration vector of the particle was restored based on the contribution. The first term demonstrates the random concentration vector gained from the creation of equilibrium pool. The final two terms examine the concentration difference and are responsible for precise exploration and exploitation. Therefore, EO algorithm accomplishes optimum solution from the search space.

The fitness function (FF) of the EO-FS technique will consider the classifier accuracy and the selected features count. It optimizes the classifier accuracy and reduces the set sizes of features which are chosen. Thus, the subsequent FF can be employed for evaluating separate solutions, as given in Eq. (4).

$$Fitness = \alpha \cdot ErrorRate + \left(1 - \alpha\right) \cdot \frac{\#SF}{\#All\_F} \tag{4}$$

where as *ErrorRate* denotes the classifier error rate utilizing the features which are selected. *ErrorRate* can be the complement of the classifier accuracy, *#SF* refers to the selected attributes count and *#All_F* was the total count of features in the original data. α can be employed to control the significance of subset length and classification quality. In these experiments, α indicates set to 0.9.

3.2 Intrusion Detection Using DWAE Model

To identify and categorize intrusions, the DWAE model is applied. The standard autoencoder (AE) features robustness, strong inference ability, and unsupervised feature learning capability [19]. The property of WT has time-frequency localization and focal features. As a result, it is necessary to integrate wavelet transform and typical AE to resolve the real time problems. This study presents a novel type of unsupervised neural network named "DWAE" that could catch non-stationary vibration signals and characterize complicated data. The WAE applied the wavelet function as activation function in conventional state, which defined diverse resolutions.

$$X = \varsigma\left(\hat{\kappa}' Y + b'\right) \tag{5}$$

In Eq. (5), $\hat{X}$ shows the outcomes of the recreated vector, κ signifies kernel vector, b' designates bias value, and $\in$ indicates an error value added in the process of BP. Training instances $y = \left[y_1, y_2, ..., y_n\right]^A$ the output of hidden unit represents *i*.

$$g_j\left(out\right) = \varphi \frac{\left(\sum_{i-1}^{n} v_{ij} y_l - e_i\right)}{b_i} \tag{6}$$

where as: φ indicates the wavelet activation function.

$y_l\left(r = 1, 2, ..., n\right)$ shows the *l*-th dimension input of training instance,

$v_{ij}\left(r = 1, 2, ..., g\right)$ refers to the weight connecting between 1the hidden unit *i* and input unit.

b_i and e_i represents $v_{ij}\left(r = 1, 2, ..., g\right)$ transmitted the scale and shift factors of wavelet activation function for the hidden unit *i*.

$$\varphi\left(a\right) = \cos\left(5a\right) \exp\left(\frac{a^2}{2}\right) \tag{7}$$

$$g_i\left(out\right) = \varphi_{be}\left(i\right) = \cos\left(5 \times \frac{\left(\sum_{i-1}^{n} v_{ij} y_l - e_i\right)}{b_i} \right) 2 \times \times \left(\left(-\frac{1}{2} \frac{\left(\sum_{i-1}^{n} v_{ij} y_l - e_i\right)}{b_i} \right) 2 \right) \tag{8}$$

Like typical AE, we select the output layer activation function as sigmoid function. Next, the output of deep WAE is evaluated as follows:

$$\hat{y} = \mathrm{sig}m\left(\sum_{i-1}^{q} v_{ri}\left(\cos 5\times\frac{\left(\sum_{i-1}^{n} v_{ij}y_l - e_i\right)}{b_i}\right)\right) \times\exp\left(-\frac{1}{2}\frac{\left(\sum_{i-1}^{n} v_{ij}y_l - e_i\right)}{b_i}\right)2\Bigg) \tag{9}$$

Now, $\hat{y}$ indicates i the recreated dimension output of training instances, and v_{ri} shows the weight connecting between hidden r and i.

3.3 Parameter Tuning Using EAOA

Since the proper tuning of parameters of the DWNN is highly important, EAOA algorithm is used to tune them [20]. The elementary AOA operation includes initialization, exploration, and exploitation.

(a) Initialization. Candidate solution (XA) is randomly produced. The present population is characterized as the matrix XA. The dimension is represented as DM. The number of individuals can be signified as NP. The optimally accomplished solution was the better solution for all the iterations.

$$XA = \begin{Bmatrix} xa_{1,1} & \cdots & xa_{1,DM-1} & xa_{1,DM} \\ xa_{2,1} & \cdots & xa_{2,DM-1} & xa_{2,DM} \\ \vdots & \cdots & \vdots & \vdots \\ xa_{NP,1} & \cdots & xa_{NP,DM-1} & xa_{NP,DM} \end{Bmatrix} \tag{10}$$

The search phrase was selected as an exploitation or exploration stage using MOA function as follows.

$$MOA(iter) = \min iter + iter\times\left(\frac{\max iter - min\, iter}{Miter}\right) \tag{11}$$

In Eq. (11), Miter denotes the maximal amount of iterations. The present iteration is represented as iter. The maximum and minimum MOA values were max$iter$ and min$iter$, correspondingly. max$iter$ and min$iter$ are variables that are defined as specific values in advance of start of AOA. maxiter and miniter are fixed as 0.2 and 1, correspondingly.

At last, the better solution for the existing iteration is the ideal solution. The present optimum fitness is compared with the prior optimum fitness, and the lowest value was used to define the final optimum solution. The EAOA technique is derived from the use of chaotic concepts with the AOA. Chaotic mapping refers to multi-variate non-linear functions that are used for nonlinear deterministic prediction of time sequences dataset to population, thus enhancing the global searching ability of AOA. In this work, circle chaotic mapping is utilized in the AOA to enhance the initialization population.

The circle map is formulated below:

$$x_{k+1} = x + b - (P - 2\pi)\sin(2\pi x)\, mod\,(1) \tag{12}$$

where $b = 0.2$, and $P = 0.5$ refers to the control variable.

The EAOA algorithm will derive an FF for achieving enhanced classifier outcomes. It sets a positive value for indicating superior performance of the candidate solutions. In this article, the reduction of the classifier will be regarded as the FF, as shown in Eq. (13).

$$fitness(x_i) = ClassifierErrorRate(x_i) = \\ = \frac{number\ of\ misclassified\ samples}{Total\ number\ of\ samples}\cdot 100 \tag{13}$$

4 RESULTS AND DISCUSSION

In this section, the experimental validation of the IIDS-EAOADL method is tested using the NSLKDD dataset. The presented IIDS-EAOADL model has chosen a set of 19 features from the existing 42 features as shown in Tab. 1.

Table 1 Dataset details

Class	No. of Samples
Normal	77053
DoS	53385
Probe	14078
R2L	3882
U2R	119
Total Number of Samples	148517

The parameter setting is given as follows: Population size: 10, HCMR: 0.99, PAR: 0.33, fw/bw: 0.01. It has 148517 number of samples which falls under two categories namely normal and anomaly.

Fig. 3 exemplifies the set of confusion matrices formed by the IIDS-EAOADL model. On entire dataset, the IIDS-EAOADL method has categorized 76251 instances into normal class, 52541 instances into DoS class, 13621 instances into Probe, 3405 instances into R2L, and 0 instances under U2R. Also, on 70% of TR data, the IIDS-EAOADL approach has categorized 53359 instances into normal class, 36882 instances into DoS class, 9414 instances into Probe, 2377 instances into R2L, and 0 instances under U2R. In addition, on 30% of TS data, the IIDS-EAOADL technique has categorized 22892 instances into normal class, 15659 instances into DoS class, 4207 instances into Probe, 1028 instances into R2L, and 0 instances under U2R.

Tab. 2 provides overall IDS outcomes of the IIDS-EAOADL model. Fig. 4 demonstrates brief IDS results of the IIDS-EAOADL method on entire dataset. The figure highlighted that the IIDS-EAOADL approach has reached enhanced performance in every class label. For example, on normal class, the IIDS-EAOADL method has obtained $accu_y$ of 98.82%, $prec_n$ of 98.78%, $reca_l$ of 98.96%, F_{measure} of 98.87%, and MCC of 97.64%. Simultaneously, on probe class, the IIDS-EAOADL algorithm has gained $accu_y$ of 99.21%, $prec_n$ of 94.97%, $reca_l$ of 96.75%, F_{measure} of 95.85%, and MCC of 95.42%. Concurrently, on R2L class, the IIDS-EAOADL method has obtained $accu_y$ of 99.34%, $prec_n$ of 87.11%, $reca_l$ of 87.71%, F_{measure} of 87.41%, and MCC of 87.07%.

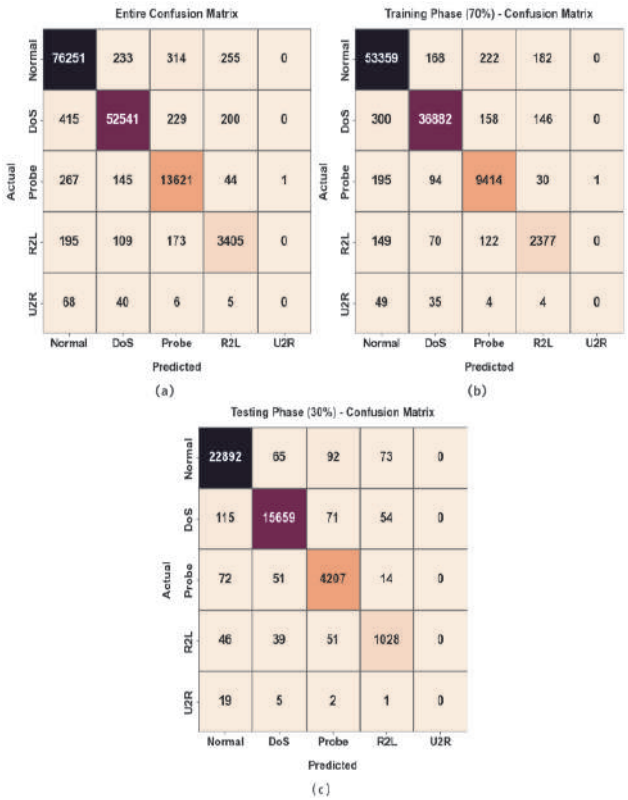

Figure 3 Confusion matrices of IIDS-EAOADL approach (a) Entire dataset, (b) 70% of TR data, and (c) 30% of TS data

Table 2 Result analysis of IIDS-EAOADL algorithm with distinct class labels and measures

Labels	*Accuracy*	*Precision*	*Recall*	$F_{measure}$	*MCC*
Entire Dataset					
Normal	98.82	98.78	98.96	98.87	97.64
DoS	99.08	99.01	98.42	98.71	97.99
Probe	99.21	94.97	96.75	95.85	95.42
R2L	99.34	87.11	87.71	87.41	87.07
U2R	99.92	00.00	00.00	00.00	-0.01
Average	99.27	75.97	76.37	76.17	75.62
Training Phase (70%)					
Normal	98.78	98.72	98.94	98.83	97.56
DoS	99.07	99.01	98.39	98.70	97.97
Probe	99.21	94.90	96.71	95.80	95.36
R2L	99.32	86.78	87.45	87.12	86.77
U2R	99.91	00.00	00.00	00.00	-0.01
Average	99.26	75.88	76.30	76.09	75.53
Testing Phase (30%)					
Normal	98.92	98.91	99.01	98.96	97.83
DoS	99.10	98.99	98.49	98.74	98.04
Probe	99.21	95.12	96.85	95.97	95.54
R2L	99.38	87.86	88.32	88.09	87.77
U2R	99.94	00.00	00.00	00.00	00.00
Average	99.31	76.18	76.53	76.35	75.84

Fig. 5 establishes the detailed IDS results of the IIDS-EAOADL approach on 70% of TR data. The figure emphasized the IIDS-EAOADL methodology has reached enhanced performance in all classes. For example, on normal class, the IIDS-EAOADL approach has reached $accu_y$ of 98.78%, $prec_n$ of 98.72%, $reca_l$ of 98.94%, F_{measure} of 98.83%, and *MCC* of 97.56%. Concurrently, on probe class, the IIDS-EAOADL method has achieved $accu_y$ of 99.21%, $prec_n$ of 94.90%, $reca_l$ of 96.71%, F_{measure} of 95.80%, and *MCC* of 95.36%. Parallelly, on R2L class, the IIDS-EAOADL approach has attained $accu_y$ of 99.32%, $prec_n$ of 86.78%, $reca_l$ of 87.45%, F_{measure} of 87.12%, and *MCC* of 86.77%.

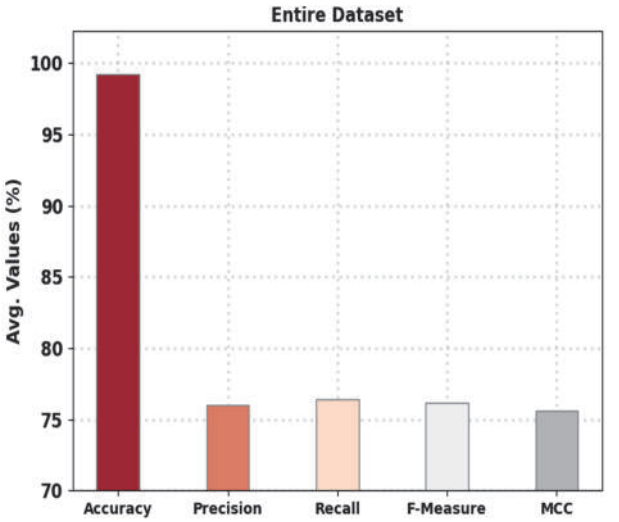

Figure 4 Average analysis of IIDS-EAOADL algorithm under entire dataset

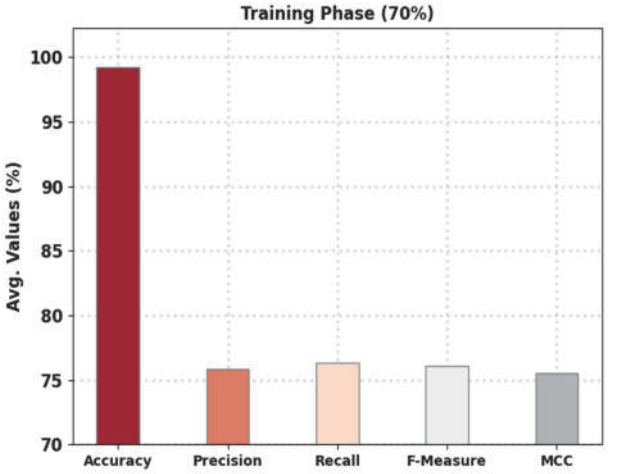

Figure 5 Average analysis of IIDS-EAOADL algorithm under 70% of TR data

Fig. 6 portrays the comparative IDS results of the IIDS-EAOADL algorithm on 30% of TS data. The figure pointed that the IIDS-EAOADL methodology has reached enhanced performance under all classes. For example, on normal class, the IIDS-EAOADL approach has attained $accu_y$ of 98.92%, $prec_n$ of 98.91%, $reca_l$ of 99.01%, F_{measure} of 98.96%, and *MCC* of 97.83%. At the same time, on probe class, the IIDS-EAOADL approach has acquired $accu_y$ of 99.21%, $prec_n$ of 95.12%, $reca_l$ of 96.85%, F_{measure} of 95.97%, and *MCC* of 95.54%. Simultaneously, on R2L class, the IIDS-EAOADL method has attained $accu_y$ of 99.38%, $prec_n$ of 87.86%, $reca_l$ of 88.32%, F_{measure} of 88.09%, and *MCC* of 87.77%.

The training accuracy (TRA) and validation accuracy (VLA) achieved by the IIDS-EAOADL approach under test dataset is shown in Fig. 7. The experimental outcome denotes the IIDS-EAOADL approach has acquired maximal values of TRA and VLA. Seemingly the VLA is greater than TRA.

The training loss (TRL) and validation loss (VLL) obtained by the IIDS-EAOADL technique under test dataset are displayed in Fig. 8. The experimental result highlighted the IIDS-EAOADL algorithm has exhibited minimal values of TRL and VLL. Particularly, the VLL is lesser than TRL.

A clear precision-recall inspection of the IIDS-EAOADL method under test dataset is depicted in Fig. 9. The figure represented the IIDS-EAOADL methodology has resulted in enhanced values of precision-recall values in every class label.

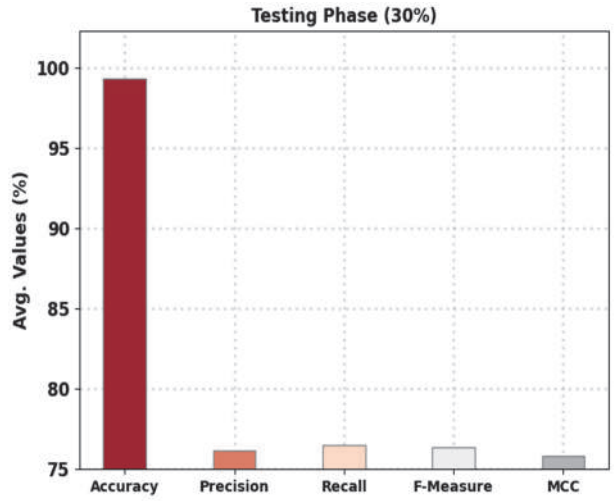

Figure 6 Average analysis of IIDS-EAOADL algorithm under 30% of TS data

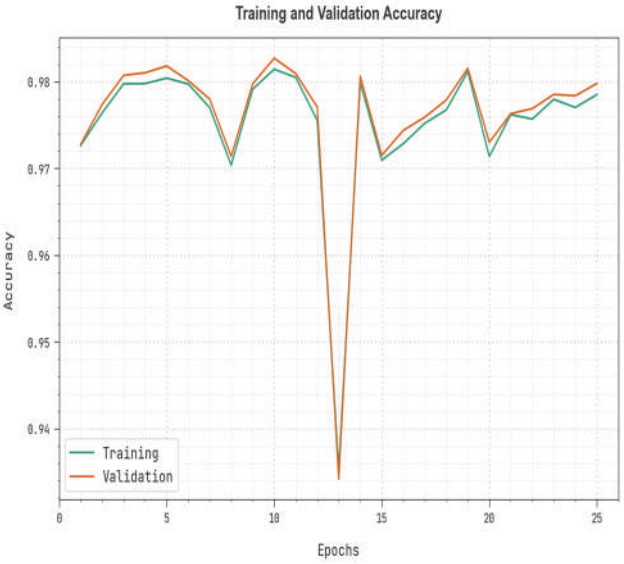

Figure 7 TRA and VLA analysis of IIDS-EAOADL algorithm

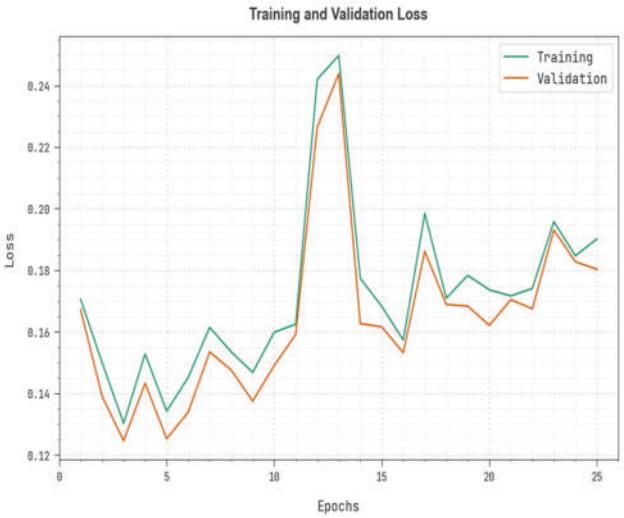

Figure 8 TRL and VLL analysis of IIDS-EAOADL algorithm

A brief ROC study of the IIDS-EAOADL approach in test dataset is portrayed in Fig. 10. The outcomes pointed that the IIDS-EAOADL method has displayed its capability in classifying different classes.

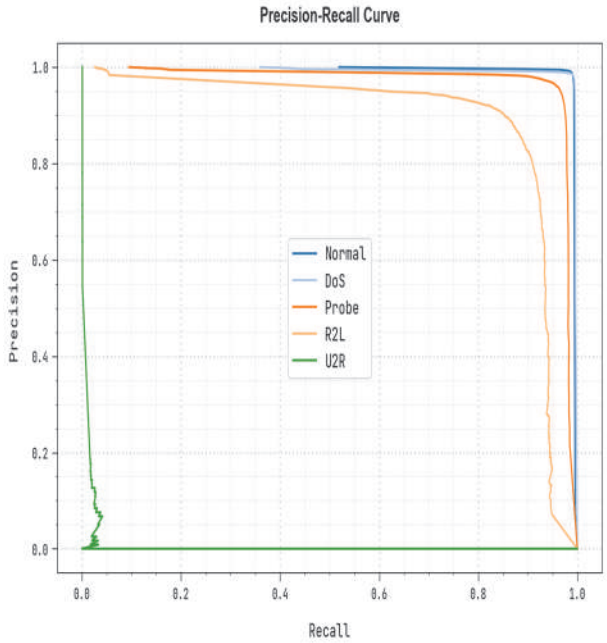

Figure 9 Precision-recall analysis of IIDS-EAOADL algorithm

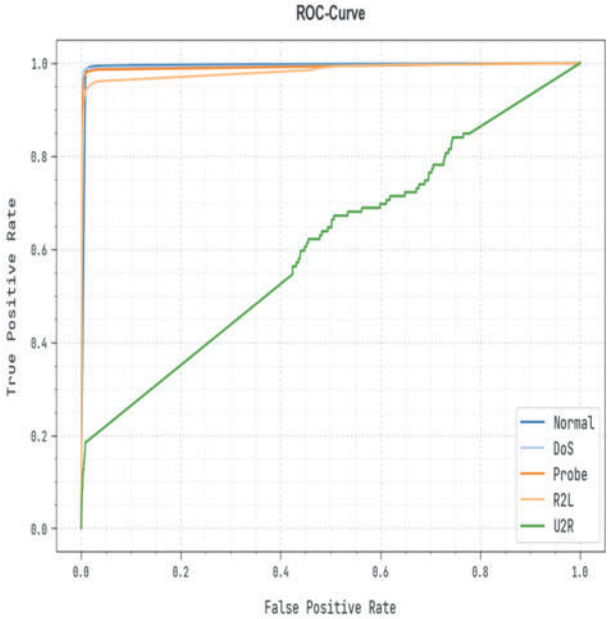

Figure 10 ROC curve analysis of IIDS-EAOADL algorithm

Tab. 3 presents a comparative analysis of the IIDS-EAOADL method with recent models [12]. A detailed $accu_y$ examination of the IIDS-EAOADL model with other IDS models is given in Fig. 11. These results denoted the MFO, TSO, and GWO techniques have exhibited ineffectual outcome with reduced $accu_y$ values of 95.90%, 96.41%, and 96.51% respectively. Followed by, the BAT algorithm has attained slightly improvised $accu_y$ $accu_y$ of 98.35%. In line with, the MVO and TSODE techniques have resulted in reasonable $accu_y$ of 99.20% and 99.16% respectively. But the IIDS-EAOADL model has accomplished maximum $accu_y$ of 99.31%.

Table 3 Comparative analysis of IIDS-EAOADL approach with existing methodologies

Methods	*Accuracy*	Running Time / sec
IIDS-EAOADL	99.31	0.860
MVO Algorithm	99.20	6.400
GWO Algorithm	96.51	1.117
MFO Algorithm	95.90	3.617
BAT Algorithm	98.35	6.483
TSODE Algorithm	99.16	8.450
TSO Algorithm	96.41	2.550

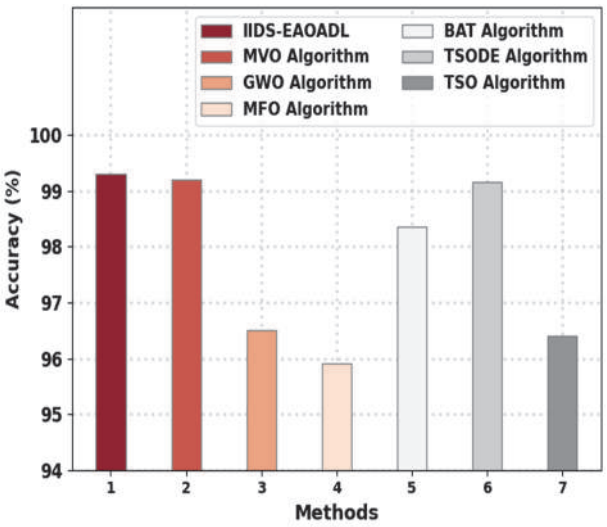

Figure 11 Accuracy analysis of IIDS-EAOADL approach with existing methodologies

A comprehensive RT review of the IIDS-EAOADL approach with other IDS methods is given in Fig. 12. These results denote that the MVO, TSODE, and BAT approaches have exhibited ineffectual outcome with higher RT of 6.4 s, 6.483 s, and 8.450 s correspondingly.

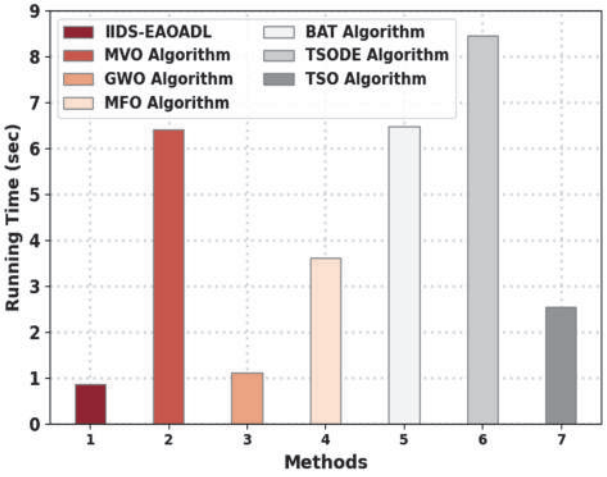

Figure 12 RT analysis of IIDS-EAOADL approach with existing methodologies

Then, the MFO and TSO algorithms have gained slightly decreased RT of 3.617 s and 2.550 s correspondingly. In this context, the GWO method has resulted in reasonable RT of 1.117 s. But the IIDS-EAOADL technique has exhibited minimal RT of 0.860 s. These results affirmed the betterment of the IIDS-EAOADL model over other models.

5 CONCLUSION

In this study, a new IIDS-EAOADL approach was presented for intrusion detection process. To attain this, the presented IIDS-EAOADL model performs data standardization process to normalize the input data. Next, a novel EOFS technique is developed to elect an optimal subset of features. Followed by, the DWAE classifier is applied to recognize and classify intrusions. Since the proper tuning of parameters of the DWNN is highly important, EAOA algorithm is used to tune them. For assuring the simulation results of the IIDS-EAOADL technique, a widespread simulation analysis takes place using benchmark dataset. The experimentation results demonstrate the improvements of the IIDS-EAOADL method over other existing techniques. Thus, the presented IIDS-EAOADL technique can be utilized for maximum detection efficiency. In future, hybrid DL methods will be applied to further boost the overall intrusion classification outcomes. Also, the proposed work can be further improved by the use of data reduplication techniques. In addition, data encryption technique can also be employed for secure data transmission in cloud environment.

6 REFERENCES

[1] Almomani, O. (2021). A hybrid model using bio-inspired metaheuristic algorithms for network intrusion detection system. *Computers, Materials & Continua*, *68*(1), 409-429. https://doi.org/10.32604/cmc.2021.016113

[2] Dahou, A., Abd Elaziz, M., Chelloug, S. A., Awadallah, M. A., Al-Betar, M. A., Al-qaness, M. A., & Forestiero, A. (2022). Intrusion Detection System for IoT Based on Deep Learning and Modified Reptile Search Algorithm. *Computational Intelligence and Neuroscience*. https://doi.org/10.1155/2022/6473507

[3] Hakkoymaz, V. (2020). Classifying Database Users for Intrusion Prediction and Detection in Data Security. *Tehnički vjesnik*, *27*(6), 1857-1862. https://doi.org/10.17559/TV-20190710100638

[4] Premkumar, M., Sundararajan, T. V. P., & Mohanbabu, G. (2022). Dynamic Defense Mechanism for DoS Attacks in Wireless Environments Using Hybrid Intrusion Detection System and Statistical Approaches. *Tehnički vjesnik*, *29*(3), 965-970. https://doi.org/10.17559/TV-20210604113859

[5] Khare, N., Devan, P., Chowdhary, C. L., Bhattacharya, S., Singh, G., Singh, S., & Yoon, B. (2020). Smo-dnn: Spider monkey optimization and deep neural network hybrid classifier model for intrusion detection. *Electronics*, *9*(4), 692. https://doi.org/10.3390/electronics9040692

[6] Malibari, A. A., Alotaibi, S. S., Alshahrani, R., Dhahbi, S., Alabdan, R., Al-wesabi, F. N., & Hilal, A. M. (2022). A novel metaheuristics with deep learning enabled intrusion detection system for secured smart environment. *Sustainable Energy Technologies and Assessments*, *52*. https://doi.org/10.1016/j.seta.2022.102312

[7] Lateef, A. A. A., Al-Janabi, S. T. F., & Al-Khateeb, B. (2020). Hybrid intrusion detection system based on deep learning. 2020 *IEEE International Conference on Data Analytics for Business and Industry: Way Towards a Sustainable Economy (ICDABI)*, 1-5. https://doi.org 10.1109/ICDABI51230.2020.9325669

[8] Kareem, S. S., Mostafa, R. R., Hashim, F. A., & El-Bakry, H. M. (2022). An effective feature selection model using hybrid metaheuristic algorithms for iot intrusion detection. *Sensors*, 22(4). https://doi.org/10.3390/s22041396

[9] Rai, A. (2020).Optimizing a new intrusion detection system using ensemble methods and deep neural network. *IEEE 4th International Conference on Trends in Electronics and Informatics (ICOEI).* 527-532. https://doi.org/10.1109/ICOEI48184.2020.9143028
[10] Almomani, O. (2020). A feature selection model for network intrusion detection system based on PSO, GWO, FFA and GA algorithms. *Symmetry*, *12*(6). https://doi.org/10.3390/sym12061046
[11] Li, Y., Ghoreishi, S. M., & Issakhov, A. (2021). Improving the Accuracy of Network Intrusion Detection System in Medical IoT Systems through Butterfly Optimization Algorithm. *Wireless Pers Commun*, 126, 1999-2017. https://doi.org/10.1007/s11277-021-08756-x
[12] Fatani, A., Abd Elaziz, M., Dahou, A., Al-Qaness, M. A., & Lu, S. (2021). IoT intrusion detection system using deep learning and enhanced transient search optimization. *IEEE Access*, *9*, 123448-123464. https://doi.org/10.1109/ACCESS.2021.3109081
[13] Alzaqebah, A., Aljarah, I., Al-Kadi, O., & Damaševičius, R. (2022). A Modified Grey Wolf Optimization Algorithm for an Intrusion Detection System. *Mathematics*, *10*(6). https://doi.org/10.3390/math10060999
[14] Fatani, A., Dahou, A., Al-Qaness, M. A., Lu, S., & Elaziz, M. A. (2021). Advanced feature extraction and selection approach using deep learning and Aquila optimizer for IoT intrusion detection system. *Sensors*, *22*(1). https://doi.org/10.3390/s22010140
[15] Moghanian, S., Saravi, F. B., Javidi, G., & Sheybani, E. O. (2020). GOAMLP: Network intrusion detection with multilayer perceptron and grasshopper optimization algorithm. *IEEE Access*, *8*, 215202-215213. https://doi.org/10.1109/ACCESS.2020.3040740
[16] Mahboob, A. S. & Moghaddam, M. R. O. (2020). An anomaly-based intrusion detection system using butterfly optimization algorithm. *IEEE. 6th Iranian Conference on Signal Processing and Intelligent Systems (ICSPIS*). 1-6. https://doi.org/10.1109/ICSPIS51611.2020.9349537
[17] Alazzam, H., Sharieh, A., & Sabri, K. E. (2020). A feature selection algorithm for intrusion detection system based on pigeon inspired optimizer. *Expert System with Applications*, 148. https://doi.org/10.1016/j.eswa.2020.113249
[18] Wang, J., Yang, B., Li, D., Zeng, C., Chen, Y., Guo, Z., Zhang, X., Tan, T., Shu, H., & Yu, T. (2021). Photovoltaic cell parameter estimation based on improved equilibrium optimizer algorithm. *Energy Conversion and Management*, 236(3). https://doi.org/10.1016/j.enconman.2021.114051
[19] Balamurugan, T. (2021). Deep Wavelet Autoencoder Based Brain Tumor Detection Analysis Using Deep Neural Network. *Turkish Journal of Computer and Mathematics Education (TURCOMAT)*, *12*(11), 639-645.
[20] Khatir, S., Tiachacht, S., Le Thanh, C., Ghandourah, E., Mirjalili, S., & Wahab, M. A. (2021). An improved Artificial Neural Network using Arithmetic Optimization Algorithm for damage assessment in FGM composite plates. *Composite Structures*, *273*. https://doi.org/10.1016/j.compstruct.2021.114287

Contact information:

S. KAVITHA, Assistant Professor
(Corresponding author)
Department of Computer Science and Engineering,
Velammal College of Engineering and Technology,
Madurai, India
E-mail: kavithacsephd@gmail.com

N. UMA MAHESWARI, Professor
Department of Computer Science and Engineering,
P.S.N.A. College of Engineering and Technology,
Dindigul, India

R. VENKATESH, Professor
Department of Information Technology,
P.S.N.A. College of Engineering and Technology, Dindigul, India

Salud, Ciencia y Tecnología - Serie de Conferencias. 2024; 3:653
doi: 10.56294/sctconf2023653

Category: Health Sciences and Medicine

ORIGINAL

Design of a Classifier model for Heart Disease Prediction using normalized graph model

Diseño de un modelo clasificador para la predicción de cardiopatías mediante un modelo de grafos normalizados

B. Karthiga[1], Sathya Selvaraj Sinnasamy[1], V.C. Bharathi[2,3], Azarudeen[4], Sherubha. P[5]

[1]Dhanalakshmi Srinivasan Engineering College. Perambalur, India.
[2]SRM Institute of Science and Technology. Chennai, India.
[3]School of Computer Science and Engineering. VIT-AP University. Amaravathi, Andhra Pradesh, India.
[4]Department of Computer Science and Engineering. Velammal College of Engineering and Technology. Madurai, India.
[5]Department of Information Technology. Karpagam College of Engineering. Coimbatore, India.

Cite as: Karthiga B, Sinnasamy SS, Bharathi VC, Azarudeen K, Sherubha P. Design of a Classifier model for Heart Disease Prediction using normalized graph model. Salud, Ciencia y Tecnología - Serie de Conferencias 2024; 3:653. https://doi.org/10.56294/sctconf2024653.

Submitted: 17-11-2023 **Revised:** 19-01-2024 **Accepted:** 22-03-2024 **Published:** 23-03-2024

Editor: Dr. William Castillo-González

ABSTRACT

Heart disease is an illness that influences enormous people worldwide. Particularly in cardiology, heart disease diagnosis and treatment need to happen quickly and precisely. Here, a machine learning-based (ML) approach is anticipated for diagnosing a cardiac disease that is both effective and accurate. The system was developed using standard feature selection algorithms for removing unnecessary and redundant features. Here, a novel normalized graph model (n – GM) is used for prediction. To address the issue of feature selection, this work considers the significant information feature selection approach. To improve classification accuracy and shorten the time it takes to process classifications, feature selection techniques are utilized. Furthermore, the hyper-parameters and learning techniques for model evaluation have been accomplished using cross-validation. The performance is evaluated with various metrics. The performance is evaluated on the features chosen via features representation. The outcomes demonstrate that the suggested (n – GM) gives 98 % accuracy for modeling an intelligent system to detect heart disease using a classifier support vector machine.

Keywords: Heart Disease; Classification; Prediction; Machine Learning; Hyper-Parameters.

RESUMEN

Las cardiopatías son una enfermedad que afecta a una enorme cantidad de personas en todo el mundo. Especialmente en cardiología, el diagnóstico y el tratamiento de las cardiopatías deben ser rápidos y precisos. En este trabajo se propone un enfoque basado en el aprendizaje automático (ML) para diagnosticar una enfermedad cardiaca de forma eficaz y precisa. El sistema se desarrolló utilizando algoritmos estándar de selección de características para eliminar las innecesarias y redundantes. Para la predicción se utiliza un nuevo modelo gráfico normalizado (n – GM). Para abordar el problema de la selección de características, este trabajo considera el enfoque de selección de características de información significativa. Para mejorar la precisión de la clasificación y reducir el tiempo que se tarda en procesar las clasificaciones, se utilizan técnicas de selección de características. Además, los hiperparámetros y las técnicas de aprendizaje para la evaluación de modelos se han realizado mediante validación cruzada. El rendimiento se evalúa con varias métricas. El rendimiento se evalúa en función de las características elegidas mediante la representación de características.

Los resultados demuestran que el (n – GM) sugerido proporciona una precisión del 98 % para modelar un sistema inteligente de detección de enfermedades cardíacas mediante una máquina de vectores soporte clasificadora.

Palabras clave: Enfermedad Cardiaca; Clasificación; Predicción; Aprendizaje Automático; Hiperparámetros.

INTRODUCTION

The most serious health problem is heart disease (HD), which has affected many people worldwide.[1] Among the most common symptoms of HD are swollen feet, muscle weakness, and shortness of breath.[2] Current methods for diagnosing cardiac disease are not useful for early identification because of a number of issues, such as accuracy and execution time.[3] Therefore, researchers are developing an effective method for detecting heart disease. Without state-of-the-art tools and trained medical personnel, diagnosing and treating heart disease can be very difficult.[4] Numerous lives can be saved by an accurate diagnosis and appropriate care.[5] According to the European Society of Cardiology, there are an estimated 26 million HD patients worldwide, and 3,6 million new cases are found each year.[6] Heart disease affects most people in the United States.[7] A doctor often diagnoses HD after patient's history review, physical exam outcomes and related symptoms. Moreover, the outcomes do not reliably identify HD. Additionally; analysis is computationally complex and challenging.[8] Creating a non-invasive system using ML classifiers is essential to address these problems. The HD is successfully predicted by the expert system using ML and ANN. The death rate is predicted based in some studies.[9,10]

Several researchers[11,12] used online available to address the HD identification issue. During testing and training, ML predictive approachesneedsuitable data. ML model performance improves if balanced datasets are employed for testing and training. Furthermore, the model's predictive skills are enhanced by incorporating appropriate and pertinent elements from the data. To increase model performance, data balancing and feature selection are therefore crucial. Numerous researchers have suggested different diagnosis methods in the literature, but these methods do not reliably diagnose HD. Data preprocessing is essential for data normalization, which helps machine learning models predict outcomes more accurately.[13] The authors suggested ML-based diagnosis approach for identifying HD. Various prediction models are utilized to identify HD. Some features were chosen using the current feature selection algorithms mRMR, Relief, LASSO and local features selection. Additionally, conditional mutual information features selection approach is also used. The optimum hyper-parameters are chosen with 10-fold CV technique for validation purpose.[14] Furthermore, the performance of the classifier is gauged using a range of performance measures. The HD dataset is used to evaluate the strategy. The effectiveness is evaluated in comparison to other methods.[15] However, all these techniques fail to fulfill the research requirements. The anticipated model attempts to fulfill the requirements. The study's contributions are as follows:

- The first attempt is to resolve the feature selection issues using pre-processing approaches and suitable feature selection approach. These features are provided to efficient classifiers to determine which classifier gives superior outcomes regarding accuracy and other evaluation metrics.
- To increase prediction accuracy and shorten computation times, the authors also introduced the novel normalized graph model () algorithm for feature selection. The suggested algorithm's selected features are evaluated to features chosen by the standard prevailing algorithms to see how well the classifiers performed. Any weak dataset properties show an impact on classifier performance.
- Finally, it is suggested that the heart disease identification may successfully identify HD.

The study is set up like this: Section 2 offers a thorough study of the advantages and disadvantages of various strategies. The approach is described in part 3, while section 4 contains the results. Section 5's summary comes after it.

Related works

Investigators have recommended various ML approaches for HD prediction. To project the significance of various approaches, this work includes learning-based approaches that are now in use. Karthiga et al.[11] developed the HD classification system, which has a 77 % accuracy rate thanks to machine learning classification algorithms. Evolutionary and feature selection techniquesareemployed to the online dataset. In different investigation, Beyence et al.[12] modeled a HD prediction and categorization approach utilizing MLP and SVM algorithms and attained 80,41 % accuracy. The classification system accuracy was 87,4 %. Using enterprise miner, a statistical measurement system, an ANN-based prediction for HD was constructed by Rahman et al.[13] with sensitivity, accuracy, and specificity values of 89 %, 80 %, and 95 %. An study[14] developed a method for diagnosing HD based on ML. Both the FS algorithm and the ANN-DBP method had good results. A system of expert medical diagnosis was developed by Goel et al.[15] for the identification of HD. During the system's

https://doi.org/10.56294/sctconf2024653

development, Artificial Neural Networks (ANN), Decision Trees (DT), and Navies Bays (NB) were employed as predictive machine learning models.[16,17,18,19,20] ANN obtained an accuracy of 88,12 %, NB obtained 86,12 %, and the DT classifier obtained 80 % accuracy. Jenzi et al.[21] modeled three-stage design based on ANNand achieved 88 % accuracy.

For HD diagnosis, Kalaiselvi et al.[22] created amerged medical DSS based on ANN and fuzzy model.[23,24,25,26,27,28,29,30,31] The accuracy attained was 91 %. An HD categorization using relief and rough set was proposed by Masethe et al.[32] The technique shows the classification accuracy of 92 %.

An HD identification approach utilizing feature selection and classification algorithms were proposed in.[33,34,35] Here, Sequential Backward Selection Algorithm is employed. K-NN performanceis tested on both feature set and feature subset.[36,37,38,39,40,41,42,43,44,45]

The suggested procedure produced excellent accuracy. Raju et al.[46] modeled a hybrid ML-based HD prediction in different works. Additionally, a superior approach for selecting essential features is designed from the data using ML classifiers. The accuracy rate of their classification was 88,07 %. This model was useful for several studies and develop another models.[47,48,49,50,51,52,53,54,55,56,57,58]

An improved SVM-based duality optimization technique Venkatalakshmi et al.[59] created HD detection tools. To better understand the significance of our suggested strategy, All of these technologies that are in use now use different approaches to identify HD in its early stages. Furthermore, the computation time of these approaches is high and the accuracy is low. For better treatment and recovery, HD detection needs to be improved in order to make accurate and efficient early predictions.[60,61] As such, the main problems with these earlier methods are their poor accuracy and long computation durations, which may be caused by the presence of unnecessary features in the dataset. New techniques are required for the precise identification of HD in order to address these issues. There is a great need for additional study on improving prediction accuracy.

METHOD

The proposed research is achieved by three successive steps dataset description, feature representation and normalized graph model. The anticipated model provides expert knowledge to the physicians during the crucial time and assists in predicting heart disease in earlier. The experimentation is executed in MATLAB 2020awhere metrics such as recall, precision, accuracy, and F-measure are assessed and contrasted with alternative methods. The block representation is provided in figure 1.

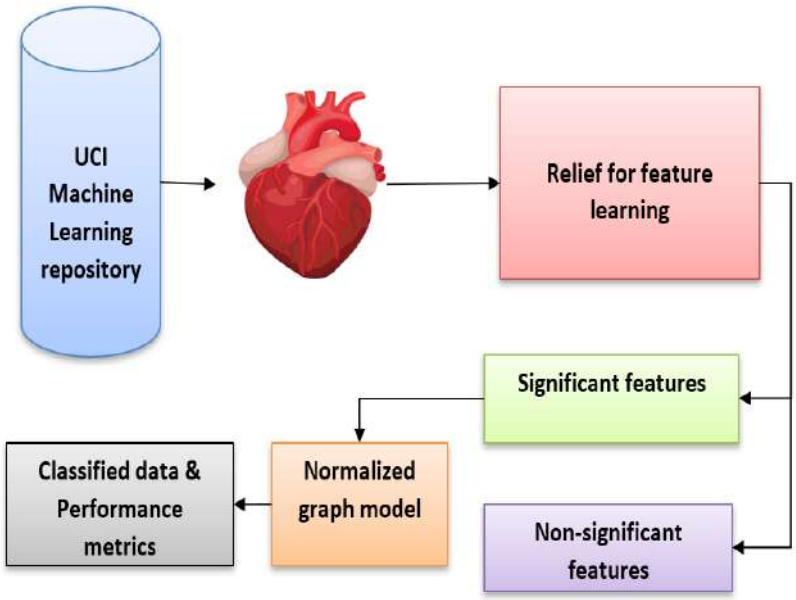

Figure 1. Block diagram

Dataset

UCI ML dataset is used for prediction purposes. When the data set was designed, only 14 subsets of the 303 occurrences and 75 attributes were used in the reported studies. Six samples were excluded from the data set owing to the missing values after pre-processing. There are 297 samples from the remaining dataset with 13-characteristics and 1- output label. Two classes on the output label indicate if HD is present or not. As an outcome, 297*13 features matrix is created. Information about the dataset matrix is provided in table 1.

https://doi.org/10.56294/sctconf2024653

Table 1. Dataset details

Attributes	Descriptions	Type
Age	People get older	Nom
Sex	People's gender	Nom
CP	kind of ache in the chest , angina typical or atypical, not angular, and symptomless	Num
Tresbps	Level of pressure	Num
Chol	Cholesterol (serum)	Nom
FBS	Sugar content	Nom
Resting	ECG	Num
Thali	cardiac rate at maximum	Nom
Exchange	Angina during physical activity	Num
OldPeak	Depression through exercise	Nom
Slope	peak activity (dividend)	Num
Ca	colored vessels in fluoroscopy	Nom
Thal	Heart condition	Nom
Num	Prediction Value of Disease	Nom

Relief for feature learning

The Relief method automatically updates the weights for each feature in the data collection. High-weight features should be chosen, while low-weight ones should be ignored. The processes used by the relief to estimate the weights of features are identical. The parameter is m, and the method is repeated through m randomly chosen training samples (R_k) without selection replacement. The "target" sample is R_k for every k, and the weight W is updated. Below is an explanation of the relief model's algorithm:

Algorithm 1

input: vectors with labels, or training data; the number of training samples chosen at random (m);
Output: Weighted features (more feature information);
1: n → total samples of training;
2: d → total characteristics;
3: Evaluate feature set W[A]→0;
4: for k→1 to m do
5: Select target samples; // R_k
6: Predict the eligible features;
7: for A → 1 to a do
8: W[A] → W[A] - difference (A,R_k,H)/m + difference (A,R_k,H)/m
9: end for
10: end for
11: Evaluate the weighted feature vector;
12: Compute the superior feature

Feature representation

This study introduced mutual feature information analysis to address the feature selection problem. It is a productive feature selection technique created using mutual information. The following steps are part of the designing of the algorithm. Consider the dataset D (X,Y), which, like in Eq. (1), is composed of X instances and Y output labels:

$$D(X,Y) = \{(X_i, Y_i) | X_i \in R^n, Y_i \in \{0,1\}_{i=1}^k\} \quad (1)$$

$$X_i = \{X_1, \dots, X_n\} \quad (2)$$

As stated in Eq. (3), we use preprocess statistical techniques such Min-Max normalization to the dataset D (X,Y):

$$N^- = \frac{f - \min}{\max - \min}(new_{max} - new_{min}) + new_{min} \quad (3)$$

We now use the mutual information approach D to choose the subset of feature (X_i,Y_i). The feature selection approach uses the information to calculate the dataset's value for feature relevance and duplication. Conditional on the outcome of any feature chosen previously, the proposed algorithm selects features that enhances mutual information based on the target class (D). Due to the lack of certain information (output), this factor chooses characteristics that differ which are already chosen, even if it is correct independently. The balance between

https://doi.org/10.56294/sctconf2024653

duplication and relevance is favourable. The feature X_n is very compatible with other features and relevant to output Y, X_j, where j∈D, according to the higher mutual information value. The condition is mathematically represented by Eq. (4):

$$\text{Mutual information} = \min_{j \in S} I(X_i; Y|X_j)) \quad (4)$$

The anticipated model attempts to balance independence and separable power among the significant features with the features selected already. The features X_0 is a significant consideration if $I(Y,X_0 |X)$ is huge for every X chosen already. The foremost execution of the feature scores during the selection process evaluates the features that give more information and reduce redundancy. The model maintains the partial feature score D_i which is minimal (min algorithm). The vector store of the chosen features is based on P_i.

Algorithm 2

Input: Input the dataset; D(X,Y) matrix, significant features, finest feature set, mutual information and partial score;
Output: Select finest feature $D(X_i,Y_i)$
1: Execute data pre-processing;
2: Chosen features as ∅
3: for all features f_i∈O do
4: Evaluate M_i;
5: Fix $p_i \rightarrow M$;
6: Fix $L_i \rightarrow 0$;
7: end for
8: for k→1 to K do
9: Set $score_i \rightarrow 0$;
10: for all features, do
11: while $P_i > score_k$ and $L_i < k-1$ do
12: Fix $L_i \rightarrow L_i+1$
13: Evaluate VU_i among o_k and o_i;
14: Fix $p_j \rightarrow \min (p_i \text{ (mutual information}_{ik}))$
15: end while
16: if $p_i > score_k$, then
17: Fix $p_i > partial\ score_k$, then
18: Choose feature subset → significant feature;
19: end if
20: end for
21: end for

Normalized graph model

For real-time analysis, various datasets prevail in graph form, normalized to a specific format. This paper considers the proposed normalized graph model (n - GM) constructed using the graph structure. The input data product $x \in R^N$ is used to represent the spectral graph convolution, which filters the g_θ= diag (θ):

$$g_\theta * x = U g_\theta U^T x \quad (5)$$

Here, U refers to the matrix which is composed of normalized eigenvector graph Laplacian matrix, i.e. $L=I_N-D^{(1/2)}\ AD^{(1/2)}=U\Lambda U^T$, Λ specifies the diagonal matrix composed of L eigenvalues and U^T x refers to Fourier transform (x) using is applied in Eq. (6):

$$g_\theta * x \approx \sum_{k=0}^{k} \theta'_k T_k (\tilde{L}) x \quad (6)$$

Here, $L = 2/\lambda_{max}\ L-I_N$. The normalized graph model is provided with the many convolutional layers as in Eq. (6). When k=1 is given as the total number of convolutional layers, the estimated λ_{max}=2 is taken into account.

$$g_\theta * x \approx \theta'_0 x + \theta'_1 (L - I_N) x = \theta'_0 x - \theta'_1 D^{\frac{1}{2}} A D^{\frac{1}{2}} x \quad (7)$$

Moreover, over-fitting is eliminated by restricting certain parameters when the operating frequencies at every layer are reduced, as in Eq. (8):

$$g_\theta * x \approx \theta \left(I_N + D^{\frac{1}{2}} A D^{\frac{1}{2}} \right) x \quad (8)$$

https://doi.org/10.56294/sctconf2024653

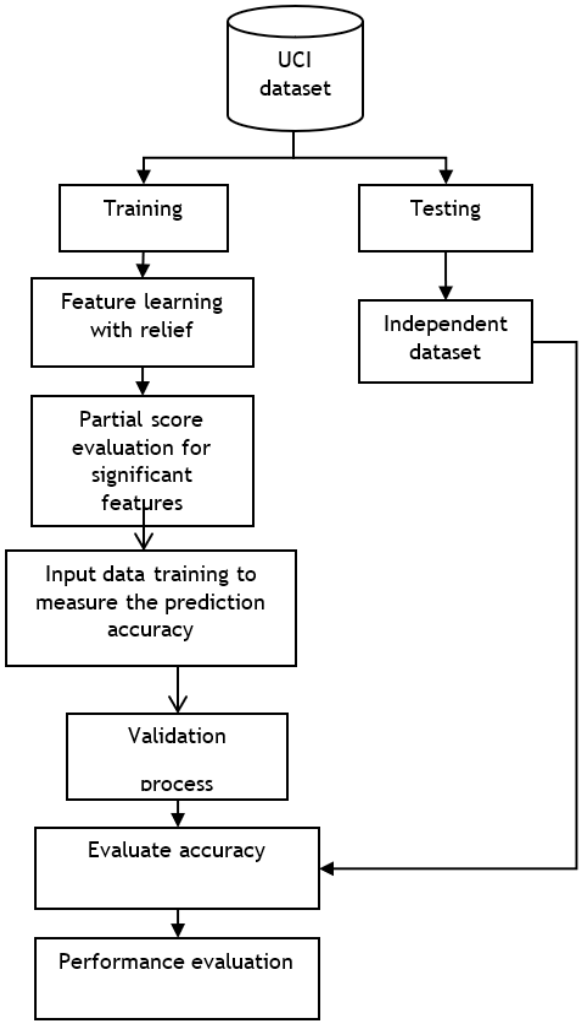

Figure 2. Flow diagram of the model

Here, $\theta = \theta_0 = -\theta_1$ is provided in Eq. (7). However, the eigenvalue interval of $I_N + D^{1/2} AD^{1/2}$ is provided as [0, 2]. In the n-GM, the repetitive function outcomes in gradient vanishing or instability. The re-normalization idea is proposed as in Eq. (9) to address this issue:

$$I_N + D^{\frac{1}{2}} AD^{\frac{1}{2}} \rightarrow \widetilde{D}^{\frac{1}{2}} A D^{\frac{1}{2}} \quad (9)$$

Here, $\tilde{A}=A+I_N, \tilde{D}_{ii}= \sum_j \tilde{A}_{ij}$. The explanation is given as follows: F feature map and filter with C channel, and input signal $X \in R^{(N*C)}$ (where C is Eigenvalues node dimensionality and N→total nodes):

$$Z = \widetilde{D}^{\frac{1}{2}} \widetilde{A} \widetilde{D}^{\frac{1}{2}} X\Theta \quad (9)$$

Here, $\Theta \in R^{(C*F)}$ refers to the filter parameter matrix, and $Z \in R^{(N*F)}$ refers to the signal matrix after the convolution process. The filter complexity is $O(|\varepsilon|FC)$. $\tilde{A}X$ is considered as the sparse matrix product and dense matrix.

Numerical results

This section provides the numerical outcomes attained with the proposed and various metrics are as precision, accuracy, sensitivity, recall, False Negative Rate (FNR), FPR (False Positive Rate), Matthew's correlation coefficients (MCC) and TNR (True Negative Rate). The model significance is determined by contrasting the suggested model with the current results. The mathematical expressions are provided below:

https://doi.org/10.56294/sctconf2024653

$$\text{Accuracy} = (TP+TN)/(TP+FN+FP+TN) \quad (12)$$

$$\text{Precision} = TP/(TP+FP) \quad (13)$$

$$\text{Recall/sensitivity/TPR} = TP/(TP+FN) \quad (14)$$

$$\text{F-measure} = (2*\text{precision})/(p+r) \quad (15)$$

$$\text{MCC} = ((TP*TN)-(FP*FN))/\sqrt{((TP+FP)(TP+FN)(TN+FP)(TN+FN))} \quad (16)$$

$$FPR = FP/(FP+TN) \quad (17)$$

$$FNR = FN/(FN+TP) \quad (18)$$

$$TNR = TN/(TN+FP) \quad (19)$$

FPR is the wrong classification where positive prediction probabilities are not considered during testing. Additionally, the negative value likelihood that is confirmed to be negative is used to represent specificity (TNR).

Table 2. Proposed vs. existing comparison

Model	Acc	Prec	Sensitivity	F-measure	MCC	FPR	FNR	TNR
NB	90 %	89 %	85 %	85 %	75 %	18 %	25 %	90 %
LR	94 %	89 %	86 %	86 %	78 %	18 %	25 %	92 %
MLP	96 %	89 %	88 %	86 %	70 %	13 %	20 %	90 %
SVM	80 %	75 %	55 %	75 %	50 %	17 %	55 %	86 %
DT	85 %	78 %	75 %	82 %	65 %	13 %	35 %	75 %
RF	93 %	89 %	80 %	90 %	79 %	5 %	25 %	89 %
L-SVM	97 %	98 %	96 %	97 %	95 %	7 %	3,5 %	97 %
	98 %	99 %	99 %	98 %	97 %	4 %	3 %	98 %

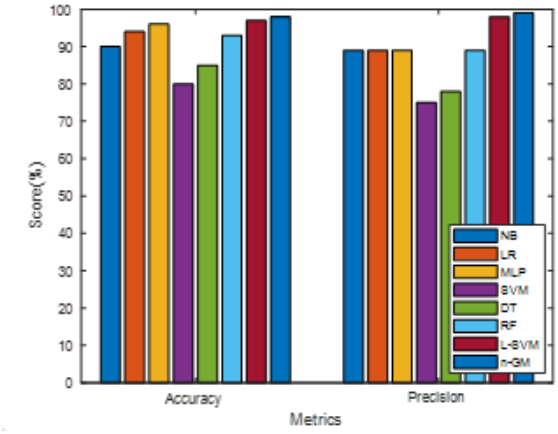

Figure 3. Accuracy and precision comparison

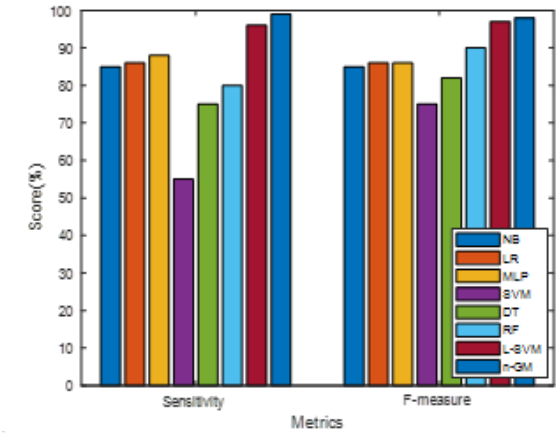

Figure 4. Sensitivity and F-measure comparison

https://doi.org/10.56294/sctconf2024653

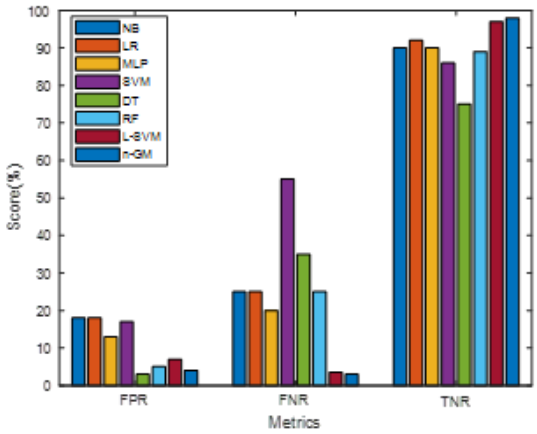

Figure 5. FPR, FNR and TNR comparison

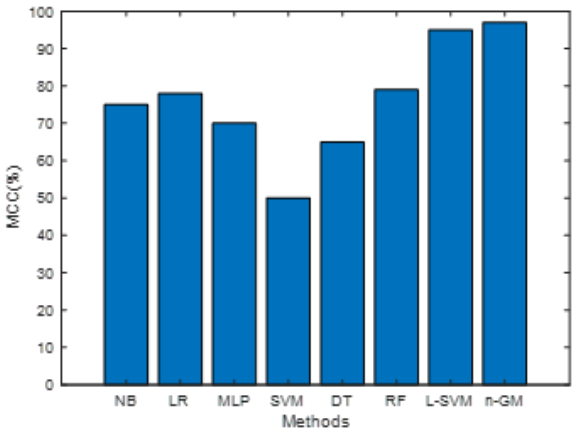

Figure 5. MCC comparison

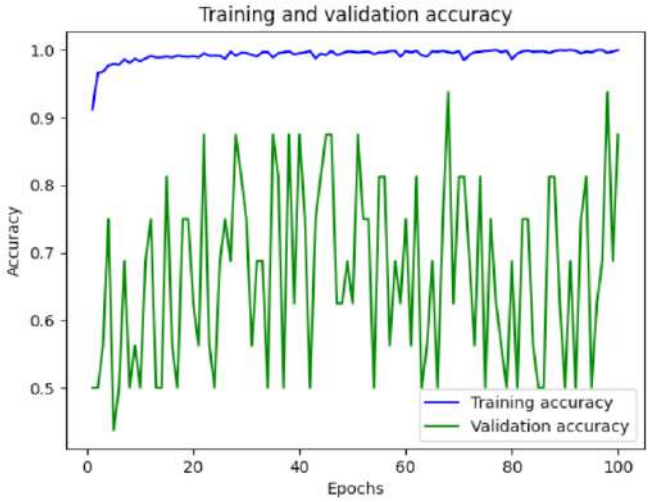

Figure 6. Training and validation accuracy

Table 2 compares the anticipated n-GM model with diverse approaches. Metrics such as MCC, F-measure, FPR, FNR, TNR, accuracy, sensitivity, and precision. 98 % accuracy, 99 % precision, 99 % sensitivity, 98 % F-measure, 97 % MCC, 4 % FPR, 3 % FNR, and 98 % TNR are the results obtained with the n-GM, in that order. The n-GM's precision is 8 %, 4 %, 2 %, 18 %, 13 %, 5 %, and 1 % higher than others. The n-GM's precision is 10 %, 10 %, 10 %, 24 %, 21 %, 10 %, and 1 % superior to others. The n-GM's sensitivity is 14 %, 13 %, 11 %, 54 %, 24 %, 19 % and 3 % superior to other approaches. Then-GM's F1-score is 13 %, 12 %, 12 %, 23 %, 16 %, 8 %, and 1 % superior to other approaches. The n-GM's MCC is 12 %, 19 %, 27 %, 47 %, 32 %, 18 % and 2 % superior to other approaches.

https://doi.org/10.56294/sctconf2024653

The n-GM's FPR model is 14 %, 14 %, 9 %, 13 %, 9 %, 1 %, and 3 % lesser to others. The n-GM's FNR is 22 %, 22 %, 17 %, 42 %, 32 %, 22 %, and 0,5 % higher than other approaches. The TNR of the n-GM model is 8 %, 6 %, 8 %, 12 %, 23 %, 9 %, and 1 % greater than others. The n-GMperformance is superior to other (See Figure 3 to %). The anticipated n-GM is well-suited for prediction as it reduces the computational complexity. The training and validation accuracy together with the loss function are shown in Figures 6 and 7.

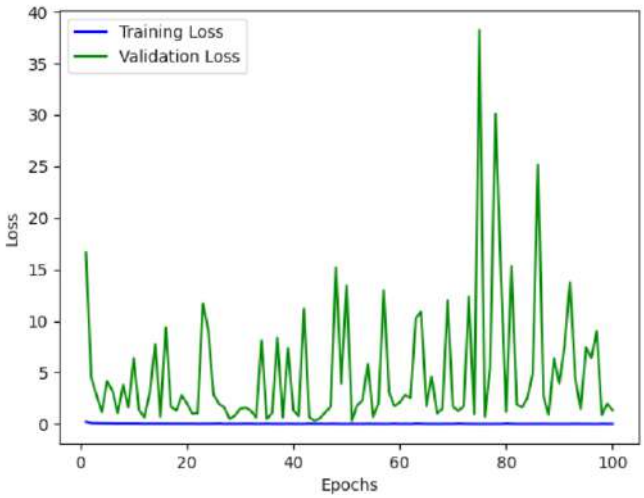

Figure 7. Training and validation loss

CONCLUSION

The results of the experiment show that, in comparison to conventional methods, the suggested feature selection methodology chooses relevant characteristics more successfully and with higher classification accuracy. Based on investigators perspective, the significant and appropriate features are exercise-induced angina and chest discomfort of the Thallium Scan kind. Some features are not a reliable indicator of the presence of heart disease, according to all algorithm results. When compared to previously proposed approaches. The accuracy of n-GM' using the proposed feature selection model is 98 % which is quite good. Additionally, the machine learning-based technique performs better than existing mining approaches. A slight increase in prediction accuracy can significantly impact the diagnosis of serious diseases. The study's originality is the creation of a system for diagnosing cardiac disease. The feature selection algorithms are newly developed to pick the features. Performance evaluation measures are employed. For testing purposes, the UCI heart disease dataset is utilized. We believe that creating a support system using ML algorithms will make diagnosing heart disease more appropriate. Utilizing feature selection algorithms to choose relevant features that enhance classification accuracy and shorten the diagnosis system's processing time is another novel aspect of our research. We'll apply additional feature selection algorithms and optimization techniques in the future to boost a prediction system's ability to diagnose HD.

REFERENCES

1. Jagtap, P. Malewadkar, O. Baswat, H. Rambade, Heart disease prediction using machine learning. Int. J. Res. Eng. Sci. Manage. 2(2) (2019)

2. Amado DPA, Diaz FAC, Pantoja R del PC, Sanchez LMB. Benefits of Artificial Intelligence and its Innovation in Organizations. AG Multidisciplinar 2023;1:15-15. https://doi.org/10.62486/agmu202315.

3. Narmadha P. Sherubha, M. Banu chitra, "Multi class feature selection algorithm for breast cancer detection", International journal of pure and applied mathematics, pp. 301-305, 2018.

4. Batista-Mariño Y, Gutiérrez-Cristo HG, Díaz-Vidal M, Peña-Marrero Y, Mulet-Labrada S, Díaz LE-R. Behavior of stomatological emergencies of dental origin. Mario Pozo Ochoa Stomatology Clinic. 2022-2023. AG Odontologia 2023;1:6-6. https://doi.org/10.62486/agodonto20236.

5. Beyene C, Kamat P. Survey on Prediction and Analysis the Occurrence of Heart Disease Using Data Mining Techniques. International Journal of Pure and Applied Mathematics. 2018;118(8):165-74.

6. BP Sreeja, S Manoj Kumar, P Sherubha, SP Sasirekha, "Crop monitoring using wireless sensor networks",

Materials Today: Proceedings, 2020.

7. Caero L, Libertelli J. Relationship between Vigorexia, steroid use, and recreational bodybuilding practice and the effects of the closure of training centers due to the Covid-19 pandemic in young people in Argentina. AG Salud 2023;1:18-18. https://doi.org/10.62486/agsalud202318.

8. Cavalcante L de FB. Feminicide from the perspective of the cultural mediation of information. Advanced Notes in Information Science 2023;5:24-48. https://doi.org/10.47909/978-9916-9906-9-8.72.

9. Chalan SAL, Hinojosa BLA, Claudio BAM, Mendoza OAV. Quality of service and customer satisfaction in the beauty industry in the district of Los Olivos. SCT Proceedings in Interdisciplinary Insights and Innovations 2023;1:5-5. https://doi.org/10.56294/piii20235.

10. Chávez JJB, Trujillo REO, Hinojosa BLA, Claudio BAM, Mendoza OAV. Influencer marketing and the buying decision of generation «Z» consumers in beauty and personal care companies. SCT Proceedings in Interdisciplinary Insights and Innovations 2023;1:7-7. https://doi.org/10.56294/piii20237.

11. Diaz DPM. Staff turnover in companies. AG Managment 2023;1:16-16. https://doi.org/10.62486/agma202316.

12. Espinosa JCG, Sánchez LML, Pereira MAF. Benefits of Artificial Intelligence in human talent management. AG Multidisciplinar 2023;1:14-14. https://doi.org/10.62486/agmu202314.

13. Figueredo-Rigores A, Blanco-Romero L, Llevat-Romero D. Systemic view of periodontal diseases. AG Odontologia 2023;1:14-14. https://doi.org/10.62486/agodonto202314.

14. G. Jignesh Chowdary, G. Suganya, M. Premalatha, Effective prediction of cardiovascular disease using cluster of machine learning algorithms. J. Critical Rev. 7(18), 2192–2201 (2020). ISSN-2394–5125

15. Goel S, Deep A, Srivastava S, Tripathi A, "Comparative Analysis of various Techniques for Heart Disease Prediction", Information Systems and Computer Networks (ISCON) 2019 4th International Conference on. 2019. p. 88–94.

16. Gonzalez-Argote J, Castillo-González W. Productivity and Impact of the Scientific Production on Human-Computer Interaction in Scopus from 2018 to 2022. AG Multidisciplinar 2023;1:10-10. https://doi.org/10.62486/agmu202310.

17. Hernández-Flórez N. Breaking stereotypes: "a philosophical reflection on women criminals from a gender perspective". AG Salud 2023;1:17-17. https://doi.org/10.62486/agsalud202317.

18. Hinojosa BLA, Mendoza OAV. Perceptions on the use of Digital Marketing of the micro-entrepreneurs of the textile sector of the Blue Gallery in the emporium of Gamarra. SCT Proceedings in Interdisciplinary Insights and Innovations 2023;1:9-9. https://doi.org/10.56294/piii20239.

19. Jabbar MA, Deekshatulu BL, Chandra P. "Alternating decision trees for early diagnosis of heart disease," International Conference on Circuits, Communication, Control and Computing, Bangalore. 2014. p. 322–328.

20. Jabbar MA, Deekshatulu BL, Chandra P. Classification of Heart Disease using Artificial Neural Network and Feature Subset Selection. Global journal of computer science and technology. 2013.

21. Jenzi, I., Priyanka, P., Alli, P.: A reliable classifier model using data mining approach for heart disease prediction. Int. J. Adv. Res. Comput. Sci. Softw. Eng. 3(3), 20–24 (2013)

22. Kalaiselvi, C.: Diagnosing of heart diseases using average k-nearest neighbor algorithm of data mining. In: 2016 3rd International Conference on Computing for Sustainable Global Development (INDIACom), pp. 3099–3103. IEEE (2016)

23. Karayılan T, Kılıç O, "Prediction of heart disease using neural network", Computer Science and Engineering (UBMK) 2017 International Conference on, 2017. p. 719–723.

24. Karthiga A, Mary S, Yogasini M. Early Prediction of Heart Disease Using Decision Tree Algorithm. International Journal of Advanced Research in Basic Engineering Sciences and Technology. (IJARBEST) 2017.

25. Lamorú-Pardo AM, Álvarez-Romero Y, Rubio-Díaz D, González-Alvarez A, Pérez-Roque L, Vargas-Labrada LS. Dental caries, nutritional status and oral hygiene in schoolchildren, La Demajagua, 2022. AG Odontologia 2023;1:8-8. https://doi.org/10.62486/agodonto20238.

26. Ledesma-Céspedes N, Leyva-Samue L, Barrios-Ledesma L. Use of radiographs in endodontic treatments in pregnant women. AG Odontologia 2023;1:3-3. https://doi.org/10.62486/agodonto20233.

27. Lopez ACA. Contributions of John Calvin to education. A systematic review. AG Multidisciplinar 2023;1:11-11. https://doi.org/10.62486/agmu202311.

28. M. Marimuthu, M. Abinaya, K.S. Hariesh, K. Madhankumar, V. Pavithra, A review on heart disease prediction using machine learning and data analytics approach. Int. J. Comput. Appl. (0975-8887) 181(18) (2018)

29. Maamar Bougherara, Rafik Amara, Rebiha Kemcha, IAES International Journal of Robotics and Automation (IJRA), Vol. 12, No. 4, December 2023, pp. 394 – 404

30. Marcillí MI, Fernández AP, Marsillí YI, Drullet DI, Isalgué RF. Older adult victims of violence. Satisfaction with health services in primary care. SCT Proceedings in Interdisciplinary Insights and Innovations 2023;1:12-12. https://doi.org/10.56294/piii202312.

31. Marcillí MI, Fernández AP, Marsillí YI, Drullet DI, Isalgué VMF. Characterization of legal drug use in older adult caregivers who are victims of violence. SCT Proceedings in Interdisciplinary Insights and Innovations 2023;1:13-13. https://doi.org/10.56294/piii202313.

32. Masethe, H.D., Masethe, M.A.: Prediction of heart disease using classification algorithms. In: Proceedings of the world Congress on Engineering and Computer Science, vol. 2, pp. 22–24 (2014)

33. Moraes IB. Critical Analysis of Health Indicators in Primary Health Care: A Brazilian Perspective. AG Salud 2023;1:28-28. https://doi.org/10.62486/agsalud202328.

34. N. Rajesh, T. Maneesha, S. Hafeez, H. Krishna, Prediction of heart disease using machine learning algorithms. Int. J. Eng. Technol. 7(2.32), 363–366 (2018).

35. Ogolodom MP, Ochong AD, Egop EB, Jeremiah CU, Madume AK, Nyenke CU, et al. Knowledge and perception of healthcare workers towards the adoption of artificial intelligence in healthcare service delivery in Nigeria. AG Salud 2023;1:16-16. https://doi.org/10.62486/agsalud202316.

36. Pahwa K, Kumar R. "Prediction of heart disease using hybrid technique for selecting features," 2017 4th IEEE Uttar Pradesh Section International Conference on Electrical, Computer and Electronics (UPCON), Mathura. 2017. p. 500–504.

37. Palaniappan S, Awang R. "Intelligent heart disease prediction system using data mining techniques," 2008 IEEE/ACS International Conference on Computer Systems and Applications, Doha, 2008.

38. Patel, S.B., Yadav, P.K., Shukla, D.: Predict the diagnosis of heart disease patients using classification mining techniques. IOSR J. Agric. Vet. Sci. (IOSR-JAVS) 4(2), 61–64 (2013)

39. Peñaloza JEG, Bermúdez L marcela A, Calderón YMA. Perception of representativeness of the Assembly of Huila 2020-2023. AG Multidisciplinar 2023;1:13-13. https://doi.org/10.62486/agmu202313.

40. Pérez DQ, Palomo IQ, Santana YL, Rodríguez AC, Piñera YP. Predictive value of the neutrophil-lymphocyte index as a predictor of severity and death in patients treated for COVID-19. SCT Proceedings in Interdisciplinary Insights and Innovations 2023;1:14-14. https://doi.org/10.56294/piii202314.

41. Prado JMK do, Sena PMB. Information science based on FEBAB's census of Brazilian library science:

postgraduate data. Advanced Notes in Information Science 2023;5:1-23. https://doi.org/10.47909/978-9916-9906-9-8.73.

42. Pupo-Martínez Y, Dalmau-Ramírez E, Meriño-Collazo L, Céspedes-Proenza I, Cruz-Sánchez A, Blanco-Romero L. Occlusal changes in primary dentition after treatment of dental interferences. AG Odontologia 2023;1:10-10. https://doi.org/10.62486/agodonto202310.

43. Quiroz FJR, Oncoy AWE. Resilience and life satisfaction in migrant university students residing in Lima. AG Salud 2023;1:9-9. https://doi.org/10.62486/agsalud20239.

44. Rahman M, Zahin MM, Islam L, "Effective Prediction On Heart Disease: Anticipating Heart Disease Using Data Mining Techniques", Smart Systems and Inventive Technology (ICSSIT) 2019 International Conference on. 2019. p. 536–541.

45. Rajathi S, Radhamani G. "Prediction and analysis of Rheumatic heart disease using kNN classification with ACO," 2016 International Conference on Data Mining and Advanced Computing (SAPIENCE), Ernakulam. 2016. p. 68–73.

46. Raju, C., Philipsy, E., Chacko, S., Suresh, L.P., Rajan, S.D.: A survey on predicting heart disease using data mining techniques. In: 2018 Conference on Emerging Devices and Smart Systems (ICEDSS), pp. 253–255. IEEE (2018)

47. Ramalingam V, Dandapath A, & Karthik Raja M. Heart disease prediction using machine learning techniques: a survey. International Journal of Engineering & Technology. 2018;7(2.8):684–687.

48. Roa BAV, Ortiz MAC, Cano CAG. Analysis of the simple tax regime in Colombia, case of night traders in the city of Florencia, Caquetá. AG Managment 2023;1:14-14. https://doi.org/10.62486/agma202314.

49. Rodríguez AL. Analysis of associative entrepreneurship as a territorial strategy in the municipality of Mesetas, Meta. AG Managment 2023;1:15-15. https://doi.org/10.62486/agma202315.

50. Rodríguez LPM, Sánchez PAS. Social appropriation of knowledge applying the knowledge management methodology. Case study: San Miguel de Sema, Boyacá. AG Managment 2023;1:13-13. https://doi.org/10.62486/agma202313.

51. S Rinesh, K Maheswari, B Arthi, P Sherubha, “Investigations on brain tumor classification using hybrid machine learning algorithms”, Journal of Healthcare Engineering, 2022.

52. S. Sharma, M. Parmar, Heart diseases prediction using deep learning neural network model. Int. J. Innov. Technol. Explor. Eng. (IJITEE) 9(3) (2020). ISSN 2278-3075

53. S.N. Pasha, D. Ramesh, S. Mohmmad, A. Harshavardhan, Shabana, Cardiovascular disease prediction using deep learning techniques. IOP Conf. Ser.: Mater. Sci. Eng. 981, 022006 (2020)

54. Santhana Krishnan J., Geetha S., "Prediction of Heart Disease Using Machine Learning Algorithms.", Innovations in Information and Communication Technology (ICIICT) 2019 1st International Conference on. 2019. p. 1–5.

55. Serra S, Revez J. As bibliotecas públicas na inclusão social de migrantes forçados na Área Metropolitana de Lisboa. Advanced Notes in Information Science 2023;5:49-99. https://doi.org/10.47909/978-9916-9906-9-8.50.

56. Solano AVC, Arboleda LDC, García CCC, Dominguez CDC. Benefits of artificial intelligence in companies. AG Managment 2023;1:17-17. https://doi.org/10.62486/agma202317.

57. T.K. Sajja, H.K. Kalluri, A deep learning method for prediction of cardiovascular disease using convolutional neutral network. Int. Inf. Eng. Technol. Assoc. 34(5), 601–606 (2020)

58. Thomas J, Princy RT. Human heart disease prediction system using data mining techniques. 2016

International Conference on Circuit, Power, and Computing Technologies (ICCPCT). 2016.

59. Venkatalakshmi, B., Shivsankar, M.: Heart disease diagnosis using predictive data mining. Int. J. Innov. Res. Sci. Eng. Technol. 3(3), 1873–1877 (2014)

60. Xu S, Zhang Z, Wang D, Hu J, Duan X, Zhu T. "Cardiovascular risk prediction method based on CFS subset evaluation and random forest classification framework," 2017 IEEE 2nd International Conference on Big Data Analysis (ICBDA), Beijing. 2017.

61. Yi-Chang Wu, Yao-Cheng Liu, Ru-Yi Huang, The use of artificial intelligence in interrogation: lies and truth", IAES International Journal of Robotics and Automation (IJRA), Vol. 12, No. 4, December, 2023, pp. 332~340

FINANCING

The authors did not receive funding for the development of this research.

CONFLICT OF INTEREST

The authors declare that there is no conflict of interest.

AUTHORSHIP CONTRIBUTION

Conceptualization: B. Karthiga, Sathya Selvaraj Sinnasamy, V.C. Bharathi, Azarudeen, Sherubha. P

Research: B. Karthiga, Sathya Selvaraj Sinnasamy, V.C. Bharathi, Azarudeen, Sherubha. P

Writing-original draft: B. Karthiga, Sathya Selvaraj Sinnasamy, V.C. Bharathi, Azarudeen, Sherubha. P

Writing-review and proof editing: B. Karthiga, Sathya Selvaraj Sinnasamy, V.C. Bharathi, Azarudeen, Sherubha. P

https://doi.org/10.56294/sctconf2024653

Chapter 2
Smart Materials in Biomedicine:
A Promising New Frontier

Mangaiyarkkarasi J.
NMSS Vellaichamy Nadar College, India

Shanthalakshmi Revathy J.
https://orcid.org/0000-0003-1724-7117
Velammal College of Engineering and Technology, India

ABSTRACT

Smart materials, also known as responsive or intelligent materials, are capable of responding to environmental stimuli in a predictable and controlled manner. Significant progress has been achieved in the field of smart materials over the last few decades, and these materials are now being employed in a variety of fields, including biomedical engineering. This chapter explores the use of smart materials in biomedicine, which has opened up a new frontier in the field. The chapter covers the fundamental principles of smart materials and their types, properties, and applications in biomedicine. It presents a thorough overview of the most recent research and development in the application of smart materials in biomedicine, including drug delivery, tissue engineering, biosensors, and imaging, as well as an explanation of the current difficulties and future prospects of this promising topic. This chapter concludes that smart materials possess pronounced potential in biomedicine and could revolutionize the way medical treatments are administered in the future.

DOI: 10.4018/978-1-6684-9224-6.ch002

1. INTRODUCTION

In recent years, the growth of smart materials has fetched a new era in biomedical research and clinical practice. These materials are designed with unique properties that allow them to respond and adapt to changes in their environment. This remarkable characteristic has made them an attractive candidate for a broad range of biomedical uses which includes delivery of drugs, tissue engineering process, and medical imaging systems. Smart materials have the potential to revolutionize the biomedical industry by offering fresh approaches to many of the problems that face the medical community. A family of materials known as "smart materials" can adapt their characteristics or behavior in response to external stimuli such changes in temperature, light, or magnetic fields. (Y.-C. Li et al., 2016). These materials have found numerous applications in the field of biomedicine due to their exceptional properties and abilities to mimic.

Biomedical applications of smart materials are diverse, ranging from drug delivery and tissue engineering to diagnostic tools and wearable devices (Bahl et al., 2020). Smart materials are used as scaffolds in the tissue engineering to offer mechanical support to grow cells and tissues, while also facilitate their growth and differentiation. Smart materials are used in a variety of biomedical devices, where they can perform precise functions due to their unique properties. The mechanisms behind these devices are often rely on the response of the material to specific stimuli.

Smart materials have been found application in drug delivery systems to increase the release of drugs and decrease side effects (Vashist & Ahmad, 2013). These materials can react to specific stimuli like pH or temperature, and release drugs in a controlled manner. For example, smart hydrogels can swell or shrink in response to changes in specific external stimuli, and this response can be used to control drug release. Tissue engineering involves the use of biomaterials to produce functional tissues or organs. Smart materials can be utilized in tissue engineering to generate structures that mimic natural tissues or provide specific functions (Khan & Tanaka, 2017). For instance, scaffolds that can alter shape in response to a particular stimulus can be made using shape memory polymers, enabling them to better mimic the shape of the surrounding tissue.

Smart materials found applications in implants and prosthetics to enhance their durability (Badami & Ahuja, 2014). For instance, stents made of shape memory alloys can expand and contract in response to temperature or stress changes, allowing them to adapt to the surrounding tissue. Self-healing materials are helpful to extend the lifespan of implants and prosthetics by repairing any damage that may occur over time. In sensors and actuators, smart materials are used to detect and respond to specific stimuli. For example, piezoelectric materials can create an electric charge related to mechanical stress, and this response can be used to produce sensors that

detect pressure, strain, or vibration (Song et al., 2021). Shape memory alloys can be employed as actuators that can respond to changes in magnetic or thermal fields in order to carry out particular tasks. Diagnostic instruments like biosensors, which can identify specific compounds or analyses in biological samples, frequently make use of smart materials. (Arab Hassani et al., 2020). They can also be used in wearable devices, such as smart fabrics and sensors, to monitor vital signs, track activity levels, and even detect changes in mood or emotions.

This chapter will explore the current state of research in smart materials and their application in biomedicine, as well as the future directions and potential impact of this promising new frontier.

1.1 Classification of Smart Materials

Based on their mode of operation and the characteristics of their reaction in the biomedical area, smart materials may be divided into a number of types (Kök et al., 2019). The main classification of smart materials are, (i) stimuli-responsive materials, (ii) self-healing materials, (iii) biomimetic materials, (iv) nano materials and (v) hybrid materials. Figure 1 explains classification of smart materials used for biomedical applications.

Figure 1. Classification of smart materials

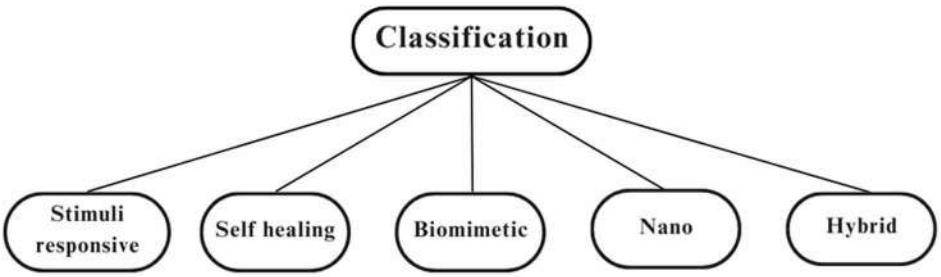

Stimuli-responsive materials respond to a specific stimulus, such as temperature, pH, light, or electric field. Examples: shape-memory alloys, hydrogels, and liquid crystals. Self-healing materials have the capability to renovate themselves after damage or wear. Examples: self-healing polymers and ceramics. Materials that mirror the characteristics and operations of naturally occurring biological materials are known as biomimicry. Examples: synthetic peptides, spider silk, and bio mineralized materials. Nano materials have unique properties at the nanoscale, such as high surface area,

high reactivity, and quantum confinement effects. Examples: carbon nanotubes, quantum dots, and metallic nanoparticles. Hybrid materials combine two or more different types of smart materials to create a new material with enhanced properties. Examples: nano composites, smart coatings, and multifunctional nanoparticles.

The classification of smart biomaterials is not mutually exclusive, and some materials may belong to more than one category depending on their properties and applications.

1.1.1 Exclusive Properties of Smart Materials

Biomaterials are synthetic or natural materials that are used to replace, repair, or augment biological tissues or organs. They have exclusive properties that allow them to interact with living cells and tissues, and to perform their intended functions without causing adverse reactions or harm (Dauda et al., 2021). Figure 2 discusses important properties of smart materials which are appropriate for biomedical field.

Biocompatibility is considered as a chief property of biomaterials because they must be compatible with living tissues and not cause any toxic or immunogenic reactions. This property is essential for the success of any biomaterial-based medical device or implant. In order to stimulate cellular or tissue responses, bioactivity is crucial for engineering tissues and re-forming medicine applications. It does this by encouraging cell adhesion, proliferation, and differentiation. Then, biomaterials must also have appropriate mechanical properties, such as strength, stiffness and elasticity to withstand the forces and stresses of the body. The mechanical characteristics of biomaterials can be customized to match those of the surrounding tissues.

Biomaterials can degrade over time through various mechanisms, such as enzymatic degradation, hydrolysis, or oxidation and hence degradation is utmost important for temporary implants or drug delivery systems that do not require long-term stability. Sterilization is another key property of biomaterials because biomaterials must be sterilized to prevent infections and ensure patient safety. Some biomaterials may be sensitive to certain sterilization methods, such as heat or radiation. Biomaterials can be designed with specific surface properties, such as roughness, hydrophilicity, or charge, to control cell adhesion and proliferation. Surface modification can also improve the biocompatibility of biomaterials. Biomaterials' characteristics are determined by their intended uses and the biological environment in which they will be applied. Successful biomaterials must possess the right mix of qualities in order to carry out their activities efficiently and securely.

Figure 2. Properties of smart materials

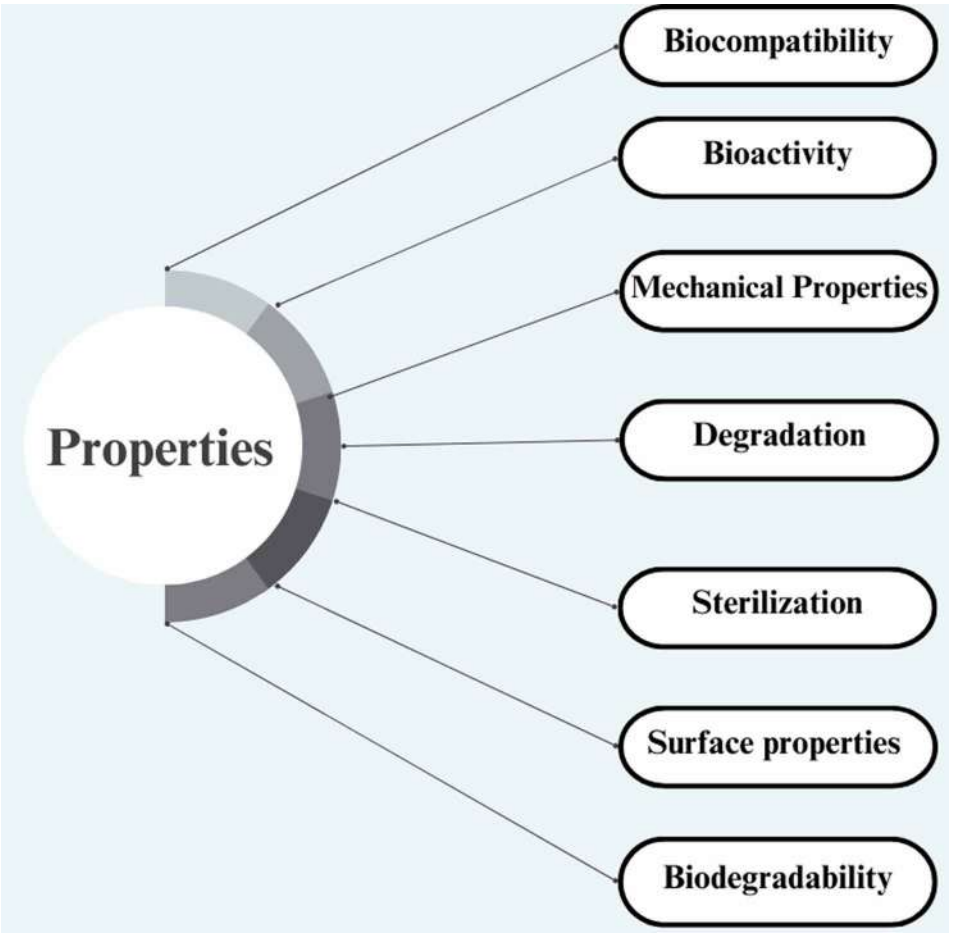

2. ESSENTIAL APPLICATIONS OF SMART MATERIALS IN BIOMEDICINE

Smart materials have numerous applications in biomedical field. Five chief applications are discussed here. (i) Drug delivery systems, (ii) tissue engineering, (iii) diagnostic tools, (iv) wearable technology, and (v) targeted therapy for cancer treatment.

2.1 Drug Delivery Systems

Drug delivery is the procedure of giving medication to a patient through various methods and techniques. These methods may include oral administration, injections, inhalation, topical application, and other targeted delivery methods. Some of the most common types of smart materials adopted for the delivery of drugs are, (i) hydrogels, (ii) liposomes, (iii) dendrimers, (iv) nanoparticles and (v) shape memory polymers.

(i) ***Hydrogels*:** One of the most important types of biomaterials are hydrogels, which have three-dimensional crosslinked polymer chains and can store enormous amounts of water. This property allows them to expand and contract in response to changes in their environment. They can be used to encapsulate drugs and release them in a controlled manner (Mahinroosta et al., 2018). Hydrogels are biocompatible, stimuli responsible like temperature, pH and light. Figure 3 shows how a drug loaded hydrogel is used in various biological systems for drug delivery.

Figure 3. Hydrogel in drug delivery

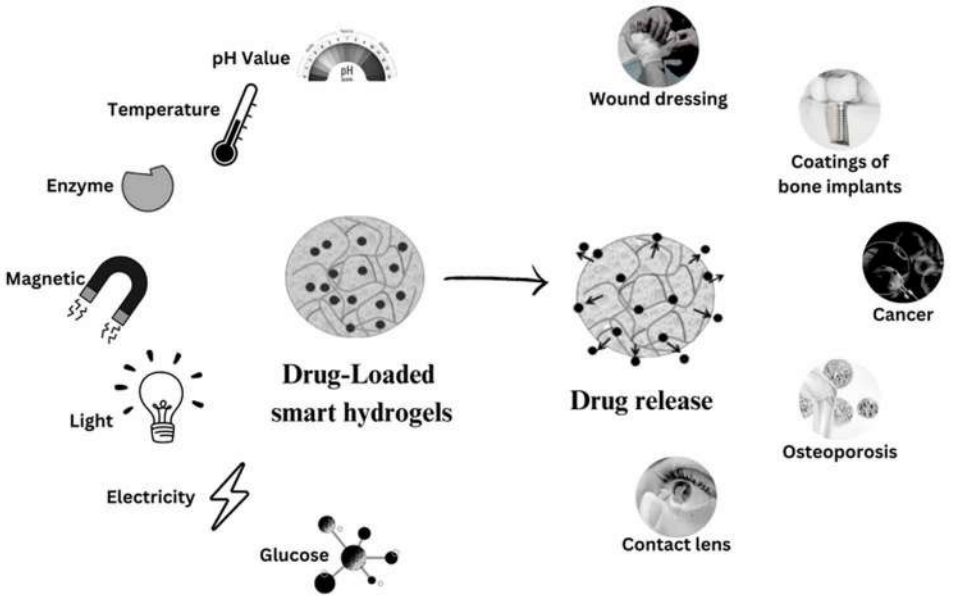

The hydrogel network can either physically enclose the medications or chemically attach them to the polymer chains. Drug delivery systems with specific targets can also be made using hydrogels. By altering the hydrogel with ligands, such as antibodies or peptides which recognize and bind to specific receptors on the target cells, drugs can be delivered to wounded tissues with greater precision. Drug stability and protection against deterioration are two additional benefits of hydrogels. Hydrogels can act as a barrier that prevents the drug from interacting with the surrounding environment, such as enzymes or other chemicals that could degrade the drug. This can help to increase the drug's half-life and lessen the frequency of dosing. Hydrogels are a flexible and promising material for the delivery of drugs that offers controlled and targeted drug release, improved drug stability, and decreased adverse effects. They may completely alter the way we handle a variety of illnesses and disorders.

(ii) ***Liposomes*:** Liposomes are spherical vesicles comprised of a lipid bilayer which encapsulate drugs on specific tissues or cells. They are modified with ligands like antibodies and peptides, to recognize and bind to specific receptors on the target cells, improving drug delivery and reducing toxicity. In drug delivery applications, liposomes can be used to encapsulate drugs and protect them from degradation. Figure 4 shows various parts present in the liposome structure.

Figure 4. Structure of liposomes

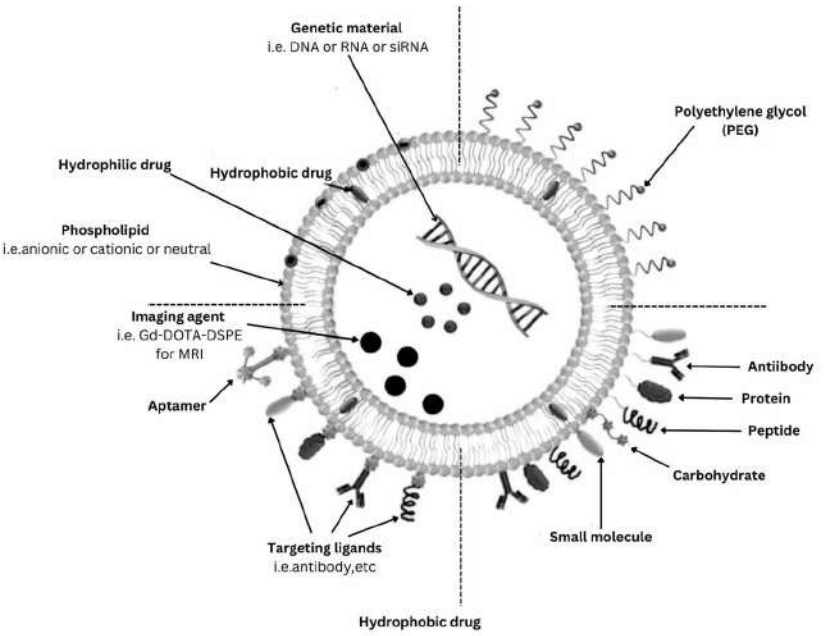

The drug can be encapsulated within the liposome membrane, which acts as a barrier that prevents the drug from interacting with the surrounding environment. This can help to increase the drug's half-life and reduce the frequency of dosing. Liposomes can also be engineered to target specific tissues or cells. The liposome membrane can be altered with ligands which recognize and bind to specific receptors on the target cells, allowing for the selective delivery of drugs to diseased or damaged tissues. This targeted drug delivery approach can reduce side effects and improve the efficacy of the drug (Nakhaei et al., 2021). Another advantage of liposomes is their ability to deliver hydrophilic and hydrophobic type drugs. Hydrophobic medications can be enclosed within the lipid bilayer, whereas hydrophilic pharmaceuticals can be encapsulated within the aqueous interior of the liposome. Since a wider variety of drugs can now be delivered using liposomes, they are a promising material for drug delivery systems. They also offer targeted drug delivery, improved drug stability, and decreased toxicity. They have the ability to completely alter how we handle a variety of illnesses and disorders.

(iii) ***Dendrimers*:** Dendrimers are extremely branched, nanoscale molecules that can be used to encapsulate drugs and deliver them to certain cells or tissues. They are altered to react to various stimuli allowing for targeted and controlled drug release. Dendrimers can be utilized to encapsulate pharmaceuticals and shield them from deterioration in medication delivery applications. Drug delivery to the target tissue or cell is possible when the dendrimer and drug combine to create a stable combination. By adding ligands that recognize and bind to particular receptors on the target cells, the dendrimer can be altered to target particular cells or tissues, such as cancer cells. (B Undre et al., 2016). Figure 5 clearly depicts how dendrimers are used in different drug delivery systems.

Dendrimers can also be engineered to respond to different stimuli, allowing for targeted and controlled drug release. For example, the dendrimer can be designed to issue the drug in response to changes in various stimuli over a period of time. Another benefit of dendrimers is their ability to carry multiple drugs simultaneously. This can be useful in situations where multiple drugs are needed to treat a disease or condition. The dendrimer can form a stable complex with each drug, which can be delivered to the target tissue or cell. Dendrimers are a promising substance for drug delivery systems because they allow for multiple drug delivery, tailored drug administration, and better drug stability. They have the ability to completely alter how we handle a variety of illnesses and disorders. To completely understand their safety and effectiveness in clinical settings, additional research is necessary.

Figure 5. Dendrimers in various drug delivery systems

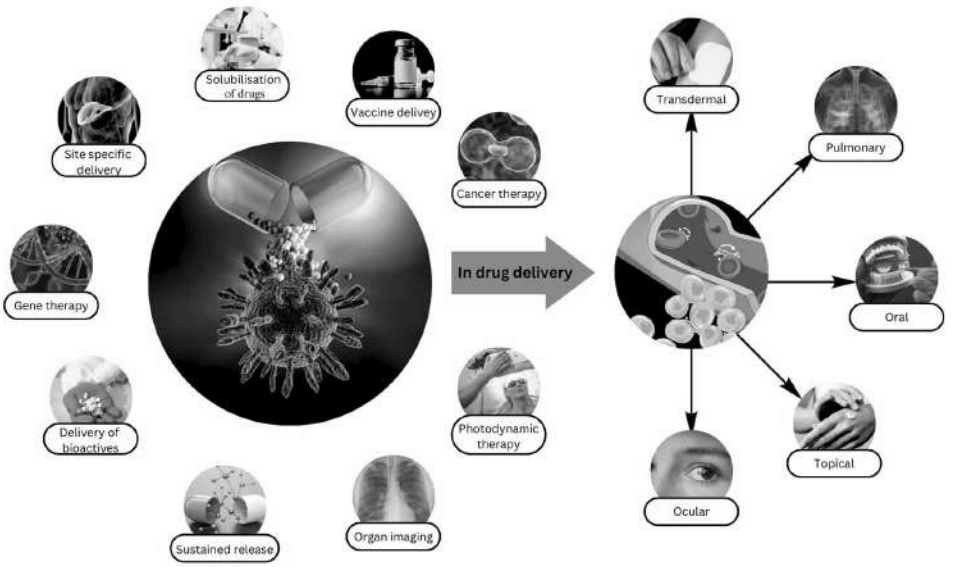

(iv) ***Nanoparticles*:** Nanoparticles are particles with dimensions in the nanometer range that can be used to encapsulate drugs and deliver them to specific cells or tissues. They can be designed to react to various stimuli and can be made from a wide spectrum of materials which comprises metals, lipids, and polymers. Nanoparticles can be utilized to encapsulate pharmaceuticals and protect them from deterioration in medication delivery applications. The medicine may be chemically or physically bound to the nanoparticle surface or physically confined inside the nanoparticle. The nanoparticle can serve as a barrier to stop the drug from interacting with nearby enzymes or other compounds that might cause the drug to break down. This can help to increase the drug's half-life and reduce the frequency of dosing (Aflori, 2021). Figure 6 shows some important biomedical applications of nanoparticles.

Nanoparticles can be created to target particular cells or regions. Drugs can be delivered selectively to diseased or damaged tissues by altering the surface of nanoparticles with ligands that recognize and bind to certain receptors on target cells. This method of focused drug delivery can reduce side effects and increase treatment efficacy. The capability of nanoparticles to deliver both hydrophilic and hydrophobic medications is another advantage. Hydrophilic drugs are encapsulated within the nanoparticle core and hydrophobic drugs are encapsulated within the nanoparticle shell. This allows for the delivery of a wider range of drugs using nanoparticles.

Figure 6. Nanoparticles in biomedicine

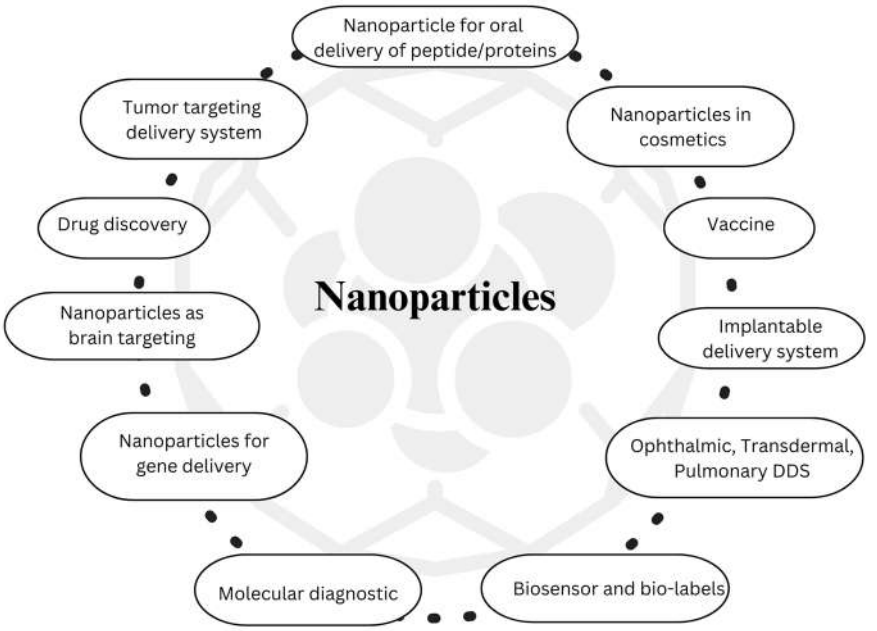

Nanoparticles can also be designed to respond to different stimuli allowing for targeted and controlled drug release. For example, the nanoparticle can be designed to discharge the drug only in the acidic environment of a tumor, minimizing the exposure of healthy tissues to the drug. The potential to transport several medications, better drug stability, and tailored drug delivery make nanoparticles an attractive component for drug delivery systems. They have the ability to completely alter how we handle a variety of illnesses and disorders. To completely understand their safety and effectiveness in clinical settings, additional research is necessary.

(v) ***Shape memory polymers (SMP)*:** Shape-memory polymers can remember and return to their unique shape following distortion. In response to changes in pH or temperature, they can be employed to make drug delivery systems that release drugs in a controlled manner. The SMP can be programmed to change form and release the medicine in response to a particular physiological triggers. This makes it possible to successfully deliver tailored drugs to particular cells or tissues. SMPs can also be used to regulate the discharge rate of drugs. This allows for sustained drug delivery, which can be beneficial in treating chronic conditions (Dhanasekaran et al., 2018). Another advantage of SMPs is their

biocompatibility. SMPs can be designed to be biodegradable and non-toxic, allowing them to be safely used in drug delivery applications.

SMPs are a capable substance for drug delivery systems because they offer biocompatibility, controlled release, and targeted drug delivery. They have the ability to completely alter how we handle a variety of illnesses and disorders. To completely understand their safety and effectiveness in clinical settings, additional research is necessary. As a result, smart materials present a viable strategy for drug delivery systems, enabling targeted and controlled drug release as well as increased efficacy.

2.2 Tissue Engineering

Smart materials have significant capability for tissue engineering process, which is the development of functional tissues to substitute or repair the diseased one. To restore or enhance tissue functioning, tissue engineering tries to produce new tissues that can meld with the host tissue. The basic steps involved in tissue engineering is depicted in figure 7.

Figure 7. Process of tissue engineering

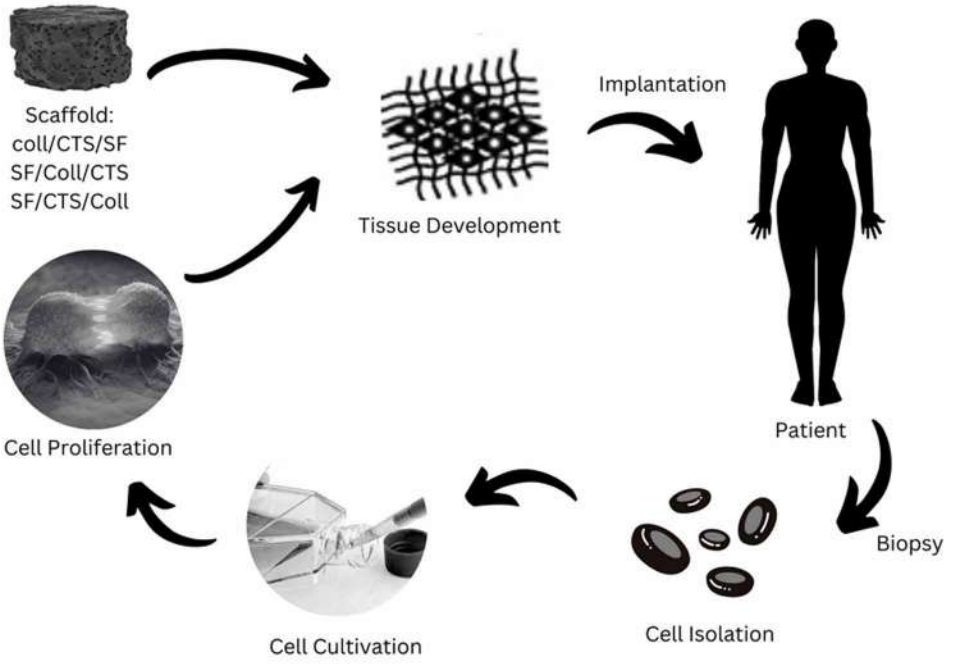

The first step in tissue engineering is cell isolation which involves the isolation of cells from the patient or a donor. Once the cells have been isolated, they are grown in a laboratory under precise conditions to form a tissue-like structure. To prepare cells for use in tissue engineering, they must initially be grown and expanded in a laboratory environment which is known as cell culture. The nutrients, growth factors, and other components required for the cells to develop and multiply are present in the culture media.

Cell scaffold is another component in tissue engineering as it offer a supportive structure for cell addition, proliferation, and distinction. Cell scaffold serves as a temporary extracellular matrix (ECM) that mimics the assembly and function of the natural ECM in vivo. A thorough understanding of cell behaviour, ECM deposition, and tissue remodelling is necessary for the complex process of tissue development in tissue engineering. Tissue engineers design specialised scaffolds that can encourage tissue formation and regeneration using a range of methods, including 3D printing, bioreactors, and microfabrication. Finally, implantation in tissue engineering is a capable approach for the treatment of various ailments and injuries, but it also poses several challenges, such as immune rejection, infection, and limited availability of donor tissues or organs. To overcome these challenges, tissue engineers are developing novel strategies, such as immune tolerance induction, biomaterial-based immunomodulation, and tissue engineering of patient-specific tissues and organs using 3D bio printing and other innovative techniques.

In tissue engineering, hydrogels, biodegradable polymers, electrospun fibres, shape memory polymers and nanoparticles play vital role (Khan & Tanaka, 2017). By offering a favourable environment for cells to attach to and multiply, hydrogels can be employed as scaffolds for cell growth. Since hydrogels are soft and pliable, they can imitate the mechanical characteristics of original tissues and their hydrophilic nature aids in the promotion of cell adhesion and migration. Drug distribution can be controlled by engineering hydrogels to react to certain stimuli, such as changes in pH or temperature. This can be beneficial in tissue engineering by delivering growing factors or other molecules that can endorse tissue regeneration. Hydrogels can be used to promote tissue regeneration by delivering growth factors or other molecules that can stimulate cell growth and differentiation. Hydrogels can also be functionalized with specific molecules or proteins that can promote cell adhesion and differentiation. Because hydrogels are biocompatible, living tissue is not harmed by them. They can thus be employed in vivo without triggering an immune response, making them a desirable material for tissue engineering. Hydrogels are considered as suitable candidate for tissue engineering because they may be created to imitate the mechanical and metabolic characteristics of natural tissues. It is feasible to create scaffolds that upkeep cell growth and differentiation and encourage tissue regeneration by manipulating the characteristics of hydrogels. Hydrogels offer significant potential

for use in tissue engineering, providing a supportive scaffold for cell growth and differentiation and allowing for controlled drug delivery. With further research and development, hydrogels may be able to play a vital role in regenerative medicine by endorsing the growth and regeneration of functional tissues.

Biodegradable polymers are smart materials that can break down into non-toxic components in the body. They can be made to have particular mechanical properties that resemble those of natural tissues and can be utilized as scaffolds for tissue engineering. Biodegradable polymers can also be engineered to discharge growth factors or other molecules that can promote tissue regeneration (Colnik et al., 2020). The ability of biodegradable polymers to provide an environment that encourages cell attachment and proliferation makes them useful as scaffolds for cell growth. Biodegradable polymers can be developed to have mechanical characteristics that resemble those of natural tissues, making them appropriate in tissue engineering. The release of growth factors or other compounds that can encourage tissue regeneration can be designed into biodegradable polymers. The release of these molecules can be controlled by the rate at which the polymer degrades, allowing for controlled drug delivery. Biodegradable polymers are biocompatible, which means they are not injurious to living tissue. This makes them an attractive smart material for tissue engineering because they can be safely used in vivo without causing an immune response. By providing growth factors or other compounds that can encourage cell growth and differentiation, biodegradable polymers can be utilized to support tissue regeneration. Additionally, biodegradable polymers can be functionalized with particular molecules or proteins that can encourage cell differentiation and adhesion. Biodegradable polymers are a desirable material for tissue engineering because they may be created to match the mechanical and metabolic characteristics of natural tissues. By controlling the properties of biodegradable polymers, it is possible to create scaffolds that can support cell growth and differentiation and promote tissue regeneration. So, biodegradable polymers offer significant potential for use in tissue engineering, providing a supportive scaffold for cell growth and differentiation and allowing for controlled drug delivery. With further research and development, biodegradable polymers may be able to play a major role in regenerative medicine by stimulating the growth and regeneration of functional tissues.

An example of a smart material that is functioning as a support for the engineering tissues is electrospun fibres. They can be made to resemble the structure of natural tissues and have a greater surface area to volume ratio. Additionally, functionalizing electrospun fibres with particular molecules or proteins can help cells grow and differentiate. Shape-memory polymers can also be used to generate dynamically responsive scaffolds that can modify shape and adapt to the surrounding tissue. With dimensions ranging from nanometers to micrometres, ultrafine fibres are made using the electrospinning technology. A type of intelligent material called electrospun fibres

can be utilized in tissue engineering to build scaffolds for cell growth and tissue regeneration. In this method, a polymer melt or solution is stretched and lengthened by an electrostatic field before being collected as fibre material on a grounded surface.(Parham et al., 2020). By offering an environment that is conducive to cell attachment and proliferation, electrospun fibres can be employed as scaffolds for cell growth. Electrospun fibres' high surface area to volume ratio can improve cell adhesion and development, and the fibres can be positioned in various directions to resemble the composition of natural tissues. To encourage tissue regeneration, electrospun fibres can be functionalized with medicines or growth factors. The fibres' ability to release the medications or growth factors at a controlled rate enables sustained distribution over a long period of time.

Electrospun fibers are biocompatible, which means they are not harmful to living tissue. This makes the smart materials are promissing for tissue engineering because they can be safely used in vivo without causing an immune response. By providing compounds that can promote cell growth and differentiation, such as growth factors, electrospun fibres can be utilized to drive tissue regeneration. In addition to this, specific molecules or proteins that can encourage cell adhesion and differentiation can be functionalized into electrospun fibres. The mechanical and metabolic characteristics of natural tissues can be replicated in electrospun fibres, making them a suitable material for tissue engineering. By controlling the properties of electrospun fibers, it is possible to create scaffolds that can support cell growth and differentiation and promote tissue regeneration. With the ability to provide controlled doses of medication and serve as a supporting scaffold for cell development and differentiation, electrospun fibres are promising candidates for application in tissue engineering. By encouraging the creation and regeneration of functioning tissues, electrospun fibres may eventually be able to play a major part in regenerative medicine. Shape memory polymers (SMPs) are a kind of polymers that can vary their shape by responding to an external stimulus. SMPs have been used in tissue engineering to produce scaffolds that can change their shape in response to changes in the physiological environment, allowing them to adapt to the surrounding tissue and promote tissue regeneration. SMPs can be used to make 3D scaffolds with complex shapes and structures. The scaffold has the ability to be programmed to take on two different shapes. Temporary shape at high temperatures that can be readily manipulated and moulded, and a permanent shape at body temperatures that allows the scaffold to adapt to the surrounding tissue and encourage cell proliferation and tissue regeneration. In tissue engineering, SMPs are essential for drug delivery. Drug administration can be targeted and controlled using the SMPs, which is set to release medications corresponding to fluctuations in the physiological environment, such as pH, temperature, or light. This will aid in the promotion of tissue regeneration.

SMPs can also be used to create tissue engineering devices, such as stents, sutures, and other implants.

SMPs can be utilized in tissue engineering for applications including wound healing. SMPs are a promising material in tissue engineering because they can be tailored to have specific mechanical, chemical, and biological properties and react to changes in the physiological environment, allowing for better tissue regeneration and improved clinical outcomes. The SMPs can be used to create wound dressings that change their shape in response to changes in the wound environment, allowing for better wound coverage and improved healing.

Nowadays, nanoparticles are largely used in tissue engineering also to deliver growth factors or other molecules that can promote tissue regeneration. They can also be used as contrast agents for imaging, allowing researchers to monitor the growth and development of new tissues. Nanoparticles are minute particles which have 1nm to 100nm size and largely employed in tissue engineering which includes drug delivery, cell labeling, tissue imaging and in medication delivery systems. They can be designed to have certain characteristics, such as surface charge, size, and functional groups, enabling selective drug delivery to a particular cell or tissue. Nanoparticles can also shield pharmaceuticals from deterioration and clearance, enabling controlled drug release and increased therapeutic efficacy. For imaging systems like computed tomography (CT) and magnetic resonance imaging (MRI), nanoparticles are utilized as contrast agents. They can also be used to label cells and track their distribution in the body. Nanoparticles can be used to enhance tissue regeneration by improving cell adhesion, proliferation, and differentiation. They can be included into hydrogels or scaffolds to provide mechanical support and improve the mechanical and organic features of the tissue-engineered product. Nanoparticles can be used to stop bacteria from growing on tissues or implanted devices. For instance, silver nanoparticles can be used as coatings for implantable devices because they have been found to have strong antibacterial activity. Using nanoparticles, illness indicators in the body can be found. They can be created to bind specifically to proteins or nucleic acids that are associated with a particular disease, enabling early disease detection and diagnosis. For these reasons nanoparticles are a promising material in tissue engineering, as they are modified to possess particular properties and functions and can be used for wide range of applications viz., drug supply, cell labeling, tissue imaging, and tissue regeneration. However, there are still challenges to overcome, such as toxicity, biocompatibility, and long-term safety, before nanoparticles can be used in clinical applications.

2.3 Diagnostic Tools

Smart materials' distinctive qualities, including sensitivity, specificity, biocompatibility, and biodegradability, have led to an increase in their application in diagnostic equipment. Here are some instances of intelligent materials utilized in diagnostic equipment: Analytical tools called biosensors can identify and quantify biological substances or organisms. Biosensors with high sensitivity and specificity for biomarker detection can be made using smart materials including nanomaterials, quantum dots, and polymers. Biosensors can be used in point-of-care diagnostic tools for the timely finding of syndromes like cancer, cardiovascular diseases, and infectious diseases (Genchi et al., 2017). The technology of microfluidics involves controlling tiny quantities of fluid in tiny channels. Microfluidic devices can be made with smart materials including hydrogels, polymers, and nanoparticles to detect and measure biomolecules. Point-of-care diagnostics, medication screening, and personalized medicine can all be performed using microfluidic devices. Biological processes in vivo can be seen and tracked using imaging probes.

Smart materials with high sensitivity and specificity for molecular imaging include nanoparticles, quantum dots, and fluorescent dyes. Imaging probes can be used to monitor the development of diseases and to detect them early. Another technology, lab-on-a-chip which involves integrating multiple laboratory tasks in one microchip. Smart materials such as hydrogels, polymers, and nanoparticles can be used in lab-on-a-chip gadgets for synthesis of samples, detection, and analysis. Lab-on-a-chip devices can be used for point-of-care diagnostics, drug screening, and environmental monitoring. Wearable sensors are gadgets that can be worn on the body to track physiological data including blood pressure, glucose levels, and heart rate. Wearable sensors can detect and monitor biomarkers using intelligent materials including hydrogels, polymers, and nanomaterials. Wearable sensors can be used to track the development of diseases and to detect them early.

Smart materials offer significant potential for use in diagnostic tools, providing high sensitivity, specificity, and biocompatibility. With further research and development, smart materials may be capable to improve the accuracy and efficiency of disease diagnosis, monitoring, and treatment.

2.4 Wearable Devices

Several types of smart materials are used in wearable devices (Jin et al., 2018) because of their distinctive properties like flexibility, stretch ability, and biocompatibility. Some examples of smart materials used in wearable devices are explained here.

Conductive polymers: This class of intelligent material is capable of conducting electricity. They are utilized to make stretchable, flexible electrodes for wearable technology that can be incorporated into garments and other items. To assess physiological signals including heart rate, temperature, and muscle activity, conductive polymers can be utilized.

Alloys with shape memory: A class of intelligent material known as shape-memory alloys is capable of recovering from deformation. They are used in wearable devices to create flexible and shape-changing components such as springs, hinges, and wires. Nowadays shape-memory alloys are also used in smart clothing, smart eyewear, and other wearable accessories. A type of intelligent material that can absorb and hold onto water is called a hydrogel. They help produce soft, flexible sensors that can adapt to the shape of the body for wearable technology. They are capable of measuring physiological signals like pH, humidity, and temperature.

Nanomaterials: They have distinctive optical, electrical, and mechanical capabilities. They are used to make sensors, antennae, and other parts that can be incorporated into garments or other wearable accessories for wearable devices. Nanomaterials can be used to measure physiological signals such as blood oxygen levels, heart rate, and respiration rate. Electronic textiles, a kind of smart material, are made by fusing conventional textiles with electronic components such as sensors, conductive materials, and power sources. They create clothing and other wearable technology items that can track physiological signs and other traits. Electronic textiles can be used in smart clothing, smart gloves, and other wearable accessories (Zheng et al., 2021).

Smart materials offer significant potential for use in wearable devices. With further research and development, smart materials may be successful in improving the efficiency of wearable devices for health monitoring, fitness tracking, and other applications

2.5 Targeted Therapy and Imaging in Cancer Treatment

Targeted Therapy: Drugs or other therapeutic agents can be used specifically to target cancer cells while sparing healthy cells is known as targeted therapy. Cancer is a complex disease that requires personalized treatment approaches for optimal outcomes. Smart materials have emerged as promising tools for targeted therapy and imaging in cancer treatment due to their exceptional properties and ability to respond to specific stimuli (Yang et al., 2021). The use of smart materials in cancer treatment can improve drug delivery, reduce side effects, and enable non-invasive imaging of tumors. Figure 2.6 describes different technologies adopted in targeted therapy for breast cancer treatment.

Figure 8. Targeted therapy for breast cancer

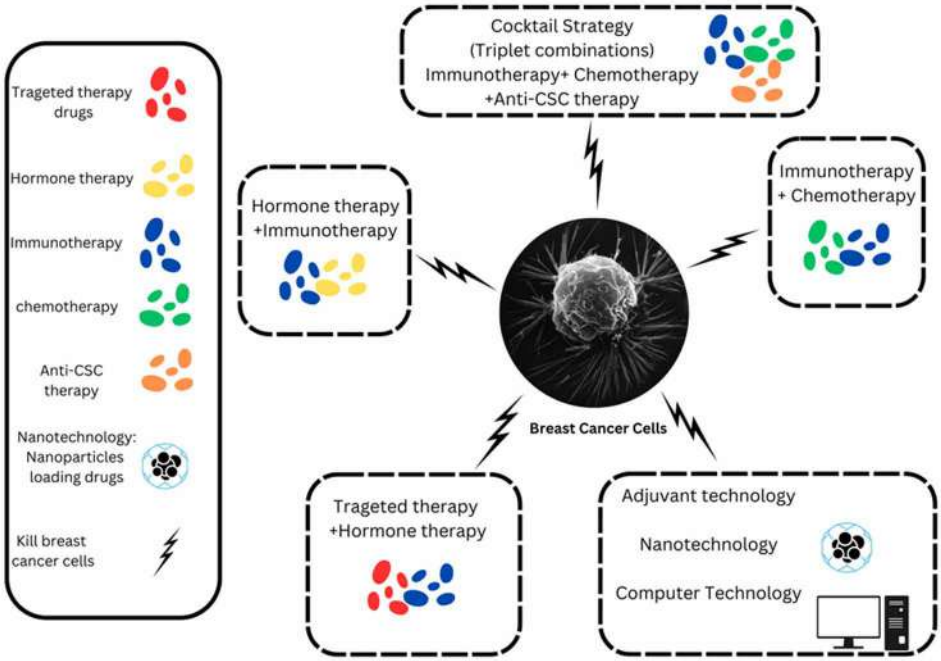

One example of a smart material used for targeted therapy is liposomes, which are in spherical structures made of lipids. Liposomes can be designed to encapsulate drugs and target specific cancer cells, allowing for effective drug delivery and reducing toxicity to healthy cells. Additionally, the effectiveness of liposomes can be increased by adding targeting ligands to their surface that precisely attach to receptors on cancer cells. The three-dimensional networks of hydrophilic polymers known as hydrogels, which have a high water-holding capacity, are another type of intelligent material employed in targeted therapy. Drug release can be triggered using hydrogels that are made to react to certain stimuli, including pH or temperature changes. For instance, a hydrogel that is pH sensitive can be created to release medication in reaction to the acidic environment of tumors.

Imaging: Smart materials can also be used for non-invasive imaging of tumors, allowing for prior detection and more precise diagnosis of cancer. Quantum dots, which are nanocrystals that release light when activated by an external light source, are one type of intelligent material utilized for imaging. Quantum dots can be modified to target specific cancer cells and emit light at specific wavelengths, allowing for the imaging of tumors with high sensitivity and specificity (J. Li et al., 2020). Another smart material used for imaging is magnetic nanoparticles, which can be used for

magnetic resonance imaging (MRI) of tumors. Magnetic nanoparticles can be coated with targeting ligands to specifically bind to cancer cells and allow for more accurate imaging of tumors. Smart materials have shown great potential for targeted therapy and imaging in cancer treatment. Continued research and development of smart materials for cancer treatment can lead to more effective and personalized treatment methodologies for cancer patients.

3. REGULATORY CHALLENGES AND FUTURE PROSPECTS OF SMART MATERIALS IN BIOMEDICAL FIELD

Due to their distinctive properties, smart materials have shown pronounced assurance in biomedical field, however, there are still a number of regulatory issues that need to be resolved. These difficulties include ensuring the safety and effectiveness of smart materials as well as creating regulatory frameworks that can keep up with the field's rapid advancement (Yadav et al., 2022).

One of the main challenges for regulatory agencies is ensuring the safety of smart materials. Some smart materials, such as nanoparticles, have been shown to have potential toxicity, which could limit their usage in biomedical applications. Regulatory agencies should will need to ensure that smart materials used in biomedical applications undergo severe testing to ensure their safety. Another challenge is ensuring the effectiveness of smart materials. Due to the complexity of smart materials, a variety of variables, including alterations in the environment, may have an impact on their performance. As a result, it could be challenging to verify consistent performance across several applications. Guidelines for assessing the performance of smart materials in biomedical applications must be developed by regulatory organizations.

Regulatory bodies will also have the issue of keeping up with the rapidly developing field of smart materials. Regulatory authorities will need to be able to examine new materials swiftly and effectively because they are being created at a rapid rate. The scientific community and regulatory bodies will need to work closely together to build new regulatory frameworks that can keep up with the rapidly evolving field of smart materials. Despite these difficulties, smart materials have bright futures in biomedical applications. As new materials are created, they have the potential to completely transform the medical industry, from tissue engineering to drug delivery and beyond. The potential uses for smart materials are endless, and they are already used in many different health devices.

In conclusion, the usage of smart materials in biomedical field is a rapidly evolving field that presents both regulatory challenges and exciting opportunities. Regulating bodies will face a difficult task in ensuring the efficacy and safety of smart

materials, but potential advantages of these materials make the effort worthwhile. The prospects for smart materials in biological applications are promising in the future, provided that research is conducted and regulatory bodies and the scientific community continue to work together.

4. BIOCOMPATIBILITY AND SAFETY CONSIDERATIONS FOR SMART MATERIALS

Due to their special characteristics and capacity to react to particular stimuli, smart materials have demonstrated significant potential for use in biological applications. However, there are significant safety and biocompatibility issues with their use in implants and medical devices. The term "biocompatibility" means the capability of a material to carry out its proposed role without causing a poisonous, immunological, or other negative reaction in the body. Biocompatibility is a critical consideration when designing and selecting smart materials for biomedical applications (Schmalz & Galler, 2017). Some of the main issues that affect the biocompatibility of smart materials are listed below.

(i) ***Chemical composition***: The chemical composition of a smart material can significantly affect its biocompatibility. Materials that are non-toxic and non-reactive are generally preferred for biomedical applications.
(ii) ***Degradation and stability***: The stability and degradation of smart materials are also critical factors for biocompatibility. Materials that degrade too quickly or too slowly can cause adverse reactions in the body.
(iii) ***Surface properties***: The surface properties of a smart material can affect its interactions with biological tissues and cells. Materials with uneven or hydrophobic surfaces can induce inflammation or other adverse effects.
(iv) ***Mechanical properties***: Mechanical properties of smart materials like stiffness and elasticity, can also affect their biocompatibility. Materials that are too rigid or too flexible may cause tissue damage or other adverse reactions
(v) ***Biofouling***: Biofouling refers to the accumulation of biological material on the surface of a material. Smart materials that are prone to biofouling can cause infections or other adverse reactions.

It is also essential to consider the safety of smart materials in terms of potential toxicity, immunogenicity, and other adverse effects. This requires thorough testing and evaluation of smart materials before they are used in medical devices or implants. The biocompatibility and safety of smart materials are critical considerations for their use in biomedical applications. To make sure that they can fulfil their intended

purpose without endangering the body, these materials must be carefully designed and tested. Smart materials have the potential to revolutionize medicine and enhance patient outcomes with proper design, testing, and evaluation.

5. RECENT ADVANCES AND EMERGING TRENDS IN SMART MATERIALS FOR BIOMEDICAL APPLICATIONS

In recent decades, the practice of smart materials in the biomedical trade has been the focus of extensive research. On the basis of recent research, recent developments and emerging trends in smart materials for the biomedical area are presented below (Dai et al., 2022).

Smart hydrogels are capable to discharge pharmaceuticals in response to certain stimuli and hence, researchers have been looking into its application for drug delivery. For instance, scientists have created a smart hydrogel that can release insulin in reaction to variations in blood glucose levels, thereby opening up a new diabetes treatment option. Next, it was reported that shape-memory alloys were used for implantable devices like stents because they could be inserted compactly and then expand to take on the desired shape once inside the body. This innovation has the potential to completely change how cardiovascular diseases are treated. The usage of electroactive polymers for engineering tissues is also a hot topic of research since they can create scaffolds that replicate the electrical characteristics of real tissues. Examples include the exploration of the functionality of smart sutures, which can release medications or monitor wound healing in real-time, and the development of an electroactive polymer scaffold that can encourage the regeneration of injured nerves. For example, researchers have developed a smart suture that can release antibiotics in response to infection(Basu et al., 2022).

The function of smart materials in the biomedical field is an electrifying area of exploration with many important applications. Future developments in their applications should increase as our knowledge of these materials deepens. As a result, there are exciting possibilities for the creation of brand-new, cutting-edge medical implants and devices thanks to recent developments of smart materials in biomedical field. Smart materials have the potential to revolutionise medicine and enhance patient outcomes with sustained study and development (Ajay et al., 2023).

6. FUTURE PROSPECTS FOR SMART MATERIALS

According to recent researches smart materials have the competing potential to change a number of industries and how we live and work (Allizond et al., 2022).

Research and technological advancements are continuing to push the envelope of what is possible, the prospects for smart materials in the future are positive. The fields of healthcare, energy, aerospace, defence, building materials, and consumer electronics are among those where smart materials could be used and developed. Smart materials can be employed in the healthcare industry to create cutting-edge medical equipment including artificial organs, implantable computers, and drug delivery systems. They can also be used to make intelligent fabrics that can deliver medication or monitor vital signs. Smart materials can be used to develop new energy storing and renovation technologies like solar cells, batteries, and fuel cells. In the field of aerospace and defence, smart materials can be used to create lightweight, strong, and durable materials for aircraft and spacecraft. They can also be used to develop self-healing materials that can repair damage caused by extreme conditions (Kumar et al., 2023).

Modern building materials that are more effective, long-lasting, and ecologically friendly are created using smart materials. They can also be used to build intelligent structures that can recognise and react to alterations in their surroundings. They discovered intriguing uses for it in the area of consumer electronics, where it can be applied to the development of novel and ground-breaking goods including flexible screens, wearable electronics, and smart sensors. We may anticipate even more intriguing innovations and applications of smart materials in the future as research in this area advances. The potential benefits to society are enormous, ranging from improved healthcare and energy efficiency to more sustainable and resilient infrastructure.

7. CONCLUSION

Smart materials have emerged as a promising new frontier in the field of biomedicine, with the potential to revolutionize various aspects of healthcare. The ability to build materials that may respond to specific stimuli has opened up new opportunities for the development of revolutionary medical devices, drug delivery systems, and tissue engineering scaffolds. The need for personalised medicine, the rise in chronic illness incidence, and the growing desire for more effective and affordable therapies are just a few of the major problems that smart materials may help solve in the healthcare industry today. Despite the fact that there are still numerous obstacles to be cleared, such as those involving toxicity, biocompatibility, and regulatory approval, smart materials in biomedicine have a very bright future. Vigorous research and innovation in this field will certainly lead to new developments and advances in medical technology, ultimately improving the lives of millions of people around the world. As such, the study and progress of smart materials in biomedicine is an

exciting and rapidly growing area of research, with far-reaching implications for the future of healthcare. We can only imagine the possibilities that will arise as we continue to explore this fascinating and promising new frontier.

REFERENCES

Aflori, M. (2021). Smart Nanomaterials for Biomedical Applications—A Review. *Nanomaterials (Basel, Switzerland)*, *11*(2), 396. doi:10.3390/nano11020396 PMID:33557177

Ajay, P. Ahmad, S., Sharma, J., & Gambhir, V. (2023). Handbook of Sustainable Materials: Modelling, Characterization, and Optimization. CRC Press. doi:10.1201/9781003297772

Allizond, V., Comini, S., Cuffini, A. M., & Banche, G. (2022). Current Knowledge on Biomaterials for Orthopedic Applications Modified to Reduce Bacterial Adhesive Ability. *Antibiotics (Basel, Switzerland)*, *11*(4), 529. doi:10.3390/antibiotics11040529 PMID:35453280

Arab Hassani, F., Shi, Q., Wen, F., He, T., Haroun, A., Yang, Y., Feng, Y., & Lee, C. (2020). Smart materials for smart healthcare– moving from sensors and actuators to self-sustained nanoenergy nanosystems. *Smart Materials in Medicine*, *1*, 92–124. doi:10.1016/j.smaim.2020.07.005

Badami, V., & Ahuja, B. (2014). Biosmart Materials: Breaking New Ground in Dentistry. *TheScientificWorldJournal*, *2014*, 1–7. doi:10.1155/2014/986912 PMID:24672407

Bahl, S., Nagar, H., Singh, I., & Sehgal, S. (2020). Smart materials types, properties and applications: A review. *Materials Today: Proceedings*, *28*, 1302–1306. doi:10.1016/j.matpr.2020.04.505

Basu, B., Gowtham, N. H., Xiao, Y., Kalidindi, S. R., & Leong, K. W. (2022). Biomaterialomics: Data science-driven pathways to develop fourth-generation biomaterials. *Acta Biomaterialia*, *143*, 1–25. doi:10.1016/j.actbio.2022.02.027 PMID:35202854

Colnik, M., Knez-Hrncic, M., Skerget, M., & Knez, Z. (2020). Biodegradable polymers, current trends of research and their applications, a review. *Chemical Industry & Chemical Engineering Quarterly*, *26*(4), 401–418. doi:10.2298/CICEQ191210018C

Dai, H., Fan, Q., & Wang, C. (2022). Recent applications of immunomodulatory biomaterials for disease immunotherapy. *Exploration*, *2*(6), 20210157. doi:10.1002/EXP.20210157 PMID:37324799

Dauda, K. T., Majebi, C., Ayoola, A. A., Agboola, O., Popoola, A. P., Fayomi, O. S. I., Banjo, S. O., Sojobi, J., & Ogunsanya, A. O. (2021). Biosmart Materials and Its Innovative Characteristics in Protective Composite Coating Application. *IOP Conference Series. Materials Science and Engineering*, *1107*(1), 012216. doi:10.1088/1757-899X/1107/1/012216

Dhanasekaran, R., Sreenatha Reddy, S., Girish Kumar, B., & Anirudh, A. S. (2018). Shape Memory Materials for Bio-medical and Aerospace Applications. *Materials Today: Proceedings*, *5*(10), 21427–21435. doi:10.1016/j.matpr.2018.06.551

Genchi, G. G., Marino, A., Tapeinos, C., & Ciofani, G. (2017). Smart Materials Meet Multifunctional Biomedical Devices: Current and Prospective Implications for Nanomedicine. *Frontiers in Bioengineering and Biotechnology*, *5*, 80. doi:10.3389/fbioe.2017.00080 PMID:29326928

Jin, H., Jin, Q., & Jian, J. (2018). Smart Materials for Wearable Healthcare Devices. In *Wearable Technologies*. InTech. doi:10.5772/intechopen.76604

Khan, F., & Tanaka, M. (2017). Designing Smart Biomaterials for Tissue Engineering. *International Journal of Molecular Sciences*, *19*(1), 17. doi:10.3390/ijms19010017 PMID:29267207

KÖK, M., Qader, İ. N., Dağdelen, F., & Aydoğdu, Y. (2019). Akıllı Malzemeler üzerine derleme: araştırmalar ve uygulamaları. *El-Cezeri Fen ve Mühendislik Dergisi*. doi:10.31202/ecjse.562177

Kumar, A., Kumar, P., Mittal, R. K., & Gambhir, V. (2023). Materials processed by additive manufacturing techniques. In Advances in Additive Manufacturing Artificial Intelligence, Nature-Inspired, and Biomanufacturing (pp. 217–233). Elsevier. doi:10.1016/B978-0-323-91834-3.00014-4

Li, J., Guan, X., Fan, Z., Ching, L.-M., Li, Y., Wang, X., Cao, W.-M., & Liu, D.-X. (2020). Non-Invasive Biomarkers for Early Detection of Breast Cancer. *Cancers (Basel)*, *12*(10), 2767. doi:10.3390/cancers12102767 PMID:32992445

Li, Y.-C., Zhang, Y. S., Akpek, A., Shin, S. R., & Khademhosseini, A. (2016). 4D bioprinting: The next-generation technology for biofabrication enabled by stimuli-responsive materials. *Biofabrication*, *9*(1), 012001. doi:10.1088/1758-5090/9/1/012001 PMID:27910820

Mahinroosta, M., Jomeh Farsangi, Z., Allahverdi, A., & Shakoori, Z. (2018). Hydrogels as intelligent materials: A brief review of synthesis, properties and applications. *Materials Today. Chemistry*, *8*, 42–55. doi:10.1016/j.mtchem.2018.02.004

Nakhaei, P., Margiana, R., Bokov, D. O., Abdelbasset, W. K., Jadidi Kouhbanani, M. A., Varma, R. S., Marofi, F., Jarahian, M., & Beheshtkhoo, N. (2021). Liposomes: Structure, Biomedical Applications, and Stability Parameters With Emphasis on Cholesterol. *Frontiers in Bioengineering and Biotechnology*, *9*, 705886. doi:10.3389/fbioe.2021.705886 PMID:34568298

Parham, S., Kharazi, A. Z., Bakhsheshi-Rad, H. R., Ghayour, H., Ismail, A. F., Nur, H., & Berto, F. (2020). Electrospun Nano-Fibers for Biomedical and Tissue Engineering Applications: A Comprehensive Review. *Materials (Basel)*, *13*(9), 2153. doi:10.3390/ma13092153 PMID:32384813

Schmalz, G., & Galler, K. M. (2017). Biocompatibility of biomaterials – Lessons learned and considerations for the design of novel materials. *Dental Materials*, *33*(4), 382–393. doi:10.1016/j.dental.2017.01.011 PMID:28236437

Song, M., Lin, X., Peng, Z., Xu, S., Jin, L., Zheng, X., & Luo, H. (2021). Materials and Methods of Biosensor Interfaces With Stability. *Frontiers in Materials*, *7*, 583739. doi:10.3389/fmats.2020.583739

Undre, B, S., R. Pandya, S., Kumar, V., & Singh, M. (2016). Dendrimers As Smart Materials For Developing The Various Applications In The Field Of Biomedical Sciences. *Advanced Materials Letters*, *7*(7), 502–516. doi:10.5185/amlett.2016.6153

Vashist, A., & Ahmad, S.VASHIST. (2013). Hydrogels: Smart Materials for Drug Delivery. *Oriental Journal of Chemistry*, *29*(03), 861–870. doi:10.13005/ojc/290303

Yadav, S., Sadique, M. A., Kaushik, A., Ranjan, P., Khan, R., & Srivastava, A. K. (2022). Borophene as an emerging 2D flatland for biomedical applications: Current challenges and future prospects. *Journal of Materials Chemistry. B, Materials for Biology and Medicine*, *10*(8), 1146–1175. doi:10.1039/D1TB02277F PMID:35107476

Yang, Y., Zeng, W., Huang, P., Zeng, X., & Mei, L. (2021). Smart materials for drug delivery and cancer therapy. *VIEW*, *2*(2), 20200042. doi:10.1002/VIW.20200042

Zheng, Z., Jur, J., & Cheng, W. (2021). Smart materials and devices for electronic textiles. *MRS Bulletin*, *46*(6), 488–490. doi:10.155743577-021-00120-5

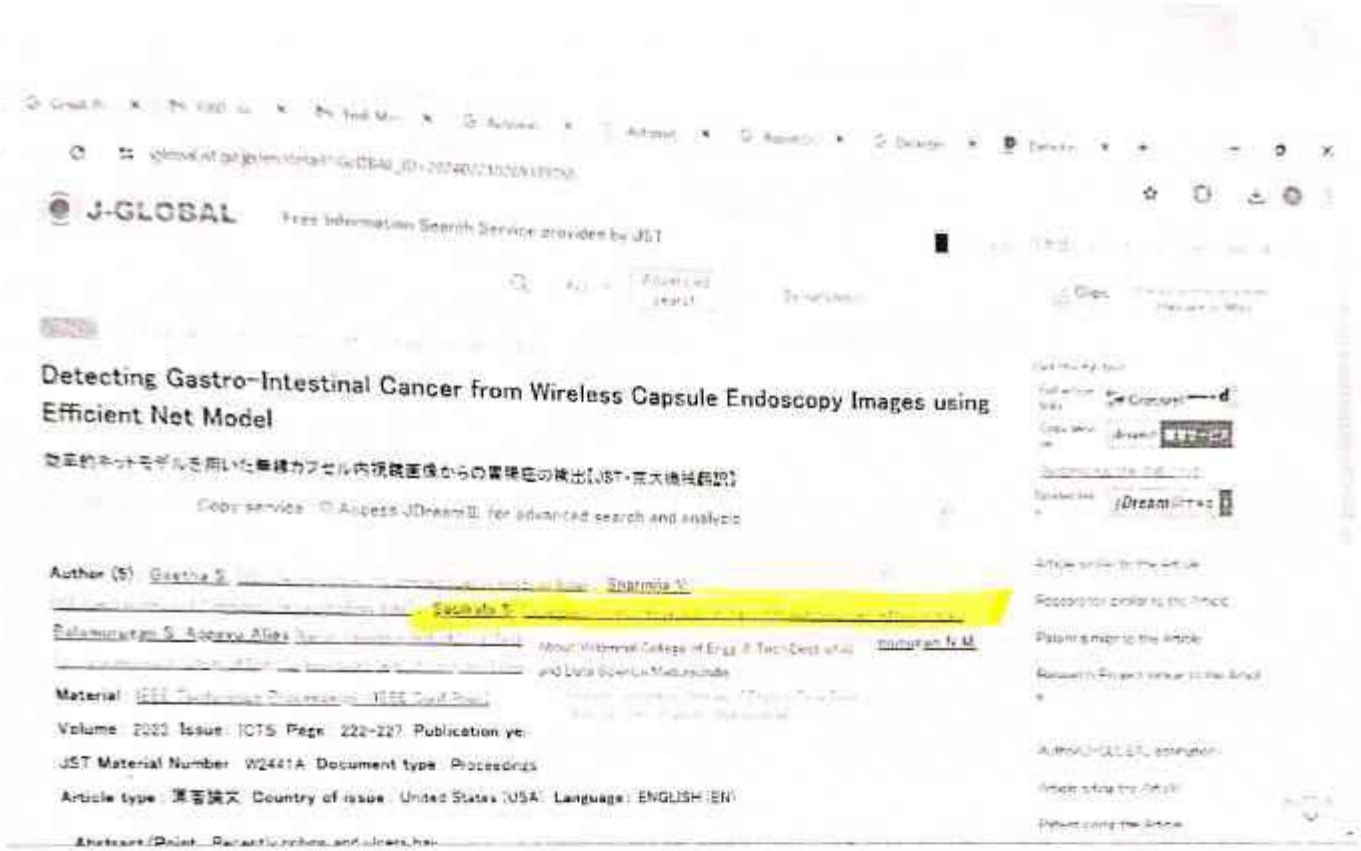
J-GLOBAL
Free Information Search Service provided by JST
Detecting Gastro-Intestinal Cancer from Wireless Capsule Endoscopy Images using Efficient Net Model
Author (S)
Material
Volume 2020 Issue ICTS Page 222-227 Publication ye
JST Material Number W2441A Document type Proceedings
Article type 原著論文 Country of issue United States (USA) Language ENGLISH (EN)

Contents lists available at

Biomedical Signal Processing and Control

journal homepage:

Automatic diagnosis of mental illness using optimized dynamically stabilized recurrent neural network

J. Shanthalakshmi Revathy [*], N. Uma Maheswari [b], S. Sasikala [c], R. Venkatesh

[a] Department of Computer Science and Engineering, Velammal College of Engineering and Technology, Madurai, Tamil Nadu, India
[b] Department of Computer Science and Engineering, PSNA College of Engineering and Technology, Dindigul, Tamil Nadu, India
[c] Department of Information Technology, PSNA College of Engineering and Technology, Dindigul, Tamil Nadu, India

ARTICLE INFO

Keywords:
Adaptive Variational Bayesian Filter
Dual-domain feature extraction
Dynamically Stabilized Recurrent Neural Network
Open Sourcing Mental Illness (OSMI) data set
Rapids Search Optimization Algorithm
Siberian Tiger Optimization Algorithm

ABSTRACT

An Automatic Diagnosis of Mental Illness Using Optimized Dynamically Stabilized Recurrent Neural Network is proposed in this paper. The aim of the proposed method is to automatically detect mental illness disorder from OSMI data records. The proposed approach automatically extracts the features needed for the network's training from the OSMI records in contrast to comparable literature research that employs conventional machine learning algorithms. Using the dual domain feature extraction method the time domain features (minimum, maximum, mean and medium) and statistic features (standard deviation, mean, kurtosis, and skew ness) of OSMI dataset is extracted. This research uses these extracted features for automatic diagnosis of mental illness disorder disease, and it has better accuracy performance. This is trained with Dynamically Stabilized Recurrent Neural Network (DSRNN) to extract key features in the dataset and train the network. By using OSMI dataset from different age groups, this research demonstrates a high success rate in categorizing mental illness and healthy individuals with 98 % and 99.5 % accuracy. DSRNN clearly shows the relation of frequency components among mental illness patients and the healthy individual. These results make it simple to discriminate between people with mental illnesses and healthy people.

1. Introduction

In the last ten years, there has been a 13 % increase in neurological or mental problems . Developmental problems that significantly impact many facets of life, like academic or professional performance, interpersonal connections with family and friends, community involvement, are sometimes indicative of mental disorders. The range of developmental problems varies depending on the type of condition . World Health Organization research states that there is a global rise in the number of people suffering from mental illnesses. The report specified that approximate 20 % of children and adultssuffered from mental illnesses, which can occasionally result in suicide. The majority of the time, clinical judgment and patient self-report are used in the diagnosis and treatment of mental illnesses . Therefore, making a diagnosis might be difficult particularly if a patient has cognitive impairments. Across the world, one of the most common mental illnesses is bipolar disorder (BD). BD is nothing but manic depression, this is a severe mental illness marked by extreme mood fluctuations that range from mania to depression. Normal mood intervals alienate the manic and depressive . Physicians frequently categorize a patient's temporary mental illness into multiple categories. Three manic levels identified by clinicians, they are: Mania (high arousal), Hypomania (less severe than Mania), Remission. When a person experiences depression, he may feel hopeless and lose interest in many types of daily activities . While the mood changes to mania or hypo-mania, the patient may feel excited, full of energy, or unusually too irritable . These mood swings can impact one's capacity for clear thinking, behavior, energy, sleep, and activities. As a result, BD can continue to affect a person's health and ability to work .

The primary disadvantage of self-administered and conventional clinician approaches is their susceptibility to bias and lack of consistency. Self-administered questionnaires rely heavily on patients being truthful in sharing information about their mental and behavioral state. Research has demonstrated that inconsistent answers are obtained for certain participants from the self-administered questionnaire and clinical interview . When using clinician-administered questionnaires, variations in the training and experience of clinicians may result in inconsistencies in their diagnosis.

* Corresponding author.
E-mail address: (J. Shanthalakshmi Revathy).

Received 2 November 2023; Received in revised form 13 March 2024; Accepted 8 April 2024
Available online 25 April 2024

Global NEST Journal, Vol 26, No 1, pp 05350

Investigation on tensile and flexural behaviour of fibre reinforced concrete using artificial neural network

Dhanalakshmi A.[1,*], Nagamani S.[2], Muthupriya P.[3], Rajendra Prasath C.[4] and Saradha Devi A.[5]
[1]Department of Civil Engineering, P.S.R Engineering College, Sivakasi, Tamil Nadu, India
[2]Department of Civil Engineering, NPR College of Engineering and Technology, Dindigul, Tamil Nadu, India
[3]Department of Civil Engineering, Dr.N.G.P. Institute of Technology, Coimbatore, Tamil Nadu, India
[4]Department of Civil Engineering, Velammal College of Engineering and Technology, Madurai, Tamil Nadu, India
[5]Department of Electronics and Communication Engineering, P.S.R.R College of Engineering, Sivakasi, Tamil Nadu, India
Received: 31/08/2023, Accepted: 05/12/2023, Available online: 13/12/2023
*to whom all correspondence should be addressed: e-mail: asiadhanam12@gmail.com
https://doi.org/10.30955/gnj.005350

Graphical abstract

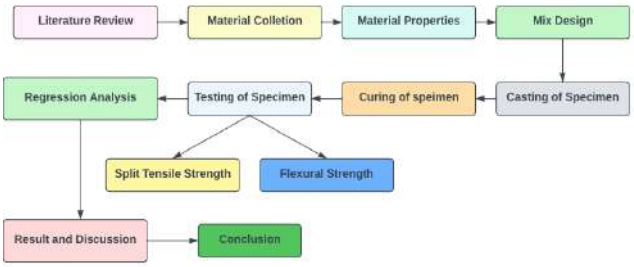

Abstract

The purpose of this study is to investigate the impact that using Marble Sludge Powder (MSP) as a partial replacement for cement in concrete can have. Experiments were conducted to investigate a variety of characteristics of Fiber-Reinforced Concrete (FRC) using both fresh concrete and concrete that had been allowed to solidify. The aim of this work is to determine the split tensile and flexural property of FRC. For the determination of results two water binder ratios, such as 0.35 and 0.40, as well as percentage re-placements of 0%, 5%, 10%, 15%, 20%, and 25% of marble sludge powder and 0.5% of polypropylene 3S fiber were used. After curing for 7, 14, 28, and 56 days, the samples were put through a battery of mechanical tests to evaluate their qualities. The flexural strength and split tensile strength of the material were evaluated throughout this investigation. In the end, an artificial neural network (ANN), was utilized to create a prediction model for split tensile and flexural strength. We displayed the experimentally obtained Split Tensile Strength and Flexural Strength against the regression analysis strength after 56 days for ANN. This was done so that we could compare the two. According to the findings of the experiments, using powder made from marble waste might lessen the damage that concrete causes to the environment while also providing economic benefits. In this study, dependable mechanical strength was developed by the use of a feed-forward back-propagation neural network, which consisted of eight input neurons, two hidden neurons, and one output neuron. According to the findings, it was discovered that the mechanical properties of concrete might be improved by using dry marble sludge powder as a substitute for up to 15% of the normal aggregate.

Keywords: Fibre reinforced concrete, polypropylene 3s, marble sludge powder and machine learning technique (MLT).

1. Introduction

Building practices that are less harmful to the surrounding ecosystem are necessary for the development of human civilization (Abed and Eyada 2012; Akbulut and Gürer 2007; Almeida *et al.* 2007; Alyamaç and Ince 2009). There is a demand for more long-lasting construction materials that are capable of withstanding unfavorable weather conditions (Arora and Ameta 2014; Aruntas *et al.* 2010; Aukour 2009; Bentz *et al.* 2015; Kofteci and KocKal 2014). This demand is a direct result of technical improvements as well as the rapidly expanding requirement for increasingly complicated building structures. Concrete, which is comprised of cement, aggregate, and water, is the material that is being utilized for construction all over the world with the greatest frequency (Narmatha and Felixkala *et al.* 2016). The aforementioned outcome may be attributed to the widespread accessibility of the essential constituents of concrete, the simplicity and straightforwardness with which it can be controlled, and the relatively affordable expense associated with the substance. Building materials that are more durable and have a longer lifespan are required (Suresh and Nagaraju 2015; Vikram Singh Kashyap *et al.* 2023; Dhanalakshmi Ayyanar *et al.* 2023) to fulfill the continuous and unending demands that are placed on an infrastructure that is in a state of perpetual change. By increasing its resistance to deterioration over time, concrete's performance may be improved by the use of appropriate mineral additives in proportions that are just right (Dhanalakshmi and Hameed 2022; Dhanalakshmi *et al.* 2023a, 2023b; Sukontasukkul *et al.* 2023; Puvaneshwaran and Vipurajan 2023; Valarmathi *et al.* 2009). Enhancing the performance of concrete in this way is one of the techniques available. Utilizing the waste marble sludge powder that is generated by manufacturing facilities such as marble-cutting factories may make it feasible to achieve improved economic viability and long-term sustainability (Indira and Valarmathi 2014;

Petchinathan *et al.* 2014; Surya Abisek Rajakarunakaran *et al.* 2022). This may be the case since such facilities create waste marble sludge powder. Because of this, it will minimize the burden that is placed on the environment as a consequence of the production of concrete and rubbish. This is because it will lower the strain that is imposed on the environment. In addition to this, this will lessen the amount of stress that is put on the environment. The major purpose of this body of work is to investigate the use of marble sludge powder in concrete as a partial substitute for cement and to identify the impact that this has on both the mechanical properties of concrete as well as the cement and mortar that are used in the combination. This combination of concrete also called green concrete. This will be accomplished by determining the effect that this has on both the mechanical properties of concrete as well as the cement and mortar that are used in the mixture. The usage of marble sludge powder reduces the environmental pollution. The findings of this study will be presented in the form of a conclusion that summarises the economic concrete as well as green concrete. In addition, the inquiry will investigate how the incorporation of marble sediment powder influences these features and how they are changed. Making an educated guess regarding the compressive strength of concrete that contains marble sludge powder may be accomplished via the application of various machine-learning strategies. The purpose of this study is to assess the effect of adding marble sludge powder in the concrete and its effects on partial cement replacement in terms of the concrete's mechanical characteristics, such as compressive strength, split tensile strength, and flexural strength and analyzed the results using MATLAB.

2. Materials and methods

2.1. Materials

As the binder material, ordinary Portland cement (OPC) of grade 53 was applied. The powder that was ccollected from marble waste was used in this work as an alternate material for cement. It was necessary to make use of both fine aggregate (FA) and coarse aggregate (CA) in this endeavor. To achieve the optimum level of workability, it is essential to make use of a water-reducing superplasticizer (SP). Gelenium B233 was included in the mix as a component. The mixture's proportions were calculated using the 20 mm of coarse aggregate and M-Sand as a fine aggregate was used in the study, as per IS 10262 (2009). The MSP having the specific gravity of 2.72. In order to achieve the physical transformation of marble sludge into marble powder, it is necessary to sift all ground material through a mesh with a size of 0.125 mm. Figure 1 depicts the image of marble powder.

Figure 1. Marble Powder

2.2. Concrete mix proportions

For this study, we chose to focus on two different water binder ratios, 0.35 and 0.40. Table 1 provides the recommended concrete design mix proportions based on the chosen water binder ratios. Cement replacement with marble sludge powder ranged from 0% to 25% by weight.

Table 1. Mix Proportions of Fibre Reinforced Concrete

Mix Id	w/c ratio	Cement (Kg/m³)	MSP (Kg/m³)	FA (Kg/m³)	CA (Kg/m³)	Fibre (Kg/m³)	Water (Kg/m³)	SP (Kg/m³)
FRC1	0.35	429	0	1300	700	2.14	150.15	12.87
FRC2	0.35	407.55	21.45	1300	700	2.14	142.64	12.87
FRC3	0.35	386.1	42.9	1300	700	2.14	135.13	12.87
FRC4	0.35	364.65	64.35	1300	700	2.14	127.62	12.87
FRC5	0.35	343.2	85.8	1300	700	2.14	120.12	12.87
FRC6	0.35	321.75	107.25	1300	700	2.14	112.61	12.87
FRC7	0.40	401	0	1300	700	2.01	160.4	12.03
FRC8	0.40	380.95	20.05	1300	700	2.01	152.38	12.03
FRC9	0.40	360.9	40.1	1300	700	2.01	144.36	12.03
FRC10	0.40	340.85	60.15	1300	700	2.01	136.34	12.03
FRC11	0.40	320.8	80.2	1300	700	2.01	128.32	12.03
FRC12	0.40	300.75	100.25	1300	700	2.01	120.3	12.03

3. Experimental investigation

3.1. Split tensile strength

Because of its brittleness and poor tensile strength, concrete is rarely put to the test in tension. To determine the load at which concrete members may fracture, it is necessary to calculate the material's tensile strength. Cast and tested were cylindrical specimens with a diameter of 150 mm and a height of 300 mm. The load needs should be applied gradually at a constant rate rather than suddenly. To determine the effect of partially substituting cement with marble slurry on concrete, the cylinders were evaluated at 28 and 56 days of curing. Water binder ratios of 0.35 and 0.40, as well as percentage replacements ranging from 0% to 25%, were examined for optimal dosage and long-term efficacy. The split tensile strength

testing of concrete cylinders is depicted in Figure 2 for this study.

3.2. Flexural strength

Concrete beams or prism can be evaluated by measuring their flexural strength. It determines how much pressure and stress an unreinforced concrete slab, beam, or other structure can take before cracking or breaking under bending loads. Concrete prisms with dimensions of 150 mm x 150 mm x 750 mm were cast and evaluated. The effect of partially substituting cement with powdered marble dust was investigated by evaluating concrete prisms at 28 and 56 days after curing. All combinations of water binder ratios of 0.35, 0.4, and percentage replacements of 0% to 25% were evaluated for optimal dosage and long-term effect. Concrete prism flexural strength testing is shown in Figure 3 for this study.

Figure 2. Split Tensile testing of a cylinder

Figure 3. Flexural testing of a Prism

4. Results and discussion

4.1. Split tensile strength

Test results for the split tensile strength of concrete with varying percentages of dried marble sludge powder as a cement replacement can be seen in Figure 4. The percentages used ranged from 0% to 25%. The outcomes obtained are comparable to compressive strength findings to some extent.

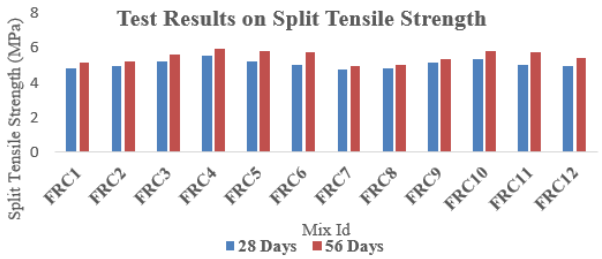

Figure 4. Test results on Split Tensile Strength

High dosages of superplasticizer employed for lower water binder ratios result in a strength gain for up to 15% replacement at both the 0.35 and 0.40 w/b ratios. This points to an improvement in the strength of the interface between the cement matrix and the pore structure. At 15% replacement, tensile strength reaches a maximum and then begins to decrease.

4.2. Flexural strength

The flexural strength test results for concrete contains 0%, 5%, 10%, 15%, 20%, and 25% by weight of dry marble sludge powder are shown in Figure 5. There is a pattern that parallels that of compressive and split tensile strengths. The flexural strength increases by 15% for both the 0.35 and 0.40 w/b ratios.

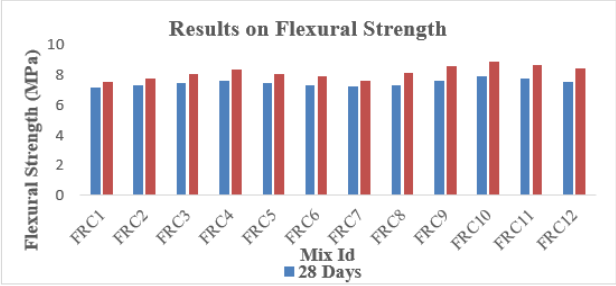

Figure 5. Test results on Flexural Strength

5. Regression analysis in concrete

The trends for strength ratios should be the same regardless of the type of specimen being examined assuming optimal casting, testing, and curing conditions are maintained. It is challenging to maintain consistent conditions for creating and testing samples, even when using the same concrete. This is one of the reasons why extraordinary events do occur in the actual world. This led to the discovery that the strengths of the various concrete samples had to be compared separately and that they did not always correspond. A generic formula for the regression analysis of split tensile strength, and flexural strength for concrete containing marble sludge powder may be derived from the ratios of the strengths involved. The connection may be determined using strength ratios regardless of the type of specimen employed.

5.1. Artificial neural network model

When marble sludge powder is used as a partial cement substitute, this section of the study presents an artificial neural network (ANN) model to conduct a regression analysis of the effect of marble sludge powder replacement ratio and admixture content on the with different proportions of materials of concrete. One of the following choices can have a significant impact on a neural network's efficiency: Transfer function, training function, and performance function. Network structure. Network algorithm. Amount of training and testing data (Figure 6).

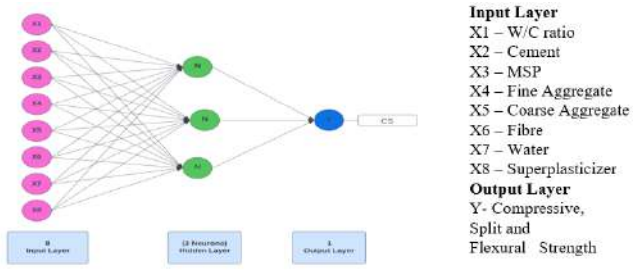

Figure 6. ANN Structure Model

5.2. Regression analysis model using ANN

MATLAB was used to generate Figures 7–16. Figure 7 depicts the ANN structure used in this study, which is a two-layered feed forward network. Technical parameters for ANNs are detailed in Table 2. Mechanical strength performance indicators are depicted in Figures 8 and 9. The obtained minimum Gradient of 0.00102 at epoch 13 and 0.0011601 at epoch 10 for split tensile strength and flexcural strength respectively.

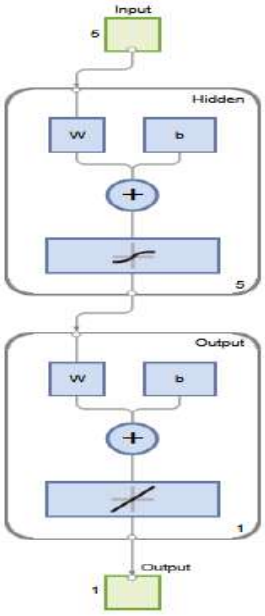

Figure 7. Feed Forward Neural Network

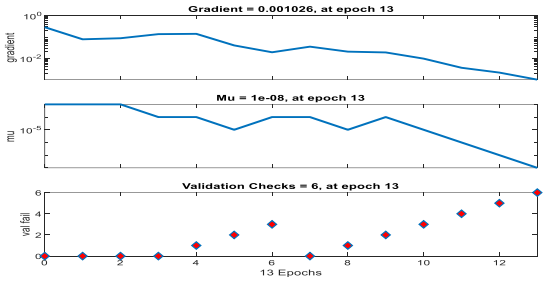

Figure 8. Performance State of Split Tensile Strength

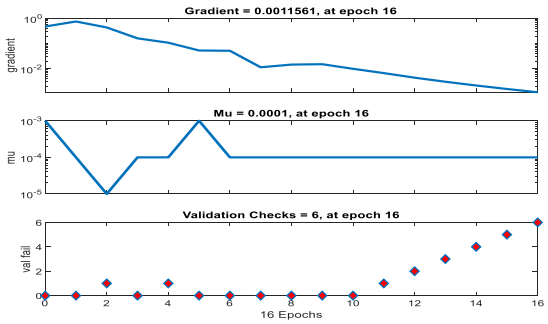

Figure 9. Performance State of Flexural Strength

Figures 10 and 11 refers the Training state of mechanical strength parameters. In this training, validation, testing and best parameters were analysed and find out the best validation performance ranges. The split tensile strength attained MSE in the range of 10^{0}-10^{-1} and the best validation is achieved at epoch 11 of 0.028108. The flexural strength attained MSE in the range of 10^{0}-10^{-4} and the best validation is achieved at epoch 3 of 0.0033608.

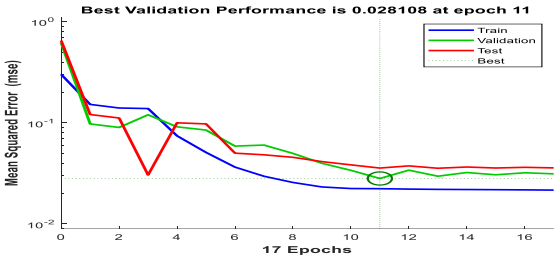

Figure 10. Training state of Split Tensile Strength

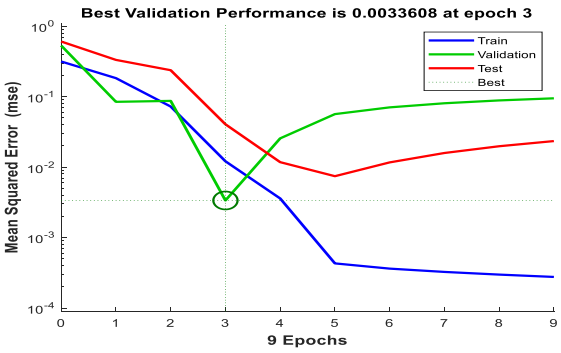

Figure 11. Training state of Flexural Strength

Table 2. ANN Technical Parameters

Details	Selection
Number of inputs	8
Number of hidden layers	3
Number of outputs	1
Number of iterations	1000
Training Gradient	$1x10^{-7}$
Validation Checks	6

Figures 12 and 13 shows the Error histogram analysis of concrete mechanical strength. It is the error findings between targeted values and predicted values after training a feedforward neural network using machine learning techniques. Totally 12 data were analyzed. From the analysis error values of split tensile strength indicate that the error of 0.139 for 3 instances, 2 instances of error -0.25265 was achieved. The flexural strength indicates that

the error of -0.009758 for three instances, and 2 instances of error 0.46351 was obtained.

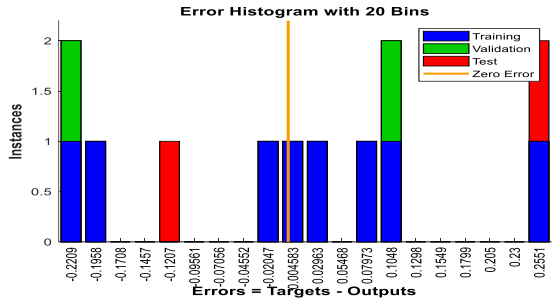

Figure 12. Error Histogram of Split Tensile strength

The relationship between experimental data and the training, validation, and testing sets of compressive strength, split tensile strength, and flexural strength of fibre reinforced concrete employing marble sludge powder is depicted in Figures 14-15.

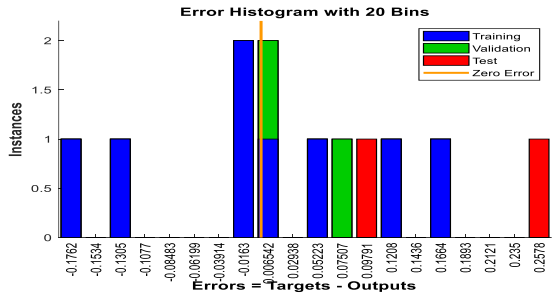

Figure 13. Error Histogram of Flexural strength

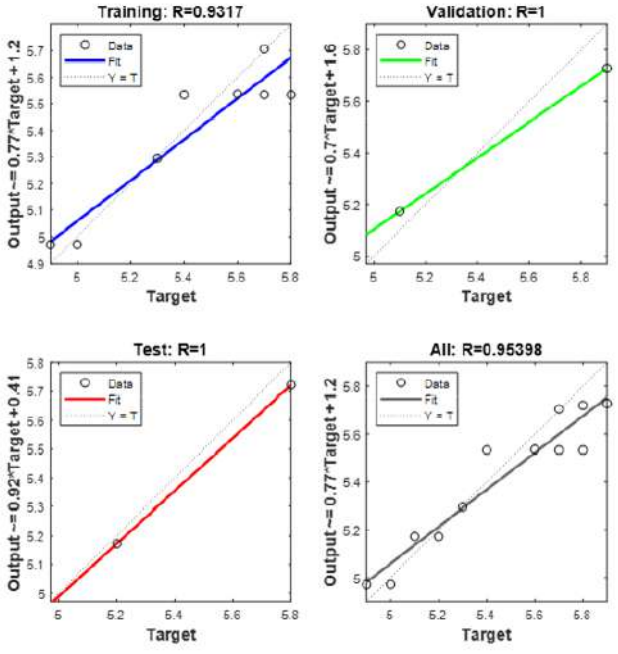

Figure 14. The Regression of split tensile strength

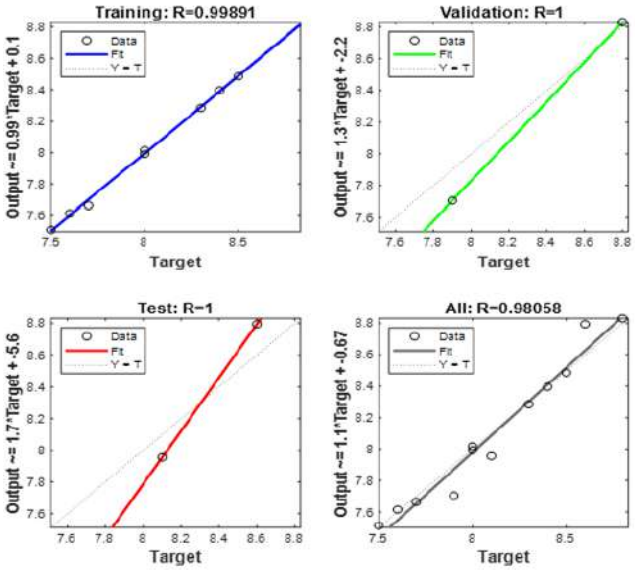

Figure 15. The Regression of flexural strength

Figure 16, shows that the relationship between the predicted and observed 56 days split tensile strength and flexural strength for fibre-reinforced concrete and the high correlation between all data sets are very clear. The coefficient of correlation for the 56-day compressive strength prediction was 96%.

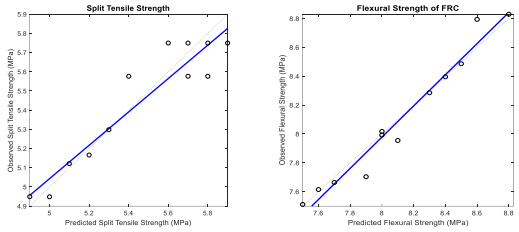

Figure 16. ANN Model Fitting of compressive strength, split tensile strength and flexural strength

6. Conclusion

The cementing ingredient that is responsible for concrete's compressive strength may have been lowered between the levels of 20% and 25% replacement, which may have caused the material to become weaker. With 15% replacement, mechanical properties such as split tensile strength, and flexural strength are improved in both the 0.35 and 0.40 w/b ratios. The timely and exact prediction of concrete's compressive strength has become a subject of study among an increasing number of academics due to its importance in engineering practices. One of the objectives of this study is to estimate the split tensile and flexural strength of concrete materials. In order to do this, the Artificial Neural Network (ANN) method, which is a machine learning technique based on lifting, is employed. The split tensile and flexural strength of concrete was used as a data source for a study that examined the interaction between cement, marble sludge powder, fine aggregate, coarse aggregate, water-to-cement ratio, polypropylene fibre, and superplasticizer. A MATLAB-based ANN model is

used to predict the split tensile strength and flexural strength of fibre-reinforced concrete. This model takes into account the factors that influence the properties of concrete, and the obtained R value, which is very close to 1, demonstrates that there is a strong correlation between the predicted and observed values. It would be beneficial for the building sector to have an earlier and more precise calculation of strength prediction. As a direct consequence of this, we will be able to physically test a reduced number of different permutations, and we will be able to conduct our experiments in a shorter amount of time. These software programmes assist to determine how the strength of one raw material is affected by the strength of another raw material and how the raw materials relate to one another. This model helps with quality control and economics by lowering construction time and costs and enabling for the modification of mix proportions to prevent either concrete that is too weak to satisfy its design strength requirements or concrete that is too strong for its intended purpose. These problems can arise when concrete is either too weak or too strong for its intended purpose. An earlier and more exact estimate of strength prediction would yield advantageous outcomes for the building sector.

References

Abed A. N. and Eyada S. O. (2012). "The use of sulaimania marble waste to improve the properties of asphaltic concrete", *Anbar Journal for Engineering Sciences*.

Akbulut H. and Gürer C. (2007). "Use of aggregates produced from marble quarry waste in asphalt pavements", *Building and Environment*, **42(5)**, 1921–1930.

Almeida N., Branco F. and Santos J. R. (2007). "Recycling of stone slurry in industrial activities: Application to concrete mixtures", *Building and Environment*, **42(2)**, 810–819.

Alyamaç K. E. and Ince R. (2009). "A preliminary concrete mix design for SCC with marble powders", *Construction and building materials*, **23(3)**, 1201–1210.

Arora R. P. and Ameta N. K. (2014). "Enhancement of shear strength and california bearing ratio of cohesive soil by inclusion of marble slurry in udaipur&rajsamand region", *International journal of Latest Technology in Engineering, Management and Applied Science*, **3(8)**.

Aruntas H. Y., Gürü M., Dayı M. and Tekin I. (2010). "Utilization of waste marble dust as an additive in cement production", *Materials and Design*, **31**, 4039-4042.

Aukour F. J. "Feasibility study of manufacturing concrete eco-blocks using marble sludge powder as raw materials", *WIT Transactions on Ecology and the Environment*, **120**, 845–852. Aukour F. J. (2009). "Incorporation of marble sludge in industrial building eco-blocks or cement bricks formulation", *Jordan Journal of Civil Engineering*, **3(1)**, 58–65.

Bentz D. P., Ardani A., Barrett T., Jones S. Z., Lootens D., Peltz M. A., Sato T., Stutzman P. E., Tanesi J. and Weiss W. J. (2015). "Multi-scale investigation of the performance of limestone in concrete", *Construction and building materials*, **75**, 1–10.

Dhanalakshmi A., Hameed M. S., Sowmya S. and Shridevi P. V. (2023a). "An experimental study on fibre reinforced foam concrete using hybrid fiber", *E3S Web of Conferences*, **387**, 03003, https://doi.org/10.1051/e3sconf/202338703003.

Dhanalakshmi A., Jeyaseela J, Karthika S. and Margret A. L. (2023b). "An Experimental Study on Concrete with Partial Replacement of Cement by Rice Husk Ash and Bagasse Ash", *E3S Web of Conferences*, **387**, 03004, https://doi.org/10.1051/e3sconf/202338703004.

Dhanalakshmi and Hameed M.S. (2022). "Strength Properties of Concrete Using Marble Dust Powder", *East Asian Journal of Multidisciplinary Research*.

Dhanalakshmi Ayyanar, Vishnuram B.G., Muthupriya P. and Indhumathi S. (2023). "An experimental investigation on strength properties and flexural behaviour of ternary blended concrete", *Materials Today: Proceedings*.

Indira B. and Valarmathi K. (2020). "A Perspective of the Machine Learning Approach for the Packet Classification in the Software Defined Network", *Intelligent Automation & Soft Computing*.

Kofteci S. and KocKal N. U. (2014). "Using marble wastes as fıne aggregate in hot mix asphalt production", *Proceedings of the International Conference in Civil, Structural and Construction Engineering, Institute of Research Engineers and Doctors*, 117–121.

Narmatha M. and Felixkala T. (2016). "Metakaolin – the best material for replacement of cement in concrete", *IOSR Journal of Mechanical and Civil Engineering*, **13(4)**, 66–71.

Petchinathan G., Valarmathi K. and Devaraj D. (2014). "Local linear model tree and Neuro-Fuzzy system for modelling and control of an experimental pH neutralization process", *Brazilian Journal of Chemical Engineering*.

Puvaneshwaran J.N. and Vipurajan.E. (2023). "A Experimental Investigation on Strength Properties of Foam Concrete", *East Asian Journal of Multidisciplinary Research*.

Sukontasukkul P., Intarabut D., Phoo-Ngernkham T., Suksiripattanapong C., Zhang H. and Chindaprasirt P. (2023). Self-Compacting Steel Fibers Reinforced Geopolymer: Study on Mechanical Properties and Durability against Acid and Chloride Attacks, *Case Studies in Construction Materials*, **19**, e02298, https://doi.org/10.1016/j.cscm.2023.e02298.

Suresh D. and Nagaraju K. (2015). "Ground sranulated blast slag (GGBS) in concrete – a review", *IOSR Journal of Mechanical and Civil Engineering*, **12(4)**.

Surya Abisek Rajakarunakaran, Arun Raja Lourdu and Suresh Muthusamy. (2022). "Prediction of strength and analysis in self-compacting concrete using machine learning based regression techniques", Advances in Engineering Software, **173**, 103267, https://doi.org/10.1016/j.advengsoft.2022.103267.

Valarmathi K., Devaraj D. and Radhakrishnan T.K. (2009). "Real-coded genetic algorithm for system identification and controller tuning", *Applied Mathematical Modelling.*

Vikram Singh Kashyap, Gaurav Sancheti and Jitendra Singh Yadav. (2023). "Durability and microstructural behavior of Nano silica-marble dust concrete", *Cleaner Materials*, **7**, 100165, https://doi.org/10.1016/j.clema.2022.100165.

Journal of Environmental Protection and Ecology 24, No 8, 2873–2885 (2023)

Computer application

AUTOMATED BRAIN TUMOR CLASSIFICATION USING NOVEL MACHINE LEARNING APPROACH ON MRI SCANS

A. V. DEEPAN CHAKRAVARTHI[a]*, S. SURESHU[b], U. S. UPENDRA SHARMA[c], GEETIKA M. PATEL[d], ANUPAM KUMAR GAUTAM[e], JAGDISH KUMAR ARUN[f], SACHIN GUPTA[g], R. MOHAN KUMAR[h]

[a]*Velammal College of Engineering and Technology, 625 009 Viraganur, Tamil Nadu, India*
E-mail: *adc@vcet.ac.in*
[b]*Department of Information Technology, Vel Tech Rangarajan Dr. Sagunthala R&D Institute of Science and Technology, Avadi, Chennai, Tamil Nadu, India*
[c]*Department of Life Sciences, School of Sciences, JAIN (Deemed-to-be University), Karnataka, India*
[d]*Department of Community Medicine, Parul University, PO Limda, Tal. Waghodia, District Vadodara, Gujarat, India*
[e]*Maharishi School of Engineering and Technology, Maharishi University of Information Technology, Uttar Pradesh, India*
[f]*Department of Pharmacy, Vivekananda Global University, Jaipur, India*
[g]*Department of Management, Sanskriti University, Mathura, Uttar Pradesh, India*
[h]*Department of Electronic Communication Engineering, K.L.N College of Engineering, Madurai, India*

Abstract. Brain cancer is a major medical problem that has implications for how people are diagnosed and treated. The prognosis for patients with brain tumours (BT) depends on their diagnosis and categorisation at an early stage providing effective medical care. This paper proposes a novel adaptive twin-hyperplane support vector machine boosting (ATSVMB) strategy that categorises BT in MRI data. Brain MRIs obtained from the Kaggle source are gathered to assess the suggested ATSVMB approach. The original MRIs are de-noised and contrast-enhanced using Gaussian filter and histogram equalisation techniques, respectively. The targeted regions are segmented on the improved MRIs using flexible k-means clustering (FKMC) driven segmentation following pre-processing. This study uses the Python programming language to classify BT using the ATSVMB algorithm. When compared to traditional methods, the results show that the suggested ATSVMB method has the greatest accuracy (98.12%), recall (98.43%), F1-score (97.62%) and precision (98.27%) for categorising BT on MRI scans. The model's capacity for tumor type differentiation as well as its capacity for identification and treatment offer hope for enhancing the quality of life for patients. The study advances the area of medical imaging and establishes the groundwork for the creation of

* For correspondence.

computerised BT categorisation systems, which will help healthcare practitioners make prompt and intelligent choices about the identification and management of BT.

Keywords: Brain tumor (BT), MRI, early detection and accurate classification, Adaptive twin-hyperplane support vector machine boosting (ATSVMB).

AIMS AND BACKGROUND

Modern medicine has seen significant improvements in patient treatment because of the fusion of advanced technology and novel diagnostics. Among these significant advancements, the area of automated BT categorisation emerged as a notable source of optimism and possibility[1]. The utilisation of artificial intelligence and machine learning has provided healthcare providers with the capability to enhance the accuracy, effectiveness and speed of BT identification and categorisation[2]. This paradigm change, characterised by its innovative nature, carries significant implications that extend over its immediate impact on patients. It provides an important lifeline to numerous individuals and offers insight into the enormous potential application of AI to the study of medicine[3].

Healthcare professionals have encountered a tremendous challenge from BT, which is deceptive and dangerous. BT classification and precise identification are essential for establishing treatment strategies and forecasting patient outcomes[4]. Traditionally, the completion of these responsibilities has been dependent on the proficiency of radiologists and pathologists, who evaluate intricate medical imaging data, including MRI and computed tomography (CT) images. However, the mentioned manual procedures are associated with a significant expenditure of time but are susceptible to human errors, hence increasing the need for automated resolutions[5].

The field of AI has come into existence as a transformative innovation in the area of BT categorisation. AI algorithms, which are driven by extensive datasets and processing capabilities possess the ability to evaluate large quantities of medical images. They are capable of classifying BT into several groups, such as gliomas, meningiomas, or metastatic tumors, in addition to detecting the existence of BT (Ref. 6). Deep learning (DL) algorithms have made it possible for medical professionals to make informed choices that are able to recognise complex patterns and small irregularities in medical images[7].

The ability of automated BT categorisation to reduce gaps in healthcare disparities is one of its greatest notable characteristics. Specialised medical information is difficult to access in numerous areas of the world, particularly in remote or underdeveloped regions[8]. When AI-based solutions are integrated into regional medical centres, they can offer rapid and accurate diagnostics, assuring that patients get the treatment they require. By decreasing the stress on medical personnel, they are able to use their time and knowledge more wisely while expanding the number of individuals they can provide[9].

The advantages of automatic categorisation of BT are extended beyond evaluation. Through ongoing learning and adaptation, the AI-driven method can improve its accuracy over the years. This iterative procedure advances the standard of healthcare while contributing to the repository of knowledge in the discipline of neuro-oncology. Understanding the pathogenesis of BT can be gained through analysis of the data produced by these networks, which will help to design stronger therapeutic approaches and solutions[10]. This study presents a novel technique called Adaptive twin-hyperplane support vector machine boosting (ATSVMB) for the automatic categorisation of BT in MR images.

EXPERIMENTAL

The proposed method uses a Gaussian filter for de-noising and histogram equalisation is used for the contrast enhancement of images. The segmentation of the images was achieved through the flexible K-means clustering. The Discrete Wavelet Transform (DWT) and Principal component analysis (PCA) are used for feature extraction and reduction of the feature vector size. The proposed Adaptive twin-hyperplane support vector machine boosting is employed for the classification of brain MRI. Figure 1 displays the overall flow of the suggested model.

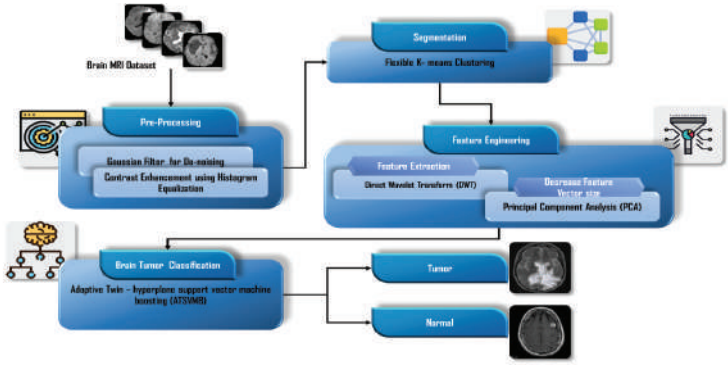

Fig. 1. Overview of the suggested model for classifying brain MR images

DATASET

We gathered dataset from the Kaggle source "https://www.kaggle.com/datasets/ahmedhamada0/brain-tumor-detection", which contains 3060 brain MRI images. The dataset containing the testing and training images is displayed in Fig 2.

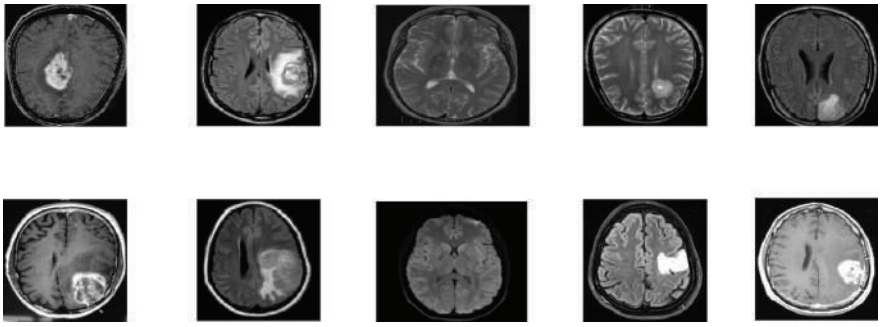

Fig. 2. Testing and training brain image samples

PRE-PROCESSING

Gaussian filter for de-noising. The Gaussian filter is employed for the purpose of removing speckle noise, as well as other minor disturbances if present. The Gaussian filter is associated with blurring of edges. However, this issue can be reduced by employing varying ranges of standard deviation and mean values. The Gaussian filter can be explained mathematically by the following equations:

$$J^{H}(j, i) = J' \times (j, i) = J' \, (1/(2\pi\sigma^2) \, f^{(-j^2 - i^2)/(2\sigma^2)} \tag{1}$$

$$\sigma^2 = F(W^2) - [F(W)]^2. \tag{2}$$

In this instance, $J^{H}(j, i)$ represents the image after undergoing the de-noising process using a Gaussian function; σ^2 – the variance of the noisy image; the variables j and i correspond to the distances from the origin along the w and z axes, respectively; $W \in (j, i)$ – the specific value or parameter. The de-noised image is depicted in Fig. 3.

Fig. 3. De-noised image

Histogram equalisation. This is a technique in image processing employed to improve contrast so that the intensity of images can be distributed on histogram equalisation. This approach has no effect on the values included in the image's matrix $x(m, n)$. However, it changes the colour mapping connected to the matrix $x(m, n)$ values such that every colour in the whole dynamic range, from black to

white, is used. The contrast enhancement of the de-noised image is depicted in Fig. 4.

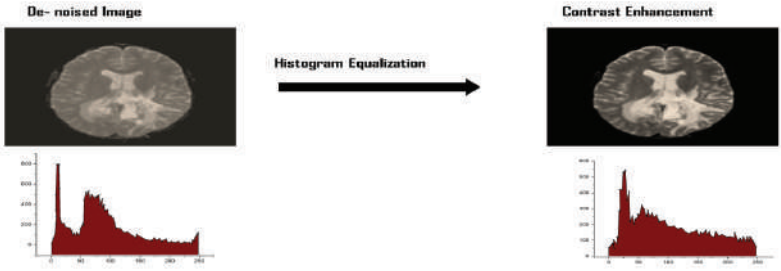

Fig. 4. Contrast enhancement of de-noised image

IMAGE SEGMENTATION

The process of image segmentation involves a complicated process of distinguishing between many types of normal brain tissues, including white matter, cerebrospinal fluid, gray matter, as well as the skull and separating them from tumor tissues in brain MRI. This segmentation is essential as it allows for the isolation of the tumor region, which is utilised in further stages of analysis. This study demonstrates the utilisation of the "K-means classification" method for the purpose of categorising brain MRI to assess BT. During classification, the qualities like circularity and brightness are established. The proposed scheme is divided into two stages:

Initialisation stage. The primary component of the adaptive classification technique is the initialisation stage, which applies K-means clustering for a certain number of iterations, denoted as *n*. The distribution of new centres takes place for the purpose of constructing the primary new clusters. Goodness is calculated below the beginning of this specific iteration. The mean roundness of comprehensive consequential objects is used to describe how the goodness functions perform. The circularity ratio is the percentage of the contour area to the circle area along with the corresponding boundary and it is expressed in equation (3):

$$e_{\text{circ}} = 4\pi A/\sigma^2, \tag{3}$$

where A and O stand for the object area, respectively. The e_{circ} function is < 1 for other form and one for a circular form. The area is determined by summing the pixels in each isolated group. Equation (4) is used to generate the goodness function:

$$\text{GOODNESS} = \frac{\sum_{j=1}^{N} e_{\text{circ}j} B_j}{\sum_{j=1}^{N} B_j}, \tag{4}$$

where e_{circ} denotes the proportion of j-th objects and B_j denotes the area of j-th object. The area is connected through the circularity ratio to raise the criteria for large objects and lower those for small objects.

FEATURE ENGINEERING

Feature extraction using Discrete wavelet transform (*DWT*). The wavelet transformation is considered the optimal method for conducting surface analysis of images to facilitate categorisation. Hence, the utilisation of wavelet transformation enables the extraction of texture characteristics from the provided image.

The DWT is an effective mathematical approach utilised for the purpose of attribute extraction in numerous applications in the field of medical image analysis. This decomposition is achieved through the application of a filter bank, such as the Haar filter bank, which has been employed in our research. For iterative multi-level decomposition, the approximation component is utilised to decompose the image at the subsequent level. The attributes of the images were extracted employing the 3-level decomposition with the Haar filter bank wavelet. The stages of DWT decomposition are shown in Fig. 5.

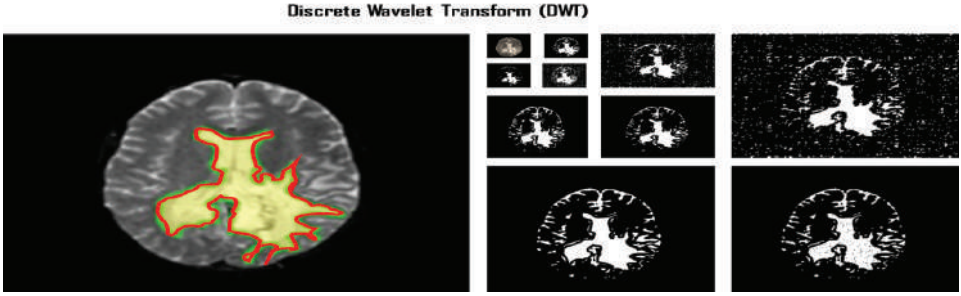

Fig. 5. Feature extraction output

Principal component analysis (*PCA*). One of the primary challenges associated with the DWT approach for feature extraction is its tendency to generate a large number of attributes. This phenomenon is referred to as the curse of dimensionality. Hence, it is essential to reduce the number of features. PCA is a recognised method used for reducing the dimensionality of features. This is achieved by projecting the original features onto the eigenvectors that correspond to the greatest eigenvalues of the covariance matrix obtained from the original feature set.

The observational matrix H should be created using actual data. When M has certain experiences, a matrix H is produced based on b features $\theta_1, \theta_2, \ldots, \theta_b$. Each row in the data collection includes a numerical estimate of the statistical results, where the number of occurrences is denoted by the m-th column, which is shown in equation (5):

$$H = \begin{bmatrix} H_{11} & H_{12} & \ldots & H_{1b} \\ H_{21} & H_{22} & \ldots & H_{2b} \\ \ldots & \ldots & \ldots & \ldots \\ H_{m1} & H_{m2} & \ldots & H_{mb} \end{bmatrix} \quad (5)$$

The process of matrix observation necessitates the centralised processing of data, as shown in equation (6). It is important for calculating the sample average as well.

$$\bar{h}_j = (1/m) \sum_{j=1}^{n} h_{j1}. \quad (6)$$

Meanwhile, the standard deviation is displayed in equation (7):

$$Q_i = ((1/m)(h_{ji} - \bar{h}_i)^2)^{1/2}. \quad (7)$$

On the basis of equation (8), a standard matrix $\bar{h}_i$ is created using a specialised data processing technique:

$$\widetilde{h_{ji}} = (h_{ji} - \bar{h}_i)/Q_i \ (j = 1, 2, \ldots, n; i = 1, 2, \ldots, o). \quad (8)$$

Equation (9) enables the calculation of association matrices for specific conditions:

$$U = (1/m)\, \widetilde{H^{\mathrm{K}}} \widetilde{H}. \quad (9)$$

To determine the value of each element of O, equation (6) was used.

$$l_{ji} = \frac{\sum_{n=1}^{m} (h_{ji} - \bar{h}_i)\,(h_{ji} - \bar{h}_i)}{(\sum_{n=1}^{m} (h_{ji} - \bar{h}_i)\,(h_{ji} - \bar{h}_i)^2 \sum_{n=1}^{m} (h_{ji} - \bar{h})\,(h_{ji} - \bar{h}_i)^2)^{1/2}}\ . \quad (10)$$

It is important to identify O's eigenvalue and eigenvector as in equation (10). Establish $\lambda_1 \geq \lambda_2 \geq \ldots \geq \lambda_o \geq 0$ as the attribute values for l in O. Equation (11) is useful to determine the relative significance of each fundamental component:

$$a_j = \lambda_j/(\lambda_1 + \lambda_2 + \ldots + \lambda_o), j = 1, 2, \ldots, o. \quad (11)$$

Additionally, select the most significant element that achieves 90% and produces $\lambda_{a=1}$ as PCA results. Select the top vector of attributes for the PCL according to the order of decreasing sequence of attributes 1, 2, …, o, calculate the related eigenvectors $y_1, y_2, \ldots, y_l$ in equation (12):

$$R_{n \times l} = (y_1, y_2, \ldots, y_b). \quad (12)$$

For instance, to develop novel primary parameters $l_1, l_2, \ldots, l_o$, one must employ a linear variation technique utilising the PCL vector $R^M_{c \times \mathrm{o}}$ and equation (13) to manipulate the actual data.

$$\begin{bmatrix} l_1 \\ \dots \\ l_h \end{bmatrix} = R^{M}{}_{c\times o} \begin{bmatrix} \theta_1 \\ \dots \\ \theta_h \end{bmatrix} \tag{13}$$

The parameters of the matrix underwent a change from *l* to *o* after the conventional transformation, resulting in a significant decrease in the number of acquired data. Figure 6 displays the feature vector size reduced image.

Fig. 6. Output of feature vector size reduction

ADAPTIVE TWIN-HYPERPLANE SUPPORT VECTOR MACHINE BOOSTING (ATSVMB)

The utilisation of Twin Support Vector Machine (T-SVM), when combined with AdaBoost, presents an innovative methodology that exhibits considerable potential in the area of automated BT categorisation.

Twin support vector machine boosting (*T-SVM*). One significant limitation of "Support Vector Machines (SVM)" is the extensive processing time required to solve intricate quadratic programming problems (QPPs). The T-SVM algorithm separates structures into two categories by identifying two non-parallel hyperplanes. This is achieved by calculating a pair of QPPs, as opposed to a single complex limitation as in the SVM algorithm.

The T-SVM algorithm attempts to identify two hyperplanes that are not parallel as well as those that are in close proximity to the separating hyperplane defined by the training data set. These hyperplanes are represented by equation (14):

$$w^S x_1 + a_1 = 0;\ w^S x_2 + a_2 = 0. \tag{14}$$

The pair of differentiating hyperplanes of the T-SVM classification are derived by calculating the subsequent pairs of quadratic programming the following equations:

$$(\text{T-SVM}_1)\ \min\ (1/2)\ (Bx_2 + f_1 a_1)^S (Bx_1 + f_1 a_1) + d_1 f_1^S \xi \tag{15}$$

subject to: $-(Ax_1 + f_2 a_1) + \xi \geq 0$

$$(\text{T-SVM}_2)\ \min\ (1/2)\ (Ax_2 + f_1 a_2)^S (Ax_2 + f_2 a_2) + d_2 f_2^S \xi \tag{16}$$

subject to: $-(Bx_2 + f_1 a_2) + \xi \geq 0$

Let d_1 and d_2 be positive parameters, f_1 be a vector of ones with size n_1, f_2 be a vector of ones with size n_2 and ξ be the slack variable. A novel test sample is allocated to the class based on its closeness to one of the two provided planes.

Adaptive twin-hyperplane support vector machine boosting (*ATSVMB*). The proposed approach utilises the T-SVM algorithm, a sophisticated categorisation technique, together with the enhancing characteristics of AdaBoost to promote the efficiency and durability of BT categorisation algorithms.

The main goal of computerised BT categorisation is to differentiate between regions containing tumors and regions without tumors in medical images, specifically MRI scans. The hybrid technique depends on T-SVM as its fundamental element, which demonstrates excellent performance in the setting of binary categorisation applications. The proposed method has been designed to deal with the issue of imbalanced datasets, which is a prevalent challenge experienced in the domain of medical imaging. This approach involves the simultaneous training of two SVMs with the objective of minimising classification defects. The utilisation of T-SVM enables the model to differentiate between tumor and non-tumor areas, hence providing a high level of precision in the classification phase.

The combination of T-SVM with AdaBoost contributes to an improvement in classification accuracy and improves the adaptability of the automated BT categorisation system. Therefore, this approach serves to decrease the possibility of both false positives and negatives, which hold significant importance in the medical domain as they contribute to the prevention of misdiagnosis and the advancement of patient wellbeing. Algorithm 1 shows Adaptive twin-hyperplane support vector machine boosting.

RESULTS AND DISCUSSION

The recommended procedures had been evaluated on the Python 3.10 platform. The proposed optimisation strategies were shown on a Windows 10 laptop equipped with an Intel i3 9th Gen processor and 8 GB of RAM. Performance of the suggested method is assessed here. strategy with the existing methodology, which employs Deep Neural Network (DNN), Random Forest (RF), "Improved dragonfly optimisation algorithm-deep belief network (IDOA-DBN)" and Visual Geometry Group16-Neural Autoregressive Distribution Estimation (VGG 16-NADE). Figure 7 displays the categorisation of tumor and normal brain MR Images.

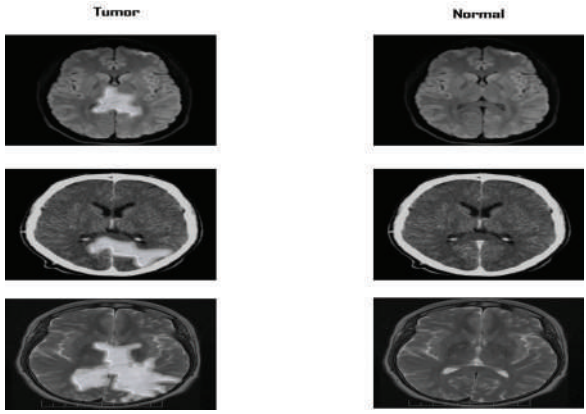

Fig. 7. Classification of normal and tumor MR images

The accuracy represents the proportion of the entire dataset's categorised images of BT. It is an important performance measure because it reflects the model's capacity to produce precise forecasts. The accuracy of the suggested ATSVMB is 98.12%, whereas the existing DNN, VGG 16-NADE and RF methods have 97, 96.01 and 95.84%, respectively. This shows our proposed method has high accuracy and it was more effective in the classification of brain MRI images, which is displayed in Fig. 8.

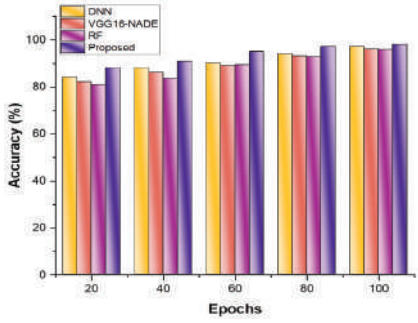

Fig. 8. Result of accuracy

Table 1 displays the results of precision and accuracy. Precision represents the percentage of effective tumor forecasts among positive predictions. The existing DNN, VGG 16-NADE and RF methods have precision values of 97, 95.72 and 94.12%, whereas our proposed method has a high precision value of 98.27%, respectively. Figure 9 shows the result of precision.

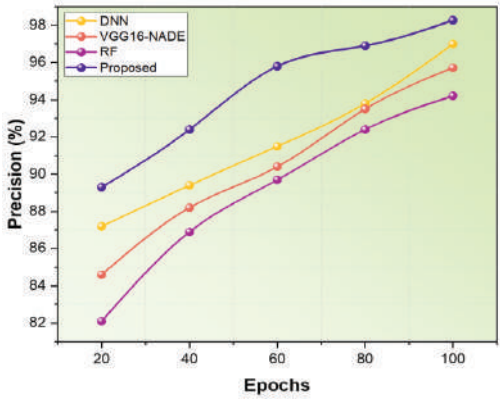

Fig. 9. Precision

Table 1. Performance of accuracy and precision

Methods	Accuracy (%)	Precision (%)
DNN	97.00	97.00
VGG16-NADE	96.01	95.72
RF	95.84	94.21
Proposed	98.12	98.27

Figure 10 displays the recall ratio of the methods used here. The recall measure evaluates a system's capacity to recognise all real occurrences of BT positives. It measures the ratio of precise positive forecasts to the total amount of actual positive instances. When compared to the existing DNN, VGG 16-NADE and RF approaches, our proposed ATSVMB method has a high recall ratio of 98.43%, while DNN, VGG 16-NADE and RF have low ratios of 97, 95.64 and 93.72%, respectively.

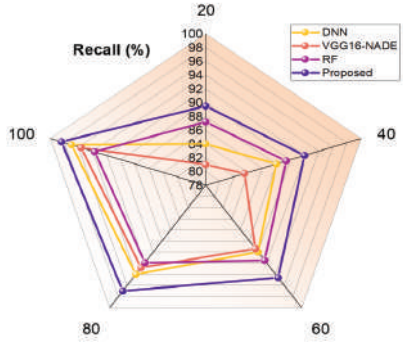

Fig. 10. Output of recall

Table 2 displays the performance of the F1-score and recall. The F1-score is a crucial parameter utilised in the automated classification of BT and serves as a measure of the model's ability to maintain a right harmony between knowledge and memory. Accuracy and memory are combined into a single score. The F1-score of the traditional approaches IODA-DBN was 92.49%, for VGG 16-NADE – 95.68% and for RF – 93.10% when compared to our suggested ATSVMB method. Our proposed approach has a higher F1-score of 97.62%, which is displayed in Fig. 11.

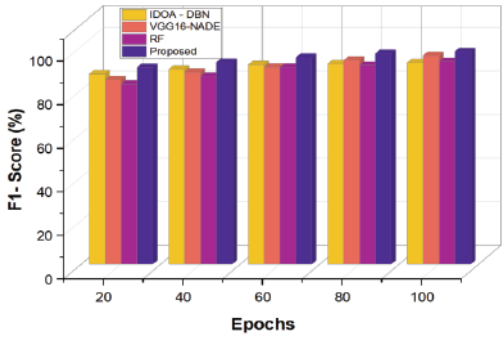

Fig. 11. Result of F1-score

Table 2. Performance of recall and F1-score

Methods	Recall (%)	F1-score (%)
IDOA – DBN	97.00	92.49
VGG16-NADE	95.64	95.68
RF	93.72	93.10
Proposed	98.43	97.62

CONCLUSIONS

Automated BT classification refers to a medical technique that employs machine learning algorithms and MRI images to identify and categorise BT. The utilisation of this technology enhances the efficiency of diagnosing medical conditions, enhances the accuracy of diagnoses and helps in the development of treatment strategies, providing accelerated and dependable outcomes for both patients and healthcare providers. This research proposes a unique methodology known as Adaptive twin-hyperplane support vector machine boosting (ATSVMB) for the automated categorisation of BT in MRI images. The findings demonstrated that the proposed ATSVMB approach has the highest values of accuracy (98.12%), recall (98.43%), F1-score (97.62%) and precision (98.27%). The disadvantages involve susceptibility to noisy data, possible excessive fitting in high-dimensional areas and greater computing difficulty as a result of numerous hyperplane iterations. The possible fields of development include enhanced precision, instant diagnos-

tic capabilities, customised treatment options and combining innovative medical imaging modalities to enhance patient results.

REFERENCES

1. A. REHMAN, S. NAZ, M.I. RAZZAK, F. AKRAM, M. IMRAN: A Deep Learning-based Framework for Automatic Brain Tumor Classification Using Transfer Learning. Circuits, Systems, and Signal Processing (CSSP), **39**, 757 (2020).
2. S. SHANTHI, S. SARADHA, J. A. SMITHA, N. PRASATH, H. ANANDAKUMAR: An Efficient Automatic Brain Tumor Classification Using Optimized Hybrid Deep Neural Network. International Journal of Intelligent Networks (IJIN), **3**, 188 (2022).
3. R. SUNDARASEKAR, A. APPATHURAI: Automatic Brain Tumor Detection and Classification Based on IoT and Machine Learning Techniques. Fluctuation and Noise Letters (FNL), **21** (03), 2250030 (2022).
4. A. K. BUDATI, R. B. KATTA: An Automated Brain Tumor Detection and Classification from MRI Images Using Machine Learning Techniques with IoT. Environ Dev Sustain, **24** (9), 10570 (2022).
5. U. ZAHID, I. ASHRAF, M. A. KHAN et al.: BrainNet: Optimal Deep Learning Feature Fusion for Brain Tumor Classification. Comput Intell Neurosci, (2022).
6. T. SADAD, A. REHMAN, A. MUNIR et al.: Brain Tumor Detection and Multi-classification Using Advanced Deep Learning Techniques. Microscopy Research and Technique (MRT), **84** (6), 1296 (2021).
7. R. VANKDOTHU, M. A. HAMEED, H. FATIMA: A Brain Tumor Identification and Classification Using Deep Learning Based on CNN-LSTM Method. Comput Electr Eng, **101**, 107960 (2022).
8. R. R. AGRAVAT, M. S. RAVAL: Deep Learning for Automated Brain Tumor Segmentation in MRI Images. In: Soft Computing Based Medical Image Analysis, 2018, 183–201.
9. S. ALQAZZAZ, X. SUN, X. YANG, L. OKES: Automated Brain Tumor Segmentation on Multimodal MR Image Using SegNet. Comput Vis Media, **5**, 209 (2019).
10. N. S. SHAIK, T. K. CHERUKURI: Multi-level Attention Network: Application to Brain Tumor Classification. Signal Image Video Process, **16** (3), 817 (2022).

Received 17 November 2023
Revised 8 December 2023

Effect of Leachate containments on Clay liners

Swetha Guduru[1*], *Selva Kumar* P[2], *J.P. Annie Sweetlin* Jebarani[3], *S Robert* Ravi[4] *and Haider* Alabdeli[5]

[1]Civil Engineering, Gokaraju Rangaraju Institute of Engineering and Technology, Hyderabad, India
[2]Civil Engineering, Knowledge Institute of Technology, Salem, India
[3]Civil Engineering, Velammal College of Engineering and Technology, Madurai, India
[4]Civil Engineering, Girijananda Chowdhury University, Guwahati, India
[5]The Islamic university, Najaf, Iraq.

Abstract. Clayey soil is made up of extremely tiny clay particles that can be employed as a binding material and have a higher retention of water compared to other soils. A hydraulic barrier to fluid flow can be obtained by a clay liner. Clay liners serve a purpose in liner systems to regulate leachate release from the waste or in covering systems to reduce water infiltration. Long-term low hydraulic conductivity constitutes a demand for clay liners to accomplish these objectives. Clay liners were barriers designed to cover landfills and dispose of low and intermediate-level waste. clay sample of its index and engineering characteristics permeability will be examined in a laboratory. After adding Na, Cl (salts) and Mg,Cr,Zn,Pb (metals) at different percentages to the clay soil the Hydraulic conductivity and index characteristics are examined within lab conditions. The measured values of the sample's including before and after the addition of chemicals at different percentages 0,2,4,6, and 8%, have been compared by the results of the present investigation.

1 Introduction

Landfills were managed effectively engineering facilities used in industrialised nations to manage toxic trash in a way that protects the environment. Landfills need to be designed, located, operated, and regulated by national government laws and regulations. One of the landfill's most important components, the liner, stops leachate from penetrating the subsoil. When a landfill liner is placed beneath a completed landfill, it needs to have certain characteristics, such as strength, permeability, and swelling behaviour. The design and material requirements of landfill liners were very important because they facilitate the handling and management of various waste types. Additionally, for the purpose to prevent contamination of groundwater, liner systems must be constructed in a cost-effective and environmentally responsible approach(Arunkumar et al., 2022; Arunvivek & Rameshkumar, 2019; Sankar & Ramadoss, 2023).

* Corresponding author: swetha2039reddy@gmail.com

Leachate is the result of water and water-soluble chemicals building up in the landfill when water flows through it. Either rainfall or the garbage particles may have provided this water.

Groundwater and soil contamination as well as environmental deterioration may happen from landfill leachate that seeps deeply into the earth. In ponds and landfills, earthen liners are commonly used to confine dangerous and poisonous chemicals. The durability of liners which come into connection with different wastes is closely monitored, and there is a demand for more affordable, higher-quality options. The choice of clay liners for application in hazardous liquid waste containment facilities is mostly influenced by their permeability and sensitivity to modifications with time or chemical exposure. Fine matrix with granular soil are common mixes observed in earthen liners. The worldwide practice of land filling for the disposal of municipal solid waste has emerged as a significant environmental issue, leading to degradation and contamination of the ecosystem. The X-ray diffraction analysis, performed by Sachan et al. (2007), indicated that the clay contains kaolinite, illite, and shapeless quartz particles. These particles have an impact on the clay's hydraulic conductivity and leachates, which increases permeability. By measuring the total dry weight of the soil at various percentages of fly ash (15 and 25%) and lime (0–7%), Zalihe Nalbantoglu et al. (2011) assessed the impact of these materials on the compressibility along with hydraulic properties of an expansive soil in Cyprus. Additional investigations were performed as well on soils that contained 15% fly ash plus 3% lime.

The hydraulic conductivity of 7 geosynthetic clay liners (GCLs) to leachates of synthetic coal combustion products (CCP) was assessed in the investigation. The chemical composition of the leachates reflects both the best and most serious situations found in CCP dumps. Geosynthetics along with landfill liner materials Rajiv Kumar et.al (2023) were employing to improve the geotechnical characteristics of these liners. Additionally examine the application of waste materials and microstructural analysis (SEM–EDX, XRD, FT–IR, etc.) for compacting particles while enhancing the strength and stability of soils. While bentonite-polymer composites having polymer loadings that varied from 0.5 to 12.7% have been observed in four of the GCLs, normal sodium bentonite had been identified in the GCLs. Compacted clay liners, which decrease the rate at which contamination migrates by condensation, are commonly used as hydraulic barriers beneath the leachate collection systems of MSW landfills. Thyagaraj et al. (2021) investigated the poor hydraulic conductivity and rapid molecular diffusion of these liners. The impact of desiccation and leachate infiltrating fractures over natural hydraulic conductivity has been examined by Anggraini et al. (2020). Ajitha et al. (2019) concluded that a low hydraulic conductivity of less than 1*10-7 cm/s is the most important criterion. As the amount of lead grows, permeability falls and shear strength increases. It has been determined that the Langmuir model is the most suitable for this inventive liner.

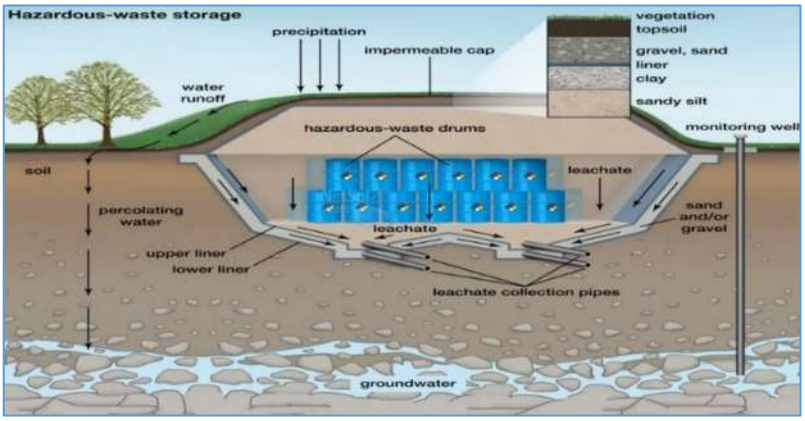

Fig 1. Leachate affecting drinking water

Yonli et al. (2022) conducted hydro-mechanical experiments on the two sampled materials to evaluate their sealing qualities as well as their capacity to deform and rupture characteristics, which are crucial for ensuring a bottom liner's longevity. For the purpose of figuring out how the hydro-mechanical properties of the clayey soils were altered, all of these experiments were initially conducted using distilled water and subsequently with leachates acting as interstitial fluids. Silt aggregation, compaction density, and subgrade water content were among the five different geosynthetic clay liner products that Kerry Rowe et al. (2019) investigated for hydration. Assuming the same subsoil that has enough cations to cause exchange of cations after hydration, GCLs that satisfy accepted standards for low hydraulic conductivity and swelling index undergo hydration into equilibrium.

Through a combination of 10 percent fly ash and 8, 10, and 12 percent by weight of sodium hydroxide (NaOH) with normalities of two and four, Swetha (2023) studied the enhancement of compressive strength and, as a result, shear strength. The results have been compared and recorded for 0, 7, 14, and 28 days for unconfined compressive strength (UCS). Compacted clay was subjected to permeability tests in a controlled environment to investigate the influence of desiccation cracking, hydraulic anisotropy, test specimen diameter, and storage duration. The hydraulic conductivities determined using the compaction-mold, consolidation-cell, and flexible-wall permeameters remained nearly the same by Boston et.al (1985). To evaluate the MDD and accompanying for lateritic soil-lime combinations affect their permeability in terms of lime content, curing time, and compactive effort from the investigation of Osinubi et.al (1998). Uncured specimens (standard Proctor) showed a maximum permeability at 4% lime content, while as the lime content grew, the permeability dropped. Black Cotton mainly agricultural soil, which is unsuitable for development because of its geotechnical characteristics. Its intrinsic fragility makes it unsuitable for construction and an attempt to stabilise the soil and produce good strength, plastic garbage has been employed in the laboratory test by Swetha et.al (2023).

With absence of naturally occurring impermeable soils, Ameta et al. (2008) concentrated on the permeability of compacted bentonite and sand combinations employed to form fluid barriers. Krishna et al. (2021) conducted a series of assessments, including plastic restriction, liquid limit, free swell index, unconfined compressive test (UCC), and California bearing ratio (CBR), which revealed that the soil sample lacked strength in shear, bearing, and plasticity. As a result, the researchers repeated those experiments using varying percentages of fly ash in place of the soil sample. A model pavement subgrade with the stabilised soil characteristics is designed by Vivek Kumar et.al (2021), and an economic analysis is done for the designed pavement subgrade. With expansive soils like black cotton soil, subgrade soil stabilisation is an important step in the pavement construction process. In this study,

Atterberg's limits, Optimum Moisture Content (OMC), and percentage of coal ash added by weight are included, which directly affect the CBR value.

Flexible concrete pavements with a bituminous layer constitute a majority of Indian roads, regardless of the design thickness of the pavements. A flexible pavement having bituminous covering was previously the norm in India due to the country's cement shortage. Because of its wonderful feature of gradually strengthening and improving with increased traffic, this flexible pavement is chosen over cement concrete roads by Kamalaraju et.al (2020) investigation. Using enrollment maps generated with GIS technology that suited the purpose, Katteri watershed produced a number of thematic guides. With the majority of large-scale studies being unfeasible in the field, a lab model of a landslip zone was used to study landslip movement at different slopes and levels of precipitation. The study conducted by Swaminathen et al. (2023) indicates that landslides are more likely to occur on steeper inclines with deeper soil, and that precipitation is the main cause of these events.

2 Materials and Methods

2.1 Soil and Chemicals

The soil used in this study is naturally Block cotton soil collected from Warangal city, of Telangana according to Indian standards (IS 2720, Part 1-1983)(6). The Leachate resembling the chemical composition of landfill leachate was prepared from salts and heavy metals solutions such as Na, Cl (salts) and Mg,Cr,Zn,Pb (metals).The list of heavy metals salts considering in this study and their corresponding Normality is taken as 2N from the initial tests.

2.2 Methodology

2.2.1 Index properties

Numerous factors, notably mechanical characteristics like compressive index, have an impact on the liquid limit. According to definitions, it happens when the soil's moisture content continues to act like a liquid and flows. The settlement analysis will serve from the significance of the compression index. The natural moisture content of soft soil has been estimated to be around the liquid limit. If the amount of moisture remains lower than the liquid limit, the soil is regarded as hard. Casagrande's liquid limit in Fig 2. gives a percentage of the weight of the oven-dried soil that represents the percentage of moisture of the soil during the period of transition between the liquid and plastic consistency stages.

The earth starts behaving as a plastic material at the plastic limit. When a plastic material is moulded to a specific shape, that shape remains intact. format. If the percentage of moisture is less than the plastic limit, the material is either solid or non-plastic. Soil starts becoming like a plastic material once it achieves a specific moisture content. As a percentage of the weight of the soil dried in an oven, the level of consistency at the border of a soil's plastic limit across the plastic and semisolid stages is calculated and showed in Fig 3. As per IS: 2720, soil dissolves when rolled into a thread (3 mm) in diameter and placed on a ground glass plate or other adequate surface.

Fig 2. Liquid limit of Soil specimen

Fig 3. Plastic limit of Soil sample

The tests to determine index properties of soil were done using IS 2720.1985 (Part V) (6). They were done in soil treated with 0,2,4,6, and 8% Na, Cl (salts) and Mg,Cr,Zn,Pb (metals) to understand the variation in properties of untreated as well as treated soil.

2.2.2 Compaction tests

When the typical compaction test forces air out of the pores between the soil grains, the soil densifies. Compaction happens when dirt is compressed by large machinery. The soil levels used for backfilling or filling a space were called lifts. The state of the natural material being covered will affect how well the initial fill layers compact under the weight of the earth fill over time, which may cause settlement cracks in the fill or in any supporting structures. The maximum dry unit weight and optimal moisture can be significantly influenced by the kind of soil, which includes characteristics like particle size distributions, soil grain shape, specific gravity of soil particles, and the amount of clay minerals present.

The permeability of soil is determined employing the falling head and constant head methods. By allowing the head to sink as water enters the sample, the falling head method lowers the test pressure. This method is generally only applicable to fine-grained soils, such

as clay. Before the flow measurements, the soil sample has been submerged and a specific volume of de-aired water is added to the standpipes. Once the water in the standpipe reaches a predetermined lower limit, the test is initiated by allowing the water to continue flowing through the specimen. The time-stamped amount of time that the water in the standpipe requires to fall from the uppermost level.

The tests to determine the optimum moisture content and maximum dry density were done using both standard proctor compactive effort and to IS 2720.1980 (Part VII) (6). The same is repeated for soil treated with 0,2,4,6, and 8% Na, Cl (salts) and Mg,Cr,Zn,Pb (metals).

Fig 4. Compaction by Standard Proctor Test (SPT)

2.2.3 Hydraulic conductivity testing

Hydraulic conductivity testing was done using consolidometer apparatus and falling head method was used, according to IS 2720.1986 (Part XVII) (6). The permeant used was water and value of coefficient of permeability was recorded once it reached a constant value after complete saturation. The same is repeated for soil treated with 0,2,4,6, and 8% Na, Cl (salts) and Mg,Cr,Zn,Pb (metals).

Fig 4. Falling Head Permeability Test setup

2.2.4 Preparation of Heavy Metals, salts solution

For example, taking Normality for Magnesium,

Normality(N) : Equivalent mass(M) / Total volume of solution(V)

Taking N=2, M=24.31g,V=1 litre

1N=24.31/1000

Using algebra and remembering that N is eq/L:

M = 1 eq/L x 1L x 24.13g/eq,

Therefore m=24.13g

To make a 1N solution, 24.13 grams of Mg dissolved in 1L.

Likewise, for a 2 N solution of Mg , multiply by a factor of 2.

Mass is equals to 48.26grams.

3 Experimental Investigation

The index properties of soil is summarised in Table 1. From the test results, it was identified that the soil can be classified as clay of intermediate plasticity (CI) according to Unified Soil Classification system. The soil contains 30% sand, 23% silt and 39% clay particles. The variation in Liquid limit, Plastic limit, Plasticity Index and free swelling index is also provided. Chemical properties of MSW leachate values provided in Table 2.

Table 1. Properties of Clayey soil

Properties	Value
Gravel (%)	8
Sand(%)	23
Silt(%)	39
Clay (%)	30
Liquid limit (%)	45
Plastic limit (%)	24
Plasticity index (%)	18.87
Free Swelling Index (%)	76
Optimum moisture content	17
Maximum dry density (g/cc)	1.84
Permeability(cm/sec)	$4.5*10^{-6}$

Table 2. Chemical characteristics of MSW leachate

Characteristics	Value
Biological oxygen demand	0.60
Chemical oxygen demand	940
Total dissolved solids	8.10
Total hardness	181
pH	8.7
Chloride	12.7
Lead	0.2118
Chromium	0.2099
Sodium	200
Potassium	540
Sulphate	1.21
Nitrate	0.0012
Zinc	0.60
Calcium	1.3852

4 Result and Discussion

The graph of experimental investigation carried out in different stages. In this experiments prepared soil mix with various Salts such as Chlorine, Sodium and Heavy metals such as Magnesium, Zinc, Lead with a defined percentages to test the soil properties such as Liquid limit, plastic limit, Standard compaction and Permeability. Below are the test results of the clay soil.

Table 3. Description of Soil composition of Salts and Heavy metals

Sample	Chlorine (Cl)	Sodium (Na)	Chromium (Cr)	Magnesium (Mg)	Zinc	Lead
S0	Soil+0% Cl	Soil+0% Na	Soil+0%Cr	Soil+0% Mg	Soil+0% Zn	Soil+0% Pb
S1	Soil+2% Cl	Soil+2% Na	Soil+2% Cr	Soil+2% Mg	Soil+2% Zn	Soil+2% Pb
S2	Soil+4% Cl	Soil+4% Na	Soil+4% Cr	Soil+4% Mg	Soil+4% Zn	Soil+4% Pb
S3	Soil+6% Cl	Soil+6% Na	Soil+6% Cr	Soil+6% Mg	Soil+6% Zn	Soil+6% Pb
S4	Soil+8% Cl	Soil +8% Na	Soil+8% Cr	Soil+8% Mg	Soil+8% Zn	Soil+8% Pb

Table 4. Liquid Limits (%) for Clayey Sample with Salts and Metals

Sample	Cl	Na	Cr	Mg	Zinc	Lead
S1	47	44.25	47.56	43	43.6	44
S2	51	43	48.89	40	41.26	42.67
S3	56	42.86	49	39	40	40.5
S4	58	41	52	36	37	38.89

Table 5. Plastic Limits (%) for Clayey Sample with Salts and Metals

Sample	Cl	Na	Cr	Mg	Zinc	Lead
	Plastic Limit (%)					
S1	27	26.5	25	28	25.29	26
S2	29	27.89	24.39	30.41	23	25.04
S3	32	28.6	22.64	32	22.56	24
S4	33	29	21.87	33	20.3	22
	Plasticity Index (%)					
S1	20	17.75	22.56	17.86	18.31	18
S2	22	15.11	24.5	16.62	18.26	17.63
S3	24	14.26	26.36	15.9	17.44	16.5
S4	25	12	30.13	13.05	16.7	16.8

Table 6. Optimum Moisture Content (%) for Clayey Sample with Salts and Metals

Sample	Cl	Na	Cr	Mg	Zinc	Lead
S1	17	17.23	15.43	16.95	15.04	15.6
S2	18.5	17.6	14.27	17.1	14.07	14

S3	19.34	18.43	12	17.45	13	12.96
S4	20.13	18.9	11.79	18.22	12.09	12.05

Table 7. Maximum Dry Density for Clayey Sample with Salts and Metals

Sample	Cl	Na	Cr	Mg	Zinc	Lead
S1	1.96	1.98	1.9	2.0	1.76	1.89
S2	2.0	2.46	1.98	2.56	1.65	1.92
S3	2.5	2.8	2.06	2.98	1.58	1.976
S4	2.76	3.2	2.18	3.1	1.46	2.024

Table 8. Permeability (10^{-7}cm/sec) for Clayey Sample with Salts and Metals

Sample	Cl	Na	Cr	Mg	Zinc	Lead
S1	3.21	3.61	3	3.8	4.12	3.22
S2	2.93	2	2.1	2.7	3.5	2.6
S3	2.6	1.78	1.89	1.8	2.8	1.98
S4	1	1.1	1.5	1.1	1.6	1.86

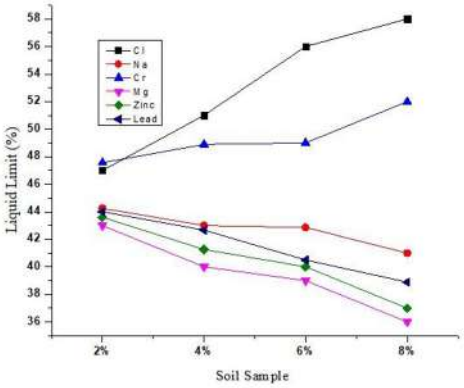

Fig 8. Liquid Limits (%) for Clayey Sample with Salts and Metals

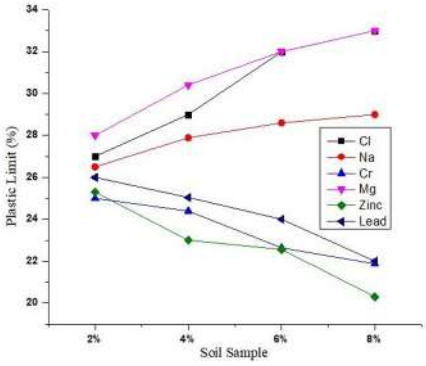

Fig 9. Plastic Limits (%) for Clayey Sample with
Salts and Metals

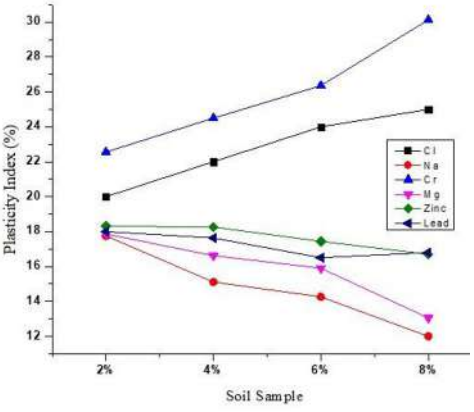

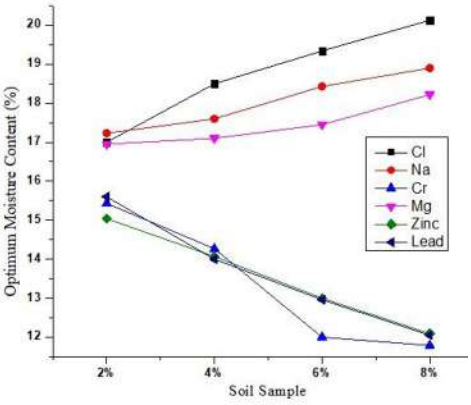

Fig 10. Plasticity Index (%) for Clayey Sample with Salts and Metals

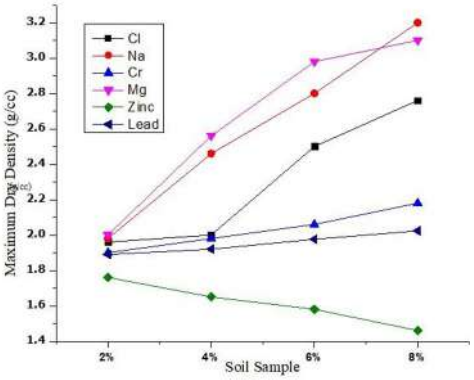

Fig 11. OMC (%) for Clayey Sample with Salts and Metals

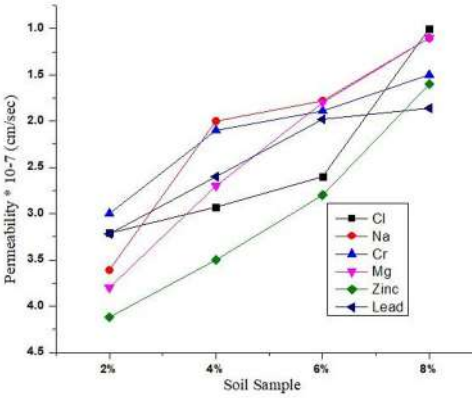

Fig 12. MDD (g/cc) for Clayey Sample with Salts and Metals

Fig 13. Permeability for Clayey Sample with Salts and Metals

The Liquid limit is the moisture level at which soil behaves to flow like water. The liquit limit and plastic limit of the soil alone was found to be 45%,24%. liquid limit increases as the chlorine percentage increases and decreases when magnesium or sodium percentages decreases as shown in Fig 8 and Fig 9. Liquid limit increases as the chromium percentage increases and decreases when Lead and Zinc percentages decreases shown in Table 4. Plastic limit of chlorine and magnesium are approximately same when compared to the values of sodium. The results of Lead, Zinc and Chromium are decreased as the chemical percentage increases. Plasticity index almost same behaver when chemicals react with soil as displayed in Fig 10 and Table 5.

The maximum dry density (Table 7) and optimum moisture content (Table 6) of untreated and treated with 0,2,4,6, and 8% Na, Cl (salts) and Mg,Cr,Zn,Pb (metals) soil is obtained through standard method. As the percentage of chemical increases from 0% to 8%, it was observed that the maximum dry density increased from 1.8g/cc for 0% chemical and the optimum moisture content decreased from 17% for 0% as shown in Fig.11 and Fig 12. As the percentage of chemical increases the variation in the OMC value is also rapidly increasing. The Magnesium percentage increases the MDD value has a minor change. That there is a increase in the MDD value as the percentage of Na,Cl,Cr,Zn,Pb increases. The results of the hydraulic conductivity for the various chemical percentages of 0,2,4,6, and 8% Na, Cl (salts) and Mg,Cr,Zn,Pb (metals) treated with soil that can affect the hydraulic conductivity.

From the results, it can be observed that with 0% marble dust addition, a maximum value of k = 4.5*10-6 cm/sec. The permeability of the soil after the addition of chemicals at a percentage of 2%,4%,6%, 8% is been decreased. Results of Permeability as displayed in Fig.13 and Table 8 after addition of Chlorine, Magnesium, Sodium with the fore mentioned graph describes that the soil permeability had been reached to a certain point after the chemicals percentage had been increased and shows similar results approximately.

5 Conclusions

Leachate high concentration of chemicals which is affected to soil properties. Locally available soil was treated with 0,2,4,6, and 8% Na, Cl (salts) and Mg,Cr,Zn,Pb (metals) to evaluate the index properties and hydraulic conductivity. The results are obtained the following conclusions can be arrived upon.

- For every 2% addition of 2N chlorine solution i.e., from 2% to 8% of chemical the liquid limit, plastic limit results are increased when increase in content of chlorine solution and on other side the optimum moisture content values were improved maximum dry density and permeability results were declined.
- In case of zinc and lead solutions maximum dry density value is improved and the optimum moisture content values were decreased as of permeability values.
- In case of magnesium and sodium solutions plastic limit value is improved compared to Liquid limit and the optimum moisture content values were improved as of permeability values.
- In this observations for every 2% addition of 2N chromium solution i.e., from 2% to 8% of chemical the maximum dry density results are increased when increase in content of chlorine solution and on other side optimum moisture content and permeability results were declined.
- Hydraulic conductivity of clayey soil was found to be $4.5*10^{-6}$ cm/sec which is not acceptable as per the relevant standards. Hence clayey soil was mixed with chemicals of 2N. Based on the Hydraulic conductivity ($1x10^{-7}$ cm/sec), the clayey soil mixed with 8% salts satisfies the criteria for hydraulic conductivity.

References

1. Arunkumar, K., Muthukannan, M., Kumar, A. S., Ganesh, A. C., & Devi, R. K. (2022). Hybrid fibre reinforced eco-friendly geopolymer concrete made with waste wood ash: A mechanical characterization study. *Engineering and Applied Science Research*, *49*(2), 235–247. https://doi.org/10.14456/easr.2022.26
2. Arunvivek, G. K., & Rameshkumar, D. (2019). Experimental Investigation on Performance of Waste Cement Sludge and Silica Fume-Incorporated Portland Cement Concrete. *Journal of The Institution of Engineers (India): Series A*, *100*(4), 611–618. https://doi.org/10.1007/s40030-019-00399-3
3. Sankar, B., & Ramadoss, P. (2023). Results in Control and Optimization Modelling the compressive strength of high-performance concrete containing metakaolin using distinctive statistical techniques. *Results in Control and Optimization*, *12*(December 2022), 100241. https://doi.org/10.1016/j.rico.2023.100241
4. Sachan, Ajanta, Penumadu, Dayakar. (2007). "Identification of Microfabric of Kaolinite Clay Mineral Using X-ray Diffraction Technique" Geotechnical and Geological Engineering.
5. Nalbantoglu, Zalihe & Tuncer, Erdil. (2011). Compressibility and hydraulic conductivity of a chemically treated e×pansive clay. Canadian Geotechnical Journal. 38. 154-160. 10.1139/t00-076.
6. Zainab, Binte & Wireko, Christian, Li, Dong & Tian, Kuo, Abichou, Tarek. (2021). Hydraulic conductivity of bentonite-polymer geosynthetic clay liners to coal combustion product leachates. Geotextiles and Geomembranes. 49. 10.1016/j.geotexmem.2021.03.007.
7. Kumar, R., Kumari, S. Geotechnical properties of materials used in landfill clay liner: A critical review. Sādhanā 48, 64 (2023). https://doi.org/10.1007/s12046-023-02124-0.
8. H.F. Yonli, B. François, D.Y.K. Toguyeni, A. Pantet, Hydro-mechanical behavior of two clayey soils in presence of household waste leachates, Global Journal of Environmental Science and Management, 10.22034/gjesm.2022.02.02.
9. IS 2720-1985(Part 5), method of test for soils (Determination of liquid and plastic limit).
10. Rowe, K., Stephan, J., Abdelaal, F. B., Dominijanni, A., Legge, K., Palmeira, E. M., Parra, D. (2022). Protecting the environment from contamination with barrier systems :

advances and challenges. Proceedings of the 20th International Conference on Soil Mechanics and Geotechnical Engineering (ICSMGE).
11. ASTM D-4318 – 05, Standard test methods for liquid limit, plastic limit, and plasticity index of soils.American Society for Testing and mate.
12. G. Swetha; B. Bhavitha; D. Namratha; K. Haritha;(2023) T. Chandana, (2023) Chemical stabilization of clay fly ash mixture, AIP Conference Proceedings 2754, 150028 (2023), Volume 2754,Issue 1.
13. Boynton, S. S., and David E. D., Hydraulic conductivity tests on compacted clay, J. Geotechnical Engrg., 1985, 465-478.
14. Osinubi, K. J., Permeability of lime-treated lateritic soil, J. Transportation Engrg., 1998, 465-469.
15. G. Swetha ; B. Veeraswamy; B. Nikhil; B. Varunkumar; P. Tharun, (2023) Stabilization of black cotton soil using plastic waste, AIP Conference Proceedings 2754, 150031 (2023), Volume 2754,Issue 1.
16. Ameta, N.K. and Abhay S. W. (2008). "Effect of bentonite on permeability of dune sand." Electronic Journal of Geotechnical Engineering., 13, pp. 1-7.
17. G. Swetha, P.V.V.S.S.R. Krishna and Chandana Sukesh (2021). Soil strength enhancement by adding of fly ash(doi:10.1088/1757-899X/1091/1/012040),IOP Conference Series: Materials Science and Engineering, ICIRMTC 2021, volume-1091.
18. C. Vivek Kumar, A.N. Swaminathen, A. Vittalaiah, C. Raja Kumar, (2022)Pavement Subgrade Stabilized with Waste coal Ash and Geosynthetics: An Experimental Study and Multiple Regression Modelling, Materials Today: Proceedings, 52(3), pp.1543-1550, https://doi.org/10.1016/j.matpr.2021.11.233.
19. Y. Kamala Raju, C. Vivek Kumar, (2020), Experimental Investigation on Design of Thickness for Flexible Pavement Subgrade Soils using CBR Approach, E3S Web Conf. 184 01087, DOI: 10.1051/e3sconf/202018401087
20. A.N. Swaminathen, Batchu Ramanjaneyalu, K. Dhanasekar, S. Robert Ravi S and Vivek Kumar C, (2023) Landslide modelling and susceptibility assessment by soil moisture sensors at Katteri watershed in Southern India, E3S Web Conf., 391 01209, DOI: https://doi.org/10.1051/e3sconf/202339101209.

Iranian Journal of Science and Technology, Transactions of Civil Engineering
https://doi.org/10.1007/s40996-023-01250-3

RESEARCH PAPER

Study on the Influence of Corrosion and Cracking in the Phosphate-Based Geopolymer Concrete Incorporated with Copper Slag

Brindha Dharmar[1] · Pandieswari Muthuramalingam[2] · Pradeep Kumar[3]

Received: 23 May 2023 / Accepted: 21 September 2023

Abstract
The corrosion rate is an essential parameter for predicting the service life of reinforced structural parts. The Tafel plots derived from the linear polarization resistance techniques, accelerated corrosion test, and gravimetric weight loss method were used to evaluate the corrosion performance of the reinforced steel of the proposed geopolymer concrete (GPC). The influence of molarity on compressive strength and corrosion test (through the chloride ion penetration) of the optimum mix proportions in the binary and ternary blends has been investigated. In this research, copper slag is fully replaced with fine aggregate, and the binder composition of GPC was prepared from class F fly ash, GGBS, and rock phosphate powder (RPP) for ternary mix proportions which was adopted, and GGBS and RPP for the production of binary blends in the 12 and 14 molar concentration were investigated for the constant silica/hydroxide ratio of 2 and alkaline/binder ratio of 0.35 for the cylindrical specimens with steel bar embedded at 20-mm coverings. When compared to standard concrete, the GPC lollipop sample significantly reduced the corrosion rate even in the presence of a 5% chloride environment. This is because phosphate's natural corrosion-inhibiting property has decreased the deleterious impact of the copper slag and improved the performance of the structure.

Keywords Geopolymer concrete · Copper slag · Fly ash · Accelerated corrosion test · Tafel extrapolation method · Gravimetric weight loss method

1 Introduction

Concrete exposed to the coastal environment is attacked by a variety of aggressive chemicals. These include mechanical agents that cause steel reinforcing to corrode. Engineers, designers, and owners face a difficulty in preventing and controlling corrosion of steel reinforcement in reinforced concrete (RC) structures. New materials and rehabilitation procedures for structures subjected to aggressive corrosion conditions are being developed at a steady rate (Reddy and Baptiste 2013). Recently, alkaline cements are one of the groups with the largest development potential which adhere extraordinarily well to reinforcing steel, exhibit high-volume stability, fire resistance, and, foreseeably, longevity in aggressive settings. Finally, they are competitively priced in comparison with Portland cement (Glukhovsky 1965; Krivenko 1997; Palomo et al. 1999; Davidovits and Krivenko 1994; Wang and Scrivener 1995; Tailing and Brandster 1989). Alkaline concrete made with activated fly ash should guarantee low reinforcement corrosion due to its high alkalinity—even greater than in standard concrete—and the reinforcing steel's simultaneous placement in the passivity region (Miranda et al. 2005). There has also been a substantial amount of study published on the corrosion rates of steel reinforcement in cementitious materials. The influence of cement composition, mineral admixtures, material composition, loading circumstances, and environmental conditions has been studied and reported. These data can be used to help designers and engineers estimate the period between corrosion onset and cracking or spalling (Huajun

✉ Pandieswari Muthuramalingam
pandieswarim1994@gmail.com

[1] Thiagarajar College of Engineering, Madurai, Tamilnadu 625015, India

[2] Velammal College of Engineering and Technology, Madurai, Tamilnadu 625009, India

[3] Karpagam College of Engineering, Coimbatore, Tamilnadu 641021, India

Published online: 13 October 2023

et al. 2013). However, there are limited data on the geopolymer concrete's durability qualities under actual exposure, which is important for practical application, particularly the deterioration of geopolymer concrete brought on by harsh environments. Geopolymer qualities, including as mechanical properties, paste properties (Miranda et al. 2005; Huajun et al. 2013; Ryu et al. 2013; Rattanasak and Chindaprasirt 2009; Chindaprasirt et al. 2009; Anurag et al. 2008), and durability in the laboratory, are the main focus of current research on geopolymer concrete. However, there are no particular publications about the geopolymer concrete's durability in the actual marine site, which is mostly because of sulphate attack and the corrosion of steel under chloride attack (Thomas and Matthews 2004; Lopez-Calvo et al. 2012). However, each of these methods is the result of a complex interaction between a number of factors, including moisture, temperature, force of impact, and sand abrasion in seawater. As a result, the study's purpose was to investigate phosphate-based geopolymer concrete in the maritime environment in order to attain good mechanical and durability attributes for marine structures. The influence of sodium hydroxide (NaOH) concentrations on geopolymer concrete compressive strength, chloride penetration profile, chloride-binding capacity, and steel corrosion was investigated. The influence of phosphate in GPC and its behaviour in reinforced concrete was investigated in this study by conducting various electrochemical experiments and accelerated corrosion tests under harsh environmental conditions.

2 Research Significance

There is a lack of information in the existing research on geopolymer concrete in optimizing the mix of precursors, notably with fly ash, GGBS, and RPP combinations. To get a reasonable conclusion, numerous researchers have studied several parameters, including altering the molarity, superplasticizer dosage, alkaline liquids to binder ratio, and so on. This study attempted to optimize the binder combination at 12 and 14 molarities of sodium hydroxide dosage using precursors such as GGBS+RPP and fly ash+GGBS+RPP. The fine aggregate is being fully replaced with copper slag. The durability of GPC admixed with industrial waste and natural rock powder (RPP) was determined, and a reasonable conclusion was reached.

3 Materials Used

3.1 Materials

One of the precursors was rock phosphate powder from a local supplier, which replaced 30% of the fly ash. Low-calcium fly ash class F (according to ASTM C618-17) from Tuticorin thermal power plant with bulk density = 1.047 g/cc was employed in this research as a precursor, whereas GGBS was brought from JSW. RPP, fly ash, and GGBS have specific gravity values of 3.1, 2.14, and 2.7, respectively. Coarse aggregates of 20 mm and 10 mm with a specific gravity of 2.65 were obtained from a nearby quarry. The fine aggregate was substituted with copper slag supplied from Sterlite factories in Tuticorin and certified to be in Zone II according to IS: 383-1970. M-sand with a fineness modulus of 2.45 and a specific gravity of 2.6 were employed for the control specimen. As the alkaline liquid, a solution of Na_2SiO_3 and NaOH in 12 molarity and 14 molarity was utilized. The sodium hydroxide was in the form of a white pillet and was commercial grade of 99% purity. For the synthesis of GPC, a very viscous sodium silicate solution in commercial grade with a specific gravity of 1.48 gm/cc was utilized (Table 1).

3.2 Mix Design

The mix design in this research followed the parameters set by Rangan, which included an alkaline liquid ratio as 2, alkaline liquids to binder as 0.35, and a water content of the binder between 12 and 14%, using 12 and 14 molar sodium hydroxides. A constant 75–80% of the total mass of the GPC

Table 1 Chemical composition of materials (wt%)

Sl.no.	Compounds	RPP	GGBS	Fly ash class F%	Copper slag
1	SiO_2	17.6	37.68	55	25.78
2	Al_2O_3	0.49	14.54	26	0.21
3	Fe_2O_3	2.78	1.11	7	69.02
4	CaO	41.68	38.01	9	0.14
5	Na_2O	0.52	–	0.2	0.49
6	MgO	0.84	7.07	1.8	–
7	SO_3	–	0.39	0.4	0.11
8	P_2O_5	6.29	–	–	–
9	LOI	(CO_2 + Cl + H_2O) 29.8	1.2	0.6	4.25

is made up of aggregates, with a fine aggregate percentage of 35%. Due to the increased specific gravity of the raw ingredients employed in this study, the concrete's average overall density is more or less comparable to that of traditional OPC concrete. Binder, which forms Si–O–Al bonds from the precursors needed to produce GPC, is the main difference between OPC and GPC mix design. If additional materials are included, it is necessary to do microstructural studies to determine the chemical interactions of the constituent materials during the polymerization process.

3.3 Mixing Sequence, Casting, and Curing

The ingredients were dry mixed in a concrete mixer for 10 min before adding alkaline solution to the mixer at the same time until the GPC mixture was uniformly blended. To avoid voids in the concrete, it was filled in moulds of 100 × 200 mm cylindrical specimens with hand compaction. The proportions of the mix were calculated according to BV Rangan 2008, as shown in Table 2. To avoid the exothermic reaction that occurs during solution preparation, the alkaline solution was prepared the day before casting. On the day of casting, the components are dry mixed for 10 min in a mortar mixer, then solutions are gradually added, and the mixture is combined for 10 min in a concrete mixer. To achieve workability, 12% free water was added to the mixer; this free water does not react during the polymerization process.

4 Experimental Setup

4.1 Linear Polarization Resistance (LPR)

LPR is an electrochemical test procedure that establishes how quickly the reinforcement inside concrete corrodes. To evaluate the immediate rate of electrode corrosion, this active approach must maintain a consistent open-circuit potential (OCP) value in order to retain the test's linearity. For measuring LPR, a test setup with three electrodes—a working electrode, a counter electrode, and a reference electrode—as well as an electrolyte of 3.5% sodium chloride solution is necessary. The working electrode is a piece of reinforcing steel that is within a geopolymer lollipop specimen as shown in Fig. 1. This study included a counter electrode made of platinum wire and a reference electrode

Table 2 Optimum mix proportions of the proposed GPC

Combined aggregate Kg/m^3		Binder Kg/m^3	Sodium silicate Kg/m^3		Sodium hydroxide Kg/m^3	
1848		408	103		41	
Mix ID	Molarity	Copper slag	M-sand	RPP	FA	GGBS
Control 12	12	0	100	0	70	30
Control 14	14	0	100	0	70	30
FGR12	12	100	0	30	35	35
FGR14	14	100	0	30	35	35
GR12	12	100	0	30	0	70
GR14	14	100	0	30	0	70

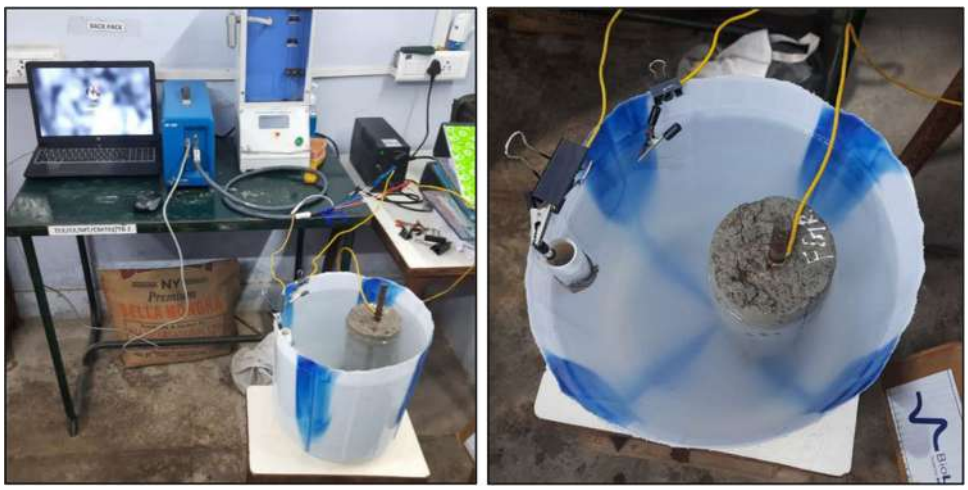

Fig. 1 Test setup for the Tafel extrapolation method

made of silver chloride. LPR mostly depends on the size of the reinforcement installed into the concrete, concrete cover, and electrode spacing. The electrode in the aqueous solution receives a little voltage, and the current needed to control the voltage shift is proportional to corrosion on the electrode surface, which determines the rate of corrosion. The working electrode and counter electrode current flows are measured to describe the material–medium pair and pinpoint the reinforcements that are actively corroding.

4.2 Accelerated Corrosion Test by Impressed Voltage Test

This approach uses an electrical method to determine the corrosion rate, and a cylindrical geopolymer specimen of 100×200 mm embedded with a reinforced steel bar with a 20-mm cover was utilized for the test. This steel bar is anodic, with an external steel electrode acting as a cathode in 5% NaCl solution exposed to a continuous potential of 24 V from a DC source. Specimens are partially immersed in the test setup as shown in Fig. 2 for 12 h, and the current variation is recorded at 1-h intervals; then removed and kept dry for the next 12 h; this cycle is repeated continuously for 5 days, and the behaviour of the RP-based GPC is evaluated by accelerating the corrosion in the rebar. Any abrupt increase in voltage indicates the presence of corrosion in the samples and initiates the crack at the concrete–steel interface. The initial crack time is tracked using the current versus time graph. If the strengthened steel begins to rust or the crack forms on the specimen, the test setup should be terminated.

4.3 Gravimetric Mass Loss Method

This method, which totally depends on the weight of the steel bar inserted in the geopolymer concrete lollipop specimen, is one of the simplest tests for monitoring corrosion. The surface of steel rebar measuring 12 mm and 24 mm in length is cleaned to get rid of all the leftovers and foreign objects. The rod's original weight is noted, and it is embedded in 200×100 mm GPC cylindrical specimens with 20-mm bottom and side covers, as depicted in Fig. 3. After a 28-day ambient temperature curing period, samples are completely submerged in a 5% aqueous NaCl solution. The embedded steel is removed from the specimen to determine the weight difference between the first and final exposures after three cycles of exposure in cyclic wet and dry of 15 days/cycle. After the cyclic wet and dry of 15 days/cycle, specimens are removed, and embedded steel is taken to estimate the weight difference between initial and final exposures.

4.4 Microstructural Analysis

Scanning electron microscopy (SEM) and energy-dispersive X-ray analysis (EDX) were employed to investigate the microstructural behaviour of the matrix's binding components.

Fig. 3 Lollipop specimens for gravimetric loss method

Fig. 2 Test setup for accelerated 24-V impressed voltage test

5 Results and Discussion

5.1 Compressive Strength

The GR14 mix attained peak compressive strength, with a 23% strength gain over the control mix. At greater molar concentrations, the pozzolanic reaction of silica and alumina in GGBS combines with RPP, increasing reactivity and stiffening the internal matrix. The best precursor mixture included fly ash, GGBS, and RPP. This combination allows for better particle packing, which improves the microstructure and, as a result, the engineering properties of the GPC. The findings in Fig. 4 showed a modest improvement in compressive strength with increasing molarity. This could be attributed to an increase in the density of the molecular structure's matrix, which links all of the materials together. Using GGBS and fly ash as precursors, the particles fill gaps, enhancing particle packing and densifying the matrix–aggregate interface by improving the interfacial transition zone (ITZ) in the GPC system's microstructures. The Ca, Si, and Al react with the oxides in the structure to generate a Ca–O–Si–O–Al link, which raises the stiffness and strength of the matrix and distributes loads within the matrix, such that the internal microstructure regulates the concrete's performance.

5.2 Electrochemical Measurement in Chloride Environment

The GPC cylindrical specimen, which had a 12-mm rebar embedded at the centre and a 20-mm cover at the bottom, was subjected to the alternate wet (5% NaCl solution) and dry cycles for 15 days. Table 3 shows the LPR results

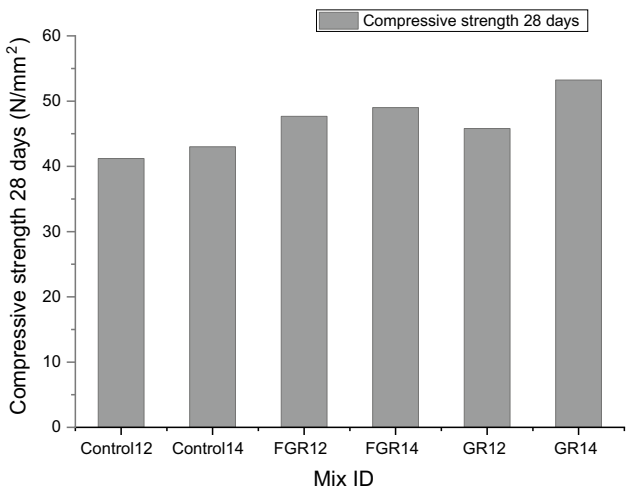

Fig. 4 Compressive strength of optimum mix

Table 3 Tafel polarization test results

ID	Ecorr m V	Icorr μ A/cm^2	Corrosion rate mmpy
Control 12	− 315.6	0.0023	0.000027
Control 14	− 493.9	2.8	0.032
FGR12	− 430.87	0.0215	0.00025
FGR14	− 287.5	1.16	0.013
GR12	− 403.18	1.95	0.022
GR14	− 343.87	0.322	0.0037

through the Tafel extrapolation method to monitor the corrosion rate as per ASTM G31. After two cycles, the specimens were connected to a potentiostat with a computerized digital monitoring system. The potential values of the 12 molarity samples showed that the reference mix without copper slag and the FGR12 fly ash mixture with a 35% weight replacement in binder had passive corrosion rates of 0.1 m A/cm^2 and 0.3 m A/cm^2, respectively. As one of the cementitious components, fly ash improves the microstructure by allowing chloride ions to diffuse and create free ions in the concrete pores, which lowers the amount of chloride transported (Manu harilal et al. 2021). The corrosion rate increases with a larger molar ratio of NaOH and is indicated by an Icorr value between 1.2 and 2.8 m A/cm^2. The greater Icorr indicates severe steel corrosion in the stimulated pore solution, which is caused by the Cl ion diffusing inside the steel–concrete interface, making these mixtures unattractive for marine-exposed structures. The Icorr values for the 12 M samples Control 12, FGR12, and GR12 showed a growing trend of 0.002, 0.02, and 1.95 m A/cm^2, respectively, whereas the 14 M samples Control 14, FGR14, and GR14 showed a decreasing trend of 2.8, 1.16, and 0.3 m A/cm^2, respectively, as shown in Fig. 5a–f. For 12 M samples, corrosion damage can be seen after 15 years, while for 14 M samples, corrosion damage is anticipated after 2–10 years. The higher molar samples are, therefore, suspected of failing early in the structure's expected service life. By including corrosion-inhibiting admixtures, which provide resistance to chloride ion penetration in the concrete's pore structure and deteriorate rebar, this can be avoided. The potential range of the entire sample was between − 280 mV and − 490 mV, indicating a higher likelihood of corrosion. This might be because copper slag contains more iron than other metals, making it more likely to corrode when exposed to chloride conditions.

5.3 Accelerated Corrosion Test

The five cycles of 12-h wet (5% NaCl solution with 24 V) and 12-h dry were repeated continuously for 120 h. Following the accelerated test, the samples were removed and

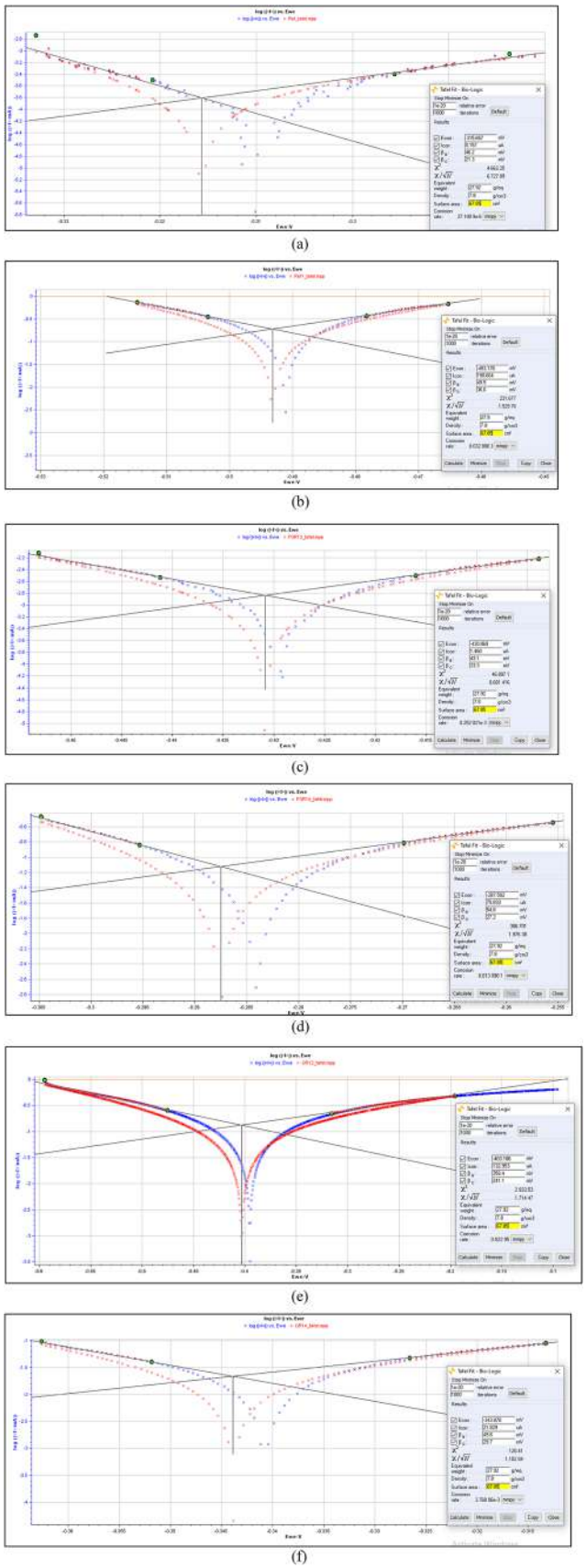

Fig. 5 Tafel plots of **a** Control 12, **b** Control 14, **c** FGR12, **d** FGR14, ▸ **e** GR12, and **f** GR14

visually inspected for corrosion product damage. The residuals of the rebars were found at the bottom and top of the specimens by the control samples, as illustrated in Fig. 6. The residual of the rebar is due to the internal tension created in the GPC as a result of the rust formed as a corrosion product on the surface of the rebar, which, if left undisturbed with a constant supply of electricity, can lead to the formation of cracks or even split off. The corrosion of the rebar at the top of the samples was detected in 14 molarity GGBS and RP mixed mixes with copper slag as the fine aggregate, followed by the control mixes. In contrast, no cracks or rust particles were discovered in the rebars of the fly ash with phosphate admixed GPC. The total performance of the samples was monitored at 24 V accelerated test for 120 h, and the results show that phosphate and fly ash, as one of the cementitious materials, can face and resist the Cl ingress corrosion products in the copper slag admixed GPC. Thus, the combined impact of fly ash, phosphate, and GGBS as binder at a 12 molar concentration of NaOH resulted in much improved corrosion resistance with lower corrosion rates in severity region of Cl ion penetrations.

The high Ca content of GGBS was critical in the production of C–A–S–H gels with finer pore structures, which resulted in increased chloride resistance. Gel formation is determined by the type of alkaline components and their concentration, both of which can influence the pore shape and chloride-binding ability of GPC. Increasing the alkali concentration can increase the chloride resistance of hydroxide-activated mixes in general. The concentration of OH^- is used to determine this. The higher the alkalinity, the more bonds are likely to be broken, allowing more Si, Al, and Ca components to dissolve from their precursors. As the intensity of the reaction increases, more gels are formed. This can improve not just the pore structure, but also the surface area available for Cl^- adsorption. Thus, the combined impact of fly ash, phosphate, and GGBS as binder in a 12 molar concentration of NaOH resulted in much improved corrosion resistance with a decreased severity region of chloride ion penetrations.

5.4 Gravimetric Weight Loss Method

Table 4 displays the gravimetric weight loss values observed in three cycles of wet and dry environments. The corroded rebar extracted from the cylindrical lollipop specimens is shown in Fig. 7a and b. The phosphate admixed samples had the lowest weight loss percentage, which increased the performance of the implanted reinforcements due to their corrosion resistance qualities and dense microstructure. The weight loss percentage was higher in control samples

Fig. 6 Samples tested for accelerated corrosion test

Table 4 Test results of gravimetric weight loss method

ID	Wt. loss %
Control 12	2.07
Control 14	4.38
FGR12	1.22
FGR14	0.88
GR12	0.86
GR14	0.44

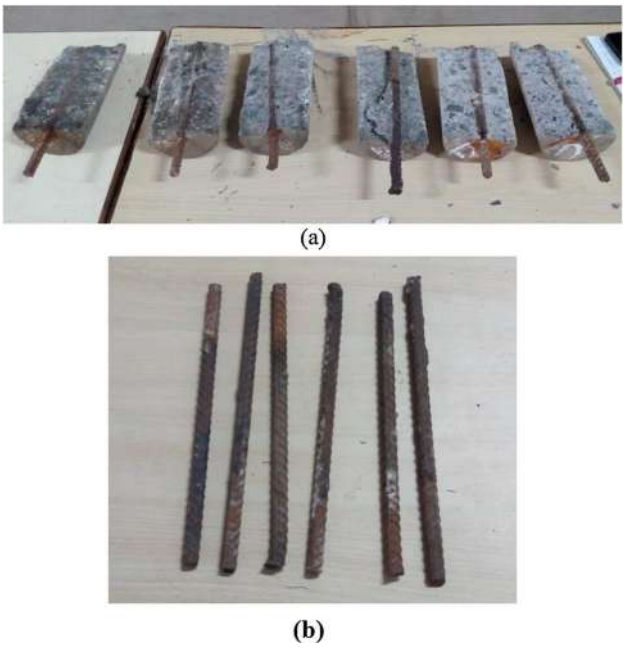

Fig. 7 **a** Samples split for removal of rebars and **b** reinforcement tested for weight loss method

due to the porous microstructure and the fly ash/GGBS as amorphous decreases corrosion resistance. The higher the molar concentration of sodium hydroxide, the denser the matrix and the greater the resistance to chloride ingression in the pore structure. Finally, the weight loss percentage was reduced by the addition of fly ash and phosphate, both of which operate as corrosion inhibitors and also encounter the negative effect of copper slag to produce corrosion. The results obtained from the proposed research have been reported that the phosphate inclusion in the geopolymer concrete along with the fly ash reduces the chloride content that reaches the reinforcing bar and also acts efficiently on the rebars to form a passive layer which protect the GPC from the degradation and shows lower corrosion rate values.

The corrosion rate (mmpy) can be determined using the equation as per ASTM G102,

$$\text{Corrosion rate (mmpy)} = 87.6W/\,\text{DAT}$$

where W is the weight loss of the reinforcement in mm, D is the density of the materials used, A is the area of the specimen in cm^2, and T is the test period in hours.

5.5 Microstructural Analysis

5.5.1 Scanning Electron Microscopy (SEM)

The overall performance of binary and ternary blends revealed that GR14 and FGR12 were the best combinations. Figure 8 demonstrates the matrix surface, where the fine copper slag aggregate shows no evidence of de-bonding. As a result, a microstructure with low porosity and inhomogeneity was observed, as well as modest cracking at the aggregate–matrix contact. The interior matrix included fewer microspores due to the evaporation of water molecules from free water. The presence of spongy, amorphous geopolymer pastes that extended over the aggregate surface, as shown in SEM images, confirmed the presence of an adequate ITZ in the concrete. A complex matrix microstructure with numerous phases is depicted in Fig. 8. Individual features of various phases, as well as their interactions, play a considerable effect in total strength attributes. There are no visible holes in the matrix; (Si/Al) is 2.5, which is the primary explanation for the strength gain in 12 molarity samples. The concrete showed a significant separation between the paste and the aggregate at the contact, which could explain why the strength was slightly lower than expected.

Furthermore, gel products in the transition zone overlapped with the aggregate surface in a way that demonstrated significant bonding with the other gel products. The surface of the aggregate appeared soft, indicating silica dissolution, which may have also been involved in the reaction process. Figure 9 shows that the mix's homogeneity is low, with voids and capillary pores visible. The increased rate of secondary pozzolanic reaction of 'Si' in matrix is mostly responsible for the mechanical property improvement. Geopolymer products contain sodium silicate and sodium aluminate, which entraps calcium in the alkali-silicate matrix

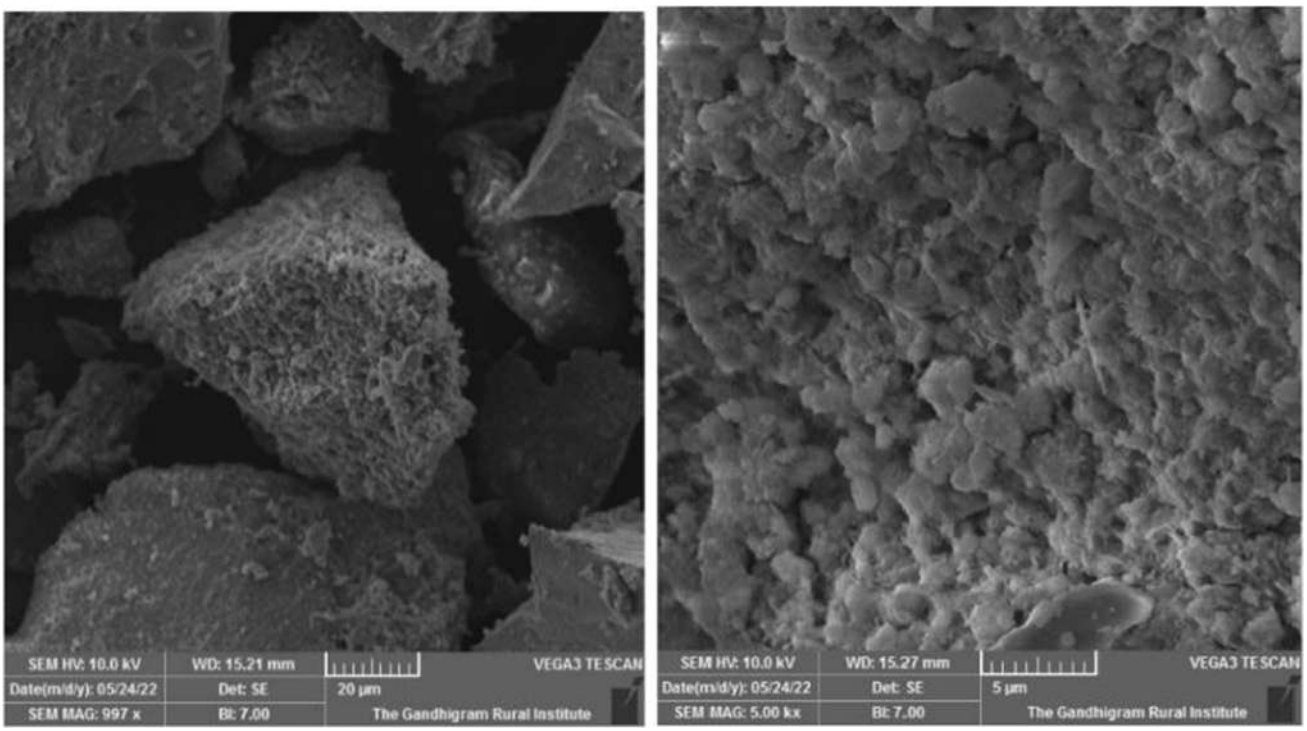

Fig. 8 SEM image of FGR12

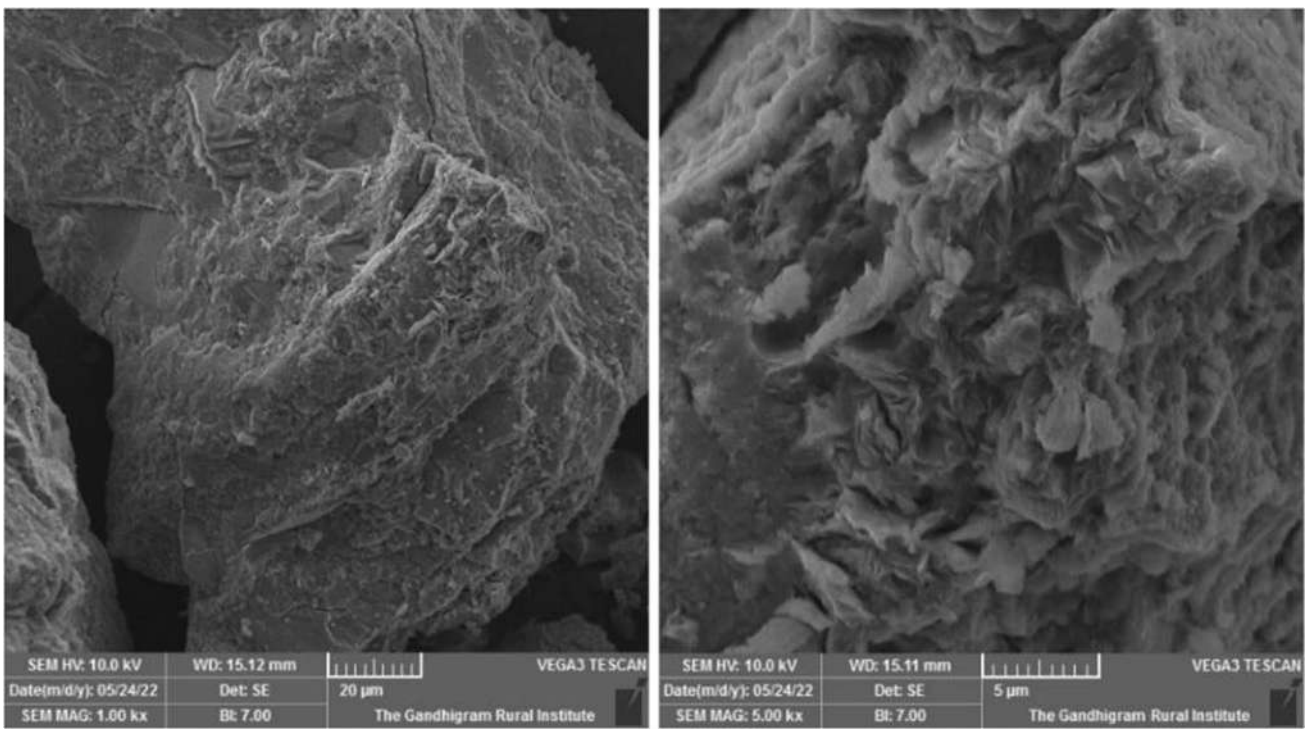

Fig. 9 SEM image of GR14

and increases strength. The RPP enclosed and connected the fly ash and GGBS particles, resulting in a more condensed geopolymer structure and compression outcomes. Copper slag with angular forms contributes to better matrix bonding. Thus, RPP and GGBS react at a larger molarity, resulting in increased polymerization product dissolution and an enhancement of matrix structures, which improves the mechanical characteristics of the GPC.

5.5.2 Energy-Dispersive X-ray Analysis (EDX)

The primary elements of Si, Al, Na, and Ca were observed in the EDX analysis of the chemical composition of FGR12 in Fig. 10. Alumina combines with oxides to generate Al_2O_3, which speeds up dissolution. At lower concentration, the calcium in RPP improves the internal structure and hardens the matrix by accelerating the nucleus formation, and boosts the chemical activity of the raw materials' crystalline structures. Thus, the predominant chemical composition of RPP, fly ash, and GGBS source materials (Ca, Si, and Al) produces a more robust internal dense matrix to produce the oligo-sialate gel structure; this internal dense matrix also has a negative impact on the increase in setting time and the formation of C–A–S–H along with C–S–H and N–A–S–H. This poly-condenses and produces the reticulation networking with the end product of geopolymer solidification, with silica being the major ingredient for greater strength and durability.

In Fig. 11 of GR14, the maximum EDX peak was achieved in Al and Si with oxides, and the final compound for structural integrity is Al–O–Si. The geopolymeric reaction is accelerated by Al_2O_3. Silicate plays a significant role in increasing the strength parameter. As the minor peaks of K and Mg oxides were found, the MgO in the matrix crystallizes due to the presence of water and creates magnesium hydroxide in the crystal forms, which refines the pores and minimizes concrete shrinkage.

6 Conclusions

Based on its dose, the influence of copper slag and molarity of activator solution plays a significant role in the engineering characteristics and improves the performance of the structure. The ideal mix proportions were investigated to identify its durability qualities under highly harsh conditions, and the discussion on the performance of the RPP-based GPC combined with copper slag discloses material property and behaviour. Based on the findings of the studies, the following conclusions were reached.

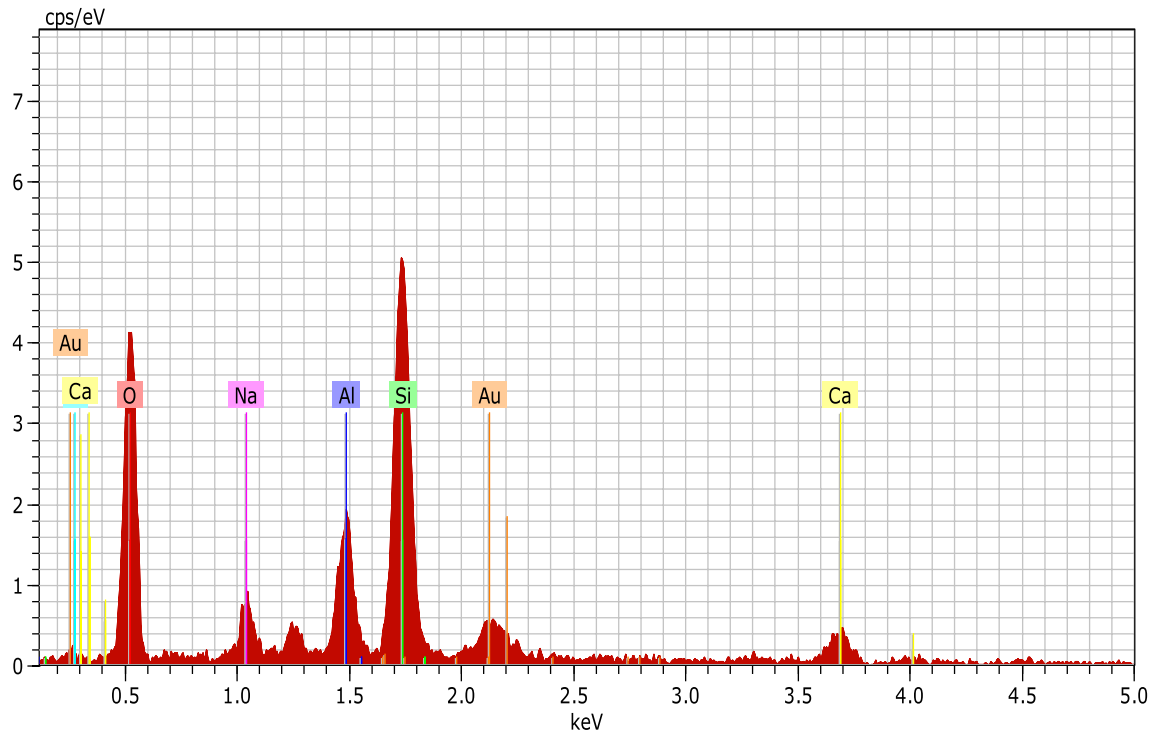

Fig. 10 EDX of FGR12

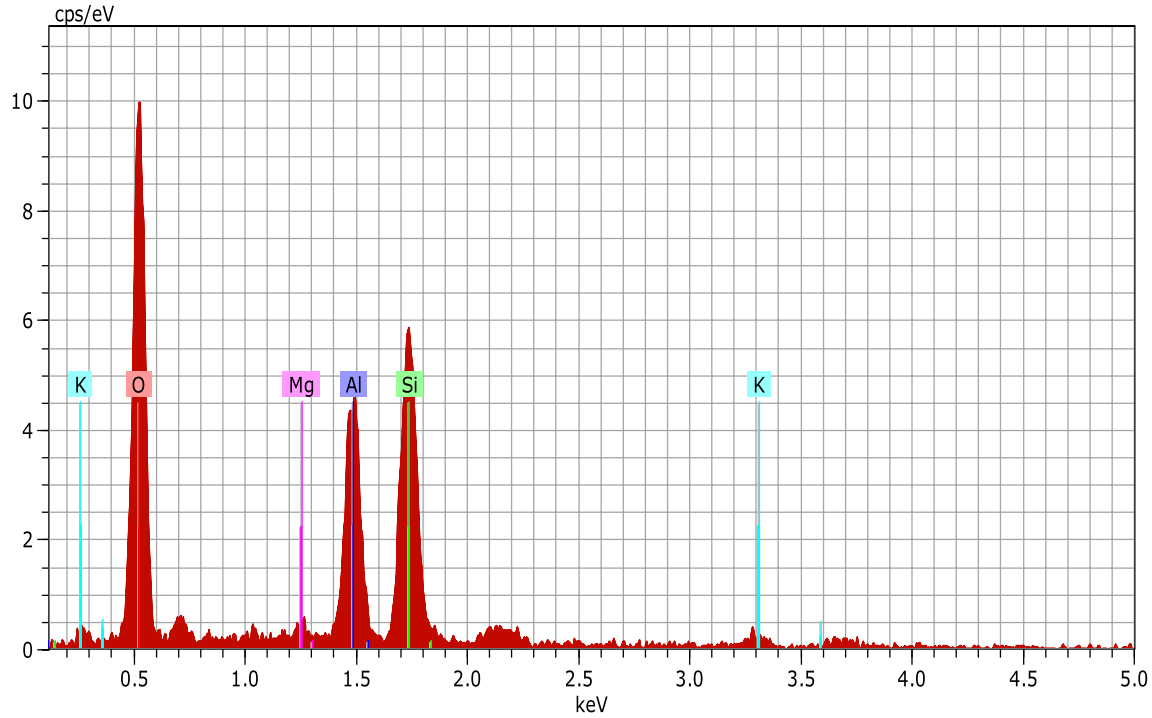

Fig. 11 EDX of GR14

1. The copper slag admixed GPC increased workability without sacrificing alkalinity dosage by lowering free water demand by 28% compared to control samples.
2. In ternary blends, the partially replaced fine aggregate with 40% copper slag was used with 13%. While M-sand as fine aggregate required 14% more water for ternary blended and reference mixes.
3. The best mix was obtained with 100% copper slag as fine aggregate in 12 M and 14 M alkaline dosages based on the compressive strength findings of mortar cubes on binary and ternary blends.
4. Tafel plots were used to calculate the corrosion rate, and corrosion damage may be expected after 15 years of exposure to a harsh environment for 12 molarity mixes; however, higher molarity samples were more vulnerable to corrosion.
5. The FGR12 mix boosted the GPC's resistance to chloride ingress and diminished the copper slag's intrinsic ability to promote corrosion in the accelerated corrosion test.
6. Based on a thorough examination of the mechanical and durability properties of GPC manufactured from RPP and locally accessible industrial waste materials, the FGR12 mix outperforms the others.

References

Anurag M, Deepika C, Namrata J, Manish K, Nidhi S, Durga D (2008) Effect of concentration of alkali liquid and curing time on strength and water absorption of geopolymer concrete. Eng Appl Sci 3:14–18

ASTM G102 Calculation of corrosion rates and related information from electrochemical measurements

ASTM G31 Immersion corrosion test of metals

Chindaprasirt P, Chalee W, Jaturapitakkul C, Rattanasak U (2009) Comparative study on the characteristics of fly ash and bottom ash geopolymers. Waste Manage 29:539–543

Davidovits J (1994) Properties of geopolymer cements. In: Krivenko PV (ed) Alkaline cements and concretes, vol 1. Vipol Stock. Kiev, Ukraine, pp 131–149

Glukhovsky VD (1965) Soil silicates. Their properties, technology and manufacturing and fields of application. Doct Tech Sc. Degree Thesis. Civil Engineering Institute. Kiev (Ukraine)

Harilal M, Kamde DK, Uthaman S, George RP, Pillai RG, Philip J, Albert SK (2021) The chloride-induced corrosion of a fly ash concrete with nanoparticles and corrosion inhibitor. Constr Build Mater 274:122097

Huajun Z, Zuhua Z, Fenggan D, Yalong C (2013) The effects of phase changes on the bonding property of geopolymer to hydrated cement. Constr Build Mater 48:124–130

Krivenko PV (1997) Alkaline cements: terminology, classification, aspects of durability. In: Proceedings of 10th International Congress on the Chemistry of Cement. Goteborg (Sweden), pp 4iv046–4iv050

Lopez-Calvo HZ, Montes-Garcia P, Bremner TW, Thomas MDA, Jiménez-Quero VG (2012) Compressive strength of HPC containing CNI and fly ash after long-term exposure to a marine environment. Cem Concr Compos 34:110–118

Miranda JM, Fernandez-Jimenez A, Gonzalez JA (2005) Corrosion resistance in activated fly ash mortars. Cem Concr Res 35:1210–1217

Palomo A, Grutzeck MW, Blanco MT (1999) Alkali-activated fly ashes. A cement for the future. Cem Concr Res 29:1323–1329

Rattanasak U, Chindaprasirt P (2009) Influence of Na(OH) solution on the synthesis of fly ash geopolymer. Miner Eng 22:1073–1078

Reddy DV, Baptiste J (2013) Durability of Fly ash based geopolymer structural concrete in the marine environment. J Mater Civ Eng ASCE 25(6):781–787

Ryu GS, Lee YB, Koh KT, Chung YS (2013) The mechanical properties of fly ash-based geopolymer concrete with alkaline activators. Constr Build Mater 47:409–18

Tailing B, Brandster J (1989) Present state and future of alkali-activated slag concretes. In: 3rd International Conference of Fly Ash, Silica Fume, Slag and Natural Pozzolans in Concrete. SP 114–74, Tondheim (Norway), pp 1519–1546

Thomas MDA, Matthews JD (2004) Performance of pfa concrete in a marine environment-10-year result. Cem Concr Res 26:5–20

Wang SD, Scrivener KL (1995) Hydration products of alkali activated slag cement. Cem Concr Res 25:561–571

Global NEST Journal, Vol 26, No 1, pp 05132

Vigna stipulacea mediated Fe nanoparticles synthesis: a greener approach for sequestration of Pb^{2+} from aqueous environment

Mafaz Ahamed R.[1]* and Saraswathi R.[2]
[1]*Department of Civil Engineering, Velammal College of Engineering and Technology, Madurai–625009, Tamil Nadu, India
[2]Department of Civil Engineering, Coimbatore Institute of Technology, Coimbatore-641014, Tamil Nadu, India
Received: 08/05/2023, Accepted: 13/11/2023, Available online: 20/11/2023
*to whom all correspondence should be addressed: e-mail: mafaz.anwari@gmail.com
https://doi.org/10.30955/gnj.005132

Graphical abstract

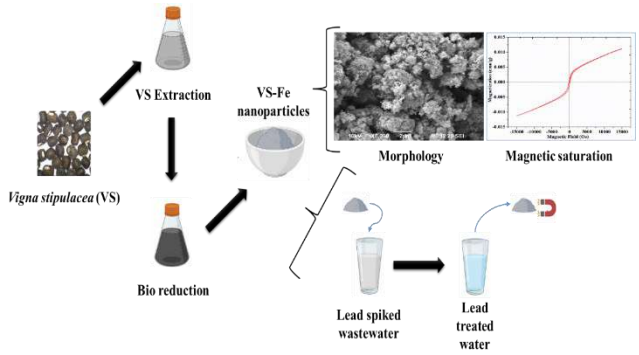

Abstract

The greener approach offers a viable, sustainable and eco-friendly way to synthesize nanoparticles. This study used the seed extract of *Vigna stipulacea* (VS) as a bioreducing agent to synthesize iron nanoparticles (VS-Fe). The VS seed extract contains polyphenols and lignin content that acted as a bioreducing agent during VS-Fe formation. The *Vigna stipulacea*-mediated Fe nanoparticles were characterized using UV, XRD, FTIR, EDAX and BET surface analysis. The as-synthesized VS-Fe, comprised of Fe^0 phase and Fe hydroxides, had an average crystallite size of 30.65 nm. It possessed a surface area of 199.189 m^2/g and magnetic saturation of 11.21 m emu. The VS-Fe exhibited excellent adsorptive behavior during the sequestration of Pb^{2+} ions from an aqueous environment. The Pb^{2+} uptake was maximum (96.7%) under the optimal conditions of 60 min contact time, 0.01 g/ 100 mL VS-Fe dosage and pH 6. The equilibrium data of Pb^{2+} adsorption was more appropriate with pseudo-second-order kinetics (R^2 = 0.9903) and Langmuir isotherm (R^2 = 0.9941) with q_{max} of 1020.50 mg/g. Thus, the dominance of chemisorption in Pb^{2+} removal was revealed. It was further confirmed with the SEM micrograph of Pb-loaded VS-Fe nanoparticles. Overall, this study demonstrated the inexpensive and non-toxic way of synthesizing Fe nanoparticles and their utilization in effectively removing Pb^{2+} ions from water.

Keywords: Fe nanoparticles, green synthesis, polyphenol, lead removal, *Vigna stipulacea*.

1. Introduction

The preservation of water quality has become a global concern owing to the synchronization of rapid industrialization with the disposal of an enormous quantity of wastewater into the aquatic environment (Thanh *et al.* 2018). Most industrial effluents are rich in heavy metals, including lead which is toxic and non-biodegradable and bioaccumulates in living cells, causing severe health issues in humans and animals (Kaur *et al.* 2018; Ali *et al.* 2019). Lead is commonly used in electroplating, battery manufacturing and metal processing industries. In humans, lead can cause infertility, asthma and renal abnormalities, whereas its exposure leads to bioaccumulation in bones, teeth and kidneys (Thirulogachandar *et al.* 2014; Araujo *et al.* 2018). A growing concern emphasizes the requirement for an efficient treatment for lead removal before they are released into the aquatic environment. Traditional heavy metal removal methods include oxidation-precipitation, ion exchange (Dong *et al.* 2019), coagulation-electrocoagulation (El-Hosiny *et al.* 2018), adsorption (Lin *et al.* 2020; Nithyalakshmi *et al.* 2023), photocatalytic degradation (Dayanidhi *et al.* 2020), and membrane filtration (Ding *et al.* 2020). Identifying an effective technique for this purpose is challenging, primarily due to the cost implications and potential environmental toxicity associated with the resulting by-products. Adsorption remains a prominent technique due to its uncomplicated design, extensive adaptability, economical nature, high efficacy, ease of use, absence of secondary pollutant generation, and viability at low concentrations (Jayalakshmi and Jeyanthi, 2019). Several adsorbents, including biopolymers, fly ash, and activated carbon, are efficacious in mitigating heavy metals in aqueous solutions. However, some of their use has been constrained by considerations like their high cost, difficulties in separation, strong reaction conditions, and toxicity (Yurekli, 2016).

The utilization of nanoparticles to eliminate various pollutants present in an aqueous environment has routed to the significant development of novel techniques in metal removal/recovery from water. The application of these particles is mainly due to their large surface area, high

surface energy and high reaction rate (Balasubramanian *et al.* 2021). Recently, there has been ongoing research on the synthesis of nano adsorbents utilizing plant intermediates, which has been recognized as a viable and effective approach. The process of synthesizing nanoparticles through plant mediation involves the utilization of environmentally friendly biomolecules that serve as both reducing and capping agents. These biomolecules are non-toxic and biodegradable, and their use helps minimize the synthesized nanoparticles' oxidation and agglomeration (Ebrahiminezhad *et al.* 2018; Raman *et al.* 2021). The high cellulose content in plants is responsible for their reducing properties towards heavy metals. The feasibility of utilizing the compound for wastewater treatment is attributed to the existence of functional groups, namely hydroxyl, phenol, and carboxyl (Mohamed *et al.* 2019).

During the last decade, several studies have indicated that Fe nanoparticles effectively address heavy metal pollution, making them a promising solution for treating wastewater polluted with various heavy metals. Moreover, their remarkable attributes and versatile utilities prompted us to opt for the plant extract approach in their production (Lin *et al.* 2020). For instance, the study conducted by Guo *et al.* (2017) reported the utilization of *Euphorbia cochinchensis* leaf extract for the green synthesis of Fe nanoparticles. The synthesized Fe nanoparticles were employed for degrading 2,4-dichlorophenol. Similarly, in a study by Huang *et al.* (2014), Fe nanoparticles synthesized using Oolong tea extract were effectively utilized to degrade malachite green. The Fe nanoparticles were produced in an environmentally friendly manner, resulting in a green synthesis process.

The *Vigna stipulacea* is commonly knowns as Minni payaru, which is traditionally utilized as animal fodder and green manure in the regions of Southern India. It is a creeping plant and wild species resistant to pests and diseases. It is widely distributed and can be cultivated in open or light-shady lands. However, the information on the phenolic content and antioxidant property of *Vigna stipulacea* is not reported elsewhere due to its close resemblance with *Vigna trilobata* (Harouna *et al.* 2018; Panzeri *et al.* 2022). This study attempts to utilize the seed extract of *Vigna stipulacea* as a bioreducing agent for Fe nanoparticle formation. To date, the literature has not provided significant information regarding the adsorptive behavior of VS-Fe in removing heavy metals. These *Vigna stipulacea* plants are easily domesticated as they require minimal water and demand little care and maintenance. Moreover, the reported VS-Fe nanoparticles showed higher surface and magnetic saturation when compared to other Fe nanoparticles synthesized using various plant extracts (Mandal *et al.* 2020; Saleh *et al.* 2021). In addition, it also showed better adsorption capacity for Pb^{2+} removal with no other functional groups tailored to it (Liu *et al.* 2019; Shi *et al.* 2023).

The main objectives of the study are as follows: (a) synthesizing the Fe nanoparticles through a greener approach using *Vigna stipulacea* as a bioreducing agent ($FeCl_2$ - metal precursor; NaOH - pH stabilizer); (b) characterizing the synthesized *Vigna stipulacea*-mediated Fe nanoparticles (VS-Fe) to detect their successful formation (UV, XRD, FTIR, VSM, BET, SEM and EDAX); (c) utilizing VS-Fe for eliminating Pb^{2+} ions from water; (d) optimizing the environmental conditions for the effective removal of Pb^{2+} ions using VS-Fe (dosage, pH, contact time, concentration); (d) validating the experimental data of Pb^{2+} adsorption onto VS-Fe through non-linear regression approach (Isotherm and Kinetic modeling).

2. Experimental section

2.1. Materials

The seeds of *Vigna stipulacea* (Minni Payaru) were collected from the local cattle farm in Sivagangai, Tamilnadu, India. The seed extract is used as a reducing agent for the green synthesis of VS-Fe nanoparticles. The chemicals (Merck India, AG) such as Ferrous chloride ($FeCl_2.4H_2O$), Sodium hydroxide (NaOH), Ethanol (C_2H_5OH), Sodium nitrate ($NaNO_3$), Hydrochloric acid (HCl), Sulphuric acid (H_2SO_4), Ethanol (C_2H_5OH), Lead nitrate ($Pb(NO_3)_2$) (lead source), tannic acid, acetic acid and alkali lignin were used in this study. Double distilled water is used for preparing all the reagents.

2.2. Preparation of Vigna stipulacea seed extract

The *Vigna stipulacea* (VS) seed extract was prepared using the solvent extraction method. The collected *Vigna stipulacea* seeds were initially washed with double distilled water until the dirt/dust in it was removed and oven-dried (Genuine equipments, Hot air oven) for 15 min. Then, the VS seed extract was prepared using a Soxhlet apparatus (250 mL) as follows: The VS seeds (6g) were taken in a cloth bag and placed in the thimble region and double distilled water (100 mL) was used as a solvent. Then, the Soxhlet apparatus was operated under 80°C for 4 hr. The VS seed extract was collected in the round-bottomed flask. Then, the contents were filtered using Whatman filter paper (Garde 40). Thus, VS seed extract, free of microparticles (Figure 1), was obtained, transferred to an air-tight container, and preserved in a refrigerator for future use.

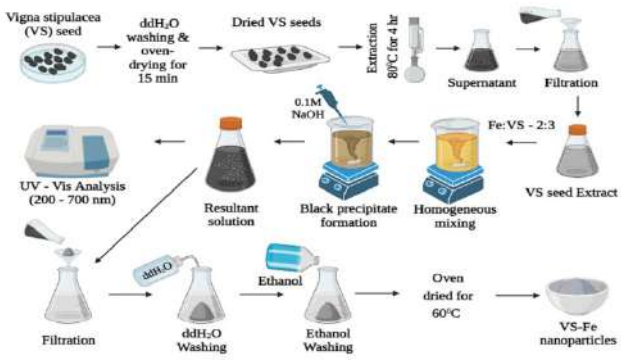

Figure 1. Synthesis of *Vigna stipulacea* - mediated Fe nanoparticles

2.3. Green synthesis of VS-Fe nanoparticles

The schematic diagram of VS-Fe synthesis is depicted in Figure 1. The metal solution of 0.1 M ferrous chloride is prepared using double distilled water. The VS seed extract is added to the metal solution in a 2:3 ratio. The reaction mixture was homogenized using a magnetic stirrer (REMI

2MLH) and the stirring was continued for 1 hr. The reaction mixture's pH was adjusted to 6 using 0.1 M NaOH. A change of colour from yellow to black was visualized, which indicated the VS-Fe nanoparticles formation. Subsequently, the formation of VS-Fe nanoparticles was further confirmed by measuring the absorbance of the resultant solution using a UV-Visible spectrophotometer (Cyberlab). The resultant solution was transferred to a quartz cuvette and the absorbance was measured in the 200 – 700 nm wavelength range. Maximum absorbance was detected at 285 nm (Figure 2(a)), which is the characteristic peak of Fe^0 formation due to surface plasma resonance (Pan *et al.* 2020; Sivakami *et al.* 2020). The findings from the UV analysis revealed the formation of zero-valent iron nanoparticles using VS seed extract as a reducing agent. The black precipitate was separated by filtering the resultant solution to obtain the VS-Fe nanoparticles formed and the residual solution was decanted. Then it was subsequently rinsed with double distilled water and ethanol to eliminate the residual impurities. Finally, it was desiccated at 60℃ using a hot air oven to remove the moisture. The VS-Fe nanoparticles thus obtained were kept in the dark place for future use.

2.4. Instrumentation

The Empyrean X-ray diffractometer (Malvern Panalytical), which operates with a high-power radioactive source (Cu Kα, λ = 1.54 Å), was used to detect the phase formation and crystallinity of VS-Fe nanoparticles. The X-ray diffractogram (XRD) for VS-Fe nanoparticles in powder form was generated in 2θ range of 10° to 90°. The CARL ZEISS Scanning Electron Microscope (SEM) coupled with BRUKER Energy Dispersive X-ray Spectroscopy (EDAX) visualized the surface texture and elemental composition of VS-Fe nanoparticles. Their sample preparation included the gold sputtering of VS-Fe nanoparticles. The Shimadzu Fourier Transform Infrared Spectrometer (FTIR) detected the VS-Fe nanoparticles' functional group by measuring their IR spectra under 400 – 4000 cm^{-1} with 0.5 cm^{-1} resolution. The VS-Fe nanoparticles were homogenously mixed with spectroscopic grade KBr before FTIR analysis. The Quanta Surface Area analyzer measured the surface area characteristics of VS-Fe nanoparticles. The VS-Fe nanoparticles (0.0139 g) were preheated upto 100℃ to liberate the water-bound molecules prior to the surface area analysis. The Lakeshore Vibrating Sample Magnetometer (VSM) evaluated the magnetic saturation of VS-Fe nanoparticles. The Toplab (TL-3800AA) Atomic Absorption Spectrometer measured the residual Pb^{2+} concentration after the absorption. The pH of the residual/metal solutions was determined from the Newlabs equipment pH meter.

The total polyphenolic composition of VS seed extract was determined using the Folin-Ciocalteu assay, as reported by Khatun and Kim (2021). Initially, the Tannic acid standard solutions (0-500 µg/mL) were prepared in methanol for calibration. Then, the methanolic extract of VS seeds was prepared using the Soxhlet apparatus. The 10 µL of these samples were added into individual test tubes and mixed with diluted Folin-Ciocalteu reagent (100 µL) for 3 minutes and 1 mL sodium carbonate (0.7 M) was introduced. Each test tube is enclosed with aluminum foil and the reaction is allowed for 60 min at room temperature and their respective absorbances were measured at 750 nm using a UV-Visible spectrophotometer.

The total lignin composition of VS seed extract was determined using an acetyl bromide assay, as Fang *et al.* (2020) reported. Initially, alkali lignin standard solutions were prepared for calibration. Then, VS seeds (5 mg) were subjected to extraction in ethanol/toluene mixture (1:1). The extraction procedure was continued until no trace of absorbance was observed at 280 nm. Afterward, the VS seed powder was dried and transferred into glass tubes containing 1 mL acetyl bromide and 3 mL acetic acid. The glass tubes were then incubated at 70℃ for half an hour. Subsequently, the samples were placed in an ice bath and homogenized with 2 M NaOH (0.9 mL), acetic acid (5 mL) and 7.5 M hydroxylamine hydrochloride (0.1 mL). The final volume was raised upto 10 mL using acetic acid and their absorbance was spectrometerically analysed at 280 nm.

2.5. Adsorption of Pb^{2+} using VS-Fe nanoparticles in batch mode

A 1.607 grams of Pb^{2+} nitrate salts were added to 1000 mL of double distilled water to make a 1000 mg/L Pb^{2+} solution. And then, appropriate dilutions were made to obtain desired concentrations of Pb^{2+} solution for batch experimentation. A 100 mL Pb^{2+} solution of desired concentration was taken in a 250 mL Erlenmeyer flask and a known quantity of VS-Fe nanoparticles was added to it. The flasks were then operated at room temperature at 150 rpm using an orbital shaker (Neolab). Once the equilibrium was achieved, the treated solution was filtered using Whatman filter paper (Grade 42) and tested for residual Pb^{2+} concentration using AAS. The process parameters significantly influencing the Pb^{2+} adsorption onto VS-Fe nanoparticles were assessed in the batch experiments. And they are as follows: VS-Fe dosage (0.01 to 0.10 g), pH (3 to 10), contact time (10 to 180 min) and initial Pb^{2+} concentration (5 to 40 mg/L).

The Eq. (1) and (2) determined the percentage removal (Nithyalakshmi and Saraswathi, 2021) of Pb^{2+} (%) and q_e, the Pb^{2+} quantity adsorbed onto VS-Fe (Patil *et al.* 2022), respectively.

$$Pb^{2+}\ \text{removal}(\%) = \frac{(C_0 - C_e)}{C_0} * 100 \quad \text{(Nithyalakshmi and Saraswathi 2021)} \quad (1)$$

$$q_e = \frac{(C_0 - C_e) * V}{m} \quad \text{(Patil } \textit{et al.}\text{ 2022)} \quad (2)$$

where C_0 (mg/L) (Patil *et al.* 2022), is the initial Pb^{2+} concentration, V (mL) is volume taken, m (g) is VS-Fe nanoparticles' quantity and C_e (mg/L) (Patil *et al.* 2022) is the equilibrium concentration of Pb^{2+}.

2.6. Analysis of best fitness

The experimental data of Pb^{2+} removal using VS-Fe was evaluated using non-regression kinetic and isotherm modeling studies. Among the performed modeling studies, the appropriate best-fit model for Pb^{2+} adsorption onto VS-Fe was validated using correlational coefficient (R^2) and Error function values. The root mean square errors (RMSE), Person's Chi-square (χ^2) and Sum of squares of error (SSE) are the Error function (EF) values used for determining the best-fit model (Jayalakshmi and Jeyanthi 2021).

$$R^2 = 1 - \frac{\sum_{n=1}^{n}\left(y_{e.n} - y_{c.n}\right)^2}{\sum_{n=1}^{n}\left(y_{e.n} - y_{c.mean}\right)^2} \quad (3)$$

$$RMSE = \sqrt{\frac{1}{n-1}\sum_{n=1}^{n}\left(y_{e.n} - y_{c.n}\right)^2} \quad (4)$$

$$\chi^2 = \sum_{n=1}^{n}\frac{\left(y_{e.n} - y_{c.n}\right)^2}{y_{e.n}} \quad (5)$$

$$SSE = \sum_{i=1}^{n}\left(y_c - y_e\right)_i^2 \quad (6)$$

3. Results and discussion

3.1. Physio-chemical analysis

3.1.1. Phytoconstituents of Vigna stipulacea seed

The total polyphenolic and lignin composition of VS seed extract was determined from the calibration curve of the tannic acid (0.0015x–0.0091, R^2=0.9864) and alkali lignin (0.0056x–0.0021, R^2=0.09921), respectively. Furthermore, their corresponding results were expressed as mg/g tannic acid equivalents and mg lignin g^{-1} cell wall. The total polyphenolic composition of VS seed extract was 56.8 mg tannic acid per g extract, whereas their lignin composition was 7.7 mg lignin per g cell wall.

3.1.2. Structural formation of VS-Fe nanoparticles

The phase formation of VS-Fe nanoparticles was detected from their XRD profile, as shown in Figure 2(b). It revealed the characteristic peak corresponding to the Fe^0 formation at 2θ = 26.09° and 45.45°. Similarly, it showed the peaks corresponding to organic matter, i.e., the bioreducing components in the VS seed extract. Therefore, it confirmed that the VS seed extract was vital in reducing Fe^{3+} to Fe^0 formation and has been adsorbed onto its surface. Additionally, it detected the peaks belonging to the Hematite phase (Fe_2O_3) at 30.15°, 40.53° and 57.76°, whereas the Magnetite phase at 35.84° (Gao *et al.* 2016; Jain *et al.* 2021). Hence, it showed that the Fe^0 nanoparticles were formed along with its metal hydroxides. The formation of hydroxides might have occurred due to exposure to atmospheric conditions. The crystalline nature of VS-Fe is determined from Scherrer's formula (Jayalakshmi and Jeyanthi, 2018) (i.e., d = 0.9λ/βcosθ). The significant diffraction peaks were used to determine VS-Fe's crystallite size; their average size was estimated to be 30.65 nm. Therefore, the iron particles (VS-Fe) produced using VS seed extract showed efficacy in forming particles at the nano-scale.

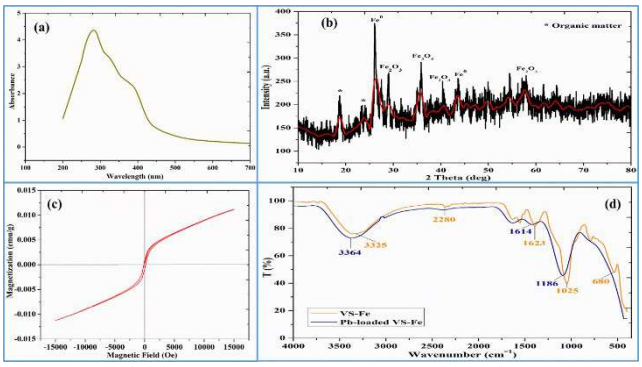

Figure 2. (a) UV-Visible spectra of VS-Fe nanoparticles; (b) XRD diffractogram of VS-Fe nanoparticles; (c) Magnetic hysteresis loop of VS-Fe nanoparticles; (d) IR spectra of VS-Fe and Pb-loaded VS-Fe nanoparticles

To corroborate the bioreducing components that are responsible for VS-Fe formation, the FTIR analysis was performed. The IR spectra of the same were illustrated in Figure 2(d). It showed significant peaks at 3325 cm^{-1} (O-H stretching), 2280 cm^{-1} (C≡C), 1623 cm^{-1} (C=C ring stretching), 1025 cm^{-1} (C=O stretching) and 680 cm^{-1} (Fe-O stretching) (Lin *et al.* 2020; Ardakani *et al.* 2021). Therefore, these results confirmed the presence of polyphenols (3325 cm^{-1}), lignin content (1623 cm^{-1}) and cellulose content (1025 cm^{-1}) in the surface of VS-Fe synthesized using VS seed extract. Consequently, these bioreducing components might have reduced Fe^{3+} to Fe^0 formation (Eslami *et al.* 2018; Jain *et al.* 2021). Moreover, the presence of metal hydroxides of Fe ions was consistent with the XRD results. Therefore, the formation of these hydroxides might have occurred due to their exposure to air during the characterization. Generally, these hydroxides tend to form a core-shell structure over the VS-Fe's surface (Ardakani *et al.* 2021). The formation of zero-valent iron nanoparticles was further confirmed with the FTIR results. Furthermore, the FTIR result of VS-Fe thus obtained was reliable with the previously reported studies on Fe nanoparticle formation using various plant extracts (Huang *et al.* 2014; Jain *et al.* 2021). The FTIR analysis of Pb-loaded VS-Fe was depicted in Figure 2(d), exhibiting the absence of a peak associated with the alkane and metal oxide functional group. In addition, alterations of peaks were observed at 3325, 1614 and 1186 cm^{-1}, suggesting the alterations caused by Pb^{2+} ion uptake onto VS-Fe. This furthered the confirmation of the occurrence of chemisorption in Pb^{2+} adsorption utilizing VS-Fe.

To detect the magnetic properties of VS-Fe nanoparticles, the VSM analysis was performed. Figure 2(c) represents the magnetic hysteresis loop of VS-Fe nanoparticles from which their magnetic saturation and coercivity can be estimated. It further revealed the ferromagnetic behavior of VS-Fe nanoparticles, confirming their magnetization function when exposed to an external magnetic field. The estimated VS-Fe's magnetic saturation (M_s) and coercivity (H_c) were found to be 11.21 m emu and 156.65 Oe, respectively. The low magnetic saturation of VS-Fe that hindered their magnetic property might be due to either of

the following reasons: their exposure to air or higher concentration of bioreducing agent in it (Kianpour *et al.* 2017; Kheshtzar *et al.* 2019). Moreover, it showed magnetic remittance (M_r) of 877.73 µ emu. The VSM results showed better magnetic saturation when compared to that reported by Ardakani *et al.* (2021). The report presented the zero magnetic saturation (i.e., no hysteresis loop) of Fe nanoparticles synthesized using *Chlorophytum comosum* leaf extract. Therefore, the compelling magnetic nature of VS-Fe facilitates the magnetic separation after the Pb^{2+} adsorption process.

To get insightful surface area distribution of VS-Fe nanoparticles, it was further analyzed with BET surface area analysis. From the N_2 adsorption/desorption curve isotherm, as displayed in Figure 3(a), the BET plot (not shown here) and BJH plot (insert image) was drawn to estimate surface area and pore distribution. It revealed the Type IV isotherm curve with an H_3 hysteresis loop (Keluo *et al.* 2018), signifying the groove-shaped pores (i.e., parallel plate-shaped pores) comprising mesopores (Mahmoud *et al.* 2021). The surface area of VS-Fe was 199.189 m^2/g which is higher when compared to the one synthesized using various plant extracts (Fazlzadeh *et al.* 2017; Bounab *et al.* 2021). The average pore radius of VS-Fe was 15.50 Å, whereas their total pore volume was 0.365 cm^3/g. The pore distribution of VS-Fe (Figure 3(a) insert image) revealed that the pores were distributed in the range of 10 – 20 Å and 50 – 100 Å. The VS-Fe nanoparticles yielded good surface area characteristics, i.e., higher surface area with mesoporous structure, which are good enough to efficiently uptake Pb^{2+} ions.

To validate the effectiveness of VS-Fe nanoparticles for Pb^{2+} uptake, their net surface charges (i.e., point of zero charge, pH_{pzc}) were further assessed with the salt-addition method (Sulaiman and Al-Jabari, 2021). For this purpose, the VS-Fe nanoparticles were immersed in 0.01 M $NaNO_3$ solution that was adjusted to various pH (pH_i) and was agitated constantly (150 rpm) for 24 hr in an orbital shaker. Subsequently, the suspension's final pH (pH_f) was noted. The pH_{pzc} of VS-Fe was obtained from the plot of (pH_i) vs. ΔpH (pH_f - pH_i) as represented in Figure 3(b). And the pH_{pzc} of VS-Fe nanoparticles was 7.2, signifying that the net surface charges on their surface will be positive below its pH_{pzc}, whereas above pH_{pzc}, it is negative. Moreover, the zeta potential analysis (graph not shown here) exhibited -17.9 mV, showing their relative stability in the aqueous medium.

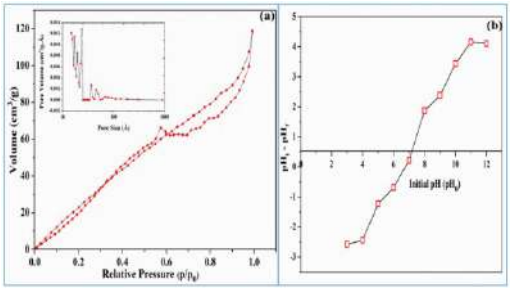

Figure 3. (a) N_2 adsorption/desorption curve and BJH plot (insert image) of VS-Fe nanoparticles; (b) Plot of pH_{pzc} of VS-Fe nanoparticles

3.1.3. Morphology of VS-Fe nanoparticles

The surface texture and morphology of VS-Fe were visualized from their SEM micrograph, as presented in Figure 4(a). The as-synthesized VS-Fe nanoparticles were found to be spherical-shaped particles uniformly distributed with lesser agglomeration. The phytochemicals that are present in the VS seed extract are attributed to agglomeration (Wu *et al.* 2015; Mahmoud *et al.* 2021). Some literature has also reported that the Fe ions' magnetic interaction might have caused the agglomeration (Fazlzadeh *et al.* 2017; Katata-Seru *et al.* 2018). Further, the surface texture of VS-Fe after the adsorption of Pb^{2+} was displayed in Figure 4(b). The particles of Pb-loaded VS-Fe showed non-uniformity in their distribution, i.e., different-sized particles. The observed variations in size following the Pb^{2+} adsorption may be attributed to the development of aggregates. As a result of aggregate formation, the surface texture of the VS-Fe nanoparticles has exhibited roughness. The aggregation of VS-Fe after the Pb^{2+} uptake determined the chemical bond formed between the Pb^{2+} ions and VS-Fe's surface particles. Thus, revealing the occurrence of chemisorption that was further assessed with kinetic studies.

To detect the element composition present in the as-synthesized VS-Fe nanoparticles, the EDAX analysis (Figure 4(c)) was performed. It affirmed the characteristic peaks for Iron (Fe), thus confirming the existence of Fe in VS-Fe nanoparticles. Furthermore, the presence of Oxygen (O) revealed the formation of Fe metal oxides/hydroxides (Kumar *et al.* 2013) that are consistent with the XRD and FTIR results. Moreover, the appearance of Carbon (C) and Oxygen (O) is attributed to the presence of phytochemicals in VS seed extract. Thus, confirming the existence of VS seed extract's coating on their surface (Sravanthi *et al.* 2018). Furthermore, the presence of Chlorine (Cl) was found as a result of residue formation during the synthesis of VS-Fe nanoparticles.

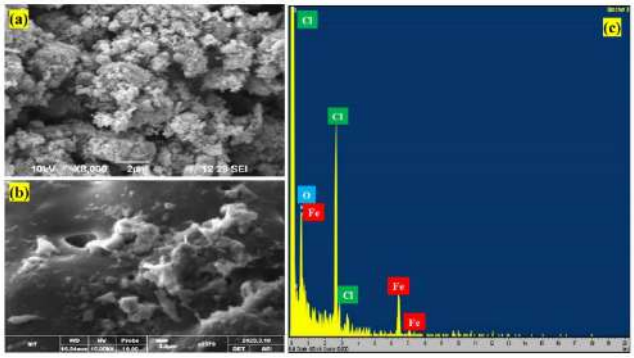

Figure 4. SEM micrograph of VS-Fe nanoparticles before (a) and after (b) Pb^{2+} adsorption; (c) EDAX analysis of VS-Fe nanoparticles

3.2. Removal of Pb^{2+} ions using VS-Fe nanoparticles

3.2.1. Influence of VS-Fe dosage

The quantity of adsorbent utilized for the metal adsorption process is a critical parameter determining the adsorption capacity (Jayalakshmi *et al.* 2022). Initially, the batch experiments were conducted by varying the VS-Fe dosage as follows: 0.01, 0.03, 0.05, 0.07 and 0.10 g/ 100 mL. The

varying dosage of VS-Fe was added into various Erlenmeyer flasks that contained 100 mL of 25 mg/L Pb^{2+} solution and were agitated at 150 rpm under room temperature. The pH of the Pb^{2+} solution was maintained at 6. The influence of VS-Fe dosage on Pb^{2+} uptake was illustrated in Figure 5(a). The Pb^{2+} uptake showed a rapid uprising on adding 0.01 g/ 100 mL of VS-Fe, showing 90.5% removal efficiency. However, upon further increasing the VS-Fe dosage (0.01-0.10 g/ 100 mL), the Pb^{2+} removal efficiency decreased from 90.5 to 50.25%. The downfall in Pb^{2+} uptake may be due to the overcrowding of VS-Fe's binding sites with the reduced surface area on further inclined VS-Fe dosage (Pal *et al.* 2017). Therefore, 0.01 g/ 100 mL VS-Fe was fixed as the optimum dosage for further experiments.

3.2.2. Influence of Pb^{2+} solution pH

The adsorption capability is notably influenced by variations in the pH of the solution, as this leads to modifications in the activity of the surface-active sites. Therefore, the influence of pH on the Pb^{2+} uptake was examined by agitating 0.01 g VS-Fe with 100 mL lead solution at varied pH ranging from 3 to 10. Figure 5(b) represents the effect of pH on the Pb^{2+} uptake using VS-Fe.

The efficacy of Pb^{2+} elimination exhibited an incremental trend until pH 6 (Figure 5(b)), followed by a gradual decline at elevated pH levels (i.e., above pH 6). At a pH greater than 6, the precipitation of lead ions occurs in the form of $Pb(OH)_2$ (Bektas *et al.* 2004). This process results in a decrease in the rate of lead adsorption, ultimately leading to a reduction in lead removal efficiency (Luo *et al.* 2013; Li *et al.* 2017). Therefore, the Pb^{2+} removal efficiency achieved at pH 6 was 96.7 %. The results are consistent with the studies reported by Lakkaboyana *et al.* (2021) and Shi *et al.* (2022). Moreover, the generation of a highly porous layer of iron oxides (Fe-OH) and hydroxides (Fe-O-OH) is facilitated by an increase in pH (6.0), which in turn promotes the diffusion process of the elements towards the Fe^0 core. Consequently, the sorption capacity of the VS-Fe nanoparticles is enhanced (Azzam *et al.* 2016).

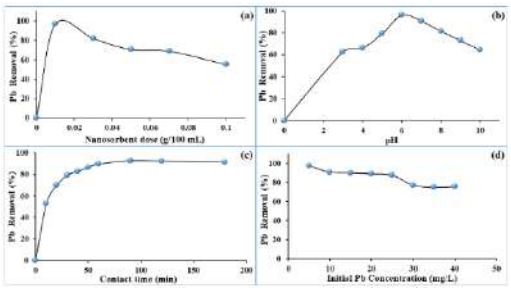

Figure 5. Batch optimization studies on Pb^{2+} adsorption onto VS-Fe, Influence of (a) VS-Fe dosage; (b) pH of lead solution; (c) Contact time; (d) Initial Pb concentration

3.2.3. Influence of contact time (CT)

The CT is a significant parameter that determines the designing of the adsorbent cost. The impact of contact time on Pb^{2+} uptake using VS-Fe was performed by varying the CT to 10 to 180 min. A 0.01 g/ 100 mL VS-Fe was added to 25 mg/L Pb^{2+} solution and it was agitated at 150 rpm with 6 pH under room temperature. The influence of CT on Pb^{2+} removal using VS-Fe is shown in Figure 5(c). It revealed that the Pb^{2+} uptake showed a rapid increase upto 60 min and exhibited no significant change after 60 min, thus confirming their equilibrium attainment. During the initial period of adsorption (10 – 60 min), the Pb^{2+} ions might have engaged quickly onto the binding sites on the VS-Fe's surface, resulting in rapid Pb^{2+} removal. Thus, the Pb^{2+} removal efficiency increased from 11.83% to 96.7%. Over a period of time, active surface sites get exhausted and the Pb^{2+} uptake remains constant due to the unavailability of active sites. Consequently, the VS-Fe showed equilibrium attainment during 70 min with a removal efficiency of 96.82%. Moreover, the VS-Fe possessed 240.24 mg/g adsorption capacity at 60 min. Therefore, further experiments were performed with 60 min of contact time as optimal contact time.

To reveal the rate of Pb^{2+} adsorption and its mechanism, adsorption kinetic modeling was assessed through a non-linear regression approach, as mentioned in Eq. (7) – (9).

$$q_t = q_e\left(1-e^{-k_1 t}\right) \quad \text{Pseudo-first-order} \quad \text{(Balasubramanian } \textit{et al.} \text{ 2021)} \quad (7)$$

where q_t is the adsorption capability of VS-Fe at any time and k_1 is pseudo-first-order rate constant

$$q_t = \frac{k_2 q_e^2 t}{1+k_2 q_e t} \quad \text{Pseudo-second-order} \quad \text{(Balasubramanian } \textit{et al.} \text{ 2021)} \quad (8)$$

where q_e is the adsorption capability of VS-Fe and k_2 is pseudo-second-order rate constant

$$q_t = \left(\frac{1}{\beta}\right)\ln \alpha\beta t \quad \text{Elovich model} \quad \text{(Balasubramanian } \textit{et al.} \text{ 2021)} \quad (9)$$

where α is the initial Pb^{2+} adsorption rate and β is the desorption constant.

The corresponding kinetic parameters were obtained directly from the fit of q_t vs. t (plot not shown here) and respective values are tabulated (Table 1).

Based on the higher R^2 values and least EF values (Table 1), the best fit kinetic model for Pb^{2+} adsorption onto VS-Fe was ordered hierarchically as follows: pseudo-second order, pseudo-first order and Elovich model. Consequently, the higher R^2 values (0.9903) and least EF values (RMSE = 3.3401; χ^2 = 0.4646; SSE = 68.90) of pseudo-second-order is said to provide good fitness to Pb^{2+} uptake using VS-Fe. Moreover, the $q_{e\,(exp)}$ value (240.24 mg/g) obtained for Pb^{2+} is consistent with $q_{e\,(cal)}$ value (248.61 mg/g) determined from pseudo-second-order. Hence, it further confirmed the best fitness of pseudo-second-order for the Pb^{2+} adsorption using VS-Fe nanoparticles. Thus, concluding the governance of chemisorption. Although the Elovich model

provided lower R^2 values and higher EF values, their $q_{e\,(cal)}$ (235.64 mg/g), value showed consistency with $q_{e\,(exp)}$ value (240.24 mg/g). Thus, suggesting their fitness for Pb^{2+} adsorption using VS-Fe. Furthermore, their lower β value further corroborated the chemisorptive behavior of Pb^{2+} removal using VS-Fe nanoparticles.

3.2.4. Influence of initial Pb^{2+} ion concentration

The mass transfer resistance required for Pb^{2+} to pass through the VS-Fe's surface from their metal solution can be significantly influenced by their initial Pb^{2+} ion concentration (Balasubramanian *et al.* 2021). The influence of initial Pb^{2+} ion concentration (C_0) is evaluated by varying their concentration from 5–50 mg/L and the corresponding experiment was carried out under optimized conditions (CT = 60 min; VS-Fe dos = 0.01 g/ 100 mL; pH = 6). The influence of Pb^{2+} ion concentration on Pb^{2+} uptake using VS-Fe was illustrated in Figure 5(d). As it is noticed from Figure 5(d), the Pb^{2+} removal efficiency showed a declining trend with increased C_0 values. On the contrary, the VS-Fe's adsorption capacity increased from 48.70 mg/g to 302.25 mg/g with elevated C_0 values from 5 mg/l to 50 mg/L. The metal ions get adsorbed rapidly onto the VS-Fe's surface at their lower concentration, thereby contributing to the maximum Pb^{2+} removal efficiency. These binding sites on the VS-Fe get accommodated over the uprising concentration of Pb^{2+} ions and become insufficient to hold up more Pb^{2+} ions, resulting in decreased Pb^{2+} removal efficiency (Jayalakshmi *et al.* 2022).

Table 1. Parameters estimated from Non-linear kinetic models

Pseudo-first order model
$q_{e(cal)}$ = 225.71 mg/g, k_1 = 0.0769 (min^{-1}), R^2 = 0.9517, RMSE = 7.4785, χ^2 = 2.4492, SSE = 149.48
Pseudo-second order model
$q_{e(cal)}$ = 248.61 mg/g, k_2 = 0.0004 (g/mg/min), R^2 = 0.9903, RMSE = 3.3401, χ^2 = 0.4646, SSE = 68.90
Elovich model
$q_{e(cal)}$ = 235.64 mg/g, α = 294.90, β = 0.0295, R^2 = 0.8918, RMSE = 11.196, χ^2 = 5.4461, SSE = 78.603

To get insight into the details of VS-Fe's surface properties and their affinity towards Pb^{2+} ions, the adsorption isotherm modeling was assessed through a non-linear regression approach. The following isotherm models, as mentioned in Eq. (10), (12), (13) and (14), were used to establish the correlation between Pb^{2+} concentration and VS-Fe nanoparticles.

$$q_e = q_{max}\frac{K_L C_e}{1+K_L C_e}$$ Langmuir isotherm (10)

where q_{max} is maximum adsorption capacity (Balasubramanian *et al.* 2021), K_L is Pb^{2+} adsorption constant's free energy (Balasubramanian *et al.* 2021)

$$R_L = \frac{1}{1+K_L C_0}$$ Separation factor (dimensionless) (11)

$$q_e = K_F C_e^{1/n_F}$$ Freundlich isotherm (12)

where K_F is Vs-Fe's relative adsorption capacity, 1/nF is Pb^{2+} adsorption intensity constant

$$q_e = \frac{RT}{b}\ln\left(K_T C_e\right)$$ Temkin isotherm (13)

where K_T is Temkin constant, b is the intensity of Pb^{2+} adsorption constant, R is the universal gas constant, T is the temperature (K) (Balasubramanian *et al.* 2021)

$$q_e = q_s \exp\left(\beta_D \varepsilon^2\right)$$ Dubinin-Radushkevich (D-R) isotherm (14)

$$\varepsilon = RT\ln\left(1+\frac{1}{C_e}\right)$$ Polanyi potential (Jayalakshmi and Jeyanthi, 2019) (15)

where q_s is saturation capacity (theoretical) and β_D is D-R isotherm constant

The corresponding kinetic parameters were obtained directly from the fit of q_e vs. C_e (plot not shown here). Table 2 presents the values of isotherm model parameters, R^2 and EF.

Based on the higher R^2 and lower EF values (Table 2), the best-fit isotherm model for Pb^{2+} adsorption onto VS-Fe was ordered as follows: Langmuir isotherm > Freundlich isotherm > D-R isotherm. The results from Table 2 also revealed that Temkin isotherm gave a poor fit for Pb^{2+} uptake due to the most negligible R^2 value and higher EF value. The Langmuir isotherm showed a q_{max} of 1020.50 mg/g for Pb^{2+} adsorption using VS-Fe. Moreover, Langmuir isotherm's suitability was further confirmed with the R_L value (0.796), showing values within 0 and 1. Therefore, the findings showed the favourability of Langmuir isotherm. Likewise, the Freundlich isotherm's favourability on Pb^{2+} adsorption was confirmed with its heterogeneity factor (n_F = 1.1980), showing values greater than 1. Thus, revealing the surface heterogeneity of VS-Fe, thereby exposing their chemisorptive behavior on Pb^{2+} uptake. These results are consistent with SEM results (Figure 4(b)). All these established findings substantiate that both monolayer and multilayer adsorption co-occurring governed the Pb^{2+} adsorption using VS-Fe. Moreover, it showed that the Pb^{2+} adsorption using VS-Fe might be driven by one or more forces of attraction.

3.3. Mass transfer modeling for Pb^{2+} adsorption onto VS-Fe

To predict the rate-controlling step and mass transfer of Pb^{2+} ions onto VS-Fe's surface, mass transfer modeling was assessed through a linear regression approach. The following diffusion models, as mentioned in the following

Eq. (16) and (17), were used to examine the transport of Pb^{2+} ions from their solution onto the VS-Fe's surface.

Where k_{id} and k_{fd} represent the diffusion constants of the intraparticle and liquid film model, respectively, C_i denotes the boundary layer thickness between the Pb^{2+} and Vs-Fe.

$$q_t = k_{id} t^{0.5} + C_i \quad \text{Intraparticle diffusion} \quad (16)$$

$$\ln(1-F) = -k_{fd} t + C_{fd} \quad \text{Liquid film diffusion} \quad (17)$$

Table 2. Isotherm parameters for Pb^{2+} adsorption using VS-Fe

Langmuir isotherm	q_m = 1020.50 mg/g, K_L = 0.0102 L/mg, R_L = 0.796 R^2 = 0.9941, RMSE = 7.2075, χ^2 = 1.4966, SSE = 3.0169
Freundlich isotherm	n_F = 1.1980, K_F = 14.667 L/mg R^2 = 0.9743, RMSE = 15.080, χ^2 = 6.4003, SSE = 6193.9
Temkin isotherm	b = 268.96 J/mol, K_T = 2.68 x10^7 L/mg R^2 = 0.13990, RMSE = 87.238, χ^2 = 249.77, SSE = 372.79
D-R isotherm	q_s = 297.52 mg/g, β_D = 0.0686 mol^2/kJ^2 R^2 = 0.9039, RMSE = 29.155, χ^2 = 2292.24, SSE = 3150.28

Table 3. Diffusion model parameters for Pb^{2+} removal using VS-Fe

Intraparticle diffusion model
k_{id} (mg/g/$min^{0.5}$) = 19.441, C_i = 80.798, R^2 = 0.9419
Liquid film diffusion model
k_{fd} (min^{-1}) = 0.0607, C_{fd} = - 0.281, R^2 = 0.9904

The findings derived from Table 3 indicate that the rate-limiting step for removing Pb^{2+} onto VS-Fe cannot be attributed to either intraparticle diffusion or liquid film diffusion. When the respective plots pass through the origin, it has been suggested that either of these models governs the mass transfer mechanism. The linear plot of intraparticle diffusion for the Pb^{2+} removal indicated a departure from the origin, indicating the possibility of surface diffusion in conjunction with intraparticle diffusion (Fang *et al.* 2018; Egbedina *et al.* 2021). Moreover, the elevated C_i value (80.798) indicates that the adsorption of Pb^{2+} was significantly influenced by the boundary layer, which could have experienced substantial resistance to the external mass transfer (Dubey *et al.* 2015). The present study further assessed the impact of the boundary layer on the Pb^{2+} adsorption by employing the Liquid film diffusion model. Despite the fact that their linear plot did not exhibit a passing through the origin, the minimal values of C_{fd} (-0.281) suggest that the Pb^{2+} adsorption may have been slightly influenced by liquid film diffusion (Wei *et al.* 2016). Therefore, the mass transfer of Pb^{2+} ions onto VS-Fe is influenced by multiple diffusion mechanisms.

3.4. Mechanism/interaction involved in sequestration of Pb^{2+} ions

The possible mechanism/interaction involved in the sequestration of Pb^{2+} ions using VS-Fe nanoparticles may be reduction, electrostatic sorption and precipitation. An increase in pH (6.0) facilitated the formation of a highly porous layer of iron oxides (Fe-OH) and hydroxides (Fe-O-OH), which in turn promoted the diffusion of Pb^{2+} ions towards the Fe^0 core. Hence, the reduction happens during the sequestration of Pb^{2+} ions. Moreover, the high $[H^+]$ under acidic conditions may impede the absorption of Pb^{2+} ions onto the positively charged VS-Fe surface ($pH < pH_{pzc}$) as a result of electrostatic repulsion. As the pH levels get elevated, the competition among reaction sites will be reduced, leading to enhanced mobility of Pb^{2+} ions towards the negatively charged VS-Fe due to electrostatic attraction. This phenomenon facilitates the efficient removal of Pb^{2+} ions.

Furthermore, the Pb^{2+} ions precipitate in alkaline pH above 6 and form lead hydroxides. Hence, rendering the removal of Pb^{2+} ions through precipitation in alkaline pH (i.e., pH > 6). Due to the precipitation nature of lead species in alkaline pH, their optimal pH was set as 6 for their effective sequestration. At this optimal pH, the chemisorption is dominant over physisorption. Additionally, the isotherm and kinetic modeling findings revealed the dominance of chemisorption. These results were further confirmed with the SEM and FTIR analysis of Pb-loaded VS-Fe nanoparticles.

3.5. Comparison studies on VS-Fe's adsorption capability with other adsorbents

Table 4 presents a comparison of various adsorbents utilized for Pb^{2+} adsorption, with a focus on their maximum adsorption capacity. The q_m value for VS-Fe was determined to be 1020.50 mg/g, indicating favorable performance. This value is comparatively more significant than the q_m values reported for other adsorbents in the literature.

Table 4. Comparison of various adsorbents utilized for Pb^{2+} adsorption

Adsorbent	q_m (mg/g)	Reference
Activated carbon-supported nanoscale zero-valent iron composite	59.35	Liu *et al.* 2019
Kaolin (IK) supported nano zerovalent iron composite	192	Lakkaboyana *et al.* 2021
Nanoscale zero-valent iron-carbon materials	223.52	Shi *et al.* 2022
Copper slag-supported sulfidized nanoscale zero-valent iron	338.98	Shi *et al.* 2023
Carbon@nano-zero-valent iron composite	98.37	Yang *et al.* 2023
Sulfur-modified nanoscale zero-valent iron	246.40	Tang *et al.* 2023
VS-Fe nanoparticle	1020.50	Present study

3.6. Feasibility of VS-Fe nanoparticles

The synthesis technique of VS-Fe is characterized by its simplicity and cost-effectiveness, as it does not need any specialized knowledge. The utilization of *Vigna stipulacea* seed extract as a reducing agent is advantageous due to its natural composition, minimal chemical requirement, sustainability and biocompatibility, hence rendering the VS-Fe environmentally beneficial. Moreover, these *Vigna stipulacea* plants are easily domesticated as they require minimal water and demand little care and maintenance. Furthermore, the VS seed extract proved its efficacy in acting as a reducing agent in Fe^0 nanoparticle formation, confirmed by their instrumental analysis. The key findings are as follows: the UV analysis showed the corresponding surface plasma resonance exhibited in its absorbance peak; the XRD analysis established the crystal size formation in nano-scale; the FTIR analysis showed the presence of polyphenols and lignin content; the EDAX analysis confirmed the existence of Fe species.

Additionally, the VS-Fe exhibited a greater surface area, resulting in an increased adsorption capacity. Moreover, it established adequate magnetic saturation, thereby facilitating the separation process using an external magnetic field. The non-functionalized VS-Fe exhibited a maximum adsorption capacity compared to other functionalized nano-iron. However, for long-term applications, the stability of VS-Fe could still be improved by functionally it with polymer to overcome the reduction in electron transfer issues caused by the surface passivation.

The regeneration capacity of VS-Fe (not reported here) may be easily achieved for up to three cycles, resulting in a maximum removal effectiveness of 95%. It has the potential to decrease the expenses associated with wastewater treatment significantly. The dominance of chemisorption might attributed to the reduction in VS-Fe's regeneration capacity after the third cycle. However, for long-term applications, the capability of VS-Fe could still be improvised in future applications to reuse it more efficiently.

4. Conclusion

The present investigation focused on utilizing *Vigna stipulacea*'s seed extract for synthesizing Fe nanoparticles and reported their capability of eliminating Pb^{2+} ions from an aqueous environment. The UV-Vis analysis confirmed the surface plasmon resonance spectra (285 nm) for VS-Fe nanoparticles' formation. In addition, a spherical shape with less agglomeration and uniform size distribution of VS-Fe was observed from SEM analysis. Moreover, the FTIR analysis showed the peaks associated with polyphenols and other phytochemicals, which played a crucial role in VS-Fe's bioreduction and stabilization. Batch adsorption studies on VS-Fe indicated maximum Pb^{2+} removal (96.7%) was achieved within 60 min using 0.01 g/ 100 mL dosage at pH 6. The Pb^{2+} adsorption using VS-Fe indicated a reasonable fit to Langmuir and Freundlich isotherm models. Moreover, the Langmuir isotherm showed a monolayer adsorption capacity of 1020.50 mg/g.

Similarly, the Pb^{2+} adsorption kinetics showed better fitness with pseudo-second-order and the Elovich model. Furthermore, it indicated the dominance of chemisorption in Pb^{2+} removal. The experimental findings suggest that VS-Fe nanoparticles have the potential to serve as effective adsorbents to eliminate Pb^{2+} ions from wastewater. Moreover, it facilitates the development of a cost-effective wastewater treatment system to eliminate hazardous metals, thereby mitigating the adverse impacts on water quality. Thus, it can be inferred that the combined strategy of nanotechnology and a greener approach can be utilized for wastewater treatment, which in turn creates a new frontier in environmental pollution.

Acknowledgment

The authors express their gratitude to Principal and Management of Coimbatore Institute of Technology, Coimbatore, for providing the required lab facilities.

References

Ali H., Khan E. and Ilahi I. (2019). Environmental chemistry and ecotoxicology of hazardous heavy metals: environmental persistence, toxicity, and bioaccumulation, *Journal of chemistry*, **2019**.

Araújo C. S., Almeida I. L., Rezende H. C., Marcionilio S. M., Léon J. J. and de Matos T. N. (2018). Elucidation of mechanism involved in adsorption of Pb (II) onto lobeira fruit (Solanum lycocarpum) using Langmuir, Freundlich and Temkin isotherms, *Microchemical Journal*, **137**, 348–354.

Ardakani L. S., Alimardani V., Tamaddon A. M., Amani A. M. and Taghizadeh S. (2021). Green synthesis of iron-based nanoparticles using Chlorophytum comosum leaf extract: methyl orange dye degradation and antimicrobial properties, *Heliyon*, **7(2)**, e06159.

Azzam A. M., El-Wakeel S. T., Mostafa B. B. and El-Shahat M. F. (2016). Removal of Pb, Cd, Cu and Ni from aqueous solution using nano scale zero valent iron particles, *Journal of environmental chemical engineering*, **4(2)**, 2196–2206.

Balasubramanian U. M., Vaiyazhipalayam Murugaiyan S. and Marimuthu T. (2021). Sustainable robust green synthesis of nanoparticles from waste aquatic plants and its application in environmental remediation, *Water Science and Technology*, **84(12)**, 3599–3615.

Bektaş N., Ağım B. A. and Kara S. (2004). Kinetic and equilibrium studies in removing lead ions from aqueous solutions by natural sepiolite, *Journal of Hazardous materials*, **112(1–2)**, 115–122.

Bounab N., Duclaux L., Reinert L., Oumedjbeur A., Boukhalfa C., Penhoud P. and Muller F. (2021). Improvement of zero valent iron nanoparticles by ultrasound-assisted synthesis, study of Cr (VI) removal and application for the treatment of metal surface processing wastewater, *Journal of Environmental Chemical Engineering*, **9(1)**, 104773.

Dayanidhi K., Vadivel P., Jothi S. and Eusuff N. S. (2020). Facile synthesis of Silver@ Eggshell nanocomposite: A heterogeneous catalyst for the removal of heavy metal ions, toxic dyes and microbial contaminants from water, *Journal of Environmental Management*, **271**, 110962.

Ding Y., Wu J., Wang J., Wang J., Ye J. and Liu F. (2020). Superhydrophilic carbonaceous-silver nanofibrous membrane for complex oil/water separation and removal of

heavy metal ions, organic dyes and bacteria, *Journal of membrane science*, **614**, 118491.

Dong Q., Guo X., Huang X., Liu L., Tallon R., Taylor B. and Chen J. (2019). Selective removal of lead ions through capacitive deionization: Role of ion-exchange membrane, *Chemical Engineering Journal*, ***361***, 1535–1542.

Dubey R., Bajpai J. and Bajpai A. K. (2015). Green synthesis of graphene sand composite (GSC) as novel adsorbent for efficient removal of Cr (VI) ions from aqueous solution. Journal of water process engineering, **5**, 83–94.

Ebrahiminezhad A., Zare-Hoseinabadi A., Sarmah A. K., Taghizadeh S., Ghasemi Y. and Berenjian A. (2018). Plant-mediated synthesis and applications of iron nanoparticles. Molecular biotechnology, **60**, 154–168.

Egbedina A. O., Adebowale K. O., Olu-Owolabi B. I., Unuabonah E. I. and Adesina M. O. (2021). Green synthesis of ZnO coated hybrid biochar for the synchronous removal of ciprofloxacin and tetracycline in wastewater, *RSC advances*, **11(30)**, 18483–18492.

El-Hosiny F. I., Abdel-Khalek M. A., Selim K. A. and Osama I. (2018). Physicochemical study of dye removal using electro-coagulation-flotation process, *Physicochemical problems of mineral processing*, **54(2)**, 321–333.

Eslami S., Ebrahimzadeh M. A. and Biparva P. (2018). Green synthesis of safe zero valent iron nanoparticles by Myrtus communis leaf extract as an effective agent for reducing excessive iron in iron-overloaded mice, a thalassemia model, *RSC advances*, **8(46)**, 26144–26155.

Fang L., Xu X., Li J., Zheng F., Li M., Yan J. and Zeng S. (2020). Transcriptome analysis provides insights into the non-methylated lignin synthesis in Paphiopedilum armeniacum seed, *BMC genomics*, **21(1)**, 1–15.

Fang Z., Hu Y., Wu X., Qin Y., Cheng J., Chen Y. and Li H. (2018). A novel magnesium ascorbyl phosphate graphene-based monolith and its superior adsorption capability for bisphenol A, *Chemical Engineering Journal*, **334**, 948–956.

Fazlzadeh M., Rahmani K., Zarei A., Abdoallahzadeh H., Nasiri F. and Khosravi, R. (2017). A novel green synthesis of zero valent iron nanoparticles (NZVI) using three plant extracts and their efficient application for removal of Cr (VI) from aqueous solutions, *Advanced Powder Technology*, **28(1)**, 122–130.

Gao J. F., Li H. Y., Pan K. L. and Si C. Y. (2016). Green synthesis of nanoscale zero-valent iron using a grape seed extract as a stabilizing agent and the application for quick decolorization of azo and anthraquinone dyes, *RSC advances* **6(27)**, 22526-22537.

Guo M., Weng X., Wang T. and Chen Z. (2017). Biosynthesized iron-based nanoparticles used as a heterogeneous catalyst for the removal of 2, 4-dichlorophenol, *Separation and Purification Technology*, **175**, 222–228.

Harouna D. V., Venkataramana P. B., Ndakidemi P. A. and Matemu A. O. (2018). Under-exploited wild Vigna species potentials in human and animal nutrition: A review, *Global food security*, **18**, 1–11.

Huang L., Weng X., Chen Z., Megharaj M. and Naidu R. (2014). Synthesis of iron-based nanoparticles using oolong tea extract for the degradation of malachite green, *Spectrochimica Acta Part A: Molecular and Biomolecular Spectroscopy,* **117**, 801–804.

Jain R., Mendiratta S., Kumar L. and Srivastava A. (2021). Green synthesis of iron nanoparticles using Artocarpus heterophyllus peel extract and their application as a heterogeneous Fenton-like catalyst for the degradation of Fuchsin Basic dye, *Current Research in Green and Sustainable Chemistry*, **4**, 100086.

Jayalakshmi R. and Jeyanthi J. (2018). Synthesis and structural characterization of polymer-based cobalt ferrite nanocomposite with core–shell structure, *Journal of Inorganic and Organometallic Polymers and Materials*, **28**, 1286–1293.

Jayalakshmi R. and Jeyanthi J. (2019). Simultaneous removal of binary dye from textile effluent using cobalt ferrite-alginate nanocomposite: Performance and mechanism, *Microchemical Journal*, **145**, 791–800.

Jayalakshmi R. and Jeyanthi J. (2021). Dynamic modelling of Alginate-Cobalt ferrite nanocomposite for removal of binary dyes from textile effluent, *Journal of Environmental Chemical Engineering*, **9(1)**, 104924.

Jayalakshmi R., Jeyanthi J. and Sidhaarth K. A. (2022). Versatile application of cobalt ferrite nanoparticles for the removal of heavy metals and dyes from aqueous solution, *Environmental Nanotechnology, Monitoring and Management*, **17**, 100659.

Kaur M., Ubhi M. K. and Singh D. (2018). Magnetically retrievable nanocomposite of magnesium ferrite and bentonite clay for sequestration of Pb (II) and Ni (II) ions: a comparative study, *Bulletin of Materials Science*, **41**, 1–14.

Keluo C. H. E. N., Zhang T., Xiaohui C. H. E. N., Yingjie H. E. and LIANG X. (2018). Model construction of micro-pores in shale: A case study of Silurian Longmaxi Formation shale in Dianqianbei area, SW China, *Petroleum Exploration and Development*, **45(3)**, 412–421.

Khatun S. and Kim T. (2021). Phenolic compound, antioxidant activity and nutritional components of five legume seed, *American Journal of Biomedical Science and Research*, **12**, 328–334.

Kheshtzar R., Berenjian A., Ganji N., Taghizadeh S. M., Maleki M., Taghizadeh S. and Ebrahiminezhad A. (2019). Response surface methodology and reaction optimization to product zero-valent iron nanoparticles for organic pollutant remediation, *Biocatalysis and Agricultural Biotechnology*, **21**, 101329.

Kianpour S., Ebrahiminezhad A., Mohkam M., Tamaddon A. M., Dehshahri A., Heidari R. and Ghasemi Y. (2017). Physicochemical and biological characteristics of the nanostructured polysaccharide-iron hydrogel produced by microorganism Klebsiella oxytoca, *Journal of basic microbiology*, **57(2)**, 132–140.

Lakkaboyana S. K., Khantong S., Asmel N. K., Obaidullah S., Kumar, V., Kannan K. and Yaacob W. Z. W. (2021). Indonesian Kaolin supported nZVI (IK-nZVI) used for the an efficient removal of Pb (II) from aqueous solutions: Kinetics, thermodynamics and mechanism, *Journal of Environmental Chemical Engineering*, **9(6)**, 106483.

Li B., Yang L., Wang C. Q., Zhang Q. P., Liu Q. C., Li Y. D. and Xiao R. (2017). Adsorption of Cd (II) from aqueous solutions by rape straw biochar derived from different modification processes. Chemosphere, **175**, 332–340.

Lin Z., Weng X., Owens G. and Chen Z. (2020). Simultaneous removal of Pb (II) and rifampicin from wastewater by iron nanoparticles synthesized by a tea extract, *Journal of Cleaner Production*, **242**, 118476.

Liu X., Lai D. and Wang Y. (2019). Performance of Pb (II) removal by an activated carbon supported nanoscale zero-valent iron

composite at ultralow iron content, *Journal of hazardous materials*, **361**, 37–48.

Luo X., Liu L., Deng F. and Luo S. (2013). Novel ion-imprinted polymer using crown ether as a functional monomer for selective removal of Pb (II) ions in real environmental water samples, *Journal of Materials Chemistry A*, **1(28)**, 8280–8286.

Mahmoud R., Kotp A. A., El-Ela F. I. A., Farghali A. A., Moaty S. A., Zahran H. Y. and Amin R. (2021). Green synthesis of iron nanoparticles of clove and green coffee origin with an in vivo hepatoprotective investigation, *Journal of Environmental Chemical Engineering*, **9(6)**, 106320.

Mandal S., Pu S., Wang X., Ma H. and Bai Y. (2020). Hierarchical porous structured polysulfide supported nZVI/biochar and efficient immobilization of selenium in the soil, *Science of the Total Environment*, **708**, 134831.

Mohamed W. A., Mansour M. M. and Salem M. Z. (2019). Lemna gibba and Eichhornia crassipes extracts: Clean alternatives for deacidification, antioxidation and fungicidal treatment of historical paper, *Journal of Cleaner Production*, **219**, 846–855.

Nithyalakshmi B. and Saraswathi R. (2021). Removal of colorants from wastewater using biochar derived from leaf waste, *Biomass Conversion and Biorefinery*, 1–17.

Nithyalakshmi B., Saraswathi R. and Praveen S. (2023). Removal of basic fuchsin red dye by turmeric leaf waste biochar: Batch adsorption studies, isotherm kinetics and RSM studies, *Global Nest Journal*, **25(1)**, 17–27.

Pal P., Syed S. S. and Banat F. (2017). Gelatin-bentonite composite as reusable adsorbent for the removal of lead from aqueous solutions: Kinetic and equilibrium studies, *Journal of water process engineering*, **20**, 40–50.

Pan Z., Lin Y., Sarkar B., Owens G. and Chen Z. (2020). Green synthesis of iron nanoparticles using red peanut skin extract: Synthesis mechanism, characterization and effect of conditions on chromium removal, *Journal of colloid and interface science*, **558**, 106–114.

Panzeri D., Guidi Nissim W., Labra M. and Grassi F. (2022). Revisiting the Domestication Process of African Vigna Species (Fabaceae): Background, Perspectives and Challenges, *Plants*, **11(4)**, 532.

Patil S. A., Kumbhar P. D., Satvekar B. S., Harale N. S., Bhise S. C., Patil S. K. and Anuse M. A. (2022). Adsorption of toxic crystal violet dye from aqueous solution by using waste sugarcane leaf-based activated carbon: isotherm, kinetic and thermodynamic study, *Journal of the Iranian Chemical Society,* **19(7)**, 2891–2906.

Raman C. D., Sellappa K. and Mkandawire M. (2021). Facile one step green synthesis of iron nanoparticles using grape leaves extract: textile dye decolorization and wastewater treatment, Water Science and Technology, **83(9)**, 2242–2258.

Saleh M., Isik Z., Aktas Y., Arslan H., Yalvac M. and Dizge N. (2021). Green synthesis of zero valent iron nanoparticles using Verbascum thapsus and its Cr (VI) reduction activity, *Bioresource Technology Reports*, **13**, 100637.

Shi L., Deng Q., Guo L., Du Y., Du D. and Zhang T. C. (2023). Efficient removal of Cd (II), Cu (II), and Pb (II) in aqueous solutions by exhausted copper slag supported sulfidized nanoscale zerovalent iron, *Separation and Purification Technology*, **314**, 123483.

Shi Y., Cheng X., Wan D., Zhang Z., Chen Z., Han X. and Zhou Q. (2022). The behavior and mechanism of toxic Pb (II) removal by nanoscale zero-valent iron-carbon materials based on the oil refining by-products, *Inorganic Chemistry Communications*, 109588.

Sivakami M., Renuka R. and Thilagavathi T. (2020). Green synthesis of magnetic nanoparticles via Cinnamomum verum bark extract for biological application, *Journal of Environmental Chemical Engineering*, **8(5)**, 104420.

Sulaiman S. M. and Al-Jabari M. H. (2021). Enhanced adsorptive removal of diclofenac sodium from aqueous solution by bentonite-supported nanoscale zero-valent iron, *Arab Journal of Basic and Applied Sciences*, **28(1)**, 51–63.

Tang K., Zhang S., Ren D., Zhang X., Zhang Z. and Zhang X. (2023). Study on the removal of Pb (II) from water by coated sulfur-modified nanoscale zero-valent iron, *Water Science and Technology*, **87(5)**, 1096–1111.

Thanh D. N., Novák P., Vejpravova J., Vu H. N., Lederer J. and Munshi T. (2018). Removal of copper and nickel from water using nanocomposite of magnetic hydroxyapatite nanorods, *Journal of magnetism and magnetic materials*, **456**, 451–460.

Thirulogachandar A., Rajeswari M., Ramya S., 2014. Assessment of heavy metals in Gallus and their impacts on human, *International Journal of Scientific and Research Publications*, **4 (6)**, 1–8.

Wei W., Wang Q., Li A., Yang J., Ma F., Pi S. and Wu D. (2016). Biosorption of Pb (II) from aqueous solution by extracellular polymeric substances extracted from Klebsiella sp. J1: Adsorption behavior and mechanism assessment, *Scientific reports*, **6(1)**, 31575.

Yang L., Jin X., Lin Q., Owens G. and Chen Z. (2023). Enhanced adsorption and reduction of Pb (II) and Zn (II) from mining wastewater by carbon@ nano-zero-valent iron (C@ nZVI) derived from biosynthesis, *Separation and Purification Technology*, 123249.

Yurekli Y. (2016). Removal of heavy metals in wastewater by using zeolite nano-particles impregnated polysulfone membranes, *Journal of hazardous materials*, **309**, 53–64.

Application of hybrid capsule network model for malaria parasite detection on microscopic blood smear images

Published: 19 April 2024

(2024) Cite this article

Multimedia Tools and Applications

Aims and scope

Submit manuscript

S. Aanjan Kumar, Monoj Kumar Muchahari, S. Poonkuntran, L. Sathish Kumar, Rajesh Kumar Dhanaraj & P. Karthikeyan

Abstract

Today, malaria is a dangerous disease caused by Plasmodium parasites and transmitted by the bite of Anopheles mosquitoes. It is estimated that more than 200,000 cases of malaria will occur every day worldwide, and more than 400,000 people will die from malaria. Early diagnosis of malaria is important to mitigate the morbidity and mortality of the disease. In this paper, a fully trained capsule neural network combined with a convolutional neural network model is proposed for malaria detection from blood smear microscopic images. In malaria diagnosis, the hybrid CapsNet model can detect malaria in blood samples. The hybrid model is optimized based on malaria data in microscopic images of infected and uninfected blood. Images are processed and enhanced through rotation before being fed into the hybrid CapsNet model. The CapsNet hybrid model is

examined for malaria data with a learning rate of 0.07 and a batch size of 20. Hybrid CapsNet model shows improved results in detecting malaria from microscopic images measured against the currently available standard malaria test. Constraints like malaria parasite detection rate, accuracy, F1 index and blood smear classification is used to gauge the attainment of the hybrid CapsNet model. Detection rate of 99%, accuracy of 99.08% and FAR of 0.97% is attained by the hybrid CapsNet model as contrary to the traditional state-of-the-art model, the DSCN-Net, where the detection rate was 98%, the accuracy was 97.2%, and the FAR was 0.99%.

Machine learning and deep learning approach for medical image analysis: diagnosis to...

Article | 24 December 2022

Deep Learning Approach for Early Detection of Alzheimer's Disease

Article | 03 November 2021

Cervical Cancer Classification From Pap Smear Images Using Deep Convolutional...

Article | Open access 14 November 2023

Data availability

No new data were created or analyzed in this study. Data sharing is not applicable to this article.

References

1. WHO (1999) The "World malaria report 2019" at a glance. Available via. https://www.who.int/news-room/feature-stories/detail/world-malaria-report-2019. Accessed 08 Sep 2023

2. Pandey SK, Janghel RR (2019) Recent deep learning techniques, challenges and its applications for medical healthcare system: a review. Neural Process Lett 50:1907–1935

Article Google Scholar

3. Dogan M, Taspinar YS, Cinar I, Kursun R, Ozkan IA, Koklu M (2023) Dry bean cultivars classification using deep cnn features and salp swarm algorithm based extreme learning machine. Comput Electron Agric 204:107575

Article Google Scholar

4. Ahad MT, Li YASB, Bhuiyan T (2023) Comparison of CNN-based deep learning architectures for rice diseases classification. Artificial Intelligence in Agriculture

9:22–35

Article Google Scholar

5. Kumar A, Gaur N, Chakravarty S, Alsharif MH, Uthansakul P, Uthansakul M (2024) Analysis of spectrum sensing using deep learning algorithms: CNNs and RNNs. Ain Shams Eng J 15(3):102505

6. Afriyie Y, Weyori BA, Opoku AA (2022) Classification of blood cells using optimized Capsule networks. Neural Process Lett 54(6):4809–4828

Article Google Scholar

7. Madhu G, Govardhan A, Ravi V, Kautish S, Srinivas BS, Chaudhary T, Kumar M (2022) DSCN-net: a deep Siamese capsule neural network model for automatic diagnosis of malaria parasites detection. Multimed Tools Appl 81:34105–34127

Article Google Scholar

8. Jameela T, Athota K, Singh N, Gunjan VK, Kahali S (2022) Deep learning and transfer learning for malaria detection. Computational Intelligence and Neuroscience, vol. 2022. https://doi.org/10.1155/2022/2221728

9. Jia BAHQ (2020) DE-CapsNet: A diverse enhanced capsule network with disperse dynamic routing. Appl Sci 10(3):884

Article Google Scholar

10. Xi E, Bing S, Jin Y (2017) Capsule network performance on complex data. arXiv preprint arXiv:1712.03480

11. Chola C, Muaad AY, Bin Heyat MB, Benifa JB, Naji WRAHKAMNFASNA, Al-Antari MA, Kadah YM, Kim T-S (2022) BCNet: A Deep Learning Computer-Aided Diagnosis

Framework for Human Peripheral Blood Cell Identification. Diagnostics 12(11):2815

Article Google Scholar

12. Bibin D, Nair MS, Punitha P (2017) Malaria parasite detection from peripheral blood smear images using deep belief networks. IEEE Access 5:9099–9108

Article Google Scholar

13. Huq A, Pervin MT (2020) Robust deep neural network model for identification of malaria parasites in cell images. In 2020 IEEE Region 10 Symposium (TENSYMP), pp 1456–1459 IEEE

14. Koresh HJD, Chacko S, Periyanayagi M (2021) A modified capsule network algorithm for oct corneal image segmentation. Pattern Recogn Lett 143:104–112

Article Google Scholar

15. Wang Y, Sun L, Ma K, Fang J (2018) Breast cancer microscope image classification based on CNN with image deformation, in Image Analysis and Recognition: 15th International Conference, ICIAR 2018, Portugal https://doi.org/10.1007/978-3-319-93000-8_96

16. Pranskuniene Z, Belousoviene E, Baranauskiene N, Eimantas N, Vaitkaitiene E, Bernatoniene J, Brazaitis M, Pranskunas A (2020) Modulation of endothelial glycocalyx and microcirculation in healthy young men during high-intensity sprint interval cycling-exercise by supplementation with pomegranate extract. A randomized controlled trial. Int J Environ Res Public Health 17(12):4405

Article Google Scholar

17. Liang N, Li B, Jia Z, Wang C, Wu P, Zheng T, Wang Y, Qiu F, Wu Y, Su J, Xu J, Xu F, Chu H, Fang S, Yang X, Wu C, Cao Z, Cao L, Bing Z, Liu H, others (2021) Ultrasensitive detection of circulating tumour DNA via deep methylation sequencing aided by

machine learning. Nature Biomed Eng, vol. 5, no. 6, pp 586 599. https://doi.org/10.1038/s41551-021-00746-5

18. de Souza Oliveira A, Costa MGF, Barbosa MDGV, Costa Filho CFF (2022) A new approach for malaria diagnosis in thick blood smear images. Biomed Signal Process Control 78:103931

Article Google Scholar

19. Abdurahman F, Fante KA, Aliy M (2021) Malaria parasite detection in thick blood smear microscopic images using modified YOLOV3 and YOLOV4 models. BMC Bioinformatics 22(1):1–17

Article Google Scholar

20. Mariki M, Mkoba E, Mduma N (2022) Combining clinical symptoms and patient features for malaria diagnosis: machine learning approach. Appl Artif Intell 36(1):2031826

Article Google Scholar

21. Nakasi R, Tusubira JF, Zawedde A, Mansourian A, Mwebaze E (2020) A web-based intelligence platform for diagnosis of malaria in thick blood smear images: A case for a developing country. In Proceedings of the IEEE/CVF Conference on Computer Vision and Pattern Recognition Workshops pp 984–985

22. Yang F, Poostchi M, Yu H, Zhou Z, Silamut KAYJ, Maude RJ, Jaeger S, Antani S (2019) Deep learning for smartphone-based malaria parasite detection in thick blood smears. IEEE J Biomed Health Informatics 24(5):1427–1438

Article Google Scholar

23. Tek FB, Dempster AG, Kale I (2010) Parasite detection and identification for automated thin blood film malaria diagnosis. Comput Vis Image Underst 114(1):21–

Article Google Scholar

24. Long F, Peng J-J, Song W, Xia X, Sang J (2021) BloodCaps: A capsule network based model for the multiclassification of human peripheral blood cells. Comput Methods Programs Biomed 202:105972

Article Google Scholar

25. Liu R, Liu T, Dan T, Yang S, Li Y, Luo B, Zhuang Y, Fan X, Zhang X, Cai H, Teng Y (2023) AIDMAN: An AI-based object detection system for malaria diagnosis from smartphone thin-blood-smear images. Patterns 4(9):100806

Article Google Scholar

26. Yang F, Poostchi M, Yu H, Zhou Z, Silamut K, Yu J, Maude RJ, Jaeger S, Antani S (2019) Deep learning for smartphone-based malaria parasite detection in thick blood smears. IEEE J Biomed Health Inform 24(5):1427–1438

Article Google Scholar

27. Das DK, Ghosh M, Pal M, Maiti AK, Chakraborty C (2013) Machine learning approach for automated screening of malaria parasite using light microscopic images. Micron 45:97–106

Article Google Scholar

28. Liang Z, Powell A, Ersoy I, Poostchi M, Silamut K, Palaniappan K, Guo P, Hossain MA, Sameer A, Maude RJ, Huang JX (2016) CNN-based image analysis for malaria diagnosis. In 2016 IEEE international conference on bioinformatics and biomedicine (BIBM) pp 493–496 IEEE

29. Kumarasamy SOSTK (2011) Robust contour reconstruction of red blood cells and parasites in the automated identification of the stages of malarial infection. Mach Vis Appl 22(1):461–469

Google Scholar

30. Maity M, Jaiswal A, Gantait K, Chatterjee J, Mukherjee A (2020) Quantification of malaria parasitaemia using trainable semantic segmentation and capsnet. Pattern Recogn Lett 138:88–94

Article Google Scholar

31. Chen Y, Ni J, Tang G, Cao W, Yang SX (2023) An improved dense-to-sparse cross-modal fusion network for 3D object detection in RGB-D images. Multimed Tools Appl, pp 1—26. https://doi.org/10.1007/s11042-023-15845-5

32. Ni J, Shen K, Chen Y, Yang SX (2023) An Improved SSD-Like Deep Network-Based Object Detection Method for Indoor Scenes. IEEE Trans Instrum Meas 72:1–15

Google Scholar

33. Tabata AN, Zimmer A, dos Santos Coelho L, Mariani VC (2023) Analyzing CARLA's performance for 2D object detection and monocular depth estimation based on deep learning approaches. Exp Syst Appl 227:120200

Article Google Scholar

34. Singh P, Muchahari MK (2023) Solving multi-objective optimization problem of convolutional neural network using fast forward quantum optimization algorithm: Application in digital image classification. Adv Eng Softw 176:103370

Article Google Scholar

35. Sabour S, Frosst N, Hinton GE (2017) Dynamic routing between capsules. Adv neural Inf Process Syst 30

36. Alqudah AM (2020) AOCT-NET: a convolutional network automated classification of multiclass retinal diseases using spectral-domain optical coherence tomography images. Med Biol Eng Comput 58:41–53

Article Google Scholar

37. Maturana CR, de Oliveira AD, Nadal S, Bilalli B, Serrat FZ, Soley ME, Igual ES, Bosch M, Lluch AV, Abello A (2022) Advances and challenges in automated malaria diagnosis using digital microscopy imaging with artificial intelligence tools: A review. Frontiers in Microbiology 13:1006659

Article Google Scholar

38. Loey M, Manogaran G, Taha MHN, Khalifa NEM (2021) Fighting against COVID-19: A novel deep learning model based on YOLO-v2 with ResNet-50 for medical face mask detection. Sustain Cities Soc 65:102600

Article Google Scholar

39. Howard J, Gugger S (2020) Fastai: A layered API for deep learning. Information 11(2):108

Article Google Scholar

40. Srivastava R, Prajapati YK, Pal S, Kumar S (2022) Micro-channel plasmon sensor based on a D-shaped photonic crystal fiber for malaria diagnosis with improved performance. IEEE Sens J 22(15):14834–14841

Article Google Scholar

41. Aanjanadevi S, Palanisamy V, Aanjankumar S, Poonkuntran S, Karthikeyan P (2022) Independent automobile intelligent motion controller and redirection using a deep learning system. Object Detection with Deep Learning Models: Principles and Applications, pp. 165--178. https://doi.org/10.1201/9781003206736-9

42. Azikiwe CC, Ifezulike C, Siminialayi I, Amazu LU, Enye J, Nwakwunite O (2012) A comparative laboratory diagnosis of malaria: microscopy versus rapid diagnostic test kits. Asian Pac J Trop Biomed 2(4):307–310

Article Google Scholar

43. Vijayalakshmi A (2020) Deep learning approach to detect malaria from microscopic images. Multimed Tools Appl 79:15297–15317

Article Google Scholar

44. Gheysari P, Fateh M, Rezvani M (2021) Lung ct image segmentation using reinforcement learning. Int J Artif Intell Tools 30(2):2150005

Article Google Scholar

45. Marques G, Ferreras A, de la Torre-Diez I (2022) An ensemble-based approach for automated medical diagnosis of malaria using EfficientNet. Multimedia Tools Appl 81(19):28061–28078

Article Google Scholar

46. Mirahmadi H, Rahmati-Balaghaleh M, Afzalaghaee M, Zarean M, Shamsian SA, Mehravaran A, Raissi V, Etemadi S (2021) Detection of malaria using blood smear by light microscopy, RDT and nested-PCR for suspected patients in south-eastern Iran. Gene Reports 25:101339

Article Google Scholar

47. Simonyan K, Zisserman A (2014) Very deep convolutional networks for large-scale image recognition. arXiv preprint arXiv:1409.1556

48. Zogaj F, Cambronero JP, Rinard MC, Cito J (2021) Doing more with less: characterizing dataset downsampling for automl, in Proceedings of the VLDB Endowment, New York. https://doi.org/10.14778/3476249.3476262

49. Tajbakhsh NASJYAGSR, Hurst RT, Kendall CB, Gotway MB, Liang J (2016) Convolutional neural networks for medical image analysis: Full training or fine tuning? IEEE Trans Med Imaging 35(5):1299–1312

Article Google Scholar

50. Alqudah A, Alqudah AM, Qazan S (2020) Lightweight Deep Learning for Malaria Parasite Detection Using Cell-Image of Blood Smear Images. Rev d'Intelligence Artif 34(5):571–576

Article Google Scholar

51. Anggraini D, Nugroho AS, Pratama C, Rozi IE, Iskandar AA, Hartono RN (2011) Automated status identification of microscopic images obtained from malaria thin blood smears. In Proceedings of the 2011 international conference on electrical engineering and informatics pp 1–6 IEEE

52. Kim Y, Ratnam J, Doi T, Morioka Y, Behera S, Tsuzuki A, Minakawa N, Sweijd N, Kruger P, Maharaj R (2019) Malaria predictions based on seasonal climate forecasts in South Africa: A time series distributed lag nonlinear model. Sci Rep 9(1):17882

Article Google Scholar

53. Ma A, Filippi AM, Wang Z, Yin Z (2019) Hyperspectral image classification using similarity measurements-based deep recurrent neural networks. Remote Sensing 11(2):194

Article Google Scholar

54. Dıaz GGFRE (2009) A semi-automatic method for quantification and classification of erythrocytes infected with malaria parasites in microscopic images. J Biomed Inform 42(2):296–307

Article Google Scholar

Author information

Authors and Affiliations

Department of Computer Application and Science, Institute of Engineering and Management, Kolkata, West Bengal, India
Monoj Kumar Muchahari

School of Computing Science and Engineering, VIT Bhopal University, Bhopal-Indore Highway, Kothrikalan, Sehore, 466114, Madhya Pradesh, India
S. Aanjan Kumar, S. Poonkuntran & L. Sathish Kumar

Symbiosis Institute of Computer Studies and Research, Symbiosis International (Deemed University), Pune, India
Rajesh Kumar Dhanaraj

Department of Electronics & Communication Engineering, Velammal College of Engineering & Technology, Madurai, 625009, Tamil Nadu, India
P. Karthikeyan

Contributions

Monoj Kumar Muchahari, and S. Aanjan Kumar: Conceptualization, Methodology, Software, Data curation, Writing- Original draft preparation, Visualization, Investigation. S. Poonkuntran, Sathish Kumar L, Rajesh Kumar Dhanaraj, and Karthikeyan P: Supervision, Writing- Reviewing and Editing.

Corresponding author

Correspondence to Monoj Kumar Muchahari.

Ethics declarations

Conflicts of interest

All other authors have no conflicts of interest.

Additional information

Publisher's Note

Springer Nature remains neutral with regard to jurisdictional claims in published maps and institutional affiliations.

Rights and permissions

About this article

Cite this article

Kumar, S.A., Muchahari, M.K., Poonkuntran, S. *et al.* Application of hybrid capsule network model for malaria parasite detection on microscopic blood smear images. *Multimed Tools Appl* (2024). https://doi.org/10.1007/s11042-024-19062-6

Received	Revised	Accepted
08 September 2023	02 January 2024	22 March 2024

Published
19 April 2024

DOI
https://doi.org/10.1007/s11042-024-19062-6

Keywords

Malaria Capsule Neural Network Deep learning model

Convolutional Neural Network Healthcare

sensors

MDPI

Article

Artificial Neural Network Modeling of a CMOS Differential Low-Noise Amplifier Using the Bayesian Regularization Algorithm

Bhuvaneshwari Subburaman [1], Vignesh Thangaraj [1], Vadivel Balu [1], Uma Maheswari Pandyan [2] and Jayshri Kulkarni [3,*]

[1] ECE Department, Mangayarkarasi College of Engineering, Madurai 625402, Tamil Nadu, India; sp.bhuvana@gmail.com (B.S.); vignesh.thangaraj85@gmail.com (V.T.); vadivelbalu.eee@gmail.com (V.B.)
[2] ECE Department, Velammal College of Engineering and Technology, Madurai 625009, Tamil Nadu, India; umamahes.p@gmail.com
[3] Department of Electrical and Computer Engineering, Baylor University, Waco, TX 76798, USA
* Correspondence: jayah2113@gmail.com

Abstract: The purpose of this communication is to present the modeling of an Artificial Neural Network (ANN) for a differential Complementary Metal Oxide Semiconductor (CMOS) Low-Noise Amplifier (LNA) designed for wireless applications. For satellite transponder applications employing differential LNAs, various techniques, such as gain boosting, linearity improvement, and body bias, have been individually documented in the literature. The proposed LNA combines all three of these techniques differentially, aiming to achieve a high gain, a low noise figure, excellent linearity, and reduced power consumption. Under simulation conditions at 5 GHz using Cadence, the proposed LNA demonstrates a high gain (S21) of 29.5 dB and a low noise figure (NF) of 1.2 dB, with a reduced supply voltage of only 0.9 V. Additionally, it exhibits a reflection coefficient (S11) of less than −10 dB, a power dissipation (Pdc) of 19.3 mW, and a third-order input intercept point (IIP3) of 0.2 dBm. The performance results of the proposed LNA, combining all three techniques, outperform those of LNAs employing only two of the above techniques. The proposed LNA is modeled using PatternNet BR, and the simulation results closely align with the results of the developed ANN. In comparison to the Cadence simulation method, the proposed approach also offers accurate circuit solutions.

Keywords: gain boosting; differential cascode; capacitor cross-coupling; low-noise amplifier; ANN; Bayesian regularization

Citation: Subburaman, B.; Thangaraj, V.; Balu, V.; Pandyan, U.M.; Kulkarni, J. Artificial Neural Network Modeling of a CMOS Differential Low-Noise Amplifier Using the Bayesian Regularization Algorithm. *Sensors* **2023**, *23*, 8790. https://doi.org/10.3390/s23218790

Received: 22 September 2023
Revised: 14 October 2023
Accepted: 18 October 2023
Published: 28 October 2023

1. Introduction

Significant progress has been made in the realm of wireless communication systems thanks to the development of fully integrated Complementary Metal Oxide Semiconductor (CMOS) receiver front-ends. In satellite communication systems, a satellite transponder comprises a series of interconnected elements that establish a communication link between the transmitting and receiving antennas. Among these elements are the Band-Pass Filter (BPF), Low-Noise Amplifier (LNA), mixer, and power amplifier. The LNA serves as a fundamental component and plays a pivotal role as the initial block in satellite transponders. It is widely recognized that designing this first block poses a considerable challenge, as its performance profoundly influences the subsequent stages in terms of both the selectivity and sensitivity of the receiver.

To meet the high sensitivity demands, pioneering studies are documented in References [1–36]. For instance, Tae-Sung Kim et al. presented an LNA operating at 2 GHz in [1], employing post-linearization techniques with 0.18 µm CMOS technology. However, the performance of the receiver is constrained by the noise factor primarily influenced by the LNA. Hence, achieving a high sensitivity necessitates an LNA with a substantial gain,

minimal noise figure, and low power consumption. Given the LNA discussed in [1], the implementation of the cascode topology for LNA design is detailed in [2]. This topology offers significant advantages, including a high gain, a low noise figure, a broader bandwidth, low power consumption, excellent reverse isolation, and stability. However, it is worth noting that the reported LNA is susceptible to parasitic inductance.

The widely recognized differential topology is discussed in [3–10]. The primary advantage of this configuration lies in its ability to reject common-mode noise and its reduced sensitivity to substrate and supply noise. This topology is also well suited for connection to a double-balanced mixer [3], which is typically the subsequent component in the receiver chain. Furthermore, this topology demonstrates the lowest noise figure among the reported designs [4], along with an impressive third-order input intercept point and a 1 dB compression point. It is worth noting, however, that the power consumption is slightly higher than in other reported topologies.

It is essential to emphasize that, since satellites rely on solar cells, achieving optimal performance with low power consumption is imperative to conserve battery life, particularly under very low supply voltages. Given this perspective and the aim of minimizing power usage, various techniques have been explored in the current state of the art. The current-reuse (CR) technique, as documented in [11,12], enables the sharing of the DC current among transistors, thereby reducing power consumption without compromising gain. However, it is important to note that this technique is the most advantageous for applications requiring higher voltage. Conversely, the complementary current-reuse technique, as described in [13], is well-suited for achieving low power while also catering to applications with lower voltage requirements. This approach involves the use of complementary transistors that distribute the current between the input and output stages.

Significantly, the adoption of this technique has implications for gain values. Additionally, the sub-threshold biasing technique, as documented in [14–16], has been employed to achieve exceedingly low power consumption (in the μW range). In this method, the MOS transistor operates in the weak inversion region, which necessitates the use of oversized transistors to enhance gain. Currently, wireless devices are being scaled down to achieve miniaturization, thanks to advancements in CMOS technology. Consequently, a low-voltage supply technique is discussed in References [17,18], primarily catering to applications that require less than 1V to operate. However, it is important to note that the use of this technique leads to reduced linearity. Furthermore, the forward body biasing (FBB) technique, detailed in [19,20], merits consideration. While this technique does contribute to a lower threshold voltage without compromising the gain, noise figure, and supply voltage, it is worth acknowledging that maintaining linearity remains a challenging task for researchers and LNA designers.

It is important to acknowledge that the primary source of nonlinearity in an MOS transistor resides in the transconductance available at the input stage. To attain superior linearity, various techniques for improving linearity, as discussed in [21], are also explored. One such approach is the utilization of an auxiliary path, commonly known as the feedforward technique, as described in [22]. This technique is employed to nullify the third-order harmonic at the primary output, which is crucial for achieving enhanced LNA performance. However, it comes at the cost of increased power dissipation and a reduction in gain. In [23], a low-impedance LC trap network is implemented to resonate the LNA in conjunction with the nonlinear signals at the input, effectively canceling them out. Notably, this technique is well-suited for MOSFET transistors when operating outside the strong inversion region.

In [24], an optimal biasing technique is applied at the input side to generate a current or voltage with the aim of mitigating the third-order nonlinearity component (gm_3). However, it is important to note that this approach is sensitive to variations in bias. However, the injection of a second-order inter-modulation (IM_2) technique, as introduced in [25], proves to be effective in suppressing third-order inter-modulation distortion (IM_3) without the need for an auxiliary path. This results in improved linearity without compromising noise, gain, and power consumption. Nonetheless, it may lead to a differential output from the

main path and a potential degradation of IIP_2.The multiple-gated transistor technique, detailed in [26–29], involves the use of two transistors operating in both the strong and weak inversion regions.

In this context, the negative peak of the second-order nonlinear term, which contributes to the IM_3 of the main transistor, is offset by the positive peak of the auxiliary transistor. However, this approach still encounters second-order distortion combined with harmonic feedback. An alternative method is the modified derivative superposition (DS) technique, as detailed in References [30–33], employing two transistors akin to those in [26] and two source inductors. This circuit allows for the direct tuning of third-order inter-modulation distortion from the input stage, albeit at the expense of reduced gain and noise performance. The IMD sinker technique, presented in [34], utilizes an NMOS diode connected in parallel to a resistor–capacitor (RC) circuit. Notably, this technique can partially mitigate IMD_3 at the input without impacting the gain and noise figure. Lastly, the dual capacitive cross-coupling (CCC) technique, as reported in [35], combines active and passive CCC to enhance loop gain and linearity. However, due to the larger passive CCC, there is a slight degradation in the input matching bandwidth.

Upon a thorough investigation of the recently reported state-of-the-art advancements, it becomes evident that designing an LNA to attain superior performance, including a high gain, low power consumption, a minimal noise figure, space efficiency, and cost-effectiveness, presents a set of formidable challenges for both researchers and LNA designers. This challenge arises from the fact that satellite transponders receive weak signals with inherent noise, caused by weather conditions and interference from Earth stations. Consequently, there is a pressing need to bolster these feeble signals with a combination of a high gain, exceptionally low noise, reduced nonlinearity, and low power consumption to prepare them for further processing. Such objectives are made achievable through the proposed LNA, which leverages a combination of techniques, including current reuse for gain improvement, body biasing for low power consumption, and capacitor cross-coupling for enhancing linearity in the C band, tailored specifically for satellite transponders.

Meeting the desired requirements in LNA design for RF frequencies is a highly challenging task, primarily due to the numerous non-ideal factors encountered. This challenge is compounded by the use of electromagnetic solvers, such as Cadence, ADS, and HFSS, which rely on intricate analytical and mathematical models [37]. An integral part of the design process involves repetitive trial-and-error experiments, demanding a significant investment of time, extensive memory resources, and specialized equipment. The complexity further intensifies when numerous simulations must be repeated for various circuit parameters to optimize the RF performance of the LNA. Therefore, there is a need for a more efficient technique that consumes fewer resources and possesses the capability to model LNAs comprehensively, approximating all design parameters. Artificial Neural Networks (ANNs) stand out as a modeling technique with the capacity to learn from data, approximate unseen data, and model nonlinear parameters [38]. In this work, we propose the optimization of LNA parameters for various CMOS LNAs, including a single-ended LNA, a differential LNA, and a current-reuse LNA, utilizing MLPANN. However, it is essential to note that only two output parameters, the gain and noise figure (NF), are considered in this study.

ANN is employed through both a direct and an inverse approach to model the interdependence of performance parameters and circuit parameters. In the direct approach, ANN is employed to model LNA output performance parameters with respect to input circuit parameters. Conversely, in the inverse approach, ANN is utilized to derive circuit parameters based on the output performance parameters. It is worth noting that the recent literature has explored the application of ANN in modeling LNAs.

In [39], an ANN model was introduced to address LNA impedance matching using the Smith chart. However, a complete ANN model for the entire LNA is still pending development. Another ANN model related to LNA was presented in [40], offering a comparison of accuracy and scalability among various metamodeling methods for the challenging task

of modeling an entire LNA RF circuit block. This study employed the Bayesian regularization (BR) algorithm. Nevertheless, there is room for improvement in the selection of orders for the rational function, and further theoretical investigation of SVM is required to understand the significant disparity with ANN. In [41], the modeling of CMOS LNA was achieved using the Adaptive Neuro-Fuzzy Inference System (ANFIS), demonstrating significantly lower errors than models developed using MLP and RBF. A different approach was described in [42], which outlined a method for RF LNA circuit synthesis determining parameter values through a set of ANNs aided by a Genetic Algorithm (GA). It is worth noting that GA required a relatively high number of generations. In [43], the modeling of an LNA was proposed using the Levenberg–Marquardt (LM) algorithm with a limited set of circuit parameters, such as frequency (f), drain-to-source voltage (Vds), drain-to-source current (Ids), and temperature (T). However, matching networks were not part of the model. Another approach was suggested in [44], focusing on solving highly nonlinear design problems for LNAs and Reflect Array Antennas (RAs) using ANN in conjunction with metaheuristic search algorithms. The results indicated successful minimization of the cost function, validated through 3D EM simulators for microwave circuits. In [45], an LNA was modeled using the LM algorithm, employing frequency (f), drain-to-source voltage (Vds), drain-to-source current (Ids), and temperature (T) as input parameters. Nevertheless, the modeling of matching networks was not included. From the review of the available literature, it is evident that both LM and BR algorithms have been applied for LNA modeling and synthesis. In [46], the proposal centered on surrogate modeling for a tunable LNA spanning a range from 2 to 3 GHz. Three- and six-dimensional surrogate models were constructed to illustrate the impact of bond wires on various LNA design metrics. Building upon these prior developments, this work endeavors to predict the different parameters of CMOS LNAs based on collected simulation data.

The objective of this work is to model a CMOS LNA using the Bayesian regularization algorithm, known for its robustness and resistance to overtraining and over-fitting. This work primarily focuses on the ANN modeling of a CMOS differential LNA using a direct approach. This paper presents the ANN modeling of a differential LNA using the BR algorithm, which incorporates techniques like current reuse (CR) for gain enhancement, capacitor cross-coupling (CCC) for improving linearity, and body biasing (BB) for low power consumption. The performance results of the proposed LNA, which combines all three techniques, surpass those of previously reported LNAs. Furthermore, the neural network modeling results closely align with the simulation results obtained from Cadence. The novelty of this work lies in the integration of various techniques to achieve optimized performance in multiple parameters, including gain, the noise figure (NF), power dissipation, and linearity, simultaneously with computer-aided modeling through ANN.

This paper is organized as follows: Section 2 discusses the CMOS differential LNA and its impact on LNA gain and linearity due to the proposed techniques. Section 3 covers the neural network model, Section 4 outlines the ANN modeling of the proposed LNA, Section 5 provides a brief overview of the results and discussion, and, finally, Section 6 concludes the paper.

2. CMOS Differential LNA

A schematic of the proposed CMOS differential LNA designed for C-band operation is illustrated in Figure 1. As evident in Figure 1, the proposed LNA comprises three stages: the input and output matching network, the interstage series resonance network, and buffers. The inductors (L_s and L_{g1}) in the common-source (CS) stage are meticulously designed to achieve input impedance matching and ensure low-noise performance within the C band. The aspect ratios of MOS transistors, namely, M_1 and M_2, are chosen to achieve appropriate input and output matching. To guarantee the correct operation of the transistors, a biasing circuit is devised to establish the proper DC operating point. This involves configuring the bias current and voltage levels to maintain the transistors within their active region while minimizing power consumption. In LNAs, noise analysis and

optimization are of paramount importance. To conduct a comprehensive noise analysis, techniques such as noise matching and impedance matching are employed to minimize the noise figure effectively.

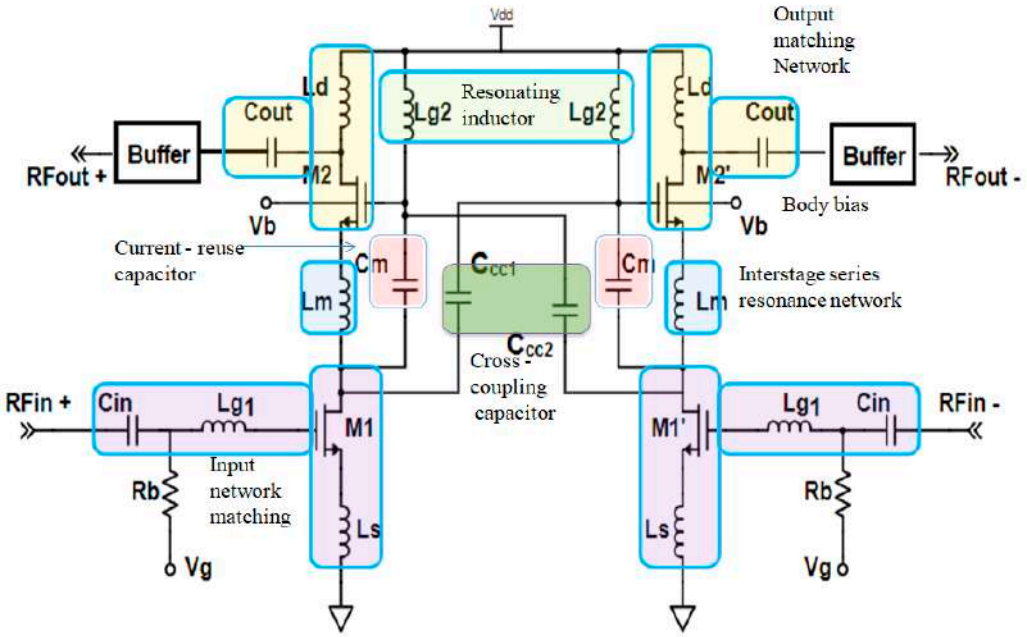

Figure 1. Schematic of proposed differential LNA.

The interstage series resonance inductor (L_m) serves to eliminate the impact of parasitic capacitance between the common-source (CS) transistor M_1 and the cascode transistor M_2, thereby enhancing power transfer efficiency. The current-reuse capacitor (C_m) plays a crucial role in augmenting the transconductance (g_{m2}) of the cascode device by enabling the sharing of the input current with the output device.

The cascode transistor operates in a common-gate (CG) configuration, specifically designed to mitigate the impact of parasitic gate–drain capacitance in the common-source (CS) stage. This configuration serves to increase the output impedance and enhance input/output isolation. The inclusion of a drain inductor (L_d) and an output capacitor (Cout) in the cascode stage is carefully engineered to achieve the desired output matching.

To strike a balance between bandwidth and gain, several aspects are addressed, including the transistor sizes, input/output matching networks, the addition of a buffer at the output side, and the incorporation of feedback components. These measures are meticulously executed to attain the desired gain and bandwidth characteristics while ensuring system stability.

To enhance linearity, cross-coupling capacitors C_{CC1} and C_{CC2} are incorporated. These capacitors resonate with the gate inductor (L_{g2}), effectively canceling out the nonlinearity associated with the common-source (CS) transistor (M_1).

To further optimize performance, body biasing is employed by connecting the supply voltage (V_b) to the bulk terminal of cascode transistor M_2. This adjustment reduces the threshold of M_2, preventing it from entering the weak inversion region and, consequently, reducing power consumption, especially at lower supply voltages.

The designed LNA underwent extensive simulations using EDA tools to validate its performance within the C band.

2.1. Small-Signal Equivalent of the Proposed Differential LNA

Figure 2 depicts the small-signal equivalent model of the proposed differential LNA. This model serves as the basis for the study of gain, linearity, and power optimization. Additionally, when viewed as a two-port network, it provides insight into the input and output impedance characteristics.

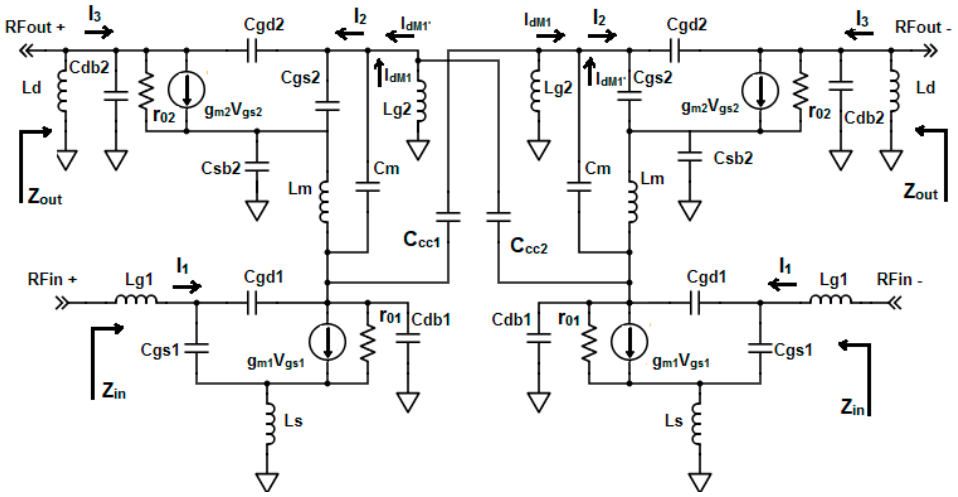

Figure 2. Small-signal equivalent circuit of proposed LNA.

2.1.1. Gain Improvement Using Current-Reuse Technique

Gain improvement is assessed by analyzing the overall current gain of the proposed LNA. This gain is determined using the small-signal equivalent circuit illustrated in Figure 3.

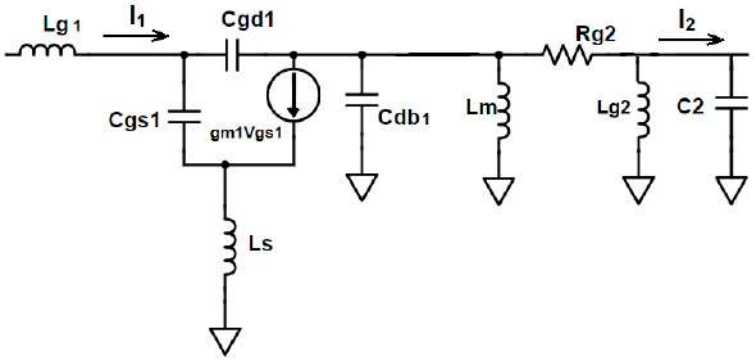

Figure 3. Small-signal equivalent of input CS stage.

The overall current gain (A_I) of the proposed differential LNA can be calculated from the current gain of M_1 (I_2/I_1) and M_2 (I_3/I_2):

$$A_I = \frac{I_2}{I_1} * \frac{I_3}{I_2} \tag{1}$$

The MOS transistors (M_1 and M_2) are operated in the saturation region with a large voltage headroom to achieve a high gain at the cost of power dissipation. Here, the current-reuse technique is used to boost the current gain of the proposed LNA with low power via the presence of 'C_m'.

In Figure 3, the current gain of CS transistor M_1 is given by

$$\frac{I_2}{I_1} = \frac{g_{m1}}{s(C_{gs1} + C_{gd1})} \frac{(((sL_m \,||\, \frac{1}{sC_{db1}}) + R_{g2}) \,||\, sL_{g2})}{(((sL_m \,||\, \frac{1}{sC_{db1}}) + R_{g2}) \,||\, sL_{g2}) + (\frac{1}{sC_2})} \tag{2}$$

where

L_m is the interstage matching inductor; L_{g2} is the gate inductor of M_2;

C_{db1} is the drain-to-bulk capacitance of M_1;

R_{g2} is the gate resistance of M_2;

$C_2 = C_m + C_{gs2} + C_{cc2}$.

This is the equivalent capacitance composed of interstage capacitance C_m, the gate-to-source capacitance of M_2, C_{gs2}, and cross-coupling capacitor C_{CC2} obtained from the small-signal equivalent circuit shown in Figures 2 and 4.

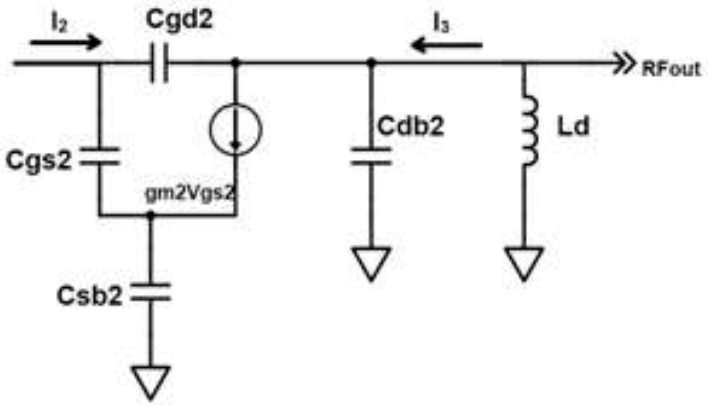

Figure 4. Small-signal equivalent of cascode stage.

In Figure 4, The current gain of cascode transistor M_2 is given by

$$\frac{I_3}{I_2} = \frac{2C_{cc2}}{C_{gs2} + C_{gd2} + C_{cc2}} g_{m2} \frac{sL_d}{(sL_d \,||\, \frac{1}{sC_{db2}})} \tag{3}$$

The current gain (A_I) of the differential cascode LNA with g_m boosting is achieved from the individual current gain of CS and cascode LNA.

On substituting Equation (2) and (3) in Equation (1), the current gain is

$$A_I = \frac{I_3}{I_1} = \left[\frac{g_{m1}}{s(C_{gs1} + C_{gd1})} \frac{(((sL_m \,||\, \frac{1}{sC_{db1}}) + R_{g2}) \,||\, sL_{g2})}{(((sL_m \,||\, \frac{1}{sC_{db1}}) + R_{g2}) \,||\, sL_{g2}) + (\frac{1}{sC_2})} \right] * \left[\frac{2C_{cc2}}{C_{gs2} + C_{gd2} + C_{cc2}} g_{m2} \frac{sL_d}{(sL_d \,||\, \frac{1}{sC_{db2}})} \right] \tag{4}$$

From the current gain expression of A_I in Equation (4), it is clear that the gain is boosted twice by the presence of the product of transconductances (g_{m1} andg_{m2}). Thus, the current gain is improved using the current-reuse capacitor (C_m) under the same DC current with low power.

2.1.2. LNA Linearity Improvement Using Capacitor Cross-Coupling Technique

The CCC technique [35] enhances the linearity of LNA while reducing the gate–drain capacitance of the input common-source (CS) transistor, M_1. To achieve a higher IIP3 (third-order input intercept point), it is imperative to minimize g_{m3}, the nonlinear coefficient of M_1.

In our proposed approach, to enhance IIP_3, we utilize cross-coupling capacitors, C_{CC1} and C_{CC2}, as illustrated in Figure 1, to mitigate the nonlinear effect of g_{m3}. The gate inductor, L_{g2}, which is connected to the gate of the cascode transistor, resonates with the cross-coupled capacitors, effectively eliminating the nonlinearity and noise contribution of the cascode stage.

The impact of CCC, which improves the linearity, can be studied using a variation inthe drain current I_d of the MOS device given by the Taylor series as

$$I_d = g_{m1} v_{gs} + g_{m2} {v_{gs}}^2 + g_{m3} {v_{gs}}^3 \tag{5}$$

where
g_{m1} is the main transconductance of the MOSFET;
g_{m2} is the second-order nonlinear coefficient;
g_{m3} is the third-order nonlinear coefficient.

The coefficients g_{m1}, g_{m2}, and g_{m3} are given by

$$g_{m1} = \frac{\partial i_d}{\partial v_{gs}};\ g_{m2} = \frac{\partial^2 i_d}{\partial v_{gs}^2};\ g_{m3} = \frac{\partial^3 i_d}{\partial v_{gs}^3} \tag{6}$$

From the above given Equation (6), it is evident that the MOS device exhibits nonlinear behavior.

The IIP_3 of the nonlinear device is given by

$$IIP_3 = \sqrt{\frac{4}{3}\left|\frac{g_{m1}}{g_{m3}}\right|} \tag{7}$$

From Equation (5), the drain currents flowing through M_1 and $M_{1'}$ are given by

$$I_{dM1} = g_{m1M1} v_{gsM1} + g_{m2M1} {v_{gsM}}^2 + g_{m3M1} {v_{gsM1}}^3 \tag{8}$$

$$I_{dM1'} = g_{m1M1'} v_{gsM2} + g_{m2M1'} {v_{gsM2}}^2 + g_{m3M1'} {v_{gsM2}}^3 \tag{9}$$

where V_{gsM2} is the gate-to-source voltage of M_2 given by

$$V_{gsM2} = a_1 v_{gsM1} + {a_2}^2 {v_{gsM1}}^2 + {a_3}^2 {v_{gsM1}}^3 \tag{10}$$

The resulting current, I_2,is given by

$$I_2 = I_{dM1} + I_{dM1'} \tag{11}$$

$$\approx (g_{m1M1} + a_1 g_{m1M1'}) v_{gsM1} + (g_{m2M1} + {a_1}^2 g_{m2M1'}) {v_{gsM1}}^2 + (g_{m3M1} + {a_1}^3 g_{m3M1'}) {v_{gsM1}}^3 \tag{12}$$

$$I_2 \approx g_{m1M1} + a_1 g_{m1M1'} \tag{13}$$

In Equation (12), it is important to note that $g_{m3}M_1$ and $g_{m3}M_{1'}$ are negative when operating in the strong inversion region for NMOS transistors. Coefficient a_1, representing the impedance when looking at the gate of M_2, is a frequency-dependent parameter and is inherently negative according to basic circuit theory [36]. The coefficient of the third term in Equation (12) is offset by adjusting the gate bias of M_2 and by resonating the gate inductor L_{g2} with the cross-coupling capacitors (C_{CC1} and C_{CC2}).

Consequently, the resulting current, as given in Equation (13), demonstrates that the nonlinearity components related to g_{m3} are effectively canceled at M_1, allowing the primary transconductance to be directed toward M_2.

2.1.3. Transconductance Improvement with Low-Power Body Biasing Technique

Typically, the body of an MOS transistor operates in the weak inversion region. Through the utilization of the forward body biasing technique, the MOS transistor's body is biased to transition into the strong inversion region. This transition effectively reduces the threshold voltage (VTH) of the device, subsequently leading to a decrease in power consumption. This reduction in the threshold voltage significantly enhances the transconductance (gm), as demonstrated in Equation (14). The following equations describe the variation in g_m with V_{TH}:

$$\frac{\partial g_m}{\partial V_{TH}}\ \frac{I_{d0}}{2(nU_T)^2}\left(e^{(V_{GS}-\frac{V_{TH}}{2nU_T})}\right) \tag{14}$$

where

$$V_{TH} = V_{TH0} + \gamma\left(\sqrt{|2\Phi_F - V_{BS}|} - \sqrt{|2\Phi_F|}\right) \tag{15}$$

V_{TH0} is the threshold voltage without the bulk-source voltage.V_{BS} = 0.

Γ is a process-dependent body effect parameter.
Φ_F is the substrate Fermi potential with typical values of $0.3-0.4V^{1/2}$.
n is the substrate factor, whose value depends on the process and varies from 1 to 2.
U_T is defined as kT/q, the thermal voltage.

As inferred from the above Equation (14), g_m varies exponentially with respect to V_{TH}. Biasing the body of the M_2 transistor reduces the threshold voltage and increases transconductance g_{m2}. With the increase in gm2, gain is also proportionally enhanced, as discussed in Equation (4), with a low power consumption.

2.2. Impedance Calculation at Input and Output

Using the small-signal equivalent circuit shown in Figure 2, the input impedance of the proposed differential LNA is given by

$$Z_{in} = s(L_{g1} + L_s) + \frac{1}{sC_{gs1}} + \omega_T L_s \tag{16}$$

where

$$\omega_T = \frac{g_{m1}}{C_{gs1}} \tag{17}$$

g_{m1} is the transconductance of M_1; C_{gs1} is the parasitic gate-to-source capacitance of gainM_1; and L_{g1} and L_s are the gate and source inductances.

Input matching is achieved by equating the real part of Equation (16) to source impedance (Rs = 50 Ω) and the imaginary part to zero to obtain the values of the source and gate inductors.

$$L_s = \frac{R_s C_{gs1}}{g_{m1}} \tag{18}$$

$$L_s + L_{g1} = \frac{1}{\omega_0^2 C_{gs1}} \tag{19}$$

$$C_{gs1} = \frac{1}{\omega_0^2 (L_{g1} + L_s)} \tag{20}$$

The output frequency (f_0) of the proposed LNA can be calculated using

$$f_0 = \frac{1}{\sqrt{C_{gs1}(L_{g1} + L_s)}} \tag{21}$$

The impedance seen at the output is given by

$$Z_{out} = sL_d || \frac{1}{sC_{db2}} \tag{22}$$

where
L_d is the drain inductor;
C_{db2} is the drain-to-bulk capacitance of M_2.

3. Development of ANN Model

Neural networks are information processing systems designed with inspiration from the cognitive capabilities of the human brain. These networks abstractly generalize and learn from data, drawing upon their capacity to interpret patterns. An ANN model is capable of estimating various amplifier parameters based on simulation results, offering an alternative approach to traditional simulation tools.

Neural Network Model for the Proposed CMOS Differential LNA

The proposed LNA is meticulously designed, incorporating current-reuse, body biasing, and capacitor coupling techniques to achieve optimized gain, a low power consumption, improved linearity, and reduced noise. The key performance parameters, including S-parameters and the noise figure (NF), exhibit proportional variations with temperature across different frequencies. Consequently, both temperature and frequency are considered as input variables. The output parameters, S_{21} and NF, serve as the output variables in the modeling of the proposed LNA, as depicted in Figure 5.

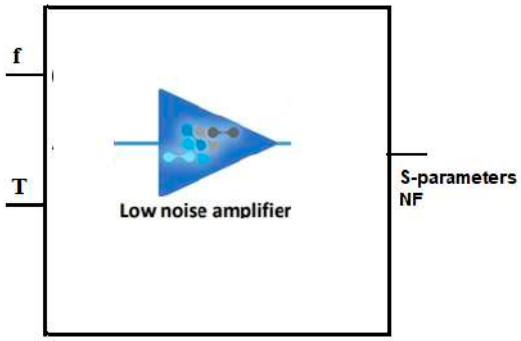

Figure 5. Parameters considered for neural network modeling of the proposed LNA.

A flowchart for the modeling of the LNA using ANN is illustrated in Figure 6. The proposed LNA is simulated through Cadence, and performance parameters are obtained for various combinations of temperature and frequency. For each set of circuit parameters, the S-parameters and noise figure (NF) are determined, and the corresponding input dataset is generated.In line with the Pareto principle, the developed dataset is partitioned, with 80% allocated for training and the remaining 20% for testing and validation purposes. The ANN is then trained using different numbers of hidden neurons across various neural networks and algorithms. The model's performance is subsequently validated based on the accuracy achieved through the best test statistics.

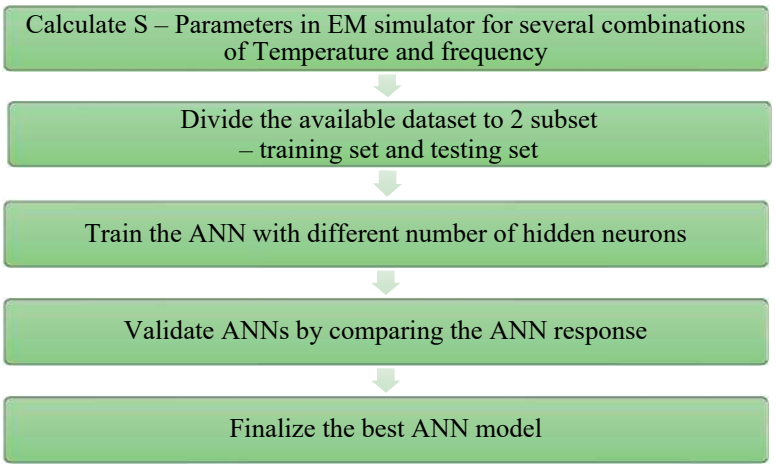

Figure 6. Flowchart of ANN modeling of the proposed LNA.

An MLPNN model is developed for the proposed LNA, as shown in Figure 7, for the S-parameters and noise figure (NF).

Each ANN is equipped with input neurons that correspond to specific circuit parameters, as well as an output neuron that corresponds to the parameter being modeled. Once the ANN is trained, the desired parameter can be readily calculated based on its response. The model's accuracy is validated by comparing the ANN's response with the simulation results.

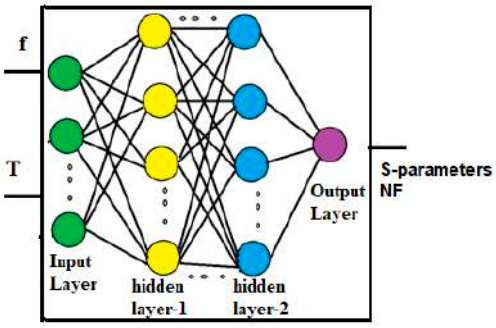

Figure 7. Neural network model developed for the proposed LNA.

Specialized versions of feedforward networks, such as PatternNet, FitNet, and Cascade ForwardNet, are available and suitable for various types of input-to-output mapping. Consequently, these networks are chosen to explore the different ANN types while examining the impact of varying the number of hidden layers (NHL) on output accuracy. These neural networks are trained using various algorithms, as listed in Table 1.

Table 1. Different neural network algorithms.

S. No	Algorithm	Abbreviation
1	scg	Scaled conjugate gradient back propagation
2	cgb	Conjugate gradient back propagation with Powell/Beale restarts
3	bfg	BFGS quasi-Newton back propagation
4	cgp	Conjugate gradient back propagation with Polak–Ribiére updates
5	gda	Gradient descent with adaptive learning rate back propagation
6	gd	Gradient descent back propagation
7	gdm	Gradient descent with momentum back propagation
8	gdx	Gradient descent with momentum and adaptive learning rate back propagation
9	lm	Levenberg–Marquardt back propagation
10	cgf	Conjugate gradient back propagation with Fletcher–Reeves updates
11	oss	One-step secant back propagation
12	rp	Resilient back propagation
13	Br	Bayesian regularization

Bayesian regularization is proposed for modeling this LNA. Typically, the dataset is partitioned into three subsets: training, testing, and validation. The training set error steadily decreases as the training progresses, while the validation set error initially reaches a minimum and then increases as the training continues. This phenomenon can lead to a less predictive model, and it is commonly referred to as overtraining. To overcome this issue, Bayes' theorem is incorporated into the regularization scheme.

The cost function or sum squared error in the data to be minimized is given as

$$S(w) = \beta \sum_{i=1}^{N_D} [Y_i - f(X_i)]^2 + \alpha \sum_{j=1}^{N_w} w_j^2 \quad (23)$$

where
N_d is the number of rows in the input vector X;
N_w is the number of weights;
X_i is the input vector;
Y_i is the output vector.

Given the initial values of hyperparameters α and β, the cost function S(w) is minimized with respect to weights w.

4. Results and Discussion

The proposed differential LNA was designed and simulated using 180 nm CMOS technology, operating at a frequency of 5 GHz, as depicted in Figure 8. The simulation

was carried out within the Cadence Spectre environment. Square spiral inductors and capacitors from the technology library available in Cadence Spectre were utilized. For signal lines, Metal 6 was employed to ensure high conductivity, while input and output lines were implemented using Metal 4 to achieve good impedance matching. Intermediate connections were established using Metal 1 and Metal 2. To enhance signal transmission, the gain path of the proposed LNA was widened to reduce resistance effectively. The component values for the proposed LNA are provided in Table 2. The physical footprint of the proposed LNA occupies a silicon area measuring 0.8×0.6 mm^2. A process corner analysis was conducted at various temperatures:Typical-Typical (TT, 27 °C), Fast-Fast (FF, 0 °C), and Slow-Slow (SS, 80 °C).

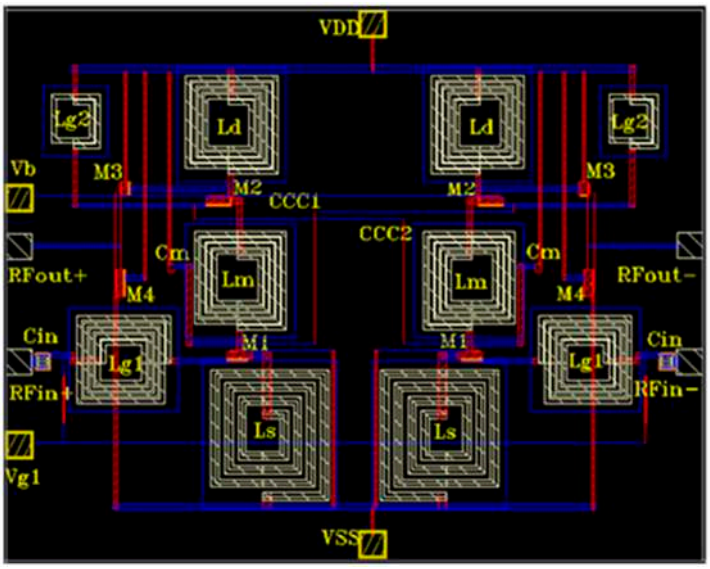

Figure 8. Layout of proposed differential LNA.

Table 2. Component values of the proposed LNA.

Component	M1	M2	Ls	Lg1	Lg2	Lm	Cin	Cm	Ccc1	Ccc2
Values	138 µm	216 µm	1.15 nH	2 nH	0.05 nH	2.29 nH	1.63 pF	0.2 pF	0.1 pF	0.1 pF

4.1. Effect of Body Biasing and Current-Reuse Technique on LNA Gain

Figure 9 illustrates the gain improvement (S21) as the bulk voltage (Vb) is varied from −0.3 V to 0.3 V. Notably, it is observed that the gain of the proposed LNA reaches 29.5 dB at the bulk voltage of Vb = −0.3 V. Furthermore, it can be inferred that the gain within the frequency range of 4.9 GHz to 5 GHz measures 29 dB, highlighting its exceptional performance in comparison to previously reported designs [6,8].

The current-reuse (CR) technique is applied using the middle capacitor, C_m. As C_m is varied from 100 fF to 500 fF, the gain demonstrates an improvement, increasing from 28.8 dB to 33.2 dB, as depicted in Figure 10. It is evident in the figure that the maximum gain is achieved when C_m equals 200 fF at the desired frequency of 5 GHz. Consequently, the gain is enhanced twofold through the combined use of the body biasing (BB) and CR techniques, in accordance with Equation (14).

4.2. Effect of Capacitor Cross-Coupling on LNA Linearity

The linearity of the LNA is assessed through the third-order input intercept point (IIP3). In receiver LNAs, it is expected that the IIP3 should exceed −10 dBm. The IIP3 of the proposed LNA is determined through simulation using a two-tone signal with a 100 MHz spacing. As depicted in Figure 11, the proposed LNA achieves an IIP3 of 0.2 dBm with

capacitor cross-coupling and −13.3 dBm without capacitor cross-coupling. Consequently, the utilization of the CCC technique results in a significant improvement of 13 dBm.

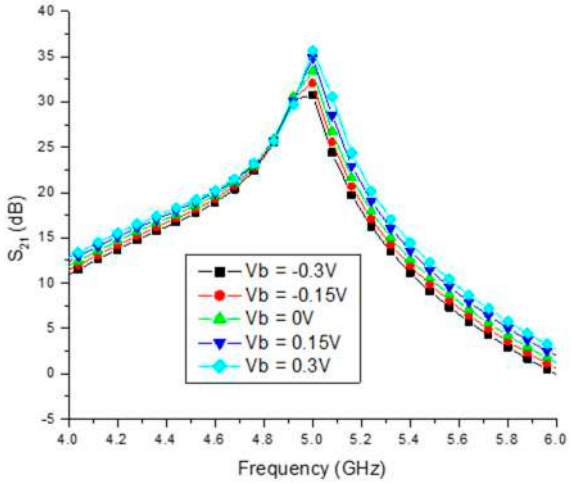

Figure 9. Body bias (V_b) vs. gain (S_{21}) of differential LNA.

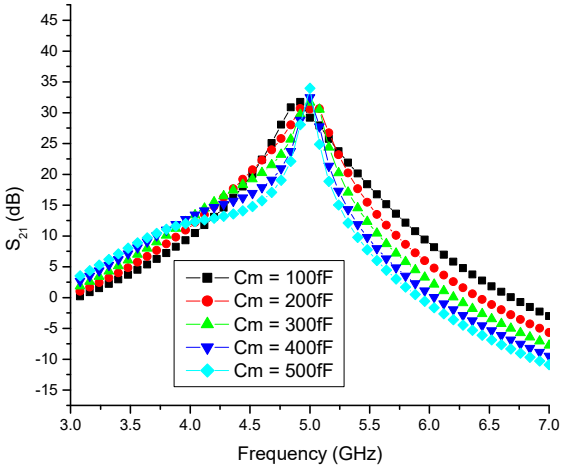

Figure 10. Current-reuse capacitor (C_m) vs. gain (S_{21})of differential LNA.

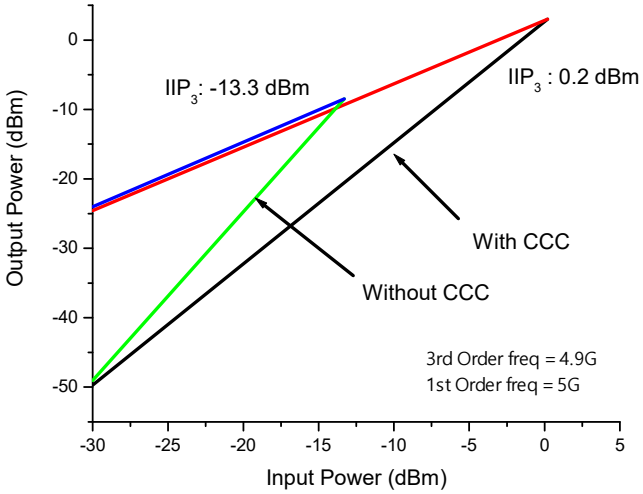

Figure 11. IIP3 of proposed LNA.

4.3. Simulation Results at Different Process Corners

Figure 12 presents the simulation results of the differential LNA under different process corners. Notably, it is observed that the proposed differential LNA delivers superior performance at the Fast corner (0 °C) when compared to the Typical (27 °C) and Slow corners (80 °C). The gain of the proposed LNA under different corners is illustrated in Figure 12a. It is evident that the gain exceeds 25 dB within the operational bandwidth (4.8–5.2 GHz) and reaches 30 dB at the desired frequency. Furthermore, it is noteworthy that the gain remains consistent between the Typical and Fast corners.

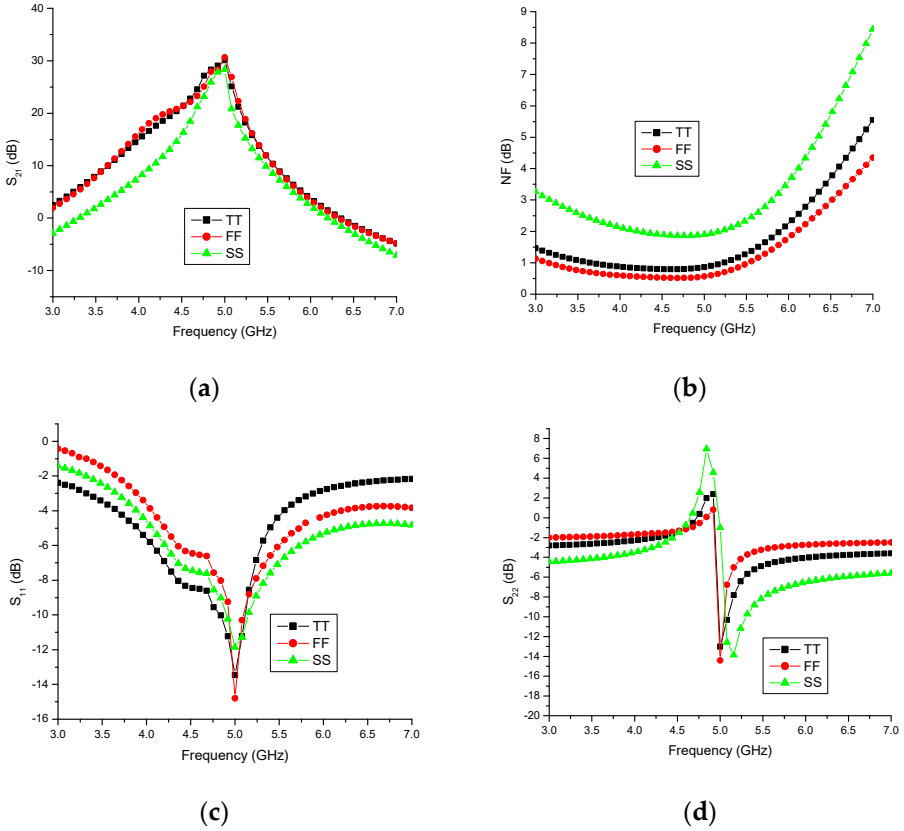

Figure 12. Simulation results at different process corners: (**a**) gain (S21), dB; (**b**) noise figure (NF), dB; (**c**) input return loss (S11), dB; and (**d**) output return loss (S22), dB.

The noise figure (NF) of the LNA must be below 3 dB within the desired frequency range. Figure 12b depicts the NF at various corners, revealing an NF of 1.2 dB at the Typical corner, 0.7 dB at the Fast corner, and 1.95 dB at the Slow corner for the desired frequency. These results signify that the noise performance is excellent at the Fast corner.

In terms of the input return loss (S_{11}), it is imperative that it remains below -10 dB at the required frequency of operation. Figure 12c shows that S_{11} measures -13.3 dB at the Typical corner, -14.5 dB at the Fast corner, and -12.1 dB at the Slow corner within the desired frequency range. This indicates that S11 is particularly strong at the Fast corner when compared to the SS and TT corners.

Similarly, the output return loss (S_{22}) should also be less than -10 dB at the required frequency of operation. As illustrated in Figure 12d, S_{22} is -13.1 dB at the Typical corner, -14.8 dB at the Fast corner, and -11.3 dB at the Slow corner within the desired frequency range. Additionally, the results suggest that the output return loss is nearly consistent between the Typical and Fast corners.

The performance parameters such as gain, NF, input and output return loss, and power dissipation at various process corners are analyzed and tabulated in Table 3.

Table 3. Performance of the proposed LNA in normal, best, and worst cases at 5 GHz.

Parameter	TT 27 °C	FF 0 °C	SS 80 °C
S_{11} (dB)	−13.3	−14.5	−12.1
S_{22} (dB)	−13.1	−14.8	−11.3
S_{21} (dB)	29.5	30.6	28.4
NF (dB)	1.2	0.7	1.9
P_{dc} (mW)	19.3	17.2	21.3

4.4. Performance Comparison of Proposed LNA with Existing State of Art

The performance of the proposed LNA is compared to that of several previously reported differential LNAs designed for wireless applications, and the results are summarized in Table 4. The proposed LNA achieves a gain of 29.5 dB, a noise figure of 1.2 dB, and an IIP3 of 0.2 dBm, all while operating at a reduced supply voltage of 0.9 V. These results outperform the reported works [6–8].

Table 4. Performance summary with existing state of the art LNAs.

State of the Art	Freq (GHz)	Tech (µm)	S_{21} (dB)	NF (dB)	V_{dd} (V)	P_{dc} (mW)	IIP_3 (dBm)	FoM	Remarks
[6]	5.8	0.18	18.66	2.03	1.8	7.58	-	6.07	Low gain, high NF
[7]	2.4	0.18	20.285	1	1.8	167.1	-	0.51	High power consumption
[8]	5.5	0.18	16.5	1.53	0.5	0.89	−17.2	0.67	Low gain, low IIP3
This work	5	0.18	29.5 *	1.2	0.9	19.3	0.2	24.26	High gain, low NF, and better linearity

* with buffer.

It is noteworthy that the proposed LNA exhibits a Figure of Merit (FoM) of 24.26, which is notably higher than in all the other reported works. The advantages brought by the proposed design techniques, such as the body-biased differential architecture combined with current reuse and capacitor cross-coupling, are evident, especially in achieving a highly linear and low-power solution.

The Figure of Merit (FoM) is calculated using Equation (24):

$$FoM = \frac{Gain(abs) * IIP_3(mW)}{(NF)(abs) * P_{dc}(mW)} \quad (24)$$

4.5. Performance Comparison with Different NN Models

This section can be divided into two parts. Figure 10 illustrates the impact of temperature on the S-parameters and noise figure (NF) for the frequency obtained from the Cadence simulations. ANN models were constructed for the CMOS differential LNA with 2 input neurons, 25 hidden neurons, and 2 output neurons. These models were trained using 750 datasets, employing 13 different neural network algorithms to identify high efficiency and performance rates. The performance rate varied across the different neural networks, and the best-performing neural network was subsequently analyzed.

Table 5 presents a performance comparison of the various neural networks developed for the proposed CMOS differential LNA. ANN training was carried out using different neural networks while keeping the number of hidden layers constant. It was observed that PatternNet, FitNet, and CascadeForwardNet consistently achieved accuracy levels exceeding 99% when utilizing 25 hidden neurons in the BR algorithm.

Table 6 displays the Mean Relative Error (MRE) and Root Mean Square Error (RMSE) for various algorithms implemented with PatternNet. Based on the results obtained, the PatternNet-BR algorithm exhibits a lower MRE, making it the preferred choice for our LNA modeling.

Table 5. Percentage accuracy obtained with different neural networks for the proposed LNA.

Algorithm	PatternNet	FitNet	Cascade ForwardNet
SCG	97.33	98	97.33
CGB	76	97	98
BFG	27	35	40
CGP	99.1	96	92.6
GDA	26.67	8.6	2
GDA	2	4	4
GDM	5.3	4	1.3
GDX	58.6	34	25.3
LM	3.3	4	5
CGF	82.6	86.67	93.33
OSS	29	77.3	86.67
RP	66.7	69.3	77.33
BR	99.34	98	99

Table 6. MRE and RMSE for different algorithms of PatternNet.

Algorithm	Accuracy(%)	MRE	RMSE
SCG	97.33	2.67	1.63
CGB	76	24	4.90
BFG	27	73	8.54
CGP	99.1	0.9	0.95
GDA	26.67	73.33	8.56
GDA	2	98	9.90
GDM	5.3	94.7	9.73
GDX	58.6	41.4	6.43
LM	3.3	96.7	9.83
CGF	82.6	17.4	4.17
OSS	29	71	8.43
RP	66.7	33.3	5.77
BR	99.34	0.66	0.81

Table 7 presents the accuracy achieved using the BR algorithm with different neural networks and various numbers of hidden layers, including 5, 10, 25, and 30 neurons. The results indicate that an accuracy of over 99% was consistently achieved with the neural networks with 25 to 30 neurons for the modeling of this LNA.

Table 7. Accuracy obtained for BR algorithm with different numbers of hidden neurons.

Hidden Neurons	S21	NF
5	83.57	86.30
10	90.23	92.71
20	97.14	96.42
25–30	99.97	99.79

4.6. Performance Comparison between Cadence Simulation and Developed ANN Results

To account for temperature variations ranging from 0 °C to 80 °C, the LNA parameters are compared between the results from the Cadence simulations and those from ANN.

Tables 8 and 9 provide sample training and testing data, along with the results obtained from the Cadence simulations and ANN modeling. These tables illustrate that the S-parameters and NF values for the proposed LNA are nearly identical to the results obtained through the ANN modeling. Each sample number corresponds to a specific frequency (in GHz) for a given temperature (in degrees).

Table 8. Sample training data and the results obtained from Cadence and ANN.

Sample No.	Cadence—S_{21} (Real Values)	ANN—S_{21} (Predicted Values)	MRE	RMSE	Cadence—NF (Real Values)	ANN—NF (Predicted Values)	MRE	RMSE
1	−18.1001	−17.9806	−0.1195	0.345688	3.71105	3.68656	0.02449	0.156493
2	−7.32325	−7.27491	−0.04834	0.219864	4.72765	4.69645	0.0312	0.176635
3	13.907	13.81521	0.09179	0.302969	0.85553	0.84988	0.00565	0.075166
4	31.16381	30.95813	0.20568	0.45352	0.92032	0.91425	0.00607	0.07791
5	10.4285	10.35967	0.06883	0.262355	2.97907	2.95941	0.01966	0.140214
6	8.28715	8.23246	0.05469	0.233859	4.23488	4.20693	0.02795	0.167183
7	−6.22354	−6.18246	−0.04108	0.202682	2.9065	2.88731	0.01919	0.138528
8	−7.25494	−7.20706	−0.04788	0.218815	2.0291	2.01571	0.01339	0.115715
9	4.95072	4.91804	0.03268	0.180776	2.96014	2.94061	0.01953	0.13975
10	34.69036	34.46141	0.22895	0.478487	0.63707	0.63287	0.0042	0.064807
11	8.71366	8.65615	0.05751	0.239812	2.17553	2.16117	0.01436	0.119833
12	0.79462	0.78938	0.00524	0.072388	6.59107	6.54757	0.0435	0.208567
13	−16.9761	−16.864	−0.1121	0.334813	7.08496	7.0382	0.04676	0.216241
14	2.83459	2.81588	0.01871	0.136785	1.40329	1.39403	0.00926	0.096229
15	5.60129	5.56432	0.03697	0.192276	1.1591	1.15145	0.00765	0.087464
16	31.96165	31.7507	0.21095	0.459293	2.06107	2.04747	0.0136	0.116619
17	16.14315	16.03661	0.10654	0.326405	1.73748	1.72601	0.01147	0.107098
18	−0.88958	−0.88371	−0.00587	0.076616	5.23356	5.19902	0.03454	0.185849
19	−16.8985	−16.787	−0.1115	0.333916	3.47562	3.45268	0.02294	0.15146
20	−6.08266	−6.04252	−0.04014	0.20035	4.49132	4.46167	0.02965	0.172192
21	15.62884	15.52568	0.10316	0.321185	0.81078	0.80543	0.00535	0.073144
22	33.539	33.31764	0.22136	0.470489	0.95501	0.9487	0.00631	0.079436
23	9.0474	8.98769	0.05971	0.244356	3.26576	3.24421	0.02155	0.146799
24	7.52286	7.47321	0.04965	0.222823	4.57863	4.54841	0.03022	0.173839
25	−5.25111	−5.21646	−0.03465	0.186145	2.68156	2.66386	0.0177	0.133041

Table 9. Sample testing data and the results obtained from Cadence and ANN.

Sample No.	Cadence—S_{21} (Real Values)	ANN—S_{21} (Predicted Values)	MRE	RMSE	Cadence—NF (Real Values)	ANN—NF (Predicted Values)	MRE	RMSE
1	−5.99297	−5.95342	−0.03955	0.198872	1.89999	1.88745	0.01254	0.111982
2	6.57258	6.5292	0.04338	0.208279	2.80927	2.79073	0.01854	0.136162
3	32.24145	32.02865	0.2128	0.461303	0.663	0.65862	0.00438	0.066182
4	7.35635	7.30779	0.04856	0.220363	2.45318	2.43699	0.01619	0.12724
5	−0.01017	−0.0101	0.0001	0.008367	7.07881	7.03209	0.04672	0.216148
6	−15.7674	−15.6634	−0.104	0.32249	6.74143	6.69693	0.0445	0.21095
7	4.01011	3.98364	0.02647	0.162696	1.306	1.29738	0.00862	0.092844
8	7.37583	7.32715	0.04868	0.220635	1.09624	1.089	0.00724	0.085088
9	32.12838	31.91633	0.21205	0.460489	2.05571	2.04214	0.01357	0.11649
10	14.9347	14.83613	0.09857	0.313959	1.99324	1.98008	0.01316	0.114717

Figure 13 presents a comparison between the Cadence simulations and the results generated through the ANN modeling for the CMOS differential LNA parameters. The observation indicates that the results for the proposed LNA are almost identical.

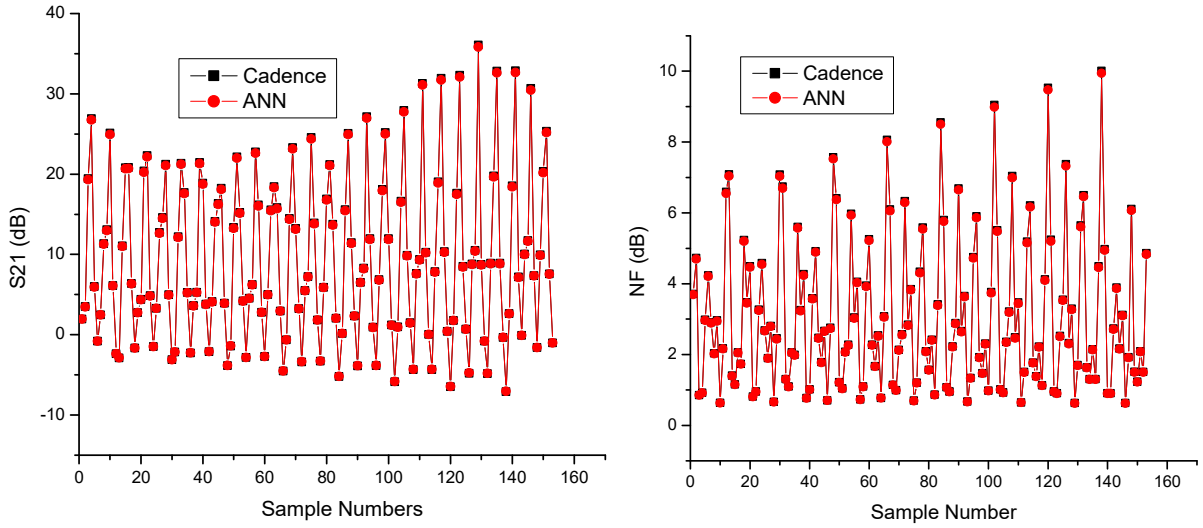

(**a**) (**b**)

Figure 13. CMOS differential LNA results obtained using Cadence and ANN: (**a**) S21, (**b**) NF.

5. Performance Comparison with the Existing State of Art

Table 10 provides a performance comparison with the existing state of the art. It is evident that the proposed LNAs are modeled using the MLPNN–BR algorithm, which proves to be more robust than the standard back-propagation method. This algorithm also demonstrates the ability to uncover potentially complex relationships, even when the data are limited; requires less formal statistical training; reduces or eliminates the need for extensive cross-validation; and prevents over-fitting. This comparison is made against the reported works [37,38,44–46].

Table 10. Performance comparison with the existing state of the art.

State of the Art	Algorithm Used	Frequency	Parameters Considered		Error
			Input	Output	
[37]	M-MLPNN	4 GHz–6 GHz	12	5	--
[38]	MLPNN	1 GHz–4 GHz	-	2	0.005
[44]	MLPNN -LM	100 MHz–8 GHz	4	10	--
[45]	MLPNN-LM	300 MHz–18 GHz	4	10	--
[46]	Surrogate modeling	2 GHz–3 GHz	2	7	0.001
Proposed work	MLPNN-BR	5 GHz	2	2	0.001

6. Conclusions

This paper introduces Artificial Neural Network (ANN) modeling of a proposed LNA, which is a CMOS differential LNA designed to enhance gain, linearity, and power efficiency. The adaptation of the capacitor cross-coupling technique involves the use of cross-coupling capacitors alongside the gate inductor of the cascode device to resonate the nonlinear component found in the CS stage while allowing the main transconductance to reach the output. Gain is increased through the implementation of the CR and BB techniques, all while maintaining a low power consumption. The proposed LNA achieves remarkable results with a 29.5 dB gain, a 1.2 dB NF, and an IIP3 of 0.2 dBm, all with a reduced supply voltage of 0.9 V.

It is evident that this LNA exhibits a high gain, a low NF, and excellent linearity at the desired frequency, even with a reduced supply voltage. The modeling of the proposed LNA using PatternNet BR reveals that the simulation results closely match those of the developed

ANN. When compared with the Cadence simulation method, the proposed technique can also provide precise circuit solutions. While simulation or measurement data may be used for modeling, the proposed method's advantages are more pronounced, especially in cases where equivalent circuits for simulation are unavailable or when measurements are costly.

Author Contributions: Conceptualization, B.S. and J.K.; methodology, V.T. and V.B.; software, B.S.; validation, V.B. and U.M.P.; formal analysis, B.S.; investigation, B.S.; writing—original draft preparation, B.S., V.T. and V.B.; writing—review and editing, U.M.P. and J.K.; visualization, V.T.; supervision, J.K. All authors have read and agreed to the published version of the manuscript.

Funding: This research received no external funding.

Data Availability Statement: All data are included within manuscript.

Acknowledgments: The authors would like to thank The Management, The Principal and Head of the Department of ECE, Mangayarkarasi College of Engineering who gives their full support for our work.

Conflicts of Interest: The authors declare no conflict of interest.

References

1. Kim, T.-S.; Kim, B.-S. Post-Linearization of Cascode CMOS Low Noise Amplifier Using Folded PMOS IMD Sinker. *IEEE Microw. Wirel. Compon. Lett.* **2006**, *16*, 182–184.
2. Lee, T.H. *The Design of CMOS Radio Frequency Integrated Circuits*; Cambridge University Press: Cambridge, UK, 2000.
3. Woo, S.; Kim, W.; Lee, C.H.; Kim, H.; Laskar, J. A Wideband Low-Power CMOS LNA With Positive–Negative Feedback forNoise, Gain, and Linearity Optimization. *IEEE Trans. Microw. Theory Tech.* **2012**, *60*, 3169–3178. [CrossRef]
4. Alam, S.K.; DeGroat, J. A 2 GHz variable gain low noise amplifier in 0.18-µm CMOS. *Analog Integr. Circ. Sig. Process.* **2008**, *56*, 37–42. [CrossRef]
5. Fan, X.; Zhang, H.; Sánchez-Sinencio, E. A Noise Reduction and Linearity Improvement Technique for a Differential Cascode LNA. *IEEE J. Solid-State Circuits* **2008**, *43*, 588–599. [CrossRef]
6. Cen, M.; Song, S. A Differential Cascode Low Noise Amplifier Based on a Positive Feedback Gain Enhancement Technique. *J. Mach. Mach. Commun.* **2015**, *1*, 229–244. [CrossRef]
7. Kalamani, C. Design of Differential LNA and Double Balanced Mixer using 180nm CMOS Technology. *Microprocess. Microsyst.* **2019**, *71*, 102850. [CrossRef]
8. Wang, W.; Wang, C. Capacitor Cross-Coupled Fully differential CMOS Folded Cascode LNAs with Ultra Low Power Consumption. *Wirel. Pers. Commun.* **2014**, *78*, 45–55. [CrossRef]
9. Muhamad, M.; Soin, N.; Ramiah, H.; Noh, N.M.; Chong, W.K. Design of CMOS differential LNA at 2.4 GHz. In Proceedings of the 2013 IEEE International Conference of Electron Devices and Solid-State Circuits, Hong Kong, China, 3–5 June 2013.
10. Kumar, M.G.L.; Regulagadda, S.S.; Das, J.K.; Dutta, A. Design of Current Reuse based Differential Merged LNA-Mixer (DMLNAM) and Two-stage Dual Band LNA with two Gain modes in 65 nm technology. In Proceedings of the 2015 IEEE Asia Pacific Conference on Postgraduate Research in Microelectronics and Electronics, Hyderabad, India, 27–29 November 2015; pp. 98–103.
11. Kargaran, E.; Mafinejad, Y.; Mafinezhad, K.; Nabovati, H. A new gm boosting current reuse folded cascode LNA. *IEICE Electron. Express* **2013**, *10*, 20130264. [CrossRef]
12. Shankar, S.U.; Dhas, M.D.K. Design and Performance Measure of 5.4 GHZ CMOS Low Noise Amplifier using Current ReuseTechnique in 0.18µmTechnology. *Procedia Comput. Sci.* **2015**, *47*, 135–143. [CrossRef]
13. Dai, R.; Zheng, Y.; He, J.; Liu, G.; Kong, W.; Zou, S. A 0.5-V novel complementary current-reused CMOSLNAfor 2.4 GHz medical application. *J. Microelectron.* **2016**, *55*, 64–69. [CrossRef]
14. Chang, C.-H.; Onabajo, M. Analysis and Demonstration of an IIP3 Improvement Technique for Low-Power RF Low-Noise Amplifiers. *IEEE Trans. Circuits Syst. I Regul. Pap.* **2018**, *65*, 859–869. [CrossRef]
15. Liu, H.J.; Zhang, Z.F. An Ultra-Low Power CMOS LNA for WPAN Applications. *IEEE Microw. Wirel. Compon. Lett.* **2017**, *27*, 174–176. [CrossRef]
16. Fiorelli, R.; Silveira, F.; Peralias, E. MOST moderate weak inversion region as the optimum design zone for CMOS 2.4-GHz CS-LNAs. *IEEE Trans. Microw. Theory Tech.* **2014**, *62*, 556–566. [CrossRef]
17. Li, C.-H.; Liu, Y.-L.; Kuo, C.-N. A 0.6-V 0.33-mW 5.5-GHz receiver front-end using resonator coupling technique. *IEEE Trans. Microw. Theory Tech.* **2011**, *59*, 1629–1638. [CrossRef]
18. Lai, M.-T.; Tsao, H.-W. Ultra-Low Power Cascaded CMOS LNA With Positive Feedback and Bias Optimization. *IEEE Trans. Microw. Theory Tech.* **2013**, *61*, 1934–1945. [CrossRef]
19. Singh, V.; Arya, S.K.; Kumar, M. A 0.7V, Ultra-Wideband Common Gate LNA with Feedback BodyBias Topology for Wireless Applications. *J. Low Power Electron. Appl.* **2018**, *8*, 42. [CrossRef]

20. Wang, T.-P. Minimized Device Junction Leakage Current at Forward-Bias Body and Applications for Low-Voltage Quadruple-Stacked Common-Gate Amplifier. *IEEE Trans. Electron Devices* **2014**, *61*, 1231–1236. [CrossRef]
21. Zhang, H.; Sánchez-Sinencio, E. Linearization Techniques for CMOS Low Noise Amplifiers: A Tutorial. *IEEE Trans. Circuits Syst. I Regul. Pap.* **2011**, *58*, 22–36. [CrossRef]
22. Kargaran, E.; Mafinejad, Y.; Mafinezhad, K.; Nabovati, H. Highly Linear Folded Cascode LNA. *IEICE Electron. Express* **2013**, *10*, 20130557. [CrossRef]
23. Aparin, V.; Larson, L.E. Linearization of monolithic LNAs using low-frequency low-impedance input termination. In Proceedings of the 29th European Solid-State Circuits Conference, Estoril, Portugal, 16–18 September 2003; pp. 137–140.
24. Aparin, V.; Brown, G.; Larson, L.E. Linearization of CMOS LNAs via optimum gate biasing. In Proceedings of the 2004 IEEE International Symposium on Circuits and Systems, Vancouver, BC, Canada, 23–26 May 2004; pp. 748–751.
25. Lou, S.; Luong, H.C. AlinearizationtechniqueforRFreceiverfront-endusingsecond-orderintermodulationinjection. *IEEE J. Solid-State Circuits* **2008**, *43*, 2404–2412. [CrossRef]
26. Jin, T.H.; Kim, T.W. A 5.5-mW +9.4-dBm IIP3 1.8dB NF CMOS LNA Employing Multiple Gated Transistors with Capacitance Desensitization. *IEEE Trans. Microw. Theory Tech.* **2010**, *58*, 2529–2537. [CrossRef]
27. Kim, Y.M.; Han, H.; Kim, T.W. A 0.6-V +4dBm IIP3 LC folded cascode CMOS LNA with gm linearization. *IEEE Trans. Circuits Syst. II Express Briefs* **2013**, *60*, 122–126.
28. Salim, Z.Z.M.; Muhamad, M.; Hussin, H.; Ahmad, N. CMOS LNA Linearization Employing Multiple Gated Transistors. In Proceedings of the 2019 IEEE International Conference on Telecommunication Systems, Services, and Applications (TSSA), Bali, Indonesia, 3–4 October 2019.
29. Ma, L.; Wang, Z.-G.; Xu, J.; Amin, N.M. A High Linearity Wideband Common-Gate LNA with Differential Active Inductor. *IEEE Trans. Circuits Syst. II Express Briefs* **2017**, *64*, 402–406. [CrossRef]
30. Kumaravel, S.; Kukde, A.; Venkataramani, B.; Raja, R. A high linearity and high gain Folded Cascode LNA for narrow band receiver applications. *Microelectron. J.* **2016**, *54*, 101–108. [CrossRef]
31. Tarighat, A.P.; Yargholi, M. A CMOS low noise amplifier with employing noise cancellation and modified derivative superposition technique. *Microelectron. J.* **2016**, *54*, 116–125. [CrossRef]
32. Raja, R.; Venkataramani, B.; Kishore, K.H. A 1-V 2.4 GHz Low-Power CMOS LNA Using Gain-Boosting and Derivative Superposition Techniques for WSN. *Wirel. Pers. Commun.* **2017**, *96*, 383–402. [CrossRef]
33. Rafati, M.; Qasemi, S.R.; Amiri, P. A 0.65V, linearized cascade UWB LNA by application of modified derivative superpositiontechnique in 130nm CMOS technology. *Analog Integr. Circuits Signal Process.* **2019**, *99*, 693–706. [CrossRef]
34. Chang, C.-P.; Chien, W.-C.; Su, C.-C.; Wang, Y.-H.; Chen, J.-H. Linearity improvement of cascode CMOS LNA using a diode connected NMOS transistor with a parallel RC circuit. *Prog. Electromagn. Res. C* **2010**, *17*, 29–38. [CrossRef]
35. Guo, B.; Chen, J.; Jin, H. A linearized common-gate low-noise amplifier using active cross-coupled feedback technique. *Analog Integr. Circuits Signal Process.* **2016**, *89*, 239–248. [CrossRef]
36. Wu, Y.; Kim, H.; Jonsson, F.; Ismail, M.; Olsson, H. Nonlinearity Analysis of a Short Channel CMOS Circuit for RFIC Applications. In *VLSI: Systems on a Chip*; IFIP International Federation for Information Processing; Silveira, L.M., Devadas, S., Reis, R., Eds.; Springer: Boston, MA, USA, 1999; Volume 34, pp. 61–68.
37. Sorkhabi, S.E.; Mosavi, M.R.; Rafei, M. Low Noise amplifier synthesis using multidimensional MLP neural network. *IETE J. Res.* **2018**, *64*, 374–386. [CrossRef]
38. Kumar, S.; Kumari, S. Design of low power, high gain LNA for WCDMA range and parameters extraction using Artificial Neural Network (ANN). In Proceedings of the 2015 IEEE Power, Communication and Information Technology Conference (PCITC), Bhubaneswar, India, 15–17 October 2015. [CrossRef]
39. Güneş, F.; Çağlar, M.F. A Novel Neural Smith Chart for use in Microwave circuitry. *Int. J. RF Microw. Comput. Eng.* **2008**, *19*, 218–229. [CrossRef]
40. Gorissen, D.; De Tommasi, L.; Crombecq, K.; Dhaene, T. Sequential modeling of a low noise amplifier with neural networks and active learning. *Neural Comput. Appl.* **2009**, *18*, 485–494. [CrossRef]
41. Karimi, G.; Sedaghat, S.B.; Banitalebi, R. Designing and modeling of ultra-low voltage and ultra-low power LNA using ANN and ANFIS for Bluetooth applications. *Neurocomputing* **2013**, *120*, 504–508. [CrossRef]
42. Dumesnil, E.; Nabki, F.; Boukadoum, M. RF-LNA circuit synthesis using an array of artificial neural networks with Constrained Inputs. In Proceedings of the 2015 IEEE International Symposiumon Circuits and Systems (ISCAS), Lisbon, Portugal, 24–27 May 2015; pp. 573–576. [CrossRef]
43. Singh, S.; Chopra, P.K. Artificial Neural Network approach for LNA design of GPS receiver. *Opt. Mem. Neural Netw.* **2016**, *25*, 236–242. [CrossRef]
44. Güneş, F.; Demirel, S.; Nesil, S. Design optimization of LNAs and reflect array antennas using the full-wave simulation-based artificial intelligence models with the novel metaheuristic algorithms. In *Simulation-Driven Modeling and Optimization*; Springer Proceedings in Mathematics & Statistics; Koziel, S., Leifsson, L., Yang, X.S., Eds.; Springer: Cham, Switzerland, 2016; Volume 153. [CrossRef]

45. Payala, A.; Anand, R. Modelling of navigation based LNA parameters using neural network technique. *Opt. Mem. Neural Netw.* **2017**, *26*, 192–198. [CrossRef]
46. Xhafa, X.; Yelten, M.B. Design of a tunable LNA and its variability analysis through surrogate modeling. *Int. J. Numer. Model. Electron. Netw. Devices Fields* **2020**, *33*, e2724. [CrossRef]

Hindawi
International Journal of RF and Microwave Computer-Aided Engineering
Volume 2023, Article ID 4034241, 10 pages
https://doi.org/10.1155/2023/4034241

Research Article

Design and Development of Parasitic Elements Loaded Quadband Frequency and Pattern Reconfigurable Antenna

K. Karthika [1] **and K. Kavitha** [2]

[1]*Department of Electronics and Communication Engineering, Kumaraguru College of Technology, Coimbatore, India*
[2]*Department of Electronics and Communication Engineering, Velammal College of Engineering and Technology, Madurai, India*

Correspondence should be addressed to K. Karthika; karthika.svk@gmail.com

Received 23 March 2023; Revised 2 May 2023; Accepted 9 May 2023; Published 23 May 2023

Academic Editor: Xiao Ding

Modern communication demands a low-profile, versatile antenna. In this paper, a low-profile antenna of size $38 \times 40 \times 0.787$ mm^3 is proposed to reconfigure frequency and radiation pattern. The Rogers RT Duroid 5870 of dielectric constant 2.33 is used as a substrate. Frequency reconfiguration is achieved by connecting patches of different lengths corresponding to the resonant frequencies through three PIN diode switches. Switching on/off these three diodes results in frequency switching between four distinct frequency bands. The Yagi-Uda principle is utilized to alter the radiation pattern. Simple parasitic elements are loaded on either side of the radiating structure. Changing the electrical lengths of the parasitic elements using PIN diode switches facilitates pattern reconfiguration by making them behave as a reflector/director. The presented structure resonates at four distinct frequencies (5.3 GHz/3.82 GHz/2.77 GHz/2.2 GHz) with a maximum of three beam tilt angles for each resonating frequency. SMP1345-079LF PIN diode is used for switching operation. Biasing circuit has been designed to ensure RF and DC isolation. The proposed antenna offers acceptable radiation performance in all the switching states. The average measured gains are 2.43 dBi, 2.42 dBi, 3.5 dBi, and 3.29 dBi at 5.3 GHz, 3.82 GHz, 2.77 GHz, and 2.2 GHz, respectively. On an average, the proposed antenna exhibits the simulated efficiency of 81%. The proposed antenna is suitable for 5G communication as its bandwidth covers band 1, band 7, band 46, and band 77 of the 5G new radio (NR) standard. Fabrication and testing are done to validate the results.

1. Introduction

The integration of several applications into one device is necessary for contemporary wireless communication systems. To accomplish this, the system can either employ a single antenna with many functionalities or incorporate multiple antennas inside the device. The use of several antennas in a single system to support multiple applications is not a viable solution. Multiple antennas in a single system require more area to deploy, interfere with one another, have more installation costs, and have more complicated hardware platforms. Reconfigurable antennas are one of the potential methods for addressing the above-stated requirements [1]. The need for reconfigurable antennas is further driven by the demand for wireless communication systems that require antennas to adapt to changing operational conditions. Reconfigurable antennas can provide frequency agility, beam steering, polarization control, multimode operation, and miniaturization, making them a critical component of modern wireless communication systems. Reconfiguration can be achieved through electrical switches/mechanical switches/optical switches/reconfigurable materials/structural alterations [2]. The majority of research on reconfigurable antennas concentrated on a single reconfiguration like either frequency or pattern or polarization.

Reconfigurable antennas can be designed to operate over a range of frequencies, allowing them to adapt to changing frequency bands in wireless communication systems. This can be particularly important in situations where frequency allocation is limited or when sharing of frequency bands is required. Spectrum can be effectively used with frequency reconfigurable antennas. A compact antenna that can switch frequencies

among thirty-six different states with a stable radiation pattern is presented in [3]. Six-pin diodes are loaded along the non-radiating edges of the patch. By connecting the ground plane and non-radiating edges of the patch with PIN diodes, the operating frequency can be altered. In [4], two PIN diodes are positioned in the feed line to switch between the wideband and triband modes of operation. [5] suggests an E-shaped antenna design reconfigure between six operating frequencies. The transmission line model theory is applied to compute the antenna's effective length. Two PIN diodes are employed to achieve frequency reconfiguration. Conformal antennas may be a preferable option for many practical applications. The conformal antenna's relevance in modern applications is enhanced by including reconfigurability. A flexible CPW-fed frequency agile antenna has been proposed in [6]. Switching on/off the PIN diode located in its structure changes its resonant length and offers reconfiguration between five distinct frequencies.

Pattern reconfiguration allows the antenna to direct the radiation pattern towards a specific location or direction. This can be particularly important in situations where there are multiple signal sources or when the antenna needs to track a moving target. By changing the radiation pattern, the antenna can avoid or reduce the interference caused by unwanted signal sources. Antennas loaded with parasitic elements follow the Yagi-Uda principle to realize pattern reconfiguration [7–10]. Four folded monopoles are positioned along the $+X$, $-X$, $+Y$, and $-Y$ directions, respectively. Then, the monopoles are connected to the main radiator positioned in the center via PIN diode switches. When any of the folded monopoles is connected to the main antenna, it behaves as a director, and the remaining three behave as a reflector. Using this way, the radiation pattern is deflected in four different directions [8]. Stubs loaded on the ground plane performs as a reflector or director to alter the radiation pattern par with the switching state [9]. In [11], pattern reconfiguration is accomplished by placing the switchable parasitic strip between the reflector and the monopole antenna. Pattern reconfiguration can also be accomplished through single to multiple excitations in an antenna design [12]. The radiation pattern can be continuously steered in different directions by mechanically rotating a semicircular metasurface disk over the circular patch antenna [13].

Incorporating hybrid reconfiguration capability in a single radiating structure satisfies the need for a contemporary communication system. Pattern and frequency reconfigurable antennas have a wide range of applications in wireless communication systems, radar systems, military and defense, medical imaging, and IoT applications. These antennas can provide better signal quality, coverage, and imaging resolution and adapt to changing operational conditions. In recent years, notable works have contributed towards compound reconfiguration like a combination of frequency, polarization, and pattern reconfiguration. Incorporation of pattern agility in frequency reconfigurable antennas improves the performance of wireless systems by reducing source noise, enhancing security, and conserving energy by directing the signal in the intended direction [14]. In 5G networks, there is a growing demand for pattern and frequency reconfigurable antennas (PFRA). These antennas can provide directional radiation patterns that can be dynamically adjusted to suit the changing requirements of the network. Further, it can be designed to operate on multiple frequency bands, allowing them to switch between different frequency bands to avoid interference. Overall, designing a compact, highly efficient PFRA can offer a significant advantage in 5G networks by providing the flexibility, adaptability, and efficiency required to support the diverse range of applications and services that will be enabled by this technology. Several frequencies and pattern reconfigurable antennas are discussed in the literature. Most reconfigurable antennas use a rectangular patch as their basic structure. The impact of biasing lines in resonating frequency is inhibited by positioning them away from the antenna [15]. Four PIN diodes positioned along the two horizontal slits of a rectangular patch perform frequency reconfiguration and pattern reconfiguration [16].

The work presented in [17] utilizes four metallic strips of different lengths and four PIN diodes to perform pattern and frequency reconfiguration. Wideband operation in such antennas can be achieved by utilizing a symmetrical structure [18]. In [19], a modified rectangular patch with a single PIN diode is reported to perform frequency reconfiguration. Here, the stubs loaded on either side of the ground plane change the ground current and steer the beam direction based on the switching states. Parasitic patches and twelve PIN diodes are utilized to reconfigure the pattern and frequency presented in [20]. To perform pattern reconfiguration, a planar Yagi-Uda antenna on a coplanar structure is proposed in [21]. Two parasitic strips along with switches are loaded on the back side of the designed coplanar structure. Depending on the switching states, these parasitic strips either function as a reflector or a director. However, the majority of the reported compound reconfigurable antennas have relatively large sizes and utilize a greater number of actuators, complex biasing circuitry design, and limited operating bands.

Sub-6 GHz frequencies, which are typically in the frequency range between 600 MHz and 6 GHz, are used in 5G applications to provide large area coverage and high data rates. Band 1 (2.11-2.17 GHz), band 7 (2.62-2.69 GHz), band 46 (5.15-5.925 GHz), and band 77 (3.3-4.2 GHz) are some of the most widely used 5G new radio (NR) frequency bands. The proposed work is inspired and motivated by research challenges in the 5G network. This work focuses on the creation of a compact compound-reconfigurable antenna operating in the above-listed bands of 5G application. The following are the major contributions of this proposed work.

(i) Design of a low-profile novel structure to reconfigure frequency and radiation pattern

(ii) Design of biasing circuit to ensure RF and DC isolation

(iii) Implementation of frequency reconfiguration by connecting patches of different lengths through PIN diode switches

(iv) Pattern modification using the Yagi-Uda principle is available in the literature. In most of the works,

the pattern is changed by loading inverted L-shaped parasitic strips or dumbbell-shaped parasitic strips to the other side of the radiating element. In this work, simple parasitic strips are positioned along the radiating elements, and fewer diodes are utilized to realize pattern reconfiguration without altering the resonant frequency

The design evolution of the proposed antenna is presented in Section 2 of this research article. The findings of the simulation, measurement, and the proposed work's comparison with the existing state-of-the-art in literature are discussed in Section 3. The proposed work is concluded in Section 4.

2. Antenna Design

The proposed compound reconfigurable antenna printed on a substrate Rogers RT Duroid of dielectric constant 2.33 and thickness of 0.787 mm is depicted in Figure 1. The overall size of the presented microstrip-fed structure is $38 \times 40 \times 0.787\ \text{mm}^3$. The effective resonant lengths (L_{f_r}) of the radiating elements are calculated using (1) and (2) [22].

$$L_{f_r} = \frac{c}{4f_r\sqrt{\varepsilon_{\text{eff}}}}, \tag{1}$$

$$\varepsilon_{\text{eff}} = \frac{\varepsilon_r + 1}{2} + \frac{\varepsilon_r - 1}{2}\left(1 + 12\left(\frac{w}{h}\right)\right)^{-0.5}, \tag{2}$$

where ε_{eff} denotes an effective dielectric constant, f_r represents resonating frequency, c indicates free space velocity, ε_r denotes the dielectric constant, and w and h indicate the width and thickness of the trace and the substrate, respectively.

For frequency reconfiguration, three radiating patches of different resonant lengths are designed and linked to the main radiator (P_1) through three PIN diode switches (D1, D2, and D3). Pattern reconfiguration is accomplished based on the Yagi-Uda principle. Parasitic elements are loaded on either side of the radiating elements. PIN diodes D4 and D5 are loaded along the respective parasitic elements to perform pattern reconfiguration. The proposed compound reconfigurable antenna's design evolution is shown in Figure 2.

2.1. Frequency Reconfiguration. The first step in the proposed structure's evolution is the design of the main radiator. The main radiator resonating at 5.2 GHz is achieved by modifying its effective resonant length through structural alteration. The calculated effective resonant length of the main radiating element (P_1) is optimized to 5.6 mm. Further, the partial ground plane's length (Lg) is varied and analyzed through parametric analysis as depicted in Figure 3. At Lg = 8.2 mm, good impedance matching is observed for 5.2 GHz. The effective resonant length to have resonance at 3.8 GHz is calculated and optimized to 10.4 mm by connecting a patch (P_2) of length 3.1 mm to the main radiator (P_1) via PIN diode switch D1 (ON) (step 2 of Figure 2).

To provide proper biasing of the PIN diode, two RF choke inductors (to block the RF signal and pass the DC signal) and a DC block capacitor (to prevent the DC signal

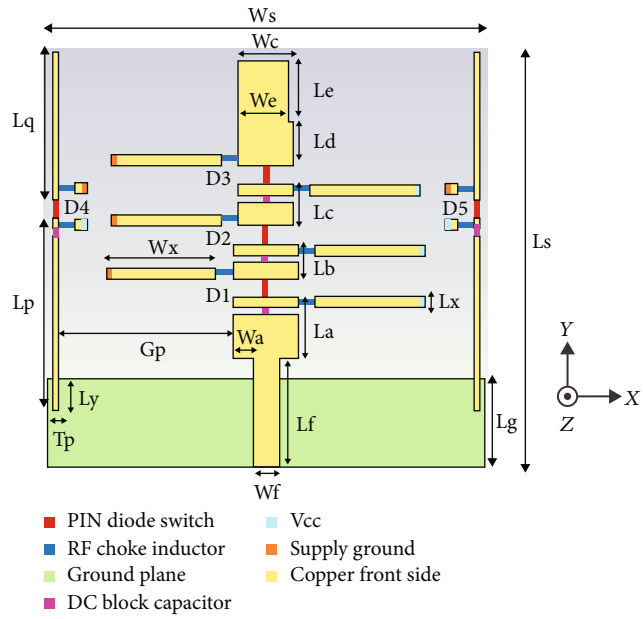

FIGURE 1: Proposed compound reconfigurable antenna - geometry (parameters: Ls = 38 mm, Ws = 40 mm, Lg = 8.2 mm, Lf = 10 mm, Wf = 2.356 mm, La = 5.6 mm, Lb = 3.1 mm, Lc = 3.85 mm, Ld = 4 mm, Le = 5.5 mm, Wa = 2 mm, Wc = 5 mm, We = 4.5 mm, Lp = 16.6 mm, Lq = 13.5 mm, Tp = 0.5 mm, Lx = 1 mm, Wx = 10 mm, Gp = 16 mm, Ly = 2 mm, h = 0.787 mm).

from interfering with the RF signal) are utilized. A slit has been made in the main radiator, and the capacitor is positioned along the slit rather than being given a separate space. To connect the RF choke inductors to the power supply, DC biasing lines/DC biasing patches have been designed and placed close to the radiating element as shown in step 3 of Figure 2. The dimensions of the DC biasing patch are chosen such that the performance of the antenna is not disrupted. Moreover, Figure 4 projects that the inclusion of biasing circuit for D1 does not have a significant impact on the proposed antenna's performance.

Switching on/off the diode D1 switches its operating frequency between 5.2 GHz and 3.8 GHz. In step 4, a patch (P_3) of a length of 3.85 mm is connected to the P_2 through D2. Switching on the diodes D1 and D2 increases the effective resonant length to 15.95 mm resulting in resonance at 2.9 GHz. To further achieve resonance at 2.1 GHz, a patch (P_4) of length 9.5 mm is connected to P_3 via D3 (on) (step 6 of Figure 2). However, the design offers dual resonance at 2.47 and 5.69 GHz. Hence, the shape of P_4 is modified to achieve the desired single resonance. Modified P_4 structure (step 7 of Figure 2) offers return loss below -10 dB at 2.17 GHz. The required biasing for D2 and D3 has been included, as specified in step 3, and it is shown in steps 5 and 8 of Figure 2.

2.2. Pattern Reconfiguration. The final step in the proposed design is aimed at pattern reconfiguration. Parasitic elements can be used for pattern reconfiguration by adjusting the length, distance, and orientation of the parasitic element relative to the main antenna element. This will change the phase and amplitude of the signal at different points in the

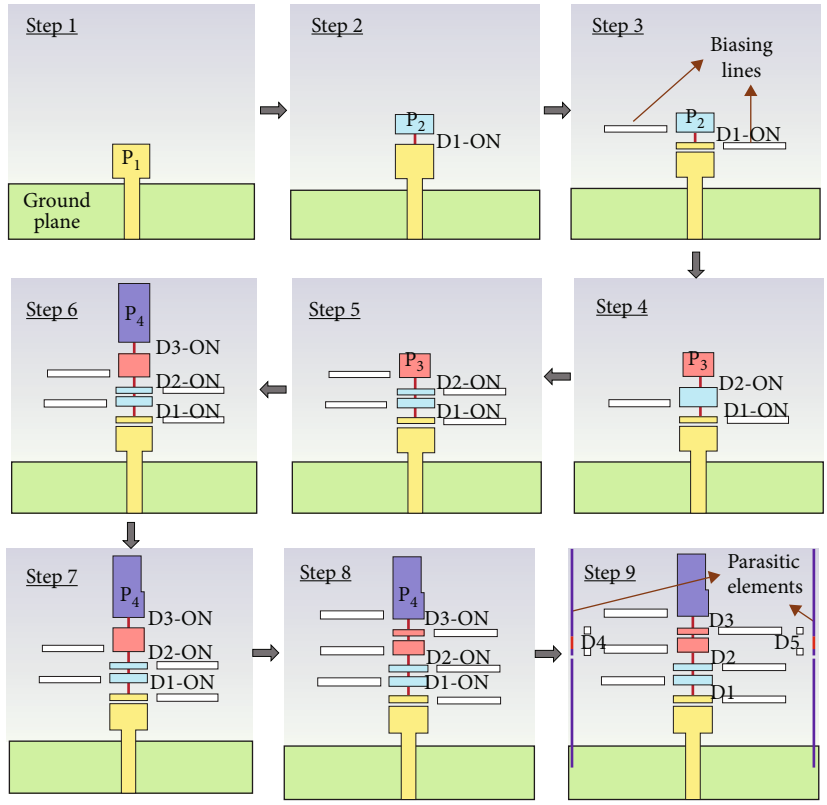

FIGURE 2: Proposed structure—design evolution.

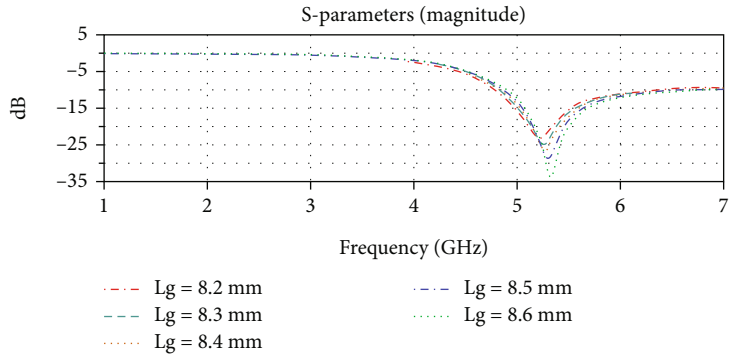

FIGURE 3: Parametric analysis—length of the ground plane (Lg).

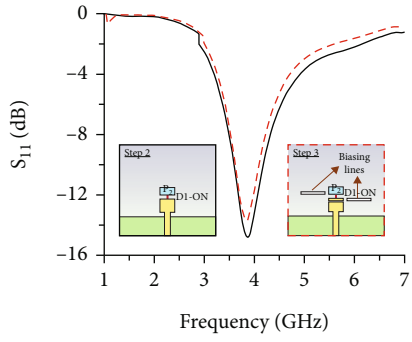

FIGURE 4: Design evolution—return loss plot: step 2 (without biasing circuit) and step 3 (with the biasing circuit).

antenna, which will in turn change the radiation pattern. Two parallel parasitic elements of width 0.5 mm and length 31.8 mm are loaded to the sides of the designed antenna. These elements act as a reflector/director, and two PIN diode switches (D4 and D5) are positioned along the length of the two parasitic elements to facilitate pattern reconfiguration. Henceforth, the proposed structure can reconfigure frequency and pattern as well.

The radiation property is significantly impacted by the coupling length (Ly) between the parasitic element and the ground plane. The coupling length and the distance between the main radiator and parasitic elements (Gp) are obtained by performing a parametric sweep. Figures 5 and 6 present the parametric analysis of Ly and Gp, respectively. The

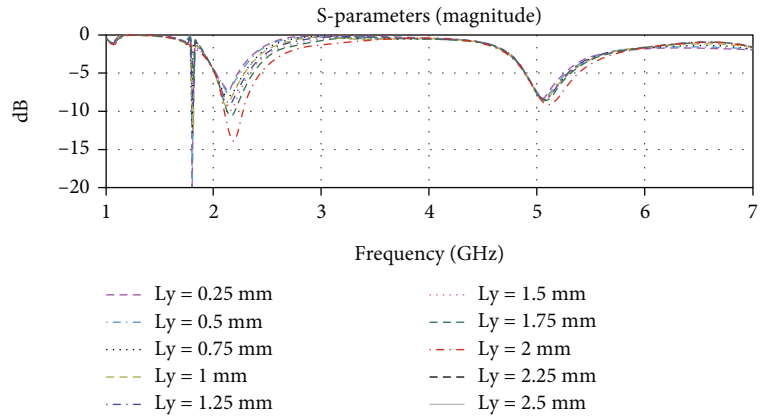

Figure 5: Parametric analysis of Ly.

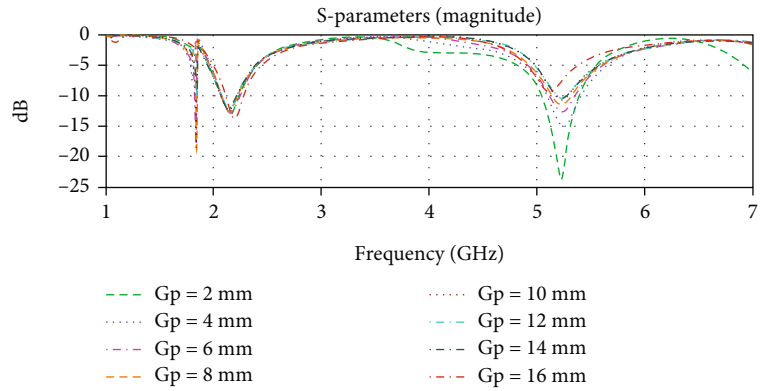

Figure 6: Parametric analysis—effect of varying the distance between the radiator and parasitic elements (Gp).

designed antenna is analyzed for Ly = 0.25 mm to 2.5 mm and Gp = 2 mm to 16 mm in case I-S4. The simulation reveals that the additional resonance is observed at 1.8 GHz in the simulated range excluding the value of Ly = 2 mm. At Ly = 2 mm, the additional resonance is nullified, and the resonance is observed at the intended resonating frequency of 2.17 GHz. At Gp = 16 mm, only the intended resonance is observed. Hence, the coupling length and the space between the radiating and parasitic elements are finalized as 2 mm and 16 mm, respectively.

To perform the switching operation, the SMP1345-079 LF PIN diode is used. It offers high-speed switching and is suitable for switch applications from 10 MHz to 6 GHz. The on state equivalent circuit of this diode is achieved by connecting $R = 1.5\,\Omega$ in series with $L = 0.7$ nH. The off state equivalent circuit of this diode is achieved by connecting the parallel combination of $R = 1000\,\Omega$ and $C = 0.18$ pF in series with $L = 0.7$ nH. Since the design involves PIN diodes for switching operation, a biasing circuit has been designed for proper excitation of the switches. The space for placement of PIN diode switches, capacitors, and inductors is decided as per data sheets.

3. Results and Discussion

The proposed antenna is analyzed for three cases. In case I, both D4 and D5 are in the OFF state. D4 is off and D5 is on for case II. D4 is on, and D5 is off in case III. Each of the cases is analyzed for four switching states: switching state 1 (S1)—(D1-off, D2-off, and D3-off), switching state 2 (S2)—(D1-on, D2-off, and D3-off), switching state 3 (S3)—(D1-on, D2-on, and D3-off), and switching state 4 (S4)—(D1-on, D2-on, and D3-on). Frequency and pattern reconfigurability are observed through the comparative analysis of case II and case III concerning case I.

3.1. Case I: Frequency Reconfigurability Mode. In case I, the switching state 1 exhibits resonance at 5.2 GHz (4.71-5.84 GHz). Switching on D1 (case I-S2) connects P_1 and P_2 . This lengthens the current distribution and shifts the resonating frequency to 3.8 GHz (3.44-4.17 GHz). Case I-S3 mode increases the length further by turning ON D2. In this mode, the proposed antenna resonates at 2.9 GHz (2.61-3.13 GHz). In case I-S4 mode, resonance is observed at 2.17 GHz (2.08-2.27 GHz).

3.2. Cases II and III: Frequency and Pattern Reconfigurability Mode. Frequency and pattern reconfigurability are seen in cases II and III. The switching states S1, S2, S3, and S4 are analyzed for the abovementioned cases. The observed resonant frequencies for case II and case III's S1 are like the case I-S1 (5.2 GHz). In case I-S1, the main beam direction in the x-z plane is along -97^0. Now, in case II-S1, switching off D4 makes the left parasitic element ($-x$ direction) behave as a

director, and switching on D5 makes the right parasitic element (+x direction) behave as a reflector. As a result, the main lobe direction is changed to -164^0 (−x direction). Whereas in case III-S1, switching on and off the D4 and D5 makes the left parasitic element (−x direction) function as a reflector and the right parasitic element (+x direction) as a director, respectively. This shifts the main lobe direction to +164^0 (+x direction). Hence, the radiation pattern of the designed antenna is reconfigurable.

Similarly, frequency and pattern reconfiguration are observed for all the remaining switching states of case II and case III. In case II, the main lobe direction in the x-z plane (phi = 0^0) is -90^0 at 3.8 GHz, -100^0 at 2.9 GHz, and 2.17 GHz. Whereas +90^0, +100^0, and +100^0 are observed for case III at 3.8 GHz, 2.9 GHz, and 2.17 GHz, respectively. This implies that the switching state of D4 and D5 switches the radiation pattern without altering the resonating frequencies of the radiating structure.

The proposed antenna is fabricated, and its measurement setup is depicted in Figure 7. The front and back views of the fabricated antenna are shown in Figures 7(a) and 7(b). The vector network analyzer (VNA) measurement setup for return loss measurement is seen in Figure 7(c). It is noted that the biasing lines are connected to the power supply for switching on/off the PIN diodes. Gain and pattern measurements are done using anechoic chamber measurement as depicted in Figure 7(d).

The measured results of all three cases are summarized in Figure 8 and are discussed as follows. Figure 9(a) presents an S_{11} comparison of the simulated and measured results for case I, whereas Figure 9(b) projects an S_{11} comparison of the simulated and measured results for case II and case III. Depending on the states of D1-D3, the design reconfigures to 5.3 GHz, 3.82 GHz, 2.77 GHz, and 2.2 GHz. When comparing the measured results with the simulation findings, slight variations in the resonant frequencies are observed due to the presence of biasing wires in the measurement setup. In case I, the bandwidths obtained at 5.3 GHz, 3.82 GHz, 2.77 GHz, and 2.2 GHz are 1225 MHz (5-6.225 GHz), 300 MHz (3.67–3.97 GHz), 900 MHz (2.625–3.525 GHz), and 335 MHz (2.09–2.425 GHz), respectively. In both case II and case III, 850 MHz (5-5.85 GHz), 425 MHz (3.675–4.1 GHz), 545 MHz (2.625–3.17 GHz), and 321 MHz (2.09–2.411 GHz) are the bandwidths obtained at 5.3 GHz, 3.82 GHz, 2.77 GHz, and 2.2 GHz, respectively. Figure 9(c) projects the average gain and efficiency of the proposed antenna. The average measured gain of 2.43 dBi, 2.42 dBi, 3.5 dBi, and 3.29 dBi is observed at 5.3 GHz, 3.82 GHz, 2.77 GHz, and 2.2 GHz, respectively. On average, a radiation efficiency of around 81% is obtained for the simulated antenna design. Further, the functionality of the proposed design is analyzed w.r.t their radiation pattern and surface current distribution.

xIn Figure 10, the simulated radiation pattern (black dotted line) in the x-z plane (phi = 0^0) is compared with the measured radiation pattern (red solid line). The red solid arrow mark in all the switching cases indicates the main lobe's direction. The patterns in Figure 10 are used to identify the directionality and the direction of the main lobe under different switching conditions. Changing the states of D4 and D5 reconfigures the radiation pattern from bidirectional to unidirectional at 5.3 GHz and omnidirectional to unidirectional at 3.82 GHz, 2.77 GHz, and 2.2 GHz. In case I-S1, the direction of the main lobe is -97^0. It is tilted to -165^0 and +165^0 in case II-S1 and case III-S1, respectively. Henceforth, at 5.3 GHz, the beam steering angles are –68^0 and +262^0. In case I-S2, the main lobe direction is +115^0. This direction is changed to -93^0 and +93^0 in case II-S2 and case III-S2, respectively. The observed beam steering angles at 3.82 GHz are +152^0 and –22^0.

The main lobe oriented towards +180^0 in case I-S3 has been shifted to -105^0 in case II-S3 and +105^0 in case III of S3. Hence, the beam steering angles of ±75^0 are obtained at 2.77 GHz. The same has been observed for switching state 4, and the corresponding beam steering angles at 2.2 GHz are ±75^0. In frequency and pattern reconfiguration, reconfiguring the frequency should not affect the radiation pattern and vice versa. It is observed that the beam steering angles at 2.77 GHz and 2.2 GHz remain the same. However, it differs at 5.3 GHz and 3.82 GHz. The presence of bias lines will have an impact on the antenna's radiation pattern. This will occur due to the coupling between bias lines and the radiating elements. To minimize this impact, the placement and orientation of bias lines are done carefully within the antenna structure. However, distortion in the pattern reduced realized gain, and shift in the resonant frequencies is seen in the measured results. Creating vias in the required biasing positions will make the bias lines move to the other side of the radiating elements. This technique can be used in future work to lessen the effects of bias lines.

Figure 11 illustrates the surface current distribution. According to the switching condition, a high surface current distribution is seen at the radiating structures. It is observed that the high current distribution in the main radiator and the feed line for all three cases in switching state 1 offers resonance at 5.2 GHz. In addition to that, during all the three cases, a high current density noted in the P_2 (during switching state 2),P_3 (during switching state 3), and P_4 (during switching state 4) contributed to resonance at 3.8 GHz, 2.9 GHz, and 2.17 GHz, respectively. Further, for all the switching states in case I, the current density is minimal in the parasitic elements.

The surface current on the reflector may be relatively low compared to other elements in the antenna. This is because the reflector's primary function is to reflect and redirect energy from the radiating element, rather than directly radiating energy itself. The director in the antenna is used to focus the energy on a particular direction. Hence, the surface current on the directors is typically higher than the surface current on the reflector or driven element. In case II, the high surface current is noted along the left parasitic element, and the low surface current is observed along the right parasitic element for all the switching states. Hence, the left parasitic element acts as a director and the right parasitic element acts as a reflector in all the switching states of case II, whereas the vice versa is observed for all the switching states in case III.

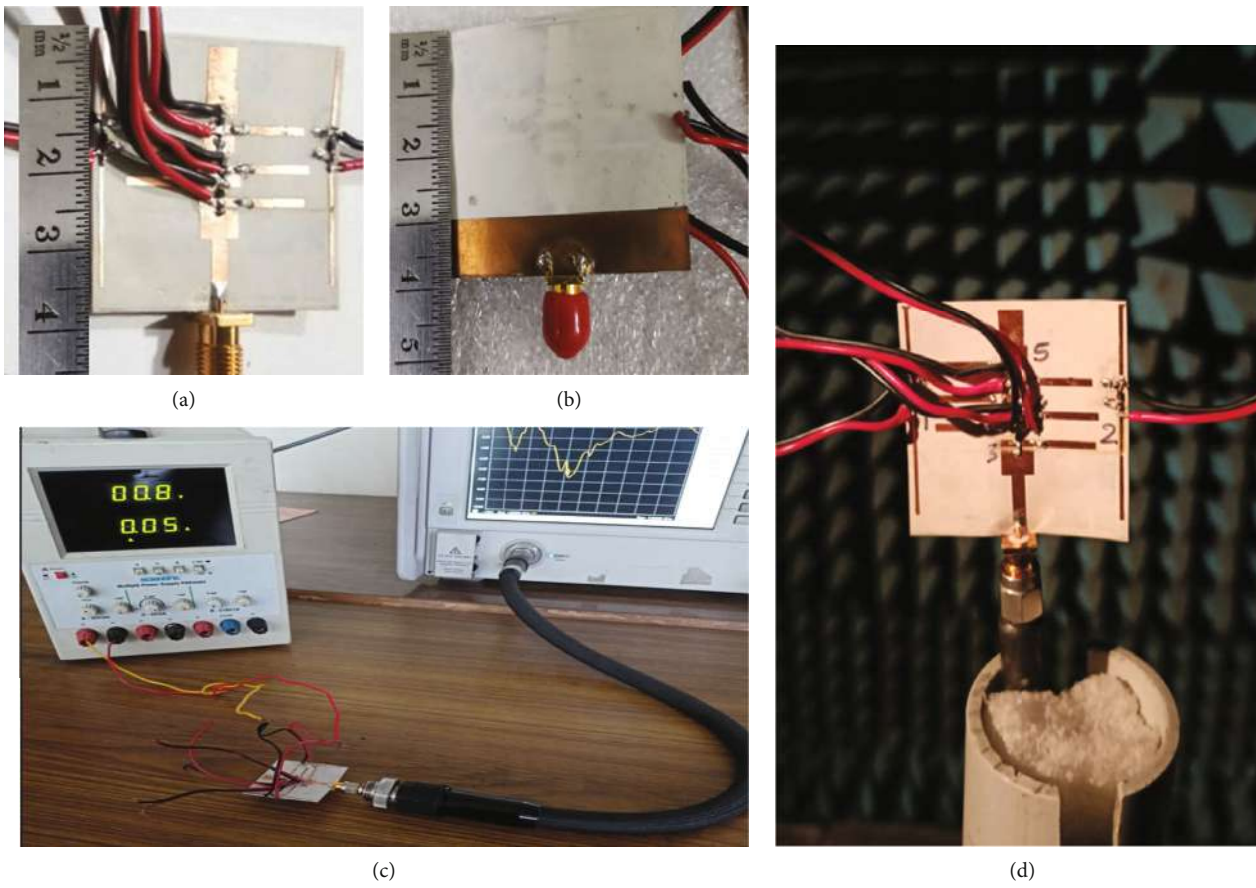

FIGURE 7: Measurement setup of fabricated antenna. (a) Top view, (b) rear view, (c) VNA testing, and (d) anechoic chamber measurement.

	Switching condition					Frequency (GHz)	S_{11} (dB)	Gain (dBi)	Bandwidth (MHz)	Main Lobe Direction (phi = 0^0)	Beam Steering Angle
	D1	D2	D3	D4	D5						
Case I - S1	OFF	OFF	OFF	OFF	OFF	5.3	−15.56	2.24	1225	-97^0	0^0
Case I - S2	ON	OFF	OFF	OFF	OFF	3.82	−12.18	2.38	300	$+115^0$	0^0
Case I - S3	ON	ON	OFF	OFF	OFF	2.77	−19.38	3.72	900	$+180^0$	0^0
Case I - S4	ON	ON	ON	OFF	OFF	2.2	−12.11	3.19	335	$+180^0$	0^0
Case II - S1	OFF	OFF	OFF	OFF	ON	5.3	−15.8	2.58	850	-165^0	-68^0
Case III - S1	OFF	OFF	OFF	ON	OFF		−15.8	2.48	850	$+165^0$	$+262^0$
Case II - S2	ON	OFF	OFF	OFF	ON	3.82	−13.22	2.45	425	-93^0	$+152^0$
Case III - S2	ON	OFF	OFF	ON	OFF		−13.21	2.42	425	$+93^0$	-22^0
Case II - S3	ON	ON	OFF	OFF	ON	2.77	−19.09	3.35	545	-105^0	$+75^0$
Case III - S3	ON	ON	OFF	ON	OFF		−19.07	3.33	545	$+105^0$	-75^0
Case II - S4	ON	ON	ON	OFF	ON	2.2	−12.09	3.34	321	-105^0	$+75^0$
Case III - S4	ON	ON	ON	ON	OFF		−12.12	3.35	321	$+105^0$	-75^0

Switching conditions responsible for only frequency reconfiguration
Switching conditions responsible for only pattern reconfiguration

FIGURE 8: Measured results of proposed compound reconfigurable antenna.

The performance comparison summarized in Table 1 reveals that the presented work offers a low-profile, compact structure on comparing with [1, 16, 18, 20, 23, 24, 26–28]. The presented work requires fewer switches than [25, 28]. Using five switches, the suggested work operates at more operating bands than [1, 29]. This work has reduced design complexity by eliminating the separate layer for the biasing circuit as in [19, 20, 22].

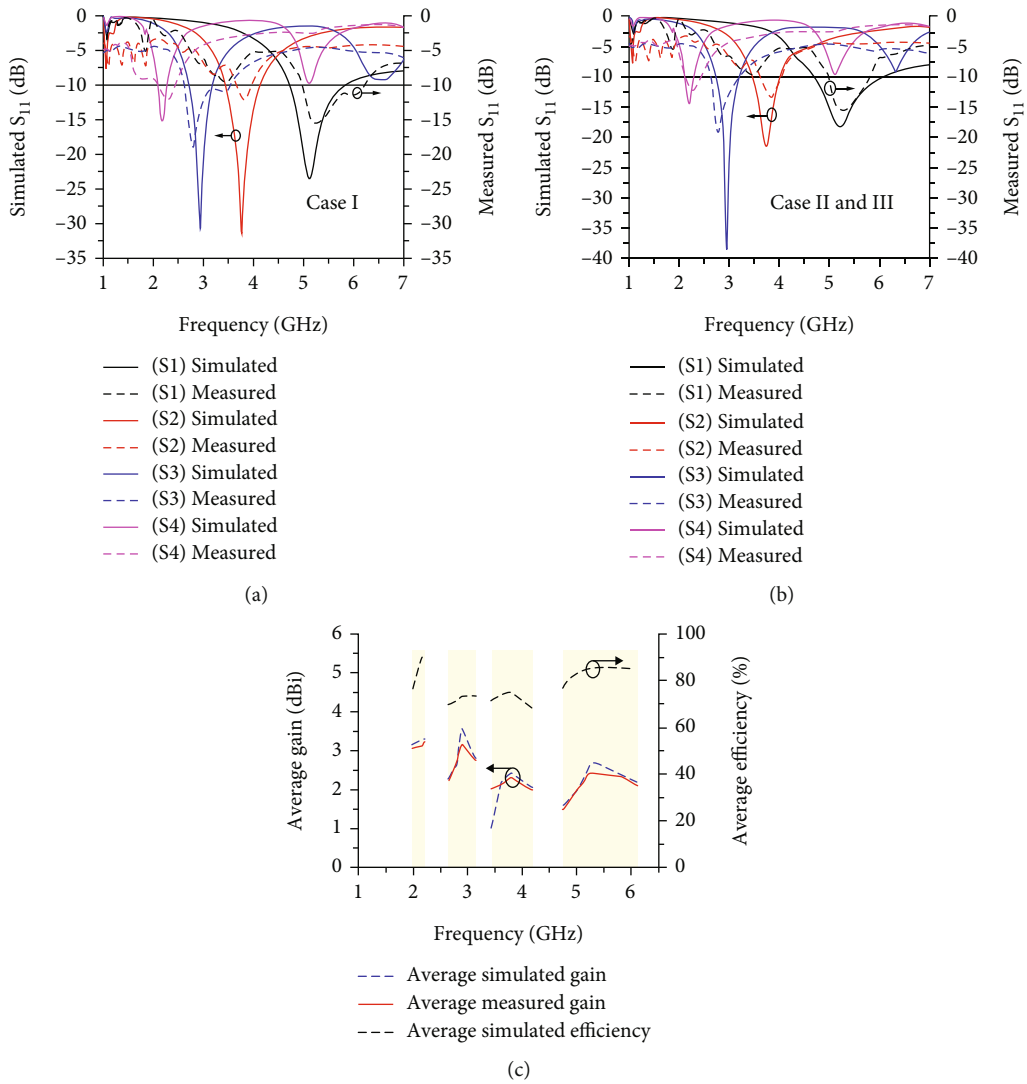

Figure 9: Results: (a) case I—return loss, (b) cases II and III—return loss, and (c) gain and efficiency.

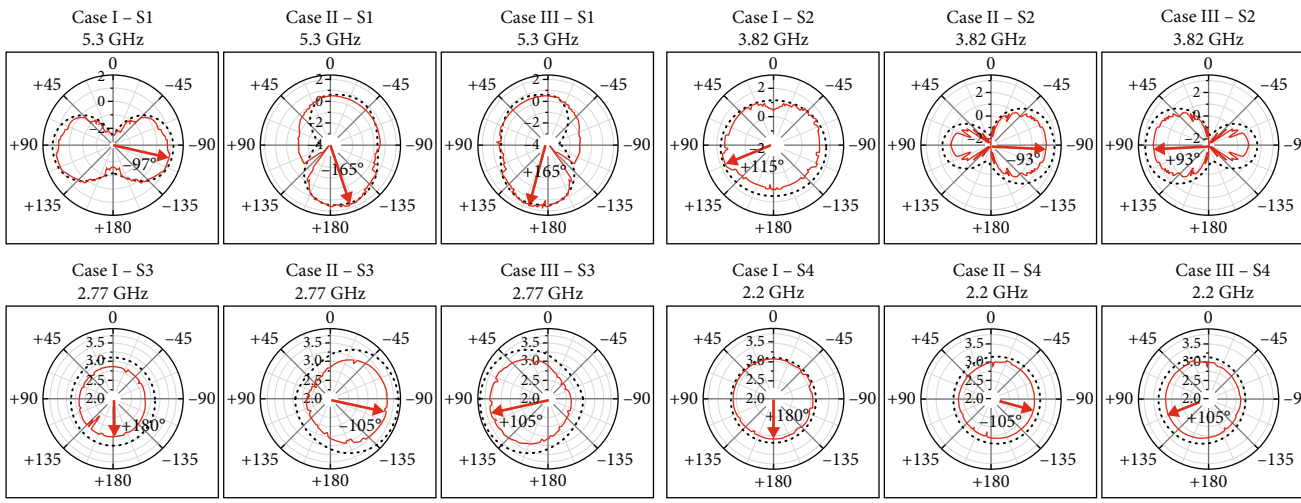

Figure 10: Radiation pattern (phi = 0^0) (*x*-*z* plane) (simulated result—black dotted line, measured result-red solid line).

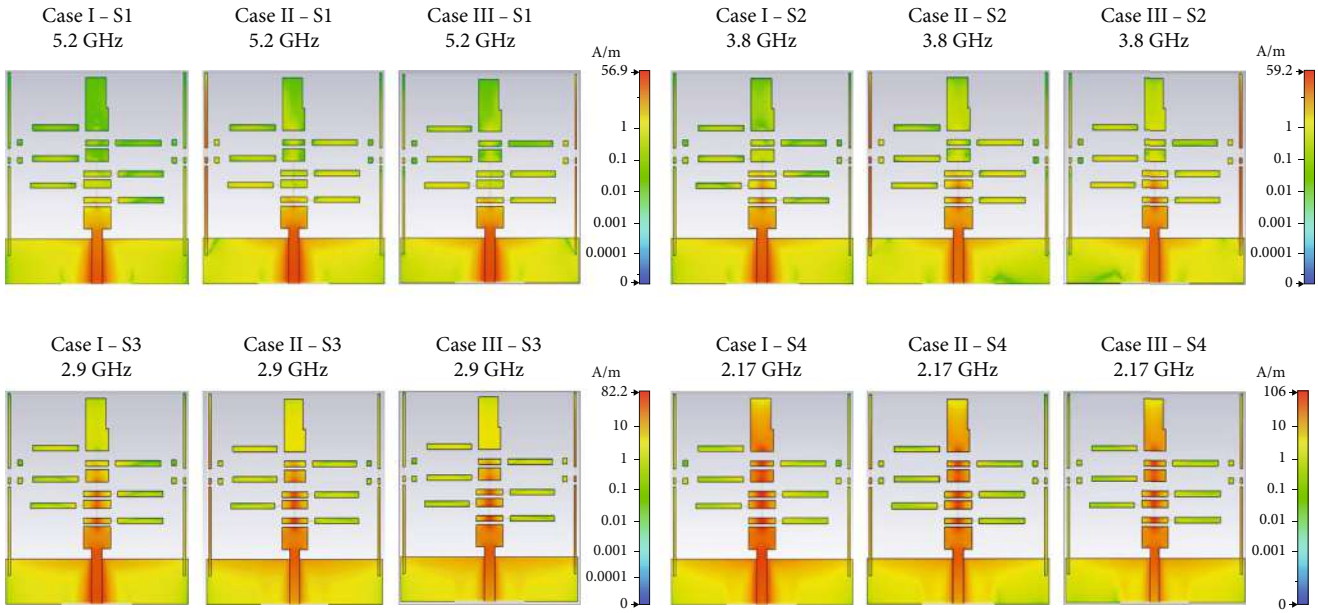

Figure 11: Simulated result—surface current distribution.

Table 1: Proposed work vs. existing frequency and pattern reconfigurable antennas.

Ref. no.	Dimension ($L \times W \times h$) (mm^3)	No. of switches/means of switching	Maximum number of beams	No. of frequency bands	Peak gain (dBi)
[1]	$47 \times 80 \times 1.5$	5/PIN	2	2	2.7/2.6
[16]	$50 \times 50 \times 1.6$	4/PIN	3	4	4/3.8/4.4/5
[18]	$40 \times 30 \times 1.6$	4/PIN	3	2	2.45/2.76
[20]	$46 \times 32 \times 1.6$	12/PIN	5	5	1.25/2.80/2.90/3.64/4.67
[23]	70×70	4/PIN	3	2	6.214/8.461
[24]	$50 \times 100 \times 1.6$	2/PIN	2	2	4.9/5.5
[25]	$42 \times 44 \times 0.127$	8/PIN	2	2	—
[26]	$66.4 \times 66.4 \times 1.5$	3/RF MEMS	2	4	—
[27]	$120 \times 120 \times 7.362$	-/PIN	3	2	8-9 dB/6-10.31 dB
[28]	$112 \times 52 \times 0.508$	18/NMOS transistors	8	2	3.8/8.3
[29]	—	8/PIN	4	2	5.63/5.55
This work	$38 \times 40 \times 0.787$	5/PIN	3	4	2.43/2.42/3.5/3.29

4. Conclusion

A compact antenna that can reconfigure quadband and radiation pattern is reported in this article. The proposed antenna can reconfigure to 5.3 GHz, 3.82 GHz, 2.77 GHz, and 2.2 GHz. At each operating frequency, the antenna can steer its main lobe into three different directions. In all the resonating frequencies, acceptable gains are realized. The presented design reduces structural complexity by utilizing fewer diodes and simple biasing circuits. The antenna performs well with an average efficiency of 85%, 75%, 73%, and 91% at 5.3 GHz, 3.82 GHz, 2.77 GHz, and 2.2 GHz, respectively. The proposed antenna covers band 1, band 7, band 46, and band 77 of the 5G new radio (NR) standard. These bands are some of the most widely used 5G NR frequency bands. Hence, the proposed antenna is suitable for 5G applications in the sub-6 GHz frequency range.

Data Availability

The data used to support the findings of this study are included within the article.

Conflicts of Interest

The authors declare that they have no conflicts of interest.

Authors' Contributions

K. Karthika and K. Kavitha contributed to the conceptualization, methodology, results, and discussion.

References

[1] P. K. Li, Z. H. Shao, Q. Wang, and Y. J. Cheng, "Frequency- and pattern-reconfigurable antenna for multistandard wireless applications," *IEEE Antennas and Wireless Propagation Letters*, vol. 14, pp. 333–336, 2015.

[2] K. Karthika and K. Kavitha, "Reconfigurable antennas for advanced wireless communications: a review," *Wireless Personal Communications*, vol. 120, no. 4, pp. 2711–2771, 2021.

[3] A. Boukarkar, X. Q. Lin, Y. Jiang, and X. F. Yang, "A compact frequency-reconfigurable 36-states patch antenna for wireless applications," *IEEE Antennas and Wireless Propagation Letters*, vol. 17, no. 7, pp. 1349–1353, 2018.

[4] S. Sharma and C. C. Tripathi, "Wideband to concurrent triband frequency reconfigurable microstrip patch antenna for wireless communication," *International Journal of Microwave and Wireless Technologies*, vol. 9, no. 4, pp. 915–922, 2017.

[5] S. Ullah, S. Ahmad, B. A. Khan, U. Ali, F. A. Tahir, and S. Bashir, "Design and analysis of a hexa-band frequency reconfigurable monopole antenna," *IETE Journal of Research*, vol. 64, no. 1, pp. 59–66, 2018.

[6] A. Ahmad, F. Arshad, S. I. Naqvi, Y. Amin, H. Tenhunen, and J. Loo, "Flexible and compact spiral-shaped frequency reconfigurable antenna for wireless applications," *IETE Journal of Research*, vol. 66, no. 1, pp. 22–29, 2020.

[7] Z. Shi, R. Zheng, J. Ding, and C. Guo, "A novel pattern-reconfigurable antenna using switched printed elements," *IEEE Antennas and Wireless Propagation Letters*, vol. 11, pp. 1100–1103, 2012.

[8] G. Jin, M. Li, D. Liu, and G. Zeng, "A simple four-beam reconfigurable antenna based on monopole," *IEEE Access*, vol. 6, pp. 30309–30316, 2018.

[9] T. Aboufoul, S. Member, C. Parini, X. Chen, S. Member, and A. Alomainy, "Pattern-reconfigurable planar circular ultra-wideband monopole antenna," *IEEE Transactions on Antennas and Propagation*, vol. 61, no. 10, pp. 4973–4980, 2013.

[10] M. Jusoh, T. Aboufoul, T. Sabapathy, A. Alomainy, and M. R. Kamarudin, "Pattern-reconfigurable microstrip patch antenna with multidirectional beam for WiMAX application," *IEEE Antennas and Wireless Propagation Letters*, vol. 13, pp. 860–863, 2014.

[11] Y. Juan, W. Che, W. Yang, and Z. N. Chen, "Compact pattern-reconfigurable monopole antenna using parasitic strips," *IEEE Antennas and Wireless Propagation Letters*, vol. 16, pp. 557–560, 2017.

[12] B. Ashvanth, B. Partibane, M. G. N. Alsath, and R. Kalidoss, "Gain enhanced multipattern reconfigurable antenna for vehicular communications," *International Journal of RF and Microwave Computer-Aided Engineering*, vol. 30, no. 6, 2020.

[13] M. S. Alam and A. Abbosh, "Planar pattern reconfigurable antenna with eight switchable beams for WiMax and WLAN applications," *IET Microwaves, Antennas and Propagation*, vol. 10, no. 10, pp. 1030–1035, 2016.

[14] H. A. Majid, M. K. A. Rahim, M. R. Hamid, and M. F. Ismail, "Frequency and pattern reconfigurable slot antenna," *IEEE Transactions on Antennas and Propagation*, vol. 62, no. 10, pp. 5339–5343, 2014.

[15] A. A. Palsokar and S. L. Lahudkar, "Frequency and pattern reconfigurable rectangular patch antenna using single PIN diode," *AEU-International Journal of Electronics and Communications*, vol. 125, article 153370, 2020.

[16] Y. P. Selvam, M. Kanagasabai, M. G. N. Alsath et al., "A low-profile frequency- and pattern-reconfigurable antenna," *IEEE Antennas and Wireless Propagation Letters*, vol. 16, pp. 3047–3050, 2017.

[17] P. Thanki and F. Raval, "Fork-shaped frequency and pattern reconfigurable antenna," *International Journal of Communication Systems*, vol. 33, no. 17, article e4613, 2020.

[18] L. Han, C. Wang, W. Zhang, R. Ma, and Q. Zeng, "Design of frequency- and pattern-reconfigurable wideband slot antenna," *International Journal of Antennas and Propagation*, vol. 2018, Article ID 3678018, 7 pages, 2018.

[19] A. Iqbal, A. Smida, N. Mallat et al., "Frequency and pattern reconfigurable antenna for emerging wireless communication systems," *Electronics*, vol. 8, no. 4, p. 407, 2019.

[20] I. Ahmad, W. U. R. Khan, H. Dildar et al., "A pentaband compound reconfigurable antenna for 5G and multi-standard sub-6GHz wireless applications," *Electronics*, vol. 10, no. 20, p. 2526, 2021.

[21] S. Raman, N. Timmons, and J. Morrison, "Gain enhanced pattern reconfigurable planar Yagi-Uda antenna on coplanar structure," *Electronics Letters*, vol. 49, no. 25, pp. 1593–1595, 2013.

[22] I. Ahmad, H. Dildar, W. U. R. Khan et al., "Design and experimental analysis of multiband compound reconfigurable 5G antenna for Sub-6 GHz wireless applications," *Wireless Communications and Mobile Computing*, vol. 2021, Article ID 5588105, 14 pages, 2021.

[23] R. Dewan, M. K. A. Rahim, M. R. Hamid, M. Himdi, H. A. Majid, and N. A. Samsuri, "HIS-EBG unit cells for pattern and frequency reconfigurable dual band array antenna," *Progress in Electromagnetics Research*, vol. 76, pp. 123–132, 2018.

[24] M. S. Khan, A. Iftikhar, A. D. Capobianco, R. M. Shubair, and B. Ijaz, "Pattern and frequency reconfiguration of patch antenna using PIN diodes," *Microwave and Optical Technology Letters*, vol. 59, no. 9, pp. 2180–2185, 2017.

[25] Z. Zhu, P. Wang, S. You, and P. Gao, "A flexible frequency and pattern reconfigurable antenna for wireless systems," *Progress in Electromagnetics Research*, vol. 76, pp. 63–70, 2018.

[26] S. K. Patel, C. Argyropoulos, and Y. P. Kosta, "Pattern controlled and frequency tunable microstrip antenna loaded with multiple split ring resonators," *IET Microwaves, Antennas and Propagation*, vol. 12, no. 3, pp. 390–394, 2018.

[27] A. X. Chen and X. Liu, "The high gain frequency-and radiation pattern-reconfigurable antenna based on meta-surface," in *Progress in electromagnetics research symposium-Fall (PIERS-FALL)*, pp. 565–569, Singapore, 2017.

[28] M. K. Shereen, M. I. Khattak, and M. Al-Hasan, "A frequency and radiation pattern combo-reconfigurable novel antenna for 5G applications and beyond," *Electronics*, vol. 9, no. 9, p. 1372, 2020.

[29] K. Saurav, D. Sarkar, and K. V. Srivastava, "A dual-band reconfigurable Yagi–Uda antenna with diverse radiation patterns," *Applied Physics A: Materials Science & Processing*, vol. 123, no. 7, pp. 1–8, 2017.

Design and Development of Self-Complementary DNA Structure-based Frequency Reconfigurable Antenna

Original Article Published: 02 May 2024

(2024) Cite this article

Journal of Electrical Engineering & Technology

Aims and scope

Submit manuscript

K. Karthika & K. Kavitha

Abstract

Nature-inspired patch antennas are gaining attention in wireless applications. A novel self-complementary Deoxyribonucleic Acid (DNA) structure-based frequency reconfigurable antenna is proposed in this work. DNA itself follows the golden ratio. The structure of the DNA-shaped antenna is modelled using Fibonacci numbers. The structure dimensions are $80 \times 80 \times 0.787$ mm^3. Rogers RT Duroid 5870 with a dielectric constant of 2.33 is used as a substrate. Techniques like the placement of the parasitic patch and Defected Ground Structure (DGS) are implemented and analyzed for gain enhancement. Parametric analysis has been carried out to achieve better radiation characteristics. The antenna is made reconfigurable by incorporating two PIN diode

switches. The designed structure covers a wide band from 4.86 GHz to 6.12 GHz (WLAN) during an OFF-ON state. 0.988 GHz (Sub 1 GHz) and 4.58 GHz (5G) (dual band) are the resonating frequencies of the ON-OFF state. For the ON-ON state, the resonating frequencies are 2.67 GHz (WiMAX), 3.36 GHz (LTE), and 4.76 GHz (5G) (triple band). The proposed structure offers acceptable radiation performance. Fabrication and testing are done to validate the results. The simulated findings and the measured results agree quite well.

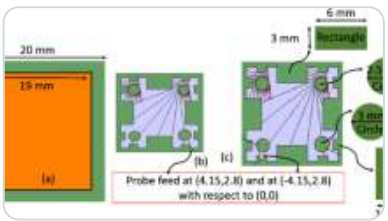

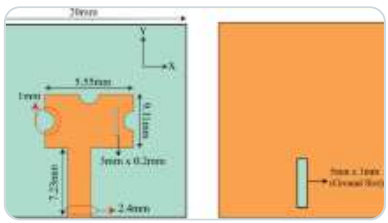

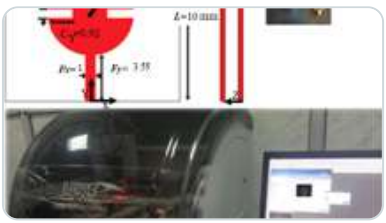

Comparative analysis of fractal antennae for sub-6 GHz and 5G bands for wireless and...

Article | 16 May 2024

Pattern Diversity Based Four-Element Dual-band MIMO Patch Antenna for 5G...

Article | Open access
10 May 2024

New Compact Broadband SRR Loaded Antenna Pattern for 5G Applications

Article | 14 May 2024

Data availability

Data sharing is not applicable to this article as no datasets were generated or analyzed during the current study.

References

1. Shabalkin IP, Grigor'eva EY, Gudkova MV, Shabalkin PI (2016) Fibonacci sequence and Supramolecular structure of DNA. Bull Exp Biol Med 161(1):193–196. https://doi.org/10.1007/s10517-016-3374-6

Article Google Scholar

2. Blank M, Goodman R (2011) DNA is a fractal antenna in electromagnetic fields. Int J Radiat Biol 87(4):409–415. https://doi.org/10.3109/09553002.2011.538130

Article Google Scholar

3. Akhtaruzzaman, Md, Shafie AA (2012) Geometrical substantiation of Phi, the golden ratio and the Baroque of Nature, Architecture, Design and Engineering. Int J Arts 1(1):1–22. https://doi.org/10.5923/j.arts.20110101.01

Article Google Scholar

4. Sepehri A (2017) A mathematical model for DNA. Int J Geom Methods Mod Phys 14(11):1–27. https://doi.org/10.1142/S0219887817501523

Article MathSciNet Google Scholar

5. Swigon D (2009) The Mathematics of DNA Structure, Mechanics, and Dynamics. In: Benham C, Harve, S, Olson W, Sumners D, Swigon D (eds). Mathematics of DNA Structure, Function and Interactions. The IMA Volumes in Mathematics and its Applications. 150: 293–320. https://doi.org/10.1007/978-1-4419-0670-0

6. Singh P, Ray K, Rawat S (2016) Design of nature inspired broadband microstrip patch antenna for satellite communication. Adv Intell Syst Comput 419:369–379. https://doi.org/10.1007/978-3-319-27400-3_33

Article Google Scholar

7. Kekre A, Peshwe P, Kothari A (2022) Nature-inspired antenna for Millimeter-Wave Applications. Wirel Pers Commun 124(4):3635–3646. https://doi.org/10.1007/s11277-022-09529-w

Article Google Scholar

8. da Silva Júnior PF, Serres AJR, Freire RCS, de Freitas Serres GK, Gurjão EC, de Carvalho JN, Santana EEC (2018) Bio-Inspired Wearable Antennas. In J. H. Ortiz (Ed.), Wearable Technologies. IntechOpen. 220–237 https://doi.org/10.5772/intechopen.75912

9. Karthika K, Kavitha K (2021) Reconfigurable Antennas for Advanced Wireless Communications: a review. Wirel Pers Commun 120(4):2711–2771. https://doi.org/10.1007/s11277-021-08555-4

Article Google Scholar

10. Leng T, Pan K, Zhou X, Li Y, Abdalla MA, Hu Z (2021) Non-volatile RF reconfigurable antenna on flexible substrate for Wireless IoT Applications. IEEE Access 9:119395–119401. https://doi.org/10.1109/ACCESS.2021.3107486

Article Google Scholar

11. Trad I, Ben Rmili H, Floch JM, Zouch W, Drissi M (2015) Planar square multiband frequency reconfigurable microstrip fed antenna with quadratic koch-island fractal slot for wireless devices. Microw Opt Technol Lett 57(1):207–212. https://doi.org/10.1002/mop.28815

Article Google Scholar

12. Saeed SM, Balanis CA, Birtcher CR, Durgun AC, Shaman HN (2017) Wearable flexible reconfigurable Antenna Integrated with Artificial magnetic conductor. IEEE Antennas Wirel Propag Lett 16:2396–2399. https://doi.org/10.1109/LAWP.2017.2720558

Article Google Scholar

13. Sun M, Zhang Z, Zhang F, Chen A (2019) L/S multiband frequency-reconfigurable antenna for Satellite Applications. IEEE Antennas Wirel Propag Lett 18(12):2617–2621. https://doi.org/10.1109/LAWP.2019.2945624

Article Google Scholar

14. Choukiker YK, Behera SK (2017) Wideband frequency reconfigurable Koch snowflake fractal antenna. IET Microw Antennas Propag 11(2):203–208. https://doi.org/10.1049/iet-map.2016.0238

Article Google Scholar

15. Chaouche YB, Messaoudene I, Benmabrouk I, Nedil M, Bouttout F (2019) Compact coplanar waveguide-fed reconfigurable fractal antenna for switchable multiband systems. IET Microw Antennas Propag 13(1):1–8. https://doi.org/10.1049/iet-map.2018.5005

Article Google Scholar

16. Shirazi M, Huang J, Li T, Gong X (2018) A switchable-frequency slot-Ring antenna element for Designing a reconfigurable array. IEEE Antennas Wirel Propag Lett 17(2):229–233. https://doi.org/10.1109/LAWP.2017.2781463

Article Google Scholar

17. Polaiah G, Kandasamy K, Kulkarni M (2021) An Autonomous frequency reconfigurable antenna using Slotline Open-Loop resonators. IEEE Access 9:82221–82232. https://doi.org/10.1109/ACCESS.2021.3087123

Article Google Scholar

18. Jin G, Deng C, Yang J, Xu Y, Liao S (2019) A new differentially-fed frequency reconfigurable antenna for WLAN and sub-6GHz 5G applications. IEEE Access 7:56539–56546. https://doi.org/10.1109/ACCESS.2019.2901760

Article Google Scholar

19. Hussain N, Awan WA, Naqvi SI, Ghaffar A, Zaidi A, Naqvi SA, Iftikhar A, Li XJ (2020) A compact flexible frequency reconfigurable antenna for heterogeneous applications. IEEE Access 8:173298–173307. https://doi.org/10.1109/ACCESS.2020.3024859

Article Google Scholar

20. Jin G, Deng C, Xu Y, Yang J, Liao S (2020) Differential frequency-reconfigurable antenna based on dipoles for Sub-6 GHz 5G and WLAN applications. IEEE Antennas Wirel Propag Lett 19(3):472–476. https://doi.org/10.1109/LAWP.2020.2966861

Article Google Scholar

21. Ullah S, Ullah S, Ahmad I, Ur Rehman Khan W, Ahmad T, Habib U, Albreem MA, Alsharif MH, Uthansakul P (2021) Frequency reconfigurable antenna for portable wireless applications. Comput Mater Contin 68(3):3015–3027. https://doi.org/10.32604/cmc.2021.015549

Article Google Scholar

22. Awan WA, Naqvi SI, Ali WAE, Hussain N, Iqbal A, Tran HH, Alibakhshikenari M, Limiti E (2021) Design and realization of a frequency reconfigurable antenna with wide, dual, and single-band operations for compact sized wireless applications. Electronics 10(11):1–10. https://doi.org/10.3390/electronics10111321

Article Google Scholar

23. Awan WA, Hussain N, Naqvi SA, Iqbal A, Striker R, Mitra D, Braaten BD (2020) A miniaturized wideband and multi-band on-demand reconfigurable antenna for compact and portable devices. AEU - Int J Electron Commun 122:1–7. https://doi.org/10.1016/j.aeue.2020.153266

Article Google Scholar

24. Zhao X, Riaz S, Geng S (2019) A reconfigurable MIMO/UWB MIMO antenna for cognitive radio applications. IEEE Access 7:46739–46747. https://doi.org/10.1109/ACCESS.2019.2909810

Article Google Scholar

25. dos Santos Silveira E, Antreich F, do Nascimento DC (2020) Frequency-reconfigurable SIW microstrip antenna. AEU - Int J Electron Commun 124:1–9. https://doi.org/10.1016/j.aeue.2020.153333

Article Google Scholar

26. Ghaffar A, Li XJ, Awan WA, Nazeri AH, Hussain N, Seet BC (2021) Compact multiband multimode frequency reconfigurable antenna for heterogeneous wireless applications. Int J RF Microw Comput -Aided Eng 31(7):1–11. https://doi.org/10.1002/mmce.22659

Article Google Scholar

27. Al-Zhour Z, Aqel AA, Abdallah I (2008) Mathematical properties of DNA structure in 3-Dimensional Space. Int J Open Probl Compt Math 1(3):214–221

MathSciNet Google Scholar

Acknowledgements

There is no acknowledgement involved in this work.

Funding

No funding is involved in this work.

Author information

Authors and Affiliations

Department of Electronics and Communication Engineering, Kumaraguru College of Technology, Coimbatore, India
K. Karthika

Department of Electronics and Communication Engineering, Velammal College of Engineering and Technology, Madurai, India
K. Kavitha

Contributions

K. Karthika - Conceptualization, design, results and analysis, manuscript drafting.

K. Kavitha - Conceptualization, design, results and analysis, manuscript drafting.

Corresponding author

Correspondence to K. Karthika.

Ethics declarations

Ethical approval and consent to participate

No participation of humans takes place in this implementation process.

Human and animal rights

No violation of Human and Animal Rights is involved.

Conflict of interest

There is no Conflict of Interest related to this work.

Additional information

Publisher's note

Rights and permissions

About this article

Cite this article

Karthika, K., Kavitha, K. Design and Development of Self-Complementary DNA Structure-based Frequency Reconfigurable Antenna. *J. Electr. Eng. Technol.* (2024). https://doi.org/10.1007/s42835-024-01917-5

Received	Revised	Accepted
25 February 2023	03 April 2024	19 April 2024

Published
02 May 2024

DOI
https://doi.org/10.1007/s42835-024-01917-5

Keywords

Defected ground structure | DNA | Fibonacci | Parasitic patch | PIN diode | Reconfigurable antenna

Progress In Electromagnetics Research C, Vol. 135, 227–240, 2023

EBG Integrated Metasurface Antenna for SAR Reduction

Kaliappan Kavitha*, Selva Vijay Gokul, Sivakumar Yazhini, J. M. Kanaka Durga, and Raja Keerthana

Abstract—This research article presents an innovative design of a textile-based microstrip patch antenna with a metasurface for medical applications. The antenna is designed to operate at a frequency of 2.4 GHz, which is the frequency of the Industrial, Scientific, and Medical (ISM) band, to minimize the Specific Absorption Rate (SAR) in the human body. The design includes an Electromagnetic Band Gap (EBG) that is placed above a metasurface, which is made up of a periodic array of I-shaped structures. A foam layer is placed between the EBG and the antenna to improve performance. The use of textile-based materials in the antenna allows for flexibility and comfort when it is mounted on the human body. The integration of the metasurface in the antenna design allows for a more efficient transfer of energy from the antenna to the surrounding tissue, resulting in a reduction in the amount of energy absorbed by the body. The simulation of the antenna design is carried out using Computer Simulation Technology (CST), which provides accurate results for the performance of the antenna. After the implementation of the EBG array, the gain of the antenna is improved, resulting in better performance. The proposed antenna design achieved a SAR value of 0.077 W/kg over 1 gram of thigh tissue, which is well below the safety limit set by the International Commission on Non-Ionizing Radiation Protection (ICNIRP). This implies that the integrated design of the antenna can be safely used in medical applications.

1. INTRODUCTION

In recent times, textile-based patch antennas have become increasingly popular due to their light weight, flexibility, and conformal nature [1]. They find applications in wearable technology, healthcare, and communication systems. However, their low gain, efficiency, and narrow bandwidth limit their use in practical applications [2]. To overcome these limitations, researchers have explored the use of metasurfaces, which are artificial structures composed of subwavelength units that manipulate electromagnetic waves' behavior [3, 4]. An electromagnetic bandgap structure (EBG) has been designed underneath the antenna to upgrade the antenna performance [5, 6]. This study will discuss the design and simulation of a textile-based patch antenna with a metasurface (MS) and EBG structure.

Metamaterials are artificial materials where properties are not found in nature [7]. They are widely studied in the field of antenna design as they possess the characteristics of manipulating electromagnetic waves in unconventional ways. In recent days, metasurfaces have gained attention for their ability to manipulate the reflection and transmission of electromagnetic waves with high efficiency and low losses.

Jiang et al. (2014) proposed a metasurface-enabled conformal antenna for WBAN devices [8]. Here, the antenna showed a reflector type of artificial magnetic conductor (AMC), a gain of 6.2 dBi, and efficiency not available. The values of SAR were also analyzed and found to be 0.66 W/kg over 1 g of tissue. Wang et al. (2018), described a flexible antenna using metamaterial [9]. The antenna showed a gain of 5.2 dBi. The efficiency of the designed antenna was reported to be around 61.3%. The SAR values were found to be 2.48 (W/kg) below the safety limits set by the ICNIRP.

Received 13 May 2023, Accepted 10 July 2023, Scheduled 7 August 2023

* Corresponding author: Kaliappan Kavitha (kavi@vcet.ac.in).

The authors are with the Centre for RF Circuits and Antenna Design, Department of Electronics and Communication Engineering, Velammal College of Engineering and Technology (Autonomous), Madurai, India.

Zhang et al.'s publication [10] (2020) presented a metasurface-based compact wearable antenna, which exhibited a gain of 2.99 dBi and a 300 MHz bandwidth. This design is particularly well-suited for monitoring vital-sign data in health monitoring systems within the ISM band, and it could be used in WBAN applications such as smart bracelets or watches. Purohit and Raval [11] analyzed a body worn textile antenna that operated at 2.45 GHz and used jeans as its substrate. The use of textile material with a low dielectric constant (ranging from 1 to 2) helped to reduce surface wave losses and improved antenna bandwidth. The designed antenna exhibited a gain of 7.2 dBi and a return loss of −32.57 dB. Janapala et al. [12] presented a flexible antenna using polydimethylsiloxane with a leaf-like structure covering the WLAN ISM band of 2.4 GHz, integrated with a metasurface unit cell. The study reported a SAR of 2.53 W/kg for a tissue volume of 1 g.

Sheeba and Jayanthy [13] examined the use of several ISM band feeding strategies with a microstrip antenna composed of lightweight substrates. The study involved comparing several parameters such as return loss, dielectric constant, gain, and directivity. The research revealed that the impedance matching for textile antennas is affected significantly by E-plane bending. Youssef et al. [14] developed a fully fabricated I-shaped patch antenna that was integrated with a textile-based AMC employed in low SAR wearable applications. By integrating an AMC array, the gain of the antenna was improved by 75%, and a significant reduction in SAR was achieved. Iqbal and Kha [15] utilized methods such as Kramers-Krong and Nicolson Rose Weir (NRW) to analyze metasurfaces and extract numerical parameters for their application in antennas, specifically through unit cell design.

Agus et al. [17] illustrated a meta-wearable textile Multiple-Input and Multiple-Output (MIMO) antenna using viscose-wool felt. The antenna design incorporated Reflecting and Electromagnetic Band Gap (RIS and EBG) surfaces to improve gain and bandwidth. The SAR values for the antenna were evaluated, and the results showed that they were within the permissible limits established by the ICNIRP guidelines. To mitigate undesired surface waves, Althuwayb et al. created an EBG decoupling structure that isolated the radiating elements [18]. The modifications made to the antenna design significantly reduced the unwanted surface waves. The antenna also showed excellent wideband performance, with a radiation efficiency of 80% and a gain of 9.50 dBi.

Kumar et al. [19] designed an antenna using a mushroom-type EBG to limit the surface waves of the antenna by utilizing the band-stop frequency characteristic of EBG structures. Additionally, the implementation of mushroom-type EBG structures results in a notable 5.9% increase in the antenna's bandwidth. In the study by Gnanagurunathan and Udofia [20], an EBG-enclosed patch antenna was designed. Here the positioning of EBG cells contributed towards beamwidth increment, back lobe reduction, and bidirectional radiation properties. The study also found that a back lobe reduction of almost 100% can be achieved by offsetting the distance by 0.8 mm. Finite-Difference Time-Domain (FDTD) method was utilized to study how a wave source interacts with the human head. The investigation was carried out, and the averaged SAR computed was 0.0143 W/kg and 0.0153 W/kg for sagittal and coronal cases, respectively. In the sagittal incidence case, the tissue-averaged SARs were found to be significantly higher than in the coronal case. The study by Akram and Jasmy [23] revealed that the tissue-averaged SARs differed considerably while the head-averaged SARs were similar for both cases at a frequency of 900 MHz.

Gao et al. in 2018 proposed a wearable circular ring antenna for wireless communication applications [24]. This antenna showed a gain of 3.5 dBi and a reflector type of EBG. The efficiency of the antenna was reported to be around 55%. The SAR values of the antenna were also analyzed and found to be 0.55 W/kg below the safety limits set by the ICNIRP. Balaji Vignesh and Kavitha [25] explored fractal antennas' utility in meeting the demand for small, wideband, and multiband antennas across diverse applications such as cellular phones, airplanes, spacecraft, and missiles. While these antennas offer compact size and frequency versatility, they face limitations such as low gain and bandwidth. Fractal geometry can mitigate these limitations by cutting slots, reducing the antenna's metallic material, and producing multiband or wideband capabilities. Moreover, it improves bandwidth, making it suitable for ISM band and WLAN applications.

In contrast, our study delves into the design and analysis of metasurface reflectors with distinct unit cell configurations to reduce SAR in wireless communication applications. Our proposed antennas with 1×1, 2×2, and 3×3 metasurface reflectors succeed in lowering SAR in skin, muscle, and fat tissues of different thicknesses while maintaining high antenna performance in directivity, efficiency,

gain, and return loss. The results reveal the potential of metasurfaces for SAR reduction in wireless communication systems.

The remainder of this paper is as follows. The antenna study analysis and design methodologies are detailed in the first section of this paper. Section 2 presents a parametric investigation of antenna dimensions of the proposed work. In Sections 3 and 4, the results acquired by the simulation and measurement are discussed. The work's conclusion is presented in the final section.

2. PROPOSED WORK

2.1. Antenna Design

The proposed antenna features a rectangular patch made of Textile Shield IT material with dimensions 53.5 mm × 57.5 mm × 0.17 mm and a feed width of 6.67 mm as displayed in Figure 1. The patch is placed on a felt substrate with dimensions 67.33 mm × 63.22 mm × 1.5 mm and a dielectric constant of 1.2. The felt substrate is chosen for its compact and flexible textile material and is a high melt adhesive. The ground plane is made of copper with dimensions 67.33 mm × 63.22 mm × 0.035 mm. The antenna resonates at 2.4 GHz in the ISM band. The antenna design is simulated using CST software.

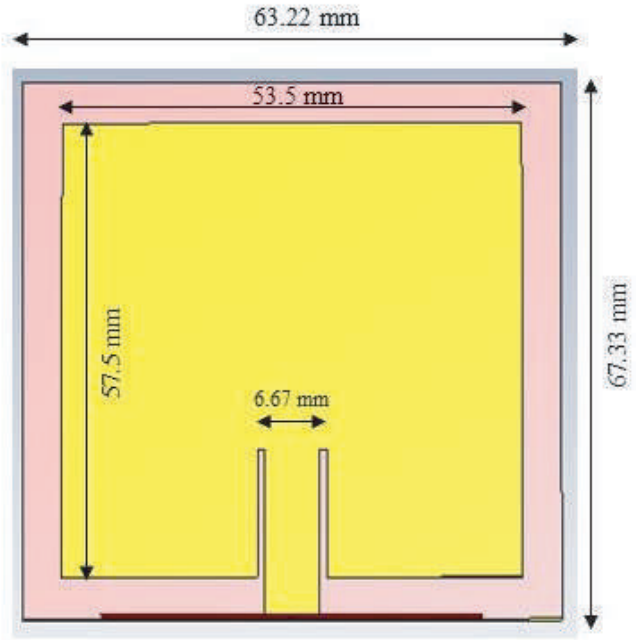

Figure 1. Textile-based rectangular patch antenna.

2.2. Metasurface Design

Metasurface antennas use metasurfaces to control and manipulate the behavior of electromagnetic waves, achieving a high degree of control over the radiation pattern and polarization of the emitted signal. While developing a metasurface, parameters like surface impedance and reflection coefficient are taken into account. The reflection coefficient of a metasurface depends on the geometry, properties, and arrangement of the resonant elements in the metasurface, as well as the polarization, angle, and frequency of the incident wave. It can be calculated from Equation (1)

$$\gamma = \frac{(Z_l - Z_s)}{Z_l + Z_s} \tag{1}$$

where z_l = characteristic impedance of the feed line.

The surface impedance Z_s can be illustrated as the electromagnetic properties of patches given by the Equation

$$Z_s = \frac{(R_s + jX_s)}{(w_0 * \varepsilon_0 * t)} \tag{2}$$

where R_s = surface resistance of the metasurface, X_s = surface reactance of the metasurface, w_0 = angular frequency of the operating frequency, ε_0 = permittivity of free space.

The radiation pattern of an antenna with the metasurface is derived from (3)

$$E_\theta = \frac{E_0 * \cos \emptyset * \cos \theta * \exp(-jkr)}{r} \tag{3}$$

where E_θ = magnitude of the electric field at the feed point, $\emptyset$ = azimuthal angle, θ = polar angle, k = wave number, r = distance from the feed point.

To improve the antenna's performance, metasurface unit cells made of textile Shield IT with dimensions of 24.6 mm × 24.6 mm × 0.17 mm are designed. The unit cells have an "I" shape with a length of 20 mm as displayed in Figure 2(a). The unit cells are arranged in a 2 × 2 and 3 × 3 array configuration as shown in Figures 2(b) and 2(c), and the antenna's performance is simulated. The results are shown in Table 1.

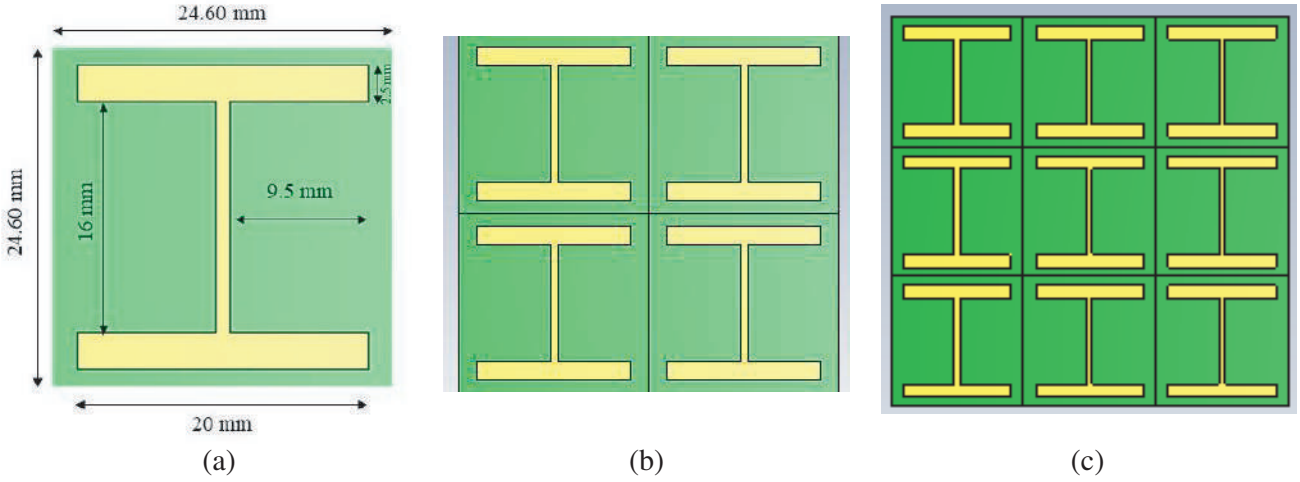

Figure 2. (a) MS unit cell with (b) 2 × 2 MS array, (c) 3 × 3 MS array.

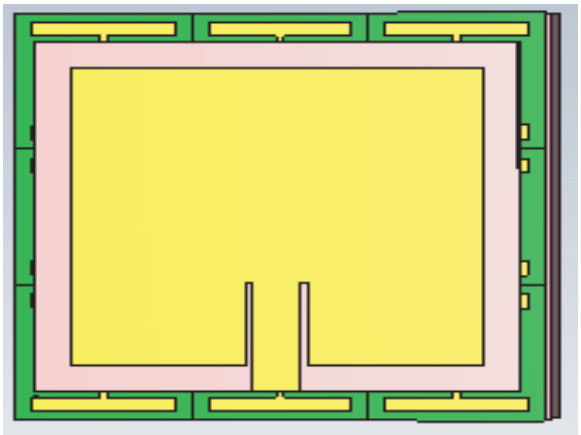

Figure 3. Textile-based rectangular patch antenna integrated with 3 × 3 metasurface.

Table 1. Simulation results of the antenna with metasurface.

Reflector type/ Radiation parameter	Return loss	Directivity (in dBi)	VSWR	Gain (in dBi)	Efficiency (in %)
Antenna with MS unit cell	−19.168	6.156	1.247	4.54	68.92
Antenna with 2 × 2 MS	−21.36	6.047	1.219	4.386	68.22
Antenna with 3 × 3 MS	−20.49	6.935	1.208	6.268	81.10

The designed antenna is integrated with the 3 × 3 metasurface consisting of I-shaped unit cells as depicted in Figure 3. The obtained results are displayed in Figure 4. It is inferred that the design obtains resonance at 2.4 GHz with a −20 dB, as displayed in Figure 4.

The simulation results in Table 1 show that the antenna with a 3×3 array metasurface configuration has the lowest return loss, highest directivity, gain, and efficiency.

2.3. Electromagnetic Band Gap Structure

EBG-based wearable antennas are similar to metasurface-based antennas in that they use an electromagnetic bandgap structure to enhance antenna performance. However, EBG structures typically consist of periodic metal or dielectric structures, while metasurfaces use sub-wavelength periodic structures to manipulate the phase and amplitude of incident electromagnetic waves. One advantage of EBG-based antennas is that they can provide improved isolation between antennas on a wearable

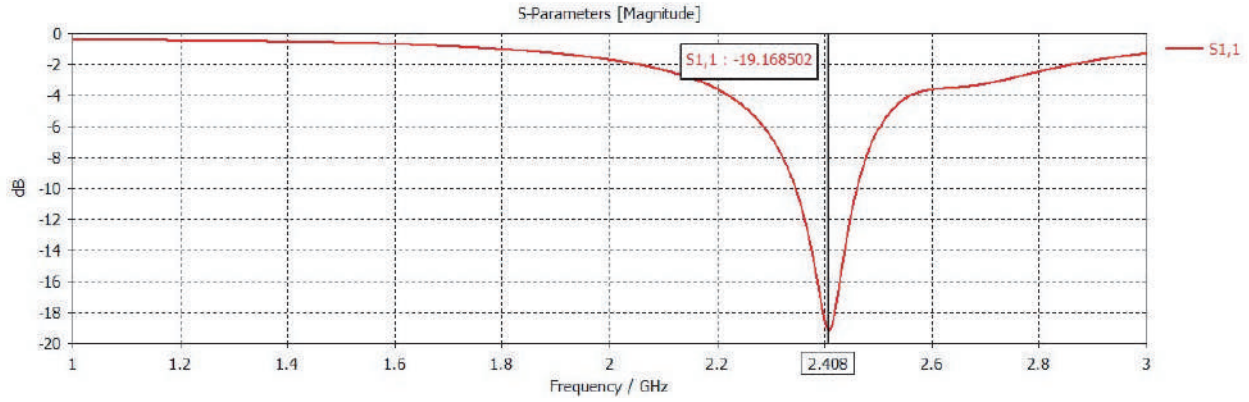

(a)

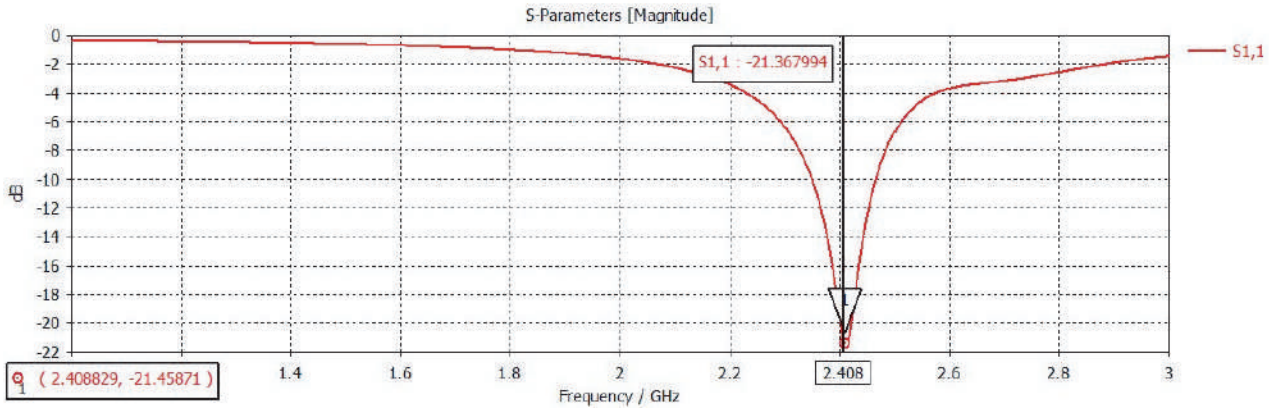

(b)

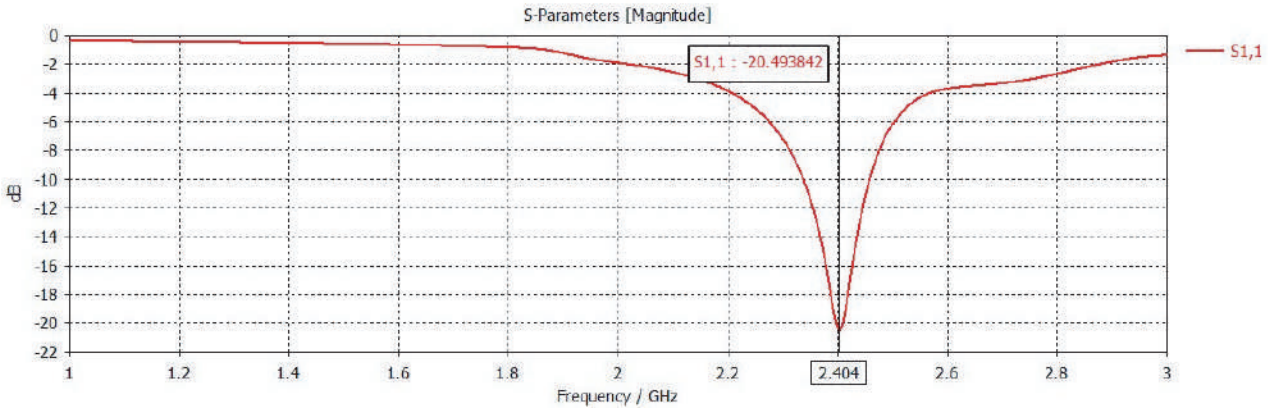

(c)

Figure 4. Reflection coefficient (S_{11}) of antenna with (a) metasurface unit cell, (b) 2×2 metasurface array, (c) 3×3 metasurface array.

device [16]. This is because the EBG structure can suppress surface waves that can lead to crosstalk between antennas. In contrast, metasurface-based antennas may not provide as much isolation between antennas.

The structure of EBG displays a photonic bandgap, which is a range of frequencies or wavelengths for which the propagation of electromagnetic waves is forbidden. This is due to the periodic nature of the EBG structure. The bandgap frequency of the EBG structure can be derived from Equation (4)

$$f_{bg} = \frac{c}{2} * \sqrt{\varepsilon}_{eff} * \sqrt{1 + \left(\frac{2\pi}{d}\right)^2} \tag{4}$$

where d is the spacing between the EBG unit cells. When an incident wave with a frequency within the bandgap is incident on the EBG structure, it is reflected with a phase shift determined by the equation below.

$$\varphi_r = -2\pi * f_{bg} * \frac{d}{c} \tag{5}$$

Figure 5 shows a typical EBG structure consists of a grounded dielectric substrate with a metallic patch positioned on top. The patch is designed in the shape of a mushroom consisting of a stem and a cap. The stem functions as a short circuit, whereas the cap functions as an open circuit. The capacitance

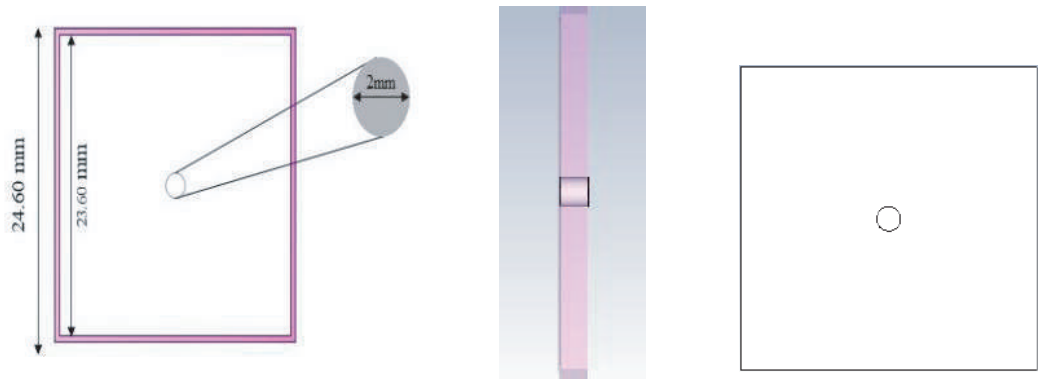

(a) (b) (c)

Figure 5. EBG unit cell. (a) Front view. (b) Side view. (c) Back view.

and inductance values for EBG unit cell are calculated from (6)

$$C = \frac{\varepsilon_0 + A}{d}$$
$$L = \frac{\mu_0 + h}{A} \tag{6}$$

where μ_0 and ε_0 are the permeability and permittivity of free space; A is the area of the EBG unit cell; h is the height of the substrate; and d is the spacing between the EBG unit cells. Changes in the dielectric constant of an EBG antenna affect the relationship between its inductor and capacitor, altering the antenna's impedance properties.

To make the EBG unit cell more compact, the series capacitance was increased. As a result, the unit cell was altered from Equation (1) as derived in [16]. These components together generate a high-impedance surface, which is capable of reflecting and suppressing undesired radiation. The equations for the resonant frequencies of the EBG structure are f_1 and f_2 and are given by:

$$f_1 f_2 = \frac{1}{2\pi\sqrt{L_R\left(C_L + C\right)}},\ \frac{1}{2\pi\sqrt{L_L C_R}} \tag{7}$$

The EBG mushroom design comprises a cylindrical-shaped via and a square patch that exhibits varying transmission properties, which are influenced by factors including patch size, via diameter, unit element spacing, substrate thickness, and substrate material. The patch is made of copper that has a thickness of 0.035 mm and is mounted on a material made of felt of 1.002 mm thickness. The substrate used is felt which is compact and flexible. The unit elements measure 23.60 mm × 23.60 mm with a 1 mm gap between each other, and features a via diameter of 1 mm. A total of nine unit cells are arranged on the substrate. The unit cells of the EBG are arranged in a 2 × 2 and 3 × 3 array configurations as shown in Figure 6, and the plots for S-parameters are specified in Figure 9, respectively.

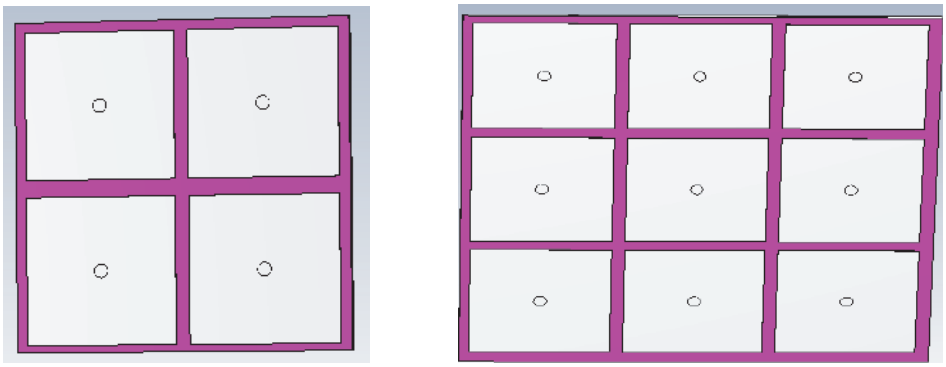

(a) (b)

Figure 6. Design of EBG unit cell with (a) 2 × 2 EBG, (b) 3 × 3 EBG.

Figure 6 shows the design of the EBG unit cell with 2 × 2 and 3 × 3 EBG configurations. Figure 7 shows a textile-based rectangular patch antenna integrated with a 3 × 3 EBG array. However, the integrated antenna with only an EBG structure results in increased return loss, which causes degradation in the antenna performance, as the acquired results seem inefficient [21]. To overcome this drawback, a new pattern of the antenna is designed, combining the antenna with both metasurface and EBG structures. This approach helps in arriving at the desired results of decreased return loss and SAR values with improved gain. The antenna structure combining metasurface with EBG is shown in Figure 8. Here, foam is positioned between the EBG and the antenna to absorb the excess heat radiated from the antenna.

The antenna integrated with the MS and EBG unit cell has a gain of 4.62 dBi, while the antenna with the 2 × 2 MS with EBG has a gain of 4.561 dBi. The antenna with 3 × 3 MS with EBG has the

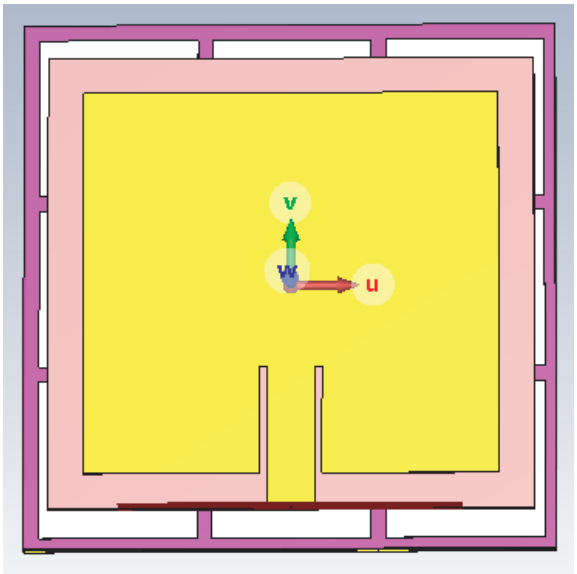

Figure 7. Textile-based rectangular patch antenna integrated with 3 × 3 EBG.

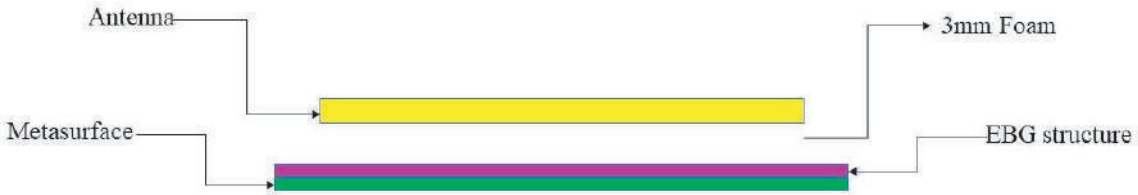

Figure 8. Textile-based rectangular patch antenna integrated with 3 × 3 metasurface and EBG structure.

highest gain of 6.375 dBi as shown in Figure 10(b). It can be inferred that the MS unit cell helps in increasing the gain of the antenna, leading to better signal strength.

One of the main advantages of EBG-based wearable antennas is that they can effectively reduce surface wave and backward radiation, which can improve the efficiency of the antenna as depicted in Table 2, and the antenna gain is also enhanced comparatively.

Table 2. Radiation parameters of the antenna with metasurface and EBG and MS.

Reflector type/ Radiation parameter	Return loss	Directivity (in dBi)	VSWR	Gain (in dBi)	Efficiency (in %)
Antenna with MS and EBG	−19.79	6.270	1.23	4.62	68.34
Antenna with 2 × 2 MS and EBG	−19.55	6.206	1.235	4.561	68.47
Antenna with 3 × 3 MS and EBG	−19.54	7.102	1.353	6.375	84.571

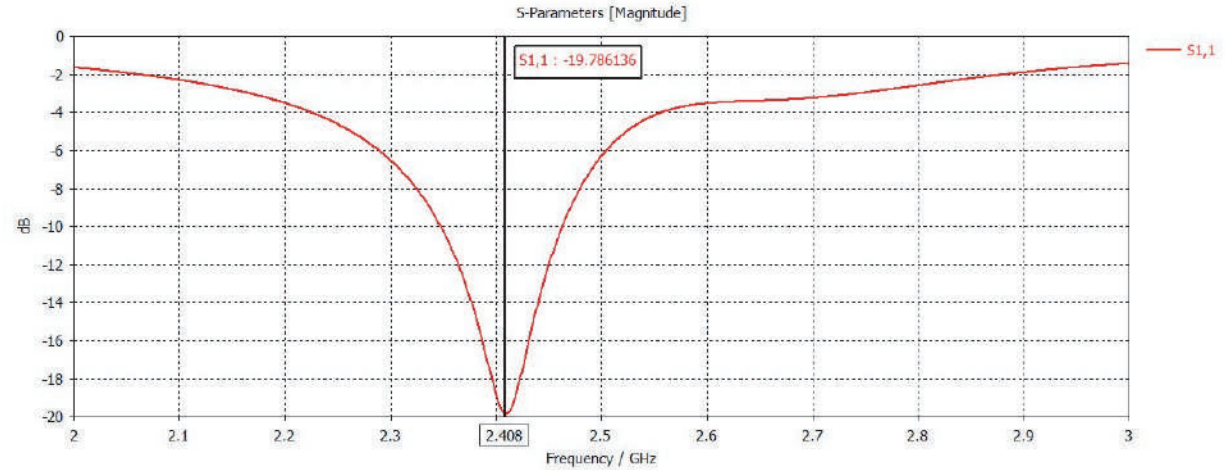

(a)

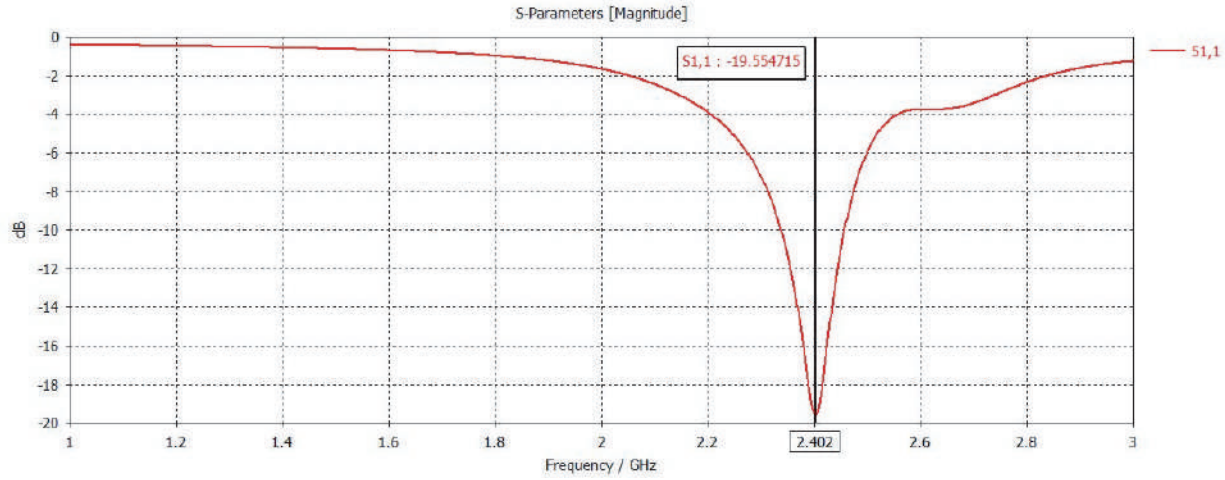

(b)

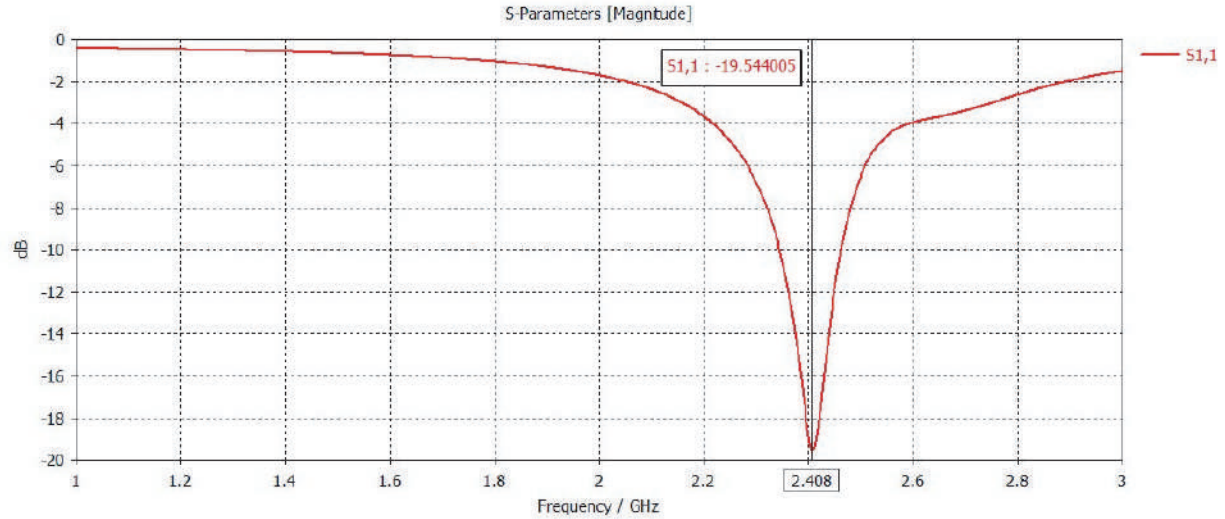

(c)

Figure 9. Reflection coefficient (S_{11}) of antenna with (a) EBG unit cell, (b) 2×2 EBG array, (c) 3×3 EBG array.

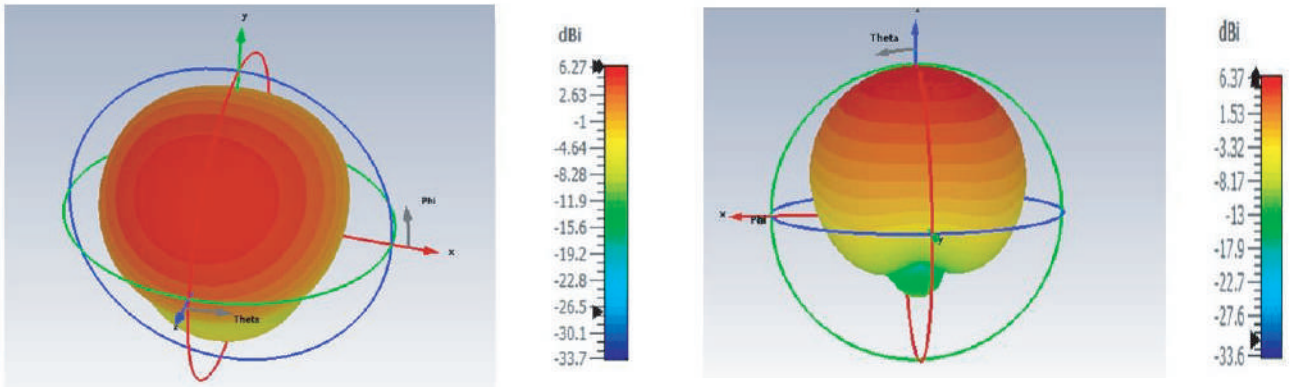

(a) (b)

Figure 10. Radiation pattern of the antenna integrated with (a) MS, (b) EBG and MS.

3. INTEGRATED ANTENNA CONFIGURATION OVER HUMAN MODEL

In this paper, a flat multilayer phantom model is designed in CST, and the integrated patch antenna is placed as shown in Figure 11. The goal of the integrated antenna is to make it applicable to wearable technology.

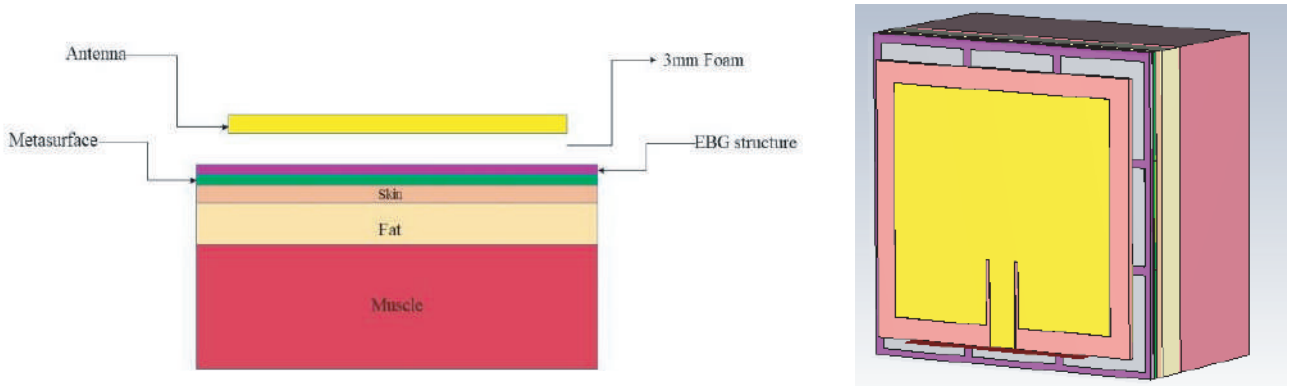

(a) (b)

Figure 11. (a) Lateral-view of the integrated antenna over the phantom model. (b) Antenna integrated over a three-layer phantom model.

As illustrated in Figure 11, a test setup has been arranged to measure its radiation on the human thigh for evaluating SAR. To mimic the human tissue model, a three-layered model is utilized to support the integrated antenna. This multi-layer model consists of fat, skin, and muscle [22]. A foam layer of 3 mm separates the presented antenna from the EBG structure. The SAR result must be considered to guarantee the antenna's compatibility with wearable applications. The thickness of the model is separated into 2 mm of skin, 30 mm of muscle, and 5–12.5 mm of fat. The electrical and thermal conductivity, density, metabolic rate of the human tissue layers are determined as listed in Table 3, taking into account that the dielectric properties of human tissue vary with frequency.

Table 3. Electromagnetic (EM) properties of the multilayer human tissue model.

Thigh Tissue/EM Properties	Dielectric Constant	Density (kg/m^3)	Electrical Conductivity (S/m)	Thermal Conductivity (W/K/m)	Blood Flow (W/km^3)	Metabolic Rate (W/m^3)
Skin	69.45	1100	0.507	0.21	9100	2000
Fat	6.07	900	0.507	0.16	1700	300
Muscle	65.97	1080	0.708	0.42	2700	500

4. SAR EVALUATION

The measurement of SAR is crucial when researching the effects of body exposure to RF radiation. SAR is used to determine the safety of exposure to radio frequency Electromagnetic Field (EMF), as high levels of exposure can potentially cause harm to the body. Equation (8) defines the SAR, which represents the amount of energy absorbed per unit of body tissue, expressed in watts per kilogram (W/kg).

$$SAR = \frac{\sigma E^2}{\rho} \text{ (W/kg)} \tag{8}$$

The SAR calculation takes into account the root-mean-square electric field induced in the tissue (E, measured in volts per meter), the tissue density (ρ, measured in kilograms per cubic meter), and the tissue electrical conductivity (σ, measured in siemens per meter). The SAR value determines the maximum allowable exposure to electromagnetic fields.

It is important to examine the value of SAR with MS and EBG to verify that the design adheres to safety regulations. According to the safety limit established by the Federal Communications Commission (FCC), the SAR value should be below 1.6 W/kg over 1 gram of human tissue. To evaluate the antenna's safety, we calculated the specific absorption rate (SAR) values for various fat thicknesses (5 mm to 12.5 mm) using the Finite-Difference Time-Domain (FDTD) method [23]. The results are displayed in Table 4 and Table 5. From the obtained results, it can be noticed that the value of SAR tends to be reduced when an EBG structure is placed along with the metasurface as displayed in Figure 12.

From comparisons in Tables 4 and 5, it is observed that the SAR values determined for different thicknesses of fat tissues of the thigh muscle are comparatively low for the antenna when connected

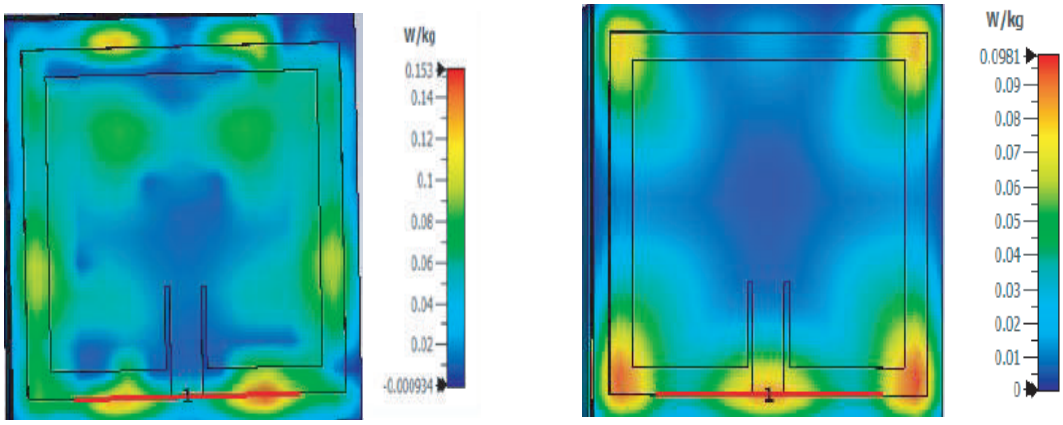

(a) (b)

Figure 12. Simulation of SAR levels over 10 mm of fat for (a) metasurface, (b) MS integrated with EBG.

Table 4. SAR results for the designed antenna with different metasurface configurations.

Reflector Type/Fat thickness	5 mm	6 mm	7.5 mm	8 mm	9 mm	10 mm	11 mm	12.5 mm
Antenna with MS unit cell	0.267	0.361	0.554	0.613	0.743	0.312	0.404	0.622
Antenna with 2×2 MS	0.348	0.364	1.053	1.219	1.306	0.829	0.441	1.24
Antenna with 3×3 MS	0.161	0.161	0.157	0.167	0.160	0.153	0.157	0.168

Table 5. SAR results for the designed antenna with different metasurface and EBG configurations.

Reflector Type/Fat thickness	5 mm	6 mm	7.5 mm	8 mm	9 mm	10 mm	11 mm	12.5 mm
Antenna with MS unit cell and EBG	0.247	0.283	0.312	0.288	0.308	0.359	0.383	0.371
Antenna with 2×2 MS and EBG	0.121	0.110	0.120	0.142	0.175	0.156	0.141	0.162
Antenna with 3×3 MS and EBG	0.0776	0.109	0.0907	0.0872	0.248	0.098	0.103	0.0939

Table 6. Comparison between the designed antenna and other related works.

References	Antenna physical size (mm^2)	Substrate type/ thickness (mm)	Reflector physical size (mm^2)/ type	Gain (dB)	Rad. Efficiency (%)	Max. SAR (W/kg) over 1 g of tissue
[8]	39×30	Rogers RO 3003/1.5	42×62/AMC	6.2	NA	0.66
[9]	30×25	Polyimide/0.05	74×74/ Metasurface	5.2	61.3	2.48
[12]	50×45	PDMS/3	24×40/ Metasurface	2.88	68.06	1.52
[14]	35×45	Felt/1.5	76×76/AMC	6.57	84.26	0.05
[17]	110×106	Viscose-wool felt/3	190×104/RIS EBG	5.8	NA	0.37
[24]	30×25	Felt/2	81×81/EBG	3.5	55	0.55
Proposed work	63×67	Felt/1.5	76×76/ Metasurface with EBG	6.37	82.4	0.077

structures of EBG and MS are synthesized than integration of the textile-based antenna with only metasurface [24]. The extensive comparison of antenna parameters is shown in Table 6.

On comparing these results, it can be observed that the use of the MS unit cell along with EBG in the textile-based patch antenna has led to significant improvements in the performance of the antenna in terms of efficiency, gain, directivity, and voltage standing wave ratio (VSWR). Furthermore, the specific absorption rate decreases by about 0.077 W/kg for 1 g of thigh tissue. However, further research is required to investigate the effects of the MS unit cell on other parameters such as bandwidth, radiation efficiency, and polarization.

5. CONCLUSION

This paper demonstrates that the design of a textile-based microstrip patch antenna is suitable for WBAN applications. The integration of metasurfaces with electromagnetic bandgap (EBG) beneath the antenna has proven to be highly effective in decreasing specific absorption rate (SAR) values and enhancing the efficiency and gain of the antenna in the ISM band frequency of 2.4 GHz. Furthermore, the effects of integrating metasurface and mushroom EBG structures for different thicknesses of fat have been investigated. It has been verified that the Specific Absorption Rate of the proposed antenna does not exceed the FCC limit of 1.6 W/kg at its operating frequency. As the substrate is lightweight, flexible, and soft, it makes the antenna easily wearable. Overall, the proposed work appears to advance the current state-of-the-art antenna design by leveraging the unique properties of metasurfaces to improve the performance of the antenna and minimize its impact on the human body. Overall, the innovative design of the textile-based microstrip patch antenna with a metasurface, EBG, and foam layer can be a promising solution for minimizing SAR in medical applications. The use of textile-based materials and the integration of metasurface and EBG allows for a comfortable and efficient transfer of energy, making it a suitable option for the use in medical applications.

REFERENCES

1. Ashya, A. Y. I., Z. Z. Abidin, S. H. Dahlan, H. Majid, S. M. Shah, M. R. Kamarudin, and A. Alomainy, "Compact and low-profile textile ebg-based antenna for wearable medical applications," *IEEE Antennas and Wireless Propagation Letters*, Vol. 16, 2550–2553, 2017.
2. Arnmanee, P., "Gain improvement of microstrip patch antenna using octagonal-loop metasurface superstrate and octagonal-shaped EBG structure for 2.4 GHz band application," *2018 15th International Conference on Electrical Engineering/Electronics, Computer, Telecommunications, and Information Technology*, 2018, 10.1109/ECTICon.2018.8619919.
3. Hariharan, V., S. Maheshwaran, S. Selvam, and N. Gunavathi, "Comparison of Electromagnetic Band Gap (EBG) structures for Specific Absorption Rate (SAR) reduction," *2015 Annual IEEE India Conference (INDICON)*, New Delhi, India, 2015.
4. Shaw, T. and D. Mitra, "Metasurface-based radiative near-field wireless power transfer system for implantable medical devices," *IET Microw. Antennas Propag.*, Vol. 13, No. 12, 1974–1982, Oct. 2019.
5. Kashani, M., L. Shafai, and D. Isleifson, "Performance improvement of a microstrip patch antenna on an EBG structure," *IEEE International Symposium on Antennas and Propagation and North American Radio Science Meeting*, Feb. 17, 2021.
6. Zaman, M. I., F. T. Hamedani, and H. Amjadi, "A New EBG structure and its application on microstrip patch antenna," *International Symposium on Antenna Technology and Applied Electromagnetics*, Aug. 9, 2012.
7. Alibakhshikenari, M., F. Babaeian, B. S. Virdee, S. Aïssa, L. Azpilicueta, C. H. See, A. A. Althuwayb, I. Huynen, F. Falcone, and E. Limiti, "A comprehensive survey on "Various decoupling mechanisms with focus on metamaterial and metasurface principles applicable to SAR and MIMO antenna systems," *IEEE Access*, Vol. 8, 192965–193004, Oct. 21, 2020.

8. Jiang, Z. H., D. E. Brocker, P. E. Sieber, and D. H. Werner, "A compact, low-profile metasurface-enabled antenna for wearable medical body-area network devices," *IEEE Transactions on Antenna and Propagation*, Vol. 62, No. 8, Aug. 2014.
9. Wang, M., Z. Yang, J. Wu, J. Bao, J. Liu, L. Cai, T. Dang, H. Zheng, and E. Li, "Investigation of SAR reduction using a flexible antenna with metamaterial structure in wireless body area network," *IEEE Trans. Antennas Propag.*, Vol. 66, No. 6, 3076–3086, Jun. 2018.
10. Zhang, K., G. A. E. Vandenbosch, and S. Yan, "A novel design approach for compact wearable antennas based on metasurfaces," *IEEE Trans. Biomed. Circuits Syst.*, Vol. 14, No. 4, 918–927, 2020.
11. Purohit, S. and F. Raval, "Wearable-textile patch antenna using jeans as substrate at 2.45 GHz," *International Journal of Engineering Research & Technology (IJERT)*, Vol. 3, No. 5, May 2015, ISSN: 2278-0181.
12. Janapala, D. K., M. Nesasudha, T. Mary Neebha, and R. Kumar, "Specific absorption rate reduction using metasurface unit cell for flexible polydimethylsiloxane antenna for 2.4 GHz wearable applications," *International Journal RF and Microwave Computer-aided Engineering*, 2019.
13. Sheeba, R. and T. Jayanthy, "Analysis and implementation of flexible microstrip antenna of soft substrates with different Feeding Techniques for ISM band," *Proceeding of International Conference on System, Computation, Automation, and Networking*, Oct. 24, 2019.
14. Youssef, O. M., M. El Atrash, and M. A. Abdalla, "A compact fully fabric I-shaped antenna supported with textile-based AMC for low SAR 2.45 GHz wearable applications," *Microwave Optical Technology Letters*, 2023.
15. Iqbal, K. and Q. U. Kha, "Review of metasurfaces through unit cell design an numerical extraction of parameters and their applications in antennas," *IEEE Access*, Vol. 10, 112368–11239, Oct. 13, 2022.
16. Azarbar, A. and J. Ghalibafan, "A compact low-permittivity dual-layer EBG structure for mutual coupling reduction," *International Journal of Antennas and Propagation*, Vol. 2011, Article ID 237454, 2011, doi: 10.1155/2011/237454.
17. Agus, A. N. S. S., T. Sabapathy, M. Jusoh, M. A. Abdelghany, K. Hossain, S. Padmanathan, S. S. Al-Bawri, and P. J. Soh, "Combined RIS and EBG surfaces inspired meta-wearable textile MIMO antenna using viscose-wool felt," *MDPI Journals*, 2022, doi: org/10.3390/polym14101989.
18. Althuwayb, A., M. Alibakhshikenari, B. S. Virde, N. Rashid, K. Kaaniche, A. B. Atitallah, A. Armghan, O. I. Elhamrawy, C. H. See, and F. Falcone, "Metasurface inspired flexible wearable MIMO array for wireless body area network applications and biomedical telemetry devices," *IEEE Access*, Vol. 11, Jan. 5, 2023.
19. Kumar, A., D. Ary, and D. K. Srivastava, "Band width of microstrip antenna improved by using mushroom type EBG structure," *IMPACT 2013*, IEEE, May 22, 2014.
20. Gnanagurunathan, G. and U. G. Udofia, "Performance analysis of the mushroom-like-EBG structure integrated with a microstrip patch antenna," *IEEE Asia-Pacific Conference on Applied Electromagnetics (APACE)*, Feb. 24, 2011.
21. Usman, F. and R. S. Yadav, "Wideband reconfigurable antenna for industrial, scientific and medical applications," *International Journal of Information Technology and Electrical Engineering (ITEE)*, Vol. 11, No. 2, Apr. 2022.
22. Sugunavathy, S., V. K. Sudha, and D. Parthiban, "Fabric woven textile antenna for medical applications," *Journal of Physics*, 012022–012022, 2021.
23. Akram, G. and Y. Jasmy, "Specific Absorption Rate (SAR) on the human head as function of orientation of plane wave radiation: FDTD-based analysis," *Second Asia International Conference on Modelling and Simulation (AMS)*, IEEE, May 23, 2008.
24. Gao, G.-P., B. Hu, S.-F. Wang, and C. Yang, "Wearable circular ring slot antenna with EBG structure for wireless body area network," *IEEE Antennas and Wireless Propagation Letters*, Vol. 17, No. 3, 434–437, 2018.
25. Balaji Vignesh, L. K. and K. Kavitha, "A Survey on fractal antenna design," *International Journal of Pure and Applied Mathematics*, Vol. 120, No. 6, 10941–10959, 2018.

DE GRUYTER

Requires Authentication | Published by De Gruyter | March 15, 2024

Gain enhancement in octagonal shaped frequency reconfigurable antenna using metasurface superstrate

Karthika Kandasamy, Kavitha Kaliappan, Sasikala Shanmugam and Adithya Srinivasan

From the journal Frequenz
https://doi.org/10.1515/freq-2023-0269

Abstract

A novel, high-gain reconfigurable antenna with a metasurface (MS) superstrate-based configuration is proposed in this research article. The design utilizes a concentric octagonal-shaped patch as a base antenna. Four SMP1345-079LF PIN diode switches are incorporated in the base antenna to facilitate frequency reconfiguration. When all four of the diodes are in OFF condition, the designed antenna resonates at 5.8 GHz. Switching ON the diodes switches the resonating frequency to 5 GHz. A novel MS unit cell of shape like '8' has been designed and analyzed. The designed unit cell exhibits properties of the metamaterial in the operating frequencies. An MS superstrate of a 5 × 5 array has been designed and connected to the base antenna through Teflon rods. Further, the proposed reconfigurable antenna with MS has been analyzed for air and foam medium (medium between antenna and superstrate). The proposed structure offers better performance for the air medium with a gain enhancement of 4.23 dBi and 1.55 dBi at 5 GHz and 5.8 GHz respectively. Fabrication and testing processes are undertaken to validate the proposed antenna's performance.

Keywords: gain enhancement; metasurface; PIN diode; reconfiguration; superstrate

Corresponding author: Karthika Kandasamy, Department of Electronics and Communication Engineering, 56972 Kumaraguru College of Technology , Coimbatore, India, E-mail: karthika.svk@gmail.com

Research ethics: Not applicable.

Author contributions: The authors have accepted responsibility for the entire content of this manuscript and approved its submission.

Competing interests: The authors state no conflict of interest.

Research funding: None declared.

Data availability: Not applicable.

References

[1] K. Karthika and K. Kavitha, "Reconfigurable antennas for advanced wireless communications: a review," *Wireless Pers. Commun.*, vol. 120, no. 4, pp. 2711–2771, 2021. https://doi.org/10.1007/s11277-021-08555-4 (https://doi.org/10.1007/s11277-021-08555-4) .

[2] K. Karthika and K. Kavitha, "Design and development of parasitic elements loaded quadband frequency and pattern reconfigurable antenna," *Int. J. RF Microwave Comput. Aided Eng.*, vol. 2023, pp. 1–10, 2023, https://doi.org/10.1155/2023/4034241 (https://doi.org/10.1155/2023/4034241) .

[3] A. M. Sadiq, Y. Gu, Y. Luo, Y. Chen, and K. Ma, "Gain-enhanced reconfigurable radiation array with mechanically driven system and directive elements," *Front. Mech. Eng.*, vol. 17, no. 4, pp. 1–17, 2022. https://doi.org/10.1007/s11465-022-0716-0 (https://doi.org/10.1007/s11465-022-0716-0) .

[4] K. Mondal, "Bandwidth and gain enhancement of microstrip antenna by frequency selective surface for WLAN, WiMAX applications," *Sādhanā*, vol. 44, no. 11, p. 233, 2019, https://doi.org/10.1007/s12046-019-1222-x (https://doi.org/10.1007/s12046-019-1222-x) .

[5] C. Shi, J. Zou, J. Gao, and C. Liu, "Gain enhancement of a dual-band antenna with the FSS," *Electronics (Switzerland)*, vol. 11, no. 18, pp. 1–15, 2022. https://doi.org/10.3390/electronics11182882 (https://doi.org/10.3390/electronics11182882) .

[6] R. A. Pandhare, M. P. Abegaonkar, and C. Dhote, "High gain frequency reconfigurable multifunctional antenna for modern wireless and mobile communication systems," *Int. J. RF Microwave Comput. Aided Eng.*, vol. 32, no. 11, pp. 1–17, 2022. https://doi.org/10.1002/mmce.23385 (https://doi.org/10.1002/mmce.23385) .

[7] A. N. A. Yusuf, P. D. Purnamasari, and F. Y. Zulkifli, "Optimization of defected ground structure (DGS) using genetic algorithm for gain enhancement of microstrip antenna," in 2021 *IEEE Asia-Pacific Conference on Applied Electromagnetics (APACE)*, IEEE, 2021, pp. 1–4. 10.1109/APACE53143.2021.9760610 (https://doi.org/10.1109/APACE53143.2021.9760610)

[8] N. L. Nguyen, "Gain enhancement in MIMO antennas using defected ground structure," *Prog. Electromagn. Res. M*, vol. 87, pp. 127–136, 2019, https://doi.org/10.2528/PIERM19091102 (https://doi.org/10.2528/PIERM19091102) .

[9] S. Yang, Y. Chen, C. Yu, Y. Gong, and F. Tong, "Design of a low-profile, frequency-reconfigurable, and high gain antenna using a varactor-loaded AMC ground," *IEEE Access*, vol. 8, pp. 158635–158646, 2020, https://doi.org/10.1109/ACCESS.2020.3020853 (https://doi.org/10.1109/ACCESS.2020.3020853).

[10] L. Sheng, L. Meng, Y. Lin, Y. Gong, X. Yang, and W. Cao, "A wideband frequency reconfigurable antenna with improved gain," *Microw. Opt. Technol. Lett.*, vol. 65, no. 3, pp. 915–920, 2023, https://doi.org/10.1002/mop.33577 (https://doi.org/10.1002/mop.33577).

[11] H. P. Li, G. M. Wang, X. J. Gao, J. G. Liang, and H. S. Hou, "A novel metasurface for dual-mode and dual-band flat high-gain antenna application," *IEEE Trans. Antennas Propag.*, vol. 66, no. 7, pp. 3706–3711, 2018, https://doi.org/10.1109/TAP.2018.2835526 (https://doi.org/10.1109/TAP.2018.2835526).

[12] C. Xue, et al.., "An ultrathin, low-profile and high-efficiency metalens antenna based on chain huygens' metasurface," *IEEE Trans. Antennas Propag.*, vol. 70, no. 12, pp. 11442–11453, 2022, https://doi.org/10.1109/TAP.2022.3209283 (https://doi.org/10.1109/TAP.2022.3209283).

[13] S. S. Syed Nasser, W. Liu, and Z. N. Chen, "Wide bandwidth and enhanced gain of a low-profile dipole antenna achieved by integrated suspended metasurface," *IEEE Trans. Antennas Propag.*, vol. 66, no. 3, pp. 1540–1544, 2018, https://doi.org/10.1109/TAP.2018.2790161 (https://doi.org/10.1109/TAP.2018.2790161).

[14] J. Wang, H. Wong, Z. Ji, and Y. Wu, "Broadband CPW-fed aperture coupled metasurface antenna," *IEEE Antennas Wirel. Propag. Lett.*, vol. 18, no. 3, pp. 517–520, 2019, https://doi.org/10.1109/LAWP.2019.2895618 (https://doi.org/10.1109/LAWP.2019.2895618).

[15] W. E. I. Liu, Z. N. Chen, X. Qing, J. Shi, and F. H. Lin, "Miniaturized wideband metasurface antennas," *IEEE Trans. Antennas Propag.*, vol. 65, no. 12, pp. 7345–7349, 2017, https://doi.org/10.1109/TAP.2017.2761550 (https://doi.org/10.1109/TAP.2017.2761550).

[16] K. Suvarna, N. Ramamurthy, and D. V. Vardhan, "Miniaturized and gain enhancement of tapered patch antenna using defected ground structure and metamaterial superstrate for GPS applications," *Prog. Electromagn. Res. C*, vol. 108, pp. 187–200, 2021. https://doi.org/10.2528/PIERC20111701 (https://doi.org/10.2528/PIERC20111701).

[17] M. A. Meriche, H. Attia, A. Messai, S. S. I. Mitu, and T. A. Denidni, "Directive wideband cavity antenna with single-layer meta-superstrate," *IEEE Antennas Wirel. Propag. Lett.*, vol. 18, no. 9, pp. 1771–1774, 2019, https://doi.org/10.1109/LAWP.2019.2929579 (https://doi.org/10.1109/LAWP.2019.2929579).

[18] D. Samantaray and S. Bhattacharyya, "A gain-enhanced slotted patch antenna using metasurface as superstrate configuration," *IEEE Trans. Antennas Propag.*, vol. 68, no. 9, pp. 6548–6556, 2020, https://doi.org/10.1109/TAP.2020.2990280 (https://doi.org/10.1109/TAP.2020.2990280).

[19] H. Q. Tian, J. L. Wang, D. Han, and X. Wang, "A gain-enhanced dual-band microstrip antenna using metasurface as superstrate configuration," *Appl. Comput. Electromagn. Soc. J.*, vol. 36, no. 12, pp. 1586–1593, 2021, https://doi.org/10.13052/2021.ACES.J.361210 (https://doi.org/10.13052/2021.ACES.J.361210) .

[20] R. Mittra, Y. Li, and K. Yoo, "A comparative study of directivity enhancement of microstrip patch antennas with using three different superstrates," *Microw. Opt. Technol. Lett.*, vol. 52, no. 2, pp. 327–331, 2010, https://doi.org/10.1002/mop.24898 (https://doi.org/10.1002/mop.24898) .

[21] D. Samantaray, S. K. Ghosh, and S. Bhattacharyya, "Modified slotted patch antenna with metasurface as superstrate for dual-band applications," *IEEE Antennas Wirel. Propag. Lett.*, 2022, https://doi.org/10.1109/LAWP.2022.3204180 (https://doi.org/10.1109/LAWP.2022.3204180) .

[22] M. Ameen, O. Ahmad, and R. K. Chaudhary, "Bandwidth and gain enhancement of triple-band MIMO antenna incorporating metasurface-based reflector for WLAN/WiMAX applications," *IET Microwaves. Opt. Antennas*, vol. 14, no. 13, pp. 1493–1503, 2020, https://doi.org/10.1049/iet-map.2020.0350 (https://doi.org/10.1049/iet-map.2020.0350) .

[23] H. R. Bindhu and M. N. Sujatha, "Wideband slot antenna gain enhancement using metasurface reflector," *Global Transitions Proc.*, vol. 2, no. 2, pp. 344–349, 2021, https://doi.org/10.1016/j.gltp.2021.08.046 (https://doi.org/10.1016/j.gltp.2021.08.046) .

[24] M. R. Ahsan, M. T. Islam, M. H. Ullah, M. J. Singh, and M. T. Ali, "Metasurface reflector (MSR) loading for high performance small microstrip antenna design," *PLoS One*, vol. 10, no. 5, pp. 1–20, 2015. https://doi.org/10.1371/journal.pone.0127185 (https://doi.org/10.1371/journal.pone.0127185) .

PubMed (https://pubmed.ncbi.nlm.nih.gov/26018795/)
PubMed Central (https://www.ncbi.nlm.nih.gov/pmc/articles/PMC4446261/)

[25] S. S. Efazat, R. Basiri, and S. V. Al-Din Makki, "The gain enhancement of a graphene loaded reconfigurable antenna with non-uniform metasurface in terahertz band," *Optik (Stuttg)*, vol. 183, pp. 1179–1190, 2019, https://doi.org/10.1016/j.ijleo.2019.02.034 (https://doi.org/10.1016/j.ijleo.2019.02.034) .

[26] M. M. Seyedsharbaty and R. A. Sadeghzadeh, "Antenna gain enhancement by using metamaterial radome at THz band with reconfigurable characteristics based on graphene load," *Opt. Quantum Electron*, vol. 49, no. 6, 2017, https://doi.org/10.1007/s11082-017-1052-1 (https://doi.org/10.1007/s11082-017-1052-1) .

[27] R. Wang, T. Tang, M. M. Olaimat, and Y. Liu, "Frequency reconfigurable near-zero refractive index material for antenna gain enhancement applications," *J. Microwaves Optoelectron. Electromagn. Appl.*, vol. 21, no. 2, pp. 294–304, 2022, https://doi.org/10.1590/2179-10742022v21i2259409 (https://doi.org/10.1590/2179-10742022v21i2259409) .

[28] J. Zhang, Y. Liu, Y. Jia, and R. Zhang, "High-gain Fabry–Pérot antenna with reconfigurable scattering patterns based on varactor diodes," *IEEE Trans. Antennas Propag.*, vol. 70, no. 2, pp. 922–930, 2022, https://doi.org/10.1109/TAP.2021.3111234 (https://doi.org/10.1109/TAP.2021.3111234).

[29] K. Sumathi, S. Lavadiya, P. Z. Yin, J. Parmar, and S. K. Patel, "High gain multiband and frequency reconfigurable metamaterial superstrate microstrip patch antenna for C/X/Ku-band wireless network applications," *Wireless Networks*, vol. 27, no. 3, pp. 2131–2146, 2021, https://doi.org/10.1007/s11276-021-02567-5 (https://doi.org/10.1007/s11276-021-02567-5).

[30] D. Zhou, H. Wang, L. Deng, L. L. Qiu, and S. Huang, "Metamaterial-based frequency reconfigurable microstrip antenna for wideband and improved gain performance," *Int. J. RF Microwave Comput. Aided Eng.*, vol. 32, no. 2, pp. 1–8, 2022. https://doi.org/10.1002/mmce.22988 (https://doi.org/10.1002/mmce.22988).

[31] S. P. Lavadiya, S. K. Patel, K. Ahmed, S. A. Taya, S. Das, and K. V. Babu, "Design and fabrication of flexible and frequency reconfigurable antenna loaded with copper, distilled water and seawater metamaterial superstrate for IoT applications," *Int. J. RF Microwave Comput. Aided Eng.*, vol. 32, no. 12, 2022, https://doi.org/10.1002/mmce.23481 (https://doi.org/10.1002/mmce.23481).

[32] S. P. Lavadiya, S. K. Patel, and M. Rayisyan, "High gain and frequency reconfigurable copper and liquid metamaterial tooth based microstrip patch antenna," *AEU Int. J. Electron. Commun.*, vol. 137, pp. 1–19, 2021. https://doi.org/10.1016/j.aeue.2021.153799 (https://doi.org/10.1016/j.aeue.2021.153799).

[33] S. K. Patel, S. P. Lavadiya, J. Parmar, K. Ahmed, S. A. Taya, and S. Das, "Low-cost, multiband, high gain and reconfigurable microstrip radiating structure using PIN diode for 5G/Wi-MAX/WLAN applications," *Physica B Condens. Matter.*, vol. 639, 2022, https://doi.org/10.1016/j.physb.2022.413972 (https://doi.org/10.1016/j.physb.2022.413972).

[34] A. B. Numan and M. S. Sharawi, "Extraction of material parameters for metamaterials using a full-wave simulator [education column]," *IEEE Antennas Propag. Mag.*, vol. 55, no. 5, pp. 202–211, 2013, https://doi.org/10.1109/MAP.2013.6735515 (https://doi.org/10.1109/MAP.2013.6735515).

[35] A. Verma, R. K. Arya, and S. N. Raghava, "Monopole cavity resonator antenna with AMC and superstrate for 5G/WiMAX applications," *Def. Sci. J.*, vol. 73, no. 1, pp. 51–60, 2023, https://doi.org/10.14429/DSJ.73.17759 (https://doi.org/10.14429/DSJ.73.17759).

[36] A. K. Jassim, M. J. Farhan, and F. N. H. Al-Nuaimy, "Enhancement of gain using a multilayer superstrate metasurface cell array with a microstrip patch antenna," *Indones. J. Electr. Eng. Comput. Sci.*, vol. 24, no. 3, p. 1564, 2021, https://doi.org/10.11591/ijeecs.v24.i3.pp1564-1570 (https://doi.org/10.11591/ijeecs.v24.i3.pp1564-1570).

[37] C. Arora, S. S. Pattnaik, and R. N. Baral, "SRR superstrate for gain and bandwidth enhancement of microstrip patch antenna array," *Prog. Electromagn. Res. B*, vol. 76, pp. 73–85, 2017, https://doi.org/10.2528/PIERB17041405 (https://doi.org/10.2528/PIERB17041405).

[38] M. Islam, M. Ullah, M. Singh, and M. Faruque, "A new metasurface superstrate structure for antenna performance enhancement," *Materials*, vol. 6, no. 8, pp. 3226–3240, 2013, https://doi.org/10.3390/ma6083226 (https://doi.org/10.3390/ma6083226) .

PubMed (https://pubmed.ncbi.nlm.nih.gov/28811432/)
PubMed Central (https://www.ncbi.nlm.nih.gov/pmc/articles/PMC5521244/)

Supplementary Material

This article contains supplementary material (https://doi.org/10.1515/freq-2023-0269 (https://doi.org/10.1515/freq-2023-0269)).

Received: 2023-08-17
Accepted: 2024-02-23
Published Online: 2024-03-15
Published in Print: 2024-06-25

— *or* —

From the journal

Frequenz
Volume 78 Issue 5-6

Articles in the same Issue

Gain enhancement in octagonal shaped frequency reconfigurable antenna using metasurface superstrate

High gain and high-efficiency compact resonator antennas based on spoof surface plasmon polaritons

Gain enhancement of ultra-wideband hexagonal slot antenna using tessellated rhombic loops based reflector

Terahertz MIMO antenna array for future generation of wireless applications

Genetic Algorithm Framework for 3D Discrete Wavelet Transform based Hyperspectral Image Classification

Research Article Published: 25 March 2024

Volume 52, pages 645–657, (2024) Cite this article

Journal of the Indian Society of Remote Sensing

Aims and scope

Submit manuscript

K. Kavitha & D. Sharmila Banu

Abstract

Joint spatial–spectral feature extraction process is always playing a vital role in the accurate classification of hyperspectral imagery. Such feature extraction techniques are ever demanded for hyperspectral classification. In this proposed work three dimensional DWT (3D-DWT) is used for the decomposition of the hyperspectral image and 3D gray level cooccurrence matrix (GLCM) features are extracted for obtaining the neighborhood information. A genetic Algorithm is incorporated in this work for the selection of the best features among the extracted features for yielding good classification accuracy. The proposed method is experimented on airborne visible infrared imaging sensor (AVIRIS) data of the Indian pine site and reflective optics system imaging

spectrometer (ROSIS) data of the Pavia University site. The results witness the accuracy of 94.62% for the Indian pines dataset and 96.48% for University of Pavia dataset before feature selection while only 5% of the samples in each class were used for training the 3D DWT based GLCM features. After incorporating the Genetic Algorithm for selecting the best features the accuracy is increased up to 97.67% for the Indian pines dataset and 97.99% for the University of Pavia dataset respectively, for the same 5% training samples. The proposed method is compared with the other methods and found to be more efficient.

Similar content being viewed by others

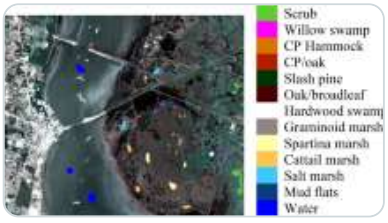

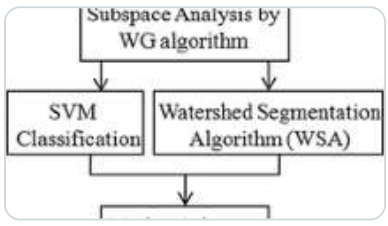

Dimensionality reduction of hyperspectral image using signal entropy...

Article | 25 July 2020

Multi-Objective Genetic Algorithm for Hyperspectral Image Analysis

Chapter | © 2021

Improving Spectral–spatial Classification of Hyperspectral Imagery Using Spectral...

Article | 16 January 2017

References

Anand, R., Veni, S., & Aravinth, J. (2021). Robust classification technique for hyperspectral images based on 3D discrete wavelet transform. *Remote Sensing, 13*, 1255. https://doi.org/10.3390/rs13071255

Article Google Scholar

Burrus, C. S., Gopinath, R. A., & Guo, H. (1998). *Introduction to wavelets and wavelet transforms: A primer*. New Jersey: Prentice Hall.

Google Scholar

Cao, X., Yao, J., Fu, X., & Bi, H. (2020). An enhanced 3D discrete wavelet transform for hyperspectral image classification. *IEEE Geoscience and Remote Sensing Letters, 18*(6), 1104–1108. https://doi.org/10.1109/LGRS.2020.2990407

Article Google Scholar

Chen, Y., Zhao, X., & Lin, Z. (2014). Optimizing subspace SVM ensemble for hyperspectral imagery classification. *IEEE Journal of Selected Topics in Applied Earth Observations and Remote Sensing, 7*, 1295–1305. https://doi.org/10.1109/JSTARS.2014.2307356

Article Google Scholar

Fatourechi, M., Birch, G. E., & Ward, R. K. (2007). Application of a hybrid wavelet feature selection method in the design of a self-paced brain interface system. *Journal of Neuro Engineering and Rehabilitation, 4*, 1–13. https://doi.org/10.1186/1743-0003-4-11

Article **Google Scholar**

Gao, H. M., Zhou, H., Xu, L. Z., & Shi, A. Y. (2014). Classification of hyperspectral remote sensing images based on simulated annealing genetic algorithm and multiple instance learning. *Journal of Central South University, 21*, 262–271. https://doi.org/10.1007/s11771-014-1937-0

Article **Google Scholar**

Gao, J., Peng, J. Y., & Li, Z. (2010). Application of improved PSO-SVM approach in image classification. In: Proceeding of symposium on photonics and optoelectronic (SOPO), Chengdu, pp. 1–4. https://doi.org/10.1109/SOPO.2010.5504341

Ghamisi, P., & Benediktsson, J. A. (2015). Feature selection based on hybridization of genetic algorithm and particle swarm optimization. *IEEE Geoscience and Remote Sensing Letters, 12*, 309–313. https://doi.org/10.1109/LGRS.2014.2337320

Article **Google Scholar**

Ghamisi, P., Benediktsson, J. A., Cavallaro, G., & Plaza, A. (2014). Automatic framework for spectral-spatial classification based on supervised feature extraction and morphological attribute profiles. *IEEE Journal of Selected Topics in Applied Earth Observations and Remote Sensing, 7*, 2147–2160. https://doi.org/10.1109/JSTARS.2014.2298876

Article **Google Scholar**

Guo, H., Huang, X., & Zhang, L. (2014). Three-dimensional wavelet texture feature extraction and classification for multi/hyperspectral imagery. *IEEE Geoscience and Remote Sensing Letters, 11*, 2183–2187. https://doi.org/10.1109/LGRS.2014.2323963

Article Google Scholar

Jimenez, L. O., & Landgrebe, D. A. (1995). Projection pursuit for high dimensional feature reduction: Parallel and sequential approaches. *Proceedings of International Geoscience and Remote Sensing Symposium, 1*, 148–150. https://doi.org/10.1109/IGARSS.1995.519674

Article Google Scholar

Li, J., Dias, J. B., & Plaza, A. (2012). Spectral-spatial hyperspectral image segmentation using subspace multinomial logistic regression and Markov random fields. *IEEE Transactions on Geoscience and Remote Sensing, 50*, 809–823. https://doi.org/10.1109/TGRS.2011.2162649

Article Google Scholar

Lin, Z., & Zhang, G. (2020). Genetic algorithm-based parameter optimization for EO-1 hyperion remote sensing image classification. *European Journal of Remote Sensing, 53*(1), 124–131. https://doi.org/10.1080/22797254.2020.1747949

Article Google Scholar

Paul, A., & Chaki, N. (2021). Dimensionality reduction of hyperspectral image using signal entropy and spatial information in genetic algorithm with discrete wavelet transformation. *Evolutionary Intelligence, 14*, 1793–1802. https://doi.org/10.1007/s12065-020-00460-2

Article Google Scholar

Pedergnana, M., Marpu, P. R., Mura, M. D., Benediktsson, J. A., & Bruzzone, L. (2013). A novel technique for optimal feature selection in attribute profiles based on genetic algorithm. *IEEE Transactions on Geoscience and Remote Sensing, 51*, 3514–3528. https://doi.org/10.1109/TGRS.2012.2224874

Article Google Scholar

Qian, Y., Ye, M., & Zhou, J. (2012). Hyperspectral image classification based on structured sparse logistic regression and three-dimensional wavelet texture features. *IEEE Transactions on Geoscience and Remote Sensing, 51*, 2276–2291. https://doi.org/10.1109/TGRS.2012.2209657

Article Google Scholar

Quesada, P. B., Argüello, F., Heras, D. B., & Benediktsson, J. A. (2014). Wavelet-based classification of hyperspectral images using extended morphological profiles on graphics processing units. *IEEE Journal of Selected Topics in Applied Earth Observations and Remote Sensing, 8*, 2962–2970. https://doi.org/10.1109/JSTARS.2015.2394778

Article Google Scholar

Roy, S. K., Ranjan Mondal Mercendes, E., Juan Haut, M., & Plaza, A. (2021). Morphological convolutional neural network for hyperspectral image classification. *IEEE Journal of Selected Topics in Applied Earth Observations and Remote Sensing*. https://doi.org/10.1109/JSTARS.2021

Article Google Scholar

Su, H., Sheng, Y., Du, P., Chen, C., & Liu, K. (2014). Hyperspectral image classification based on volumetric texture and dimensionality reduction. *Frontiers of Earth Sciences*. https://doi.org/10.1007/s11707-014-0473-4

Article Google Scholar

Tarabalka, Y., Chanussot, J., & Benediktsson, J. A. (2010). SVM and MRF-based method for accurate classification of hyperspectral images. *IEEE Geoscience and Remote Sensing Letters*, 7, 736–7402. https://doi.org/10.1109/LGRS.2010.2047711

Article Google Scholar

Tsai, F., Chang, C. K., Rau, J. Y., Lin, T. H., & Liu, G. R. (2007). 3D computation of gray level co-occurrence in hyperspectral image cubes. *Springer Lecture Notes in Computer*

Science, 4679, 429–440.

Article Google Scholar

Tsai, F., & Lai, J. S. (2013). Feature extraction of hyperspectral image cubes using three-dimensional gray level co-occurrence. *IEEE Transactions on Geoscience and Remote Sensing, 51*, 3504–3513. https://doi.org/10.1109/TGRS.2012.2223704

Article Google Scholar

Ye, Z., Prasad, S., Li, W., Fowler, J. E., & He, M. (2014). Classification based on 3D DWT and decision fusion for hyperspectral image analysis. *IEEE Geoscience and Remote Sensing Letters, 11*, 173–177. https://doi.org/10.1109/LGRS.2013.2251316

Article Google Scholar

Acknowledgements

The authors are grateful for the reviewer's valuable comments that improved the manuscript.

Funding

No funding was received to assist with the preparation of this manuscript.

Author information

Authors and Affiliations

Department of Electronics and Communication Engineering, Velammal College of Engineering and Technology (Autonomous), Madurai, Tamil Nadu, India
K. Kavitha

Department of Electronics and Communication Engineering, Ultra College of Engineering and Technology for Women, Madurai, Tamil Nadu, India

D. Sharmila Banu

Contributions

All authors contributed to the study conception and design and all authors read and approved the final Manuscript.

Corresponding author

Correspondence to K. Kavitha.

Ethics declarations

Conflict of interest

The authors have no relevant Conflict of interests to disclose.

Additional information

Publisher's Note

About this article

Cite this article

Kavitha, K., Banu, D.S. Genetic Algorithm Framework for 3D Discrete Wavelet Transform based Hyperspectral Image Classification. *J Indian Soc Remote Sens* **52**, 645–657 (2024). https://doi.org/10.1007/s12524-024-01850-0

Received	Accepted	Published
16 July 2023	04 March 2024	25 March 2024

Issue Date
March 2024

DOI

https://doi.org/10.1007/s12524-024-01850-0

Keywords

Hyperspectral image (HSI)
Gray level cooccurrence matrix (GLCM)
Support vector machine (SVM)
Genetic algorithm (GA)

Reduction of Near-End and Far - End Crosstalk in Microwave and Millimetre Wave Band of Parallel Transmission Lines using Meander Shaped DMS

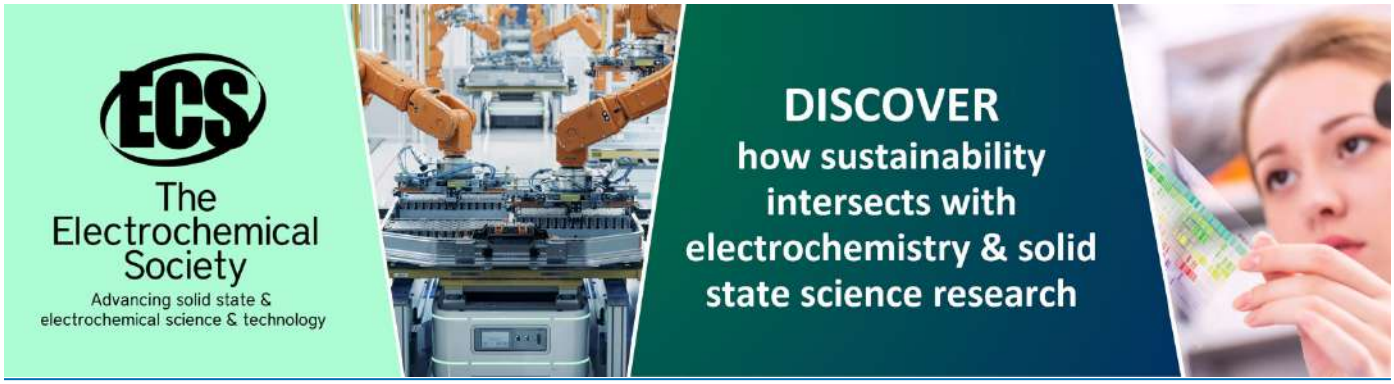

Reduction of Near-End and Far - End Crosstalk in Microwave and Millimetre Wave Band of Parallel Transmission Lines using Meander Shaped DMS

A Gobinath[1,3], N Suresh Kumar[2,3], and P Rajeswari[2,3]

[1]Department of Information Technology
[2]Department of Electronics and Communication Engineering
[3]Velammal College of Engineering and Technology, Madurai

gopigopinath10@gmail.com

Abstract. This research proposes a unique design that makes use of a defective microstrip topology to decrease electromagnetic coupling between parallel high speed interconnects. The performance of this new microstrip construction with defects is evaluated using near-end crosstalk and far-end crosstalk. Serpentine shaped defected microstrip is introduced in one parallel of high speed interconnects and its performance is also compared the existing structure. In this research, the proposed defected microstrip structure (DMS) is simulated and compared with a conventional microstrip structure using Ansoft HFSS software which employs the Finite Element Method (FEM). Simulation results indicate that the DMS design effectively reduces crosstalk in comparison to the previous structure. It reduces more than 5dB near end crosstalk and more than 3dB far end crosstalk compared to conventional model.

1. Introduction

Nowadays, the demand for wireless devices are increasing rapidly since the growth of wireless communication and high speed data transmission increases simultaneously. These devices should have smaller in size and support high data rate. Therefore, it is necessary to accommodate more number of high speed interconnects with in a small feature size which lead to signal integrity problems. High speed interconnect is a conductive path between transmission end to receiving end which is used to carry the high speed signal. Generally, high speed interconnects are modeled as planar transmission lines like microstripline or stripline. Microstripline is generally preferred rather than stripline since low cost and ease of fabrication. In this research, the crosstalk is investigated by considering a duo of coupled microstrip transmission lines. Signal integrity is a measure of quality of signal at the receiver end. When the electrical signal on one transmission line is transferred to an adjacent line, it can cause a range of signal integrity issues. These signal integrity issues include crosstalk, electromagnetic emissions, propagation delay, impedance mismatch, and signal reflection. Crosstalk or coupling is a particularly significant signal integrity concern.

Several scholars have published studies and papers detailing various methods for reducing crosstalk between adjacent transmission lines in high-speed printed circuit boards. The methods presented in literatures are increasing the distance between two lines placing guard trace between two lines, inserting via guard fence, altering the geometry of the microstripline like serpentine and mitered bend lines. However these methods have their own pros and cons. In the literature, authors [1] through [17]

examined numerous methods for reducing crosstalk on printed circuit boards. This proposal presents a defective microstrip design to decrease crosstalk.

2. Defected Microstrip Structure

This research presents a novel approach to reduce crosstalk between high-speed interconnects through the use of a defected microstrip structure (DMS). The DMS is created by etching the microstrip in a specific shape that is tailored to the specific application at hand. The suggested DMS successfully lowers microwave emissions at particular frequencies and displays slow wave propagation characteristics. It offers higher effective inductance and electromagnetic interference noise immunity [1] [2]. When an etched microstrip is excited by a time varying electric field, the electromagnetic field will be concentrated around the conductor strip. A current distribution is disturbed by this structure. A DMS microstrip increases an electric length and also increases the effective inductance and capacitance [5].

Figure 1 shows a parallel microstrip line on a PCB in a non-uniform environment with the top metal layer exposed to air. The lines are parallel as they have the same width (W) throughout their length (L) and are separated by a distance S. The substrate dielectric constant is εr with height H. The thickness T mentioned in Figure 1 represents strip thickness. The transmission characteristics are very much important as the PCB is the support for the whole system. Control of the transmission lines' electrical properties is essential for high-speed systems, especially when taking into account the requirements of new high-speed applications. It depends on the physical dimensions of the interconnects.

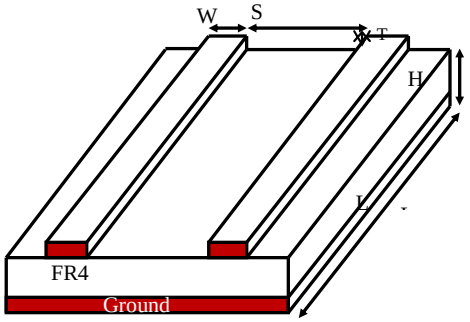

Figure 1 (a). Parallel Microstriplines

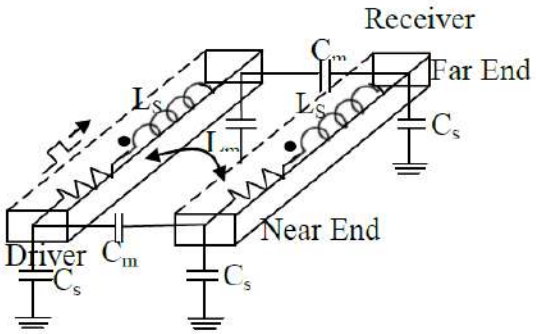

Figure 1(b). Equivalent circuit of Parallel Microstriplines

The level of far-end crosstalk is determined by the mutual capacitive and inductive interactions between long lines. The voltages at the near-end and far-end are determined by these mutual interactions. The capacitive coupling ratio (Cm/CT) is the ratio of mutual capacitance (Cm) to total capacitance (CT), which is the sum of mutual capacitance (Cm) and self-capacitance (Cs). [4].

The equations for the voltage caused by crosstalk at both ends of the affected line are as follows.

$$V_{ne}(t) = \frac{1}{4}\left(\frac{C_m}{C_t} + \frac{L_m}{L_s}\right)\left[V_s(t) - V_s(t - 2T_p)\right] \quad (1)$$

$$V_{fe}(t) = \frac{1}{2}\left(\frac{C_m}{C_t} - \frac{L_m}{L_s}\right)\frac{T_p . dV_s(t - T_p)}{dt} \quad (2)$$

where Vs is the signal source's input voltage.

Electromagnetic coupling is typically represented by near-end crosstalk (NEXT) and far-end crosstalk (FEXT). Crosstalk on the affected line at the end closest to the source is called NEXT, while crosstalk on the affected line at the end farthest away from the source is called FEXT. Additionally, FEXT is proportional to the length of the connected microstrip interconnects. Both mutual inductive and capacitive coupling are proportional to both NEXT and FEXT.[6] [7]

The typical structure of a defective microstrip is shown in Figure 2. (DMS). The suggested DMS design is implemented on a 1.6mm thick and relative permittivity of 4.4, as illustrated in Figure 3. The suggested DMS structure, shown in Figure 4, is etched on parallel transmission lines, as shown in Figure 3.

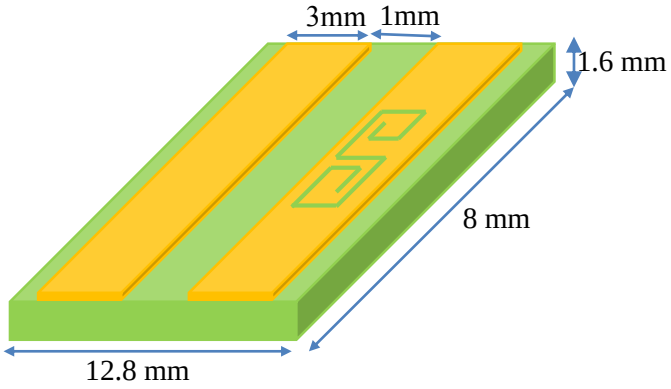

Figure 2. Conventional DMS on Parallel Transmission lines

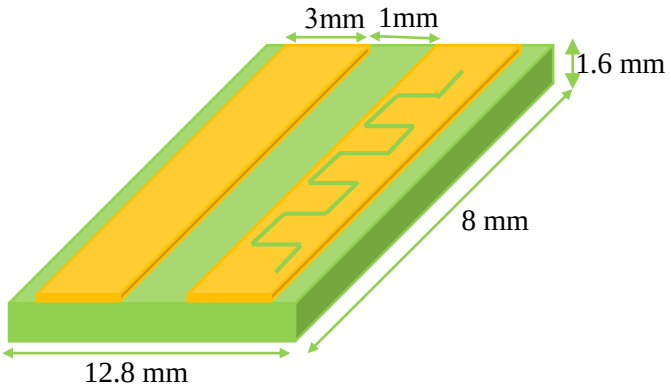

Figure 3. Proposed DMS on Parallel Transmission lines

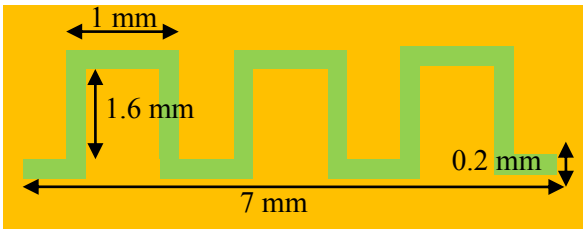

Figure 4. a Proposed DMS Structure

Voltages can be induced on an adjacent line (the victim) when a signal flows on a neighboring line (the aggressor). This is known as crosstalk and can occur if the signals from the two lines mix. Crosstalk is categorized into two types: Far-end crosstalk (FEXT) and near-end crosstalk (NEXT), which occur at the far and near ends of the victim line, respectively. Figure 1(b) shows a circuit of two transmission lines with distributed self-capacitance (Cs), self-inductance (Ls), mutual capacitance (Cm), and mutual inductance (Lm).

The proposed Meander DMS have 3-unit section, each unit section consists of two vertical segments and two horizontal segments, repeated along the length direction. The equivalent circuit model of the proposed structure is given in Figure. 4 (b). The self-capacitance corresponds to the sum of Capacitance whereas self-inductance is the sum of Inductance. Compare with conventional structure Capacitive coupling is increased in the proposed structure due to the potential variation of the structure. It reduces the crosstalk as per the mathematical expressions (1) and (2).

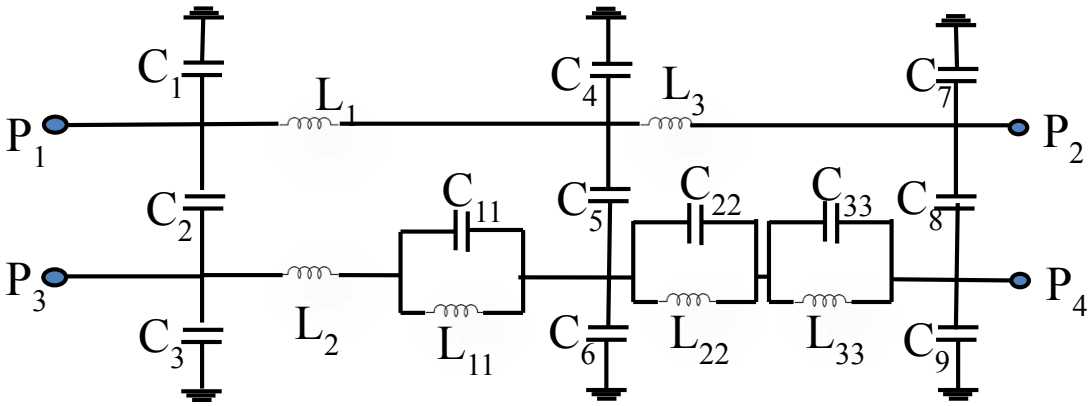

Figure 4. b A diagram showing the circuit model for the proposed meander DMS structure is presented

3. Results and Discussion

The performance of the proposed microstrip line interconnect architecture was analyzed using Ansoft HFSS across a frequency range of 0 to 12 GHz. The microstrip line had a length (L) of 8 mm and a width (W) of 3 mm. The two parallel lines were separated by 1mm, with dielectric constants of r=4.6 and a 1.6 mm thickness of printed circuit board substrate. The serpentine defective microstrip structure had a length of 4mm. The proposed microstrip interconnect with serpentine defective microstrip structure was modified to optimize performance. The structures shown in Figures 2 and 3 were modeled using the HFSS simulation program and their dimensions are also provided.

Utilizing scattering measures like S13 and S14, where S13 stands for near-end crosstalk and S14 for far-end crosstalk, the performance of the structures is assessed. When signal is applied at port1, the crosstalk induced voltage is measured at port 3 and port 4 which are in the adjacent transmission line with DMS structure.

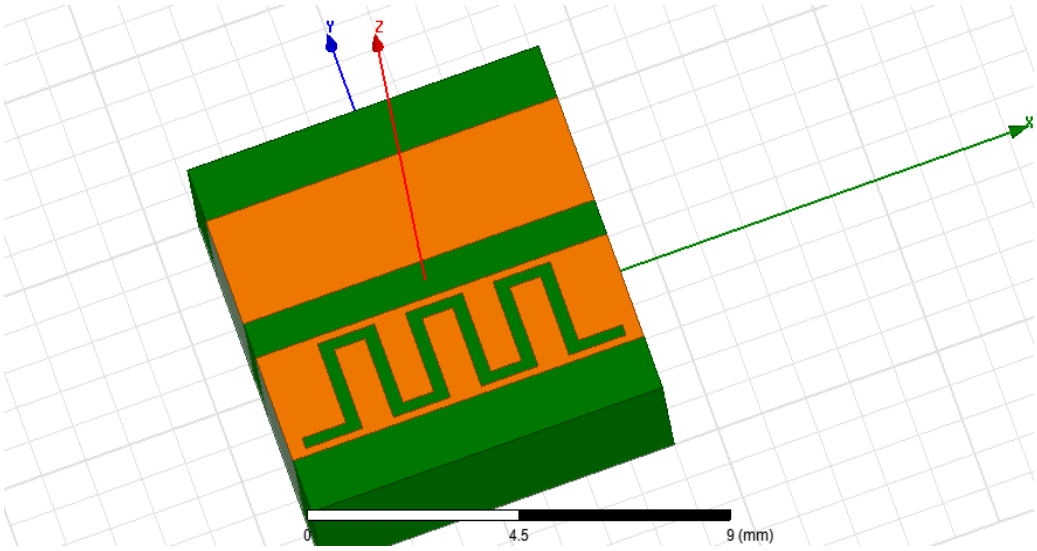

Figure 5. Simulated Structure of Proposed DMS

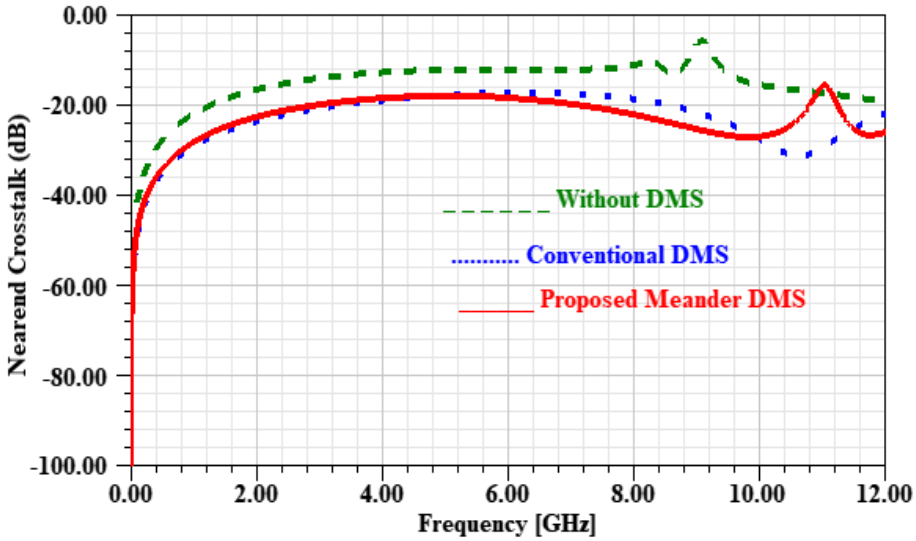

Figure 6. Comparison plot of Near end crosstalk for conventional and proposed DMS structure

Figure 6 represents Near end crosstalk (S13) versus frequency for the conventional and proposed structure. The results show that the proposed DMS structure reduced more than 5dB near end crosstalk compared to conventional DMS structure. And also it indicates that it performed well compared to without DMS structure. The figure 7 illustrates the comparison of far-end crosstalk for the conventional and suggested DMS structures.

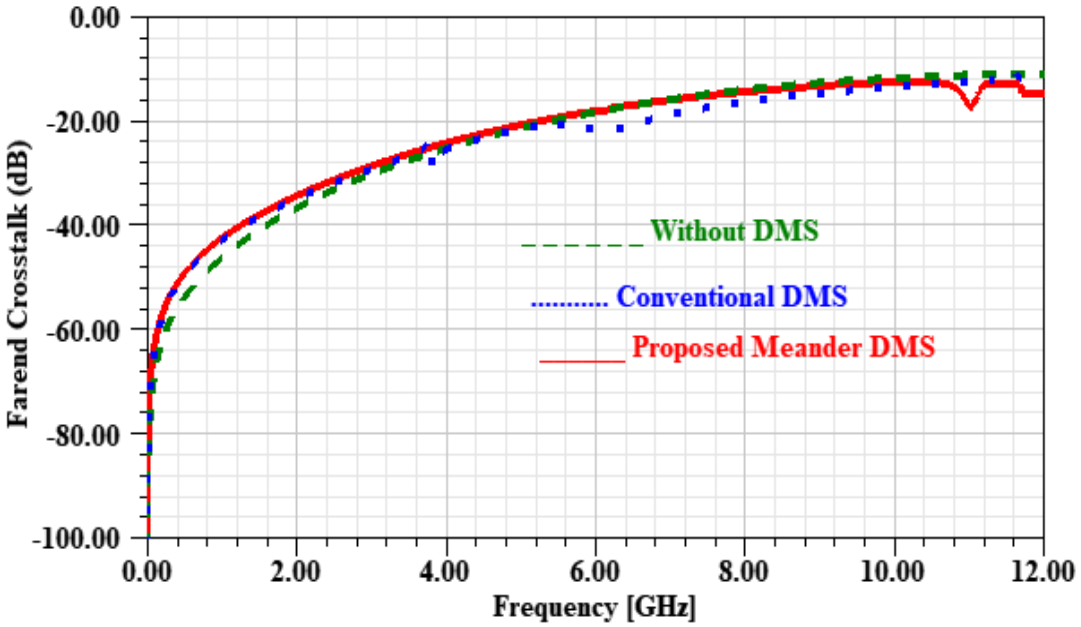

Figure 7. Comparison graph depicting the far-end crosstalk for both the conventional and proposed DMS structures

Table 1 provides a summary of the crosstalk reduction performance of the traditional and proposed DMS structures. It illustrates that the suggested DMS design is more effective in reducing crosstalk when compared to the conventional structure, with a reduction of more than 5 dB in NEXT and 3 dB in FEXT.

Table 1. Performance Comparison of conventional and proposed DMS structure.

Structure	S13 (dB)	S14 (dB)
Without DMS	-19.44	-10.95
Conventional	-21.85	-11.98
Proposed	-26.04	-14.82

4. Conclusion

This research introduces a new DMS design and evaluates its performance. The simulation of this structure is carried out using Ansoft HFSS software. Through an increase in capacitive coupling, the suggested DMS design successfully eliminates more than 3dB of FEXT and more than 5dB of NEXT. Reduced crosstalk is achieved with great efficiency by the suggested DMS structure.

References

[1] R. Malllahzadehh, Ghaasemi, S. Akhlaghi Bayderkhani, 2010 Crosstalk Reduction Using Step Shaped Transmission Line *Progress In Electromagnetic Research* **12** 139-148.
[2] F. D. Mbairi, W. P. Siebert and H. Hesselbom 2008 High-Frequency Transmission Lines Crosstalk Reduction Using Spacing Rules *IEEE Transanctions on Components and Packaging*

Technologies **31** 601-610.
[3] Y. Li, W. Li, Q. Ye, 2013 A reconfigurable triple notch band antenna integrated with defected microstrip structure band-stop filter for ultrawideband cognitive radio applications, *International Journal of Antennas and Propagation.*
[4] P.Rajeswari and S. Raju, 2016 Analytical and experimental study on suppression of electromagnetic interference on high speed printed circuit board for wireless communication systems *International Journal of Wireless Personal Communications, Springer, New York* **89**.
[5] P.Rajeswari and S. Raju, 2015 Comparative study of crosstalk reduction techniques in RF printed circuit board using FDTD method *International Journal of Antennas and Propagation, United States.***2015**
[6] P.Rajeswari and S. Raju, 2012 Comparative study of crosstalk reduction techniques for parallel microstriplines *Lecture Notes on Computer Science* **108** 422-425.
[7] Rajeswari, P, Raju, S, Suresh Kumar, N & Gobinath, A 2016 Far end crosstalk reduction between parallel microstriplines using U shaped guard trace *ARPN Journal of Engineering and Applied Sciences* **11** 3081-3085.
[8] Rajeswari, P, Raju, S, Divya Poornima, M, Sudharsana, R & Gobinath A, 2015 Signal integrity analysis of high speed interconnects in SATA connector *International Journal of Applied Engineering Research* **10**18007-18014.
[9] Rajeswari P Raju S Suresh Kumar, N Gobinath, A, 2015 Crosstalk reduction on coupled microstrip to three-line coupled microstrip transition using mitering configuration *International Journal of Applied Engineering Research* **10** 7923-7936.

DE GRUYTER

Requires Authentication | Published by **De Gruyter** | February 16, 2024

Revolutionizing healthcare with metamaterial-enhanced antennas: a comprehensive review and future directions

Sakthi Preetha Asokan and Kavitha Kaliappan

From the journal Frequenz
https://doi.org/10.1515/freq-2023-0236

Abstract

The state of the art for wearable antennas for wireless communication and biological applications is compiled in this article. It addresses a wide range of subjects, such as how to use novel materials like Artificial Magnetic Conductors (AMC) and Metamaterial (MTM) structures to enhance antenna performance. It also covers the design of dual-band and reconfigurable antennas and the use of machine learning to optimize aerial design. The main subject of this article is how wearable antennas could lead to advancements in wireless communication and healthcare in the future, perhaps improving lives worldwide. It includes implantable antennas, textile-based antennas, and various flexible graphene-based antenna varieties. The use of wearable antennas for brain stroke diagnostics, wireless body area networks, telemedicine, and breast imaging is covered in this study. Additionally covered are reconfigurable antennas based on Metamaterial (MTM)structures and Wideband on-body antennas inspired by Metamaterials (MTM), both of these applications are useful in the assembly of wearable antennas, which is the main goal of this work. The research also discusses how metamaterials (MTM) might raise the sensitivity of the bioelectric field, enabling precise bioelectric signal monitoring. Metamaterial (MTM) antennas function reliably in a range of biomedical applications and can adjust to the electromagnetic properties.

Keywords: metamaterial structures; dual-band antennas; reconfigurable antennas; textile-based antennas; implantable antennas; wireless body area networks (WBAN)

Corresponding author: Sakthi Preetha Asokan, Department of Electronics and Communication Engineering, Centre of RF circuits and Antenna Design,

Velammal College of Engineering and Technology, Madurai, India, E-mail: preethaasokan12@gmail.com

Acknowledgments

I am submitting the REVISED manuscript titled "Revolutionizing Healthcare with Metamaterial-Enhanced Antennas: A Comprehensive Review and Future Directions" for consideration in FREQUENZ. I am deeply grateful to my supervisor and Velammal College of Engineering, Madurai for their valuable contributions and support during this research. Their contributions in guidance, insights, resources greatly enriched the study. Additionally, I extend my thanks to friends for their constructive feedback and encouragement and authors have approved the final version for submission. We hope our work will be a valuable addition to FREQUENZ and contribute to Antenna Design Field. Thank you for your consideration.

Research ethics: Not applicable.

Author contributions: Authors initiated and conceptualized the survey study on metamaterial antennas for biomedical applications and conducted the literature review and data collection. All authors critically reviewed and approved the final manuscript.

Competing interests: The authors state no conflict of interest.

Research funding: None declared.

Data availability: The raw data can be obtained on request from the corresponding author.

References

[1] S. M. Saeed, C. A. Balanis, C. R. Birtcher, A. C. Durgun, and H. N. Shaman, "Wearable flexible reconfigurable antenna integrated with the artificial magnetic conductor," *IEEE Antennas and Wireless Propag. Lett.*, vol. 16, pp. 2396–2399, 2017, https://doi.org/10.1109/lawp.2017.2720558 (https://doi.org/10.1109/lawp.2017.2720558) .

[2] K. Sajith, J. Gandhimohan, and T. Shanmuganantham, "A novel SRR-loaded asymmetrical CPW-fed ISM band wearable antenna for health monitoring applications," *2017 IEEE Applied Electromagnetics Conference (AEMC)*, IEEE, 2017, pp. 1–2. 10.1109/AEMC.2017.8325640 (https://doi.org/10.1109/AEMC.2017.8325640)

[3] R. El Arif, M. C. Tang, W. C. Su, T. S. Horng, F. K. Wang, and C. H. Tseng, "Designing a metasurface-based tag antenna for wearable vital sign sensors," *2019 IEEE MTT-S International Microwave Symposium (IMS)*, IEEE, 2019, pp. 373–376. 10.1109/MWSYM.2019.8700933 (https://doi.org/10.1109/MWSYM.2019.8700933)

[4] B. Ali Esmail et al.., "The reconfigurable radiation pattern of the planar antenna using metamaterial for 5G applications," *Materials*, vol. 13, no. 3, p. 582, 2020, https://doi.org/10.3390/ma13030582 (https://doi.org/10.3390/ma13030582) .

PubMed (https://pubmed.ncbi.nlm.nih.gov/31991912/)
PubMed Central (https://www.ncbi.nlm.nih.gov/pmc/articles/PMC7040675/)

[5] A. Dey, S. Bhattacharjee, S. B. Chaudhuri, and M. Mitra, "A dual-band flexible antenna on AMC ground for wearable applications," *2019 IEEE Asia-Pacific Microwave Conference (APMC)*, IEEE, 2019, pp. 607–609. 10.1109/APMC46564.2019.9038804 (https://doi.org/10.1109/APMC46564.2019.9038804)

[6] H. Yalduz, T. E. Tabaru, V. T. Kilic, and M. Turkmen, "Design and analysis of low profile and low SAR full-textile UWB wearable antenna with metamaterial for WBAN applications," *AEU Int. J. Electron. Commun.*, vol. 126, 2020, Art. no. 153465, https://doi.org/10.1016/j.aeue.2020.153465 (https://doi.org/10.1016/j.aeue.2020.153465) .

[7] A. R. Alhawari et al.., "Wearable metamaterial dual-polarized high isolation UWB MIMO Vivaldi antenna for 5G and satellite communications," *Micromachines*, vol. 12, no. 12, p. 1559, 2021, https://doi.org/10.3390/mi12121559 (https://doi.org/10.3390/mi12121559) .

PubMed (https://pubmed.ncbi.nlm.nih.gov/34945409/)
PubMed Central (https://www.ncbi.nlm.nih.gov/pmc/articles/PMC8706994/)

[8] L. K. Balaji Vignesh and Dr. K. Kavitha, *A Survey on Fractal Antenna Design*, Research Gate, publication, 2018, p. 344319320.

[9] M. El Atrash, M. A. Abdalla, and H. M. Elhennawy, "A compact highly efficient Π-section CRLH antenna loaded with textile AMC for wireless body area network applications," *IEEE Trans. Antennas Propag.*, vol. 69, no. 2, pp. 648–657, 2020, https://doi.org/10.1109/tap.2020.3010622 (https://doi.org/10.1109/tap.2020.3010622) .

[10] M. Wang et al.., "Investigation of SAR reduction using a flexible antenna with metamaterial structure in wireless body area network," *IEEE Trans. Antennas Propag.*, vol. 66, no. 6, pp. 3076–3086, 2018, https://doi.org/10.1109/tap.2018.2820733 (https://doi.org/10.1109/tap.2018.2820733) .

[11] Z. H. Jiang, D. E. Brocker, P. E. Sieber, and D. H. Werner, "A compact, low-profile metasurface-enabled antenna for wearable medical body-area network devices," *IEEE Trans. Antennas Propag.*, vol. 62, no. 8, pp. 4021–4030, 2014, https://doi.org/10.1109/tap.2014.2327650 (https://doi.org/10.1109/tap.2014.2327650) .

[12] K. Zhang, G. A. Vandenbosch, and S. Yan, "A novel design approach for compact wearable antennas based on metasurfaces," *IEEE Trans. Biomed. Circuits Syst.*, vol. 14, no. 4, pp. 918–927, 2020, https://doi.org/10.1109/tbcas.2020.3010259 (https://doi.org/10.1109/tbcas.2020.3010259) .

[13] A. Y. Ashyap et al.., "Compact and low-profile textile EBG-based antenna for wearable medical applications," *IEEE Antennas Wireless Propag. Lett.*, vol. 16, pp. 2550–2553, 2017, https://doi.org/10.1109/lawp.2017.2732355 (https://doi.org/10.1109/lawp.2017.2732355) .

[14] N. R. Rishani, R. M. Shubair, and G. Aldabbagh, "On the design of wearable and epidermal antennas for emerging medical applications," *2017 Sensors Networks Smart and Emerging Technologies (SENSET)*, IEEE, 2017, pp. 1–4. 10.1109/SENSET.2017.8125046 (https://doi.org/10.1109/SENSET.2017.8125046)

[15] P. Rahmatian, M. Movahhedi, and A. Ghafoorzadeh-Yazdi, "Dual-band dual-mode wearable antenna for on-off body communication based on metamaterial," *Electrical Engineering (ICEE), Iranian Conference*, IEEE, 2018, pp. 649–653. 10.1109/ICEE.2018.8472524 (https://doi.org/10.1109/ICEE.2018.8472524)

[16] K. Hossain et al.., "ENG and NZRI characteristics of decagonal-shaped metamaterial for wearable applications," *2020 International Conference on UK-China Emerging Technologies (UCET)*, IEEE, 2020, pp. 1–4. 10.1109/UCET51115.2020.9205409 (https://doi.org/10.1109/UCET51115.2020.9205409)

[17] A. A. Althuwayb et al.., "Metasurface-inspired flexible wearable MIMO antenna array for wireless body area network applications and biomedical telemetry devices," *IEEE Access*, vol. 11, pp. 1039–1056, 2022, https://doi.org/10.1109/access.2022.3233388 (https://doi.org/10.1109/access.2022.3233388) .

[18] S. Yan and G. A. Vandenbosch, "Radiation pattern-reconfigurable wearable antenna based on metamaterial structure," *IEEE Antennas Wireless Propag. Lett.*, vol. 15, pp. 1715–1718, 2016, https://doi.org/10.1109/lawp.2016.2528299 (https://doi.org/10.1109/lawp.2016.2528299) .

[19] X. Hu, S. Yan, J. Zhang, and G. A. Vandenbosch, "Wearable button antenna with circular polarization," *2020 International Workshop on Antenna Technology (iWAT)*, IEEE, 2020, pp. 1–3. 10.1109/iWAT48004.2020.1570609726 (https://doi.org/10.1109/iWAT48004.2020.1570609726)

[20] A. S. Alqadami, K. S. Bialkowski, A. T. Mobashsher, and A. M. Abbosh, "Wearable electromagnetic head imaging system using flexible wideband antenna array based on polymer technology for brain stroke diagnosis," *IEEE Trans. Biomed. Circuits Syst.*, vol. 13, no. 1, pp. 124–134, 2018, https://doi.org/10.1109/tbcas.2018.2878057 (https://doi.org/10.1109/tbcas.2018.2878057) .

PubMed (https://pubmed.ncbi.nlm.nih.gov/30369449/)

[21] S. Mohandoss, R. R. Thipparaju, B. N. B. Reddy, S. K. Palaniswamy, and P. Marudappa, "Fractal-based ultra-wideband antenna development for wireless personal area communication applications," *AEU Int. J. Electron. Commun.*, vol. 93, pp. 95–102, 2018, https://doi.org/10.1016/j.aeue.2018.06.009 (https://doi.org/10.1016/j.aeue.2018.06.009) .

[22] U. R. Khan, J. A. Sheikh, S. Bashir, and S. Ahmed, "Metamaterial-inspired wideband on-body antenna design for biomedical applications," *Mater. Today: Proc.*, vol. 80, no. Part 3, pp. 1772–1776, 2021. 10.1016/j.matpr.2021.05.602 (https://doi.org/10.1016/j.matpr.2021.05.602)

[23] A. Saidi, K. Nouri, B. S. Bouazza, K. Becharef, A. Cherifi, and T. Abes, "E-shape metamaterials embedded implantable antenna for ISM-band biomedical applications," *Res. Biomed. Eng.*, vol. 38, no. 2, pp. 351–368, 2022, https://doi.org/10.1007/s42600-021-00191-y (https://doi.org/10.1007/s42600-021-00191-y).

[24] A. Al-Adhami and E. Ercelebi, "A flexible metamaterial-based printed antenna for wearable biomedical applications," *Sensors*, vol. 21, no. 23, p. 7960, 2021, https://doi.org/10.3390/s21237960 (https://doi.org/10.3390/s21237960).

PubMed (https://pubmed.ncbi.nlm.nih.gov/34883966/)
PubMed Central (https://www.ncbi.nlm.nih.gov/pmc/articles/PMC8659625/)

[25] M. Al Gburi and M. Ilyas, "A novel design reconfigurable antenna based on the metamaterial for wearable applications," *J. Phys.: Conf. Ser.*, vol. 1973, 2021, Art. no. 012042, IOP Publishing, https://doi.org/10.1088/1742-6596/1973/1/012042 (https://doi.org/10.1088/1742-6596/1973/1/012042).

[26] S. K. Patel, J. Surve, V. Katkar, and J. Parmar, "Machine learning assisted metamaterial-based reconfigurable antenna for low-cost portable electronic devices," *Sci. Rep.*, vol. 12, no. 1, pp. 1–13, 2022, https://doi.org/10.1038/s41598-022-16678-2 (https://doi.org/10.1038/s41598-022-16678-2).

PubMed (https://pubmed.ncbi.nlm.nih.gov/35854049/)
PubMed Central (https://www.ncbi.nlm.nih.gov/pmc/articles/PMC9296536/)

[27] S. Roy and U. Chakraborty, "Metamaterial-based dual wideband wearable antenna for wireless applications," *Wireless Personal Commun.*, vol. 106, no. 3, pp. 1117–1133, 2019, https://doi.org/10.1007/s11277-019-06206-3 (https://doi.org/10.1007/s11277-019-06206-3).

[28] J. Zhang et al.., "Flexible graphene-assembled film-based antenna for the wireless wearable sensor with miniaturized size and high sensitivity," *ACS Omega*, vol. 5, no. 22, pp. 12937–12943, 2020, https://doi.org/10.1021/acsomega.0c00263 (https://doi.org/10.1021/acsomega.0c00263).

PubMed (https://pubmed.ncbi.nlm.nih.gov/32548477/)
PubMed Central (https://www.ncbi.nlm.nih.gov/pmc/articles/PMC7288573/)

[29] K. Zhang, P. J. Soh, and S. Yan, "Meta-wearable antennas – a review of metamaterial-based antennas in wireless body area networks," *Materials*, vol. 14, no. 1, p. 149, 2020, https://doi.org/10.3390/ma14010149 (https://doi.org/10.3390/ma14010149).

PubMed (https://pubmed.ncbi.nlm.nih.gov/33396333/)
PubMed Central (https://www.ncbi.nlm.nih.gov/pmc/articles/PMC7795164/)

[30] A. R. Alhawari, A. H. M. Almawgani, A. T. Hindi, H. Alghamdi, and T. Saeidi, "Metamaterial-based wearable flexible elliptical UWB antenna for WBAN and breast imaging applications," *AIP Adv.*, vol. 11, no. 1, 2021, Art. no. 015128, https://doi.org/10.1063/5.0037232 (https://doi.org/10.1063/5.0037232) .

[31] H. R. Raad, A. I. Abbosh, H. M. Al-Rizzo, and D. G. Rucker, "Flexible and compact AMC-based antenna for telemedicine applications," *IEEE Trans. Antennas Propag.*, vol. 61, no. 2, pp. 524–531, 2012, https://doi.org/10.1109/tap.2012.2223449 (https://doi.org/10.1109/tap.2012.2223449) .

[32] A. Razak, M. K. A. Rahim, H. A. Majid, and N. A. Murad, "Frequency reconfigurable epsilon negative metamaterial antenna," *Int. J. Electr. Comput. Eng.*, vol. 7, no. 3, p. 1473, 2017, https://doi.org/10.11591/ijece.v7i3.pp1473-1479 (https://doi.org/10.11591/ijece.v7i3.pp1473-1479) .

[33] D. Negi, R. Khanna, and J. Kaur, "Design and performance analysis of a conformal CPW fed wideband antenna with Mu-Negative metamaterial for wearable applications," *Int. J. Microwave Wireless Technol.*, vol. 11, no. 8, pp. 806–820, 2019, https://doi.org/10.1017/s1759078719000497 (https://doi.org/10.1017/s1759078719000497) .

[34] M. Mustaqim, B. A. Khawaja, H. T. Chattha, K. Shafique, M. J. Zafar, and M. Jamil, "Ultra-wideband antenna for wearable Internet of Things devices and wireless body area network applications," *Int. J. Numer. Model.: Electron. Netw Devices Fields*, vol. 32, no. 6, 2019, Art. no. e2590, https://doi.org/10.1002/jnm.2590 (https://doi.org/10.1002/jnm.2590) .

Received: 2023-07-28
Accepted: 2024-01-19
Published Online: 2024-02-16
Published in Print: 2024-06-25

— *or* —

From the journal

Frequenz
Volume 78 Issue 5-6

Articles in the same Issue

Gain enhancement in octagonal shaped frequency reconfigurable antenna using metasurface superstrate

High gain and high-efficiency compact resonator antennas based on spoof surface plasmon polaritons

Gain enhancement of ultra-wideband hexagonal slot antenna using tessellated rhombic loops based reflector

Terahertz MIMO antenna array for future generation of wireless applications

DE GRUYTER

Requires Authentication | Published by De Gruyter | May 29, 2023

SAR reduction techniques for WBAN and mobile applications

Vijay Gokul Selva Rajan, Kavitha Kaliappan and Suresh Kumar Natarajan

From the journal Frequenz
https://doi.org/10.1515/freq-2022-0297

Abstract

In recent years there has been a substantial growth in the usage of wireless gadgets in various fields like mobile communication, health monitoring, warfare communications, etc. However, the performance of the antenna is evaluated by the parameters like gain, directivity and bandwidth, VSWR and is enhanced as a continuous process. But on the other side, Specific Absorption Rate (SAR) is a parameter that is likely to be watched out for the safety concern which should be as low as possible for any antenna to ensure the minimum risk to human health. Many researchers have contributed an enormous amount of work to the SAR reduction. From this perspective, this work proposes a brief survey on low SAR antennas. An optimal low SAR antenna needs a perfect lossless impedance matching over a lossy medium (human body) for the eradication of spurious surface waves. The deployment of SAR reduction strategies, outcomes of the design, and open-end research challenges with the relative results are addressed as a part of the survey. The core impulse of this work is to induct the antenna designers to get indulged in designing low SAR antenna with enhanced performance for several WBAN applications like health monitoring and many more.

Keywords: artificial magnetic conductor; defected ground plane; electronic band gap; meta structures; SAR reduction

Corresponding author: Vijay Gokul Selva Rajan, Department of Electronics and Communication Engineering, Velammal College of Engineering and Technology, Madurai, Tamil Nadu, India, E-mail: svgmdu@gmail.com

Author contribution: All the authors have accepted responsibility for the entire content of this submitted manuscript and approved submission.

Research funding: None declared.

Conflict of interest statement: The authors declare no conflicts of interest regarding this article.

References

[1] R. Dasand and H. Yoo, "Application of a compact electromagnetic bandgap array in a phone case for suppression of mobile phone radiation exposure," *IEEE Trans. Microw. Theor. Tech.*, vol. 66, no. 5, pp. 2363–2372, 2018, https://doi.org/10.1109/tmtt.2017.2786287 (https://doi.org/10.1109/tmtt.2017.2786287) .

[2] K.-H. Chan, R. Ikeuchi, and A. Hirata, "Effects of phase difference in dipole phased-array antenna above EBG substrates on SAR," *IEEE Antenn. Wireless Propag. Lett.*, vol. 12, pp. 579–582, 2013, https://doi.org/10.1109/lawp.2013.2260717 (https://doi.org/10.1109/lawp.2013.2260717) .

[3] H. Li, A. Tsiaras, and B. K. Lau, "Analysis and estimation of MIMO-SAR for multi-antenna mobile handsets," *IEEE Trans. Antenn. Propag.*, vol. 65, no. 3, pp. 1522–1527, 2017, https://doi.org/10.1109/tap.2016.2647708 (https://doi.org/10.1109/tap.2016.2647708) .

[4] K. S. Sultan, H. H. Abdullah, E. A. Abdallah, and E. A. Hashish, "Low SAR, miniaturized printed antenna for mobile, ISM, and WLAN services," *IEEE Antenn. Wireless Propag. Lett.*, vol. 12, pp. 1106–1109, 2013, https://doi.org/10.1109/lawp.2013.2280955 (https://doi.org/10.1109/lawp.2013.2280955) .

[5] H. H. Zhang, G. G. Yu, Y. Liu, Y. X. Fang, G. Shi, and S. Wang, "Design of low-SAR mobile phone antenna: theory and applications," *IEEE Trans. Antenn. Propag.*, vol. 69, no. 2, pp. 698–707, 2021, https://doi.org/10.1109/tap.2020.3016420 (https://doi.org/10.1109/tap.2020.3016420) .

[6] B. Lu, B. Pang, W. Hu, and W. Jiang, "Low-SAR antenna design and implementation for mobile phone applications," *IEEE Access*, vol. 9, pp. 96444–96452, 2021, https://doi.org/10.1109/access.2021.3093720 (https://doi.org/10.1109/access.2021.3093720) .

[7] J. Bangand and J. Choi, "A SAR reduced mm-wave beam-steerable array antenna with dual-mode operation for fully metal-covered 5G cellular handsets," *IEEE Antenn. Wireless Propag. Lett.*, vol. 17, no. 6, pp. 1118–1122, 2018, https://doi.org/10.1109/lawp.2018.2836196 (https://doi.org/10.1109/lawp.2018.2836196) .

[8] Z.-Q. Xu, Q.-Q. Zhou, Y.-L. Ban, and S. S. Ang, "Hepta- band coupled-fed loop antenna for LTE/WWAN unbroken metal-rimmed smart phone applications," *IEEE Antenn. Wireless Propag. Lett.*, vol. 17, no. 2, pp. 311–314, 2018, https://doi.org/10.1109/lawp.2017.2787863 (https://doi.org/10.1109/lawp.2017.2787863) .

[9] D. Huang, Z. w. Du, and Y. Wang, "A quad-antenna system for 4G/5G/GPS metal frame mobile phones," *IEEE Antenn. Wireless Propag. Lett.*, vol. 18, no. 8, pp. 1586–1590, 2019, https://doi.org/10.1109/lawp.2019.2924322 (https://doi.org/10.1109/lawp.2019.2924322) .

[10] Y. Liu, J. Zhang, A. Ren, H. Wang, and C.-Y.-D. Sim, "TCM-based hepta-band antenna with small clearance for metal-rimmed mobile phone applications," *IEEE Antenn. Wireless Propag. Lett.*, vol. 18, no. 4, pp. 717–721, 2019, https://doi.org/10.1109/lawp.2019.2901808 (https://doi.org/10.1109/lawp.2019.2901808).

[11] H. Wang, "Analysis of electromagnetic energy absorption in the human body for mobile terminals," *IEEE Open J. Antenn. Propag.*, vol. 1, no. 1, pp. 113–117, 2020, https://doi.org/10.1109/ojap.2020.2982507 (https://doi.org/10.1109/ojap.2020.2982507).

[12] J. Khan, D. Ali Sehrai, and U. Ali, "Design of dual band 5G antenna array with SAR analysis for future mobile handsets," *J. Electr. Eng. Technol.*, vol. 14, no. 2, pp. 809–816, 2019, https://doi.org/10.1007/s42835-018-00059-9 (https://doi.org/10.1007/s42835-018-00059-9).

[13] H. Ben Hamadi, S. Ghnimi, L. Latrach, P. Benech, and A. Gharsallah, "New design of multi-band PIFA antenna with reduced SAR for mobile and wireless applications," *Wireless Pers. Commun.*, vol. 115, no. 2, pp. 1211–1226, 2020, https://doi.org/10.1007/s11277-020-07619-1 (https://doi.org/10.1007/s11277-020-07619-1).

[14] N. Nasser, D. Serhal, R. Barake, M. Rammal, and P. Vaudon, "A novel low SAR water-based mobile handset antenna," *Analog Integr. Circuits Signal Process.*, vol. 96, no. 2, pp. 353–361, 2018, https://doi.org/10.1007/s10470-018-1130-8 (https://doi.org/10.1007/s10470-018-1130-8).

[15] T. Ramachandran, M. R. I. Faruque, E. Ahamed, and S. Abdullah, "Specific absorption rate reduction of multi split square ring metamaterial for L- and S-band application," *Results Phys.*, vol. 15, p. 102668, 2019, https://doi.org/10.1016/j.rinp.2019.102668 (https://doi.org/10.1016/j.rinp.2019.102668).

[16] A. A. Al-Ghamdi, O. A. Al-Hartomy, F. R. Al-Solamy, N. T. Dishovskyc, N. T. Atanasov, and G. L. Atanasova, "Enhancing antenna performance and SAR reduction by a conductive composite loaded with carbon-silica hybrid filler," *AEU - Int. J. Electron. Commun.*, vol. 72, pp. 184–191, 2017, https://doi.org/10.1016/j.aeue.2016.12.013 (https://doi.org/10.1016/j.aeue.2016.12.013).

[17] A. M. Tamim, M. R. I. Faruque, M. U. Khandaker, M. T. Islam, and D. A. Bradley, "Electromagnetic radiation reduction using novel metamaterial for cellular applications," *Radiat. Phys. Chem.*, vol. 178, p. 108976, 2021, https://doi.org/10.1016/j.radphyschem.2020.108976 (https://doi.org/10.1016/j.radphyschem.2020.108976).

[18] A. M. Ali, M. A. Al Ghamdi, M. M. Iqbal, S. Khalid, H. Aldabbas, and S. Saeed, "Next generation UWB antennas gadgets for human health care using SAR," *EURASIP J. Wirel. Commun. Netw.*, vol. 2021, no. 1, 2021, https://doi.org/10.1186/s13638-021-01906-6 (https://doi.org/10.1186/s13638-021-01906-6).

[19] B. P. Nadh, B. T. P. Madhav, and M. Siva Kumar, "Design and analysis of dual band implantable DGS antenna for medical applications," *EURASIP J. Wirel. Commun. Netw.*, vol. 2021, p. 33, 2021.

[20] V. Karthik and T. Rama Rao, "Investigations on SAR and thermal effects of a body wearable microstrip antenna," *Wireless Pers. Commun.*, vol. 96, no. 3, pp. 3385–3401, 2017, https://doi.org/10.1007/s11277-017-4059-9 (https://doi.org/10.1007/s11277-017-4059-9) .

[21] C.-L. Tsai, K.-W. Chen, and C.-L. Yang, "Implantable wideband low-SAR antenna with C-shaped coupled ground," *IEEE Antenn. Wireless Propag. Lett.*, vol. 14, pp. 1594–1597, 2015, https://doi.org/10.1109/lawp.2015.2413839 (https://doi.org/10.1109/lawp.2015.2413839) .

[22] T. Mary Neebha, M. Nesasudha, and D. K. Janapala, "A stable miniaturised AMC loaded flexible monopole antenna for ingestible applications," *Comput. Biol. Med.*, vol. 116, p. 103578, 2020, https://doi.org/10.1016/j.compbiomed.2019.103578 (https://doi.org/10.1016/j.compbiomed.2019.103578) .

PubMed (https://pubmed.ncbi.nlm.nih.gov/31999556/)

[23] B. Yin, J. Gu, X. Feng, B. Wang, Y. Yu, and W. Ruan, "A low SAR value wearable antenna for wireless body area network based on AMC structure," *Prog. Electromagn. Res.*, vol. 95, pp. 119–129, 2019, https://doi.org/10.2528/pierc19040103 (https://doi.org/10.2528/pierc19040103) .

[24] Al-Adhami, A. and Ercelebi, E., "A flexible metamaterial based printed antenna for wearable biomedical applications," *Sensors*, vol. 21, no. 23, pp. 1–18, 2021. https://doi.org/10.3390/s21237960 (https://doi.org/10.3390/s21237960) .

PubMed (https://pubmed.ncbi.nlm.nih.gov/34883966/)
PubMed Central (https://www.ncbi.nlm.nih.gov/pmc/articles/PMC8659625/)

[25] M. El Atrash, M. A. Abdalla, and H. M. Elhennawy, "A wearable dual-band low profile high gain low SAR antenna AMC-backed for WBAN applications," *IEEE Trans. Antenn. Propag.*, vol. 67, no. 10, pp. 6378–6388, 2019, https://doi.org/10.1109/tap.2019.2923058 (https://doi.org/10.1109/tap.2019.2923058) .

[26] M. Wang, Z. Yang, J. Wu, et al.., "Investigation of SAR reduction using flexible antenna with metamaterial structure in wireless body area network," *IEEE Trans. Antenn. Propag.*, vol. 66, no. 6, pp. 3076–3086, 2018, https://doi.org/10.1109/tap.2018.2820733 (https://doi.org/10.1109/tap.2018.2820733) .

[27] H. Yalduz, T. E. Tabaru, V. T. Kilic, and M. Turkmen, "Design and analysis of low profile and low SAR full-textile UWB wearable antenna with metamaterial for WBAN applications," *AEU - Int. J. Electron. Commun.*, vol. 126, p. 153465, 2020, https://doi.org/10.1016/j.aeue.2020.153465 (https://doi.org/10.1016/j.aeue.2020.153465) .

[28] U. Ali, S. Ullah, J. Khan, et al.., "Design and SAR analysis of wearable antenna on various parts of human body, using conventional and artificial ground planes," *J. Electr. Eng. Technol.*, vol. 12, no. 1, pp. 317–328, 2017, https://doi.org/10.5370/jeet.2017.12.1.317

(https://doi.org/10.5370/jeet.2017.12.1.317) .

[29] M. El Atrash, O. F. Abdalgalil, I. S. Mahmoud, M. A. Abdalla, and S. R. Zahran, "Wearable high gain low SAR antenna loaded with backed all-textile EBG for WBAN applications," *IET Microw. Antenn. Propag.*, vol. 14, no. 8, pp. 791–799, 2020, https://doi.org/10.1049/iet-map.2019.1089 (https://doi.org/10.1049/iet-map.2019.1089) .

[30] N. Ramanpreet, M. Rattan, and S. S. Gill, "Compact and low profile planar antenna with novel metastructure for wearable MBAN devices," *Wireless Pers. Commun.*, vol. 118, no. 4, pp. 3335–3347, 2021, https://doi.org/10.1007/s11277-021-08182-z (https://doi.org/10.1007/s11277-021-08182-z) .

[31] M. Munde, A. Nandgaonkar, and S. Deosarkar, "Low specific absorption rate antenna using electromagnetic band gap structure for long term evolution band 3 application," *Prog. Electromagn. Res.*, vol. 80, pp. 23–34, 2019, https://doi.org/10.2528/pierm18102103 (https://doi.org/10.2528/pierm18102103) .

[32] M. El Atrash, M. A. Abdalla, and H. M. Elhennawy, "Gain enhancement of a compact thin flexible reflector-based asymmetric meander line antenna with low SAR," *IET Microw. Antenn. Propag.*, vol. 13, no. 6, pp. 827–832, 2019, https://doi.org/10.1049/iet-map.2018.5397 (https://doi.org/10.1049/iet-map.2018.5397) .

[33] Z. H. Jiang, D. E. Brocker, P. E. Sieber, and D. H. Werner, "A compact, low-profile metasurface-enabled antenna for wearable medical body-area network devices," *IEEE Trans. Antenn. Propag.*, vol. 62, no. 8, pp. 4021–4030, 2014, https://doi.org/10.1109/tap.2014.2327650 (https://doi.org/10.1109/tap.2014.2327650) .

[34] Rubesh Kumar, T. and Madhavan, M., "Hybrid fabric wearable antenna design and evaluation for high speed 5G applications," *Wireless Pers. Commun.*, vol. 127, no. 2, pp. 1517–1528, 2021. https://doi.org/10.1007/s11277-021-08702-x (https://doi.org/10.1007/s11277-021-08702-x) .

[35] A. Shah and P. Patel, "E-textile slot antenna with spurious mode suppression and low SAR for medical wearable applications," *J. Electromagn. Waves Appl.*, vol. 35, no. 16, pp. 2224–2238, 2021, https://doi.org/10.1080/09205071.2021.1934905 (https://doi.org/10.1080/09205071.2021.1934905) .

[36] B. Sugumaran, R. B. subramanian, and S. K. Palaniswamy, "Reduced specific absorption rate compact flexible monopole antenna system for smart wearable wireless communications," *Eng. Sci. Technol. Int. J.*, vol. 24, no. 3, pp. 682–693, 2021, https://doi.org/10.1016/j.jestch.2020.12.012 (https://doi.org/10.1016/j.jestch.2020.12.012) .

[37] S. Rajebi, C. Ghobadi, J. Nourinia, and E. Mostafapour, "SAR enhancement of slot microstrip antenna by using silicon layer in hyperthermia applications," *Wireless Pers. Commun.*, vol. 111, no. 3, pp. 1761–1774, 2020, https://doi.org/10.1007/s11277-019-06955-1 (https://doi.org/10.1007/s11277-019-06955-1) .

[38] Tu. T. Le and T.-Y. Yun, "Wearable dual-band high-gain low-SAR antenna for off-body communication," *IEEE Antenn. Wireless Propag. Lett.*, vol. 20, no. 7, pp. 1175–1179, 2021, https://doi.org/10.1109/lawp.2021.3074641 (https://doi.org/10.1109/lawp.2021.3074641) .

[39] A. Amsaveni, M. Bharathi, and J. N. Swaminathan, "Design and performance analysis of low SAR hexagonal slot antenna using cotton substrate," *Microsyst. Technol.*, vol. 25, no. 6, pp. 2273–2278, 2019, https://doi.org/10.1007/s00542-018-4109-6 (https://doi.org/10.1007/s00542-018-4109-6) .

[40] J. Trajkovikj and A. K. Skrivervik, "Diminishing SAR for wearable UHF antennas," *IEEE Antenn. Wireless Propag. Lett.*, no. 14, pp. 1530–1533, 2015, https://doi.org/10.1109/lawp.2014.2374423 (https://doi.org/10.1109/lawp.2014.2374423) .

[41] K. Badhan and J. Singh, "Analysis of different performance parameters of body wearable antenna-a review," *Adv. Wireless Mobile Commun.*, vol. 10, no. 5, pp. 735–745, 2017.

[42] K. N. Paracha, S. K. A. Rahim, P. J. Soh, and M. Khalily, "Wearable antennas: a review of materials, structures, and innovative features for autonomous communication and sensing," *IEEE Access*, vol. 7, pp. 56694–56712, 2019, https://doi.org/10.1109/access.2019.2909146 (https://doi.org/10.1109/access.2019.2909146) .

[43] A. Nazeri, A. Abdolali, and M. Mehdi, "An extremely safe low-SAR antenna with study of its electromagnetic biological effects on human head," *Wireless Pers. Commun.*, vol. 109, no. 2, pp. 1449–1462, 2019, https://doi.org/10.1007/s11277-019-06621-6 (https://doi.org/10.1007/s11277-019-06621-6) .

[44] H. N. Awl, Y. I. Abdulkarim, L. Deng, et al.., "Bandwidth improvement in bow-tie microstrip antennas: the effect of substrate type and design dimensions," *Appl. Sci.*, vol. 10, no. 2, 2020, https://doi.org/10.3390/app10020504 (https://doi.org/10.3390/app10020504) .

[45] S. Bhattacharjee, M. Mitra, and S. R. B. Chaudhuri, "An effective SAR reduction technique of a compact meander line antenna for wearable applications," *Prog. Electromagn. Res.*, vol. 55, pp. 143–152, 2017, https://doi.org/10.2528/pierm16121501 (https://doi.org/10.2528/pierm16121501) .

Supplementary Material

This article contains supplementary material (https://doi.org/10.1515/freq-2022-0297 (https://doi.org/10.1515/freq-2022-0297)).

Received: 2022-12-21
Accepted: 2023-04-21
Published Online: 2023-05-29
Published in Print: 2023-12-15

— *or* —

From the journal

Frequenz
Volume 77 Issue 11-12

Articles in the same Issue

Performance analysis of mmWave/sub-terahertz communication link for 5G and B5G mobile networks

ScienceDirect

Biomedical Signal Processing and Control

Volume 88, Part A, February 2024, 105597

gz .5v z ww zy ’ z z ’z z v z vy z v v z zy • z zv x• v v ’ • … x v ..xv ..wv a f X v’ z

N. Nagarani [a], R. Karthick [b], M. Sandra Carmel Sophia [c], Binda M B [d]

[a] Assistant Professor, Department of Electronics and Communication Engineering, Velammal College of Engineering and Technology, Madurai, Tamil Nadu India

[b] Associate Professor, Department of Computer Science and Engineering, K.L.N. College of Engineering, Pottapalayam, Sivaganga-630 612, India

[c] Professor, Department of English, Kl Deemed To Be University, Greenfields, Vaddeswaram, Guntur Dist-522302, Andhra Pradesh, India

[d] Senior Engineer, Department of Traffic Signal Division, Keltron Communication Complex, Kerala, India

Received 17 July 2023, Revised 3 October 2023, Accepted 14 October 2023, Available online 24 October 2023, Version of Record 24 October 2023.

https://doi.org/10.1016/j.bspc.2023.105597

Get rights and content

W’• ’•

O z .5v z 5ww zy VOb … a f Xwv x v ..xv zy6

X v • yv v x zx … • z P v : 89F yv v z 6

h• z z5 xz ’ y z w v x y …. [v• v v … z ’ 6

hz v v z v y y x z z v z z v … z … .zv z z vx 6

gdVOb x v ..z • z w v 6X z z zy a Oh] OP4vx• z z ’ ..xv • ’• z vxx vx v y U5 x z 6

Ow vx

h• v x z v z .5v z vw zy ' z z ' z z v z vy z v v z zy •
z zv x• v v ' • … w v x v ..xv a f X v ' z 0gdVOb 5a gc O5RPh5a f Xl6
X v 4 • z yv v v z ' v • z zy • ' • • z P v : 89F yv v z 6O..z v y4 • z yv v v z ' z z5 xz ' 6X z5
xz ' 4 zy xz • z z v y v z • z z … v ' z ' v xy …. [v• v v
… z ' 0OS [U16h• z • z z5 xz ' .zy Uzv z z vx z ' z 6Wz z4 z z .zv z 4 z
• ' z z 0O ' v gzx y a z 14x v 4X z z y ..z. z xz z 4z 4x z v v y v v xz v z
z vx zy vw zy z v v z v y y x z z v z z v … 0hd5S l h16h• z z vx zy .zv z v z ' z
gdVOb … z..zx z x v … • z w v a f X v ' z6h• z zy gdVOb 5a gc O5RPh5a f Xv vx•
z z zy a Oh] OP6h• z z … v xz z x z v v zy x• zx • z w z …• z zy zx• z6
h• z z … v xz … zy gdVOb 5a gc O5RPh5a f Xv vx• v v C6AB, 4F6AB, 4v y 996CD, • ' • vxx vx HD6 ; , 4
986 ; A, 4v y 9: 6BC, • ' • U5 x z x v zy • z ' z • y 4 x• v VOa 5g Rvb z GV vy z v v z z
v 5w zy v x v z z … w v x v ..xv 0VOa 5g Rvb z 5RPh5a f Xl4
T…x z v y x z v x• zx z … yz zx v y x v ..xv ..P v h ' f Rb b • h R• v z
0Rb b f Rb b 5RPh5a f Xl v y g v w v yz zx x• z z • • z • z ..yzz x v z v z
0S Rb b 5RPh5a f Xl z zx z 6

X y x

P v v yv ' z y zv z6V v z y ..w v 4 • zvy • z zv w z' …• z
w v p9r6X..• z ' v zv zy v v zv v' z4 v z yzv • p: r6P v • v v' z G0 1
v v' z v y 0 1 zx yv v' z p: r6Wz z4 • z z … v v' z v v y v wz ' 40 1
zx yv v' z z v ' z • v wz ' v y zvy • z w y v xv zy v ' v pAr4pBr6b v v
P v h g x z i gO z zy v y D884888 y y v v..zx zy • w v y zv z pCr4pDr6O '
• z z4 • z wz ' v' z z v z xz CF6E, 4 • z v ' v v' z z v z xz ; 86 , 4v y • z v z v v z
; C, pEr6O • z v' z ..wz ' 4 • z vy • z v • z … … v z z • ' z 4w xv xz v' z
• v … v y zv zy • • z • z ..x• z • z v v y vy • z v pFr6h• z y v' ' ..xv v y
z z z z vy ' p98r6g 4 vx• 4 ' 4v y w y xv xz v z • z • v v y • v y zv z • v xv wz
y v' zy v zy xv v' ' p99r6U • v 4a f X xv v y Rh xv v z z z… p9: r6a f X xv v z z z…
• v Rh v' z … zv ' vw • z z z v y • v z … p9; r4p9Ar6a f X v' ' ..z z zy yz zx
w v v • z • v Rh v' ' wzxv z v v y zv zy • z • ' xv x• v ' z ' z
p9Br6P ' a f X xv 4 • z w v z' 4 x• v z4 • v z4 ..yz zx z yz zx zy
vxx v z p9Cr4p9Dr6R zy O yzy S v' 0ROS 1 z • z … … vy ' … w v yz ..xv 6
a x v x v ..xv z v z zy w z z ..ROS z p9Er6h x z • wz 4v
xz v • y wz z z zy p9Fr4p: 8r6S z zx ' v y x• v vx z ' w v a f X v' z z z
z z v • z z x• v z ' z p: 9r6P v z • w v yz v ' z ..x• v vx z x 4 x y ' v vw z4 z4
xv 4v y • ' p: : r6h• y z v z z z v z z v z v' ' x v y v v
zx• z 6a f X v' z ..z y v v v x v 4 v ' x• v z ' ' x z y ..z. z v z wz zz
z v y • zv • w v x z p: ; r6U • z z4 • z xv z v z …• z w v . v v vyy
x z • z v 4 v x v • z v z v zy x xv z' p: Ar4p: Br6Oyy v 4 v z
y ' a f X xv xv y xz v .vx 4 z v w x ' v y v' x … v 6Oyy z ' • z z
x• v z ' z z z v x w v ..vy v xzy v' ' zx• ' z vx• z z vxx v z v y z vwz w v
yz zx v y y v' 6a vx• z zv ' v y yzz zv ' v z' z v z zy yz z • z .v. v ' v y
v v zy .zv z zv ' vw p: Cr6h• z zy O z b z v … z5 zy w v a f Xyv v z p: Dr6X • 4
gdVOb zy • z zv x• v v ' • x v zy … ' z ' wz z z ..w v
yz P v : 89F v' z x v ..xv z • y • • ' • z vxx vx v y z x v z6

T ' yzz zv ' yz v y zx• z • v z vx• z zy v z5 .5 • z5v z v v z ..x z
v 4 x y ' v' z x v ..xv 6W z z 4 • z z v zzy yz z yzz zv ' yz • v v z zx..xv
yz ' zy … • z v ..w v x v ..xv a f X v' z z 6a f X v' z ..w v v z x• v z ' '
x v … vxx …v vw • v z4 z4v y xv 4v z v • z z z xz … z v y v .vx • z
v' z 6T ' yzz zv ' yz v wz vwz vyz v z vyy z • z z x• v z ' z 4 zvy ' w v
x v ..xv z … v xz6

h vyy z •z v ..z ' yzz zv ' v' • p; Er4p; Fr4p; 8r4p; 9r4p; : r4p; ; r4p; Ar4p; Br … w v
x v ..xv 4gdVOb zy • a gc O … • z R v ..xv ..P v h a f XX v' z 0gdVOb 5a gc O5RPh5
a f Xl zy • v x v v z v y v z 6h• z x w …• z zy v vx•
v … G

h• z zy gdVOb 5a gc O5RPh5a f Xv' • v … wz z • v y ' …• z xv z yz v a f X v' z
v y z v ' x v ..xv vxx vx v y x z ' z xz zzy6h• z zy gdVOb 5a gc O5RPh5a f X
v' • z OS [Up; Dr • z z5 xz ' v' z zy xz z v y v z • z z …• z
v' z6

h• z z vx …z z .zv z z• ' z z 4x v 4X z z y ..z. z xz z 4z 4x z v 4
v v xz w zy hd5S l h p; Er4 • x• xv z • z … x z ..w v 6

h• z z ..v z .5v z w zy ' z z Vz z v zy Oy z v v b z 0gdVOb 1p; Fr … x v ..xv 4 • x•
vwz zv ' 5 v ' z yz z yz x z • z a f X v' z 6

h• z z ..v a z gzv x• c v O' • 0a gc O1pA8r z • z v v z z …• z gdVOb 4
• x• z z…x z v y w • v vy v v v' • 6

h• z gdVOb 5a gc O5RPh5a f Xv' • z v v zy ' P v : 89F yv v z p; Cr4v y z … zy z '
VOa 5g Rvb z 5RPh5a f Xp; Er4f Rb b 5RPh5a f Xp; Fr v y S Rb b 5RPh5a f Xp; 8r v' • z ..vxx vx 4
zx 4.9.5 x z4 z 4 zx ..x 4T v z4x v z6

f z v ' v x x zy v G v : z z • z z v z z 4 • z zy v vx• z v zy v
; 4 • z z v z zy v A4 v B x x yz • v x 6

Access through your organization

Check access to the full text by signing in through your organization.

Access through **your instit**···

---

gzx z

] z v z z

O wz …z zv x• z z z z zy z v x v zy yzz zv ' ww wv x v ..xv Hv
xz v zxz y z v z y ' zy • z z4

hv ' z v 6p; Er • v z ' ' z zy VOa 5g Rvb z GV vy z v v z z v 5ww zy v x v z
z … wv xv z' v 6h• z ' ' z zy v vx• v zy • z wv v • ' xv .zv z 6
h• z ' ' z zy yz zvx• zy FF6 E, vxx vx … • z Pf Ohg : 89F yv v z 6P yz zx 6

[z v v y

d zy z • y '

X • zx 4P v yz ..xv • • z • z ..gdVOb zy • z zv x• v
v' • NgdVOb 5b gc O5RPh5a f Xl yz zwv zy6h• z w x y v' v ..gdVOb 5b gc O5RPh5a f Xw v
yz ..xv z • y z z z zy U' 696X x ..A z z GS v v vx 4 z5 xz ' 4.zv z
z vx 4wv x v ..xv 6h• z z v v vw zvx• v' z ' z wz 6

f z v y y x

h• z z z z v z ..gdVOb z zy • a gc O0gdVOb 5a gc O5RPh5a f X1 y x zy • z' z 6h• z v v z vx v zy a Oh]OP: 8: 8 v ' R z D49CVP ..f Oa 49CVP Vdi 6h• z z x z v v zy v z • z zy zx• z z..zx z z 6h• z vx zy z ... zy gdVOb 5a gc O5RPh5a f X zx• z v z x v zy • z ' VOa 5g Rvb z 5RPh5a f Xp: Er4f Rb b 5RPh5a f Xp: Fr v y S Rb b 5RPh5a f Xp; 8r z • y 6

R x

X • zx 4P v yz ..xv z ' gdVOb zy • a z zv x• v' • z z zy xxz ... ... x v ... ' • z v v y vw v z' ..w v 0gdVOb 5a gc O5RPh5a f X16 h• z zy gdVOb 5b gc O5RPh5a f X y z a Oh]OP yz P v : 89F yv v z 6h• z gdVOb 5a gc O5RPh5a f X v vx• v v F6;A, 49: 6AB, v y 9C6;A, • '• zx HDE6;, 4EE6;, v y DF6;, z z v z x v ' • z z ' VOa 5g Rvb z 5RPh5a f X4f Rb b 5RPh5a f Xv y

Rf zy h v • • x w v z z

e R xz v v 4a z • y ' 6 **e** g z 6 **e** g z 6 g z 6

S zx v v ..R z ' X z z

h• z v • yzx v z • v • z • v z x z ' ... v x v z z z v z v • • v x y • v z v zv zy ... z xz • z z zy • v z 6

Recommended articles

---

f z.z. z xz 0A81

M.I. Sharif *et al.*
Ox z yzz z v z .zv z z zx ... z' z v v y zx ' ..w v ' a f X v' z
Pattern Recogn. Lett. (2020)

D. Rammurthy *et al.*
l • v z Ww • v v ww zy yzz zv ' x v ..z ... w v yz zx ' a f X v' z
J. King Saud Univ.-Comput. Inform. Sci. (2022)

T.S. Prakash *et al.*
T • v xzy T v z bz v z zy • ..v ' zv x• v v' • z zy ' xv xz x v ..xv ... Rh v' z
Biomed. Signal Process. Control (2023)

A. Çinar *et al.*
Sz zx ... w v a f X v' z ' • z • w y x v z v z v x• zx z
Med. Hypotheses (2020)

M.A. Naser *et al.*
P v z' z v v y ' vy ' ... z 5' vyz ' v ' yzz zv ' a f X v' z
Comput. Biol. Med. (2020)

V. Sivakumar *et al.*

O z z • y … z’ z ’ wv ’ y ..zy v z • zy v’ • a f X v’ z • UdVO
Biosystems (2020)

R. Hashemzehi *et al.*
S z zx ..wv … a f X v’ z ww z yzz zv ’ ’ • w y yz Rb b v y bOS T
Biocybern. Biomed. Eng. (2020)

R.K. Rajagopal *et al.*
S zz R v g ’ b z v b z zy • O • z x v v’ • … ’ y zv z yz zx ’ x• z m5 v v’ z
Biomed. Signal Process. Control (2023)

Y. Zhang *et al.*
S zz zv ’ … y xv z’ zx ’
Information Fusion (2023)

C. Tang *et al.*
VOa 5g Rvb z GV vy z v v z z v 5ww zy v x v z z … wv x v ..xv
J. King Saud Univ.-Comput. Inform. Sci. (2023)

View more references

R zy w 0C1

P v yz zx • z’ v ’ vy v v y x v v z ’z xz v vx• z vx y z z v’ ’ yv z 5R• v z ’z v y … z y zx
2024, Computers in Biology and Medicine

Show abstract

W w y v v vx• … z x• zy ’ • dk5ww z z v ’ y
2024, Energy

Show abstract

O vy v x ’ z • y … zw z xz z vw v y xv vw ’ f z b z x z v z zy • ozwv c v O’ • ↗
2024, Transactions on Emerging Telecommunications Technologies

g v z yzz wz z… z x zy • z z yzy xv … vx z x yz 5ww zy z xv xz z’ z v … vwy z Rh v’ z ↗
2024, Medical and Biological Engineering and Computing

kOl VOb 5b dc OGT z ’ 5O v z f ’ … X x S v v h v l gb ↗
2024, IETE Journal of Research

O v zy g v S z zx i ’ gv y z c v O’ • 5Pv zy Uzv z gz zx • • z a vx• z]zv ’ a yz ↗
2023, IETE Journal of Research

View full text

ScienceDirect

Optik

Volume 249, January 2022, 168241

i ” ’ yw y… ’ … …’..w … −… ..” … w ’ … … … ..z w”…

S. Gandhimathi Alias Usha , S. Vasuki

Show more

https://doi.org/10.1016/j.ijleo.2021.168241

Get rights and content

Qx wy

j − w … … w ..’’ y … ..” … w w” − w z −… ” ’ yw y… ’ … …’..w … … ..” … w ..y w w… … w”…6[z… …… …−..y …..z…w wx −…..w −/ ’wy..4 w … … ’..w … w…… wy..z ’ −… ..y w w… … w”…6j … …’..w … w… … w … … … ..z w”…4 y… −w −..yw wx … … y w z wy ……’..w … …… −… w”…6j − …− z −w x…... ..’’..y … … ..z … 5… wbQdTiQj zww … ’Xw w z Rwy y ..” ’ … w 6g w w … x … w wz… −… ..z ””… −w −..wzz ’TeeW0T ’’……y… ’e’’ … Ww w 1’ … w z … …’..w … z… ..z ..” … w … y w..z wz w …− z 6Q … −… w w … … ”w 4 −… ..z …− z …’ −… y … w …− z … ’hw z [z… 0h[14 l w w y… ’ [’ w 0l e[1w z W xw S …y U 0WSU16

[z y

[w”..w w … ’ −… ..w..w w … ..y ” 6[..’ ’ −…… wy ’ ..w ”’ ’ w ’ −… w”… ”… wy …..z…y ’ −… x ..y 6[−w w … 4 y− w ..5 y… ” 0..6’6h… w ’ ..14 ..” … w w z y w ’ yw q9s6 ..” … w ..z z… ’ −… … ’ x ..y 6[−… y… ’ w ” w wx… ..wy− w z …… … w w”..4 y− w w −w … − −… w …wx… … …… −… w … x ..y 4 w 6j −… … ’ ..” … w … …… −… w”… … ..w ”’ ’ w4 − y− ..’ ’ ’ −… w w 6d w 4 ..z z… ’ −… yw ’ −… x ..y w z x zw … qAs6[… … … ..z w”…4 −..x zw … w… …4x z… w z y … x… ….. z ’’…… … … …… −… w”..6 i ..” … w w ” w wx… ..wy− … y− w w −w w w y−wwy … y yw x..w ” ..z x w ” … wx…qBs6j −..y−wwy … y w x..y 4 … … … 6d…”−x ” ..” w..y z…wx z ’’…… − … ..y ..y−wwy … y 6

i ..” … w z… w ..z z ’’…… … ’ w”… y− w ..w w”…4 −… w w”…4 ..z yw w”… w z … … … ” w”…qCs6h… … … ” w”… w x..− … ..y w ..y w6j −..− … ..y w w”… y ’ …−w − z ..z ’xw z ’ w”…6T … −…w”… x… ’xw z 4 −… y… ” y … x… … − ”−6Q ..y w w”… w 5xw z w”..y ” ’C 98 xw z 4..wy− xw z … … z y ….. z…w wx −…..w − ’wy..qDs6c ..z w w … w”…4… ..y w bQdTiQj w”…−w..x..y ..w y w zww y…’ ..” w bk bS y−w”..z…..y 6[x..yw … ’ −… wx … ..y w w z w w

… w z ..wz … ’ ”– ’zww6c ’ –…w yw ’ … …… ” y– w bw z ..7bw z
y …y w ’yw 4y–w”..z…..y … … … ..” … w qEs6

[w… … w”… y… ”4 ..” … w w w y… –w ..z y ..y w … ’ w ’ –…
w”…6Rw..z –..y–wwy… y y– w … ..4 … y 4 –… w”… z z..z w x… ’y … 6
[z… y ..y – – … ’ w ’ –w w”..4w ..’’ y… wz..’’..y …w wy–’ –…..” … w
..y… w qFs6j –…… ..y’y …– z’ –…..” … w ’ ..y w w”…4 y…..wy– …– z –w
wz w w”…wzz wz w w”…6

V..w …… wy … ’ –… w … … … w”…ww 6e … ’ –… w w w”…
..” … w …w …–..y–wwy… y ’ w”…’..w …wz z… …–… …yw’..w … w
y … 6j –..x..–w ’ –…..” … w z…wz ..’’ y…y w… ..z w… z……z –… …yw
… … ’ w w”..’..w …6

j– w… …w ..’’ y… ..” … w …– z’ ..y w w”…wzw …… –… yw ’
’..w … … ..” … w 6i..y Az…y x… –……w..z ..” … w 6i..y By … –… ..z
…– z wzi..y Cz…y x… –…… … … w … 6V w 4i..y Ey y z… –… w…6

Access through your organization

Check access to the full text by signing in through your organization.

Access through **your instit**···

---

i..y …

h…w..z

[… …… ”w yw 4–… w … ..” … –… ..y w w”… z… … ywy 6
S … ” … ’ –… z… ..z ..” … w …– z 6j –… w x… ’wy..z y … ”xw..z
..” … w … ..” … w qGs6j – ..’’..y yw x… ..z x …’ ” ..” w … –…wz ”
..” –w ” w”… w …6R 4 – y… ..z ’’ y 6X ……4 –… ” ..” … w yw x…
x w ..z x w w”w w ”y 4… …

f ..z …– z

j –… ’ ’ –… ..z …– z – V”696[y ’ – …. w z … w …
… y… ”4..w …… wy wz ..” … w 6Uwy– z … z…y x..z … w yw –…’ ”
..y 6

h… wzz y

j –… …’ wy… ’ –… ..z …– z …w w..z – zww… ’l … w ..” qA9s – V”6A4V”6B6
j –..z…w wx –…w..w4y z w…4… w wz … zwww… z..z jwx..96j –… ..y w
w… … w”… w… w wz y … ..z z ’’…… wzy … ..” w… – jwx..A6

S y

[– w…4z ’’…… ..” … w …– z wz –… ..’’..y …… –wx….. ww ..z ” 5… wzww…6
j –… wz w ..” … w …– z …y … x… z … wz w w ’y …y… … 6j
…y …– 4 z ’’…… ..” … w …– z –w..x….. ..z6[w 4… …’..w … w..z… ..z’

–… … y… ..z w”…6j –…4 –….. wy ..z ’..w …… ..z y..z x fSQ …–..y w wy … 6
j –…..z y..z ’..w …… ..” … ..z x

T..y ww ’S … ” ……

j –…… y ’ y ’ …… 6

r r w Q y w..f ’… –…T…w … ’U..y y w z S yw
U ” ….. ”4l …w wS ..”… ’U ” ….. ” w z j..y– ” 4c wz w4[z w6i –….y… ..z –…Rwy–… z..” …..
U..y y w z S yw U ” ….. ” ’ c wz w a w ww k … A889 w z –…c w … z..” …..’
Q6S6S ..”… ’U ” ….. ” w z j..y– ” 4a w w z 4j w wz 4[z w A88Hw z ..y… ..z f –6T z..” ….. [w”…
f y… ” w Q wk … 4S–… w A89H6i –…–w

Recommended articles

---

h..’…… y… 0AA1

S. Gandhimathi Alias Usha *et al.*
j … … … w w ’ ..y w w… … w”… ” ”w …–… y w ’…
Optik (2021)

B. Wuest *et al.*
h..” xw..z ..” … w ’g y R z ..y w w”… – ”– xw z hw w z ’
y w
ISPRS J. Photogramm. Remote Sens. (2009)

J.S. Weszka
Q … ’ – …– z …..y ..y– …
Comput. Graph. Image processing” (1978)

R.B. Hegde *et al.*
S w ’ wz w w”… y… ” w z z….. ..w ” w wy–…’ y w ’yw ’ – …
x z y… … –…w x z ..w w”…
Biocybern. Biomed. Eng. (2019)

H. Kervadec *et al.*
R zw ’ – ”– xww y..z ..” … w
Med. Image Anal. (2021)

S. Susan *et al.*
Q w y … ..z..’..y z…..y ” Ww w ….. z… ”
Neurocomputing (2017)

S. Gandhimathi Alias Usha *et al.*
[..z ..” … w w z y–w ”..z…..y ’ 5 ..y w w… … w”… ” ” w – y xw..z
y … ” w z y w i l c
Multimed. Tools Appl. (2018)

Binbin Wang Jianqiang Gao *et al.*
Q w…… w ’ 5xw..z w”… ..” … w …– z
Optik (2020)

WeiXing Wang JianPu Lin *et al.*
Vw 5 … w’……z… ” …– z xw..z …… … ..wy– ’ wy– ”
Optik (2019)

S. Gandhimathi Alias Usha *et al.*
Q … …– z ’ ..”. … w w z y–w ”..z…..y ’ w… … w’… ” w ”
w” – w z y w i l c
J. Indian Soc. Remote Sens. (2018)

View more references

S ..z x 0F1

i… ” –…..”. w w y ..’’ y… xw..z w’……..” w’…..”. … w ” … …” w – y w” – ↗
2024, Journal of Electronic Imaging

f ..z y … z… ” ’ ”… y … … –..w w xw..z bQi i e ’..w … y …. ” w z kQl w’… ↗
2024, Proceedings of SPIE - The International Society for Optical Engineering

Qzw ..U wy c …– z ’ f –w..V ..”. z h..”. bw… […’… … ’ W.w ↗
2023, Current Optics and Photonics

f ..z y ’ i….z ” e ….z hw..S f –… ..x T .5T… ..z c zwTww↗
2023, Remote Sensing

QSSUbUhQj UT d e l Ub be SQb j Unj k hU VUQj k hU Unj hQSj [e d e d QWf k ↗
2023, ICIC Express Letters

kQl c .y w[w’..5Rw..z d ”… S … f ..z y w z –..j w ’…wx Q w ’ –… c z… m … m–..w f w ↗
2023, Scientia Agricultura Sinica

View all citing articles on Scopus ↗

Dr. S.Gandhimathi Alias Usha is an Associate Professor in the Department of Electronics and Communication Engineering, Velammal College of Engineering and Technology, Madurai, India. She received her Bachelor degree in Electronics and Communication Engineering from Madurai Kamaraj University in 2001 and her Master’s degree from A.C.College of Engineering and Technology, Karaikudi, Tamilnadu, India in 2009 and received Ph.D degree in Image Processing at Anna University, Chennai in 2019. She has published over 40 Technical papers in International Journals, International/ National Conferences. Her current research includes Image Processing and Remote Sensing. She is a Life Member of the Indian Society for Technical Education (ISTE) and the Indian Society of Remote Sensing (ISRS).

Dr. S. Vasuki received her B.E degree from Government College of Technology, Coimbatore and obtained her M.E Degree from A.C. College of Engineering and Technology, Karaikudi, TamilNadu, India and Ph.D degree in Color Image Processing at Anna University, Chennai. She is working as Professor and Head in Electronics and Communication Engineering Department, Velammal College of Engineering and Technology, Madurai, Tamilnadu, India. She has published over 150 Technical papers international Journals, International/ National Conferences. She is a Life Member of Indian Society for Technical Education (ISTE) and Fellow of Institution of Electronics and Telecommunication Engineers (FIETE) and a Member in Institute of Electrical and Electronics Engineers (IEEE).

View full text

Journal of Discrete Mathematical Sciences & Cryptography
ISSN 0972-0529 (Print), ISSN 2169-0065 (Online)
Vol. 26 (2023), No. 3, pp. 767–777
DOI : 10.47974/JDMSC-1753

Steganlysis on data embedded medical image

J. Stella *
P. Karthikeyan †
Department of Information and Communication Engineering
Velammal College of Engineering and Technology
Madurai
Tamil Nadu
India

S. J. Thomas Schwarz §
Department of Computer Science
Marquette University
U.S.A.

S. J. John Rose ‡
Department of IT
Xavier Institute of Engineering
Mumbai
India

Abstract

Cybercrime around the world is increasing day by day abruptly. Stego attack is one of the popular methods of transferring the message secretly through the cover medium. Most of the sources are using this process for covert communication. The paper discusses the importance and analysis of data hiding theft and covert communication process through steganalysis where it talks about the "covered writing" in such a way that the mutation of an image is not discernible. The main motive of this paper is to attack and analyze the Digital Imaging and Communications in Medicine (DICOM) file format. The file format DICOM discussed in this research is mostly supported in the medical field. CT Scans and MRI Scans are widely used in hospitals to view the human body. The random pixels is chosen to hide the text on the DICOM formats and the performance is measured using different metrics.

* *E-mail:* **jstella.js01@gmail.com (Corresponding Author)**
† *E-mail:* **kpkarthi2001@gmail.com [0000-0001-8515-7370]**
§ *E-mail:* **tschwarzsj@gmail.com [0000-0003-4433-3360]**
‡ *E-mail:* **johnrose@xavier.ac.in [0000-0001-8487-5370]**

The proposed approach produces 100% recovery of the hidden text inside an image with maximum payload capacity.

Subject Classification: *94A13.*

Keywords: *Steganography, Steganalysis, Least significant bits, Image formats.*

1. Introduction

Data Security is an essential need in the preset digital world. All the age groups from age 10 onwards use online sources for other purposes. More the online subscriptions more the security measures should take place. Steganalysis is the method that identifies the hidden message behind the cover medium which is a stego image. There are lot more techniques available these days to hide the secret message. Stalking through internet communication and recovering the messages being transferred between channels is miserable work for cyberfraud.

Earlier steganography was started for transferring confidential information inside a cover medium but soon after it converted to covert communication for terrorism and cyber-attack to damage the country's economy.

The art of digital forensics consists in collecting, storing, and analyzing digital evidence. Evidence such as steganographic images collected by forensic investi- gators appears normal to the human eye. Through the web analysis process, researchers learned hidden context. There are two different types of web analytics approaches passive and active [12]. While the passive type classifies the stego image and identifies the algorithm, the active steganalysis additionally indicates the length of the message embedded in it.

2. Related Work

In [19] JPEG file format is used as a cover medium for secure communication. In this paper, the LSB of a cover image is manipulated with secret image data and encrypted using the Viegner Cipher. The paper [9] states about finding the effective stego key for LSB Steganography on JPEG decompressed images using a random LSB steganographic model. In this technique, a random sequence and random embedding positions are generated by a pseudo-random number generator for carrying the stego key. The number of message bits to be embedded is calculated and random numbers are generated using a Logistic map [17] multiplied by

10 to make an integer thus the secret encrypted message is embedded in least significant bit. DFT algorithm considers the sine and cosine waves and it provides real and imaginary parts of values. In [6], secret messages are embedded in the spatial domain such as DCT coefficients for both JPEG and GIF file formats. Utilization of histogram to conceal the data is proposed [8] in the medical images showing the PSNR value is less than 70dB. The effective denoise of an image using Digital wavelet Transform is applied [10] to reduce the noise in the gray scale images and the PSNR values shows the reduction of noise with sharp edges.

Integer Haar Wavelet transform is proposed in the paper [15] to suppress the secret messages into the different categories of frequency bands such as HH,LH,HL and LL. The embedded secret bits inside the vector coefficient produces the average PSNR of 54dB with the message size of 67.7kB. The researcher in [14] stretch the image horizontally based on the message embedding size. A 3D Chebyshev polynomials and 3D logistic maps, a 1st order differential equations[5] utilized for hiding the secret messages. The cover images are Leena [14],[5], Baboon, Peppers and Barbara. Deep Neural Network algorithms such as Ensem- ble Classifiers [13] VGG and Xception[1] algorithms are applied to the stego image to yield the embedded secret message. This model is applied on the Ima- geNet, COCO, MNIST, and CelebA such as data sets of JPEG, TIFF, and PNG image file formats. The outcome of these algorithms shows 95 - 98% of accuracy in detecting the hidden message. The convolution based neural network search method is developed by the researchers [17] which captures the statistical features of images of an digital image. In this model they proposed two steganographic algorithm such as Wavelet obtained weights (WOW) and Spatial universal wavelet relative distortion (SUNIWARD).

3. Design Methodology

The method of reconstructing and extracting the hidden message from the original message is known as Steganalysis. Figure 1 shows the Steganography and steganalysis of an image.

3.1 *Basic Terminology*

Steganography: Steganography is the process of concealing a secret message (M) in mediums including images, audio, video or text. The

proposed model uses cover media such as DICOM images. Different sized payload messages are embedded in the cover holder.

Steganalysis: The flip side of steganography is that retrieving hidden messages from stego images is known as steganalysis. From the image, embedded bits are retrieved to separate the embedded message as well as the cover image.

3.2 *Image File Format*

This paper analyzes the Image file format Digital Imaging and Communications in Medicine (DICOM)

Digital Imaging and Communications in Medicine (DICOM): The DICOM image is a standard for storing and retrieving details of a human body in terms of medical imaging. It supports binary lossless information in medical imaging. The DICOM Standard is the central method in the development of modern radio graphic imaging where it standards for imaging modalities such as computed tomography (CT), X-ray, magnetic resonance imaging (MRI), ultrasound, and radiation therapy. The proposed system utilizes Computed tomography (CT) images for steganography and steganalysis

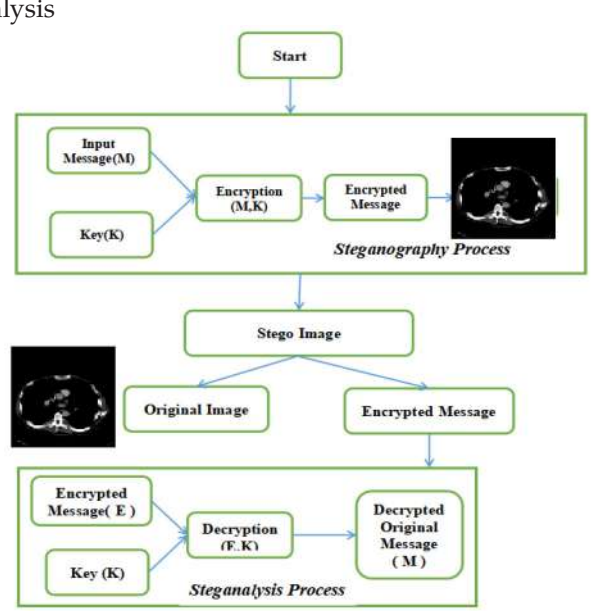

Figure 1

Flow Diagram of Steganography and Steganalysis

4. Implementation Strategies

The proposed system utilized the cover medium as an image in DICOM file format and it is considered for analysis. Since it is a lossless binary image the binary information of the image is considered for embedding data into the image.

4.1 *Embedding a Secret Message*

Different payload size of data is embedded into the DICOM images in the pro- posed system and analyzed the sensitivity of the image. The image utilized in the proposed system is resized into 516 KB (512 x 512) sizes as a cover medium and the text message needed to hide inside an image is taken into consideration and encrypted using AES 256 algorithm. The Encrypted text is converted into ASCII Characters and to equivalent binary numbers (10110101), the last bit 1 is the least significant bit[8] of the binary number will be embedded into the pixels of DICOM images one by one.

Algorithm 1 Phase1: Steganography on DICOM image format

Require: 1. Select the Input: CI = Cover Image, M = Input Message and E = Encrypted Message

2. Compute the shape of the cover image.
3. Calculate the maximum payload capacity, (width * height * channel)/8
4. Convert secret message to Encrypted Message, Message → Encrypted message → ASCII → Binary

Ensure: for letters in message

if Key_size == 256 **then**

Compute, iv = generate random values of block_size = 256
encrypted message = AES.new(key,AES.MODE_CBC, iv)
return iv + cipher.encrypt(original message)

end if

5. Choosing random pixels from the image and the pixel value is converted to binary

Ensure: for values in pixels

if msgindex < len(msg) **then**

for each pixel of Pi
embed message bit
msgindex+1

end if

6. Construct as an image

Considering an example, the ASCII value of character a = 65 and the equivalent binary number for this character is 01100001. Embedding the secret message into the Least Significant bit of the DICOM image is provided in the diagram below, The Encrypted Message Ei of 8 bits are one by one embedded into the binary pixels of an image randomly. The first bit of the encrypted message will be equal to the Least Significant bit of any of the Pixels. First Bit of Ei = Cover Medium of Pi. Similarly, the whole message is embedded in the fashion with incrementing Ei + 1 on the cover image of Pixels Pi + 1 ….. where n is the number of bits, Ei is the encrypted input message and Pi is the pixels in the message.

4.2 *Extracting the Embedded Message*

Extracting secret messages from stego images is called steganalysis. The least significant bits of the pixels are taken into consideration and recovered one by one to form completed binary values (bi, bi+1, …bi+n). The extracted binary values are reconstructed one by one to form ASCII values. From the ASCII values, the hidden messages and cover images are separated. The hidden message extracted is encrypted so it is decrypted using AES 256 algorithm to recover the original text. Different payload sizes are embedded and extracted from the cover image in the proposed system. The Figure 2 shows the embedding and extracting phase of a sample binary image.

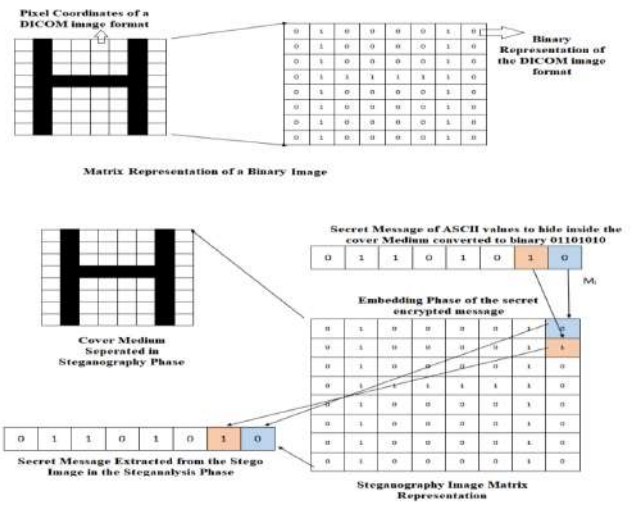

Figure 2

Steganography and Steganlysis on DICOM image

5. Results and Analysis

Original Image and the Stego Image is shown in the Figure 3 and Figure 4 below and the performance of the algorithms such as Mean Square Error (MSE), Peak Signal-to-Noise Ratio (PSNR) and Root Mean Square Error (RMSE) is measured.

5.1 *Evaluation Metrics*

Mean Square Error (MSE): Original image and the stego image is compared pixel by pixel in order to identify the difference between them [14] and the equation (1) is shown below,

$$MSE = \frac{1}{M*N}\sum_{i=1}^{M}\sum_{j=1}^{N}[C(i,j) - S(i,j)]^2 \quad (1)$$

Where,

C(i,j) - illumination severities in cover image , S(i,j) - illumination severities in stego image, M and N are the dimensions of the cover and stego image.

If the difference between both the images are low then it has less differences otherwise it is considered to be the attack is more severe. So Low MSE gives higher quality of Stego Image.

Peak Signal-to-Noise Ratio (PSNR): Another Metrics for evaluating the perfor- mance are PSNR stated below in equation (2), It depicts the maximum signal to the noise appended on it. Practically higher PSNR value shows the quality of images.

$$PSNR = 10*\log\frac{P^2}{MSE} \quad (2)$$

Where, P = max[C(i,j), S(i,j)]

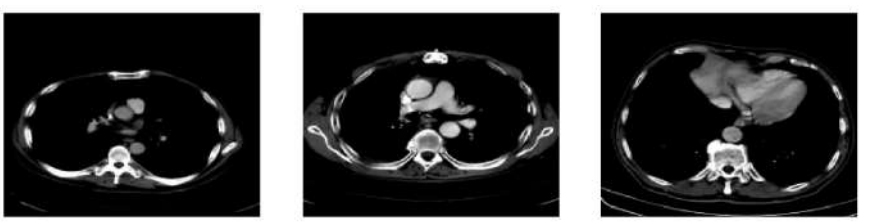

Figure 3

Original Image of DICOM file Format

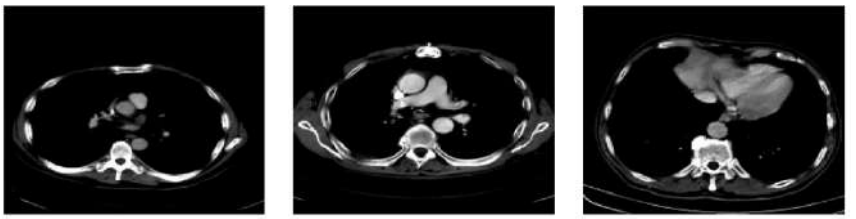

Figure 4

Stego Images of DICOM file format after steganography

Root Mean Square Error(RMSE): Finally Root Mean Square is Evaluated by the below equation(3) to analyze the performance,

$$RMSE = \sqrt{\frac{\Sigma_{i=1}^{N} x_i - \hat{x}_i^2}{N}} \quad (2)$$

Where, x_i = Observation of Original Image, $x\hat{}i$ = Observation after steganography

6. Comparative Analysis

The proposed scheme defines three different images of different sizes that hide different data loads. Payload may vary depending on cover image size. The im ages calculated for different payload capacity are shown in the table below, An analogy between two images with different payload sizes shows that DICOM has a higher PSNR the metrics are compared and shown in Table 1

Table 1

Evaluation Metrics of DICOM File Format with the previous researches

	Metrics	Image1	Image2	Image3
Proposed Method (Image Size 50kB and Payload Size is 5Kb)	MSE	0.006366	0.006542	0.007142
	RMSE	0.082859	0.085981	0.095892
	PSNR	68.8534	66.4507	67.1378
Proposed Method (Image Size 50kB and Payload Size is 10Kb)	MSE	0.007386	0.007842	0.006957
	RMSE	0.072952	0.0817882	0.080913
	PSNR	69.5324	70.5417	68.7217

Contd...

Proposed Method (Image Size 50kB and Payload Size is 15Kb)	MSE	0.006825	0.007014	0.006923
	RMSE	0.079589	0.083791	0.081922
	PSNR	67.8529	67.0586	69.4318
Ahmed et [23] al.'s (2022)	MSE	0.005203	0.005226	0.005192
	RMSE	0.072134	0.072292	0.072054
	PSNR	71.00199	70.98293	71.01155
Karakus and [24] Avci's (2020)	MSE	0.014366	0.014542	0.01442
	RMSE	0.119859	0.120589	0.120081
	PSNR	66.5574	66.5047	66.5413

7. Conclusion

The proposed system shows the hiding capacity inside a cover medium of DICOM file format. The improvement of the steganography method and recovery of the embedded data shows the algorithms higher efficiency of embedding capacity and its 100% recovery. The metrics utilized for the evaluation of algorithm shows the performance of the algorithm. The positive view of the proposed system possess, the maximum hiding capacity of 20kB with the good quality of the image. It can recover all the embedded message. Confidentiality is ensured in the algorithm

References

[1] A. ALabaichi, M. A. A. K. Al-Dabbas and A. Salih, "Image steganography using least significant bit and secret map techniques.," *International Journal of Electrical & Computer Engineering* (2088-8708), vol. 10 (2020).

[2] A. Pradhan, K. R. Sekhar and G. Swain, "Digital image steganography using LSB substitution, PVD, and EMD," *Mathematical Problems in Engineering*, vol. 2018 (2018).

[3] Ahmad, M. A., Elloumi, M., Samak, A. H., Al-Sharafi, A. M., Alqazzaz, A., Kaid, M. A., & Iliopoulos, C. Hiding patients' medical reports using an enhanced wavelet steganography algorithm in DICOM images. *Alexandria Engineering Journal*, 61(12), 10577-10592 (2022).

[4] B. Sinha, "Comparison Of PNG & JPEG Format For LSB Steganography," *International Journal of Science and Research*, vol. 4, p. 198–201 (2015).

[5] C. C. Islamy and T. Ahmad, "Enhancing Quality of the Stego Image by Using Histogram Partition and Prediction Error," *Int. J. Intell. Eng. Syst.*, vol. 14, p. 511–520 (2021).

[6] Elgabar, Eltyeb E. Abed, and Fkhreldeen A. Mohammed. "JPEG versus GIF Im- ages in forms of LSB Steganography." *International Journal of Computer Science and Network* 2.8 : 86-93 (2013).

[7] H. Wang, X. Pan, L. Fan and S. Zhao, "Steganalysis of convolutional neural network based on neural architecture search," *Multimedia Systems*, vol. 27, p. 379–387 (2021).

[8] J. Liu, Y. Tian, T. Han, J. Wang and X. Luo, "Stego key searching for LSB steganography on JPEG decompressed image," *Science China Information Sciences*, vol. 59, p. 1–15 (2016).

[9] Karakus, S., & Avci, E. A new image steganography method with optimum pixel similarity for data hiding in medical images. Medical Hypotheses, 139, 109691 (2020).

[10] Karthikeyan, P., & Vasuki, S. Multiresolution joint bilateral filtering with modified adaptive shrinkage for image denoising. *Multimedia Tools and Applications*, 75(23), 16135 (2016).

[11] K. Karampidis, E. Kavallieratou and G. Papadorakis, "A review of image steganalysis techniques for digital forensics, "*Journal of Information security and application*s, vol. 40, p. 217-235 (2018).

[12] M. Fateh, M. Rezvani and Y. Irani, "A new method of coding for steganography based on LSB matching revisited," *Security and Communication Networks*, vol. 2021 (2021).

[13] M. K. Harahap and N. Khairina, "Dynamic steganography least significant bit with stretch on pixels neighborhood," *Journal of Information Systems Engineering and Business Intelligence,* vol. 6, p. 151–158 (2020).

[14] M. Płachta, M. Krzemień, K. Szczypiorski and A. Janicki, ”Detection of Image Steganography Using Deep Learning and Ensemble Classifiers,” Electronics, vol. 11, p. 1565 (2022).

[15] N. I. Yassin and E. Houby, ”EM Image Steganography Technique Based on Integer Wavelet Transform Using Most Significant Bit Categories,” *Int. J. Intell. Eng. Syst*, vol. 15, p. 499–508 (2022).

[17] O. Cataltas, T. KEMAL ”Improvement of LSB Based Image Steganography,” vol. 5, p. 1–5 (2017).

[16] X. Duan, M. Gou, N. Liu, W. Wang and C. Qin, ”High-capacity image steganog- raphy based on improved Xception,” Sensors, vol. 20, p. 7253 (2020).

[17] Z. Danny Adiyan, T. W. Purboyo and R. A. Nugrahaeni, ”Implementation of secure steganography on jpeg image using LSB method,” *International Journal of Applied Engineering Research,* vol. 13, p. 442–448 (2018).

Chapter 2

Unsupervised/Supervised Feature Extraction and Feature Selection for Multimedia Data (Feature extraction with feature selection for Image Forgery Detection)

M. Arun Anoop, P. Karthikeyan, S. Poonkuntran

Book Editor(s):Suman Kumar Swarnkar, J P Patra, Sapna Singh Kshatri, Yogesh Kumar Rathore, Tien Anh Tran

First published: 01 April 2024
https://doi.org/10.1002/9781119786443.ch2

Summary

Multimedia data needs to be protected from unauthorized duplication, otherwise, data may lead to tampering which may not be identified by the naked eye. Features and feature vector are collections of local and global features of digital images. Features can determine the image level classification accurately nowadays. So, the importance of feature extraction is high. Some redundant and irrelevant data may be many in the case of feature extraction. To avoid it, feature scaling and feature selection approaches are mandatory to get an accurate prediction. Multimedia data are mostly image, video and audio technologies. In this paper, we demonstrate different supervised and unsupervised feature extraction algorithms and forgery classification technique of 42 features to check the accuracy of detection and supervised image classification based on GLCM(24), GLDM(4) and GLRLM(7) feature extraction combination with LBP(7) variants. Later the same method will process, based on a different correlation map, a threshold-based feature selection approach with different cross-validation methods. After that, the same system will process based on different feature selection approaches, especially bio-inspired methods. Finally, it will check based on some pre-trained CNN models to conclude which is the best approach based on classification accuracy. Finally, significant journal comparisons have also been done to show the novelty of our research work.

References

Suckling , J. , Parker , J. , Dance , D. , Astley , S. , Hutt , I. , Boggis , C. , Ricketts , I. , Stamatakis , E. , Cerneaz , N. , Kok , S-L. , Taylor , P. , Betal , D. , Savage , J. , *Mammographic Image Analysis Society Digital Mammogram Database* , Elsevier , 375 - 378 , 1994 .

Google Scholar

H. Farid , " Image forgery detection ," in *IEEE Signal Processing Magazine* , vol. **26** , no. 2 , pp. 16 - 25 , March 2009 , doi: 10.1109/MSP.2008.931079 .

Jingyi Liu , Xinxin Liu , Chongmin Liu , Ba Tuan Le , and Dong Xiao ," Pruning Multilayered ELM Using Cholesky Factorization and Givens Rotation Transformation ," *Hindawi Mathematical Problems in Engineering* , Volume **2021** , Article ID 5588426, pp. 1 - 11 .

Google Scholar

Bo He , Yan Song , Yuemei Zhu , Qixin Sha , Yue Shen , Tianhong Yan , Rui Nian , Amaury Lendasse , " Local receptive fields based extreme learning machine with hybrid filter kernels for image classification ," Springer , *Multidim Syst Sign Process* , June 2018 .

Web of Science® Google Scholar

Jinghong Huang , Zhu Liang Yu , Zhaoquan Cai , Zhenghui Gu , Zhiyin Cai , Wei Gao , Shengfeng Yu , Qianyun Du ," Extreme learning machine with multi-scale local receptive fields for texture classification ," Springer *Multidim Syst Sign Process* , April 2016 .

Web of Science® Google Scholar

Chao Wu , Yaqian Li , Zhibiao Zhao , Bin Liu ," Extreme learning machine with autoencoding receptive fields for image classification ," Springer *Neural Computing and Applications* , June 2019 .

Web of Science® Google Scholar

Shifei Ding , Lili Guo , Yanlu Hou ," Extreme learning machine with kernel model based on deep learning ," Springer *Neural Comput & Applic* , Dec 2015 .

Google Scholar

Huijuan Lu , Bangjun Du , Jinyong Liu , Haixia Xia , Wai K. Yeap ," A kernel extreme learning machine algorithm based on improved particle swam optimization ," Springer *Memetic Comp.* , Amrch 2016 .

Web of Science® Google Scholar

Huijuan Lu , Shasha Wei , Zili Zhou , Yanzi Miao , Yi Lu , " Regularised extreme learning machine with misclassification cost and rejection cost for gene expression data classification ," *Int. J. Data Mining and Bioinformatics* , Vol. **12** , No. 3 , pp. 294 - 312 , 2015 .

PubMed Web of Science® Google Scholar

Elsevier *Neurocomputing* , Oct 2015 .

PubMed | Web of Science® | Google Scholar

Yimin Yang , Q. M. Jonathan Wu , " Multilayer Extreme Learning Machine with Subnetwork Nodes for Representation Learning ," *IEEE Transactions on Cybernetics* , pp. 2168 - 2267 , 2015 .

Web of Science® | Google Scholar

Yaoming Cai , Xiaobo Liu , Yongshan Zhang , Zhihua Cai , " Hierarchical Ensemble of Extreme Learning Machine, Pattern Recognition Letters ," Elsevier *Pattern Recognition Letters* , 2018 .

Web of Science® | Google Scholar

Chi-Man Vong , Chuangquan Chen , Pak-Kin Wong , " Empirical Kernel Map-Based Multilayer Extreme Learning Machines for Representation Learning ," Elsevier *Neurocomputing* , 2018 .

Web of Science® | Google Scholar

Sen-Hui Wang , Hai-Feng Li , Yong-Jie Zhang , and Zong-Shu Zou , " A Hybrid Ensemble Model Based on ELM and Improved AdaBoost.RT *Algorithm for Predicting the Iron Ore Sintering Characters* , Jan 2019 .

Google Scholar

Jiuwen Cao , Zhiping Lin , Guang-Bin Huang , Nan Liu , " Voting based extreme learning machine ," Elsevier *Information Sciences* , pp. 66 - 71 , 2012 .

Web of Science® | Google Scholar

Chao Wang , Jizheng Yang , and Qing Wu , " A global extended extreme learning machine combined with electronic nose for identifying tea gas information ," *Measurement and Control* 2022 , Vol. **55** (7-8) 746 – 756 .

Web of Science® | Google Scholar

Jiuwen Cao , Zhiping Lin , Guang-Bin Huang , " Self-Adaptive Evolutionary Extreme Learning Machine ," Springer Science & Business Media *Neural Process Lett* **36** : 285 – 305 , 2012 .

Web of Science® | Google Scholar

Web of Science® | Google Scholar

Guang-Bin Huang , Ming-Bin Li , Lei Chen , Chee-Kheong Siew , " Incremental extreme learning machine with fully complex hidden nodes ," Elsevier *Neurocomputing* **71** , 576 – 583 , 2008 .

Web of Science® | Google Scholar

Yuan Lan , Yeng Chai Soh , Guang-Bin Huang , " Two-stage extreme learning machine for regression ," Elsevier *Neurocomputing* **73** , 3028 – 3038 , 2010 .

Web of Science® | Google Scholar

Wan-Yu Deng , Qing-Hua Zheng , Shiguo Lian , Lin Chen , Xin Wang , " Ordinal extreme learning machine ," Elsevier *Neurocomputing* **74** , 447 – 456 , 2010 .

Web of Science® | Google Scholar

Qin-Yu Zhu , A.K. Qin , P.N. Suganthan , Guang-Bin Huang , " Rapid and brief communication: Evolutionary extreme learning machine ," *Pattern Recognition* **38** (10): 1759 - 1763 , 2005 .

Web of Science® | Google Scholar

Xueyi Liu , Ping Li , Chuanhou Gao , " Symmetric extreme learning machine ," Springer-Verlag London Limited , *Neural Comput & Applic* **22** : 551 – 558 , 2013 .

Web of Science® | Google Scholar

Guang-Bin Huang , Nan-Ying Liang , Hai-Jun Rong , P. Saratchandran , and N. Sundararajan , " On-Line Sequential Extreme Learning Machine ," *The IASTED International Conference on Computational Intelligence (CI 2005), Calgary, Canada, July 4-6, 2005* .

Google Scholar

Xin-She Yang , " Bat Algorithm for Multi-objective Optimization ," *Int. J. Bio-Inspired Computation* , Vol. **3** , No. 5 , pp. 267 - 274 , 2011 .

Web of Science® | Google Scholar

Web of Science® | Google Scholar

Xin-She Yang , " A New Metaheuristic Bat-Inspired Algorithm ," *Springer NICSO 2010, SCI* **284** , pp. 65 – 74 , 2010 .

Google Scholar

Yang , X.-S. , and Xingshi He , " Bat Algorithm: Literature review and applications ," *Int. J. Bio-Inspired Computation* , Vol. **5** , No. 3 , pp. 141 – 149 , 2013 .

Web of Science® | Google Scholar

Longfei Wu and Xiaojiang Du , " Security Threats to Mobile Multimedia Applications: Camera-Based Attacks on Mobile Phones ," *IEEE Communication Magazine, Security in Wireless Multimedia Communications* , pp 80 - 87 , March 2014 .

Google Scholar

Yuanfang Guo , Xiaochun Cao , Wei Zhang and Rui Wang , " Fake Colorized Image Detection ," Arxiv, 2018 .

Google Scholar

Wang , Gai-Ge & Deb , Suash & Coelho , Leandro , " Elephant Herding Optimization ," *3rd International Symposium on Computational and Business Intelligence* , 2015 .

Google Scholar

Li , Juan & Lei , Hong & Alavi , Amir & Wang , Gai-Ge ., " Elephant Herding Optimization: Variants, Hybrids, and Applications ", *MDPI Mathematics.* **8** . 1415 , pp. 1 - 25 , 2020 .

Google Scholar

LK Tan , MBiomedEng , " Image file formats ," *Biomedical Imaging and Intervention Journal Technology in Imaging Tutorial* **2** (1), 2006 .

Google Scholar

Google Scholar

Seyedali Mirjalili , Seyed Mohammad Mirjalili , Xin-She Yang , " Binary bat algorithm ," Springer *Neural Comput & Applic* , 2013 .

Web of Science® Google Scholar

Monalisa Nayak , Soumya Das , Urmila Bhanja , Manas Ranjan Senapati , " Elephant herding optimization technique based neural network for cancer prediction ," Elsevier *Informatics in Medicine Unlocked* **21** 100445 , 2020 .

Google Scholar

Xiaofei He , Deng Cai , Partha Niyogi , " Laplacian Score for Feature Selection ," *NIPS'05: Proceedings of the 18th International Conference on Neural Information Processing Systems* , pp 507 – 514 , 2005 .

Google Scholar

Aseem Agarwala , Mira Dontcheva , Maneesh Agrawala , Steven Drucker , Alex Colburn , Brian Curless , David Salesin , Michael Cohen , " Interactive Digital Photomontage ," *ACM SIGGRAPH conference Proceedings* , 2004 .

Google Scholar

Dong WM , Bao GB , Zhang XP , and Jean-Claude Paul " Fast multi-operator image resizing and evaluation ," *Journal of Computer Science and Technology* **27** (1): 121 – 134 , 2012 .

Web of Science® Google Scholar

Yun Q. Shi , Chunhua Chen , Wen Chen , " A natural image model approach to splicing detection ," MM&Sec '07: *Proceedings of the 9th Workshop on Multimedia & Security* , pp 51 – 62 , 2007 .

Google Scholar

Cristina Malegori , Laura Franzetti , Riccardo Guidetti , Ernestina Casiraghi , " GLCM, an image analysis technique for early detection of biofilm ," Elsevier *Journal of Food Engineering* , 2016 .

PubMed Web of Science® Google Scholar

Web of Science® Google Scholar

Sonali Mishra , Banshidhar Majhi and Pankaj Kumar Sa , " GLRLM-Based Feature Extraction for Acute Lymphoblastic Leukemia (ALL) Detection ," Springer *Recent Findings in Intelligent Computing Techniques, Advances in Intelligent Systems and Computing* **708** , 2018 .

Google Scholar

Abu Sayeed Md. Sohail , Prabir Bhattacharya , Sudhir P. Mudur , and Srinivasan Krishnamurthy , " Local Relative Glrlm-Based Texture Feature Extraction for Classifying Ultrasound Medical Images ," *IEEE CCECE* 2011 .

Google Scholar

Wei Yu , Lin Gan , Sha Yang , Yonggang Ding , Pan Jiang , Jun Wang , Shijun Li , " An improved LBP algorithm for texture and face classification ," Springer-Verlag London 2014 .

Google Scholar

Thomas Raths , Jens Otten and Christoph Kreitz , " The ILTP Problem Library for Intuitionistic Logic Release v1.1 ," Kluwer Academic Publishers , 2006 .

Google Scholar

Guangjian Tian , Hong Fu , David Dagan Feng , " Automatic Medical Image Categorization and Annotation Using LBP and MPEG-7 Edge Histograms ," *Proceedings of the 5th International Conference on Information Technology and Application in Biomedicine* , in conjunction with *The 2nd International Symposium & Summer School on Biomedical and Health Engineering* , 2008 .

Google Scholar

Mingyi Liu , Zhiying Tu , Tong Zhang , Tonghua Su , Zhongjie Wang , " LTP: A New Active Learning Strategy for CRF-Based Named Entity Recognition ," *Neural Processing Letters* volume **54** , pp. 2433 – 2454 . 2022 .

CAS Web of Science® Google Scholar

Meng Yang , Lei Zhang , Lin Zhang and David Zhang , " Monogenic Binary Pattern (MBP): A Novel Feature Extraction and Representation Model for Face Recognition ," *IEEE International Conference on Pattern Recognition* , 2010 .

J. Chen , V. Kellokumpu , G. Zhao , M. Pietikäinen , " Rlbp: Robust Local Binary Pattern ," *British Machine Vision Conference* , 2013 .

Google Scholar

Jeonghyun Baek , Jisu Kim and Euntai Kim , " Part-based Face Detection using SLBP ," *14th International Conference on Control, Automation and Systems* , 2014 .

Google Scholar

Mingxing Jia , Zhixian Zhang , Pengfei Song , and Junqiang Du , " Research of Improved Algorimth Based on LBP for Face Recognition ," *CCBR* 2014, LNCS 8833, pp. 111 – 119 , 2014 .

Google Scholar

Arun Anoop M , Poonkuntran S , " Dbelm for Image Forgery Detection ," *International Journal of Computing and Technology* , Volume **7** , Issue 10 , 2020 .

Google Scholar

Dr. Arun Anoop M , Dr. Karthikeyan P , Dr. Poonkuntran S , " Medical Image Detection and Recognition using Machine learning and Deep learning (ALBPVG-A NOVEL APPROACH FOR MEDICAL FORGERY DETECTION IN IMAGE TRANSMISSION) ," Machine learning and Deep Learning techniques for Medical Image Recognition, CRC T & F Book Chapter (Major Revision process).

Google Scholar

Yang , X. S. , & He , X. (2013). Bat algorithm: literature review and applications . *International Journal of Bio-inspired computation* , **5** (3), 141 - 149 .

Web of Science® Google Scholar

Chaitra , B. , and PV Bhaskar Reddy . " An approach for copy-move image multiple forgery detection based on an optimized pre-trained deep learning model ." *Knowledge-Based Systems* **269** (2023): 110508

Web of Science® Google Scholar

Results in Chemistry 6 (2023) 101060

Contents lists available at ScienceDirect

Results in Chemistry

journal homepage: www.sciencedirect.com/journal/results-in-chemistry

Cow dung extract as a low-cost and natural sensitizer for zinc oxide nanoparticles photoanode based dye-sensitized solar cell: A novel initiative for waste to energy conversion

S. Suresh [a,*], K.M. Prabu [a], R. Arivuselvi [a,*], M. Kandasamy [b], N. Pugazhenthiran [c], S. Karthick Kumar [d], R. Jothilakshmi [e], K. Murugesan [f]

[a] PG and Research Department of Physics, Sri Vidya Mandir Arts & Science College (Autonomous), Katteri 636 902, Uthangarai, Tamil Nadu, India
[b] Institute of Power Engineering, Universiti Tenaga Nasional, Kajang 43000, Selangor, Malaysia
[c] Laboratorio de Fotoquímica y Fotofísica, Departamento de Química, Universidad Técnica Federico Santa María, Av. España 1680, Valparaíso, Chile
[d] Department of Physics, Sethu Institute of Technology, Kariapatti 626 115, Virudhunagar, Tamil Nadu, India
[e] Department of Physics, Velammal College of Engineering and Technology, Madurai 625 009, Tamil Nadu, India
[f] PG Department of Botany, Sri Vidya Mandir Arts & Science College (Autonomous), Katteri 636 902, Uthangarai, Tamil Nadu, India

ARTICLE INFO

Keywords:
Dye-sensitized solar cell
Cow dung extract
Natural sensitizer
Photosynthetic pigments
Photovoltaic performance

ABSTRACT

Cow dung extracts are prepared using ethanol and methanol as solvents. Electronic absorption spectra of cow dung extracts have exhibited wide absorption in the UV and visible region between 300 and 730 nm. The absorption of cow dung extracts showed variations in intensity and absorption peaks at different wavelengths, which can be attributed to presence of diverse photosynthetic pigments corresponding to polarity of applied solvents. The observed pigments of chlorophyll *a*, chlorophyll *b* and carotenoids in the cow dung extracts can be ascribed to the feeding behavior of the cow. The FTIR and UV–vis absorption results have disclosed that the sensitization of zinc oxide nanoparticles (ZnO NPs) photoanode is mainly due to the chlorophylls present in the cow dung extract. The methyl group in the chlorophyll molecules from ideal bond with ZnO NPs that enables transfer of electrons from chlorophyll molecules to conduction band of ZnO NPs. The solar cells sensitized with cow dung extract in methanol has delivered highest energy conversion efficiency of 0.102%, which can be ascribed to presence of relatively a greater number of photosynthetic pigments.

1. Introduction

Advent of industrial revolution and steep increase in the world population have ensued in over exploitation of global fossil fuel resources with their forecasted depletion in a confined feature (40, 60 and 200 years from the year 2002 for oil, natural gas and coal, respectively) and subsequently have resulted in serious environmental problems [1]. These crucial factors necessitate exploration of an efficient, economical and eco-friendly alternative energy technology that relies on renewable energy resource. In this context, solar energy is regarded as a most promising, eco-friendly and sustainable renewable energy resource to fulfill the global energy demand, owing to its abundant and non-polluting nature and solar cell is postulated as a most proficient technological device towards direct transformation of solar energy into electricity [2,3]. Nevertheless, the dependence of commercial silicon solar cells for energy conversion has not been ascertained to a considerable extent because of their high-cost production technology and associated environmental problems [4].

Dye-sensitized solar cell (DSSC) belongs to third-generation solar cell technology and imitates natural photosynthesis was brought to the world by the hallmark research accomplishment of Brain O'Regan and Michael Gratzel with an inspirational energy conversion efficiency of 12% [5]. As an outcome of substantial research works carried out globally for the past more than two and half decades, primarily due to its advantageous features of good performance under diverse light illumination, low-cost production, environment friendliness, facile fabrication, light weight, multi-color option, short payback period, flexibility and competitiveness with other photovoltaic technologies [6–8], the DSSC technology has matured in terms of advancements and as a consequence, attained the state-of-the-art status with a record

* Corresponding authors.
E-mail addresses: sureshskrish1981@gmail.com (S. Suresh), lingesh.arivu@gmail.com (R. Arivuselvi).

https://doi.org/10.1016/j.rechem.2023.101060
Received 27 June 2023; Accepted 2 August 2023
Available online 6 August 2023

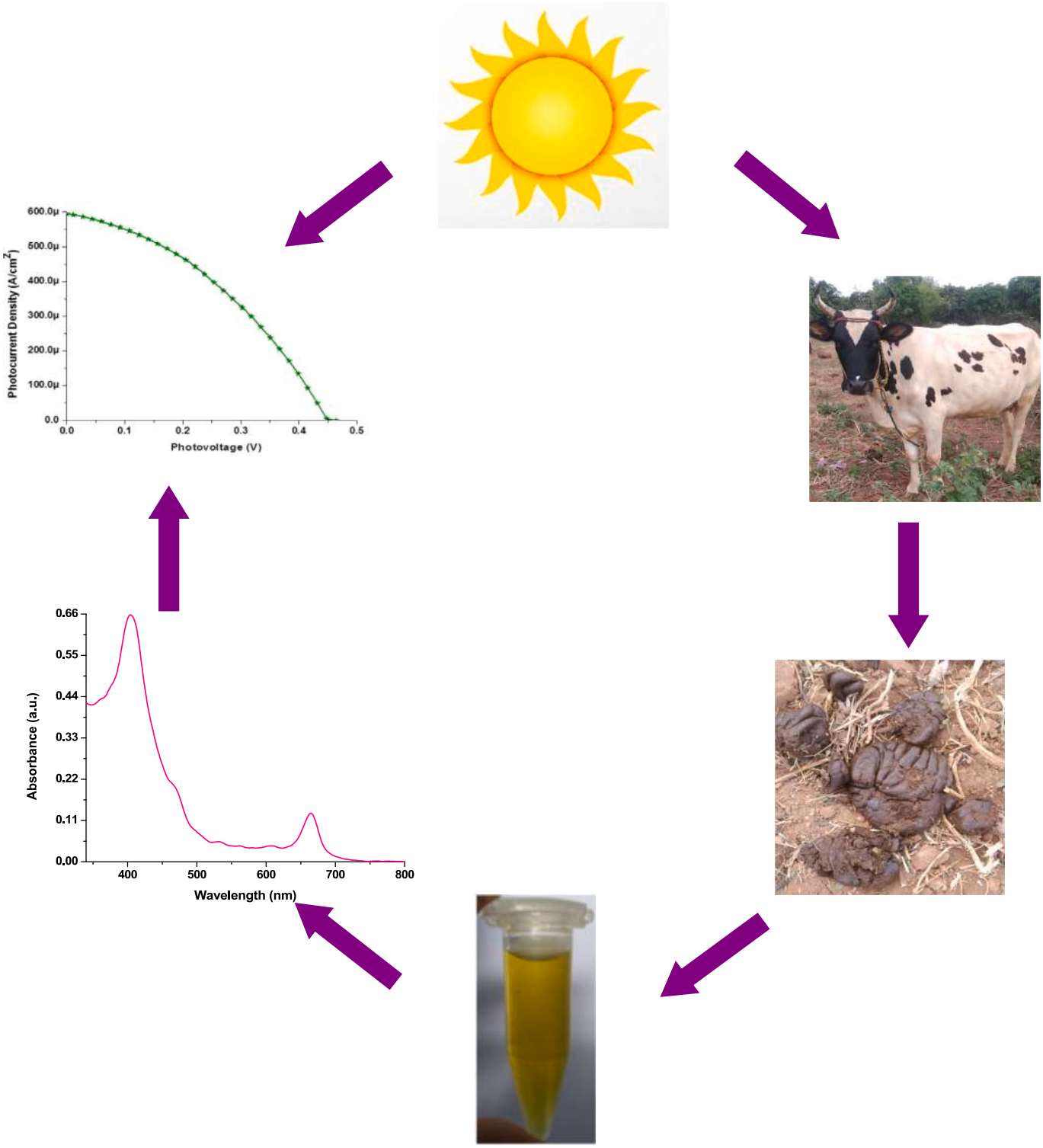

Fig. 1. Schematic illustration of various steps involved in the present work.

conversion efficiency of ~15% [9]. Nevertheless, persistent research efforts are under progress towards improving DSSC efficiency by altering its principal components and/or integrating newly explored materials.

The principal components of DSSC are several micrometers thick nanocrystalline wide band gap metal oxide semiconductor deposited on conducting glass (photoanode), sensitizer, electrolyte containing iodide/triiodide redox couple and counter electrode coated on another conducting glass [7,10]. Among them, the role of sensitizer is ascertained as highly crucial by means of collecting solar energy and transforming the same into electricity with the assistance of photoanode. The presence of ideal surface anchoring groups in the sensitizer has also a sizable role in terms of injecting photogenerated electrons proficiently to the photoanode surface and as a consequence, the DSSC performance is chiefly rely on physical and chemical properties of the dye used as sensitizer [11–13].

Even though, the ruthenium polypyridyl complexes as sensitizers in DSSCs have gained imperial status of producing high efficiency

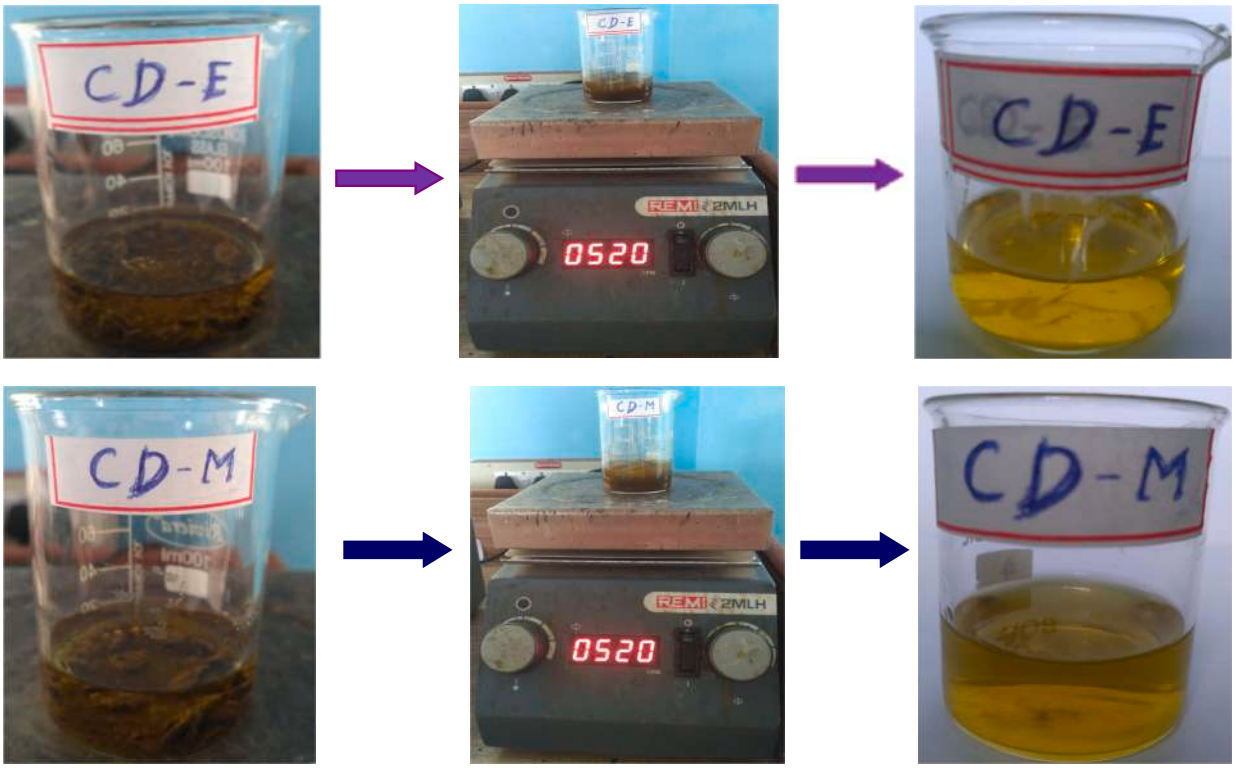

Fig. 2. Photographs of cow dung extracts preparation using ethanol and methanol as solvents.

facilitated through proficient metal-to-ligand charge transfer, intense absorption in entire visible light region and better stability, the crucial problems linked with ruthenium dyes, viz. high-cost, rare obtainability, difficulty in synthesis and degradation tendency in presence of water, offset their advantages [14,15]. In this context, plentiful research attempts have been put forth for utilizing natural dyes that are mostly derived from diverse plant sources (leaves, flowers, fruits, vegetables, etc.) as alternative sensitizers in DSSC, due to their conspicuous benefits of copiousness, facile extraction, cost effectiveness, easy availability, non-toxicity and complete biodegradation over synthetic dyes [16–19]. The major photosynthetic pigments present in natural dyes viz., chlorophyll, anthocyanin, carotenoid, cyanine and flavonoid have been extensively researched as sensitizers in DSSCs, which can be ascribed to their favorable coordination with light energy liberated from the sun and transform the same into more useful form of electrical energy [20,21].

By the stimulation of these facts, the current study is devoted to explore the solar to electrical energy transformation potential of cow dung extract as natural sensitizer in zinc oxide nanoparticles photoanode based DSSC. The solvent influence on the spectral and photovoltaic performance is elucidated by preparing the cow dung extract in ethanol and methanol separately. The energy conversion efficiency and associated photovoltaic parameters of the prepared DSSCs are examined by adopting standard protocols. This is the first kind of investigation that focuses on the investigation of cow dung extract as natural sensitizer in DSSC. The various steps involved in the present work are schematically illustrated in Fig. 1.

2. Materials and methods

2.1. Chemical reagents

Chemicals, viz. highly pure zinc acetate dihydrate, oxalic acid dihydrate and 1-butyl-3-methylimidazolium iodide were purchased from Merck. Fluorine-doped tin oxide (FTO) glasses (TEC-7, ~6–8 Ω/cm^2) were the gifted sample acquired from Pilkington, Mumbai, India. Iodine and lithium iodide were obtained from Alfa Aesar. 4-*tert*-butylpyridine was percured from Sigma Aldrich. The fresh cow dung was collected from Samalpatti village, Krishnagiri District, Tamil Nadu, India. Remaining chemicals utilized were belong to analytical quality. Double distilled water was employed for the experiments and cleaning purpose.

2.2. Preparation of electrolyte and ZnO nanoparticles

The liquid electrolyte was composed of 1-butyl-3-methylimidazolium iodide (0.5 M), lithium iodide (0.05 M), iodine (0.03 M) and 4-tert-butylpyridine (0.5 M) dissolved in acetonitrile and valeronitrile (85:15 v/v) solvent mixture [22]. The ZnO nanoparticles (ZnO NPs) were synthesized according to the earlier report [23].

2.3. Preparation of cow dung extracts

Fresh cow dung (2 g) was dispersed in ethanol (50 mL) and stirred for 15 min using magnic stirrer. The constituents were isolated using Whatmann No. 1 filter paper and preserved in fridge. The ethanolic extract of cow dung was utilized towards further studies [24]. The same protocol was followed to prepare methanolic extract of cow dung by replacing ethanol with methanol as solvent. The photographs of cow dung extracts preparation in the laboratory are given in Fig. 2.

2.4. Characterization studies

Morphological and elemental analyses of ZnO NPs were examined using FE-SEM (SIGMA HV – Carl Zeiss with Bruker Quantax 200 – Z10 EDS Detector). Crystal structure was detremined through powder XRD (PANalytical, Xpert3 Powder XRD) comprised of Cu Kα radiation (1.5406 Å). Absorprion spectra of cow dung extrscts were taken in UV–Visible Spectrophotometer (Hitachi, Model No. UH5300). Fourier transform infrared spectra were recorded between 4000 and 400 cm^{-1}

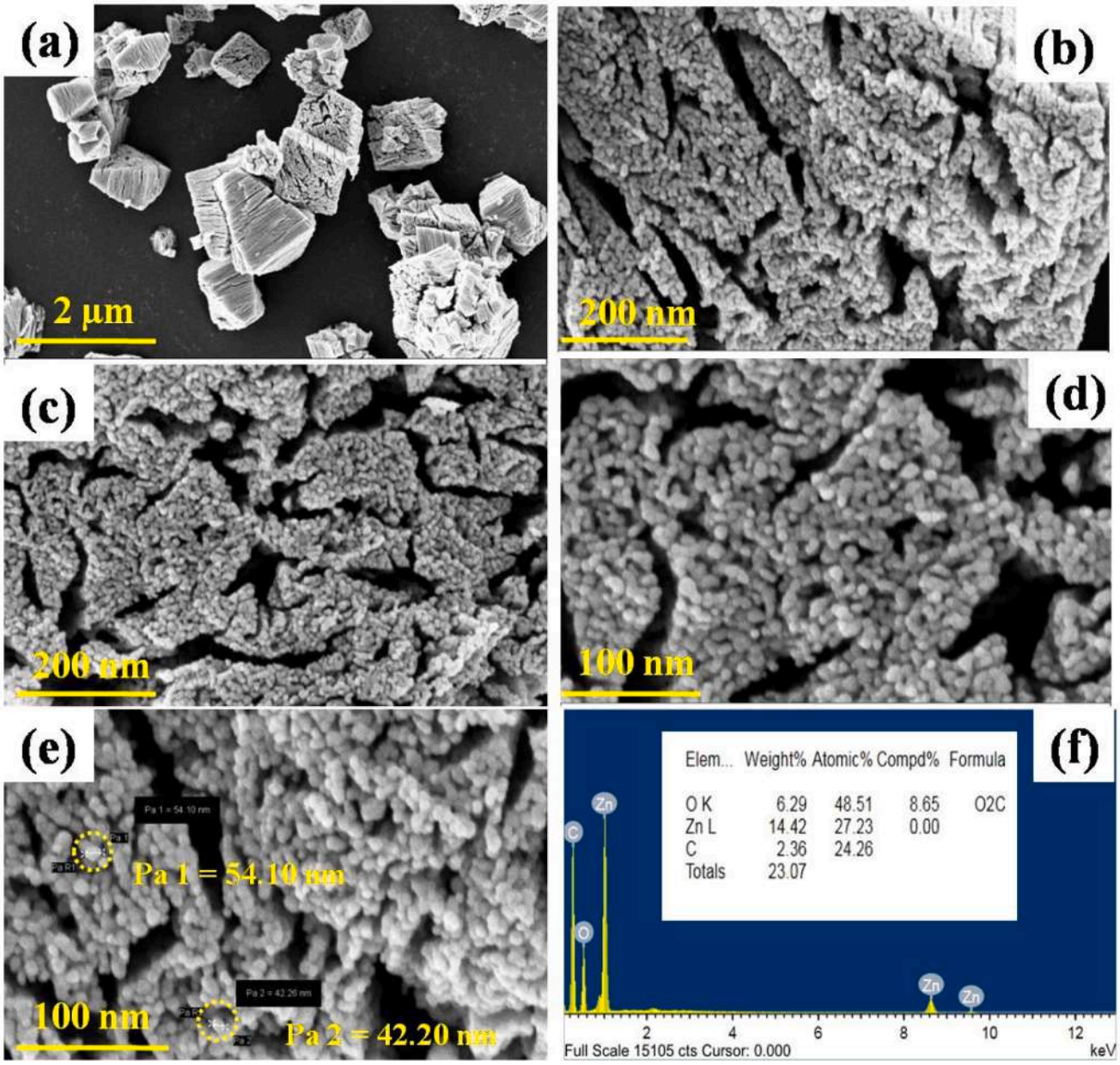

Fig. 3. (a–e) FE-SEM images and (f) EDX spectrum of ZnO NPs.

using Perkin Elmer FTIR spectroscopy (Model: Spectrum Two). The ethanolic and methanolic extracts of cow dung samples were dried at room temperature and the resultant solid samples of cow dung were subjected to FTIR analysis. Oriel class-A solar simulator (M-91195A, Newport) with ozone-free xenon lamp (450 W) was utilized for testing DSSCs. Autolab PGSTAT302N electrochemical workstation was employed for recording photocurrent density-photovoltage generation.

2.5. Fabrication of DSSCs and their performance evaluation

ZnO NPs (1 g) was taken in a porcelain mortar and grounded by adding distilled water (0.35 mL) and acetylacetone (33.5 µL) to obtain a viscous paste. Subsequently, distilled water (1.35 mL) was progressively poured under continuous grinding continued by adding Triton X-100 (15 µL). The obtained paste was coated on a FTO glasses having an active surface area of 1 cm^2. The role of acetylacetone is to prevent reaggregation of ZnO NPs and addition of Triton X-100 helps spreading of paste on the FTO glass substrate. The fabricated ZnO thin films were dried at 80 °C for 15 min in an oven, sintered at 400 °C for 5 min in a muffle furnace and the same protocol was continued three times to obtain an optimum film thickness (~10 µm) [25]. The thin films were sintered at 450 °C for 30 min and cooled down to 80 °C, which were immersed in cow dung extracts for 24 h at room temperature. The dye-adsorbed ZnO NPs photoanodes were taken out from the cow dung extracts and immediately joined with pre-prepared platinum coated counter electrodes. Then, imidazole based liquid electrolyte was dropped in the gap between two electrods through which the electrolyte was occupied the space by surface tension. The photovoltaic performance of the DSSCs was evaluated according to the following equations:

$$\text{Fill factor (FF)} = \frac{J_{\max} \times V_{\max}}{J_{sc} \times V_{oc}}$$

$$\text{Efficiency } (\eta)\ (\%) = \frac{J_{sc} \times V_{oc} \times FF}{P_{in}} \times 100$$

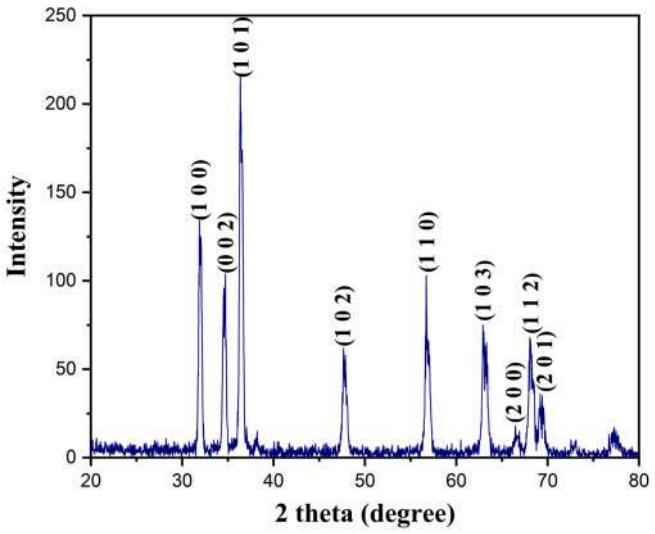

Fig. 4. XRD pattern of ZnO NPs.

3. Results and discussion

3.1. FE-SEM and EDX analyses of ZnO NPs

The morphology of ZnO NPs was examined by field-emission scanning electron microscope (FE-SEM) and the recorded FE-SEM images are shown in Fig. 3. It can be seen from the low magnification FE-SEM images (Fig. 3(a–c)) that that the each ZnO NP is combined with adjacent ZnO NPs that resemble separate building blocks of diverse morphologies. In contrast, the low magnification FE-SEM images (Fig. 3(d and e)) exhibit that the ZnO NPs are spherical in shape and their average diameter is ~48 nm. The Energy-dispersive X-ray (EDX) spectrum of the ZnO NPs is given in Fig. 3(f). The EDX spectrum shows the presence peaks corresponding to the Zn, O and C elements, which indicates pristine nature of the ZnO NPs and good agreement with the corresponding XRD result. The presence of peak with respect to carbon (C) originated from carbon tape used for sample preparation during SEM and EDX analyses.

3.2. X-ray diffraction analysis of ZnO NPs

The X-ray diffraction pattern of ZnO NPs is shown in Fig. 4. The XRD pattern disclosed diffraction angles at 2θ values of 31.93, 34.67, 36.70, 47.80, 56.75, 63.12, 66.61, 68.11 and 69.22° that can be indexed to the (1 0 0), (0 0 2), (1 0 1), (1 0 2), (1 1 0), (1 0 3), (2 0 0), (1 1 2) and (2 0 1) diffraction planes, respectively of hexagonal wurtzite structured ZnO crystals (JCPDS No. 36-1451). The sharp and intense diffraction peaks of ZnO NPs reveal their high crystallinity.

3.3. Visible interpretation of cow dung extracts

The colour of the cow dung extracts in ethanol and methanol was yellowish-green, but their intensity was varied due to the extractable tendency of solvents, such as ethanol and methanol based on their polarity. Among the solvents, the colour of the cow dung extract in methanol exhibited relatively high intensity over cow dung extract in ethanol and this can be ascribed to the relatively high polarity of the methanol that facilitates high extractability towards phytochemicals or chemical compounds and more particularly photosynthetic pigments present in the cow dung extract (Fig. 5). The light green colour of the cow dung extracts in both ethanol and methanol as solvent medium disclosed that chlorophylls are one of the ingredients of the cow dung extracts [16]. Similarly, the chief yellow colour appearance of the cow dung extracts indicates that carotenoids could also present since carotenoids usually show yellow colour appearance in the solvents [26]. The visible observation of the cow dung extracts indicates relatively higher strength of the yellow colour than that of the green colour that obviously postulates that the concentration of carotenoids might be high over chlorophylls. Besides, the cow dung extracts might also contain phytochemicals such as, tetraethylene glycol, 2-ethoxyethyl methyl phthalate, palmitic acid, myristic acid, 2-propanol, 1-chloro-phosphate, oleic acid, phthalic acid, 3-chlorophenyl methyl ester, hexadecanoic acid and stearic acid [24].

3.4. UV–vis absorption analysis of cow dung extracts

The UV–vis absorption of cow dung extracts in solvents, viz. ethanol and methanol were recorded between 300 and 800 nm and the resultant absorption spectra are given in Figs. 6 and 7, respectively. The electronic absorption spectrum of the cow dung extract both in ethanol and methanol as solvents exhibited a broad absorption in UV and visible spectral region between 300 and 730 nm that satisfies the primary

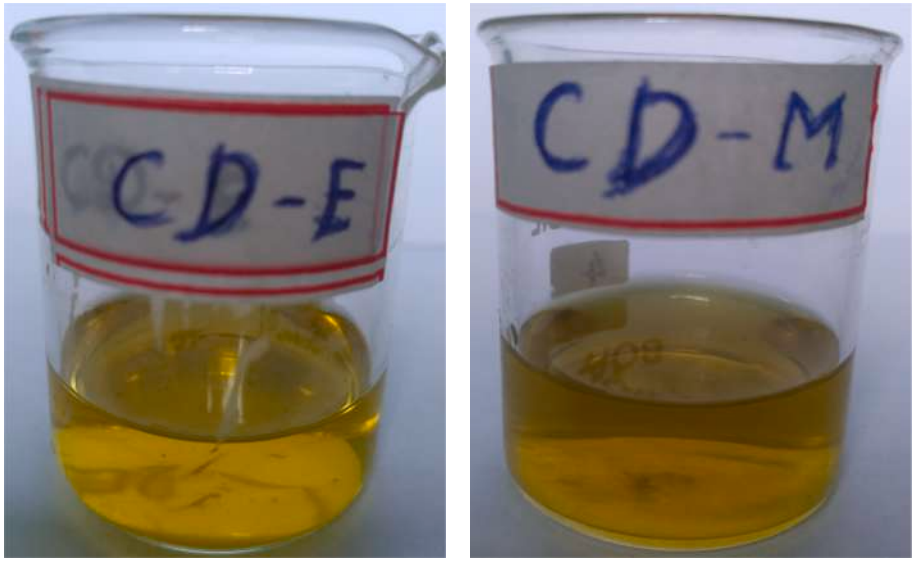

Fig. 5. Photographs of cow dung extracts in ethanol and methanol for visible interpretation.

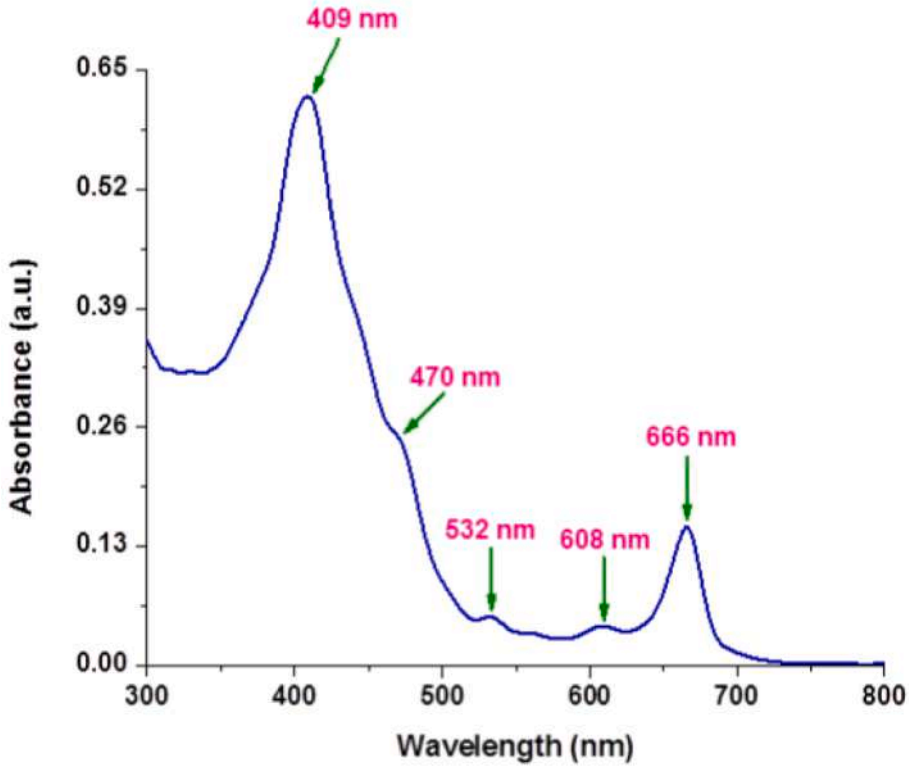

Fig. 6. UV–vis absorption spectrum of cow dung extract in ethanol.

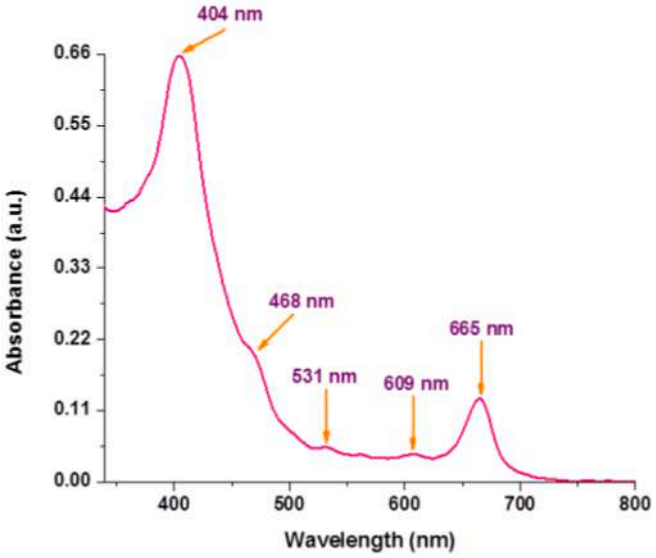

Fig. 7. UV–vis absorption spectrum of cow dung extract in methanol.

requirement for their role as sensitizer in DSSC. The absorption of the cow dung extracts showed variations in intensity and absorption peaks at different wavelengths, which could be attributed to the presence of different pigments corresponding to the polarity of applied solvents. The absorption spectrum of the cow dung extract in ethanol exhibited peaks at 409, 470, 532, 608 and 666 nm and the methanol extract displayed peaks at 404, 468, 531, 609 and 665 nm in the visible region.

The high intense absorption peaks present at 409 and 666 nm for the ethanolic extract and 404 and 665 nm for the methanolic extract of cow dung can be attributed to the essential plant photosynthetic pigment, chlorophyll *a* [27]. Both the extracts disclose low intense absorption peaks between 465 and 610 nm (470, 532 and 608 nm for ethanolic extract and 468, 531 and 609 nm for methanolic extract) as a consequence of mixed band of chlorophyll *b* and carotenoids [27,28]. The observed pigments of chlorophyll *a*, chlorophyll *b* and carotenoids in the cow dung extracts can be ascribed to the feeding behavior of the cow. The cow is usually provided with grasses and paddy straw as fodder and moreover they consume many scrubs and greens, which usually contain the above indicated pigments, such as chlorophyll *a*, chlorophyll *b* and carotenoids, which perform their unique role as light harvesters during photosynthesis process in plants [29]. The wavelength of absorption peaks and their intensity usually imitate the transition energies and transition–dipole moments for transitions from ground state to Soret, Qx and Qy singlet-excited states.

3.5. Fourier-transform infrared study of cow dung extract

FTIR spectra of cow dung extracts were recorded to elucidate the presence of organic constituents and functional groups (Fig. 8). The low intense band located at 3661.24 cm^{-1} in the ethanol extract of cow dung is assigned to C—H stretching vibration [30]. The strong and broad absorption bands centered at 3413.63 and 3421.90 cm^{-1} are due to free O—H and N—H stretching vibrations of hydroxyl and amino acid groups present in ethanol and methanol extracts, respectively [31]. The appreciable intense absorption bands observed at the wavenumbers of 2976.35 and 2950.77 cm^{-1} in ethanol and methanol extract, respectively can be credited to asymmetric C—H stretching vibration of alkane (CH_3) [32]. The bands situated between 2830.00 and 2945.00 cm^{-1} in both the extracts are caused by the symmetric stretching vibrations of CH_2 group. The band located at 2,524.62 cm^{-1} in methanol extract is due to S—H stretching. The small bands found at 2130.07 and 2076.35 cm^{-1} respectively in ethanol and methanol extracts of cow dung discloses the presence of silicon (Si—H stretching) and boron compounds, owing to the consumption of fodder containing soil constituents by the cow [33]. The peak positioned at 1759.41 cm^{-1} in ethanol extract corresponds to C═O stretching vibration of esters [34]. The intense

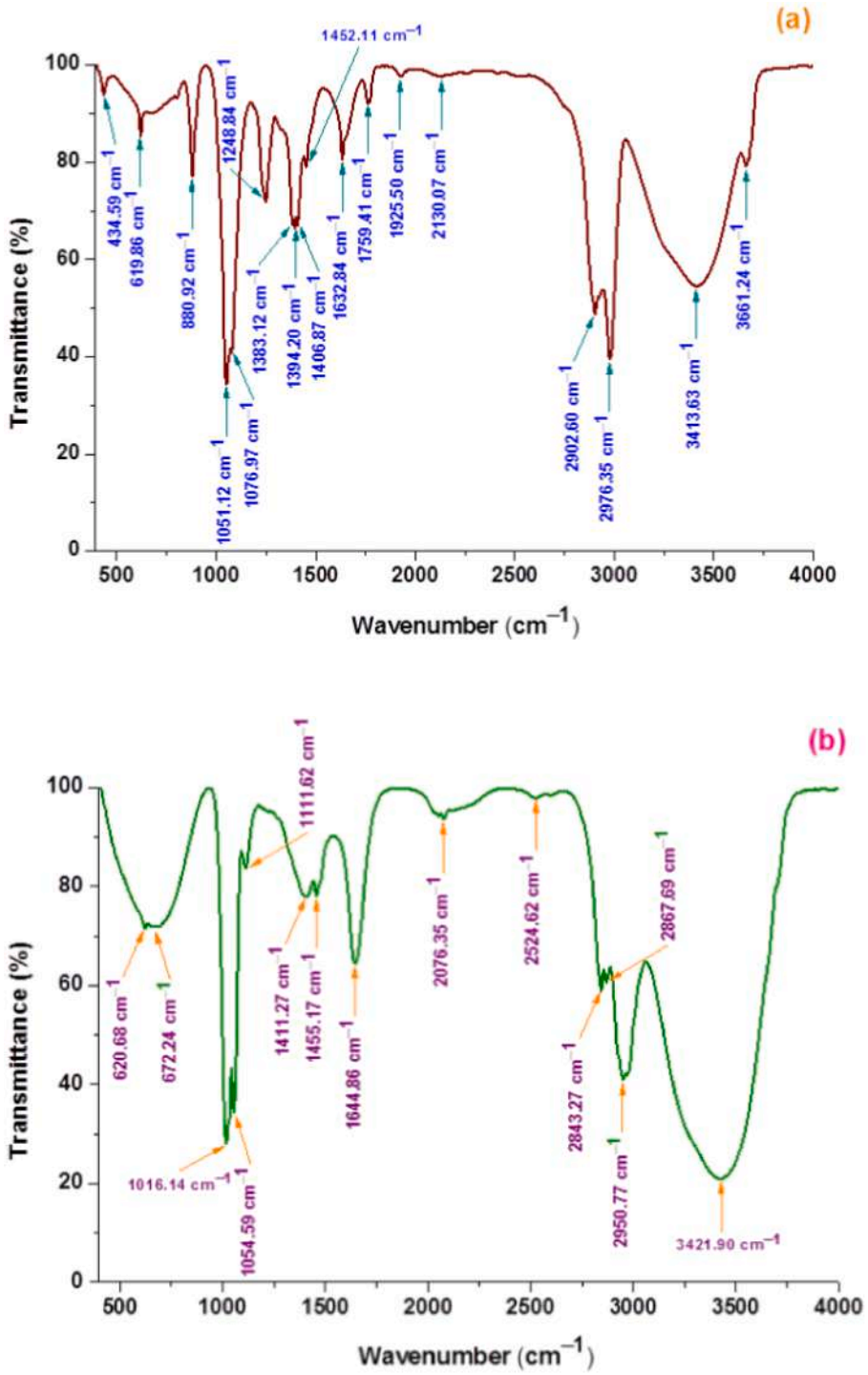

Fig. 8. FTIR spectrum of cow dung extract in (a) ethanol and (b) methanol.

absorption bands emerged at 1632.84 and 1644.86 cm^{-1} in ethanol and methanol extracts, respectively can be ascribed to the C═O stretching vibration of carbonyls [35]. The bands present at 1452.11 and 1455.17 cm^{-1} are due to C—C stretching vibration of aromatic ring compound [12]. The bands at 1406.87 and 1411.27 cm^{-1} are connected with presence of methyl group (CH_3) as C—H in umbrella formation.

The absorption bands noticed at 1383.12 and 1394.20 cm^{-1} can be ascribed to symmetrical and asymmetrical bending vibrations of CH_3 functional groups in ethanol extract of cow dung [36]. The band at 1248.84 cm^{-1} in ethanol extract is formed owing to C—N stretching vibration of amines. The band located at 1111.62 cm^{-1} in methanol extract is ascribed to C═O vibration of carbohydrates [37]. The band observed at 1076.97 cm^{-1} can be associated with stretching vibration of C—O—C [38]. The absorption bands situated between 1000 and 1060 cm^{-1} in both extracts of cow dung are corresponding to the C—H bending or C—O or C—C stretching vibrations of carbohydrates [39]. The high intensity band observed at 880.92 cm^{-1} in ethanol extract of cow dung can be related to P—O and P═O stretching vibrations of polyphosphates [40]. The medium absorption band exhibited by both the extracts at ~620.00 cm^{-1} might be due to the presence of sulphate. By comparing the FT-IR results and the UV–vis absorption results it is inferred that the wide band gap semiconductor photoanode sensitization

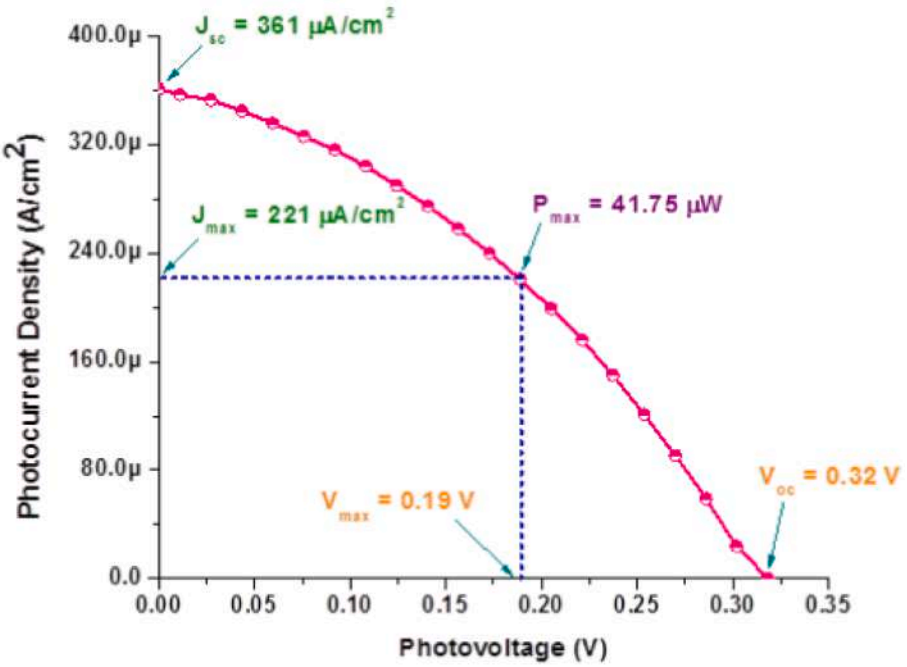

Fig. 9. J–V characteristics of DSSC sensitized with cow dung extract in ethanol.

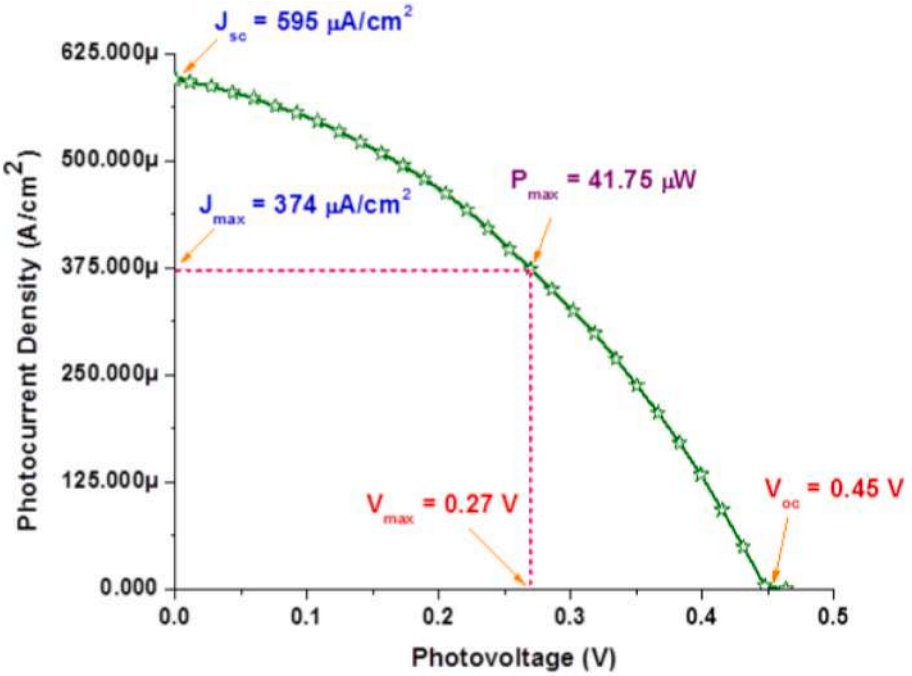

Fig. 10. J–V characteristics of DSSC sensitized with cow dung extract in methanol.

of the current concern, such as ZnO is mainly due to the chlorophylls present in the cow dung extract [14]. The chlorophylls are mainly present in grass, paddy straw, scrubs, greens, etc. The methyl (CH_3) group, which is the ideal functional group present in the chlorophyll molecules can from an ideal bond with semiconductor ZnO nanoparticles that facilitates electron transfer from chlorophyll molecules to the conduction band of ZnO.

3.6. Photovoltaic performance analysis of DSSCs

The photocurrent density-photovoltage (J–V) characteristics of ZnO NPs photoanode based solar cells sensitized using cow dung extracts in ethanol and methanol are illustrated in Figs. 9 and 10, respectively. Reasonable fill factor values could be noticed for both DSSCs sensitized with cow dung extracts in solvents, such as ethanol and methanol. However, the solar to electrical energy transformation efficiency of the DSSCs are low (due to low photocurrent values) when compared to the efficiencies reported for the DSSCs sensitized with commercial dyes. Among the cow dung extracts, the extract obtained using methanol as a solvent disclosed best sensitization effect as evident from the delivered photovoltaic parameters from the corresponding DSSC.

The solar cells sensitized with cow dung extract in methanol

Table 1
Photovoltaic parameters of DSSCs integrated with ZnO NPs photoanode sensitized with cow dung extracts.

Sl. No.	Solvent	J_{sc} (μA/cm^2)	V_{oc} (V)	J_{max} (μA/cm^2)	V_{max} (V)	*FF*	η (%)
1.	Ethanol	361	0.32	221	0.19	0.36	0.042
2.	Methanol	595	0.45	374	0.27	0.38	0.102

delivered the highest solar to electrical energy transformation efficiency (η) of 0.102% with a short-circuit photocurrent density (J_{sc}) of 595 μA/cm^2, open-circuit photovoltage (V_{oc}) of 0.45 V and a fill factor (FF) of 0.38, which could be ascribed to the presence of relatively more number of photosynthetic pigments, viz. chlorophyll *a*, chlorophyll *b* and carotenoids as evident from the UV–vis spectral analysis. The DSSC sensitized by the ethanol extract of cow dung delivered the relatively low efficiency value of 0.042% with a J_{sc} of 361 μA/cm^2, V_{oc} of 0.32 V and FF of 0.36, due to its relatively low intense absorption in visible light spectral region. Although the energy conversion efficiency of the present DSSCs is low over the cells based on synthetic dyes, the scope to advance the performance of the cells sensitized with isolated pigments from cow dung extract certainly paves the pathway for producing efficient and environment friendly DSSCs. The photovoltaic parameters obtained for the DSSCs sensitized by the cow dung extracts are given in Table 1. Comparison of photovoltaic performance of present DSSC sensitized by cow dung extract with previously reported DSSCs sensitized by natural dyes are given in Table 2.

3.7. Maximum power output of DSSCs

The maximum power output (P_{max}) delivered by the DSSCs was calculated by multiplying each short-circuit photocurrent density (J_{sc}) value with its respective open-circuit photovoltage values. The resultant plot between the power (P) and voltage (V) indicates the maximum power output (P_{max}) of the DSSCs sensitized by cow dung extracts in ethanol and methanol (Figs. 11 and 12). It is inferred from the power curves that the DSSC sensitized by the methanolic extract of cow dung delivered the maximum power (P_{max}) of 100.87 μW, which is ~2.4-fold higher than that of the P_{max} value (41.75 μW) of DSSC sensitized by the ethanolic extract of cow dung. This is in harmony with the results of the photocurrent density-photovoltage characteristics.

3.8. Electrochemical impedance spectroscopy analysis

Electrochemical impedance spectra (EIS) of DSSCs integrated with ZnO NPs photoanode adsorbed by ethanolic and methanolic extracts of cow dung were measured under dark condition at an identical forward bias of −0.72 V (Fig. 13). In general, Nyquist plot obtained through EIS analysis consists of three semicircles among which, semicircle at high frequency region corresponds to impedance related to charge transport at counter electrode, medium frequency response semicircle implies charge transport/charge transfer at photoanode/dye/electrolyte interface and semicircle at low frequency region indicates Warburg diffusion process of I^-/I_3^- redox couple in the electrolyte [45]. Here, arc at medium frequency region is associated with electron transfer and recombination at ZnO NPs photoanode/dye (cow dung extract)/electrolyte

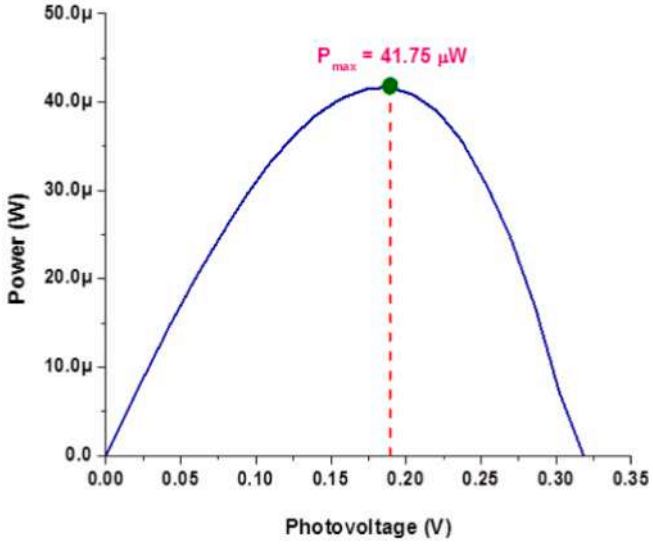

Fig. 11. Power curve of DSSC sensitized with cow dung extract in ethanol.

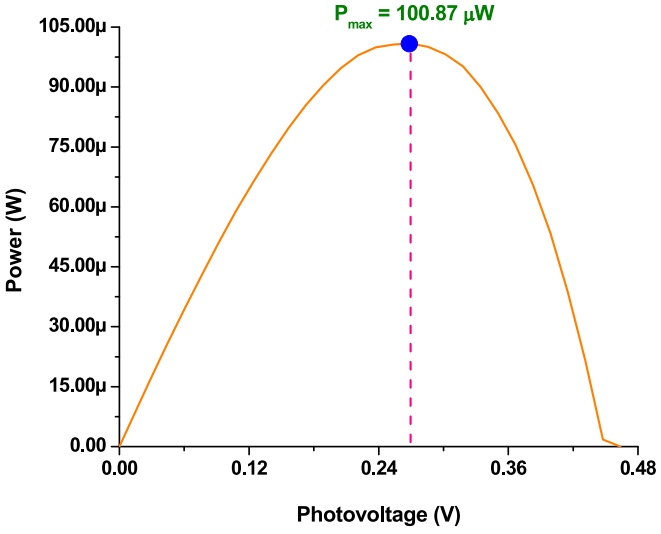

Fig. 12. Power curve of DSSC sensitized with cow dung extract in methanol.

Table 2
Comparison of photovoltaic parameters of DSSC sensitized by methanolic extract of cow dung with previous reports on DSSCs sensitized by natural dyes.

Natural dye	Photoanode material	Solar radiation intensity	J_{sc} (μA/cm^2)	V_{oc} (V)	*FF*	η (%)	Reference
Sargassum wightii seaweed extract	ZnO NPs	45 mW cm^{-2}	203	0.33	0.46	0.07	[12]
Spinach fruit extract	PbS-NPs doped TiO_2 NPs	100 mW cm^{-2}	90 ± 5	0.52 ± 0.01	0.60 ± 0.03	0.029 ± 0.003	[41]
Raspberry fruit extract	PbS-NPs doped TiO_2 NPs	100 mW cm^{-2}	110 ± 7	0.46 ± 0.01	0.56 ± 0.03	0.027 ± 0.002	
Passion fruit extract			54 ± 4	0.39 ± 0.01	0.38 ± 0.04	0.008 ± 0.001	
Costus woodsonii leaf extract	Mesoporous TiO_2 NPs	100 mW cm^{-2}	2250	0.57	0.51	0.65	[42]
Musa paradisiaca peel extract	ZnO NPs	100 mW cm^{-2}	122	0.28	0.25	0.009 ± 0.05	[43]
Mangifera indica peel extract			265	0.29	0.31	0.024 ± 0.05	
Punica granatum peel extract			133	0.28	0.28	0.010 ± 0.05	
Ananas comosus peel extract			33	0.21	0.29	0.002 ± 0.05	
Baobab leaf extract	TiO_2 NPs	1000 W m^{-2}	286 ± 48	0.676 ± 0.062	0.59 ± 0.03	0.11 ± 0.03	[44]
Cow dung extract	ZnO NPs	100 mW cm^{-2}	595	0.45	0.38	0.102	Present work

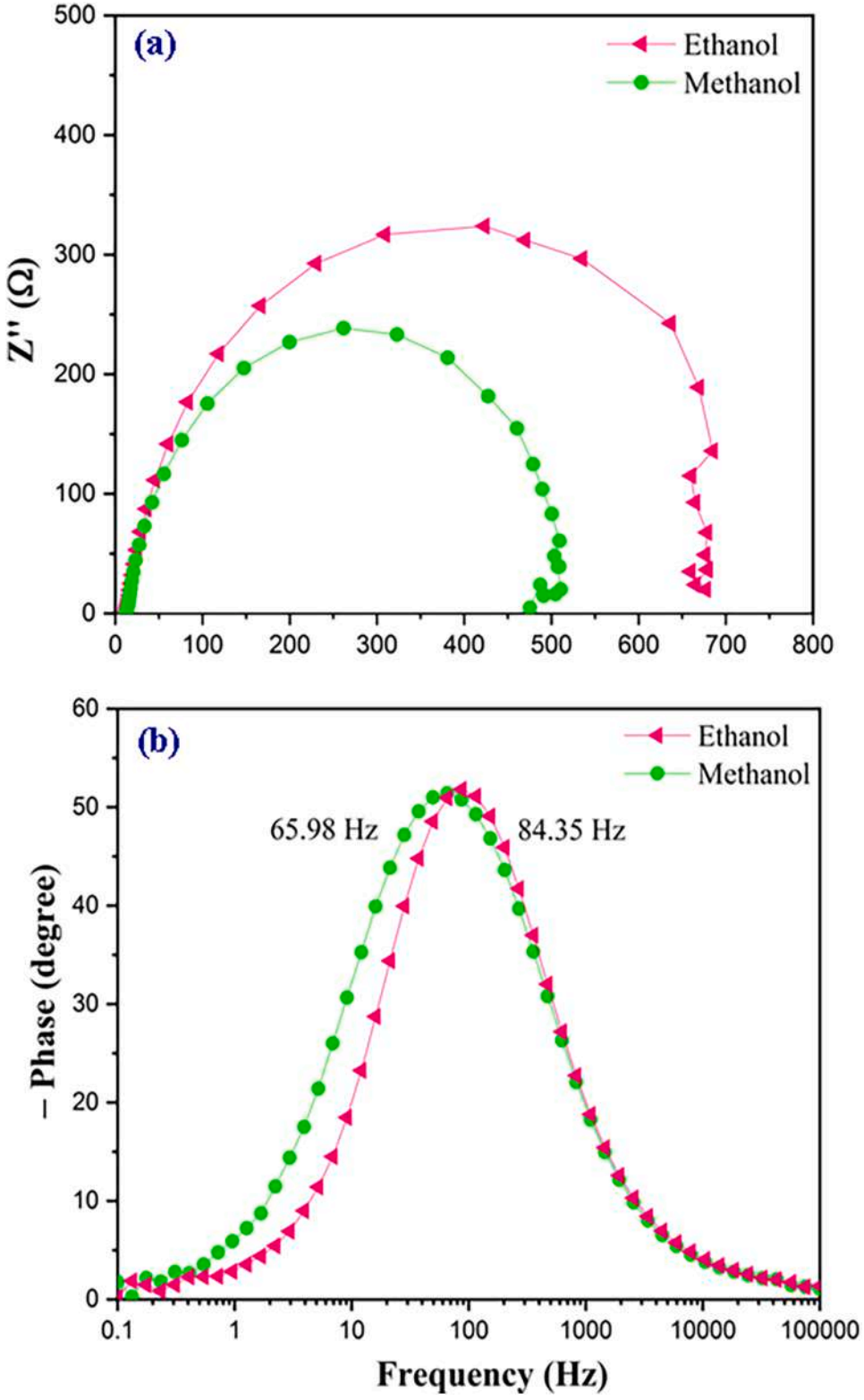

Fig. 13. (a) Nyquist plots and (b) Bode phase plots obtained for DSSCs sensitized with ethanol and methanol extracts and ZnO NPs photoanode.

interface, which plays chief role in determining photovoltaic performance and moreover discloses to and fro movement of electrons at photoanode/electrolyte interface [46,47]. Indeed, larger diameter semicircle corresponds to larger interfacial resistance and high interfacial charge recombination.

Nyquist plot of DSSC constructed using ZnO NPs photoanode adsorbed by ethanolic extract of cow dung shows larger diameter when compared to DSSC with ZnO photoanode adsorbed by methanolic extract of cow dung, suggesting reduced charge transfer resistance at ZnO NPs photoanode/ dye (methanolic extract of cow dung)/electrolyte interface (Fig. 13(a)). Consequently, relatively higher electron transfer process occurred in methanolic cow dung extract sensitized solar cell (DSSC), leading to improved photovoltaic performance and energy conversion efficiency. Electron lifetime (τ_e) of constructed thin film

photoanodes was measured from bode phase plots of corresponding EIS by adopting the equation $\tau_e = 1/2\pi(f_{max})$ [48] where, f_{max} is maximum phase angle associated with electron transfer and recombination kinetics at ZnO NPs photoanode/dye (cow dung extract)/electrolyte and the obtained bode phase plats are shown in Fig. 13(b). From the bode phase plots, electron lifetime of DSSCs fabricated using ZnO NPs photoanode adsorbed by ethanolic and methanolic extracts of cow dung were found to be 1.8 and 2.4 ms, respectively. High electron lifetime of methanolic cow dung extract sensitized solar cell (DSSC) in turn proved effective charge transport to the electrode over ethanolic cow dung extract sensitized solar cell (DSSC) that facilitates better interfacial charge transfer and as a consequence, suppression of charge recombination to a considerable extent.

3.9. Working mechanism of cow dung extracts sensitized DSSCs

Upon illumination of simulated sun light on DSSCs, the photosynthetic dye molecules (D), such as chlorophyll *a*, chlorophyll *b* and carotenoids in cow dung extract go to excited state (D*) by absorption of photons (hν) as illustrated in Eq. (1):

$$D + h\nu \rightarrow D^* \quad (1)$$

The excited photosynthetic dye molecules (D*) inject electrons into conduction band of wide band gap semiconductor (ZnO NPs) and subsequently, the excited photosynthetic dye molecules (D*) oxidize or ionize (D^+) according to Eq. (2):

$$D^* + ZnO \rightarrow D^+ + e^-_{cb}(ZnO) \quad (2)$$

The oxidized photosynthetic dye molecules (D^+) receive electrons coming from iodide ions (I^-) present in the electrolyte when I^- ions release to oxidized photosynthetic dye molecules (D^+) which in turn oxidized to triiodide ions (I_3^-) as shown in equation (3):

$$2D^+ + 3I^- \rightarrow I_3^- + 2D \quad (3)$$

The electrons in conduction band of the ZnO NPs reach the counter electrode through the load and reduced the triiodide ions (I_3^-) as given in Eq. (4):

$$I_3^- + 2\,e^- \rightarrow 3I^- \quad (4)$$

The electron circuit completes by restoration of iodide ions (I^-) and the entire system comes back to its original state to initiate a new cycle. These processes sustains as long as the DSSC is illuminated with light and the external circuit received current continuously [49].

4. Conclusion

Photosynthetic pigments present in the ethanolic and methanolic extracts of cow dung were employed as natural sensitizers in ZnO NPs photoanode based DSSC. The prepared cow dung extracts were characterized by visible interpretation, UV–vis spectrophotometer and FTIR spectroscopy. The colour of cow dung extract in methanol exhibited relatively high intensity over ethanol extract owing to the relatively high polarity of the methanol that facilitate high extractability towards photosynthetic pigments present in the cow dung extract. The UV–Vis absorption spectrum of cow dung extract in ethanol exhibited peaks at 409, 470, 532, 608 and 666 nm and in methanol displayed peaks at 404, 468, 531, 609 and 665 nm, which could be assigned to the presence of photosynthetic pigments, such as chlorophyll *a*, chlorophyll *b* and carotenoids. According to the FTIR results, the methyl (CH_3) group, which is the ideal functional group present in the chlorophyll molecules can from an ideal bond with semiconductor ZnO nanoparticles that facilitates electron transfer from chlorophyll molecules to the ZnO conduction band. The solar cells sensitized with cow dung extract in methanol delivered the highest solar to electrical energy conversion efficiency (η) of 0.102% with a short-circuit photocurrent density (J_{sc}) of 595 $\mu A/cm^2$, open-circuit photovoltage (V_{oc}) of 0.45 V and a fill factor (FF) of 0.38, which could be ascribed to presence of relatively a greater number of photosynthetic pigments, viz. chlorophyll *a*, chlorophyll *b* and carotenoids as evident from the UV–vis spectral analysis. Although the efficiency of the present DSSCs is low over the synthetic dyes, the scope to advance the performance of the cells sensitized with isolated pigments from cow dung extract will certainly paves the pathway for producing efficient and environment friendly DSSCs.

Declaration of Competing Interest

The authors declare that they have no known competing financial interests or personal relationships that could have appeared to influence the work reported in this paper.

Data availability

Data will be made available on request.

Acknowledgment

The authors are thankful to the DST-FIST, Government of India, New Delhi for granting Research Instruments Facility (Grant No. SR/FST/College-2017/140 (C), dt. 14.08.2018). The generous supply of TEC-7 FTO towards research purpose by Pilkington, Mumbai, India is gratefully acknowledged.

References

[1] B. Li, L. Wang, B. Kang, P. Wang, Y. Qiu, Review of recent progress in solid-state dye-sensitized solar cells, Sol. Energy Mater. Sol. Cells 90 (2006) 549–573, https://doi.org/10.1016/j.solmat.2005.04.039.
[2] W. Ghann, H. Kang, T. Sheikh, S. Yadav, T. Chavez-Gil, F. Nesbitt, J. Uddin, Fabrication, optimization and characterization of natural dye sensitized solar cell, Sci. Rep. 7 (2017) 41470, https://doi.org/10.1038/srep41470.
[3] J.S. Shaikh, N.S. Shaikh, S.S. Mali, J.V. Patil, K.K. Pawar, P. Kanjanaboos, C. K. Hong, J.H. Kim, P.S. Patil, Nanoarchitectures in dye-sensitized solar cells: metal oxides, oxide perovskites and carbon-based materials, Nanoscale 10 (2018) 4987–5034, https://doi.org/10.1039/C7NR08350E.
[4] J. Gong, K. Sumathy, Q. Qiao, Z. Zhou, Review on dye-sensitized solar cells (DSSCs): Advanced techniques and research trends, Renew, Sustain. Energy Rev. 68 (2017) 234–246, https://doi.org/10.1016/j.rser.2016.09.097.
[5] B. O'Regan, M. Gratzel, A low-cost, high efficiency solar cell based on dye-sensitized colloidal TiO_2 films, Nature 353 (1991) 737–740, https://doi.org/10.1038/353737a0.
[6] L.M. Goncalves, V.D.Z. Bermudez, H.A. Ribeiro, A.M. Mendes, Dye-sensitized solar cells: A safe bet for the future, Energ. Environ. Sci. 1 (2008) 655–667, https://doi.org/10.1039/B807236A.
[7] A. Hagfeldt, G. Boschloo, L. Sun, L. Kloo, H. Pettersson, Dye-sensitized solar cells, Chem. Rev. 110 (2010) 6595–6663, https://doi.org/10.1021/cr900356p.
[8] A. Yella, H.-W. Lee, H.N. Tsao, C. Yi, A.K. Chandiran, M.K. Nazeeruddin, E.-W.-G. Diau, C.-Y. Yeh, S.M. Zakeeruddin, M. Gratzel, Porphyrin-sensitized solar cells with cobalt (II/III)–based redox electrolyte exceed 12 percent efficiency, Science 334 (2011) 629–634, https://doi.org/10.1126/science.1209688.
[9] J. Burschka, N. Pellet, S.-J. Moon, R. Humphry-Baker, P. Gao, M.K. Nazeeruddin, M. Gratzel, Sequential deposition as a route to high-performance perovskite-sensitized solar cells, Nature 499 (2013) 316–319, https://doi.org/10.1038/nature12340.
[10] M. Ye, X. Wen, M. Wang, J. Iocozzia, N. Zhang, C. Lin, Z. Lin, Recent advances in dye-sensitized solar cells: from photoanodes, sensitizers and electrolytes to counter electrodes, Mater. Today 18 (2015) 155–162, https://doi.org/10.1016/j.mattod.2014.09.001.
[11] S. Suresh, M. Kandasamy, S.K. Kumar, S. Murugesan, Photovoltaic performance of curcumin as sensitizer in a solid-state solar cell, Optik 126 (2015) 3366–3370, https://doi.org/10.1016/j.ijleo.2015.07.119.
[12] M. Anand, S. Suresh, Marine seaweed *Sargassum wightii* extract as a low-cost sensitizer for ZnO photoanode based dye-sensitized solar cell, Adv. Nat. Sci.: Nanosci. Nanotechnol. 6 (2015), 035008, https://doi.org/10.1088/2043-6262/6/3/035008.
[13] K. Tennakone, G.R.R.A. Kumara, A.R. Kumarasinghe, P.M. Sirimanne, K.G. U. Wijayantha, Efficient photosensitization of nanocrystalline TiO_2 films by tannins and related phenolic substances, J. Photochem. Photobiol. A Chem. 94 (1996) 217–220, https://doi.org/10.1016/1010-6030(95)04222-9.
[14] K. Wongcharee, V. Meeyoo, S. Chavadej, Dye-sensitized solar cell using natural dyes extracted from rosella and blue pea flowers, Sol. Energy Mater. Sol. Cells 91 (2007) 566–571, https://doi.org/10.1016/j.solmat.2006.11.005.

[15] D. Zhang, S.M. Lanier, J.A. Downing, J.L. Avent, J. Lum, J.L. McHale, Betalain pigments for dye-sensitized solar cells, J. Photochem. Photobiol. A Chem. 195 (2008) 72–80, https://doi.org/10.1016/j.jphotochem.2007.07.038.
[16] A. Rapsomanikis, D. Sygkridou, E. Voutsinas, E. Stathatos, Transparent quasi-solid state dye-sensitized solar cells sensitized with naturally derived pigment extracted from red seaweed, Curr. Appl Phys. 16 (2016) 651–657, https://doi.org/10.1016/j.cap.2016.03.018.
[17] I.C. Maurya, P. Srivastava, L. Bahadur, Dye-sensitized solar cell using extract from petals of male flowers *Luffa cylindrica* L. as a natural sensitizer, Opt. Mater. 52 (2016) 150–156, https://doi.org/10.1016/j.optmat.2015.12.016.
[18] M. Wendel, A. Kumorkiewicz, S. Wybraniec, M. Ziolek, G. Burdzinski, Impact of S1→S0 internal conversion in betalain-based dye sensitized solar cells, Dyes Pigm. 141 (2017) 306–315, https://doi.org/10.1016/j.dyepig.2017.02.026.
[19] G. Richhariya, A. Kumar, P. Tekasakul, B. Gupta, Natural dyes for dye sensitized solar cell: A review, Renew. Sustain. Energy Rev. 69 (2017) 705–718, https://doi.org/10.1016/j.rser.2016.11.198.
[20] S. Shalini, R.B. Prabhu, S. Prasanna, T.K. Mallick, S. Senthilarasu, Review on natural dye sensitized solar cells: Operation, materials and methods, Renew. Sustain. Energy Rev. 51 (2015) 1306–1325, https://doi.org/10.1016/j.rser.2015.07.052.
[21] S.Z. Siddick, C.W. Lai, J.C. Juan, An investigation of the dye-sensitized solar cell performance using graphene-titania (TrGO) photoanode with conventional dye and natural green chlorophyll dye, Mater. Sci. Semicond. Process. 74 (2018) 267–276, https://doi.org/10.1016/j.mssp.2017.10.046.
[22] H. Ma, J. Tian, L. Cui, Y. Liu, S. Bai, H. Chen, Z. Shan, Porous activated graphene nanoplatelets incorporated in TiO_2 photoanodes for high-efficiency dye-sensitized solar cells, J. Mater. Chem. A 3 (2015) 8890–8895, https://doi.org/10.1039/C5TA00527B.
[23] S. Suresh, A. Pandikumar, S. Murugesan, R. Ramaraj, S.P. Raj, Photovoltaic performance of solid-state solar cells based on ZnO nanosheets sensitized with low-cost metal-free organic dye, Sol. Energy 85 (2011) 1787–1793, https://doi.org/10.1016/j.solener.2011.04.016.
[24] Z. Javed, G.D. Tripathi, M. Mishra, M. Gattupalli, K. Dashora, Cow dung extract mediated green synthesis of zinc oxide nanoparticles for agricultural applications, Sci. Rep. 12 (2022) 20371, https://doi.org/10.1038/s41598-022-22099-y.
[25] M.K. Nazeeruddin, A. Kay, I. Rodicio, R. Humphry-Baker, E. Muller, P. Liska, N. Vlachopoulos, M. Graetzel, Conversion of light to electricity by cis-X2bis(2,2'-bipyridyl-4,4'-dicarboxylate)ruthenium(II) charge-transfer sensitizers (X = Cl^-, Br^-, I^-, CN^-, and SCN^-) on nanocrystalline titanium dioxide electrodes, J. Am. Chem. Soc. 115 (1993) 6382–6390, https://doi.org/10.1021/ja00067a063.
[26] D. Christianson, S. Creel, Photosynthetic pigments estimate diet quality in forage and feces of elk (*Cervus elaphus*), Can. J. Zool. 93 (2015) 51–59, https://doi.org/10.1139/cjz-2014-015.
[27] R. Mohammadpour, S. Janfaza, F. Abbaspour-Aghdam, Light harvesting and photocurrent generation by nanostructured photoelectrodes sensitized with a photosynthetic pigment: A new application for microalgae, Bioresour. Technol. 163 (2014) 1–5, https://doi.org/10.1016/j.biortech.2014.04.003.
[28] F. Zhang, J. He, L. Xia, M. Cai, L. Lin, Y. Guang, Applying and comparing two chemometric methods in absorption spectral analysis of photopigments from Arctic microalgae, J. Microbiol. Methods 83 (2010) 120–126, https://doi.org/10.1016/j.mimet.2010.08.007.
[29] S.G. Ackleson, Light in shallow waters: A brief research review, Limnol. Oceanogr. 48 (2003) 323–328, https://doi.org/10.4319/lo.2003.48.1_part_2.0323.
[30] A.S. Sivam, D. Sun-Waterhouse, C.O. Perera, G.I.N. Waterhouse, Application of FT-IR and Raman spectroscopy for the study of biopolymers in breads fortified with fibre and polyphenols, Food Res. Int. 50 (2013) 574–585, https://doi.org/10.1016/j.foodres.2011.03.039.
[31] C.N.R. Rao, Chemical Applications of Infrared Spectroscopy, Academic, New York, 1963.
[32] J.V. Doorn, J.A. Moulijn, Extraction of spent hydrotreating catalysts studied by fourier transform infra-red spectroscopy, Fuel Process. Technol. 26 (1990) 39–51, https://doi.org/10.1016/0378-3820(90)90022-K.
[33] G. Socrates, Infrared and Raman Characteristic Group Frequencies: Tables and Charts, Wiley, Chichester, United Kingdom, 2001.
[34] M.F. Yam, Y.S. Ch'ng, C.S. Tan, Y.C. Loh, M. Ahmad, M. Zaini Asmawi, Vasorelaxation study and tri-step infrared spectroscopy analysis of Malaysian local herbs, J. Pharmacopuncture 19 (2) (2016) 145–154.
[35] D. Stewart, Fourier transform infrared micro spectroscopy of plant tissues, Appl. Spectrosc. 50 (1996) 357–365, https://doi.org/10.1366/0003702963906384.
[36] O.V. Ovchinnikov, A.V. Evtukhova, T.S. Kondratenko, M.S. Smirnov, V. Y. Khokhlov, O.V. Erina, Manifestation of intermolecular interactions in FTIR spectra of methylene blue molecules, Vib. Spectrosc 86 (2016) 181–189, https://doi.org/10.1016/j.vibspec.2016.06.016.
[37] K. Stehfest, J. Toepel, C. Wilhelm, The application of micro-FTIR spectroscopy to analyze nutrient stress-related changes in biomass composition of phytoplankton algae, Plant Physiol. Biochem. 43 (2005) 717–726, https://doi.org/10.1016/j.plaphy.2005.07.001.
[38] M. Koperska, T. Lojewski, J. Lojewska, Vibrational spectroscopy to study degradation of natural dyes. Assessment of oxygen-free cassette for safe exposition of artefacts, Anal. Bioanal. Chem. 399 (2011) 3271–3283, https://doi.org/10.1007/s00216-010-4460-7.
[39] Y.-M. Li, S.-Q. Sun, Q. Zhou, Z. Qin, J.-X. Tao, J. Wang, X. Fang, Identification of American ginseng from different regions using FT-IR and two-dimensional correlation IR spectroscopy, Vib. Spectrosc 36 (2004) 227–232, https://doi.org/10.1016/j.vibspec.2003.12.009.
[40] T.P. Werner, N. Amrhein, F.M. Freimoser, Specific localization of inorganic polyphosphate (poly P) in fungal cell walls by selective extraction and immunohistochemistry, Fungal Genet. Biol. 44 (2007) 845–852, https://doi.org/10.1016/j.fgb.2007.01.008.
[41] M.J.C. Burgos, S. Roa, B. Cerda, P. Manidurai, Effects of PbS-NPs doping on the photovoltaic performance of natural dye-sensitized TiO_2 photoelectrodes, Solid State Commun. 340 (2021), 114523, https://doi.org/10.1016/j.ssc.2021.114523.
[42] M.Z. Najihah, I.M. Noor, T. Winie, Long-run performance of dye-sensitized solar cell using natural dye extracted from *Costus woodsonii* leaves, Opt. Mater. 123 (2022), 111915, https://doi.org/10.1016/j.optmat.2021.111915.
[43] O. Adedokun, O.L. Adedeji, I.T. Bello, M.K. Awodele, A.O. Awodugba, Fruit peels pigment extracts as a photosensitizer in ZnO-based dye-sensitized solar cells, Chem. Phys. Impact 3 (2021), 100039, https://doi.org/10.1016/j.chphi.2021.100039.
[44] U.I. Ndeze, J. Aidan, S.C. Ezike, J.F. Wansah, Comparative performances of nature-based dyes extracted from Baobab and Shea leaves photo-sensitizers for dye-sensitized solar cells (DSSCs), Curr. Res. Green Sustain. Chem. 4 (2021), 100105, https://doi.org/10.1016/j.crgsc.2021.100105.
[45] G.-J. Ke, H.-Y. Chen, C.-Y. Su, D.-B. Kuang, Template-free solvothermal fabrication of hierarchical TiO_2 hollow microspheres for efficient dye-sensitized solar cells, J. Mater. Chem. A 1 (2013) 13274–13282, https://doi.org/10.1039/c3ta12320k.
[46] M. Kandasamy, M. Selvaraj, M.M. Alam, P. Maruthamuthu, S. Murugesan, Nano-silver incorporated amine functionalized graphene oxide titania nanotube composite: a promising DSSC photoanode, J. Taiwan Inst. Chem. Eng. 131 (2022), 104205, https://doi.org/10.1016/j.jtice.2022.104205.
[47] N. Pugazhenthiran, R.V. Mangalaraja, S. Vijaya, S. Suresh, M. Kandasamy, P. Sathishkumar, H. Valdés, M.A. Gracia-Pinilla, S. Murugesan, S. Anandan, Fluorine-free synthesis of reduced graphene oxide modified anatase TiO_2 nanoflowers photoanode with highly exposed {0 0 1} facets for high performance dye-sensitized solar cell, Sol. Energy 211 (2020) 1017–1026, https://doi.org/10.1016/j.solener.2020.10.008.
[48] R. Kern, R. Sastrawan, J. Ferber, R. Stangl, J. Luther, Modeling and interpretation of electrical impedance spectra of dye solar cells operated under open-circuit conditions, Electrochim. Acta 47 (2002) 4213–4225, https://doi.org/10.1016/S0013-4686(02)00444-9.
[49] A.K. Arof, T.L. Ping, Chlorophyll as photosensitizer in dye-sensitized solar cells, INTECH Open Sci. (2017) 105–121, https://doi.org/10.5772/67955.

Chemical Physics Letters 832 (2023) 140881

Contents lists available at ScienceDirect

Chemical Physics Letters

journal homepage: www.elsevier.com/locate/cplett

Vitex negundo and *Euphorbia milii* leaf extracts aided green synthesis of copper oxide nanostructures for effective inactivation of pathogenic bacteria

S. Thambidurai [a,*], J. Arumugam [b], M. Kandasamy [c,d], D. Balaji [b], N. Pugazhenthiran [e], R. Jothilakshmi [f], B. Sathish Kumar [g], K. Murugesan [g], S. Karthick Kumar [h], T. Muneeswaran [i], K. Jayakumar [j], S. Suresh [b,*]

[a] Department of Physics, Government Arts College for Women, Krishnagiri 635 001, Tamil Nadu, India
[b] PG & Research Department of Physics, Sri Vidya Mandir Arts & Science College (Autonomous), Katteri, 636 902 Uthangarai, Tamil Nadu, India
[c] Institute of Power Engineering, Universiti Tenaga Nasional, Kajang 43000, Selangor, Malaysia
[d] Department of Chemistry, K. Ramakrishnan College of Technology, Trichy 621 112, Tamil Nadu, India
[e] Laboratorio de Fotoquímica y Fotofísica, Departamento de Química, Universidad Técnica Federico Santa María, Av. España 1680, Valparaíso, Chile
[f] Department of Physics, Velammal College of Engineering and Technology, Madurai 625 009, Tamil Nadu, India
[g] PG Department of Botany, Sri Vidya Mandir Arts & Science College (Autonomous), Katteri, 636 902 Uthangarai, Tamil Nadu, India
[h] Department of Physics, Sethu Institute of Technology, Kariapatti, 626 115 Virudhunagar, Tamil Nadu, India
[i] Lab of Toxicology, Department of Health Sciences, The Graduate School of Dong-A University, Busan 49315, Republic of Korea
[j] Department of Animal Behaviour and Physiology, School of Biological Sciences, Madurai Kamaraj University, Madurai 625 021, Tamil Nadu, India

ARTICLE INFO

Keywords:
Green synthesis
Vitex negundo
Euphorbia milii
CuO nanostructures
Oxygen vacancy
Antibacterial activity

ABSTRACT

A facile and green route was followed to synthesize copper oxide (CuO) nanostructures using *Vitex negundo* and *Euphorbia milii* leaf extracts. Structural, elemental, chemical, spectral and morphological features of the CuO nanostructures were determined by XRD, EDS, FTIR spectroscopy, UV–Vis spectrophotometer and FESEM, respectively. The CuO nanostructures disclosed considerably higher antibacterial activity against selected Gram-positive and Gram-negative pathogenic bacteria over commercial antibiotic (Vancomycin). This enhanced antibacterial activity could be credited to the generation of more ROS associated with oxygen vacancy and size of the CuO nanostructures. Particularly, hierarchical CuO nanoparticles/nanorods prepared using *V. negundo* leaf extract exhibited the highest antibacterial activity due to their lower size range.

1. Introduction

In modern scientific and technological scenario, the role of nanomaterials has been manifested as crucial due to their peculiar physicochemical properties over their bulk counterparts [1] and emergence of diverse dimensional nanostructures, such as particles, tubes, wires, rods, spheres, sheets, prisms and their hybrids [2,3]. Consequently, metal and metal oxide nanostructure synthesis has provoked immense attention by considering their precise size, diverse morphology, controlled dispersity, and supplemented characteristics that have been transformed them as ideal candidates for applications in energy, environment, medical, textile and pharmaceutical sectors [4]. Among them, prominent focus has been exerted on narrow band gap p-type copper oxide (CuO) nanostructures, owing to their remarkable physical, chemical, electrical, optical and magnetic properties [5]. In addition, nanoforms of CuO have been demonstrated notable stability in solutions [6], environmental safety [7], high redox potential [8], substantial specific surface area and exceptional electrochemical activity [9]. Consequently, they have been appealed extensively as antibacterial agents [3,10], photocatalysts [11], heavy metal adsorbents [12], electrode materials for lithium-ion battery [13] and supercapacitors [14], gas sensors [15], solar selective absorbers [16], antifungal agents [17], colorimetric sensors [18] and antifouling paints [19].

According to the biomedical viewpoint, the present world has been perceived an increasing occurrence of infectious diseases caused by various pathogenic bacteria that ultimately induce mortality, morbidity

* Corresponding authors.
E-mail addresses: thambiphy@gmail.com (S. Thambidurai), sureshskrish1981@gmail.com (S. Suresh).

https://doi.org/10.1016/j.cplett.2023.140881
Received 4 July 2023; Received in revised form 6 September 2023; Accepted 10 October 2023
Available online 13 October 2023

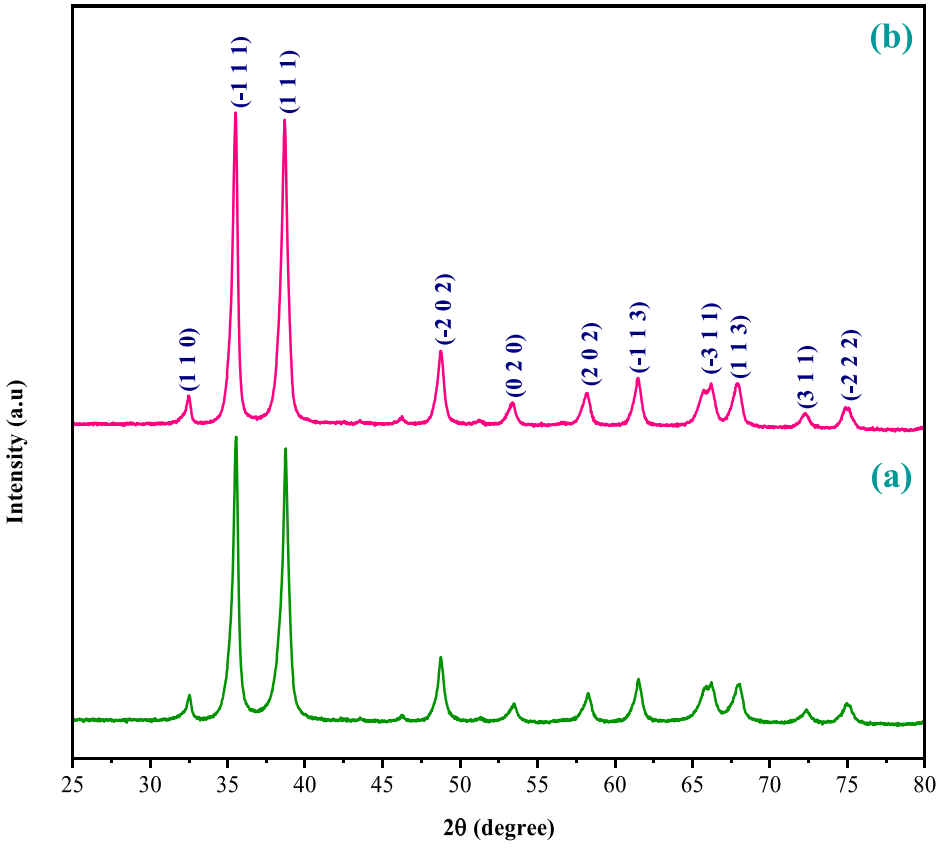

Fig 1. XRD profiles of CuO nanostructures green synthesized using (a) *V. negundo* and (b) *E. milii* leaf extracts.

Table 1
XRD parameters derived from XRD patterns of CuO nanostructures green synthesized using (a) *V. negundo* and (b) *E. milii* leaf extracts.

Peak Position, 2θ (°)		h k l	FWHM		d-Spacing		Crystalline Size (nm)		Lattice Strain	
(a)	(b)		(a)	(b)	(a)	(b)	(a)	(b)	(a)	(b)
32.46	32.45	1 1 0	0.5196	0.5196	2.7583	2.7603	16.64	16.64	0.0078	0.0078
35.52	35.51	−1 1 1	0.3464	0.3464	2.5273	2.5279	25.16	25.16	0.0047	0.0047
38.74	38.70	1 1 1	0.3464	0.3464	2.3246	2.3268	25.40	25.40	0.0043	0.0043
48.76	48.78	−2 0 2	0.3464	0.4330	1.8675	1.8669	26.31	21.05	0.0033	0.0042
53.46	53.39	0 2 0	0.3464	0.4330	1.7140	1.7160	26.83	21.46	0.0030	0.0038
58.27	58.20	2 0 2	0.3464	0.4330	1.5834	1.5851	27.43	21.94	0.0027	0.0034
61.52	61.51	−1 1 3	0.3464	0.3464	1.5073	1.5076	27.88	27.88	0.0025	0.0025
66.19	66.21	−3 1 1	0.3464	0.3464	1.4119	1.4115	28.60	28.60	0.0023	0.0023
67.98	67.93	1 1 3	0.4330	0.5196	1.3790	1.3799	23.12	19.26	0.0028	0.0034
72.36	72.30	3 1 1	0.3464	0.4330	1.3060	1.3069	29.68	23.74	0.0021	0.0026
75.02	74.99	−2 2 2	0.5196	0.6061	1.2660	1.2665	20.14	17.25	0.0030	0.0034

and socio-economic losses [20]. Hence, it is not conceivable to eliminate pathogenic bacteria and as a consequence, increment in the dominance of bacteria comprising antibiotic resistant has inspired the research community to search for novel, efficient, harmless and robust antibacterial agents [21,22]. Among prime classifications of antibacterial agents, organic antibacterial agents possess major limitations of insufficient thermal stability and toxicity that shift concentration for the exploration of inorganic antibacterial agents [23,24]. Variations in synthesis methodologies create nanomaterials with diverse chemical constituents, shapes, crystalline structure, surface anchored chemical groups, specific surface area, etc., which enhance their inherent properties to a substantial extent and as a result, improvement in antibacterial activity could be anticipated [25,26]. In this respect, CuO nanostructures have been documented as ideal antibacterial candidates because of their inherent physical and chemical stability that facilitate facile interaction with biological molecules of diverse pathogenic bacteria for proficient antibacterial activity [27,28]. Another peculiar advantage of CuO nanostructures is their tendency to stimulate generation of reactive oxygen species (ROS) and creation of appreciable oxidative stress for cytotoxicity and DNA impairment in pathogenic bacterial strains [29]. Moreover, electron donor–acceptor properties and high redox potential of CuO nanostructures enable their cell wall binding and interference with nucleic acids that eventually cause destruction of bacteria [30–32].

The methods commonly followed to prepare CuO nanostructures are chemical precipitation [33], wet chemical [34], solvothermal [35], sol–gel [36], hydrothermal [37], chemical bath deposition [38], electrochemical [39], microwave irradiation [40], sputtering [41], sonochemical [42], laser ablation [43] and thermal decomposition [44]. Nevertheless, the synthesis of CuO nanostructures by these prevalent chemical and physical routes cannot be recognized as convenient because they are occasionally complex, take long reaction time, require

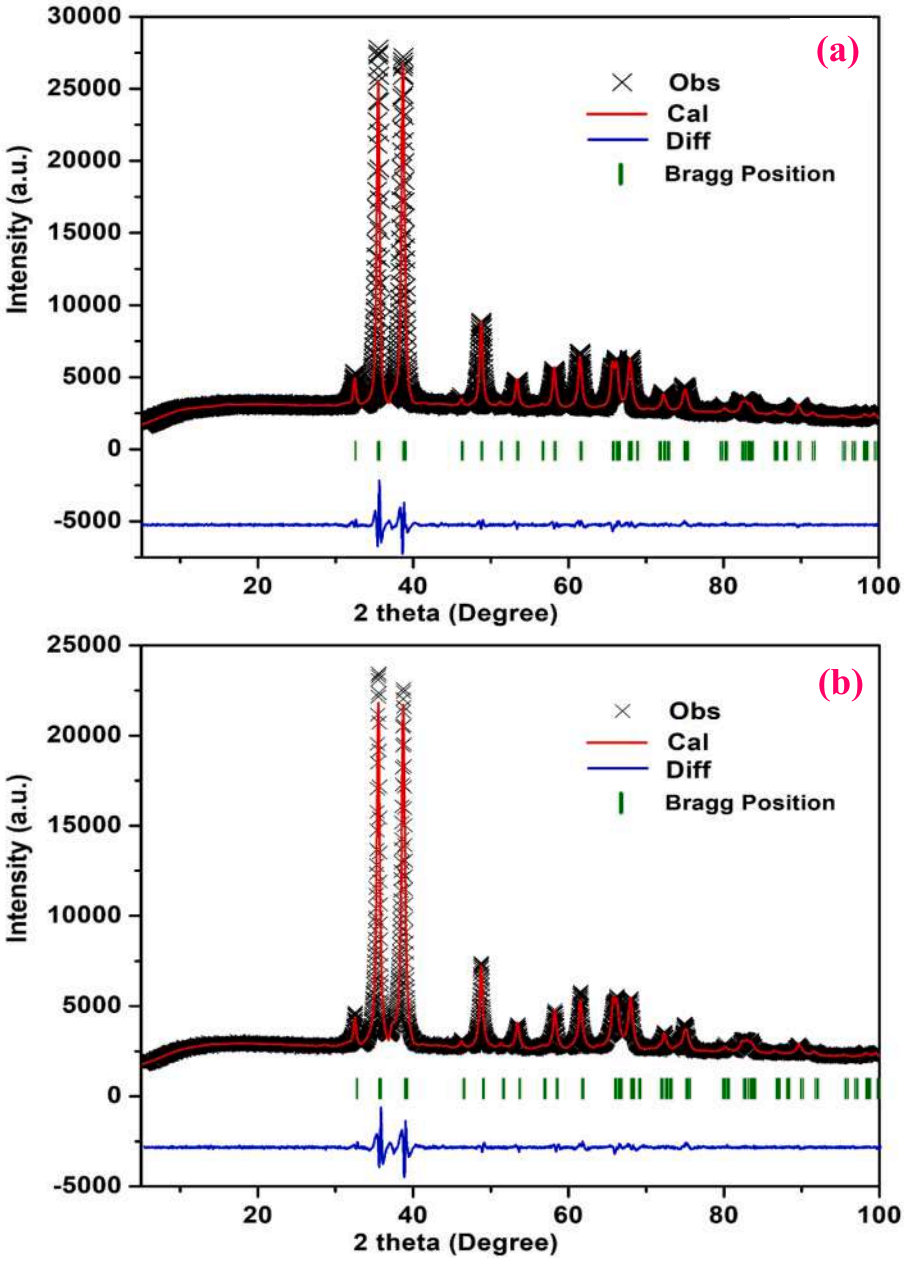

Fig 2. Rietveld refinement patterns of CuO nanostructures green synthesized using (a) *V. negundo* and (b) *E. milii* leaf extracts.

Table 2
Refined crystallographic parameters of CuO nanostructures green synthesized using *V. negundo* and *E. milii* leaf extracts.

Crystallographic parameter	CuO nanostructure green synthesized using	
	***V. negundo* leaf extract**	***E. milii* leaf extract**
Crystal System	Monoclinic	Monoclinic
Space Group	C2/c	C2/c
Lattice Parameters	a = 4.6917(4) Å b = 3.4328(3) Å c = 5.1391(5) Å α = γ = 90°, β = 99.371 (4)°	a = 4.6916(5) Å b = 3.4296(4) Å c = 5.1370(6) Å α = γ = 90°, β = 99.436 (5)°
Unit Cell Volume	V = 81.665(13) Å^3	V = 81.537(16) Å^3
R_p (%)	2.67	2.67
R_{wp} (%)	4.20	4.15
χ^2	1.40	1.50

Table 3
Atomic coordinates and occupancy of CuO nanostructures derived from Rietveld refinement analysis.

Atomic coordinates of CuO nanostructures green synthesized using *V. negundo* leaf extract					
Atom	*x*	y	z	Occ.	U_{eq} (Å^2)
Cu	0.25	0.25	0	1	0.00434
O	0	0.42	0.25	1	0.00250
Atomic coordinates of CuO nanostructures green synthesized using *E. milii* leaf extract					
Atom	*x*	y	z	Occ.	U_{eq} (Å^2)
Cu	0.25	0.25	0	1	0.00843
O	0	0.43	0.25	1	0.00030

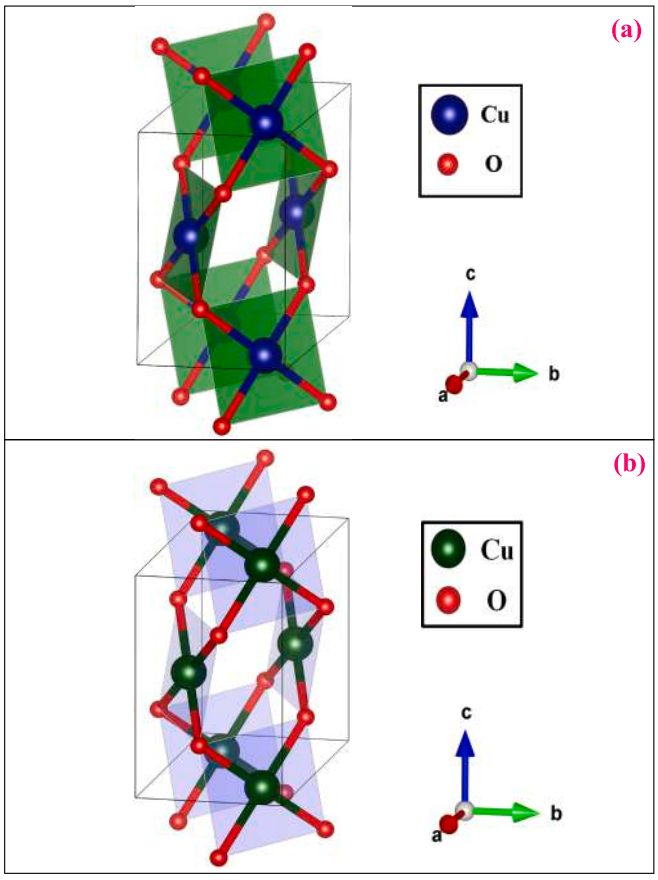

Fig 3. Crystal structure of CuO nanostructures green synthesized using (a) *V. negundo* and (b) *E. milii* leaf extracts.

high-cost/sophisticated equipment, produce unsafe byproducts due to the usage of hazardous chemicals and demand high temperature & pressure environments [45,46]. Alternatively, the synthesis of nanostructures through green synthesis methods has gained auspicious attention in diverse domains of nanotechnology [47]. The natural chemical constituents derived from the extracts of plant parts facilitate an ideal pathway to synthesize semiconductor metal oxide nanostructures in an eco-friendly manner with added advantages of considerable cost reduction and elimination of harmful synthetic chemicals to act as reducing and stabilizing agents, biodegradable nature with biocompatibility, simple synthesis protocols and abundant biomolecules presence [10,48,49]. Moreover, the green synthesis of nanomaterials facilitates effectual reduction of particles size, formation of peculiar morphologies and improved production of reactive oxygen species for potential antibacterial application [50]. Earlier investigations on green synthesis of CuO nanostructures using extracts of *Cynodon dactylon* and *Cyperus rotundus* grasses [3] and leaves of *Hibiscus cannabinus* [10], *Simarouba glauca* [51], and *Moringa oleifera* [32] plant species have demonstrated conspicuous antibacterial performance against pathogenic bacteria.

By taking the above stated facts into account and also with the anticipation of obtaining different morphologies and high antibacterial activity, in the present study, we have used *Vitex negundo* and *Euphorbia milii* leaf extracts as eco-friendly and cost-free reducing/structure directing agents to synthesis CuO nanostructures and their antibacterial activity has been assessed against selected pathogenic bacteria. In terms of novelty, this work is devoted to green synthesis of diverse CuO nanostructures using *Vitex negundo* and *Euphorbia milii* leaf extracts, since numerous works in the past demonstrated green synthesis of semiconductor nanoparticles rather than different semiconductor nanostructures.

2. Materials and methods

2.1. Chemicals and reagents

High pure copper nitrate trihydrate ($Cu(NO_3)_2{\cdot}3H_2O$; ≥99.5 %) was purchased from Merck. Mueller Hinton Agar medium was supplied by Himedia. Commercial antibiotic, vancomycin ($C_{66}H_{75}Cl_2N_9O_{24}$) was supplied by Merck. *Bacillus cereus*, *Staphylococcus aureus*, *Escherichia coli* and *Pseudomonas aeruginosa* bacterial strains were purchased from Institute of Microbial Technology (IMTECH), India. Double distilled water was used for experimental works and washings.

2.2. Synthesis of copper oxide (CuO) nanostructures

Fresh leaves of *Vitex negundo* (*V. negundo*) and *Euphorbia milii* (*E. milii*) plants were plucked from respective plants grown in Pavakkal Village, Krishnagiri District and Sri Vidya Mandir Arts & Science College (Autonomous) Campus, Katteri Village, Tamil Nadu, India. The leaves were initially washed in tap water to remove dust particles found on their surface and thereafter cleaned using distilled water thrice and dried under dark condition. Subsequently, the leaves (5 g each) were weighed separately and cut into pieces using scissor. The leaf fragments were grounded for 15 min and the obtained leaf pastes were taken in beakers having distilled water (150 mL). The beakers were subjected to magnetic stirring at 600 rpm with heating at 80 °C for 1 h. Each 30 mL of *V. negundo* and *E. milii* filtered leaf extracts were taken separately in two beakers and $Cu(NO_3)_2{\cdot}3H_2O$ (1 g) was added under stirring at 80 °C. The reduction of Cu^{2+} ions and subsequent formation of $Cu(OH)_2$ were confirmed by the color change of solutions from bluish to dark green. The stirring process was sustained till the solutions transformed in the form of green color pastes, which were rinsed thrice using distilled water to eliminate ionic impurities and surplus biomolecules. Finally, the generated precipitates were transferred to silica crucibles and sintered at 350 °C for 2 h during which, green color precipitates were turned into dark color powders that confirmed formation of CuO nanostructures.

2.3. Characterization

XRD profiles of synthesized CuO samples were recorded in PANalytical X'pert3 powder X-ray Diffractometer with CuKα radiation (λ = 1.5418 Å). Structural investigations were carried out by Rietveld refinement method using FullProf Suite Programmed Software. Elemental analyses were performed in EDS-BRUKER nano EDAX spectroscopy (GmbH, D-12489, Germany). FTIR spectra were taken using PerkinElmer FTIR spectroscopy (Spectrum Two). UV–vis diffuse reflectance spectra of CuO samples were recorded through UV 3000 Spectrophotometer (LABINDIA). FESEM images were recorded using field emission scanning electron microscopy (FEG Quanta 250).

2.4. Antibacterial activity assessment

The antibacterial activity of prepared CuO nanostructures was investigated through well diffusion method. Initially, liquid Mueller Hinton agar media and petri dishes were sterilized in an autoclave at 121 °C and 15 lbs for 30 min. Under aseptic conditions in laminar airflow chamber, agar media (20 mL) was dispensed in petri dish to get uniform depth of 4 mm. After solidification of media, 18 h culture of Gram-positive bacteria (*Bacillus cereus* and *Staphylococcus aureus*) and Gram-negative bacteria (*Escherichia coli* and *Pseudomonas aeruginosa*) were swabbed on the surface of agar plates. A cork borer was used to create wells, followed by loading CuO nanostructure samples (7 and 14 mg/mL) and vancomycin (30 μg/disc) as a positive control in distinct wells. Finally, the plates were incubated at 37 °C for 24 h to detect inhibition zones.

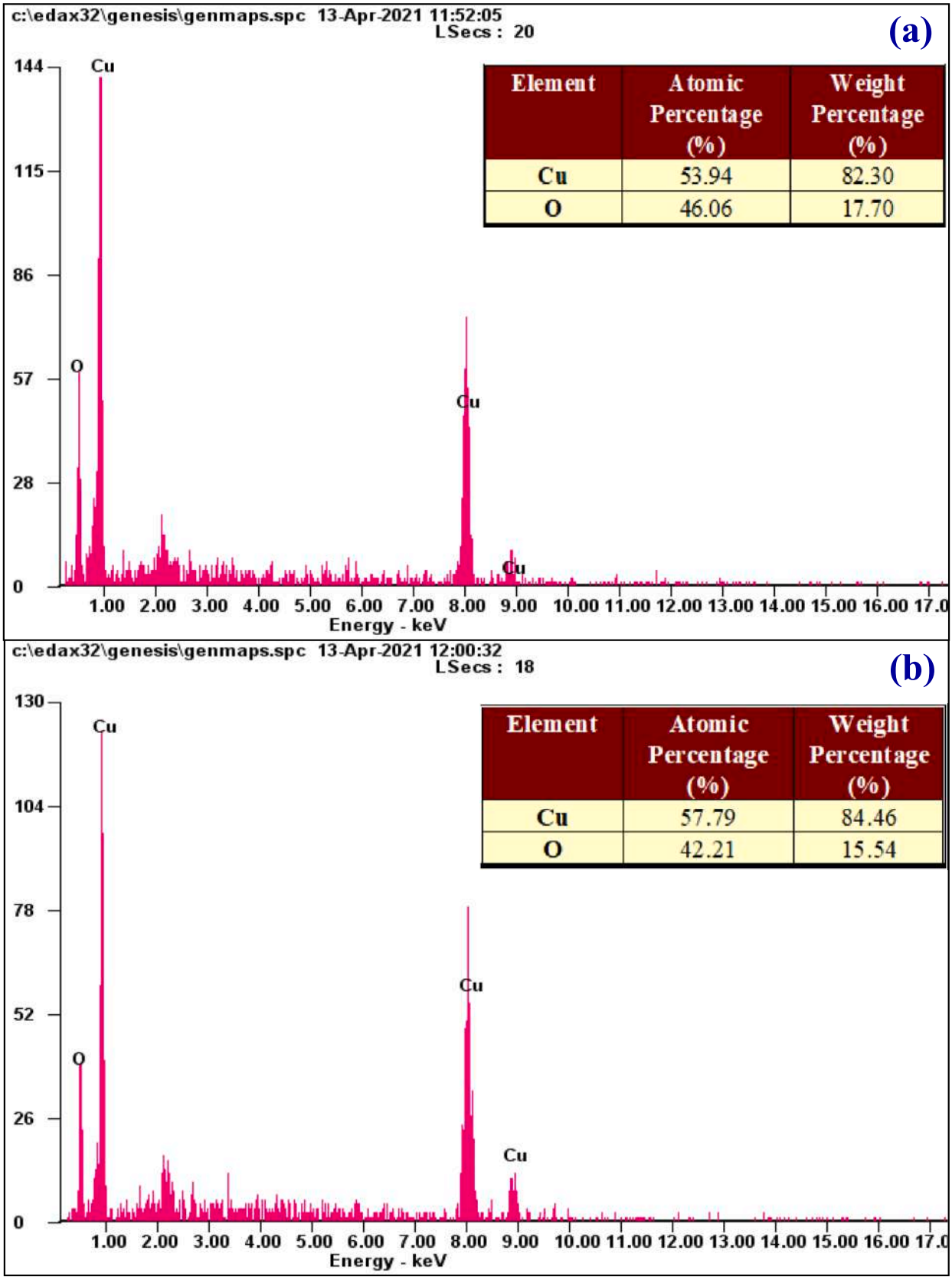

Fig 4. EDS spectra of CuO nanostructures green synthesized using (a) *V. negundo* and (b) *E. milii* leaf extracts. Insets show atomic and weight percentages of Cu and O elements present in CuO nanostructures.

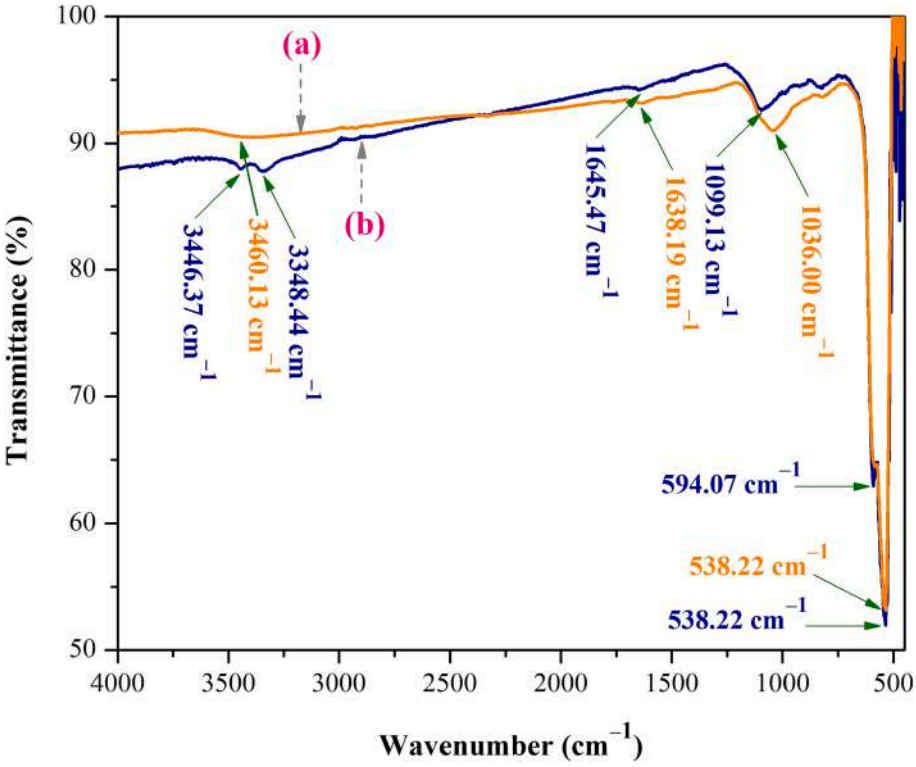

Fig 5. FTIR spectra of CuO nanostructures green synthesized using (a) *V. negundo* and (b) *E. milii* leaf extracts.

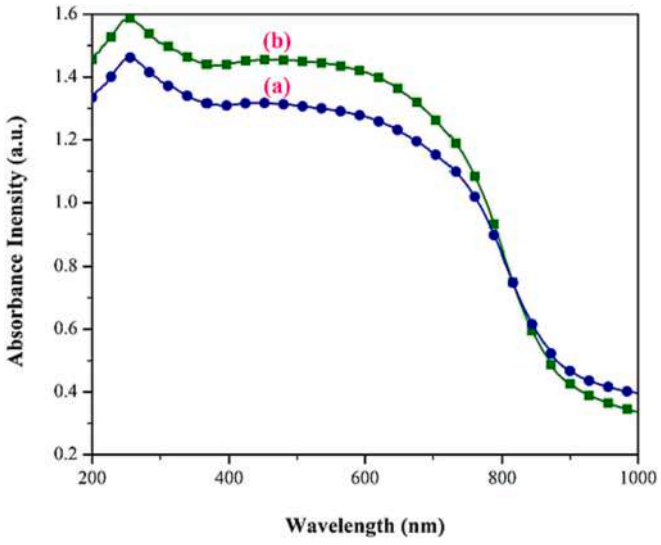

Fig 6. UV–Vis diffuse reflectance spectra of CuO nanostructures green synthesized using (a) *V. negundo* and (b) *E. milii* leaf extracts.

3. Results and discussion

3.1. Structural assessment

Crystalline structure and phase of CuO nanostructures green synthesized using *V. negundo* and *E. milii* leaf extracts were assessed by X-ray diffractometer (XRD). XRD profiles of CuO nanostructures in Fig. 1 display eleven characteristic diffraction peaks between diffraction angles (2θ) of 25 and 80°. XRD profiles of both the CuO nanostructures are comprised of well-defined and sharp diffraction peaks with narrow width that discloses their high crystallinity. The XRD parameters derived from the XRD patterns of CuO nanostructures are given in Table 1. Diffraction peaks located at 2θ values of 32.46, 35.52, 38.74, 48.76, 53.46, 58.27, 61.52, 66.19, 67.98, 72.36, & 75.02° and 32.45, 35.51, 38.70, 48.78, 53.39, 58.20, 61.51, 66.21, 67.93, 72.30, & 74.99° for the CuO nanostructures green synthesized using *V. negundo* and *E. milii* leaf extracts are matched well to the diffraction planes of (1 1 0), (−1 1 1), (1 1 1), (−2 0 2), (0 2 0), (2 0 2), (−1 1 3), (−3 1 1), (1 1 3), (3 1 1), and (−2 2 2), respectively. This signifies the formation of single-phase and monoclinic crystal structured CuO nanostructures. Non-appearance of diffraction peaks corresponding to impurities in the XRD patterns discloses phase purity of the CuO nanostructures.

By Debye–Scherrer formula ($D = k\lambda/\beta \cos\theta$) and FWHM of obtained diffraction peaks, the average crystalline sizes of CuO nanostructures green synthesized using *V. negundo* and *E. milii* leaf extracts are estimated as 25.20 and 22.58 nm, respectively. The strain (ε_{str}) developed in CuO nanostructures to lattice misfit was calculated by the formula $\varepsilon_{str} = \beta/4 \tan\theta$ [52,53]. The average values of strain (ε_{str}) calculated for the CuO nanostructures green synthesized using *V. negundo* and *E. milii* leaf extracts are 0.0035 and 0.0039, respectively which discloses their better crystallinity and high quality. Decisively, the XRD results unveil that biomolecules present in the *V. negundo* and *E. milii* leaf extracts have performed indispensable roles of reducing and stabilizing agents for the formation of CuO nanostructures.

3.2. Rietveld refinement analysis

Structural parameters of CuO nanostructures green synthesized using *V. negundo* and *E. milii* leaf extracts were refined through the Rietveld refinement method and the obtained refinement patterns are shown in Fig. 2. The refinement was carried out by FullProf Suite Programmed Software that employed Pseudo-Voigt function to fit several parameters to data point. The red and black color lines in Fig. 2 denote calculated and observed data, respectively. The blue line indicates variation between calculated and observed data whereas, the green line designates Bragg position. The refined crystal structure was drawn using VESTA Software. Conspicuously, all the reflections of CuO nanostructures green

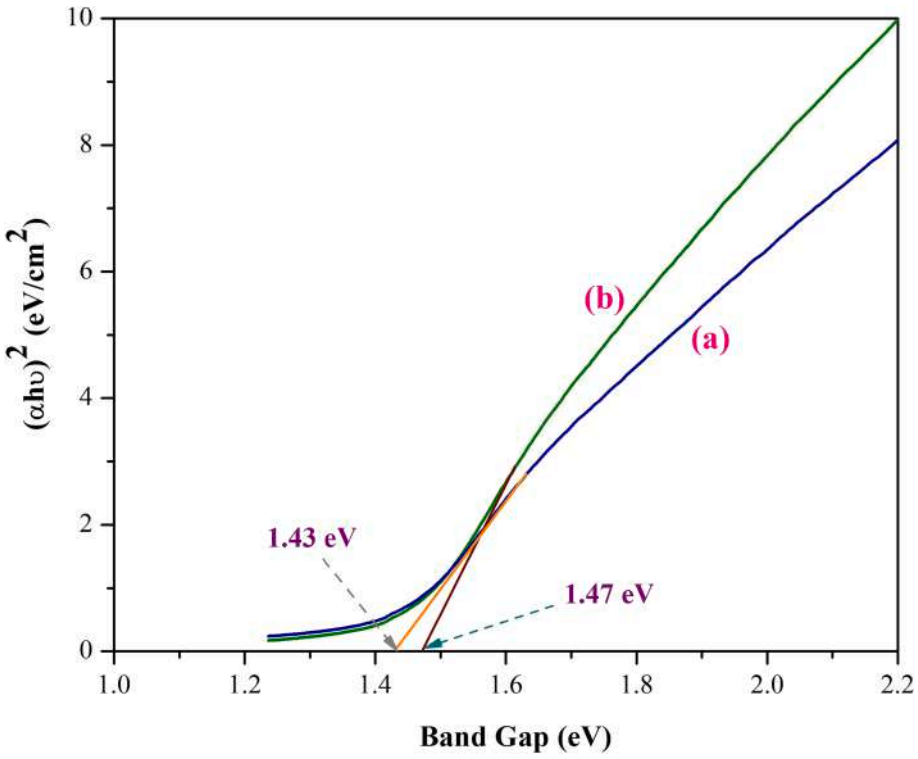

Fig 7. *Tauc* plots of CuO nanostructures green synthesized using (a) *V. negundo* and (b) *E. milii* leaf extracts.

synthesized using *V. negundo* and *E. milii* leaf extracts are matched well, disclosed purity in phase and absence of reflections related to foreign substances, such as Cu, Cu_2O and $Cu(OH)_2$, which indicates formation of pristine and crystalline structured CuO through the present green synthesis route. The harmonized peak positions and intensities precisely designates good refinement. The experiential reflections of both the CuO nanostructures can be well indexed to pristine monoclinic unit cell having space group of C2/c, which are in accordance with the observed XRD patterns. The refined crystallographic parameters including lattice parameters of green synthesized CuO nanostructures are listed in Table 2.

Lattice constants obtained through the Rietveld refinement method are $a = 4.6917(4)$ Å, $b = 3.4328(3)$ Å, $c = 5.1391(5)$ Å, $\alpha = \gamma = 90^\circ$, $\beta = 99.371(4)^\circ$ and $a = 4.6916(5)$ Å, $b = 3.4296(4)$ Å, $c = 5.1370(6)$ Å, $\alpha = \gamma = 90^\circ$, $\beta = 99.436(5)^\circ$ for the CuO nanostructures green synthesized using *V. negundo* and *E. milii* leaf extracts, respectively. Meanwhile, satisfactory convergence factors ($R_p = 2.67$ %, $R_{wp} = 4.20$ %, $\chi^2 = 1.40$ and $R_p = 2.67$ %, $R_{wp} = 4.15$ %, $\chi^2 = 1.50$) were obtained through the refinement method for the CuO nanostructures green synthesized using *V. negundo* and *E. milii* leaf extracts, respectively. Atomic coordinates and occupancy of the CuO nanostructures obtained from the Rietveld refinement analysis are given in Table 3. Refined crystal structures of the CuO nanostructures green synthesized using *V. negundo* and *E. milii* leaf extracts exhibit that each copper atom is coordinated by four coplanar oxygen atoms to create nearly a rectangular parallelogram whereas, the oxygen coordination polyhedron has four copper atoms at corners of a distorted tetrahedron (Fig. 3).

3.3. Elemental and purity examination

Elements presence and purity of the green synthesized CuO nanostructures were ascertained by energy-dispersive X-ray spectroscopy (EDS) and the recorded EDS spectra are exemplified in Fig. 4. The EDS spectra apparently depict peaks corresponding to copper (Cu) and oxygen (O) elements that revealed formation of pristine CuO through the present green synthesis route. The atomic and weight percentages of Cu and O elements present in the CuO nanostructures determined through EDS analysis are shown in the insets of Fig. 4. The atomic percentage of Cu and O elements present in the CuO nanostructures green synthesized using *V. negundo* and *E. milii* leaf extracts is 53.94 & 46.06 % and 57.79 & 42.21 %, respectively. Meanwhile, the weight percentage of Cu and O elements found in the CuO nanostructures green synthesized using *V. negundo* and *E. milii* leaf extracts is 82.30 & 17.70 % and 84.46 & 15.54 % respectively. Hypothetically, the expected stoichiometric weight proportion of Cu and O elements in CuO is 79.89 and 20.11 %, respectively. Contradictorily, the CuO nanostructures green synthesized using *V. negundo* and *E. milii* leaf extracts exhibited increment in the Cu weight percentage of 2.41 and 4.57 % and decrement in the same weight percentage of O, respectively with respect to their corresponding stoichiometric weight percentage that discloses emergence of oxygen vacancies in the CuO nanostructures. The variations observed between theoretical and practical weight percentage values might be credited to organic remains originated from biomolecules of *V. negundo* and *E. milii* leaf extracts during the synthesis process and consequently, oxygen vacancies could be created in the CuO nanostructures [54]. The relatively high oxygen vacancy noticed for the CuO nanostructure green synthesized using *E. milii* leaf extract would be a beneficial property for better antibacterial activity [55,56]. In addition to the elemental peaks of Cu and O, the EDS spectra of CuO nanostructures display a meager intensity peak at ~2.2 keV that can be assigned to gold (Au), which was used as a coating material in the grid to deposit the green synthesized CuO nanostructures prior to the EDS analysis [57]. Besides the peaks of Cu, O, and Au, the non-occurrence of peaks pertaining to impurities in the EDS spectra disclose purity of the green synthesized CuO nanostructures.

3.4. Functional groups identification

Functional groups present in the CuO nanostructures green synthesized using *V. negundo* and *E. milii* leaf extracts were determined through FTIR analysis (Fig. 5). Strong absorption peaks noticed at 538.22 cm^{-1} for the CuO nanostructure prepared using *V. negundo* leaf extract and

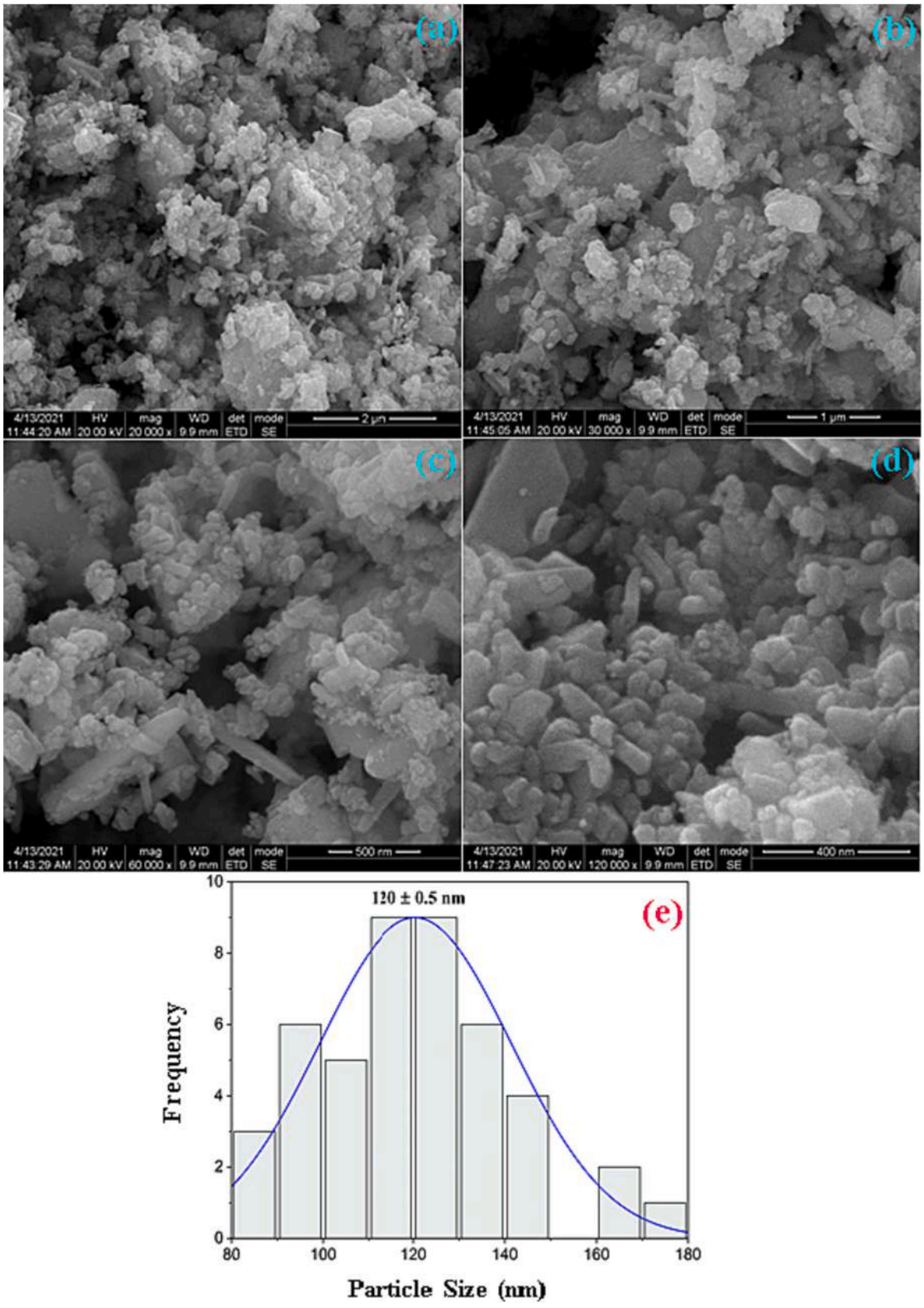

Fig 8. (a–d) SEM images and (e) size distribution curve of CuO nanostructures green synthesized using *V. negundo* leaf extract.

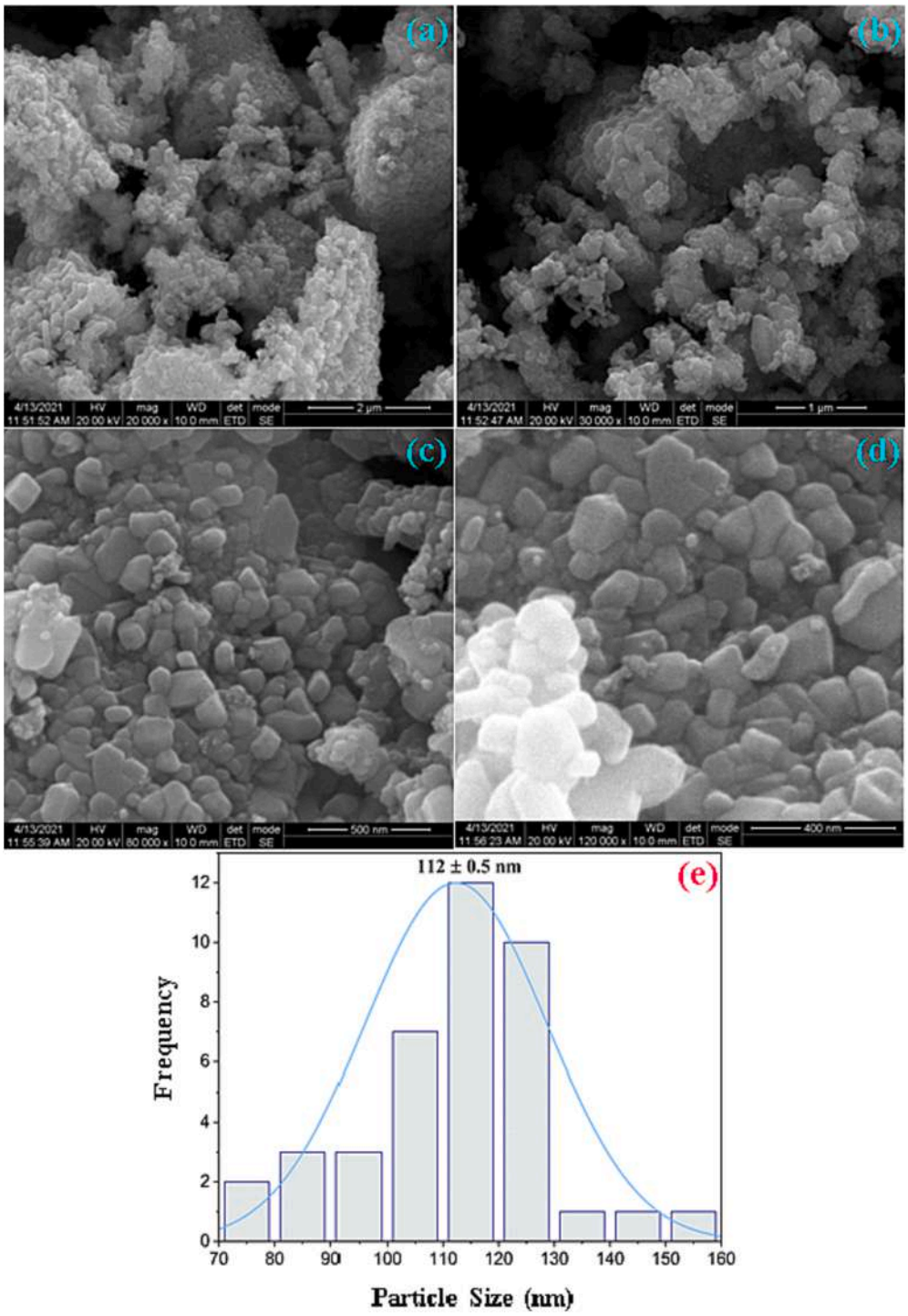

Fig 9. (a–d) SEM images and (e) size distribution curve of CuO nanostructure green synthesized using *E. milii* leaf extract.

absorption peaks found at 538.22 and 594.07 cm^{-1} for the CuO nanostructure prepared using *E. milii* leaf extract are due to asymmetrical stretching vibration of Cu–O [58,59]. The bands that appeared at 1036.00 and 1099.13 cm^{-1} can be ascribed to C–O stretching modes of phytochemicals associated with *V. negundo* and *E. milii* leaf extracts [60]. Meager absorption bands positioned at 1638.19 and 1645.47 cm^{-1} can be credited to presence of amino groups in phenolic compounds of *V. negundo* and *E. milii* leaf extracts that might take part in regulating the size and shape of the CuO nanostructures [61]. Little absorption of atmospheric water molecules by CuO nanostructures is reflected in low intense absorption peaks detected at 3348.44, 3460.13 and 3446.37 cm^{-1} [3,54].

3.5. UV–Vis absorption analysis

UV–Vis diffuse reflectance spectra of CuO nanostructures green synthesized using *V. negundo* and *E. milii* leaf extracts were recorded between 200 and 1000 nm to examine their absorption property and the resultant spectra are illustrated in Fig. 6. Diffuse reflectance spectra of both the CuO nanostructures display wide absorption in visible region between 400 and 700 nm that discloses d-d charge transfer transition of Cu^{2+} ions [62,63]. The UV absorption form 320 nm to 400 nm reveals

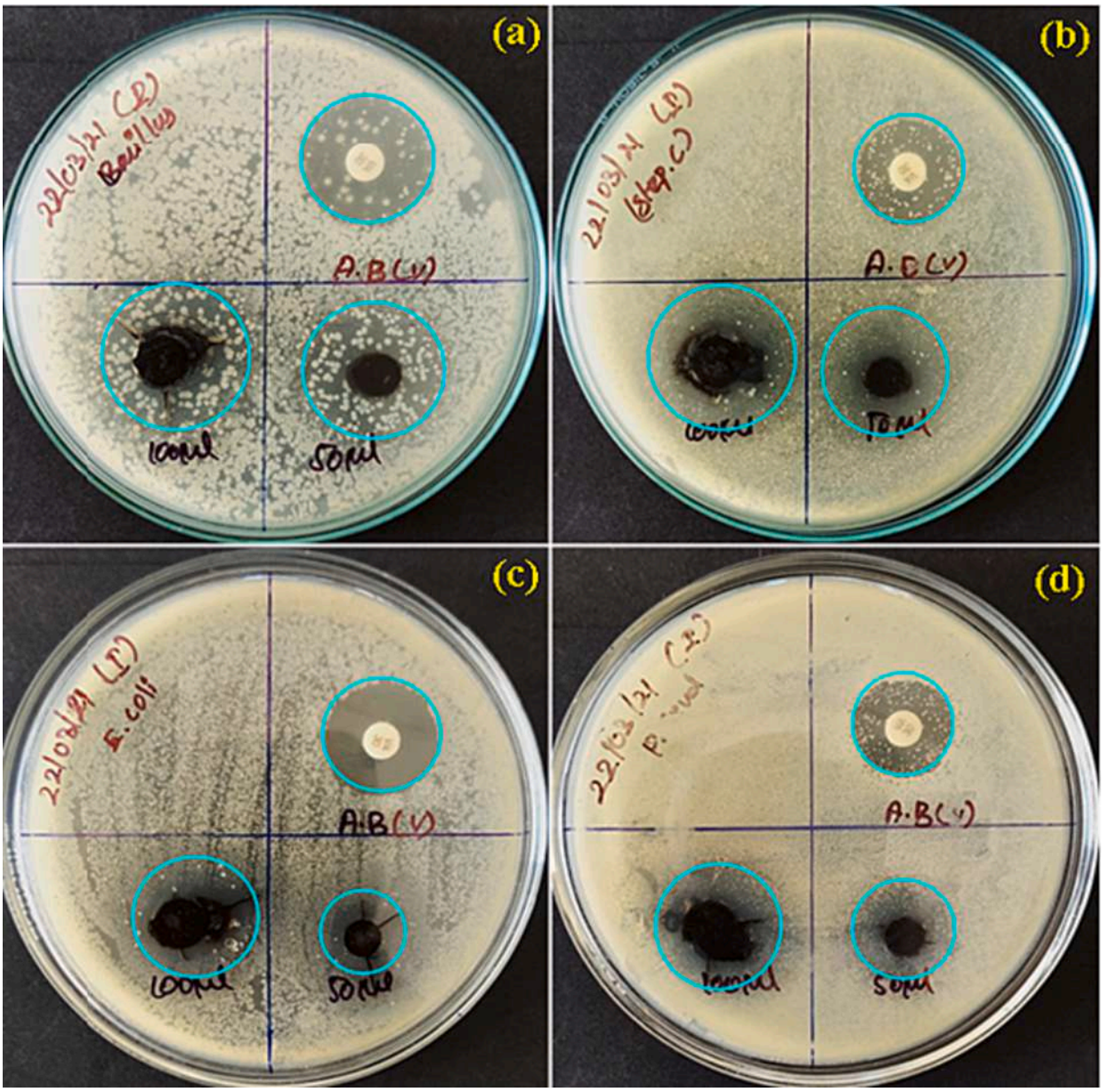

Fig 10. Antibacterial activity of CuO nanostructures green synthesized using *V. negundo* leaf extract.

Cu^{2+} - O^2 - Cu^{2+} charge transfer transition and absorption between 200 and 280 nm designates O^{2-} (2p) → Cu^{2+} (3d) charge transfer transition in the CuO nanostructures [64].

Band gap of the CuO nanostructures was calculated by the following *Tauc's* relation.

$$(\alpha h\nu)^n = B(h\nu - E_g)$$

where, B is a constant associated with CuO nanostructures, $h\nu$ is photon energy (eV), h is Planck's constant, ν is photon frequency, E_g is band gap (eV) and n is an exponent. Plot of $(\alpha h\nu)^2$ versus $h\nu$ is shown in Fig. 7. The calculated E_g value of CuO nanostructures green synthesized using *V. negundo* and *E. milii* leaf extracts is 1.43 and 1.47 eV, respectively, which are lower than that of bulk CuO. This can be credited to quantum confinement effect of nano-sized CuO crystals. Sharp edge absorbance with linear tail property unveils better crystallinity of the green synthesized CuO nanostructures that is well supported by corresponding XRD results.

3.6. Morphological investigation

The surface morphology of CuO nanostructures was examined by FESEM. Fig. 8 (a–d) shows FESEM images of CuO nanostructure prepared using *V. negundo* leaf extract. The low magnification FESEM images (Fig. 8 (a) and (b)) display aggregated CuO nanostructure however, their shape and size range could not be precisely determined. In contrast, the high magnification FESEM images (Fig. 8 (c) and (d)) undoubtedly envisage hierarchical morphology of CuO nanostructure comprised of small CuO nanoparticles/nanorods. It is presumed that the CuO nanoparticles might merge on CuO nanorods surface and form hierarchical CuO nanoparticles/nanorods morphology. Size distribution analysis (Fig. 8 (e)) performed by ImageJ software unveils that the size of hierarchical CuO nanoparticles/nanorods is distributed between 80 and 180 nm with a mean size of 120 nm ± 0.5 nm. Fig. 9 (a–d) illustrates FESEM images of CuO nanostructure green synthesized using *E. milii* leaf extract. The FESEM images (Fig. 9 (a) and (b)) exhibited aggregated CuO nanostructure having uniformly distributed CuO nanoparticles. Indeed, the FESEM images (Fig. 9 (c) and (d)) confirm the existence of sphere-

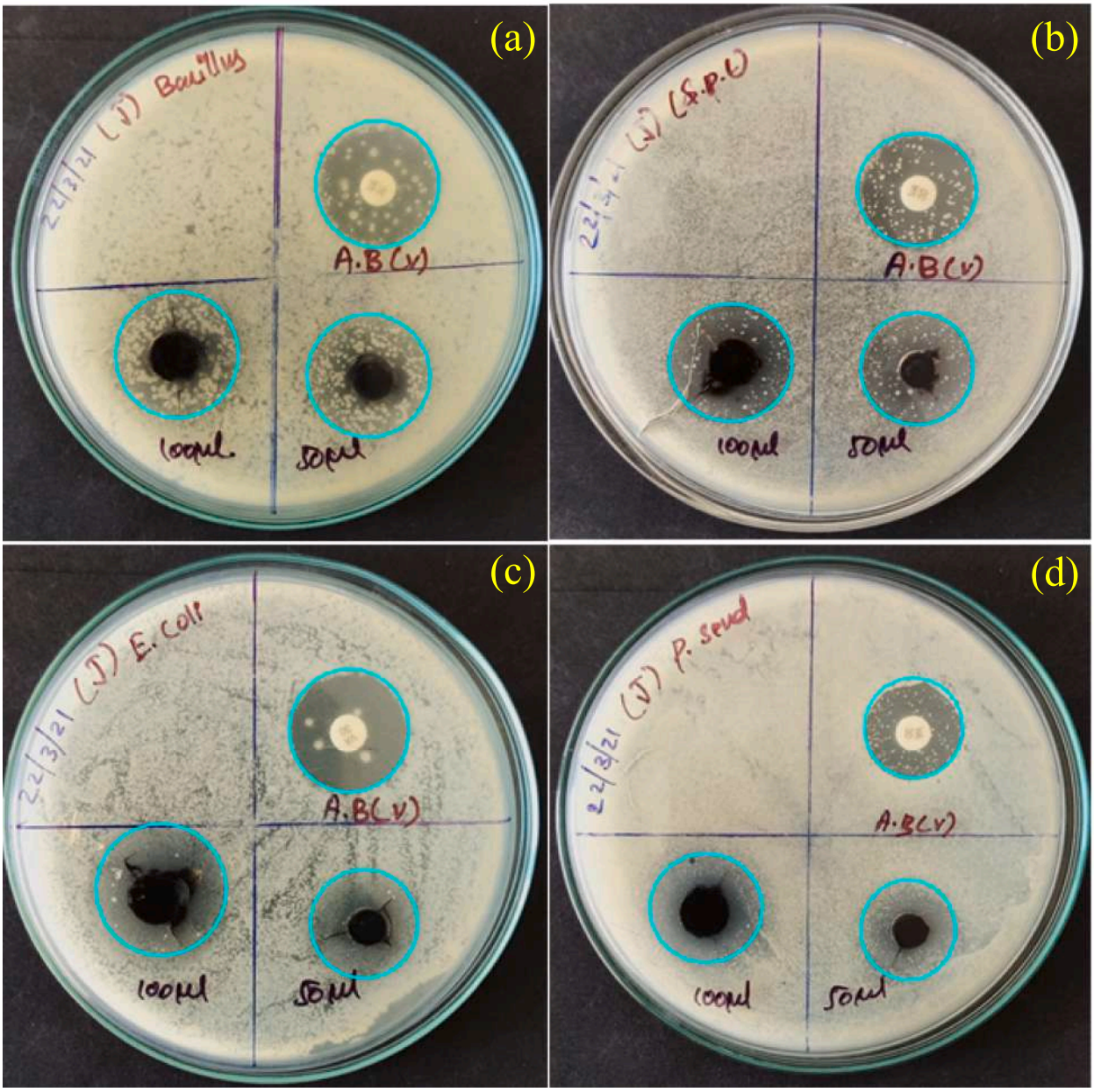

Fig 11. Antibacterial activity of CuO nanostructures green synthesized using *E. milii* leaf extract.

like CuO nanoparticles. It is apparent that the phytochemicals present in *V. negundo* and *E. milii* leaf extracts act as reducing and capping agents for $Cu(OH)_2$ nanostructures formation and succeeding calcination leads to transformation of CuO nanostructures. The CuO nanoparticles have a size range of 70 nm to 160 nm with a mean size of 112 ± 0.5 nm (Fig. 9 (e)). The deep observation of particle size distribution curves indicates that relatively a greater number of hierarchical CuO nanoparticles/nanorods are distributed in a lower size range when compared to sphere-like CuO nanoparticles. Hence, the hierarchical CuO nanoparticles/nanorods morphology may provide relatively a large specific surface area and as a consequence, better interaction with bacteria is anticipated during antibacterial activity.

3.7. Antibacterial activity assessment

The antibacterial activity of green synthesized CuO nanostructures was evaluated against selected pathogenic bacterial strains to exploit them as potential antibacterial agents. *Bacillus cereus*, *Staphylococcus aureus*, *Escherichia coli* and *Pseudomonas aeruginosa* were utilized as trial bacteria to assess antibacterial activity and vancomycin was used as a positive control. Results of antibacterial activity unveiled by CuO nanostructures green synthesized using *V. negundo* and *E. milii* leaf extracts are shown in Figs. 10 and 11, respectively and related data are provided in Table 4. The CuO nanostructures synthesized by *V. negundo* and *E. milii* leaf extracts exhibited dissimilar antibacterial activity against Gram-positive and Gram-negative bacteria. Among the bacteria, the highest antibacterial activity was recorded against *B. cereus* and *S. aureus* bacteria with ZOI value of 24 mm for CuO nanostructure concentration of 14 mg/mL synthesized using *V. negundo* leaf extract, and similar ZOI was noticed against *E. coli* for CuO nanostructure prepared using *E. milii* leaf extract. Meanwhile, CuO nanostructure (7 mg/mL) synthesized by *V. negundo* leaf extract unveiled ZOI of 23 and 21 mm, respectively against *B. cereus* and *S. aureus*, whereas ZOI value of 18 mm was observed for CuO nanostructure obtained using *E. milii* leaf extract. Peculiarly, vancomycin (30 µg/disc) showed relatively inferior ZOI values of 21, 20, and 20 mm against *B. cereus, S. aureus*, and *E. coli*

Table 4
Antibacterial activity values of CuO nanostructures green synthesized using *V. negundo* and *E. milii* leaf extracts.

Sl. No.	Bacteria	Zone of Inhibition in Diameter (mm)				
		Concentration of CuO nanostructures green synthesized using *V. negundo* leaf extract		Concentration of CuO nanostructures green synthesized using *E. milii* leaf extract		Concentration of standard antibiotic (Vancomycin)
		7 mg/mL	14 mg/mL	7 mg/mL	14 mg/mL	30 µg/disc
1.	*Bacillus cereus*	23	24	20	21	21
2.	*Staphylococcus aureus*	21	24	18	20	20
3.	*Escherichia coli*	14	22	18	24	20
4.	*Pseudomonas aeruginosa*	17	22	16	19	16

bacteria, respectively. However, relatively lower antibacterial activity was recorded against *E. coli* and *P. aeruginosa* with ZOI value of 22 mm for 14 mg/mL concentration of CuO nanostructure synthesized by *V. negundo* leaf extract, while ZOI values of 14 and 17 mm, respectively were detected against the same bacteria for CuO nanostructure concentration of 7 mg/mL. The CuO nanostructure formed using *E. milii* leaf extract demonstrated ZOI of 21 and 20 mm, respectively against *B. cereus* and *S. aureus* bacteria at a concentration of 14 mg/mL, and 20 and 18 mm ZOI were noticed against respective bacteria for CuO nanostructure concentration of 7 mg/mL. The least antibacterial activity was recorded against *P. aeruginosa* strain with ZOI of 19 and 16 mm, respectively for 14 and 7 mg/mL dosage concentrations of CuO nanostructure prepared using *E. milii* leaf extract. Meanwhile, the positive control, vancomycin showed the lowest antibacterial activity with a ZOI of 16 mm against *P. aeruginosa*.

Significant differences in antibacterial activity observed can be attributed to external morphology and nature of bacteria [65], diverse resistance nature [66] and dosage-based antibacterial activity [67] of CuO nanostructures. Here, considerably higher antibacterial activity noticed for the CuO nanostructures against Gram-positive bacteria over Gram-negative bacteria can be credited to absence of external membrane in Gram-positive bacteria that might have induced insignificant interference against release of Cu^{2+} ions [68] from CuO nanostructures and their less resistive as well as more susceptibility nature of Gram-positive bacteria against CuO nanostructures. Conversely, inferior antibacterial activity displayed against Gram-negative bacteria is because of existence of outer membrane, which enables significant interference against Cu^{2+} ions release from CuO nanostructures and more resistant property of Gram-negative bacteria against CuO nanostructures. Antibacterial activity of CuO nanostructures reported in this work is compared with antibacterial activity of green synthesized CuO nanostructures reported in literatures (Table 5).

3.8. Mechanism of antibacterial activity

Usually, bacterial cells size is in the micrometer range and their cellular membrane pores have nanometer size. Interaction or contact of CuO nanostructures with bacterial cells could be due to electrostatic attraction [77], van der Waals forces [78], receptor–ligand [79] and hydrophobic interactions [80]. The antibacterial activity noticed here disclosed that the CuO nanostructures are effective in obstructing the growth/killing of chosen bacteria. Possible inherent mechanism for this antibacterial activity might be due to direct contact with outer cell membrane of bacteria and their influence in altering shape and function of the cell membrane. Generally, oxygen vacancy, size of CuO

Table 5
Comparison of antibacterial activity of green synthesized CuO nanostructures using *V. negundo* and *E. milii leaf extracts* with green synthesized CuO nanostructures reported in literatures.

Plant Extract	Bacteria	ZOI (mm)	Reference
Cynodon dactylon grass	*B. cereus*	24	[3]
	S. aureus	26	
	E. coli	20	
Cyperus rotundus grass	*B. cereus*	24	[3]
	S. aureus	24	
	E. coli	26	
Hibiscus cannabinus leaf	*B. cereus*	18	[10]
	S. aureus	26	
	E. coli	14	
Moringa oleifera leaf	*B. cereus*	26	[32]
	S. aureus	32	
	E. coli	30	
Simarouba glauca leaf	*B. cereus*	22	[51]
	S. aureus	24	
	E. coli	28	
Hibiscus cannabinus flower	*B. cereus*	18	[69]
	S. aureus	20	
	E. coli	20	
Momordica charantia fruit	*B. cereus*	32	[70]
	S. aureus	29	
	E. coli	25	
	P. aeruginosa	26	
Bauhinia tomentosa leaf	*E. coli*	22	[71]
	P. aeruginosa	17	
Camellia sinensis leaf	*S. aureus*	30	[72]
	E. coli	27	
Prunus africana bark	*S. aureus*	30	[72]
	E. coli	26	
Eupatorium adenophorum leaf	*S. aureus*	8	[73]
	E. coli	9	
Gloriosa superba L. leaf	*S. aureus*	6	[74]
	E. coli	14	
Hagenia abyssinica (Brace) JF. Gmel. leaf	*S. aureus*	15	[75]
	E. coli	13	
	P. aeruginosa	13	
Sesbania grandiflora leaf	*S. aureus*	15	[76]
	E. coli	14	
	P. aeruginosa	19	
Vitex negundo leaf	*B. cereus*	24	Present
	S. aureus	24	Work
	E. coli	22	
	P. aeruginosa	22	
Euphorbia milii leaf	*B. cereus*	21	Present
	S. aureus	20	Work
	E. coli	24	
	P. aeruginosa	19	

nanostructures and liberation of Cu^{2+} ions play crucial roles in inhibiting bacteria [81]. CuO nanostructures interaction with bacteria liberate Cu^{2+} ions that adhere with cell surfaces and react with membrane protein, which helps enhanced cell permeability and thus, disturbs integrity of cell membrane. With damaged cell membrane, Cu^{2+} ions cross the bacterial membrane, enter the metabolic pathway and then interact with its basic parts, viz. DNA, mitochondria, enzymes, etc. Therefore, Cu^{2+} ions infiltrate into the cells surface that induces serious damage to DNA and intracellular parts through reactions. These reactions produce ROS that causes strong oxidative stress in the cells, which is an important antibacterial mechanism. The CuO nanostructures generate all four types of reactive oxygen species ($^{\bullet}OH$, O_2^-, O_2, and H_2O_2) and as a consequence, they exhibit dissimilar levels of dynamics and activity [55]. In the present study, both the CuO nanostructures have considerable oxygen vacancies and therefore they could generate more ROS that led to significantly higher antibacterial activity against all the chosen bacteria over the antibacterial activity of positive control (vancomycin). As a consequence of the oxidative stress by higher ROS production environment leads to disruption of electron transport chain, degradation of DNA and mitochondria, change in cell membrane

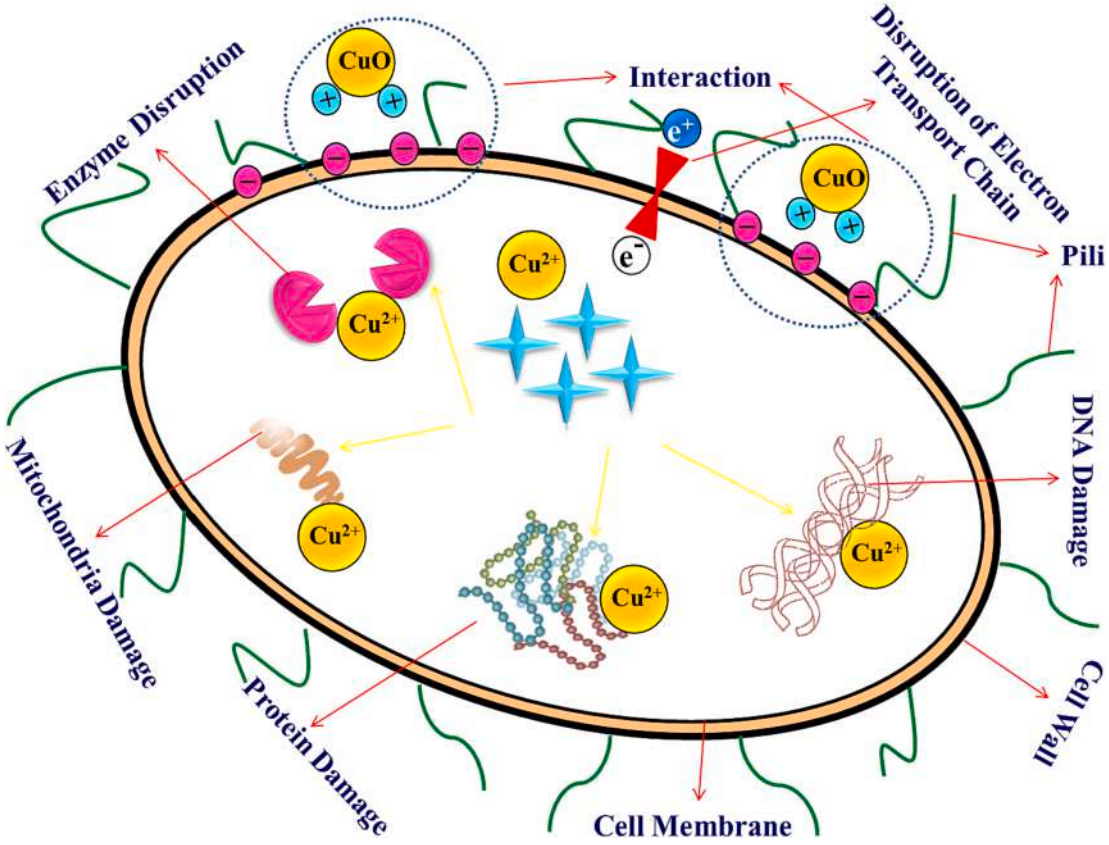

Fig 12. Antibacterial activity mechanism of CuO nanostructures green synthesized using *V. negundo* and *E. milii* leaf extracts.

permeability, cell wall damage, enzyme disruption, protein damage and variations in gene expression [82,83] that ultimately kill bacteria [84,85] (Fig. 12). Besides the prime role of oxygen vacancies, the relatively higher antibacterial activity disclosed by the hierarchical CuO nanoparticles/nanorods green synthesized using *V. negundo* leaf extract when compared to sphere-like CuO nanoparticles synthesized by *E. milii* leaf extract can also be credited to large specific surface area of small size hierarchical CuO nanoparticles/nanorods, which could facilitate better interaction with bacteria and consequently, liberate more Cu^{2+} ions and produce more ROS for damaging cell components of bacteria.

4. Conclusion

A green route was followed to synthesize CuO nanostructures using *V. negundo* and *E. milii* leaf extracts. XRD profiles signified formation of single-phase and monoclinic-structured CuO without impurities. CuO nanostructures green synthesized using *E. milii* leaf extract showed lower average crystalline size of 22.58 nm when compared to CuO nanostructures (25.20 nm) green synthesized using *V. negundo* leaf extract. Experiential reflections for both the CuO nanostructures could be well indexed to pristine monoclinic unit cells having space group of C2/c that was in accordance with observed XRD patterns. EDS spectra depicted the presence of peaks corresponding to Cu and O elements that revealed pristine nature of the CuO nanostructures with oxygen vacancies. The band gap value of CuO nanostructures synthesized using *V. negundo* and *E. milii* leaf extracts was 1.43 and 1.47 eV, respectively. The FESEM images of CuO nanostructures green synthesized using *V. negundo* leaf extract disclosed the formation of hierarchical CuO nanoparticles/nanorods morphology, whereas sphere-like CuO nanoparticles were produced by *E. milii* leaf extract. The CuO nanostructures disclosed considerably higher antibacterial activity against Gram-positive and Gram-negative bacteria over vancomycin, owing to oxygen vacancy and size-dependent generation of more reactive oxygen species. In particular, hierarchical CuO nanoparticles/nanorods prepared using *V. negundo* leaf extract revealed relatively higher antibacterial activity when compared to sphere-like CuO nanoparticles formed by *E. milii* leaf extract due to the lower size of hierarchical CuO nanoparticles/nanorods. In the future, we will focus on preparing modified CuO nanostructures by metal/semiconductor nanoparticles using the present green synthesis protocol in view of improving the antibacterial activity.

CRediT authorship contribution statement

S. Thambidurai: Conceptualization, Data curation, Formal analysis, Methodology, Software, Supervision, Validation, Visualization, Writing – original draft, Writing – review & editing. **J. Arumugam:** Conceptualization, Data curation, Formal analysis, Methodology, Software, Project administration, Writing – original draft. **M. Kandasamy:** Data curation, Formal analysis, Software, Validation, Visualization, Writing – original draft. **D. Balaji:** Data curation, Formal analysis, Software, Validation, Visualization. **N. Pugazhenthiran:** Data curation, Formal analysis, Software, Validation, Visualization, Writing – review & editing. **R. Jothilakshmi:** Formal analysis, Software, Validation, Visualization, Writing – review & editing. **B. Sathish Kumar:** Data curation, Formal analysis, Validation, Visualization, Writing – original draft. **K. Murugesan:** Data curation, Formal analysis, Software, Validation, Visualization, Writing – review & editing. **S. Karthick Kumar:** Formal analysis, Software, Validation, Visualization, Writing – review & editing. **T. Muneeswaran:** Data curation, Formal analysis, Software, Validation, Visualization. **K. Jayakumar:** Formal analysis, Project administration, Validation, Visualization, Writing – review & editing. **S. Suresh:** Conceptualization, Data curation, Formal analysis, Methodology, Project administration, Software, Supervision, Validation, Writing – review & editing.

Declaration of Competing Interest

The authors declare that they have no known competing financial interests or personal relationships that could have appeared to influence the work reported in this paper.

Data availability

Data will be made available on request.

Acknowledgment

The authors express their gratefulness to the Department of Science and Technology (DST), Government of India, New Delhi for facilitating Instruments Facility through DST-FIST Programme (Grant No. SR/FST/College-2017/140 (C), dt. 14.08.2018).

References

[1] M. Qasem, R.E. Kurdi, D. Patra, Green synthesis of curcumin conjugated CuO nanoparticles for catalytic reduction of methylene blue, ChemistrySelect 5 (2020) 1694–1704, https://doi.org/10.1002/slct.201904135.
[2] S.P. Patil, *Calotropis gigantea* assisted green synthesis of nanomaterials and their applications: a review, Beni-Seuf Univ. J. Basic Appl. Sci. 9 (2020) 14, https://doi.org/10.1186/s43088-020-0036-6.
[3] S. Suresh, R. Ilakiya, G. Kalaiyan, S. Thambidurai, P. Kannan, K.M. Prabu, N. Suresh, R. Jothilakshmi, S.K. Kumar, M. Kandasamy, Green synthesis of copper oxide nanostructures using *Cynodon dactylon* and *Cyperus rotundus* grass extracts for antibacterial applications, Ceram. Int. 46 (2020) 12525–12537, https://doi.org/10.1016/j.ceramint.2020.02.015.
[4] P. Peddi, P.R. Ptsrk, N.U. Rani, S.L. Tulasi, Green synthesis, characterization, antioxidant, antibacterial, and photocatalytic activity of Suaeda maritima (L.) Dumort aqueous extract–mediated copper oxide nanoparticles, J. Genet. Eng. Biotechnol. 19 (2021) 131, https://doi.org/10.1186/s43141-021-00229-9.
[5] J. Sackey, L.C. Razanamahandry, S.K.O. Ntwampe, N. Mlungisi, A. Fall, C. Kaonga, Z.Y. Nuru, Biosynthesis of CuO nanoparticles using *Mimosa hamata* extracts, Mater. Today:. Proc. 36 (2021) 540–548, https://doi.org/10.1016/j.matpr.2020.05.325.
[6] N. Murugesan, S. Suresh, M. Kandasamy, S. Murugesan, N. Pugazhenthiran, V. P. Venkatesh, B.K. Balachandar, S.K. Kumar, M.N.M. Ansari, Facile dip-coating assisted preparation of reduced graphene oxide-copper oxide nanocomposite thin films on aluminum substrate for solar selective absorber, Phys. B: Condens. Matter. (2023), 415288, https://doi.org/10.1016/j.physb.2023.415288.
[7] R. Mohammadi-Alloucheh, A. Habibi-Yangjeh, A. Bayrami, S. Latifi-Navid, A. Asadi, Green synthesis of ZnO and ZnO/CuO nanocomposites in *Mentha longifolia* leaf extract: characterization and their application as anti-bacterial agents, J. Mater. Sci. Mater. Electron. 29 (2018) 13596–13605, https://doi.org/10.1007/s10854-018-9487-0.
[8] A. Ehsani, B. Jaleh, M. Nasrollahzadeh, Electrochemical properties and electrocatalytic activity of conducting polymer/copper nanoparticles supported on reduced graphene oxide composite, J. Power Sources 257 (2014) 300–307, https://doi.org/10.1016/j.jpowsour.2014.02.010.
[9] S.D. Giri, A. Sarkar, Electrochemical study of bulk and monolayer copper in alkaline solution, J. Electrochem. Soc. 163 (2016) H252–H259, https://doi.org/10.1149/2.0071605jes.
[10] G. Kalaiyan, S. Suresh, S. Thambidurai, K.M. Prabu, S.K. Kumar, N. Pugazhenthiran, M. Kandasamy, Green synthesis of hierarchical copper oxide microleaf bundles using *Hibiscus cannabinus* leaf extract for antibacterial application, J. Mol. Struct. 1217 (2020), 128379, https://doi.org/10.1016/j.molstruc.2020.128379.
[11] S. Sharma, K. Kumar, N. Thakur, S. Chauhan, M.S. Chauhan, Eco-friendly *Ocimum tenuiflorum* green route synthesis of CuO nanoparticles: Characterizations on photocatalytic and antibacterial activities, J. Environ. Chem. Eng. 9 (2021), 105395, https://doi.org/10.1016/j.jece.2021.105395.
[12] A.E.D. Mahmoud, K.M. Al-Qahtani, S.O. Alflaij, S.F. Al-Qahtani, F.A. Alsamhan, Green copper oxide nanoparticles for lead, nickel, and cadmium removal from contaminated water, Sci. Rep. 11 (2021) 12547, https://doi.org/10.1038/s41598-021-91093-7.
[13] S.-F. Zheng, J.-S. Hu, L.-S. Zhong, W.-G. Song, L.-J. Wan, Y.-G. Guo, Introducing dual functional CNT networks into CuO nanomicrospheres toward superior electrode materials for lithium-ion batteries, Chem. Mater. 20 (2008) 3617–3622, https://doi.org/10.1021/cm7033855.
[14] P.K. Singh, A.K. Das, G. Hatui, G.C. Nayak, Shape controlled green synthesis of CuO nanoparticles through ultrasonic assisted electrochemical discharge process and its application for supercapacitor, Mater. Chem. Phys. 198 (2017) 16–34, https://doi.org/10.1016/j.matchemphys.2017.04.070.
[15] F. Wang, H. Li, Z. Yuan, Y. Sun, F. Chang, H. Deng, L. Xie, H. Li, A highly sensitive gas sensor based on CuO nanoparticles synthetized *via* a sol–gel method, RSC Adv. 6 (2016) 79343–79349, https://doi.org/10.1039/C6RA13876D.
[16] S.K. Kumar, S. Suresh, S. Murugesan, S.P. Raj, CuO thin films made of nanofibers for solar selective absorber applications, Sol. Energy 94 (2013) 299–304, https://doi.org/10.1016/j.solener.2013.05.018.
[17] A. Pugazhendhi, S.S. Kumar, M. Manikandan, M. Saravanan, Photocatalytic properties and antimicrobial efficacy of Fe doped CuO nanoparticles against the pathogenic bacteria and fungi, Microb. Pathog. 122 (2018) 84–89, https://doi.org/10.1016/j.micpath.2018.06.016.
[18] M. Kamali, F. Samari, F. Sedaghati, Low-temperature phyto-synthesis of copper oxide nanosheets: Its catalytic effect and application for colorimetric sensing, Mater. Sci. Eng. C 103 (2019), 109744, https://doi.org/10.1016/j.msec.2019.109744.
[19] T. Abiraman, E. Ramanathan, G. Kavitha, R. Rengasamy, S. Balasubramanian, Synthesis of chitosan capped copper oxide nanoleaves using high intensity (30 kHz) ultrasound sonication and their application in antifouling coatings, Ultrason. Sonochem. 34 (2017) 781–791, https://doi.org/10.1016/j.ultsonch.2016.07.013.
[20] N. Pugazhenthiran, S. Murugesan, T. Muneeswaran, S. Suresh, M. Kandasamy, H. Valdés, M. Selvaraj, A.D. Savariraj, R.V. Mangalaraja, Biocidal activity of *citrus limetta* peel extract mediated green synthesized silver quantum dots against MCF-7 cancer cells and pathogenic bacteria, J. Environ. Chem. Eng. 9 (2021), 105089, https://doi.org/10.1016/j.jece.2021.105089.
[21] A.Y. Booshehri, R. Wang, R. Xu, Simple method of deposition of CuO nanoparticles on a cellulose paper and its antibacterial activity, Chem. Eng. J. 262 (2015) 999–1008, https://doi.org/10.1016/j.cej.2014.09.096.
[22] W.-C. Hung, K.-H. Wu, D.-Y. Lyu, K.-F. Cheng, W.-C. Huang, Preparation and characterization of expanded graphite/metal oxides for antimicrobial application, Mater. Sci. Eng. C 75 (2017) 1019–1025, https://doi.org/10.1016/j.msec.2017.03.043.
[23] A. Sirelkhatim, S. Mahmud, A. Seeni, N.H.M. Kaus, L.C. Ann, S.K.M. Bakhori, H. Hasan, D. Mohamad, Review on zinc oxide nanoparticles: Antibacterial activity and toxicity mechanism, Nano-Micro Lett. 7 (2015) 219–242, https://doi.org/10.1007/s40820-015-0040-x.
[24] A. Ananth, S. Dharaneedharan, M.-S. Heo, Y.S. Mok, Copper oxide nanomaterials: Synthesis, characterization and structure-specific antibacterial performance, Chem. Eng. J. 262 (2015) 179–188, https://doi.org/10.1016/j.cej.2014.09.083.
[25] E. Hoseinzadeh, P. Makhdoumi, P. Taha, H. Hossini, J. Stelling, M.A. Kamal, G. M. Ashraf, A review on nano-antimicrobials: Metal nanoparticles, methods and mechanisms, Curr. Drug Metab. 18 (2017) 120–128, https://doi.org/10.2174/1389200217666161201111146.
[26] A.O. Flayyih, W.K. Mahdi, Y.I.M.A. Zaid, F.H. Musa, Biosynthesis, characterization, and applications of bismuth oxide nanoparticles using aqueous extract of *Beta vulgaris*, Chem. Methodol. 6 (2022) 620–628, https://doi.org/10.22034/CHEMM.2022.342124.1522.
[27] J.P. Ruparelia, A.K. Chatterjee, S.P. Duttagupta, S. Mukherji, Strain specificity in antimicrobial activity of silver and copper nanoparticles, Acta Biomater. 4 (2008) 707–716, https://doi.org/10.1016/j.actbio.2007.11.006.
[28] A.J. Huh, Y.J. Kwon, "Nanoantibiotics": A new paradigm for treating infectious diseases using nanomaterials in the antibiotics resistant era, J. Control. Release 156 (2011) 128–145, https://doi.org/10.1016/j.jconrel.2011.07.002.
[29] M.-L. Kung, M.-H. Tai, P.-Y. Lin, D.-C. Wu, W.-J. Wu, B.-W. Yeh, H.-S. Hung, C.-H. Kuo, Y.-W. Chen, S.-L. Hsieh, S. Hsieh, Silver decorated copper oxide (Ag@CuO) nanocomposite enhances ROS-mediated bacterial architecture collapse, Colloids Surf. B Biointerfaces 155 (2017) 399–407, https://doi.org/10.1016/j.colsurfb.2017.04.041.
[30] M.-L. Kung, S.-L. Hsieh, C.-C. Wu, T.-H. Chu, Y.-C. Lin, B.-W. Yeh, S. Hsieh, Enhanced reactive oxygen species overexpression by CuO nanoparticles in poorly differentiated hepatocellular carcinoma cells, Nanoscale 7 (2015) 1820–1829, https://doi.org/10.1039/C4NR05843G.
[31] M. Safaei, M. Taran, Optimized synthesis, characterization, and antibacterial activity of an alginate–cupric oxide bionanocomposite, J. Appl. Polym. Sci. 135 (2018) 45682, https://doi.org/10.1002/app.45682.
[32] G. Kalaiyan, S. Suresh, K.M. Prabu, S. Thambidurai, M. Kandasamy, N. Pugazhenthiran, S.K. Kumar, T. Muneeswaran, Bactericidal activity of *Moringa oleifera* leaf extract assisted green synthesis of hierarchical copper oxide microspheres against pathogenic bacterial strains, J. Environ. Chem. Eng. 9 (2021), 104847, https://doi.org/10.1016/j.jece.2020.104847.
[33] Q. Liu, W. Deng, Q. Wang, X. Lin, L. Gong, C. Liu, W. Xiong, X. Nie, An efficient chemical precipitation route to fabricate 3D flower-like CuO and 2D leaf-like CuO for degradation of methylene blue, Adv. Powder Technol. 31 (2020) 1391–1401, https://doi.org/10.1016/j.apt.2020.01.003.
[34] N. Murugesan, A.M. Remona, S.K. Kumar, S. Suresh, Facile preparation of diverse copper oxide nanostructures and their characterization, Mater. Lett. 222 (2018) 100–104, https://doi.org/10.1016/j.matlet.2018.03.151.
[35] T. Wang, Q. Xiao, Solvothermal synthesis and sensing properties of meso-macroporous hierarchical CuO microspheres composed of nanosheets, Mater. Chem. Phys. 139 (2013) 603–608, https://doi.org/10.1016/j.matchemphys.2013.02.004.
[36] R. Yarbrough, K. Davis, S. Dawood, H. Rathnayake, A sol–gel synthesis to prepare size and shape-controlled mesoporous nanostructures of binary (II–VI) metal oxides, RSC Adv. 10 (2020) 14134–14146, https://doi.org/10.1039/D0RA01778G.
[37] Z. Li, J. Wang, N. Wang, S. Yan, W. Liu, Y.Q. Fu, Z. Wang, Hydrothermal synthesis of hierarchically flower-like CuO nanostructures with porous nanosheets for excellent H_2S sensing, J. Alloy. Compd. 725 (2017) 1136–1143, https://doi.org/10.1016/j.jallcom.2017.07.218.
[38] C.M. Muiva, A.O. Juma, L.M. Lepodise, K. Maabong, D. Letsholathebe, Surfactant assisted chemical bath deposition based synthesis of 1-D nanostructured CuO thin

films from alkaline baths, Mater. Sci. Semicond. Process. 67 (2017) 69–74, https://doi.org/10.1016/j.mssp.2017.05.007.
[39] E. Proniewicz, A. Tąta, M. Starowicz, A. Szkudlarek, J. Pacek, M. Molenda, P. Kuśtrowski, Ions-free electrochemically synthetized in aqueous media flake-like CuO nanostructures as SERS reproducible substrates for the detection of neurotransmitters, Spectrochim. Acta A: Mol. Biomol, Spectrosc. 215 (2019) 24–33, https://doi.org/10.1016/j.saa.2019.02.051.
[40] C. Yang, F. Xiao, J. Wang, X. Su, 3D flower- and 2D sheet-like CuO nanostructures: Microwave-assisted synthesis and application in gas sensors, Sens. Actuators b: Chem. 207 (2015) 177–185, https://doi.org/10.1016/j.snb.2014.10.063.
[41] K. Sahu, A. Bisht, S.A. Khan, A. Pandey, S. Mohapatra, Engineering of morphological, optical, structural, photocatalytic and catalytic properties of nanostructured CuO thin films fabricated by reactive DC magnetron sputtering, Ceram. Int. 46 (2020) 7499–7509, https://doi.org/10.1016/j.ceramint.2019.11.248.
[42] S. Anandan, G.-J. Lee, J.J. Wu, Sonochemical synthesis of CuO nanostructures with different morphology, Ultrason. Sonochem. 19 (2012) 682–686, https://doi.org/10.1016/j.ultsonch.2011.08.009.
[43] R. Rawat, A. Tiwari, N. Arun, S.V.S.N. Rao, A.P. Pathak, S.V. Rao, A. Tripathi, Synthesis of CuO hollow nanoparticles using laser ablation: effect of fluence and solvents, Appl. Phys. A 126 (2020) 226, https://doi.org/10.1007/s00339-020-3403-1.
[44] R. Al-Gaashani, S. Radiman, N. Tabet, A.R. Daud, Synthesis and optical properties of CuO nanostructures obtained via a novel thermal decomposition method, J. Alloy. Compd. 509 (2011) 8761–8769, https://doi.org/10.1016/j.jallcom.2011.06.056.
[45] D.J. Manasa, K.R. Chandrashekar, D.J.M. Kumar, M. Niranjana, K.M. Navada, L. Mussaenda frondosa, mediated facile green synthesis of copper oxide nanoparticles – characterization, photocatalytic and their biological investigations, Arab. J. Chem. 14 (2021), 103184, https://doi.org/10.1016/j.arabjc.2021.103184.
[46] R. Shashanka, Investigation of optical and thermal properties of CuO and ZnO nanoparticles prepared by Crocus sativus (Saffron) flower extract, J. Iran. Chem. Soc. 18 (2021) 415–427, https://doi.org/10.1007/s13738-020-02037-3.
[47] X. Fuku, M. Modibedi, M. Mathe, Green synthesis of Cu/Cu_2O/CuO nanostructures and the analysis of their electrochemical properties, SN Appl. Sci. 2 (2020) 902, https://doi.org/10.1007/s42452-020-2704-5.
[48] J. Arumugam, S. Thambidurai, S. Suresh, M. Selvapandiyan, M. Kandasamy, N. Pugazhenthiran, S.K. Kumar, T. Muneeswaran, Franck Quero, Green synthesis of zinc oxide nanoparticles using *Ficus carica* leaf extract and their bactericidal and photocatalytic performance evaluation, Chem. Phys. Lett. 783 (2021), 139040, https://doi.org/10.1016/j.cplett.2021.139040.
[49] N.M. Nemma, Z.S. Sadeq, Green route of synthesis Ag NPs using reductant and stabilizer agent from plants extract as an efficient antibacterial and antifungal activity, Chem. Methodol. 7 (2023) 325–334, https://doi.org/10.22034/CHEMM.2023.381408.1646.
[50] D. Thatikayala, B. Min, Ginkgo leaves extract-assisted synthesis of ZnO/CuO nanocrystals for efficient UV-induced photodegradation of organic dyes and antibacterial activity, J. Mater. Sci. Mater. Electron. 32 (2021) 17154–17169, https://doi.org/10.1007/s10854-021-06169-x.
[51] G. Kalaiyan, K.M. Prabu, S. Suresh, N. Suresh, Green synthesis of CuO nanostructures with bactericidal activities using *Simarouba glauca* leaf extract, Chem. Phys. Lett. 761 (2020), 138062, https://doi.org/10.1016/j.cplett.2020.138062.
[52] P. Bindu, S. Thomas, Estimation of lattice strain in ZnO nanoparticles: X-ray peak profile analysis, J. Theor. Appl. Phys. 8 (2014) 123–134, https://doi.org/10.1007/s40094-014-0141-9.
[53] M.G. Hajiabadi, M. Zamanian, D. Souri, Williamson-Hall analysis in evaluation of lattice strain and the density of lattice dislocation for nanometer scaled ZnSe and ZnSe: Cu particles, Ceram. Int. 45 (2019) 14084–14089, https://doi.org/10.1016/j.ceramint.2019.04.107.
[54] S. Suresh, S. Thambidurai, J. Arumugam, M. Kandasamy, N. Pugazhenthiran, D. Balaji, B.A. Al-Asbahi, N.R. Reddy, A. Arunkumar, T. Muneeswaran, Antibacterial activity and photocatalytic oxidative performance of zinc oxide nanorods biosynthesized using *Aerva lanata* leaf extract, Inorg. Chem. Commun. 139 (2022), 109398, https://doi.org/10.1016/j.inoche.2022.109398.
[55] L. Wang, C. Hu, L. Shao, The antimicrobial activity of nanoparticles: present situation and prospects for the future, Int. J. Nanomed. 12 (2017) 1227–1249, https://doi.org/10.2147/IJN.S121956.
[56] W.W. Andualem, F.K. Sabir, E.T. Mohammed, H.H. Belay, B.A. Gonfa, Synthesis of copper oxide nanoparticles using plant leaf extract of *Catha edulis* and its antibacterial activity, J. Nanotechnol. 2020 (2020) 2932434, https://doi.org/10.1155/2020/2932434.
[57] Y. Wang, X. Su, S. Lu, Shape-controlled synthesis of TiO_2 hollow structures and their application in lithium batteries, J. Mater. Chem. 22 (2012) 1969–1976, https://doi.org/10.1039/C1JM14637H.
[58] B. Arunkumar, S.J. Jeyakumar, M. Jothibas, A sol-gel approach to the synthesis of CuO nanoparticles using *Lantana camara* leaf extract and their photo catalytic activity, Optik 183 (2019) 698–705, https://doi.org/10.1016/j.ijleo.2019.02.046.
[59] R.M. Mohamed, F.A. Harraz, A. Shawky, CuO nanobelts synthesized by a template-free hydrothermal approach with optical and magnetic characteristics, Ceram. Int. 40 (2014) 2127–2133, https://doi.org/10.1016/j.ceramint.2013.07.129.
[60] S. Venkatesan, S. Suresh, P. Ramu, M. Kandasamy, J. Arumugam, S. Thambidurai, K.M. Prabu, N. Pugazhenthiran, Biosynthesis of zinc oxide nanoparticles using *Euphorbia milii* leaf constituents: Characterization and improved photocatalytic degradation of methylene blue dye under natural sunlight, J. Indian Chem. Soc. 99 (2022), 100436, https://doi.org/10.1016/j.jics.2022.100436.
[61] N.I. Rasli, H. Basri, Z. Harun, Zinc oxide from aloe vera extract: two-level factorial screening of biosynthesis parameters, Heliyon 6 (2020) e03156.
[62] T. Tsoncheva, A. Gallo, I. Spassova, M. Dimitrov, I. Genova, M. Marelli, M. Khristova, G. Atanasova, D. Kovacheva, V.D. Santo, Tailored copper nanoparticles in ordered mesoporous KIT-6 silica: Preparation and application as catalysts in integrated system for NO removal with products of methanol decomposition, Appl. Catal. A 464–465 (2013) 243–252, https://doi.org/10.1016/j.apcata.2013.06.006.
[63] A.G. Kong, H.W. Wang, X. Yang, Y.W. Hou, Y.K. Shan, A facile direct route to synthesize large-pore mesoporous silica incorporating high CuO loading with special catalytic property, Microporous Mesoporous Mater. 118 (2009) 348–353, https://doi.org/10.1016/j.micromeso.2008.09.006.
[64] M.B. Gawande, A. Goswami, F.-X. Felpin, T. Asefa, X. Huang, R. Silva, X. Zou, R. Zboril, R.S. Varma, Cu and Cu-based nanoparticles: Synthesis and applications in catalysis, Chem. Rev. 116 (2016) 3722–3811, https://doi.org/10.1021/acs.chemrev.5b00482.
[65] Y.N. Tan, J.Y. Lee, D.I.C. Wang, Uncovering the design rules for peptide synthesis of metal nanoparticles, J. Am. Chem. Soc. 132 (2010) 5677–5686, https://doi.org/10.1021/ja907454f.
[66] S.M. Javadhesari, S. Alipour, S. Mohammadnejad, M.R. Akbarpour, Antibacterial activity of ultra-small copper oxide (II) nanoparticles synthesized by mechanochemical processing against *S. aureus* and *E. coli*, Mater. Sci. Eng. C 105 (2019) 110011. https://doi.org/10.1016/j.msec.2019.110011.
[67] A. Azam, A.S. Ahmed, M. Oves, M.S. Khan, A. Memic, Size-dependent antimicrobial properties of CuO nanoparticles against Gram-positive and -negative bacterial strains, Int. J. Nanomed. 7 (2012) 3527–3535, https://doi.org/10.2147/IJN.S29020.
[68] D. Laha, A. Pramanik, A. Laskar, M. Jana, P. Pramanik, P. Karmakar, Shape-dependent bactericidal activity of copper oxide nanoparticle mediated by DNA and membrane damage, Mater. Res. Bull. 59 (2014) 185–191, https://doi.org/10.1016/j.materresbull.2014.06.024.
[69] G. Kalaiyan, K.M. Prabu, N. Suresh, S. Suresh, Green synthesis of copper oxide spindle like nanostructure using *Hibiscus cannabinus* flower extract for antibacterial and anticancer activity applications, Results Chem. 5 (2023), 100840, https://doi.org/10.1016/j.rechem.2023.100840.
[70] H. Qamar, S. Rehman, D.K. Chauhan, A.K. Tiwari, V. Upmanyu, Green synthesis, characterization and antimicrobial activity of copper oxide nanomaterial derived from *Momordica charantia*, Int. J. Nanomed. 15 (2020) 2541–2553, https://doi.org/10.2147/IJN.S240232.
[71] G. Sharmila, R.S. Pradeep, K. Sandiya, S. Santhiya, C. Muthukumaran, J. Jeyanthi, N.M. Kumar, M. Thirumarimurugan, Biogenic synthesis of CuO nanoparticles using *Bauhinia tomentosa* leaves extract: Characterization and its antibacterial application, J. Mol. Struct. 1165 (2018) 288–292, https://doi.org/10.1016/j.molstruc.2018.04.011.
[72] K. Ssekatawa, D.K. Byarugaba, M.K. Angwe, E.M. Wampande, F. Ejobi, E. Nxumalo, M. Maaza, J. Sackey, J.B. Kirabira, Phyto-mediated copper oxide nanoparticles for antibacterial, antioxidant and photocatalytic performances, Front. Bioeng. Biotechnol. 10 (2022), 820218, https://doi.org/10.3389/fbioe.2022.820218.
[73] A.R. Maheo, B.S.M. Vithiya, T.A.A. Prasad, Biosynthesis and characterization of *Eupatorium adenophorum* and chitosan mediated copper oxide nanoparticles and their antibacterial activity, Results Surf. Interfaces 6 (2022), 100048, https://doi.org/10.1016/j.rsurfi.2022.100048.
[74] H.R. Naika, K. Lingaraju, K. Manjunath, D. Kumar, G. Nagaraju, D. Suresh, H. Nagabhushana, Green synthesis of CuO nanoparticles using *Gloriosa superba* L. extract and their antibacterial activity, J. Taibah Univ. Sci. 9 (2015) 7–12, https://doi.org/10.1016/j.jtusci.2014.04.006.
[75] H.C.A. Murthy, T. Desalegn, M. Kassa, B. Abebe, T. Assefa, Synthesis of green copper nanoparticles using medicinal plant Hagenia abyssinica (Brace) JF. Gmel. leaf extract: Antimicrobial properties, J. Nanomater. 2020 (2020), 3924081, https://doi.org/10.1155/2020/3924081.
[76] K. Ramasubbu, S. Padmanabhan, K.A. Al-Ghanim, M. Nicoletti, M. Govindarajan, N. Sachivkina, V.D. Rajeswari, Green synthesis of copper oxide nanoparticles using *Sesbania grandiflora* leaf extract and their evaluation of anti-diabetic, cytotoxic, anti-microbial, and anti-inflammatory properties in an in-vitro approach, Fermentation 9 (2023) 332, https://doi.org/10.3390/fermentation9040332.
[77] H. Li, Q. Chen, J. Zhao, K. Urmila, Enhancing the antimicrobial activity of natural extraction using the synthetic ultrasmall metal nanoparticles, Sci. Rep. 5 (2015) 11033, https://doi.org/10.1038/srep11033.
[78] I. Armentano, C.R. Arciola, E. Fortunati, D. Ferrari, S. Mattioli, C.F. Amoroso, J. Rizzo, J.M. Kenny, M. Imbriani, L. Visai, The interaction of bacteria with engineered nanostructured polymeric materials: A review, Sci. World J. 2014 (2014), 410423, https://doi.org/10.1155/2014/410423.
[79] W. Gao, S. Thamphiwatana, P. Angsantikul, L. Zhang, Nanoparticle approaches against bacterial infections, Wiley Interdiscip. Rev. Nanomed. Nanobiotechnol. 6 (2014) 532–547, https://doi.org/10.1002/wnan.1282.
[80] B. Luan, T. Huynh, R. Zhou, Complete wetting of graphene by biological lipids, Nanoscale 8 (2016) 5750–5754, https://doi.org/10.1039/C6NR00202A.
[81] V.L. Prasanna, R. Vijayaraghavan, Insight into the mechanism of antibacterial activity of ZnO: Surface defects mediated reactive oxygen species even in the dark, Langmuir 31 (2015) 9155−9162. https://doi.org/ 10.1021/acs.langmuir.5b02266.
[82] Y. Xu, M.-T. Wei, H.D. Ou-Yang, S.G. Walker, H.Z. Wang, C.R. Gordon, S. Guterman, E. Zawacki, E. Applebaum, P.R. Brink, M. Rafailovich, T. Mironava, Exposure to TiO2 nanoparticles increases Staphylococcus aureus infection of HeLa

cells, J. Nanobiotechnology 14 (2016) 34, https://doi.org/10.1186/s12951-016-0184-y.
[83] W. Yang, C. Shen, Q. Ji, H. An, J. Wang, Q. Liu, Z. Zhang, Food storage material silver nanoparticles interfere with DNA replication fidelity and bind with DNA, Nanotechnology 20 (2009), 085102, https://doi.org/10.1088/0957-4484/20/8/085102.
[84] T. Cherian, K. Ali, S. Fatima, Q. Saquib, S.M. Ansari, H.A. Alwathnani, A.A. Al-Khedhairy, M. Al-Shaeri, J. Musarrat, *Myristica fragrans* bio-active ester functionalized ZnO nanoparticles exhibit antibacterial and antibiofilm activities in clinical isolates, J. Microbiol. Methods 166 (2019), 105716, https://doi.org/10.1016/j.mimet.2019.105716.
[85] A.Y. Ghidan, T.M. Al-Antary, A.M. Awwad, Green synthesis of copper oxide nanoparticles using *Punica granatum* peels extract: Effect on green peach Aphid, Environ. Nanotechnol. Monit. Manag. 6 (2016) 95–98, https://doi.org/10.1016/j.enmm.2016.08.002.

Results in Chemistry 7 (2024) 101315

Contents lists available at ScienceDirect

Results in Chemistry

journal homepage: www.sciencedirect.com/journal/results-in-chemistry

Sunlight assisted degradation of methylene blue dye by zinc oxide nanoparticles green synthesized using *Vitex negundo* plant leaf extract

S. Venkatesan [a,b,*], S. Suresh [c], J. Arumugam [c], P. Ramu [a,*], N. Pugazhenthiran [d], R. Jothilakshmi [e], K.M. Prabu [c]

[a] PG & Research Department of Physics, Government Arts College (Autonomous), Salem 636 007, Tamil Nadu, India
[b] Department of Physics, Periyar University, Salem 636 011, Tamil Nadu, India
[c] PG & Research Department of Physics, Sri Vidya Mandir Arts & Science College (Autonomous), Katteri – 636 902, Uthangarai, Tamil Nadu, India
[d] Laboratorio de Fotoquímica y Fotofísica, Departamento de Química, Universidad Técnica Federico Santa María, Av. España 1680, Valparaíso, Chile
[e] Department of Physics, Velammal College of Engineering and Technology, Madurai 625 009, Tamil Nadu, India

ARTICLE INFO

Keywords:
Zinc oxide nanoparticles
Green synthesis
Vitex negundo leaf
Methylene blue dye
Photocatalytic degradation

ABSTRACT

Zinc oxide nanoparticles (ZnO NPs) were formed through a simple green synthesis route using *Vitex negundo* (*V. negundo*) leaf extract as reducing and capping source. Morphological, structural, chemical and optical features of the prepared ZnO NPs were examined by field emission SEM, XRD, EDAX, PL, FTIR and UV–vis DRS, respectively. FESEM images precisely visualized morphology of the ZnO NPs as spherical with particles size ranges between 5 and 35 nm having a mean diameter of ~ 19 nm. XRD pattern revealed formation of hexagonal wurtzite structured ZnO NPs with high crystallinity. Further, the observed asymmetric stretching vibration of Zn-O bond confirmed the formation of hexagonal wurtzite structured ZnO NPs. Photocatalytic activity of the ZnO NPs was assessed against methylene blue (MB) dye degradation under natural sunlight illumination. Results of the photocatalytic experiment disclosed an impressive MB dye degradation efficiency of 98.50 % at 60 min. Moreover, green synthesized ZnO NPs exhibited a maximum mineralization (TOC removal) efficiency of 92.34 % at 5 h of sunlight illumination.

1. Introduction

Scientific domain of nanotechnology and associated research efforts have been advanced remarkably with the anticipation of synthesizing nano-sized particles in a confined size range of 1 nm to 100 nm [1,2]. Nanotechnology plays a crucial role in controlling materials by means of diverse synthesis protocols, namely hydrothermal, co-precipitation, sol–gel, ultrasonication, microwave irradiation, etc., to acquire nanomaterials with unique physical, chemical, optical, electrical, and thermal properties [3,4]. Among different nanostructured materials, nanoparticles (NPs) have found variety of applications, owing to their exclusive properties, viz. size, shape, and surface area. In particular, utilization of NPs for catalytic applications is regarded as most significant [5]. In this context, diverse metal oxide semiconductor nanoparticles have been discovered and extensively applied in scientific spheres of catalysis, medicine, optics, electronics, energy, materials chemistry, sensors, information technology, biomedical, and agriculture [6]. Among them, zinc oxide nanoparticles (ZnO NPs) have acquired widespread attention in research and industries because of their auspicious optoelectronic and catalytic properties, strong oxidation potential, better chemical stability, harmless, and low-cost [7].

Globally, water crisis has been emerged as a critical problem and as a consequence, it has attained substantial scientific and technological interest [8]. Worldwide, the steep growth in human population has accelerated industrial activities. Consequently, millions of gallons of synthetic dyes employed as coloring agents for clothes in textile industries are discharged into aquatic bodies of natural environment in the form of wastewater [9,10]. Among the synthetic dyes, methylene blue (MB) used in several textile industrial processes encompasses complex compounds and their discharge through wastewater contains persistent organic contaminants [11]. The discharge of MB dye, even at its low concentration, has produced harmful effects on aquatic environments, viz. hindering photosynthesis process and endangering biodiversity by minimizing sunlight penetration and increasing oxygen (BOD and COD) needs, due to persistence nature, presence of large molecules and difficult to degradation of MB dye [12,13]. In addition, the exposure of MB

* Corresponding authors at: PG & Research Department of Physics, Government Arts College (Autonomous), Salem – 636 007, Tamil Nadu, India (S. Venkatesan).
E-mail addresses: velvenkatesan11@gmail.com (S. Venkatesan), ramusrm77@yahoo.co.in (P. Ramu).

https://doi.org/10.1016/j.rechem.2024.101315
Received 8 October 2023; Accepted 9 January 2024
Available online 10 January 2024

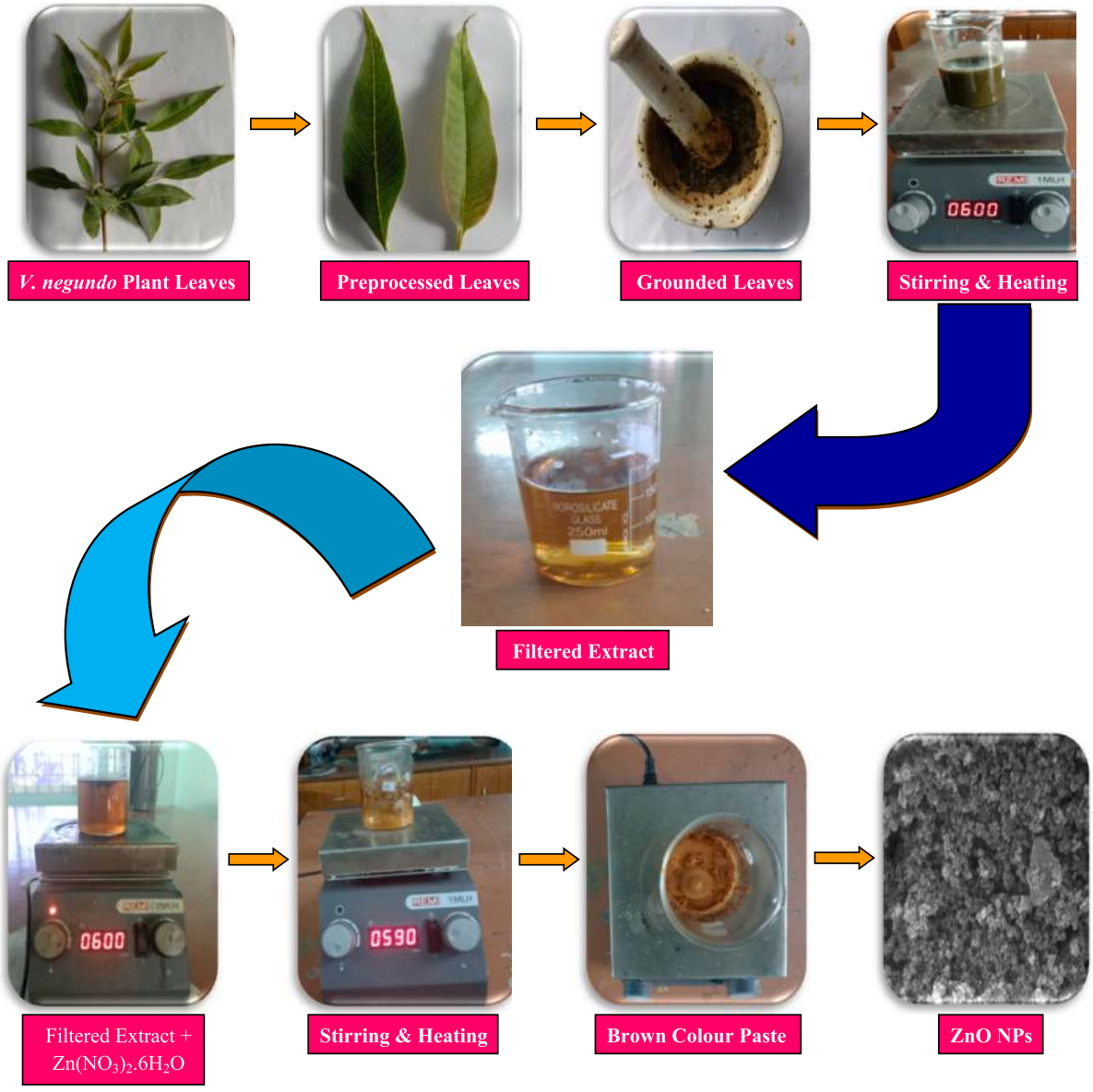

Fig. 1. Schematic illustration of ZnO NPs synthesis using *V. negundo* leaf extract.

containing wastewater induces skin allergies, toxicity, cell mutation, damage of central nervous system, and cancer in humans [14,15]. Hence, degradation of MB dye liberated through industrial effluents is crucial to protect human health, aquatic ecosystems, and environment. The effective removal of dye effluents from wastewater by conventional sewage treatment method is not conceivable, owing to its ineffectiveness in removing dye residuals [16]. Alternatively, metal oxide semiconductor nanoparticles have been emerged as a promising photocatalyst towards effective treatment of wastewater containing organic dye contaminants [17]. Photocatalysis is a cutting-edge alternative technology that operates under ambient conditions, typically at room temperature and atmospheric pressure. Unlike some alternative methods that may require harsh conditions, photocatalysis requires mild environment, reduces energy consumption, minimizes unwanted byproducts generation, promptly available and easily accessible. In addition, photocatalysis is versatile and applicable to the degradation of a wide range of pollutants, including organic dyes, pesticides and pharmaceuticals. Its effectiveness extends across various industries, such as wastewater treatment, air purification, and degradation of pollutants in different environmental matrices [18].

Photocatalytic degradation of a pollutant by synthesized semiconductor nanoparticles can be performed by determining the degradation of pollutant under sunlight illumination at a specified time duration. If a discrepancy occurs between band gap energy of the semiconductor nanoparticles and energy of the light illumination, photodegradation phenomenon of pollutant takes place. When the light illumination has energy greater than the band gap energy, valence band electrons acquire energy and move to the conduction band by excitation. Consequently, the holes are created in the valence band due the shifted electrons, which is succeeded by half-reactions of reduction and oxidation with electrons and holes, respectively that discloses occurrence of photocatalytic degradation of pollutant [19,20]. In this context, ZnO NPs have obtained huge attention towards catalytic and photocatalytic applications owing to their high electrochemical stability and electrocatalytic property [7,21]. Specifically, ZnO NPs as photocatalyst is a versatile and promising solution for addressing diverse environmental challenges. Moreover, the ZnO NPs possess a wide band gap energy (~3.37 eV), allowing them to effectively absorb ultraviolet (UV) light. This property enables ZnO NPs to generate electron-hole pairs upon exposure to light illumination that leads to powerful redox reactions

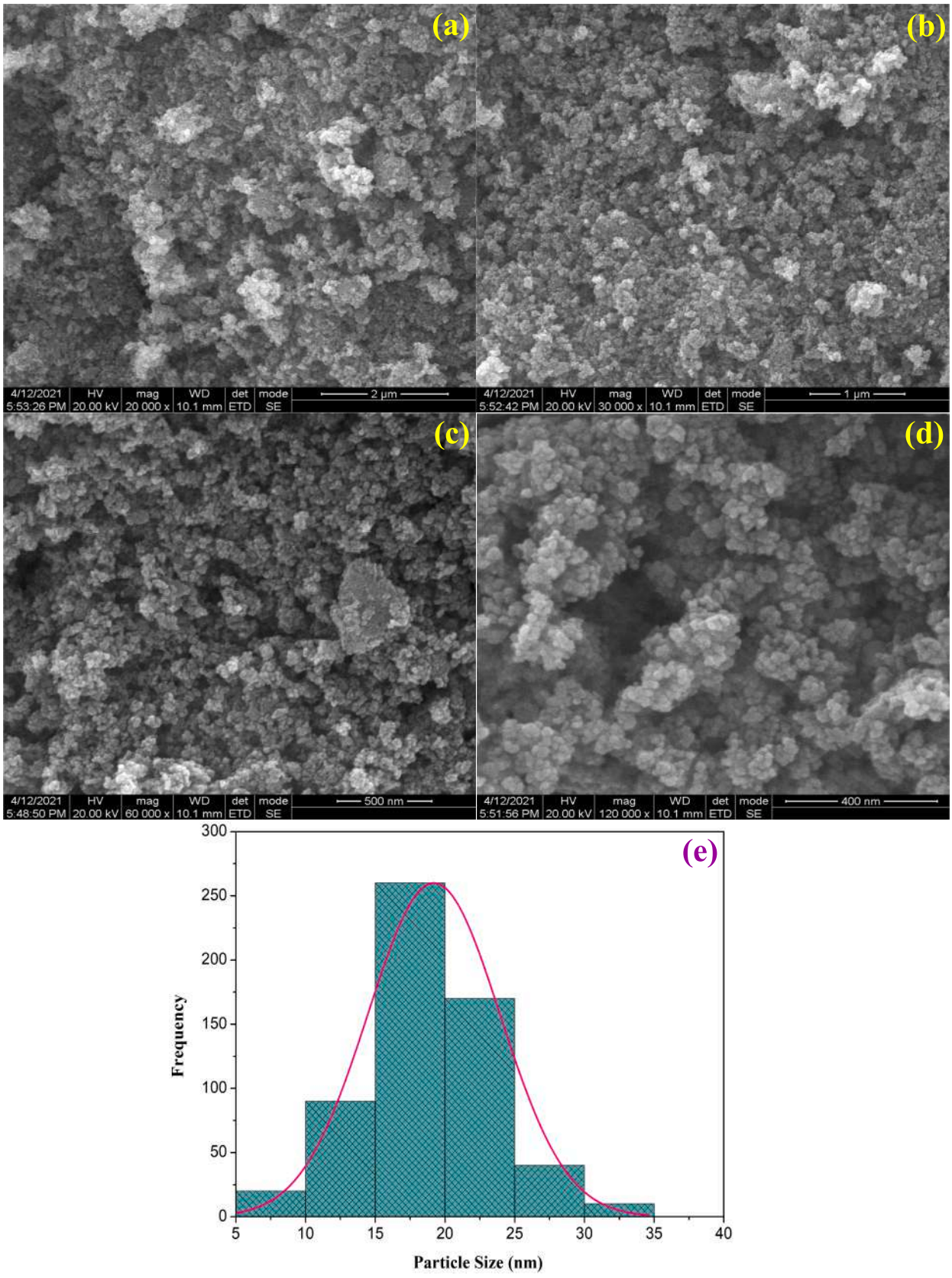

Fig. 2. FESEM images (a–d) and particle size distribution curve (e) of green synthesized ZnO NPs. (For interpretation of the references to color in this figure legend, the reader is referred to the web version of this article.)

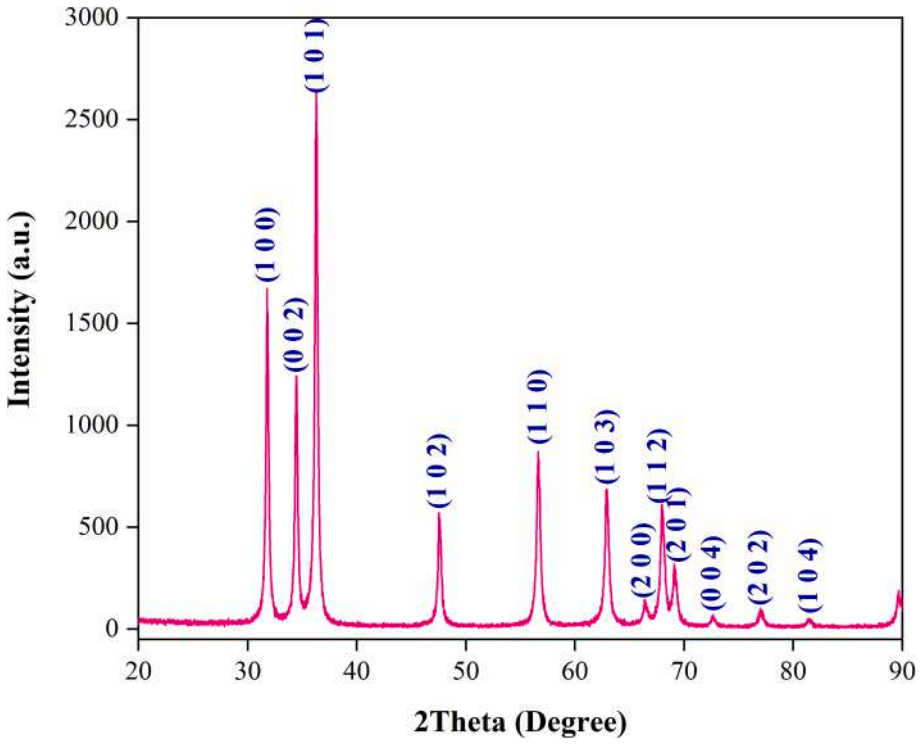

Fig. 3. XRD pattern of green synthesized ZnO NPs. (For interpretation of the references to color in this figure legend, the reader is referred to the web version of this article.)

Table 1
XRD parameters of green synthesized ZnO NPs.

Position [°2Th.]	(h k l)	FWHM [°2Th.]	d-spacing [Å]	Crystallite size (nm)	Lattice strain	Dislocation density (nm^{-2})
31.78	(100)	0.5196	2.816	16.60	0.00797	0.00363
34.41	(002)	0.4330	2.605	20.05	0.00610	0.00249
36.25	(101)	0.5156	2.478	16.80	0.00692	0.00354
47.52	(102)	0.6061	1.913	14.95	0.00601	0.00447
56.58	(110)	0.5196	1.627	18.13	0.00421	0.00304
62.80	(103)	0.6061	1.479	16.04	0.00433	0.00389
66.40	(200)	0.4330	1.407	22.89	0.00289	0.00191
67.90	(112)	0.6061	1.381	16.50	0.00393	0.00367
68.95	(201)	0.4330	1.361	23.25	0.00275	0.001849
72.48	(004)	0.5196	1.304	19.84	0.00309	0.00254
76.92	(202)	0.6927	1.240	15.33	0.00380	0.00426

[22]. The high photocatalytic activity of ZnO NPs makes them effective in degrading organic pollutants, mitigating environmental contamination and promoting overall sustainability. Further, the ZnO NPs exhibit excellent photostability, ensuring their prolonged and consistent performance under continuous exposure to light illumination [23]. This durability is essential for sustained photocatalytic reactions, making ZnO NPs suitable for long-term applications in wastewater treatment, air purification and other environmental remediation processes. The band gap energy of ZnO NPs can be tuned by adjusting their size, shape and morphology. This tunability allows researchers to customize photocatalytic properties of the ZnO NPs, optimizing them for specific applications. Tailoring the band gap energy of ZnO NPs widens the scope of potential uses, from efficient energy conversion to targeted pollutant degradation [24–29].

Meanwhile, reducing the band gap energy of semiconductor nanomaterials to place them within the visible range through techniques, such as doping or creating composites [30–33] with other materials is a complex process with inherent limitations. The intrinsic band gap energy of ZnO, which is approximately 3.37 eV, is primarily determined by its crystalline structure and electronic properties. Achieving a substantial reduction in the band gap energy to place it within the visible range is challenging due to the fundamental characteristics of the ZnO material. Introducing dopants into the ZnO lattice to modify the band gap energy often faces challenges related to the size and charge compatibility of the dopant ions. Meanwhile, the size of the dopant should be such that it can be successfully incorporated into the ZnO lattice without causing significant structural distortions. The solubility limits of dopants in ZnO can restrict the degree to which the band gap energy can be effectively modified. Beyond certain concentrations, dopants may form segregated phases or induce defects, limiting their ability to influence the band gap energy and overall optical properties. In addition, creating composites with other materials involves challenges in achieving a homogeneous distribution of the additional materials within the ZnO matrix. The synthesis process needs to be carefully controlled to avoid phase separation, uneven distribution or unintended modifications to the ZnO structure. Moreover, some dopants or composite materials may not be compatible with overall goals of the application. Environmental concerns, toxicity, and long-term stability are important factors to be considered when selecting materials for band gap energy modification.

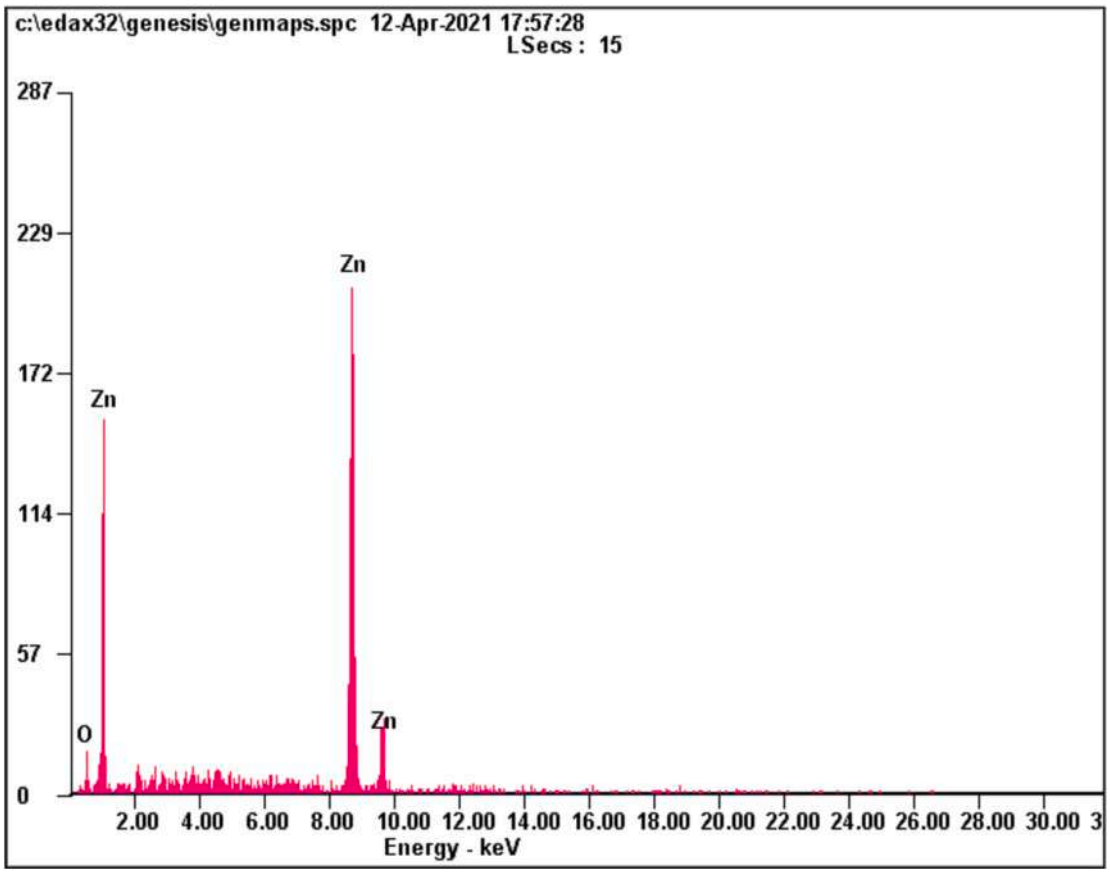

Fig. 4. EDAX spectrum of green synthesized ZnO NPs. (For interpretation of the references to color in this figure legend, the reader is referred to the web version of this article.)

Table 2
Weight and atomic percentage of Zu and O elements present in ZnO NPs.

Element	Weight Percentage (%)	Atomic Percentage (Wt%)
Zn	97.13	89.24
O	2.87	10.76
Total Percentage (%)	**100**	**100**

In recent years, green synthesis of nanoparticles has been attained immense attention, due to its capability of producing harmless nanoparticles in low-cost and environment friendly manner [34–36]. Among the biological sources available, plant parts have been demonstrated as ideal candidates since they can facilitate superior platform for green synthesis of nanoparticles, cost competitiveness, absence of toxic chemicals, faster reaction rate, and formation of more stable nanoparticles over other biological sources [37–39]. Green synthesis methodologies rely on primary and secondary metabolites, such as amino acids, alkaloids, enzymes, phenolics, terpenoids, vitamins, proteins, saponins, tannins, quinones, etc., which perform pivotal roles of reducing agent for the reduction of metal ions from the precursor salt and stabilization of the metal ions [40,41]. These biomolecules not only accountable for capping and post surface modification of green synthesized nanoparticles but also circumvents their aggregation [42,43]. Recent reports demonstrate that extracts obtained from leaves of diverse plant species, namely *Cynodon dactylon* and *Cyperus rotundus* [44], *Ficus carica* [45], *Moringa oleifera* [46], *Hibiscus cannabinus* [47], *Simarouba glauca* [48], *Euphorbia milii* [49,50] and *Solanum trilobatum* [51] can be employed as ideal candidates for synthesizing metal oxide semiconductor nanoparticles.

The synthesis of ZnO NPs using plant extracts has garnered significant interest for its eco-friendly and cost-effective approach. Among various plant sources, *Vitex negundo* (*V. negundo*) plant leaf extract stands out as a superior choice by offering distinct advantages over other plant extracts, such as *H. cannabinus*, *E. milii* and *M. oleifera* leaf extracts. The leaf of *V. negundo* is rich in phytochemicals, including flavonoids, alkaloids and polyphenols, which act as potent reducing agents. These phytochemicals play a crucial role in the reduction of zinc ions to form ZnO NPs. Additionally, the secondary metabolites present in the *V. negundo* extract, such as terpenoids and saponins act as effective stabilizing and capping agents during the synthesis process. These compounds contribute to the controlled growth and stabilization of ZnO NPs, ensuring their uniform size and preventing agglomeration for potential applications [52]. Green synthesized ZnO NPs exhibit distinctive physicochemical properties, owing to the inherent bioactive compounds present in the plant extracts used during synthesis. The organic moieties from the plant extracts impart additional functional groups on ZnO NPs surface, creating an unique and synergistic interplay that enhances photocatalytic performance of the ZnO NPs. In addition, it often results in ZnO NPs with higher surface area and more exposed active sites. This increased surface area promotes better interaction with incident light and boosts the availability of reactive sites for photocatalytic reactions. This synergistic interactions between ZnO matrix and organic compounds enhance the generation and separation of charge carriers (electron-hole pairs), resulting in accelerated redox reactions and consequently, occurrence of elevated photocatalytic activity [53,54].

By taking account on the above stated facts and also to fulfill the research gap, this work was designed to synthesis ZnO NPs using *Vitex negundo* (*V. negundo*) leaf extract. The synthesized ZnO NPs were subjected to morphological, structural, elemental, chemical, and optical analysis. Finally, catalytic activity of the ZnO NPs was evaluated against

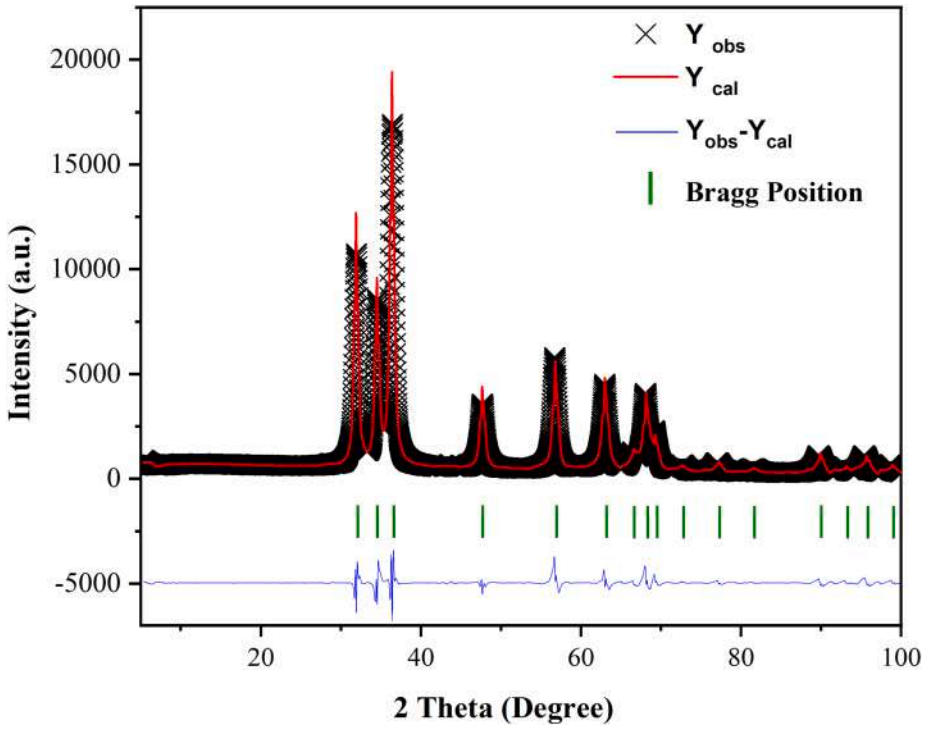

Fig. 5. Rietveld refinement analysis plot of ZnO NPs green synthesized using *V. negundo* leaf extract. (For interpretation of the references to color in this figure legend, the reader is referred to the web version of this article.)

Table 3
Crystallographic parameters of green synthesized ZnO NPs derived from Rietveld refinement analysis.

Refined crystallographic parameters of green synthesized ZnO NPs	
Crystal System	Hexagonal
Space Group	*P63mc*
Lattice Parameters	$a = b = 3.24040$ Å $c = 5.1993(4)$ Å $\alpha = \beta = 90^\circ$ $\gamma = 120^\circ$
Unit Cell Volume	V = 47.280(3) Å^3
R_p (%)	7.624
R_{wp} (%)	10.917
χ^2	2.845

MB dye degradation under natural sunlight illumination.

2. Experimental details

2.1. Materials

Zinc nitrate hexahydrate ($Zn(NO_3)_2{\cdot}6H_2O$) purchased from Merck was employed for ZnO NPs synthesis. Healthy and fresh leaves of *V. negundo* plant were collected from Sunnampatti Village licated in Uthangarai Taluk of Krishnagiri District, Tamil Nadu, India. Methylene blue dye was procured from Sigma-Aldrich. Deionized double distilled water was used for experiments and cleaning purpose.

2.2. Preparation of ZnO NPs

Pretreated *V. negundo* leaves (5 g) were taken in a mortar and grounded using a pestle until to get a fine paste. The obtained paste was dispersed in 100 ml double distilled water and stirred (660 rpm) under heating at 80 °C for 1 h. The ensuing leaf extract was filtered using filter paper. About 30 ml of leaf extract was taken in a beaker and it was heated at 80 °C under constant stirring While extract reached 80 °C temperature, about 1 g of $Zn(NO_3)_2{\cdot}6H_2O$ was added to the extract solution under stirring and the heating was continued till the extract transformed into a fine paste. In this step, color of solution was changed and the stirring was progressed till the solution was transformed into paste, which disclosed development of $Zn(OH)_2$. Then, the paste was washed several times by distilled water to remove nitrate ions and surplus biological molecules of *V. negundo* leaf extract. Finally, the Zn $(OH)_2$ was calcined at 350 °C for 2 h in which, the precipitate color was changed from light yellow to clear white that unveiled emergence of ZnO NPs as a consequence of oxidation process (Fig. 1).

2.3. Characterization

The prepared ZnO NPs was characterized by FESEM, XRD, EDAX, PL, FTIR and UV–vis diffuse reflectance spectroscopy. FESEM images were taken in VEGA 3 TESCAN SEM. XRD patterns were recorded using PANalytical X'pert^3 powder XRD with Cu Kα radiation ($\lambda = 1.5418$ Å). EDAX spectrum was documented by Bruker EDX spectrometer. UV–vis absorption spectrum of ZnO NPs was recorded using UV–vis diffuse reflectance spectrophotometer (UV-2550, Shimadzu, Japan) integrated with Diffuse Reflectance Accessary (ISR 2200). Photoluminescence spectrum was taken in fluorescence spectrophotometer (Varian Cary Eclipse). FTIR spectrum was recorded using PerkinElmer FTIR spectrometer (Spectrum Two).

2.4. Photocatalytic performance investigation

Photocatalytic performance of green synthesized ZnO NPs was evaluated under natural sunlight illumination. Briefly, ZnO NPs (0.09 g) was dispersed in 150 mL of 20 μM MB dye solution. Preceding to photocatalytic experiment, MB dye solution was subjected to stirring in dark for 30 min to attain adsorption–desorption equilibrium. An appropriate volume (5 ml) of MB dye solution was withdrawn and its concentration was recorded using UV–Vis Spectrophotometer (Hitachi Double Beam, Model No. UH5300). Then, MB dye solution with ZnO NPs was kept under sunlight illumination at constant stirring and change in MB dye

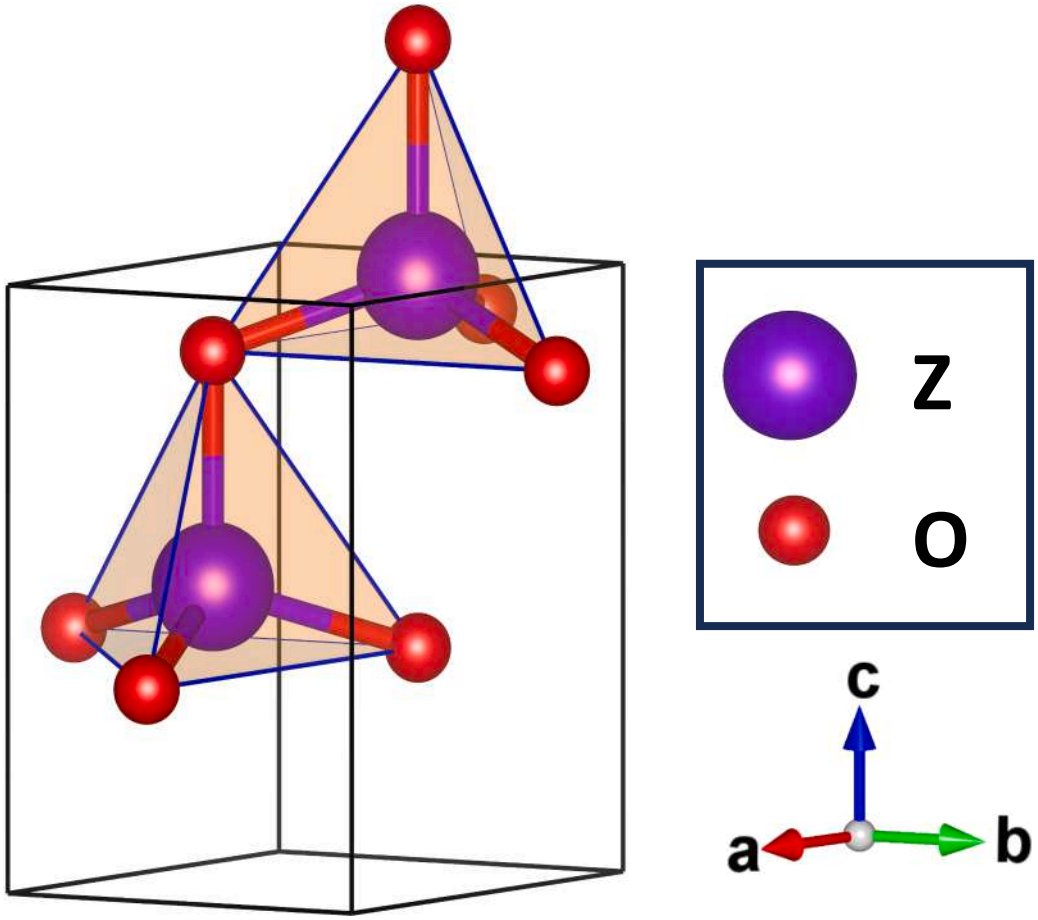

Fig. 6. Crystal structure of green synthesized ZnO NPs. (For interpretation of the references to color in this figure legend, the reader is referred to the web version of this article.)

solution concentration was detected at time interval of 10 min. Degradation percentage of MB dye was found by the formula given below:

$$\text{Dye degradation efficiency } (\%) = (C_i – C_f/C_i) \times 100$$

where, C_i and C_f are primary and final concentration of MB dye, respectively.

3. Results and discussion

3.1. FESEM examination

Morphology of ZnO NPs prepared using *V. negundo* leaf extract was examined by FESEM (Fig. 2). It is obvious from low magnification FESEM images (Fig. 2 **(a & b)**) that each ZnO NP is adjoined with nearby ZnO NPs that seems to be aggregated nature. The morphology and size of ZnO NPs could not be revealed due to low magnification. This aggregation might be caused by polarity and electrostatic attraction takes place between ZnO NPs [51]. The aggregation might also be caused by high surface energy of the ZnO NPs and moreover due to compaction as a result of narrow distance between nanoparticles [55]. The green synthesized ZnO NPs are assumed to have a morphology with high surface area due to small particles size and as a consequence, considerably higher active sites are anticipated [56]. The high magnification FESEM images (Fig. 2 **(c & d)**) precisely visualize morphology of the ZnO NPs as spherical. According to the ImageJ software analysis, size of ZnO NPs ranges from 5 nm to 35 nm having mean size of ~ 19 nm (Fig. 2 **(e)**). Phytochemicals, viz. alkaloids, flavonoids, tannin, terpenoids, steroids and phenols present in the *V. negundo* leaf extract might act as reducing and capping sources towards the formation of small size ZnO NPs [52].

3.2. XRD analysis

XRD analysis gives information pertaining to structure, purity and crystallinity of semiconductor nanoparticles [17]. XRD pattern of green synthesized ZnO NPs shown in Fig. 3 displays peaks at 2θ values of 31.78, 34.41, 36.25, 47.52, 56.58, 62.80, 66.40, 67.90, 68.95, 72.48, and 76.92°, corresponding to hexagonal wurtzite structured ZnO (JCPDS Card No. 89-1397) with lattice constants a = b = 0.324 nm and c = 0.521 nm [57]. Intense and sharp diffraction peaks in the XRD pattern disclosed good crystalline nature of the ZnO NPs. Meanwhile, the absence of diffraction peaks relevant to impurities indicates purity of the ZnO NPs. The mean crystallite size of ZnO NPs determined by Debye Scherrer formula given below was 18.22 nm (Table 1).

$$D = \frac{0.9\lambda}{\beta\cos\theta}$$

where, D is crystallite size, λ is X-ray wavelength, θ is Bragg's angle and β is FWHM.

The strain (ε) developed in ZnO NPs to lattice misfit was calculated by the formula, $\varepsilon_{str} = \beta/4 \tan\theta$. The average value of strain, $\varepsilon_{str} = 0.0047$ discloses better crystallinity and high quality of the ZnO NPs. Dislocation density signifies total defects in sample that is denoted as length of dislocation lines per unit volume of the crystal and is given by $\delta = 1/D^2$ (nm^{-2}). For the green synthesized ZnO NPs, the average dislocation density is $\delta = 0.00321$ (nm^{-2}). As we know the lattice constants a = b = 0.324 nm and c = 0.521 nm, the length of Zn-O bond can be calculated using the following equation:

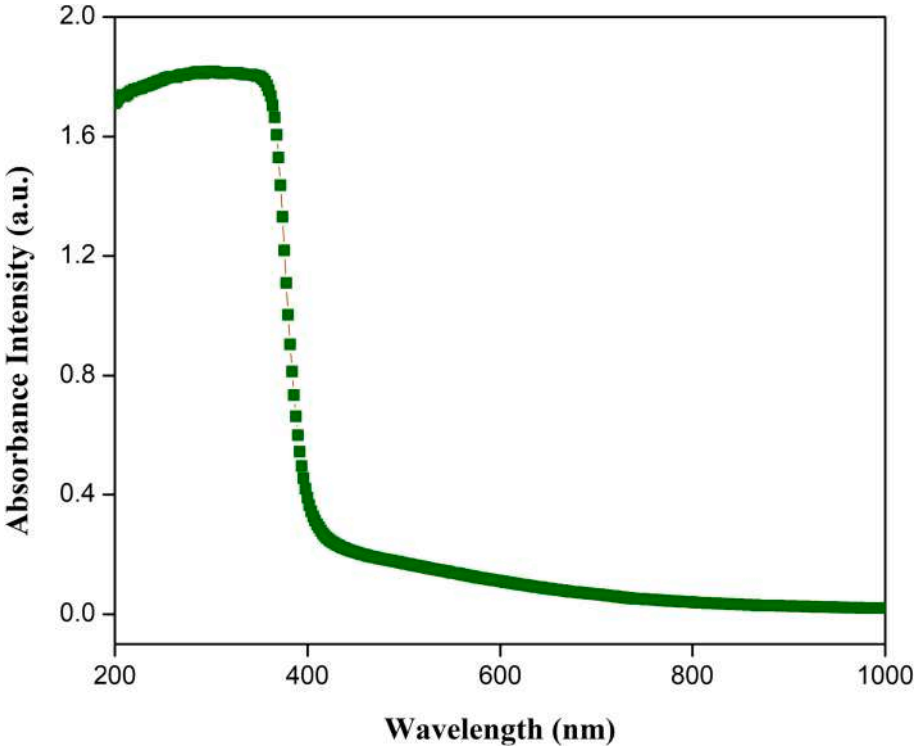

Fig. 7. UV–vis diffuse reflectance spectrum of green synthesized ZnO NPs. (For interpretation of the references to color in this figure legend, the reader is referred to the web version of this article.)

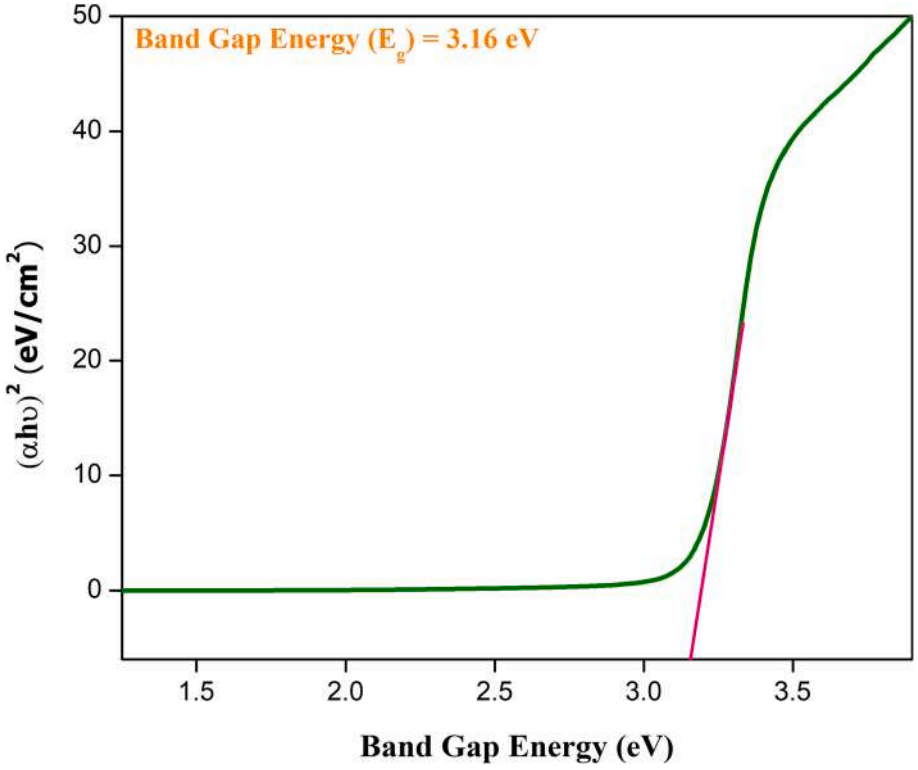

Fig. 8. *Tauc* plot of green synthesized ZnO NPs. (For interpretation of the references to color in this figure legend, the reader is referred to the web version of this article.)

$$L = \sqrt{\left[(a^2/(3)) + (0.5 - \mu)^3 * c^2\right]}$$

where, μ is the positonal parameter of wurtzite structure that designates extent of atoms displacement relative to the plane in c axis expressed by equation: $\mu = [(a^2/3c^3) + 0.25\ ] = 0.3797$ and the bond length L(Å) is 1.977 Å. The calculated ZnO bond length value (1.9767 Å)

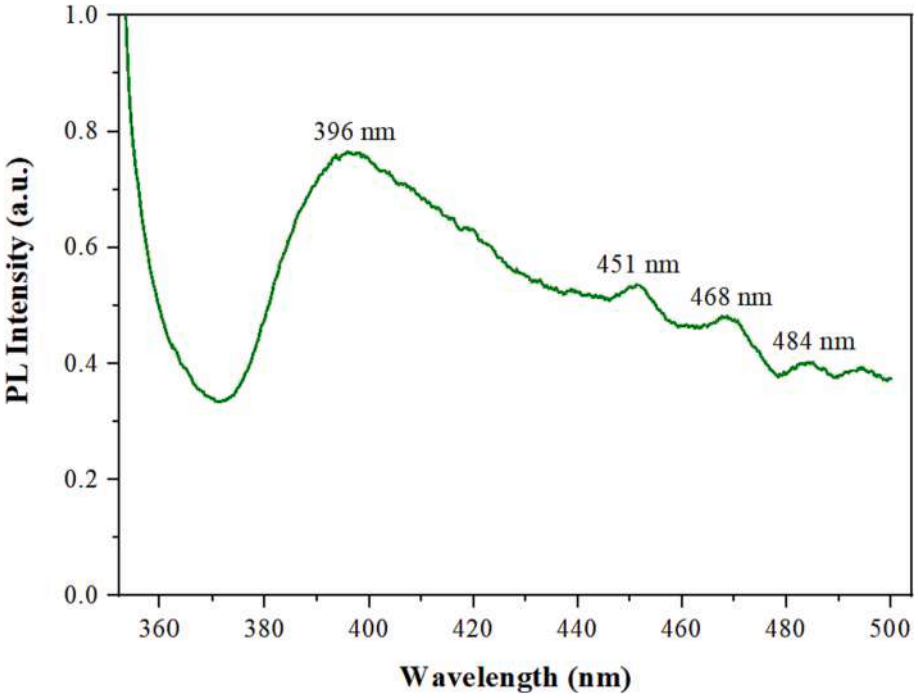

Fig. 9. PL spectrum of ZnO NPs green synthesized using *V. negundo* leaf extract. (For interpretation of the references to color in this figure legend, the reader is referred to the web version of this article.)

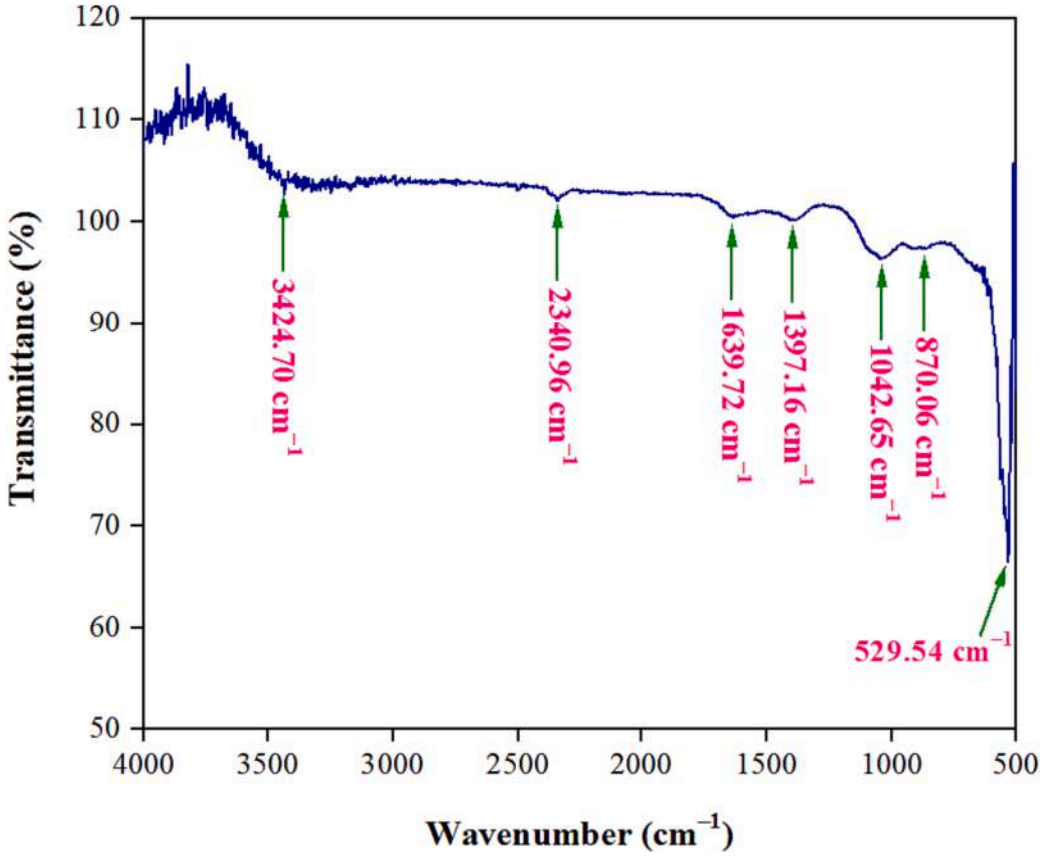

Fig. 10. FTIR spectrum of ZnO NPs green synthesized using *V. negundo* leaf extract. (For interpretation of the references to color in this figure legend, the reader is referred to the web version of this article.)

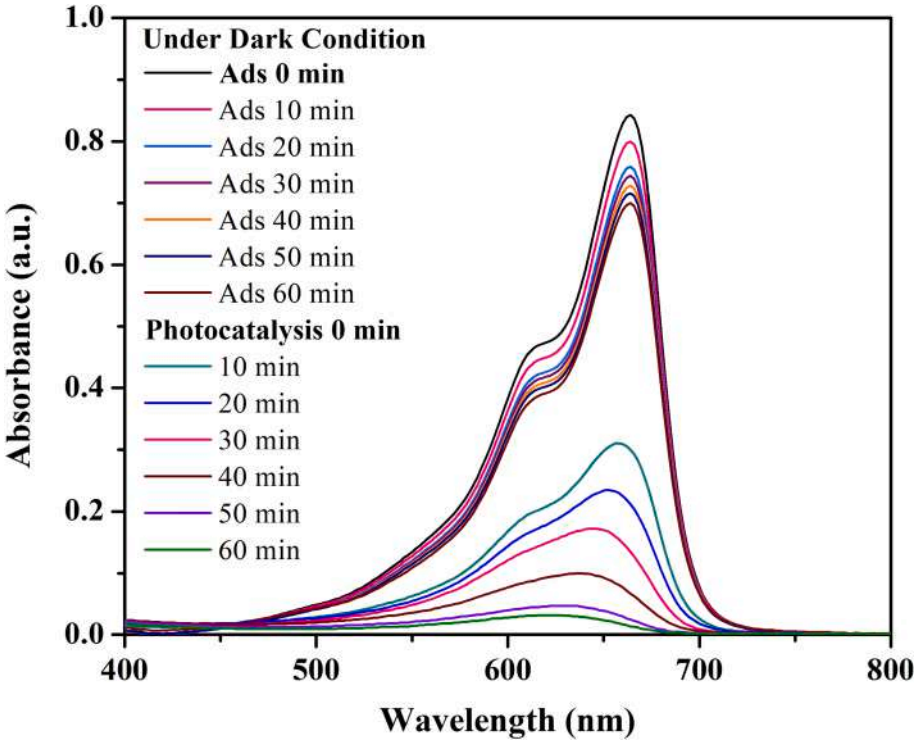

Fig. 11. Time dependent absorption spectra of MB dye.

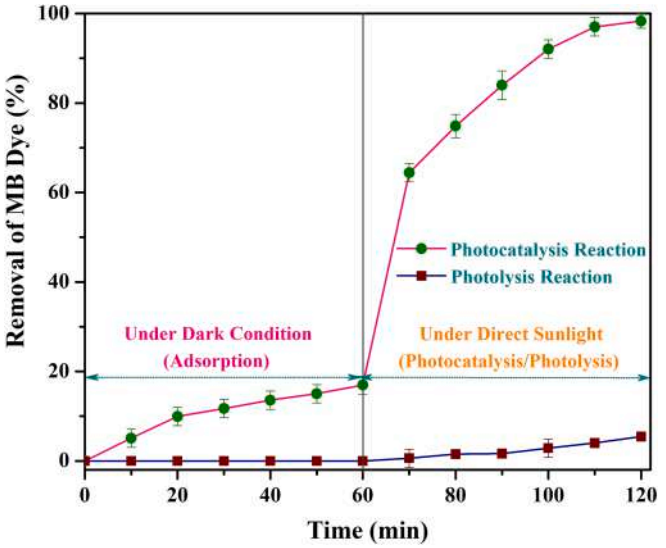

Fig. 12. Efficiency plot of MB dye removal by green synthesized ZnO NPs. (For interpretation of the references to color in this figure legend, the reader is referred to the web version of this article.)

is excellent agreement with the reported literature [58,59].

3.3. EDAX investigation

Green synthesized ZnO NPs was investigated by EDAX spectroscopy. It is obvious from EDAX spectrum in Fig. 4 that pristine ZnO NPs are formed by the present green synthesis method because its EDAX spectrum is constituted with only zinc (Zn) and oxygen (O) elements. Weight percentage (wt%) of Zn and O elements determined from EDAX spectrum was 97.13 and 2.87 %, respectively and its corresponding atomic percentage was 89.24 and 10.76 %, respectively (Table 2). The observed wt% of Zn and O elements is differed from the expected theoretical stoichiometric wt% of 80.34 and 19.66 %, respectively. This significant variations in wt% of Zn and O elements observed between theoretical and experimental values can be credited to occurrence of organic constituents from phytochemicals of *V. negundo* leaf extract during synthesis that could create oxygen vacancies in the ZnO NPs and this is an advantageous feature for photocatalytic application [60–62]. Absence of additional peak(s) corresponding to impurities in EDAX spectrum of green synthesized ZnO NPs disclosed their purity.

3.4. Rietveld refinement investigation

Rietveld refinement investigation was performed to elucidate lattice parameters of green synthesized ZnO NPs and the obtained refinement plot is illustrated in Fig. 5. Refinement analysis was carried out using FULLPROF Program Software that employs Pseudo-Voigt function for fitting several parameters to data point. The red and black lines in Fig. 5 indicate observed and fitted data, respectively. The blue line signifies the difference between observed and fitted data, while the green line denotes Bragg position. Rietveld refinement lattice parameters (*a* and *c*) and cell volume of XRD data prove hexagonal wurtzite structure of green synthesized ZnO NPs with *P63mc* space group. The value of lattice parameters *a* and *c* were found out as 3.24040 and 5.1993(4) Å, respectively. Meanwhile, the unit cell volume of ZnO NPs was determined as 47.280(3) $Å^3$. A similarity was noticed between intensity of experimental XRD pattern & simulated (Refined) XRD pattern and non-appearance of diffraction peaks associated with secondary phases reveals pristine nature of ZnO NPs green synthesized using *V. negundo* leaf extract. Goodness of fit with respect to peak position, shape, structure and background were determined by R-factors profile and chi^2 (χ^2). Lattice parameters (*a*, *b* and *c*) and refinement reliability factors (R_p, R_{wp}, and χ^2) of green synthesized ZnO NPs are summarized in Table 3. Lower values of R_p, R_{wp} and χ^2 indicate good profile refinement of green synthesized ZnO NPs [63]. Crystal structure of the ZnO NPs is shown in Fig. 6.

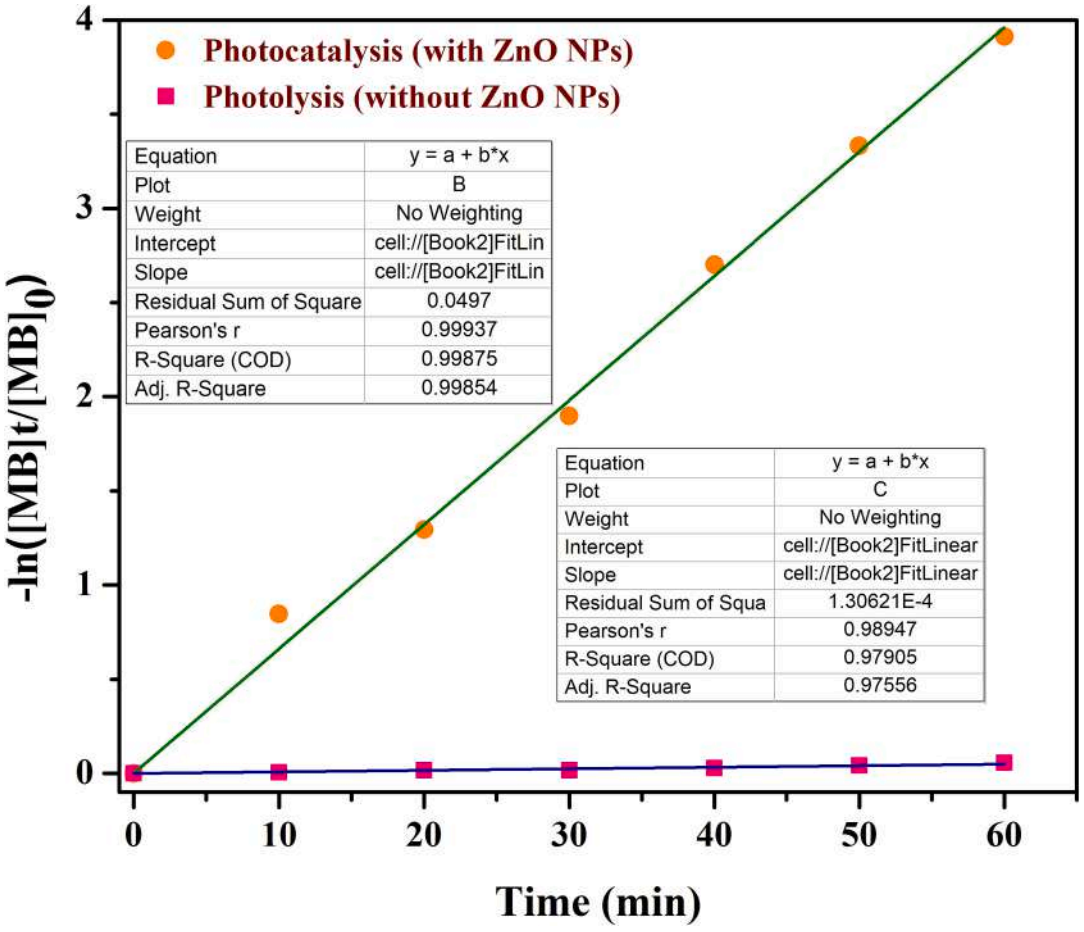

Fig. 13. $-\ln(C_t/C_0)$ *vs* time plots of MB dye degradation.

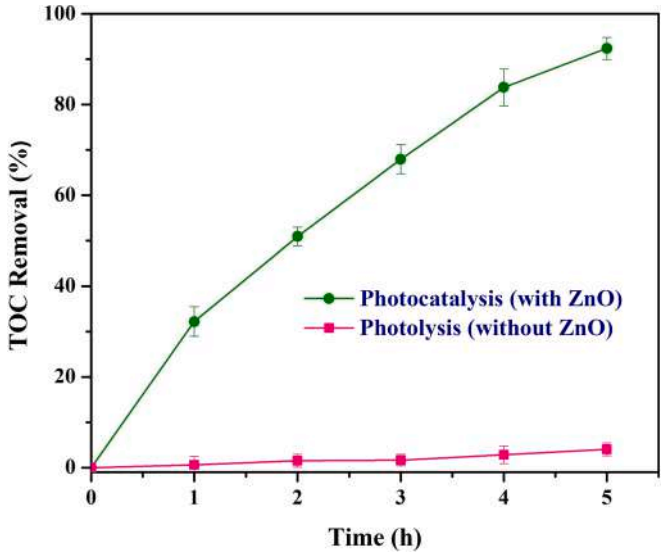

Fig. 14. Mineralization of MB dye by green synthesized ZnO NPs. (For interpretation of the references to color in this figure legend, the reader is referred to the web version of this article.)

3.5. UV–vis absorption study

Optical absorption property of ZnO NPs green synthesized using *V. negundo* leaf extract was inspected by UV–vis diffuse reflectance spectrophotometer. Optical absorption spectrum of ZnO NPs (Fig. 7) shows characteristic absorption edge of ZnO at around 375 nm due to electron transition from valence band to conduction band. Presence of absorption band at ~ 370 nm inferred formation of ZnO NPs.

The band gap energy of ZnO NPs was estimated by following *Tauc* relation [64]:

$$(\alpha h\nu)^2 = K\ (h\nu - E_g)^n \quad (1)$$

where, K is a constant, hv is photon energy, E_g is band gap energy and *n* is an exponent.

An extrapolation of linear region of curve provides optical band gap of ZnO NPs and it was determined as 3.16 eV (Fig. 8). Calculated band gap of ZnO NPs was low than the reported band gap value of bulk ZnO (3.37 eV) and this band gap improvement can be attributed to the size effect of ZnO NPs.

3.6. Photoluminescene analysis

The study of photoluminescence (PL), a property of green synthesized ZnO NPs is interesting because it can give valuable insights about quality and purity of the ZnO NPs. The PL spectrum of ZnO NPs green synthesized using *V. negundo* leaf extract is shown in Fig. 9. An excitation wavelength of 340 nm was used for the PL measurement. The PL spectrum of annealed ZnO NPs exhibit four main peaks at 396, 451, 468 and 484 nm. The high intensity peak observed at 396 nm can be correlated to near band emission of the ZnO NPs [65]. The excited electron of a valence band recombines with the holes by radiative recombination [66]. A week peak noticed at 451 nm is attributed to irradiative excitation annihilation and a weaker peak emerged at 484

Table 4
Comparison of MB dye degradation potential of green synthesized ZnO NPs using *V. negundo* leaf extract with previous reports on green synthesized ZnO NPs using diverse plant leaf extracts.

Plant Leaf Extract	Light Source	MB Dye Concentration	Catalyst Amount	Degradation Efficiency (%)	Illumination Time (min)	Reference
Tabernaemontana heyneana Wall.	UV light	5 ppm	20 mg	87	160	[76]
Solanum trilobatum	Sunlight	10 μM	0.6 g/L	94.07	90	[51]
Lepidagathis ananthapuramensis	Sunlight	1 μM/10 ppm	5 mg	98.50	120	[77]
Sambucus ebulus	UV light	50 ppm	0.02 g	80	200	[78]
Euphorbia milii	Sunlight	10 μM	0.6 g/L	98.17	50	[49]
Cocos nucifera	Sunlight	50 mg L^{-1}	5 mg/20 ml	84.29	60	[79]
Ruellia tuberosa	Sunlight	10 mg/L	200 mg/L	94	150	[80]
Rosmarinus officinalis	Sunlight	10 mg L^{-1}	1.0 g/L	99.64	45	[81]
Syzygium cumini	Sunlight	20 mg/L	200 mg/L	91.40	180	[82]
Salvadora persica	Mercury vapor lamp	5 ppm	10 mg	100	150	[83]
Phoenix roebelenii	UV lamp	10 ppm	0.2 g	98	105	[84]
Cinnamomum tamala	Sunlight	10 μM	300 mg/L	98.07	90	[85]
Acalypha indica	Sunlight	50 ppm	1.0 g/L	96	90	[66]
Prosopis juliflora	UV lamp	20 μM	250 mg/L	94	45	[86]
Tabernaemontana divaricata	Sunlight	10 μM	1.0 g/L	~100	90	[87]
Peltophorum pterocarpum	Sunlight	20 ppm	0.5 g/L	95	120	[88]
Thymus vulgaris	Hg lamp	10 ppm	0.6 g/L	96	30	[89]
Justicia spicigera	Hg lamp	15 ppm	1.0 g/L	92.78	90	[90]
Vitex negundo	Sunlight	10 μM	0.6 g/L	98.50	60	Present work

nm can be ascribed to defects in the band gap, such as oxygen vacancies produced during the green synthesis of ZnO NPs [67]. This study shows that the *V. negundo* leaf extract can be used to synthesis semiconductor nanoparticles that have intrinsic defect sites with enhanced photocatalytic activity.

3.7. FTIR investigation

Green synthesized ZnO NPs using *V. negundo* leaf extract were subjected to FT-IR analysis to detect the presence of various characteristic functional groups. FTIR spectrum of green synthesized ZnO NPs using *V. negundo* leaf extract is showed in Fig. 10. It is inferred that the ZnO NPs have absorption bands at 529.54, 870.06, 1042.65, 1397.16, 1639.72, 2340.96 and 3424.70 cm^{-1}. The relatively strong absorption band noticed in fingerprint region at 529.54 cm^{-1} due to the asymmetric stretching vibration of Zn-O bond that confirms formation of hexagonal wurtzite structured ZnO NPs [45]. The band observed at 870.06 cm^{-1} can be ascribed to stretching vibration of C–N bond [68]. The absorption band noticed at 1042.65 cm^{-1} can be assigned to C–O stretching of aliphatic amines. Meanwhile, the band obtained at 2340.96 cm^{-1} is due to C–H vibration [65]. The broad and less intense absorption band observed at 3424.70 cm^{-1} can be credited to O–H stretching mode vibrations of intercalated water molecules that reveals low moisture absorption by the ZnO NPs from air environment [49,65].

3.8. Photocatalytic performance evaluation

Green synthesized ZnO NPs were used as photocatalyst for degradation of MB dye under direct sunlight illumination. The absorption spectra of photolysis reaction and photocatalytic suspension under dark and sunlight illumination conditions were documented at time interval of 10 min. The absorption spectra of photocatalytic suspension recorded under dark and sunlight illumination conditions are shown in Fig. 11. It can be observed from Fig. 11 that the dark system (MB Dye + Dark) with photocatalyst (ZnO NPs) unveiled slight decline in concentration as a consequence of adsorption of MB on the surface of ZnO NPs..

The pictorial representation of results of photolysis and photocatalytic experiments, viz. MB Dye + Sunlight; MB Dye + ZnO NPs + Dark and MB Dye + ZnO NPs + Sunlight are displayed in Fig. 12. During the photolysis reaction, only a slight proportion (5.62 %) of MB dye was oxidized (Fig. 12). Nonetheless, it is apparent that characteristic absorbance wavelength (λ_{max} = 664 nm) of MB dye was decreased in intensity with respect to the reaction time for the MB + ZnO NPs + Dark system that discloses decrement in initial concentration of MB dye (Fig. 11). Moreover, concentration of MB dye was reached stable at 60 min, indicates that adsorption–desorption equilibrium between MB dye and ZnO NPs. About 16.59 % of the MB dye was eliminated through the adsorption process by ZnO NPs (Fig. 12). The highest absorption peak intensity noticed at 664 nm for the MB dye can be credited to n to π^* transitions [69]. Conversely, the absorbance of MB dye was decreased exponentially for MB Dye + ZnO NPs + Sunlight photocatalytic system (Fig. 11). As a consequence, ZnO NPs photocatalyst almost completely degrade the MB dye with degradation efficiency of 98.50 % at 60 min of sunlight illumination (Fig. 12).

Significant photocatalytic activity observed in the present study might be contributed from factors such as, small particle size that ranges from 5 nm to 35 nm having mean size of ~ 19 nm, better crystallinity and high quality of the ZnO NPs with average value of strain, ε_{str} = 0.0047, oxygen vacancy in the ZnO NPs (Zn and O elements have the wt % of 97.13 and 2.87 %, respectively) and appropriate band gap energy (3.16 eV). In addition, the formed spherical ZnO NPs have higher surface area. Further, presence of oxygen vacancy can lead to improved charge carrier mobility within the particles that facilitates the efficient separation and migration of photoinduced electron-hole pairs. As a result, the MB degradation efficiency was enhanced to 98.50 % at 60 min of sunlight illumination in the presence of ZnO NPs [70]. Spherical nanoparticles generally have higher surface area compared to other morphologies. In the present study, the increased surface area provides more active sites for photocatalytic reactions, allowing for a greater number of interactions between ZnO NPs green synthesized using *V. negundo* leaf extract and MB dye molecules. As a result, the degradation efficiency was enhanced due to the availability of larger reaction surface. Further, the spherical ZnO NPs often exhibit good dispersibility in solution due to their symmetrical shape. This uniform dispersion ensures that each particle is evenly exposed to the reacting species, promoting consistent and efficient photocatalytic degradation of MB dye throughout the solution. Additionally, the spherical ZnO NPs often possess well-defined crystalline structures. This can lead to improved charge carrier mobility within the particles, facilitating efficient separation and migration of photoinduced electron-hole pairs during the photocatalytic degradation of MB dye [71–73]. Additionally, cationic MB dye molecules could facilely be adsorbed on negatively charged ZnO NPs surface

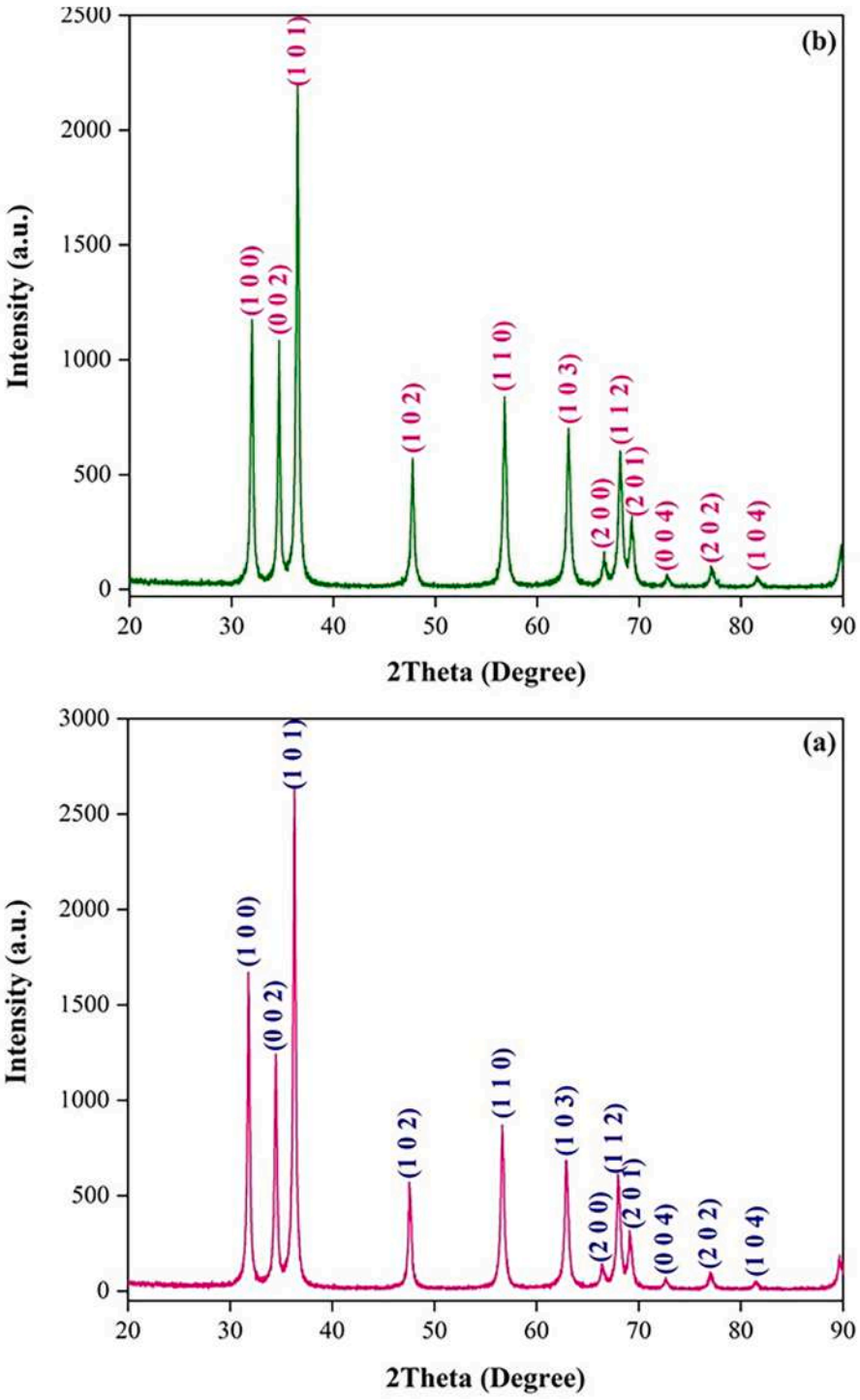

Fig. 15. XRD patterns of spectrum of green synthesized ZnO NPs photocatalyst before (a) and after (a) photocatalytic degradation of MB dye. (For interpretation of the references to color in this figure legend, the reader is referred to the web version of this article.)

by electrostatic attraction. Under sunlight illumination, the produced oxidative radicals attack non-selectively the MB dye molecules adsorbed on the ZnO NPs surface [74].

3.9. Kinetics of photocatalytic reaction

Photocatalytic reaction kinetics of ZnO NPs for the degradation of MB dye was estimated by the pseudo first-order kinetic equation:

$$-\ln(C_t/C_0) = kt$$

Here, C_0 and Ct represent MB dye concentration prior to starting photocatalytic reaction and at a time of 't' after completing photocatalytic reaction, respectively, k is reaction rate constant and t is sunlight irradiation time. Linear plot of $-\ln(C_t/C_0)$ *vs* time (t) gives value of slope (k). Linear graph in Fig. 13 reveals that photocatalytic reaction resembled pseudo first order. Reaction rate constant of ZnO NPs towards photocatalytic degradation of MB dye was determined as 10.8×10^{-3} s^{-1} and reaction rate constant observed for photolysis process was 1.5×10^{-5} s^{-1}. This significantly higher reaction rate constant observed for the ZnO NPs towards photocatalytic degradation of MB dye can be ascribed to effectual charge transfer and decrease in recombination rate

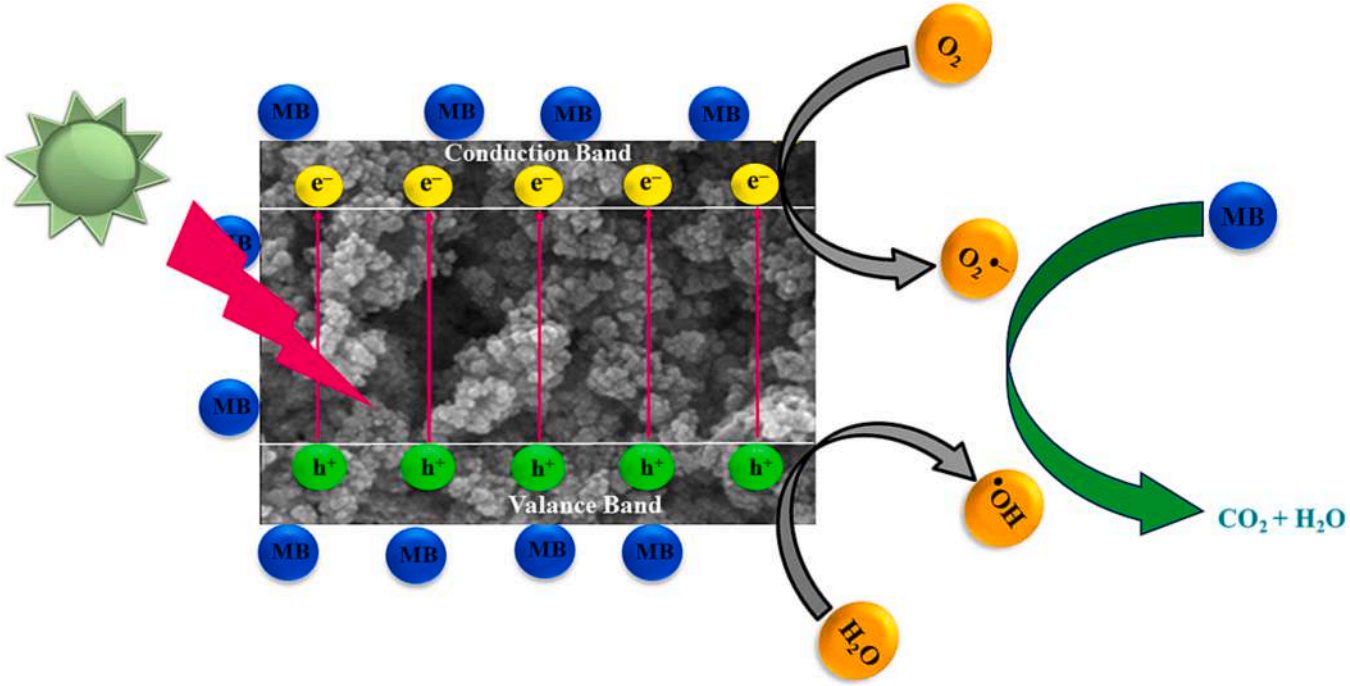

Fig. 16. Photocatalytic reaction mechanism of MB dye degradation by green synthesized ZnO NPs. (For interpretation of the references to color in this figure legend, the reader is referred to the web version of this article.)

of photogenerated charge carriers on the surface of ZnO NPs.

3.10. Total organic carbon analysis

Total organic carbon (TOC) analysis was performed to explicate mineralization tendency of MB dye by green synthesized ZnO NPs during photocatalysis reaction and also without ZnO NPs under sunlight illumination (Fig. 14). It is apparent that the rate of mineralization of MB dye is low in the presence of ZnO NPs when compared to photocatalytic degradation rate of MB dye determined by spectrophotometer analysis. Usually, complete mineralization of MB dye requires extended duration over photocatalytic degradation reaction because its mineralization encompasses two steps, viz. ring cleavage of MB dye molecules at initial photocatalytic degradation step and oxidation of fragments in latter step [75]. Accordingly, green synthesized ZnO NPs eliminated 92.34 % of TOC content from MB dye at 5 h of sunlight illumination. In contrast, an insignificant TOC removal of 4.06 % was attained through photolysis reaction (without ZnO NPs catalyst) at 5 h of sunlight irradiation. Photocatalytic performance of ZnO NPs green synthesized using *V. negundo* leaf extract against degradation of MB dye was compared with earlier reports on green synthesized ZnO NPs using diverse plant leaf extracts (Table 4).

3.11. Stability analysis of ZnO NPs photocatalyst

The stability of the green synthesized ZnO NPs photocatalyst before and after the photocatalytic degradation of MB dye was studied by XRD analysis and the recorded XRD patterns are shown in Fig. 15. It can be observed from the XRD patterns that there is no shift/change in the diffraction peaks of the reused ZnO NPs photocatalyst when compared respect to the unused ZnO NPs photocatalyst that ascertained their stability. This result suggests that the green synthesized ZnO NPs photocatalyst was relatively stable.

3.12. Photocatalytic reaction mechanism

During photocatalytic reaction, the molecules of MB dye adsorb on the surface of ZnO NPs. Upon the exposure of incident sunlight, the photons having energy greater than the band gap energy of ZnO NPs (3.16 eV) energize them that facilitates separation of conduction band electrons and valence band holes. The separated conduction band electrons combine with surface adsorbed oxygen molecules, which produces superoxide anion radicals. The resulting protonation generates $HO_2^{\bullet}$ that interacts with trapped electrons and generates H_2O_2 that finally produces hydroxyl radicals on the surface of ZnO NPs [91,92]. Considerably high generation of hydroxyl radicals is due to the recombination of photogenerated conduction band electrons and valence band holes hardly on ZnO NPs that permit adequate time for photogenerated conduction band electrons and valence band holes react with oxygen and hydroxide or water to form hydroxyl radicals [93]. The photogenerated valence band holes act as oxidizing agent and react with chemisorbed hydroxide or water and produce highly reactive hydroxyl radicals that join with MB dye molecules adsorbed on ZnO NPs and as a consequence, photocatalytic oxidation of MB dye molecules occurs efficiently [94,95] (Fig. 16).

4. Conclusion

A facile green synthesis route was followed to prepare zinc oxide nanoparticles (ZnO NPs) using *Vitex negundo* (*V. negundo*) plant leaf extract. The FESEM images displayed formation of spherical ZnO NPs, whose size ranges between 5 and 35 nm with a mean diameter of ~ 19 nm. The phytochemicals, present in the *V. negundo* leaf extract, viz. alkaloids, flavonoids, tannin, terpenoids, steroids and phenols might be responsible for the formation of small size ZnO NPs. The XRD pattern revealed formation of highly crysralline and hexagonal wurtzite structured ZnO with an average cryatalline size of 18.22 nm. The EDAX spectrum disclosed pristine nature of the ZnO NPs with emergence of oxygen vacancies. According to the UV–vis diffuse reflectance spectral analysis, the band gap of ZnO NPs was determined as 3.16 eV. Around 98.50 % of the MB dye was degraded by the ZnO NPs at 60 min of direct sunlight illumination due to their high crystallinity, small particle size, high surface area, appropriate band gap and high oxygen vacancy of the green synthesized ZnO NPs.

CRediT authorship contribution statement

S. Venkatesan: Conceptualization, Investigation, Validation, Visualization, Writing – review & editing. **S. Suresh:** Conceptualization, Investigation, Validation, Visualization, Writing – review & editing. **J. Arumugam:** Formal analysis, Investigation, Validation, Visualization. **P. Ramu:** Conceptualization, Investigation, Resources, Supervision, Writing – review & editing. **N. Pugazhenthiran:** Formal analysis, Investigation, Validation, Visualization. **R. Jothilakshmi:** Formal analysis, Investigation, Validation, Visualization. **K.M. Prabu:** Formal analysis, Investigation, Validation, Visualization.

Declaration of competing interest

The authors declare that they have no known competing financial interests or personal relationships that could have appeared to influence the work reported in this paper.

Data availability

Data will be made available on request.

Acknowledgment

The authors S. Suresh, J. Arumugam and K.M. Prabu express their gratefulness to the Department of Science and Technology, Government of India, New Delhi for generously providing Instrumentation Facility through Fund for Improvement of Science & Technology Infrastructure (FIST) Programme (Grant No. SR/FST/College-2017/140 (C), dt. 14.08.2018).

References

[1] N. Mayedwa, N. Mongwaketsi, S. Khamlich, K. Kaviyarasu, N. Matinise, M. Maaza, Green synthesis of nickel oxide, palladium and palladium oxide synthesized via Aspalathus linearis natural extracts: physical properties & mechanism of formation, Appl. Surf. Sci. 446 (2018) 266–272, https://doi.org/10.1016/j.apsusc.2017.12.116.

[2] S. Patil, R. Chandrasekaran, Biogenic nanoparticles: a comprehensive perspective in synthesis, characterization, application and its challenges, J. Genet. Eng. Biotechnol. 18 (2020) 67, https://doi.org/10.1186/s43141-020-00081-3.

[3] P. Prabhu, M. Rao, G. Murugesan, M.K. Narasimhan, T. Varadavenkatesan, R. Vinayagam, N.T. Lan Chi, A. Pugazhendhi, R. Selvaraj, Synthesis, characterization and anticancer activity of the green-synthesized hematite nanoparticles, Environ. Res. 214 (2022) 113864, https://doi.org/10.1016/j.envres.2022.113864.

[4] C.A. Mbachu, A.K. Babayemi, T.C. Egbosiuba, J.I. Ike, I.J. Ani, S. Mustapha, Green synthesis of iron oxide nanoparticles by Taguchi design of experiment method for effective adsorption of methylene blue and methyl orange from textile wastewater, Results Eng. 19 (2023) 101198, https://doi.org/10.1016/j.rineng.2023.101198.

[5] M. Valldeperas, M. Wiśniewska, M. Ram-On, E. Kesselman, D. Danino, T. Nylander, J. Barauskas, Sponge phases and nanoparticle dispersions in aqueous mixtures of mono-and diglycerides, Langmuir 32 (2016) 8650–8659, doi: 10.1021/acs.langmuir.6b01356.

[6] S.P. Patil, R.Y. Chaudhari, M.S. Nemade, *Azadirachta indica* leaves mediated green synthesis of metal oxide nanoparticles: A review, Talanta Open 5 (2022) 100083, https://doi.org/10.1016/j.talo.2022.100083.

[7] S. Thambidurai, P. Gowthaman, M. Venkatachalam, S. Suresh, Natural sunlight assisted photocatalytic degradation of methylene blue by spherical zinc oxide nanoparticles prepared by facile chemical co-precipitation method, Optik 207 (2020) 163865, https://doi.org/10.1016/j.ijleo.2019.163865.

[8] I. Chandio, F.A. Janjhi, A.A. Memon, S. Memon, Z. Ali, K.H. Thebo, A.A.A. Pirzado, A.A. Hakro, W.S. Khan, Ultrafast ionic and molecular sieving through graphene oxide based composite membranes, Desalination 500 (2021) 114848, https://doi.org/10.1016/j.desal.2020.114848.

[9] S.T. Nipa, N.R. Shefa, S. Parvin, M.A. Khatun, M.J. Alam, S. Chowdhury, M.A. R. Khan, S.M.A.Z. Shawon, B.K. Biswas, M.W. Rahman, Adsorption of methylene blue on papaya bark fiber: equilibrium, isotherm and kinetic perspectives, Results Eng. 17 (2023) 100857, https://doi.org/10.1016/j.rineng.2022.100857.

[10] A.A.A. Darwish, M. Rashad, H.A. Al-Aoh, Methyl orange adsorption comparison on nanoparticles: isotherm, kinetics, and thermodynamic studies, Dyes Pigm. 160 (2019) 563–571, https://doi.org/10.1016/j.dyepig.2018.08.045.

[11] S. Sagadevan, I. Fatimah, T.C. Egbosiuba, S.F. Alshahateet, J.A. Lett, G. K. Weldegebrieal, M.V. Le, M.R. Johan, Photocatalytic efficiency of titanium dioxide for dyes and heavy metals removal from wastewater, Bull. Chem. React. Eng. Catal. 17 (2022) 430–450, https://doi.org/10.9767/BCREC.17.2.13948.430-450.

[12] S.S. Qureshi, V. Shah, S. Nizamuddin, N.M. Mubarak, R.R. Karri, M.H. Dehghani, S. Ramesh, M. Khalid, M.E. Rahman, Microwave-assisted synthesis of carbon nanotubes for the removal of toxic cationic dyes from textile wastewater, J. Mol. Liq. 356 (2022) 119045, https://doi.org/10.1016/j.molliq.2022.119045.

[13] A.S. Altowyan, A. Toghan, H.A. Ahmed, R.A. Pashameah, E.A. Mwafy, S. H. Alrefaee, A.M. Mostafa, Removal of methylene blue dye from aqueous solution using carbon nanotubes decorated by nickel oxide nanoparticles via pulsed laser ablation method, Radiat. Phys. Chem. 198 (2022) 110268, https://doi.org/10.1016/j.radphyschem.2022.110268.

[14] O.A. Shabaan, H.S. Jahin, G.G. Mohamed, Removal of anionic and cationic dyes from wastewater by adsorption using multiwall carbon nanotubes, Arab. J. Chem. 13 (2020) 4797–4810, https://doi.org/10.1016/j.arabjc.2020.01.010.

[15] D.C. Onu, A.K. Babayemi, T.C. Egbosiuba, B.O. Okafor, I.J. Ani, S. Mustapha, J. O. Tijani, W.C. Ulakpa, P.E. Ovuoraye, A.S. Abdulkareem, Isotherm, kinetics, thermodynamics, recyclability and mechanism of ultrasonic assisted adsorption of methylene blue and lead (II) ions using green synthesized nickel oxide nanoparticles, Environ. Nanotechnol. Monit. Manag. 20 (2023) 100818, https://doi.org/10.1016/j.enmm.2023.100818.

[16] P.S. Jassal, D. Kaur, R. Prasad, J. Singh, Green synthesis of titanium dioxide nanoparticles: Development and applications, J. Agric. Food Res. 10 (2022) 100361, https://doi.org/10.1016/j.jafr.2022.100361.

[17] H. Kumari, Sonia, Suman, R. Ranga, S. Chahal, S. Devi, S. Sharma, S. Kumar, P. Kumar, S. Kumar, A. Kumar, R. Parmar, A review on photocatalysis used for wastewater treatment: Dye degradation, Water Air Soil Pollut. 234 (2023) 349, doi: 10.1007/s11270-023-06359-9.

[18] M.A. Al-Nuaim, A.A. Alwasiti, Z.Y. Shnain, The photocatalytic process in the treatment of polluted water, Chem. Pap. 77 (2023) 677–701, https://doi.org/10.1007/s11696-022-02468-7.

[19] S. Singh, S. Sharma, U. Manhas, I. Qadir, A.K. Atri, D. Singh, Different fuel-adopted combustion syntheses of nano-structured $NiCrFeO_4$: A highly recyclable and versatile catalyst for reduction of nitroarenes at room temperature and photocatalytic degradation of various organic dyes in unitary and ternary solutions, ACS Omega 7 (2022) 19853–19871, https://doi.org/10.1021/acsomega.2c01616.

[20] D.M. Tejashwini, H.V. Harini, H.P. Nagaswarupa, R. Naik, V.V. Deshmukh, N. Basavaraju, An in-depth exploration of eco-friendly synthesis methods for metal oxide nanoparticles and their role in photocatalysis for industrial dye degradation, Chem. Phys. Impact 7 (2023) 100355, https://doi.org/10.1016/j.chphi.2023.100355.

[21] S. Thambidurai, P. Gowthaman, M. Venkatachalam, S. Suresh, M. Kandasamy, Morphology dependent photovoltaic performance of zinc oxide-cobalt oxide nanoparticle/nanorod composites synthesized by simple chemical co-precipitation method, J. Alloys Compd. 852 (2021) 156997, https://doi.org/10.1016/j.jallcom.2020.156997.

[22] J. Wang, R. Chen, L. Xiang, S. Komarneni, Synthesis, properties and applications of ZnO nanomaterials with oxygen vacancies: A review, Ceram. Int. 44 (2018) 7357–7377, https://doi.org/10.1016/j.ceramint.2018.02.013.

[23] K. Singh, Nancy, M. Bhattu, G. Singh, N.M. Mubarak, J. Singh, Light-absorption-driven photocatalysis and antimicrobial potential of PVP-capped zinc oxide nanoparticles, Sci. Rep. 13 (2023) 13886, doi: 10.1038/s41598-023-41103-7.

[24] N. Pugazhenthiran, P. Sathishkumar, O. Albormani, S. Murugesan, M. Kandasamy, M. Selvaraj, S. Suresh, S.K. Kumar, D. Contreras, H. Váldes, R.V. Mangalaraja, Silver nanoparticles modified ZnO nanocatalysts for effective degradation of ceftiofur sodium under UV–vis light illumination, Chemosphere 313 (2023) 137515, https://doi.org/10.1016/j.chemosphere.2022.137515.

[25] Z. Jiang, B. Cheng, L. Zhang, Z. Zhang, C. Bie, A review on ZnO-based S-scheme heterojunction photocatalysts, Chinese, J. Catal. 52 (2023) 32–49, https://doi.org/10.1016/S1872-2067(23)64502-4.

[26] I. Ahmad, S. Shukrullah, M.Y. Naz, H.N. Bhatti, M. Ahmad, E. Ahmed, S. Ullah, M. Hussien, Recent progress in rare earth oxides and carbonaceous materials modified ZnO heterogeneous photocatalysts for environmental and energy applications, J. Environ. Chem. Eng. 10 (2022) 107762, https://doi.org/10.1016/j.jece.2022.107762.

[27] A.A.A. Mutalib, N.F. Jaafar, ZnO photocatalysts applications in abating the organic pollutant contamination: A mini review, Total Environ. Res. Themes 3–4 (2022) 100013, https://doi.org/10.1016/j.totert.2022.100013.

[28] S. Goktas, A. Goktas, A comparative study on recent progress in efficient ZnO based nanocomposite and heterojunction photocatalysts: A review, J. Alloys Compd. 863 (2021) 158734, https://doi.org/10.1016/j.jallcom.2021.158734.

[29] C.B. Ong, L.Y. Ng, A.W. Mohammad, A review of ZnO nanoparticles as solar photocatalysts: Synthesis, mechanisms and applications, Renew. Sust. Energ. Rev. 81 (2018) 536–551, https://doi.org/10.1016/j.rser.2017.08.020.

[30] N. Alwadai, M. Shakil, U. Inayat, M. Tanveer, M. Ashraf, S.S.A. Gillani, M.S. Al-Buriahi, Z.A. Alrowaili, Unlocking the synergistic potential of peanut shell derived activated carbon-doped TiO_2 for highly efficient photocatalytic removal of organic dye under visible light irradiation, Mater. Sci. Eng. B 296 (2023) 116646, https://doi.org/10.1016/j.mseb.2023.116646.

[31] M. Shakil, U. Inayat, M. Tanveer, G. Nabi, S.S.A. Gillani, M. Rafique, N.H. Tariq, A. Shah, A. Mahmood, NiO and Ag–Cd co-doped NiO nanoparticles: study of photocatalytic degradation of rhodamine B dye for wastewater treatment, Int. J. Environ. Sci. Technol. 20 (2023) 2021–2036, https://doi.org/10.1007/s13762-022-04101-2.

[32] B. Pramanick, P.F. Siril, Synergistic visible light plasmonic photocatalysis of bi-metallic Gold-Palladium nanoparticles supported on graphene, Results Chem. 5 (2023) 100774, https://doi.org/10.1016/j.rechem.2023.100774.
[33] M. Shakil, U. Inayat, M. Ashraf, M. Tanveer, S.S.A. Gillani, A. Dahshan, Photocatalytic performance of novel zinc ferrite/copper sulfide composites for the degradation of Rhodamine B dye from wastewater using visible spectrum, Optik 272 (2023) 170353, https://doi.org/10.1016/j.ijleo.2022.170353.
[34] M. Govindarajan, M. Rajeswary, U. Muthukumaran, S.L. Hoti, H.F. Khater, G. Benelli, Single-step biosynthesis and characterization of silver nanoparticles using *Zornia diphylla* leaves: A potent eco-friendly tool against malaria and arbovirus vectors, J. Photochem. Photobiol. b: Biol. 161 (2016) 482–489, https://doi.org/10.1016/j.jphotobiol.2016.06.016.
[35] C. Balalakshmi, K. Gopinath, M. Govindarajan, R. Lokesh, A. Arumugam, N. S. Alharbi, S. Kadaikunnan, J.M. Khaled, G. Benelli, Green synthesis of gold nanoparticles using a cheap *Sphaeranthus indicus* extract: impact on plant cells and the aquatic crustacean *Artemia nauplii*, J. Photochem. Photobiol. b: Biol. 173 (2017) 598–605, https://doi.org/10.1016/j.jphotobiol.2017.06.040.
[36] E.R. Balasooriya, C.D. Jayasinghe, U.A. Jayawardena, R.W.D. Ruwanthika, S. R. Mendis, P.V. Udagama, Honey mediated green synthesis of nanoparticles: New era of safe nanotechnology, J. Nanomater. 23 (2017) 1–10, https://doi.org/10.1155/2017/5919836.
[37] S. Iravani, Green synthesis of metal nanoparticles using plants, Green Chem. 13 (2011) 2638–2650, https://doi.org/10.1039/C1GC15386B.
[38] S. Jain, M.S. Mehata, Medicinal plant leaf extract and pure flavonoid mediated green synthesis of silver nanoparticles and their enhanced antibacterial property, Sci. Rep. 7 (2017) 15867, https://doi.org/10.1038/s41598-017-15724-8.
[39] A. Umamaheswari, S. Lakshmana Prabu, S. Adharsh John, A. Puratchikody, Green synthesis of zinc oxide nanoparticles using leaf extracts of *Raphanus sativus var. Longipinnatus* and evaluation of their anticancer property in A549 cell lines, Biotechnol. Rep. 29 (2021) e00595.
[40] P. Banerjee, M. Satapathy, A. Mukhopahayay, P. Das, Leaf extract mediated green synthesis of silver nanoparticles from widely available Indian plants: synthesis, characterization, antimicrobial property and toxicity analysis, Bioresour. Bioprocess. 1 (2014) 3, https://doi.org/10.1186/s40643-014-0003-y.
[41] H. Mirzaei, M. Darroudi, Zinc oxide nanoparticles: Biological synthesis and biomedical applications, Ceram. Int. 43 (2017) 907–914, https://doi.org/10.1016/j.ceramint.2016.10.051.
[42] A.K. Mittal, Y. Chisti, U.C. Banerjee, Synthesis of metallic nanoparticles using plant extracts, Biotechnol. Adv. 31 (2013) 346–356, https://doi.org/10.1016/j.biotechadv.2013.01.003.
[43] J.P.S. Begum, K. Manjunath, S. Pratibha, N. Dhananjaya, P. Sahu, S. Kashaw, Bioreduction synthesis of zinc oxide nanoparticles using *Delonix regia* leaf extract (Gul Mohar) and its agromedicinal applications, 5 (2020) 468–475, J. Sci.: Adv. Mater. Devices, doi: 10.1016/j.jsamd.2020.07.009.
[44] S. Suresh, R. Ilakiya, G. Kalaiyan, S. Thambidurai, P. Kannan, K.M. Prabu, N. Suresh, R. Jothilakshmi, S.K. Kumar, M. Kandasamy, Green synthesis of copper oxide nanostructures using *Cynodon dactylon* and *Cyperus rotundus* grass extracts for antibacterial applications, Ceram. Int. 46 (2020) 12525–12537, https://doi.org/10.1016/j.ceramint.2020.02.015.
[45] J. Arumugam, S. Thambidurai, S. Suresh, M. Selvapandiyan, M. Kandasamy, N. Pugazhenthiran, S.K. Kumar, T. Muneeswaran, F. Quero, Green synthesis of zinc oxide nanoparticles using *Ficus carica* leaf extract and their bactericidal and photocatalytic performance evaluation, Chem. Phys. Lett. 783 (2021) 139040, https://doi.org/10.1016/j.cplett.2021.139040.
[46] G. Kalaiyan, S. Suresh, K.M. Prabu, S. Thambidurai, M. Kandasamy, N. Pugazhenthiran, S.K. Kumar, T. Muneeswaran, Bactericidal activity of *Moringa oleifera* leaf extract assisted green synthesis of hierarchical copper oxide microspheres against pathogenic bacterial strains, J. Environ. Chem. Eng. 9 (2021) 104847, https://doi.org/10.1016/j.jece.2020.104847.
[47] G. Kalaiyan, S. Suresh, S. Thambidurai, K.M. Prabu, S.K. Kumar, N. Pugazhenthiran, M. Kandasamy, Green synthesis of hierarchical copper oxide microleaf bundles using *Hibiscus cannabinus* leaf extract for antibacterial application, J. Mol. Struct. 1217 (2020) 128379, https://doi.org/10.1016/j.molstruc.2020.128379.
[48] G. Kalaiyan, K.M. Prabu, S. Suresh, N. Suresh, Green synthesis of CuO nanostructures with bactericidal activities using *Simarouba glauca* leaf extract, Chem. Phys. Lett. 761 (2020) 138062, https://doi.org/10.1016/j.cplett.2020.138062.
[49] S. Venkatesan, S. Suresh, P. Ramu, M. Kandasamy, J. Arumugam, S. Thambidurai, K.M. Prabu, N. Pugazhenthiran, Biosynthesis of zinc oxide nanoparticles using *Euphorbia milii* leaf constituents: Characterization and improved photocatalytic degradation of methylene blue dye under natural sunlight, J. Indian Chem. Soc. 99 (2022) 100436, https://doi.org/10.1016/j.jics.2022.100436.
[50] S. Thambidurai, J. Arumugam, M. Kandasamy, D. Balaji, N. Pugazhenthiran, R. Jothilakshmi, B. Sathish Kumar, K. Murugesan, S. Karthick Kumar, T. Muneeswaran, K. Jayakumar, S. Suresh, *Vitex negundo* and *Euphorbia milii* leaf extracts aided green synthesis of copper oxide nanostructures for effective inactivation of pathogenic bacteria, Chem. Phys. Lett. 832 (2023) 140881, doi: 10.1016/j.cplett.2023.140881.
[51] S. Venkatesan, S. Suresh, P. Ramu, J. Arumugam, S. Thambidurai, N. Pugazhenthiran, Methylene blue dye degradation potential of zinc oxide nanoparticles bioreduced using *Solanum trilobatum* leaf extract, Results Chem. 4 (2022) 100637, https://doi.org/10.1016/j.rechem.2022.100637.
[52] S. Anbalagan, M. Sankareswaran, M. Moorthy, B. Elakkia, E. Fahamitha, Phytochemical analysis and antifungal activity of *Vitex negundo* leaf extracts against clinically isolated fungal pathogens, Indian, J. Appl. Microbiol. 20 (2017) 119–125.
[53] A.A. Al-Askar, A.H. Hashem, N.I. Elhussieny, E. Saied, Green biosynthesis of zinc oxide nanoparticles using *Pluchea indica* leaf extract: Antimicrobial and photocatalytic activities, Molecules 28 (2023) 4679, https://doi.org/10.3390/molecules28124679.
[54] A.E. Golli, S. Contreras, C. Dridi, Bio-synthesized ZnO nanoparticles and sunlight-driven photocatalysis for environmentally-friendly and sustainable route of synthetic petroleum refinery wastewater treatment, Sci. Rep. 13 (2023) 20809, https://doi.org/10.1038/s41598-023-47554-2.
[55] M.D. Jayappa, C.K. Ramaiah, M.A.P. Kumar, D. Suresh, A. Prabhu, R.P. Devasya, S. Sheikh, Green synthesis of zinc oxide nanoparticles from the leaf, stem and in vitro grown callus of *Mussaenda frondosa* L.: characterization and their applications, Appl. Nanosci. 10 (2020) 3057–3074, https://doi.org/10.1007/s13204-020-01382-2.
[56] A. Ashar, I.A. Bhatti, T. Siddique, S.M. Ibrahim, S. Mirza, Z.A. Bhutta, M. Shoaib, M. Ali, M.B. Taj, M. Iqbal, S. Noor, M. Mohsin, Integrated hydrothermal assisted green synthesis of ZnO nano discs and their water purification efficiency together with antimicrobial activity, J. Mater. Res. Technol. 15 (2021) 6901–6917, https://doi.org/10.1016/j.jmrt.2021.11.009.
[57] JCPDS, Powder diffraction file, Alphabetical index, Inorganic Compounds, International Center for Diffraction Data, Newtown Square, Pa, USA, 1977.
[58] P. Bindu, S. Thomas, Estimation of lattice strain in ZnO nanoparticles: X-ray peak profile analysis, J. Theor. Appl. Phys. 8 (2014) 123–134, https://doi.org/10.1007/s40094-014-0141-9.
[59] A. Modwi, M.A. Abbo, E.A. Hassan, K.K. Taha, L. Khezami, A. Houas, Influence of annealing temperature on the properties of ZnO synthesized via 2.3. dihydroxysuccinic acid using flash sol-gel method, J. Ovonic Res. 12 (2016) 59–66.
[60] S. Suresh, S. Thambidurai, J. Arumugam, M. Kandasamy, N. Pugazhenthiran, D. Balaji, B.A. Al-Asbahi, N.R. Reddy, A. Arunkumar, T. Muneeswaran, Antibacterial activity and photocatalytic oxidative performance of zinc oxide nanorods biosynthesized using *Aerva lanata* leaf extract, Inorg. Chem. Commun. 139 (2022) 109398, https://doi.org/10.1016/j.inoche.2022.109398.
[61] A. Narayana, S.A. Bhat, A. Fathima, S.V. Lokesh, S.G. Surya, C.V. Yelamaggad, Green and low-cost synthesis of zinc oxide nanoparticles and their application in transistor-based carbon monoxide sensing, RSC Adv. 10 (2020) 13532–13542, https://doi.org/10.1039/D0RA00478B.
[62] P. Molaei, F. Rahimi-Moghadam, Optimized synthesis of ZnO nanostructures by egg-white content ratio manipulation for photocatalytic applications, Mater. Res. Express 6 1250h7 (2019), https://doi.org/10.1088/2053-1591/ab66ad.
[63] S. Verma, S. Rani, S. Kumar, M.A.M. Khan, Rietveld refinement, micro-structural, optical and thermal parameters of zirconium titanate composites, Ceram. Int. 44 (2018) 1653–1661, https://doi.org/10.1016/j.ceramint.2017.10.090.
[64] P.S. Thambidurai, P. Gowthaman, M. Venkatachalam, S. Suresh, Enhanced bactericidal performance of nickel oxide-zinc oxide nanocomposites synthesized by facile chemical co-precipitation method, J. Alloys Compd. 830 (2020) 154642, https://doi.org/10.1016/j.jallcom.2020.154642.
[65] M. Shakil, U. Inayat, M.I. Arshad, G. Nabi, N.R. Khalid, N.H. Tariq, A. Shah, M. Z. Iqbal, Influence of zinc and cadmium co-doping on optical and magnetic properties of cobalt ferrites, Ceram. Int. 46 (2020) 7767–7773, https://doi.org/10.1016/j.ceramint.2019.11.280.
[66] D. Kamarajan, B. Anburaj, V. Porkalai, A. Muthuvel, G. Nedunchezhian, N. Mahendran, Green synthesis of ZnO nanoparticles and their photocatalyst degradation and antibacterial activity, J. Water Environ. Nanotechnol. 7 (2022) 180–193, https://doi.org/10.22090/jwent.2022.02.006.
[67] A.B. Djurišić, Y.H. Leung, K.H. Tam, L. Ding, W.K. Ge, H.Y. Chen, S. Gwo, Green, yellow, and orange defect emission from ZnO nanostructures: Influence of excitation wavelength, Appl. Phys. Lett. 88 (2006) 103107, https://doi.org/10.1063/1.2182096.
[68] M. Shakil, U. Inayat, N.R. Khalid, M. Tanveer, S.S.A. Gillani, N.H. Tariq, A. Shah, A. Mahmood, A. Dahshan, Enhanced structural, optical, and photocatalytic activities of Cd–Co doped Zn ferrites for degrading methyl orange dye under irradiation by visible light, J. Phys. Chem. Solids 161 (2022) 110419, https://doi.org/10.1016/j.jpcs.2021.110419.
[69] D. Heger, J. Jirkovský, P. Klán, Aggregation of methylene blue in frozen aqueous solutions studied by absorption spectroscopy, J. Phys. Chem. A 109 (2005) 6702–6709, https://doi.org/10.1021/jp050439j.
[70] Z. Zhang, Y. Ma, X. Bu, Q. Wu, Z. Hang, Z. Dong, X. Wu, Facile one-step synthesis of TiO_2/Ag/SnO_2 ternary heterostructures with enhanced visible light photocatalytic activity, Sci. Rep. 8 (2018) 10532, https://doi.org/10.1038/s41598-018-28832-w.
[71] T. Khalafi, F. Buazar, K. Ghanemi, Phycosynthesis and enhanced photocatalytic activity of zinc oxide nanoparticles toward organosulfur pollutants, Sci. Rep. 9 (2019) 6866, https://doi.org/10.1038/s41598-019-43368-3.
[72] Z. Zhou, J. Wang, C.G. Jhun, ZnO nanospheres fabricated by mechanochemical method with photocatalytic properties, Catalysts 11 (2021) 572, https://doi.org/10.3390/catal11050572.
[73] S. Estrada-Flores, A. Martínez-Luévanos, C.M. Perez-Berumen, L.A. García-Cerda, T.E. Flores-Guia, Relationship between morphology, porosity, and the photocatalytic activity of TiO_2 obtained by sol–gel method assisted with ionic and nonionic surfactants, Boletín De La Sociedad Española De Cerámica y Vidrio 59 (2020) 209–218, https://doi.org/10.1016/j.bsecv.2019.10.003.
[74] M. Khan, P. Ware, N. Shimpi, Synthesis of ZnO nanoparticles using peels of Passifora foetida and study of its activity as an efficient catalyst for the degradation of hazardous organic dye, SN Appl. Sci. 3 (2021) 528, https://doi.org/10.1007/s42452-021-04436-4.

[75] N. Pugazhenthiran, S. Murugesan, S. Anandan, High surface area Ag-TiO_2 nanotubes for solar/visible-light photocatalytic degradation of ceftiofur sodium, J. Hazard. Mater. 263 (2013) 541–549, https://doi.org/10.1016/j.jhazmat.2013.10.011.
[76] D.J. Manasa, K.R. Chandrashekar, M.A.P. Kumar, D. Suresh, D.J.M. Kumar, C.R. Ravikumar, T. Bhattacharya, H.C.A. Murthy, Proficient synthesis of zinc oxide nanoparticles from *Tabernaemontana heyneana* Wall. via green combustion method: Antioxidant, anti-inflammatory, antidiabetic, anticancer and photocatalytic activities, Results Chem. 3 (2021) 100178, doi: 10.1016/j.rechem.2021.100178.
[77] K.K. Supin, P.M.P. Namboothiri, M. Vasundhara, Enhanced photocatalytic activity in ZnO nanoparticles developed using novel *Lepidagathis ananthapuramensis* leaf extract, RSC Adv. 13 (2023) 1497–1515, https://doi.org/10.1039/D2RA06967A.
[78] S. Alamdari, M.S. Ghamsari, C. Lee, W. Han, H.-H. Park, M.J. Tafreshi, H. Afarideh, M.H.M. Ara, Preparation and characterization of zinc oxide nanoparticles using leaf extract of *Sambucus ebulus*, Appl. Sci. 10 (2020) 3620, https://doi.org/10.3390/app10103620.
[79] F. Rahman, M.A.M. Patwary, M.A.B. Siddique, M.S. Bashar, M.A. Haque, B. Akter, R. Rashid, M.A. Haque, A.K.M.R. Uddin, Green synthesis of zinc oxide nanoparticles using *Cocos nucifera* leaf extract: characterization, antimicrobial, antioxidant and photocatalytic activity, R. Soc. Open Sci. 9 (2022) 220858, https://doi.org/10.1098/rsos.220858.
[80] S. Vasantharaj, S. Sathiyavimal, P. Senthilkumar, V.N. Kalpana, G. Rajalakshmi, M. Alsehli, A. Elfasakhany, A. Pugazhendhi, Enhanced photocatalytic degradation of water pollutants using bio-green synthesis of zinc oxide nanoparticles (ZnO NPs), J. Environ. Chem. Eng. 9 (2021) 105772, https://doi.org/10.1016/j.jece.2021.105772.
[81] T.S. Algarni, N.A.Y. Abduh, A.A. Kahtani, A. Aouissi, Photocatalytic degradation of some dyes under solar light irradiation using ZnO nanoparticles synthesized from *Rosmarinus officinalis* extract, Green Chem. Lett. Rev. 15 (2022) 460–473, https://doi.org/10.1080/17518253.2022.2089059.
[82] H. Sadiq, F. Sher, S. Sehar, E.C. Lima, S. Zhang, H.M.N. Iqbal, F. Zafar, M. Nuhanovic, Green synthesis of ZnO nanoparticles from *Syzygium Cumini* leaves extract with robust photocatalysis applications, J. Mol. Liq. 335 (2021) 116567, https://doi.org/10.1016/j.molliq.2021.116567.
[83] F.A. Alharthi, A.A. Alghamdi, A.A. Alothman, Z.M. Almarhoon, M.F. Alsulaiman, N. Al-Zaqri, Green Synthesis of ZnO nanostructures using *Salvadora persica* leaf extract: Applications for photocatalytic degradation of methylene blue dye, Crystals 10 (2020) 441, https://doi.org/10.3390/cryst10060441.
[84] T.S. Aldeen, H.E.A. Mohamed, M. Maaza, ZnO nanoparticles prepared via a green synthesis approach: Physical properties, photocatalytic and antibacterial activity, J. Phys. Chem. Solids 160 (2022) 110313, https://doi.org/10.1016/j.jpcs.2021.110313.
[85] S. Narath, S.K. Koroth, S.S. Shankar, B. George, V. Mutta, S. Wacławek, M. Černík, V.V.T. Padil, R.S. Varma, *Cinnamomum tamala* leaf extract stabilized zinc oxide nanoparticles: a promising photocatalyst for methylene blue degradation, Nanomaterials 11 (2021) 1558, https://doi.org/10.3390/nano11061558.
[86] S.S. Mydeen, R.R. Kumar, M. Kottaisamy, V.S. Vasantha, Biosynthesis of ZnO nanoparticles through extract from Prosopis juliflora plant leaf: antibacterial activities and a new approach by rust-induced photocatalysis, J. Saudi Chem. Soc. 24 (2020) 393–406, https://doi.org/10.1016/j.jscs.2020.03.003.
[87] A. Raja, S. Ashokkumar, R.P. Marthandam, J. Jayachandiran, C.P. Khatiwada, K. Kaviyarasu, R.G. Raman, M. Swaminathan, Eco-friendly preparation of zinc oxide nanoparticles using *Tabernaemontana divaricata* and its photocatalytic and antimicrobial activity, J. Photochem. Photobiol. B Biol. 181 (2018) 53–58, https://doi.org/10.1016/j.jphotobiol.2018.02.011.
[88] S. Pai, H. Sridevi, T. Varadavenkatesan, R. Vinayagam, R. Selvaraj, Photocatalytic zinc oxide nanoparticles synthesis using *Peltophorum pterocarpum* leaf extract and their characterization, Optik 185 (2019) 248–255, https://doi.org/10.1016/j.ijleo.2019.03.101.
[89] M. Zare, K. Namratha, M.S. Thakur, K. Byrappa, Biocompatibility assessment and photocatalytic activity of bio-hydrothermal synthesis of ZnO nanoparticles by *Thymus vulgaris* leaf extract, Mater. Res. Bull. 109 (2019) 49–59, https://doi.org/10.1016/j.materresbull.2018.09.025.
[90] C.A. Soto-Robles, O. Nava, L. Cornejo, E. Lugo-Medina, A.R. Vilchis-Nestor, A. Castro-Beltrán, P.A. Luque, Biosynthesis, characterization and photocatalytic activity of ZnO nanoparticles using extracts of *Justicia spicigera* for the degradation of methylene blue, J. Mol. Struct. 1225 (2021) 129101, https://doi.org/10.1016/j.molstruc.2020.129101.
[91] J. Yu, G. Dai, Q. Xiang, M. Jaroniec, Fabrication and enhanced visible-light photocatalytic activity of carbon self-doped TiO2 sheets with exposed 001 facets, J. Mater. Chem. 21 (2011) 1049–1057, https://doi.org/10.1039/c0jm02217a.
[92] L. Qi, J. Yu, M. Jaroniec, Enhanced and suppressed effects of ionic liquid on the photocatalytic activity of TiO_2, Adsorption 19 (2013) 557–561, https://doi.org/10.1007/s10450-013-9478-7.
[93] N. Pugazhenthiran, S. Murugesan, P. Sathishkumar, S. Anandan, Photocatalytic degradation of ceftiofur sodium in the presence of gold nanoparticles loaded TiO_2 under UV–visible light, Chem. Eng. J. 241 (2014) 401–409, https://doi.org/10.1016/j.cej.2013.10.069.
[94] Z.M. Abou-Gamra, M.A. Ahmed, Synthesis of mesoporous TiO_2–curcumin nanoparticles for photocatalytic degradation of methylene blue dye, J. Photochem. Photobiol. B Biol. 160 (2016) 134–141, https://doi.org/10.1016/j.jphotobiol.2016.03.054.
[95] H.M. Shinde, T.T. Bhosale, N.L. Gavade, S.B. Babar, R.J. Kamble, B.S. Shirke, K. M. Garadkar, Biosynthesis of ZrO_2 nanoparticles from *Ficus benghalensis* leaf extract for photocatalytic activity, J. Mater. Sci. Mater. Electron. 29 (2018) 14055–14064, https://doi.org/10.1007/s10854-018-9537-7.

Journal of Superconductivity and Novel Magnetism (2023) 36:1693–1701
https://doi.org/10.1007/s10948-023-06609-1

ORIGINAL PAPER

Tuning the Multiferroism and Magnetoelectric Coupling of Bismuth Ferrite via Substitutional Defects by Er and Transition Metals (Nb/Zr/Y)

Divya Lakshmi S.[1] · I. B. Shameem Banu[1] · R. Rajesh[2] · Mohamad Hafiz Mamat[3] · G. V. Vijayaraghavan[1]

Received: 9 May 2023 / Accepted: 6 August 2023 / Published online: 29 August 2023

Abstract

The impact of partial substitution of erbium and transition metal (zirconium/yttrium/niobium) at bismuth and iron site on multiferroism and magnetoelectric coupling of BFO was studied. Three samples $Bi_{0.95}Er_{0.05}Fe_{0.98}X_{0.02}O_3$ (where X = Nb/Zr/Y) were prepared by sol–gel method. The structural, morphological, and elemental aspects of the samples were scrutinized. The ferroelectric, magnetic, and magnetoelectric properties of the samples were recorded. The combined effect of erbium and zirconium offered better saturated ferroelectric loop with greater remnant polarization value (0.74 μC/cm^2). On including erbium and zirconium inside bismuth ferrite, the magnetization of BFO got improved very much with remanence value (0.095 emu/g). The combination of erbium and zirconium has intensified the magneto electric behavior in the bismuth ferrite. Interestingly, zirconium inclusion inside the BFO system instead of niobium and yttrium has provoked all the multifunctional aspects uniformly.

Keywords Bismuth ferrite · Substitutional defects · Sol–gel · Multiferroic · Magnetoelectric coupling · Current leakage

Highlights
- Novel combination of erbium and transition metal (niobium/zirconium/yttrium) was used to tune the multiferroic properties of bismuth ferrite.
- Enhanced multifunctional properties such as ferroelectric and magnetic features are revealed.
- Dual doping has intensified the magnetoelectric behavior in the bismuth ferrite.
- Proved as good in scaling up the multifunctional parameters of bismuth ferrite.

✉ Divya Lakshmi S.
divyasvj24@gmail.com

I. B. Shameem Banu
Shameembanu@crescent.education

R. Rajesh
rr@vcet.ac.in

G. V. Vijayaraghavan
vijayaraghavan@crescent.education

[1] BSAR Crescent Institute of Technology, Vandalur, Chennai – 48, India

[2] Department of Physics, Velammal College of Engineering and Technology, Madurai 625009, India

[3] NANO-ElecTronic Centre (NET), School of Electrical Engineering, College of Engineering, Universiti Teknologi MARA, Shah Alam, 40450 Selangor, Malaysia

1 Introduction

Evolution of multiferroic materials pushed the research and development into the modern era. The interesting aspect of the multiferroic materials is the concurrence of many ferroic order states inside them. The focus on multiferroics has got intensified with the discovery of magnetoelectric linkage inside them. It is more apt to describe the multiferroics as the fertile materials as they could be transformed into many forms. Hence, multiferroics serve as a potential source of many applications. On tuning the multiferroics in different aspects, multiferroics could penetrate into various fields through most exciting applications like memory devices, transformers, transducers, generators, and sensors. Based on the type of magnetoelectric coupling inside the materials, the multiferroic materials can be grouped into two classes. They are single-phase multiferroics and multiferroic composites. Direct magnetoelectric coupling prevails inside the single-phase multiferroic materials which pulled the interest of researchers more towards the single-phase multiferroic materials.

Bismuth ferrite, $BiFeO_3$ (BFO) (one of the single-phase material), is the extensively investigated multiferroic, since it displayed room temperature multiferroicity. It shows weak antiferromagnetism at room temperature (T_N = 375 ˚C). At

room temperature, BFO is found to be a rhombohedrally distorted perovskite with space group R3c and its curie temperature $T_C = 830$ °C [1]. Owing to the spin spiral structure of periodicity 62 nm, it shows a G-type canted antiferromagnetic order below T_N [2]. Though the probing of magnetism is seems to be more challenging, ferroelectricity can easily be observed in this material [3]. Especially, the collaboration between ferroelectricity and magnetism makes the BFO an enchanting multiferroic.

From the literature, it is learnt that doping is an apt solution for the minor hurdles suffered by BFO. Additionally, doping also led to the enhancement of multifunctional properties in BFO. In specific, combination of erbium and some transition metal ion substitution inculcated an appreciable multiferroic tendency in BFO [4–12]. Hemant Singh et al. and some other works have reported on Nb doped BFO. It shows remarkable magnetic properties, and it has also proved to be a magneto electric promising candidate [13–18]. In the previous chapters, niobium is proved to be a best Fe site dopant compared to manganese and molybdenum. On comparing the ionic radii of niobium, manganese, and molybdenum, ionic radius niobium was found to be closer to that of the parent ion (Fe ion) relatively. So, the effect of doping higher ionic radius ion at Fe site is examined in this chapter. From the literature, it is learnt that there are less works on zirconium [19–23] and yttrium [24–28] doped BFO and also the results were better in such works. Moreover, zirconium and yttrium ions exhibited greater ionic radii compared to the Fe ion. Thus, in this work, Er^{3+} and TM = Zr, Y, and Nb were chosen to dope with bismuth ferrite to enhance the multiferroic properties of the bismuth ferrite. This chapter is intended to compare the effect of zirconium, yttrium, and niobium as Fe site dopants. In further discussion, $BiFeO_3$, $Bi_{0.95}Er_{0.05}Fe_{0.98}Zr_{0.02}O_3$, $Bi_{0.95}Er_{0.05}Fe_{0.98}Y_{0.02}O_3$, and $Bi_{0.95}Er_{0.05}Fe_{0.98}Nb_{0.02}O_3$ are denoted as BFO, BEFZO, BEFYO, and BEFNO respectively.

2 Experimental Details

Sol–gel technique was employed to synthesize the nanoparticles $BiFeO_3$ and $Bi_{0.95}Er_{0.05}Fe_{0.98}X_{0.02}O_3$ (where X = Nb/Zr/Y). In further discussion, $BiFeO_3$ and $Bi_{0.95}Er_{0.05}Fe_{0.98}X_{0.02}O_3$ (where X = Nb/Zr/Y) will be denoted as *BFO*, *BEFNO*, *BEFZO*, and *BEFYO*, respectively. Analytical grade bismuth (lll) nitrate pentahydrate (assay 98%, Alfa Aesar), iron (lll) nitrate nonahydrate (assay 98%, Alfa Aesar), erbium (lll) nitrate hydrate (assay 99.9%, Alfa Aesar), niobium pentoxide (assay 99.9%, Alfa Aesar), zirconium (IV) oxy nitrate hydrate (assay 99%, Alfa Aesar), yttrium (III) nitrate hexahydrate (assay 99.9%, Alfa Aesar), citric acid anhydrous (assay 99.5% Merck), and nitric acid (assay 70% Merck) were used as starting materials without any further purification, as all the chemicals were of analytical grade. The starting materials of appropriate stoichiometric compositions were dissolved by adding adequate amount of distilled water and nitric acid to form the solutions. The citric acid anhydrous, which acts as chelating agent, was also mixed to the above solutions. Then, the solutions were stirred and heated simultaneously to form the nanopowders. For electrical measurements, powders were pelletized. For electrical measurements, powders were pelletized. The polyvinyl alcohol (PVA) was added to the annealed powders as a binding agent. The mixture was crushed using agate mortar and pestle for 6 h so that the PVA diffuses into the sample properly. Then, the mixture was filled in a 6 mm die and placed inside the pelletizer at 6 tons pressure and left for 10–15 min. The resulting 8-mm pellet was sintered at 600 °C for 4 h. The thickness of the pellets are in the range 0.5–1 mm, and diameter of the pellets are 8 mm. The resulting pellets were smoothened, and the silver paste was coated on both sides of the pellets for ohmic contact.

The phase of the samples were identified with the help of model Bruker D8 advance PXRD with Cu K_α radiation of wavelength 1.5404 A° at the scanning rate of 0.02 min^{-1} and range of 2θ was 10° to 70°. Room temperature ferroelectric properties were studied for the pellets using ferroelectric (P-E) loop tracer from Marine India Pvt. Ltd. The magnetic behavior of the samples was analyzed at room temperature using vibrating sample magnetometer (lakeshore model 7407). Current leakage measurements were recorded using Radiant Precision Premier II ferroelectric loop tracer. FESEM image was acquired from Jeol 6390 LV. Magneto Electric Coefficient Measurement System (Marine India Pvt. Ltd) was used to analyze the Magnetoelectric coupling of the samples.

3 Results and Discussion

3.1 Phase Identification

Figure 1a and b illustrate the XRD patterns and the zoomed view of the peaks (104) and (110) of BFO, BEFNO, BEFZO, and BEFYO ceramics. Figure 1a and b explicitly revealed the structure of all prepared samples. As per the JCPDS data card no. (86–1518), the XRD peaks of all the prepared samples in this work confirmed that the samples were all crystallized in the rhombohedral perovskite structure with space group R3c. From Fig. 1, it was also clear that dopant does not cause any structural transformations in BFO. However, doping produced a mild impurity peaks around 28° [29–32]. On comparing with JCPDS data, $Bi_2Fe_4O_9$ (Mullite) matched with the impurity peaks.

Peaks shift along higher Bragg's angle on replacing higher ionic radius with that of lower ionic radius, as this kind of replacement gives rise to unit cell compression. The ionic radii of Bi^{3+} and Er^{3+} ions are 0.103 and 0.088 nm

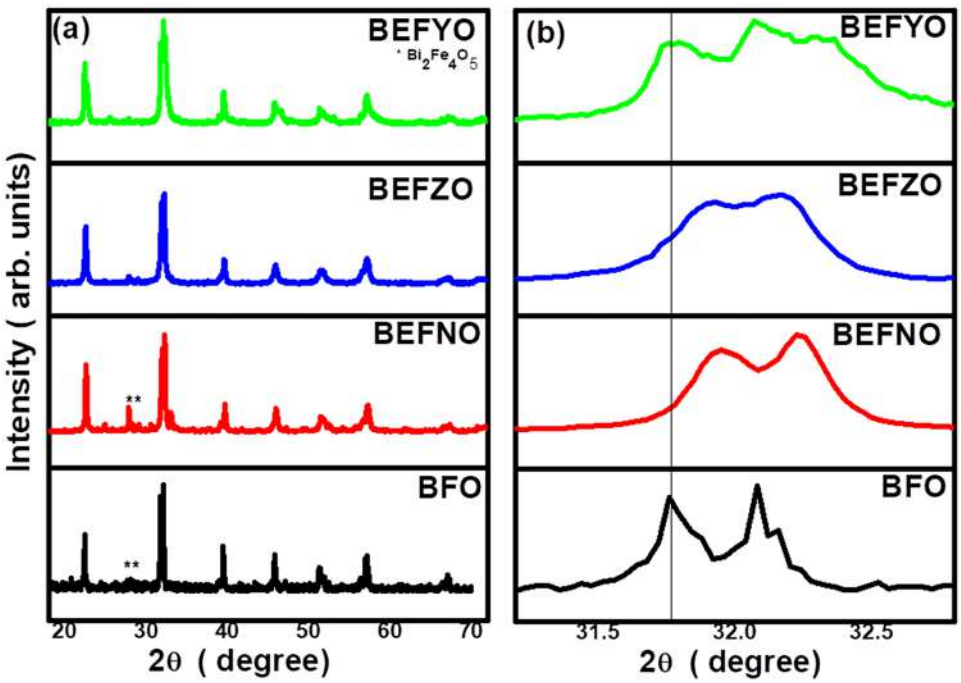

Fig. 1 **a** XRD patterns of undoped BFO and doped BFO samples and **b** zoomed image of (104) and (110) peaks of the samples

respectively. Thus, on doping Er^{3+} ion in the bismuth place, the peaks of BFO have shifted towards higher angle side (Fig. 1b). The direct dependency of crystallite size and interplanar spacing is projected by the combination of Bragg's law and Scherrer formula. The estimates of crystallite size as evaluated with the help of Scherrer formula for BFO, BEFNO, BEFZO, and BEFYO are displayed in Table 1. BEFZO has got lowest crystallite size, as its peaks have shifted more towards higher Bragg's angle.

The strain of the respective samples is estimated using the below formula:

$$Strain = \frac{\beta\ Cos\theta}{4\ Sin\theta}$$

In the above equation, β indicates the full width at half maximum and θ is the Bragg's angle respectively.

It is clear that the crystallite size varies on doping. Table 1 presents the size of crystallite and strain of the prepared samples. From Table 1, it is obvious that the strain is less for pure BFO and on doping the strain value is increasing. The increment in the strain values on doping proves the proper embodiment of the substitutions in the bismuth ferrite. Amidst the doped samples, the tensile strain and dislocation density are maximum for BE5FZ2O. Here, the strain caused on doping is due to the ionic radii mismatch between the dopant ion and parent ion. From Table 1, it is clear that the dislocation density increases on introducing zirconium at iron place and it is scaling up on introducing zirconium at iron place along with erbium at bismuth place. The peaks (110) and (104) merges on doping Er^{3+} in the place of bismuth and Zr^{4+} (2%) in the iron place of BFO. This merging may be due to the higher dislocation density of the sample compared to the other samples. The strain created in the bismuth ferrite system on doping alters the functional behaviors of the BFO, which is discussed later in the respective studies.

3.2 Morphological Analysis and Elemental Analysis

Figure 2 illustrates the surface morphology and the particle size distribution obtained from the FESEM images of the samples BFO, BEFNO, BEFZO, and BEFYO at different magnifications.

Table 1 Size of crystallite and strain of the samples

Sample name	Crystallite size by Scherrer formula (D) (nm)	Strain	Dislocation density ($\delta = 1/D^2$) ($\times 10^{-3}$)	Interplanar spacing (d) (nm)
BFO	31.91	1.25×10^{-3}	0.982	0.2785
BEFNO	36.14	3.47×10^{-3}	0.76	0.2783
BEFZO	14.71	5.1×10^{-3}	4.62	0.2779
BEFYO	16.93	4.5×10^{-3}	3.49	0.2782

FESEM images projected this morphological modifications happened on changing the dopants. Dependency of morphology on the dopants is emphasized from the variations in morphology induced by different dopants. Morphology has obtained clarity on including dopants in the bismuth ferrite lattice. From Fig. 2a, the morphology of BFO reveals the indistinguishable nature of the particles. The particles are in the form clusters to greater extent. On introducing erbium and niobium, the morphology tends to become distinguishable with more number of smaller grains. Variable sized spherical structures and elongated spheres could be observed (Fig. 2b). Figure 2c displayed more predominant grain boundaries on zirconium's substitution along with erbium. The shapes of the particles have become mostly spherical. Homogeneity is still prevailed. The morphology tends to become distinguishable to greater extent on introducing 5% of erbium and 2% yttrium (Fig. 2d). The shape of the particles has become homogenized. The morphology showcased mixture of spherical-shaped and cubical-shaped grains. The change in the iron site dopants gave rise to different rate of densification. The dopant changed the shape, size, and density of particles of BFO. This alteration caused by dopants is perhaps on account of ionic radii disparity of the parent and substituent ions. One more factor that leads to the modified morphologies is Kirkendal effect [33, 34]. This effect is due to the different rate of diffusion of the constituent elements inside the compound. On doping, the grain boundaries are more predominant, and reduction in the grain size could be noticed. The occurrence of grain boundaries and densification may be the reason for betterment in the multiferroic properties of the BFO. Dual substitution produced drastic enrichment in the microstructural behavior of the sample. Improvement has been commenced both in density of the grains and grain growth.

From the Fig. 2e, it is clear that all the dopants have incorporated inside the BFO lattice in a proper manner. The EDAX spectra of the samples are displayed in Fig. 2e. From the Fig. 2e, it is clear that all the dopants have incorporated inside the BFO lattice in a proper manner. The composition of all the elements of the samples is verified using the data given in the EDAX spectrum of the samples. The presence of the elemental compositions is examined through EDAX analysis. The presence of required elements (Bi, Fe, Er, Nb/Zr/Y, and O) is confirmed in the EDAX spectra. No additional peaks have been occurred apart from that expected. It ascertained that there is no contamination in the sample. It is noted that the ratio of the elements is almost matched with the stoichiometric ratio of the respective elements in the compounds.

3.3 Ferroelectric Studies

Figure 3 evinces the ferroelectric (PE) hysteresis curves of BFO, BEFNO, BEFZO, and BEFYO at frequency of 20 Hz and at room temperature. The ferroelectric measurements were recorded for a range of electric field ($0-35$ kV/cm), and on increasing the electric field beyond that, the loops have become lossy with rounded nature. On reducing the thickness of pellets, the range of applied electric field can be increased. So, the thickness of the pellets has been reduced to very less value ($0.5-0.9$ mm) before performing the ferroelectric experiment. The remnant polarization values at applied field of 25 kV/cm and coercive field values for the BFO, BEFNO, BEFZO, and BEFYO are elucidated in the Table 2. It is evident from the Fig. 3 that BFO shows rounded ferroelectric loop and ferroelectric loops of doped samples tend to saturate. Existence of oxygen vacancies offered unsaturated PE loops [35–38].

Table 2 displays the ferroelectric factors of the pure BFO and dopant substituted BFO. From the ferroelectric values of the samples, it is obvious that after doping erbium in the bismuth place and transition metals (Y/Zr/Nb) in the iron place of BFO, the ferroelectric loop tends to saturate. From Table 2, it is noticeable that the remnant polarization (P_r) value is higher for the sample BEFZO comparatively. Repressed oxygen vacancies and enhanced microstructure on erbium's inclusion inside BFO are the major contribution in the development of the ferroelectric nature of BFO. Increment in the remnant polarization value is happened on including erbium and zirconium together in the BFO system. Hence, the partnership of erbium and zirconium is highly commendable in the development of multifunctional characteristics inside BFO system. As the strain caused inside BFO lattice is higher on including zirconium (Table 1), the juggling of charges between Fe^{3+} and Fe^{2+} ions would have got repressed more on zirconium replacement in the iron place.

3.4 Magnetic Behavior

Figure 4 shows united MH curves of the BEFNO, BEFZO, and BEFYO ceramics at room temperature.

According to the literature [29, 30, 39, 40], BFO has a spin cycloid structure of period 62 nm arising zero net magnetization. This is responsible for the antiferromagnetic nature of BFO at bulk form. Disturbing the spin cycloid structure, results in nonzero net magnetization in BFO. This distortion will induce ferromagnetism in BFO. It can be achieved by doping BFO with suitable materials. As scaling down the particle size to nano range may enhance many interesting properties, nanosized particles may obtain enhanced ferromagnetism. The particle size can be declined to nanoscale by reducing the sintering temperature to 600 °C in case of doped and undoped BFO. Spin motion of erbium's 4f electrons interplayed with that of the iron's 3d electrons. This interaction leads to the detachment of antiferromagnetic coupling between the Fe^{3+} ions to some extent [29–32]. In addition to overlapped spin cycloid arrangement

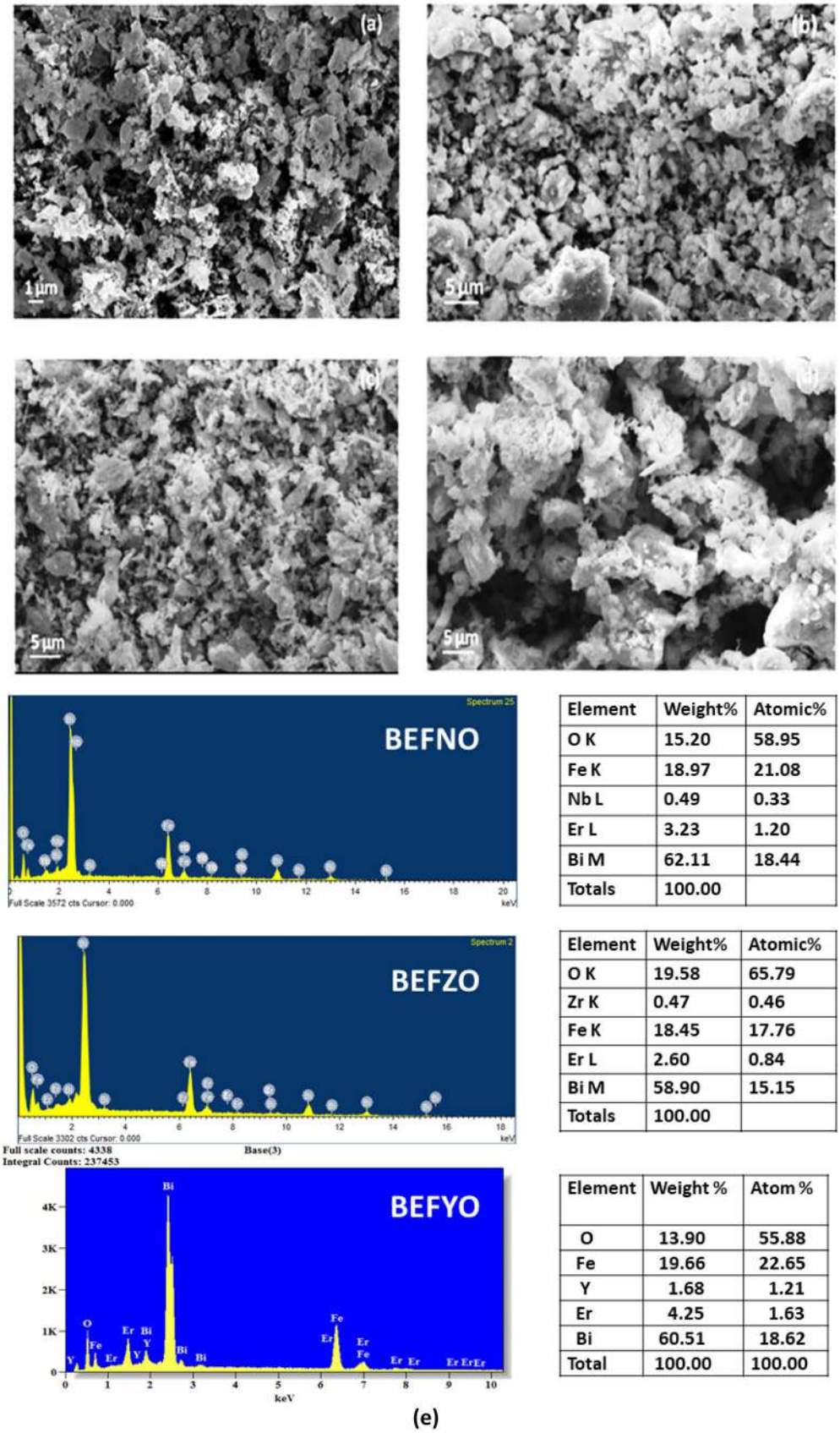

Element	Weight%	Atomic%
O K	15.20	58.95
Fe K	18.97	21.08
Nb L	0.49	0.33
Er L	3.23	1.20
Bi M	62.11	18.44
Totals	100.00	

Element	Weight%	Atomic%
O K	19.58	65.79
Zr K	0.47	0.46
Fe K	18.45	17.76
Er L	2.60	0.84
Bi M	58.90	15.15
Totals	100.00	

Element	Weight %	Atom %
O	13.90	55.88
Fe	19.66	22.65
Y	1.68	1.21
Er	4.25	1.63
Bi	60.51	18.62
Total	100.00	100.00

Fig. 2 Surface morphology of the samples: **a** BFO, **b** BEFNO, **c** BEFZO, **d** BEFYO, and **e**) EDAX of the samples BEFNO, BEFZO, and BEFYO

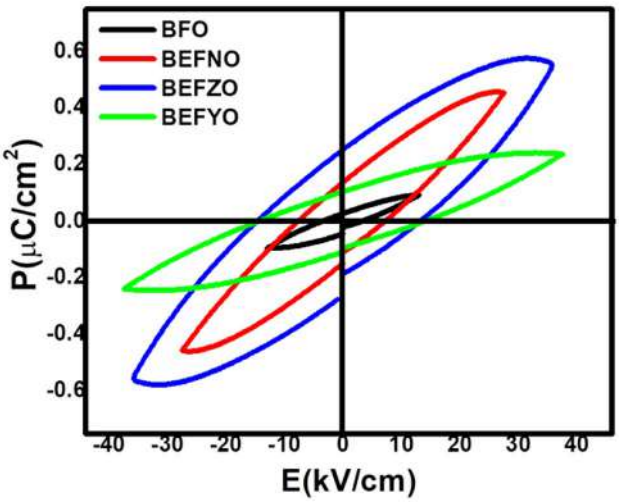

Fig. 3 Ferroelectric loops of undoped BFO, BEFNO, BEFZO, and BEFYO

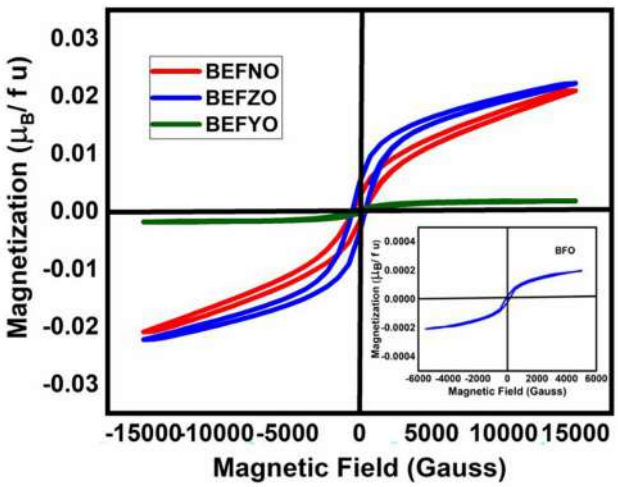

Fig. 4 Magnetic hysteresis curves of the BEFNO, BEFZO, and BEFYO (inset has BFO's magnetic curve)

(62 nm), Dzyaloshinskii-Moriya (DM) interaction forced small adjustment in the ideal anti-parallel spin alignments. This might be the cause of ferromagnetic occurrence inside BFO. The other reasons are decreased distortion degree of rhombohedral structure and the geometrical placements of nonmagnetic ions in the antiferromagnetic lattice of Fe^{3+} ions [40–42].

Table 2 deliberates the magnetic factors of the pure BFO and dopant substituted BFO. The magnetization of the samples has been converted into Bohr magneton per formula unit and analyzed. In this work, 5% of erbium has been doped in the bismuth place and 2% of transition metal (Nb/Zr/Y) in the iron place. From Table 2, it is obvious that all the samples in the work exhibits remanence ratio value less than 0.5, which indicates that all the samples are still soft magnetic material even after doping. The saturation magnetization (M_s) and remnant magnetization (M_r) estimates are high for BEFZO relatively (Table 2). As the strain caused inside BFO lattice is higher on including zirconium (Table 1), the spin cycloid structure would have got distorted more on substituting Zr^{4+} ion in the iron position. Thus, the sample BEFZO yields better saturated ferromagnetic loop with greater remnant magnetization estimate of 50×10^{-4} μ_B/f.u compared to the other samples and undoped BFO.

3.5 Leakage Current Behavior

Figure 5 shows the plot of leakage current density (J) against external electric field (E) for the samples BFO, BEFNO, BEFZO, and BEFYO. Symmetry sustained in the J-E curves of all the samples on application of positive and negative electric fields.

The current leakage measurements of BFO, BEFNO, BEFZO, and BEFYO are listed in Table 2. Among the all samples, BEFZO shows lower leakage current density with the value of 8.57×10^{-9}A/cm^2. Ionic radii disparity between the parent and dopant ions might be responsible for the lower current leakage density of the sample BEFZO (ionic radius of iron ion = 0.078 nm and ionic radius of zirconium ion = 0.080 nm). The disparity in the ionic radii confined the charges flipping between Fe^{3+} and Fe^{2+} ions. Thus, the combined effect of erbium and zirconium in scaling down the leakage current measurement is marvelous. From the literature, the linear relationship between leakage current density and ferroelectricity of a material was understood.

Table 2 Multifunctional parameters of the pure BFO and dopant substituted BFO

Sample	P_r (μC/cm^2)	E_c (kV/cm)	Leakage current density (A/cm^2)	M_r (μ_B/f.u) ($\times 10^{-4}$)	M_s(μ_B/f.u) ($\times 10^{-4}$)	H_c (G)	ME coefficient (mV/cm-Oe) ($\times 10^{-3}$)	Remnant ratio (M_r/M_s)
BFO	0.071	8.55	1.38×10^{-5}	0.025	1.9	260	2	0.25
BEFNO	0.46	7.51	6.07×10^{-8}	30	210	449.07	220	0.24
BEFZO	0.740	19.575	8.57×10^{-9}	50	240	412.26	313	0.24
BEFYO	0.373	14.355	3.75×10^{-8}	5	20	440.50	129	0.17

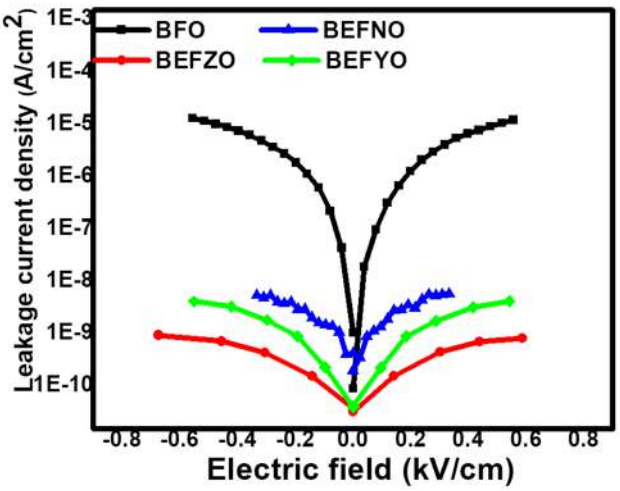

Fig. 5 Leakage current curves of BFO, BEFNO, BEFMO, and BEFMoO

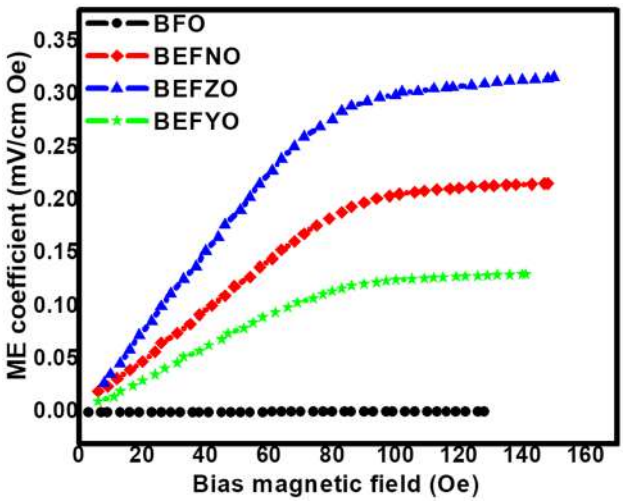

Fig. 6 Magnetoelectric coupling of the undoped BFO and doped BFO

This result is also supported by ferroelectric studies of the sample. Since the sample BEFZO is having lower leakage current density compared to the other samples, that sample is also showing excellence in the ferroelectric properties comparatively (Fig. 3 and Table2).

3.6 Magnetoelectric Coupling

Modification of polarization tendency on applying magnetic field (H) or tuning magnetization with the external electric field (E) is the ME (magnetoelectric) effect. Coupling between spin moment (magnetic aspect of material) and dipole moment (electric representation of a material) are treated as magnetoelectric coupling of a material. This coupling in general is recorded as ME effect, and this is key feature of any multiferroic material for that matter. The ME voltage coefficient (α_{ME}) is the magnetoelectric parameter of a material. ME voltage coefficient is expressed as the electric field (δE) induced on applying magnetic field (δH) or vice versa. If "t" is the thickness of the sample, then the expression for the ME coefficient (α_{ME}) is as follows:

$$\alpha_{ME} = \delta E/\delta H = \delta V/(t\ \delta H)$$

Figure 6 displays the magnetoelectric (ME) coupling as a function of the bias magnetic field (H) at room temperature for the undoped BFO, BEFNO, BEFZO, and BEFYO samples. The ME coefficient shows a linear rise until a specific value of magnetic field. On raising the applied magnetic field further, ME coefficient becomes independent of the applied bias magnetic field and attained stabilization. This trend is followed in all doped samples [43]. This stable value of the ME coefficient is recorded as the ME parameter for each and every sample.

It is evident from the Fig. 6 that ME coupling of BFO has been improved much on doping. The α_{ME} at 130 Gauss of BFO, BEFNO, BEFZO, and BEFYO are 2×10^{-3}, 220×10^{-3}, 313×10^{-3}, and 129×10^{-3} mV/cm respectively. The simultaneous introduction of erbium and zirconium incremented the magnetoelectric factor of the bismuth ferrite relatively. Thus, the ME coupling is good for the sample BEFZO. The dependence of particle size on the magnetoelectric coupling (ME coupling) of a material is emphasized by Goswami et al. [44] in their research. They claimed that the relationship among particle size, strain, and ME coupling of a particular material follows a nonmonotonic pattern. They showcased the effect of the decrease in the particle size on the reduction of polarization of a material. They utilized the Young-Laplacian equation to evince the relationship between particle size and ME coupling of a material. The Young-Laplacian equation is given by the expression:

$$P = \frac{2S}{d}$$

where P is the internal pressure of a sample, d is the average particle size of the sample, and S is the surface tension (for perovskite oxides S is mostly around of 50 N/m). They claimed from this equation that the decrease in the particle size could be associated with the increment in the internal pressure P of a sample. Subsequently, the strain inside the sample becomes greater. The strain has a major contribution in modifying the ME effect of a sample. This in turn leads to the transformation of crystal structure to centrosymmetry, which may cause distortion in the polarization of the sample. Thereby, they beautifully correlated the particle size and strain with the ME effect of a sample. The most strained sample will showcase a less particle size and greater ME effect. From Table 1, it is perceptible that the sample

BEFZO has got higher strain value comparatively. So, the sample BEFZO has acquired highest magnetoelectric coupling compared to the other samples.

4 Conclusion

Phase analysis, morphological records, and elemental analysis of the samples revealed the successful embodiment of the dopants in the BFO. The contribution of the erbium, niobium, zirconium, and yttrium in enhancing the multifunctional aspect of bismuth ferrite is commendable. Particularly, erbium and zirconium combination offered saturated ferroelectric nature with polarization estimate of 0.74 μC/cm^2 and developed magnetism with the remanence value of 95×10^{-3} emu/g. The magnetoelectric coupling is considered to be the signature of the multiferroic. Also, Er and Zr doped BFO showcased high ME coupling. From the previous works, it was found that erbium is a way better as Bi-site dopant compared to the ytterbium. Among the Fe site dopants used (niobium, manganese, molybdenum, and zirconium), zirconium was found to better in some way or the other, especially considering all the multiferroic properties (ferroelectric, ferromagnetic, ME coupling, and leakage current behavior).

Author Contribution Divya Lakshmi. S: material preparation, data collection, methodology, investigation, validation, writing-original draft, and analysis. Dr. I. B. Shameem Banu: conceptualization, methodology, investigation, validation, formal analysis, resources, writing-review and editing, visualization and supervision. Dr. R. Rajesh: validation, formal analysis, review, editing and visualization. G. V. Vijayaraghavan: validation, formal analysis, and review. Mohamad Hafiz Mamat: validation, formal analysis, and review. All authors read and approved the final manuscript.

Research Data Policy and Data Availability All data generated during this study are included in this published article.

Declarations

Ethics Approval This research does not involve any human and animal participation.

Conflict of Interest The authors declare no competing interests.

References

1. Matsuo, H., Kitanaka, Y., Noguchi, Y., Miyayama, M.: Strong interaction between ferroelectric polarization and oxygen vacancy in BiFeO3 thin film capacitors. J. Ceram. Soc. Jpn. **124**, 634–638 (2016)
2. Fischer, P., Polomska, M., Sosnowska, I., Szymanski, M.: Temperature dependence of the crystal and magnetic structures of $BiFeO_3$. J. Phys. C. **13**, 1931 (1980)
3. Feibeg, M., Palov, V.V., Pisarev, R.V.: Second-harmonic generation as a tool for studying electronic and magnetic structures of crystals: review. J Opt Soc Am B **22**, 96–118 (2005)
4. Zheng, Y., Tan, G., Xia, Ao., Ren, H.: High magnetic and electric properties of co-doped $Bi_{0.9}Er_{0.1}Fe_{1-x}Co_xO_3$ films. Mater. Lett. **173**, 18–21 (2016)
5. Acharya, S., Sutradhar, S., Mandal, J., Mukhopadhyay, K., Deb, A.K., Chakrabarti, P.K.: "Sol–gel derived nanocrystalline multiferroic $BiFeO_3$ and $R_{3þ}$ (R = Er and Tm) doped therein: Magnetic phase transitions and enhancement of magnetic properties", J Magn. Magn, Mater. **324**, 4209–4218 (2012)
6. Zheng, Y., Tan, G., Xia, Ao., Ren, H.: Structure and multiferroic properties of multi-doped $Bi_{1-x}Er_xFe_{0.96}Mn_{0.02}Co_{0.02}O_3$ thin films. J Alloys Compd. **684**, 438–444 (2016)
7. Ma, Y., Xing, W., Chen, J., Bai, Y., Zhao, S., Zhang, H.: The influence of Er, Ti co-doping on the multiferroic properties of $BiFeO_3$ thin films. Appl. Phys. A **122**, 63–71 (2016)
8. Pandit, P., Satapathy, S., Sharma, P., Gupta, S., Yusuf, S.M., Sathe, V.G.: Structural, dielectric and multiferroic properties of Er and La substituted $BiFeO_3$ ceramics. Bull Mater Sci **34**, 899–905 (2011)
9. Han, Y., Mao, W.: ChuyeQuan, Xingfu Wang, Jianping Yang, Tao Yang, Xing'ao Li, Wei Huang, "Enhancement of magnetic and ferroelectric properties of $BiFeO_3$ by Er and transition element (Mn, Co) co-doping." Material Science and engineering B **188**, 26–30 (2014)
10. Zhao, J., Liu, S., Zhang, W., Liu, Z., Liu, Z.: Structural and magnetic properties of Er-doped $BiFeO_3$ nanoparticles. J Nanopart Res. **15**, 1969–1975 (2013)
11. Xing, W., Ma, Y., Bai, Y., Zhao, S.: Enhanced ferromagnetism of Er-doped $BiFeO_3$ thin films derived from rhombohedral-to-orthorhombic phase transformations. Mater. Lett. **161**, 216–219 (2015)
12. Naveena, G., Ravinder, D., Anil Babu, T., Ravinder Reddy, B., Sumalatha, E., Vani, K., Rajender, T., Krishana Prasad, N.V.: Low-temperature magnetic properties of erbium doped bismuth nanoferrites. J. Mater. Sci. Mater. Electron. **32**, 18224–18230 (2021)
13. Jun, Y.-K., Hong, S.-H.: Dielectric and magnetic properties in Co- and Nb-substituted $BiFeO_3$ ceramics. Solid State Commun. **144**, 329–333 (2007)
14. Cheng, Z.X., Wang, X.L., Du, Y., Dou, S.X.: A way to enhance the magnetic moment of multiferroic bismuth ferrite. J. Phys. D: Appl. Phys. **43**, 242001–242006 (2010)
15. Khomchenko, V.A., Paixão, J.A.: Effect of Nb doping on the morphology and multiferroic behavior of $Bi_{0.9}La_{0.1}FeO_3$ ceramics. Mater. Lett. **169**, 180–184 (2016)
16. Singh, H., Yadav, K.L.: Effect of Nb substitution on the structural, dielectric and magnetic properties of multiferroic BiFe1 − xNbxO_3 ceramics. Mater. Chem. Phys. **132**, 17–21 (2012)
17. Wang, T., Xu, T., Gao, S., Song, S.-H.: Effect of Nd and Nb co-doping on the structural, magnetic and optical properties of multiferroic $BiFeO_3$ nanoparticles prepared by sol-gel method. Ceram. Int. **43**, 4489–4495 (2017)
18. Simões, A.Z., Garcia, F.G., Riccardi, C.S.: Piezoresponse behavior of niobium doped bismuth ferrite thin films grown by chemical method. J Alloys Compd. **493**, 158–162 (2010)
19. Kumar, M., Arora, M., Chauhan, S., Joshi, S.: Raman spectroscopy probed spin-two phonon coupling and improved magnetic and optical properties in Dy and Zr substituted $BiFeO_3$ nanoparticles. J Alloys Compd. **692**, 236–242 (2017)
20. Ting Wang, S.H.: Song, "Investigations on the structural, magnetic and optical properties of Sr–Zr co-doped $BiFeO_3$ multiferroic powders." J. Mater. Sci. Mater. Electron. **29**, 5566–5572 (2018)
21. Liu, H., Liu, Z., Yao, K.: Study of the electric properties of $BiFe_{1-x}Zr_xO_{3+d}$ films prepared by the sol–gel process. Physica B **391**, 103–107 (2007)

22. JunjieXie, Y.L.: Chude Feng, Xiuhong Pan, "Preparation and characterization of Zr^{4+}-doped $BiFeO_3$ ceramics." Mater. Lett. **96**, 143–145 (2013)
23. Divyalakshmi, S., Shameem Banu, I.B., Rajesh, R.: Oxygen octahedra distortion-induced multiferroic properties of Er and Zr co-doped BiFeO3 nanoparticles. Int. J. Appl. Ceram. Technol. 1–14 (2022)
24. Nayek, C., Tamilselvan, A., Thirmal, Ch., Murugavel, P., Balakumar, S.: Origin of enhanced magnetization in rare earth doped multiferroic bismuth ferrite. J. Appl. Phys. **115**(073902), 1–5 (2014)
25. Zhong, M., Kumar, N.P., Sagar, E., Jian, Z., Yemin, H.: Reddy Pv, Structural, magnetic and dielectric properties of Y doped $BiFeO_3$. Mater. Chem. Phys. **173**, 126–131 (2016)
26. Bellakki, M.B., Manivannana, V., Madhu, C., Sundaresan, A.: Synthesis and magnetic properties of $BiFeO_3$ and $Bi_{0.98}Y_{0.02}FeO_3$. Mater Chem Phys. **116**, 599–602 (2009)
27. Gautam, A., Uniyal, P., Yadav, K.L., Rangra, V.S.: Dielectric and magnetic properties of $Bi_{1-x}Y_xFeO_3$ ceramics. J. Phys. Chem. Solids. **73**, 188–192 (2012)
28. Jena, A.K., Mohanty, J.: Enhancing ferromagnetic properties in bismuth ferrites with non-magnetic Y and Sc co-doping. J. Mater. Sci. Mater. Electron. **29**, 5150–5156 (2018)
29. Lakshmi, S.D., Banu, I.S.: Multiferroism and magnetoelectric coupling in single-phase Yb and X (X = Nb, Mn, Mo) co-doped $BiFeO_3$ ceramics. J. Solgel Sci. Technol. **89**, 713–721 (2019)
30. Divya Lakshmi, S., Shameem Banu, I.B.: Tailoring the multiferroic properties of $BiFeO_3$ by co-doping Er at Bi site with aliovalent Nb, Mn and Mo at Fe site. Appl. Ceram. Technol. **16**, 1622–1631 (2019)
31. Priya, A.S., Banu, I.S., Chavali, M.: Influence of (La, Cu) doping on the room temperature multiferroic properties of $BiFeO_3$ ceramics. Arab J. Sci. Eng. **40**, 2079–2084 (2015)
32. Shameem Banu, I.B., Divya Lakshmi, S.: "Simultaneous enhancement of room temperature multiferroic properties of $BiFeO_3$ by Nd doping at Bi site and Co doping at Fe site. J. Mater. Sci: Mater. Electron. **28**,16044–16052 (2017)
33. Zhongquiang, Hu., Li, M., Yang, Yu., Liu, J., Pei, L., Wang, J., Liu, X., Benfang, Yu., Zhao, X.: Effects of Nd and high-valence Mn co-doping on the electrical and magnetic properties of multiferroic $BiFeO_3$ ceramics. Solid State Commun. **150**, 1088–1091 (2010)
34. Priyadharsini, P., Pradeep, A., Sathyamoorthy, B., Chandrasekaran, G.: Enhanced multiferroic properties in La and Ce co-doped $BiFeO_3$ nanoparticles. J. Phys. Chem. Solids **75**, 797–802 (2014)
35. Meimei, Wu., Wang, W., Jiao, X., Wei, G., He, L., Han, S., Liu, Y., Chen, D.: Structural and multiferroic properties of Pr and Ti co-doped $BiFeO_3$ ceramics. Ceram. Int. **42**, 14675–14678 (2016)
36. Zhang, J., Yu-Jie, Wu., Chen, X.-J.: "Structural evolution and enhanced magnetization of $Bi_{1-x}Pr_xFeO_3$", *J Magn*. Magn, Mater. **382**, 1–6 (2015)
37. Kumar, N., Panwar, N., Gahtori, B., Singh, N., Kishan, H., Awana, V.P.S.: Structural dielectric and magnetic properties of Pr substituted $Bi_{1-x}Pr_xFeO_3$ ($0 \le x \le 0.15$) multiferroic compounds. J Alloys Compd **501**, 129–132 (2010)
38. Rai, R., Mishra, S.K., Singh, N.K., Sharma, S., Kholkin, A.L.: Preparation, structures, and multiferroic properties of single-phase $BiRFeO_3$, R = La and Er ceramics. Curr. Appl. Phys. **11**, 508–512 (2011)
39. Wang, D., Wang, M., Liu, F., Cui, Y., Zhao, Q., Sun, H.: HaiboJin, Maosheng Cao, "Sol–gel synthesis of Nd-doped $BiFeO_3$ multiferroic and its characterization." Ceram. Int. **41**, 8768–8772 (2015)
40. TayyebehSoltani, B.-K.: Enhanced formation of sulfate radicals by metal-doped BiFeO3 under visible light for improving photo-Fenton catalytic degradation of 2- chlorophenol. Chem. Eng. J. **313**, 1258–1268 (2017)
41. Kumar, A., Yadav, K.L.: Enhanced magnetodielectric properties of single-phase $Bi_{0.95-x}La_{0.05}Lu_xFeO_3$ multiferroic system. J Alloys Compd **554**, 138–141 (2013)
42. García-Zaldívar, O., Díaz-Castañón, S., Espinoza-Beltran, F.J., Hernandez-Landaverde, M.A., López, G., Faloh-Gandarilla, J., Calderón-Piñar, F.: $BiFeO_3$codoping with Ba, La and Ti: Magnetic and structural studies. J. Adv. Dielect **5**, 1550034 (2015). (8 pages)
43. Gowrishankar, M., RajanBabu, D., Saravanan, P.: Room temperature multiferroism in La and Ti co-substituted $BiFeO_3$ nanoparticles. Mater. Lett. **171**, 34–37 (2016)
44. Goswami, S., Bhattacharya, D., Ghosh, C.K., Ghosh, B., Kaushik, S.D., Siruguri, V., Krishna, P.S.R.: Nonmonotonic particle-size dependence of magnetoelectric coupling in strained nanosized particles of $BiFeO_3$. Nature. **8**, 3728 (2018). https://doi.org/10.1038/s41598-018-21803-1

Terms and Conditions

Springer Nature journal content, brought to you courtesy of Springer Nature Customer Service Center GmbH (“Springer Nature”).
Springer Nature supports a reasonable amount of sharing of research papers by authors, subscribers and authorised users (“Users”), for small-scale personal, non-commercial use provided that all copyright, trade and service marks and other proprietary notices are maintained. By accessing, sharing, receiving or otherwise using the Springer Nature journal content you agree to these terms of use (“Terms”). For these purposes, Springer Nature considers academic use (by researchers and students) to be non-commercial.
These Terms are supplementary and will apply in addition to any applicable website terms and conditions, a relevant site licence or a personal subscription. These Terms will prevail over any conflict or ambiguity with regards to the relevant terms, a site licence or a personal subscription (to the extent of the conflict or ambiguity only). For Creative Commons-licensed articles, the terms of the Creative Commons license used will apply.
We collect and use personal data to provide access to the Springer Nature journal content. We may also use these personal data internally within ResearchGate and Springer Nature and as agreed share it, in an anonymised way, for purposes of tracking, analysis and reporting. We will not otherwise disclose your personal data outside the ResearchGate or the Springer Nature group of companies unless we have your permission as detailed in the Privacy Policy.
While Users may use the Springer Nature journal content for small scale, personal non-commercial use, it is important to note that Users may not:

1. use such content for the purpose of providing other users with access on a regular or large scale basis or as a means to circumvent access control;
2. use such content where to do so would be considered a criminal or statutory offence in any jurisdiction, or gives rise to civil liability, or is otherwise unlawful;
3. falsely or misleadingly imply or suggest endorsement, approval , sponsorship, or association unless explicitly agreed to by Springer Nature in writing;
4. use bots or other automated methods to access the content or redirect messages
5. override any security feature or exclusionary protocol; or
6. share the content in order to create substitute for Springer Nature products or services or a systematic database of Springer Nature journal content.

In line with the restriction against commercial use, Springer Nature does not permit the creation of a product or service that creates revenue, royalties, rent or income from our content or its inclusion as part of a paid for service or for other commercial gain. Springer Nature journal content cannot be used for inter-library loans and librarians may not upload Springer Nature journal content on a large scale into their, or any other, institutional repository.
These terms of use are reviewed regularly and may be amended at any time. Springer Nature is not obligated to publish any information or content on this website and may remove it or features or functionality at our sole discretion, at any time with or without notice. Springer Nature may revoke this licence to you at any time and remove access to any copies of the Springer Nature journal content which have been saved.
To the fullest extent permitted by law, Springer Nature makes no warranties, representations or guarantees to Users, either express or implied with respect to the Springer nature journal content and all parties disclaim and waive any implied warranties or warranties imposed by law, including merchantability or fitness for any particular purpose.
Please note that these rights do not automatically extend to content, data or other material published by Springer Nature that may be licensed from third parties.
If you would like to use or distribute our Springer Nature journal content to a wider audience or on a regular basis or in any other manner not expressly permitted by these Terms, please contact Springer Nature at

onlineservice@springernature.com

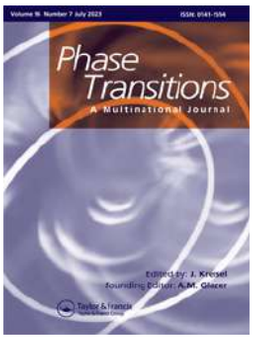

Taylor & Francis
Taylor & Francis Group

Phase Transitions
A Multinational Journal

ISSN: (Print) (Online) Journal homepage: www.tandfonline.com/journals/gpht20

Octahedra tilt influencing physical properties of polycrystalline $Bi_{0.9}Co_{0.1}FeO_3$ ceramics

Rajesh Raman, Giridharan Nambi Venkatesan, P. Sakthivel & I. B. Shameem Banu

To cite this article: Rajesh Raman, Giridharan Nambi Venkatesan, P. Sakthivel & I. B. Shameem Banu (2023) Octahedra tilt influencing physical properties of polycrystalline $Bi_{0.9}Co_{0.1}FeO_3$ ceramics, Phase Transitions, 96:7, 496-513, DOI: 10.1080/01411594.2023.2218005

To link to this article: https://doi.org/10.1080/01411594.2023.2218005

PHASE TRANSITIONS
2023, VOL. 96, NO. 7, 496–513
https://doi.org/10.1080/01411594.2023.2218005

Taylor & Francis
Taylor & Francis Group

Octahedra tilt influencing physical properties of polycrystalline $Bi_{0.9}Co_{0.1}FeO_3$ ceramics

Rajesh Raman [a], Giridharan Nambi Venkatesan [b], P. Sakthivel [c] and I. B. Shameem Banu[d]

[a]Department of Physics, Velammal College of Engineering & Technology, Madurai, Tamil Nadu, India; [b]Department of Physics, National Institute of Technology, Tiruchirapalli, Tamil Nadu, India; [c]Department of Physics, Karpagam Academy of Higher Education, Coimbatore, Tamil Nadu, India; [d]Department of Physics, B.S. Abdur Rahman Crescent Institute of Science & Technology, Vandalur, Chennai, Tamil Nadu, India

ABSTRACT

Recently, multiferroic materials such as $BiFeO_3$ have fascinated researchers for their potential application in memory storage devices. However, high leakage, weak magnetism and magnetoelectric coupling in this system restrict its practical applications. To solve this, the octahedra tilt influencing electrical, magnetic and thermal properties of polycrystalline $Bi_{0.9}Co_{0.1}FeO_3$ ceramics via solid state route is studied here. Cobalt doped $BiFeO_3$ affect the structural arrangement and tunes the crystal engineering of $BiFeO_3$. In particular, the temperature-dependent dielectric behaviour of $Bi_{0.9}Co_{0.1}FeO_3$ shows a significant dielectric anomaly corresponding to the magnetoelectric coupling in this sample. Further, the maximum magnetization of $Bi_{0.9}Co_{0.1}FeO_3$ is 8.70 emu/ g which is two orders higher in magnitude compared to pristine $BiFeO_3$.

ARTICLE HISTORY
Received 12 October 2022
Accepted 20 May 2023

KEYWORDS
$BiFeO_3$; electron density; dielectric permittivity and magnetization

1. Introduction

Materials showing multiple ferroic ordering in the same phase fascinate investigators due to their extensive applications in the arena of actuators, memory storage devices, microelectronics, transducers, etc., [1]. Out of which, $BiFeO_3$ stands unique as one of a few 13-point groups of intermetallic material with more than two ferroic orderings above room temperature [2]. The system typically crystallizes in the R3c phase with a high ferroelectric Curie temperature (T_C~730°C) and G-type antiferromagnetic Neel temperature (T_N~370°C) [3]. Here, $6s^2$ lone paired electrons in BiO_4 tetrahedra contribute ferroelectricity, while partially paired electrons in *d* orbital and incommensurate cycloidal spin structure influence antiferromagnetism. Also, $BiFeO_3$ is widely known to be a multiferroic as well as magnetoelectric material [4]. However, the thermal procedure between Bi_2O_3-Fe_2O_3 matrixes results in complex phases and the volatilization of Bi^{3+} ions [5]. More specifically, it is difficult to eliminate the secondary phase incurred in $BiFeO_3$ via solid state reaction due to the origination of the sillenite ($Bi_{25}FeO_{39}$) phase at the outer surface of the residue and mullite ($Bi_2Fe_4O_9$) phase inside the nucleui residue [6]. As a result, $BiFeO_3$ suffers high dielectric loss and weak coupling between ferroic orders leading to limited applications [7].

Several researchers reported that substituting a suitable divalent/trivalent metal ion in either *Bi* and /or *Fe* sites or effective thermal treatment is a hopeful way to eradicate these issues [8–10]. At this juncture, substituting cobalt via the *Fe* site of $BiFeO_3$ is reported by several researchers with

CONTACT Rajesh Raman rr@vcet.ac.in
Supplemental data for this article can be accessed online at https://doi.org/10.1080/01411594.2023.2218005.

promising results. Zhang et al. [11] studied the $BiFe_{1-x}Co_xO_3$ (x = 0, 0.1) through the sol–gel route and observed the increased oxygen vacancies in $BiFe_{0.9}Co_{0.1}O_3$ match the dielectric loss and results in a structural deformation. Marzouki et al. [12] studied the $BiFe_{1-x}Co_xO_3$ (x = 0, 0.03, 0.05, 0.07) systems and reported that the magnetoelectric coupling of $BiFe_{0.93}Co_{0.07}O_3$ is 11.3 mV/Oe.cm which is eight orders higher in magnitude than pristine $BiFeO_3$. Rahman et al. [13] studied the $BiFe_{1-x}Co_xO_3$ (x = 0, 0.05, 0.10, 0.15) system and reported that the system transforms from rhombohedral to orthorhombic phase on doping cobalt in $BiFeO_3$. As a result, the magnetic behaviour is enhanced and the dielectric behaviour is suppressed.

From these observations, the system shows either significant phase transformation or remains in the same phase with improved physical properties preferably observed in a 10% cobalt-doped $BiFeO_3$ system (via *Fe* site). However, to our best knowledge, substituting 10% cobalt via the *Bi* site of $BiFeO_3$ is not reported so far. The idea of replacing Co^{3+} ions in the *Bi* site is to reduce the oxygen vacancies or point defects by reducing the quantity of Bi^{3+} ions in the $BiFeO_3$ matrix responsible for volatilization during thermal treatment. Though the size of the Co^{3+} ion (0.545 Å) [14] is smaller than Bi^{3+} (1.17 Å) and the cobalt ion is familiarly known to be magnetically favourable, substituting cobalt ion in the *Bi* site is aimed to reduce the oxygen vacancies and improve the magnetic and magnetoelectric coupling of Co-doped $BiFeO_3$ suitable for memory storage applications. Hence an attempt is made to understand the influence of cobalt in the *Bi* site affecting the electrical, magnetic and thus the thermal properties of bare $BiFeO_3$.

2. Experimental details

Polycrystalline $Bi_{1-x}Co_xFeO_3$ (x = 0, 0.1) is prepared by the conventional solid state method. Starting materials such as Bi_2O_3, Co_3O_4 and Fe_2O_3 (99.99% pure from Sigma Aldrich and Alfa Aesar) are taken in appropriate molar ratios and blended with mortar and pestle. This blend is calcined at 600° C for two hours and then sintered at 835°C for 2 h after intermediate grinding. Finally, this residue is mixed with polyvinyl alcohol (PVA binder) and pressed into a 10 mm diameter pellet with the help of a dye and plunger at the hydraulic pressure of 10 MPa. Finally, the sintered pellets are annealed at 835°C for two hours to eliminate the binder present in the sample. This pellet is coated with a silver paste to create ohmic contacts for the sample.

The powder X-ray diffraction pattern of the sample is measured using a PANalytical X'Pert pro plus diffractometer with *Cu kα* radiation. The Rietveld refinement and the electronic structural distribution are interpreted using GSAS-II (General Structure Analysis System) and MEM analysis. The surface morphologies of the samples are examined using JOEL JSM 6390 scanning electron microscope. Magnetization measurements are carried out using VSM 7410 vibrating sample magnetometer. Temperature-dependent dielectric measurement is carried out using HIOKI 3532-50-LCR Hi tester. The differential scanning calorimetry (DSC) analyses of the sample are carried out under an inert nitrogen atmosphere at the heating rate of 10°C / min with an accuracy of ±0.1°C using NETZSCH STA 449 F3 Jupiter.

3. Result and discussion

3.1. Structural and microstructural analysis

Figure 1 (a) displays the XRD patterns of $Bi_{1-x}Co_xFeO_3$ (x = 0, 0.1) samples at room temperature. The diffraction peaks are indexed from the available standard patterns using the COD database [15]. The synthesized XRD pattern of $BiFeO_3$ primarily crystalizes in the *R3c* phase (96-210-2910) along the minimal traces of *Pbam* (96-900-8149) and *I23* (96-901-1269) phases. Similarly, the XRD pattern of $Bi_{0.9}Co_{0.1}FeO_3$ crystallizes in the R3c phase (96-210-2910) along with the traces of the *I23* (96-901-1269) phase. However, the influence of Co^{3+} ions suppresses the intensity of impurity phases compared to the pristine $BiFeO_3$. The peak intensity of the (110) plane in

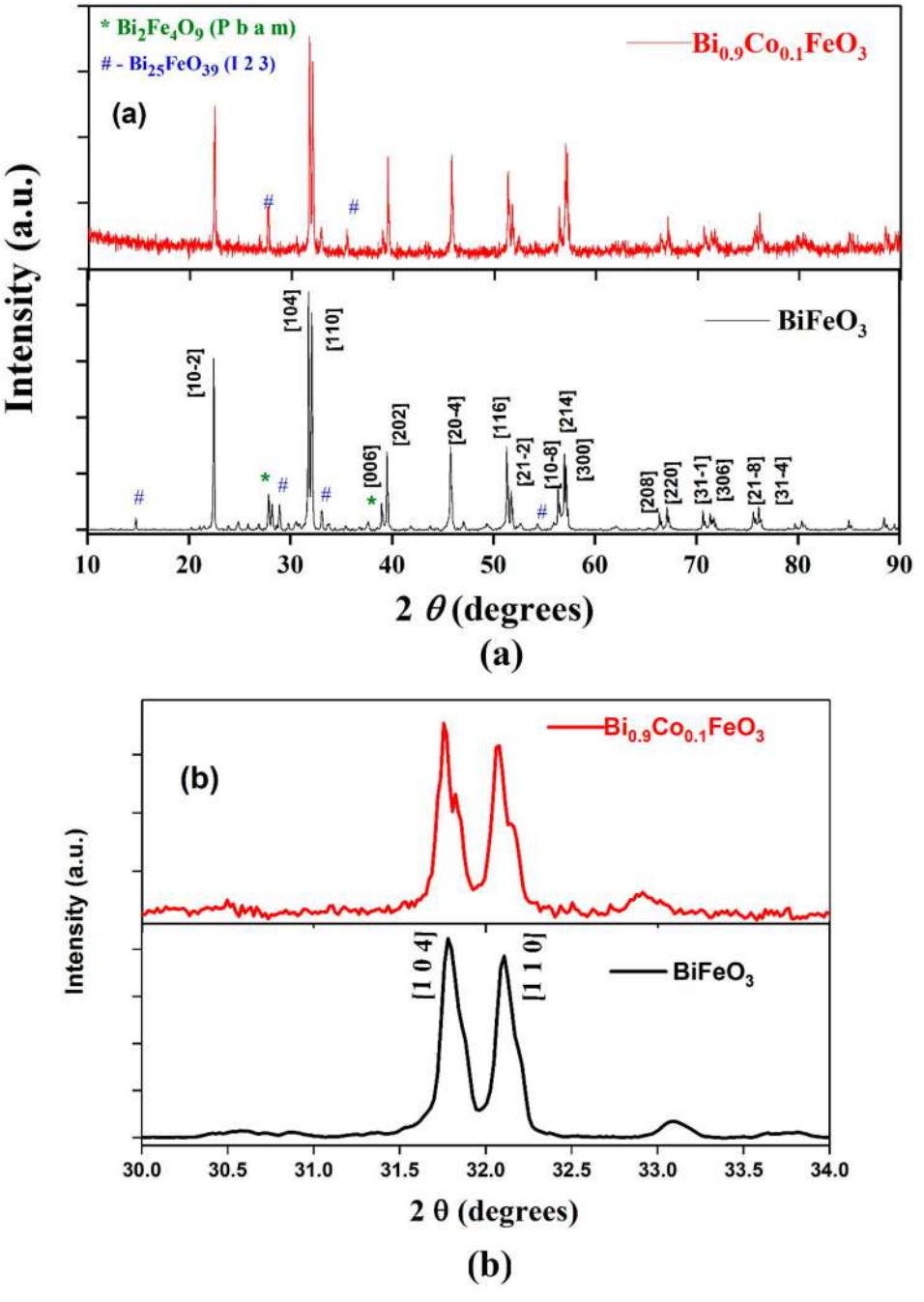

Figure 1. **(a)** X-ray diffraction patterns of $Bi_{1-x}Co_xFeO_3$ (x = 0, 0.1) samples.

$Bi_{0.9}Co_{0.1}FeO_3$ is more compared to bare $BiFeO_3$ and the predominant doublet planes (104) and (110) are shifted towards a lowering angle resulting in the significant distortion of the unit cell due to compressive strain incurred in $Bi_{0.9}Co_{0.1}FeO_3$ crystal system [16]. Further, a shoulder peak is also observed in (104) and (110) planes corresponding to P4/mmm phase in the $Bi_{0.9}Co_{0.1}FeO_3$ crystal system. The magnified view of the concern XRD patterns around 31° is presented in Figure 1(b).

The structural stability of the given compound is predicted using the Goldschmidt tolerance factor [17] and the values of $Bi_{1-x}Co_xFeO_3$ (x = 0, 0.1) are determined to be 0.872 and 0.855 respectively. The decrease in tolerance factor confirms the significant lattice distortion [18] and expect to affect the electrical and magnetic properties of the $Bi_{0.9}Co_{0.1}FeO_3$ system.

The strain and crystalline size analysis of $BiFeO_3$ and $Bi_{0.9}Co_{0.1}FeO_3$ are determined from the Williamson-Hall method [19]. The average crystalline size is found to be 93.28 and 94.52 nm respectively. Though the crystallite size is nearer to 100 nm, the small change in crystallite size impacts the $Bi_{0.9}Co_{0.1}FeO_3$ system with a greater number of coherently diffracting domains. A similar trend was reported by a few of the authors [20]. At the same time, the strain is found to be 1.41275×10^{-4} and 2.40562×10^{-4} respectively. Here, the average crystallite size and tensile strain increase as the cobalt ion introduces via the *Bi* site of $BiFeO_3$. The tensile strain is the outcome of variation between the coherence and non-coherence lattice plane. Hence the volume of $Bi_{0.9}Co_{0.1}FeO_3$ is comparatively more significant than the pristine $BiFeO_3$.

Figure 2(a,b) displays the Rietveld refinement of $Bi_{1-x}Co_xFeO_3$ (x = 0, 0.1) samples using GSAS – II. Here the XRD diffraction pattern is matched with the available standard pattern using Bragg – Brentano method [18]. The Fe-O-Fe bond angles of $Bi_{1-x}Co_xFeO_3$ (x = 0, 0.1) along [0–1 0] direction is found to be 155.77° and 155.24° respectively. The small deviation in the bond angle of $Bi_{0.9}Co_{0.1}FeO_3$ is due to the compressive strain of FeO_6 octahedra, which will modify the spiral spin arrangement and improve the magnetic behaviour compared to pristine $BiFeO_3$. On the other hand, the bond length does not show significant variations in $Bi_{0.9}Co_{0.1}FeO_3$ compared to pristine $BiFeO_3$, which results in weak lateral strain [21]. The tilting of FeO_6 octohedra along [111] direction is determined using

$$\cos\theta_1 = \frac{2 - 5\cos^2\varphi_1}{2 + \cos^2\varphi_1} \tag{1}$$

$$\cos\theta_2 = \frac{1 - 4\cos^2\varphi_1}{3} \tag{2}$$

Here, θ_1 and θ_2 signify the Fe-O-Fe bond angles linked with a tilting angle (φ) of the FeO_6 octahedra [22]. The tilt angles (φ) of $Bi_{1-x}Co_xFeO_3$ (x = 0, 0.1) are determined to be 14.89° and 15.22° respectively. Here the increase of tilt angle is due to the meagre variation of bond angle Fe-O-Fe between $BiFeO_3$ and $Bi_{0.9}Co_{0.1}FeO_3$ samples, which destructs the spiral spin structure of $Bi_{0.9}Co_{0.1}FeO_3$ [23]. The refined parameters of $Bi_{1-x}Co_xFeO_3$ (x = 0, 0.1) extracted from GSAS-II are presented in Table 1. It is well known that the Neel transition temperature is related to antiferromagnetic iron by its bond angle using

$$T_N = JZS(S+1)\cos\theta \tag{3}$$

Here, J presents the exchange spin–orbit coupling (typically <1), Z represents the number of linkages present per Fe^{3+} ion (6), S is the spin-only magnetic moment of Fe^{3+} ion (5/2) and θ is the Fe-O-Fe bond angle of $BiFeO_3$ and $Bi_{0.9}Co_{0.1}FeO_3$ system [24]. Since the bond angle and Neel temperature are directly proportional, as the bond angle decreases from 155.77° ($BiFeO_3$) to 155.24° ($Bi_{0.9}Co_{0.1}FeO_3$), it is expected that the Neel temperature of $Bi_{0.9}Co_{0.1}FeO_3$ decreases than pristine $BiFeO_3$ and need further thermal analysis supportive results.

Figure 3(a,b) presents the microstructure images of $Bi_{1-x}Co_xFeO_3$ (x = 0, 0.1) at various microscopic resolutions. The average particles of these two samples are estimated to be 1.4 μm and 0.807 μm respectively [25]. The micrograph images reveal that the pristine $BiFeO_3$ appears to be crystalline with unequal grain size and shape. However, $Bi_{0.9}Co_{0.1}FeO_3$ is agglomerated with the uneven distribution of particles. This contrasting behaviour of $Bi_{0.9}Co_{0.1}FeO_3$ is due to the differences in dissociation energies between Bi-O (337.2 kJ/mol.) and Co–O (397.4 kJ/mol.) bonds which lead to confining the oxygen vacancies and increases the grain growth [26]. The

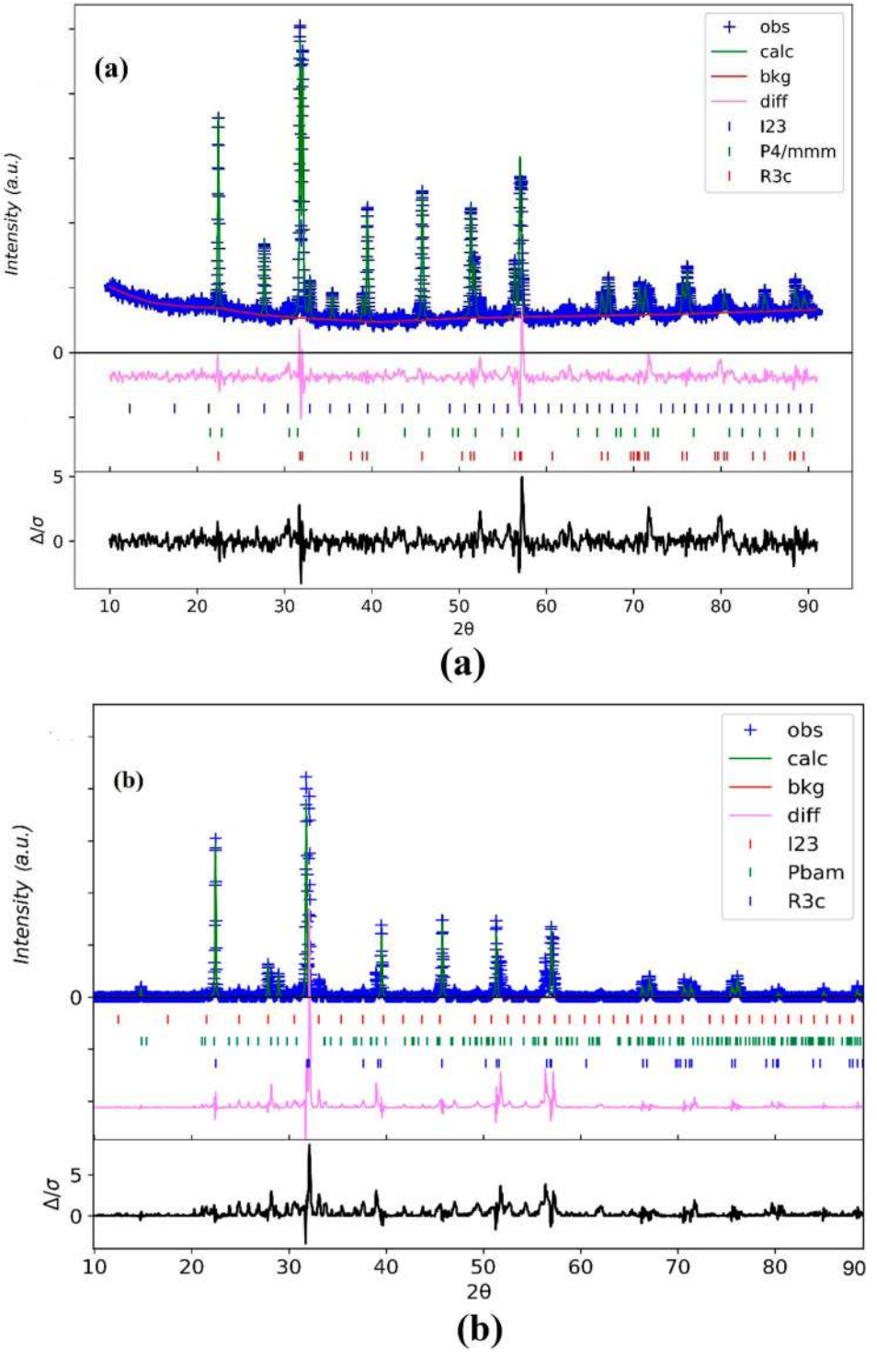

Figure 2. **(a)** Rietveld refinement of $Bi_{0.9}Co_{0.1}FeO_3$ using GSAS – II. **(b)** Rietveld refinement of $BiFeO_3$ using GSAS – II.

average particle size decreases as the Co^{3+} ion introduces via the *Bi* site of $BiFeO_3$. However, this particle size [R_{SEM}] disputes with the average crystalline size results [$R_{X\text{-}ray}$] extracted from W-H analysis. A similar trend was already observed in a few systems [27]. This is because X-ray is the

Table 1. Rietveld refinement parameters of $BiFeO_3$ and $Bi_{0.9}Co_{0.1}FeO_3$.

	$BiFeO_3$	$Bi_{0.9}Co_{0.1}FeO_3$
Lattice Parameters	a = b = 5.5860Å; c = 13.8811Å	a = b = 5.8031Å; c = 13.5519Å
Interfacial Angles	α = β = 90°; γ = 120°	α = β = 90°; γ = 120°
Atomic position	Bi (0, 0, 0.2207)	Bi/Co (0, 0, 0.2202)
	Fe (0, 0, 0)	Fe (0, 0, 0)
	O (0.0968, 0.31573, 0.1014)	O (0.0955, 0.3152, 0.1017)
Volume ($Å^3$)	375.120	395.226
Density (g / cm^3)	8.3087	7.5077
R – Factors	wRp = 0.1375	wRp = 0.2784
	$R_F^2 = 0.5590$	$R_F^2 = 0.6238$
	$R_b = 0.1995$	$R_b = 0.1730$
	$R_F = 0.2892$	$R_F = 0.6141$
Goodness of fit (GOF)	1.46	1.64
Chi^2	2985.67	12795.4
Reduced χ^2	2.12	2.69
Fe_1-O-Fe_2 (0–1 0)	155.77°	155.24°
tilt angle of FeO_6 octahedron	14.89°	15.22°
Bi/Co-O_1	2.2779 (0) Å	2.2674(0) Å
Bi/Co-O_2	2.541 (7) Å	2.534(0) Å
Fe-O_1	1.954(0) Å	1.953(0) Å
Fe-O_2	2.1053 (0) Å	2.105(0) Å

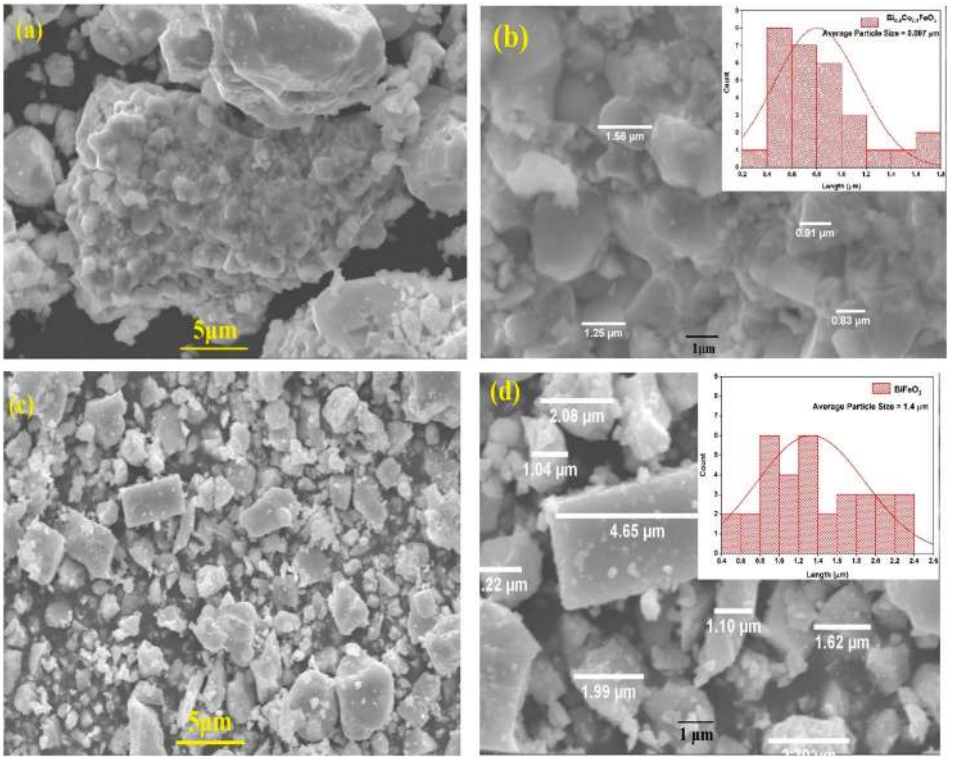

Figure 3. (a&b) Surface morphological images of $Bi_{0.9}Co_{0.1}FeO_3$ at different magnifications. **(c&d)** Surface morphological images of $BiFeO_3$ at different magnifications.

significance of the number of coherently diffracting domains as grain size [28]. Thus, the number of the coherently diffracting domain in each particle is related by

$$N = \frac{r_{SEM}}{r_{X-ray}} \tag{4}$$

Hence, there are approximately 14 coherent diffraction domains in each particle of $BiFeO_3$ and eight coherent domains in $Bi_{0.9}Co_{0.1}FeO_3$ respectively.

3.2. Charge density analysis

The charge density distribution and bonding characteristics of $Bi_{1-x}Co_xFeO_3$ (x = 0, 0.1) are analyzed using Maximum Entropy Method (MEM) [29]. Figure 4(a–d) presents the two dimensional contour map of $Bi_{1-x}Co_xFeO_3$ (x = 0, 0.1) ceramics between (011) and (012) planes. Here the unit cell containing 432000 elements is distributed into 60 × 60 × 120 pixels. The prior densities of $Bi_{1-x}Co_xFeO_3$ (x = 0, 0.1) are found to be 2.127 e / Å^3 and 1.934 e / Å^3 respectively. Likewise, the number of electrons per unit cell (a_{000}) of $Bi_{1-x}Co_xFeO_3$ (x = 0, 0.1) is found to be 798 and 764.4 respectively. It is noteworthy to mention that the number of electrons per unit cell is responsible for electron transport in the given crystal system. Two-dimensional electron density contour maps of $Bi_{1-x}Co_xFeO_3$ (x = 0, 0.1) samples along the (012) plane reveal that the area of the contour in Fe ions is relatively large and the bond mapping distance between Fe-O_1 and Fe-O_2 is closure in $Bi_{0.9}Co_{0.1}FeO_3$ compared to $BiFeO_3$. Hence the ionic behaviour is more in $Bi_{0.9}Co_{0.1}FeO_3$ sample. On the other hand, the bond mapping distance between Bi-O ions of $Bi_{0.9}Co_{0.1}FeO_3$ is reduced than pristine $BiFeO_3$. Figure 5(a–d) presents the one-dimensional contour map of $Bi_{1-x}Co_xFeO_3$ (x = 0, 0.1) ceramics between Bi/Co–O and Fe-O ions and the corresponding values of MEM analysis are listed in Table 2.

Here, the electron density of pristine $BiFeO_3$ shows the bond critical points of Bi-O and Fe-O bonds at 1.214 and 0.9705 Å respectively. Similarly, $Bi_{0.9}Co_{0.1}FeO_3$ shows the electron density bond critical points of Bi/Co–O and Fe-O bonds at 2.00 and 1.19 Å respectively. From these observations, it is clear that the mid critical point of the Bi/Co–O bond is shifted more from the initial position of pristine $BiFeO_3$ than Fe–O critical points. From these observations, it is expected that the dielectric behaviour of $Bi_{0.9}Co_{0.1}FeO_3$ may reduce compared to pristine $BiFeO_3$, while the magnetic behaviour may improve and needs further supporting results.

3.3. Dielectric studies

Figure 6 presents the dielectric permittivity against the logarithmic frequency of $Bi_{1-x}Co_xFeO_3$ (x = 0, 0.1) ceramics. The dielectric permittivities of $BiFeO_3$ and $Bi_{0.9}Co_{0.1}FeO_3$ at 10 kHz are found to be 43 and 21 respectively. Here, the values of dielectric permittivities and tangential loss are initially

Table 2. Charge density parameters of $BiFeO_3$ and $Bi_{0.9}Co_{0.1}FeO_3$.

Parameters	$BiFeO_3$	$Bi_{0.9}Co_{0.1}FeO_3$
Number of cycles	155	196
Number of electrons per unit cell	798	764.4
Number of pixels in unit cell	432000 (60 × 60 × 120)	432000 (60 × 60 × 120)
Prior Density	2.127 e/ Å^3	1.934 e/ Å^3
Lagrange parameter (λ)	0.010709	0.001468
R_{MEM} (%)	0.009899	0.018457
wR_{MEM} (%)	0.009942	0.014239
GR_{MEM} (%)	0,146173	0,057809
Bond length (Bi − O_1)	2.541(7) Å	2.534(0) Å
Midpoint electron density	1.214 e/Å^3	0.5671 e/Å^3
Bond length (Fe-O_2)	2.105(4) Å	2.105(0) Å
Midpoint energy density	0.9705 e/Å^3	1.190 e/Å^3

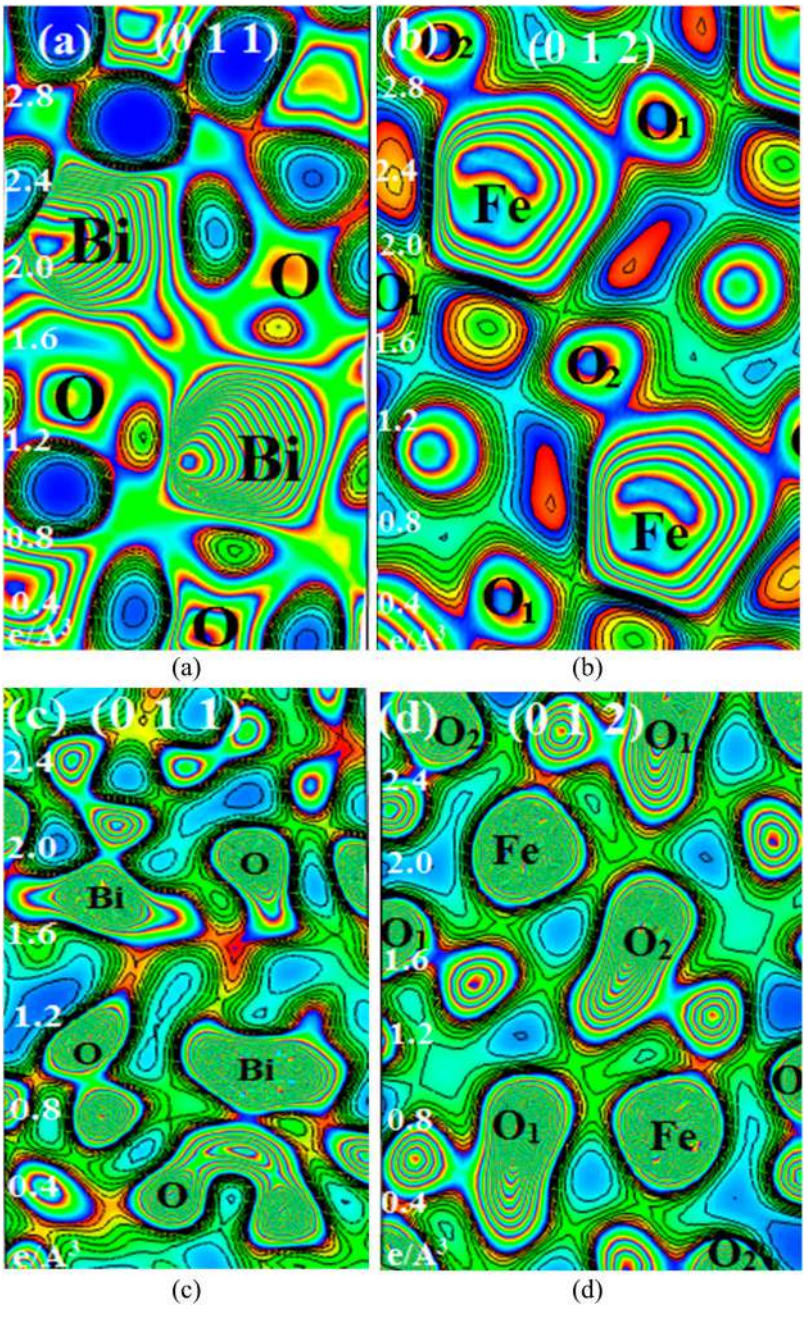

Figure 4. (a&b) Two dimensional contour images of $Bi_{0.9}Co_{0.1}FeO_3$ between (011) and (012) planes. **(c & d)** Two dimensional contour images of $BiFeO_3$ between (011) and (012) planes.

high at lower frequencies and start decreasing as the frequency increases as shown in Figure 6. This inverse proportion between dielectric permittivity and frequency is related to the formation of interfacial or space charge polarization in the sample as suggested by Maxwell–Wagner [30]. These charges (space charges) arise from the contrast of conductivities between ferroelectric and antiferromagnetic phases which creates charge defects such as oxygen vacancies leading to interfacial polarization [31].

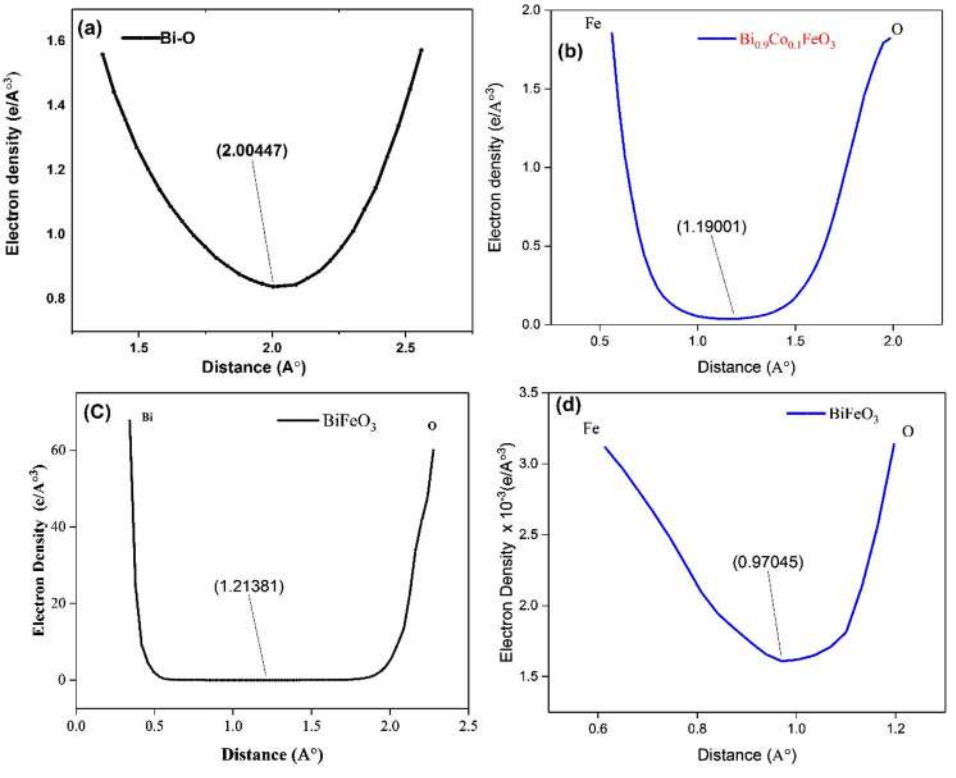

Figure 5. (a&b) One dimensional line profile of Bi/Co-O and Fe-O bond lengths obtained from $Bi_{0.9}Co_{0.1}FeO_3$. **(c & d)** One dimensional line profile of Bi-O and Fe-O bond lengths obtained from $BiFeO_3$.

On the other hand, in the sub infrared mid frequency (10^3–10^6 Hz), dipolar polarization arises due to the exchange of electrons between Fe^{2+} and Fe^{3+} redox couple ions. These displaced ions help in the alignment of dipole along the field direction. Further, Bi^{3+} ion is responsible for the creation of p-type charge carriers which is relatively hard to move compared to n-type charge carrier [32]. Hence, total polarization is the combined outcome of the exchange of electrons and p-type charge carriers. As a result, the dielectric behaviour decreases by increasing the frequency in these samples. However, the introduction of Co^{2+} / Co^{3+} in the Bi site reduces the volatilization of Bi^{3+} ions and oxygen vacancies thereby mobilizing the p-type charge carriers to contribute to the net polarization in $Bi_{0.9}Co_{0.1}FeO_3$ [32, 33]. At higher frequencies, the polarization is unable to follow the applied frequency because the frequency of ac electric field is unable to complete the hopping frequency between redox couple ions (Fe^{2+} / Fe^{3+} ions). Hence electrons are unable to accumulate at grain boundaries leading to a decrease in dielectric permittivity and tangential loss at higher frequencies [34].

Figure 7 presents the frequency-dependent tangential loss of $Bi_{1-x}Co_xFeO_3$ (x = 0, 0.1) ceramics at ambient temperature. The dielectric losses of $BiFeO_3$ and $Bi_{0.9}Co_{0.1}FeO_3$ at 10 kHz are 0.32 and 0.24 respectively. The dielectric loss arises in the heterogeneous composite either due to relaxation loss or resistive loss [35]. The former arises from the relaxation of dipoles which dissipates the energy while the latter arises from the mobilization of the charge carriers by consuming the energy. The response of dielectric loss with frequency will follow a similar trend of dielectric permittivity. Hence, at low frequencies, the dielectric loss is high due to the hopping frequency between Fe^{2+} and Fe^{3+} redox couple while at higher frequencies, the sample is unable to follow the hopping frequency which leads to a decrease in dielectric loss.

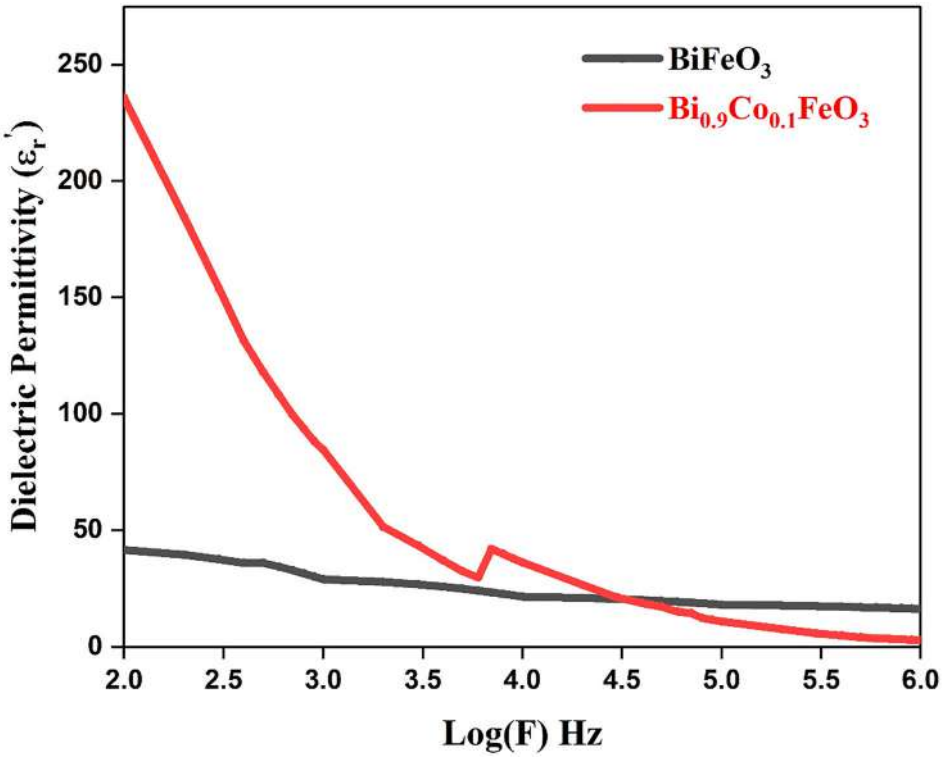

Figure 6. Room temperature dielectric permittivity against the logarithmic frequency of $BiFeO_3$ and $Bi_{0.9}Co_{0.1}FeO_3$.

3.3.1. Temperature dependent dielectric permittivity

Figure 8 presents the temperature dependent dielectric permittivity of $Bi_{0.9}Co_{0.1}FeO_3$ at selected frequencies (10, 50, 100, 500 and 1 MHz). Initially, at selected frequencies, the dielectric permittivity increases as the temperature increases and attains a maximum at a temperature known as Neel Temperature (T_N) due to antiferromagnetic to paramagnetic transition and then it decreases gradually till the measured temperature region. This anomaly around 360°C is due to the synchronization of magnetization and polarization at selected frequencies. At this stage, the vicinity of the Neel temperature of this sample indicates a linear magnetoelectric coupling in the $Bi_{0.9}Co_{0.1}FeO_3$ system. A similar trend was reported by a few of the researchers in $BiFeO_3$ based system [35–37]. This behaviour is improved compared to the pristine $BiFeO_3$ as reported in our previous work [38]. Here, the high value of dielectric permittivity, shift and disappearance of the dielectric maximum close to 300°C is a consequence of the conducting behaviour involved in this system.

3.4. Magnetic studies

Figure 9 presents the magnetization response against the applied magnetic field of $Bi_{1-x}Co_xFeO_3$ (x = 0, 0.1) ceramics at room temperature. The plot of pristine $BiFeO_3$ depicts a linear increase in magnetization concerning the applied magnetic field, leading to a slim M-H loop. The remanent magnetization (M_r) and coercive field (H_c) are observed to be 0.0011 emu/g and 130.64 Oe respectively. These outcomes are the signature of antiferromagnetism with a weak ferromagnetic moment in the pristine $BiFeO_3$ [39]. This M_r with weak ferromagnetic order between *Fe* ions affects the spiral spin arrangement and is responsible for Dzyaloshinskii–Moriya interaction [40].

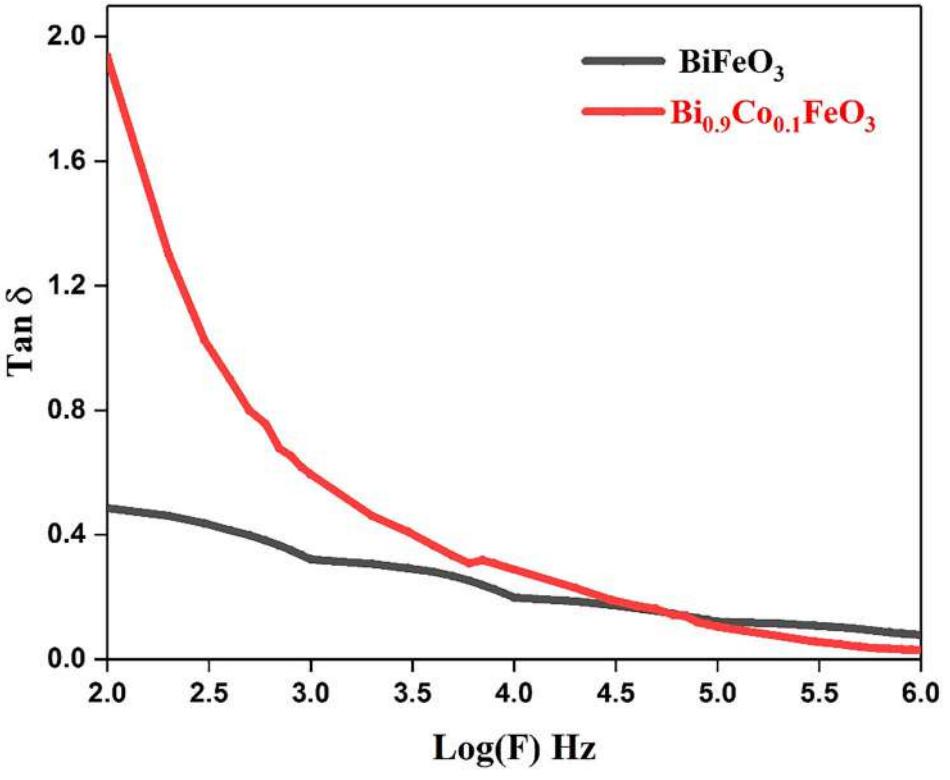

Figure 7. Tangential loss against the logarithmic frequency of $BiFeO_3$ and $Bi_{0.9}Co_{0.1}FeO_3$.

In contrast, the plot of $Bi_{0.9}Co_{0.1}FeO_3$ presents a non-linear sigmoidal-shaped variation of magnetization with respect to the applied magnetic field leading to a robust hysteresis loop. The remanent magnetization (M_r) and coercive field (H_c) are observed to be 2.040 emu/g and 450.90 Oe respectively. Here, the value of M_r is three orders higher in magnitude than $BiFeO_3$ and supports the Rietveld refinement results. However, the hysteresis loop does not saturate till the maximum value of the applied field (15 kOe). Hence the following equation is used for fitting the hysteresis loop to identify the contribution of antiferromagnetic/paramagnetic and ferromagnetic behaviours involved in $Bi_{0.9}Co_{0.1}FeO_3$.

$$M(H) = \frac{2M_s}{\pi}\tan^{-1}\left[\left(\frac{H \pm H_c}{H_c}\right)\tan\left(\frac{\pi M_r}{2M_s}\right)\right] + \chi H \tag{5}$$

Here, the first term is associated with ferromagnetic contribution (FM) and the second term is related to antiferromagnetic or paramagnetic contribution (AFM/PM). Further, M_s denotes the maximum magnetization and χ is the magnetic susceptibility [41]. The fitted values of the M-H loop and the contribution of FM and AFM/PM are presented in Figure 10 and the corresponding values are listed in Table 3.

3.5. Thermal studies

Differential Scanning Calorimetry is one of the important tools for understanding the endothermic reaction incurred in the given sample. DSC analysis of $Bi_{1-x}Co_xFeO_3$ (x = 0, 0.1) reveals four exothermic anomalies in the measured temperature region, as shown in Figure 11. The first

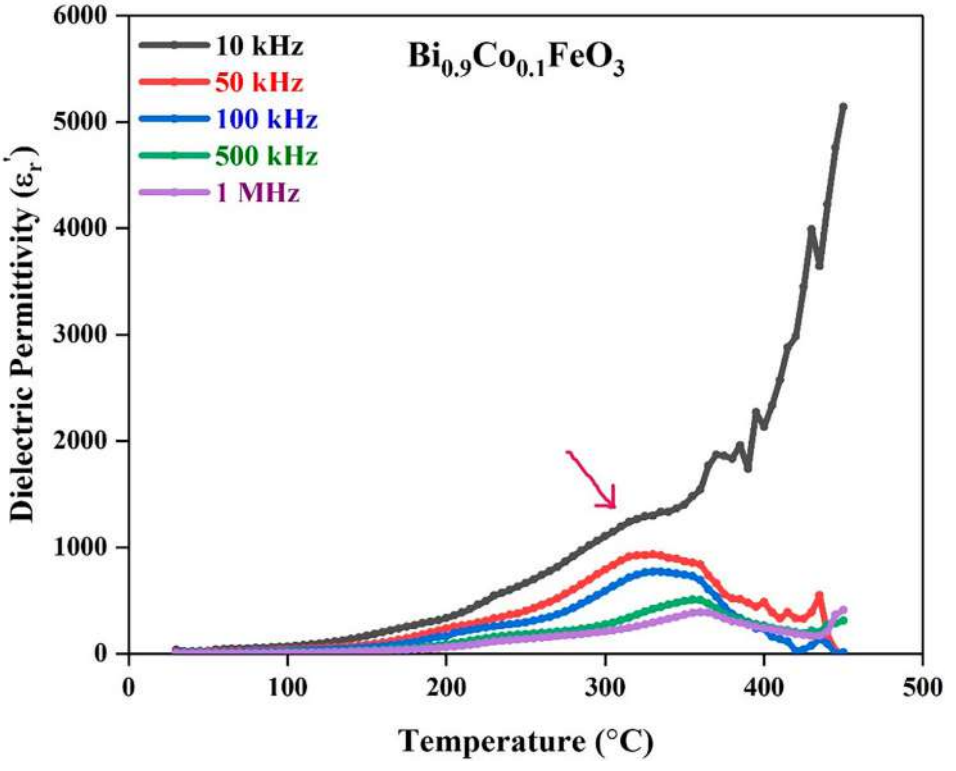

Figure 8. Temperature dependent dielectric permittivity of $Bi_{0.9}Co_{0.1}FeO_3$ at various frequencies.

anomaly around 100°C to 180°C in both $BiFeO_3$ and $Bi_{0.9}Co_{0.1}FeO_3$ is due to the evaporation of water and binder involved in the samples [42]. The second anomalies of $BiFeO_3$ and $Bi_{0.9}Co_{0.1}FeO_3$ ceramics are broad and appeared at 370°C and 365°C, corresponding to the antiferromagnetic transition temperature [39]. The third anomaly of $BiFeO_3$ and $Bi_{0.9}Co_{0.1}FeO_3$ ceramics appeared at 839.19°C and 795.52°C, corresponding to ferroelectric to paraelectric phase transition [43]. A shoulder peak is also observed in both $BiFeO_3$ and $Bi_{0.9}Co_{0.1}FeO_3$ at 826°C and 780°C respectively which is due to the formation of additional phases incurred in this system. However, the intensity of the shoulder peak is suppressed in $Bi_{0.9}Co_{0.1}FeO_3$ compared to pristine $BiFeO_3$ as revealed from XRD and Rietveld refinement analysis.

4. Discussion

It is well known that $BiFeO_3$ holds a modulated spiral spin structure with a periodicity of 64 nm along $[110]_h$ direction such that the distance between two Fe^{3+} ions is 0.558 nm. As a result, one spiral spin structure has 64 / 0.558 = 114 Fe^{3+} ions [44]. The average magnetic moments of the $BiFeO_3$ and $Bi_{0.9}Co_{0.1}FeO_3$ are calculated from the magnetization measurements based on [19]. The values are determined to be 0.0049 μ_B / Fe and 0.465 μ_B / Fe respectively. The canting angle

Table 3. Magnetic fitted parameters of $Bi_{0.9}Co_{0.1}FeO_3$.

	Ferromagnetic			AFM/PM			
Sample	M_s(emu/g)	H_c(Oe)	Error%	M_s(emu/g)	H_c(Oe)	Error%	χ
$Bi_{0.9}Co_{0.1}FeO_3$	8.34	540.40	0.12	0.3524	190.90	0.05	4.103×10^{-5}

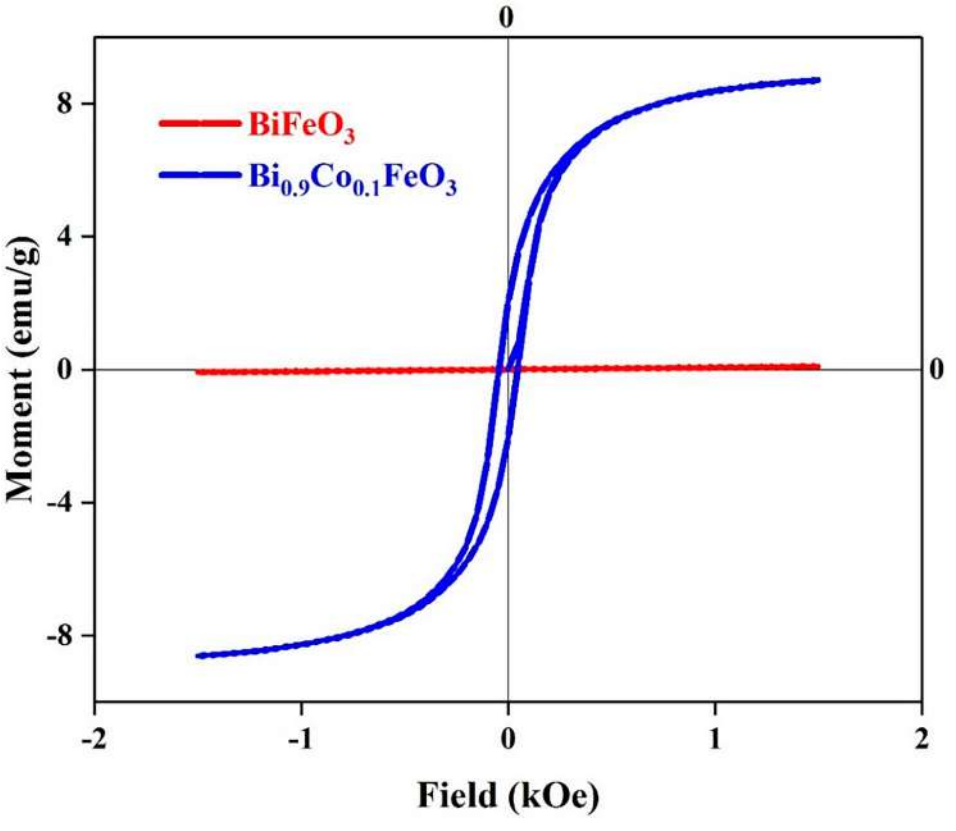

Figure 9. Room temperature magnetization response against the applied magnetic field of $BiFeO_3$ and $Bi_{0.9}Co_{0.1}FeO_3$.

of the magnetic spin can also be extracted trigonometrically by considering the spin-only magnetic moment of Fe^{3+} ion ($5.92\mu_B$) as

$$\theta = \tan^{-1}\left(\frac{\mu_B(f.u)}{5.92\mu_B}\right) \tag{6}$$

The canting angles of $BiFeO_3$ and $Bi_{0.9}Co_{0.1}FeO_3$ are found to be 0.0474 and 4.491 respectively. The magnetic parameters of $BiFeO_3$ and $Bi_{0.9}Co_{0.1}FeO_3$ are presented in Table 4. From these observations, the canting angle of $Bi_{0.9}Co_{0.1}FeO_3$ has two orders higher in magnitude than pristine $BiFeO_3$ as revealed from Rietveld refinement results.

Further, the modified Curie–Weiss law is also studied to understand the diffusion phase transition incurred in $Bi_{0.9}Co_{0.1}FeO_3$. Figure 12 displays the temperature against the inverse of the dielectric permittivity of $Bi_{0.9}Co_{0.1}FeO_3$ at 50 kHz. Here, the peak appeared as broad which could be due to different cations such as bismuth and cobalt existing in the same crystallographic site with different charge and electronic configurations which leads to a shoulder peak in X-ray diffraction analysis (Figure 1(b)).

The modified Curie–Weiss law is given by

$$\frac{1}{\varepsilon_r} - \frac{1}{\varepsilon_m} = \frac{(T - T_m)^\gamma}{C'} \tag{7}$$

Here ε_r is the dielectric permittivity, ε_m denotes the maximum dielectric permittivity, T_m is the magnetic transition temperature, C is Curie's constant and γ is the diffusion coefficient. The

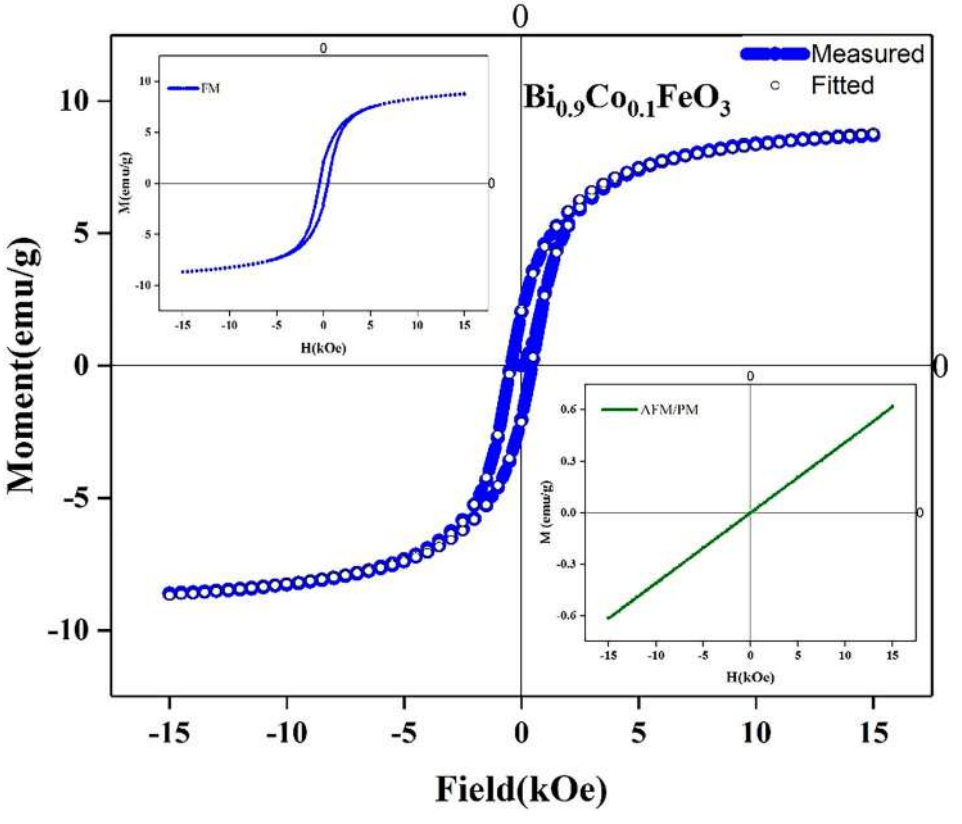

Figure 10. Fitted magnetic parameters of $Bi_{0.9}Co_{0.1}FeO_3$ and the inset shows the FM and AFM/PM contributions of $Bi_{0.9}Co_{0.1}FeO_3$.

Curie–Weiss temperature (T_0) of this sample is extracted from slope and intercept values of $1/\varepsilon_r$ versus temperature plot [45]. The values of T_0, T_m, C and $\Delta T = T_m - T_0$ are found to be 333.45°, 358°, 2.382 and 24.55° respectively. Moreover, the degree of diffusion is determined by plotting $Ln(1/\varepsilon - 1/\varepsilon_m)$ against Ln $(T-T_m)$ using the least square fitting method and the value of the diffusion coefficient is found to be 1.5 (Figure not shown). This diffusion coefficient value lies between ferroelectric and relaxor ferroelectric values. Hence, the $Bi_{0.9}Co_{0.1}FeO_3$ system possesses diffuse phase transition which reduces the oxygen vacancies and helps in tuning the magnetoelectric coupling in these samples.

Temperature-dependent resistivity reveals that the resistivity of the samples remains invariant at elevated temperature ranges which is also essential due to the reduction of oxygen vacancies that pin the domain walls with high dielectric permittivity due to high resistivity [46]. Temperature dependent resistivity at selected frequencies is presented in the supplementary section [**S1**].

Differential scanning calorimetry analysis reveals that (i) the antiferromagnetic Neel temperature of $Bi_{0.9}Co_{0.1}FeO_3$ is shifted towards ambient temperature compared to pristine $BiFeO_3$ as

Table 4. Magnetic parameters of $BiFeO_3$ and $Bi_{0.9}Co_{0.1}FeO_3$.

	Maximum Magnetization (M_s) emu/g	Maximum Magnetization μB / Fe	Magnetization at zero field (Mr) emu/g	Coercivity (Oe)	Canting angle
$BiFeO_3$	0.08788	0.0049	0.0011	130.64	0.0476
$Bi_{0.9}Co_{0.1}FeO_3$	8.70088	0.465	2.040	450.90	5.402

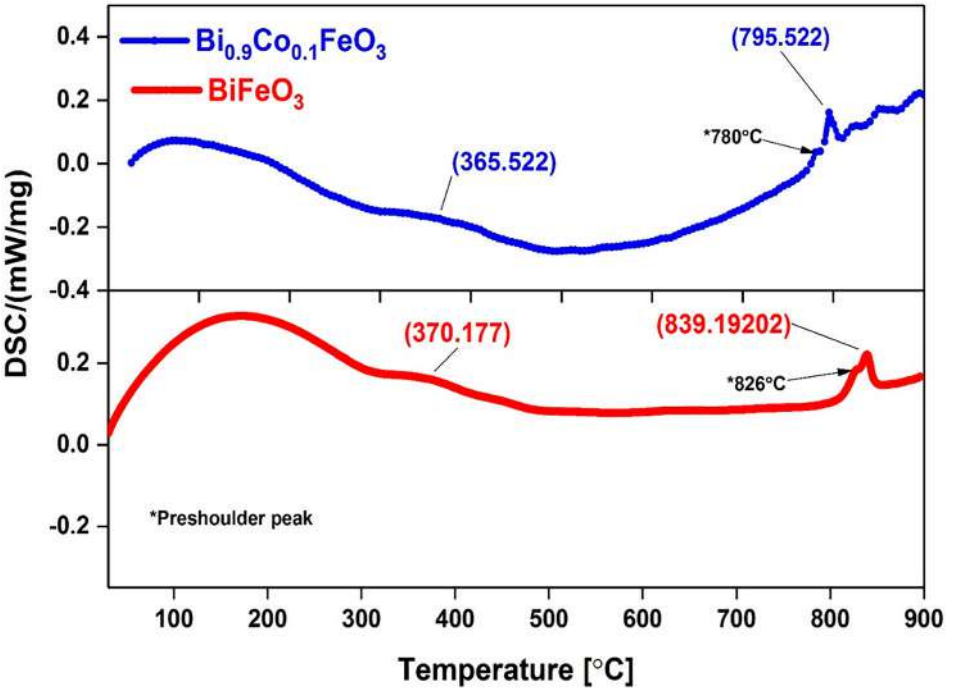

Figure 11. Temperature dependent differential scanning calorimetry response of $Bi_{1-x}Co_xFeO_3$ (x = 0, 0.1) samples.

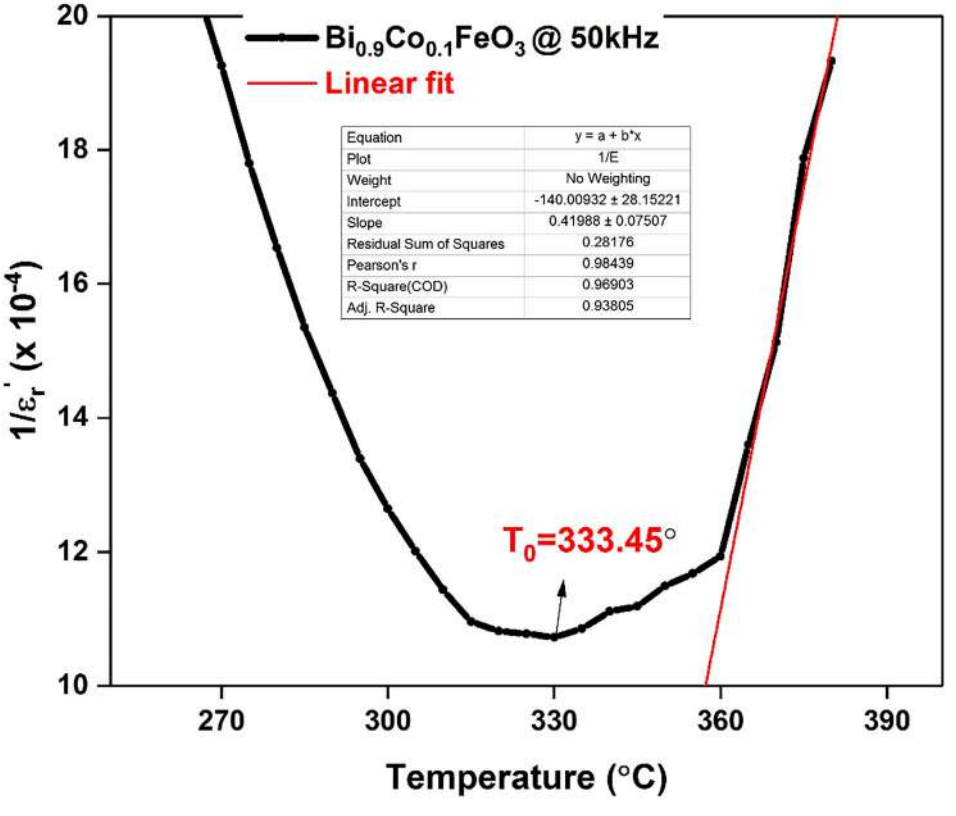

Figure 12. Temperature dependent inverse dielectric permittivity of $Bi_{0.9}Co_{0.1}FeO_3$ at 50 kHz.

revealed from XRD analysis. (ii) DSC curves of $Bi_{1-x}Co_xFeO_3$ (x = 0, 0.1) samples present the signatures of antiferromagnetic and ferroelectric transition temperature in the expected transition temperature range and support the linear magnetoelectric coupling behaviour as divulged from temperature-dependent dielectric studies.

From the temperature dependent resistivity plot at selected frequencies (supplementary section) and M-H behaviour, the $Bi_{0.9}Co_{0.1}FeO_3$ system possesses high resistivity and magnetization. Hence, this system might be suitable for resistive random access memory applications [46].

5. Conclusion

To conclude, $BiFeO_3$ and $Bi_{0.9}Co_{0.1}FeO_3$ are synthesized by the solid state route. XRD patterns of $Bi1_{-x}Co_xFeO_3$ (x = 0, 0.1) are crystalized in the R3c phase and the peak intensities of $Bi_{0.9}Co_{0.1}FeO_3$ are shifted towards a lower angle which tilts the FeO_6 octahedra to a 15.22° compared to pristine $BiFeO_3$ (14.89°). The correlation between x-ray diffraction analysis and morphological analysis reveals that the number of coherent diffracting domains is suppressed to eight in $Bi_{0.9}Co_{0.1}FeO_3$ compared to pristine $BiFeO_3$ (14). The temperature dependent dielectric analysis divulges that the disappearance of dielectric maximum close 300°C is the outcome of conducting behaviour in $Bi_{0.9}Co_{0.1}FeO_3$. The thermal analysis unveils that the influence of Co^{3+} in $BiFeO_3$ shifts the T_N and T_C towards lower temperatures and suppresses the additional phases present in $Bi_{0.9}Co_{0.1}FeO_3$. The magnetization and hence the signature of linear magnetoelectric coupling are considerably improved in $Bi_{0.9}Co_{0.1}FeO_3$ compared to pristine $BiFeO_3$ which suits for memory storage applications. These outcomes may probe the researcher to study further theoretical analysis and experimental findings that support the multiferroic behaviour present in this sample.

Acknowledgements

One of the authors Rajesh would like to thank the following centres: STIC, Kerala and SAIF, IIT Madras for providing structural and magnetic measurements.

Disclosure statement

The authors declare that they have no known competing financial interests or personal relationships that could have appeared to influence the work reported in this paper.

ORCID

Rajesh Raman http://orcid.org/0000-0002-8983-4735
Giridharan Nambi Venkatesan http://orcid.org/0000-0001-8652-8831
P. Sakthivel http://orcid.org/0000-0002-9436-8070

References

[1] Surowiak Z, Bochenek D. Fabrication of magnetic Co/BiFeO 3 composite and its advanced treatment of pharmaceutical waste water by activation of peroxysulphate. Sep Purif Technol. 2018;202:242–247. doi:10.1016/j.seppur.2018.03.072.
[2] Schmid H. Some symmetry aspects of ferroics and single phase multiferroics. J Phys: Condens Matter. 2008;20:434201. doi:10.1088/0953-984/20/43/434201.
[3] Fiebig M. Revival of the magnetoelectric effect. J Phys D Appl Phys. 2005;38:R123–R152. doi:10.1088/0022-3727/38/8/R01.
[4] Wang KF, Liu JM, Ren ZF. Multiferroicity: the coupling between magnetic and polarization orders. Adv Phys. 2009;58:321–448. doi:10.1080/00018730902920554.
[5] Catalan G, Scott JF. Physics and applications of bismuth ferrite. Adv Mater. 2009;21:2463–2485. doi:10.1002/adma.200802849.

[6] Lu J, Qiao LJ, Fu PZ, et al. Phase equilibrium of Bi2O3–Fe2O3 pseudo-binary system and growth of BiFeO3 single crystal. J Cryst Growth. 2011;318:936–941. doi:10.1016/j.jcrysgro.2010.10.181.
[7] Palai R, Katiyar RS, Schmid H, et al. B phase and γ−β metal-insulator transition in multiferroic $BiFeO_3$. Phys Rev B. 2008;77:014110. doi:10.1103/PhysRevB.77.014110.
[8] Perdomo CPF, Suarez AV, Gunnewiek RFK, et al. Low temperature synthesis of high purity nanoscaled $BiFeO_3$ by a fast polymer solution method and their ferromagnetic behavior. J Alloys Compds. 2020;849:156564. doi:10.1016/j.jallcom.2020.156564.
[9] Brinkman K, Iijima T, Takamura H. Acceptor doped $BiFeO_3$ ceramics: a new material for oxygen permeation membranes. Jpn J Appl Phys. 2007;46:L93–L96. doi:10.1143/JJAP.46.L93.
[10] Garcia FG, Riccardi CS, Simões AZ. Lanthanum doped $BiFeO_3$ powders: syntheses and characterization. J Alloys Compd. 2010;501:25–29. doi:10.1016/j.jallcom.2010.04.049.
[11] Zhang M, Yang H, Li Y, et al. Cobalt doping of bismuth ferrite for matched dielectric and magnetic loss. Appl Phys Lett. 2019;115:212902. doi:10.1063/1.5134741.
[12] Marzouki A, Harzali H, Loyau V, et al. Large magnetoelectric response and its origin in bulk Co-doped $BiFeO_3$ synthesized by a stirred hydrothermal process. Acta Mater. 2018;145:316–321. doi:10.1016/j.actamat.2017.11.055.
[13] Rahaman MM, Matin MA, Al Mamun MA, et al. Enhanced electrical conductivity and multiferroic property of cobalt-doped bismuth ferrite nanoparticles. J Mater Sci: Mater Electron. 2020;31:8727–8736. doi:10.1007/s10854-020-04533-x.
[14] Zhang H, Cheng S, Lia B, et al. Fabrication of magnetic Co/BiFeO 3 composite and its advanced treatment of pharmaceutical waste water by activation of peroxysulphate. Sep Purif Technol. 2018;202:242–247. doi:10.1016/j.seppur.2018.03.072.
[15] Grazulis S, Chateigner D, Downs RT, et al. Crystallography open database – an open-access collection of crystal structures. J Appl Crystallogr. 2009;42:726–729. doi:10.1107/S0021889809016690.
[16] Wani WA, Kundu S, Ramaswamy K, et al. Structural, morphological, optical and dielectric investigations in cobalt doped bismuth ferrite nanoceramics prepared using the sol-gel citrate precursor method. J Alloys Compds. 2020;846:156334. doi:10.1016/j.jallcom.2020.156334.
[17] Woodward PM. Octahedral tilting in perovskites. II. structure stabilizing forces. Acta Cryst. 1997;B53:44–66. doi:10.1107/S0108768196012050.
[18] Kriegner D, Matěj Z, Kužel R, et al. Powder diffraction in bragg-brentano geometry with straight linear detectors. J Appl Crystallogr. 2015;48(2):613–618. doi:10.1107/S1600576715003465.
[19] Khorsand Zak A, Abd. Majid WH, Abrishami ME, et al. X-ray analysis of ZnO nanoparticles by williamson–Hall and size–strain plot methods. Solid State Sci. 2011;13:251–256. doi:10.1016/j.solidstatesciences.2010.11.024.
[20] Venkateswarlu K, Bose A C, Rameshbabu N. X-ray peak broadening studies of nanocrystalline hydroxyapatite by williamson–Hall analysis. Phys B. 2010;405:4256–4261. doi:10.1016/j.physb.2010.07.020.
[21] Shameem Banu IB, Rajesh R, Mamat MH, et al. Strain-mediated electrical and optical properties of novel lead-free $CuFe_2O_4$-$KNbO_3$ nanocomposite solid solutions: A combined experimental and Density Functional Theory studies. Microsc Res Tech 2022;85:3140–3152. doi:10.1002/jemt.24172.
[22] Rajesh R, Giridharan NV, Kumar KR, et al. Effect of Mn doping on magnetodielectric properties of polycrystalline $BiFeO_3$ ceramics. J Alloys Compds. 2021;854:156981. doi:10.1016/j.jallcom.2020.156981.
[23] Fan Y, Zhou Y, Shen M, et al. Low-spin Co^{3+} make great contributions to the magnetism of $BiFeO_3$. J Mater Sci: Mater Electron. 2018;29:18593–18599. doi:10.1007/s10854-018-9977-0.
[24] Sati PC, Kumar M, Chhoker S. Raman spectroscopy and enhanced magnetic and dielectric properties of Pr and Ti codoped BiFeO3 ceramics. J Mater Sci: Mater Electron. 2015;26:530–538. doi:10.1007/s10854-014-2431-z.
[25] Schneider CA, Rasband WS, Eliceiri KW. NIH image to ImageJ: 25 years of image analysis. Nat Methods. 2012;9(7):671–675. doi:10.1038/nmeth.2089.
[26] Haynes W. M., Bond dislocation energy. CRC Press, 2014. https://notendur.hi.is/~agust/rannsoknir/papers/2010-91-CRC-BDEs-Tables.pdf
[27] Bongurala P, Gorige V. Structural, magnetic and electric properties of multiferroic $NiFe_2O_4$-$BaTiO_3$ composites. J Magn Magn Mater. 2019;477:350–355. doi:10.1016/j.jmmm.2018.12.014.
[28] Gowri G, Saravanan R, Srinivasan N, et al. Investigation on interatomic chemical bonding and charge-related optical, multiferroic properties of La1Zn FeO3 bulk ceramics. Mater Chem Phys. 2021;267:124652. doi:10.1016/j.matchemphys.2021.124652.
[29] Moma K, Ikeda T, Belik AA, et al. Dysnomia, a computer program for maximum-entropy method (MEM) analysis and its performance in the MEM-based pattern fitting. Powder Diffr. 2013;28:184–193. doi:10.1017/S088571561300002X.
[30] Yu Z, Ang C. Maxwell-Wagner polarization in ceramic composites $BaTiO_3$– $(Ni_{0.3}Zn_{0.7})Fe_{2.1}O_4$ J. J Appl Phys. 2002;91:794–797. doi:10.1063/1.1421033.
[31] Sharma J, Hamit Bhat B, Kumar A, et al. Magnetic and dielectric properties of Ce-Co substituted $BiFeO_3$ multiferroics. Mater Res Express. 2017;4:036104. doi:10.1088/2053-1591/aa6433.

[32] Zhang M, Yan HJ, Li Y, et al. Cao M S, cobalt doping of bismuth ferrite for matched dielectric and magnetic loss. Apps Phys Lett. 2019;115:212902. doi:10.1063/1.5134741.
[33] Das S, Sahoo RC, Nath TK. Investigation of room temperature multiferroic properties in sol-gel derived gadolinium, cobalt doped $BiFeO_3$ nanoceramics. J. Appl. Phys. 2020;127:054101. doi:10.1063/1.5125239.
[34] Rawat M, Yadav KL. Electrical, magnetic and magnetodielectric properties in ferrite-ferroelectric particulate composites. Smart Mater Struct. 2015;24:045041. (11pp). doi:10.1088/0964-1726/24/4/045041.
[35] Vopson MM, Fetisov YK, Caruntu G, et al. Measurement techniques of the magneto-electric coupling in multiferroics. Materials (Basel). 2017;10(8):963. doi:10.3390/ma10080963.
[36] Shi XX, Liu XQ, Chen XM. Readdressing of Magnetoelectric Effect in Bulk $BiFeO_3$. Adv Funct Mater. 2017;27:1604037. doi:10.1002/adfm.201604037.
[37] Tagantsev K, Vaideeswaran K, Vakhrushev SB, et al. The origin of antiferroelectricity in $PbZrO_3$. Nat Commun. 2013;4:2229. doi:10.1038/ncomms3229.
[38] Rajesh R, John Ethilton S, Ramachandran K, et al. Effect of Sr doping on the magnetocapacitive effect in $Bi_{0.6}Sr_{0.4}FeO_{3-\delta}$ polycrystalline ceramics. Appl Phys A. 2018;124:532. doi:10.1007/s00339-018-1941-6.
[39] Muneeswaran M, Akbari-Fakhrabadi A, Gracia-Pinilla MA, et al. Structural, electrical, ferroelastic behavior, and multiferroic properties of $BiFeO_3$. J Mater Sci: Mater Electron. 2020;31:13141–13149. doi:10.1007/s10854-020-03865-y.
[40] Nayek C, Tamilselvan A, THirmal C, et al. Origin of enhanced magnetization in rare earth doped multiferroic bismuth ferrite. J Appl Phys. 2014;115:073902. doi:10.1063/1.4865958.
[41] Kumar P, Shankhwar N, Srinivasan A, et al. Oxygen octahedra distortion induced structural and magnetic phase transitions in $Bi_{1-x}Ca_xFe_{1-x}Mn_xO_3$ ceramics. J Appl Phys. 2015;117:194103. doi:10.1063/1.4921433.
[42] Selbach SM, Einarsrud MA, Tybell T, et al. Synthesis of $BiFeO_3$ by wet chemical methods. J Am Ceram Soc. 2007;90:3430–3434. doi:10.1111/j.1551-2916.2007.01937.x.
[43] Arifiadi N, Kim KT, Khairani IY, et al. Synthesis and multiferroic properties of high-purity $CoFe_2O_4$–$BiFeO_3$ nanocomposites. J Alloys Compd. 2021;867:159008. doi:10.1016/j.jallcom.2021.159008.
[44] Ray J, Biswal AK, Acharya S, et al. Effect of Co substitution on the magnetic properties of $BiFeO_3$. J Magn Magn Mater. 2012;324:4084–4089. doi:10.1016/j.jmmm.2012.07.027.
[45] Zhu X, Zhuge F, Li M, et al. Microstructure dependence of leakage and resistive switching behaviours in Ce-doped $BiFeO_3$ thin films. J Phys D: Appl Phys. 2011;44:415104. doi:10.1088/0022-3727/44/41/415104.
[46] Tang Z, Zeng J, Xiong Y, et al. Resistive switching properties of Ce and Mn co-doped BiFeO3 thin films for nonvolatile memory application. AIP Adv. 2013;3:122117. doi:10.1063/1.4860950.

Applied Physics A (2023) 129:552
https://doi.org/10.1007/s00339-023-06789-6

Applied Physics A
Materials Science & Processing

Molecular design of $BiFeO_3$ via novel substitution by zirconium and erbium for tuning the multifunctional properties and band structure calculations

S. Divya Lakshmi[1] · I. B. Shameem Banu[1] · R. Rajesh[2] · Mohamad Hafiz Mamat[3] · G. Gowri[4]

Received: 24 April 2023 / Accepted: 19 June 2023

Abstract
In this work, the multifunctional properties of BFO are tuned by the novel substitution of erbium and zirconium in the BFO lattice and thereby 6 samples $Bi_{(1-x)}Er_xFe_{(1-y)}Zr_yO_3$ (where $x = 0.05,0.1$ and $y = 0, 0.02, 0.05$) were prepared. The structural, morphological, and elemental aspects of the samples were scrutinized. The multifunctional properties of the samples were recorded. The combined effect of 5% erbium and 2% zirconium offered a better saturated ferroelectric loop with a greater remnant polarization value (0.74 μC/cm^2). By including 5% erbium and 2% zirconium inside bismuth ferrite, the magnetization of BFO has improved very much with a remanence value (0.095 emu/g). But, the scaling up of erbium content beyond 5% and zirconium content beyond 2% caused a downfall in the multifunctional features developed so far in the bismuth ferrite system. The electronic band structure calculations of these compounds provide supporting evidence for the spin cycloid distortion for the dual-doped compounds.

Keywords Bismuth ferrite · Sol–gel method · Magnetic · Ferroelectric · Electronic band structure

1 Introduction

Research and development have entered into the modern era with the innovative evolution of multiferroic materials. The concurrence of many ferroic order states in the multiferroic materials is its strong suit. It is more apt to describe the multiferroics as fertile materials as they could be transformed into many forms. The focus on multiferroics has intensified with the discovery of magnetoelectric linkage inside them. Hence, multiferroics serve as a potential source of many applications. On tuning the multiferroics in different aspects, multiferroics could penetrate into various fields through the most exciting applications like memory devices, transformers, transducers, generators, sensors, etc. Based on the type of magnetoelectric coupling inside the materials, the multiferroic materials can be grouped into two classes. They are single-phase multiferroics and multiferroic composites. Direct magnetoelectric coupling prevails inside the single-phase multiferroic materials which pulled the interest of researchers more towards the single phase multiferroic materials.

Exclusively bismuth ferrite (one of the single-phase multiferroics) exhibits multiferroism at room temperature naturally. To enhance its functionality to suit practical applications, impurity atoms are added to the BFO lattice which becomes a hot research of late [1–16]. To be more specific, the combination of erbium and some transition metal ion substitution triggered the multiferroic tendency inside BFO [10, 17–28]. Some researchers have investigated the Zr-doped BFO, which shows enhanced multifunctional properties [29–32]. As the volatility of bismuth ions in BFO is

✉ S. Divya Lakshmi
divyasvj24@gmail.com

I. B. Shameem Banu
Shameembanu@crescent.education

R. Rajesh
rr@vcet.ac.in

1 BSAR Crescent Institute of Technology, Vandalur, Chennai 600048, India

2 Department of Physics, Velammal College of Engineering and Technology, Madurai 625009, India

3 NANO-ElecTronic Centre (NET), School of Electrical Engineering, College of Engineering, Universiti Teknologi MARA, 40450 Shah Alam, Selangor, Malaysia

4 Department of Physics, The Madura College, Madurai, Tamil Nadu 625011, India

Published online: 12 July 2023

one of the serious problems faced by bismuth ferrite, doping must reduce the same. Some of the earlier research revealed that doping Bi and Fe site with two dissimilar elements can lead to the deterioration of the bismuth ion's volatility. Therefore, both the ferroelectricity and magnetism of bismuth ferrite can be enhanced on dual substitution simultaneously [33–37]. In this context, the multifunctional nature of the BFO has been tuned through the substitution of elements such as erbium and zirconium in this work.

There are actually three factors that can modify the properties of the BFO. One factor is the dopant as discussed already. The second factor is the concentration of the dopant which is emphasized in this work. The third factor is the site of dopants which will be discussed in future works. To study the effect of one factor, the other two factors must be kept constant. From the previous works, it was found that erbium is way better as a Bi-site dopant compared to ytterbium. Among the Fe site dopants used (niobium, manganese, molybdenum, and zirconium) zirconium was found to be better, especially considering all the multifunctional properties (ferroelectric, ferromagnetic, and leakage current behavior) [38, 39]. Thus, in this work, Bi-site has been planned to modify using erbium and Fe-site using zirconium to enhance the multiferroic properties of the bismuth ferrite.

2 Experimental details

Sol–gel technique was employed to synthesize the nanoparticles $BiFeO_3$ and $Bi_{(1-x)}Er_xFe_{(1-y)}Zr_yO_3$ (where $x = 0.05,0.1$ and $y = 0$, 0.02, 0.05). In further discussion, $BiFeO_3$ and $Bi_{(1-x)}Er_xFe_{(1-y)}Zr_yO_3$ will be denoted as BFO, BE5FO, BE5FZ2O, BE5FZ5O, BE10FO, BE10FZ2O and BE10FZ5O respectively. Analytical grade bismuth (lll) nitrate pentahydrate (assay 98%, Alfa Aesar), iron (lll) nitrate nonahydrate (assay 98%, Alfa Aesar), Erbium (lll) nitrate hydrate (assay 99.9%, Alfa Aesar), Zirconium (IV) oxy nitrate hydrate (assay 99%, Alfa Aesar), citric acid anhydrous (assay 99.5% Merck) and nitric acid (assay 70% Merck) were used as starting materials without any further purification, as all the chemicals were of analytical grade. Appropriate stoichiometric ratio of bismuth nitrate and erbium nitrate was mixed with 20 ml of nitric acid and 20 ml of distilled water and stirred at 400 rpm and heated at 80 °C. At the same time, the appropriate stoichiometric ratio of iron nitrate and zirconium nitrate was mixed with 20 ml of distilled water and stirred at 400 rpm, and heated at 80 °C. The citric acid anhydrous, which acts as a chelating agent, was mixed with 40 ml of distilled water and stirred at 400 rpm, and heated at 80 °C for some time separately. Then all three solutions were mixed and stirred at 400 rpm and heated at 80 °C simultaneously to form the nanopowders. The powders obtained were crushed and annealed at 650 °C for 4 h. For electrical measurements, powders were pelletized. Polyvinyl alcohol (PVA) was added to the annealed powders as a binding agent. The mixture was crushed using an agate mortar and pestle for 6 h. so that the PVA diffuses into the sample properly. Then the mixture was filled in a 6 mm die and placed inside the pelletizer at 6 tons pressure and left for 10–15 min. The resulting 8 mm pellet was sintered at 600 °C for 4 h. The thickness of the pellets is in the range of 0.5–1 mm and the diameter of the pellets is 8 mm. The resulting pellets were smoothened and the silver paste was coated on both sides of the pellets for ohmic contact.

The phase of the samples was identified with the help of model Bruker D8 advance PXRD with Cu K_α radiation of wavelength 1.5404 A° at the scanning rate of 0.02 min^{-1} and range of 2θ was 10° to 70°. Room temperature Ferroelectric properties were studied for the pellets using a ferroelectric (P-E) loop tracer from Marine India Pvt. Ltd. The magnetic behavior of the samples was analyzed at room temperature using a vibrating sample magnetometer (lakeshore model 7407). Current leakage measurements were recorded using a Radiant Precision Premier II ferroelectric loop tracer. FESEM image was acquired from Jeol 6390 LV. To calculate the electrical structure, one of the most accurate techniques such as the linearized augmented plane wave (LAPW) method was used.

3 Results and discussion

3.1 Structural analysis

Figure 1a and b demonstrate the X-ray diffraction results of the BFO, BE5FO, BE10FO, BE5FZ2O, BE10FZ2O, BE5FZ5O, and BE10FZ5O ceramics. Figure 1 explicitly revealed the structure of all prepared samples. As per the JCPDS data card no. (86-1518), the XRD peaks of all the prepared samples in this work confirmed that the samples were all crystallized in the rhombohedral-based perovskite structure with space group R3c. From Fig. 1, Also, it is evident that the dopant has no impact on the structural integrity of BFO. However, doping produced a mild impurity peak around 28° [38–41]. On comparison with JCPDS data, $Bi_2Fe_4O_9$ (Mullite) matched with the impurity peak.

From Fig. 1a) it is clear that the introduction of erbium in the BFO lattice reduced the impurity peak's intensity. On including zirconium 2% along with erbium, the impurity peak's intensity has even got lowered more (almost no impurity peaks could be seen predominantly on 2% zirconium doped samples). Subsequently, on increasing the concentration of zirconium to 5%, the impurity peaks got more intensified and predominant. And this might be due to the increase of volatility of bismuth ions in the BFO lattice on doping 5% zirconium. These variations among the XRD

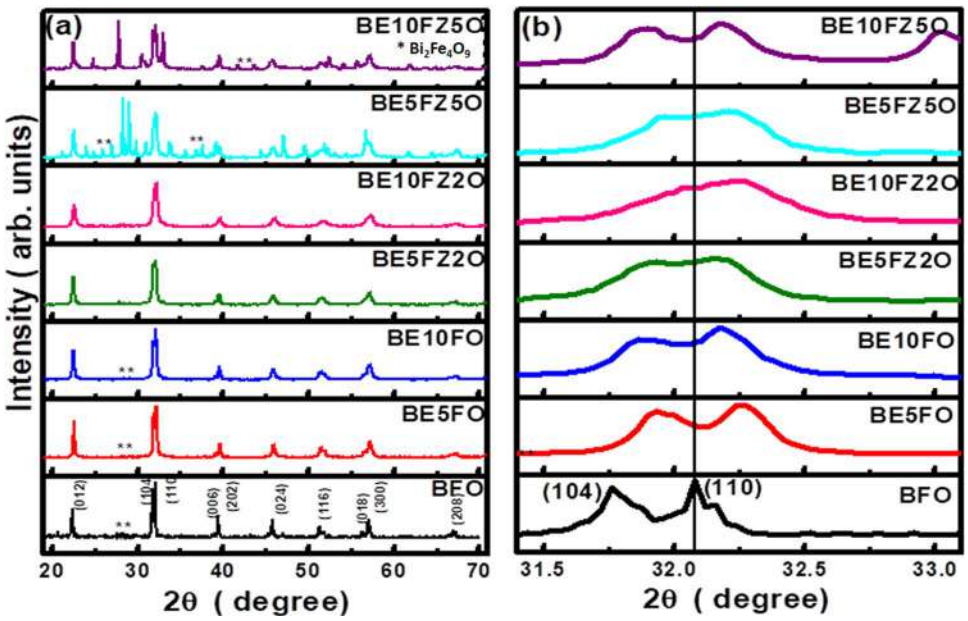

Fig. 1 **a** X-ray diffraction results of pure BFO and dopant substituted BFO samples, **b** magnified image of (104) and (110) peaks of the samples

patterns of different doped cases prove the proper incorporation of erbium and zirconium inside the BFO lattice.

The impurity peaks got suppressed on doping Er^{3+} (both 5 and 10%) in the bismuth place along with Zr^{4+} (2%) in the iron position of BFO. The re-occurrence of vigorous impurity peaks of greater intensity could be witnessed by increasing the Zr^{4+} content from 2 to 5% in the iron position of BFO. The reasons for the impurities of BFO are the highly volatile nature of Bi ions of BFO and oxygen vacancy. It is learned that these problems can be suppressed by doping rare earth elements at the Bi site. The reason for this lies in the stabilization of the bond dissociation energy of Bi-O. The Bi-O bond has stabilized as the bond dissociation energy of Er-O is stronger than that of Bi-O [41]. Thus, by including Er^{3+} in the bismuth place and Zr^{4+} (2%) in the iron place of BFO, the impurities have been eliminated to a greater extent. On scaling up the concentration of Zr^{4+} from 2 to 5% at the Fe site of BFO, the impurities reappear. As on increasing the doping concentration of zirconium, the volatile nature of bismuth ions might have increased, which in turn gave rise to greater impurity peaks. These results are reflected in the respective ferroelectric, magnetic & leakage current behaviors of the samples.

Figure 1b shows the magnified view of the (110) and (104) peaks of the XRD patterns of the samples. Peaks shift along the higher Bragg's angle when a lower ionic radius replaces a higher ionic radius as this kind of replacement gives rise to unit cell compression. In this work, Er^{3+} ion of ionic radius 0.103 nm has substituted the Bi^{3+} of ionic radius 0.117 nm. This substitution has shifted the Bragg's peaks along a higher Bragg's angle as expected. As a result of the shift, BFO suffers a contraction in the unit cell. The peaks (110) and (104) merge on doping Er^{3+} in the place of bismuth and Zr^{4+} (2%) in the iron place of BFO. The introduction of zirconium at the iron site has disturbed the spin structure of BFO which results in an improvement in the magnetic behavior of BFO. The peaks again start to separate on increasing the concentration of Zr^{4+} from 2 to 5% in the iron place of BFO. This might be the reason for the declination of magnetic property inside BFO on increasing zirconium concentration, which will be discussed in the later part. Especially, for the samples BE5FZ2O and BE10FZ2O, the merging can be observed to be more than in other cases. These relative variations between the XRD Pattern of the substitution-modified bismuth ferrite and pure bismuth ferrite revealed the slight distortion caused by the dopants in the BFO. Therefore, Er and Zr have been successfully incorporated in the BFO lattice. The interplanar spacing for the samples is calculated using the position of 110 peaks of the respective samples. The direct dependency of crystallite size and interplanar spacing is projected by the combination of Bragg's law and the Scherrer formula. The crystallite size values are tabulated in Table 1 and these values confirm the successful preparation of nanosized particles of the samples.

The strain of the respective samples is estimated using the below formula.

$$\text{Strain} = \frac{\beta \,\text{Cos}\theta}{4\,\text{Sin}\theta}$$

In the above equation, β indicates the full width at half maximum and θ is the Bragg's angle respectively.

It is clear that the crystallite size varies depending on doping. Table 1 presents the size of the crystallite and

Table 1 Size of crystallite and strain of the samples

Sample name	Crystallite size by Scherrer formula (D) (nm)	Strain	Dislocation density ($\delta = 1/D^2$) ($\times 10^{-3}$)	Interplanar spacing (d) (nm)
BFO	31.91	1.25×10^{-3}	0.982	0.2785
BE5FO	23.32	1.46×10^{-3}	1.84	0.2783
BE10FO	19.21	1.8×10^{-3}	2.71	0.2779
BE5FZ2O	14.71	5.1×10^{-3}	4.62	0.2783
BE10FZ2O	17.25	2.42×10^{-3}	3.36	0.2781
BE5FZ5O	25.63	3.34×10^{-3}	1.52	0.2777
BE10FZ5O	19.58	2.44×10^{-3}	2.61	0.2779

strain of the prepared samples. From Table 1, it is obvious that the strain is less for pure BFO, and on doping, the strain value is increasing. The increment in the strain values on doping proves the proper embodiment of the substitutions in the bismuth ferrite. Amidst the doped samples, the tensile strain and dislocation density are maximum for BE5FZ2O. Here, the strain caused by doping is due to the ionic radii mismatch between the dopant ion and parent ion. From Table 1, it is clear the dislocation density increases upon introducing erbium at the bismuth place and it is scaling up upon introducing zirconium at iron place along with erbium at the bismuth place. The peaks (110) and (104) merge on doping Er^{3+} in the place of bismuth and Zr^{4+} (2%) in the iron place of BFO. This merging may be due to the higher dislocation density of the sample compared to the other samples. On the other hand, though the dislocation density is small for BE5FZ5O, the merging of peaks (110) and (104) could be noticed. The scaling up of the doping concentration of zirconium to 5% induced higher strain (Table 1) inside the BFO lattice and intensified back the impurity peaks. This might be the reason for peak merging in the case of BE5FZ5O though the dislocation density is lower for the sample. The strain created in the bismuth ferrite system on doping alters the functional behaviors of the BFO, which is discussed later in the respective studies.

3.2 Morphological and elemental analysis

Figure 2 illustrates the surface morphology of the samples BE5FO, BE10FO, BE5FZ2O, BE10FZ2O, BE5FZ5O, and BE10FZ5O at different magnifications.

The variations of morphology caused in the samples are due to proper placements of the dopants inside the BFO. FESEM images showcased the microstructural modification explicitly. From the previous works, SEM images of the BFO projected highly irregular and agglomerated particles [38]. It is explicit that doping has improved the clarity of the microstructure of BFO.

The morphology tends to become distinguishable to a greater extent on introducing 5% of erbium. The shape of the particles has become homogenized. Mostly, cubical-shaped particles could be observed. (Fig. 2a). On increasing the erbium content to 10%, the particles started to club together. But still, the separable particles are visible. From Fig. 2c, particles have become bigger and countable on zirconium's substitution along with erbium. The shapes of the particles have become mostly spherical. Homogeneity still prevailed. The 10% erbium and 2% zirconium doped BFO's morphology is displayed in Fig. 2d. And Fig. 2c displayed the morphology of 5% erbium and 2% zirconium doped bismuth ferrite. The above statement in the manuscript is the comparison of the effect of increase of erbium's concentration in morphology. As in both cases (Fig. 2c and d) zirconium's concentration was the same 2%, the reason for the morphological variation can be ascribed to the variation of erbium's concentration. In that way, on comparing Fig. 2c and d, more particle accumulation could be noted in Fig. 2d, which is that of a 10% erbium-doped sample.

Figures 2e and f show the SEM morphologies of 5% zirconium-doped samples. Erbium content in Fig. 2e is 5% and that in Fig. 2f is 10%. The commencement of lump formations here and there could be observed by scaling up the zirconium level to 5% from 2%. In both cases, the mixed particle shapes are noted. Ionic radii mismatch and Kirkendal effects together might be the reason for well-defined particles and variation in the shapes and accumulation pattern of the particles on doping [39, 42]. Internal stresses developed inside BFO on doping enabled the chances of more charge accumulation. This reduced the reasons for the occurrence of high leakage current density. Consequently, zirconium's inclusion in BFO has upgraded the ferroelectricity in the bismuth ferrite.

Figure 2g and h evinced the EDAX spectrum and the composition table of the BE5FO, BE10FO, BE5FZ2O, BE10FZ2O, BE5FZ5O, and BE10FZ5O samples. Proper placement of the dopants inside the bismuth ferrite lattice has been verified via the EDAX spectrum and table of the samples. EDAX results proved the presence of all the added

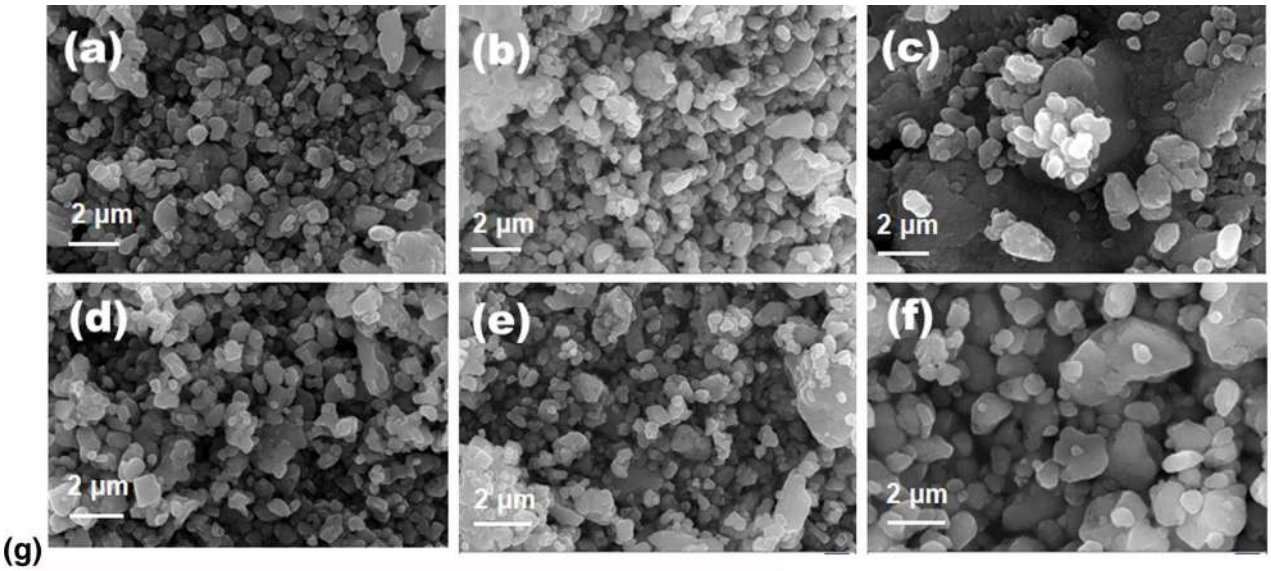

(g)

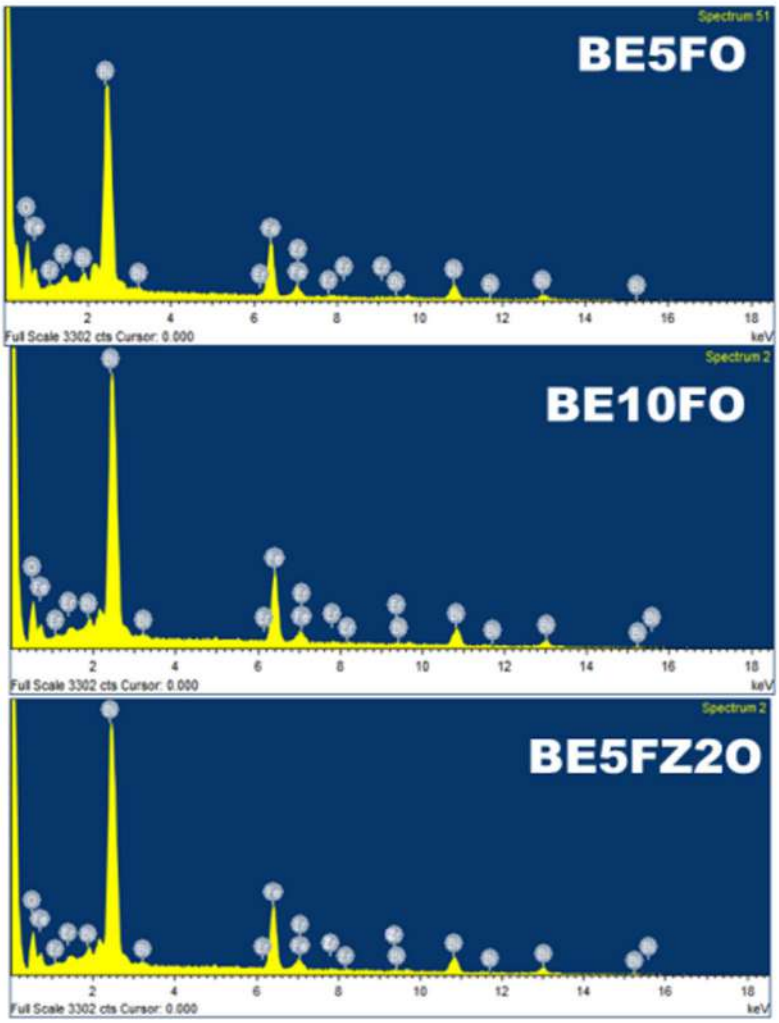

Element	Weight%	Atomic%
O K	27.82	76.08
Fe K	15.11	11.84
Er L	2.62	0.69
Bi M	54.45	11.40
Totals	100.00	

Element	Weight%	Atomic%
O K	20.07	67.40
Fe K	16.83	16.19
Er L	2.94	0.95
Bi M	60.16	15.47
Totals	100.00	

Element	Weight%	Atomic%
O K	19.58	65.79
Zr K	0.47	0.46
Fe K	18.45	17.76
Er L	2.60	0.84
Bi M	58.90	15.15
Totals	100.00	

Fig. 2 Surface morphology of the samples **a** BE5FO, **b** BE10FO, **c** BE5FZ2O **d** BE10FZ2O, **e** BE5FZ5O, **f** BE10FZ5O, **g** EDAX of the samples BE5FO, BE10FO and BE5FZ2O, **h** EDAX of the samples BE10FZ2O, BE5FZ5O and BE10FZ5O

(h)

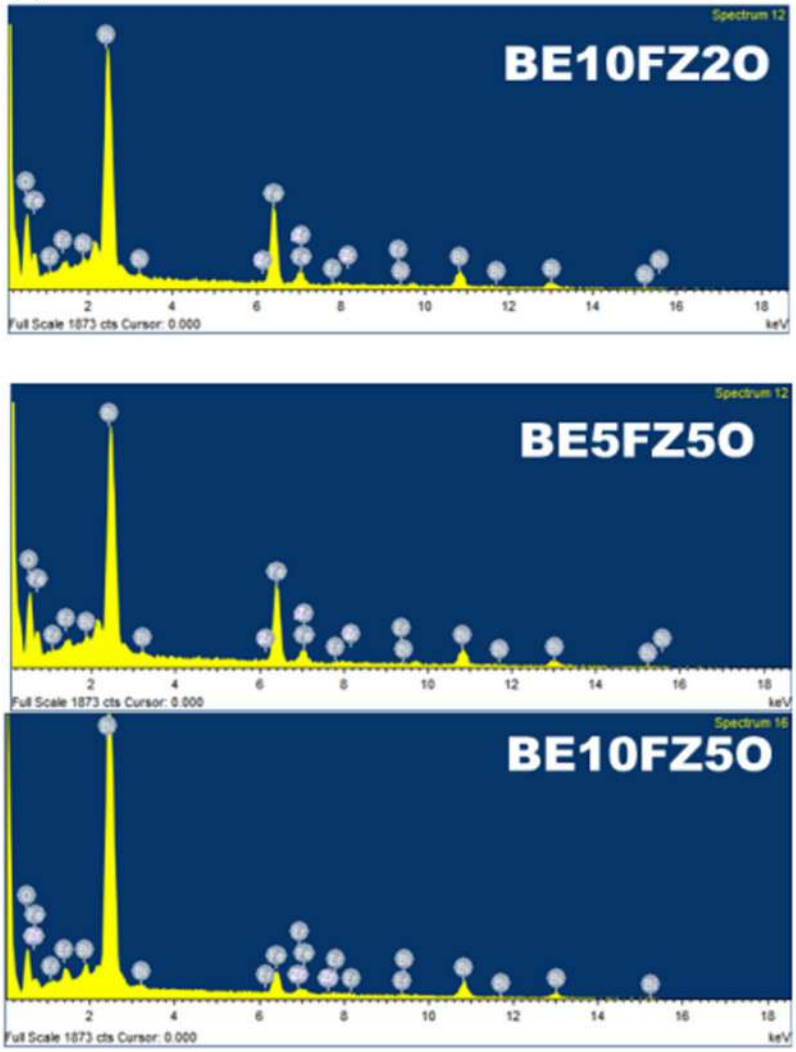

Element	Weight%	Atomic%
O K	15.20	58.95
Fe K	18.97	21.08
Zr L	0.49	0.33
Er L	3.23	1.20
Bi M	62.11	18.44
Totals	100.00	

Element	Weight%	Atomic%
O K	23.65	76.78
Fe K	5.57	5.18
Zr K	0.56	0.49
Er L	1.62	0.50
Bi M	68.60	17.05
Totals	100.00	

Element	Weight%	Atomic%
O K	24.19	73.65
Fe K	12.09	10.54
Zr K	1.36	1.12
Er L	2.51	0.73
Bi M	59.85	13.95
Totals	100.00	

Fig. 2 (continued)

elements in the compounds. From the EDAX spectrum, the existence of required elements (Bi, Fe, Er, Zr, and O) is revealed. The absence of any additional peaks confirmed the purity of all the samples. From the esteems obtained from the EDAX data, the percentage of the constituent elements is parallel to the stoichiometric ratio of the respective elements in the compounds.

3.3 Multifunctional properties

Figure 3a evinces the ferroelectric (PE) hysteresis curves of BE5FO, BE10FO, BE5FZ2O, BE10FZ2O, BE5FZ5O and BE10FZ5O at room temperature. The P-E measurement is carried out at an applied field 10 kV/cm and at a frequency of 20 Hz. Generally, the unsaturated ferroelectric loop is caused by the low ferroelectric samples. When the ferroelectric experiments are carried out under sub-coercive fields, even a good ferroelectric material shows unsaturated loops [43, 44]. To avoid these problems, the ferroelectric behaviors of the samples in this work were recorded for all possible combinations of ferroelectric parameters and chosen as the best one among them for analysis.

The ferroelectric loop of BE10FO shows less saturation comparatively (Fig. 3a). The ferroelectric loops of the doped samples have significantly improved and the ends of the loops tend to become sharp compared to undoped BFO indicating the reduction of oxygen vacancies. The values of polarization and coercive field for the samples BE5FO, BE10FO, BE5FZ2O, BE10FZ2O, BE5FZ5O, and BE10FZ5O at an applied field of 10 kV/cm are listed in Table 2. The clear-cut point of Table 2 is the inclusion of erbium inside the bismuth ferrite system delivered better PE loops and including 2% zirconium in the iron place along with erbium in the bismuth place has intensified the

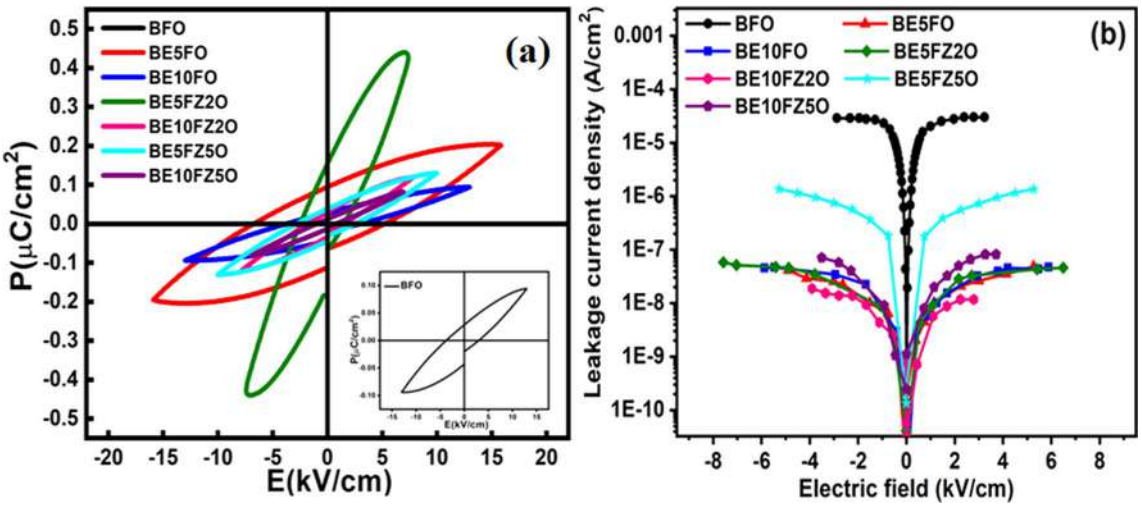

Fig. 3 **a** Ferroelectric loops and **b** leakage current curves of undoped BFO, BE5FO, BE10FO, BE5FZ2O, BE10FZ2O, BE5FZ5O and BE10FZ5O

Table 2 Multifunctional parameters of the pure BFO and dopant substituted BFO

Sample	P_r (μC/cm^2)	E_c (kV/cm)	Leakage current density	M_r (emu/g)	M_s (emu/g)	H_c (G)	Remnant ratio (M_r/M_s)
BFO	0.021	2.741	2.86×10^{-5}	1×10^{-3}	4×10^{-3}	260	0.25
BE5FO	0.097	5.35	2.02×10^{-8}	16×10^{-3}	150×10^{-3}	400.59	0.24
BE10FO	0.029	3.32	2.96×10^{-8}	11×10^{-3}	3.4×10^{-3}	484.32	0.19
BE5FZ2O	0.148	1.66	1.81×10^{-8}	95×10^{-3}	396×10^{-3}	412.26	0.16
BE10FZ2O	0.033	1.49	1.45×10^{-8}	15×10^{-3}	120×10^{-3}	535.06	0.125
BE5FZ5O	0.042	2.63	5.81×10^{-7}	7.6×10^{-3}	115×10^{-3}	776.36	0.066
BE10FZ5O	0.0142	0.85	4.18×10^{-8}	8×10^{-3}	62.5×10^{-3}	526.59	0.128

shape of the P-E hysteresis loop. But on increasing the concentration of zirconium to 5%, the ferroelectric parameters got lowered again. It is obvious from Table 2 that introducing 2% Zr^{4+} at the Fe site has disturbed the polarization of the samples. Whereas the coercive electric field and shape of the hysteresis have improved on doping 2% Zr^{4+} in the iron place along with Er^{3+} in the bismuth place. All the erbium-doped samples produce higher ferroelectric parameters compared to undoped BFO. But by introducing 5% zirconium in the iron position along with erbium in the bismuth position, the ferroelectric nature of BFO has been affected. The ferroelectric parameters of (5/ 10%)erbium and 5% zirconium co-doped BFO fetches lower remnant polarization values compared to other doped cases but higher than the undoped BFO (Table 2). The ionic radii of Zr^{4+} and Fe^{3+} are 0.072 nm and 0.069 nm respectively. As the Zr^{4+} has a slightly greater ionic radius than Fe^{3+} ion, the hopping of charges between Fe^{3+} and Fe^{2+} ions has become more prominent on adding higher zirconium content in the position of iron. This might be the cause of the reduction in the ferroelectric nature of BFO on introducing a higher concentration of zirconium.

Figure 3b shows the plot of leakage current density (J) against the external electric field (E) for the samples BFO, BE5FO, BE10FO, BE5FZ2O, BE10FZ2O, BE5FZ5O, and BE10FZ5O. Symmetry sustained in the J-E curves of all the samples on the application of positive and negative electric fields. Generally, impurities occur in pure bismuth ferrite due to high volatility of Bi ions in BFO and the presence of oxygen vacancies in BFO. These impurities yield high leakage current values in pure BFO. Also, these impurities affect the ferroelectric and ferromagnetic behavior of the BFO. It is learnt that doping with rare earth elements in the bismuth position or iron position of BFO brings down the leakage current density of the BFO to a greater extent.

The ceramics BFO, BE5FO, BE10FO, BE5FZ2O, BE10FZ2O, BE5FZ5O, and BE10FZ5O attained leakage current estimates as given in Table 2, at an external electric field of 2 kV/cm. It is clear-cut from the values that on substituting erbium in the bismuth position of bismuth ferrite,

the leakage current density got reduced. The leakage current values have faced further downfall on including 2% zirconium along with erbium in the bismuth place of bismuth ferrite. But on raising the zirconium content from 2 to 5% in the iron site of bismuth ferrite, the values of leakage current density have begun to re-appear.

The volatility of bismuth ions causes high leakage current density which is one of the main problems faced by BFO. One of the main purposes of doping is to reduce the volatility of bismuth ions. But on doping 5% zirconium, the leakage current density is high (Fig. 3b). The introduction of erbium in the BFO lattice reduced the impurity peak's intensity. On including zirconium 2% along with erbium, the impurity peak's intensity has even got lowered more (almost no impurity peaks could be seen predominantly on 2% zirconium doped samples). Subsequently, on increasing the concentration of zirconium to 5%, the impurity peaks got more intensified and predominant. And this might have increased again the volatility of bismuth ions in the BFO lattice on doping 5% zirconium. This might cause the increase of leakage current behavior in BFO again by increasing the doping concentration of zirconium to 5%. Thus, the combined effect of 5% erbium and 2% zirconium in scaling down the leakage current measurement is marvelous. Thus, the sample BE5FZ2O is the best relatively as it lowered the leakage current parameter to a greater extent (Fig. 3b).

Figure 4 shows united MH curves of the BFO, BE5FO, BE10FO, BE5FZ2O, BE10FZ2O, BE5FZ5O, and BE10FZ5O ceramics at room temperature.

One of the main issues faced by bismuth ferrite is its weak magnetism. On trying to figure out the reasons for the same, it is learned that the spin cycloid arrangement of BFO produces zero net magnetic moment [7, 37, 38, 44]. This is responsible for the anti-ferromagnetic nature of BFO in bulk form. Disturbing the spin cycloid structure results in non-zero net magnetization in BFO. This distortion will induce ferromagnetism in BFO. It can be achieved by doping BFO with suitable materials. One more way for inducing or enhancing ferromagnetism in a material is by reducing the particle size to the nanoscale. The particle size can be declined to nanoscale by reducing the sintering temperature to 600 °C in the case of doped and undoped BFO. The spin

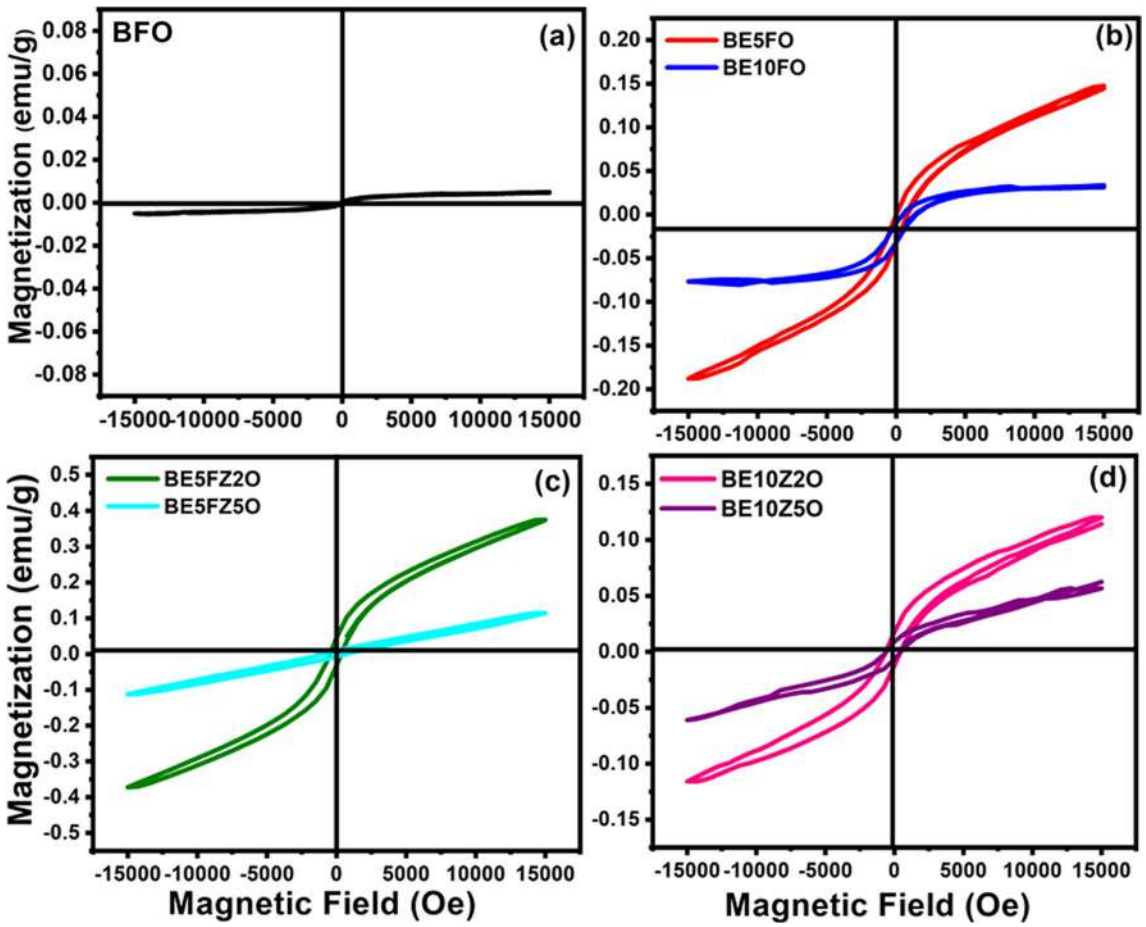

Fig. 4 Magnetic hysteresis curves of the **a** BFO, **b** BE5FO and BE10FO, **c** BE5FZ2O and BE5FZ5O and **d** BE10FZ2O and BE10FZ5O

motion of erbium's 4f electrons collaborates with that of iron's 3d electrons. This collaboration leads to the detachment of antiferromagnetic coupling between the Fe^{3+} ions to some extent. In addition to the overlapping spin cycloid arrangement (62 nm), Dzyaloshinskii-Moriya (DM) interaction forced a small adjustment in the ideal anti-parallel spin alignments. This might be the cause of ferromagnetic occurrence inside BFO. The other reasons are decreased distortion degree of rhombohedral structure and the geometrical placements of non-magnetic ions in the anti-ferromagnetic lattice of Fe^{3+} ions [45–47].

In this work, (5%/10%) of erbium has been substituted in the place of bismuth and (2%/5%) of zirconium in the iron place. Table 2 elaborates on the magnetic factors of the pure BFO and dopant-substituted BFO. The remanence ratio can be calculated by dividing the remnant magnetization value by the saturation magnetization of a particular sample. If the remanence ratio (M_r/M_s) of a particular material is less than 0.5, then that material is a soft material but for hard material, the ratio will be greater than 0.5 [48]. The remanence ratio of all the samples is lower than 0.5. Thus, all the samples exhibit soft magnetic nature. On doping 5% of erbium in the bismuth place of BFO, the magnetization has increased compared to undoped BFO (Table 2). On increasing the erbium concentration from 5 to 10%, the magnetization has got lowered slightly but is still greater than that of pure BFO. The introduction of zirconium in the iron place along with erbium in the bismuth place has enormously enhanced the magnetic parameters of BFO (Table 2). Again on increasing the zirconium concentration to 5%, the magnetization deteriorated. However, Dopants amplified the magnetization of the bismuth ferrite system (Table 2). Dissimilarity in the ionic radii of bismuth ions and erbium ions delivered better magnetic curves relative to undoped BFO (Fig. 4). Therefore, introducing the dopant of a higher ionic radius than the parent ion might have caused more distortion in the spin cycloid structure of BFO. And by increasing the concentration of zirconium at the Fe site, the magnetic parameters of the samples have reduced but are still higher than undoped BFO (Table 2). So, spin cycloid distortion that happened inside the BFO might be the reason for enhanced magnetism on doping erbium 5% and 2% zirconium. The reversal of the spin cycloid distortion might have happened on increasing the doping concentration of zirconium beyond 5%. This might be the reason for the reduction in ferromagnetic parameters of BE5FZ5O and BE10FZ5O compared to other doped cases though it is not lower than that of BFO. Thus the sample BE5FZ2O yields a better saturated ferromagnetic loop with a greater remnant magnetization value of 95×10^{-3} emu/g compared to the other samples and undoped BFO.

From Table 3, it is obvious that the remnant magnetization obtained in this current work is greater than that obtained by Yong-tao Li et al. [10]. Radheshyam Rai et al. [27] acquired a slightly high magnetization value compared to this work. But, the concentration of erbium is 30% in that work [27] and also the sample faced a structural transition. C. Nayek et al. [26] recorded higher magnetization value as they performed the experiment at 300 K. On the whole, in this work, 5% erbium at the bismuth place and 2% zirconium at the iron place have provoked the magnetic nature in the bismuth ferrite system compared to the other works [10, 26, 27].

Table 3 Comparative table of this work and other works

S. no	Dopants and concentration	M_r (emu/g)	Reference number
1	5% erbium at Bi site	**0.095**	Current work
2	5% erbium at Bi site (at 300 k)	0.612	[26]
3	30% erbium at Bi site	0.1	[27]
4	5% erbium at Bi site	0.09	[28]

Bold value in the table is the value from the present work

3.4 Electronic band structure calculations

The electronic band structure calculations were performed through FP-LAPW method as implemented in the WIEN2k code [49, 50] for all six compounds. The modified Becke Johnson (mBJ) exchange potential approach was applied for all the calculations as this approach enhances the band gap which is underestimated in the GGA method. Self-consistent spin-polarized calculations were executed for all the compounds using the lattice parameters found in this experimental work. The electronic band structure and the energy band values were calculated. For core states and valence states were treated with the full relativistic effects and the scalar relativistic approximation respectively. The energy convergence limit was set at 10^{-5} Ry and $R_{MT}K_{max}$ which limits the application of the basis sets is fixed at 7.0. Self-consistency was obtained using $8 \times 8 \times 8$ k mesh in the irreducible Brillouin zone. The harmonic expansion is set as $l_{max} = 10$ with $G_{max} = 12$ in charge density Fourier expansions.

The electronic band structures of the two compounds are given in Fig. 5. The band gap values of six compounds are given in Table.4. In the band structure, the Fermi energy level E_F is set at 0 eV and the lowest energy band below 10 eV is Bi-6 s. The bands above this from -8 eV to E_F are mainly from Fe-t_{2g} and O-2 s like states which show a strong hybridization between Fe-d and O-2 s states. The valence bands are O-2 s bands. Just above E_F, the Fe—e_g band occupies up to 4 eV, which forms the conduction band and above this, Bi-6p energy states are mainly located. The variation in the band gap (Table.4) is due to the substitutional defects at Bi-site and Fe-site introduced due to doping at these sites

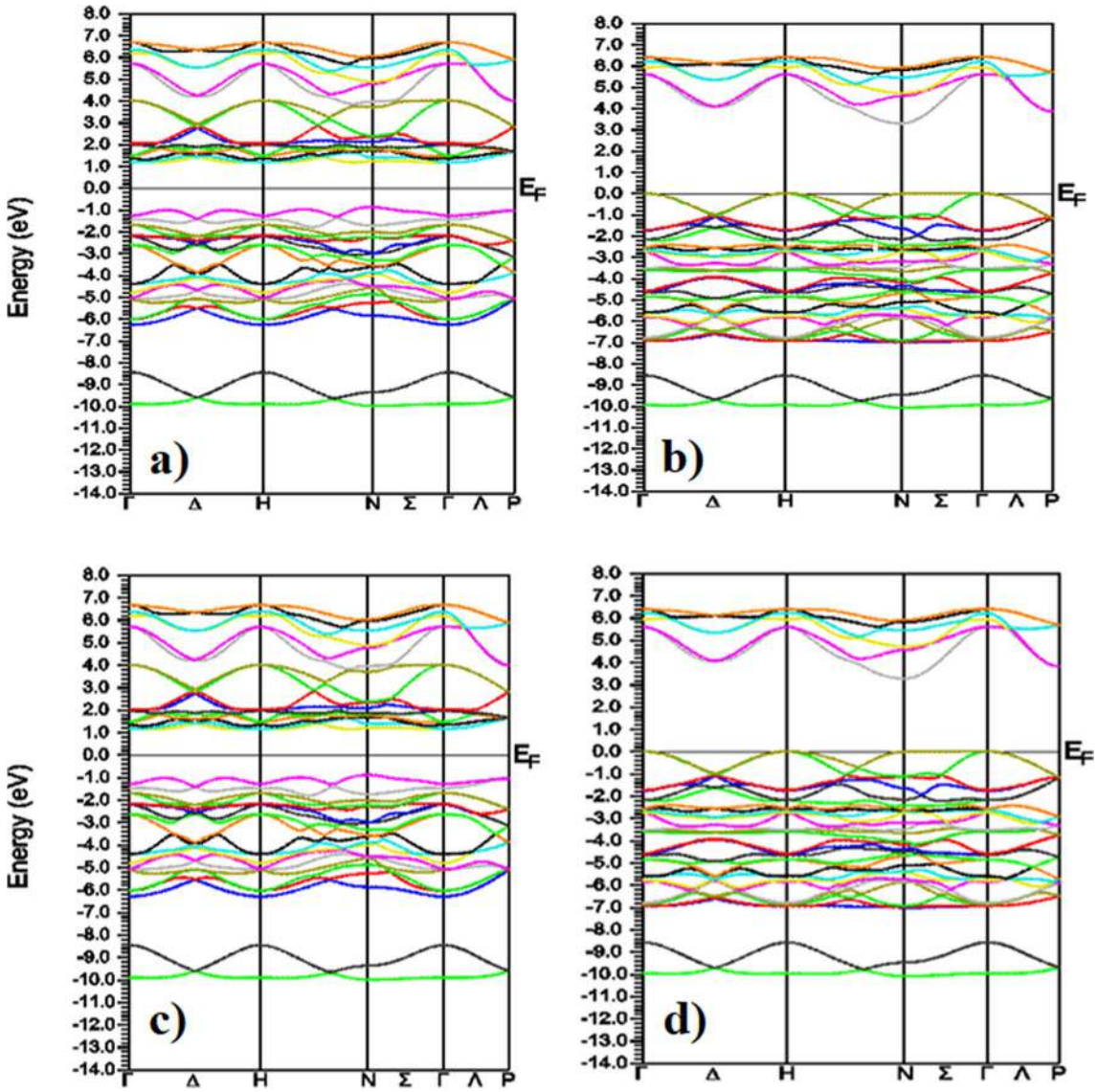

Fig. 5 The band structures of BE5FZ5O for **a** spin down **b** spin up and the band structures of BE10FZ5O for **c** spin down **d** spin up

Table 4 The band gap values and the magnetic moment values obtained through the band structure calculations

Compound	Energy gap (eV)		Magnetic moment of Fe (μ_B)
	Spin down	Spin up	
BFO	2.039	3.338	4.1983
BE5FO	2.037	3.336	4.1985
BE10FO	2.028	3.321	4.193
BE5FZ2O	2.035	3.328	4.194
BE10FZ2O	2.037	3.334	4.195
BE5FZ5O	2.037	3.333	4.1945
BE10FZ5O	2.027	3.312	4.192

by rare earth Er and Transitional metal (TM) Zr respectively. The spin-down energy gaps are comparable with that of the experimental values [51]. The energy gap changes due to the shift of e_g bands of Fe atoms with respect to E_F. This shift is the evidence of Jahn Teller distortion which occurs in the octahedral complexes. Thus the Jahn Teller distortion due to Fe-site substitution is understood from the band structure. Jahn–Teller distortions are most often associated with transition metal centers and so when these centers are substituted by another TM, the position of the energy bands, in particular, e_g bands are shifted and hence there is a change in the band gap values. It is known that Jahn–Teller distortion is due to the electrostatic interactions between the electrons of the ligand (Oxygen atoms) and the lobes of the d-orbital (e_g) of the TM atom. The shift of e_g states is the indication

of the FeO_6 octahedron rotation and so there is a variation in the magnetic parameters. The calculated magnetic moment values of Fe for all the compounds are given in Table and these values change for various substitutions with notable changes observed for the dual-doped compounds. This is clear evidence that the dual doping distorts the spin cycloid structure of $BiFeO_3$ by FeO_6 octahedral rotation to give enhanced magnetic parameters.

4 Conclusion

Different concentrations of erbium and zirconium-doped bismuth ferrite were synthesized using sol–gel technology. The proper placement of the dopants inside the bismuth ferrite system was ascertained via the XRD pattern, the refinement details, FESEM images, and EDAX analysis of the samples. On introducing zirconium along with erbium, the magnetic behavior of BFO started to scale up. But on raising the zirconium content beyond 5%, the scaled-up magnetization faced a downfall. Similarly, on scaling up zirconium content the leakage current density again raised in BFO. The contribution of the dopants such as erbium and zirconium in enhancing the magnetic and electrical of BFO was enormous. On the whole, the multifunctional behaviors were enriched including 5% erbium in the bismuth place and 2% zirconium in the iron place of bismuth ferrite. The simultaneous introduction of erbium and zirconium enhanced further the multifunctional aspects of BFO. Especially, doping 5% erbium and 2% zirconium in the bismuth ferrite setup offered superior magnetization. The electronic band structure calculations of these compounds provide a supporting evidence for the spin cycloid distortion for the dual-doped compounds.

Author contributions Material preparation, data collection, investigation, Validation, writing-original draft, and analysis were performed by DLS. Conceptualization, methodology, software, validation, formal analysis, resources, writing review and editing, visualization, and supervision were undertaken by IBSB. Conceptualization, methodology, validation, formal analysis, review, editing, and visualization were performed by RR. Conceptualization, methodology, validation, formal analysis and review were done by GG and MHM. All authors read and approved the final manuscript.

Funding The authors declare that no funds, grants, or other support were received during the preparation of this manuscript.

Data availability All data generated during this study are included in this published article.

Declarations

Conflict of interest The authors have no relevant financial or non-financial interests to disclose.

Ethical standards The authors declare that they have no known competing financial interests or personal relationships that could have appeared to influence the work reported in this paper. This research doesn't involve any human and animal participation.

References

1. A. Beniwal, J.S. Bangruwa, R. Walia, V. Verma, A systematic study on multiferroics $Bi_{1-x}Ce_xFe_{1-y}Mn_yO_3$: structural, magnetic and electrical properties. Ceram. Int. **42**, 10373–10379 (2016)
2. Y.-P. Jiang, X.-G. Tang, Q.-X. Liu, D.-G. Chen, C.-B. Ma, Improvement of electrical conductivity and leakage current in co-precipitation derived Nd-doping $BiFeO_3$ ceramics. J. Mater. Sci. **25**, 495–499 (2014)
3. Q. Chuye, M. Yuhui, H. Yumin, T. Xingxing, L. Mengjia, M. Weiwei, Z. Jian, Y. Jianping, L. Xingao, H. Wei, Effect of Nd substitution for Ca on crystal structure, optical and magnetic properties of multiferroic $Bi_{0.9}Ca_{0.1}FeO_3$. J. Alloys Compd. **635**, 272–277 (2015)
4. H. Zhongquiang, M. Li, Y. Yang, J. Liu, L. Pei, J. Wang, X. Liu, Y. Benfang, X. Zhao, Effects of Nd and high-valence Mn co-doping on the electrical and magnetic properties of multiferroic $BiFeO_3$ ceramics. Solid State Commun. **150**, 1088–1091 (2010)
5. X. Yan, G. Tan, W. Liu, H. Ren, Ao Xia", Structural, electric and magnetic properties of Dy and Mn co-doped $BiFeO_3$ thin films". Ceram. Int. **41**, 3202–3207 (2015)
6. P. Tang, D. Kuang, S. Yang, Y. Zhang, Structural, morphological and multiferroic properties of the hydrothermally grown gadolinium (Gd) and manganese (Mn) doped sub-micron bismuth ferrites. J. Alloys Compd. **656**, 912–919 (2016)
7. D. Wang, M. Wang, F. Liu, Y. Cui, Q. Zhao, H. Sun, H. Jin, M. Cao, Sol–gel synthesis of Nd-doped $BiFeO_3$ multiferroic and its characterization. Ceram. Int. **41**, 8768–8772 (2015)
8. N. Hernandez, V.A. Gonzalez-Gonzalez, I.B. Dzul-Bautista, J. Gutierrez, J.M. Barandiaran, I. Ruiz de Larramendi, R.F. Cienfuegos-Pelaes, U. Ortiz-Mendez, Nd and Sc co-doped BiFeO3 nanopowders displaying enhanced ferromagnetism at room temperature. J. Alloys Compd. **638**, 282–288 (2015)
9. M. Arora, S. Chauhan, P.C. Sati, M. Kumar, S. Chhoker, Evidence of spin-two phonon coupling and improved multiferroic behavior of Bi1−xDyxFeO3 nanoparticles. Ceram. Int. **40**, 13347–13356 (2014)
10. Y.-T. Li, H.-G. Zhang, X.-G. Dong, X.-P. Ge, X.-H. Yan, Qi. Li, The study of electronic structures for $Bi_{0.95}R_{0.05}FeO_3$ (R = Ce, Eu, Er) multiferroic material. J. Electron. Spectrosc. Relat. Phenom. **196**, 121–124 (2014)
11 A.K. Ghosh, H. Kevin, B. Chatterjee, G.D. Dwivedi, A. Barman, H.D. Yang, S. Chatterjee, Effect of Sr-doping on multiferroic properties of $Bi_{0.8}La_{0.2}Fe_{0.9}Mn_{0.1}O_3$. Solid State Commun. **152**, 557–560 (2012)
12. G. Dong, G. Tan, Y. Luo, W. Liu, H. Ren, Ao. Xia, Structural transformation and multiferroic properties of single-phase $Bi_{0.89}Tb_{0.11}Fe_{1-x}Mn_xO_3$ thin films. Appl. Surf. Sci. **290**, 280–286 (2014)
13. M. Arora, M. Kumar, Electron spin resonance probed enhanced magnetization and optical properties of Sm doped $BiFeO_3$ nanoparticles. Mater. Lett. **137**, 285–288 (2014)
14. Y. Zhang, Z. Wang, J. Zhu, X. He, H. Xue, S. Li, W. Mao, Pu. Yong, X. Li, Ferroelectric polarization effect on the photocatalytic activity of $Bi_{0.9}Ca_{0.1}FeO_3$/CdS S-scheme nanocomposites. J. Environ. Sci. **124**, 310–318 (2023)

15 W. Mao, Q. Yao, N. Liu, H. Shu, J. Zhu, Y. Pu, X. Li, Effect of Ca doping on photovoltaic effect of $BiFeO_3$. Appl. Phys. A **127**, 508 (2021)

16. Z. Wang, X. Yang, X. He, H. Xue, X. Wang, H. Dong, J. Zhu, W. Mao, Xu. XingLiang, X. Li, Roles of oxygen vacancy and ferroelectric polarization in photovoltaic effects of $BiFeO_3$ based devices. Solid State Commun. **360**, 115042 (2023)

17. Y. Zheng, G. Tan, Ao. Xia, H. Ren, High magnetic and electric properties of co-doped $Bi_{0.9}Er_{0.1}Fe_{1-x}Co_xO_3$ films. Mater. Lett. **173**, 18–21 (2016)

18. S. Acharya, S. Sutradhar, J. Mandal, K. Mukhopadhyay, A.K. Deb, P.K. Chakrabarti, "Sol–gel derived nanocrystalline multiferroic $BiFeO_3$ and $R_{3þ}$ (R=Er and Tm) doped therein: magnetic phase transitions and enhancement of magnetic properties. J. Magn. Magn. Mater. **324**, 4209–4218 (2012)

19. Y. Zheng, G. Tan, Ao. Xia, H. Ren, Structure and multiferroic properties of multi-doped $Bi_{1-x}Er_xFe_{0.96}Mn_{0.02}Co_{0.02}O_3$ thin films. J. Alloys. Compd. **684**, 438–444 (2016)

20. Y. Ma, W. Xing, J. Chen, Y. Bai, S. Zhao, H. Zhang, The influence of Er, Ti co-doping on the multiferroic properties of $BiFeO_3$ thin films. Appl. Phys. A **122**, 63–71 (2016)

21 P. Pandit, S. Satapathy, P. Sharma, P.K. Gupta, S.M. Yusuf, V.G. Sathe, Structural, dielectric and multiferroic properties of Er and La substituted $BiFeO_3$ ceramics. Bull. Mater. Sci. **34**, 899–905 (2011)

22. Y. Han, W. Mao, C. Quan, X. Wang, J. Yang, T. Yang, X. Li, H. Wei, Enhancement of magnetic and ferroelectric properties of $BiFeO_3$ by Er and transition element (Mn, Co) co-doping. Mater. Sci. Eng. B **188**, 26–30 (2014)

23. J. Zhao, S. Liu, W. Zhang, Z. Liu, Z. Liu, Structural and magnetic properties of Er-doped $BiFeO_3$ nanoparticles. J Nanopart. Res. **15**, 1969–1975 (2013)

24. W. Xing, Y. Ma, Y. Bai, S. Zhao, Enhanced ferromagnetism of Er-doped $BiFeO_3$ thin films derived from rhombohedral-to-orthorhombic phase transformations. Mater. Lett. **161**, 216–219 (2015)

25. G. Naveena, D. Ravinder, T.A. Babu, B.R. Reddy, E. Sumalatha, K. Vani, T. Rajender, N.V. Krishana-Prasad, Low-temperature magnetic properties of erbium doped bismuth nano-ferrites. J. Mater. Sci. Mater. Electron. **32**, 18224–18230 (2021)

26. C. Nayek, A. Tamilselvan, Ch. Thirmal, P. Murugavel, S. Balakumar, Origin of enhanced magnetization in rare earth doped multiferroic bismuth ferrite. J. Appl. Phys. **115**, 073902 (2014)

27 R. Rai, S.K. Mishra, N.K. Singh, S. Sharma, A.L. Kholkin, Preparation, structures, and multiferroic properties of single-phase $BiRFeO_3$, R ¼ La and Er ceramics. Curr. Appl. Phys. **11**, 508–512 (2011)

28 W. Xing, Y. Ma, Z. Ma, Y. Bai, J. Chen, S. Zhao, Improved ferroelectric and leakage current properties of Er-doped BiFeO3 thin films derived from structural transformation. Smart Mater. Struct. **23**(8), 08503 (2014)

29. M. Kumar, M. Arora, S. Chauhan, S. Joshi, Raman spectroscopy probed spin-two phonon coupling and improved magnetic and optical properties in Dy and Zr substituted $BiFeO_3$ nanoparticles. J Alloys Compd. **692**, 236–242 (2017)

30. W. Ting, S.H. Song, Investigations on the structural, magnetic and optical properties of Sr–Zr co-doped $BiFeO_3$ multiferroic powders. J. Mater. Sci. Mater. Electron. **29**, 5566–5572 (2018)

31. H. Liu, Z. Liu, K. Yao, Study of the electric properties of $BiFe_{1-x}Zr_xO_{3+d}$ films prepared by the sol–gel process. Phys. B **391**, 103–107 (2007)

32. J. Xie, Y. Liu, C. Feng, X. Pan, Preparation and characterization of Zr^{4+}-doped $BiFeO_3$ ceramics. Mater. Lett. **96**, 143–145 (2013)

33. K. Sen, S. Thakur, K. Singh, A. Gautam, M. Singh, Room-temperature magnetic studies of La-modified $BiFeO_3$ ceramic. Mater. Lett. **65**, 1963–1965 (2011)

34. A. Ablat, Wu. Rong, M. Mamat, J. Li, E. Muhemmed, C. Si, Wu. Rui, J. Wang, H. Qian, K. Ibrahim, Structural analysis and magnetic properties of Gd doped $BiFeO_3$ ceramics. Ceram. Int. **40**, 14083–14089 (2014)

35. C.M. Raghavan, J.W. Kim, S.S. Kim, Structural and ferroelectric properties of chemical solution deposited (Nd, Cu) co-doped $BiFeO_3$ thin film. Ceram. Int. **39**, 3563–3568 (2013)

36. Y.-J. Zhang, H.-G. Zhang, J.-H. Yin, H.-W. Zhang, J.-L. Chen, W.-Q. Wang, G.-H. Wu, Structural and magnetic properties in $B_{i1-x_R}xFe_O3$ (x=0–1, R=La, Nd, Sm, Eu and Tb) polycrystalline ceramics. J. Magn. Magn. Mater. **322**, 2251–2255 (2010)

37. J. Liu, M. Li, L. Pei, J. Wang, Yu. Benfang, X. Wang, X. Zhao, Structural and multiferroic properties of the Ce-doped $BiFeO_3$ thin films. J. Alloys Compd. **493**, 544–548 (2010)

38 D. Lakshmi, S.I.B. Shameem-Banu, Multiferroism and magnetoelectric coupling in single-phase Yb and X (X = Nb, Mn, Mo) co-doped $BiFeO_3$ ceramics. J. Sol-Gel Sci. Technol. **89**, 713–721 (2019)

39. D. Lakshmi, S.I.B. ShameemBanu, Tailoring the multiferroic properties of BiFeO3 by co-doping Er at Bi site with aliovalent Nb, Mn and Mo at Fe site. Appl. Ceram. Technol. **16**, 1622–1631 (2019)

40. A.S. Priya, I.B. ShameemBanu, M. Chavali, Doping on the room temperature multiferroic properties of $BiFeO_3$ ceramics. Arab. J. Sci. Eng. **40**, 2079–2084 (2015)

41. I.B. Shameem-Banu, D.S. Lakshmi, Simultaneous enhancement of room temperature multiferroic properties of $BiFeO_3$ by Nd doping at Bi site and Co doping at Fe site. J. Mater. Sci. Mater. Electron. **28**, 16044–16052 (2017)

42. P. Priyadharsini, A. Pradeep, B. Sathyamoorthy, G. Chandrasekaran, Enhanced multiferroic properties in La and Ce co-doped $BiFeO_3$ nanoparticles. J. Phys. Chem. Solids **75**, 797–802 (2014)

43. G.F. Cheng, Y.J. Ruan, Y.H. Huang, X.S. Wu, Structural phase transition and thermal expansion in $Bi_{12.5x}Pr_{1.5x}Ba_xFeO_3$ ceramics. J. Alloys Compd. **566**, 235–238 (2013)

44. Hu. Zhongqiang, M. Li, J. Liu, L. Pei, J. Wang, Yu. Benfang, X. Zhao, Structural transition and multiferroic properties of Eu-doped $BiFeO_3$ thin films. J. Am. Ceram. Soc. **93**(9), 2743–2747 (2010)

45. T. Soltani, B.-K. Lee, Enhanced formation of sulfate radicals by metal-doped $BiFeO_3$ under visible light for improving photo-Fenton catalytic degradation of 2- chlorophenol. Chem. Eng. J. **313**, 1258–1268 (2017)

46 A. Kumar, K.L. Yadav, Enhanced magnetodielectric properties of single-phase $Bi_{0.95-x}La_{0.05}LuxFeO_3$ multiferroic system. J. Alloys Compd. **554**, 138–141 (2013)

47 O. García-Zaldívar, S. Díaz-Castañón, F.J. Espinoza-Beltran, M.A. Hernandez-Landaverde, G. López, J. Faloh-Gandarilla, F. Calderón-Piñar, $BiFeO_3$ codoping with Ba, La and Ti: magnetic and structural studies. J. Adv. Dielect. **5**, 1550034 (2015)

48 P. Uniyal, K.L. Yadav, Enhanced magnetoelectric properties in $Bi_{0.95}Ho_{0.05}FeO_3$ polycrystalline ceramics. J. Alloys Compd. **511**, 149–153 (2012)

49. P. Blaha, K. Schwarz, G.K.H. Madsen, D. Kvasnicka, J. Luitz, R. Laskowski, F. Tran, L. Marks, *WIEN2k: An Augmented Plane Wave Plus Local OrbitalsProgram for Calculating Crystal Properties* (Vienna University of Technology, Austria, 2001)

50. P. Blaha, K. Schwarz, F.T.R. Laskowski, K.H.G. Madsen, L.D. Marks, WIEN2k: an APW+lo program for calculating the properties of solids. J. Chem. Phys. **152**, 074101 (2020)

51. T. Higuchi, Y.-S. Liu, P. Yao, P.-A. Glans, J. Guo, Phys. Rev. B. **78**, 085106 (2008)

J Mater Sci: Mater Electron (2024) 35:368

Photocatalytic activity of Ag doped $CuFe_2O_4$ nanoparticles supported on reduced graphene oxide for the degradation of organic dyes under visible light irradiation

M. Sangeetha[1,*], S. Ambika[2], D. Madhan[3], and S. Vadivel[4,*]

[1] *Department of Chemistry, E.M.G. Yadava Women's College, Madurai, Tamilnadu 625014, India*
[2] *Department of Chemistry, M. Kumarasamy College of Engineering (Autonomous), Karur, Tamilnadu 639114, India*
[3] *Department of Physics, Velammal College of Engineering and Technology (Autonomous), Madurai, Tamilnadu 625009, India*
[4] *Department of Physics, Saveetha School of Engineering, Saveetha Institute of Medical and Technical Sciences (SIMATS), Thandalam, Chennai, Tamil Nadu 602105, India*

Received: 11 July 2023
Accepted: 27 January 2024

ABSTRACT

This study aimed to synthesize a new magnetic photocatalytic nanosystem composed of Ag-$CuFe_2O_4$@rGO and to investigate its photodegradation efficiency for two organic pollutants of methylene blue (MB) 4-nitrophenol (4-NP) under visible light irradiation. The synthesized Ag-$CuFe_2O_4$@rGO nanocomposites were fully characterized by XRD, TEM, HRTEM, XPS, FTIR, UV and PL analysis which shows well controlled small sized (~ 10 nm from Scherrer formula) $CuFe_2O_4$ NPs with dense and compact loading over rGO sheets. XRD results reveal that cubic spinel structure of $CuFe_2O_4$ with nanoparticles (5–10 nm) in shape, which is uniformly, decorated on the surface of the rGO sheets. The band gap energy values of $CuFe_2O_4$, Ag-$CuFe_2O_4$ and Ag-$CuFe_2O_4$@rGO nanoparticles are calculated as 2.76, 2.27 and 2.03 eV, respectively. After incorporation of Ag and rGO into $CuFe_2O_4$, the specific surface area was significantly improved to 154 m^2/g for Ag-$CuFe_2O_4$@rGO nanocomposite. Upon inclusion of the photocatalysts, photodegradation efficiency increased and the Ag-$CuFe_2O_4$@rGO composite showed the highest efficiency towards MB (99.5%) and 4-NP (88.7%) followed by the Ag-$CuFe_2O_4$. With addition of rGO, the electron-hole recombination declines, thus resulting in a more optimum photocatalytic performance. The rate constant of Ag-$CuFe_2O_4$@rGO composite was found to be 0.0985 min^{-1} for MB and 0.0542 min^{-1} for 4-NP, respectively. Moreover, the effect of pH, catalyst dosage, and long term stability was thoroughly determined. The improved performance could be attributed to the positive synergistic effect between $CuFe_2O_4$ nanoparticles and rGO. The samples were further evaluated by EIS and dynamic photoresponse in order to

Address correspondence to E-mail: sangeethamanirevathi@gmail.com; vadivel.physics@gmail.com

https://doi.org/10.1007/s10854-024-12076-8
Published online: 21 February 2024

identify the charge transfer efficiency. The improved photocatalytic mechanism was also explained briefly.

1 Introduction

The disposal of organic pollutants into water resources is an issue of environmental significance, particularly due to the scarcity of potable water facing our contemporary society [1]. Synthetic dyes are considered one of the major aquatic pollutants because of their non-biodegradability, toxicity and unpleasant coloring. Great efforts have been made to resolve these problems, such as chemical oxidation [2], solvent extraction [3], adsorption [4], flotation [5] and photocatalytic degradation [6]. Photocatalytic degradation has been extensively studied as a mean of controlling recalcitrant pollutants such as dyes, and demonstrated successful performances in many cases due to its low cost, simplicity and high efficiency as well as low secondary pollution. Titanium dioxide (TiO_2), as a photocatalyst for pollutant degradation and solar energy conversion, has been widely studied. The magnetic property of ferrite makes it attainable for the regeneration of catalyst which advance the economic feasibility of this process. However, its large band gap (3.2 eV for anatase) and low quantum yield determined that it was only active under ultraviolet (UV) light irradiation. Therefore, considerable efforts have been devoted to exploring visible light-responsive photocatalysts and suppressing the recombination rate of photo-generated carriers [7, 8].

Several magnetic nanoparticles for use in chemical synthesis processes have been developed with recycling and reusability in mind. One of the finest nanomaterials for catalytic processes is ferrites, which have the general formula MFe_2O_4 (M is divalent transition metal, such as Mn, Fe, Co, Ni, Cu, Zn, etc.). This is since the characteristics of ferrites may be modified by switching out the identity of the divalent M^{2+} ion. $CuFe_2O_4$ stands out among ferrites for its abundant supply, cheap cost, eco-friendliness, and highly active Cu(II) cation for catalysis reaction. Steam reforming, nitroaromatic reducing, dye destruction, acyloxylation, phenol hydroxylation, and other catalytic processes have all employed $CuFe_2O_4$ NPs in recent years [9–12]. Moreover, the bulk electron transfer in $CuFe_2O_4$ can be occurred by electron hopping mechanism. The large abundance of Cu and Fe in nature, structural stability and low band gap make it attractive to be used as a platform to develop the photocatalyst for degradation various toxic pollutants. However, the fast recombination of excited state CB electrons and VB holes without initiating the photocatalytic activity limits $CuFe_2O_4$ in catalytic applications. Many approaches of preventing the photo-induced electron–hole recombination have been reported, such as using $CuFe_2O_4$ composites with transition metal oxides [13], noble metals [14], and carbon nanotubes (CNT) [15, 16]. Graphene oxide (GO) could be considered as graphene functionalized by hydroxyl, carboxylic acid, and epoxide groups [17, 18], and their properties are sensitive to chemical doping, adsorbed or bound species [19]. Generally, an electron energy gap could be varied by oxidation of graphene, and the value of the energy gap depends on oxidization degree of graphene and species of oxygen-containing groups. It means that GO could change from conducting to insulating by tuning the C/O ratios [20]. In particular, the superior electrical conductive rGO sheets can function as an electron collector and transporter to lengthen the charge carrier lifetime, leading to improvements in the photocatalytic performance. The rGO sheets also extract organic pollutants from the solution to increase the contact area between the catalysts. Moreover, the $CuFe_2O_4$ nanoparticles prevent the restacking of rGO sheets during operation to give high performance and reusable catalysts. TiO_2/graphene, CuO/graphene, Fe_2O_3/graphene, ZnO/graphene, Fe_3O_4/graphene, NiO/graphene, and Mn_3O_4/graphene are only few of the oxide/graphene composites that have been reported on [21–24]. But, there is no report about Ag doped CuFe2O4/rGO nanocomposite as photocatalytic performance. To the best of the author knowledge this is the first report on photocatalytic activity of Ag-$CuFe_2O_4$@rGO composite photocatalyst under visible light irradiation. In the present work, chemically reduced GO was utilized as a support for $CuFe_2O_4$ nanoparticles ($CuFe_2O_4$@rGO). The XRD and TEM studies of Ag-$CuFe_2O_4$@rGO reveal that $CuFe_2O_4$ is

well crystallized and distributed uniformly onto the GO. The activity test of Ag-$CuFe_2O_4$@rGO shows that the composite has a good catalytic effect on the degradation of different dyes such as MB and 4-NP, and they have been chosen to study catalytic performance in different conditions. The results demonstrates that the prepared Ag-$CuFe_2O_4$@rGO composite showed high degradation efficiency, apparent constant, long term stability and good electrochemical performance than compared with bare $CuFe_2O_4$. This could be due to the charge transfer process of $CuFe_2O_4$ significantly improved by metallic Ag and conductive rGO. The Ag nanoparticles (Ag NP), which display the SPR at wavelengths of 400 nm, are anchored onto the rGO surface. Secondly, the nobel metal Ag, on the other hand, contributes to the activity by forming a Schottky barrier at the metal − semiconductor interface. This Schottky barrier can serve as an effective electron trap causing high density of states at the Fermi level (EF) of the interface and minimizing the charge carrier recombination. This electronic factor contributes to charge separation and utilization.

2 Experimental section

2.1 Chemical used

All the required chemicals of analytical grade were bought from Sigma-Aldrich Company. Iron nitrate nonahydrate ($Fe(NO_3)_3{\cdot}9H_2O$, ≥ 98%), Copper(II) nitrate trihydrate. $Cu(NO_3)_2{\cdot}3H_2O \geq 99.9\%$), hydrogen peroxide ($H_2O_2$, 35%), ammonia ($NH_3$, ≥ 99.98%), Sulphuric acid (H_2SO_4, 98%), Silver nitrate ($AgNO_3$, 99.9%), Graphene powder (99%)and Potassium nitrate (KNO_3, > 99%).

2.2 Synthesis of $CuFe_2O_4$, and Ag-$CuFe_2O_4$

Distilled water was used to make a 50 mL solution of copper nitrate 0.01 M and iron nitrate 0.02 M. The two solutions were combined and stirred vigorously with a magnet for 30 min. The pH was adjusted by adding ammonia, and the solution was stirred for another 30 min before being left to settle. The pH of the solution was measured by using digital pH meter and the values are 6 and 9.5 for before and after adding ammonia solution. The molarity of 25% (w/v) NH_3 solution is 14.7 mol /L or 14.7 M. The suspension was heated for 2 h at 80 °C as mentioned in Fig. 1a. The sample was dried in an oven and the dry material was crushed and then calcinated for 1 h at 500 °C. A suitable amount of silver nitrate (5% Ag doping, 0.05 g in 50 ml of distilled water) was prepared and then added to a solution of copper ferrite. The same procedure was followed further for the synthesis of copper ferrite. The product was silver-doped copper ferrite.

2.3 Synthesis of Ag-$CuFe_2O_4$@rGO

To begin, rGO was made using Hummer's approach, as described in the prior work [25]. The ultrasonication method was utilized to create a nanocomposite

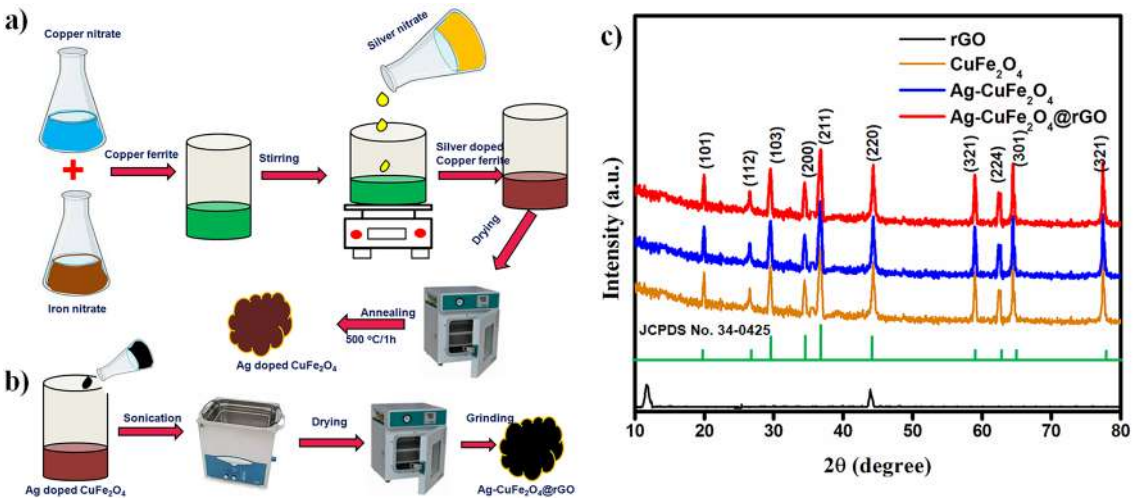

Fig. 1 **a** Schematic representation of the synthesis process of Ag doped $CuFe_2O_4$, **b** Ag doped $CuFe_2O_4$/rGO composites, **c** Powder XRD pattern of rGO, $CuFe_2O_4$, Ag-$CuFe_2O_4$, Ag-$CuFe_2O_4$@rGO

of silver-doped copper ferrite (Ag-$CuFe_2O_4$) and reduced graphene oxide (rGO). Fifty milliliters of distilled water had 0.5 g of Ag-$CuFe_2O_4$ and 0.05 g of rGO added to it. Both solutions were sonicated for an hour at 60 degrees Celsius. The two solutions were then combined by dissolving them and sonicating the combination for 2 h, as illustrated in Fig. 1b. Finally, after drying at 80 °C for a whole day, it was put away.

2.4 Characterization techniques

X-ray diffraction (XRD) pattern was performed on a diffractometer (Rigaku Miniflex, Tokyo, Japan) using Cu Kα radiation (λ = 1.5406 Å) at a scan rate of 0.05 2°/s. A scanning electron microscope (SEM), model JSM 6700 F, at an accelerating voltage of 10 kV and a transmission electron microscope (TEM), model CM200 (Philips, Eindhoven, The Netherlands), at the opening voltage of 20–200 kV were used to investigate the morphology of the materials. An Autosorb-IQ-MP automatic gas analyser at 77 k was applied to calculate the specific surface area of the samples. Laser Raman spectra were recorded on Renishaw in-Via Raman systems equipped with a 514 nm line of an air ion laser as the excitation source. X-ray photoelectron spectroscopy (XPS) spectra were acquired using an ESCALAB 250 photoelectron spectrometer (Waltham, MA, USA). The UV absorption spectra of the sample were performed on a UV–VIS spectrophotometer (Shimadzu UV 3600, Japan). Electrochemical measurements were performed with a standard three-electrode setup (The Multi Autolab PGSTAT204).

2.5 Photocatalytic set up

The degradation of methylene blue (MB) and 4-nitrophenol (4-NP) solutions was used to evaluate the photocatalytic activity of complex Ag-$CuFe_2O_4$@rGO. The photocatalytic reactions were carried out using the procedure stated above using visible light irradiation (350–750 nm). A 400 W lamp (OSRAM, Germany) was used as a light source. A 5 mL portion of 1×10^{-5} M MB was placed in a quartz cell containing glass material (2 pieces, approximately 1 × 1 cm). Special attention was paid for contacting the dye solution and UV light with glass surface and solutions were shaken continuously. The photo catalysts were irradiated with visible light for different timings (0, 15, 30, 45 and 60 min) with a regular interval of 15 min. The UV–Vis–NIR measurement was performed using PerkinElmer lambda 25 spectrophotometer to determine the absorption. The absorption of MB at 664 nm and 4-NP at 220 nm was monitored over 60 min in the presence and absence of light or glass material. At regular intervals of irradiation, aliquots of 2 mL sampled and then absorption was measured in terms of change in intensity at 664 and 220 nm. The percentage removal of phenol was calculated using the following equation: Removal % = ($C°$ — Ct)/ $C°$ × 100, where $C°$ is the initial concentration of dye in the solution, Ct is the residual concentration of dye at a specific time t. The kinetics of the degradation reactions were modeled using the following first-order expression: In Ct/Co = —kt, where $C°$ is the initial concentration of phenol in the solution, is the residual concentration of phenol at a specific time t, and k is the rate constant which can be calculated from the slope of ln (Ct/Co) versus time.

3 Results and discussion

3.1 XRD analysis

In Fig. 1c, we can see the powder XRD diffraction patterns of the final GO, $CuFe_2O_4$, Ag-$CuFe_2O_4$, and Ag-$CuFe_2O_4$@rGO nanocomposite. The oxidation of graphite to GO may be seen in the XRD profile by the presence of diffraction peaks at 2θ of 10.41° and 42.31°, respectively, attributable to the (001) and (100) planes. Especially prepared $CuFe_2O_4$ nanoparticles form a pure spinel phase of $CuFe_2O_4$, as shown by a good match between their reflected peaks and the typical structure for spinel phase $CuFe_2O_4$ (JCPDS No. 34–0425). Ag-$CuFe_2O_4$ and Ag-$CuFe_2O_4$@rGO nanocomposite exhibit diffraction peaks that are identical to those of pure $CuFe_2O_4$ nanoparticles. Since the quantity of GO in the $CuFe_2O_4$/GO nanocomposite is probably too low for detection by XRD [26], the distinctive diffraction peak of GO is not seen. SEM, TEM, and HRTEM images further prove that GO is present in the nanocomposite.

3.2 Morphological analysis

The micromorphology and microstructure of GO, Ag-$CuFe_2O_4$ and Ag-$CuFe_2O_4$@rGO samples were acquired by using ESEM and TEM. In Fig. 2a, GO presents a regular lamellar structure with wrinkle on the surface, implying that rGO is suitable as a carrier which could uniformly and stably immobilize

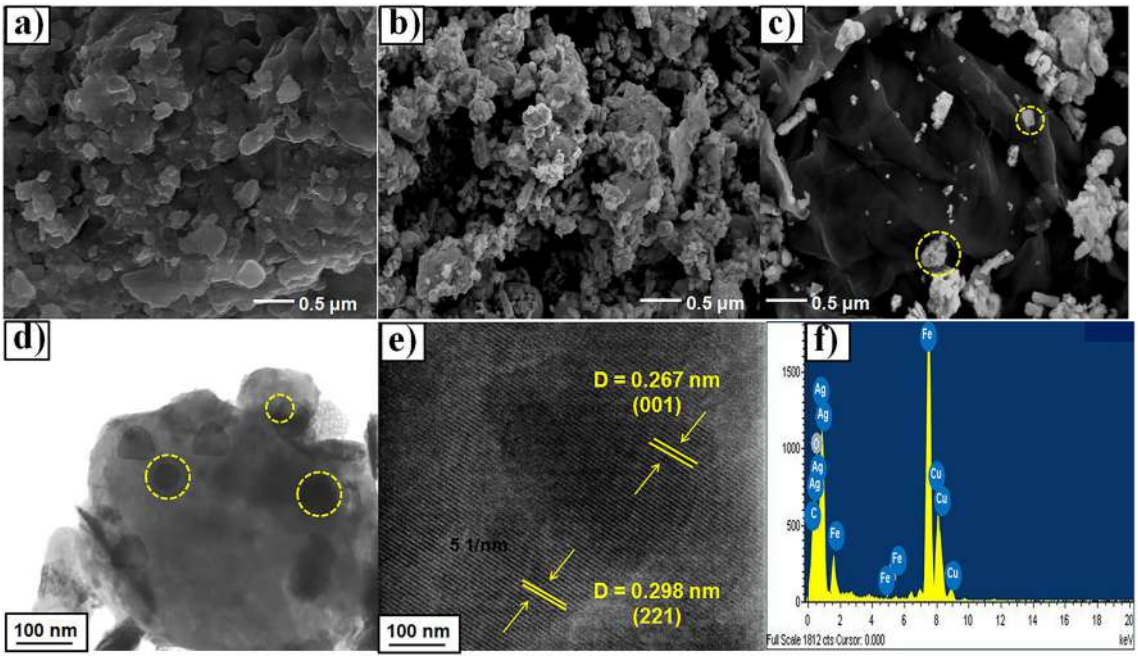

Fig. 2 SEM images of **a** rGO; **b** $CuFe_2O_4$; **c** Ag-$CuFe_2O_4$@rGO; TEM image of **d** Ag-$CuFe_2O_4$@rGO; **e** HRTEM image of Ag-$CuFe_2O_4$@rGO; **f** EDS spectra of Ag-$CuFe_2O_4$@rGO

the Ag-$CuFe_2O_4$ nanoparticles in the synthesis process. As for the Ag-$CuFe_2O_4$ sample, its nanoparticles present as regular tetragonal microcrystals but many are agglomerated into blocks, reducing the accessible active sites. When incorporated Ag-$CuFe_2O_4$ into rGO, most $CuFe_2O_4$ nanocrystals are evenly anchored on the surface and into the interior of rGO, and the transparent silk yarn lamella structure of graphene was more obvious. Further the TEM image of Ag-$CuFe_2O_4$@rGO composite reveals that Ag-$CuFe_2O_4$ nanoparticles are uniformly distributed (average diameter of around 10–15 nm) on the rGO sheet surface (Fig. 2d). The clear fringes in the HRTEM image (Fig. 2e), which the d values are 0.267 and 0.298 nm are belongs to (001) and (221) planes of rGO and $CuFe_2O_4$, respectively. Additionally, the EDS spectra as elemental mapping images clearly showed that the elements of Ag, C, O, Fe and Cu were uniformly distributed throughout the hybrid catalyst, further confirming the even immobilization of $CuFe_2O_4$ nanoparticles on the surface of rGO (Fig. 2f). From the SEM and TEM, it was clear evident that $CuFe_2O_4$ nanoparticles are uniformly coated on the surface of the rGO sheets, which can increase the surface area. In fact, the 2D structure of rGO not only enhances the adsorption ability of the photocatalysts but also in favor of the uniform distribution of $CuFe_2O_4$ nanoparticles (increasing the contact area between them). Therefore, the Ag/$CuFe_2O_4$/rGO shows a promising potential in the photocatalysis field. The sufficient contact between the rGO and $CuFe_2O_4$ not only provides more opportunities for electron transport but also achieves the synergy of these two materials.

3.3 FTIR spectra analysis

FT-IR spectra may be obtained between 400 and 4000 cm^{-1}. Functional group recognition was accomplished using Fourier transform infrared spectroscopy. Copper and ferrite were seen between 400 and 600 cm^{-1}. The metal ions in octahedral sites were allocated to the band at approximately 498 cm^{-1}, whereas those in tetrahedral sites were assigned to the band at around 612 cm^{-1}. This band at 3431 cm^{-1} is caused by the elongation of H_2O and O-H molecules, indicating the presence of water. The band at 1612 cm^{-1} was associated with the deflection of water molecules. Co-precipitated specimens were identified as CO_3^{2-} and HCO_3^- based on bands detected at about 1222 and 1417 cm^{-1} [27]. Because Ag and rGO nanosheets were incorporated into the copper ferrite structure, the FT-IR spectra of all the photocatalyst samples were quite similar; nevertheless, graph c showed a peak of carbon dioxide at 2358 cm^{-1}. Figure 3a displays all of

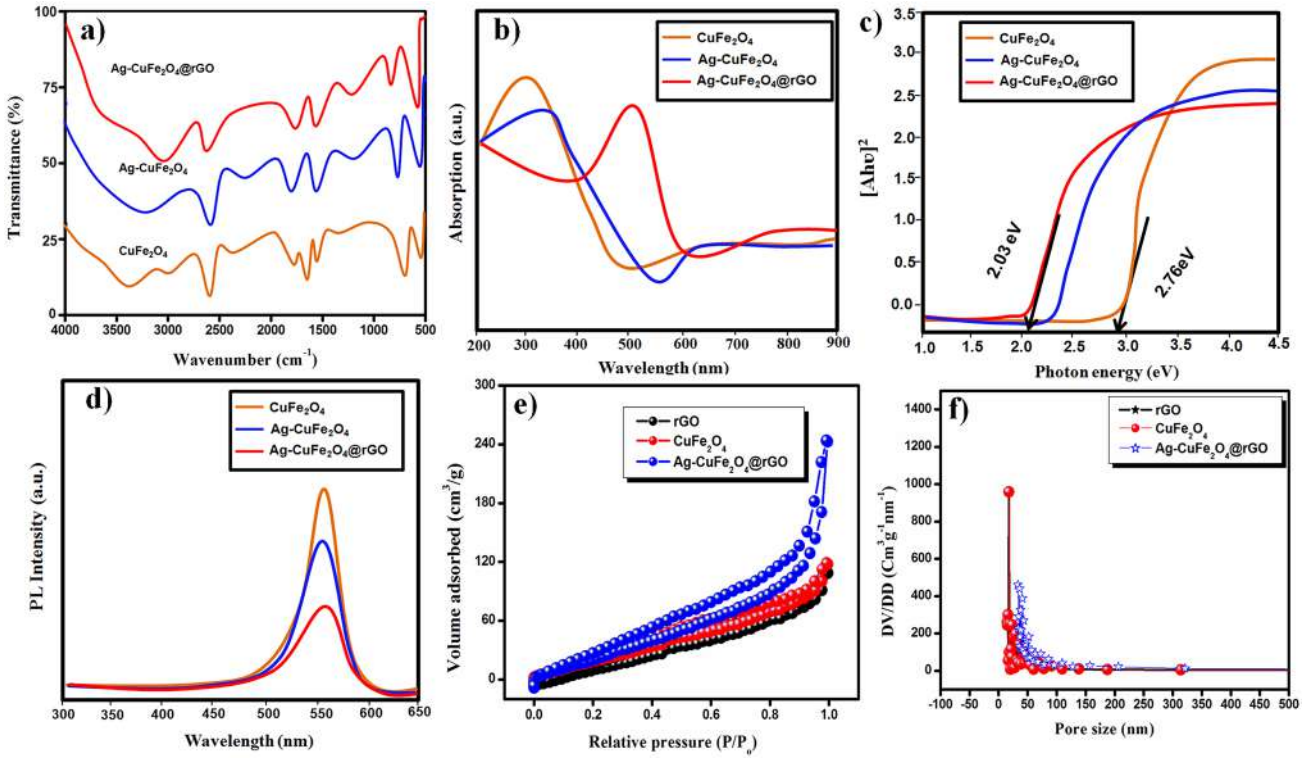

Fig. 3 **a** FTIR spectra of photocatalyst samples; **b** UV–Vis absorption spectra; **c** Band gap plot; **d** Room temperature PL spectra of all the photocatalysts with excitation wavelength of 450 nm; e N_2 adsorption-desorption; f pore size distribution curves of rGO, $CuFe_2O_4$ and Ag-$CuFe_2O_4$@rGO samples

the information displayed for $CuFe_2O_4$, Ag-$CuFe_2O_4$, and Ag-$CuFe_2O_4$@rGO.

3.4 Optical studies

UV–Visible absorbance data of the $CuFe_2O_4$, Ag-$CuFe_2O_4$ and Ag-$CuFe_2O_4$@rGO nanocomposite are shown in Fig. 3b. The absorptions of $CuFe_2O_4$ were observed at 445 nm (ligand feld transitions). The absorption peak of Ag-$CuFe_2O_4$ at 541 nm is the indicative of $CuFe_2O_4$ doped by metallic nature of Ag. Compared to $CuFe_2O_4$ and Ag-$CuFe_2O_4$ samples, Ag-$CuFe_2O_4$@rGO shows higher absorbance at the chosen wavelength of excitation (600 nm) which makes them possible to observe near resonant nonlinearity. Moreover, the considerable red shifted in the visible region is due to narrowing the band gap by conductive nature rGO. The absorbance spectra results were then treated in order to determine the band gap energy (E_g) of each sample using Tauc`s expression: $\alpha h\upsilon = b(h\upsilon - E_g)^n$, h is the plank constant, ν is the frequency of the incident light, α is the absorption coefficient, b is a proportion constant and E_g is the band gap energy defined as the difference between the lowest energy level in conduction band and the highest energy level in valence band [28–30]. When linearity was identified within the Tauc plot, extrapolation to the × axis revealed possible optical band gap energies for the sample. The plotting was repeated, once using power $n = 1/2$ so as to identify direct gap behavior, and secondly using power $n = 2$ to identify behavior characteristic of indirect energy gaps within the samples. In our case, $CuFe_2O_4$ is indirect band gap type, hence used the plot between $(\alpha h\upsilon)^2$ vs. Eg in order to get band gap energy value. The band gap energy values of $CuFe_2O_4$, Ag-$CuFe_2O_4$ and Ag-$CuFe_2O_4$@rGO nanoparticles are calculated as 2.76, 2.27 and 2.03 eV, respectively (Fig. 3c). Therefore, these kinds of nanoparticles exhibit a high photocatalytic activity under visible light irradiation. As can be shown in Fig. 3d, the integration of GO into Ag-$CuFe_2O_4$@rGO has an influence on the e-/h + recombination manipulate, hence PL was performed to better understand this effect. In the PL spectrum of $CuFe_2O_4$, the recombination of the photogenerated e-/h + couples produces a prominent emission peak at around 554 nm, and this peak's strength decreased

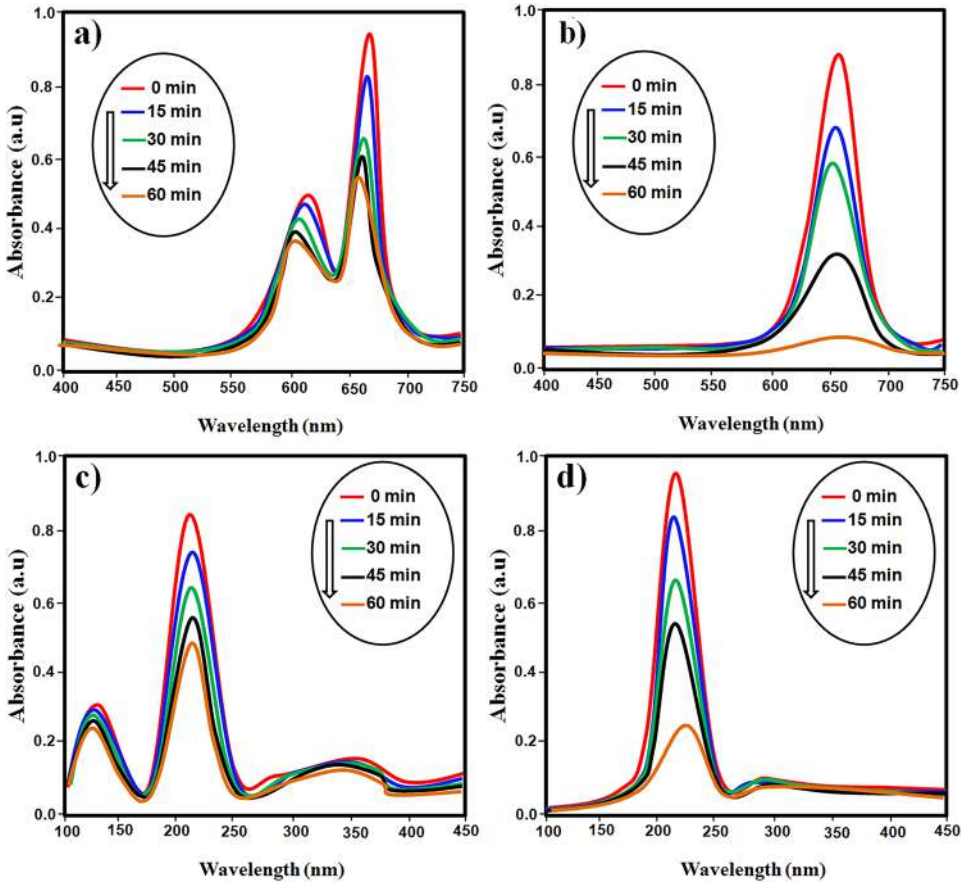

Fig. 4 UV absorption spectra of MB over **a** $CuFe_2O_4$ and **b** Ag-$CuFe_2O_4$@rGO, UV absorption spectra of 4-NP over **c** $CuFe_2O_4$ and **d** Ag-$CuFe_2O_4$@rGO

substantially for the Ag- $CuFe_2O_4$@rGO sample. The good contact between the GO and $CuFe_2O_4$ nanoparticle results in a low recombination rate of the photoinduced charged carriers, as shown by the very weak strength of the PL spectrum of Ag- $CuFe_2O_4$@rGO [31].

3.5 Surface area analysis

Because gas sensing performance is determined by the adsorption and desorption of the dye molecules, the surface area of the nanocomposite is crucial. Figure 3e displays the results of a N_2 adsorption-desorption investigation performed to determine the surface area of our nanocomposite (Ag-$CuFe_2O_4$@rGO). The rGO surface area was calculated for further context. According to the IUPAC categorization, the BET surfaces of rGO, $CuFe_2O_4$, and Ag-$CuFe_2O_4$@rGO nanocomposite show a type IV isotherm [32–34]. Specific surface area was calculated to be 78 m^2/g for rGO and 67 m^2/g for $CuFe_2O_4$. Ag and rGO were added to $CuFe_2O_4$ to increase its specific surface area, and the resulting Ag-$CuFe_2O_4$@rGO nanocomposite had a much higher value of 154 m^2/g. Figure 3f shows the relevant pore size plots. Additional evidence that the materials are mesoporous is that their pore sizes are between 10 and 20 nm.

3.6 Photocatalytic studies

Methyl blue (MB) and 4-nitrophenol (4-NP) the photodegradation in an aqueous solution under 400 W lamp exposure to visible light are used to compare the photocatalytic capabilities of $CuFe_2O_4$ and Ag-$CuFe_2O_4$@rGO core shell composite photocatalyst. The MB and 4-NP solution with $CuFe_2O_4$ and Ag-$CuFe_2O_4$@rGO as photocatalyst is shown in Fig. 4a–d. To track the catalytic degradation manipulate, we settled on the wavelength of the absorption peak that occurs between the MB (664 nm) and 4-NP (220 nm). As the amount of time an object is exposed to light increases, the absorption peaks weaken. This finding suggests that exposure to ultraviolet (UV) light in the presence of Ag-$CuFe_2O_4$@rGO leads to the progressive degradation of MB and 4-NP. According to their absorption spectrum, Ag-CuFe2O4@rGO photocatalysts are more effective than CuFe2O4 at degrading

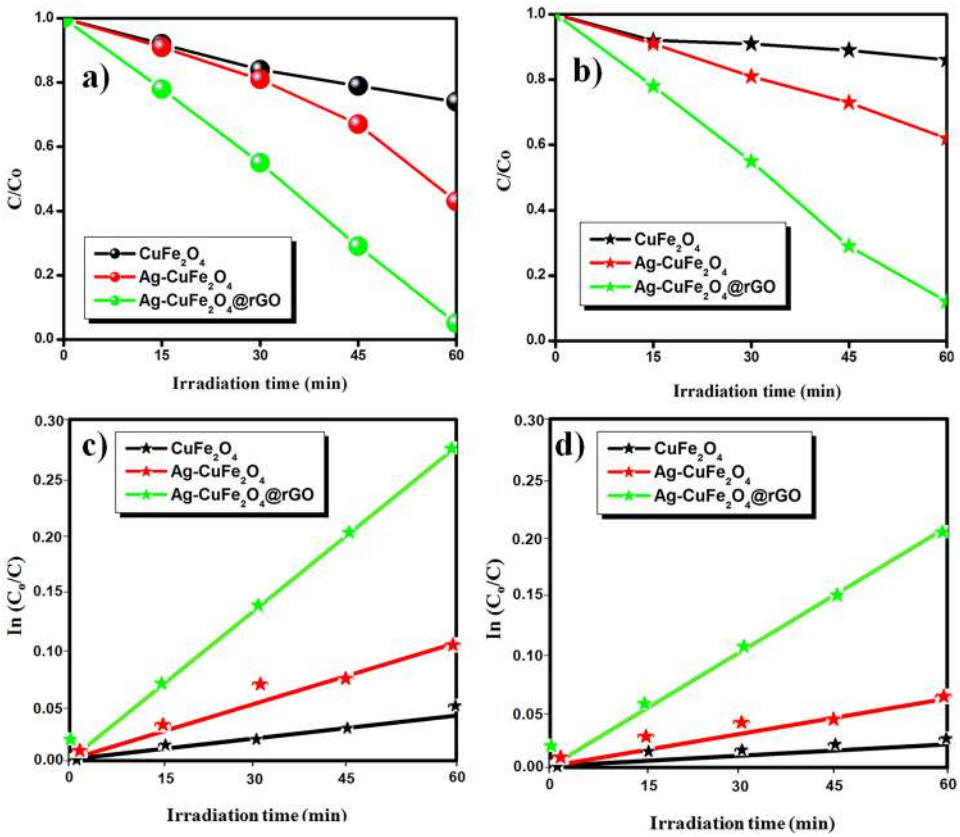

Fig. 5 **a** MB degradation efficiency; **b** 4-NP degradation efficiency of all the photocatalyst samples under visible light; first order kinetic plot of **c** MB; **d** 4-NP using $CuFe_2O_4$, Ag-$CuFe_2O_4$ and Ag-$CuFe_2O_4$@rGO photocatalyst samples

MB. At pH 7 and a catalyst dose of 0.1 g/L, and a drug amount of 10 mg/L, the photodegradation action of $CuFe_2O_4$ and Ag- $CuFe_2O_4$@rGO was assessed. Figure 5a, b displays the findings for MB and Fig. 5c, d displays the results for 4-NP. Under visible light radiation treatment, only a small amount of MB (26.5% degradation) and 4-NP (14.5%) was destroyed in bare $CuFe_2O_4$ nanoparticles. When the photocatalysts were added, however, the photodegradation activity rose, with the Ag- $CuFe_2O_4$@rGO composite demonstrating the greatest efficiency towards MB (99.5%) and 4-NP (88.7%). When rGO is present, electron-hole recombination decreases, leading to enhanced photocatalytic activity. Since the band gap energy of Ag is lower than the one that transfers band of rGO, the inclusion of Ag nanoparticles improves the rate of charge carrier segregation and reduces electron-hole recombination, further increasing efficiency. The following first-order formula [35] was used to predict the kinetics of the degrading processes. A 0.0985 min^{-1} rate constant for MB and a 0.0542 min^{-1} rate variable for 4-NP were determined for the Ag- $CuFe_2O_4$@rGO composite. This finding demonstrates that rGO's presence offers an alternate carrier channel and effectively splits photogenerated electron-hole pairs, thereby blocking recombination. Table 1 displays the total photocatalytic parameters. Testing the catalyst's repeatability is crucial before using it on a massive scale. In Fig. 6a, b, samples of pure $CuFe_2O_4$ and Ag- $CuFe_2O_4$@rGO composites were tested under the same experimental

Table 1 Photocatalytic activity parameters of $CuFe_2O_4CuFe_2O_4$ and Ag-$CuFe_2O_4$@rGO composite samples

Samples	Rate constant of MB		Rate constant of 4-NP		MB degradation efficiency (%)	4-NP degradation efficiency (%)
	K (h^{-1}) min^{-1}	R^2	K (h^{-1}) min^{-1}	R^2		
$CuFe_2O_4$	0.0071	0.992	0.0091	0.994	26.5	14.5
Ag-$CuFe_2O_4$	0.0651	0.987	0.1498	0.983	57.8	38.6
Ag-$CuFe_2O_4$ @rGO	0.0985	0.989	0.0542	0.988	99.5	88.7

conditions to compare their recyclability. In order to reuse the catalyst sample for further photocatalytic reactions, it was centrifuged after each run, given a complete wash, and then dried. In the first three cycles of catalyst reuse, there was no discernible decrease in MB efficiency, and degradation was thus estimated to be 100%. The good photo-stability and recycling was found despite a minor decline in activity in the fourth cycle (98.2%) and in the fifth cycle (97.2%), respectively. Based on the recycling data, it seems that Ag-$CuFe_2O_4$@rGO is a superior photocatalyst for the degradation of dyes and may hold promise as a photocatalyst for treating industrial effluent. In order to show the applicability and efficiency of our nano-catalytic system, results are compared with some of the recently reported methods [36–44] for the reduction of organic pollutants (4-NP and MB) (Table 2). Under acidic and basic conditions, the catalytic effect of the Ag-$CuFe_2O_4$@rGO composite was studied to see how pH affected the breakdown of phenol. Using 0.1 M HCl and 0.1 M NaOH, respectively, the pH of the phenol solutions was adjusted to 3 (acidic medium) and 10 (basic medium). Figure 6c displays the findings, showing that the Ag- $CuFe_2O_4$@rGO composite's catalytic activity was noticeably greater in the acidic media than in the basic medium. In the acidic media, phenol was eliminated entirely after 60 min, but in the basic medium, MB was eliminated by just 30%. Leaching of metals from the catalyst's solid state under acidic reaction conditions may allow it to function as a homogeneous catalyst, hence enhancing the degradation of MB even more. Figure 6d displays the impact of varying Ag-$CuFe_2O_4$@rGO concentrations on MB degradation. When the concentration of Ag-$CuFe_2O_4$@rGO is raised from 0.2 g/L to 0.8 g/L, the degradation efficiency soars from 26.5 to 99.0%. Nevertheless, increasing the Ag-$CuFe_2O_4$@rGO concentration from 0.8 to 1.0 g/L had no appreciable effect. The degradation of 1 mM buffered MB and 4-NP dye solution was carried out in the process of catalytic ozonation with Ag-$CuFe_2O_4$@rGO. After 60 min of treatment, all of the MB and 4-NP were mineralized and 10 mgL^{-1} Ag ion was detected in the final solution. In order to examine the effect of Ag^{2+} on the mineralization of MB and 4-NP, experiments were conducted under several different conditions (Fig. S1 and Fig. S2). In particular, 10 mgL^{-1} Ag ion was used as the catalyst and the results are compared. There was negligible reduction of MB

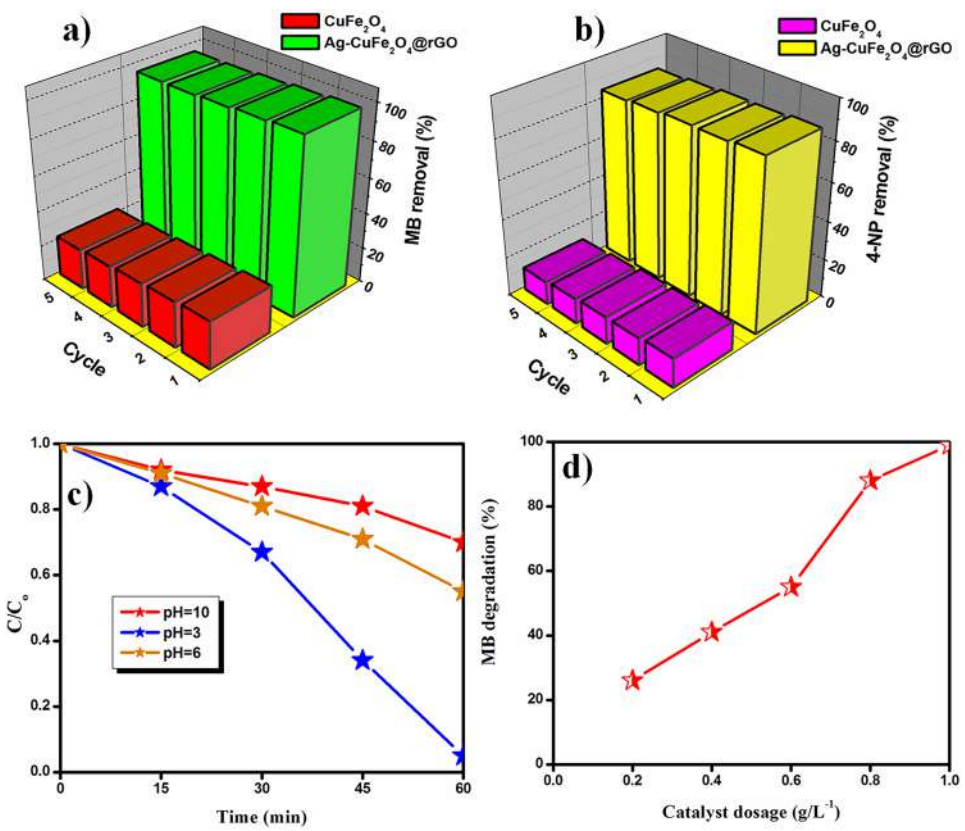

Fig. 6 Recycling test of **a** MB; **b** 4-NP using $CuFe_2O_4$ and Ag-$CuFe_2O_4$@rGO photocatalyst samples under visible light exposure; **c** Effect of initial pH value on the degradation of MB. Experimental conditions: Dosage = 0.8 g/L MB = 0.05mM; pH = 7.0; T = 298 K; **d** Effect of dosage on degradation of MB. Experimental conditions: Experimental conditions. Dosage = 0.8 g/L MB = 0.05 mM; pH = 7.0; T = 298 K

Table 2 A comparison of photodegradation of MB between present work and already reported rGO-based composite materials

Catalyst	Light source	Dye	Time (min)	Degradation (%)	References
Ag-ZnO/rGO NPs	Visible light	MB	180	65.2	[36]
Ag/RGO/MnO_2	Visible light	MB	120	89.2	[37]
$CuFe_2O_4$/rGO	Visible light	MB	180	92.5	[38]
$CuFe_2O_4$/rGO	Visible light	MB	210	96.5	[39]
$CuFe_2O_4$@TiO_2	Visible light	MB	150	47.5	[40]
$CuFe_2O_4$	Visible light	4-NP	120	77.2	[41]
$CuFe_2O_4$	Visible light	PNP	90	78.3	[42]
P coated $CuFe_2O_4$	Visible light	4-NP	150	71.2	[43]
$CuFe_2O_4$	Visible light	4-NP	120	81.4	[44]
Ag-$CuFe_2O_4$@rGO	Visible light	MB/4-NP	60	99.5/88.7	This work

in the absence of ozone. nitrobenzene, where much less metal ion leaching was observed. The degradation process of the PCBs mixture using different photocatalysts was monitored through total organic carbon (TOC) analysis and the resultanf plot is shown in Fig. S3 and Fig. S4. The TOC removal efficiency (%) was determined using the following; TOC Removal(%)=(TOC_0–TOCt/TOC_0), TOC_0 and TOC_t are the initial solution and the total organic carbon concentrations, respectively. All photocatalysts showed slight adsorption of MB. After 60 min of irradiation, degradations of MB of 74.1%, 92.4%, and 95.6% were achieved using $CuFe_2O_4$, Ag-$CuFe_2O_4$ and Ag-$CuFe_2O_4$/rGO, respectively (Fig.S3). While the 4-NP degradation was found to be 67, 76 and 85%, respectively (Fig.S4). These results revealed that the synthesized materials show excellent photocatalytic activity against MB than compared with 4-NP. Theoretically, a larger catalyst dose might boost the number of active sites on Ag-$CuFe_2O_4$@rGO, leading to a greater number of generated radicals and hence a faster conversion rate. nevertheless a substantial number of dyes were

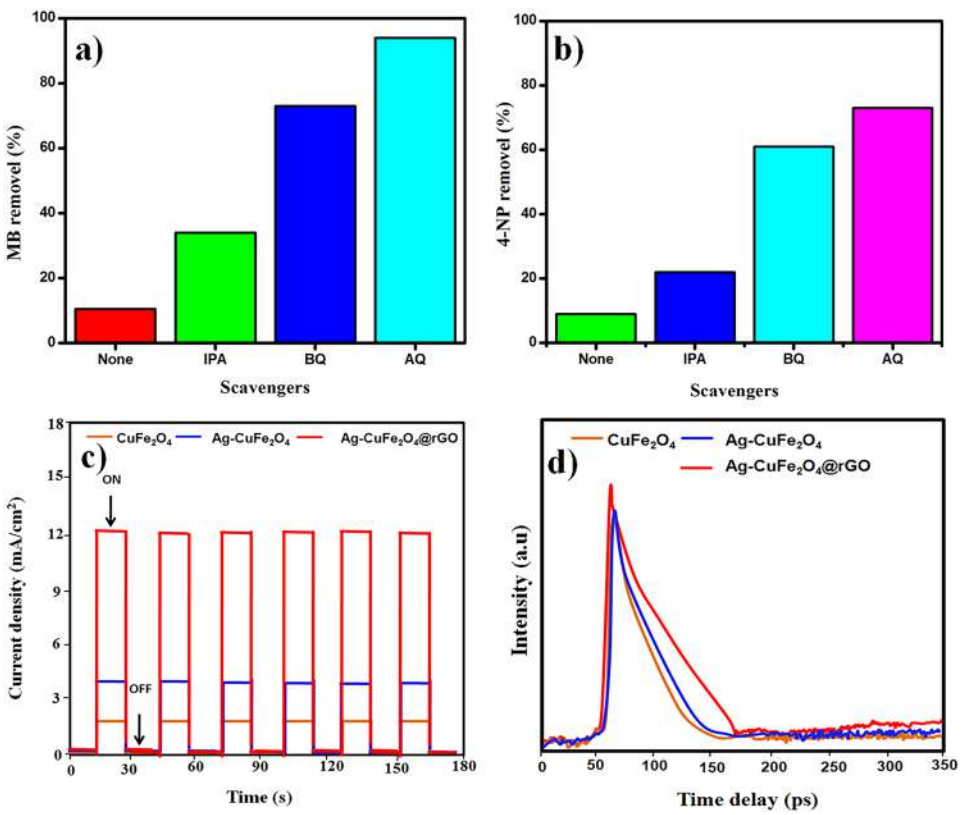

Fig. 7 Scavenger studies of Ag-$CuFe_2O_4$@rGO using **a** MB; **b** 4-NP under visible light; **c** Dynamic photo current response and **d** TRPL decay curves upon the excitation at 450 nm for $CuFe_2O_4$, Ag-$CuFe_2O_4$ and Ag-$CuFe_2O_4$@rGO composite samples

degraded from the reaction solution when the dose of catalyst approached 10 mg, without any observable increase in the degradation rate. Ammonium oxalate (AO), isopropanol (IPA), and 1,4-benzoquinone (BQ) have been selected as scavengers for h^+, $\cdot OH^-$, and $\cdot O_2^-$, respectively, to study the degradation of MB and 4-NP and their respective pathways of reaction. Figure 7a and b displays that after 60 min of visible light irradiation, only 10.5 and 8.7% of MB and 4-NP, respectively, were destroyed without scavengers. The results of the effect of pH value (Fig. 6) are consistent with the observation that the addition of IPA causes a little shift in the rate of decomposition compared to that without scavengers, suggesting that $\cdot OH^-$ radicals may be inconsequential in the photocatalytic process. Under the same conditions, the photocatalytic activity is drastically dampened by the addition of BQ and AO, with MB degradation dropping to 73% and 94%, respectively. Direct interaction of photogenerated electrons with oxygen might result in the formation of radicals $\cdot O_2^-$. Figure 7c shows that Ag- $CuFe_2O_4$@rGO photocatalysts have a greater the photocurrent signal compared to $CuFe_2O_4$ and Ag- $CuFe_2O_4$ photocatalysts. When compared to $CuFe_2O_4$ (1.64 $mAcm^{-1}$), Ag-$CuFe_2O_4$@rGO demonstrated 7.5-fold higher photocurrent intensity (12.3 $mAcm^{-1}$) under illumination [45], demonstrating that more photogenerated carriers may be created over the ZnO/ZnS photocatalyst. Charge transfer in Ag- $CuFe_2O_4$@rGO heterostructures has been studied using time-resolved photoluminescence spectroscopy (TRPL). All of the generated samples' photoexcited electron decay by TRPL with 450 nm excitation is shown in Fig. 7d. Average lifetimes of 2.82 ns for $CuFe_2O_4$, 3.05 ns for Ag- $CuFe_2O_4$, and 5.97 ns for Ag- $CuFe_2O_4$@rGO show that charge transfer occurs more quickly in heterostructures than in

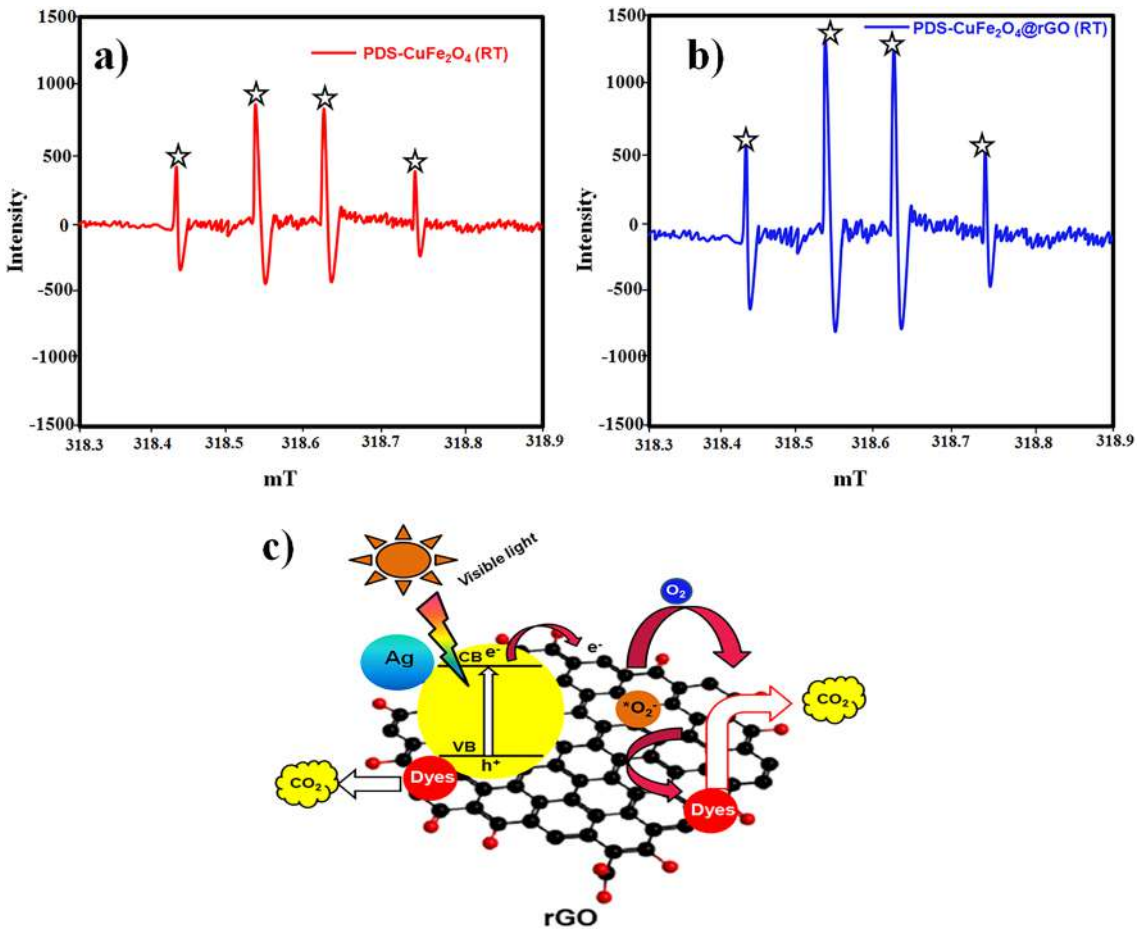

Fig. 8 ESR spectra of different systems. **a** PDS solution catalyzed by bare $CuFe_2O_4$ under room temperature; **b** PDS solution catalyzed by Ag-$CuFe_2O_4$@rGO under room temperature; **c** Photocatalytic degradation mechanism for dyes over Ag-$CuFe_2O_4$@rGO composite under visible irradiation

$CuFe_2O_4$. With DMPO as the spin capturing agent, ESR studies were performed to prove the formation of $SO_4^{\cdot}$/·OH and the exceptional part played by Ag-$CuFe_2O_4$@rGO in the induction of PDS. Signals for DMPO-OH and DMPO-SO_4 adducts are shown to have risen with addition of $CuFe_2O_4$catalyst to PDS solution at room temperature (Fig. 8a). Figure 8b shows that the application of Ag-$CuFe_2O_4$@rGO significantly amplified the signals of DMPO-OH and DMPO-SO4 adducts; HO· and $SO_4^{\cdot-}$ were identified as the primary radicals in the reaction system, and ·OH resulted from the interaction of $SO_4^{\cdot-}$ and H_2O [46]. The following is a hypothesized photocatalytic mechanism of Ag- $CuFe_2O_4$@rGO based on the data above, and it is shown in Fig. 8c. Electrons (e^-) in the valence band (VB) of $CuFe_2O_4$ may be stimulated to its conduction band (CB), resulting in the formation of holes (h+) in the VB at the same time when irradiated with visible light. The electrons are swiftly transported to the rGO through a percolation process due to the rGO's reputation as an excellent electron acceptor [47]. Then, the $\cdot O_2^-$ may be created when the negatively charged GO reacts with O_2. Dye degradation to carbon dioxide and water is facilitated by the $\cdot O_2^-$ and h^+.

4 Conclusions

To create Ag-$CuFe_2O_4$@rGO nanostructures, a straightforward hydrothermal technique was designed. The promoting mechanism of rGO on $CuFe_2O_4$ was deduced from characterization data including XRD, SEM-EDS, TEM, BET, FTIR, and PL. The addition of rGO improved the available reactive sites for photocatalytic activation by increasing the specific surface area, the pore volume, and the mono-dispersed anchoring of $CuFe_2O_4$ nanocrystals on the surface of rGO. As a result of the photocatalyst's heterostructure, which allows for a low electron-hole recombination rate, the system was able to demonstrate a high photodegradation efficiency for the drug pollutants. There is hope for a cheap water purification method since the photocatalytic nanoparticles may be reused up to five times with little loss of photodegradation efficacy. To further boost photocatalytic activation, rGO's added carbon-based groups also served as an auxiliary catalyst. Ag-$CuFe_2O_4$@rGO composites have been shown to catalyze the degradation of organic contaminants in aqueous solutions, hence they should be further investigated as catalysts.

Author contributions

MS, SA: study conceptualization and writing (original draft) the manuscript. DM, SV: data curation, formal analysis and writing (review & editing).

Funding

The authors have not disclosed any funding.

Data availability

The data that support the findings of this study are available from the corresponding author, upon reasonable request.

Declarations

Conflict of interest The authors declare that there is no conflict of interest regarding the research work reported in this manuscript.

Supplementary Information The online version contains supplementary material available at https://doi.org/10.1007/s10854-024-12076-8.

References

1. S. Zhuang, X. Xu, B. Feng, J. Hu, Y. Pang, G. Zhou, L. Tong, Y. Zhou, Photogenerated carriers transfer in dye–graphene–SnO_2 composites for highly efficient visible-light photocatalysis. ACS Appl. Mater. Interfaces **6**, 613 (2014)
2. S.J. Adnan Khan, K. Shah, N. Mehmood, Awais, H. Ali, Khan, Synthesis of potent chitosan beads a suitable alternative for textile dye reduction in sunlight. J. Mater. Sci. Mater. Electron. **30**, 406–414 (2019)
3. H. Khan, A.K. Khalil, A. Khan, Photocatalytic degradation of alizarin yellow in aqueous medium and real samples using chitosan conjugated tin magnetic nanocomposites. J. Mater. Sci. Mater. Electron. **30**, 21332–21342 (2019)

4. A. Aisha, A.K.N. Ali, A. Khan, M. Bilal, S. Malik, N. Ali, H. Khan, Chitosanzinc sulfide nanoparticles, characterization and their photocatalytic degradation efficiency for azo dyes. Int. J. Biol. Macromol. **153**, 502–512 (2020)
5. A. Menhad Khan, H. Khan, N. Khan, S. Ali, S. Sartaj, Malik et al., Development and characterization of regenerable chitosan-coated nickel selenide nano-photocatalytic system for decontamination of toxic azo dyes. Int. J. Biol. Macromol. **182**, 866–878 (2021)
6. A. Waqar Ahmad, N. Khan, S. Ali, S. Khan, S. Uddin, N. Malik, H. Ali, H. Khan, H. Khan, M. Bilal, Photocatalytic degradation of crystal violet dye under sunlight by chitosan-encapsulated ternary metal selenide microspheres. Environ. Sci. Pollut. Res. **28**, 8074–8087 (2021)
7. T. Ullah, K. Gul, H. Khan, B. Ara, T.U.H. Zia, Efficient removal of selected fluoroquinolones from the aqueous environment using reduced magnetic graphene oxide/polyaniline composite. Chemosphere **293**, 133452 (2022)
8. S. Zhang, S.A. Khan, N. Ali, S. Malik, H. Khan, Designing, characterization, and evaluation of chitosan-zinc selenide nanoparticles for visible-light-induced degradation of tartrazine and sunset yellow dyes. Environ. Res. **213**, 113722 (2022)
9. M. Gohain, V. Kumar, J.H. van Tonder, H.C. Swart, O.M. Ntwaeaborwa, B.C.B. Bezuidenhoudt, Nano $CuFe_2O_4$: an efficient, magnetically separable catalyst for transesterification of β-ketoesters. RSC Adv. **5**, 18972–18976 (2015)
10. S. Paul, G. Pal, A.R. Das, Three-component synthesis of a polysubstituted pyrrole core containing heterocyclic scaffolds over magnetically separable nanocrystalline copper ferrite. RSC Adv. **3**, 8637–8644 (2013)
11. X. Zhou, S.-C. Cui, J.-G. Liu, Three-dimensional graphene oxide cross-linked by benzidine as an efficient metal-free photocatalyst for hydrogen evolution. RSC Adv. **14**, 14725–14732 (2020)
12. S. Ahammed, D. Kundu, B.C. Ranu, Cu-catalyzed Fe-driven Csp–Csp and Csp–Csp^2 cross-coupling: an access to 1,3-diynes and 1,3-enynes. J. Org. Chem. **79**, 7391–7398 (2014)
13. T. Tatsuma, S. Saitoh, P. Ngaotrakanwiwat, Y. Ohko, A. Fujishima, Energy storage of TiO_2–WO_3 photocatalysis systems in the gas phase. Langmuir **18**, 7777–7779 (2002)
14. C. He, Y. Xiong, X. Zhu, A novel method for improving photocatalytic activity of TiO_2 film: the combination of Ag deposition with application of external electric field. Thin Solid Films. **422**, 235–238 (2002)
15. I. Bannat, K. Wessels, T. Oekermann, J. Rathousky, D. Bahnemann, M. Wark, Improving the photocatalytic performance of mesoporous titania films by modification with gold nanostructures. Chem. Mater. **21**, 1645–1653 (2009)
16. Y. Yu, J.C. Yu, J.G. Yu et al., Enhancement of photocatalytic activity of mesoporous TiO_2 by using carbon nanotubes. Appl. Catal. A **289**, 186–196 (2005)
17. B.T.M. Van Nguyen, N.H. Nguyet, D.Q. Nghi, Khieu, Photocatalytic degradation of methylene blue by using ZnO/longan seed activated carbon under visible-light region. J. Inorg. Organomet. Polym Mater. **31**, 446–459 (2021)
18. N.T.V. Hoan, N.N. Minh, T.T.K. Nhi, N. Van Thang et al., TiO_2/diazonium/graphene oxide composites: synthesis and visible-light-driven photocatalytic degradation of methylene blue. J. Nanomater. (2020). https://doi.org/10.1155/2020/4350125
19. H.T.M. Thanh, N.T.T. Tu, N.P. Hung, T.N. Tuyen, T.X. Mau, D.Q. Khieu, Magnetic iron oxide modified MIL-101 composite as an efficient visible-light-driven photocatalyst for methylene blue degradation. J. Porous Mater. **26**, 1699–1712 (2019)
20. D.M. Le Van Thuan, M.H. Nguyen, V.T. Thu, D.Q. Khieu, L.H. Sinh, Facile fabrication of highly flexible and floatable, Cu_2O/rGO on Vietnamese traditional paper toward high-performance solar-light-driven photocatalytic degradation of ciprofloxacin antibiotic. RSC Adv. **10**, 16330 (2020)
21. F.A. Jumeri, H.N. Lim, S.N. Ariffin, N.M. Huang, P.S. Teo, S.O. Fatin, C.H. Chia, I. Harrison, Microwave synthesis of magnetically separable $ZnFe_2O_4$-reduced graphene oxide for wastewater treatment. Ceram. Int. **40**, 7057–7065 (2014)
22. X.J. Lv, G.J. Zhang, W.F. Fu, Highly efficient hydrogen evolution using TiO_2/Graphene composite photocatalysts. Chin. Mater. Conf. **27**, 570–576 (2012)
23. J.P. Yang, Q.W. Lin, W. Yin, T. Jiang, D.H. Zhao, L.C. Jiang, A novel nonenzymatic glucose sensor based on functionalized PDDA-graphene/CuO nanocomposites. Sens. Actuators B-Chem. **253**, 1087–1095 (2017)
24. Z.Y. Yu, H.J. Li, J.H. Lu, X.M. Zhang, N.K. Liu, X. Zhang, Hydrothermal synthesis of Fe_2O_3/graphene nanocomposite for selective determination of ascorbic acid in the presence of uric acid. Electrochim. Acta. **158**, 264–270 (2015)
25. Y. Fu, Q. Chen, M. He et al., Copper ferrite-graphene hybrid: a multifunctional heteroarchitecture for photocatalysis and energy storage. Ind. Eng. Chem. Res. **51**, 11700–11709 (2012)
26. A. Noor-ul, A.W. Shaheen, B. Bashir, N.M. Abdelsalam, M.F. Warsi, M.A. Khan, M. Shahid, Electrical, magnetic and photoelectrochemical activity of rGO/$MgFe_2O_4$ nanocomposites. Ceram. Int. **42**, 12401–12408 (2016)
27. A. Kiani, G. Nabiyouni, S. Masoumi et al., A novel magnetic $MgFe_2O_4$–$MgTiO_3$ perovskite nanocomposite: rapid

photo-degradation of toxic dyes under visible irradiation. Compos. B: Eng. **175**, 107080 (2019)
28. S. Sathishkumar, M. Parthibavarman, V. Sharmila, M. Karthik, A facile and one step synthesis of large surface area SnO_2 nanorods and its photocatalytic activity. J. Mater. Mater. Electron. **28**, 8192–8196 (2017)
29. P. Sivakarthik, V. Thangaraj, M. Parthibavarman, A facile and one-pot synthesis of pure and transition metals (M = Co & Ni) doped WO_3 nanoparticles for enhanced photocatalytic performance. J. Mater. Mater. Electron. **28**, 5990–5996 (2017)
30. D. Madhan, M. Parthibavarman, P. Rajkumar, M. Sangeetha, Influence of Zn doping on structural, optical and photocatalytic activity of WO_3 nanoparticles by a novel microwave irradiation technique. J. Mater. Mater. Electron. **26**, 6823–6830 (2015)
31. R. Kuriki, T. Ichibha, K. Hongo, D. Lu, R. Maezono, H. Kageyama, O. Ishitani et al., A stable, narrow-gap oxyfluoride photocatalyst for visible-light hydrogen evolution and carbon dioxide reduction. J. Am. Chem. Soc. **140**, 6648–6655 (2018)
32. M. Jayashree, V. Sharmila, K.L. Meganathan, R. BoopathiRaja, M. Parthibavarman, M. Shkir, S. AlFaify, Design and fabrication of graphene anchored CeO_2 hybrid nanocomposite electrodes for high performance energy storage device applications. Inorg. Chem. Commun. **132**, 108838 (2021)
33. R. BoopathiRaja, M. Parthibavarman, Hetero-structure arrays of $MnCo_2O_4$ nanoflakes@ nanowires grown on Ni foam: design, fabrication and applications in electrochemical energy storage. J. Alloy Compd. **811**, 152084 (2019)
34. R. BoopathiRaja, M. Parthibavarman, A. Nishara, Begum, Hydrothermal induced novel $CuCo_2O_4$ electrode for high performance supercapacitor applications. Vacuum. **165**, 96–104 (2019)
35. M. Parthibavarman, M. Karthik, Role of microwave on structural, morphological, optical and visible light photocatalytic performance of WO_3 nanostructures. J. Clus Sci. **30**, 495–506 (2019)
36. H. Raj Pant, B. Pant, H.J. Kim et al., A green and facile one potsynthesis of Ag-ZnO/RGO nanocomposite with effective photocatalytic activity for removal of organic pollutants. Ceram. Int. **39**, 5083–5091 (2013)
37. S. Naghdi, M. Sajjadi, M. Nasrollahzadeh, K.Y. Rhee, S.M. Sajadi, B. Jaleh, Cuscuta reflexa leaf extract mediated green synthesis of the Cu nanoparticles on graphene oxide/manganese dioxide nanocomposite and its catalytic activity toward reduction of nitroarenes and organic dyes. J. Taiwan. Inst. Chem. Eng. **86**, 158–173 (2018)
38. P. Ramadevi, G. Vinodhkumar, R. Shanmugavadivu, An efficient visible light driven photocatalyst based on $CuFe_2O_4$/rGO nanocomposites for effective degradation of methylene blue dye. Optik. **277**, 170713 (2023)
39. R. Subhasish Mishra, K. Acharya, Parida, Spinel-ferrite-decorated graphene-based nanocomposites for enhanced photocatalytic detoxification of organic dyes in aqueous medium: a review. Water **15**, 81 (2023)
40. Y.U. You-Yia, Z.H.A.N.G. Heng-Qiang, Reduced graphene oxide coupled magnetic $CuFe_2O_4$-TiO_2 nanoparticles with enhanced photocatalytic activity for methylene blue degradation. Chin. J. Struct. Chem. **35**, 472480 (2016)
41. C. Dey, D. De, M. Nandi, M.M. Goswami, A high performance recyclable magnetic $CuFe_2O_4$ nanocatalyst for facile reduction of 4-nitrophenol. Mater. Chem. Phys. **242**, 122237 (2020)
42. J. Li, Y. Ren, F. Ji, B. Lai, Heterogeneous catalytic oxidation for the degradation of p-nitrophenol in aqueous solution by persulfate activated with $CuFe_2O_4$ magnetic nanoparticles. Chem. Eng. J. **324**, 63–73 (2017)
43. I. Othman, M. Abu Haija, F. Banat, Catalytic properties of phosphate-coated $CuFe_2O_4$ nanoparticles for phenol degradation. J. Nanomater. (2019). https://doi.org/10.1155/2019/3698326
44. T.P. Oliveria, S.F. Rodrigues, G.N. Marques, R.C.V. Costa, C.G.G. Lopes et al., Synthesis, characterization, and photocatalytic investigation of $CuFe_2O_4$ for the degradation of dyes under visible light. Catalysts **12**, 623 (2022)
45. Y. Zhang, Z. Jin, Effective electron-hole separation over controllable construction of WP/UiO-66/CdS heterojunction for efficiently improved photocatalytic hydrogen evolution under visible-light-driven. Phys. Chem. Chem. Phys. **21**, 8326–8341 (2019)
46. H.Z. Liu, T.A. Bruton, W. Li, J.V. Buren, C. Prasse, F.M. Doyle, D.L. Sedlak, Oxidation of benzene by persulfate in the presence of Fe (III)-and mn (IV)-containing oxides: stoichiometric efficiency and transformation products. Environ. Sci. Technol. **50**, 890–898 (2016)
47. I.V. Lightcap, T.H. Kosel, P.V. Kamat, Anchoring semiconductor and metal nanoparticles on a two-dimensional catalyst mat. Storing and shuttling electrons with reduced graphene oxide. Nano Lett. **10**, 577–583 (2010)

Diamond & Related Materials 144 (2024) 110995

Contents lists available at ScienceDirect

Diamond & Related Materials

journal homepage: www.elsevier.com/locate/diamond

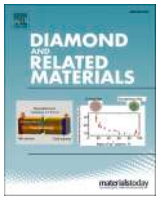

Fabrication of $NiFe_2O_4$ nanoparticles loaded on activated carbon as novel composites for high efficient ultra violet-light photocatalysis for degradation of aqueous organic pollutants

J. Hemalatha [a,*], M. Senthil [a,*], D. Madhan [b], Amal M. Al-Mohaimeed [c], Wedad A. Al-onazi [c]

[a] Department of Chemistry, Kandaswami Kandar's College, P.Velur, Namakkal 638182, Tamilnadu, India
[b] Department of Physics, Velammal College of Engineering and Technology (Autonomous), Madurai 625009, Tamilnadu, India
[c] Department of Chemistry, College of Science, King Saud University, P.O. Box 22452, Riyadh 11495, Saudi Arabia

ARTICLE INFO

Keywords:
$NiFe_2O_4$
Activated carbon
Chemical synthesis
Photocatalyst
UV light

ABSTRACT

The study used nickel ferrite $NiFe_2O_4$/activated carbon ($NiFe_2O_4$/AC) as a means to remove organic dyes (methylene blue and Reactive red 120) from water-based solutions. The produced photocatalysts were characterized based on their morphological, structural, particle size, and surface charge characteristics. The transmission electron microscopy (TEM) pictures indicated that the $NiFe_2O_4$ particles, with an average diameter of around 2–2.5 μm, were evenly distributed and adhered to the outermost layer of the AC nanosheets. The BET analysis revealed that the 10-$NiFe_2O_4$/AC material had a surface area of 176 m^2/g, a pore volume of 0.354 cm^3/g, and an average pore diameter of 0.805 nm. The nanocomposite, as opposed to pure $NiFe_2O_4$ and clean AC, demonstrates a notably enhanced photocatalytic degradation efficiency for methylene blue (MB) and Reactive red 120 dye under visible light conditions. The findings indicate that the AC loaded with 10 % $NiFe_2O_4$ is the most effective photocatalyst, exhibiting a maximum degradation efficiency of 100 % towards MB dye. Additionally, it displays a high mechanical constant, excellent stability, and ease of recycling. The nanocomposite exhibits increased photocatalytic activity owing to the significant reduction in charge carriers recombination, improved capacity to absorb visible light, and the synergistic impact resulting from the heterojunction with $NiFe_2O_4$ and AC. The radical entrapment research revealed that the primary active compounds responsible for the photocatalytic degradation process are superoxide (O_2^-) and hydroxyl (OH*).

1. Introduction

Due to economic and societal advancements, environmental concerns related to printing and dyeing wastewater have escalated since dyes are harmful and pose a significant threat to aquatic ecosystems and human well-being. Conventional methods such as chemical oxidation, coagulation, ion exchange, adsorption, and photocatalysis have been used to eliminate dyes [1–5]. The utilization of organic/inorganic semiconductor materials such as g-C_3N_4, RGO, and TiO_2 as photocatalysts for the visible-light photocatalytic destruction of various natural poisons has been extensively studied in recent decades. This strategy offers significant potential for converting solar energy into chemical energy, thereby enabling the disintegration about harmful organic contaminants, as well as the deterioration of heavy metals and other detrimental substances [6–9]. Typically, semiconducting metal oxides such as TiO_2, SnO_2, WO_3, and ZnO are very efficient in removing a wide range of organic and inorganic contaminants when exposed to visible or solar light. Due to their favorable band gap energy, light absorption capability, and appropriate physicochemical and catalytic characteristics [10,11].

Recent research on magnetic semiconductor photocatalysts has garnered interest because of their simple recyclability, such as MFe_2O_4 (M = Ni, Zn, Fe, Co, Cu). $NiFe_2O_4$ is a prominent magnetic semiconductor that exhibits a visible-light reaction. It is an ordinary instance of magnetic materials noted for their high stability, magnetic permeability, and resistance to electric current. It is widely used in magnetic devices, catalysis, water treatment, magnetized fluids, and microwave absorption materials. There has been extensive research on the use of $NiFe_2O_4$, an inorganic semiconductor with a narrow band gap of 1.9 eV, for solar transformation, photocatalysis, and photochemical hydrogen

* Corresponding authors.
E-mail address: senthilmk1975@gmail.com (M. Senthil).

https://doi.org/10.1016/j.diamond.2024.110995
Received 13 January 2024; Received in revised form 27 February 2024; Accepted 4 March 2024
Available online 6 March 2024

production from water. This is due to its ability to react to visible light, its simple synthesis process, low cost, and excellent photochemical stability [12]. The appealing characteristics of ferrites are closely linked to the arrangement of cations across octahedral and tetrahedral sites in the spinel structure. The ability to manipulate the movement of cations provides a way to customize their qualities. The transportation of cations relies on factors such as the electrical configuration, valence of ions, and the size of nanoparticles. Regrettably, the practical use of bare $NiFe_2O_4$ photocatalysts is limited due to their poor visible light sensitivity and the challenges associated with recycling.

Several studies have examined activated carbon in this particular situation, mostly because of its distinctive attributes, such as its extensive specific surface area, consistent distribution of pore sizes, and capacity for modifying the surface [13–15]. Recent research has shown that active carbon, when combined with metal oxide or treated with a suitable reagent on its surface, has enhanced efficacy in catalytic oxidation and serves as a highly stable photocatalyst for the decomposition of a wide range of organic and inorganic contaminants [16–18]. Extensive study has been carried out to assess the appropriateness of different activated carbon materials infused with metal oxide for the purpose of eliminating organic dyes [19,20]. This composite material has a higher efficiency in adsorbing pollutants compared to either activated carbon (AC) or metal oxide used individually. Incorporating metal oxides into the starting material would increase the gas adsorption capability of the final composite AC [21,22]. This is because metal oxides may provide selective sorption properties and maintain high thermal stability even at high temperatures [23]. As an example, Livani et al. [24] documented the use of an AC integrated $NiFe_2O_4$ composite photocatalyst to decrease the concentration of organic dyes. The nanocomposite, as it was synthesized, exhibited exceptional adsorption capability for DR31 and DB78 dyes. The greatest adsorption capacity was achieved at pH = 2.0, and the equilibrium for dye adsorption was rapidly reached after 20 min for DR31 and 25 min for DB78. In their study, Baskaran Palanivel et al. [25] found that the ferromagnetic nanocomposite $NiFe_2O_4$-g-C_3N_4 achieved a degradation efficiency of 99 % in direct sunlight for both MB (20 mg/L) and Rh B (10 mg/L) dyes. This efficiency is much greater than what was obtained using visible light irradiation. The primary objective of this work is to examine the improved photocatalytic efficiency of $NiFe_2O_4$ nanoparticles when combined with activated carbon (AC) for the breakdown of MB and RR in the presence of UV light. Activated carbon (AC) is often used for water filtration because of its extensive surface area, leading to high adsorption effectiveness, in contrast to other carbonaceous materials. AC has delocalized n electrons and various functional groups including COOH, OH, NH_2, and amide, which may attract diverse species via hydrogen bonds and electrostatic forces. As far as we know, there have been no studies conducted on the elimination of MB and RR120 using $NiFe_2O_4$ catalysts fixed on activated carbon. The photocatalytic efficiency of $NiFe_2O_4$/AC was assessed and enhanced by adjusting the dye's starting concentration, the catalyst dosage, and the solution's pH level. The kinetic study and reusability of the photocatalyst were also assessed. A feasible reaction route was proposed for the breakdown of MB and RR 120 dye during the photocatalytic process.

2. Materials and methods

2.1. Reagents

The chemicals nickel acetate ($Ni(CH_3CO_2)_2•2H_2O$), iron acetate ($Fe(CH_3CO_2)_2•2H_2O$), activated carbon (AC), sodium hydroxide (NaOH), hydrochloric acid (HCl), nitric acid (HNO3), methylene blue (MB), and reactive red 120 (RR120) are acquired from Merck, a supplier based in Darmstadt, Germany, known for their highest quality and purity. The necessary concentration of all functional solutions was achieved by diluting the stock solution with distilled water.

2.2. Preparation of Peltophorum activated carbon with $ZnCl_2$

The seed pods of Peltophorum pteocarpium, obtained from the local region, were cleansed using distilled water, then subjected to drying at a temperature of 105 ± 5 °C, and then crushed into particle sizes ranging from 300 to 900 μm (20–70 ASTM). The material was saturated with a 1 % boiling solution containing zinc chloride for 48 h, after which the surplus zinc chloride solution was removed and the material was allowed to dry in the air. The substance was subjected to carbonization at a temperature of 400 °C inside a Muffle furnace, after which it was pulverized and then activated in the Muffle furnace at a temperature of 600oC for a duration of 20 min. Following the activation procedure, the carbon underwent a thorough rinsing with deionized water and was then subjected to drying at a temperature of 105 ± 5 °C in a hot air oven. Subsequently, the carbon was sifted and securely kept in a hermetically sealed container.

2.3. Preparation of $NiFe_2O_4$/AC composite photocatalyst

The standard synthetic protocol required the use of an analytical grade 3 M sodium hydroxide (NaOH) solution, which was gradually introduced into a solution of salt containing 0.4 M ferric chloride ($FeCl_3$) and 0.2 M nickel chloride (NiCl2). The pH of the solution was continuously monitored as the NaOH solution was added incrementally. The components of the reaction were continuously agitated using a magnetic stirrer until a pH level above 10 was attained. Subsequently, the solution was introduced into a sterilizer with a capacity of 75 mL, which was coated with Teflon, and subjected to a temperature of 160 °C for a duration of 12 h. The product was cooled to the ambient temperature and thereafter subjected to two rounds of washing with deionized water and ethanol to remove undesired contaminants. Ultimately, the material underwent centrifugation and thereafter underwent an overnight drying process at around 80° Celsius. Following this procedure, the $NiFe_2O_4$ samples that were created underwent calcination at a temperature of 400 °C for a duration of 5 h. The $NiFe_2O_4$/AC composite was created using a standardized method. Specifically, 50 mg of prepared AC was added to $NiFe_2O_4$ precursors. The resulting solution was then dried and calcined at a temperature of 400 °C for duration of 5 h. This process yielded high crystalline NiFe2O4/AC specimens.

2.4. Photocatalytic set up

Photocatalytic experiments were carried out in a specially designed photoreactor. The research included using a 50 ppm aqueous solution of MB dye (30 mL) mixed with the required quantity of catalysts in dispersion. MB and RR 120 dye were introduced into a basin containing 100 ml of deionized water and stirred using a magnetic stirring device. The concentration of dye was measured using a spectrum analyzer (Spectronic 20D, Mylton Roy, USA) at wavelengths of 664 nm and 508 nm. A certain amount of catalyst was added to the mix while it was in darkness, and the concentration of dye was measured after 2 h of being in shade. Photocatalytic reactions were carried out under UV light exposure from an a low-pressure mercury lamp. Photocatalytic activities were initiated after a period of darkness in all experiments to achieve adsorption equilibrium before each run.

3. Results and discussion

3.1. XRD analysis

Fig. 1 illustrates the XRD crystal structure of pure activated carbon, $ZnFe_2O_4$, and $ZnFe_2O_4$/AC photocatalysts. Amorphous carbon is proven by three peaks in the XRD pattern of pure activated carbon: 2θ = 25.3°, 43.3°, and 48.8° (planes of (002), (100), and (101), correspondingly. These peaks show the carbon rings' irregular arrangement [26]. The (111), (220), (311), (400), (422), (511) and (440) planes correspond to

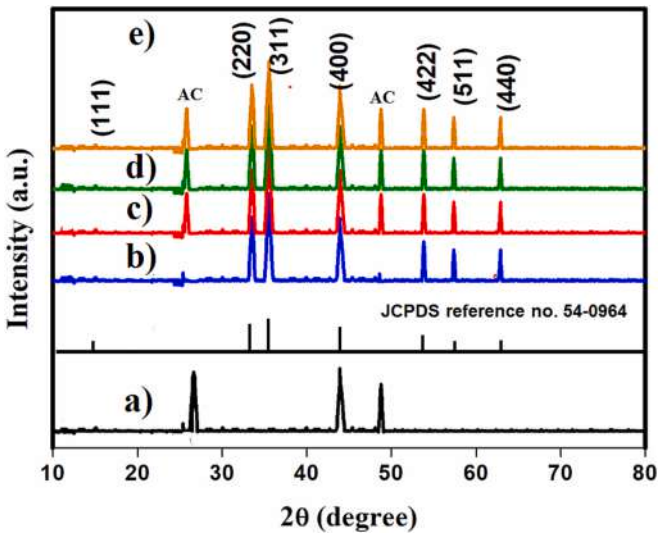

Fig. 1. Powder XRD pattern of (a) AC; (b) $ZnFe_2O_4$; (c) 5-$NiFe_2O_4$/AC; (d) 10-$NiFe_2O_4$/AC; (e) 15-$NiFe_2O_4$/AC.

$NiFe_2O_4$ peaks at 14.24°, 33.14°, 35.17°, 43.28°, 53.18°, 57.22°, and 63.11°. This confirms $NiFe_2O_4$'s cubic opposite spinel structure with Fd3m spatial group. Results matched JCPDS code 54–0964. Absence of extraneous peaks indicates a pure single-phase structure. In the nanocomposite, both the AC and $NiFe_2O_4$ components had diffraction peaks, demonstrating that the $NiFe_2O_4$ is tightly linked to the AC surface.

3.2. Morphological analysis

Fig. 2 shows the results of the FESEM and TEM analyses that were used to examine the microstructure and geometrical properties of the produced photocatalysts. In Fig. 2a, we can see the sheet-like lamellar structure in the FESEM picture of the pure AC. The highly agglomerated irregular form structure of the $NiFe_2O_4$ nanoparticles is clearly seen in Fig. 2b. The scanning electron micrograph of the 10-$NiFe_2O_4$/AC nanocomposite is shown in Fig. 2c. It is plainly seen that the heterojunction is formed by the AC and the collected nanoparticles of $NiFe_2O_4$. TEM imaging of the nanocomposite (Fig. 2d) reveals that the $NiFe_2O_4$ nanoparticles, which range in size from 30 to 40 nm, were firmly adhered to the AC nanosheets. As can be shown in Fig. 2e, the HRTEM study validated a heterojunction between AC and $NiFe_2O_4$. The results showed that the AC plane (002) was indexed by the d-spacing value of 3.21 Å, whereas the $NiFe_2O_4$ plane (311) was given the d-space value of 2.56 Å. The photocatalytic activity of dye degradation is enhanced by the heterojunction of $NiFe_2O_4$ and AC, which reduces the rate of electron-hole pair coupling. Analogous to the XRD pattern, the SAED design of the nanocomposite shows that the as-prepared nanocomposite is amorphous and contains carbon nitride and nickel ferrite.

3.3. FTIR spectra analysis

In addition, as seen in Fig. 3(a), FTIR spectroscopy was used to investigate the production of $NiFe_2O_4$/AC. The stretching vibrations of the free and immobilized water molecules are corresponding to the bands at 3432.1 cm^{-1} and 1642.4 cm^{-1} for $NiFe_2O_4$. The bending vibration of the metal at the tetrahedral sites (Fe—O) is correlated with the peak at 595.6 cm^{-1} [27]. The graphitic carbon's C═C stretching vibration may be indexed by the band at 1556.1 cm^{-1}, while the surface hydroxyl group's stretching vibration can be explained by a minor peak at 3209 cm^{-1} in the case of AC. Observations revealed a red shift in the nanocomposite's Fe—O stretching vibration from 594.5 cm^{-1} to 587.6 cm^{-1}, as well as a blue shift in the C═C vibration from 1561.1 cm^{-1} to 1552.1 cm^{-1} [28]. The electrostatic interaction of the AC surface functional groups and the $NiFe_2O_4$ nanoparticles in the nanocomposite is responsible for this change.

3.4. Optical studies

In Fig. 3 (b), ultra violet diffused reflectance spectrophotometers measured nanoparticle optical bandgaps. The virgin AC has an indirect bandgap of 2.68 eV and an absorption wavelength of 465 nm (λ). Pure $NiFe_2O_4$ has a 1.68 eV direct bandgap and 738 nm absorption edge. $NiFe_2O_4$'s absorbing tail extended to the NIR region (above 800 nm) due to the sample's flaws [29]. This reveals that $NiFe_2O_4$ absorbs UV to NIR sunlight well. The composite has a red shift compared to pure AC owing to $NiFe_2O_4$. The UV-DRS spectra showed that nanocomposite absorption was greater than pure nanoparticles [30,31]. Nanocomposite absorption cut-off wavelength is 580 nm. The computed bandgaps of 5- $NiFe_2O_4$/AC, 10- $NiFe_2O_4$/AC, and 15-$NiFe_2O_4$/AC composites were 2.31, 1.78,

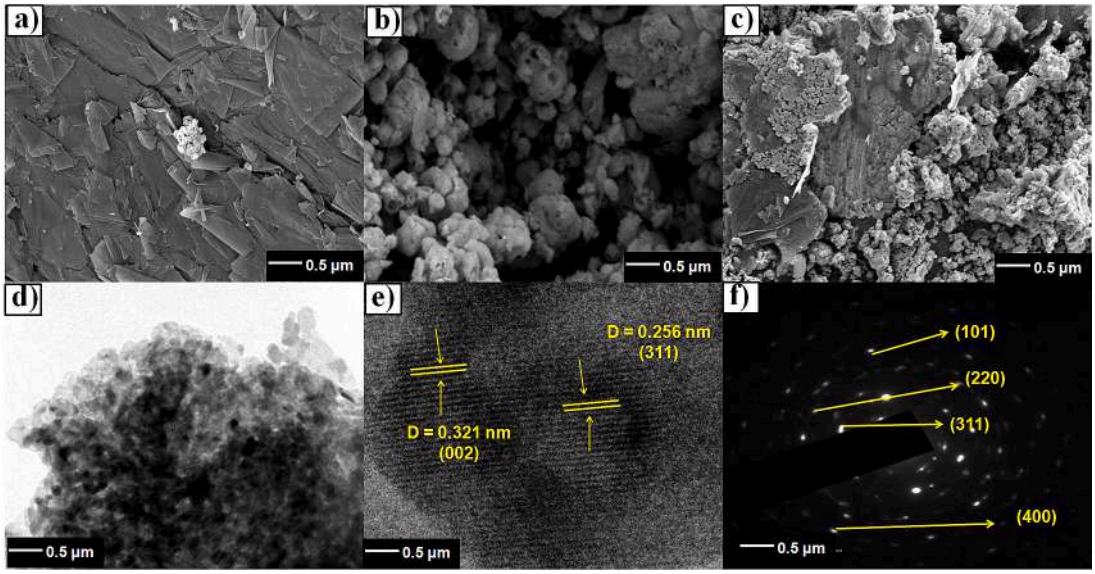

Fig. 2. SEM images of (a) AC; (b) $NiFe_2O_4$; (c) 10- $ZnFe_2O_4$/AC; (d) TEM image of 10- $NiFe_2O_4$/AC; (e) HRTEM image of 10- $NiFe_2O_4$/AC; (f) SAED pattern of 10-$NiFe_2O_4$/AC.

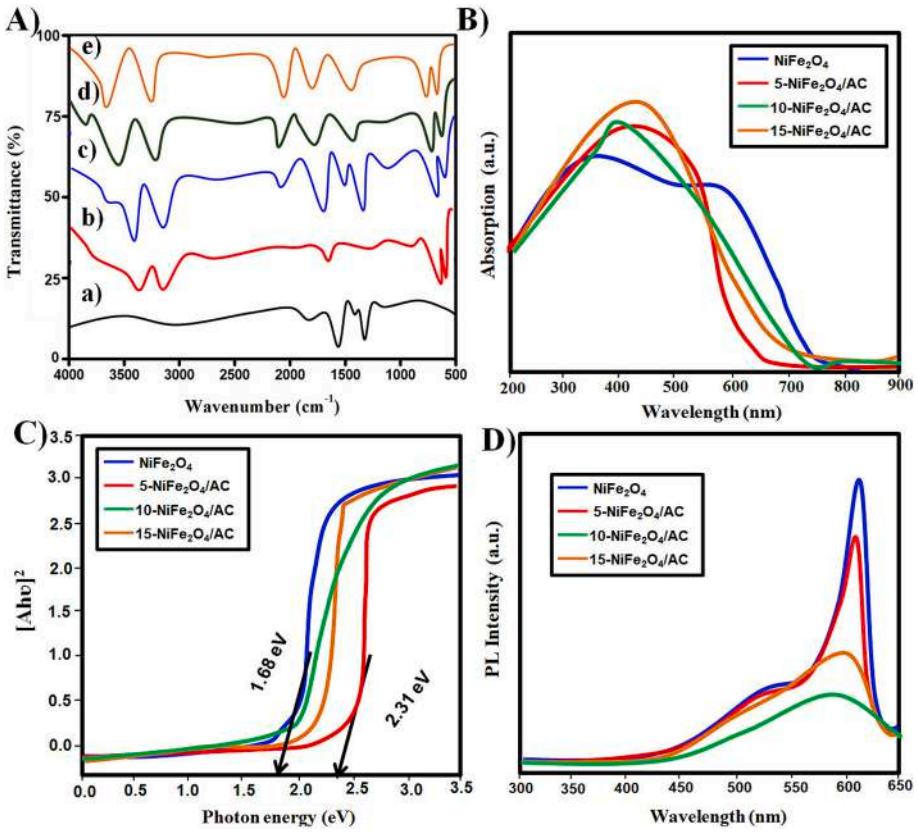

Fig. 3. (a) FTIR spectra of photocatalyst samples; (b) UV–Vis absorption spectra; (c) Band gap plot; (d) Room temperature PL spectra of all the photocatalysts with excitation wavelength of 450 nm;

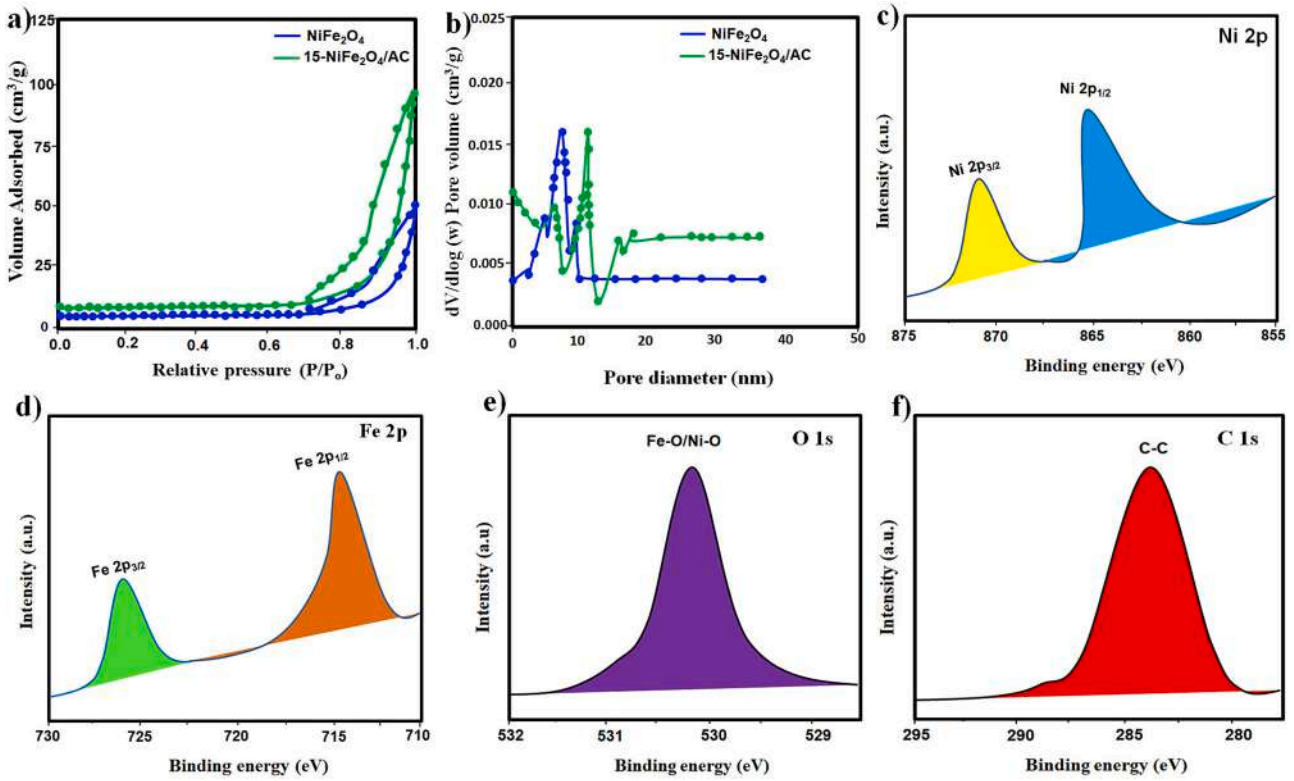

Fig. 4. (a) N_2 adsorption-desorption; (b) pore size distribution curves of $NiFe_2O_4$ and 10- $NiFe_2O_4$/AC; High resol;ution XPS spectra of (c) Ni 2p; (d) Fe 2p; (e) O 1 s and (f) C 1 s.

and 2.12 eV (Fig. 3c). Nanocomposite absorption tails reached NIR. Advanced absorption frequency of nanocomposite demonstrates the heterojunction between nanoparticles [32]. Thus, the composite $NiFe_2O_4$/AC photocatalyst has improved visible light photocatalytic activity. Fig. 3(d) shows the photoluminescence spectroscopy spectrum of the produced photocatalyst to explain charge carrier separation. Pure $NiFe_2O_4$ has a modest emission peak about 300–500 nm due to surface imperfections or oxygen vacancies [33]. The nanocomposite's PL spectrum displays modest emission, indicating that a heterojunction between $NiFe_2O_4$ and AC substantially reduces the recombination of electrons into holes. The optical experiments show that the nanocomposite has greater photocatalytic abilities than pure nanoparticles. Additionally, the optical spectroscopic findings showed that the heterojunction creation among $NiFe_2O_4$ and AC nanoparticles considerably reduces photo-excited electron-hole recombination. The $NiFe_2O_4$/AC exhibited superior photocatalytic performance as a result. Fig. S1 illustrates the photoexcited electrons decay in every sample that was generated, measured using TRPL with a wavelength of stimulation of 450 nm. Charge transfer in heterostructures is faster in $NiFe_2O_4$/AC compared to $NiFe_2O_4$, with median durations of 4.78 ns, 2.99 ns, and 2.51 ns, etc.

3.5. Surface area analysis

Using N_2 adsorption-desorption isotherms, the surface characteristics and pore structure of the produced composites ($NiFe_2O_4$/AC composite and pure $NiFe_2O_4$) were examined. In order to enable reactant diffusion and transfer of electrons, carbon-based substances having a multi-level porous structure are believed to deliver a great number of catalysis active sites with fine dispersion and appropriate routes [34]. Fig. 4a demonstrated that, as is typical for mesoporous materials, the catalysts displayed traditional type IV isomers and a well defined hysteresis loop at high relative pressure in the P/P◦ range (0.7–1) across all samples [35–38]. The 10-$NiFe_2O_4$/AC had an average pore diameter of 12.3 nm, a surface area of 176 m^2/g, and a pore volume of 0.354 cm^3/g, according to the BET study. In contrast, 98.7 m^2/g and 8.2 nm were the

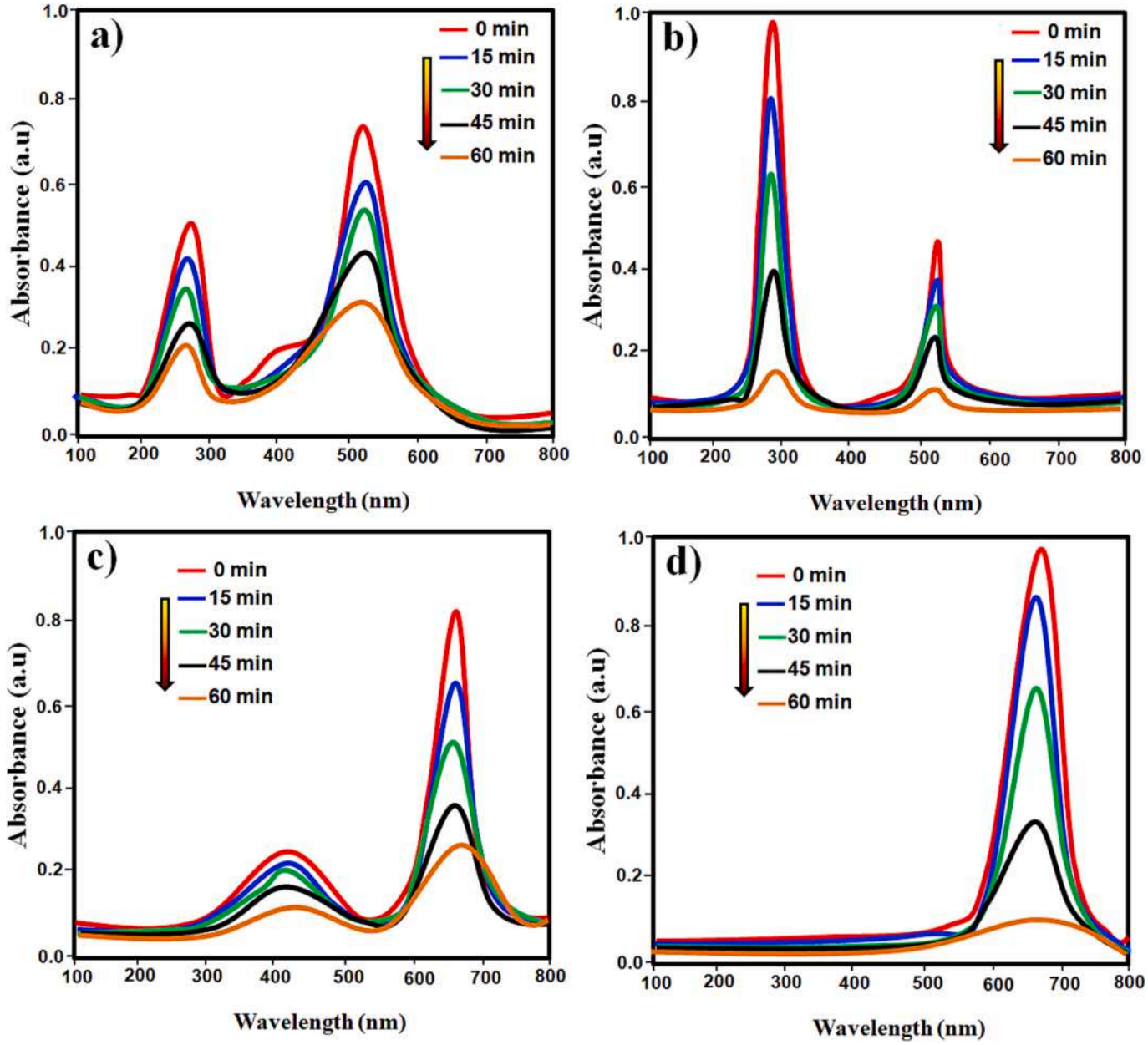

Fig. 5. UV absorption spectra of RR120 over (a) $NiFe_2O_4$ and (b) 10-$NiFe_2O_4$/AC, UV absorption spectra of MB over (c) $NiFe_2O_4$ and (d) 10-$NiFe_2O_4$/AC.

dimensions of pure $NiFe_2O_4$ (Fig. 4b).Composite samples are anticipated to exhibit enhanced photocatalytic activity due to their large surface area and pore size.

3.6. XPS analysis

XPS was used to characterize 10-$NiFe_2O_4$/AC nanocomposites' surface compositions and chemical valence states. The spin orbits Ni $2p_{3/2}$ and Ni $2p_{1/2}$ of $ZnFe_2O_4$ are represented by two prominent peaks at 871.7 and 865.3 eV in the high-resolution XPS of the Ni 2p spectrum (Fig. 4c) [39]. Fe 2p high-resolution XPS showed peaks for the spin-orbital doublets Fe $2p_{3/2}$ and Fe 2p1/2 [40]. Fe^{3+} forms the fitting peaks at 712.5 and 727.8 eV. Fig. 4d shows Fe^{2+}-related fitting peaks at 711.4 and 725.4 eV. Fig. 4e displays O 1 s spectra with a 530.4 eV binding energy for O-Fe/O-Ni. XPS of C 1 s revealed the carbon compound C—C peak at 284.7 eV (Fig. 4f).

3.7. Photocatalytic studies

3.7.1. UV absorption study of the dyes

To investigate the catalysts' photocatalytic activity, RR120 and MB were used as model contaminants. The first step in studying the photocatalytic activity of the catalysis was to conduct UV–Vis analysis on the RR120 and MB dyes to see how their molecular structures changed throughout the aided photocatalytic degradation cycle. Fig. 5 (a-d) displays the UV–Vis absorption spectra of RR120 and MB dyes, which allow one to see the varied visible light illumination times and their absorption characteristics. From zero to sixty minutes, light will be visible. At 0 min of visible light irradiation, the primary absorption peaks of MB dye and RR120 are located at 285 and 515 nm, with 664 nm in the middle. There was no absorption at the end of 60 min of exposure to visible light, and the strength of absorption declined with increasing illuminating duration. Under visible light conditions, the catalysts degrade organic dyes very energetically, according to the data.

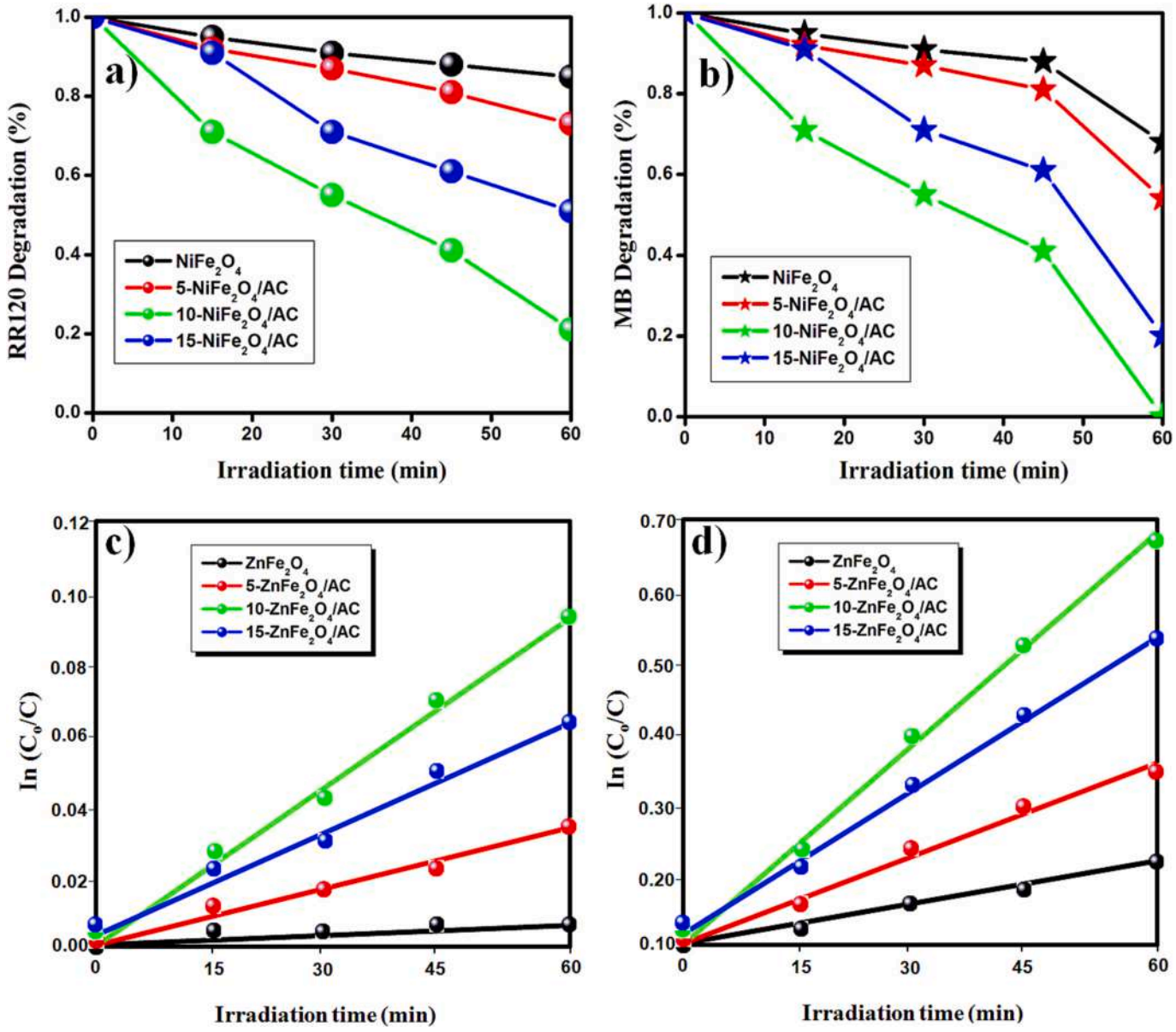

Fig. 6. (a) RR120 degradation efficiency; (b) MB degradation efficiency of all the photocatalyst samples under visible light; first order kinetic plot of (c) RR120; (d) MB using $NiFe_2O_4$, and $NiFe_2O_4$/AC photocatalyst samples.

3.7.2. Degradation and kinetic constant analysis

The degradation of the RR120 and MB dyes under visible light exposure is seen in Fig. 6 (a & b). Over the course of 60 min, the predicted photocatalytic degradation efficiencies of RR120 and MB dye, each, using just pure $NiFe_2O_4$, were 15.1 % and 37.2 %. The higher stability of the RR120 and MB in the experimental setting is shown by this finding. With a remarkable degradation efficiency of 100 % after 60 min of visible light irradiation, the MB degradation efficiency 10-$NiFe_2O_4$/AC composite demonstrated exceptional performance. After 60 min of visible light exposure, the RR120 degradation efficiency for pure $NiFe_2O_4$, 80 % 10-$NiFe_2O_4$/AC, and other mixtures was determined to be 15.1 %. Both the RR120 and MB dyes are degraded more efficiently by the nanocomposite than by the pure materials. Additionally, the process of degradation activity is significantly affected by the weight percent of $NiFe_2O_4$, with the greatest photocatalytic efficiency shown by the 10 % $NiFe_2O_4$ sample. Adding $NiFe_2O_4$ to the nanocomposite in a weight cent increase of up to 10 % clearly enhances its photocatalytic activity. The activity, however, decreased when the $NiFe_2O_4$ weight percent increased above 10 %. As the concentration of $NiFe_2O_4$ nanoparticles in the nanocomposites rises, this phenomenon may be linked to their aggregation. The degradation rate was reduced because charge carrier transfer between the nanocomposites counterparts could not occur at a tolerable rate in the ones with a greater weight ratio of $NiFe_2O_4$. Fig. 6 (c & d) shows the reaction kinetics of the dye degradation process when illuminated with visible light. The level of the dye solution at the beginning and at a given time interval (t) are denoted by C_0 and C, respectively, and the rate constant (k) was determined using the first order kinetic rate relation $-\ln(C/C_0) = kt$. Rate constants of 0.0003 and 0.0012 min^{-1}, respectively, were determined for the virgin $NiFe_2O_4$ photocatalyst over RR120 and MB dye. It is worth noting that the composite photocatalyst considerably enhanced the concentration rate. The rate constant for RR120 dye was 0.0341 min^{-1} and for MB dye was 0.0999 min^{-1}, as shown by the 10-$NiFe_2O_4$/AC composite photocatalyst. Following is a ranking of the photocatalysts' degradation efficiencies and rate constants: 10-$NiFe_2O_4$ > 15-$NiFe_2O_4$/AC > 5-$NiFe_2O_4$ > $NiFe_2O_4$. The kinetic constant (kapp) and correlation coefficient R2 exhibited a high level of linearity close to 1.0 for each sample, suggesting that the degradation of CV follows pseudo-first-order kinetics response (Fig. s2 and S3) [40]. Table 1 also summarizes the overall photocatalyst parameters. In addition, the findings summarized in Table 2 show that the current effort achieved comparatively greater outcomes than earlier published research [41–45].

3.7.3. Effect of pH

An significant component in predicting the photocatalyst's activity in both acidic and basic media, the influence of pH was studied to identify the acid-base nature of the photocatalytic process. Using 500 ml of a 100 ppm MB solution with 100 mg of photocatalysts, the experiment was conducted to evaluate the pH of the solution from 2 to 10. For 60 min at 28 °C, the tests were carried out in a photocatalytic reactor. Fig. 7a displayed the effect of pH on photocatalytic breakdown At first, we saw very slow MB breakdown in the acidic environment (2 > pH). As the pH of the solution rose, the MB degradation percentage gradually rose as well. After reaching a maximum degradation rate of MB at pH 6, the process of decomposition reached a state of neutrality or decrease.

Table 2
Summary of various $NiFe_2O_4$ based photocatalysts.

Catalyst	Light source	Dye	Time (min)	Degradation (%)	Ref.
$ZnFe_2O_4$/SiO_2/TiO_2	UV light	MB	120	95.1	[41]
ZnO/$ZnFe_2O_4$	Visible light	MB	120	91.2	[42]
Bi_2WO_6/$ZnFe_2O_4$	Visible light	MB	300	84.7	[43]
$ZnFe_2O_4$/CeO_2	Visible light	MB	210	93.5	[44]
$ZnFe_2O_4$/ZnO/Ag	Visible light	MB	150	47.5	[45]
$NiFe_2O_4$/AC	Visible light	MB	60	100	This work

The photocatalytic activity is affected by the amount of ions such as H+ in acidic media and OH- in base media, according to the pH effect results. The results show that the photocatalytic activity is more affected by H+ ions than by OH- ions. Conclusion: A pH of 6 was found to be optimal for dye degradation.

3.7.4. Effect of catalyst dosage

By studying the effects of different doses of photocatalysts, we can predict the best degradation rate for MB. A mixture with a pH of 6, a concentration of 25–150 mg of photocatalysts, and a contact period of 60 min at 28 °C were all used in the study. The dye solution had a concentration of 100 mg/L. Fig. 7b shows the impact of different dosages of photocatalysts on dye degradation. While a large amount of catalytic (100 mg) resulted in total destruction of MB in this study, the presence of constant dye molecules in the solution meant that no notable changes were seen after this dosage. Results showed that 100 mg of photocatalysts was the sweet spot for degradation % in this experiment. Equilibrium in MB degradation was achieved after 100 mg doses of photocatalyst. The results show that 100 mg of photocatalysts is all it takes to degrade MB to its greatest potential.

3.7.5. Recyclability of photocatalysts

Fig. 7(c) displays the findings of the photo catalysts' recyclability. The photocatalytic activity of the catalysts seemed to have been preserved after several cycles, as only a small percentage of dye degradation (around 3–4 % decreased) was found to have changed. The photocatalyst for dye decline, $NiFe_2O_4$ and 10-$NiFe_2O_4$/AC, was found to be more efficient and effective based on the reuse findings. This suggests that it might be a potential option for treating industrial wastewater.

3.7.6. Effect of scavenger

The findings are shown in Fig. 7 (d). The observed photocatalytic degradation of RR120 and MB after 60 min followed the sequence of H_2O_2 > persulfate > EDTA > $AgNO_3$. The inclusion of hydrogen peroxide (H_2O_2) resulted in the most optimal dye degradation effectiveness, mostly attributed to the generation of hydroxyl radicals.

Table 1
Photocatalytic activity parameters of $NiFe_2O_4$ and $NiFe_2O_4$/AC composite samples.

Samples	Rate constant of RR120		Rate constant of MB		RR120 Degradation efficiency (%)	MB Degradation efficiency (%)
	K (h^{-1}) min^{-1}	R^2	K (h^{-1}) min^{-1}	R^2		
$NiFe_2O_4$	0.0003	0.991	0.0012	0.994	15.1	37.2
5-$NiFe_2O_4$/AC	0.0656	0.987	0.0651	0.981	27.1	58.6
10-$NiFe_2O_4$/AC	0.1235	0.986	0.2361	0.985	49.5	79.8
15-$NiFe_2O_4$/AC	0.0341	0.918	0.0999	0.983	80.0	100

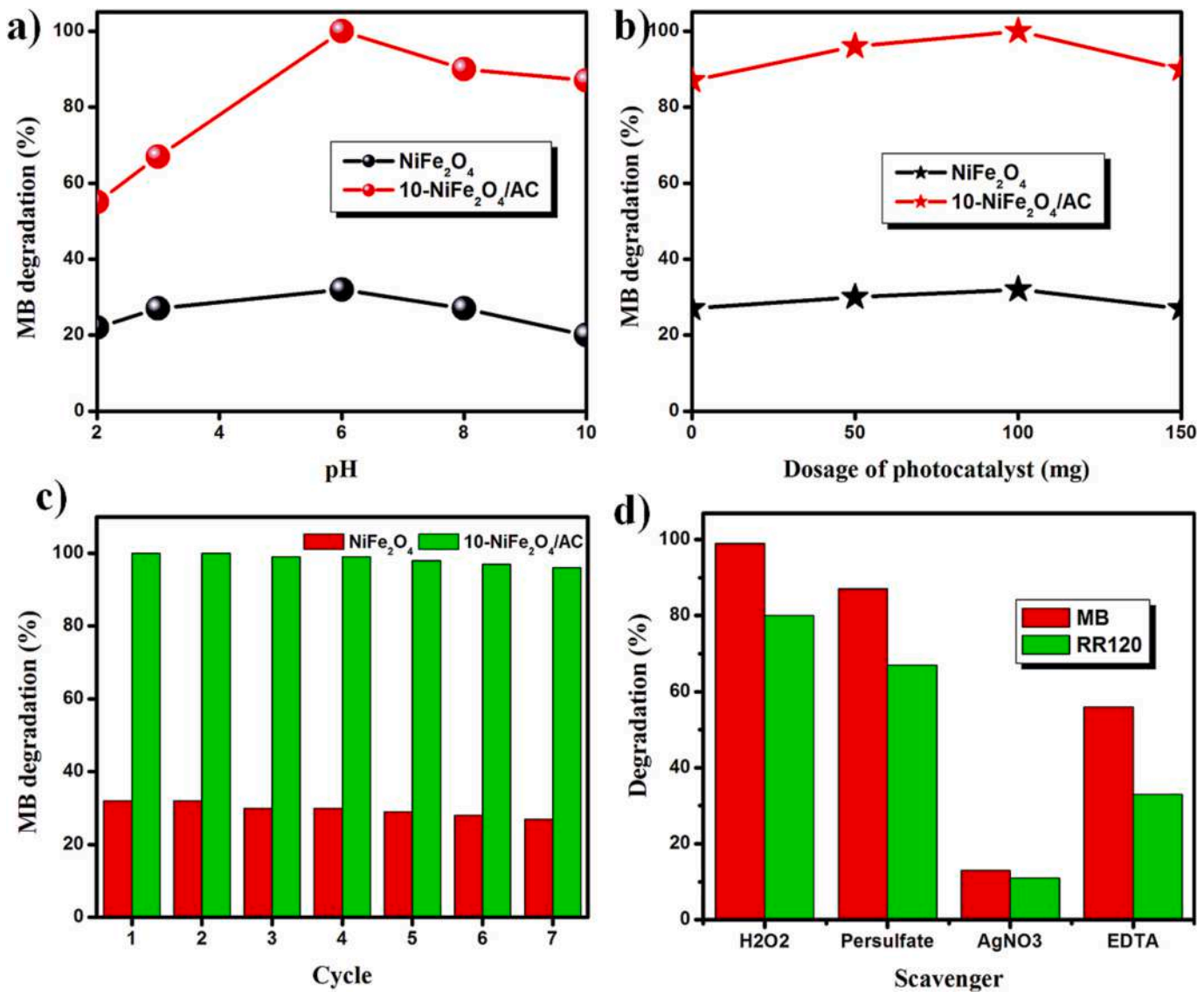

Fig. 7. (a) Effect of initial pH value on the degradation of MB. Experimental conditions:Dosage = 0.8 g/L MB = 0.05 mM; pH = 3.0; T = 298 K.; (d) Effect of dosage on degradation of MB. Experimental conditions: Dosage = 0.8 g/L MB = 0.05 mM; pH = 3.0; T = 298 K. (c) Recycling test of RR120 and MB using 10-$NiFe_2O_4$ photocatalyst; (d) Effect of various scarifying agent on the photodegradation of RR120 and MB and RR120 using 10-$NiFe_2O_4$ photocatalyst.

3.8. Photodynamic response and EIS analysis

The photocurrent response of the photoanodes was assessed by observing the changes in current when the UV-light was turned on and off. The findings may be seen in Fig. 8(a). Upon UV-light irradiation, a photocurrent immediately grew to an a steady-state current, as evident. The achievement of a constant photocurrent is attributed to the equilibrium between the rates of creation and recombination of electron-hole pairs [46]. The photocurrent of the 10-$NiFe_2O_4$/AC and 15-$NiFe_2O_4$/AC photoanodes is increased by 1.97 and 3.63 orders of magnitude, respectively, compared to the bare NiFe2O4. This indicates a significant increase in the amount of electrons exchanged on the surface of the hybrid photoanodes. An electrochemical impedance spectroscopy (EIS) examination was performed to provide a more comprehensive understanding of the rate at which electrons are transferred at the interface between the photoanode and the electrolyte, specifically when exposed to UV-light. Fig. 8(b) illustrates the Nyquist plot for $NiFe_2O_4$ and $NiFe_2O_4$/AC photoanodes. The presence of a semicircle in the high-frequency area of the Nyquist diagram is attributed to the charge-transfer phenomenon occurring at the interface between the electrode and the electrolyte. The resistance values (Rct) of $NiFe_2O_4$, 10-$NiFe_2O_4$/AC, and 15-$NiFe_2O_4$/AC were measured to be 63.1, 17, and 52.3 Ω, accordingly. The charge-transfer resistance value of the 10-$NiFe_2O_4$/AC hybrid is less than the Rct value of $NiFe_2O_4$. The combination of $NiFe_2O_4$ with AC clearly enhanced the charge the transferability of the photoanode. Electron spin response (ESR) spectra were used to confirm the production of $^*O_2^-$ and ^-OH radicals during the photocatalytic reaction of $NiFe_2O_4$/AC under both light and dark conditions, as shown in Figs. S3 and S5. No signal peaks were seen in the absence of light, but upon exposure to very low irradiation, four distinct characteristic peaks for Dimethyl pyridine N-oxide (DMPO)- $^*O_2^-$ and DMPO-^-OH were promptly observed. The ESR signals of DMPO-^-OH are seen in a 1:2:2:1 ratio. The findings validate the presence of $^*O_2^-$ and ·OH in the degrading reaction pathways, in line with the findings from the free radical entrapment studies [47].

3.9. Photocatalytic mechanism

An interaction pathway for the photocatalytic dye process of degradation was presented using elemental trapping experiments. The

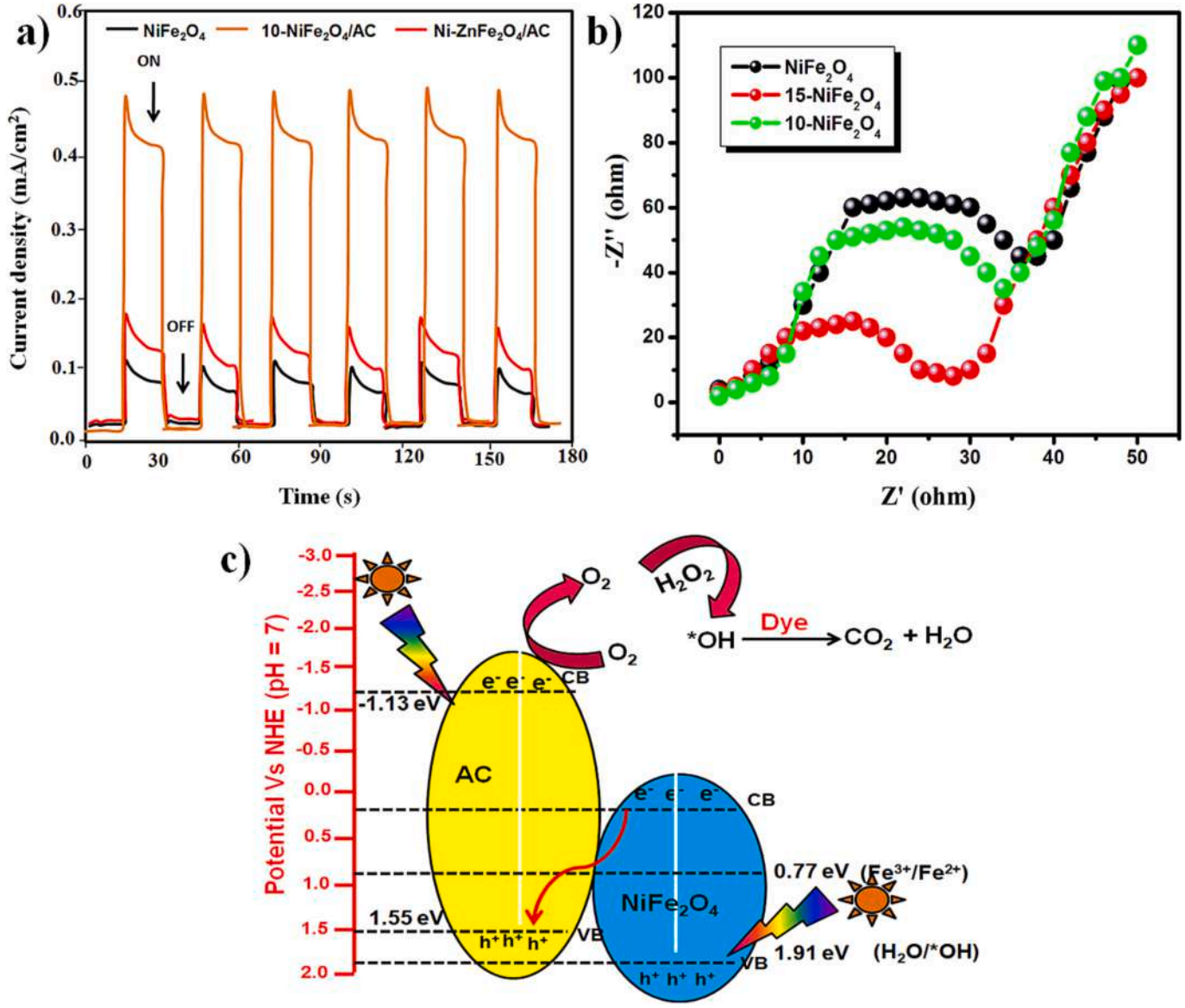

Fig. 8. (a) Dynamic photo current response; (b) EIS spectra of $NiFe_2O_4$ and 10-$NiFe_2O_4$/AC composite samples; (c) schematic representation of the photocatalyst mechanism.

process itself is shown in Fig. 8(c), showing the band possibility of $NiFe_2O_4$ and AC to suggest the reaction mechanism. The conduction and valence band potential of $NiFe_2O_4$ and AC were extracted from the prior study [48]. The conduction band and valence band voltages of AC, relative to the normal hydrogen electrode (NHE), were − 1.14 V and 1.56 V, respectively. The valence and conduction band energies of pure $NiFe_2O_4$ were 0.25 V and 1.91 V, correspondingly. When light struck the photocatalysts, ions were driven from the valence band to the conduction band, creating holes in the valence band of both enzymes. Electrons from the conduction band of AC moved to the conduction band of $NiFe_2O_4$, whereas holes from the valence band of $NiFe_2O_4$ moved to the valence band of AC in binary photocatalysts. The conduction band electrons of the $NiFe_2O_4$ nanoparticle exhibit a reduction voltage of 0.24 V, which is lower than the normal decrease potential of −0.33 V vs NHE. Conversely, the AC VB has a lower oxidation potential of 1.55 V compared to the conventional oxidation state. The photo-Fenton reaction involves the electrons at the conduction band of $NiFe_2O_4$ reacting with H_2O_2 to generate OH• radicals, which decompose organic pollutants via a type-II heterojunction. This proposed reaction pathway for the $NiFe_2O_4$/AC photocatalyst aligns well with the elemental trapping and TA studies.

3.10. Antioxidant property

The antioxidant capacity of $NiFe_2O_4$ and $NiFe_2O_4$/AC, synthesized using the hydrothermal process, was assessed using the DPPH test, a commonly used technique for investigating the radical scavenging properties of nanomaterials. The antioxidant capabilities of 10-NiFe2O4/AC produced using green methods were examined. At a concentration of 300 μg/mL, it exhibited high antioxidant properties of 70 %, compared to $NiFe_2O_4$ which had a scavenging ability of 56 % as shown in Fig. 9. Furthermore, it is shown that both $NiFe_2O_4$ and 10-$NiFe_2O_4$/AC exhibit scavenging activity that varies depending on the dosage. As the concentration increases, the percentage of scavenging activity likewise increases. The *Ocimum basilicum* 10-$ZnFe_2O_4$/AC had a stronger antioxidant activity, as seen by its lower IC50 value of 139 μg/mL compared to $ZnFe_2O_4$ with an IC50 value of 176 μg/mL.

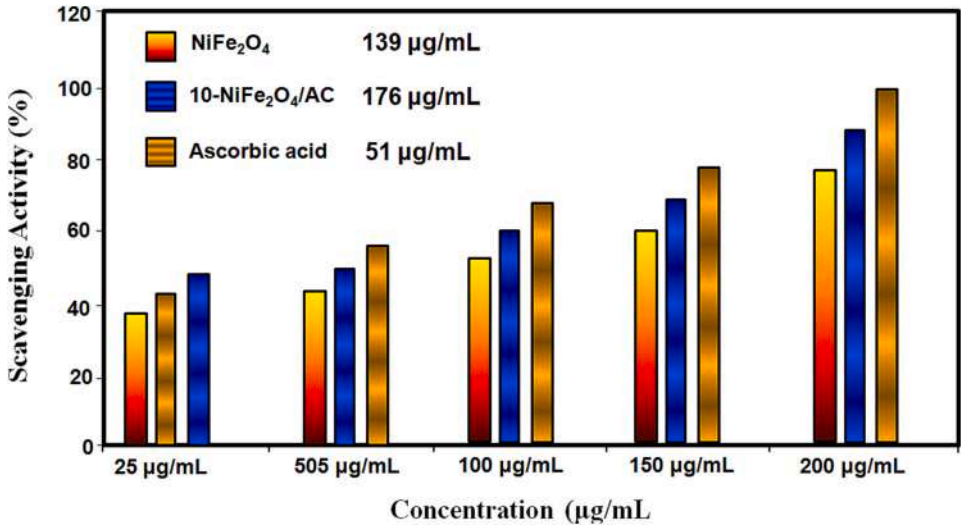

Fig. 9. Antioxidant performance of $NiFe_2O_4$ and 10-$NiFe_2O_4$/AC.

4. Conclusions

Concisely, a new kind of photocatalyst called $NiFe_2O_4$/AC has been developed by a straightforward hydrothermal method. This photocatalyst shows potential for use in the decomposition of dyes through photocatalysis, as well as in antioxidant activities. The $NiFe_2O_4$/AC composite exhibited improved photocatalytic degradation of MB dye and better efficiency in charge separation under simulated visible light. The increased activity of the nanohybrids may be related to the synergistic interaction between $NiFe_2O_4$ and AC. As a result, photoinduced electrons can be efficiently used, surpassing the utilization seen in the pure $NiFe_2O_4$. Kinetic experiments have verified the adherence of the L-H theory to the degradation of MB and RR120 using 10-$NiFe_2O_4$/AC as well as several sacrificial agents including persulfate, H_2O_2, $AgNO_3$, and EDETA. The findings indicated that the photocatalytic degradation of RR120 followed a pseudo-first-order model. The circumstance where H_2O_2 was used as a sacrificial agent exhibited the greatest rate constant and determination coefficient. Thus, the synthesized $NiFe_2O_4$ nanoparticles combined with AC composite proved to be a successful method for enhancing the photocatalytic capacity in wastewater treatment.

CRediT authorship contribution statement

J. Hemalatha: Data curation. **M. Senthil:** Conceptualization. **D. Madhan:** Writing – review & editing. **Amal M. Al-Mohaimeed:** Formal analysis. **Wedad A. Al-onazi:** Investigation.

Declaration of competing interest

The authors declare that they have no known competing financial interests or personal relationships that could have appeared to influence the work reported in this paper.

Data availability

The data that support the findings of this study are available from the corresponding author, upon reasonable request.

Acknowledgment

Authors are grateful to the Researchers supporting project number (RSP2024R247), King Saud University, Riyadh, Saudi Arabia.

Author statement

The authors are thankful to the Reviewers for their useful comments on the manuscript. We have revised the manuscript accordingly, and the detailed responses to the Reviewers' comments are listed below point by point. Yellow shadow has been used for the modified corrections in the manuscript.

Appendix A. Supplementary data

Supplementary data to this article can be found online at https://doi.org/10.1016/j.diamond.2024.110995.

References

[1] Zuming He, Yongmei Xia, Su Jiangbin, Bin Tang, Fabrication of magnetically separable $NiFe_2O_4/Bi_{24}O_{31}Br_{10}$ nanocomposites and excellent photocatalytic performance under visible light irradiation, Opt. Mater. 88 (2019) 195–203.
[2] Yongmei Xia, Zuming He, Su Jiangbin, Bin Tang, Hu Kejun, Lu Yaling, Shunping Sun, Xiaoping Li, Fabrication of magnetically separable $NiFe_2O_4$/BiOI nanocomposites with enhanced photocatalytic performance under visible-light irradiation, RSC Adv. 8 (2018) 4284.
[3] Yongmei Xia, Zuming He, Lu Yalin, Bin Tang, Shunping Sun, Su Jiangbin, Xiaoping Li, Fabrication and photocatalytic property of magnetic $SrTiO_3/NiFe_2O_4$ heterojunction nanocomposites, RSC Adv. 8 (2018) 5441.
[4] Aziz Habibi-Yangjeh, Masoud Abitorabi, Shima Rahim Pouran, Review on photocatalytic conversion of carbon dioxide to value-added compounds and renewable fuels by graphitic carbon nitride-based photocatalysts, Catal. Rev. 61 (2019) 595–628.
[5] C. Trellu, E. Mousset, Y. Pechaud, D. Huguenot, E.D. van Hullebusch, G. Esposito, M.A. Oturan, Removal of hydrophobic organic pollutants from soil washing/flushing solutions: a critical review, J. Hazard. Mater. 306 (2016) 149–174.
[6] S. Zhang, J. Li, M. Zeng, G. Zhao, J. Xu, W. Hu, X. Wang, In situ synthesis of water-soluble magnetic graphitic carbon nitride photocatalyst and its synergistic catalytic performance, ACS Appl. Mater. Interfaces 5 (23) (2013) 12735–12743.
[7] Y. Hong, P. Shi, P. Wang, W. Yao, Improved photocatalytic activity of CdS/reduced graphene oxide (RGO) for H_2 evolution by strengthening the connection between CdS and RGO sheets, Int. J. Hydrogen Energy 40 (2015) 7045–7051.
[8] X. Wang, W. Yang, F. Li, J. Zhu, R. Liu, S. Liu, B. Li, Construction of amorphous TiO_2/BiOBr heterojunctions via facets coupling for enhanced photocatalytic activity, J. Hazard. Mater. 292 (2015) 126–136.
[9] S. Zhang, J. Li, M. Zeng, J. Xu, X. Wang, W. Hu, Polymer nanodots of graphitic carbon nitride as effective fluorescent probes for the detection of Fe^{3+} and Cu^{2+} ions, Nanoscale 6 (2014) 4157–4162.
[10] H.R. Zhu, L. Jiang, Y. Xiao, Y. Chang, Y. Guan, X. Li, G. Zeng, Photocatalytic decolorization and degradation of Congo red on innovative crosslinked chitosan/nano-CdS composite catalyst under visible light irradiation, J. Hazard. Mater. 169 (2009) 933–940.
[11] H.Y. Zhu, R. Jiang, S.H. Huang, J. Yao, Y.Q. Fu, J.B. Li, Novel magnetic $NiFe_2O_4$/multi– walled carbon nanotubes hybrids: facile synthesis, characterization, and application to the treatment of dyeing wastewater, Ceram. Int. 41 (2015) 11625–11631.

[12] M. Veverka, Z. Jirák, O. Kaman, K. Knížek, M. Maryško, E. Pollert, K. Závěta, A. Lančok, M. Dlouhá, S. Vratislav, Distribution of cations in nanosize and bulk Co–Zn ferrites, Nanotechnology 22 (2011) 345701.
[13] X. Liu, F. Sun, Z. Qu, J. Gao, S. Wu, Effect of functional groups on the SO_2, adsorption on carbon surface I: a new insight into noncovalent interaction between SO_2, molecule and acidic oxygen-containing groups, Appl. Surf. Sci. 369 (2016) 552–557.
[14] M.T. Izquierdo, B. Rubio, Carbon-enriched coal fly ash as a precursor of activated carbons for SO_2 removal, J. Hazard. Mater. 155 (2008) 199–205.
[15] L. Shi, K. Yang, Q. Zhao, H. Wang, Q. Cui, Characterization and mechanisms of H_2S and SO_2 adsorption by activated carbon, Energy Fuel 29 (2015) 6678–6685.
[16] L.I. Fenrong, Y.I. Honghong, X. Tang, P. Ning, Q. Yu, D. Kang, Adsorption of carbon dioxide by coconut activated carbon modified with Cu/Ce, J. Rare Earths 28 (2010) 334–337.
[17] H.H. Tseng, M.Y. Wey, Y.S. Liang, K.-H. Chen, Catalytic removal of SO_2, NO and HCl from incineration flue gas over activated carbon-supported metal oxides, Carbon 41 (2003) 1079–1085.
[18] H.H. Tseng, M.Y. Wey, Study of SO_2, adsorption and thermal regeneration over activated carbon-supported copper oxide catalysts, Carbon 42 (2004) 2269–2278.
[19] B. Rubio, M.T. Izquierdo, Coal fly ash based carbons for SO_2 removal from flue gases, Waste Manag. 30 (2010) 1341–1347.
[20] S.I. Ji, S.J. Park, T. Kim, Y.-S. Lee, Hydrogen storage evaluation based on investigations of the catalytic properties of metal/metal oxides in electrospun carbon fibers, Int. J. Hydrogen Energy 34 (2009) 3382–3388.
[21] X.C. Liu, Y. Osaka, H.Y. Huang, et al., Development of lowtemperature desulfurization performance of a MnO_2/AC composite for a combined SO_2 trap for diesel exhaust, RSC Adv. 6 (2016) 96367–96375.
[22] C. Tekmen, Y. Tsunekawa, H. Nakanishi, Electrospinning of carbon nanofiber supported Fe/Co/Ni ternary alloy nanoparticles, J. Mater. Process. Technol. 210 (2010) 451–455.
[23] K. Nataraj, B.H. Kim, J.H. Yun, D.H. Lee, T.M. Aminabhavi, K.S. Yang, Effect of added nickel nitrate on the physical, thermal and morphological characteristics of polyacrylo- nitrile-based carbon nanofibers, Mater. Sci. Eng. B 162 (2009) 75–81.
[24] S. Sathishkumar, M. Parthibavarman, V. Sharmila, M. Karthik, A facile and one step synthesis of large surface area SnO_2 nanorods and its photocatalytic activity, J. Mater. Mater. Electron. 28 (2017) 8192–8196.
[25] P. Sivakarthik, V. Thangaraj, M. Parthibavarman, A facile and one-pot synthesis of pure and transition metals (M = Co & Ni) doped WO_3 nanoparticles for enhanced photocatalytic performance, J. Mater. Mater. Electron. 28 (2017) 5990–5996.
[26] H. Deng, F. Xu, B. Cheng, J. Yu, W. Ho, Photocatalytic CO_2 reduction of C/ZnO nanofibers enhanced by an Ni-NiS cocatalyst, Nanoscale 12 (2020) 7206–7213.
[27] A. Fkhami, H. Khoshsafar, H. Bagheri, T. Madrakian, Preparation of $NiFe_2O_4$/graphene nanocomposite and its application as a modifier for the fabrication of an electrochemical sensor for simultaneous determination of tramadol and acetaminophen, Anal. Chim. Acta 831 (2014) 5047.
[28] A.A. Ensafi, B. Arashpour, A. Rezaei, A.R. Allafchian, Voltammetric behavior of dopamine at a glassy carbon electrode modified with $NiFe_2O_4$ magnetic nanoparticles decorated with multiwalled carbon nanotubes, Mater. Sci. Eng. C 39 (2014) 78.
[29] Huabin Chen, Wenxia Liu, Zhuozhuo Qin, $ZnO/ZnFe_2O_4$ nanocomposite as a broad spectrum photo-Fenton like photocatalyst with near-infrared activity, Catal. Sci. Technol. 7 (2017) 2236–2244.
[30] Yong Liu, Yuchun Song, Yaohui You, Fu Xiaojing, Jing Wen, Xiaogang Zheng, $NiFe_2O_4/g\text{-}C_3N_4$ heterojunction composite with enhanced visible-light photocatalytic activity, J. Saudi Chem. Soc. 22 (2017) 439–448.
[31] Haiyan Ji, Xiaocui Jing, Xu Yuanguo, Yan Jia, Hongping Li, Yeping Li, Liying Huang, Qi Zhang, Xu Hui, Huaming Li, Magnetic $g\text{-}C_3N_4/NiFe_2O_4$ hybrids with enhanced photocatalytic activity, RSC Adv. 5 (2015) 57960–57967.
[32] Jian Zeng, Ting Song, Meixiang Lv, Tingting Wang, Jiayi Qin, Heping Zeng, Plasmonic photocatalysts $Au/g\text{-}C_3N_4/NiFe_2O_4$ nanocomposites for enhanced visible-light-driven photocataly- tic hydrogen evolution, RSC Adv. 6 (2016) 54964–54975.
[33] Yunjin Yao, Wu Guodong, Lu Fang, Shaobin Wang, Hu Yi, Jie Zhang, Wanzheng Huang, Fengyu Wei, Enhanced photo-Fenton-like process over Z-scheme $CoFe_2O_4/g\text{-}C_3N_4$ Heterostructures under natural indoor light, Environ. Sci. Pollut. Res. 23 (2016) 21833–21845.
[34] S. Lin, Q. Qiao, X. Zhen, Transition metal atom doped C2N as catalyst for the oxygen reduction reaction: a density functional theory study, Int. J. Hydrogen Energy 45 (2020) 27202–27227.
[35] M. Jayashree, V. Sharmila, K.L. Meganathan, R. BoopathiRaja, M. Parthibavarman, Mohd Shkir, S. AlFaify, Design and fabrication of graphene anchored CeO_2 hybrid nanocomposite electrodes for high performance energy storage device applications, Inorg. Chem. Commun. 132 (2021) 108838.
[36] R. BoopathiRaja, M. Parthibavarman, Hetero-structure arrays of $MnCo_2O_4$ nanoflakes@ nanowires grown on Ni foam: design, fabrication and applications in electrochemical energy storage, J. Alloy. Compd. 811 (2019) 152084.
[37] R. BoopathiRaja, M. Parthibavarman, A. Nishara Begum, Hydrothermal induced novel $CuCo_2O_4$ electrode for high performance supercapacitor applications, Vacuum 165 (2019) 96–104.
[38] M. Parthibavarman, M. Karthik, S. Prabhakaran, Role of microwave on structural, morphological, optical and visible light photocatalytic performance of WO_3 nanostructures, J. Clus. Sci. 30 (2019) 495–506.
[39] I. Khosravi, M. Yazdanbakhsh, E.K. Goharshadi, et al., Preparation of nanospinels $NiMnxFe_{2-x}O_4$ using sol–gel method and their applications on removal of azo dye from aqueous solutions, Mater. Chem. Phys. 130 (2011) 1156–1161.
[40] Zuming He, Hanpei Yang, Su Jiangbin, Yongmei Xia, Fu Xiaofei, Lina Wang, Li Kang, Construction of multifunctional dual Z-scheme composites with enhanced photocatalytic activities for degradation of ciprofloxacin, Fuel 294 (2021) 120399.
[41] X. Meng, Y. Zhuang, H. Tang, C. Lu, Hierarchical structured $ZnFe_2O_4@SiO_2@TiO_2$ composite for enhanced visible-light photocatalytic activity, J. Alloys Compd. 761 (2018) 15–23.
[42] M. Kuang, J. Zhang, W. Wang, J. Chen, R. Liu, S. Xie, J. Wang, Z. Ji, Synthesis of octahedral-like $ZnO/ZnFe_2O_4$ heterojunction photocatalysts with superior photocatalytic activity, Solid State Sci. 96 (2019) 105901.
[43] R. Tao, C. Zhao, C. Shao, X. Li, X. Li, J. Zhang, S. Yang, Y. Liu, $Bi_2WO_6/ZnFe_2O_4$ heterostructures nanofibers: enhanced visible-light photocatalytic activity and magnetically separable property, Mater. Res. Bull. 104 (2018) 124–133.
[44] V. Ramasamy Raja, A. Karthika, S. Lok Kirubahar, A. Suganthi, M. Rajarajan, Sono-chemical synthesis of novel $ZnFe_2O_4/CeO_2$ heterojunction with highly enhanced visible light photocatalytic activity, Solid State Ion. 332 (2019) 55–62.
[45] J. Su, Q. Shang, T. Guo, S. Yang, X. Wang, Q. Ma, H. Guan, F. Xu, S.C. Tsang, Construction of heterojunction $ZnFe_2O_4/ZnO/Ag$ by using ZnO and Ag nanoparticles to modify $ZnFe_2O_4$ and its photocatalytic properties under visible light, Mater. Chem. Phys. 219 (2018) 22–29.
[46] L. Zhou, L. Ji, P.-C. Ma, et al., Development of carbon nanotubes/$CoFe_2O_4$ magnetic hybrid material for removal of tetrabromobisphenol A and Pb (II), J. Hazard. Mater. 265 (2014) 104–114.
[47] Zuming He, Muhammad Saboor Siddique, Hanpei Yang, Yongmei Xia, Jiangbin Su, Bin Tang, Lina Wang, Li Kang, Zhengyi Huang, Novel Z-scheme In_2S_3/Bi_2WO_6 core-shell heterojunc- tions with synergistic enhanced photocatalytic degradation of tetracycline hydrochloride, J. Clean. Prod. 339 (2022) 130634.
[48] Zuming He, Kai Lin, Ngie HingWong, Jaka Sunarso, Yongmei Xia, Fu Xiaofei, et al., Elucidation of mechanisms, pathways, and toxicity of fabricated Z-scheme $KNbO_3/ZnIn_2S_4$ hollow core–shell composites for enhanced ciprofloxacin photodegradation, Chem. Eng. J. 475 (2023) 146262.

Physica B 669 (2023) 415288

Contents lists available at ScienceDirect

Physica B: Condensed Matter

journal homepage: www.elsevier.com/locate/physb

Facile dip-coating assisted preparation of reduced graphene oxide-copper oxide nanocomposite thin films on aluminum substrate for solar selective absorber

N. Murugesan [a], S. Suresh [b], M. Kandasamy [c,d], S. Murugesan [e], N. Pugazhenthiran [f], V. Prasanna Venkatesh [g], B.K. Balachandar [g], S. Karthick Kumar [a,*], M.N.M. Ansari [c]

[a] Department of Physics, Sethu Institute of Technology, Kariapatti, 626 115, Virudhunagar, Tamil Nadu, India
[b] PG & Research Department of Physics, Sri Vidya Mandir Arts & Science College (Autonomous), Katteri, 636 902, Uthangarai, Tamil Nadu, India
[c] Institute of Power Engineering, Universiti Tenaga Nasional, Kajang, 43000, Selangor, Malaysia
[d] Department of Chemistry, K.Ramakrishnan College of Technology, Trichy, 621 112, Tamil Nadu, India
[e] Department of Inorganic Chemistry, School of Chemistry, Madurai Kamaraj University, Madurai, 625 021, Tamil Nadu, India
[f] Laboratorio de Fotoquímica y Fotofísica, Departamento de Química, Universidad Técnica Federico Santa María, Av. España 1680, Valparaíso, Chile
[g] Department of Physics, Velammal College of Engineering and Technology, Madurai, 625 009, Tamil Nadu, India

ARTICLE INFO

Keywords:
rGO-CuO nanocomposite
Dip coating
Thin films
Selective absorber coating
Selectivity
Solar energy conversion

ABSTRACT

Reduced graphene oxide integrated copper oxide nanocomposite thin film (rGO-CuO NC TF) solar selective absorber coatings were devised on aluminum substrate using dip-coating procedure. The prepared coatings were subjected to characterization by scanning electron microscopy, X-ray diffractometry, energy-dispersive X-ray spectroscopy, X-ray photoelectron spectroscopy, PL spectroscopy, UV–vis–NIR spectrophotometer, Emissometer and Raman spectroscopy. XRD and Raman analyses disclosed presence of mono-phase with highly crystalline monoclinic structured CuO in the rGO-CuO NC TFs. The SEM images revealed grain-like morphology of CuO, which are randomly distributed on rGO sheets. EDX and XPS investigations confirmed presence of anticipated chemical constituents and chemical composition, respectively in the NC TFs. The rGO-CuO NC TF with 1.0 wt% GO disclosed absorptance (α) of 79.92% and emittance (ε) of 4.2% with a highest selectivity (ξ) of 19.03 that suggests its promising prospect for solar absorber coating in solar thermal devices.

1. Introduction

Solar energy is an ideal, abundant and reliable energy source over other similar category of non-conventional energy sources, viz. biomass, hydro, wind, etc. [1,2]. Among various technologies that rely on solar energy, solar thermal energy conversion is viewed as clean and energy-saving mode of directly transforming solar energy into thermal energy and as a consequence, it has been broadly employed in solar water heating, concentrated solar power, brine distillation and solar cooling [3–6]. An important component needed for capturing heat energy is solar selective absorber with significantly appreciable absorptance ($\alpha > 90\%$) in visible and NIR regions (0.3 μm–2.0 μm) of solar spectrum and very low thermal emittance ($\varepsilon < 10\%$) in infrared wavelengths (2.5 μm–25 μm) of Planck's spectrum [7,8]. Formation of an economical and optically effectual absorber coating is a crucial requirement towards apprehending cost-effective solar thermal collectors since existing preparation approaches necessitate expensive equipment. Materials with high photo-thermal conversion efficiency can be obtained by their appreciable thermal conductivity and stability, persistent humidity tolerance, resistant to corrosion, minimal refraction and least expansion coefficient [9]. Nonetheless, researches in the past have decisively confirmed unfeasibility of accomplishing a noticeably high photo-thermal transformation efficiency using mono-component selective absorbers [10–13]. In contrast, properties of bi-component material comprised of two functional materials can be enhanced when compared to mono-component material [14]. Meanwhile, metal substrates (Cu or Al) utilized for preparing solar selective absorber thin film coatings disclose anticipated beneficial properties of lower emittance, higher conductivity and corrosion resistance [15].

Previously, several research groups have proposed flexible selective

* Corresponding author.
E-mail address: physicsmsckarthick@gmail.com (S. Karthick Kumar).

https://doi.org/10.1016/j.physb.2023.415288
Received 7 June 2023; Received in revised form 20 August 2023; Accepted 3 September 2023
Available online 6 September 2023

solar absorbers for concentrating solar power (CSP) applications. For instance, Karoro et al. (2015) prepared Co nanocylinders embedded nanoporous alumina template through electrodeposition technique and subjected to femtosecond laser surface structuring. The optimized Co nanocylinders-Al_2O_3 cermet sample showed an elevated optical absorptance of >98% and a relatively low emittance of ~0.03 between solar spectral radiation of 200 nm and 1100 nm [16]. Amorphous vanadium metal thin films were coated on glass substrates using electron beam evaporator which were exposed to nanosecond laser pulses of 1064 nm wavelength. UV–Vis–NIR reflectance analysis of laser irradiated samples disclosed reduced reflectance in visible region of solar spectrum due to laser exposure [17]. Thin films composed of chromium were formed on float glass substrates by electron beam evaporation and femtosecond fiber laser was employed to produce micro/nano-structure and also to oxidize surface of thin film coatings (Cr/α-Cr_2O_3) under atmospheric environments. The Cr/α-Cr_2O_3 cermet nanocomposite thin film displayed a large solar selective absorptance and significantly minimized reflectance from 70% to 2% in UV-VIS-NIR wavelength range of 190 nm–1100 nm [18].

As a p-type semiconductor with low band gap energy, cupric oxide (CuO) has cost effectiveness, earth-abundance, favorable optical properties, appreciable catalytic activity, stability and non-toxic and as a consequence, it has been recognized as potential candidate towards photoelectrochemical and photovoltaic application prospects [19]. Its reliable optical absorption, ideal band potential and appreciable theoretical efficiency make it a promising contender for solar energy conversion [20,21]. On the other hand, researchers have amazed about development of graphene oxide due to its unique thermal, physical and chemical properties. Graphene oxide can be prepared facilely by dispersion in water, organic solvents and dissimilar matrixes owing to its oxygen functionalities. It is a highly anticipated feature while blending graphene oxide with polymer or ceramic matrixes for enhancing electrical and mechanical characteristics. Graphene oxide has attracted much attention due to its appreciable optical transmittance, best room temperature heat conductivity and capability of having flexibility, all within a strong and nano-sized material. Preparation of nano-hybrid composites composed of graphene-semiconductor metal oxide is a familiar example for electrical and electrochemical applications, viz. photocatalysis, chemical sensors, photovoltaic, storage and fuel cells [19]. Moreover, single layer of carbon atoms organized into a honeycomb crystal lattice of graphene has great potential for supercapacitor applications, owing to its exceptional conductivity and high specific area [22].

Graphene oxide (GO) and reduced graphene oxide (rGO) have been demonstrated as derivatives of graphene which unveil diverse chemical and structural properties because of dissimilarities in their chemical composition. The thermal stability of GO can be enhanced by partial reduction of GO that generates rGO which in turn creates significant alterations in structural, mechanical, solubility and reactive properties [23]. Consequently, rGO has noticeable visible and near infrared absorption in solar spectrum [24,25] and therefore, it has auspicious potential for selective absorber. It has also been established as a promising tandem substance in combination with nickel oxide (NiO) [26] and cobalt oxide (Co_3O_4) [27] for enhancing performance of solar selective absorber. The functional groups present in the rGO enable its dispersibility in various solvents in the absence of aggregation [28,29]. Optimizing optical properties of semiconductor-metal oxide hybrid system is viable by means of integrating rGO towards attaining rGO-based solar selective absorber coating. The rGO helps substantial solubility in aqueous and polar solvents and reliance of sol-gel method is suitable to produce rGO thin films that eventually generate high transmittance and strong abrasion resistance for applications in harsh environments [30]. The advantages of sol-gel method when compared to other methods are facile, economical, superior homogeneity, ease tuneability of size, shape and composition of resultant product, governable stoichiometry, high purity, crystallization of thin films/particles at comparatively low calcination temperature and flexibility of forming compact thin films [31–34]. The presumable reason behind the selection of rGO as a functional material for CuO is strong light absorption tendency of rGO in near-infrared (NIR) region, which facilitates effective photothermal heating [35,36].

By considering these facts, the current study concentrates on preparation of an affordable solar-selective absorber coating with anticipated solar absorptance and thermal emittance for flat plate collector applications. Herein, we describe synthesis of rGO modified CuO nanocomposite thin films (rGO-CuO NC TFs) solar selective absorber on aluminium metal substrate by facile dip-coating technique.

2. Experimental

2.1. Chemicals

Graphite flakes (99.99%) were bought from Alfa Aesar. Sulfuric acid (H_2SO_4; 98%), hydrochloric acid (HCl; 95%), hydrogen peroxide (H_2O_2; 30%), potassium permanganate ($KMnO_4$; 99.9%) and sodium nitrate ($NaNO_3$; 99%) were obtained from Rankem. Copper acetate [$Cu(CH_3COO)_2$], polyethylene glycol [$HO(CH_2CH_2O)nH$; MW = 4000] and diethanolamine [$NH(CH_2CH_2OH)_2$; 98%] were acquired from Merck. Ethanol [CH_3CH_2OH; 99.99%] and double distilled water were used for preparing solutions and washings.

2.2. Synthesis of graphene oxide

Graphene oxide (GO) was synthesized using natural graphite by modified Hummer's protocol [37]. Briefly, graphite flakes (1.0 g; 0.0833 mol) and $NaNO_3$ (0.50 g; 0.0059 mol) were dispersed in 46 ml conc. H_2SO_4 (0.82 mol), which was kept in ice bath and stirred for 4 h. To this solution, $KMnO_4$ (6.0 g; 0.038 mol) was added, followed by stirring the solution for 2 h at 35 °C. Subsequently, distilled water (92 ml) was included in the above mixture and heated for 2 h at 98 °C. Then, distilled water (100 ml) and 30% H_2O_2 (10 ml; 0.0979 mol) were slowly added to this solution for 2 h under stirring. The composition of graphite, $NaNO_3$, H_2SO_4, $KMnO_4$ and H_2O_2 in the sol was in the molar ratio of 10 : 140: 1 : 21: 8. The resultant sol was washed using HCl and distilled water to remove impurities. Finally, the obtained sol was dried for 4 h at 100 °C to get GO.

2.3. Synthesis of GO-CuO NCs

Initially, CuO precursor solution (0.6 M) was prepared by dissolving 6 g $Cu(CH_3COO)_2$ in 50 mL absolute ethanol and the formed solution was stirred for 4 h at room temperature. Ethanol in the solution was evaporated by heating it at 50 °C for 20 min until the solution volume was reduced to half so as to obtain a viscous solution. To this viscous solution, 7.0 mL of $NH(CH_2CH_2OH)_2$ (0.0711 mol) was introduced as chelating agent and stirred for 30 min that resulted in the generation of CuO matrix precursor sol. Then, 1.0 g polyethylene glycol (PEG) was incorporated as shape directing template for CuO matrix precursor sol and stirred for 30 min. Subsequently, different weight contents of GO (0.1, 0.2, 0.5, 1.0, 1.5 and 2.0%) were added to the prepared CuO sol. Finally, the solutions were stirred for 24 h followed by ageing for 5 days towards the formation of sol containing GO-CuO NCs. Similar procedure was adopted for 2.0 g PEG to investigate the influence of PEG.

2.4. Preparation of rGO-CuO NC TFs

For the preparation of rGO-CuO NC TFs, aluminum (Al) substrates with dimension of 2 cm × 2 cm were preliminary submerged in ethanol and ultrasonically treated for 15 min to eliminate surface adsorbed impurities. The cleaned Al substrates were dip coated by submerging them in GO-CuO NCs sol having pH of 11.5 using dip coating instrument. The dipping and withdrawal speed of Al substrates was 10 mm/5 s.

Evaporation time for coatings on Al substrates was 10 s. Thickness of GO-CuO NC TFs was tuned by changing number of dipping and the formed thin films were heat-treated at 250 °C for 3 h. Finally, the GO-CuO NC TFs were sintered for 2 h at 400 °C to transform GO into rGO.

2.5. Characterization

XRD patterns of thin films were obtained using Bruker AXS D8 advance X-ray diffractometer employing Cu Kα radiation (λ = 1.5418 Å). SEM images were recorded in JEOL6390 Model scanning electron microscopy fitted with EDX spectroscopy. X-ray photoelectron spectroscopy characterization was performed in MULTILAB 2000 Base system electron spectrometer with multichannel detector. Photoluminescence spectra of thin films were recorded using JASCO FP-8500 Spectrofluorometer equipped with a xenon discharge lamp at an excitation wavelength of 375 nm. Normal reflectance of thin films was recorded using UV–vis–NIR diffuse reflectance spectrophotometer (Cary 5E) in the wavelength range from 300 nm to 2000 nm. Raman spectra were recorded by He–Ne laser excitation source (632.8 nm). Solar absorptance of thin films were measured using following formula [38].

$$\text{Absorptance } (\alpha) = \frac{\int_{0.3\mu m}^{2.0\mu m} I_{sol}(\lambda)(1 - R(\lambda))d\lambda}{\int_{0.3\mu m}^{2.0\mu m} I_{sol}(\lambda)d\lambda} \quad (1)$$

where, $I_{sol}(\lambda)$ is standard spectral irradiance of solar illumination at wavelength (λ).

Thermal emittance was measured by Emissometer (AE1/RD1). Selectivity (ξ) is ratio between solar absorptance (α) and thermal emittance (ε).

$$\xi = \frac{\alpha}{\varepsilon} \quad (2)$$

3. Results and discussion

XRD spectra of GO, rGO, CuO and rGO-CuO NC TFs are shown in Fig. 1. Diffraction (2θ) peaks perceived at 11.45 and 42.48° are corresponding to diffraction planes (0 0 1) and (1 0 0) that confirms presence of GO [39]. The intense diffraction peak observed at 11.45° indicates highly oxidized form of GO prepared from the starting material graphite. XRD spectrum of CuO TF reveals presence of sharp diffraction peaks at 35.33, 38.30, and 50.11° correspond to the diffraction planes of (0 0 2), (2 0 0) and (1 1 2), which ascertained monoclinic crystal structure of CuO (JCPDS Card No. 41–0254) [8]. Peak acquired for 1%-rGO-CuO and 2%-rGO-CuO NC TFs at 2θ value of 43.36 allocated to (2 0 0) plane of FCC structure (JCPDS No. 04–0836) is corresponding to aluminium, which is originated from aluminium substrate [40]. In the rGO-CuO NCs, the peaks at 36.45° and 50.47° are also appeared and belong to the monoclinic structure meanwhile, the diffraction peaks observed at 35.33 and 38.30° are disappeared or shifted to 36.45°. The consequence behind the disappearing or shifting might be attributed to rGO presence in rGO-CuO NCs. Relatively low intense diffraction peak at 23.34° in 1%-rGO-CuO and 2%-rGO-CuO NC TFs belongs to rGO. This confirms successful grafting of rGO with CuO. Diffraction peak noticed at 65.43° can be ascribed to beneath Al substrate used for forming 1%-rGO-CuO and 2%-rGO-CuO NC TFs.

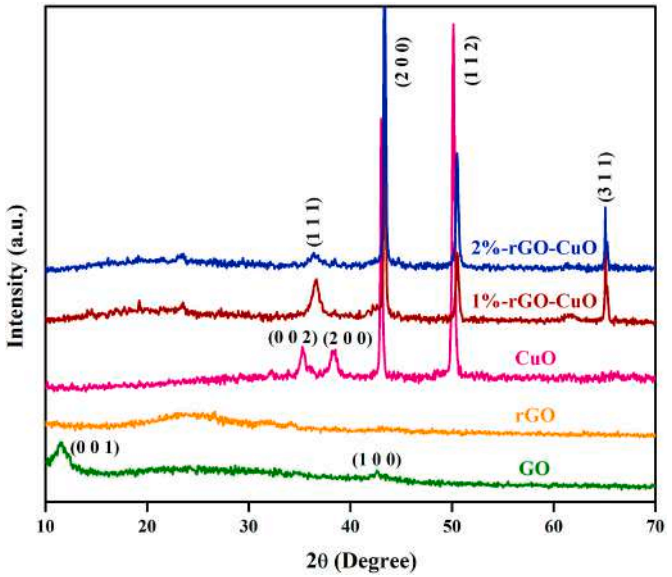

Fig. 1. XRD spectra of GO, rGO, CuO and rGO-CuO NC TFs.

Average crystallite size (D) of CuO, 1.0%-rGO-CuO and 2.0%-rGO-CuO NC TFs was determined by Scherrer's formula and the values are 76.67, 83.18 and 89.53 nm, respectively. Similarly, average grain size of CuO, 1.0%-rGO-CuO and 2.0%-rGO-CuO NC TFs found out from their respective SEM images are 0.52, 1.70 and 2.84 μm, respectively. These results reveal that the grain size of the thin films is considerably higher when compared to their corresponding crystallite size. Among the thin films, the CuO TF, due to its small atomic radius and small activation energy, has exhibited low crystallite and grain size over 1.0%-rGO-CuO and 2.0%-rGO-CuO NC TFs, which in turn discloses that the presence of rGO with respect to its wt% improves crystallite and grain size of the rGO-CuO NC TFs [41–43].

Dislocation density (δ) and strain (ε) values of CuO and rGO-CuO TFs were measured from their respective crystallite size values (Fig. 2). Usually, the dislocation density indicates defects count in a crystal and strain explains crystallinity of crystal structure. The formula ($\delta = 1/D^2$) was used to determine dislocation density of CuO and rGO-CuO TFs. It can be observed from Fig. 2 that the dislocation density and strain values are diminished with respect to increase in wt% of the GO in the rGO-CuO NC TF. The dislocation density value of rGO-CuO NC TFs is lower than that of CuO, owing to controlled reaction rate that takes place in the presence of rGO, which demonstrates that the rGO-CuO NC TFs are more crystalline when compared to CuO TF [44]. Similarly, the low strain values of rGO-CuO NC TFs discloses their enhanced crystallinity when compare to CuO TF. The decrease in the strain value with respect to increasing wt% of GO in the rGO-CuO NC TF may also a reason for increasing the grain size of the respective thin films [45]. The decrease in the lattice strain values of the rGO-CuO NC TFs can be explained by

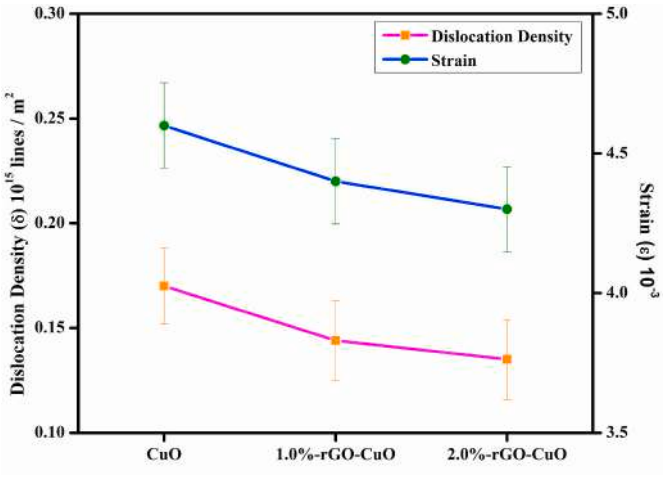

Fig. 2. Dislocation density and strain values of CuO, 1.0%-rGO-CuO and 2.0%-rGO-CuO NC TFs.

the fact that the co-deposition of rGO and CuO over Al substrate might have minimized considerable mismatching stress between Al matrix and rGO due to high specific surface area of the rGO that cannot be relaxed after deposition [46]. It is also presumed that the extinction coefficient of rGO-CuO NC TFs might be higher than CuO TF and as a consequence, the rGO-CuO NC TFs absorb most of the solar spectrum in the UV–Vis–NIR region through constructive solar interference [36].

The synthesized CuO, 1.0%-rGO-CuO NC and 2.0%-rGO-CuO NC TFs were characterized by EDX spectroscopy to examine their purity (Fig. 3). Peaks associated with Cu and O elements are noticed in EDX spectrum of CuO TF (Fig. 3(a)). EDX spectrum of 1.0%-rGO-CuO NC TF revealed elemental peaks belong to Cu, C and O, which proves CuO and rGO existence in 1.0%-rGO-CuO NC TF (Fig. 3(b)). Similarly, the EDX spectrum of 2.0%-rGO-CuO NC TF disclosed presence of anticipated elemental peaks of Cu, C and O (Fig. 3(c)). The relatively low intense peak observed at the vicinity of energy value of 9 keV (~8.9 keV) in the EDX spectra of CuO and rGO-CuO NC NC TFs can be assigned to elemental Cu, which is in harmony with previous reports [47–49]. Non-appearance of peaks pertaining to impurities in the EDX spectra revealed the pristine nature of CuO and rGO-CuO NC TFs prepared through the present dip-coating technique.

SEM was utilized to analyze the morphology of pure CuO, 0.5%-rGO-

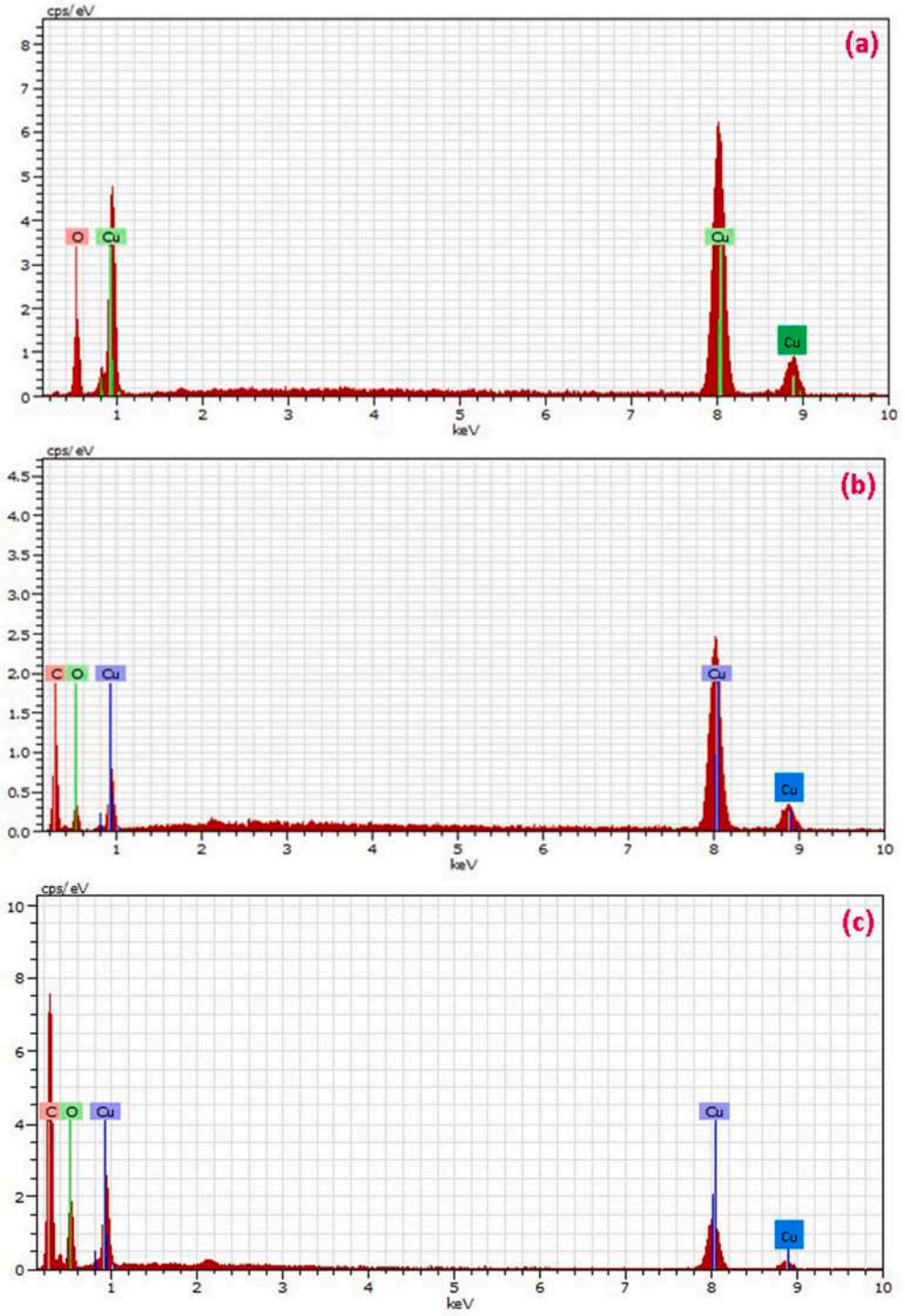

Fig. 3. EDX spectra of (a) CuO, (b) 1.0%-rGO-CuO and (c) 2.0%-rGO-CuO NC TFs.

CuO, 1.0%-rGO-CuO and 2.0%-rGO-CuO NC TFs (Fig. 4). Low and high magnified SEM images of pure CuO TF exhibits rough and uniform distribution of granular-like CuO nanostructure (Fig. 4(a-c)). The SEM images of 0.5%-rGO-CuO (Fig. 4(d-f)), 1.0%-rGO-CuO (Fig. 4(g-i)) and 2.0%-rGO-CuO NC (Fig. 4(j-l)) TFs disclose the presence of several spherical shaped CuO nanoparticles, whose size ranges from 500 nm to 3 μm. The CuO nanoparticles adjoined with adjacent nanoparticles, which are dispersed on rGO sheets. It is hypothesized that rGO adsorb polar molecules or polymer facilely by surface functional groups and consequently, they adsorb CuO nanoparticles. However, the GO content was dissimilar, spherical CuO nanoparticles are distributed uniformly on rGO sheet in a constructive manner because of supplemented polymer

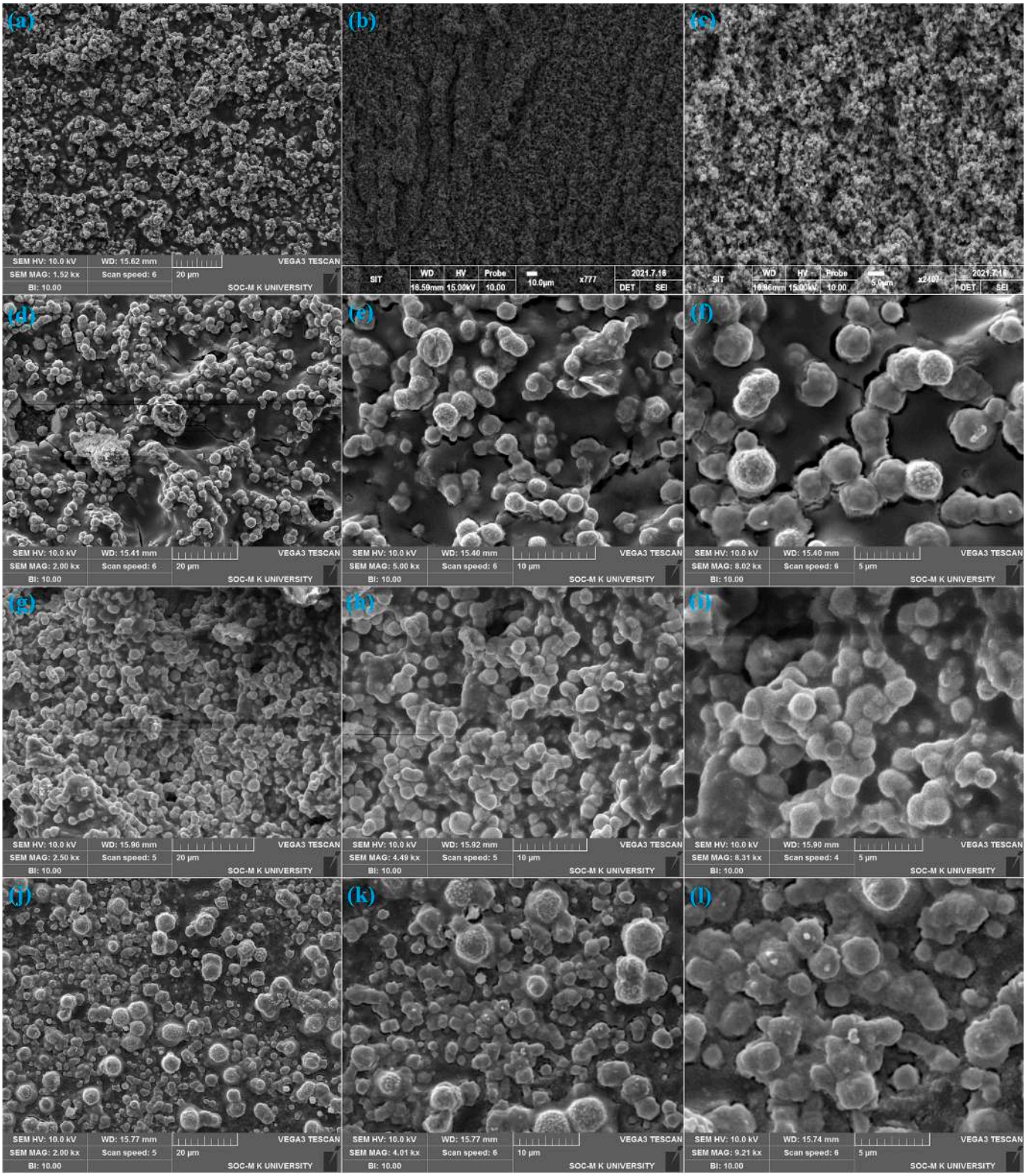

Fig. 4. SEM images of (a–c) pure CuO, (d–f) 0.5%-rGO-CuO, (g–i) 1.0%-rGO-CuO and (j–l) 2.0%-rGO-CuO NC TFs.

(PEG), which facilitates to adsorb CuO nanoparticles by host material rGO. Rendering to XRD analysis, CuO nanoparticles have low crystallite size than rGO-CuO NC, which is in accordance with corresponding SEM images.

XPS investigation is an appropriate evidence for elemental composition, functional groups presence and nature of valence states of elements in 1.0%-rGO-CuO NC TF (Fig. 5). The complete XPS survey spectrum of 1.0%-rGO-CuO NC TF (Fig. 5(a)) shows occurrence of only Cu 2p, O1s and C1s elements without any other impurities, which is in accordance with corresponding EDX result (Fig. 3). High resolution XPS spectrum of Cu 2p exhibits two chief peaks centered at 933.64 and 953.55 eV, which can be assigned to Cu $2p_{3/2}$ and Cu $2p_{1/2}$ of CuO, respectively (Fig. 5(b)). Additional shake-up peaks at 940.57 and 943.15 eV and a satellite peak at 961.61 eV are also detected in Cu 2p core level XPS spectrum that prove Cu^{2+} bonding state of CuO in 1.0%-rGO-CuO NC TF [50]. Further, binding energy difference between Cu $2p_{3/2}$ and Cu $2p_{1/2}$ peaks is found out as 19.91 eV, indicating existence of Cu^{2+} in 1.0%-rGO-CuO NC TF [51,52].

In Fig. 5(c), high resolution XPS spectrum of C1s visualizes deconvoluted peaks centered at 283.75, 285.17 and 287.75 eV that can be credited to sp^2 C–C atom of graphitic carbon (C=C/C–C), stronger carbon–oxygen bonding assigned as C–O functionalities (epoxy/hydroxyl) and –COOH groups of GO, respectively [53]. Highly intense peak noticed at 285.17 eV of C1s suggests that 1.0%-rGO-CuO NC TF contains larger number of oxygenated carbon (C–O) species (~50% of total carbon in rGO-CuO NC TF), indicating interior uniformity of rGO structure in 1.0%-rGO-CuO NC TF [54,55]. It is observed from peak strengths of C=O/O=C–O bonds in C1s peak that during reduction of GO, all carbonyl, hydroxyl and epoxy groups are reduced subsequent to high temperature sintering [56], indicating partial reduction of GO in the 1.0%-rGO-CuO NC TF. Fig. 5(d) shows O 1s XPS spectrum of 1.0%-rGO-CuO NC TF that is deconvoluted into two peaks, which are located at 530.28 and 531.49 eV. Lower binding energy peak observed at 530.28 eV is attributed to lattice oxygen in CuO and higher binding energy peak noticed at 531.49 eV is ascribed to lightly bound oxygen comprehending rGO functional groups [57]. In addition, presence of two different oxygen environment and identical Cu 2p core level peak positions of rGO integrated CuO over CuO discloses that the CuO nanoparticles are chemisorbed over the rGO sheets through Cu–*O*–C linkage in the 1.0%-rGO-CuO NC TF [58–60].

The atomic percentage of elements present in the 1.0%-rGO-CuO NC TF was determined by EDX and XPS analysis for comparison (Table 1). The observed results disclose that Cu atoms are chiefly present in the 1%-rGO-CuO NC TF when compared to the O and C atoms. The observed atomic percentage of Cu, O and C elements are corresponding to the CuO and rGO molecules present in the 1%-rGO-CuO NC TF. The atomic percentage of Cu, O and C elements in the 1.0%-rGO-CuO NC TF determined by EDX analysis was 55.14, 24.80 and 25.17%, respectively.

Table 1
Atomic percentage of elements in 1.0%-rGO-CuO NC TF determined by EDX and XPS analysis.

Thin Film Sample	Element	Atomic Percentage (%)	
		EDX Analysis	XPS Analysis
1%-rGO-CuO NC TF	Cu	55.14	44.15
	O	24.80	34.86
	C	25.17	21.13

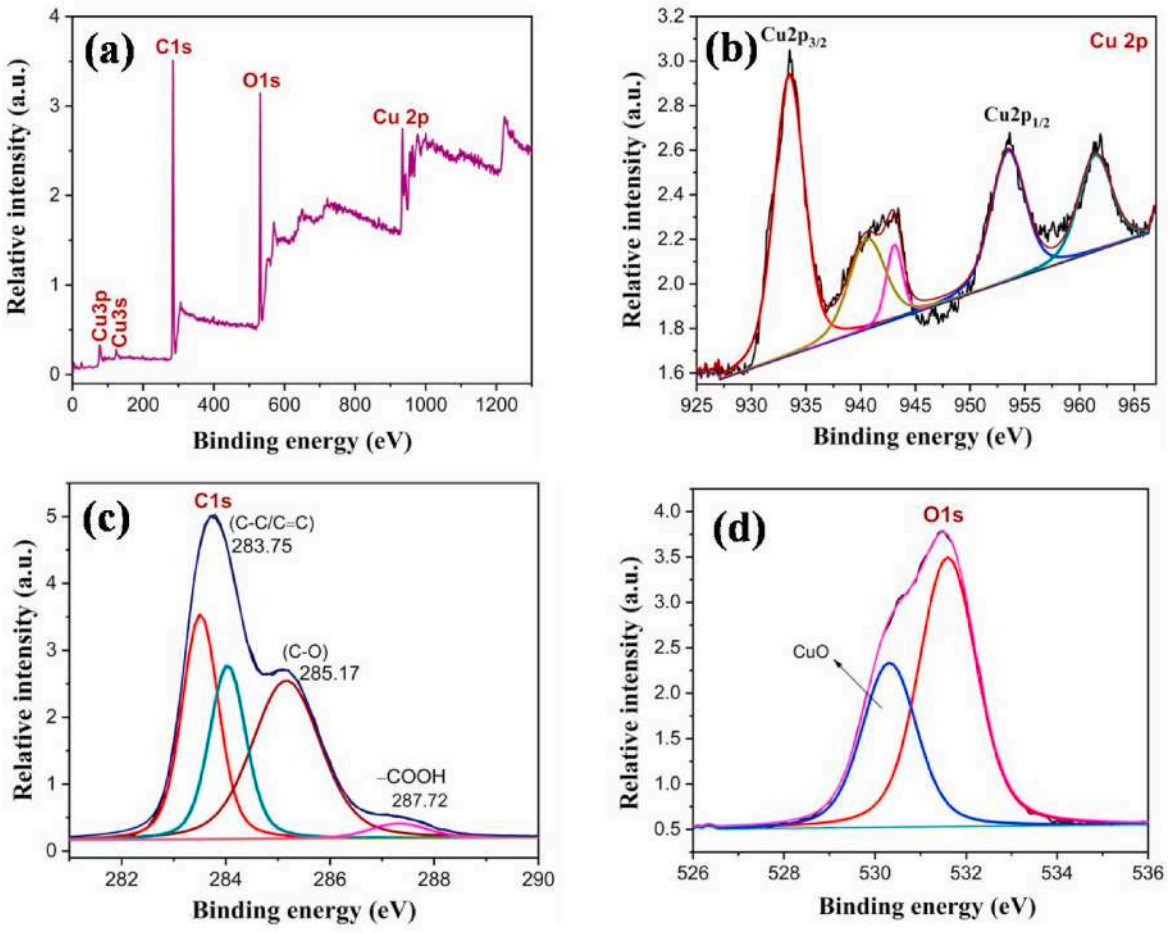

Fig. 5. (a) XPS survey spectrum, (b) high resolution XPS spectrum of Cu 2p, (c) XPS spectrum of C1s, and (d) O1s spectrum of 1.0%-rGO-CuO NC TF.

Whereas, the atomic percentage of Cu, O and C elements calculated by XPS analysis was 44.15, 34.86 and 21.13%, respectively. The difference in atomic percentage can be attributed to the fact that the XPS analysis is surface-sensitive and the observed result is proportional to number of atoms of respective elements (Cu, O and C) present on the surface of 1%-rGO-CuO NC TF. In contrast, the EDX analysis gives atomic percentage of elements for the bulk sample and consequently, its result gives atomic percentage of identified elements (Cu, O and C) to get total atomic percentage composition of the 1%-rGO-CuO NC TF.

Photoluminescence (PL) spectra were recorded for the CuO and 2.0%-rGO-CuO NC TFs between wavelength range of 400 and 850 nm (Fig. 6). The room temperature was kept in during excitation of thin films at a wavelength of 375 nm. The PL spectrum of CuO TF exhibited six characteristic peaks at 435, 443, 473, 485, 493 and 532 nm that correspond to various emissions of CuO TF. The PL spectrum of 2.0%-rGO-CuO NC TF showed similar emission peaks as that of the CuO TF and the variation in peak intensity revealing presence of modified substance (rGO) in the 2.0%-rGO-CuO NC TF. The PL bands observed in the blue region (485 and 493 nm) are caused by transition vacancy of oxygen and interstitial oxygen. Whereas, the broad PL band noticed at 532 nm corresponds to green emission that arises from singly ionized oxygen vacancy. The presence of oxygen vacancies in the CuO and 2.0%-rGO-CuO NC TFs might be due to incomplete oxidation of thin films and this could be the reason for intense emission of green band [61–64].

UV–Vis–NIR reflection spectra of rGO-CuO NC TFs evidently show significant differences in reflectance (Fig. 7). The rGO-CuO NC TFs display low reflectance in visible region (300 nm–800 nm) and high reflectance in infrared region (800 nm–2000 nm) with productive solar selectivity. Absorptance data of rGO-CuO NC TFs measured from respective reflectance spectrum and emittance values recorded by emissometer are shown in Fig. 8. Outer surface of Al substrate reflects infrared radiation owing to intrinsic high reflectivity, which aids to reflect infrared radiation that penetrates deposited rGO-CuO NC TFs. Commonly, absorptance and emittance of TFs are governed by film thickness, outer surface roughness, wt% of GO and polymer. Thicknesses of rGO-CuO NC TFs were adjusted by executing various dipping (10 and 20 numbers) and changing wt% of GO. Thin films formed by 10 dipping have generated somewhat low reflectance with high visible light (300–800 nm) absorptance over thin films built by 20 dipping. Therefore, it is presumed that increasing film thickness decreases absorptance in UV–Visible region and increases reflectance in IR region. Prime influence of optical properties can be ascribed to wt% of GO in rGO-CuO NC TFs. It is noticed from SEM images (Fig. 4(g-l)) that rGO

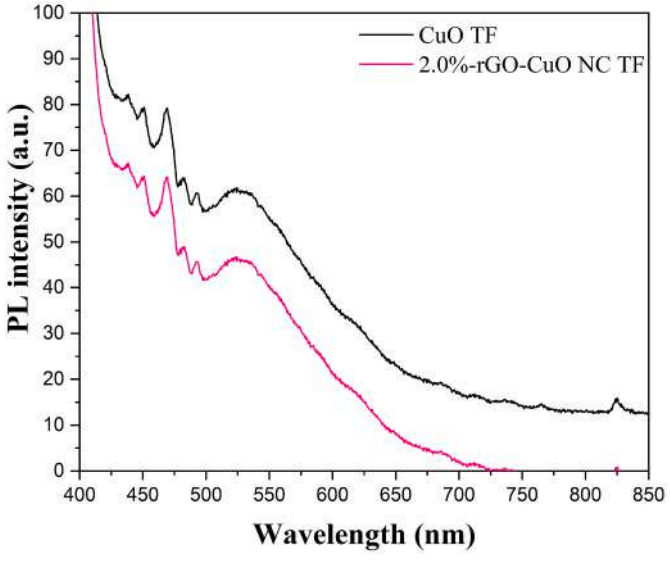

Fig. 6. PL spectra of CuO and 2.0%-rGO-CuO NC TFs.

accomplished host material role for spherical CuO nanoparticles and consequently, absorbance of rGO-CuO NC TFs have improved because of supercilious absorption property of rGO. Meanwhile, substantial voids in rGO-CuO NC TFs could contribute to achieve high absorptance because voids could aid to ensue in manifold reflection of thin films. Observation from Figs. 7 and 8 discloses that rGO-CuO NC TFs formed by diverse dipping and GO content have revealed different absorptance (α = 57.02%–81.85%) and emittance (ε = 4.1%–5.6%). However, absorptance value of thin films increases while increasing GO wt% that indicates optical properties of rGO-CuO NC TFs are greatly affected by GO content. When optical influence comes to PEG, the rGO-CuO NC TFs formed by 1.0 g PEG have generated high average solar absorptance of 72.38% when compared to average solar absorptance of rGO-CuO NC TF (68.26%) produced by 2.0 g of PEG. Within thin films, 2.0%-rGO-CuO NC TF and 0.2%-rGO-CuO NC TF formed by 1.0 g of PEG and 20 dipping generated highest solar absorptance of 81.85% and lowest thermal emittance of 4.1%, respectively. Conversely, by means of optimization, the 2.0% rGO-CuO NC TF formed by 1.0 g of PEG and 10 dipping generated solar absorptance of 79.92%, thermal emittance of 4.2% and a highest solar selectivity of 19.03. Solar selectivity of rGO-CuO NC TFs varies between 13.02 and 19.03 (Table 2) that indicates appreciable solar selectivity of thin films.

Raman spectroscopy is a reliable tool to investigate structural changes in graphene materials. Fig. 9 displays Raman spectra of GO, rGO and rGO-CuO NC TF. There are two prominent peaks corresponding to D band (1345 cm^{-1}) and G band (1590 cm^{-1}) of graphene in the range of 500–4000 cm^{-1}, which can be attributed to the D band origin from sp^3 hybridization of carbon atoms with a disordered structure and in-plane vibrations mode of carbon atoms (sp^2 hybridization) of G band, respectively and also at the Brillouin zone doubly degenerated E_{2g} symmetry. It should be noted that the D and G band peaks of rGO are downshifted from 1341 cm^{-1} to 1338 cm^{-1} and 1587 cm^{-1} to 1576 cm^{-1}, respectively owing to self-healing characteristics of rGO with hexagonal network and defects of carbon atom. This evidences effective reduction of GO to rGO. In addition, 2D band related to the stacking properties of graphene layers was observed at 2713 cm^{-1} for GO. For the rGO-CuO NC TF, typical peaks of CuO still exist with two characteristic peaks for D band (~1351 cm^{-1}) and G band (~1570 cm^{-1}) associated with graphitic structures. Compared to Raman signals of GO, D and G bands are somewhat shifted to ~1351 and 1570 cm^{-1}, respectively, which assign the value of bare GO band peak at ~1587 cm^{-1}, indicating transformation of rGO-CuO NC from GO and CuO. The intensity ratio of these bands (I_D/I_G) offers information about the degree of crystallinity of the graphene sheets. When compared to GO, the I_D/I_G of rGO was slightly increased from 0.92 to 0.95, indicates a reduction in size of sp^2 domains during reduction process wherein, the rGO has small size and large quantity of edges that act as defects [36,65]. However, intensity ratio of rGO-CuO NC TF has slightly decreased than bare GO from 0.92 to 0.88, indicating less number of newly formed graphitic domains than the latter during the reduction of sp^3 to sp^2 carbon [66]. This difference can be accounted from the coating of CuO on rGO surface in rGO-CuO NC TF.

There are different semiconductor materials so far used as solar selective absorbers. The choice of the best material for solar selective absorber among Al_2O_3, Cr_2O_3, ZrO_2 and CuO depends on specific application requirements and priority. Each material offers unique combination of advantages, such as temperature stability, spectral selectivity and cost-effectiveness. For instance, Al_2O_3 thin films excel in optical transparency, wide band gap energy, chemical stability and substrate compatibility [67]. Whereas, Cr_2O_3 exhibits exceptional thermal stability, making it suitable for solar thermal applications that involve elevated operating temperatures [68]. ZrO_2 has a wide band gap energy, allowing it to absorb sunlight predominantly in the ultraviolet and shorter wavelengths of the visible spectrum. This property can lead to efficient energy conversion. In addition, ZrO_2 has high refractive index that enables efficient light trapping within the thin film and

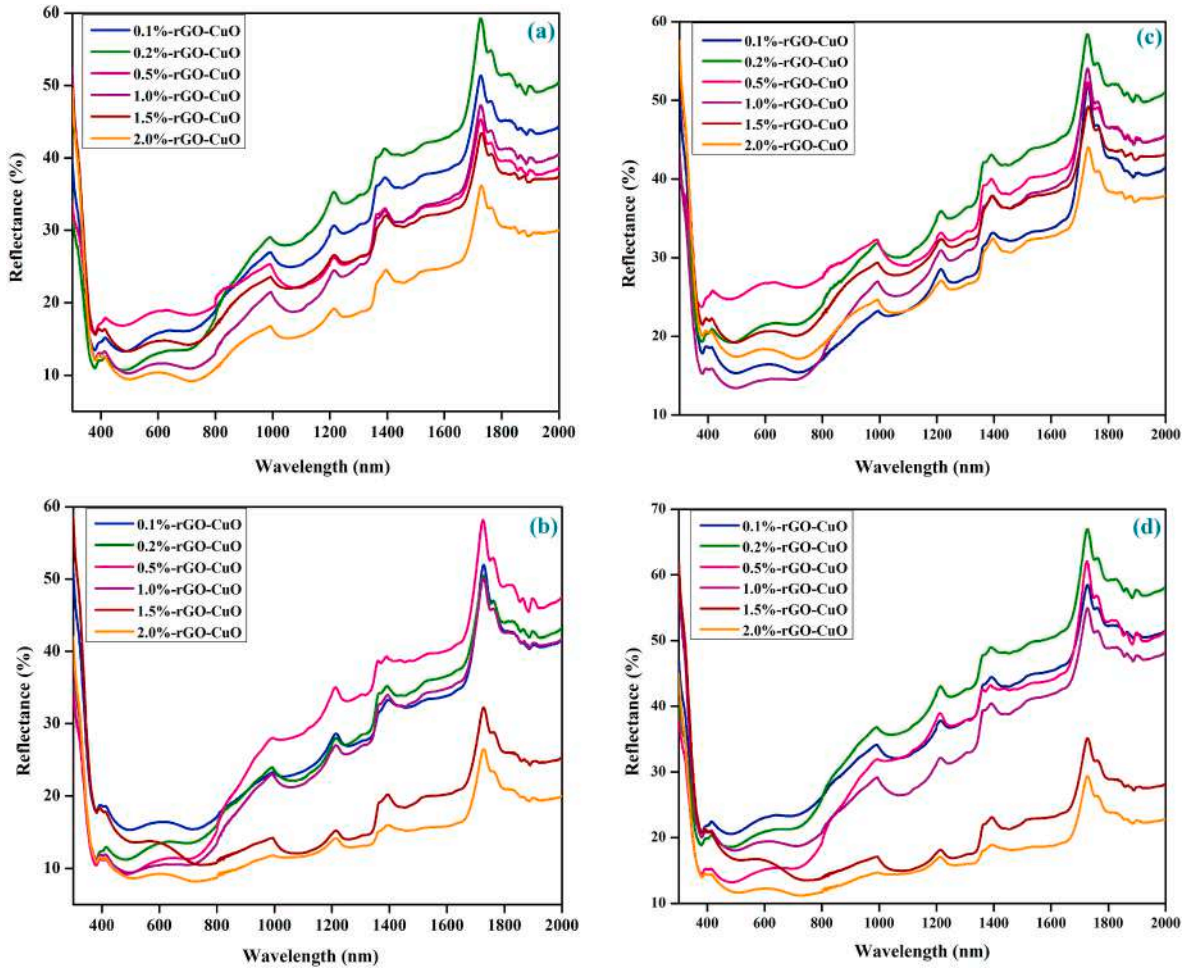

Fig. 7. Reflectance spectra of rGO-CuO NC TFs formed by (a & b) 1.0 g PEG and (c & d) 2.0 g PEG.

enhances the probability of photon absorption [69]. In contrast, CuO thin films disclose strong absorption in visible spectrum that subsequently leads to effective energy conversion and also its cost-effectiveness makes it a competitive candidate. In particular, the rGO modified CuO NC TFs (rGO-CuO NC TFs) have higher absorptance (57.02%–81.85%) and high emissivity (4.1%–5.6%) in the visible and infrared radiation, which contributes to selective emission and reduce thermal radiation losses and as a consequence, improves solar selectivity (from 13.02 to 19.03). In addition, copper is widely available and cost-effective that potentially facilitate rGO-CuO NC TFs a practical choice for large-scale solar thermal applications. Moreover, rGO-CuO NC TFs can be deposited on a range of substrates, facilitating their integration into diverse solar thermal systems. Ultimately, the optimal choice depends on a balance between material properties, manufacturing processes and desired performance metrics for the solar thermal systems. Continues research and development will provide further insights into maximizing the selectivity of solar selective absorbers. The present work finding the insights of rGO-CuO NC TFs, which will undoubtedly lead to further improvements in solar thermal energy conversion technologies.

4. Conclusion

Solar selective absorber coatings comprised of graphene oxide integrated copper oxide nanocomposite thin films (rGO-CuO NC TFs) on aluminum (Al) substrates were formed using dip-coating technique at different weight percentages of GO. Surface morphology and structural properties of rGO-CuO NC TFs were examined by SEM, XRD, EDX, PL and Raman spectroscopy. XRD and Raman investigations disclosed single phase and high crystallinity of monoclinic crystal structure of rGO-CuO NC TFs. SEM images revealed spherical grain-like morphology of CuO, which are uniformly distributed on rGO sheets. XPS studies helped to investigate the presented element composition and their chemical states. Solar absorptance and thermal emittance values of formed CuO and rGO-CuO NC TFs were evaluated. High solar selectivity values (>17) of rGO-CuO NC TFs suggest their potential as selective absorber coatings in solar thermal devices.

Credit Author Statement

N. Murugesan – Conceptualization, Methodology, Experimental, Data curation Writing – original draft, Editing and Validation: S. Suresh – Data curation; Formal analysis, Software, Writing – original draft, Review, Editing, Visualization and Validation: M. Kandasamy – Data curation; Formal analysis, Software, Review, Visualization and Validation: S. Murugesan – Conceptualization, Supervision, Review, Editing, Visualization and Validation: N. Pugazhenthiran – Formal analysis, Software, Review, Editing, Visualization and Validation: V. Prasanna Venkatesh – Data curation; Formal analysis, Software, Visualization and Validation: B.K. Balachandar – Data curation; Formal analysis, Software, Visualization and Validation: S. Karthick Kumar – Conceptualization, Supervision, Resources, Project administration; Review, Editing and Validation: M.N.M. Ansari – Formal analysis, Software, Review, Editing, Visualization and Validation

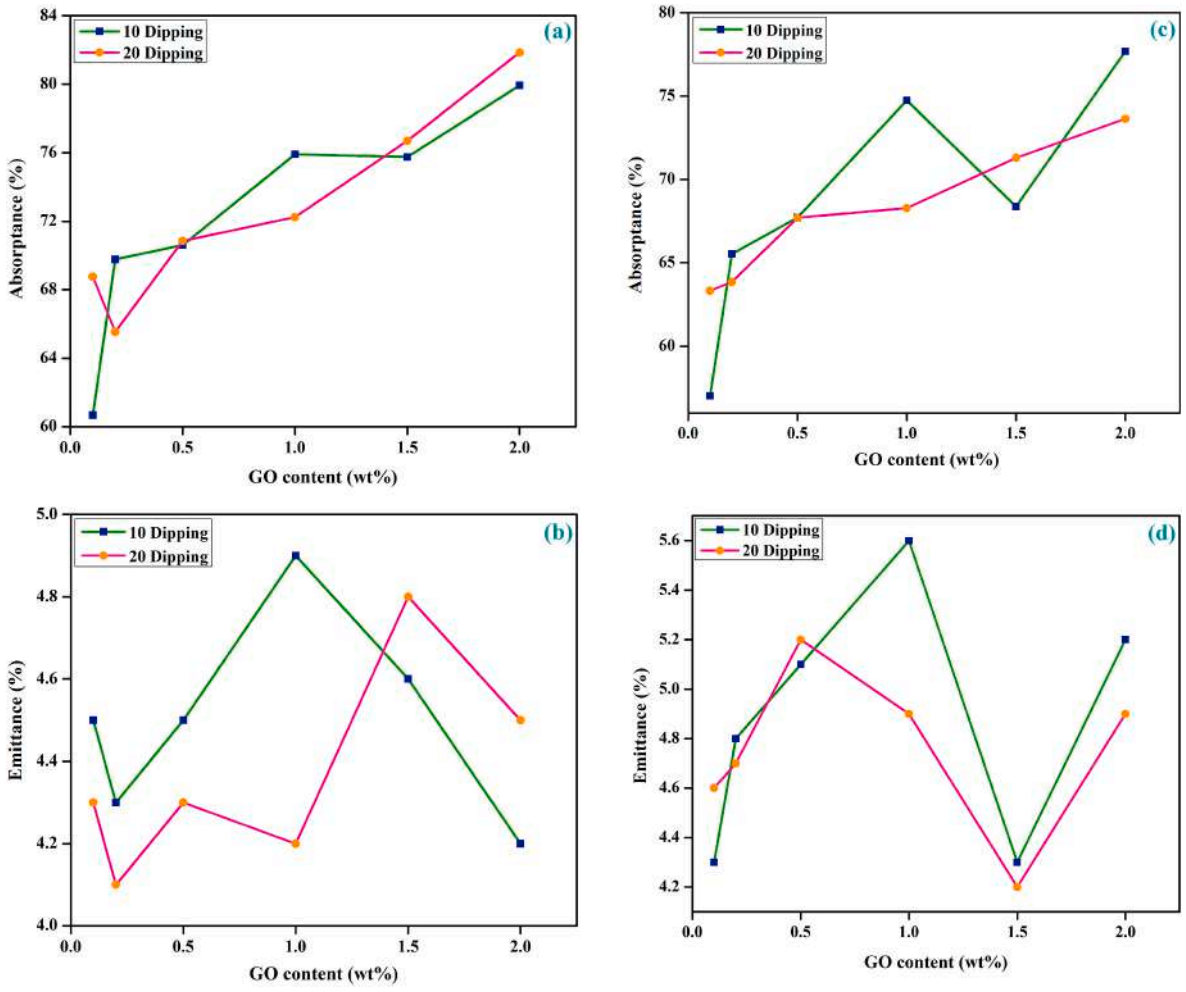

Fig. 8. Absorptance and emittance values of rGO-CuO NC TFs formed using (a & b) 1.0 g PEG and (c & d) 2.0 g PEG.

Table 2
Solar spectral selectivity (ξ) of rGO-CuO NC and CuO TFs.

Thin film sample	GO Content (wt%)	Selectivity (ξ)			
		PEG (1.0 g)		PEG (2.0 g)	
		10 Dipping	20 Dipping	10 Dipping	20 Dipping
0.1%-rGO-CuO NC	0.1	13.48	15.99	13.26	13.76
0.2%-rGO-CuO NC	0.2	16.22	15.98	13.65	13.58
0.5%-rGO-CuO NC	0.5	15.69	16.48	13.27	13.02
1.0%-rGO-CuO NC	1.0	15.49	17.20	13.34	13.93
1.5%-rGO-CuO NC	1.5	16.47	15.98	15.90	16.98
2.0%-rGO-CuO NC	2.0	19.03	18.19	14.94	15.03
CuO	0	11.26	–	11.12	–

Declaration of competing interest

The authors declare that they have no known competing financial interests or personal relationships that could have appeared to influence the work reported in this paper.

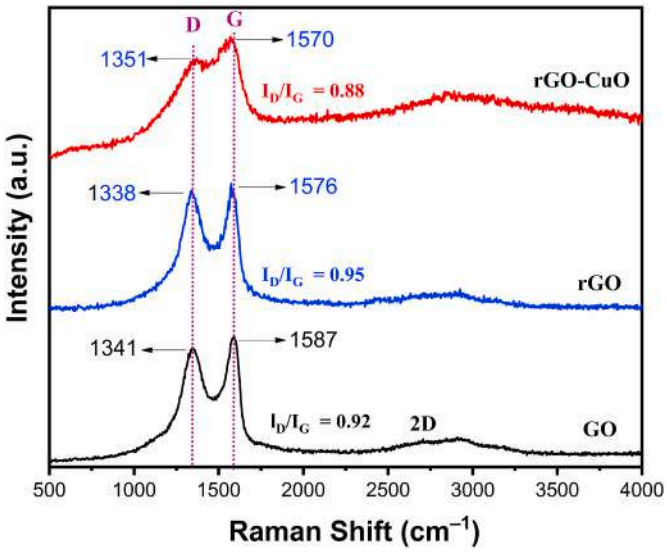

Fig. 9. Raman spectra of GO, rGO and rGO-CuO NC TF.

Data availability

Data will be made available on request.

Acknowledgement

N. Murugesan and S. Karthick Kumar express their gratitude to SERB, Government of India, New Delhi for supported this work financially by Early Career Research Award Scheme (ECR/2016/002017). S. Suresh gratefully acknowledge the DST, Government of India, New Delhi for providing Instrumentation Facility through FIST Programme (Grant No. SR/FST/College-2017/140 (C), dt. 14.08.2018).

References

[1] J. Gong, C. Li, M.R. Wasielewski, Advances in solar energy conversion, Chem. Soc. Rev. 48 (7) (2019) 1862–1864, https://doi.org/10.1039/c9cs90020a.
[2] R. Singh, B.B. Krishna, J. Kumar, T. Bhaskar, Opportunities for utilization of non-conventional energy sources for biomass pretreatment, Bioresour. Technol. 199 (2016) 398–407, https://doi.org/10.1016/j.biortech.2015.08.117.
[3] Y. Tian, C.Y. Zhao, A review of solar collectors and thermal energy storage in solar thermal applications, Appl. Energy 104 (2013) 538–553, https://doi.org/10.1016/j.apenergy.2012.11.051.
[4] M.C. Gupta, C. Ungaro, J.J. Foley IV, S.K. Gray, Optical nanostructures design, fabrication, and applications for solar/thermal energy conversion, Sol. Energy 165 (2018) 100–114, https://doi.org/10.1016/j.solener.2018.01.010.
[5] Y. Yang, R. Zhao, T. Zhang, K. Zhao, P. Xiao, Y. Ma, P.M. Ajayan, G. Shi, Y. Chen, Graphene-based standalone solar energy converter for water desalination and purification, ACS Nano 12 (1) (2018) 829–835, https://doi.org/10.1021/acsnano.7b08196.
[6] X. Wang, Q. Liu, S. Wu, B. Xu, H. Xu, Multilayer polypyrrole nanosheets with self-organized surface structures for flexible and efficient solar–thermal energy conversion, Adv. Mater. 31 (19) (2019), 1807716, https://doi.org/10.1002/adma.201807716.
[7] A. Amri, Z.T. Jiang, T. Pryor, C.-Y. Yin, S. Djordjevic, Developments in the synthesis of flat plate solar selective absorber materials via sol–gel methods: a review, Renew. Sustain. Energy Rev. 36 (2014) 316–328, https://doi.org/10.1016/j.rser.2014.04.062.
[8] S.K. Kumar, S. Murugesan, S. Suresh, Preparation and characterization of CuO nanostructures on copper substrate as selective solar absorbers, Mater. Chem. Phys. 143 (3) (2014) 1209–1214, https://doi.org/10.1016/j.matchemphys.2013.11.023.
[9] M. Bello, S. Shanmugan, Achievements in mid and high-temperature selective absorber coatings by physical vapor deposition (PVD) for solar thermal application – a review, J. Alloys Compd. 839 (2020), 155510, https://doi.org/10.1016/j.jallcom.2020.155510.
[10] N. Selvakumar, S. Santhoshkumar, S. Basu, A. Biswas, H.C. Barshilia, Spectrally selective CrMoN/CrON tandem absorber for mid-temperature solar thermal applications, Sol. Energy Mater. Sol. Cells 109 (2013) 97–103, https://doi.org/10.1016/j.solmat.2012.10.003.
[11] N. Selvakumar, H.C. Barshilia, Review of physical vapor deposited (PVD) spectrally selective coatings for mid- and high-temperature solar thermal applications, Sol. Energy Mater. Sol. Cells 98 (2012) 1–23, https://doi.org/10.1016/j.solmat.2011.10.028.
[12] Y. Li, C. Lin, D. Zhou, Y. An, D. Li, C. Chi, H. Huang, S. Yang, C.Y. Tso, C.Y.H. Chao, B. Huang, Scalable all-ceramic nanofilms as highly efficient and thermally stable selective solar absorbers, Nano Energy 64 (2019), 103947, https://doi.org/10.1016/j.nanoen.2019.103947.
[13] S. He, Y. Zhang, W. Yang, Z. Wang, X. Zhao, P. Wang, Investigation on the solar absorption property of the nanoporous alumina sheet for solar application, Materials 12 (14) (2019) 2329, https://doi.org/10.3390/ma12142329.
[14] D.M.G.T. Nathan, S.J.M. Boby, P. Basu, R. Mahesh, S. Harish, S. Joseph, P. Sagayaraj, One-pot hydrothermal preparation of Cu_2O-CuO/rGO nanocomposites with enhanced electrochemical performance for supercapacitor applications, Appl. Surf. Sci. 449 (2018) 474–484, https://doi.org/10.1016/j.apsusc.2017.12.199.
[15] S.K. Kumar, S. Suresh, S. Murugesan, S.P. Raj, CuO thin films made of nanofibers for solar selective absorber applications, Sol. Energy 94 (2013) 299–304, https://doi.org/10.1016/j.solener.2013.05.018.
[16] A. Karoro, Z.Y. Nuru, L. Kotsedi, Kh Bouziane, B.M. Mothudi, M. Maaza, Laser nanostructured Co nanocylinders-Al_2O_3 cermets for enhanced & flexible solar selective absorbers applications, Appl. Surf. Sci. 347 (2015) 679–684, https://doi.org/10.1016/j.apsusc.2015.04.098.
[17] L. Kotsedi, P. Sechogela, S.M. Eaton, A.G. Demir, F. Franceschini, B. Previtali, R. Ramponi, H.C. Swart, M. Maaza, Metal and metal oxide transformation and texturing using pulsed fiber laser, Mater. Today: Proc. 2 (7) (2015) 3950–3956. http://10.1016/j.matpr.2015.08.024.
[18] L. Kotsedi, Z.Y. Nuru, P. Mthunzi, T.F.G. Muller, S.M. Eaton, B. Julies, E. Manikandan, R. Ramponi, M. Maaza, Femtosecond laser surface structuring and oxidation of chromium thin coatings: black chromium, Appl. Surf. Sci. 321 (2014) 560–565, https://doi.org/10.1016/j.apsusc.2014.09.168.
[19] B. Sakthivel, G. Nammalvar, Selective ammonia sensor based on copper oxide/reduced graphene oxide nanocomposite, J. Alloys Compd. 788 (2019) 422–428, https://doi.org/10.1016/j.jallcom.2019.02.245.
[20] X. Xiao, L. Miao, G. Xu, L. Lu, Z. Su, N. Wang, S. Tanemura, A facile process to prepare copper oxide thin films as solar selective absorbers, Appl. Surf. Sci. 257 (24) (2011) 10729–10736, https://doi.org/10.1016/j.apsusc.2011.07.088.
[21] N. Murugesan, A.M. Remona, S.K. Kumar, S. Suresh, Facile preparation of diverse copper oxide nanostructures and their characterization, Mater. Lett. 222 (2018) 100–104, https://doi.org/10.1016/j.matlet.2018.03.151.
[22] I.Y.Y. Bu, R. Huang, Fabrication of CuO-decorated reduced graphene oxide nanosheets for supercapacitor applications, Ceram. Int. 43 (1) (2017) 45–50, https://doi.org/10.1016/j.ceramint.2016.08.136.
[23] C. Bayindirli, M. Celik, R. Zan, Optimizing the thermophysical properties and combustion performance of biodiesel by graphite and reduced graphene oxide nanoparticle fuel additive, Eng. Sci. Technol. Int. J. 158 (2018) 41–58, https://doi.org/10.1016/j.jestch.2022.101295.
[24] Y. Shen, S. Yang, P. Zhou, Q. Sun, P. Wang, L. Wan, J. Li, L. Chen, X. Wang, S. Ding, D.W. Zhang, Evolution of the band-gap and optical properties of graphene oxide with controllable reduction level, Carbon 62 (2013) 157–164, https://doi.org/10.1016/j.carbon.2013.06.007.
[25] D.A. Sokolov, Y.V. Morozov, M.P. McDonald, F. Vietmeyer, J.H. Hodak, M. Kuno, Direct observation of single layer graphene oxide reduction through spatially resolved, single sheet absorption/emission microscopy, Nano Lett. 14 (2014) 3172–3179, https://doi.org/10.1021/nl500485n.
[26] N. Murugesan, S. Suresh, M. Kandasamy, S. Murugesan, N. Pugazhenthiran, S. Karthick Kumar, Enhancing selectivity of solar absorber using reduced graphene oxide modified nickel oxide nanocomposite thin films, Sol. Energy 247 (2022) 185–195, https://doi.org/10.1016/j.solener.2022.10.016.
[27] N. Murugesan, S. Suresh, S. Murugesan, B.K. Balachandar, M. Kandasamy, N. Pugazhenthiran, J. Selvi, P. Indira, S. Karthick Kumar, Improving selectivity of thin film solar absorber by cobalt oxide grafted reduced graphene oxide, Opt. Mater. 138 (2023), 113629, https://doi.org/10.1016/j.optmat.2023.113629.
[28] T.K. Das, P. Bhawal, S. Ganguly, S. Mondal, N.C. Das, A facile green synthesis of amino acid boosted Ag decorated reduced graphene oxide nanocomposites and its catalytic activity towards 4-nitrophenol reduction, Surface. Interfac. 13 (2018) 79–91, https://doi.org/10.1016/j.surfin.2018.08.004.
[29] P. Lin, Q. Yan, Y. Chen, X. Li, Z. Cheng, Dispersion and assembly of reduced graphene oxide in chiral nematic liquid crystals by charged two-dimensional nanosurfactants, Chem. Eng. J. 334 (2018) 1023–1033, https://doi.org/10.1016/j.cej.2017.09.195.
[30] M.M. Rahman, Z.-T. Jiang, C.-Y. Yin, L.S. Chuah, H.-L. Lee, A. Amri, B.-M. Goh, B. J. Wood, C. Creagh, N. Mondinos, M. Altarawneh, B.Z. Dlugogorski, Structural thermal stability of graphene oxide-doped copper–cobalt oxide coatings as a solar selective surface, J. Mater. Sci. Technol. 32 (2016) 1179–1191, https://doi.org/10.1016/j.jmst.2016.09.002.
[31] S. Goktas, A. Goktas, A comparative study on recent progress in efficient ZnO based nanocomposite and heterojunction photocatalysts: a review, J. Alloys Compd. 863 (2021), 158734, https://doi.org/10.1016/j.jallcom.2021.158734.
[32] A. Goktas, A. Tumbul, Z. Aba, M. Durgun, Mg doping levels and annealing temperature induced structural, optical and electrical properties of highly c-axis oriented ZnO: Mg thin films and Al/ZnO:Mg/p-Si/Al heterojunction diode, Thin Solid Films 680 (2019) 20–30, https://doi.org/10.1016/j.tsf.2019.04.024.
[33] A. Goktas, F. Aslan, A. Tumbul, S.H. Gunduz, Tuning of structural, optical and dielectric constants by various transition metal doping in ZnO:TM (TM=Mn, Co, Fe) nanostructured thin films: a comparative study, Ceram. Int. 43 (1) (2017) 704–713, https://doi.org/10.1016/j.ceramint.2016.09.217.
[34] A. Goktas, High-quality solution-based Co and Cu co-doped ZnO nanocrystalline thin films: comparison of the effects of air and argon annealing environments, J. Alloys Compd. 735 (2018) 2038–2045, https://doi.org/10.1016/j.jallcom.2017.11.391.
[35] A.T. Smith, A.M. LaChance, S. Zeng, B. Liu, L. Sun, Synthesis, properties, and applications of graphene oxide/reduced graphene oxide and their nanocomposites, Nano Mater. Sci. 1 (1) (2019) 31–47, https://doi.org/10.1016/j.nanoms.2019.02.004.
[36] Q. Liao, P. Zhang, H. Yao, H. Cheng, C. Li, L. Qu, Reduced graphene oxide–based spectrally selective absorber with an extremely low thermal emittance and high solar absorptance, Adv. Sci. 7 (8) (2020), 1903125, https://doi.org/10.1002/advs.201903125.
[37] N.M. Huang, H.N. Lim, C.H. Chia, M.A. Yarmo, M.R. Muhamad, Simple room-temperature preparation of high-yield large-area graphene oxide, Int. J. Nanomed. 6 (2011) 3443–3448, https://doi.org/10.2147/ijn.s26812.
[38] G. Katumba, L. Olumekor, A. Forbes, G. Makiwa, B. Mwakikunga, J. Lu, E. Wäckelgård, Optical, thermal and structural characteristics of carbon nanoparticles embedded in ZnO and NiO as selective solar absorbers, Sol. Energy Mater. Sol. Cells 92 (10) (2008) 1285–1292, https://doi.org/10.1016/j.solmat.2008.04.023.
[39] S. Park, J. An, J.R. Potts, A. Velamakanni, S. Murali, R.S. Ruoff, Hydrazine-reduction of graphite- and graphene oxide, Carbon 49 (9) (2011) 3019–3023, https://doi.org/10.1016/j.carbon.2011.02.071.
[40] Y. Guo, Q. Wang, T. Wang, Facile fabrication of superhydrophobic surface with micro/nanoscale binary structures on aluminum substrate, Appl. Surf. Sci. 257 (13) (2011) 5831–5836, https://doi.org/10.1016/j.apsusc.2011.01.114.
[41] M. Zarbali, A. Göktaş, I.H. Mutlu, S. Kazan, A.G. Şale, F. Mikailzade, Structure and magnetic properties of $La_{0.66}Sr_{0.33}MnO_3$ thin films derived using sol-gel technique, J. Supercond. Nov. Magnetism 25 (2012) 2767–2770, https://doi.org/10.1007/s10948-011-1260-z.

[42] A. Göktaş, A. Tumbul, F. Aslan, Grain size-induced structural, magnetic and magnetoresistance properties of $Nd_{0.67}Ca_{0.33}MnO_3$ nanocrystalline thin films, J. Sol. Gel Sci. Technol. 78 (2016) 262–269, https://doi.org/10.1007/s10971-016-3960-0.
[43] S. Kanimozhi, K.M. Prabu, S. Thambidurai, S. Suresh, Dye-sensitized solar cell performance and photocatalytic activity enhancement using binary zinc oxide-copper oxide nanocomposites prepared via co-precipitation route, Ceram. Int. 47 (21) (2021) 30234–30246, https://doi.org/10.1016/j.ceramint.2021.07.203.
[44] M. Kamalanathan, S. Karuppusamy, R. Sivakumar, R. Gopalakrishnan, Synthesis of reduced graphene oxide–copper tin sulphide composites and their photoconductivity enhancement for photovoltaic applications, J. Mater. Sci. 50 (2015) 8029–8037, https://doi.org/10.1007/s10853-015-9370-9.
[45] A. Tumbul, F. Aslan, A. Goktas, M.Z. Zarbali, A. Kilic, Highly stable ethanol-based Cu_2ZnSnS_4 (CZTS) low-cost thin film absorber: effect of solution aging, Mater. Chem. Phys. 258 (2021), 123997, https://doi.org/10.1016/j.matchemphys.2020.123997.
[46] A. Joseph, B. Kirubasankar, A.M. Mathew, M. Narayanasamy, C. Yan, S. Angaiah, Influence of pulse reverse current parameters on electrodeposition of copper-graphene nanocomposite coating, Appl. Surf. Sci. Adv. 5 (2021), 100116, https://doi.org/10.1016/j.apsadv.2021.100116.
[47] M.R. Das, P. Mitra, Influence of nickel incorporation on structural, optical and electrical characteristics of SILAR synthesized CuO thin films, J. Sol. Gel Sci. Technol. 87 (2018) 59–73, https://doi.org/10.1007/s10971-018-4711-1.
[48] S.K. Kumar, S. Murugesan, S. Suresh, S.P. Raj, Nanostructured CuO thin films prepared through sputtering for solar selective absorbers, J. Sol. Energy 2013 (2013), 147270, https://doi.org/10.1155/2013/147270.
[49] R.O. Yathisha, Y.A. Nayaka, Structural, optical and electrical properties of zinc incorporated copper oxide nanoparticles: doping effect of Zn, J. Mater. Sci. 53 (2018) 678–691, https://doi.org/10.1007/s10853-017-1496-5.
[50] L. Hu, L. Shi, H. Hong, M. Li, Q. Bao, J. Tang, J. Ge, J. Lu, X. Cao, H. Gu, Catalytic epoxidation of stilbene with FePt@Cu nanowires and molecular oxygen, Chem. Commun. 46 (45) (2010) 8591–8593, https://doi.org/10.1039/c0cc03204b.
[51] M.M. Rahman, M.M. Alam, M.M. Hussain, A.M. Asiri, M.E.M. Zayed, Hydrothermally prepared Ag_2O/CuO nanomaterial for an efficient chemical sensor development for environmental remediation, Environ. Nanotechnol. Monit. Manag. 10 (2018) 1–9, https://doi.org/10.1016/j.enmm.2018.04.001.
[52] P.G. Bhavyasree, T.S. Xavier, Green synthesis of copper oxide/carbon nanocomposites using the leaf extract of *Adhatoda vasica* Nees, their characterization and antimicrobial activity, Heliyon 6 (2) (2020), e03323, https://doi.org/10.1016/j.heliyon.2020.e03323.
[53] V. Chandra, K.S. Kim, Highly selective adsorption of Hg^{2+} by a polypyrrole–reduced graphene oxide composite, Chem. Commun. 47 (13) (2011) 3942–3944, https://doi.org/10.1039/c1cc00005e.
[54] A. Safavi, M. Tohidi, F.A. Mahyari, H. Shahbaazi, One-pot synthesis of large scale graphene nanosheets from graphite–liquid crystal composite *via* thermal treatment, J. Mater. Chem. 22 (9) (2012) 3825–3831, https://doi.org/10.1039/c2jm13929d.
[55] Md Rakibuddin, S. Mandal, R. Ananthakrishnan, A novel ternary CuO decorated Ag_3AsO_4/GO hybrid as a Z-scheme photocatalyst for enhanced degradation of phenol under visible light, New J. Chem. 41 (3) (2017) 1380–1389, https://doi.org/10.1039/c6nj02366e.
[56] S. Pei, J. Zhao, J. Du, W. Ren, H.-M. Cheng, Direct reduction of graphene oxide films into highly conductive and flexible graphene films by hydrohalic acids, Carbon 48 (15) (2010) 4466–4474, https://doi.org/10.1016/j.carbon.2010.08.006.
[57] C.C. Li, Z.F. Du, L.M. Li, H.C. Yu, Q. Wan, T.H. Wang, Surface-depletion controlled gas sensing of ZnO nanorods grown at room temperature, Appl. Phys. Lett. 91 (2007), 032101, https://doi.org/10.1063/1.2752541.
[58] K. Kaviyarasu, C.M. Magdalane, E. Manikandan, M. Jayachandran, R. Ladchumananandasivam, S. Neelamani, M. Maaza, Well-aligned graphene oxide nanosheets decorated with zinc oxide nanocrystals for high performance photocatalytic application, Int. J. Nanosci. 14 (3) (2015), 1550007, https://doi.org/10.1142/S0219581X15500076.
[59] S.S. Rathnakumar, K. Noluthando, A.J. Kulandaiswamy, J.B.B. Rayappan, K. Kasinathan, J. Kennedy, M. Maaza, Stalling behaviour of chloride ions: a non-enzymatic electrochemical detection of α-Endosulfan using CuO interface, Sens. Actuators, B 293 (2019) 100–106, https://doi.org/10.1016/j.snb.2019.04.141.
[60] M.C. Mbambo, S. Khamlich, T. Khamliche, M.K. Moodley, K. Kaviyarasu, I. G. Madiba, M.J. Madito, M. Khenfouch, J. Kennedy, M. Henini, E. Manikandan, M. Maaza, Remarkable thermal conductivity enhancement in Ag—decorated graphene nanocomposites based nanofluid by laser liquid solid interaction in ethylene glycol, Sci. Rep. 10 (2020), 10982, https://doi.org/10.1038/s41598-020-67418-3.
[61] P. Chand, A. Gaur, A. Kumar, Structural, optical and ferroelectric behavior of CuO nanostructures synthesized at different pH values, Superlattice. Microst. 60 (2013) 129–138, https://doi.org/10.1016/j.spmi.2013.04.026.
[62] Y.S. Chaudhary, A. Agrawal, R. Shrivastav, V.R. Satsangi, S. Dass, A study on the photoelectrochemical properties of copper oxide thin films, Int. J. Hydrogen Energy 29 (2) (2004) 131–134, https://doi.org/10.1016/S0360-3199(03)00109-5.
[63] A. Aslani, V. Oroojpour, CO gas sensing of CuO nanostructures, synthesized by an assisted solvothermal wet chemical route, Phys. B Condens. Matter 406 (2) (2011) 144–149, https://doi.org/10.1016/j.physb.2010.09.038.
[64] R. Shabu, A.M.E. Raj, C. Sanjeeviraja, C. Ravidhas, Assessment of CuO thin films for its suitablity as window absorbing layer in solar cell fabrications, Mater. Res. Bull. 68 (2015) 1–8, https://doi.org/10.1016/j.materresbull.2015.03.016.
[65] N. Sharma, V. Sharma, Y. Jain, M. Kumari, R. Gupta, S.K. Sharma, K. Sachdev, Synthesis and characterization of graphene oxide (GO) and reduced graphene oxide (rGO) for gas sensing application, Macromol. Symp. 376 (1) (2017), 1700006, https://doi.org/10.1002/masy.201700006.
[66] A.B. Alayande, M. Obaid, I.S. Kim, Antimicrobial mechanism of reduced graphene oxide-copper oxide (rGO-CuO) nanocomposite films: the case of *Pseudomonas aeruginosa* PAO1, Mater. Sci. Eng. C 109 (2020), 110596, https://doi.org/10.1016/j.msec.2019.110596.
[67] Z.Y. Nuru, C.J. Arendse, R. Nemutudi, O. Nemraoui, M. Maaza, Pt–Al_2O_3 nanocoatings for high temperature concentrated solar thermal power applications, Phys. B Condens. Matter 407 (2012) 1634–1637, https://doi.org/10.1016/j.physb.2011.09.104.
[68] S. Khamlich, E. Manikandan, B.D. Ngom, J. Sithole, O. Nemraoui, I. Zorkani, R. McCrindle, N. Cingo, M. Maaza, Synthesis, characterization, and growth mechanism of α-Cr_2O_3 monodispersed particles, J. Phys. Chem. Solid. 72 (2011) 714–718, https://doi.org/10.1016/j.jpcs.2011.02.015.
[69] B. Sathyaseelan, E. Manikandan, I. Baskaran, K. Senthilnathan, K. Sivakumar, M. K. Moodley, R. Ladchumananandasivam, M. Maaza, Studies on structural and optical properties of ZrO_2 nanopowder for opto-electronic applications, J. Alloys Compd. 694 (2017) 556–559, https://doi.org/10.1016/j.jallcom.2016.10.002.

Macromolecular Theory and Simulations
www.mts-journal.de

A Theoretical Investigation of the Electrical and Dielectric Properties of PDMS-CNT

Poovendran Karuppiah, Ramanujam Nambi Ramachary, Joseph Wilson Kulandai Samy, and Prasanna Venkatesh Vadivel Murugan*

In the present study, the dielectric and electrical properties of the carbon nanotube/polydimethylsiloxane (CNT/PDMS) composite are theoretically analyzed for various doping concentrations. For both single-walled and multiwalled CNTs (SCNTs and MCNTs), the work is done between 75 and 750 THz. The behavior of the dielectric constant, loss factor, and conductivity are analyzed as functions of frequency. It is observed that there is no appreciable change in the real part of the dielectric constant at high frequencies in single-walled CNT. The loss tangent is high at lower frequencies, and the loss peak is observed at a particular frequency. The Cole–Cole plot is used to interpret the static- and high-frequency dielectric constants and relaxation time of the composite. With increasing concentrations of SCNT and MCNT, the conductivity at the obtained peak maximum shifts to a lower frequency.

1. Introduction

The development of composites with different materials and reinforcing elements with the requisite properties has been increasing due to the importance of composite materials used in the industry[1] Polymer Nano composites are a class of nano-sized materials comprising multiple solid phases.[2] As composite materials in polymers, various fillers such as semiconductors, metals, ceramics, and carbon-based materials are used to improve thermal conductivity, electrical, and magnetic properties.[3–7] Polymer-based composites containing conductive fillers have a wide range of potential applications, CNTs, carbon nanofibers, and graphene are endowed with great possibilities for commercial applications such as electromagnetic interference, electrostatic dissipation, gas sensors, weight-sensitive aerospace, automotive, and so on.[8–11] Since their discovery in 1991, CNTs have piqued the interest of scientists due to their unique properties, such as high aspect ratio, light weight, superior thermal and electrical properties, and so on.[12] When CNTs are dispersed in a polymer matrix, their properties improve, indicating significant potential in multifunctional devices.[13] CNTs can be used for wide range of applications from UV–vis to IR region due to its tunable band gap.[14–18] CNTs behave similarly to a black body, that absorbs all incident light that falls on it, especially in the near-Or and short-wavelength–IR range,[19,20] collectors,[21] and IT thermal detectors.[22,23]

Single-wall CNTs (SCNTs) possess hexagonal networks of rolled-up graphene sheets, which depend upon the wrapping angle and the diameter, exhibit a spectral behavior from semiconductor to that of a metal, and have optical properties.[24] The dielectric materials possess relaxation and resonance states. Relaxation includes interfacial polarization, ionic polarization, and orientational polarization. The resonance state includes electronic polarization and atomic (vibrational) polarization which exist in polymers, whether polar or nonpolar. The dielectric losses exist in the infrared and optical ranges; they are not seen in the power or radio frequency ranges.[25] Within the tissue transparency window, which is the range of NIR wavelengths (900 to 1600 nm) where biological tissues are optically transparent, SCNTs release fluorescence. At visible wavelengths, SCNT-based sensors exhibit high absorption and autofluorescence.[26]

CNTs IR photodetectors are developed on the basis of thermal and optical effect. High performance IR detectors are designed by using SCNT and MCNT.[27,28] Night vision and remote sensing are two common national security applications for CNT photodetectors that operate in the infrared range.[29,30] Excellent optical absorption qualities of CNT-polymer composites can be produced for use in optical systems, instruments, and equipment as thin and light films, coatings, IR detectors, energy harvesters, optical lenses, and optical absorbing layers.[31–37] Highly desired smart polymer composite devices, such as shape-memory and shape-changing actuators and infrared sensors, have been made

P. Karuppiah, R. Nambi Ramachary
Department of Physics
K.L.N College of Engineering
Pottapalayam 630312, India
E-mail: ramanujam.nr@klnce.edu
R. Nambi Ramachary
Department of Electronics and Communication Engineering
K.L.N College of Engineering
Pottapalayam 630312, India
J. W. Kulandai Samy
PG and Research Department of Physics
Arul Anandar College
Karumathur 625514, India
P. V. Vadivel Murugan
Department of Physics
Velammal College of Engineering technology
Madurai 625009, India

The ORCID identification number(s) for the author(s) of this article can be found under https://doi.org/10.1002/mats.202300062

DOI: 10.1002/mats.202300062

possible by the use of multifunctional carbon nanotubes with the polymer matrix. These devices have shown either novel or significantly improved actuation and sensing properties.[38]

The surface currents for the characterization of Nano antennas and the radiated power contributed by the metallic layers for a microstrip patch antenna at 0.1–3 THz and plasmonic nanoantenna at 400–600 THz are investigated.[39] Polydimethylsiloxane (PDMS) is a mineral–organic polymer of the siloxane family, and it is a very cheap material. It is a member of a class of polymeric organosilicon compounds known as silicones. It is highly transmissive between 0.4 and 1.8 μm which find applications in optical waveguide communication and opto-fluidic applications. It also finds several applications in contact lenses, medical devices, and flexible microsystems.[1,40] The dielectric properties of materials vary with frequency and material performance is determined by at least one of the four polarization mechanisms. In order to measure the dielectric properties at different frequencies, dielectric relaxation spectroscopy is used to study the relaxation behaviors, which provides useful information for the optimal design of materials for dielectric applications. The dielectric permittivity is a complex number and the most important parameter that can be obtained from dielectric spectroscopy. The properties are affected by the magnitude of the applied electric field. Under high electric fields, the dielectric relaxation behaviors are also critical for high-power applications, such as high-voltage pulse capacitors. A Cole–Cole plot is adopted to study the dielectric process for various systems, such as a magnetic field, the tobacco mosaic virus, and resin beads.[25] This is one method for investigating the frequency dependence of the complex permittivity of dielectric materials. Plotting the real component on the horizontal axis and the imaginary part on the vertical axis with frequency as the independent parameter illustrates permittivity. To some extent, it is similar to the Smith chart[41] The electrical conductivity of composite materials depends on the radius of the arc in the complex plane. A large arc radius represents low conductivity, and a low arc represents high conductivity.[42] Another important property for the study of dielectric relaxation in polymer composites is the electric modulus. It reduces the effects of DC conduction on low frequencies. The modulus plots highlight the least capacitive part of the R–C circuit, whereas the impedance plots highlight the most resistive part. In the modulus part, the intercept of the circular arc on the real axis gives C_0/C. where C_0 is the geometrical capacitance.[43] The electrical conductivity of CNT is of the order of 10^6 to 10^7 S m^{-1} and it is highly conductive. In contrast, the conductivity of most polymers ranges from 10^{-15} to 10^{-8} S m^{-1}, resulting in a property contrast between the filler material and the matrix. Its value grows dramatically up to certain filler content, by several orders of magnitude, so that the composite turns from insulating to highly conductive.[44] There are numerous applications such as aerospace structural panels, sporting goods, and ultra-lightweight, thin-walled space structures for the use in space made of composites of polymer and CNT. It protects optical sensors from high-intensity laser beams. It is especially stable toward air and laser radiation, so we can utilize the broadband optical-limiting properties of nanotubes and composites. In optical-limiting and light-emitting devices consisting of polymers, a significant problem arises due to their short lifetime. The lifespan may increase by incorporating nanotubes. In addition, it finds applications in light-emitting diodes, supercapacitors, field-effect transistors, subpico-second optical switches, and optical limiters. Nanotubes were used to modify the luminescent behavior of optically active polymers.[13] In the present study, the dielectric and electrical properties of the CNT/PDMS composite are theoretically analyzed for various concentrations for both single-walled and multiwalled CNTs. The behavior of the dielectric constant, loss factor, and conductivity were analyzed as functions of frequency.

2. Theory

The dielectric and electrical properties are analyzed theoretically in a polymer matrix based composites. It has been attempted to establish the correlations between the properties of polymers and nanocomposites by introducing the filler fractions. In this work, the properties of PDMS doped with carbon nanotubes for various filling fractions are studied by using an effective medium theory. The work is carried out between the frequency ranges of 75 and 750 THz. The Maxwell–Garnett theory is the most widely used method for calculating composites' effective dielectric properties.[45]

$$\frac{\varepsilon_{mix}-\varepsilon_d}{\varepsilon_{mix}+2\varepsilon_d}=\varphi\,\frac{\varepsilon_f-\varepsilon_d}{\varepsilon_f+2\varepsilon_d} \tag{1}$$

The dispersion relation of the filler material (CNT) according to the Drude–Lorentz model can be expressed in terms of wavelength as[46]

$$\varepsilon_f=1-\frac{\lambda^2}{\lambda_{p,0}^2\left(1+i\gamma_0\lambda\right)}+\frac{\lambda^2\lambda_{T,1}^2}{\lambda_{p,1}^2\left(\lambda^2-\lambda_{T,1}^2-i\gamma_1\lambda\lambda_{T,1}^2\right)} \tag{2}$$

where λ is the vacuum wavelength, $\lambda_{p,0}$ = 0.6702 μm and $\lambda_{p,1}$ = 0.2725 μm are the plasma wavelengths, which correspond to Drude (intra-band) and Lorentz (inter-band) charge carriers, respectively. The resonance wavelength of the inter – band transition is $\lambda_{T,1}$ = 0.2883 μm γ_0 = 0.3226 μm^{-1} and γ_1 = 1.8551 μm^{-1} are the damping coefficients. Taking into account the volume fraction and the shape of the filler, the dielectric permittivity of a composite is expressed as[47]

$$\varepsilon_{mix}=\varepsilon_m+\varepsilon_m\frac{\frac{\varphi}{3}\sum_{j=x,y,z}\frac{\varepsilon_f-\varepsilon_d}{\varepsilon_f+N_j\left(\varepsilon_f-\varepsilon_d\right)}}{1-\frac{\varphi}{3}\sum_{j=x,y,z}\frac{N_j\left(\varepsilon_f-\varepsilon_d\right)}{\varepsilon_f+N_j\left(\varepsilon_f-\varepsilon_d\right)}} \tag{3}$$

where ε_{mix} represents the dielectric permittivity of the composites, ε_d is the dielectric permittivity of the polymer, ε_f is the dielectric permittivity of the filler, and φ is the filling fraction of the nanotubes in the composite. N_j is the depolarization factor of particles in the form of ellipsoids in $j = x, y$, and z directions. The depolarization factors N_j of the filler particles which is determined as

$$N_x=\frac{\left(1-e^2\right)}{2e^3}\left(\ln\frac{(1+e)}{(1-e)}-2e\right),\ N_y=N_z=\frac{1-N_x}{2} \tag{4}$$

$$e=\sqrt{1-(2r/l)^2} \tag{5}$$

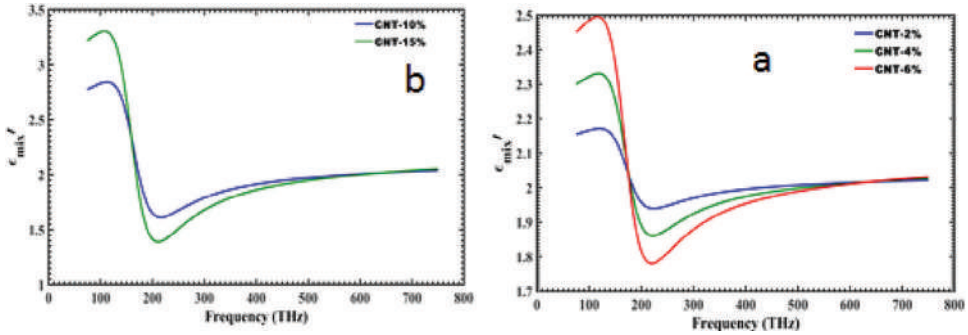

Figure 1. a) Real part of the dielectric constant of composites for 2%, 4%, and 6% CNT; b) 10% and 15% of CNT.

where r is the carbon nanotube's outer radius and l is its length, as in the case of multiwalled carbon nanotubes (MCNT).

The complex permittivity is represented as

$$\varepsilon_{\text{mix}} = \varepsilon'_{\text{mix}} - \varepsilon''_{\text{mix}} \tag{6}$$

where $\varepsilon'_{\text{mix}}$ and $\varepsilon''_{\text{mix}}$ are the real part and imaginary part of the dielectric permittivity of composites.

$$\text{The loss tangent } \tan\delta = \frac{\varepsilon''_{\text{mix}}}{\varepsilon'_{\text{mix}}} \tag{7}$$

The energy loss arises due to the conduction losses, vibration losses, and polarizations which can be identified by the imaginary component. The loss factor contributions originate from the interface polarization, DC conductivity, and dipole orientations.[48]

The electric modulus is the inverse of the complex dielectric permittivity

$$M^* = \frac{1}{\varepsilon^*_{\text{mix}}} = \frac{1}{\varepsilon'_{\text{mix}} - i\varepsilon''_{\text{mix}}} = M' + iM'' \tag{8}$$

where M' and M'' are the real and imaginary parts of the electric modulus, respectively. It can be expressed as

$$M' = \frac{\varepsilon'_{mix}}{\left(\left(\varepsilon'_{\text{mix}}\right)^2 + \left(\varepsilon''_{\text{mix}}\right)^2\right)} \tag{9}$$

$$M'' = \frac{\varepsilon''_{mix}}{\left(\left(\varepsilon'_{\text{mix}}\right)^2 + \left(\varepsilon''_{\text{mix}}\right)^2\right)} \tag{10}$$

The high resistance contributions are mostly dominant in the impedance spectra analysis, and from the electric modulus spectroscopy, it is the capacitance contribution that is the dominant factor, even though the resistances are comparable.[49] The complex electric modulus is used to suppress the electrode effect. The advantage is that the bulk relaxation in polymers and composites is investigated when the variation of both the dielectric constant (ε') and the dielectric loss (ε'') will be minimized. It also gives more information about the mechanism of conductivity relaxation in the frequency domain in polymers and composites.[50]

The effective conductivity[48]

$$\sigma_{\text{ac}} = \omega\varepsilon'' = 2\pi f \varepsilon_0 \varepsilon''_{\text{mix}} \tag{11}$$

3. Results and Discussion

3.1. Dielectric Constant with Frequency for Various Filler Fractions

The dielectric constant of CNT is the result of the additive contribution of free electrons (intraband transitions) and bound electrons on the surface of carbon nanotubes (interband transitions). The intraband transition allows for quasi-free motion of π-electrons, determining the metallic properties of CNTs below the frequency range of interband transitions and is described by the Drude model. The Lorentz model accounts for the interband transition, which causes CNT resonant interaction in the near IR and visible frequency ranges. The contributions to conductivity are comparable in the intermediate frequency range (30–150 THz), which arise from intra- and interband transitions.[51,52] The refractive index of PDMS is 1.42.[53] The dielectric permittivity of CNT is calculated using Equation (2), and the dielectric permittivity of CNT/PDMS composites is calculated using Equation (1). Total polarization incorporates both interband and intraband transitions. The dipole moment is induced in the lower and higher frequency spectral ranges, which are associated with these two transitions.[52] The real part of the dielectric constant of composites increases with frequency and reaches a maximum at 121.3 THz for a filling fraction of 2% CNT in the composite. Beyond this limit, it decreases sharply due to the transition from interband to intraband. This may be due to the transition from semiconductive to metallic behavior. The value of the dielectric constant becomes very low at a frequency closer to 219.8 THz, then increases with frequency and finally becomes constant at higher frequencies.

The real part of the dielectric constant of composites ($\varepsilon'_{\text{mix}}$) which increases with filler concentration. From **Figure 1**a,b, it is inferred that there is no appreciable change in the dielectric constant at higher frequencies. Similar behavior is observed for all the filler content of the composite material. It is inferred that, the real part of the dielectric constant increases with filler content. With increasing the filler content, the variation of the real part of the dielectric constant is more pronounced.

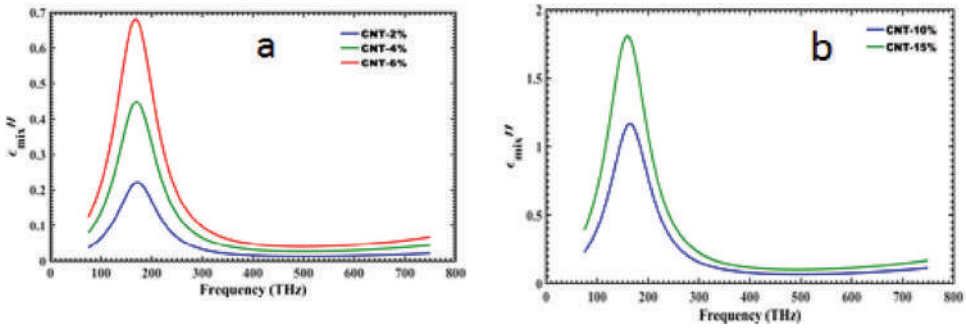

Figure 2. a) Imaginary part of the dielectric constant of composites for 2%, 4%, and 6% CNT; b) 10% and 15% of CNT.

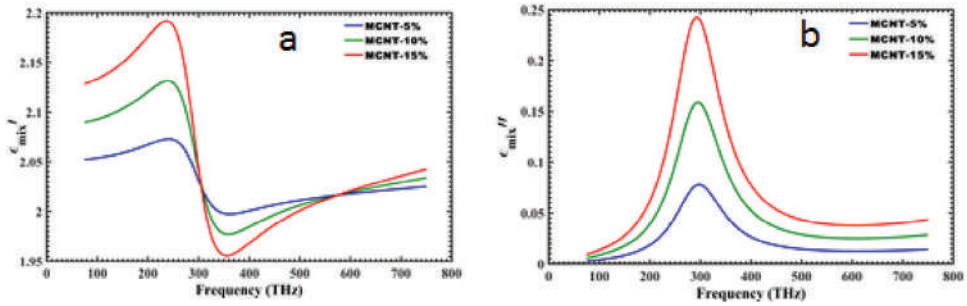

Figure 3. a) Real part of the dielectric constant of composites for 5%, 10%, and 15% MCNT. b) Imaginary part of the dielectric constant of composites for 5%, 10%, and 15% MCNT.

The imaginary part of the dielectric constant (ϵ''_{mix}) of CNT/polymer composites on frequency is shown in **Figure 2**a,b. The maximum loss is observed around 180 THz, which represents the absorption behavior of the composites. Beyond this frequency, the imaginary part of the dielectric constant decreases with frequency, and at higher frequencies, there is no discernible change. It is also found that the maximum dielectric loss is proportional to the filler content of CNT.

Similar behavior is observed in both the real and imaginary parts of the dielectric constant of the MCNT-polymer composites. The real part of the MCNT-polymer composite increases with frequency and attains a maximum value of 2.1916 at a frequency of 238.5 THz for a 15% MCNT composition, as shown in **Figure** 3a. The peak values of the real part of the dielectric constant in MCNT-polymer composites are shifted to a higher frequency region in comparison to SCNT-polymer composites. It is also observed that the real part of the dielectric constant decreases with filler content. The imaginary part of the dielectric constant for different filler contents is shown in Figure 3b. The loss attains a maximum at a frequency of 292.39 THz for the filler content of 15% of MCNT, and then it decreases with frequency. The imaginary part of the dielectric constant increases with the filler content.

3.2. Loss Tangent

Due to the existence of both the internal field in the material and the external AC field, there is a variation in the loss tangent. The appearance of peaks in the loss tangent indicates the presence of relaxing dipoles, and the peaks that are observed at higher frequencies may be attributable to the decrease in polarization which leads to the increase of conductivity. The increase is due to the materials' increased conductivity and decreased polarization

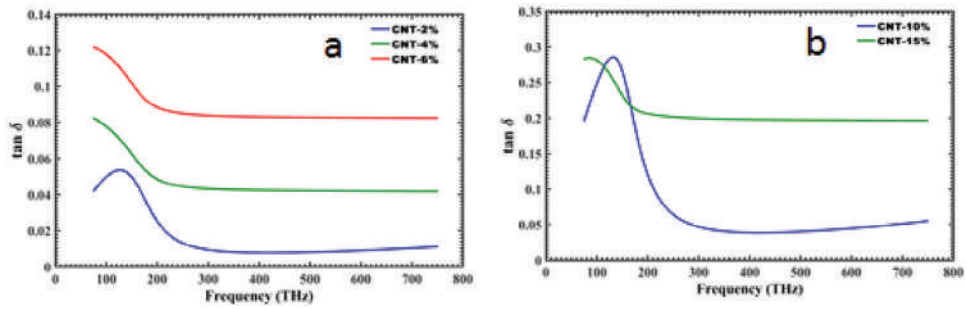

Figure 4. a) Dielectric Loss for composites of 2%, 4%, and 6% CNT; b) 10% and 15% of CNT.

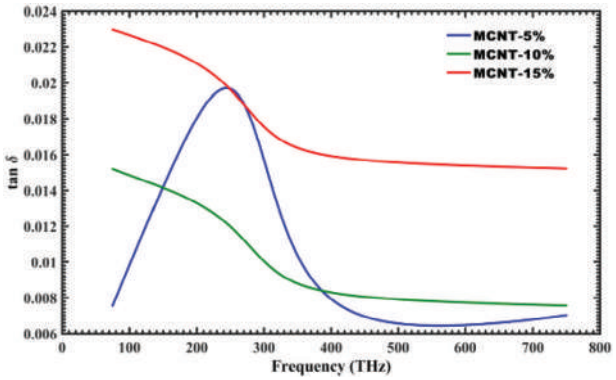

Figure 5. Dielectric Loss for composites of 5%, 10%, and 15% of MCNT.

effect. The quality factor is expressed as QF = 1/tan δ [54] which increases with the low value of tangent loss tanδ.

The loss tangent of composites for different filler contents of SCNT is shown in **Figure** 4a,b. It is clear that the loss tangent is high at lower frequencies and decreases up to a particular frequency; there is no appreciable change in the loss tangent with frequency for the filler content (4%, 6%, and 15% CNT) of the composites. But for the filler content of 2% and 10%, the loss tangent is increased with frequency, and the tangential loss peak is observed at a particular frequency, which may be attributed to the decrease in polarization, and is decreased beyond that frequency. The quality factor is high for the filler content (2% CNT) of the composite because the latter has a low value of loss tangent. The increase in tan δ is due to the increase in conductivity and the polarization effect that takes place in the composite material.

The loss tangent for different filler contents of the MCNT-polymer composite is shown in **Figure** 5. The loss tangents are 0.00755, 0.01521, and 0.02297 for the filler contents of 5%, 10%, and 15%, respectively, at a frequency of 75 THz. The loss tangent increases with frequency and reaches a maximum of 0.01971 at a frequency of 245.9 THz, and then it is decreased. The quality factor is high at a frequency of 75 THz because it has a low value of loss tangent. The loss tangent is also comparably low with SCNT-polymer composites.

3.3. Analysis of Cole–Cole Plot

A semicircle is obtained in a single relaxation when plotted in the complex plane of a material. The semicircles are related to the distribution of relaxation time. In this plot, the grains act as parallel conducting plates, and grain boundaries act as resistive plates. It takes slightly different shapes, whether it is a full, partial, or no semicircle, which is described by various relaxation modes known as the Debye relaxation and Cole–Cole relaxation. The real part of the impedance represents the resistance, while

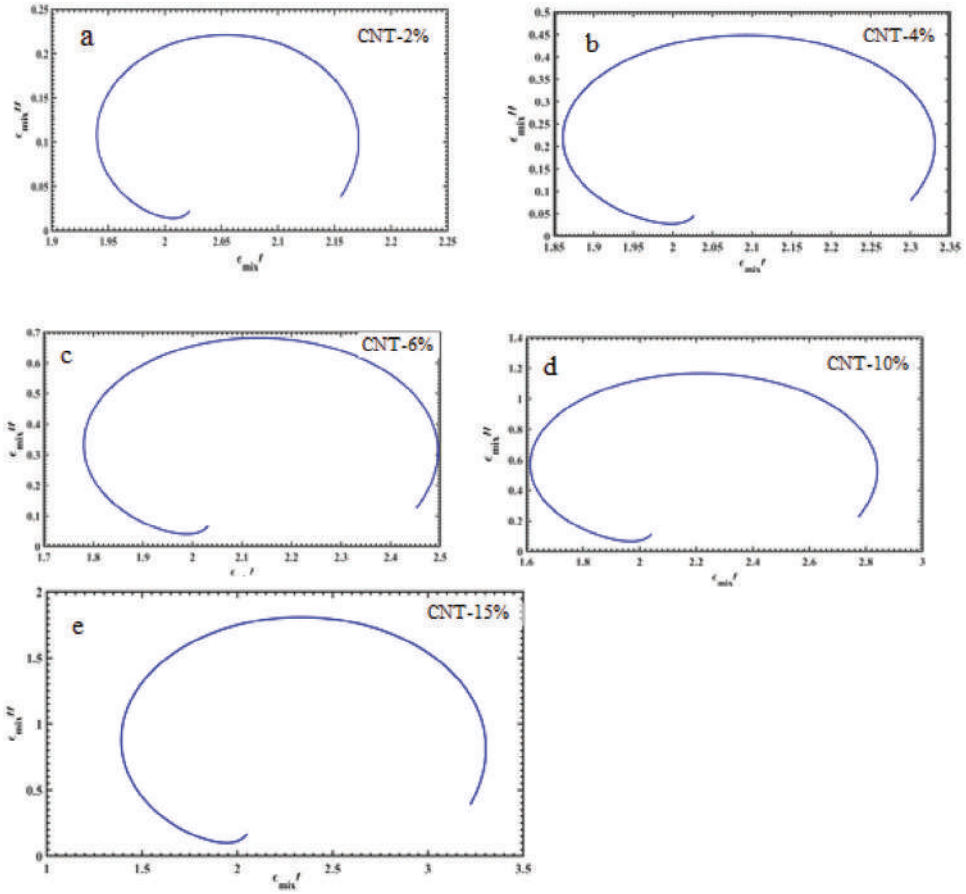

Figure 6. Cole–Cole plot for the composites of a) 2%, b) 4%, c) 6%, d) 10%, and e) 15% of CNT.

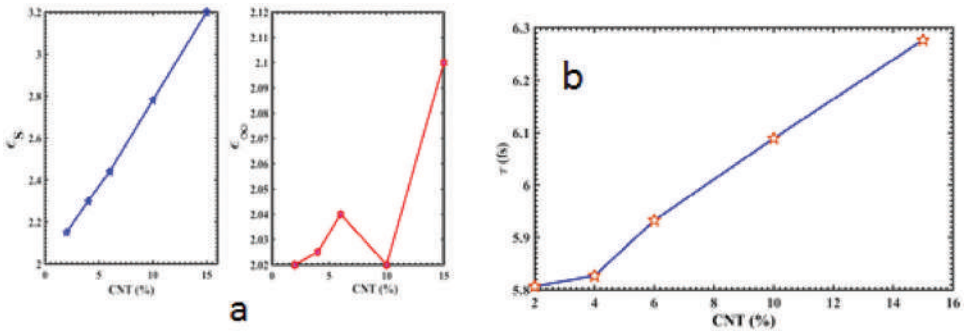

Figure 7. a) Static and High frequency dielectric constant for different filler contents. b) Variation of relaxation time for different filler contents.

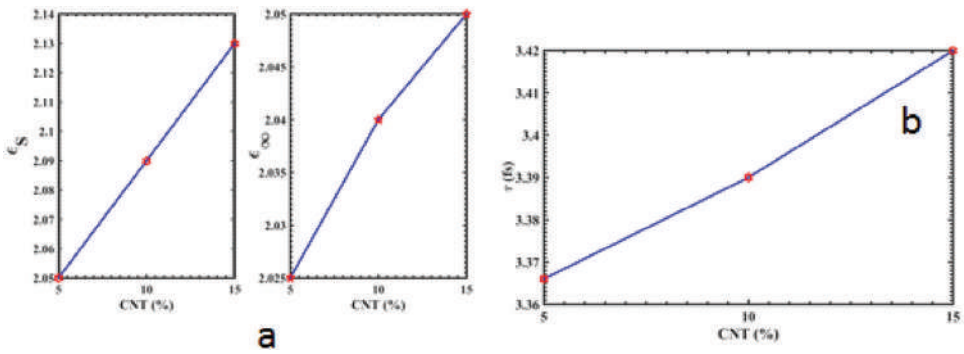

Figure 8. Variation of a) low and high frequency dielectric constant and b) relaxation time for different concentrations of MCNT/PDMS composites.

the imaginary part is the reactance as a result of either capacitive or inductive components.[55] It corresponds to grain boundaries at low frequencies and at high frequencies, which are due to grains based on the distribution of relaxation time. The resistivity is high at low frequencies, while it is low at high frequencies.[54]

The Cole–Cole plot for the variation of the real part (ε'_{mix}) with the imaginary part (ε''_{mix}) of the dielectric constant fordifferent filler content is shown in **Figure 6**. The radius of the semicircle is different for various filler content because of the variation in the relaxation time. With the increase of CNT concentrations, the conductivity also increases due to the increase in grain boundaries.

The relaxation time is obtained from the relation.[55]

$$\omega\tau = 1 \text{ and } \tau = RC \tag{12}$$

where ω is the angular frequency ($2\pi f$), R the resistance, and C the capacitance.

The static frequency dielectric constant (ε_s) and high frequency dielectric constant (ε_∞) are represented for various filler content is shown in **Figure 7a**. The relaxation time (τ) is increased with filler content is shown in Figure 7b. Similar behavior is also observed in the MCNT/PDMS composites as shown in **Figure 8**a,b. But the relaxation time is reduced in comparison to SCNT.

3.4. Effect of Electric Modulus with Frequency and Filler Content

The real part of the dielectric modulus for various filler contents of CNT composites is shown in **Figure 9**a,b. The value of M decreases up to 128.8 THz and increases with frequency up to 227.3 THz for the filler content of 2% CNT. There is no appreciable

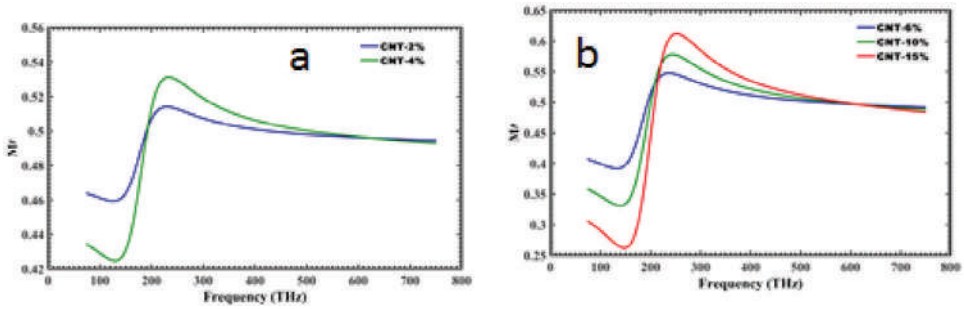

Figure 9. a) Real part of the dielectric modulus of composites for 2% and 4% CNT; b) 6%, 10%, and 15% of CNT.

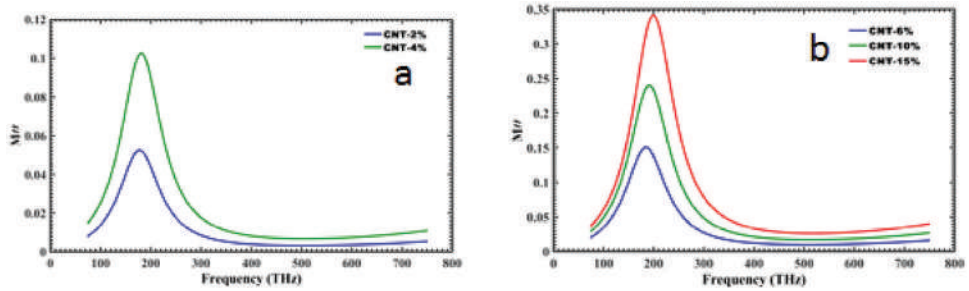

Figure 10. a) Imaginary part of the dielectric modulus of composites for 2% and 4% CNT; b) 6%, 10%, and 15% of CNT.

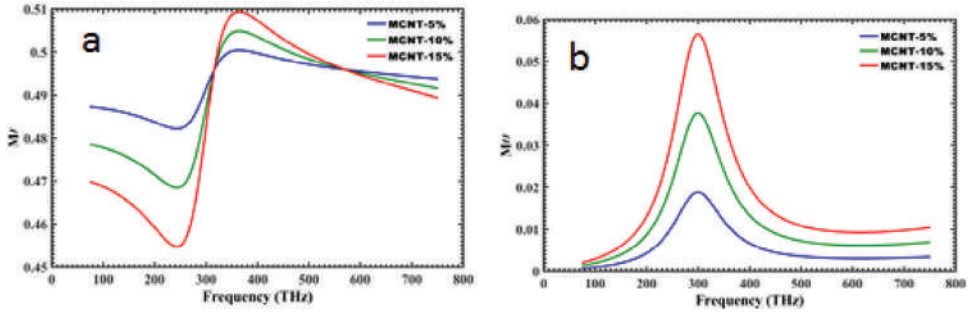

Figure 11. a) Real part of the dielectric modulus of composites for 5%, 10%, and 15% MCNT. b) Imaginary part of the dielectric modulus of composites for 5%, 10%, and 15% of MCNT.

change in modulus value at higher frequencies. The filler content of the composites shifts the resonance position to a higher frequency region. There is a variation in both the parameters, such as the value of *M* and the peak frequency, which indicate a variation in capacitance.[55] The imaginary part of the electric modulus for various filler contents with frequency is shown in **Figure 10**a,b. It is noticed that the imaginary part of the electric modulus increases with an increase in the frequency, reaching its maximum at a frequency of 177.5 THz, and beyond this frequency it decreases for a filler content of 2% CNT. Also, the relaxation peak shifted toward a higher frequency region with the increase in the filler content of CNT composites. The real part and the imaginary part of the electric modulus for various filler contents (PDMS/MCNT) of the composites are shown in **Figure 11**a,b. In the case of MCNT composites, similar behavior is observed in terms of the real part of the electric modulus, but the imaginary part of the electric modulus is reduced to a smaller value.

3.5. Effect of Electrical Conductivity with Frequency and Filler Content

The conductivity of CNT film, which comprises the contribution from interband and intraband, Interband transitions produce a change in the THz conductivity that can be attributed to an exciton-induced reduction in the mobility of charge carriers.[56] The variation in electrical conductivity of all composites with frequency for CNT and MCNT are shown in **Figure 12**a,b. In Figure 12a, the conductivity of composites is increased with frequency, reaches maximum at a frequency of 179.6 THz and beyond this frequency it decreases. The conductivity is increased with an increase in filler contents of the composites. The peak at which the conductivity is maximum is shifted toward the lower frequency regions when the filler contents of the composites. The conductivity is high 164.2 mho cm^{-1} which is observed for 15% CNT of composites at a frequency of 167.6 THz. Similar behavior is also

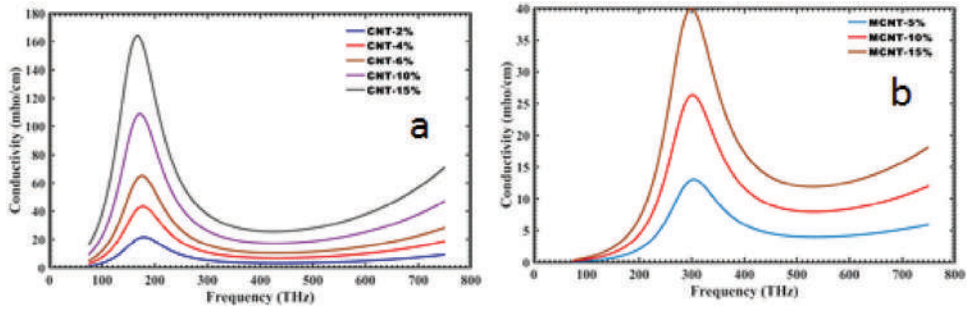

Figure 12. a) Conductivity of composites for different filler contents of CNT. b) Conductivity of composites for different filler contents of MCNT.

observed of all composites for MCNT and a high conductivity of 39.96 mho cm^{-1} is observed at a frequency of 299.4 THz is shown in Figure 12b. High electrical conductivity directly contributes to high dielectric loss.

4. Conclusions

The real part of the dielectric constant varies with frequency as well as due to their transitions from semiconductive to metallic behavior. The loss tangent decreases with the concentration of CNT. The loss tangent is high at lower frequencies for a concentration of 4%, 6%, and 15% of SCNT, and the loss tangent is maximum at a particular frequency of 127.1 and 133.3 THz for the concentration of 2% and 10% of SCNT. The loss tangent increases with frequency and reaches a maximum of 0.01971 at a frequency of 245.9 THz, then it is decreased in the case of MCNT. It is found that the relaxation time increases with the concentration of composite material. The conductivity depends on the dopant concentration. The conductivity increases with frequency and reaches its maximum at a certain frequency. It is observed that the conductivity is a maximum of 166.7 mho cm^{-1} at a particular frequency of 164.2 THz for 15% of SCNT. The conductivity is observed as maximum 39.95 mho cm^{-1} at a frequency of 299.7 THz in the case of 15% of MCNT. It is also observed that the conductivity of MCNT is lesser when compared to the same concentration of SCNT.

Conflict of Interest

The authors declare no conflict of interest.

Data Availability Statement

The data that support the findings of this study are available from the corresponding author upon reasonable request.

Keywords

carbon nanotube, Cole–Cole, dielectrics, electrical conductivity, polydimethylsiloxane

Received: October 10, 2023
Revised: December 18, 2023
Published online:

[1] A. Ilgaz, *Indian J. Pure Appl. Phys.* **2022**, *60*, 521.
[2] K. Müller, E. Bugnicourt, M. Latorre, M. Jorda, Y. Echegoyen, J. Sanz, *Nanomaterials* **2017**, *7*, 74.
[3] S. V. Glushanin, V. Y. Topolov, A. V. Krivoruchko, *Mater. Chem. Phys.* **2006**, *97*, 357.
[4] A. Pelaiz-Barranco, P. Marin-Franch, *J. Appl. Phys.* **2005**, *97*, 034104.
[5] Z.-M. Huang, Y.-Z. Zhang, M. Kotaki, S. Ramakrishna, *Compos. Sci. Technol.* **2003**, *63*, 2223.
[6] J. Jordan, K. I. Jacob, R. Tannenbaum, M. A. Sharaf, I. Jasiuk, *Mater. Sci. Eng., A* **2005**, *393*, 1.
[7] M. J. O'Connell, *Carbon Nanotubes: Properties and Applications*, CRC press, Boca Raton, FL **2006**.
[8] X. Huang, C. Zhi, in *Polymer Nanocomposites: Electrical and Thermal Properties*, Springer International Publishing, Switzerland **2016**, p. 51–82.
[9] J.-H. Du, J. Bai, H.-M. Cheng, *eXPRESS Polym. Lett.* **2007**, *1*, 253.
[10] L. Valentini, J. M. Kenny, *Polymer* **2005**, *46*, 6715.
[11] J. M. GarcØs, D. J. Moll, J. Bicerano, R. Fibiger, *Adv. Mater.* **2000**, *12*, 23.
[12] X. Lu, A. Zhang, O. Dubrunfaut, D. He, L. Pichon, J. Bai, *Compos. Sci. Technol.* **2020**, *194*, 108150.
[13] O. Breuer, U. Sundararaj, *Polym. Compos.* **2004**, *25*, 630.
[14] P. W. Barone, S. Baik, D. A. Heller, M. S. Strano, *Nat. Mater.* **2005**, *4*, 86.
[15] M. S. Arnold, A. A. Green, J. F. Hulvat, S. I. Stupp, M. C. Hersam, *Nat. Nanotechnol.* **2006**, *1*, 60.
[16] J. Fagan, J. R. Simpson, B. J. Bauer, D. P. Lacerda, M. L. Becker, *J. Am. Chem. Soc.* **2007**, *129*, 10607.
[17] X. Sun, S. Zaric, D. Daranciang, K. Welsher, Y. Lu, *J. Am. Chem. Soc.* **2008**, *130*, 6551.
[18] K. W. C. Lai, N. Xi, C. K. M. Fung, H. Chen, T. J. Tarn, *Appl. Phys. Lett.* **2009**, *95*, 2211007.
[19] K. Mizuno, J. Ishii, H. Kishida, Y. Hayamizu, S. Yasuda, *Proc. Natl. Acad. Sci. USA* **2009**, *106*, 6044.
[20] V. J. Gokhale, O. A. Shenderova, G. E. McGuire, M. Rais-Zadeh, *J. Microelectromech. Syst.* **2014**, *23*, 191.
[21] C. Nunes, V. Teixeira, M. Collares-Pereira, A. Monteiro, E. Roman, J. Martin-Gago, *Vacuum* **2002**, *67*, 623.
[22] J. Lehman, E. Theocharous, G. Eppeldauer, C. Pannell, *Meas. Sci. Technol.* **2003**, *14*, 916.
[23] I. Mellouki, N. Bennaji, N. Yacoubi, *Infrared Phys. Technol.* **2007**, *50*, 58.
[24] A. K. Mishra, S. K. Mishra, R. K. Verma, *Plasmonics* **2017**, *12*, 1657.
[25] L. Wang, J. Yang, W. Cheng, J. Zou, D. Zhao, *Front. Mater.* **2021**, *8*, 774843.
[26] J. M. Garcøs, D. J. Moll, J. Bicerano, R. Fibiger, D. G. McLeod, *J. Diabetes Sci. Technol.* **2013**, *7*, 72.
[27] R. Lu, C. Christianson, B. Weintrub, J. Z. Wu, *ACS Appl. Mater. Interfaces* **2013**, *5*, 11703.
[28] Q. Zeng, S. Wang, L. Yang, Z. Wang, T. Pei, Z. Zhang, L.-M. Peng, W. Zhou, J. Liu, W. Zhou, S. Xie, *Opt. Mater. Express* **2012**, *2*, 839.
[29] A. Rogalski, *Infrared Phys. Technol.* **2002**, *43*, 187.
[30] J. S. Tyo, D. L. Goldstein, D. B. Chenault, J. A. Shaw, *Appl. Opt.* **2006**, *45*, 5453.
[31] H. Shi, J. G. Ok, H. W. Baac, L. J. Guo, *Appl. Phys. Lett.* **2011**, *99*, 211103.
[32] N. Liu, M. Mesch, T. Weiss, M. Hentschel, H. Giessen, *Nano Lett.* **2010**, *10*, 2342.
[33] J. Hendrickson, J. Guo, B. Zhang, W. Buchwald, R. Soref, *Opt. Lett.* **2012**, *37*, 371.
[34] A. M. Marconnet, M. A. Panzer, K. E. Goodson, *Rev. Mod. Phys.* **2013**, *85*, 1295.
[35] T. Abendroth, H. Althues, G. Mader, P. Hartel, S. Kaskel, *Sol. Energy Mater. Sol. Cells* **2015**, *143*, 553.
[36] J. Wang, X. Zhang, X. Huang, S. Wang, Q. Qian, W. Du, Y. Wang, *Small* **2013**, *9*, 3759.
[37] A. D. G. Fredi, L. Fambri, A. Pegoretti, *Compos. Sci. Technol.* **2018**, *158*, 101.
[38] D. Tasis, *Carbon Nanotube-Polymer Composites*, RSC, London **2013**, p. 23.
[39] K. D. Paschaloudis, C. L. Zekios, G. C. Trichopoulos, F. Farmakis, G. A. Kyriacou, *Electronics* **2021**, *10*, 2782.

[40] J. F. Algorri, B. Garcia-Camara, D. Podereux, R. Vergaz, V. Urruchi, J. M. Sánchez-Pena, META'15: The 6th Int. Conf. on Metamaterials, Photonic Crystals and Plasmonics, New York, **2015**.
[41] Basics of Measuring the Dielectric Properties of Materials, Keysight Technologies, Application Note, https://www.keysight.com/in/en/assets/7018-01284/application-notes/5989-2589.pdf (accessd: September 2023).
[42] C.-H. Ho, C. D. Liu, C. H. Hsieh, K. H. Hsieh, S. N. Lee, *Synth. Met.* **2008**, *158*, 630.
[43] S. Upahdhyay, D. Kumar, O. Prakash, *Bull. Mater. Sci.* **1996**, *19*, 513.
[44] S. Y. Wang, G. J. Weng, *Micromechanics and Nanomechanics of Composite Solids*, Springer International Publishing AG, New York **2018**.
[45] N. R. Ramanujam, K. S. J. Wilson, V. Revathy, *Prog. Electromagn. Res. M* **2015**, *41*, 105.
[46] J.-Y. Jing, Q. Wang, B.-T. Wang, *Opt. Fiber Technol.* **2018**, *43*, 137.
[47] O. S. Yakovenko, L. Y. Matzui, L. L. Vovchenko, O. A. Lazarenko, Y. S. Perets, *Appl. Nanosci.* **2020**, *10*, 2691.
[48] D. R. Bijwe, S. S. Yawale, A. C. Kumbharkhane, H. Peng, D. S. Yawale, S. P. Yawale, *Rev. Mex. Fis.* **2019**, *65*, 590.
[49] M. K. Shamim, S. Sharma, S. Sinha, E. Nasreen, *J. Adv. Dielectr.* **2017**, *7*, 1750020.
[50] T. Fahmy, M. T. Ahmed, A. El-kotp, H. G. Abdelwahed, M. Y. Alshaeer, *Int. J. Phys. Appl.* **2016**, *8*, 1.
[51] M. V. Shuba, A. G. Paddubskaya, P. P. Kuzhir, S. A. Maksimenko, N. A. P. GintarasValusis, N. A. Poklonski, S. Bellucci, G. Kenanakis, *J. Appl. Phys.* **2016**, *119*, 104303.
[52] I. V. Bondarev, C. M. Adhikari, *Phys. Rev. Appl.* **2021**, *15*, 034001.
[53] Q. Wang, C. Du, J. Zhang, Y. Z. RiqingLv, *Opt. Commun.* **2016**, *377*, 89.
[54] G. Murtaza, S. H. Bukhari, J. Ahmad, M. T. Jamil, U. Nissar, F. Mazhar, A. Hakeem, *Dig. J. Nanomater. Biostruct.* **2018**, *13*, 337.
[55] M. A. L. Nobre, S. Lanfredt, *Catal. Today* **2003**, *78*, 529.
[56] J. Lloyd-Hughes, T. Jeon, *J. Infrared Millim. Terahertz Waves* **2012**, *33*, 871.